IMMC 2021
"in Digital Platform"

20th
International Metallurgy and Materials Congress
Uluslararası Metalurji ve Malzeme Kongresi

10-12
June / Haziran 2021
"in Digital Platform"

e-Book

immc2021

www.immc-mtm.com
immc@immc-mtm.com

METEM

UCTEA CHAMBER OF METALLURGICAL AND MATERIALS ENGINEERS
TMMOB METALURJİ VE MALZEME MÜHENDİSLERİ ODASI

20th INTERNATIONAL METALLURGY MATERIALS CONGRESS

10-12 June 2021

"in Digital Platform"

IMMC 2021

"in Digital Platform"

immc2021

IMMC
2021
“in Digital Platform”

20th International Metallurgy and Materials Congress

10 - 12 June 2021

“in Digital Platform”

METEM
UCTEA CHAMBER of METALLURGICAL and
MATERIALS ENGINEERS'S TRAINING CENTER

CONGRESS PROCEEDINGS e-BOOK
KONGRE BİLDİRİLER e-KİTABI

ISBN No: 978-605-01-1411-9

UCTEA CHAMBER OF METALLURGICAL AND MATERIALS ENGINEERS
TMMOB METALURJİ ve MALZEME MÜHENDİSLERİ ODASI

20th INTERNATIONAL METALLURGY MATERIALS CONGRESS
10-12 June
2021
“in Digital Platform”

Sponsors of Congress
Kongre Sponsorları

IMMC 2021
"in Digital Platform"

Sponsors of Congress
Kongre Sponsorları

AVEKS

Çolakoğlu Metalurji

DEMİSAŞ

ANKIROS
TURKCAST

inteKno

KİLTAŞ®
Refrakter Malzeme San. ve Tic. A.Ş.
43 yıl

sarkuysan
ELEKTROLİTİK BAKIR SANAYİ VE TİCARET A.Ş.

20th
INTERNATIONAL METALLURGY MATERIALS CONGRESS

10-12 June
2021

"in Digital Platform"

Organizing Board
Organizasyon Kurulu

Organizing Board / Organizasyon Kurulu

Başkan / Chair

Prof. Dr. C. Hakan GÜR
Middle East Technical University

Prof. Dr. Özgül KELEŞ
Istanbul Technical University

Prof. Dr. Gökhan ORHAN
Istanbul University - Cerrahpaşa

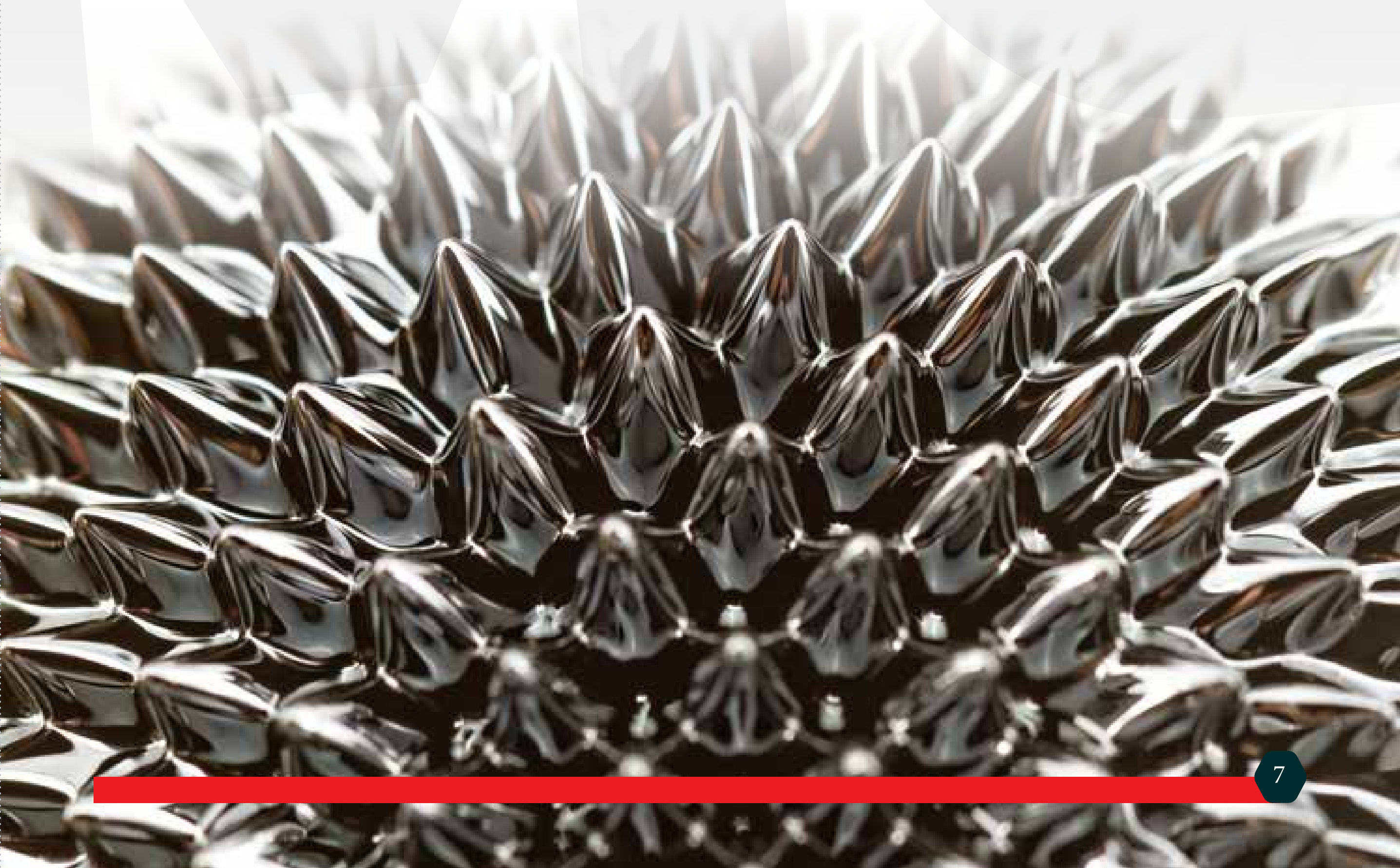

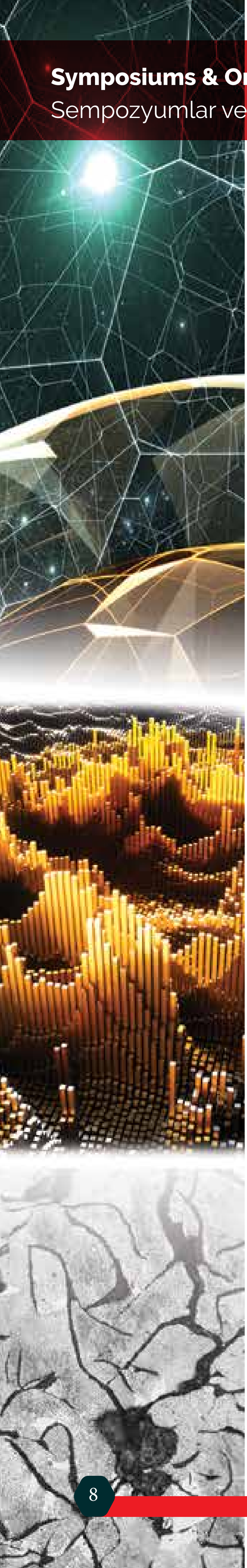

Symposiums & Organization Committee Members

Sempozyumlar ve Yürütme Komitesi Üyeleri

Advanced Alloys and Processes for Aerospace Symposium

Prof. Dr. Mustafa GÜDEN	Izmir Institute of Technology
Assoc. Prof. Dr. Benat KOÇKAR	Hacettepe University
Assoc. Prof. Dr. Havva KAZDAL ZEYTİN	TUBITAK MAM - Marmara Research Center

Biomaterials Symposium

Assoc. Prof. Dr. İpek AKIN KARADAYI	İstanbul Technical University
Prof. Dr. Caner DURUCAN	Middle East Technical University
Assoc. Prof. Dr. Batur ERCAN	Middle East Technical University
Prof. Dr. Gültekin GÖLLER	İstanbul Technical University

Casting Symposium

Yaşar Uğur AKI	Demisaş Iron Casting Company
Dr. Arda ÇETİN	Ekstrametal Foundry
Prof. Dr. Ali KALKANLI	Middle East Technical University
Assoc. Prof. Dr. Necip ÜNLÜ	İstanbul Technical University

Ceramics, Glass, Refractory Materials Symposium

Prof. Dr. Çekdar VAKIFAHMETOĞLU	İzmir Institute of Technology
Prof. Dr. Ender SUVACI	Eskişehir Technical University
Prof. Dr. Filiz ÇINAR ŞAHİN	İstanbul Technical University
Prof. Dr. Abdullah ÖZTÜRK	Middle East Technical University

Composite and Polymer Materials Symposium

Prof. Dr. Cevdet KAYNAK	Middle East Technical University
Prof. Dr. Bora MAVİŞ	Hacettepe University

Corrosion and Wear Symposium

Prof. Dr. Kürşat KAZMANLI	İstanbul Technical University
Assist. Prof. Dr. Levent ORGAN	Yeditepe University

Materials for Energy Symposium

Assist. Prof. Dr. Gökçe HAPÇI AĞAOĞLU	İstanbul University - Cerrahpaşa
Assist. Prof. Dr. Billur Deniz POLAT	Medipol University
Prof. Dr. Tayfur ÖZTÜRK	Middle East Technical University

Mechanical Metallurgy Symposium

Prof. Dr. Murat BAYDOĞAN	İstanbul Technical University
Prof. Dr. Osman ÇULHA	Manisa Celal Bayar University
Dr. Mert EFE	Pacific Northwest National Lab.
Assist. Prof. Dr. Mehmet YILDIRIM	Konya Technical University

Nanomaterials Symposium

Assoc. Prof. Dr. Z. Göknur BÜKE	TOBB-ETU
Prof. Dr. Sebahattin GÜRMEN	İstanbul Technical University
Prof. Dr. Burak ÖZKAL	İstanbul Technical University
Prof. Dr. Hüsnü Emrah ÜNALAN	Middle East Technical University

Non-Ferrous Metals Symposium

Assist. Prof. Dr. Murat ALKAN	Dokuz Eylül University
Assoc. Prof. Dr. Cem KAHRUMAN	Bursa Technical University
Assist. Prof. Dr. Ahmet TURAN	Yalova University

Quality Management and Non-Destructive Testing Symposium

Prof. Dr. Ahmet TOPUZ	İstanbul Arel University
Res. Assist. H. İlker YELBAY	Middle East Technical University

Recycling and Sustainability Symposium

Erman CAR	METEM
Assoc. Prof. Dr. Şeref SÖNMEZ	İstanbul Technical University

Steelmaking Symposium

Prof. Dr. Arcan F. DERİCİOĞLU	Middle East Technical University
Prof. Dr. Bora DERİN	İstanbul Technical University
Prof. Dr. Ender KESKİNKILIÇ	Atılım University

Surface Treatment and Heat Treatment Symposium

Assist. Prof. Dr. Metehan ERDOĞAN	Ankara Yıldırım Beyazıt University
Prof. Dr. Ahmet KARAASLAN	Yıldız Technical University
Prof. Dr. İshak KARAKAYA	Middle East Technical University
Assoc. Prof. Dr. Caner ŞİMŞİR	Middle East Technical University

Welding Metallurgy Symposium

Özgür AKÇAM	GSI-SLV-TR
Dr. Caner BATIGÜN	Middle East Technical University
Dr. Mustafa KOÇAK	İstanbul Gedik University

International Scientific Committee
Uluslararası Bilim Komitesi

Title	Name, Surname	Institution	Country
Prof.Dr.	A. Herman YUWONO	Universitas Indonesia	Indonesia
Prof.Dr.	Abdel-Monem EL-BATAHGY	Central Metallurgical Research Institute	Egypt
Assoc.Prof.Dr.	Abdul MATEEN	Institute of Space Technology	Pakistan
Prof.Dr.	Ahmad Fauzi Mohd NOOR	Universiti Sains Malaysia	Malaysia
Dr.	Ali ABOUIMRANE	Hamad Bin Khalifa University	Qatar
Prof.Dr.	Bach Thành CÔNG	VNU University of Science	Vietnam
Assist.Prof.Dr.	Bhim Prasad KAFLE	Kathmandu University	Nepal
Prof.Dr.	Cong WANG	Northeastern University	China
Prof.Dr.	Debes BHATTACHARYYA	University of Auckland	New Zealand
Prof.Dr.	Ding JUN	National University of Singapore	Singapore
Prof.Dr.	Emilio E. BUNEL	Catolic University of Chile	Chile
Prof.Dr.	Fahmida GULSHAN	Bangladesh University of Engineering and Technology	Bangladesh
Dr.	Francisco Alfredo Garcia PASTOR	National Polytechnic Institute	Mexico
Prof.Dr.	Frank MÜCKLICH	Saarland University	Germany
Res.Assoc.Prof.	George E. TOTTEN	Portland State Univ.	USA
Assoc.Prof.Dr.	Giulio TIMELLI	University of Padova	Italy
Prof.Dr.	Hans-Werner ZOCH	IWT Bremen	Germany
Prof.Dr.	Herman POTGIETER	University of the Witwatersrand	South Africa

National Advisory Committee / Ulusal Danışma Komitesi

Title	Name, Surname	Institution
Dr.	Evren TAN	Aselsan
Prof.Dr.	Eyüp Sabri KAYALI	İstanbul Technical University
Prof.Dr.	Fahrettin ÖZTÜRK	Türk Havacılık Uzay Sanayi A.Ş.
	Hayrettin ÇAYCI	Sarkuysan A.Ş.
Prof.Dr.	Lütfi ÖVEÇOĞLU	İstanbul Technical University
Prof.Dr.	Macit ÖZENBAŞ	Middle East Technical University
Dr.	Mertol GÖKELMA	İzmir Institute of Technology
Dr.	Murat KURTULUŞ	Roketsan
Prof.Dr.	Mustafa ÜRGEN	İstanbul Technical University
Dr.	N. Kaan ÇALIŞKAN	TÜBİTAK -SAGE
Prof.Dr.	Naci SEVINÇ	Middle East Technical University
Dr.	Oğuz GÜNDÜZ	Ereğli Demir Çelik A.Ş.
Prof.Dr.	Onuralp YÜCEL	İstanbul Technical University
Dr.	Önder ORHANER	Akdaş Döküm
Prof.Dr.	Servet TIMUR	İstanbul Technical University
Prof.Dr.	Tayfur ÖZTÜRK	Middle East Technical University
	Yaylalı GÜNAY	Günay Danışmanlık

International Scientific Committee
Uluslararası Bilim Komitesi

Title	Name, Surname	Institution	Country
Prof.Dr.	Hernán G. SVOBODA	University of Buenos Aires	Argentina
Prof.Dr.	Hyoung Seop KIM	POSTECH	South Korea
Prof.Dr.	Ibn Khaldoun LEFKAIER	Université de Laghouat	Algeria
Prof.Dr.	Igor ALEXANDROV	Ufa State Aviation Technical University	Russia
Prof.Dr.	Iulian Vasile ANTONIAC	University Polytehnica of Bucharest	Romania
Prof.Dr.	Janez GRUM	Ljubljana University	Slovenia
Prof.Dr.	Jilt SIETSMA	Delft University of Technology	Netherlands
Prof.Dr.	Lars ÖSTERLUND	Uppsala University	Sweden
Dr.	Larysa SUDNIK	National Academy of Sciences of Belarus	Belarus
Prof. Emeritus	Lauri HOLAPPA	Aalto University	Finland
Prof.Dr.	Laurice CANALE	University of São Paulo	Brazil
Prof.Dr.	Luis M. Liz-MARZÁN	BioNanoPlasmonics Lab., CIC biomaGUNE	Spain
Assoc.Prof.Dr.	M. Cecilia POLETTI	Graz University of Technology	Austria
Assoc.Prof.Dr.	Makoto HASEGAWA	Yokohama National University	Japan
Prof.Dr.	Marcel A.J. SOMERS	Technical University of Denmark	Denmark
Assoc.Prof.Dr.	Mathieu BROCHU	McGill Univ.	Canada
Assoc.Prof.Dr.	Ming-Xin HUANG	University of Hong Kong	Hong Kong
Prof.Dr.	Mohammad TOROGHINEJAD	Isfahan University of Technology	Iran
Assist.Prof.Dr.	Muhammad FAROOQ	University of Engineering and Technology Lahore	Pakistan
Prof.Dr.	Nikos MICHAILIDIS	Aristotle University of Thessaloniki	Greece
Prof.Dr.	Obikwelu Daniel Oraegbuna NNAMDI	University of Nigeria	Nigeria
Prof.Dr.	Orest M. IVASISHIN	G.V. Kurdyumov Institute for Metal Physics, NASU	Ukraine
Dr.	Pavels ONUFRIJEVS	Riga Technical University	Latvia
Prof.Dr.	Peter HODGSON	Deakin University	Australia
Prof.Dr.	Peter ŠUGÁR	Slovak University of Technology	Slovakia
Prof.Dr.	Pranut POTIYARAJ	Chulalongkorn University	Thailand
Assoc.Prof.Dr.	Rachman CHAIM	Technion-Israel Institute of Technology	Israel
Dr.	Richard MOAT	School of Engineering and Innovation, The Open University	UK
Prof.Dr.	Rodrigo Ferrão de Paiva MARTINS	New University of Lisbon	Portugal
Prof.Dr.	Romeu CHELARIU	Gheorghe Asachi Technical University of Iasi	Romania
Dr.	Roza ABDULKARIMOVA	Al-Farabi Kazakh National University	Kazakhstan
Prof.Dr.	Somnath BASU	Indian Institute of Technology Bombay	India
Assoc.Prof.Dr.	Tadeusz PIECZONKA	AGH University of Science and Technology	Poland
Prof.Dr.	Tatsumi ISHIHARA	Kyushu University	Japan
Assoc.Prof.Dr.	Waseem HAIDER	Central Michigan Univ.	USA
Assoc.Prof.Dr.	Yansong SHEN	University of New South Wales	Australia
Prof.Dr.	Zdenka Zovko BRODARAC	University of Zagreb	Croatia
Prof.Dr.	Zeljko KAMBEROVIC	University of Belgrade	Serbia
Prof.Dr.	Zoltan GACSI	Miskolc University	Hungary

Scientific Advisory Committee / Bilimsel Danışma Komitesi

Title	Name, Surname	Institution	Country
Prof.Dr.	Ahmet Tugrul ALPAS	Univ. of Windsor	Canada
Prof.Dr.	Ali COSKUN	Univ. of Fribourg	Switzerland
Dr.	Ali ERDEMIR	Argonne National Lab.	USA
Assist.Prof.Dr.	Ali Gokhan DEMIR	Politecnico di Milano	Italy
Dr.	Bilge Saruhan-BRINGS	Institute of Materials Research	Germany
Dr.	Burçak EBIN	Chalmers University of Technology	Sweden
Assist.Prof.Dr.	Can AYAS	Delft Univ. of Technology	Netherlands
Prof.Dr.	Cengiz OZKAN	Univ. of California-Riverside	USA
Dr.	Cenk AKTAS	Christian Albrechts Univ.	Germany
Assist.Prof.Dr.	Derya BARAN	KAUST	Saudi Arabia
Assist. Prof.Dr.	E. Koray AKDOGAN	Rutgers Univ.	USA
Prof.Dr.	I. Cevdet NOYAN	Columbia University	USA
Prof.Dr.	Ibrahim KARAMAN	Texas A&M University	USA
Prof.Dr.	Ilhan AKSAY	Princeton Univ.	USA
Dr.	Kazım OZBAYSAL	Siemens Energy Inc.	USA
Prof.Dr.	Mehmet SARIKAYA	Univ. of Washington	USA
Prof.Dr.	Mihri OZKAN	Univ. of California-Riverside	USA
Assoc.Prof.Dr.	Mihriban PEKGULERYUZ	McGill Univ.	Canada
Prof.Dr.	Mustafa YAVUZ	University of Waterloo	Canada
Prof.Dr.	Mufit AKINC	Iowa State Univ.	USA
Assist.Prof.Dr.	Neslihan DOGAN	McMaster Univ.	Canada
Dr.	O. Levent ERYILMAZ	Argonne National Lab.	USA
Dr.	Ozge KAHVECIOGLU	Argonne National Lab.	USA
Assist.Prof.Dr.	Ozgur KELES	San Jose State University	USA
Prof.Dr.	Pamir ALPAY	Connecticut University	USA
Prof.Dr.	Rauf Hurman ERIC	Witwatersrand University	S.Africa
Distinguished Prof.	Safa KASAP	University of Saskatchewan	Canada
Dr.	Salih GUNGOR	Open Univ.	UK
Prof.Dr.	Taner AKBAY	Kyushu Univ.	Japan
Assoc.Prof.Dr.	Volkan ORTALAN	University of Connecticut	USA

20th

INTERNATIONAL
METALLURGY
MATERIALS
CONGRESS

10-12 June
2021

"in Digital Platform"

immc2021

20th
INTERNATIONAL
METALLURGY
MATERIALS
CONGRESS
10-12 June
2021
“in Digital Platform”

Invited Speakers
Davetli Konuşmacılar

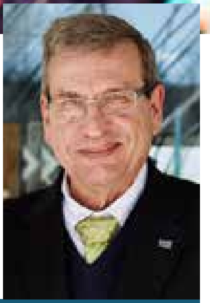

Rodrigo Martins
(Prof. Dr.)
President of the
European Academy
of Sciences, Portugal

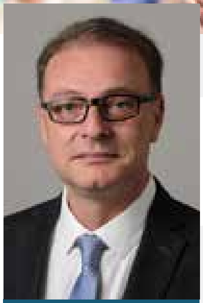

S. Pamir Alpay
(Prof. Dr.)
University of
Connecticut, USA

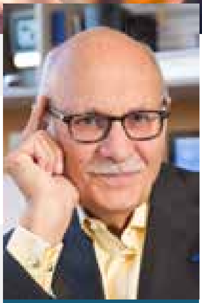

Diran Apelian
(Prof. Dr.)
University of
California,
USA

Ahmed Elmarakbi
(Prof. Dr.)
Northumbria
University,
UK

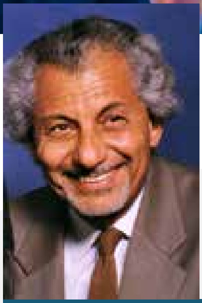

Fathi Habashi
(Prof.Dr.)
Laval University,
Canada

Makoto Hasegawa
(Prof. Dr.)
Yokohama National
University,
Japan

Alpagut Kara
(Prof. Dr.)
Eskişehir Technical
University,
Turkey

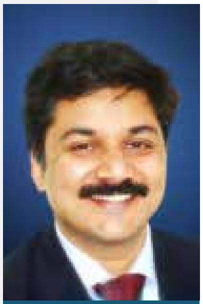

Sanjay Mathur
(Prof. Dr.)
University of
Cologne,
Germany

Frank Mücklich
(Prof. Dr.)
Saarland University,
Germany

Maria Omastova
(Dr.)
Slovak Academy of
Sciences,
Slovakia

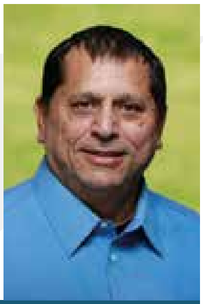

Cengiz Özkan
(Prof. Dr.)
University of
California,
USA

Marcel A. J. Somers
(Prof. Dr.)
Technical
University of
Denmark, Denmark

Mingyue Sun
(Prof. Dr.)
Chinese Academy
of Sciences,
China

Muhammet S. Toprak
(Prof. Dr.)
KTH Royal Institute
of Technology,
Sweden

Cong Wang
(Prof. Dr.)
Northeastern
University,
China

20th
INTERNATIONAL
METALLURGY
MATERIALS
CONGRESS
10-12 June
2021
“in Digital Platform”

SCHEDULE of EVENTS

10.June.2021 Thursday

	Hall 1	Hall 2	Hall 3
10:00 11:00	10:00 **S'S1** Steelmaking Symposium1 11:00	10:00 **CGRM'S1** Ceramic, Glasses and Refractory Materials Symposium1 11:10	10:00 **BM'S1** Biomaterials Symposium1 11:20
12:00	11:20 **S'S2** Steelmaking Symposium2 12:40	11:20 **CGRM'S2** Ceramic, Glasses and Refractory Materials Symposium2 12:50	
13:00		13:00 **PLENARY SESSION1** 13:30	
14:00	13:30 **S'S3** Steelmaking Symposium3 14:50	13:30 **CGRM'S3** Ceramic, Glasses and Refractory Materials Symposium3 14:30	13:30 **NM'S1** Nanomaterials Symposium1 15:00
15:00 16:00	15:10 **S'S4** Steelmaking Symposium4 16:30	15:10 **CGRM'S4** Ceramic, Glasses and Refractory Materials Symposium4 16:30	15:10 **NM'S2** Nanomaterials Symposium2 16:40
17:00 18:00	16:50 **S'S5** Steelmaking Symposium5 18:10		16:50 **MM'S1** Mechanical Metallurgy1 18:20

11.June.2021 Friday

	Hall 1	Hall 2	Hall 3	Hall 4
10:00	10:00 **AAPA'S1** Advanced Alloys and Processes for Aerospace Symposium1 11:00	10:00 **STHT'S1** Surface Treatment and Heat Treatment Symposium1 11:00	10:00 **NFM'S1** Non-Ferrous Metals Symposium1 11:00	10:00 **C'S1** Casting Symposium1 11:40
11:00				
11:20	11:20 **AAPA'S2** Advanced Alloys and Processes for Aerospace Symposium2 12:40	11:20 **STHT'S2** Surface Treatment and Heat Treatment Symposium2 12:10	11:20 **NFM'S2** Non-Ferrous Metals Symposium2 12:40	
12:00				
13:00		13:00 **PLENARY SESSION2** 13:30		
13:30	13:30 **AAPA'S3** Advanced Alloys and Processes for Aerospace Symposium3 14:50	13:30 **STHT'S3** Surface Treatment and Heat Treatment Symposium3 14:50	13:30 **NFM'S3** Non-Ferrous Metals Symposium3 14:30	13:30 **ME'S1** Materials for Energy Symposium1 15:00
14:00				
15:00				
15:10	15:10 **AAPA'S4** Advanced Alloys and Processes for Aerospace Symposium4 16:10	15:10 **STHT'S4** Surface Treatment and Heat Treatment Symposium4 16:00	15:10 **CW'S1** Corrosion and Wear Symposium1 16:10	15:10 **ME'S2** Materials for Energy Symposium2 16:10
16:00				
16:50	16:50 **AAPA'S5** Advanced Alloys and Processes for Aerospace Symposium5 17:50	16:50 **STHT'S5** Surface Treatment and Heat Treatment Symposium5 17:50	16:50 **CW'S2** Corrosion and Wear Symposium2 17:50	16:50 **ME'S3** Materials for Energy Symposium3 17:50
17:00				
18:00				

12.June.2021 Saturday

	Hall 1	Hall 2	Hall 3
10:00	10:00 **AAPA'S6** Advanced Alloys and Processes for Aerospace Symposium6 11:00	10:00 **CPM'S1** Composite And Polymer Materials Symposium1 11:50	10:00 **RS'S1** Recycling and Sustainability Symposium1 11:00
11:00	11:20 **AAPA'S7** Advanced Alloys and Processes for Aerospace Symposium7 12:10		11:20 **RS'S2** Recycling and Sustainability Symposium2 12:20
12:00			
13:00	13:30 **AAPA'S8** Advanced Alloys and Processes for Aerospace Symposium8 14:40	13:30 **CPM'S2** Composite And Polymer Materials Symposium2 14:30	13:30 **RS'S3** Recycling and Sustainability Symposium3 14:50
14:00			
15:00	15:10 **WM'S1** Welding Metallurgy Symposium1 16:20	15:10 **CPM'S3** Composite And Polymer Materials Symposium3 16:10	15:10 **RS'S4** Recycling and Sustainability Symposium4 16:30
16:00	16:20 **CLOSEING CEREMONY** 16:40		
17:00			
18:00			

20th INTERNATIONAL METALLURGY MATERIALS CONGRESS

10-12 June
2021
“in Digital Platform”

PROGRAM

HALL - 2

10.June.2021 Thursday

OPENING CEREMONY

09:15 - 09:50

Prof. Dr. C. Hakan GÜR
Congress Organizing Board, Chairman
Kongre Organizasyon Kurulu Başkanı

Ata ÖZDEMİRLER
METEM Chairman of the Executive Committee
METEM Yürütme Kurulu Başkanı

A. İrfan TÜRKKOLU
MMEC Chairman of the Board // MMMO Yönetim Kurulu Başkanı

09:50 - 10:00 PLAQUETTE CEREMONY (for Sponsors)

HALL - 1

10.June.2021 Thursday

STEELMAKING-1

Session Chairman

F. Arcan DERİCOĞLU

10:00 - 10:20	**Modelling of Mechanical Strength by Examining Hot Rolling Mill Parameters in Structural Steels** **Cemre KEÇECİ, Muhammet BİLEN, Serdar GÜNBAY, Hasan YILDIRIM, Z. Özlem TUNÇ, Tayfun KOCABAŞ, A. Mesud ÇAKIR, Burcu SOYSAL ATAN, İlyas AÇIKGÖZ** İskenderun Demir ve Çelik A. Ş., Oyak Maden Metalurji Grubu Operasyonel Mükemmellik Direktörlüğü Turkey
10:20 - 10:40	**Coking Process, Optimization of Coke Quality Parameters and Investigation of Effects in Blust Furnace** **Hüseyin KALAY, Zekeriya ÖZER** İskenderun Demir ve Çelik A. Ş. Turkey
10:40 - 11:00	**Affects of Coke Quenching Methods on Coke Reactivity Index** **Ömer ECE, Hüseyin ZÜMRÜT, Erman KAYA** İskenderun Demir ve Çelik A. Ş. Turkey

HALL - 1

10.June.2021 Thursday

STEELMAKING-2

Session Chairman

Ender KESKİNKILIÇ

11:20 - 11:40	**Maintenance Management System Installation in Integrated Iron and Steel Plants & Innovative Approches** **Hasan BULUT, Merih YAMAN, Serkan KESKİ, Ali KESKİN** İskenderun Demir ve Çelik A. Ş., Ereğli Demir ve Çelik A.Ş. Turkey
11:40 - 12:00	**Analysis of Annealing & Pickling Processes for AISI 304 Stainless Steel Sheet Corrosion Resistance** **Onur AY[1], Ayşegül BİLEN[2], Erdem GÜLER[1], Bedirhan GÜRAYDIN[1], Hamdi EKİCİ[1], İ. Cemre TÜRÜ[2], Eda DAĞDELEN[1]** [1]Trinox Metal San. ve Tic. A.Ş., [2]Yıldız Technical University Turkey
12:00 - 12:20	**Centralization and Reduction of Human Factor in the Control of Water Supply and Circulation Plants in the Iron and Steel Industry** **İsmail GÜVEN, Erkin Yekda GEDİK, Engin KARABEYOĞLU, Gencer BİRKAN** İskenderun Demir ve Çelik A. Ş. Turkey
12:20 - 12:40	**Investigation of Distinct Strain Rates on Hydrogen Permeability Properties of Enamel Steel** **Ramazan UZUN[1], Ümran BAŞKAYA[1], Zafer ÇETİN[1], Oğuz GÜNDÜZ[1], Yasemin KILIÇ[1], Adem BAKKALOĞLU[2]** [1]Eregli Iron and Steel Works, Co., [2]Yıldız Technical University Turkey

HALL - 1

10.June.2021 Thursday

STEELMAKING-3

Session Chairman

Bora DERİN

13:30 - 13:50	**Effect of Thermomechanical Rolling Process on the Mechanical Properties of 46MnV56 Microalloyed Steel** **Funda OZMEL[1], Dogan CAMLI[1], Mert ULKER[1], Kenan ACAR[1], Arcan F. DERİCİOGLU[1,2]** [1]Asil Çelik San. ve Tic. A.Ş., [2]Middle East Technical University Turkey
13:50 - 14:10	**Development of New Generation Steel Alloy and Forging Process** **Fulya EYÇİN[1], Tuğçe YAĞCI[2,3], Adem KORKMAZ[3], Serhat BARDAKÇI[3], Osman ÇULHA[2,3]** [1]Tirsan Kardan San. ve Tic. A.Ş., [2]Manisa Celal Bayar University, [3]Twin R&D Engineering Company Turkey
14:10 - 14:30	**The Characterization After Normalizing Treatment of Hot Forged 16MnCr5 and 20MnCr5 Cementation Steels** **Nuray BEKÖZ ÜLLEN[1], Mustafa ERSOY[2]** [1]İstanbul University-Cerrahpaşa, [2]Batı Heat Treatment Turkey
14:30 - 14:50	**Reverse Ageing Phenomena in Hyper-Eutectoid Wire Rod Steels** **Cemre KEÇECİ, Erhan SAKALLI, Sadık POLAT, M. Eriş DURMUŞOĞLU, Ali KOCA, Ahmet SAĞLAM** İskenderun Demir ve Çelik A. Ş., Ereğli Demir ve Çelik Fabrikaları T.A.Ş. Turkey

HALL - 1

10.June.2021 Thursday

STEELMAKING-4

Session Chairman

F. Arcan DERİCİOĞLU

15:10 - 15:30	Data Mining Applications in Iron and Steel Plants **Ahmet BEŞKARDEŞ** İskenderun Demir ve Çelik A. Ş. Turkey
15:30 - 15:50	Modelling the Turbidity-Suspended Solids Relationship and Optimizing the Polyelectrolyte Dosage **Mehmet Burak ATAN, Erkin Y. GEDİK, Gökhan GÜNGÖR, Onur MARTI, Arif AKSOY, İsmail GÜVEN, Gencer BİRKAN, A. Mesud ÇAKIR, Fatih ÇELİK** İskenderun Demir ve Çelik A. Ş., Operasyonel Mükemmellik Müdürlüğü Turkey
15:50 - 16:10	Modelling and Digitalization of Mix Slab Applications **İlker AYÇİÇEK, Kübra AKGÜN, Güven SAĞDIÇ, Murat PERÇEM, Burak Emre IŞIK, Arif SAĞBUR, Tayfun KOCABAŞ, A. Mesud ÇAKIR, Fatih ÇELİK, İlyas AÇIKGÖZ** İskenderun Demir ve Çelik A. Ş., Oyak Maden Metalurji Grubu Operasyonel Mükemmellik Direktörlüğü Turkey
16:10 - 16:30	Slab Movement Optimization **Ertan CULHACI, Mahmut KAYHAN, Timur KAYNAK, Ugur OKTAY, Halim SADE, Abdurrahman Mesud ÇAKIR, Fatih ÇELİK** İskenderun Demir ve Çelik A. Ş. Turkey

HALL - 1

10.June.2021 Thursday

STEELMAKING-5

Session Chairman

C. Fahir ARISOY

16:50 - 17:10	**A Case Study for Tool Steel Deformation: Crack Investigation of a Cold Work Tool Steel Used for Trimming Operations** **Yekta Berk SÜSLÜ[1], Berkay SAVAŞKAN[1,2], Onur ÖZCAN[1], Muammer MUTLU[1], Özgül KELEŞ[2]** [1]Mita Kalıp ve Döküm Sanayii AŞ, [2]Istanbul Technical University Turkey
17:10 - 17:30	**The Effect of FeSiMn Usage on Deoxidation at Low Carbon Silicon Restricted Steel Grades** **Zafer ÇETİN, Onur KART, Recep TOPAL, Davut ÇELİK, Özcan BAHAROĞLU, Oğuz GÜNDÜZ** Eregli Iron and Steel Works, Co. Turkey
17:30 - 17:50	**The Impact of Additive Aluminum Bullions Upon Recycle of Alloying Elements in Secondary Metallurgy** **Mert TURFANDA, Emrecan ZORBA, Oğuzhan SAKARYA, Uğur CENGİZ** Bilecik Demir Çelik San. Tic. A.Ş Turkey
17:50 - 18:10	**The Effect of Different Isolation Practice of Dolomite Steel Ladles on Energy Consumption of Ladle Furnace** **Oğuzhan SAKARYA, Mert TURFANDA, Burak EKİN, Uğur CENGİZ, Muammer BİLGİÇ** Bilecik Demir Çelik San. Tic. A.Ş Turkey

HALL - 2

10.June.2021 Thursday

CERAMICS, GLASS, REFRACTORY MATERIALS-1

Session Chairman

Ender SUVACI

10:00 - 10:30 **Invited Speaker**	**Current Status of Industrial and Advanced Ceramics in Turkey** **Alpagut KARA** Eskişehir Technical University Turkey
10:30 - 10:50	**Development of Geopolymer Based Thermal Insulation Material for Industrial Applications** **G. Can TATLISU[1,3], Cem ACIKSARI[1,2], Yesim TEKE[2], Cuneyt KARAKAYA[2], Ozge AKARCAY[2], Emre KELES[1,3], Serdar CELEBI[2], Servet TURAN[1,3]** [1]Eskişehir Technical University, [2]TUPRAS R&D Center, [3]Ceramic Research Center Turkey
10:50 - 11:10	**Effect of Brazing Parameters on the Microstructural and Mechanical Characteristics of Ceramic Matrix Composite/ Titanium Alloy Brazed Joints** **Simge TÜLBEZ[1,2], Ziya ESEN[3], Arcan Fehmi DERİCİOĞLU[1]** [1]Middle East Technical University, [2]Roketsan Industries Inc., [3]Çankaya University Turkey

HALL - 2

10.June.2021 Thursday

CERAMICS, GLASS, REFRACTORY MATERIALS-2

Session Chairman

Çekdar VAKIFAHMETOĞLU

11:20 - 11:50 **Invited Speaker**	**Synthesis of Nanoceramic Powders and Their Biomedical Applications** **Muhammet TOPRAK** KTH Royal Institute of Technology Sweden
11:50 - 12:10	**Reactive Hydrothermal Liquid-Phase Densification (rHLPD) - Low Temperature Densification Concept: A Case Study of $BaTiO_3$** **Levent KARACASULU, Melike TOKKAN, Umut ADEM, Cekdar VAKIFAHMETOGLU** Izmir Institute of Technology Turkey
12:10 - 12:30	**Hydrothermal Synthesis of Zinc Tin Oxide (Zn_2SnO_4) Particles for High Purity Sputtering Targets** **Cem ACIKSARI[1,2], Umut SAVACI[1], Emel OZEL[1], Servet TURAN[1], Ender SUVACI[1]** [1]Eskişehir Technical University, [2]TUPRAS R&D Center Turkey
12:30 - 12:50	**Open and Partially Closed Porosity SiOC Ceramics** **Tugce SEMERCI[1], Murilo Daniel de Mello INNOCENTINI[2], Gian Domenico SORARU[3],Cekdar VAKIFAHMETOGLU[1]** [1]Izmir Institute of Technology, [2]University of Ribeirão Preto (UNAERP), [3]Università di Trento [1]Turkey, [2]Brazil, [3]Italy

HALL - 2

10.June.2021 Thursday

PLENARY SESSION 1

Session Chairman

C. Hakan GÜR

13:00 - 13:30 **Invited Speaker**	**Materials Recovery and Reuse for the 21st Century: A Call for Action and the Need for a Paradigm Change** **Diran APELIAN** University of California USA

HALL - 2

	10.June.2021 Thursday
	CERAMICS, GLASS, REFRACTORY MATERIALS-3
	Session Chairman **Filiz ŞAHİN**
13:30 - 13:50	**Investigation of the Effect of Low Cost Graphene on the Mechanical and Thermal Properties of the SiAlON Based Ceramics** **Emre KELES[1,3], Cuneyt KARAKAYA[2], Cem ACIKSARI[1,2], Umut SAVACI[1,3], Servet TURAN[1,3]** [1]Eskişehir Technical University, [2]TUPRAS, 3Ceramic Research Center Turkey
13:50 - 14:10	**$CaCO_3$ Doped AlON Ceramics Fabricated by Reactivxe Spark Plasma Sintering** **Demet AYDOGMUS, Samet KAYA, Gultekin GOLLER, Onuralp YUCEL, Filiz SAHIN** Istanbul Technical University Turkey
14:10 - 14:30	**TiC Synthesis from Oxide Raw Materials Through Self-Propagating High-Temperature Synthesis** **Tuğçe ERGÜL, Umay ÇINARLI, Mehmet BUĞDAYCI, Ahmet TURAN** Yalova University Turkey

HALL - 2

10.June.2021 Thursday

CERAMICS, GLASS, REFRACTORY MATERIALS-4

Session Chairman

Abdullah ÖZTÜRK

15:10 - 15:30	**Fabrication of High Density Alumina Ceramics from Nanopowders through Colloidal Processing** **Hüseyin Utkucan KAYACI, Simge ÇINAR** Middle East Technical University Turkey
15:30 - 15:50	**Synthesis of Magnetic Bioactive Glass** **Cansu TAŞAR, Batur ERCAN** Middle East Technical University Turkey
15:50 - 16:10	**Relationship Between Surface Roughness and Adherence Perfomance of Cast Iron Enamel Coatings** **Aykut AK[1,2], Nurullah ÇÖPOĞLU[1,2], Yasin Bozkurt YILMAZ[1,2], Tamer CENGİZ[2], Buğra ÇİÇEK[1]** [1]Yıldız Technical University, [2]Gizemfrit Turkey
16:10 - 16:30	**The Investigation of Permanent Linear Change (PLC) Properties of Monolithic Refractories** **Oğuzhan SAKARYA, Mert TURFANDA, Emrecan ZORBA, Uğur CENGİZ** Bilecik Demir Çelik San. Tic. A.Ş Turkey

HALL - 3

10.June.2021 Thursday

BIOMATERIALS-1

Session Chairman
İpek AKIN KARADAYI

10:00 - 10:20	**Anodization of 316L Stainless Steel for Implant Applications** **Yaşar Kemal ERDOĞAN, Batur ERCAN** Middle East Technical University Turkey
10:20 - 10:40	**Polylactic Acid / Calcium Sulfate Composite Production for Bone Tissue Engineering** **Ayşe KAPLAN[1,2], Cem Bülent ÜSTÜNDAĞ[2]** [1]Yıldız Technical University, [2]Alvimedica Medical Technologies Turkey
10:40 - 11:00	**Effect of GTA Vapor Crosslinking Time and Temperature on the Physico-Chemical Properties of Electrospun Gelatin Scaffolds** **Aslıhan CALHAN[1,2], Mustafa SENGOR[1], Oguzhan GUNDUZ[1]** [1]Marmara University, [2]Yildiz Technical University Turkey
11:00 - 11:20	**3D Silk Fibroin Scaffolds for Tissue Engineering Applications** **Melisa KAFALI, Batur ERCAN** Middle East Technical University Turkey

HALL - 3

10.June.2021 Thursday

NANOMATERIALS-1

Session Chairman

Emrah ÜNALAN

13:30 - 14:00 **Invited Speaker**	**Chemically Processed Inorganic Nanostructures for Energy and Health Applications** **Sanjay MATHUR** University of Cologne Germany
14:00 - 14:20	**Preparation and Photocatalytic Activity of Solar Light Sensitive g-C_3N_4/TiO_2 Heterojunction Nanocomposites** **Pelin GÜNDOĞMUŞ[1], Jongee PARK[2], Abdullah ÖZTÜRK[1]** [1]Middle East Technical University, [2]Atılım University Turkey
14:20 - 14:40	**Novel Synthesis of Boron Containing TiO_2 Nanostructures with Variable Morphologies by Sol-Gel and Hydrothermal Processing** **Cansu NOBERİ[1], Cengiz KAYA[2]** [1]İstanbul Gelişim University, [2]Sabancı University Turkey
14:40 - 15:00	**Characterization of Cellulose Nanocrystals Produced via Acid Hydrolysis Method** **Burcu SARI, Cevdet KAYNAK** Middle East Technical University Turkey

HALL - 3

10.June.2021 Thursday

NANOMATERIALS-2

Session Chairman

Burak ÖZKAL

15:10 - 15:40 **Invited Speaker**	**Novel Advanced Automotive Graphene Nanocomposites: Challenges and Future Perspectives** **Ahmed ELMARAKBI** Northumbria University United Kingdom
15:40 - 16:00	**Synthesis of Metallic Striped and Janus Particles** **Mert ULUSEL, Ozan ŞAHİN, Orçun DİNÇER, Bayram YILDIZ, Simge ÇINAR** Middle East Technical University Turkey
16:00 - 16:20	**Morphological Evolution of Boron Carbide Particles: Sol-Gel Synthesized Highly Crystalline B_4C Whiskers** **Suna AVCIOĞLU, Figen KAYA, Cengiz KAYA** Yıldız Technical University Turkey
16:20 - 16:40	**Solid Solution Strenghtening in Amorphous-Crystalline Metallic Composites** **Sevda FATHIPOUR[1], Amir MOTALLEBZADEH[2], Özgür DUYGULU[3], Sezer ÖZERİNÇ[1]** [1]Middle East Technical University, [2]Koç University, [3]TÜBİTAK Marmara Research Center Turkey

HALL - 3

10.June.2021 Thursday

MECHANICAL METALLURGY-1

Session Chairman

Murat BAYDOĞAN

16:50 - 17:20 **Invited Speaker**	**Addressing Fundamental Problems in Metallurgy via First Principles Models: Point Defects, Surface Chemistry, and Initial Stages of Precipitation** **S. Pamir ALPAY** University of Connecticut USA
17:20 - 17:40	**Simulation of the Friction Coeefficent Effect on Wire Drawing Proses** **Sevim Gökçe ESEN[1], Zeynep Şeyma SERDAROĞLU[1], Osman ÇULHA[2]** [1]Çelik Halat ve Tel Sanayii A.Ş, [2]Manisa Celal Bayar University Turkey
17:40 - 18:00	**Effect of Manganese and Titanium and Heat Treatment on Microstructure and Friction Behavior of Hadfield Steel** **Ugur GUROL[1], Ozan COBAN[2,3], Suleyman Can KURNAZ[1]** [1]Sakarya University, [2]İstanbul Gedik University, [3]İstanbul Technical University Turkey
18:00 - 18:20	**Determination of Die Geometry Effect on Mechanical Properties of Wire by Numerical Simulation Method** **Sevim Gökçe ESEN[1], Osman ÇULHA[2]** [1]Çelik Halat ve Tel Sanayii A.Ş, [2]Manisa Celal Bayar University Turkey

HALL - 1

11.June.2021 Friday

ADVANCED ALLOYS AND PROCESSES FOR AEROSPACE-1

Session Chairman

Hakan YAVAŞ

10:00 - 10:20	**Mechanical Behavior and Failure Modes of Hybrid Jointed Lap Shear Joints** **Tansu GÖYNÜK[1,2], Uğur Can UYSAL[1], Duygu KARAÇAL[1,2], Cengiz Kayahan ÖZLAV[1]** [1]Roketsan A.Ş., [2]Middle East Technical University Turkey
10:20 - 10:40	**Effect of Heat Treatment on Microstructure and Mechanical Properties of Additively Manufactured 18Ni300 Maraging Steels** **İbrahim AYDIN[1], Aydın YAĞMUR[2], Süha TİRKEŞ[1], C. Hakan GÜR[1]** [1]Middle East Technical University, [2]EOS GmbH Electro Optical Systems [1]Turkey, [2]Germany
10:40 - 11:00	**Advanced Braze Repair of Nickel Base Superalloys for Gas Turbine Applications** **Kazım ÖZBAYSAL** Siemens Energy Inc USA

HALL - 1

11.June.2021 Friday

ADVANCED ALLOYS AND PROCESSES FOR AEROSPACE-2

Session Chairman

Havva KAZDAL ZEYTİN

11:20 - 11:40	**The Effect of Recycled Powder Characteristics on the Properties of Additively Manufactured 17-4 PH Stainless Steel** **Ece KAHRAMAN[1], Mertcan BAŞKAN[1], Gökhan ÇELİK[1], Mert KELEŞ[1], Andaç ÖZSOY[1], Orkun ÖNEM[1], Bilgehan ÖGEL[2]** [1]Roketsan A.S., [2]Middle East Technical University Turkey
11:40 - 12:00	**Process Parameter Optimization for Wire and Arc Additive Manufacturing (WAAM) of 316LSi Steel** **Mertcan BAŞKAN, Erkan Buğra TÜREYEN, Gökhan CAN, Mert KELEŞ, Ece KAHRAMAN, Orkun Umur ÖNEM, Oğuzhan YILMAZ** Roketsan Turkey
12:00 - 12:20	**Comparison of Mechanical and Microstructural Properties of AISI321 Alloy after ESR and ESR+VAR Processes** **Sertaç ALPTEKİN, Ömür Can ODABAŞ, Kaan DEMİRALAY, Lütfi YAKUT, Bülent BAHADIR, Havva KAZDAL ZEYTİN** Materials Institute of Marmara Research Center of The Scientific and Technological Research Council of Turkey Turkey
12:20 - 12:40	**Improving the Thermal Stability of Laser Clad NiCrBSi Coatings** **Natalia SOBOLEVA, Aleksey MAKAROV, Irina MALYGINA** Ural Branch of the Russian Academy of Sciences Russia

HALL - 1

11.June.2021 Friday

ADVANCED ALLOYS AND PROCESSES FOR AEROSPACE-3

Session Chairman

Ziya ESEN

13:30 - 13:50

Development of Fire-Resistant Wrought Mg-Zn- Y-Ca Alloys for Civil Aircraft Applications

Önder TUNA[1,2], Halil DEMİRTAŞ[1,2], Deniz Sultan AYDIN[1], Özgür DUYGULU[1], Havva KAZDAL ZEYTİN[1], Metin USTA[1,2], Youngkil JUNG[3], Wonseok YANG[3], Hyun Kyu LIM[3]

[1]TUBITAK MAM, Materials Institute, [2]Gebze Technical University,
[3]Korea Institute of Industrial Technology (KITECH)

[1,2]Turkey, [3]Korea

13:50 - 14:10

The Effect of Heat Treatment on the Fracture and Micro-Mechanical Behavior of the Selective Laser Melted AlSi10mg

Ahmet Alptuğ TANRIKULU[1], Hakan YAVAŞ[1], Sertaç ALTINOK[1,2], Burcu ARSLAN HAMAT[1,2], Gülten KAFADAR[1,2], Mustafa GÜDEN[3]

[1]Turkish Aerospace Industries Inc., [2]Middle East Technical University, [3]İzmir Institute of Technology

Turkey

14:10 - 14:30

Validation of Important Simulation Parameters to Predict Porosity Defects in ALSI12 Casting

Muharrem AKKAYA[1], Nuri DURLU[1], M. Akif ŞAHİN[2], M. Bülent ÖZER[2], Yiğit TAŞÇIOĞLU[3]

[1]TOBB University of Economics and Technology,
[2]Middle East Technical University, [3]TED University

Turkey

14:30 - 14:50

The Effect of Casting Temperature and Withdrawal Rate on Laue Misorientation in CMSX-4 SLS Single Crystal Turbine Blade Production

Serra BAYRAM, Ecem ANNAŞLI, Furkan Ferhat BONCUK, Sertaç ALPTEKİN, Lütfi YAKUT, Ömür Can ODABAŞ, Havva KAZDAL ZEYTİN

TUBITAK Marmara Research Center
Turkey

HALL - 1

11.June.2021 Friday

ADVANCED ALLOYS AND PROCESSES FOR AEROSPACE-4

Session Chairman

Caner DURUCAN

15:10 - 15:30	**Effect of Post-Processing Heat Treatment on the Mechanical Properties of Inconel 718 Fabricated by Selective Laser Melting (SLM)** Seren OZER[1,2], G. Mert BILGIN[1], Ziya ESEN[3], Arcan F. DERICIOGLU[1] [1]Middle East Technical University, [2]Atılım University, [3]Çankaya University Turkey
15:30 - 15:50	**Optimizing the Heat Treatment Parameters of Additively Manufactured IN718 Components** Tuğçe KALELİ[1], Aydın YAĞMUR[2], Süha TİRKEŞ[1], C. Hakan GÜR[1] [1]Middle East Technical University, [2]EOS GmbH Electro Optical Systems [1]Turkey, [2]Germany
15:50 - 16:10	**An Investigation on the Effect of Reuse and Recycling on Powder Characteristics in Electron Beam Melting** Evren YASA[1], Mutlu KARAŞOĞLU[2], Evren TAN[3], Berkay GÜMÜŞ[3], Emrecan SOYLEMEZ[4], Kuntay AKTAŞ[5] [1]Eskişehir Osmangazi University, [2]Eskişehir Technical University, [3]Aselsan Elektronik Sanayi ve Ticaret A.Ş., [4]Istanbul Technical University, [5]Btech Innovation Turkey

HALL - 1

11.June.2021 Friday

ADVANCED ALLOYS AND PROCESSES FOR AEROSPACE-5

Session Chairman

Levent ORGAN

16:50 - 17:10	**Structural and Mechanical Characterization of Scale-Up FeCoCrNiCux, High Entropy Alloys (HEAs)** **Z. Anıl ERDAL[1], Gökhan POLAT[1,2], Doğuhan SARITÜRK[1], Y. Eren KALAY[1]** [1]Middle East Technical University, [2]Necmettin Erbakan University Turkey
17:10 - 17:30	**Effect of Sintering Parameters on MoTiNbFeCr High Entropy Alloy (HEA) Produced by Mechanical Alloying (MA)** **Gökhan POLAT, M. Fatih BAŞ, Hasan KOTAN** Necmettin Erbakan University Turkey
17:30 - 17:50	**High-Temperature Gas Sensing Materials for Combustion Process Monitoring** **Bilge SARUHAN[1], Roussin Lontio FOMEKONG[1,2]** [1]German Aerospace Center, [2]University of Yaounde [1]Germany, [2]Cameroon

HALL - 2

	11.June.2021 Friday
	SURFACE TREATMENT AND HEAT TREATMENT-1
	Session Chairman **Metehan ERDOĞAN**
10:00 - 10:20	Modification of Nitride Layer Applied on the Surface of DIN 1.2344 Hot Work Tool Steel with Boron Yaşar AKÇA[1], Gökhan ÖZER[1], Ahmet KARAASLAN[2] [1]Fatih Sultan Mehmet Vakıf University, [2]Yıldız Technical University Turkey
10:20 - 10:40	A Novel Technique for Phase Homogenization in CRTD-Bor: Periodically Interrupted Current Oğuz Kağan COŞKUN, Mehtap ARSLAN, Mehran KARIMZADEKHOEI, Güldem KARTAL ŞİRELİ, Servet TİMUR İstanbul Technical University Turkey
10:40 - 11:00	Development of Chrome-Free Etching for Electroless Coating of Polymeric Materials Mehtap ARSLAN, Oguz Kagan COSKUN, Guldem KARTAL SIRELİ, Servet TIMUR İstanbul Technical University Turkey

HALL - 2

11.June.2021 Friday

SURFACE TREATMENT AND HEAT TREATMENT-2

Session Chairman

C. Hakan GÜR

11:20 - 11:50 **Invited Speaker**	**New Surfaces by Direct Laser Interference Patterning: Optimal Functional Properties due to Fast and Precise Micro-Nano Structuring** **Frank MUCKLICH** Saarland University Germany
11:50 - 12:10	**Effects of Multistep Surface Preparation of PU on Surface Properties of Metallic Coatings** **Büşra ÜNLÜ[1,2], Yahya ÖZ[2], Metehan ERDOĞAN[3], İshak KARAKAYA[1]** [1]Middle East Technical University, [2]Turkish Aerospace, [3]Ankara Yıldırım Beyazıt University Turkey

HALL - 2

11.June.2021 Friday

PLENARY SESSION 2

Session Chairman

Özgül KELEŞ

13:00 - 13:30 **Invited Speaker**	The Future of Extractive Metallurgy Fathi HABASHI Laval University Canada

HALL - 2

11.June.2021 Friday

SURFACE TREATMENT AND HEAT TREATMENT-3

Session Chairman

Batur ERCAN

13:30 - 13:50	**Using Laser Ultrasonics to Study Austenite Grain Growth Kinetics of Carburizing Steels** **Kemal DAVUT[1], Rasim Köksal ERTAN[2], Yasin DEMİRKOL[2], Caner ŞİMŞİR[3]** [1]Atılım University, [2]Simultura Malzeme Teknolojileri, [3]Middle East Technical University Turkey
13:50 - 14:10	**Influence of Methane Content on Control of Carburizing** **M. Tarik BOYRAZ, Heinrich KLUMPER-WESTKAMP, Matthias STEINBACHER** Leibniz-Institut für Werkstofforientierte Technologien Germany
14:10 - 14:30	**Investigating the Optimal Parameters of Electro Spark Deposition Coating Method on Inconel 718 with Aluminum** **Ahmet KAVUKCU, Kemal KORKMAZ** Gebze Technical University Turkey
14:30 - 14:50	**The Effect of Destabilization Holding Time on the Tribological Behaviour of a Hypoeutectic High Chromium Cast Iron Alloy** **U. Pranav NAYAK[1], María Agustina GUITAR[1], Valentin PESNEL[3], Frank MUCKLICH[1,2]** [1]Saarland University, [2]Materials Engineering Center Saarland (MECS), [3]EEIGM, Université de Lorraine [1,2]Germany, [3]France

HALL - 2

11.June.2021 Friday

SURFACE TREATMENT AND HEAT TREATMENT-4

Session Chairman

Caner ŞİMŞİR

15:10 - 15:40 **Invited Speaker**	**Microstructure Optimization in Additively Manufactured Metals through Heat and Surface Treatment** **Marcel A. J. SOMERS** Technical University of Denmark Denmark
15:40 - 16:00	**Influence of Heat Treatment of 1.4462 and 1.4501 Duplex Stainless Steels on Microstructure and Wear Resistance** **Gülüzar YALÇINER[1], Rıdvan GECÜ[1], Alptekin KISASÖZ[2], Ahmet KARAASLAN[1]** [1]Yıldız Technical University, [2]Kırklareli University Turkey

HALL - 2

11.June.2021 Friday

SURFACE TREATMENT AND HEAT TREATMENT-5

Session Chairman

Sezer ÖZERİNÇ

16:50 - 17:10	**Microstructural Characterization of Ferritic Nitro Carburized Layer on the Gray Cast Iron Brake Discs** Ekrem ALTUNCU[1], Recep AKYÜZ[2], Ozan DEMİRDALMIŞ[3], Bilgi ÇENGELLİ[4] [1]Sakarya University of App. Sci., [2]Tofas Automotive, [3]Kale Balata, [4]Bodycote Istaş Turkey
17:10 - 17:30	**Investigation of Wear Behavior of Vacuum Gas Nitrided Crankshafts** Sayid HAS[1,2], Mehmet YILDIRIM[2], Rabia CENGİZ[1,2], Ali KELEŞ[1,3] [1]Motus Automotive Inc., [2]Konya Technical University, [3]Dokuz Eylül University Turkey
17:30 - 17:50	**Investigating the Optimal Parameters of Hot-Dip Aluminizing Method on Inconel 718 Superalloy** Ahmet KAVUKCU[1,2], Faiz MUHAFFEL[1], Murat BAYDOĞAN[1] [1]Istanbul Technical University, [2]Gebze Technical University Turkey

HALL - 3

11.June.2021 Friday

NON-FERROUS METALS-1

Session Chairman

Cem KAHRUMAN

10:00 - 10:20	**The Outlook of Zinc Mining and Metallurgy** **Umut Doğan TURUNÇ[1,2], Cem KAHRUMAN[3]** [1]İstanbul University-Cerrahpaşa, [2]Esan Eczacıbaşı, [3]Bursa Technical University Turkey
10:20 - 10:40	**Solvent Extraction of Lithium from Tuz Lake** **Merve ÖZTÜRK[1], Gökhan KADINKIZ[2], Memet PEKGÖZ[2], Bedirhan ERDENER[2], Ş. Samet KAPLAN[1], Nurgul ÇELİK BALCI[1], M. Şeref SÖNMEZ[1]** [1]İstanbul Technical University, [2]General Directorate of Mineral Research and Exploration Turkey
10:40 - 11:00	**The Effects of Calcium Addition and the Thermomechanical Processing on the Corrosion Resistance and Ignition Temperature of Mg Alloys** **Halil DEMİRTAŞ[1,2], Önder TUNA[1,2], Özgür DUYGULU[1], Deniz Sultan AYDIN[1], Havva KAZDAL ZEYTİN[1], Metin USTA[1,2]** [1]TUBITAK MAM Materials Institute, [2]Gebze Technical University Turkey

HALL - 3

11.June.2021 Friday

NON-FERROUS METALS-2

Session Chairman

Mertol GÖKELMA

11:20 - 11:40	**Cooling Slope Casting of 7075 Aluminum Alloy with Various Tilt Angles for Thixotropic Feedstock Production** **Serhat ACAR, İzel KOCABAŞ, İbrahim TÜTÜK, Ayberk KÖÇKEN, Ali DOLU, Kerem Altuğ GÜLER** Yıldız Technical University Turkey
11:40 - 12:00	**Effect of Sn Alloying Element Addition on Microstructural Change in Al-Mg-Si Alloys** **Osman Halil ÇELİK, Mehmet Buğra GÜNER, Görkem ÖZÇELİK** ASAŞ Alüminyum A.Ş. Turkey
12:00 - 12:20	**Behaviour of Al_2O_3 and Al_4C_3 Particles during Sedimentation and Gas Purging Processes in Aluminium Melts** **Mertol GOKELMA[1], Bernd FRIEDRICH[2], Gabriella TRANELL[3]** [1]Izmir Institute of Technology, [2]RWTH Aachen University, [3]Norwegian University of Science and Technology [1]Turkey, [2]Germany, [3]Norway
12:20 - 12:40	**Characterization of the Semi-Continuous Casted AlSi Alloy Microstructure in Function of Solidification Parameters** **Agota KAZUP, Viktor KARPATI, Balazs GASCI, Greta GERGELY, Zoltan GACSI** University of Miskolc Hungary

HALL - 3

11.June.2021 Friday

NON-FERROUS METALS-3

Session Chairman
Murat ALKAN

13:30 - 13:50	**High Temperature Deformation Behavior of NiCoCrAlY Alloy** **Makoto HASEGAWA, Yuji KUBOTA, Nozomi TAKAHASHI** Yokohama National University Japan
13:50 - 14:10	**Structural and Mechanical Characterization of $Al_{35}Ti_{35}V_{20}Cr_5Mn_5$ Lightweight High Entropy Alloy (LWHEA)** **Gökhan POLAT[1,2], Ziya Anıl ERDAL[1], Yusuf Eren KALAY[1]** [1]Middle East Technical University, [2]Necmettin Erbakan University Turkey
14:10 - 14:30	**Effect of CuAg0.1 Wire Rod Solidification on Continuous Extrusion Process** **Zeynep SİREL, Murat ÖNEY, Orçun ZIĞINDERE, Mehmet Ali AKOY** Sarkuysan Elektrolitik Bakır Sanayi ve Ticaret A.Ş. Turkey

HALL - 3

11.June.2021 Friday

CORROSION AND WEAR-1

Session Chairman

Çiğdem TOPARLI

15:10 - 15:30	**The Effects of Nitriding and TiCrN Coating by Cathodic Arc PVD Method on DIN1.2379 Cold Work Steel Substrate** **Seda ATAŞ BAKDEMİR[1], M. Cenk TÜRKÜZ[2], Elif UZUN KART[3], Serdar SALMAN[1]** [1]National Defence University, Naval Academy, [2]Titanit Ultra Hard PVD Coating Company, [3]Marmara University Turkey
15:30 - 15:50	**Development of Wear Resistant Coatings for Drilling Equipments** **Emre YAVUZ[1,2], Nuri DURLU[1]** [1]TOBB University of Economics and Technology, [2]Turkish Petroleum Corporation Turkey
15:50 - 16:10	**Microscale Fracture Toughness Testing on Hard Coatings** **Burçin KAYGUSUZ[1], Amir MOTALLEBZADEH[2], Özcan Doğu KARADAYI[3], Kürşat KAZMANLI[4], Sezer ÖZERİNÇ[1]** [1]Middle East Technical University, [2]Koç University, [3]Ionbond Turkey Yüzey Teknolojileri A.Ş.,[4]İstanbul Technical University Turkey

HALL - 3

11.June.2021 Friday

CORROSION AND WEAR-2

Session Chairman

Çiğdem TOPARLI

16:50 - 17:10	**Environmental Impact on the Corrosion Behavior of Marine Grade Steel in the Arabian Sea Conditions - A Comparative Analysis of Field and Laboratory Based Corrosion Tests** **Muntazir ABBAS[1], Nigel SIMMS[1], Liyun LAO[1], Owais A. MALIK[2], Luqman ASHRAF[2]** [1]Cranfield University, [2]National University of Science & Technology, PNEC [1]United Kingdom, [2]Pakistan
17:10 - 17:30	**A Predictive Model for Corrosion Under Insulation** **Guodong WANG[1], Luyao MEI[1], Prafull SHARMA[2], Hoi YEUNG[1,2], Liyun LAO[1]** [1]Cranfield University, [2]CorrosionRADAR Ltd United Kingdom
17:30 - 17:50	**Corrosion Resistance of Electroless NiB Coatings Synthesized in a Bath Free of Stabilizing Agent** **Muslum YUNACTI[1], Alexandre MEGRET[1], Alex MONTAGNE[2], Véronique VITRY[1]** [1]Université de Mons, [2]ENSAM Lille [1]Belgium, [2]France

HALL - 4

11.June.2021 Friday

CASTING-1

Session Chairman

Necip ÜNLÜ

10:00 - 10:20	**Evaluation of a New Eco-Friendly Sodium Silicate-Based Binder System for Chromite Sand Application** **Necip ÜNLÜ[1], Ahmet ODABAŞ[2]** [1]Istanbul Technical University, [2]Alazan Casting Chemicals & Industry Metal Inc. Co. Turkey
10:20 - 10:40	**The Effect of Nodularizer Type on the Microstructure and Mechanical Properties of EN-GJS-700-2 Nodular Cast Iron** **Ali KELEŞ[1], Sayid HAS, Rabia CENGİZ[1], Mehmet YILDIRIM[2], Muhammed KIRICI[1]** [1]Motus Automotive Company, [2]Konya Technical University Turkey
10:40 - 11:00	**Squeeze Pin Application on the HPDC Process for Improving Part Quality** **Ekrem ALTUNCU[1], Naci EKMEN[2], Ali OZKAN[2]** [1]Sakarya University of Applied Sciences, Material and Manufacturing Technologies Application And Research Center (SUMAR), [2]Arpek High Pressure Die Casting Company Turkey
11:00 - 11:20	**Irregular Eutectic Solidification: Coupled or Uncoupled Growth?** **Samira MOHAGHEGHI[1], Shabnam Fadaei CHATROUDI[1], Sabine BOTTIN-ROUSSEAU[2], Silvère AKAMATSU[2], Melis ŞEREFOĞLU[1]** [1]Koç University, [2]Sorbonne Université Turkey
11:20 - 11:40	**3D Numerical Simulation and Experimental Investigation of Pure Tin Solidification Under Natural and Forced Convection** **SARI Ibrahim[1,2], HACHANI Lakhdar[1], ZAIDAT Kader[2], FAUTRELLE Yves[2]** [1]Université Amar Telidji-Laghouat, [2]Université Grenoble Alpes [1]Algeria, [2]France

HALL - 4

11.June.2021 Friday

MATERIALS FOR ENERGY-1

Session Chairman

Tayfur ÖZTÜRK

13:30 - 14:00 **Invited Speaker**	**Design of Materials for Advanced Energy Storage** **Cengiz S. ÖZKAN** University of California USA
14:00 - 14:20	**Combinatorial Development of Active Materials for Energy Storge and Conversion** **Fatih PİŞKİN[1,3], Hasan AKYILDIZ[2], Tayfur ÖZTÜRK[3]** [1]Sıtkı Koçman University, [2]Konya Technical University, [3]Middle East Technical University Turkey
14:20 - 14:40	**High Performance and Flexible Supercapacitor Cells for Energy Storage from Renewable Energy Sources** **Apurba RAY, Delale KORKUT, Jenny ROTH, Bilge SARUHAN** German Aerospace Center (DLR) Germany
14:40 - 15:00	**On the Surfaces of Complex Oxides** **Taner AKBAY[1], John A. KILNER[2,3], Tatsumi ISHIHARA[3]** [1]Yeditepe University, [2]Imperial College London, [3]Kyushu University [1]Turkey, [2]United Kingdom, [3]Japan

HALL - 4

11.June.2021 Friday

MATERIALS FOR ENERGY-2

Session Chairman

Billur Deniz KARAHAN

15:10 - 15:30	**Production of Modified Iron Oxide with the Addition of Me (Me: Co,Ni) and Investigation of its Energy Storage Performance** **Mehmet Feryat GÜLCAN[1], Billur Deniz KARAHAN[2]** [1]Istanbul Technical University, [2]Istanbul Medipol University Turkey
15:30 - 15:50	**Nickel Cobalt Aluminum Oxide (NCA) Cathode Production for Lithium-Ion Battery** **Dila SIVLIN, Ozgul KELES** Istanbul Technical University Turkey
15:50 - 16:10	**Investigation of the Performance of Colloidal $LiFePO_4$ Particles in Suspension Flow Battery** **Bayram YILDIZ[1], Yasemin AŞKAR[1], Elif COŞKUN[1], Bora MAVİŞ[2], Simge ÇINAR[1]** [1]Middle East Technical University, [2]Hacettepe University Turkey

HALL - 4

11.June.2021 Friday

MATERIALS FOR ENERGY-3

Session Chairman

Gökçe HAPÇI AĞAOĞLU

16:50 - 17:10	**Graphene Alternative 2D Materials: Mxene** **Mesut Ramazan EKİCİ, Ahmet ATASOY** Sakarya University of Applied Science Turkey
17:10 - 17:30	**Recent Development in 2D Metal Carbides and Nitrides (MXenes) for Energy Storage** **Müslüm DEMİR** Osmaniye Korkut Ata University Turkey
17:30 - 17:50	**Improved Ionic Conductivity in NASICON-Type Ce^{3+} Doped $LiZr_2(PO_4)_3$ for Li-Ion Batteries** **Farah LAMARA, Nedjemeddine BOUNAR** University of Jijel Algeria

HALL - 1

12.June.2021 Saturday

ADVANCED ALLOYS AND PROCESSES FOR AEROSPACE-6

Session Chairman

Murat ALKAN

10:00 - 10:20	**Effect of Cold Rolling on the Shape Memory Behavior of Ni Rich NiTiHf High Temperature Shape Memory Alloy** H. Onat TUGRUL, Ogulcan AKGUL, Mustafa S. VELIPASAOGLU, Benat KOCKAR Hacettepe University Turkey
10:20 - 10:40	**The Effect of Lattice Periodicity on the Compression Behavior of the E-Beam Melted Bcc-Like Ti6Al4V Lattices** Alican Tuncay ALPKAYA[1], Burak HIZLI[1], Burcu ARSLAN HAMAT[2], Hakan YAVAŞ[2], Ahmet Alptuğ TANRIKULU[2], Mustafa GÜDEN[1] [1]İzmir Institute of Technology, [2]Turkish Aerospace Industries Turkey
10:40 - 11:00	**In Situ High Temperature Characterization of 3D-Printed Ti-6Al-4V Alloy** F. R. KASCHEL[1], R. K. VIJAYARAGHAVAN[2], P. McNALLY[2], D. P. DOWLING[1], M. CELIKIN[1] [1]University College Dublin, [2]Dublin City University Ireland

HALL - 1

	12.June.2021 Saturday
	ADVANCED ALLOYS AND PROCESSES FOR AEROSPACE-7
	Session Chairman **Mustafa GÜDEN**
11:20 - 11:50 **Invited Speaker**	**Novel Technology for Manufacturing Heavy Steel and Superalloy Forgings** Mingyue SUN Chinese Academy of Sciences China
11:50 - 12:10	**Nature Inspired Macro-Atomistic Design Approach in Additive Manufacturing** Hakan YAVAŞ[1], A. Alptuğ TANRIKULU[1], Alican Tuncay ALPKAYA[2], Mustafa GÜDEN[2] [1]Turkish Aerospace Industries Inc., [2]İzmir Institute of Technology Turkey

HALL - 1

12.June.2021 Saturday

ADVANCED ALLOYS AND PROCESSES FOR AEROSPACE-8

Session Chairman

Benat KOÇKAR

13:30 - 14:00 **Invited Speaker**	**Advances in Thermal Barrier Coatings: Current Status and Future Perspectives** **Makoto HASEGAWA** Yokohama National University Japan
14:00 - 14:20	**Investigation of the Effect of Chemical Vapor Aluminizing Process Time and Heat Treatment on Nickel Aluminide Coating** **Ahmet Arda İNCEYER[1,2], Gökhan GÜVEN[2], Kaan DEMİRALAY[2], Havva KAZDAL ZEYTİN[2], Metin USTA[1,2]** [1]Gebze Technical University, [2]Materials Institute of Marmara Research Center of The Scientific and Technological Research Council of Turkey Turkey
14:20 - 14:40	**Investigation of High Temperature Oxidation Behavior of Additively Manufactured in 939 Alloy** **Batuhan BAŞBOZKURT, Cevat SARIOĞLU** Marmara University Turkey

HALL - 1

12.June.2021 Saturday

WELDING METALLURGY-1

Session Chairman

Caner BATIGÜN

15:10 - 15:40 **Invited Speaker**	**Creep Cracking Mechanisms of Welded Joints for Cr-Mo Heat-Resistant Pressure Vessel Steels** **Cong WANG** Northeastern University China
15:40 - 16:00	**Investigation of Microstructure and Mechanical Properties of Ferritic Stainless Steels Processed with Laser Welding** **Günseli GÜÇ, Onuralp YÜCEL** Istanbul Technical University Turkey
16:00 - 16:20	**Calculating Effectiveness Of Filler Metals in Reducing Solidification Cracking Susceptibility of AZ31 Mg Alloy** **Tayfun SOYSAL** Igdir University Turkey

HALL - 2

12.June.2021 Saturday

COMPOSITE AND POLYMER MATERIALS-1

Session Chairman

Cevdet KAYNAK

10:00 - 10:30 **Invited Speaker**	**Polymeric Composites with Novel 2D Nanofillers Mxenes** **Mária OMASTOVA** Polymer Institute Slovak Academy of Sciences Slovakia
10:30 - 10:50	**Simultaneous Activation of Multiple Toughening Mechanisms: Interleaving Layered Composites with Blends of Thermoplastic Polymers** **Melike KILIÇOĞLU[1], Erhan BAT[2], Güngör GÜNDÜZ[2], Bora MAVİŞ[1]** [1]Hacettepe University, [2]Middle East Technical University Turkey
10:50 - 11:10	**Fabrication and Compressive Behaviour of B_4C Reinforced Al Foam** **Bilgehan Cem TURAN, Mevlüt GÜRBÜZ** Ondokuz Mayıs University Turkey
11:10 - 11:30	**Development of Resistance Welding Process for Fiber-Reinforced Thermoplastic Matrix Composites: Experimental Analysis and Multiphysics Modeling** **Elvan ATEŞ[1], Oğuzhan BAŞ[1], Mete BAKIR[1,2], Fahrettin ÖZTÜRK[1,2]** [1]Ankara Yıldırım Beyazıt Üniversitesi, [2]Türk Havacılık ve Uzay Sanayii A.Ş. Turkey
11:30 - 11:50	**Recovered Carbon Blacks for Enviromentally Friendly EPDM Based Sealing Systems** **Yusuf GÜNER, Yasemin DURMUŞ, Ali Erkin KUTLU** Standard Profil Automotive A.S. Turkey

HALL - 2

12.June.2021 Saturday

COMPOSITE AND POLYMER MATERIALS-2

Session Chairman

Bora MAVİŞ

13:30 - 13:50	**Spark Plasma Sintering and Characterization of B_4C- TiB_2 Composites** **Leyla YANMAZ[1], S. Ege PARIM[2], Gültekin GÖLLER[1], Onuralp YÜCEL[1], Filiz Çınar ŞAHİN[1]** [1]Istanbul Technical University, [2]Gebze Technical University Turkey
13:50 - 14:10	**The Effect of B_4C Amount on the Wear Properties of Al-B_4C Composites Obtained by High Energy Ball Milling** **Sezgin YAŞA, Ahmet KABİL, Burak BİROL** Yıldız Technical University Turkey
14:10 - 14:30	**Production and Characterization of Graphene Reinforced Al-10Si Matrix Composites via Powder Metallurgy** **Berk ŞENYURT[1], Nazlı AKÇAMLI[1], Duygu AĞAOĞULLARI[2], Hasan GÖKÇE[2]** [1]Bursa Technical University, [2]Istanbul Technical University Turkey

HALL - 2

12.June.2021 Saturday

COMPOSITE AND POLYMER MATERIALS-3

Session Chairman

Bora MAVİŞ

15:10 - 15:30	**Development of Novel Production Method for LaFeSi Based Materials and Its Room Temperature Magnetic Properties** **Semih ATEŞ[1], Doğaç TARI[1], Şerzat SAFALTIN[1], Sebahattin GÜRMEN[1], Öznur KARAAĞAÇ[2], Hakan KÖÇKAR[2]** [1]Istanbul Technical University, [2]Balıkesir University Turkey
15:30 - 15:50	**Liquid Crystal Self-Assembly: A Route for Anisotropic Composites** **Selin SENGUL, Emre BUKUSOGLU** Middle East Technical University Turkey
15:50 - 16:10	**Development and Characterization of SAC305 Alloy Matrix Composites** **Zoltán GYOKER, Gréta GERGELY, Zoltán GACSI** University of Miskolc Hungary

HALL - 3

12.June.2021 Saturday

RECYCLING AND SUSTAINABILITY-1

Session Chairman

Burçak EBİN

10:00 - 10:20	**Retrofitting and Recycling Approaches on Aluminium Industry with Computer Aided Engineering and Physical Simulations to Sustain Circular Economy within Retrofeed Project** **Zeynep Tutku ÖZEN[1], Tolga DEMİRKIRAN[1], Görkem ÖZÇELİK[1], Hasan Basri TAŞKIN[1], Akın OBALI[2], Kadir KÖSOĞLU[2], Deniz ÜRK[2], Aleksandra KIEDRZYNSKA[3], Beata GLOT[3], Jaroslaw HERCOG[3]** [1]ASAŞ Alüminyum A.Ş., [2]Sistem Teknik Endüstriyel Fırınlar Ltd., [3]Institute of Power Engineering [1,2]Turkey, [3]Poland
10:20 - 10:40	**New Regulation Estimation for Efficient and Environmentally Friendly Lamp Recycling in Turkey** **S. Samet KAPLAN[1], M. Şeref SÖNMEZ[1], Zeynep AKKAYA[2], Elif KARA[2], Mustafa ÇETİN[2]** [1]İstanbul Technical University, [2]AGİD, Aydınlatma Gereçleri İmalatçıları Derneği Turkey
10:40 - 11:00	**Design of Laboratory Type Electric Arc Furnace and Production of Copper Alloy From E-Waste** **Rıdvan ORMAN, Barış DARYAL, Oğuz Kağan COŞKUN, Mehtap ARSLAN, Servet İbrahim TİMUR** İstanbul Technical University Turkey

HALL - 3

12.June.2021 Saturday

RECYCLING AND SUSTAINABILITY-2

Session Chairman
Onuralp YÜCEL

11:20 - 11:40	An Overview of Pyrometallurgical Concepts for Recycling of Metals from Waste Electrical and Electronic Equipment **Mertol GÖKELMA, Alireza HABİBZADE** Izmir Institute of Technology Turkey
11:40 - 12:00	White Dross Benefication by Pyrometallurgical Methods **İlayda Elif ÖNER, Buse Tuğçe POLAT, Selçuk KAN, Kağan BENZEŞİK, Onuralp YÜCEL** İstanbul Technical University Turkey
12:00 - 12:20	Production of Mo_2FeB_2-Fe Composites by Using Mill Scale via Self Propagating High-Temperature Synthesis **Bora DERİN, Buse YILMAZ, Faruk KAYA** İstanbul Technical University Turkey

HALL - 3

12.June.2021 Saturday

RECYCLING AND SUSTAINABILITY-3

Session Chairman

Mertol GÖKELMA

13:30 - 13:50	**Industrial Study on the Recovery of Platinum Group Metals from the Catalytic Converter** **H. Hande CEBECİ[1,3], Berk GÜLÖRTEN[3], Mahmut KARADAŞ[3], Safiye TANRIVERDİ[2,3]** [1]Yıldız Technical University, [2]Istanbul University – Cerrahpaşa, [3]Proses Rafinasyon ve Metal Geri Kazanım Makina Sistemleri San. ve Tic. Ltd. Şti Turkey
13:50 - 14:10	**Leaching of Spent Ni-W Hydrodesulphurization Catalyst in H_2SO_4 Solution** **Aycan DEMIR, Aycan ISCAN, Ahmet Orkun KALPAKLI, Mert ZORAGA, Sedat ILHAN** Istanbul University-Cerrahpaşa Turkey
14:10 - 14:30	**Liberation and Extraction of Valuable Components From Li-ion Battery Waste via Supercritical Carbon Dioxide System** **Yuanpeng FU[1,2], Burçak EBİN[2]** [1]China University of Mining and Technology, [2]Chalmers University of Technology [1]China, [2]Sweden
14:30 - 14:50	**Thermodynamic and Experimental Study of the Fluoride Recovery from Spent Pot Lining Recycling Process by Precipitation of Calcium Fluoride** **Anna Mas HERRADOR[1,2], Jonas SCHUSTER[1], Yuanpeng FU[1,3], Martina PETRANIKOVA[1], Burçak EBİN[1]** [1]Chalmers University of Technology, [2]Universitat Politècnica de Catalunya, [3]China University of Mining and Technology [1]Sweden, [2]Spain, [3]China

HALL - 3

12.June.2021 Saturday

RECYCLING AND SUSTAINABILITY-4

Session Chairman

M. Şeref SÖNMEZ

15:10 - 15:30	**Recovery of Valuable Metals from Waste Lithium-Ion Batteries by Metallurgical Routes** **Sepehr ABTAHI[1], Kağan BENZEŞİK[1], Ahmet TURAN[2], Onuralp YÜCEL[1]** [1]Istanbul Technical University, [2]Yalova University Turkey
15:30 - 15:50	**Indium Recovery from Model Leach Solutions by Solvent Extraction** **Doğaç TARI[1], Semih ATEŞ[1], Burçak EBİN[2], Sebahattin GÜRMEN[1]** [1]İstanbul Technical University, [2]Chalmers University of Technology [1]Turkey, [2]Sweden
16:10 - 16:30	**Precious Metals Recovery from Residue of the Copper Concentrate Bioleaching Process** **Mohammad MOKMELI[1], Amin KHOSHNEVISAN[2], Sina SHAKIBANIA[1], Amin RAFATI[3]** [1]University of Tehran, [2]Iranian Fartak Research & Innovation Center, [3]Middle East Meyar Sanat Engineering Company Iran

HALL - 1

12.June.2021 Saturday

CLOSING CEREMONY

Prof. Dr. C. Hakan GÜR
Congress Organizing Board, Chairman

16:20 - 16:40

Prof. Dr. Rodrigo MARTINS
President of the European Academy of Sciences
President Elected of the International Union of Materials Research Societies,
New University of Lisbon
Portugal

"Future Perspectives of Materials Research"

Invited Speaker

20th
INTERNATIONAL
METALLURGY
MATERIALS
CONGRESS
10-12 June
2021
"in Digital Platform"

POSTERS

POSTERS

IMMC-P01	**Air Hardened Bainitic Forging Steel** **İ. İsmail İrfan AYHAN[1], Caner GÜNEY[1], N. Başak DÜRGER[1], Emre ALAN[1], Ersoy ERİŞİR[2,3]** [1]ÇEMTAŞ R&D Center, [2]Kocaeli University, [3]OBER R&D Turkey
IMMC-P02	**The Site and Phase Preferences of Mo Element in a Model Ni-Al-Mo Superalloy** **Rasim ERİŞ, M. Vedat AKDENİZ, Amdulla O. MEKHRABOV** Middle East Technical University Turkey
IMMC-P03	**Numerical Simulation and Experimental Analysis of the Dynamic Behaviour of Ternary Metal Alloy (Ga-In-Sn) Flow Driven by Tubular Electromagnetic Stirrer** **Brahim HIBA[1], Lakhdar HACHANI[1], Abdallah NOURI[1], Kader ZAIDAT[2], Yves FAUTRELLE[2]** [1]Université Amar Telidji de Laghouat, [2]SIMAP-EPM PHELMA, University of Grenoble Alpes [1]Algeria, [2]France
IMMC-P04	**The Effect of Heat Input on Mechanical Properties of Trip Steels in MAG Welding** **Gökhan ERİAN[1], Adem KURT[2]** [1]Turkish Accreditation Agency, [2]Gazi Univ. Turkey

IMMC-P05

Invar Anomaly of Cu-Doped Fe64Ni36 Alloys

Ebru GEZGİN[1], Melike Nur ENGELOĞLU[1], Aslı ÇAKIR[1], Uğur Can ÖZÖĞÜT[1], Tolga TAVŞANOĞLU[1], Mehmet ACET[2]

[1]Muğla Sıtkı Koçman University, [2]Duisburg-Essen University

[1]Turkey, [2]Germany

IMMC-P06

Effect of Electro-Discharge Machining (EDM) on the Microstructure of Selective Laser Melting Processed 17-4 PH Stainless Steels

Andac OZSOY[1,2], Mert KELES[2], Ziya ESEN[3], Arcan F. DERICIOGLU[1]

[1]Middle East Technical University, [2]Roketsan Industries Inc., [3]Çankaya University

Turkey

IMMC-P07

Effect of Submerged Arc Welding on High Temperature Tensile Properties of P91 Type Steel

Junaid ASLAM, Caner BATIGÜN, C. Hakan GÜR

Middle East Technical University

Turkey

IMMC-P08

Production and Characterization of Mg and WE43 Infiltrated Ti6Al7Nb Matrix Composites

Ezgi BÜTEV ÖCAL[1], Ziya ESEN[2], Arcan F. DERİCİOĞLU[1]

[1]Middle East Technical University, [2]Çankaya University

Turkey

IMMC-P09

Hydration Efficiency of Metallic-Ion Incorporated Calcium Phosphate Cement Bone Analogs

Bersu BASTUG AZER, Caner DURUCAN

Middle East Technical University

Turkey

IMMC-P10

Production and Characterization of Si_3N_4 Reinforced Ti_6Al_4V Composites

Erdem SAYIN, Mevlüt GÜRBÜZ

Ondokuz Mayıs University
Turkey

IMMC-P11

Setting of $CaSO_4$ Based Bone Cements in the Presence of Eggshell Membrane Protein

Şule KARAGÜLLEOĞLU, M. Utku YILDIRIM, Bora MAVİŞ

Hacettepe University
Turkey

IMMC-P12

Investigation of Natural Hydroxyapatite Originated from Salmon Fish Bone Wastes

Merve BAS[1], Sibel DAGLILAR[1], Nilgun KUSKONMAZ[1], Cevriye KALKANDELEN[2], Oguzhan GUNDUZ[3]

[1]Yıldız Technical University, [2]Istanbul University- Cerrahpasa, [3]Marmara university
Turkey

IMMC-P13

Hydroxyapatite Production in Solution Combustion Synthesis Using Different Fuels

Deniz ALTAN ALTINBAŞ[1], Şevki Samet KAPLAN[1], Sadia ILYAS[2], M. Şeref SÖNMEZ[1]

[1]Istanbul Technical University, [2]Jeonbuk National University
[1]Turkey, [2]Korea

IMMC-P14

The Operational and Quality Effects of Dynamic Superheat Control During the Continuous Casting Process

İsa KESKİN, Sergen Ali KAT

Heraeus Electro-Nite Turkey, Ekinciler Demir Çelik A.Ş.
Turkey

IMMC-P15

Optimization of High Pressure Die Casting Parameters for the Minimization of Porosities in Aluminium AlSi9Cu3 Casting Parts

Leyla ŞİMŞEK[1,2], Ahmet TURAN[2], M.Cahit ENSARİ[2]

[1]Kırpart Inc., [2]Yalova University
Turkey

IMMC-P16

Hardness and Microstructural Evaluation of the Graphene Reinforced Al Composites Using Waste Beverage Cans

Özgür YILMAZ, Mevlüt GÜRBÜZ

Ondokuz Mayıs University
Turkey

IMMC-P17

An Analytical Approach to Fortification Walls of Ephesos Lysimakhos

Cansu NOBERİ, Fırat BARANAYDIN

İstanbul Gelişim Üniversitesi
Turkey

IMMC-P18

A Preliminary Study on TiO_2 Coating Deposited on the AISI 2205 by High Energy Ball Milling

Serhat ACAR[1], Burak BİROL[1], Alptekin KISASÖZ[2]

[1]Yıldız Technical University, [2]Kırklareli University
Turkey

IMMC-P19

Evaluation of Glass Waste in Ceramic Glazes

Fatma GÖL[1], Ali YILMAZ[1], Selin ŞİMŞEK[1], Emre KAÇAR[1], Zeynep Gizem SARITAŞ[1], Çiğdem TÜRE[1], Melek ARSLAN[1], Fatih ŞEN[1,2]

[1]Keramika Ceramics, Ünsa Mining, Tourism, Energy, Ceramics, Forest Products, Electricity Production Industry, [2]Dumlupınar University
Turkey

IMMC-P20

Enhancing the Ductility of 3D-Printed Polylactic Acid

Burçin KAYGUSUZ, Sezer ÖZERİNÇ

Middle East Technical University
Turkey

IMMC-P21

Synthesis of Barium Strontium Titanate (BST) Ceramics for Tunable Polymer Matrix Composite Substrates

Nazlı ÖZKARAGÖZ, Başar SÜER, Arcan F. DERİCİOĞLU

Middle East Technical University
Turkey

IMMC-P22

Production and Characterization of B_4C Reinforced Al-8.5Si-3.5Cu Matrix Composites via Powder Metallurgy

Berk ŞENYURT, Nazlı AKÇAMLI

Bursa Technical University
Turkey

IMMC-P23

Electrostatic Flocking of Small-Sized Flocks

M. Utku YILDIRIM[1], Erhan BAT[2], Bora MAVİŞ[1]

[1]Hacettepe University, [2]Middle East Technical University
Turkey

IMMC-P24

Hollow Glass Microsphere and Glass Bead-Polyamide 12 Composites Production by Selective Laser Sintering Method

Burçin ÖZBAY[1,2], İ. Ersin SERHATLI[2], M. Enes BULDUK[1]

[1]Fatih Sultan Mehmet Vakif University, [2]Istanbul Technical University
Turkey

IMMC-P25	**Corrosion and Wear Resistance of Aluminum Bronze Increased by Heat Treatment** **Aleattin KULAKLI, Talip ÇİTRAK, Serdar TOZKOPARAN, Aydın Barış ŞİMŞİR, Edanur KASAP** Sağlam Metal A.Ş. Turkey
IMMC-P26	**Fabrication of Colloidal and Conductive $LiFePO_4$ Particles for Suspension Flow Batteries** **Yasemin AŞKAR[1], Bayram YILDIZ[1], Bora MAVİŞ[2], Simge ÇINAR[1]** [1]Middle East Technical University, [2]Hacettepe University Turkey
IMMC-P27	**Bimetallic Metal-Organic Frameworks for Wearable Energy Storage Systems** **Farzaneh HEKMAT, Husnu Emrah UNALAN** Middle East Technical University Turkey
IMMC-P28	**Synthesis of Lithium Iron Phosphate with Controlled Size and Shape** **Elif ÇOŞKUN[1], Bayram YILDIZ[1], Yasemin AŞKAR[1], Bora MAVİŞ[2], Simge ÇINAR[1]** [1]Middle East Technical University, [2]Hacettepe University Turkey
IMMC-P29	**Fractographic and Metallurgical Analysis Investigations of the Failure of HP Turbine Blade** **M.A. DJERIDANE[1], M. FERHAT[2], H.A. BENHORMA[2]** [1]Sonatrach-Direction Maintenance Laghouat Company, [2]University of Laghouat Algeria

IMMC-P30

A Study on The Failure Mechanisms of Various Milling Inserts

Nuray Beköz ÜLLEN, Gizem KARABULUT

Istanbul University-Cerrahpaşa

Turkey

IMMC-P31

Effect of Coating on Surface Integrity of Tools and End Products after Piercing Operation

Fuat Can AĞARER[1], Hatice SANDALLI[1], M. Burak TOPARLİ[2], İ. Etem SAKLAKOĞLU[3]

[1]Norm Somun San. ve Tic. A.Ş.,
[2]Nedu Bağlantı Elemanları San. ve Tic. A.Ş., [3]Ege Üniversitesi

Turkey

IMMC-P32

Microstructure, High Strength and Electrical Conductivity of the Ufg Cu-0.5%Cr-0.2%Zr Alloy Processed by HPT

Igor ALEXANDROV[1], Wei WEI[2], Elena SARKEEVA[1], Vil SITDIKOV[1]

[1]Ufa State Aviation Technical University, [2]Changzhou University

[1]Russia, [2]China

IMMC-P33

Morphological, Optical and Electrochromic Properties of Vanadium Pentoxide Thin Films Prepared by Ultrasonic Spray Deposition Method

Yusuf TUTEL, Seyma KOC, Mete Batuhan DURUKAN, Serkan KOYLAN, Husnu Emrah UNALAN

Middle East Technical University

Turkey

IMMC-P34

Fabrication of P-type CuI Nanowires Networks for Transparent Flexible Electronics

Alptug CALASIN[1], Aleyna ASCIOGLU[1], Serkan KOYLAN[1], Sensu TUNCA[1], Sahin COSKUN[2], Husnu Emrah UNALAN[1]

[1]Middle East Technical University, [2]Eskisehir Osmangazi University

Turkey

IMMC-P35

Functionalization of Glass Fiber Woven Fabrics by Transparent Conducting Oxide (TCO) Thin Films and Characterization of Their Electromagnetic Properties

**Merve OZDIL, Tilbe BETIN, Caner DURUCAN,
Arcan F. DERICIOGLU**

Middle East Technical University

Turkey

IMMC-P36

Determination of the Effectiveness of the Conservation Area by Using Nano Particles on Archaic Stones with $CaCO_3$ Content

Halit S. CANOL[1], Cem B. ÜSTÜNDAĞ[2], Rıza G. AKGÜN[3]

[1]Mimar Sinan Fine Art University, [2]Yıldız Technical University,
[3]Maltepe University

Turkey

IMMC-P37

Characterization of Zirconium-Tantalum Metallic Glass Coatings Produced by Combinatorial Sputtering

**Ali Bagheri BEHBOUD[1], Gökhan TARMAN[2],
Amir MOTALLEBZADEH[3], Sezer ÖZERİNÇ[1]**

[1]Middle East Technical University, [2]TOBB University of Economics and Technology,
[3]Koç University

Turkey

IMMC-P38

A Comparative Study in the Economy of the Hydrometallurgical and Pyrometallurgical Copper Extraction from Low-Grade Chalcopyrite Ores

**Mohammad MOKMELI[1], Masoumeh Torabi PARIZI[2],
Hassan Sahraei PARIZI[2]**

[1]University of Tehran, [2]R&D Center of Sarcheshmeh Copper Complex

Iran

IMMC-P39	**Industrial Study of Tantalum Metal Production from Ore with Alkaline Process** **Safiye TANRIVERDİ[1,2], H. Hande CEBECİ[2,3], Cem KAHRUMAN[1]** [1]İstanbul University – Cerrahpaşa, [2]Proses Rafinasyon ve Metal Geri Kazanım Makina Sistemleri San. ve Tic. Ltd. Şti, [3]Yıldız Technical University Turkey
IMMC-P40	**Effect of Building Direction and Thermo-Hydrogen Processing on the Microstructure and Texture of Electron Beam Melting (EBM) Processed Ti6Al4V Alloy** **Merve N. DOĞU[1,3], Ziya ESEN[2], Kemal DAVUT[3,4], Evren TAN[5], Berkay GÜMÜŞ[5], Arcan F. DERİCİOĞLU[1]** [1]Middle East Technical University,[2] Çankaya University, [3]Atılım University, [4]Metal Forming Center of Excellence, [5]ASELSAN A.Ş. Turkey
IMMC-P41	**Characterization of Interfaces Between Intermetallic Precipitates and Matrix in Some Magnesium Alloys** **Uğur Can ÖZÖĞÜT[1], Servet TURAN[2], Ali Arslan KAYA[3]** [1]Muğla Sıtkı Koçman University, [2]Eskişehir Technical University Turkey
IMMC-P42	**Nanostructured High Entropy Alloys with High Strength** **Ö. Gökhan TARMAN[1], M. Yiğit KÖHNETARFUN[1], Amir MOTALLEBZADEH[2], Sezer ÖZERİNÇ[3]** [1]TOBB University of Economics and Technology, [2]Koç University, [3]Middle East Technical University Turkey

IMMC-P43

Determination of Mixing Ratio of Alloy Materials in Manufacturing of Power Transmission Line Aluminium Alloy Conductor

İ. BİNBUĞA, Ü. UNCU, E. KISTI, H. AYKANAT, İ. GÖK, S. ÖZER

EMTA Conductor &Cable
Turkey

IMMC-P44

Determination, Examination and Improvement of Breaking Problems in Wire Drawing Processes of 6101 Series 9,5 mm Diameter Aluminum Alloy Wire Rods

Necati OCAK[1], U. G. UNCU[1], İ. BİNBUĞA[1], S. ASLAN[2], E. DURU[2]

[1]Emta Conductor&Cable, [2]Sakarya University
Turkey

IMMC-P45

Investigation, Development of Parameters Affecting the Technical Properties of ACCC Lisbon Aluminium Conductor and Comparison with ACSR Hawk Conventional Conductor

Necati OCAK[1], U.G. UNCU[1], E. BİLDİK[1], E. KISTI[1], C. DURMAZ[1], Serdar ASLAN[2]

[1]Emta Conductor&Cable, [2]Sakarya University
Turkey

IMMC-P46

The Effect of Tin Addition and T6 Heat Treatment on the Mechanical Properties of A356 Aluminum Alloy

Selda HASÇELİK, Işıl KERTİ

Yıldız Technical University
Turkey

IMMC-P47

Fire Resistant Composite Doors Concepts and Smart Modular Design

Cem MEHMETALİOĞLU, Murat KONAR, Görkem ÖZÇELİK, Zafer ZORLU, Tutku ÖZEN

ASAŞ Alüminyum Sanayi ve Ticaret A.Ş.
Turkey

IMMC-P48

Production and Analysis of Cu and CuNi Nano Particles with Solution Combustion Synthesis

Mustafa Çağrı ALTINBAŞ[1], Şevki Samet KAPLAN[1],
Sadia ILYAS[2], M. Şeref SÖNMEZ[1]

[1]Istanbul Technical University, [2]Jeonbuk National University
[1]Turkey, [2]Korea

IMMC-P49

Evaluation of Determination of Aluminum Wire Rod Surface and Subsurface Defects by Eddy Current Method

Ebru KISTI[1], Necati OCAK[1], U.G. UNCU[1], Yıldız Y. OZBEK[2]

[1]Emta Conductor&Cable, [2]Sakarya University
Turkey

IMMC-P50

Recovery of Rare Earth Elements (Nd, Gd, and Dy) from Apatite Concentrate, Esfordi Mine-Yazd Province

Ghazale KOHOOLAT, Sina SHAKIBANIA,
Mohammad MOKMELI

University of Tehran
Iran

IMMC-P51

Production of Alumina-Based Ceramics from Aluminium Black Dross

Umay ÇINARLI, Ahmet TURAN

Yalova University
Turkey

IMMC-P52

Production of FeCo from Mill Scale Through Aluminothermic Reduction

Mehmet BUGDAYCI[1], Ahmet TURAN[1], Levent ONCEL[2]

[1]Yalova University, [2]Sinop University
Turkey

IMMC-P53

Effect of Flash Design on Efficiency in Hot Forging Process

Fulya EYÇİN[1], Tuğçe YAĞCI[2,3], Adem KORKMAZ[2], Serhat BARDAKÇI[3], Osman ÇULHA[2,3]

[1]Tirsan Kardan San. ve Tic. A.Ş., [2]Manisa Celal Bayar University, [3]Twin R&D Engineering Company

Turkey

IMMC-P54

Recovery of WC and Co-Based Compunds from Waste Cutting Tools through Hydrometallurgical Route

Hakan KUŞDEMİR[1,2], Ahmet TURAN[3], Onuralp YÜCEL[1]

[1]Istanbul Technical University, [2]Körfez Döküm Sanayi ve Ticaret A.Ş., [3]Yalova University

Turkey

IMMC-P55

Solid State Synthesis of Li_4SiO_4 Using Different Kind Steel Slags as SiO_2 Source

Fatih Kutay METE[1], Kağan BENZEŞİK[1], Ahmet TURAN[2], Onuralp YÜCEL[1]

[1]Istanbul Technical University, [2]Yalova University

Turkey

IMMC-P56

The Influence of Change in Microstructure by Heat Treatment on Drill Quality of Hot Forged AISI 4140 Steel

Nuray BEKÖZ ÜLLEN[1], Tuğba ÖNENÇ[2]

[1]Istanbul University-Cerrahpasa, [2]ULPATEC Air Filter Technology

Turkey

IMMC-P57

Effects of Microalloying Elements on Microstructure and Mechnical Properties of Leaf Sprig Steels

İ. İrfan AYHAN[1], Caner GÜNEY[1], Emre ALAN[1],
N. Başak DÜRGER[1], M. Fatih KAYADEĞİRMENİ[2],
Gülbeniz YILDIZ[2], Yakup YÜREKTÜRK[2], Nazlı AKÇAMLI[2]

[1]ÇEMTAŞ Çelik Mak. San. Tic. A. Ş. R&D Center,
[2]Bursa Technical University

Turkey

IMMC-P58

Effects of Pre-Heat Treatment on Mechanical and Microstructural Properties of Q&T and Bainitic Steels

İ. İrfan AYHAN[1], Caner GÜNEY[1], Emre ALAN[1],
N. Başak DÜRGER[1], Ö. Faruk ŞENSOY[2], Sedanur KARDAŞ[2], Betül ÖZER[2], Nazlı AKÇAMLI, Yakup YÜREKTÜRK[2]

[1]ÇEMTAŞ Çelik Mak. San. Tic. A. Ş. R&D Center,
[2]Bursa Technical University

Turkey

IMMC-P59

Increasing the Rate of Hot Charging and Reducing Energy Consupmtion by the Hot Rolling Mill Monitoring Screen Approach

Gökhan BİLMEZ, Burak Emre IŞIK, Murat PERÇEM,
Uğur OKTAY, Erhan KORKMAZ, Erman KAYA, Yavuz DEMİRCİ

İskenderun Demir ve Çelik A. Ş.

Turkey

IMMC-P60

Increasing the Quality of the Surface with Transformation from Adhesive Scale to Easy to Remove Scale

Koray ARAY, Turgut ARSLAN, Kübra AKGÜN,
Gökhan BİLMEZ, Serdar GÜNBAY, Hasan YILDIRIM,
Tayfun KOCABAŞ, A. Mesud ÇAKIR, Burcu SOYSAL ATAN, İlyas AÇIKGÖZ

İskenderun Demir ve Çelik A. Ş., Oyak Maden Metalurji Grubu Operasyonel Mükemmellik Direktörlüğü

Turkey

IMMC-P61

Power Transformer Fault Diagnosis with Fuzzy Logic Based Oil Dissolved Gas Analysis

Ahmet BEŞKARDEŞ, Serdar YILDIRIM, Emre TOPDEMİR

Iskenderun Iron & Steel Works Company
Turkey

IMMC-P62

Effect of Sintering Conditions on Microstructural and Mechanical Properties of Injection Molded 420 Martensitic Stainless Steel

Lütfi YAKUT[1,2], Sertaç ALPTEKİN[2], H. Özkan GÜLSOY[1]

[1]Marmara University, [2]TUBITAK MRC
Turkey

IMMC-P63

The Effect of Crystallographic Texture and Microstructure on Hydrogen Permability of Enamel Steels

Ümran BAŞKAYA[1], Kemal DAVUT[2], Ramazan UZUN[1], Yasemin KILIÇ[1], Oğuz GÜNDÜZ[1]

[1]Eregli Iron and Steel Works, Co., [2]Atılım University
Turkey

IMMC-P64

Influence of Hydrochloric Acid Temperature on Pickling Efficiency Before Wire Drawing

Murat Alper CEDİMAĞAR

Çelik Halat ve Tel Sanayii A.Ş
Turkey

IMMC-P65

Boriding of AISI 304L Stainless Steel via CRTD-BOR Method

Mehran KARIMZADEHKHOEI, Merve SERT,
Oguz Kagan COSKUN, Mehtap ARSLAN,
Guldem KARTAL SİRELİ, Servet TİMUR

İstanbul Technical University
Turkey

IMMC-P66	**Comparison of Microstructural and Optical Properties of TiO_2 Thin Films Synthesized by Sol-Gel Dip Coating and Spin Coating Techniques** Özge ÖZGÜN, Muhammed NAJAR, Aslı ÇAKIR, Tolga TAVŞANOĞLU Muğla Sıtkı Koçman University Turkey
IMMC-P67	**Investigation of Delaying Cold Heading Crack Formation with Shot Peening Process** Cenk KILIÇASLAN, M. Burak TOPARLI, Sezgin YURTDAŞ, Doğuş ZEREN, Barış TANRIKULU Norm Cıvata San. ve Tic A.Ş. Turkey
IMMC-P68	**Effect of Heat Treatment Parameters on the Microstructure and Mechanical Properties of 30CrNiMo8 Steel** Hakan ERÇAY[1], Gürcan TATLICAN[1], Tuncay DİKİCİ[2] [1]Özkan Iron and Steel Industry, [2]Dokuz Eylul University Turkey
IMMC-P69	**Temperature Distribution Analysis of Thin Metal Surfaces by Induction Heating** Basar SUER, Arcan F. DERICIOGLU Middle East Technical University Turkey
IMMC-P70	**Improvement of Orbital Cutting Blade Life With Tin Coating** Muhammed Cemil ENSAROĞLU, Bedri Onur KÜÇÜKYILDIRIM Yıldız Technical University Turkey

IMMC-P71

Microstructural and Mechanical Characterization of Spot Welds on AISI 430 Ferritic Stainless Steel Sheets

Maazouz MURAD[1,2], Allaoui OMAR[1],
Belhocine ABDELGHANI[1], Djendel MOKHTAR[1,3]

[1]Amar Telidji University of Laghouat,
[2]Mohamed Boudief University of M'sila,
[3]University Mohamed EL-Bachir El-Ibrahimi

Algeria

IMMC-P72

The Optimization of Super Impact MIG Welding Process of ETIAL 171 Alloy Diameter Parts Produced By Die Casting

Hafizittin Hakan YUDAR, Ahmet ÇALIM, Deniz KARABULUT, Güliz TURHAN, Gizem KAPLAN

Demircioğlu Şase A.Ş.

Turkey

IMMC-P73

New Ideas in X-Ray Diffractive Characterization of Nanomaterials

Hande ÖZTÜRK[1], I. Cevdet NOYAN[2]

[1]Özyeğin University, [2]Columbia University

[1]Turkey, [2]USA

IMMC-P74

A Microstructural Investigation of 1 Mol% H3BO3 and 0.5 Mol% MnO Added ZnO Ceramics

Berat YÜKSEL PRICE, Gökhan HARDAL

Istanbul University-Cerrahpaşa

Turkey

IMMC-P75

Preparation and Structural Characterization of $NiMn_2O_4$ Ceramics

Berat YÜKSEL PRICE, Gökhan HARDAL

Istanbul University-Cerrahpaşa

Turkey

IMMC-P76

Experimental Study of the Solidification of Sn-10wt.%Pb Alloy Under Forced and Natural Convection in Benchmark Experiment

Abdelhafid ABDELHAKEM[1], Lakhdar HACHANI[1], Kader ZAIDAT[2], Yves FAUTRELLE[2]

[1]Université Amar Telidji de Laghouat,
[2]CNRS Grenoble Institute of Technology

[1]Algérie, [2]France

IMMC-P77

The Effect of Cooling Rate on the Mechanical Properties, Microstructure and Formation of Oxide Scale in Welding Wire Rod Grade for Submerged Arc Welding

Ahmet SAĞLAM, Erdi GÖNÜLALAN

İskenderun Demir ve Çelik A. Ş.

Turkey

IMMC-P78

Definition of Martensite Structures by XRD Method in Carbon Steel (C80)

Sadık POLAT, Onur OREL, Memduh Kağan KELER

İskenderun Demir ve Çelik A. Ş.

Turkey

IMMC-P79

Bf No4 Slag Granulation (INBA) Facility Solution of Chimney Floor Abrasion Problems

İbrahim ÇAKMAK, Mehmet Atıl TUNÇ, Ümit GEBENLİ

İskenderun Demir ve Çelik A. Ş.

Turkey

IMMC-P80

The Microstructural Effects of Positioning in Manufacturing on Selective Laser Melted AlSi10Mg

Gülten KAFADAR[1,2], Sertaç ALTINOK[1,2], Burcu ARSLAN HAMAT[1,2], Ahmet Alptuğ TANRIKULU[1], Akın DAĞKOLU[1], Hakan YAVAŞ[1]

[1]Turkish Aerospace Industries Inc., [2]Middle East Technical University

Turkey

IMMC-P81

Production and Characterization of Electron Beam Melted (EBM) Ti-6Al-4V Parts

Burcu Arslan Hamat[1,2]; Ahmet Alptuğ Tanrıkulu[1],
Gülten Kafadar[1,2], Sertaç Altınok[1,2] Akın Dağkolu[1],
Hakan Yavaş[1]

[1]Turkish Aerospace Industries Inc., [2]Middle East Technical University

Turkey

IMMC-P82

Production of PLA/Hydroxyapatite/Graphene Oxide Nanosuctured Composite Scaffold

Büşra OKTAY[1], Esma ÖZEROL[1], Oğuzhan GÜNDÜZ[2],
Cem Bülent ÜSTÜNDAĞ[1]

[1]Yildiz Technical University, [2]Marmara University

Turkey

IMMC-P83

Polycarbonate / Graphene Oxide Composite Membrane Production

Meryem MUSLU[1], Muhammed Enes Oruc[2],
Cem Bulent USTUNDAG[1], Hasan SADIKOGLU[1]

[1]Yildiz Technical University, [2]Gebze Technical University

Turkey

IMMC-P84

Production of $AlFe_2B_2$ Intermetallic Compound by Using Mill Scale via Self Propagating High Temperature Synthesis Method

Ecem Turhan, Faruk Kaya, Bora Derin

Istanbul Technical University

Turkey

IMMC-P85

A Review of Composite Lattica Structures: Properties, Design, Manufacturing and Applications

Tayfun DURMAZ[1], Ronan O'HIGGINS[1], Robert TELFORD[2]

[1]University of Limerick, [2]ATG-Innovation

Ireland

IMMC-P86

Microstructural and Morphological Characterization of Directionally Solidfied Copper-Boron Eutectic System

Samira MOHAGHEGHI, Shabnam Fadaei CHATROUDI, Melis ŞEREFOĞLU

Koç University

Turkey

IMMC-P87

On the Role of Both Pulse Current and Electrolyte Bath on the Mechanical Behavior of Ni Foam

Mansooreh Jafari ESFAD, Ahmad MOLOODI

Academic Center for Education, Culture and Research (ACECR)

Iran

METEM
UCTEA CHAMBER of METALLURGICAL and
MATERIALS ENGINEERS'S TRAINING CENTER

UCTEA CHAMBER OF METALLURGICAL AND MATERIAL ENGINEERS'S TRAINING CENTER

METEM (TMMOB Chamber of Metallurgical and Materials Engineers Training Center) gathers whole sector and cooperate for sustainable development and transformation of the sector. Also, it combines the qualified knowledge of industry, university and colleagues;

- Aims to be integrated to the world, with national and international symposiums, congresses, conferences, seminars,
- Provides highly qualified trainings and consultancy with scientific, technical and practical approach,
- Support sectoral and social developments with own projects,
- Acts as an powerful and active center by providing information, new aspects, relationships, and cooperation to create new opportunities.

METEM organizes many activities in order to reach the increasing knowledge accumulation, to share the experiences and to evaluate them in production processes.

Many such as the EFRS International Iron and Steel Symposium, IMMC International Metallurgy and Materials Congress, ISRS International Steel Rolling Symposium, ALUS International Aluminum Symposium, MCHTSE Mediterranean Heat Treatment and Surface Engineering Conference, congresses, conferences and symposium organization carries out.

In addition, it provides in-house training and consultancy services open to general participation. Engineers, scientists, researchers and production managers; in order to review and discuss new challenges, recent developments and issues.

For that purpose, by bringing together highly qualified and experienced experts from the university and industry, we are able to; technical, managerial and engineering knowledge to refresh, making business development related to the sector's problems, occupational health and safety in problem solving, quality and to increase awareness and thus aim to provide value-added training and events planning, engages.

METEM also demonstrates "researches of Turkish metallurgy industry and universities" to the world, by organizing "international congresses, conferences and symposiums".

METEM is at the service of our sector with its trust, diligence, beliefs and values for improvement.

METEM
TMMOB METALURJİ VE MALZEME
MÜHENDİSLERİ ODASI EĞİTİM MERKEZİ

TMMOB METALURJİ VE MALZEME MÜHENDİSLERİ ODASI EĞİTİM MERKEZİ

METEM (TMMOB Metalurji ve Malzeme Mühendisleri Odası Eğitim Merkezi) tüm sektörü bir araya getirerek sektörün gelişimi ve dönüşümü için çalışmaktadır. Sanayi, üniversite ve meslektaşlarının nitelikli birikimlerini birleştiren METEM;

- Geliştirdiği ve planladığı tüm ulusal ve uluslararası sempozyum, kongre, konferans, seminer gibi organizasyonlarıyla dünyaya entegre olabilmek üzere çalışan,
- Bilimsel, teknik ve uygulamaya yönelik nitelikli eğitim ve danışmanlık hizmetleri veren,
- Sektörel ve toplumsal gelişimi planladığı projelerle destekleyen,
- Bilgi, yeni açılımlar, ilişkiler, fırsatlar yaratma konusunda işbirlikleri sağlama üzerinden hareket eden güçlü bir etkinlik merkezidir.

Artan bilgi birikimine hızla ulaşmak, edinilen deneyimleri paylaşmak ve bunları üretim süreçlerinde değerlendirmek üzere, METEM bünyesinde birçok etkinlik düzenlenmektedir.

EFRS Uluslararası Demir Çelik Sempozyumu, IMMC Uluslararası Metalurji ve Malzeme Kongresi, ISRS Uluslararası Hadde Sempozyumu, ALUS Uluslararası Alüminyum Sempozyumu, MCHTSE Akdeniz Isıl İşlem ve Yüzey Mühendisliği Konferansı gibi birçok; kongre, konferans ve sempozyum organizasyonları gerçekleştirmektedir.

Bunun yanı sıra genel katılıma açık, şirketiçi eğitimler ve danışmanlık hizmetleri vermektedir. Mühendislere, bilim adamlarına, araştırmacılara ve üretim yöneticilerine; alanlarında yeni zorlukları, son gelişmeleri ve ortaya çıkan konuları gözden geçirip tartışabilecekleri ortamlar hazırlamaktadır.

Yine bu amaçla, üniversite ve sanayide yer alan, yüksek bilgi ve deneyime sahip uzmanları bir araya getirerek, sektöre ve sektör çalışanlarına yönelik; teknik, yönetsel ve mühendislik bilgilerini tazelemeyi, sektörün sorunlarına ilişkin iş geliştirmeler yapmayı, çalışan sağlığı ve güvenliğinde sorun çözmeyi, nitelik ve farkındalık kazandırmayı ve böylece katma değer sağlamayı hedefleyen, eğitimler ve etkinlikler planlayıp yürütmektedir.

METEM gerçekleştirdiği uluslararası etkinlikler ile Türkiye metalurji sektörünün ve akademik araştırmalarının dünyaya tanıtılmasına katkı sağlamaktadır.

METEM, güven, çalışkanlık, iyiye ve değişime olan inanç ve değerleriyle sektörümüzün hizmetindedir.

20th

INTERNATIONAL METALLURGY MATERIALS CONGRESS

10-12 June 2021

“in Digital Platform”

PROCEEDINGS

CONTENTS

Steelmaking

Ceramics, Glass, Refractory Materials

Biomaterials

Nanomaterials

Mechanical Metallurgy

Advanced Alloys and Processes for Aerospace

Surface Treatment and Heat Treatment

Non-Ferrous Metals

Corrosion and Wear

Casting

Materials for Energy

Advanced Alloys and Processes for Aerospace

Welding Metallurgy

Composite and Polymer Materials

Recycling and Sustainability

POSTERS

20th
INTERNATIONAL
METALLURGY
MATERIALS
CONGRESS
10-12 June
2021
"in Digital Platform"

Steelmaking

immc2021

Modelling of Mechanical Strength by Examining Hot Rolling Mill Parameters in Structural Steels

Cemre KEÇECİ, Muhammet BİLEN, Serdar GÜNBAY, Hasan YILDIRIM, Z. Özlem TUNÇ, Tayfun KOCABAŞ, A. Mesud ÇAKIR, Burcu SOYSAL ATAN, İlyas AÇIKGÖZ
İskenderun Demir ve Çelik A. Ş., Oyak Maden Metalurji Grubu Operasyonel Mükemmellik Direktörlüğü
Turkey

Abstract
Carbon steels of various qualities are produced for use in structural steel manufacturing. During the production of this type of steel, the desired mechanical properties are created by chemical analysis and process parameters. With this study mechanical values obtained in rolled products with different chemical analysis and process parameters were analyzed. With the analyzed test results, the main parameters affecting the mechanical properties were determined and statistical data analysis was carried out on the formation of the mathematical model. Multiple linear regression analysis was performed to find the best model that predicts mechanical strength.

As a result of this study, the relationship between yield and tensile strength with chemical analysis and process parameters has been mathematically modeled.

1. Introduction

Structural Steels; Non-alloy or low-alloy steels, defined by tensile strength and yield limit.

The mechanical properties depend on the amount of carbon and manganese as well as the amount of alloys added in the top grades.

It is used for applications requiring high strength rather than shaping.

The lowest quality group has at least 235 Mpa yield and 360 Mpa tensile value, while the top quality group has 355 Mpa yield and 510 MPa tensile value.

For this quality group, which generates more than 50% of the production amount of Isdemir, it is aimed to model the mechanical test results and compare them with the actual realization. In this context, firstly statistical studies were made from existing data sets, and the normality of the process and process adequacy analysis were carried out.

2. Experimental Procedure

Multiple linear regression analysis was performed to find the best model that predicts mechanical strength.

Different statistical analysis was done for Group1, Group2, Group3 grades within the scope of structural steel groups.

Our inputs were chosen as hot rolling process values such as coiling temperature, run-out table cooling rate, along with chemical analysis such as C, Mn, Si. Outputs were determined as yield and tensile strength.

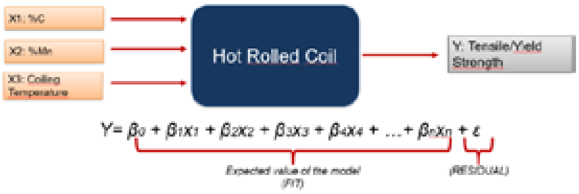

Figure 1. Multiple Linear Regression Analysis Method

After the model study for Group 1 grades, the R square value was found to be 73.68%.

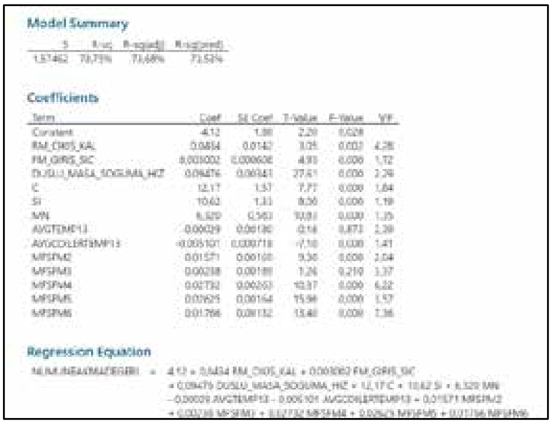
Model Summary

Coefficients

Regression Equation

Figure 2. Statistical Model Studies - Group1 Qualities Yield Strength Mathematical Model

After the model study for the group 2-3 grades, the R square value was found to be 81.65%. In the regression formula, C, Mn, Si, Cr, Ti, NB chemical elements were included along with process data such as FM inlet temperature, coiling temperature, run-out table speed etc. Unlike group 1, Nb and Ti alloy values are also added to the model. They contribute directly to the yield and tensile values as a micro alloy element in these grades for high strength value requirements.

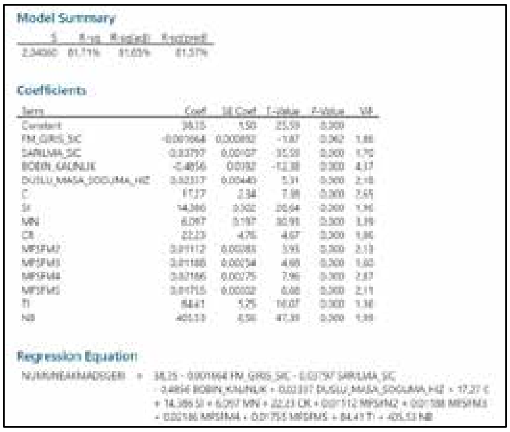

Model Summary

S	R-sq	R-sq(adj)	R-sq(pred)
2.34060	81.71%	81.65%	81.57%

Coefficients

Term	Coef	SE Coef	T-Value	P-Value	VIF
Constant	38.15	1.50	25.59	0.000	
FM_GIRIS_SIC	-0.001664	0.000892	-1.87	0.062	1.88
SARILMA_SIC	0.03797	0.00107	35.58	0.000	1.70
BOBIN_KALINLIK	-0.4856	0.0392	-12.38	0.000	4.17
DUSLU_MASA_SOGUMA_HIZ	0.02317	0.00440	5.31	0.000	2.18
C	17.27	2.34	7.38	0.000	2.65
SI	14.386	0.502	28.64	0.000	1.96
MN	6.097	0.197	30.93	0.000	1.19
CR	22.23	4.76	4.67	0.000	1.86
MPSFM2	0.01112	0.00283	3.93	0.000	2.13
MPSFM3	0.01188	0.00254	4.68	0.000	1.60
MPSFM4	0.02186	0.00275	7.96	0.000	2.87
MPSFM5	0.01755	0.00262	6.68	0.000	2.11
TI	84.41	5.25	16.07	0.000	1.38
NB	405.53	8.56	47.39	0.000	1.99

Regression Equation

NUMUNEAKMADEGERI = 38.15 - 0.001664 FM_GIRIS_SIC - 0.03797 SARILMA_SIC - 0.4856 BOBIN_KALINLIK + 0.02317 DUSLU_MASA_SOGUMA_HIZ + 17.27 C + 14.386 SI + 6.097 MN + 22.23 CR + 0.01112 MPSFM2 + 0.01188 MPSFM3 + 0.02186 MPSFM4 + 0.01755 MPSFM5 + 84.41 TI + 405.53 NB

Figure 3. Statistical Model Studies – Group2/3 Qualities Yield Strength Mathematical Model

For the tensile strength, a different regression analysis was not made and modeling was made over the yield value.

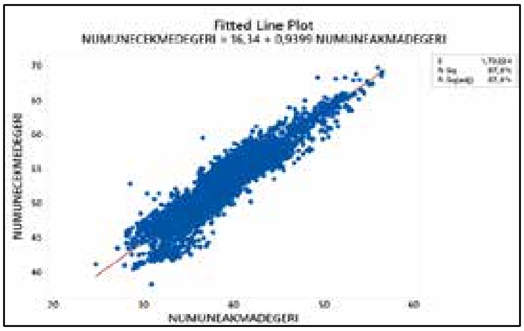

Figure 4. Statistical Model Studies – Group2/3 Qualities Tensile Strength Mathematical Model

The resulting formulation was used for different chemical analyzes. Compliance of new designs that may occur with different carbon and manganese values to the desired standard strength limits was checked. After this study, it was determined that group 2 and group 3 grades could respond to the desired strengths with lower carbon and manganese alloys.

Since C and Mn are reduced, the microstructure is more suitable and has a more homogeneous grain structure without banding, and the product with a higher impact value was obtained by increasing the grain size according to the ASTM E45 standard. In the continuation of this study, the effect of similar mechanical test results obtained with different chemical analyzes on the microstructure was investigated. For example, microstructure studies obtained with different carbon, manganese and micro alloy elements in S55JR quality were carried out in a laboratory environment.

Samples from hot rolled coils produced in 12 MM thickness were etched with nital and examined with different magnifications. In the review photo, the top, center and bottom edge microstructures of the coil along 12 mm thickness were compared with the previous productions. It has been observed that perlite banding, which was present in previous productions, was considerably decreased especially in the central regions of the coil. With this result, notch impact test results were realized with higher energy compared to previous productions.

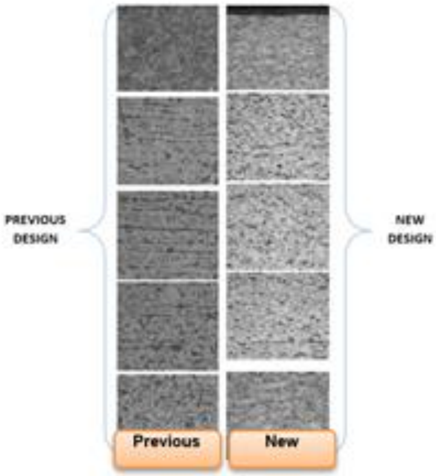

Figure 5. Micro Structure Comparison (X500)

4. Conclusion

With the statistical study made from the historical data, the test results were predictable without the need for new production.

In steel grades alloyed with different chemical elements, the effects of the elements on the product were examined. With this study since a predictable mechanical test result can be detected in advance, possible different realizations can be taken into consideration.

In the experimental study, it was observed that different designs that can meet customer expectations at a high level can be made with different chemical analysis and process parameters.

References

[1] Erdemir Product Catalogue 2017
[2] Isdemir Production Management System

Coking Process, Optimization of Coke Quality Parameters and Investigation of Effects in Blust Furnace

Hüseyin KALAY, Zekeriya ÖZER
İskenderun Demir ve Çelik A. Ş.
Turkey

Abstract

Coking is the phenomenon of heating the coal in an airless environment at certain temperatures, losing its volatile substances and forming a hard and porous structure with high carbon content. This structure, which has very high carbon content, is called coke. The obtained coke is used in liquid raw iron production process in blast furnaces, the coke used for this process must provide some quality parameters. These quality parameters include ash, volatility, fixed carbon, sulfur content, calorie content, humidity, stability, hardness, CRI and CSR values. These values should be optimized and the suitability of the coke for use in blast furnaces should be ensured. In this study, the coke, coking process, optimization of quality parameters and its effect on blast furnaces in the Iskenderun Iron and Steel Co. (ISDEMIR) coke batteries were investigated.

1. Introduction

Coal is a type of rock formed by fossilizing plants with the effect of time and natural events. The main components of coal are carbon, hydrogen, oxygen, sulfur and nitrogen. Plants around marshes and water-containing soils begin to settle down after a certain period of time. Underground plants turn into gels by breaking down with appropriate temperature and humidity values over time. Thanks to the mud and sand around this jelly-like structure, it reacts and turns into a rock.Temperature is an important parameter for these reactions to take place and is obtained by natural events such as tectonic movements and plate movements. The shematical representation of the coaling is given in the Figure 1.

Coals have different chemical and physical properties according to the fossilization stages.These differences affecting the quality of coal caused the coal to be divided into groups such as peat, lignite, hard coal, anthracite and graphite. The coal type used for coking process is hard coke that is the highest quality coal with the highest calorific value. Since hard coal is a high calorie type, the energy obtained from hard coal is more than the energy obtained from lignite. The fact that it has high energy has provided many applications in the industry. It has great importance in providing energy to blast furnaces and producing liquid raw iron especially in iron and steel industry. Apart from these coals described above, there are non-fossil based coals such as charcoal and coke. Coking coal, on the other hand, is a type of coal that is not found in nature, obtained by chemical methods. It is a chemical product obtained by removing all the volatile components of hard coal at a certain time and pressure at certain temperatures and in an airless environment [1].

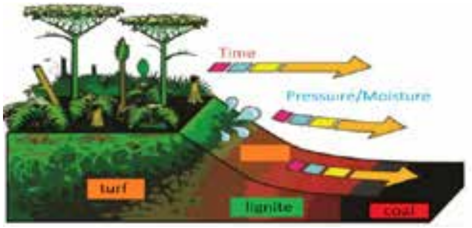

Figure 1: Shematical representation of coaling process

Coking coal is the most expensive and most important raw material, especially in the iron and steel industry. Coking coal obtained from this hard coal is the most widely used energy source in integrated iron and steel plants and there is no alternative source. The place where coke is most used is blast furnaces where liquid raw iron is obtained. Also, coke gas is one of the most important energy sources used in the operation of battery furnaces. In this study, the coking process, quality parameters and optimization for coking coal and the effect of coking coal on blast furnaces were investigated.

1.1. Coking Process and Process Steps

The coals used in the coking process must have certain parameters. The first step of the process is to supply suitable hard coal. More than one type of coal imported is passed through crushers and blended in certain proportions. The main reason for passing the coal through the crushers is to adjust its size, 80% of the coals to be used in the process is expected to be under 3 mm. The coals of the desired size are sent to the batteries for charging with the help of tapes. The coals coming into the batteries are charged according to the capacity. The capacity of the batteries varies between 20 and 32 tons. Capacity can be increased further, but it varies in all parameters that can affect the process depending on the capacity. Capacity is the most decisive factor in the design phase before the batteries are installed. All subsequent stages vary depending on capacity. Charging takes place continuously after each furnace is pushed in the batteries, after charging the furnaces according to a certain capacity, coking begins. The coking period also varies depending on the capacity. Coals coming to furnaces in certain proportions coke at a certain time and temperature. The coking period ranges from approximately 18-22 hours. In order to obtain coke in desired parameters, coking time should be optimized well [2].

Coking is the phenomenon of losing its volatile substances by heating the coal in an airless environment and forming a hard and porous structure. The product with a high percentage of carbon obtained as a result of coking is called coke. The coals charged to the coke ovens begin to coke with the heat, gases such as $CO2$ and $CH4$ are removed and thermal expansion begins. The heated coal starts to soften in the next stage. In this event, which takes place between 200-400 ºC, the volume of the coal becomes smaller, and the temperature increases towards the furnace center. Therefore, melting starts to occur towards the center and plastic zone is formed. As the temperature value reaches 450-550 °C, swelling occurs in the coal. Because in this temperature range, the plastic zone creates a barrier to the raw coke gas outlet. Consequently, coal swelling occurs because the coke gas is exposed to resistance. After the plastic zone hardens, the first half coking event occurs by forming a porous structure. The processes of graphitization and crack formation coke continue successively. In the light of this information, a schematic representation of the completed coking process is given in Figure 2.

Figure 2: Completed coking process

The plastic zone is the most decisive part in the coking process. In this section, semi-coking occurs. The plastic region is defined as the region which contains the softening, melting, shrinking, swelling, and the particles sticking to each other during the heating of the coal, and the final product is formed in the last stage. Good coking coal must have plastic properties and must necessarily include the specified steps. The energy source used in the coking process is coke gas. The coke gas produced during coking is used in the process again after a series of processes in the by-products facility. It contains approximately 4500 kcal / kg energy. In the system, blast furnace gas can be used as well as coke gas. Coal quality is the determining factor in coking, but operating conditions should not be forgotten. A good heating regime and coking times directly affect quality. The coking is inwards from the furnace walls and the combination of it from the middle point indicates that coking is completed well. The slip occurring in the middle of the furnace indicates whether coking is completed on one hand or not[3].

1.2 Coke Quality Parameters

The coke produced in the batteries is sent to the blast furnaces with the help of tapes to meet the energy needs. Coke is a universal fuel used in blast furnaces. It is also a very important parameter for production cost. No coke is obtained from every hard coal. Therefore, not every coke can be used in processes in blast furnaces. In order to meet the energy need during the production of liquid raw iron in blast furnaces, the produced coke must provide some quality parameters. The main quality parameters required for the produced coke can be listed as follows: moisture, ash, volatility, fixed carbon, sulfur content, stability, hardness, CRI, CSR, phosphorus, $Na2O$, $K2O$ etc.

The amount of moisture in the coke is very important. When 1% humidity increase occurs, it increases coke consumption by 5 kg per ton of pig iron. Therefore, the temperature of the air blown from the tuyeres should be increased by 100 ºC. Coke moisture must remain at a constant value. Because the heat balance of the furnace and the excessive cooling in the furnace directly affect the production of liquid raw iron. Ideally, the amount of moisture in the coke should be between 0 and 3%. Ash is the sum of the oxides formed by the inert materials remaining after the coal burns and has an inert structure. It also reduces the carbon content in the coke by an amount equivalent to its own. Therefore, it is undesirable to have ash in the structure of the coke to be used in blast furnaces. Ash increases the cost of the process in blast furnaces because it melts and passes to the slag, it is used with limestone because of its acidic character. Reducing the amount of ash in the coke by 1% saves 10 kg per ton of cast iron production. Alkalines such as $Na2O$ and $K2O$ reduce productivity in blast furnaces, reduces the load permeability and increases the coke rate to be used. It is necessary to pay attention to the alkali ratio in coal purchases, this ratio should not exceed 2%. Alkalines affect the oven operation in 3 ways: they reduce coke strength, they cause slippage and sling in the upper parts of the oven they penetrate and damage the refractory in the furnace structure. Phosphorus control is one of the most important features in quality parameters. Especially in coal purchases, coals with a phosphorus value below 0.06% are preferred. Sulfur content directly affects the quality of cast iron. According to the information obtained, 70 - 95% of sulfur comes from the coke. The amount of sulfur in the charge affects slag basicity, slag volume and temperature, oxygen potential (FeO + MnO) and iron quality. 1% increase in sulfur content in Blast Furnaces process causes 32 kg more coke consumption for hot metal production per ton. The amount of sulfur in metallurgical coke should not exceed 0.6% (± 0.17).

Coke reactivity (CRI) and coke resistance (CSR) are among the important variables affecting the furnace process. Coke reactivity can be expressed as the rate of the carbon in the coke to react with oxidizing gases such as air, CO2, O2 and steam. Increased coke reactivity will lead to excessive consumption of coke in the blast furnace, thereby increasing the coke consumption rate, and thus a decrease in blast furnace performance. The effect of coke resistance on blast furnace performance is quite high. Because the decrease in coke strength means that the coke breaks to smaller dimensions. The coke strength has an optimum value for certain furnace size and material composition used. If the coke strength is lower than this optimum value, it directly affects the coke rate and indirectly the production, efficiency of the furnace. ASTM stability value should be greater than 58% and ASTM hardness value should be greater than 65%. The fixed carbon content of the coke used in the process in blast furnaces is very important. This value is expected to be approximately 85-88%. High carbon content becomes an important step for the process by joining the structure of iron [4].

1.3 The Usage of Coke in The Blust Furnaces

The most commonly used energy source in blast furnaces is coke. Coal is used both as coke and as an injection fuel in blast furnaces. Quality coke required for efficient and efficient production in blast furnaces is obtained only from coals that have some features. Metallurgical coke generally meets the energy requirement in the blast furnace, helps the reduction processes and prevents the charging material from hanging. The role of this coke in blast furnaces is divided into 3 groups as physical, chemical and thermal. Its use in blast furnaces can be listed as follows: it is a heat source for chemical reactions, it helps to reduce iron oxide, provides CO formation, reduces metal and metal oxides, it allows the melting point to decrease as a result of the carburization process of iron, it provides permeability and provides mechanical support. It provides the passage of mines and slag to the chamber and hot gases to the top of the furnace [5,6].

The coke that will be used in blast furnaces should not be broken down during transportation processes. This coke should be so durable that it cannot be crushed under heavy working conditions of the blast furnace and under high pressure. The size of the coke should not be too large to burn as desired [7].

1.4.The Effect of Coke Features on Blust Furnace Productivity

Blast furnaces are 30-90m sized furnaces used for melting iron-containing raw materials with coke and limestone. Most of the steel production in the world takes place in blast furnaces. In order to obtain liquid raw iron in blast furnaces, materials such as ore, pellet and sinter are used as iron-containing raw materials. Raw materials such as lime powder and dolamite are used to obtain slag and adjust the properties of the slag obtained. Coke, tar and fuel oil are carbon-containing raw materials used to obtain heat. The average amount of coke required to obtain 1 ton of crude iron in blast furnaces is 450-800kg. The product obtained from blast furnaces is called pig iron, pig iron is obtained approximately 10-15h after the blast furnace is burned. Schematic representation of the blast furnace is given in Figure 3. Blast furnace consists of 5 parts: throat, body, waist, abdomen and chamber. There is a bell system with or without a bell in the upper area, so that the raw materials are input. If the raw materials expand with the effect of high temperature and pressure, the diameter of the body expands downwards so that they can move more comfortably. The waist region starts from where the body ends and its diameter is fixed, it is the widest part of the blast furnace. The melting of metals and slags begins in this region. In the next section, the abdomen is in the form of an inverted cone, the lower part merges with the chamber. Melting processes in the abdominal region are completed and slag is formed, then they accumulate in the chamber section. The shape of the blast furnaces used may differ, the parameters that are important in this change are the method, the temperature and the type of material used. Blast furnace auxiliary units are feeding systems, furnace charging system, injection system, control room etc. [8].

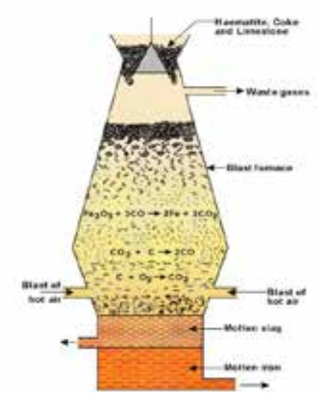

Figure 3 : Schematic representation oh blast furnace

Coking coal is one of the most important and most expensive raw material inputs among blast furnace charging materials. At the same time, coke has a very important place in iron and steel production. The chemical and physical properties of the coke used in blast furnaces affect blast furnace operating conditions, hot mine quality and fuel rate. Coke constitutes 55% of the total volume of the blast furnace and 75% of the reaction zone. Therefore, it is thought that 75% of the blast furnace problems in general are caused by coke. The operating performance of blast furnaces can change instantly depending on many parameters, so furnace operators must constantly check the process. In the process of blast furnaces, mechanical strength is the most important feature desired in coke, the coke must maintain its mechanical resistance against these harsh conditions. Moreover, in order to provide the high amount of heat required for blast furnaces, the carbon amount of the coke must be maximum, that is, the amount of ash, sulfur and volatile matter must be minimum [9]. As a result, if the quality of the coke used is low, the amount of flue gas transported increases, the gas permeability decreases and therefore the furnace internal pressure increases. Depending on all this, the production amount decreases, the furnace starts to work unbalanced, feather burns will occur. In order to avoid these, it is important that the coke has the desired quality parameter values.

2. Experimental Procedure

Short, elemental and thermal analyzes were performed to determine the quality and coking properties of coal in coal samples. After necessary sample preparations, physical and chemical analyzes of coal samples and metallurgical cokes were made in accordance with TSE standards at Coke Laboratory of Iskenderun Iron and Steel Co. (ISDEMIR). In this study, analyzes were performed for samples taken daily in January 2020. According to the results of the analysis, the average monthly values obtained for coke produced are 12.50% ash content, 0.98% volatility, 86.52% fixed carbon, 0.56% sulfur, 5.71% moisture, 56.08% stability, 65.19% hardness, 21.47% CRI, 69.09% CSR, 0.36% phosphorus and 0.83% alkali. For coking coal, the obtained average monthly values are 9.5% humidity, 9.75% ash, 25.26% volatility, 64.99% fixed carbon, 0.62% sulfur. Table 1 shows the values obtained for the coke and coking coal obtained in the 10th, 17th and 24th days from the analyzes made in this month.

Table 1: January 2020 coke and coal quality parameters analysis results

ANALYSIS	SAMPLE	10th. January	17th. January	24th. January
Moisture	Coal	9,10	9,20	9,20
	Coke	5,39	5,25	5,30
Ash	Coal	9,27	10,25	9,12
	Coke	11,6	12,15	12,25
Alkaline	Coal	🟥	🟥	🟥
	Coke	0,90	0,70	0,70
Phosphorus	Coal	🟥	🟥	🟥
	Coke	0,255	0,447	0,413
Sulphur	Coal	0,60	0,55	0,67
	Coke	0,58	0,55	0,54
Fixed Carbon	Coal	66	64,80	65
	Coke	87,20	86,60	86,70
Volatility	Coal	24,2	24,80	25,60
	Coke	0,90	1,15	0,95
Hardness	Coal	🟥	🟥	🟥
	Coke	66	64,90	65,65
Stability	Coal	🟥	🟥	🟥
	Coke	55,70	55,10	56,40
CRI	Coal	🟥	🟥	🟥
	Coke	22	21,70	21,30
CSR	Coal	🟥	🟥	🟥
	Coke	67,30	69,10	69,65

3. Results and Discussion

The quality and structure of the metallurgical coke obtained as a result of the coking process directly affects blast furnace working processes and blast furnace efficiency. The quality of the coke obtained depends on the structural and physical properties of hard coal used in coking processes. Moisture, ash, alkali amount, stability, CSR and CRI values of coke are effective in blast furnace efficiency and quality of the product obtained. If any of these values are not at the desired level in the metallurgical coke obtained, the efficiency of the blast furnace will be negatively affected, production stops and quality production becomes impossible. In coal purchases, especially ash, sulfur, alkali, phosphorus, moisture, fixed carbon, volatility values that affect the quality of metallurgical coke should be limited at certain intervals. Also, the petrographic properties, oxidation state and grain size distribution of coal must be thoroughly investigated before coal is purchased. It should be taken into consideration that the coal is at the lowest level in impurities such as sodium, potassium, iron, etc. The values obtained for coking coal and coke as a result of the analyzes are given in Table 1. It is undesirable that the increase in the amount of volatile substances will cause an increase in coke consumption in ovens. The acceptable amount of volatile matter is within the limits of 0.75-2% for coke. [10] The values obtained as a result of the 1-month analysis are close to the lower limit. The fixed carbon amount of the metallurgical coke to be used in blast furnaces should be in the range of 85-90%. [10] The values obtained in the analysis results vary between 86-87% and are among the desired values. The fixed carbon amount of coal that will provide this feature is in the range of 55-65%. Sulfur content of hard coal samples varies between 0.55-0.67%. In parallel, the sulfur values in the coke obtained range from 0.54% to 0.58%. It is an undesirable feature due to the acceleration of coke reactions and narrowing of the furnace volume in ovens with high total alkali. These values should be low in the coke obtained, values in analysis results change between 0.70-0.90%. The ash content of coals after coking is theoretically about 1.33 times compared to coal [11]. According to the results of the analysis, this ratio was found to be 1.26. Increasing the amount of moisture in coke is an undesirable feature, as it increases energy consumption in ovens. Coke reactivity is the rate at which the carbon in the coke reacts. Increasing CRI value, which is directly related to coal, increases the rate of coke to react in high blast furnaces, causes early combustion, decreases efficiency and increases coke consumption. The CRI value is aimed to be between 25-35%, the values obtained are close to the lower limit. CSR values obtained are in the range of 65-75%.

4. Conclusion

In this study, coking process, optimization of coke quality parameters and its effect on blast furnace were investigated. The physical and chemical properties of the coke obtained as a result of the coking process directly affect the process efficiency and the production of quality products in blast furnaces. The excessive amount of moisture in the coal requires more energy for the coking process and increases the transportation costs. The high amount of moisture in the coke is caused by the disintegration of the coke in the blast furnaces, the thermal balance cannot be achieved. The high ash content increases the slag volume and decreases the yield, so it is an undesirable feature. When the coke ash content is high, less products are obtained in blast furnaces and more energy is used. 80% of the amount of sulfur in coal passes into the coke, and the liquid obtained directly is a parameter affecting the quality of the raw iron. The alkali elements in the coal directly increase the reactivity of the coke and increase the disintegration rate of the coke in the blast furnaces. Therefore, the amount of coking coal and alkali in coke should be low. CRI and CSR values show the durability of the coke for the reactions occurring in the ovens. The CSR value represents the stability of the coke as a result of the reactions. Increasing this value reduces coke consumption in blast furnaces. Analysis shows that the hard coal used and the coke produced must have the specified specifications to not affect the blast furnace efficiency and ensure safe production without disturbing the flow of the process. These parameters should be taken into account during coal intake and coking processes.

5. References

[1] https://www.bilgeyik.com/komur-nasil-olusur-komur-cesitleri-nelerdir 281.

[2]https://acikders.ankara.edu.tr/pluginfile.php/109089/mod_resource/content/1/K%C3%B6m%C3%BCr%20Kokla%C5%9Fma%20Teknolojisi-2019.pdf

[3] Burak BULUT, Yüksek Fırınlarda Verim Artırmak Amacıyla Koklaşabilir Yerli Ve İthal Kömürlerin Optimum Harmanlama Özelliklerinin Belirlenmesi, Yüksek Lisans Tezi,Maden Mühendisliği Anabilim Dalı Adana, 2010.

[4] Díez, M. ., Alvarez, R., & Barriocanal, C. (2002). Coal for metallurgical coke production: predictions of coke quality and future requirements for cokemaking. International Journal of Coal Geology, 50(1-4), 389–412. doi:10.1016/s0166-5162(02)00123-4

[5]Doç. Dr. ÖZKAN ÖZDEMİR Doç. Dr. Uğur Özsaraç – Demır-Çelık Metalurjısı Ders Notu 2015.

[6]Bertling, H., Lanzer, W., & Lüngen, H. B. (1999). Coke quality and behavior of coke in the blast furnace. Revue de Métallurgie, 96(3), 295–308. doi:10.1051/metal/199996030295 .

[7]Prof.Dr.Kenan YILDIZ,Demir – Çelik Metalurjisi, Sakarya Üniversitesi/Metalurji Ve Malzeme Mühendisliği,Şubat 2017.

[8] Hardarshan S. Valia, Scientist, Coke Production For Blast Furnace Ironmaking,Ispat Inland Inc,

[9]Kojima, K., Nishi, T., Yamaguchi, T., Nakama, H., & Ida, S. (1977). Changes in the Properties of Coke in Blast Furnace. Transactions of the Iron and Steel Institute of Japan, 17(7), 401–409. doi:10.2355/isijinternational1966.17.401

[10] Graham, J.P., 1969, Specification of the Properties of Coke for Ironmaking: UK Blast-Furnace Coke Specifications,Conference on Coke in Ironmaking, The Iron and Steel Institute and the Institute of Fuel, London,

[11] AĞUŞ, M., 2008, Kardemir A.Ş. Kok Fabrikaları Tanıtım Notları, 6, Karabük (Kardemir A.Ş. Kok Fabrikaları, Arşivi)

Affects of Coke Quenching Methods on Coke Reactivity Index

Ömer ECE, Hüseyin ZÜMRÜT, Erman KAYA
İskenderun Demir ve Çelik A. Ş.
Turkey

Abstract

There are three types of quenching methods in traditional coke production. The Iskenderun Iron and Steel Co. (ISDEMIR) use dry and wet quenching methods in the coke plant. When laboratory test results of coke reactivity index are examined, the differences between two extinguishing techniques are attracting the attention. In this research, it is shown how the same coke battery oven, same blend and the same conditions affects the CRI by wet and dry quenching methods.

1. Introduction

Coke is produced by subjecting coking coals to heat in coke oven batteries in the absence of air. While coking, volatile matter of coal is extracted as coke oven gas (COG). COG is used as energy source in both heating of coke oven batteries and other units of an integrated iron and steel plant. The solid residue of coal carbonization, which is coke, has unique properties for blast furnace process that satisfy above necessities. Coke is a carbon rich fuel. The exothermic reactions below between coke and oxygen provides the heat needed to melt iron.

$2\ C + O_2 \rightarrow 2\ CO$ + heat

The product of the chemical reaction above,

carbon monoxide, reduces iron oxide.

$FeO + CO \rightarrow Fe + CO_2$

Carbon dioxide also reacts with carbon and regenerates reducing agent, carbon monoxide.

$CO2 + C \rightarrow 2\ CO$

There are four main parameters, which are standardized by ASTM, in evaluating coke quality. These are listed below with their ASTM standards and common targets.

1. Coke Stability (ASTM D3402) (> 60 %)
2. Coke Hardness (ASTM D3402) (> 70 %)
3. Coke Reactivity Index (ASTM D5341) (< 25 %)
4. Coke Strength After Reaction (ASTM D5341) (> 65 %)

There are also some coke quality parameters such as sulphur, ash, alkali content ($Na_2O + K_2O$) in ash etc., however, they are controlled by raw material selection and blend design. That is why these four parameters are more important.

Coke Reactivity, which is the subject of our research, is explained as the reaction rate of the carbon in the coke with the oxidizing gases. 200 g coke sample in a size range of -22,4 + 19 mm is subjected to CO_2 for 2 hours at 1100 °C. Percent of mass loss represents coke reactivity index. [1]

Figure 1. Hot coke view

The Iskenderun Iron and Steel Co. (ISDEMIR) coke plants have 2 different types of quenching systems called wet and dry quenching.

In coke wet quenching (CWQ) system, the red-hot coke (approx 1050 °C) extruded from the coke oven is cooled by spraying it with water. The water used for cooling is vaporized and released into the atmosphere. An issue with this system is the energy loss when the thermal energy of the red-hot coke is converted into heat that is vaporized andreleased unused. Another drawback is that the wet quenching system also produces airborne coke dust.

Figure 2. Wet Quenching System

In the coke dry quenching (CDQ) system, the red-hot coke is cooled by gas circulating in an enclosed system, thereby preventing the release of airborne coke dust. The thermal energy of the red-hot coke, which is lost in the CWQ system, is collected and reused as steam in the CDQ system. This technology uses less fossil fuel and results in lower CO_2 emissions, thereby contributing to the prevention of global warming. [2]

Figure 3. Dry Quenching System

2. Experimental Procedure

In order to examine the effects of the coke quenching method on the quality parameters, experiments have been made in industrial dimensions.

Isdemir Coke Battery No. 1 works with wet quenching system, while Battery No. 4 works with dry quenching system.

In our experimental study, the coke of Battery No. 4 quenched both in Battery No. 1' s wet quenching system and in its own system (CDQ).

During the experiments,

- Coal blend has not been changed.
- Made in the same coking conditions.
- Made in the same heating regime.
- Same coking period is used.
- The same ovens are used.

Samples taken under the above conditions were sent to the coke laboratory.

In the laboratory, coke quality parameters were examined within the ASTM standards.

3.Results and Discussion

The results reached after the experiments are given in the table below.

Table 1. Experiment results

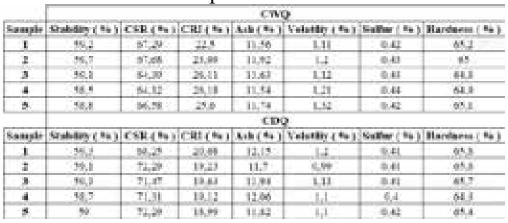

	CWQ						
Sample	Stability (%)	CSR (%)	CRI (%)	Ash (%)	Volatility (%)	Sulfur (%)	Hardness (%)
1	59,2	67,29	22,5	11,56	1,11	0,42	65,2
2	59,7	67,68	23,09	11,92	1,2	0,43	65
3	59,2	64,39	26,11	11,63	1,12	0,41	64,8
4	58,9	64,12	26,18	11,54	1,21	0,44	64,9
5	58,8	66,58	25,6	11,74	1,32	0,42	65,1

	CDQ						
Sample	Stability (%)	CSR (%)	CRI (%)	Ash (%)	Volatility (%)	Sulfur (%)	Hardness (%)
1	59,3	68,25	20,09	12,15	1,2	0,41	65,8
2	59,1	72,29	19,23	11,7	0,99	0,41	65,8
3	59,0	71,47	19,63	11,98	1,13	0,41	65,7
4	58,7	71,31	19,12	12,06	1,1	0,4	64,1
5	59	72,29	18,99	11,82	1,1	0,42	65,4

As seen in the table, coke quality parameters other than CRI and CSR are not affected by the quenching technique.

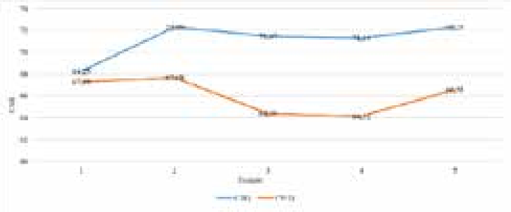

Figure 4. Variation of CSR in different quenching methods

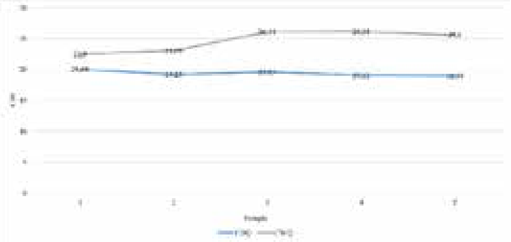

Figure 5. Variation of CRI in different quenching methods

As can be seen in the graphic above, the CRI value of the coke quenched in the CDQ system has decreased significantly.

It was seen that the results reached also support the literature.

4. Conclusion

When the experiments carried out in laboratory dimensions were applied under the conditions of the production facility, the results supporting each other were achieved.

Quenching the same coke with different techniques only created differences in CSR and CRI values.

In the literature, a high linear correlation between CRI and coke strength after reaction (CSR) values was observed. The relation between those two parameters analysed in the current study is presented in Figure 2. On the basis of the obtained data, it was observed that increase in CRI values resulted in the decrease in CSR; however, the correlation coefficient was lower than those obtained in the literature (R2 = 0.8157). Such low value could result from different origins of cokes obtained from different producers.

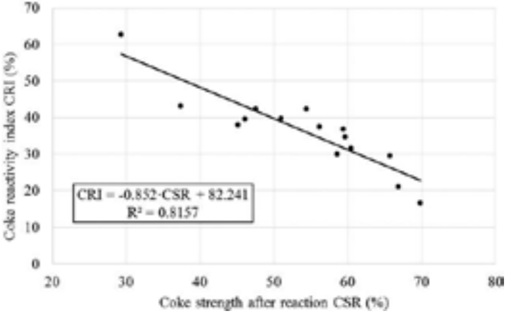

Figure 6. Relation between CRI and CSR

Reactivity is an indication of how quickly the coke reacts with CO_2 in the blast furnace, and thus how much it can maintain its mass. Coke reactivity in general terms; It can be defined as the rate at which the carbon in the coke reacts with typical oxidizing gases such as air, CO_2, O_2 and steam. It indicates the rate of conversion of carbon reacts with CO_2 gas under certain gas flow and temperature conditions to carbon monoxide (CO). Increased coke reactivity will lead to excessive consumption of coke in the blast furnace, thereby increasing the coke consumption rate and thus the decrease in blast furnace performance. When the high reactivity coke reaches the high temperature zone (raceway) region of the blast furnaces, it will decrease in quantity and reach a weak coke, will decrease the gas and fluid permeability in the raceway region, and will significantly decrease the furnace efficiency.

In wet quenching, the hot coke comes into direct contact with water (thermal shock), while more capillary cracks have been observed in the coke. During the cracked structure reactivity analysis, CRI value was high as it would react more with the carbon dioxide gas.

In dry quenching, the hot coke is gradually quenched with nitrogen gas for 8 hours. Less capillary cracks occur in the dry quenched coke compared to the wet quenched coke. It was observed that it decreased the CRI result due to the small structure with cracks. [3], [4], [5]

References

[1] B. Unsal, Investigation of Factors Affecting Coke Strength after Reaction (CSR) and Developing a Statistical Model for CSR Prediction

[2] K. Itakura, Introduction of Current Technologies for Coke Dry Quenching System

[3] K. Lech, S. Jursova, P. Kobel, P. Pustejovska, JiriBilik, A. Figiel & L. Romański, The Relation Between CRI, CSR Indexes, Chemical Composition and Physical Parameters of Commercial Metallurgical Cokes

[4] B. Bulut, Determination of Optimum Blending Characteristics of Coking Domestic And Imported Coals to Increase Productivity at Blast Furnaces

[5] Clean Coal Technologies in Japan, İron Making and General İndustry Technologies (İron Making Technologies); Part 2 CCT

Maintenance Management System Installation in Integrated Iron and Steel Plants & Innovative Approches

Hasan BULUT, Merih YAMAN, Serkan KESKİ, Ali KESKİN
İskenderun Demir ve Çelik A. Ş., Ereğli Demir ve Çelik A.Ş.
Turkey

Abstract
In order to increase the competitiveness of the companies and to ensure their continuity in the marketplace, the most important factor they have emphasized's been productivity. Maintenance of equipment, which is among the topics discussed in terms of efficiency, is an important element in order to ensure the facilities are sustainable and reliable. As a result of this, "Maintenance Management System" software becomes a necessity in order to plan, perform and monitor maintenance activities effectively and efficiently, to reduce the cost of unplanned downtimes, maintenance and inventory by cost analysis, to increase the useful lives of facilities and to contribute occupational health and safety.

In this study, the installation of common used Maintenance Management System in integrated iron and steel plants named Iskenderun Iron and Steel Co. (ISDEMIR) and Eregli Iron and Steel Co. (ERDEMIR) and the application of innovative approaches to maintenance processes with Industry 4.0 will be explained.

1. Introduction

First of all, it is important to state an essential issue; if we want to manage an event or a process, we have to make it measurable. In asset management, the best way is using computerized systems in order to get better measurement data.

Today, there are many different type of computerized asset management software solution in the market. Would it be a solution to buy such a ready software and apply it to our company? We must say with regret that the answer to this question is a huge no! For us, in order to have a successful computerized software application, the following issues must be resolved within the company;

- Awareness and support of top management
- A knowledgeable and experienced project team and team leader who knows what they want
- Software solution partner that can transfer the requirements into software as desired
- Employee profile who can adapt to change
- Technological infrastructure and IT support for Industry 4.0

Providing these conditions is a prerequisite for successful work. So what did we do? First of all, we can say that we have substantially met the conditions mentioned above. After this stage, we have prepared the general structure of fiction. Based on this fiction, we created the "analysis and conceptual design document" together with our software solution partner. In parallel with all these studies, we've worked to establish the infrastructure that can measure the process' critical success factors for our company. Ultimately, we designed effective reports. Today, we can say that we have the right tool to measure critical success factors and KPI values of the asset management process effectively.

Of course, it's not just software. The approach of stakeholders using this software, accepting the change, and internalizing the philosophy created is another matter. As we are aware of this situation, necessary information have been shared with the relevant stakeholders at every stage of the project, and project's been proceeded by providing all kinds of support.

2. Experimental Procedure

In this section, the main topics an asset management software should have are discussed separately:

2.1. Asset Tree Structure:

For the computerized maintenance management system application, it is primarily necessary to create a well-established asset tree structure. During this phase, you first need to decide how you want to track the assets. There are basically three types of information on each asset;

- Asset's main information
- Process information
- Performance information

Wherein said asset's main information is meant by; the definition of the asset, its type, the specification group, maintenance unit, maintenance plans etc. The healthier this information is the more productive work will be done. Likewise, the process information is any activity made and measurement information etc. on the asset. Finally, as process information occurs, automatically calculated performance information is generated on the equipment.

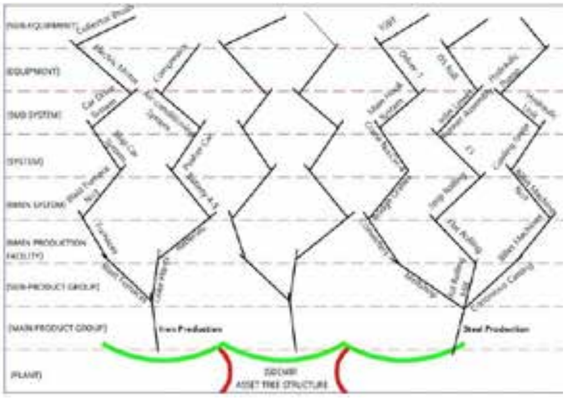

Figure 1. Tree Structure Breaks

Asset tree structure may vary depending on the structure of the company. All asset managers should decide together how many levels should the asset structure be depending on companies' needs. For the common approach, each level should be well-defined.

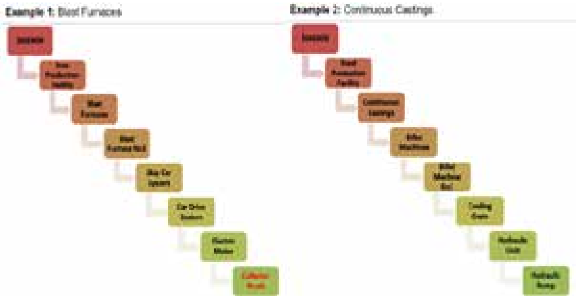

Figure 2. Examples of Tree Structure

2.2. Classification of Assets:

After the asset structure is created, the most important issue is the classification of the assets. With a properly made classification study, the company will be able to focus on business' prioritized jobs, inventory optimization and improvement plans in the most effective way independent of individuals.

The classification here means the importance level of a system, machine or equipment for the company. For example, assets could be classified as;

- Critical
- Important
- Normal

Determining the classification parameters of the assets in advance and embedding it in the software is very important. It is also important to well-define the parameters and spread it through the stakeholders effectively. It is precisely the case for the software to update these classifications over time. The participation of all departments responsible for asset management in these studies should be adopted as an indispensable admission. Where necessary, support should be obtained from Occupational Health and Safety, Environmental and Quality Departments.

In particular, a risk-centered equipment classification will reveal a more dynamic structure. Each equipment will be replaced in probability x intensity matrix and the most appropriate class will be selected. Using probability in the calculation here will allow you to classify your equipment according to the risk status, which is exactly the target level of maturity.

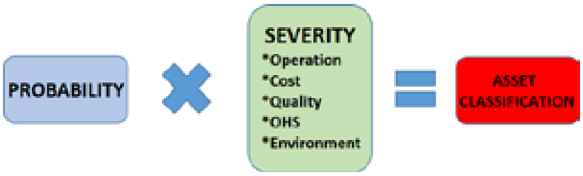

Figure 3. Asset Classification Calculation Logic

Table 1. Environmental Impact Probability v. Severity Matrix

ENVIRONMENT		PROBABILITY				
		1	2	3	4	5
SEVERITY	1	1	2	3	4	5
	2	6	7	9	10	11
	3	8	12	13	14	15
	4	16	17	18	19	20
	5	21	22	23	24	25

In asset classification, each dimension should be examined separately and finally a consolidated result should be revealed.

Table 2. Risk-Centered Asset Classification

ASSET DEFINITION			PROBABILITY	SEVERITY							CRITICALITY					TOTAL	Maintenance Approach	
				OPERATION		COST	QUALITY	OHS	ENVIRONMENT									
Level of Tree Structure	Upper Location Definition	Asset Definition	Failure Frequency	Production Loss	Process Impact	Cost Impact	Quality Loss	Safety risk	Enviton mental Impact	OPERATION	COST	QUALITY	OHS	ENVIRONMENT			Maintenance Plan	Spare Part Requirement
Ekipman	Ana Kaldırma Sistemi	Elektrik Motoru	1	2	5	1	1	1	2	15	1	1	1	6	24	Preventive Maintenance (predictive maintenance is mandatory)	Strategic Reserve
Ekipman	Ana Kaldırma Sistemi	Elektrik Motoru	1	2	5	1	1	1	2	4	1	1	1	2	9	Preventive Maintenance (predictive maintenance is mandatory)	Strategic Reserve
Ekipman	Bobin Sarma Sistemi	Pinch Roll	1	1	5	1	2	1	1	15	1	6	1	1	24	Preventive Maintenance (predictive maintenance is mandatory)	Strategic Reserve
Ekipman	Descale Sistemi	Descale Pompa	2	1	5	1	2	2	3	15	2	7	7	11	42	Preventive Maintenance (predictive maintenance is mandatory)	Strategic Reserve
Ekipman	Vinç Ana Besleme Sistemi	AFE	2	1	3	1	1	3	1	7	2	2	12	2	25	Preventive Maintenance	Depends on Requirement
Ekipman	Konverter Devirme Sistemi	Dişli Kutusu	1	3	5	5	1	1	1	15	13	1	1	1	31	Preventive Maintenance (predictive maintenance is mandatory)	Strategic Reserve
Ekipman	Elektrik Odası İklimlendirme Sistemi	Elektrik Odası Kliması	3	1	4	1	1	1	1	13	3	3	3	3	25	Preventive Maintenance	Necessary
Ekipman	Gemi Doldurma Sistemi	Katran Pompası	2	1	3	1	1	2	4	7	2	2	7	13	31	No resource allocated until it enters the first 20% asset group	None
Ekipman	İtici Araba İklimlendirme Sistemi	MCC Odası Kliması	3	1	4	3	4	1	1	13	15	19	3	3	53	Preventive Maintenance (predictive maintenance is mandatory)	Strategic Reserve
Ekipman	Kepçe Sistemi	Halatlı Kepçe	3	4	4	1	1	1	1	19	3	3	3	3	31	Preventive Maintenance (predictive maintenance is mandatory)	Strategic Reserve
Ekipman	Lans Sistemi	Lans	5	2	4	1	1	1	1	17	9	5	5	5	41	Preventive Maintenance (predictive maintenance is mandatory)	Strategic Reserve
Ekipman	Köprü Yürütme Sistemi	Sürücü	3	1	1	5	1	1	1	3	20	3	3	3	32	Preventive Maintenance (predictive maintenance is mandatory)	Strategic Reserve
Ekipman	Ana Kaldırma Sistemi	Dişli Kaplin	2	2	2	2	1	4	3	7	5	2	18	11	43	Emergency Plan + Preventive Maintenance	Depends on Requirement
Ekipman	İtici Araba Hidrolik Sistemi	Hidrolik Pompa	3	1	4	3	3	1	3	13	15	13	3	14	58	Preventive Maintenance	Necessary

2.3. Preventive Maintenance:

Preventive maintenance activities are basically divided into two classes. These are;

- Periodic maintenance conducted by maintenance units
- Autonomous maintenance conducted by operational units

The main expectation from preventive maintenance is to provide the highest performance level and reliability of the assets with optimum maintenance cost.

Figure 4. Acquisitions of Preventive Maintenance

All preventive maintenance activities of an asset should be defined together by all relevant departments and the performance of those activities should constantly be monitored. If necessary, revisions on preventive maintenance definitions should be done as soon as possible.

Preventive maintenance definitions, which is one of the most important issues in any asset management software, should be tailored to the requirements. Preventive maintenance work orders should be created automatically from the system based on defined calendar, measurement and/or asset's status. In order for an effective resource planning, the upcoming preventive maintenance activities should be identifiable and traceable to guide relevant units.

Figure 5. Types of Preventive Maintenance

The preventive maintenance types conducted by the maintenance units are given in Figure 5. Similarly, autonomous maintenance should be defined by the operators of the machines and the maintenance activities defined by both operational and maintenance groups should be synchronized and complement each other.

2.4. Source Applications:

There are various resources used during the maintenance activities that are carried out in order to have the maximum asset performance level. Accessing these resources from a single point, planning and optimization are expected from a good asset management software. These sources are;

- Manpower
- Spare Parts
- Insourcing
- Outsourcing
- Auxiliary equipment

Every user responsible for asset management should have access to the specified resources from a single point. Moreover, with mobile applications, users should be able to access the system at any time, wherever they are.

Figure 6. Mobile Application Screens

2.5. Special Applications:

Nowadays, it is expected that the asset management software will have different features other than maintenance records. In this section, some features that have been specially developed in the asset management software of Oyak Mining and Metallurgy Group (OMMG) will be examined.

1) Breakdown Inspection Form: What does breakdown means? It is the first issue that should be emphasized precisely to know this definition within the company. Especially in very large companies, if this definition is not the same for everyone, a holistic approach is often not shown.

The breakdowns' effect should be able to be classified on the software and the classification conditions should be changed dynamically. The root cause analysis of company's major breakdowns should be done and recorded in the asset management software.

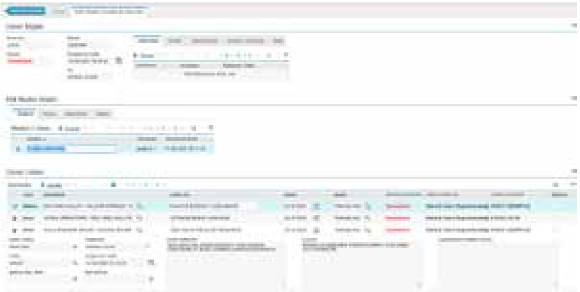

Figure 7. Breakdown Inspection Form

The form should allow root cause analysis to be analyzed in different dimensions, such as human, method, material and machine, within at least 5 steps. In addition, it should be suitable for collective studies and include the approval processes. The tasks and the deadlines for the correction of the root causes determined should be traceable.

2) Planned Shutdown Application: In integrated facilities, maintenance work generally concerns too many teams and needs to be done on a planned basis. It is important that a planned maintenance to be performed in any facility can be planned, implemented and the results can be monitored by all stakeholders within the scope of asset management software.

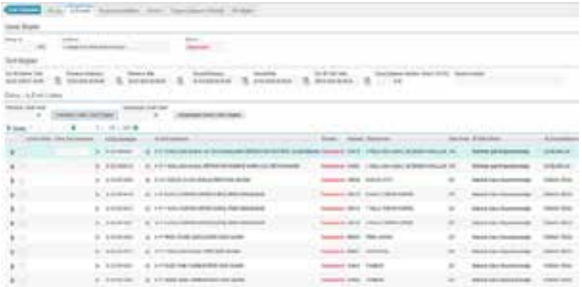

Figure 8. Planned Shutdown Application

A planned shutdown application should have the following features;

- All units that will operate in the specific planned shutdown should be able to reach the specific record and enter their planned work orders within system.
- Resource analysis of all planned works should be possible.
- Planned shutdown should enable communication via auto e-mails.
- Planning and implementation should be done visually with the Gantt Chart feature.
- Monitoring of planned shutdown performance should be possible.
- The timeline should be systematically trackable.

3) Calendar Application: One of the most important issues in integrated facilities is to ensure that planned shutdowns, preventive maintenance and future tasks should able to be monitored.

Figure 9. Asset Planned Maintenance Calendar Application

For this purpose, calendar application has been developed in OMMG Asset Management software. With this application, the tasks (work orders, preventive maintenance tasks, planned shutdowns etc.) to be performed in any facility in the future periods and the tasks that any unit should perform in the future can be seen on a single screen.

The users can run the application for each/all of the following three topics;

- Planned shutdowns
- Preventive maintenance activities
- Planned work orders

Each time the user runs the application, they can get into the details of related tasks and analyze their resource needs for any time period, instantly.

4) Asset Health and Industry 4.0 Application: A successful asset management system software should be able to keep up with new technologies and changes, easily and effectively. This topic is gathered under two main topics within the scope of OMMG asset management system software.

- Data acquisition from sensors on assets
- Online monitoring of asset health

In a traditional asset management software, preventive maintenance is generally triggered on a calendar basis. Maintenance staff take manually the measurement data from field and process data through the system. With the feature of the software, it is possible to transfer all kinds of instant and cumulative measurement data from sensors to the software. For example, the temperature information of an asset, the production quantity of a facility, etc. These data are then used in any action desired, such as triggering measurement-based preventive maintenance.

Asset health is another topic that we emphasize with a special emphasis. With this application, the health of many equipment, especially critical equipment, can instantly be tracked over the given parameters. Our technical staff who are experts in their fields carry out determination of parameters and mathematical calculation methods. As a next step, artificial intelligence studies have been partially started.

Impact of Asset Age on Health 20%

Life Expectancy : 20 years
Installation Date : March 2010
Equipment Age : 10 years
Score : 50%

Impact of Asset's Working Time on Health 30%

Exp. Working Time : 20.000 h
Asset Work. Time : 5.000 h
Formula [illegible]
Score : 75%

Impact of Asset's Vibration Value on Health 40%

Vibration : 6 mm/sn2
Formula : [illegible]
Score : 65%

Impact of Ambient Temperature on Asset Health 10%

Ambient Temp. : 20 degrees
Formula [illegible]
Score : 98%

ASSET HEALTH
(50%*20%) + (75%*30%) + (65%*40%) + (98%*10%)
68%

Figure 10. Asset Health Calculation Example

2.6. Reports:

All reports from the software are designed by project team members. Each report has its own authorization group and some reports are sent via auto e-mail to the relevant people and groups at certain times. Basically, the reports measure two main results;

- Critical success factors of asset maintenance management
- Asset management KPIs

Report examples;

- Asset Performance Reports
- Asset Cost Reports
- Executive Summary Report (via e-mail)
- Cockpit Report
- Preventive Maintenance Analysis Reports
- Planned Shutdown Performance Report
- Breakdown Inspection Form Efficiency Report
- Activity Impact Analysis Report

3. Conclusion:

Nowadays, it has been inevitable for companies to use computerized software to manage their assets. A computerized maintenance management system is a valuable tool to help companies to increase asset life, reduce the cost of maintenance, improve productivity, reduce downtime and lower the total cost of assets' ownership. However, in order to achieve successful results, besides the use of the software, it is also important to design the software in accordance with the company's mission, vision and strategies.

This article describes the importance of computerized maintenance management software (CMMS) and its installation and implementation in integrated iron and steel plants named Iskenderun Iron and Steel Co. (ISDEMIR) and Eregli Iron and Steel Co. (ERDEMIR).

The main issues to be considered during the identification process of the required software and the features that should be included in the asset management software are explained in detail. In particular, the importance of all processes and resources required in asset management on a single system are specified. In addition, Industry 4.0 applications in asset management and the outcomes of these applications were emphasized. Given all these points, with the right tool and the right conceptual design, a CMMS software can be capture critical data for making good decisions to help your company save time and money.

References

[1] IBM Maximo Enterprise Asset Management (EAM) Software
[2] ISDEMIR Risk-Centered Equipment Leveling Guide Dated: 26.11.2018
[3] ISDEMIR Maintenance Management Procedure Dated: 18.10.2019

Analysis of Annealing & Pickling Processes for AISI 304 Stainless Steel Sheet Corrosion Resistance

Onur AY[1], Ayşegül BİLEN[2], Erdem GÜLER[1], Bedirhan GÜRAYDIN[1], Hamdi EKİCİ[1],
İ. Cemre TÜRÜ[2], Eda DAĞDELEN[1]
[1]Trinox Metal San. ve Tic. A.Ş., [2]Yıldız Technical University
Turkey

Abstract

AISI 304 quality stainless steel has become an indispensable material for daily use thanks to its high corrosion resistance, high heat conductivity, formability and visual properties [1-2]. Stainless steel flat materials are produced with hot rolling, annealing and cold rolling after the casting process and then it is prepared for service processes by ensuring annealing and surface passivation.
In this study, the effect of annealing temperature, time and the difference of acidification processes on the corrosion resistance of the material is investigated.

1. Introduction

1.1. Surface Passivation in Stainless Steel

The next stage in stainless steel plate production is surface passivation after cold rolling process. Surface passivation is usually done in 2 phases. In the first stage, the descaling which caused by the annealing process on the surface of the plate with a specific acid solution is resolved.
After that, descaling surface will be passivated with a specific acid solution. Thus, the material will regain its stainless property.

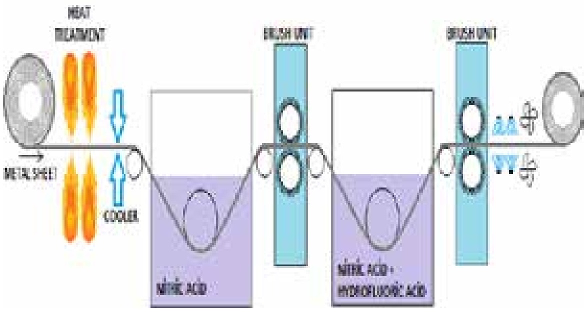

Figure 1: Trinox Metal Annealing and Pickling Process Machinery

In the passivation process, the material is submerged in nitric acid for firstly descaling operation and surface is prepared to passivation. The following reactions occur here:

$$Fe + 4H^+ + NO^-_3 \rightarrow Fe^{3+} + NO + 2H_2O$$
$$Cr + 4H^+ + NO^-_3 \rightarrow Cr^{3+} + NO + 2H_2O$$
$$3Ni + 8H^+ + 2NO^-_3 \rightarrow 3Ni^{2+} + 2NO + 4H_2O$$

The material is submerged in nitric asid and hydrofluoric acid tank fort he passivation after the nitric tank operation. In this bath, following reactions occur:

$$Fe + 4H^+ + NO^-_3 \rightarrow Fe^{3+} + NO + 2H_2O$$
$$Cr + H^+ + NO^-_3 \rightarrow Cr^{3+} + NO + 2H_2O$$
$$3Ni + 8H^+ + 2NO^-_3 \rightarrow 3Ni^{2+} + 2NO + 4H_2O$$

$$3HF + Fe^{3+} \rightarrow FeF_3 + 3H^+$$
$$2HF + Fe^{3+} \rightarrow FeF_2^+ + 2H^+$$
$$3HF + Cr^{3+} \rightarrow CrF_3 + 3H^+$$
$$2HF + Cr^{3+} \rightarrow CrF_2^+ + 2H^+$$
$$HF + Ni^{2+} \rightarrow NiF^+ + H^+$$

The schematic representation of the reactions is given in figure 2. [3]

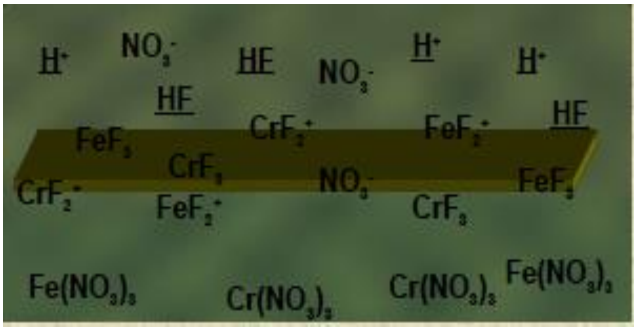

Figure 2: Chemical reactions in the pickling process

In this point, HNO3 is used as H^+ Source, oxidizing and shining agent. HF is used as a complex agent for $Fe^{3+,}$ Cr^{3+}, $Nİ^{2+,}$ and H $^+$Supplier.

The physical effect of the HNO_3 / HF mixture on the surface of the sheet is like in Figure 3. [3]

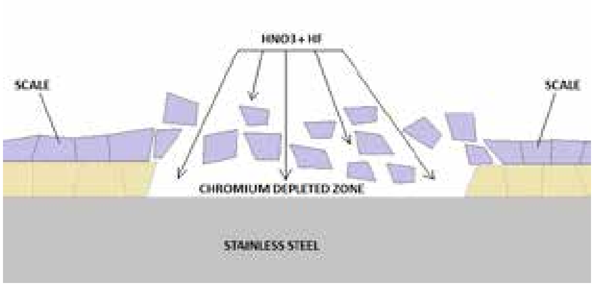

Figure 3: Effect of pickling chemicals on material surface

The relationship between the acid concentration and the concentration of metal in the acid baths should be under control to make the passivation process well done. [4]

Figure 4 shows the areas belonging to this relationship, and in Figure 5 shows the surface images of the plate that arise depending on these regions.

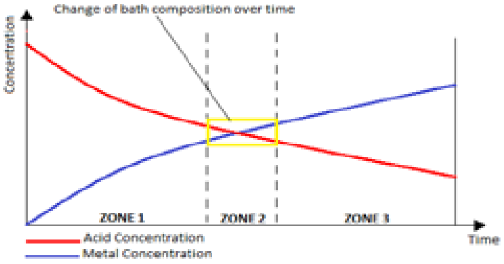

Figure 4: Connection of metal and acid concentrations

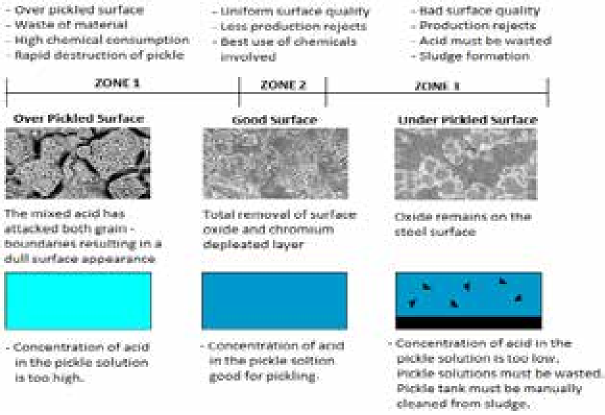

Figure 5: Material surface depending on metal amount and acid concentrations [4]

1.2. Pitting Corrosion in Stainless Steel

Corrosion is an electrochemical phenomenon that causes various problems depending on the conditions in which the engineering alloys are used. Stainless steels are also alloys produced for conditions where corrosion resistance is required. Although stainless steels have good corrosion resistance alloys, the conditions of use and unsuitable operations on the material surface can cause undesirable consequences.

Corrosion resistance of stainless steel is most fundamentally dependent on alloying elements. Then, the surface layers resulting from process conditions become important for corrosion. [5]

Especially in aggressive conditions or when the surface is subjected to a physical effect along with a chemical effect, the protective passive layer is deteriorated by a localized effect, resulting in a very narrow area of pitting corrosion.

The determination of this type of corrosion is difficult and a dangerous situation occurs because it handles the material from very small areas to the inside

On the basis of pitting corrosion which is a type of galvanic corrosion due to the potential difference of electrochemical between the weakened passive layer and the strong passive plate. As corrosion progresses, the weaker passive layer becomes weaker, In this case, the potential difference of the electrochemical between the weak layer and the strong layer will increase more. The corrosion of the pitting will progression rapidly increasing.

This is the direction that makes the çukurcuk corrosion aggressive. Starting from a very small area, it is difficult to detect and quickly processes the material deeper into the material. And there will be no significant weight loss during this time, so the progressive corrosion may not be detected. [1].

The nonmetallic structures contained in the environment are not sufficient to initiate the pitting corrosion alone. Especially the presence of an oxidizing catheter (Fe^{3+}, Cu^{2+}, Hg^{2+} etc.) creates a reaction starting point for weak areas in the protective layer. However, especially in the presence of oxygen, all chlorides become dangerous. In the environment where there is an oxygen or an oxyhydrogen component, the corrosion of the pitting becomes much more aggressive.[6]

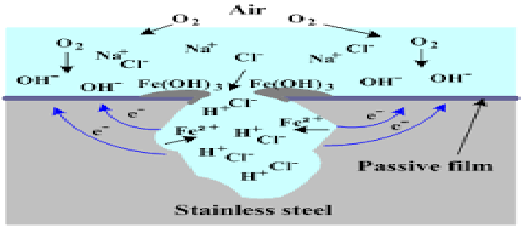

Figure 6: Pitting corrosion apperance [7]

Austenitic stainless steels are the largest and most important group in the stainless steel family. Austenitic stainless steels are alloys with high welding ability, high formability capabilities as well as high corrosion resistance

As the passive chromium oxide layer on the surface provides corrosion resistance. The nickel element in the inner structure stabilises the austenitic phase, preventing carbide precipitating and releasing the chrome. Thus, even if the passive chromium oxide layer on the surface is grazed by a mechanical effect, a passive chromium oxide layer may occur again in the same region.[3]

But over time, this resistance can be broken. In different conditions, the material may become corrosion resistant. This is an acceptable state of engineering for stainless steels; The important thing is to produce the appropriate material in the appropriate process conditions and to find optimum harmony with the environmental conditions [4-5]

There are basically 2 ways to protect the material from corrosion because it is caused by the interaction between the environment and the material.

1. Create appropriate environmental conditions
2. Create a layer of passive film as uniform and deep as possible on the surface of the material [5]

The aim of this study is to create the appropriate material surface as stated in article 2.

2. Experimental Procedure

2.1. Prepare to sample

15x20 cm in size 54 pieces of the 304 stainless steel plate samples are processed annealing operation in different temperature and times in the laboratory type of furnace. Then, the samples are cooled in the air environment. (54 pieces are 0,9 mm thickness)
The work was conducted in the Trinox Metal product and process development laboratory. A passivation process with H_2SO_4, HNO_3 and HNO_3/HF solutions was applied to the annealing specimens at different time and concentrations, respectively.

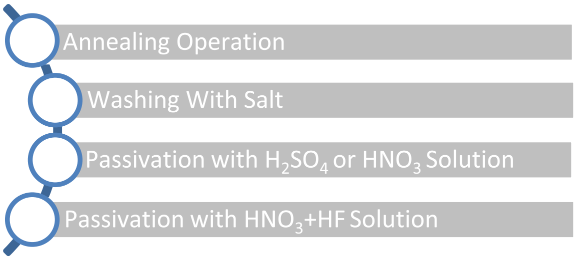

Figure 7. Sample processing steps

Figure 8. Sample appearance after annealing process

2.2. Comparative Corrosion Test

The prepared specimens are insulated to be tested for the surface area of 25 cm^2 for corrosion testing. Isolated specimens weighed.

Figure 9: Weighing of prepared material

Samples were placed in pools containing 3.5% NaCl solution. The uninsulated area has been considered to be immersed in the pool.

Figure 10: Placement of samples

Samples and cathodes are connected to the power supply set according to the circuit connection in Figure 11.

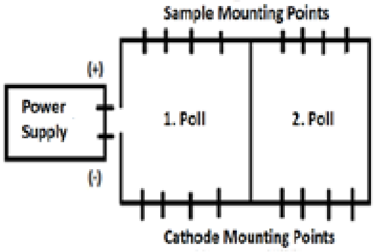

Figure 11: Circuit connection type

After making the necessary connection, 4A Current was given and corrosion test was carried out 0,5 hour.

3. Results and Discussion

3.1. Hardness Test Result

Table 1. Experimental Data of Hardness

Subject	Temperature	Annealing Time (s)	Hardness(Hv1)
1	1100	164,0473628	146
2		164,0473628	152
3		164,0473628	149
4		164,0473628	147
5		164,0473628	144
6		164,0473628	144
7		164,0473628	148
8		164,0473628	145
9		164,0473628	146
10		99,02534113	155
11		99,02534113	154
12		99,02534113	158
13		99,02534113	157
14		99,02534113	156
15		99,02534113	155
16		99,02534113	153
17		99,02534113	155
18		99,02534113	154
19		164,0473628	149
20		164,0473628	147
21		164,0473628	144
22		164,0473628	146
23		164,0473628	147
24		164,0473628	147
25		164,0473628	144
26		164,0473628	148
27		164,0473628	146
28		99,02534113	150
29		99,02534113	153
30		99,02534113	157
31		99,02534113	156
32		99,02534113	152
33		99,02534113	155
34		99,02534113	154
35		99,02534113	155
36		99,02534113	153
37	900	99,02534113	195
38		99,02534113	188
39		99,02534113	190
40		99,02534113	191
41		99,02534113	191
42		99,02534113	179
43		99,02534113	188
44		99,02534113	181
45		99,02534113	190
46		99,02534113	190
47		99,02534113	191
48		99,02534113	183
49		99,02534113	191
50		99,02534113	183
51		99,02534113	189
52		99,02534113	195
53		99,02534113	186
54		99,02534113	192

3.2. Surface Roughness Test Result

Table 2. Experimental Data of Roughness

Subject	Temperature	Annealing Time (s)	Rz
1	1100	164,0473628	5327
2		164,0473628	7816
3		164,0473628	5891
4		164,0473628	6773
5		164,0473628	7179
6		164,0473628	6409
7		164,0473628	2957
8		164,0473628	8133
9		164,0473628	5792
10		99,02534113	8428
11		99,02534113	4202
12		99,02534113	6015
13		99,02534113	4656
14		99,02534113	7020
15		99,02534113	6424
16		99,02534113	4037
17		99,02534113	2860
18		99,02534113	7387
19		164,0473628	2476
20		164,0473628	2698
21		164,0473628	1262
22		164,0473628	1067
23		164,0473628	2485
24		164,0473628	1937
25		164,0473628	2731
26		164,0473628	2561
27		164,0473628	1973
28		99,02534113	3729
29		99,02534113	2240
30		99,02534113	2545
31		99,02534113	2366
32		99,02534113	2983
33		99,02534113	2225
34		99,02534113	2698
35		99,02534113	2107
36		99,02534113	4662
37	900	99,02534113	1969
38		99,02534113	1084
39		99,02534113	1646
40		99,02534113	1705
41		99,02534113	1773
42		99,02534113	881
43		99,02534113	1222
44		99,02534113	1082
45		99,02534113	1314
46		99,02534113	808
47		99,02534113	675
48		99,02534113	1039
49		99,02534113	1388
50		99,02534113	510
51		99,02534113	1674
52		99,02534113	996
53		99,02534113	1867
54		99,02534113	1,774

3.3. Corrosion Test Result

Table 3. Experimental Data of Corrosion

Subject	(%15 Sulphiric) + (%2,5 HNO3 + %0,5 HF)	(%15 Sulphiric) + (%5 HNO3 + %1 HF)	(%15 Sulphiric) + (%7,5 HNO3 + %1,5 HF)	(%7,5 HNO3) + (%2,5 HNO3 + %0,5 HF)	(%7,5 HNO3) + (%5 HNO3 + %1 HF)	(%7,5 HNO3) + (%7,5 HNO3 + %1,5 HF)	Corrosion Variation
1	54,66 x 109,32						5
2	54,66 x 109,33						3
3	54,66 x 109,34						2
4		54,66 x 109,32					7
5		54,66 x 109,33					1
6		54,66 x 109,34					4
7			54,66 x 109,32				8
8			54,66 x 109,33				6
9			54,66 x 109,34				4
10	33x66						4
11	33x66						4
12	33x66						2
13		33x66					5
14		33x66					7
15		33x66					6
16			33x66				2
17			33x66				4
18			33x66				2
19				109,32 x 109,32			4
20				109,32 x 109,33			2
21				109,32 x 109,34			4
22					109,32 x 109,32		2
23					109,32 x 109,33		4
24					109,32 x 109,34		5
25						109,32 x 109,32	6
26						109,32 x 109,33	5
27						109,32 x 109,34	4
28				66x66			3
29				66x66			4
30				66x66			6
31					66x66		3
32					66x66		6
33					66x66		5
34						66x66	5
35						66x66	5
36						66x66	2
37	33x66						2
38	33x66						8
39	33x66						4
40		33x66					8
41		33x66					3
42		33x66					3
43			33x66				3
44			33x66				9
45			33x66				5
46				66x66			4
47				66x66			10
48				66x66			5
49					66x66		21
50					66x66		6
51					66x66		11
52						66x66	4
53						66x66	1
54						66x66	4

4. Conclusion

4.1. Hardness

Regression Equation in Uncoded Units

Hardness = 353,35 - 0,16972 Temperature - 0,1222 Annealing Time

Analysis of Variance

Source	DF	Adj SS	Adj MS	F-Value	P-Value
Model	2	35640,2	17820,1	1936,08	0,000
Linear	2	35640,2	17820,1	1936,08	0,000
Temperature	1	20740,1	20740,1	2253,32	0,000
Annealing Time	1	1136,1	1136,1	123,43	0,000
Error	105	966,4	9,2		
Lack-of-Fit	2	181,9	90,9	11,94	0,000
Pure Error	103	784,6	7,6		
Total	107	36606,7			

Model Summary

S	R-sq	R-sq(adj)	R-sq(pred)
3,07814	97,36%	97,23%	97,04%

4.2. Roughness

Regression Equation in Uncoded Units

Roughness Rz = -6186 + 6,28 Temperature + 17,50 Annealing Time

Coded Coefficients

Term	Coef	SE Coef	T-Value	P-Value	VIF
Constant	2554,7	77,7	32,87	0,000	
Tav Sıcaklığı	541,0	77,7	6,96	0,000	1,33
Daldırma Süresi	566,7	77,7	7,29	0,000	1,33

Model Summary

S	R-sq	R-sq(adj)	R-sq(pred)
659,516	67,20%	65,59%	63,23%

4.3. Corrosion

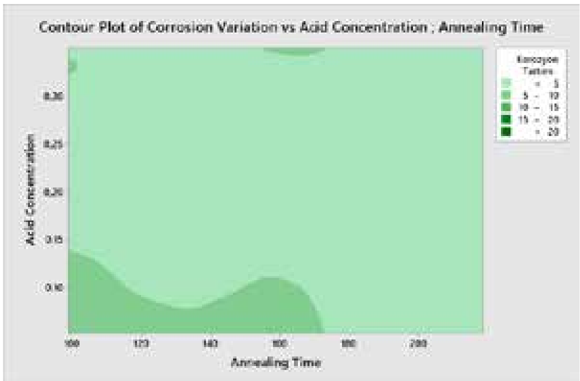

Figure 12: Relatinship Between Temperature-Annealing Time-Acid Concentration and Corrosion Variation

4.4. SEM Images

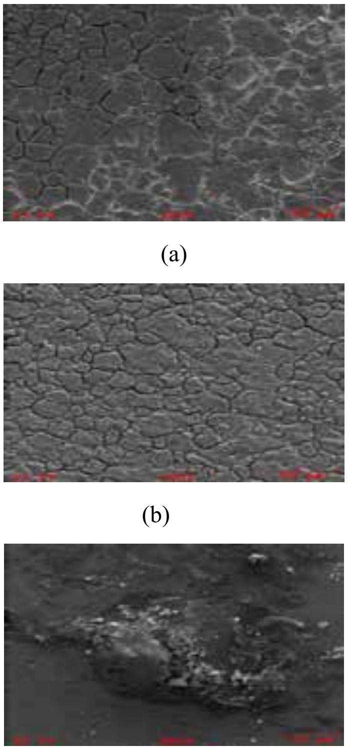
(a)

(b)

(c)

Figure 13: (a) 1100 C, 164s, %15H2SO4, %2,5HNO3+%0,5HF Process Subject No:1 (It is pickled surface) and **(b)** 1100 C, 99s, %15H2SO4, %2,5HNO3+%0,5HF Process Subject No:1 (It is pickled surface) **(c)** 900 C, 99s, %15H2SO4, %2,5HNO3+%0,5HF Process Subject No:1 (It isn't pickled surface) [4]

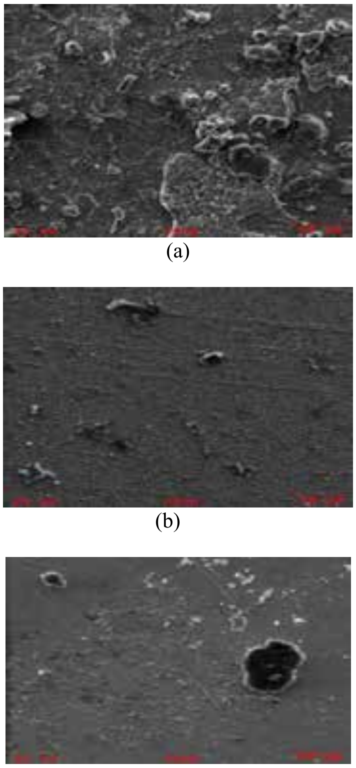
(a)

(b)

(c)

Figure 14: **(a)** 1100 C, 164s, Process Subject No:1 (It isn't pickled surface) and **(b)** 1100 C, 99s, Process Subject No:1 (It isn't pickled surface) **(c)** 900 C, 99s, Process Subject No:1 (It isn't pickled surface)

References

[1] European Steel Technology Platform (ESTEP). Strategic Research Agenda. A Vision for the Future of the Steel Sector; European Commission: Brussels, Belgium, 2005

[2] Andersson, R.; Schedin, E.; Magnusson, C.; Ocklund, J.; Persson, A. Stainless steel components in automotive vehicles. In Proceedings of the 4th European Stainless Steel Science and Market Congress, Paris, France, 10–13 June 2002; p. 57.

[3] Pitting Corrosion, Multimedia corrosion guide 2nd edition,http://www.cdcorrosion.com/mode_corrosion/corrosion_pitting.htm

[4] Fossati, A., Borgioli, F., Galvanetto, E., Bacci, T., Corrosion resistance properties of glow- discharge nitrided AISI 316L, austenitic stainless steel in NaCl solutions. Corrosion Science 48(6), 1513-1527 (1996)

[5] Gouda, V.K., Hashem A, Al. International Conference on Advances in Corrosion and Protection, UMIST, UK (1992)

[6] Szklarska-Smialowska, Z. Pitting Corrosion of Metals, NACE, Houston (1986) 218

[7] Willert-Porada M. Electrochemical Metal Corrosion. http://www.lswv.unibayreuth.de/de/download/documents/skripten/Electrochemical_Metal_corrosion.pdf

Centralization and Reduction of Human Factor in the Control of Water Supply and Circulation Plants in the Iron and Steel Industry

İsmail GÜVEN, Erkin Yekda GEDİK, Engin KARABEYOĞLU, Gencer BİRKAN
İskenderun Demir ve Çelik A. Ş.
Turkey

Abstract

Production under competitive conditions in which the whole world has become an open market; making it fast, standard, safe and efficient has become an inevitable necessity. In industry, this requirement corresponds to automation. Since 1970, 8 plants that provide the supply and distribution of the circulation and cooling water required by the main operating units in Isdemir were completely human-controlled without automation system. The aim of this study is to establish an automation system in these 8 facilities and to provide remote control and controllability with 10 other facilities located at different points in the factory area. The control of distant plants started to be made from the Central Control Room of Water Plants Management.

1. Introduction

Communities from past to present have managed to store, dispatch and filter water according to the climate and geography conditions of their location. Over time, the importance of water increases with the increase in the population, the advancement of technology and the increase in industrialization [1].

Water is one of the most essential production factors in the industry. 7 billion m^3 annual amount of water consumed for industrial activities in Turkey [2]. The World Steel Association (WSA) stated that water is one of the most important issues for the continuation of the steel industry [3]. The iron and steel industry consumes a large amount of water in its production processes. In İsdemir, the consumption of water for the steel production are 716 million m^3 in 2019; consumption per ton of steel produced is 6.4 m^3. These large water consumption shows that Water Management has become a very crucial requirement for the iron and steel industry.

One of the main requirements for the management of water is the presence of an effective automation system. The automation system used for water management basically consists of three parts; instrumentation, communication systems and logical control program. The existing infrastructure in industrial facilities may be insufficient for transition to automation system. Therefore, technological deficiencies in the facilities can be overcome by replacing innovative equipment, installing sufficient instrumentation and sustainable methods. A properly designed and commissioned automation system provides the most efficient supply and use of water. In addition, efficient equipment use, cost reduction, increase in quality, decrease in human necessity are some of the other positive results [4].

In this paper, an application is proposed to manage the water supply and circulation plants located at different points in a factory with the automation system and to control all these facilities from a single center with few operator.

2. Materials and Methods

Water plants which are distributed to different points inside and outside of the factory and have an automation infrastructure will be managed from a single point.

The study consists of two stages;

- Modernization of old technology facilities and making them manageable with automation system.
- Installing communication infrastructure and building a Central Control Room. Then, moving SCADA screens of all facilities to this room.

Thus, the facilities can be managed from this center.

2.1. Automation System Modernization

An automation system should be installed to the facility. The basic components of the automation system to be installed are as in figure 1.

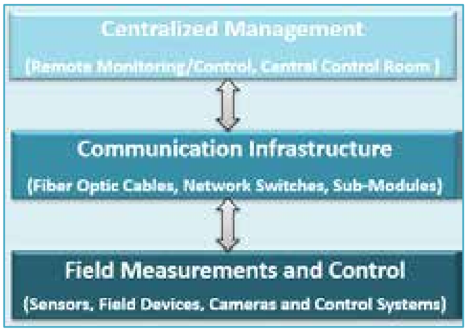

Figure 1. Areas of Proposed Topology

In order to create this structure, Programmable Logic Controller (PLC) system should be used in the facility and an automation program that can control the facility locally / manually / automatically should be written in accordance with the operation scenario. In order to monitor and control the facility, an understandable and functional Supervisory Control and Data Acquisition (SCADA) system should be designed and put into use. SCADA provides monitoring and surveillance of all units from the control of all equipment to production planning. Communication infrastructure that provides the necessary communication between the field and PLC system, PLC system and SCADA should be created and commissioned. Instruments should be mounted at every required point in the facility, and this information should be transmitted to PLC and monitored over SCADA, and all required data can be archived for future use. Electric motors and valves should be able to operate remotely by revising their control circuits. In order to enable the unmanned operation of the facility, it should be ensured that the camera system is installed without remaining any blind spots in the facility and these images are recorded. By creating alarm and warning systems, the operator should be immediately informed about the bad situations, hence the facility should be operated safely by interventing the system in a short time.

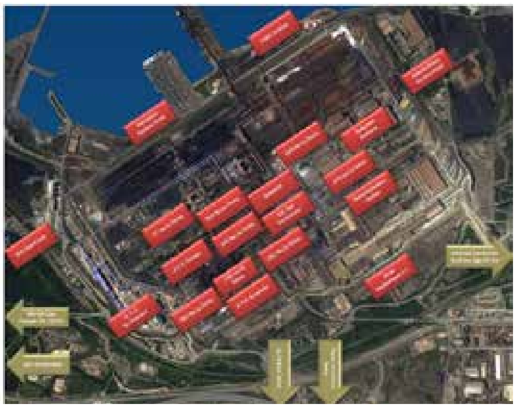

Figure 2. Layout Plan of Distributed Plants in the Factory

2.2. Centralization of Water Management

The SCADA screens of all facilities controlled by the automation system should be monitored and controlled from a single center with the communication system to be installed. For this purpose, a central control room should be built and a sufficient number of televisions should be mounted to monitor each facility. Besides, sufficient number of televisions should be installed in order to monitor all camera images. A communication infrastructure consisting of fiber optic cables should be established between the facilities located at different points in the factory and the central control room. Each monitor in the central control room should be connected to one operator computer located in the facility through the thin client computers via a remote desktop connection and all the information should be transferred to the Central Control room.

2.2. Field Applications

Eight plants that provide the supply and distribution of the circulation and cooling water required by the main operating units in Isdemir were completely human controlled without automation system over 45 years. Employees were worked in three shifts at each facility for controlling.

Figure 3. Central Control Room

Within the scope of the study, PLC system was installed in each facility, and automation software was prepared according to the facility needs. In order to manage and monitor the facility, SCADA control systems have been created. PLC and SCADA brands used in modernized facilities were selected as the same brand at other ten facilities which the automation system previously available. The aim of this is providing standardization.

Central Control Room was built in order to manage SCADA screens in 18 remote control rooms which are placed in different points in the factory as shown in figure 3. Remote desktop connection settings were established to operator computers in all facilities. Each plant's SCADA system can be monitored on any screen in central control room. A secure, isolated fiber communication network has been built for the facilities to communicate with this center. In order to avoid being affected by possible interruptions in this isolated communication network, the factory general intranet network can be used as a backup network. Besides, the infrastructure was created to be available for future expansion.

The images of all the cameras in the field can be monitored online on the screens in the central control room. History records are archived.

In order to eliminate the risk of failing to manage facilities due to power cuts, an Uninterruptable Power Supplies (UPS) were installed in all automation systems and central control room.

A rotation plan was prepared for all personnel who work in the central control room, and they worked for a certain period of time at every facility in the field. They were trained during these periods. Thus, they had sufficient knowledge about the operation of the all plants.

3. Results and Discussion

Within the scope of this project, 35 SCADA screens in 18 control rooms, over 3700 proses objects (pump motor, instrument, valve etc.), over 70.000 tags of data and 119 camera videos were collected and concentrated in one control center. The main benefits of the project are detailed below.

- Personnel efficiency; Previously, each facility was operated as 3 shifts per day and with a minimum of 2 personnel per shift. Now all facilities can be managed by only 3 personnel per shift. Thus, 17 number of personnel's costs were saved.
- The facilities have become safer in terms of Occupational Health and Safety (OHS).
- Coordination between the facilities is achieved.
- Fault detection time decreased.
- Emergency management has been made more effective.
- In terms of engineering, intervention to the failure has been made faster.
- The control of maintenance and troubleshooting works in terms of OHS and process has been increased by monitoring the cameras.
- Good differences between the facilities were identified and applied to others. Steps were taken to standardize the facilities.
- During the local control, while the operating personnel only dominated their own facilities, they were now informed about the operation of other facilities.
- Process safety and efficiency are increased.
- The operations that depend on the human factor such as dosing, chlorination etc. have been made automatic.
- Report and archiving of all data can be achieved.
- Connection and data transferring between level 1 and level 2 automation systems is provided.
- Centralization of data backup has increased time savings and backup reliability.

In spite of the fact that a centralized water management and reduction of human factor are provided at the end of these efforts, the facilities need to be adapted to industry 4.0 in order to build a complete control mechanism. Thus, the human factor will be completely eliminated in the management of the facilities and all operations will be carried out automatically in the most efficient and secure way.

4. Conclusion

As a result of the studies, an integrated management and control platform has been formed to achieve long-distance, large-scale centralized operation. It has been ensured that all processes are monitored, inspected, data archiving-reporting and controlled from one center. In emergency situations, the management of the entire facilities has been ensured. Since the need to have employees in each facility is eliminated, cost savings were achieved. Safer production has been provided in terms of Occupational Health Safety and a serious decrease has been observed in malfunctions caused by human error, hence the commitment to humanity has decreased.

References

[1] <http://www.vatekcevre.com/blog/endustride-suyun-yeri> Dated: 11.05.2020.

[2] <http://www.dsi.gov.tr/docs/stratejik-plan/dsi-2018-faaliyet-raporu.pdf?sfvrsn=2> Dated: 11.05.2020.

[3] Y. Tong, Q. Zhang, J. Cai, C. Gao, L. Wang, and P. Li, "Water consumption and wastewater discharge in China's steel industry," *Ironmak. Steelmak.*, vol. 45, no. 10, pp. 868–877, 2018.

[4] P. Gaonkar and M. Kande, "Challenges and opportunities of automation system for water and waste water applications," in *2014 IEEE International Conference on Industrial Technology (ICIT)*, 2014, pp. 682–688.

Investigation of Distinct Strain Rates on Hydrogen Permeability Properties of Enamel Steel

Ramazan UZUN[1], Ümran BAŞKAYA[1], Zafer ÇETİN[1], Oğuz GÜNDÜZ[1], Yasemin KILIÇ[1], Adem BAKKALOĞLU[2]

[1]Eregli Iron and Steel Works, Co., [2]Yıldız Technical University

Turkey

Abstract

Enamel steels are used in the white goods industry thanks to good formability and enamelability. Different plastic deformation ratios, enamel coating and curing processes are respectively performed on enamel steel according to product type (kitchen equipment, oven, boiler, storage water heater, etc.). Each applied process causes make some difference in the microstructure of the steel. This issue affects the hydrogen permeability properties as well. In this study, different strain levels (from as received to 40%) on hydrogen permeability properties were investigated. It was seen that hydrogen permeation properties were improved by increasing strain level, which makes crushing effect on inclusion/precipitation.

1. Introduction

Ultra-low carbon Ti-bearing steel is widely used in enamelling operation due to its good formabilty properties and better fish scale resistance [1]. Fish scale formation is occurred on the surface of enamelled part due to hydrogen mobility [2]. In the firing process, the atomic hydrogen diffuses into the steel. While cooling, the atomic hydrogen diffusion is started to the steel-enamel layer and hydrogen atoms recombine as molecular hydrogen. After a while, fish scale problem occurs due to pressure of hydrogen in the interface of enamel and steel [3]. Steel and frit quality, enamelling process (enamelling baking temperature, dew point of furnace), thickness of the steel and forming process are significant to evaluate the fish scale problem. Trap sites are crucial to prevent fish scale formation, the resistance of fish scaling could be enhanced by increasing the number of hydrogen traps. Nitrides, carbides, sulfides, carbonitrides, non-metallic inclusions, grain boundaries, dislocations, vacancies and microvoids are additional trap sides for enamel steel grades.

2. Materials and Methods

Deep drawing test device (Zwick BUP600) was used for marciniak test. Different strain levels were applied on samples. Hydrogen diffusion coefficient was measured by Helios II system. Microstructure characterization studies were carried out with scanning electron microscopy (SEM/Jeol JSM 7100F). The automated inclusion/particle analyses were run in the Thermoscientific Explorer-4 (TSE-4).

3. Conclusions

In this study, the effect of strain on microstructure and hydrogen permeability properties were investigated. It was detected that precipitation/inclusion become smaller by the effect of deformation and crushing. Thus, while number of them per mm^2 increase, their size decrease. Microcavities increase thanks to new smaller precipitation/inclusions and create new additional trapping sides for hydrogen atoms. Hydrogen diffusion coefficient was decreased dramatically because of increasing strain ratio. Hydrogen permeability resistance is twice better in the sample applied with 40% strain compared to the sample with no strain applied.

4. References

[1] ASM Handbook, Volume 1, Properties and Selection: Irons, Steels and High Performance Alloys, 10th edition, 1993.

[2] Fu-tao D., Lin-xiu D., Xiang-hua L., Jun H., Fei x., Effect of Ti(C N) Precipitation on Texture Evolution and Fish-Scale Resistance of Ultra-Low Carbon Ti-Bearing Enamel Steel, JOURNAL OF IRON AND STEEL RESEARCH, INTERNATIONAL. (2013), No 20(4), pp.39-45.

[3] Fábián E., Szabó P., Effect of Texture on Hydrogen Permeability in Low Carbon Al-Killed Steels, Materials Science Forum Vol. 659 (2010) pp. 301-306.

Effect of Thermomechanical Rolling Process on the Mechanical Properties of 46MnV56 Microalloyed Steel

Funda OZMEL[1], Dogan CAMLI[1], Mert ULKER[1], Kenan ACAR[1], Arcan F. DERİCİOGLU[1,2]
[1]Asil Çelik San. ve Tic. A.Ş., [2]Middle East Technical University
Turkey

1. Abstract

Thermomechanical rolling (TMR) is a modified hot rolling process which is characterized by the deformation of austenite without any recrystallization. The main purpose of TMR is to control the microstructure and provide the material with the desired properties by rolling. In the present study, 46MnVS6 grade microalloyed steel bars with a diameter of 55.6 mm were produced by TMR along with conventional rolling (CR) in Asil Çelik. Effect of TMR process parameters on the microstructure and mechanical properties of this particular steel grade was investigated in comparison to those of the same steel grade processed by CR.

2. Introduction

The purpose of the TMR process is inhibiting the recrystallization of the grains by conducting the final rolling at the appropriate temperature. Multiple critical temperatures exist during the course of the hot rolling process. The first one is known as the T_{NR} (temperature of no recrystallization) below which complete static recrystallization no longer occurs for a given holding time. Subsequent critical temperatures are the phase transformation temperatures upon cooling (Ar_3, Ar_1) [1]. Deformation above the T_{NR} results in equiaxed recrystallized grains. Without further recrystallization, the grains could increase in size through grain growth. Deformation below T_{NR} results in elongation of grains and formation of deformation bands, which act as nucleation sites for proeutectoid ferrite formation. For identical prior austenite grain size, rolling below the T_{NR} would result in finer ferrite grains than rolling above the T_{NR} due to higher grain boundary surface area to grain volume ratio achieved [2].

3. Experimental Study

At the beginning of the study material property simulations were conducted to determine the critical temperatures (Ar_3, Ar_1, T_{NR}) which are used to guide the processes. Based on these results, the hot rolling process line was modified according to TMR process requirements, and after several rolling trial runs optimum process parameters were determined. Consequently, effect of TMR process on the microstructure and mechanical properties was examined in comparison to those obtained by CR.

4. Conclusion

Results of this study has shown that TMR process had no dramatic effect on the strength and hardness of the 46MnVS6 grade steel when compared to those of the same grade processed by CR process. However, it is seen that ductility and toughness is considerably improved by the TMR process due to the refinement in the grain structure, which eventually has a positive impact on the fatigue behavior of this material.

5. References

[1] Y. Woo Kim, S. Weon Song, S. Jong Seo, S. Hong and C. Soo Lee, POSCO Technical Research Laboratories, Development of Ti and Mo Micro-Alloyed Hot-Rolled High Strength Sheet Steel by Controlling Thermomechanical Controlled Processing Schedule, Gwangyang 545-090, Republic of Korea, 2013.

[2] C. N. Homsher, Influence of Processing Parameters and Alloying Additions on the Mechanically Determined No-Recrystallization Temperature in Niobium Microalloyed Steels, M.Sc. Thesis, Colorado School of Mines, 2016.

Development of New Generation Steel Alloy and Forging Process

Fulya EYÇİN[1], Tuğçe YAĞCI[2],[3], Adem KORKMAZ[3], Serhat BARDAKÇI[3], Osman ÇULHA[2],[3]
[1]Tirsan Kardan San. ve Tic. A.Ş., [2]Manisa Celal Bayar University,
[3]Twin R&D Engineering Company

Turkey

Abstract

The main aim of this study is development a new generation steel alloy and forging process supported by numerical simulation and computational material engineering (CME) techniques. Based on the basic principles of CME, determination of the type and amount of alloying elements showing carbide-nitride and/or carbonitride formation, and the change of the mechanical properties of final product, depending on the hot forging and cooling regime will be revealed by using the material data created by the numerical simulation. In this context, by applying integrated simulation techniques, the production chain from steel alloy to final product will be designed in virtual environment and the results will be used to lighten existing / new drive shaft designs made of steel.

In this study, the flow curves of alloys 1 and 2 (A1, A2) with different compositions microalloyed steels which were hot forged at 1200 ℃ in are obtained in virtual environment. At the end of the simulation of the forging process, controlled cooling was applied to the material and TTT and CCT diagrams of the alloys were obtained. Within the scope of these studies, A1 and A2 microalloyed steels were hot forged in a simulation environment at 1200 ℃ in 5 operations that are upsetting 1 and 2, pre-forging, final forging and ironing. The phase distributions and hardness values of the forged materials were revealed. As a result of this study, the mechanical properties of new generation microalloyed steel grades with different chemical compositions were compared.

1. Introduction

Forging helps to produce steel parts with superior mechanical properties. Among all metal forming processes, forging has an important place with minimum waste of material. The forging process starts with raw material with simple geometry and ends with the production of complex geometry parts with plastic deformation [1]. The final product geometry is achieved in a very short time, usually by one or several strokes of a press or hammer strokes. In this respect, the forging process provides potential savings in time, energy and material. In addition, for a given weight, forged parts exhibit better mechanical and metallurgical properties and reliability than those produced by casting or machining [1,2]. All these capabilities emphasize the superior aspects of the forging method between metal forming processes.

In hot forging, the temperature reaches above the recrystallization point of the material. Metals are plastically deformed above their recrystallization temperature, which allows the material to retain its deformed shape as it cools [3]. Hot forging process contains lots of important engineering phenomenon and parameters such as the forging temperature, the amount of deformation, the mold-operation design, the cooling process-phase transformation relationship [4,5]. Also, the amount and type of alloying elements in a steel composition play an important role in hot deformation properties of the raw material and process parameters.

Recently, validation and development researches of product / process designs, through computational material engineering, modeling and simulation applications, form the basis of both academic and industrial R&D activities. According to the composition of the material, there are many simulation software used in determining the hot forging process parameters and cooling regimes. These computer aided tools have an important place in the engineering applications of the steel forging industry. Product and process simulations are a frequently used method to solve complex engineering problems in steel industry. Revealing the variables-related behaviors of the existing material and process in a virtual environment provides an advantage in industrial competition. In another respect, it is possible to make the existing system more efficient with simulation and verification studies, and it is possible to design a new process and product [6]. Simufact Forming, one of the commercial forming simulation sofware, offers the appropriate functionality for any forming process such as forging, rolling, extrusion, sheet metal forming, heat treatment, mechanical joint and pressure welding. The application module of hot forging brings special functionalities for the simulation of hot forging processes and enables also the process of hot die forging as well as further core processes like clamping and cooling, cutting, prior deformation and also extrusion processes [7].

On the basis of this study, i) digitizing and indexing the properties of steel alloy compositions, ii) forging and cooling process design studies with finite volume method studies were carried out.

2. Experimental Procedure

In this study, two different new generation microalloyed steel compositions (A1 and A2) were used. Since the relevant alloys are currently in the patenting process, detailed information on their elemental composition cannot be provided. Alloy development studies were carried out with simulation supported via Simufact forming software based on the computational materials engineering techniques.

After the virtual data of the alloys were indexed, hot forging simulations were carried out with *Simufact Forming* software. First of all, the contact pressures of the flange yoke work piece to the mold were calculated in five steps. The simulation results of the contact pressure for A1 and A2 alloy is given in Figure 1 and Figure 2, respectively. For A1 steel alloy, the maximum contact pressure value was identified as approximately 1033 MPa in the pre-forging. Similarly, the maximum value of contact pressure was 330 MPa, in 3rd step.

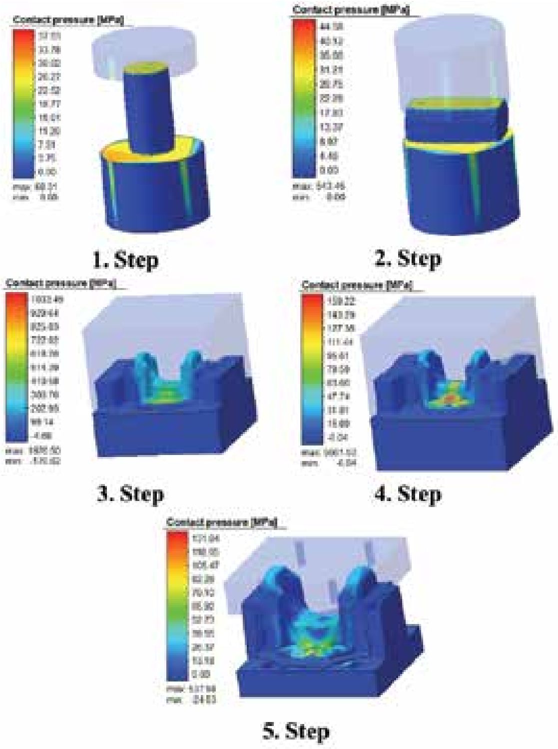

Figure 1. Simulation results of the contact pressure for A1 alloy.

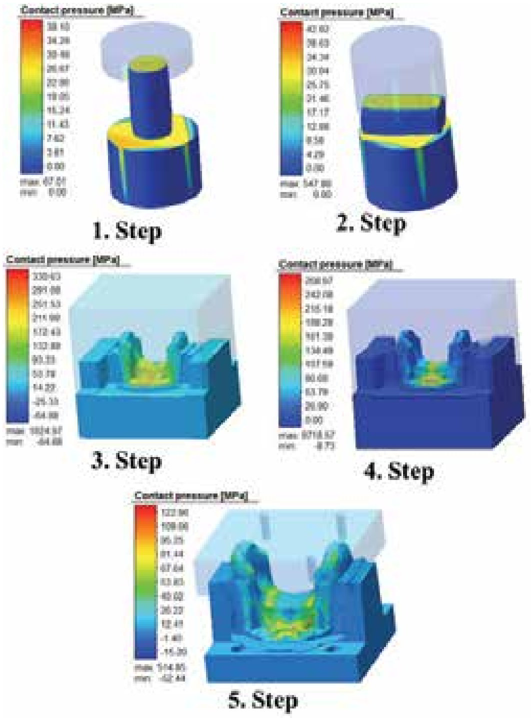

Figure 2. Simulation results of the contact pressure for A2 alloy.

The force-displacement curves of upsetting and ironing steps for new steel alloys A1 and A2 are given in Figure 3 and Figure 4. Figure 3 represents the A1 steel alloy, at the 1st step, the maximum force is 179 tons and the last one is 238 tons. For A2 steel alloy, these values are 180 tons and 258 tons, respectively.

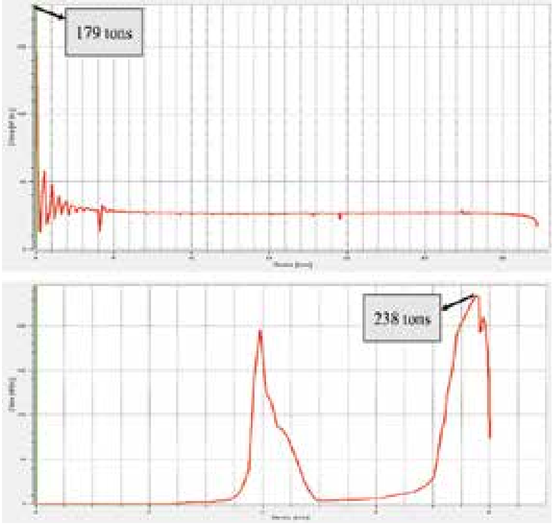

Figure 3. Force-displacement curves of steps 1 and 5 for steel alloy A1.

In addition, Figure 5 and Figure 6 show the simulation results of the material flow in die cavity for the A1 and A2 alloy.

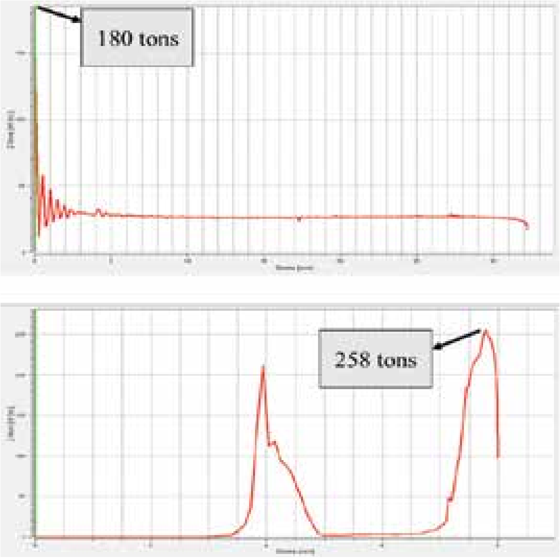

Figure 4. Force-displacement curves of steps 1 and 5 for steel alloy A2.

C

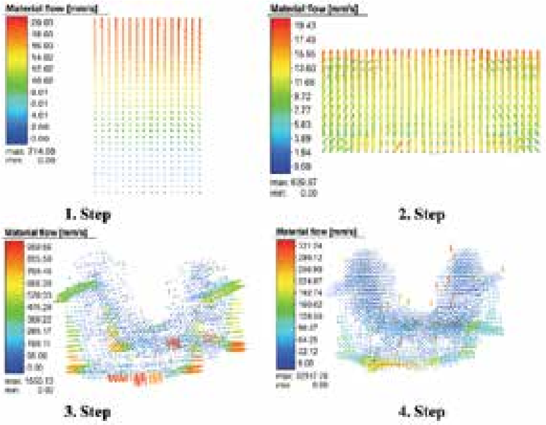

Figure 5. Simulation results of the material flow for A1 alloy.

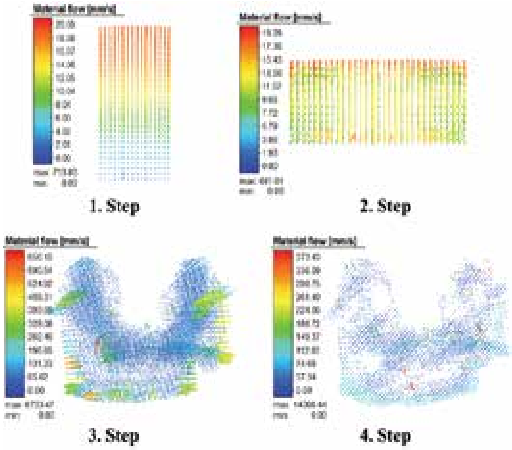

Figure 6. Simulation results of the material flow for A2 alloy.

In other respects, the simulation results of controlled cooling process for A1 and A2 steel grades are given in Figure 7 and Figure 8. As a result of controlled cooling simulation process, the microstructure of microalloyed steels contains the bainite, ferrite and pearlite phase. When looking at the major phase index of alloys, martensite and austenite are not found in the microstructure for both A1 and A2 alloys. In addition to all these data, hardness results in HV from critical parts of the workpiece are also given in Figure 9 and Figure 10.

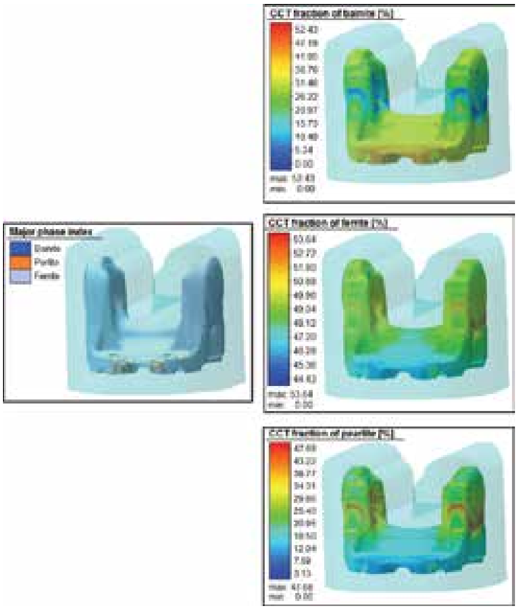

Figure 7. The phase fraction index of A1 alloy.

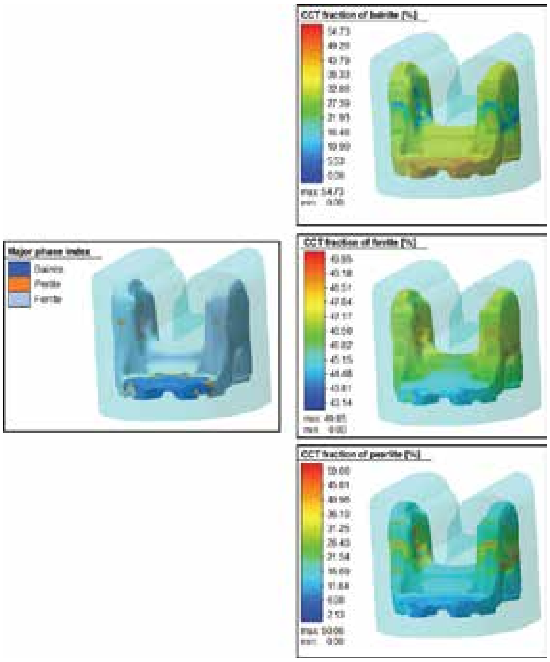

Figure 8. The phase fraction index of A2 alloy.

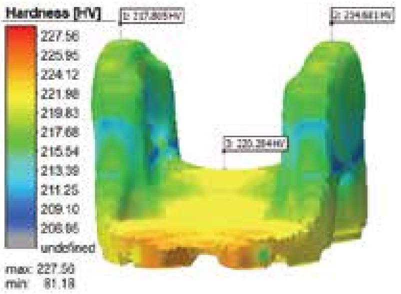

Figure 9. Hardness values of the simulated forged A1 alloy after cooling process in HV.

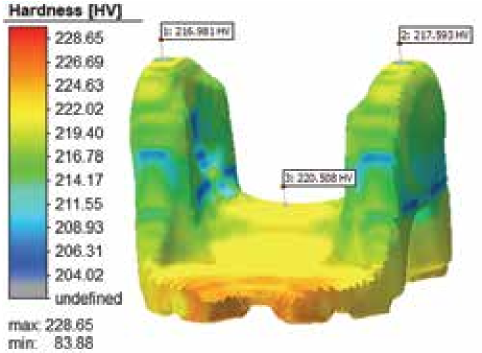

Figure 10. Hardness values of the simulated forged A2 alloy after cooling process in HV.

4. Conclusion

With this research, new generation microalloyed steel compositions have been developed for using in the hot forging process to produce flange yoke part of the cardan shaft. Computational Materials Engineering approaches were used for alloy development studies. Whether these alloys developed as an alternative to existing steel alloys are suitable for real production conditions have been checked by both simulation and experimental studies. The mechanical properties of the new alloys are intended to be superior to the conventional alloys currently used. With the help of simulation programs, the producibility of A1 and A2 alloys has been investigated and the results have been reported in detail.

Acknowledgment

In this study, we would like to express our special thanks to TWIN R&D Engineering Company for providing consultancy services to our company.

References

[1] Ed. Altan, T., Ngaile, G., Shen, G., ASM International, Cold and Hot Forging Fundamentals and Applications, 2005, United States of America, pp. 1-9.

[2] Kayalı, E. S., Ensari, C., Metallere Plastik Şekil Verme-İlke ve Uygulamaları, İ.T.Ü. Kimya-Metalurji Fakültesi Ofset Baskı Atölyesi, 1986 İstanbul.

[3] Levon ÇAPAN, Metal Forming Handbook, 2010, İstanbul.

[4] Makas, T., General Overview of Hot Forging. 2016.

[5] S. Fujikawa, Application of CAE for hot-forging of automotive components, 98(2): pp. 176-181

[6] BIM, "Digital Twin" (2018). <https://assets.new.siemens.com/siemens/assets/api/uuid:610b5974-241d-4321-8ae6-55c6167446bf/version:1562849283/bim-digitwin-ru.pdf>, Dated: 14.06.2020.

[7] <https://www.simufact.com/module-hot forging.html> Dated: 15.06.2020.

The Characterization After Normalizing Treatment of Hot Forged 16MnCr5 and 20MnCr5 Cementation Steels

Nuray BEKÖZ ÜLLEN[1], Mustafa ERSOY[2]
[1]İstanbul University-Cerrahpaşa, [2]Batı Heat Treatment
Turkey

Abstract
Low carbon steels such as 16MnCr5 and 20MnCr5 are a widely used grade of steel in almost every industry including aerospace, transportation, power transmission for manufacturing of gears, camshafts, piston, pins and bearing due to its suitable properties such as toughness, ductility, high tensile strength, good resistance to corrosion. In this study, different heat treatments have been applied to improve the properties of hot forged parts. The microstructure and mechanical properties of the hot-forged samples have been examined in three different processes; after normalizing was applied, cementation and tempering applied without normalizing, and cementation, tempering was applied on the normalized parts. As a result, when normalization is applied before the carburization and tempering processes an increase in core hardness and fatigue lives were observed for the examined parts.

1. Introduction

Cementation steels are defined as low carbon content structural steels containing 0.1 to 0.2 %C before carburizing. Due to its low carbon content, it has good toughness with the low hardness of steel before the thermochemical treatment. The carburization process is a surface hardening process to increase surface hardness and improve the wear resistance of steel but maintains the toughness and fatigue strength of the core. These steels are classified as unalloyed and low alloy steels (Cr, Mn-Cr, Mo-Cr, Ni-Cr, Cr-Ni-Mo etc.) according to different alloy compositions. The selection of proper alloying elements obtains the required hardenability from the surface to the core [1]. The carburization process is applied to low carbon steels used in gears, ball bearings, railway wheels applications that create a hard and wear-resistant surface and to maintain their ductility. Carburized steels commonly used in these applications include AISI 1018, 4320, 5120, 8620 and 9310; their international grades are 20MnCr5, 16MnCr5, ZIF-7B, 20MoCr4 and V2525 [2].

16MnCr5 and 20MnCr5 steels are frequently used in manufacturing industrial and automobile components (bolts, gears, internal combustion engine parts and valve bodies) and also used in railway vehicle, machine tools, steel rolling equipment and mining machine transmission shaft were investigated [3]. 20MnCr5 and 16MnCr5 show different properties due to different composition amounts. Compositions of the 20MnCr5 and 16MnCr5 steels are given in Table 1. The carbon percentages in the steels affect their hardening. The increase in manganese content provides an increase in strength and hardness. The increase in chromium content increases the depth of hardenability and refines the grain structure. Phosphorus, silicon and sulphur contents of steels are the same, so it has no effect on hardening and strength [4]. Toughness, high fatigue strength and hardness properties are desired in these steels, which are mostly preferred in automotive components. In order to achieve these features, hot forging process and after hot forging process carburization and tempering process applied to the steels are generally used in the industry. However, after these processes, various and undesired anomalies occur in the structure of the materials such as residual stresses, grain growth and distortion. Heat treatment is applied to reduce or eliminate them.

In this study, normalizing is applied and its effect on the parts is examined. Normalization process reduces the internal stresses formed in the production processes of steel. It also improves microstructural homogeneity and response to subsequent heat treatment and increases stability by imparting a thermal memory for other lower temperature processes [5]. In literature; there are several separate studies on these steels [6-8], but no studies which both examined together. The aim of this study is to resolve this lack of literature.

2. Experimental Procedure

The compositions of the materials examined in the study are given in Table 1.

Table 1. Composition of the steels [9]

	%C	%Si	%Mn	%P (max)	%S (max)	%Cr
16MnCr5	0,14-0,19	≤0,40	1,0-1,3	0,035	0,035	0,80-1,10
20MnCr5	0,17-0,22	≤0,41	1,10-1,40	0,03	0,035	1,0-1,30

Normalizing, carburizing and tempering heat treatments applied on the forged 20MnCr5 and 16MnCr5 steels and were examined. The materials were normalized at 960 °C for 30 minutes in the furnace atmosphere containing 0.15

%C. Then materials were cooled in air. In the cementation process, the materials were held in the furnace for 300 minutes and until the temperature reached 935 °C in a carbon atmosphere at 0.4 %C. After the temperature was reached at 935 °C, the carbon atmosphere was increased to 1 %C and samples held for 10 minutes in the furnace. Then, Atmosphere was reduced to 0.67 %C and held for 30 minutes at 850 °C. After the process was completed, materials are quenched was carried out by placed it in the 70 °C oil bath. After the cementation process, tempering was applied to the materials at 140 °C for 120 minutes. The atmosphere, time, temperature and cooling information of the processes applied to the steels are given in Table 2.

Table 2. Parameters of heat treatment processes

Process	Atmosphere (%C)	Temperature (°C)	Time (min.)	Cooling
Normalizing	0.15	960	30	Air cooling
Carburizing	0.4	935	300	Oil quenching (T_{oil}=70°C)
	1	850	10	
	0.67	850	30	
Tempering	-	140	120	Air cooling

After the processes, 8 different samples were examined; hot forged and untreated parts, normalized parts, after normalizing, carburized and tempered parts and without normalizing, carburized and tempered parts. Microstructure, hardness and fatigue strength of the samples were investigated. Metallographic steps were applied for samples microstructure analysis. 2% Nital was used as etching reagent. Fatigue strength testing conditions; fatigue frequency is 120 cycles per minute (2 Hz) and the shape change range (stroke) of the up and down rod arms during the test is 30 mm. The parts were applied bending stress of 400 MPa. The fatigue test for each bar was continued until the bar broke, life comparison was made under the same test conditions. Fatigue life is defined by the number of cycles until the bar breaks under dynamic loads.

3. Results and Discussion

Microstructures of examined samples 16MnCr5 are given in Figure 1 and 20MnCr5 in Figure 2. In the microstructure images of hot forged steels, besides the ferrite phase, there is also a finely dispersed pearlite structure. After normalization heat treatment, microstructures that are ferrite and fine-grained pearlite were obtained with the effect of air cooling in both steels. After normalization, the structure is observed to be dispersed homogeneously. Microstructures of 16MnCr5 and 20MnCr5 resulted similarly to each other after normalizing. The steels have a ferritic-pearlitic structure, and the areas that are carbon diffused turns into a martensite structure is formed after the carburization process. This indicates that the cementation process has been carried out correctly. The microstructure of steel that is correctly applied to heat treatment and tempering process consists mainly of tempered martensite [10]. Tempered martensite was formed in the samples after tempering. However; the structure, amount and properties of martensite change from surface to core. 20MnCr5 has phases with more homogeneous distribution after heat treatments. The reason for this, it is the difference of alloying elements in its content [9].

Hardness values of the tested 20MnCr5 and 16MnCr5 steels are given in Table 3. It was observed that, after normalizing, the core hardness values of the samples which are applied to cementation and tempering processes were higher than the non-normalized samples. No change in surface hardness has been observed**.** Although the normalization process reduces the hardness values of the untreated part, it enabled the subsequent processes to increase the hardness value.

Table 3. Hardness values of the samples

Sample	Code	16MnCr5		20MnCr5	
		Core (HV1)	Surface (HRC)	Core (HV1)	Surface (HRC)
Untreated	S1	295	17	305	19
Normalized	S2	171	4,5	189	9
Without Normalizing, Carburized and Tempered	S3	313	63-64	401	63-64
After Normalizing, Carburized and Tempered	S4	378	63-64	467	63-64

Results of the fatigue test are given in Table 4. It is one of the most important factors affecting the fatigue strength of the microstructure of materials. The microstructure is one of the most important factors affecting the fatigue strength of materials. The fatigue strength of the materials increases with the microstructure becoming more homogeneous. In heat treatments made after normalization, it is seen that martensite plates do not change much in both samples. This explains the higher fatigue strength. Normalizing treatment before hardening is mainly for homogenization and refinement of microstructure and softening the steel. Homogenization and microstructure refinement improve mechanical properties and prevent distortion or cracking of parts with complicated shapes during hardening while softening reduces machining costs [11].

In Figure 3, the fracture cross-sections after the fatigue test of materials are given. The brittle fracture occurred in all rods after fatigue test. Cracks formed as a result of hot forging, which caused the fatigue life to decrease, were removed by heat treatment. Umashankaran et al. [6], in their study, examined the suitability of a crankshaft made of 20MnCr5 by applying the same processes. It was observed that the hardness and fatigue resistance of the structure increased with the heat treatments applied in the study. The results of this study are compatible with the literature.

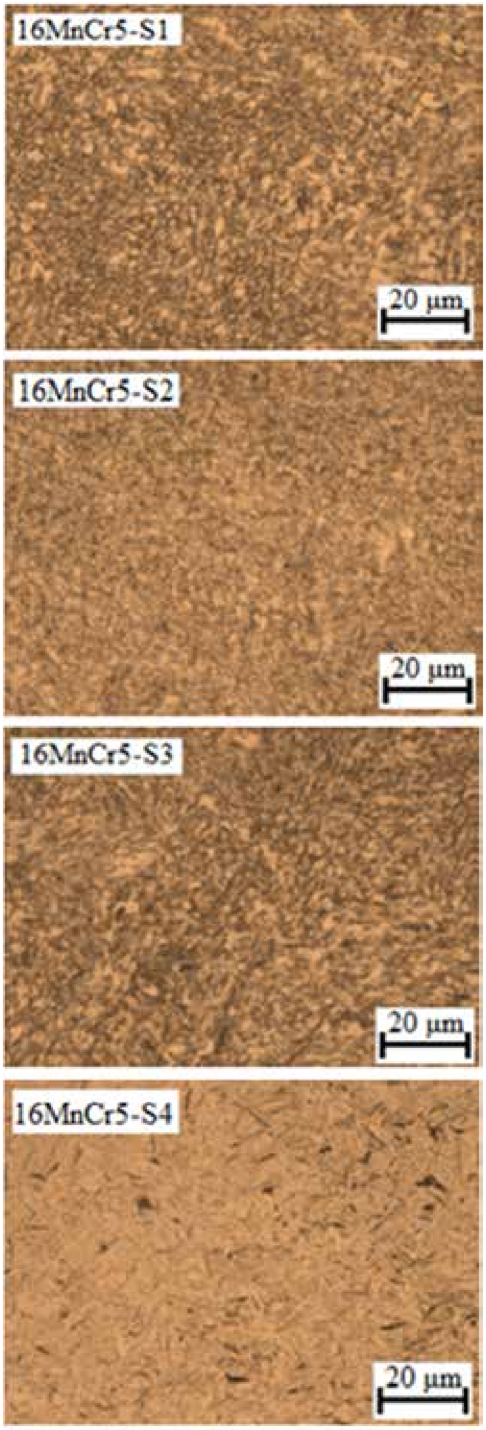

Figure 1. Microstructures of 16MnCr5 examined samples

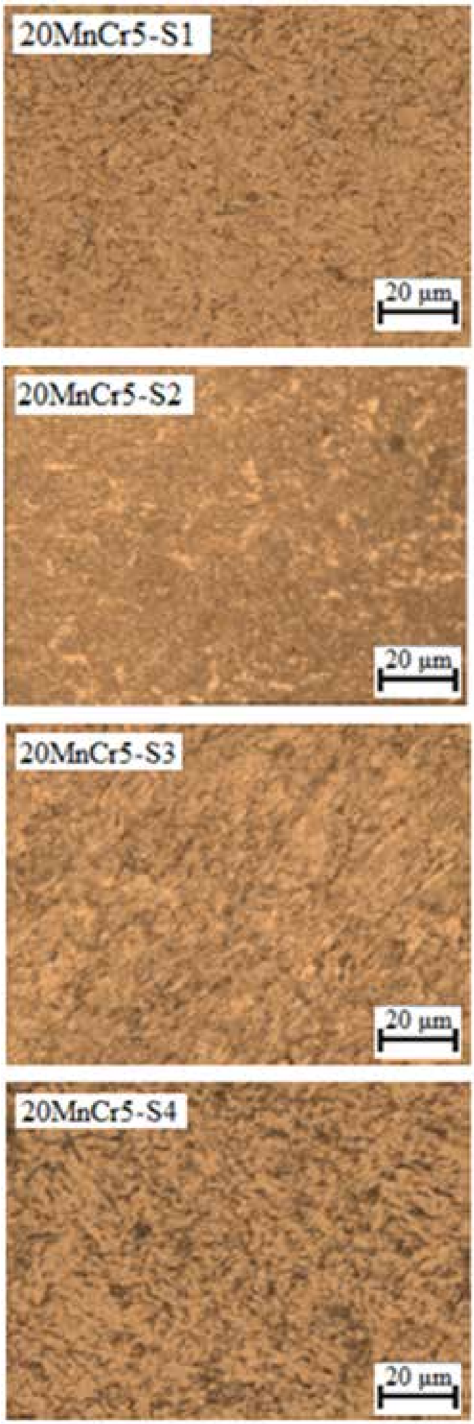

Figure 2. Microstructures of 20MnCr5 examined samples

Table 4. Results of the fatigue test

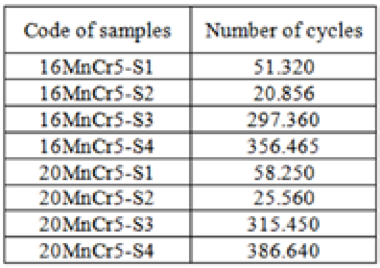

Code of samples	Number of cycles
16MnCr5-S1	51.320
16MnCr5-S2	20.856
16MnCr5-S3	297.360
16MnCr5-S4	356.465
20MnCr5-S1	58.250
20MnCr5-S2	25.560
20MnCr5-S3	315.450
20MnCr5-S4	386.640

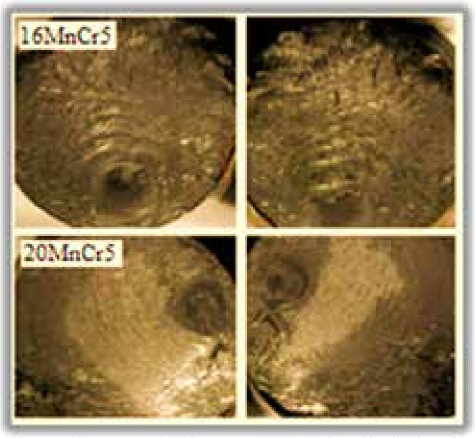

Figure 3. Image of the samples broken in fatigue test

4. Conclusion

The present study focused on the effects of the normalization heat treatment before cementation and tempering heat treatment on the microstructures, hardness and fatigue strength of 16MnCr5 and 20MnCr5.

- After the normalization process was applied to the untreated samples, a more homogeneous distribution of fine-pearlite structure was obtained. Homogenization of the structure reduced the hardness values. However, it has created a more compatible microstructure for the subsequent processes. After carburization, martensite was formed to decrease from the surface to the center. Tempered martensite was formed in the samples after tempering and the structure, amount and properties of martensite change from surface to core.
- Core hardness has been increased in the samples that after normalization applied carburizing and tempering. No change in surface hardness has been observed**.**
- The brittle fracture occurred in all parts after fatigue test. The parts were broken at very low lifetimes. However, the fatigue life of the normalized before the heat treatment is longer than the heat-treated samples without normalization. According to the number of cycles in which the parts are broken, the parts that have been heat-treated by normalizing can be resisted up to approximately 6 times the number of cycles of the untreated part, while the non-normalized parts have resisted up to 5 times the number of cycles.

References

[1] S. Kladarić, I. Kladarić, M. Gudelj, M. Pejnović, The Effect of Carburizing on the Properties of Steel 20MnCr5 and 18CrNi8, 9th International Scientific and Expert Conference under the auspices of the International TEAM Society, 10-12 October 2018, Novi Sad, Srbija, pp. 71-75.

[2] J.R. Davis, Gear Materials, Properties, and Manufacture, ASM International, 2005, United States of America, 1-18.

[3] S.A. Rizvi, W. Ali, Integration of Grey-Based Taguchi Technique for the Optimization of Process Parameters During the Turning Operation of 16MnCr5 Steel, International Journal of Industrial Engineering & Production Research, 16 September 2019, Vol. 30, No 3, pp. 245-254.

[4] D. Shastri, S. Ramamurthy and Parab, P., Strategies For Automobile Gear Material Selection, Fifth International SAE India Mobility Conference on Emerging Automotive Technologies Global and Indian Perspective, SAE Technical Paper, 2008, pp. 382-390.

[5] R. Singh, L. Pal Singh, Industrial Engineering Journal, Volume 13:4 (2020).

[6] M. Umashankaran, J.H. Vignesh, A.S. Kumar, R. Shyamaprasad, R.S. Prabhu, Metallurgical Test on 20MnCr5 Steel: To Suggest as a Suitable Crankshaft Material. In Emerging Trends in Science, Engineering and Technology Springer, 2012, India, pp. 273-28.

[7] N. Mohan, S. Arul, Materials Today: Proceedings, 5:11, (2018), 25265-25275.

[8] S. C. Harichand, S. Sharma, International Journal of Engineering Science and Technology, 4:3, (2012), 998-1004.

[9] <http://www.nsccelik.com/en/case-hardening-steels.html> Dated: 08.04.2020.Dated: 18.06.2020.

[10] B.L. Bramfitt, A.O. Benscoter, Metallographer's Guide: Practice and Procedures for Irons and Steels, 2002, 63, pp 23-48.

[11] G. Vukelic, J. Brnic, Journal of materials in civil engineering, 27:3, (2015) 04014132.

Reverse Ageing Phenomena in Hyper-Eutectoid Wire Rod Steels

Cemre KEÇECİ, Erhan SAKALLI, Sadık POLAT, M. Eriş DURMUŞOĞLU, Ali KOCA, Ahmet SAĞLAM

İskenderun Demir ve Çelik A.Ş., Ereğli Demir ve Çelik Fabrikaları T.A.Ş.

Turkey

Abstract

Production of high carbon steel wire rods with high diameter (8-16mm) are increasing yearly. Hot rolled wire rods have special properties for industrial usage. Obtaining this properties needs some studies because of the material behaviour. By the end of the production of some of the wire rod qualities tensile test results show low ductility (low % RA and % Elongation) and brittle fracture. Tensile specimens show a brittle fracture before reaching the maximum load during tensile tests. This phenomena prevents the wire rods quality approval because of the failed tensile tests. Therefore, for achieving a good ductility and proper test results, some ageing processes were developed. This ageing processes were done by holding the tensile test specimens in furnace at different holding times. In this study, ageing process results and failed tensile test specimen failure analysis were investigated.

1. Introduction

After the production of high carbon eutectoid steels, failed tests are frequently encountered, especially in thicker sizes (11-16 mm diameter in the tensile tests performed. In general, tensile test results between 11 and 16 mm diameter coils are not successful. The steel compositon was determined by optical emission spectroscopy (Table1).

Table 1. Chemical Analysis of the Material (wt%)

C	Mn	P	S	Si	Cr	V
0,82	0,72	0,012	0,007	0,20	0,26	0,030

In this study, some trials are carried out to complete the tensile tests before the need for retesting. For that reason the tensile test results and tensile sample fracture surfaces were examined in macro size. In the samples in Figure1, the fracture surfaces of the failed tensile test sample and normal sample were given.

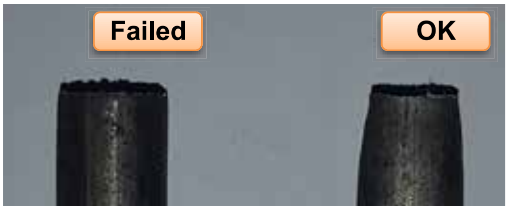

Figure 1. Brittle Fracture and Ductile Fracture Samples

When the broken sample surfaces were examined, it was seen that the samples of failed tests broke without necking.

Before reaching the maximum load required for fracture and without giving the sample elongation, the test have finished. With this results, some aging trials have been planned in order to test samples without necking without having a brittle fracture (Figure 2-4).

Figure 2. Ductile Fracture Surface (15,0 mm C82D)

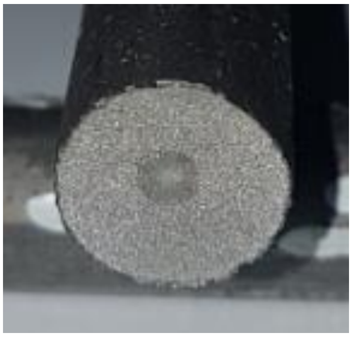

Figure 3. Brittle Fracture Surface (15,0 mm C82D)

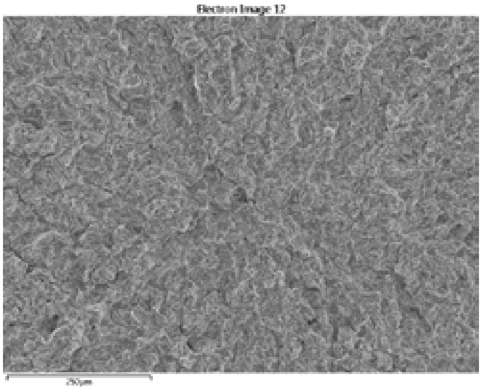

Figure 4. Brittle Fracture Surface (SEM)

A different determination was found that the tests were completed normally performed after the coil samples were kept under room conditions for a certain period of time.

With this information, an experimental designed to speed up the elapsed time by providing heating conditions with the furnace and to simulate the positive tensile test results in the sample.

2. Experimental Procedure

A total of 40 samples were extracted from the coil of a cast produced in C82D quality in 15 mm size and 4 tests were performed from 10 different experiments.

In the experiment, the samples were kept in the oven at a certain temperature within the time specified in the Table 2. At the end of the holding period, it was allowed to cool at room temperature and afterwards a tensile test was carried out.

In the first 7 experimental sets, heat treatment was carried out. 8th Samples were kept for 10 days in room conditions without heat treatment. 9th Samples were kept for 30 days in room conditions without heat treatment and finally the 10th test set was tested on the same day as production without any treatment.

Table 2. 10 Trials Set

Trial No	Heat Treatment	Holding Time	Testing Time
1.	100 °C	15 min	After holding at room temp
2.	100 °C	30 min	After holding at room temp
3.	100 °C	60 min	After holding at room temp
4.	100 °C	90 min	After holding at room temp
5.	100 °C	120 min	After holding at room temp
6.	200 °C	60 min	After holding at room temp
7.	200 °C	90 min	After holding at room temp
8.	None	-	10 days later
9.	None	-	30 days later
10.	None	-	After production

After the tensile tests performed, ductile fracture was detected in all 40 samples. Tensile strength, % elongation and% cross sectional results were compared in Figure 5-7.

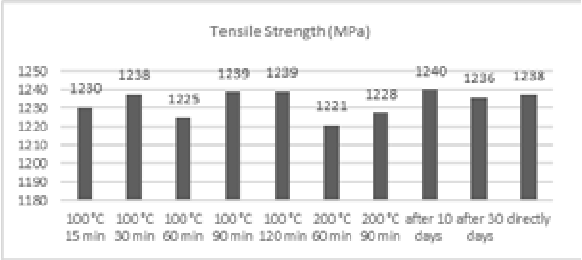

Figure 5. Tensile Test Results

When the tensile test results were examined, the relationship between the holding time in the furnace, its temperature and the holding day duration could not be determined clearly.

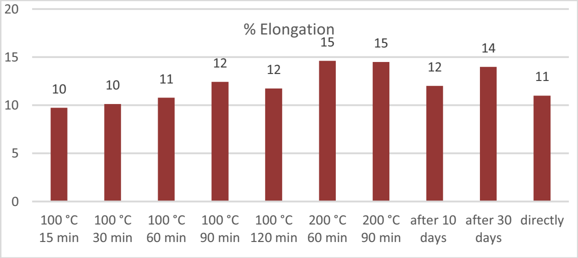

Figure 6. Elongation Results%

When the % elongation values are taken into consideration, the lowest values were determined in the samples that were left at 100 °C for 15-30 and 60 minutes with the tests performed immediately without heat treatment. The highest values were encountered in samples tested at 200 °C without heat treatment after 60 and 90 minutes and 30 days.
Results close to the values obtained at the end of 30 days are considered to be successful.

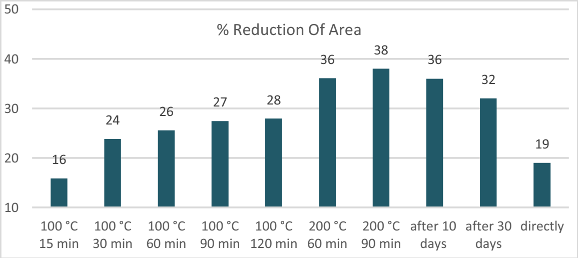

Figure 7. Results of% Reduction of Area

When the results of % RA were examined, it was observed that there was a 32% RA in the samples after the test obtained at the end of 30 days. The increase in reduction of area as the time and temperature can be seen in Figure 7.

As a result of 10 different experiments and 40 tests, the holding period of the coils in stock was simulated in the furnace and this was reflected in the results. It can be seen that the coils have been transformed from brittle to ductile by holding in the stock or in the furnace.

3.Results and Discussion

The wire rods grounded and polished by the conventional metallographic methods and etched in %2 nital solution. In micro examinations, there was no martensite structure that could cause fracture. The structure was fully pearlitic (Figure 8).

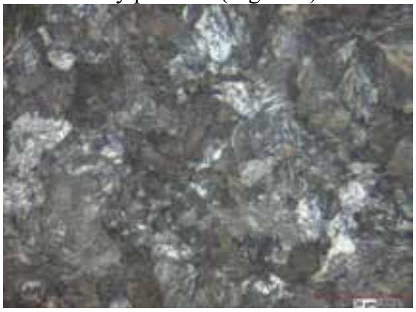

Figure 8. X500 Micro Structure

According to the results of 10 different experiments, the tensile strength,% elongation and% cross sectional averages are given in the Table 3.

Table 3. Test Results

Test Type	Tensile Strength (MPa)	% Elongation	% Reduction Of Area
100 °C 15 min	1230	10	16
100 °C 30 min	1238	10	24
100 °C 60 min	1225	11	26
100 °C 90 min	1239	12	27
100 °C 120 min	1239	12	28
200 °C 60 min	1221	15	36
200 °C 90 min	1228	15	38
after 10 days	1240	12	36
after 30 days	1236	14	32
directly	1238	11	19

Micro-examination showed no difference in ductile and brittle fractured samples. In this subject, in further studies it is planned to design new experiments with hydrogen measurement in tundish and finished products. It is known that the amount of hydrogen decreases over time in solid product.

For this reason, hydrogen change will be examined from the product during the production and after holding in stockyard and furnace.

References

[1] Reverse ageing in hot-rolled high-carbon steel wire rod T. Chand

[2] Microstructure Control and Strengthening of High-carbon Steel Wires Toshimi Tarui, Naoki Maruyama, Jun Takahashi, Seiki Nishida, Hitoshi Tashiro

[3] Strain ageing in ultra-high strength drawn pearlitic steels Nicholas Tauj, Widdrington Davie

Data Mining Applications in Iron and Steel Plants

Ahmet BEŞKARDEŞ
İskenderun Demir ve Çelik A. Ş.
Turkey

Abstract

In large facilities such as iron and steel factories, a large amount of data is produced in areas such as planning, design, assembly, production, quality, process control, fault detection, and maintenance. Data mining methods are needed to make this data useful. Recently, developments in data mining technology have directed iron and steel plants to use these methods. Good use of data mining technologies is essential for companies aiming to compete with the world in order to prevent quality defects, increase production, reduce costs and ensure continuous improvement in production processes. In this study, data mining methods are explained and current applications in recent years are described.

1. Introduction

Competition in the iron and steel industry makes it compulsory to increase production efficiency for all companies. In order to achieve and maintain an advantageous position on a global level, it is necessary to provide the desired quality and continuity as well as low-cost production [1]. Using data mining techniques at all stages of iron and steel production will bring businesses one-step ahead to produce the desired high-quality product.

Data mining is the extraction of useful meaningful information from data of different shapes and patterns collected from various sources. In this adventure, information is obtained from data, knowledge is obtained from information, and wisdom is obtained from knowledge [2]. Useful information that makes sense for the company is achieved through operations such as selecting, extracting, converting, combining, from databases, the internet environment, all kinds of text, sound, and image records. There is a great need for data mining techniques in the iron and steel industry as well as in the engineering, marketing, advertising, and education sectors.

There are many interrelated sub-plants especially in an integrated iron and steel factories. In these facilities, enormous data is collected, such as instant data from processes, laboratory results, employee inputs, and outputs produced by model applications. Many researchers have been working to process and evaluate this data to increase production, reduce costs, and ensure the desired quality. In this article, data mining techniques will be summarized and a few of the most successful applications will be examined.

2. Knowledge Discovery in Databases

There are a number of studies that need to be done to obtain useful information from different patterns and shapes and useless data stacks. Useful information is obtained with this process, which is expressed as knowledge discovery in databases (KDD) [3] and shown in Figure 1.

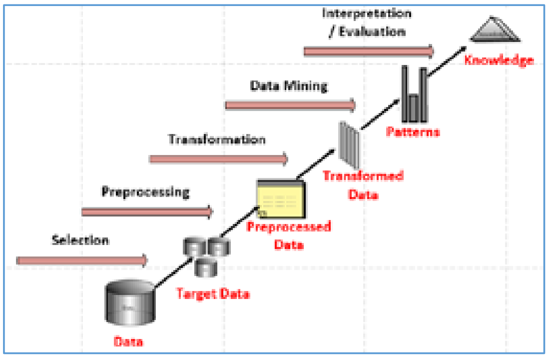

Figure 1. KDD processes

As seen in Figure 1, knowledge is obtained after selection, pre-processing, conversion, data mining, and interpretation. Data selection is the selection of only the relevant data from a large number of data in a database. The aim is to keep the data selection process continuous, fast, and up-to-date. Preprocessing is the process of filtering dirty or noisy data. In the preprocessing phase, missing or incorrect data are corrected and mismatch problems between the data are eliminated. Preprocessing can be handled in two subheadings. The first one is the imputation method. Here, records with missing data are deleted by methods such as listwise deletion, pairwise deletion. Their field is filled with methods such as mean imputation, regression imputation, and last observation carried forward. In the second subgroup, methods such as binning, clustering, regression, and human inspection are used to organize erroneous data. Transformation is the adaptation of the data to data mining by applying various conversion processes on the data that was cleared in the previous stage. For example, determining the dimensions of the data, reducing the data to meaningful intervals, generalizing the data, and even making new features over the data are discussed at this stage. Basically, smoothing, aggregation, generalization, normalization, and attribute construction processes are applied. Data mining is the processing of data that has been made available to serve information that has meaningful results and that is suitable for interpretation over the data received up to this stage. Interpretation is the questioning of the meaning of the pattern extracted from the data mining stage [4]. After all these processes, the process is controlled by decision-making mechanisms, and the necessary interventions for the continuity and stability of the system are made on time.

3. Data Mining Applications

The main purpose of the companies that give importance to quality and efficient production is to prevent defects in production and to ensure flawless production. This can only be done by scientific methods. Data mining and techniques, one of the scientific methods in the production sector, have been used effectively in corporate and large enterprises. Data mining methods have important contributions to business managers. It enables us to find meaningful relationships between large data stacks in the business and to use them in a way that works [5]. Before developing a smart application that targets efficiency, quality, or production stability, the first thing to do is to optimize the available data. There are many studies in the literature on converting data into useful information.

After the data are made meaningful, activities such as classification, prediction, estimation, association, clustering, control, explanation and visualization are performed [1]. In this study, examples of clustering, predicting and control applications, which are among the most common activities within the scope of data mining, will be given.

3.1. Clustering

Clustering is the task of dividing a different group into similar subgroups or clusters. The difference between clustering and classification is that the cluster is not based on predefined classes. Many clustering algorithms have been developed. Clustering is divided into categories such as partitioning methods, hierarchical methods and grid-based methods. This method is used in many stages of iron and steel production.

In the sintering process, it is aimed both to keep energy efficiency at the highest level and not to compromise on quality. However, economic and technical criteria are contradictory and optimization solutions are required in this case. Li et al. obtained the parameters required for this optimization by clustering the process data. Then they used online sequential extreme-learning machine (OS-ELM) to understand the effect of each cluster on FeO content. After their study considering fuel rate, productivity, FeO content and strength criteria, they saved 0.5 kg of fuel per ton without deviating from the quality targets [6].

Shnayder et al. used self-regulating Kohonen neural networks for cluster analysis of nonlinear and interacting blast furnace operating parameters. With the expert system, they have developed based on Kohonen neural networks, they have succeeded in decreasing coke consumption while increasing efficiency [7].

Kumar and Vijayachitra used data mining methods to determine the alloy components required for the desired steel quality in a ladle station. Since the proportions of the alloy elements to be added during the ladle refining process have an uncertain structure, they first applied the clustering technique to find the most suitable cluster centers. The optimal cluster centers acquired were then fed into the neural network using the Levenberg Marquardt algorithm. Their results show that they calculate alloy ratios with a minimized error rate [8].

3.2. Prediction

In the prediction process, historical data is used to create a model that describes current behavior. The relationship between dependent variables and independent variables from previous data is taught to the model. When this model is applied to new (actual) entries, the new result is predicted. Artificial neural networks, support vector machines and various regression methods are used for estimation.

In the sinter plant, the burn-through point (BTP) point gives important information about the thermal state on the pallet and the sintering process. This point is found not by measurement, but by evaluating other temperature data. Calculation or estimation of the BTP value has an important place in the studies related to the sintering process. Cao et al. used a Fast Fourier Transform (FFT) to preprocess and clear the abnormal data to determine the frequency band and select the model order to estimate the BTP value. Then, they increased the sensitivity of the model with the subspace modeling approach and the grid search algorithm [9]. Du et al. used the time series trend for BTP estimation. With the Mann-Kendal test, the BTP trend variable was determined and this value was used as the input of the fuzzy controller [10].

In sinter plants, BTP is a measure of the stability of the sintering process as well as the coke rate is a measure of carbon efficiency. In another study, Du et al. focused on an optimization model for both production and carbon efficiency. They first estimated the coke rate with the back propagated neural network and then optimized it with particle swarm optimization (PSO). On the other hand, they provided BTP control with a fuzzy controller. With the simplified structure given in Figure 2, they presented a model with stable results in carbon efficiency and sintering [11]. In this study, preprocessing was done with Spearman correlation analysis, data mining was performed with PSO and comprehensive coke ratio (CCR) prediction model, and interpretation was performed with intelligent integrated controller intelligent control application.

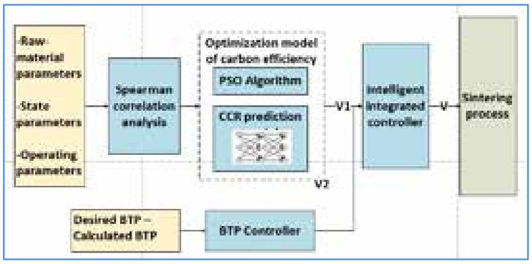

Figure 2. Control structure of the BTP control

In another data mining application developed for the sintering process, Jiang and others designed the nonlinear autoregressive model with exogenous (NARX) model for moisture control. 23 different parameters were reduced to 7 basic parameters with basic component analysis, and then they passed the data pre-processing process and provided effective learning [12].

Working on estimating the sinter quality index, Song et al. collected, cleaned, and integrated data from the sintering process. Tumbler index and screening index were analyzed by cluster analysis. Sinter quality was evaluated synthetically with cluster results and sinter iron grade. Then, important variables related to the sinter quality index were scanned by recursive feature screening, stability selection, and random forest selection. The comprehensive classification model of sinter quality and the regression model of the total iron content of the sinter has been created using various machine learning algorithms [13]. The model developed in this study is outlined in Figure 3.

Blast furnaces, one of the most important plants of an integrated iron and steel factories, have a multivariate, nonlinear, and complex structure. To optimize furnace efficiency and stability and increase the life of the furnace, it is very important to manage material and fuel consumption correctly. Researchers have done many studies to ensure production efficiency and stability in the blast furnace. Tunckaya and Koklukaya tried to better manage the oxygen enrichment, coke/ore ratio, and pulverized coal injection (PCI) parameters by estimating the flame temperature with an artificial neural network (ANN), multiple linear regression (MLR) and autoregressive integrated moving average (ARIMA) [14].

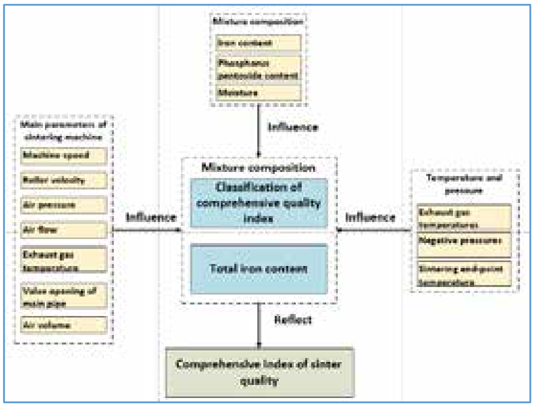

Figure 3. Input and output parameters of model

Barbasova et al focused on the prediction of the thermal status indicators of the blast furnace. They tried to provide better operational control by estimating the silicon ratio with 90% accuracy with the matrix pen method and Elman neural networks [15]. In another study on silicone estimation, Beşkardeş et al. estimated the silicon ratio from charge, fuel, analysis, and production information in the third blast furnace of İsdemir. First, 19 input variables of the blast furnace were subjected to normalization. Then, by using an artificial neural network, the silicon rate for the next casting was estimated, so that the interventions that need to be done without the need for waiting for the analysis result were made earlier [16]. Zhou et al. used a sliding window Takagi Sugeno fuzzy neural network (SW-TS-FNN) for silicon estimation and recorded 90% hits [17].

Ghosh and Chakraborty predicted solidification defects for a continuous castings plant, one of the facilities in the iron and steel plants, using a data-driven multi-layer perceptron (MLP) based neural network model. The inputs of this model are various parameters such as the percentage of aluminum, the percentage of carbon drop in steel production, the percentage of iron oxide in the sand mold, the percentage of carbon, the percentage of sulfur, the fraction solid percentage and the critical temperature. Casting defects of the steel alloy from these inputs have been estimated quantitatively consistently [18].

3.3. Control Applications

After reaching the requested information with KDD applications, it is time to evaluate this information. Rule tables, decision trees, and fuzzy logic-based control systems stand out as process control applications. In fact, intelligent control systems or expert systems can be considered as decision-making mechanisms that perform the operations related to the data from the first stage and give the process that should be done in the last stage.

Lei et al. determined the main factors affecting the sinter production rate according to data mining methods. After determining the inputs of the production rate model, other parameters are defined by the fuzzy c-means (FCM) clustering algorithm and the recursive least squares method (RLS). Finally, the T-S fuzzy model is obtained for the estimation of the sinter product ratio. Data mining stages in this study are shown in Figure 4 [19].

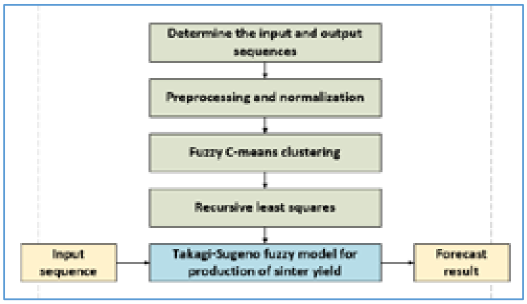

Figure 4. The process of sinter yield model

Beşkardeş et al. conducted a study on the estimation and subsequent control of RDI value, which is one of the sinter quality parameters [20]. In this study, data mining methods were applied to keep the RDI value within the desired range at the İsdemir sinter plant. RDI value was estimated with high accuracy from the laboratory, dosing, and process data. Later, with the fuzzy logic-based intelligent control application, the necessary interventions were made automatically to keep the RDI value within the desired range.

In the continuous casting process, Feng et al. designed a fuzzy PID controller based on the operating condition definition to increase the control accuracy of the mold level and prevent fluctuations in steady operating conditions. First, a model of the mold level was created, after analyzing the properties of the model with data mining, the continuous casting process was divided into different operating conditions. Then, PID parameters were determined by fuzzy rules [21].

Another control application was applied the cold rolling mill by Chen et al. In the study conducted with the Fuzzy neural network online prediction model, strip surface roughness can be controlled online and in real-time [22].

4. Conclusion

Data mining techniques are often used in the iron and steel industry for improvements in production, productivity, and quality. Especially in recent studies, techniques such as time series analysis, artificial neural networks, swarm optimization algorithms, and fuzzy logic are common. Each stage of iron and steel production consists of complex processes that affect each other, including non-linear, multiple parameters with time differences. Companies need to make the most of their data mining techniques to manage these complex processes correctly and achieve the highest efficiency and quality goals. Utilizing data mining techniques will take them one step ahead of the global challenging competition.

References

[1] S. Umeshini, C.P. Sumathi, A Survey on Data Mining in Steel Industries, International Journal of Computer Science & Engineering Survey (IJCSES), Vol.8, No.2, (2017)

[2] I. Spiegler, Knowledge Management: A New Idea Or a Recycled Concept?, Communications of the Association for Information Systems, 3 (2000)

[3] J. Han, M. Kamber and J. Pei, Data Mining: Concepts and Techniques, Elsevier, Morgan Kauomann Publishers, Third edition, pp.17

[4] S.E. Seker, Business Intelligence and Data Mining, emo.org.tr

[5] I.B. Akinci, F. Ersoz, Determination of Production Defects in Iron and Steel Sector by Data Mining, 978-1-7281-3789-6/19/$31.00 ©2019 IEEE

[6] Z. Li, X. Fan, G. Chen, G.Yang and Y. Sun, Optimization of iron ore sintering process based on ELM model and multi-criteria evaluation, Neural Comput & Applic, 28:2247–2253, (2017)

[7] D. A. Shnayder, T. A. Barbasova and Y. V. Lapteva, Enhancing Blast Furnace Control Efficiency Based on Self-Organizing Kohonen Neural Networks, International Conference on Industrial Engineering, Applications and Manufacturing (ICIEAM) 2018

[8] P. Kumar, S. Vijayachitra, Soft Computing Techniques for Ladle Refining Process in Steel Making, International Journal of Advanced Engineering Technology, March 2016

[9] W. Cao, Y. Zhang, J. She, M. Wu and Y. Cao, A Dynamic Subspace Model for Predicting Burn-Through Point in Iron Sintering Process, Information Sciences 466 1–12 , (2018)

[10] S. Du, M. Wu, L. Chen, K. Zhou, J. Hu, W. Cao and W. Pedrycz, A Fuzzy Control Strategy of Burn-Through Point Based on the Feature Extraction of Time Series Trend for Iron Ore Sintering Process, IEEE Transactions On Industrial Informatics, (2019)

[11] S. Du, M. Wu and J. She, An Intelligent Control Scheme for Burn-Through Point to

Carbon Efficiency Optimization in Iron Ore Sintering Process, Proceedings of the 37th Chinese Control Conference July 25-27, (2018), Wuhan, China

[12] Y. Jiang, N. Yang, Q.Yao, Z. Wu and W Jin, Real-time Moisture Control in Sintering Process Using Offline–Online NARX Neural Networks, Neurocomputing, April 30, 2019;12:50

[13] L. Song, L.Qing, L. Xiaojie and S. Yanqin, Synthetically predicting the quality index of sinter using machine learning model, Institute of Materials, Minerals and Mining, (2019)

[14] Y. Tunckaya, E. Koklukaya, Comparative Performance Evaluation of Blast Furnace Flame Temperature Prediction Using Artificial Intelligence and Statistical Methods, Using Gas in Oil Analysis, Turkish Journal of Electrical Engineering & Computer Sciences, 24: 1163 – 1175, (2016)

[15] T.A. Barbasova, Y.V. Lapteva and D.D. Salov, Application of Recurrent Neural Network and Matrix Pencil Method in Predicting Blast Furnace Thermal International Russian Automation Conference (RusAutoCon), (2018)

[16] A. Beskardes, S. Turkoglu and C. Aci, Prediction of the Hot Metal Silicon Content in the Blast Furnace, 978-1-5090-1679-2/16/$31.00 ©2016 IEEE

[17] H. Zhou, C. Yang, W. Liu and T. Zhuang, A Sliding-Window T-S Fuzzy Neural Network Model for Prediction of Silicon Content in Hot Metal, International Federation of Automatic Control (IFAC), (2017)

[18] I. Ghosh, N. Chakraborty, An Artificial Neural Network Model for the Comprehensive Study of the Solidification Defects During the Continuous Casting of Steel, Computer Communication & Collaboration Vol. 6, Issue 1-2, (2018)

[19] Q. Lei, G. Zhao, X. Chen and M. Wu, Sinter Product Rate Forecasting Based on T-S Fuzzy Model, Proceedings of the 36th Chinese Control Conference July 26-28, (2017), Dalian, China

[20] A. Beskardes, Y. Hames, S. Cevik, K. Kaya and E. Ozdemir, Fuzzy Logic Based Sinter RDI Optimization, The 4th International Conference on Power Electronics and their Applications (ICPEA), 25-27 September 2019, Elazig, Turkey

[21] Y. Feng, M. Wu, X. Chen, L. Chen and S. Du, Fuzzy PID Control Based on Working Condition Identification for Mould Level in Continuous Casting Process, 12th Asian Control Conference (ASCC), (2019)

[22] S. Chen, J. Wang and T. Gu, An Online Intelligent Control Method for Surface Roughness of Cold-Rolled Strip Steel, Proceedings of the 37th Chinese Control Conference July 25-27, 2018, Wuhan, China

Modelling the Turbidity-Suspended Solids Relationship and Optimizing the Polyelectrolyte Dosage

Mehmet Burak ATAN, Erkin Y. GEDİK, Gökhan GÜNGÖR, Onur MARTI, Arif AKSOY, İsmail GÜVEN, Gencer BİRKAN, A. Mesud ÇAKIR, Fatih ÇELİK

İskenderun Demir ve Çelik A. Ş., Operasyonel Mükemmellik Müdürlüğü

Turkey

Abstract

1400-1700 Nm3 Blast Furnace Gas is produced for each ton of pig iron produced in Blast Furnaces. These gases are burned as needed and energy is gained. Gases coming out of the blast furnace contain 10-20 g / Nm3 dust and moisture. If this gas is not subjected to any conditioning, it will cause the thermal effect to decrease and the combustion efficiency will decrease. Blast Furnaces are sent to gas cleaning plants at approximately 3500 m3 / h flow rate to cool and clean the gas which is exiting the furnace. The blasted and contaminated water returned from the Blast Furnaces gas purification system is settled in 4 settling tank, and it is sent to the cooling towers for cooling 3-10 0C and reusing the heated water in the circulation system.

During the process, circulation water absorbs the pollution of the gas. Polluted water comes to radial pools for cleaning. During resting of water in radial pools, it is provided to coagulate by bringing the suspended solids together to the bottom. In order for this process to be carried out more effectively within the timeframe permitted by the system, it is imperative to apply auxiliary chemicals to accelerate this precipitation. The performance of radial pools is specified by the design firms as the upper level of Suspended Solids. The amount of suspended solids is determined by drying and cooling the remaining substances on the filter. Since the system control parameter TDS cannot be measured instantly, automatic polyelectrolyte dosage cannot be made and the chemical dosage amount cannot be changed according to the TDS which varies depending on the process.

In the study, multiple linear regression analysis was performed to find the best model that predicts the value of TDS and the parameter of TDS was made instantly measurable. In this context, process data were analyzed by using MiniTab software. The equipment and software work that can automate the amount of chemicals that must be dosed according to the determined TDS value has been completed and commissioned. As a result of the study, the compliance rate of the TDS target value was increased from 90% to 100%, and the variability is also decreased..

1. Introduction

1400-1700 Nm3 Blast Furnace Gas is produced for each ton of liquid crude iron produced in Blast Furnaces. These gases are burned as needed and energy is gained. Gases coming out of the blast furnace contain 10-20 g / Nm3 dust and moisture. If this gas is not subjected to any conditioning, it will cause the thermal effect to decrease and the combustion efficiency will decrease. Blast Furnaces are sent to gas cleaning plants at approximately 3500 m3 / h flow rate to cool and clean the gas which is exiting the furnace. The blasted and contaminated water returned from the Blast Furnaces gas purification system is settled in 4 settling tank, and it is sent to the cooling towers for cooling 3-10 0C and reusing the heated water in the circulation system.

During the process, circulation water absorbs the pollution of the gas. Polluted water comes to radial pools for cleaning. During resting of water in radial pools, it is provided to coagulate by bringing the suspended solids together to the bottom. In order for this process to be carried out more effectively within the timeframe permitted by the system, it is imperative to apply auxiliary chemicals to accelerate this precipitation. The performance of radial pools is specified by the design firms as the upper level of Suspended Solids. The amount of suspended solids is determined by drying and cooling the remaining substances on the filter. Since the system control parameter TDS cannot be measured instantly, automatic polyelectrolyte dosage cannot be made and the chemical dosage amount cannot be changed according to the TDS which varies depending on the process.

The chemical used for this process in İSDEMİR; high molar mass polyelectrolyte (polyacrylamid).
Two different mechanisms work during the process;

1. Flocculation. The process of settling the solid particles in a colloid that cannot be deposited because it is very fine-grained by adding suitable substances, bringing them together and growing them.
2. Coagulation is the process of making colloid-sized solid particles in the water that cannot be deposited by their own weight, with the help of various chemicals.

2. Experimental Procedure

System control parameter TDS cannot be measured instantly and chemical dosage amount cannot be changed according to TDS which varies depending on the process. With the work to be done, making the amount of Suspended Solids instantaneous, to make the chemical dosage dynamic. It is to keep the radial pool outlet water within the facility design parameters.

For measurement studies:

Measuring devices for pH, temperature and turbidity, which are instantly measurable values of the system, are integrated into the system. Measurement values of the devices are provided to be carried on the SCADA screen. The records of the measurements started to be archived through the program.

In order to compare the measurement values of the devices with the AKM, laboratory samples were taken at determined periods and analysis was sent.

Factors that may have an impact on the desired TDS value and can be measured online have been moved to the SCADA screen. At different times, samples were taken from the Inlet and Outlet water and a data set was made by performing AKM analysis in the laboratory. Factors that may be effective;

- Turbidity (NTU)
- Temperature (^{0}C)
- pH

A total of 93 analyzes were made and a data set was created. A few of these data are given in the table below.

Date	Hour	Turbidity	Temparature	TDS	pH	Sample Location
5.05.2019	15:30	106,0	42,7	748,0	6,34	Login
6.05.2019	09:30	69,2	36,8	313,0	6,36	Login
6.05.2019	13:30	47,4	38,3	365,0	6,39	Login

Table 1: sampling in the analysis

After the data set of TDS, Temperature and pH parameters were created, basic statistical data analyzes were made. In terms of mean, variability, parameters were examined.

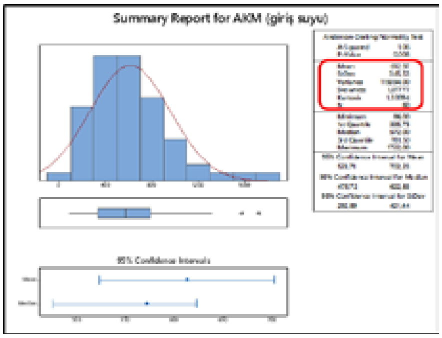

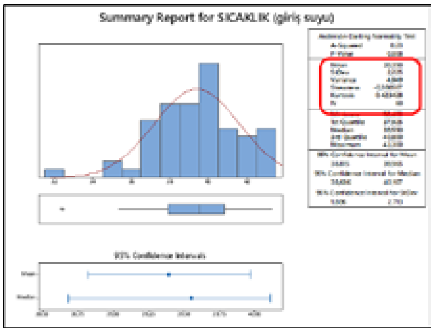

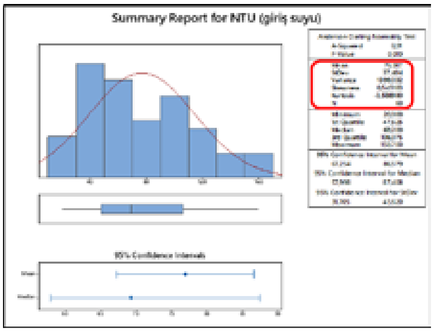

Graphic 1: Summary Report of water parameters

Mean Value of Inlet Water	
Turbidity (NTU)	76,92
Temperature (^{0}C)	39,39
TDS (ppm)	612,97

Mean Value of Outlet Water	
Turbidity (NTU)	2,66
Temperature (^{0}C)	40,07
TDS (ppm)	25,52

Multiple linear regression analysis was performed to find the best model that predicts the value of AKM. The best subset regression analysis was preferred to decide which of the 3 input factors we have to use.

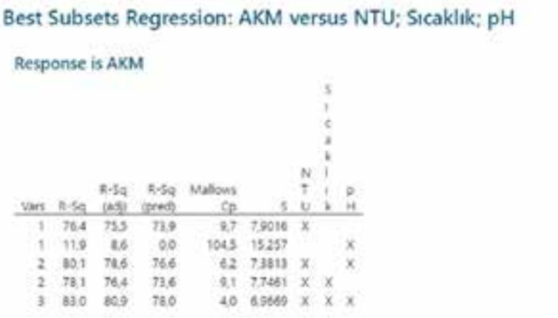

Best Subsets Regression: AKM versus NTU; Sıcaklık; pH

Response is AKM

Vars	R-Sq	R-Sq (adj)	R-Sq (pred)	Mallows Cp	S	NTU	Sıcaklık	pH
1	76,4	75,5	73,9	9,7	7,9016	X		
1	11,9	8,6	0,0	104,5	15,257			X
2	80,1	78,6	76,6	6,2	7,3813	X		X
2	78,1	76,4	73,6	9,1	7,7461	X	X	
3	83,0	80,9	78,0	4,0	6,9669	X	X	X

Table 2: Regression analysis water parameters

NTU (turbidity) value was higher than the other two factors when explaining TDS.

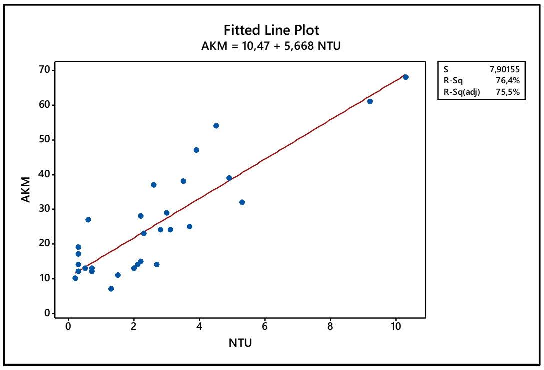

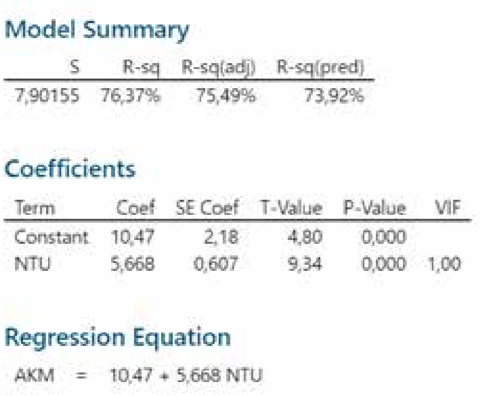

Model Summary

S	R-sq	R-sq(adj)	R-sq(pred)
7,90155	76,37%	75,49%	73,92%

Coefficients

Term	Coef	SE Coef	T-Value	P-Value	VIF
Constant	10,47	2,18	4,80	0,000	
NTU	5,668	0,607	9,34	0,000	1,00

Regression Equation

AKM = 10,47 + 5,668 NTU

Graphic 2: TDS mathematics model

By creating a model between turbidity and TDS in the study. TDS parameter has been made instantly measurable.

In parallel with the work carried out, an automation infrastructure was created, allowing system data to flow to the SCADA screen online. In addition, a frequency converter is integrated into the single speed running polyelectrolyte pumps, and variable operation is provided.

Since the inlet water could not be measured, the system was based on the outlet water values. After the TDS data came, experiments were made for 2, 5 and 10 minutes to determine how many minutes the pump speed should change, and a stable TDS value could be achieved in the form of operation after 10 minutes. The system was set up to adjust the dosage amount 10 minutes after the data it received.

3. Results and Discussion

The TDS value, which was 48.3 ppm on average before the project, decreased to 18.5 ppm after the project. In addition, variability has decreased. As a result of the study, the compliance rate of the TDS target value was increased from 90% to 100%, and the variability also decreased. With the improvements made;

TDS analysis made once a week has been made instantly measurable.

Blockages that may occur in the system are prevented, Cleaner gas was obtained, thus high combustion efficiency was achieved.

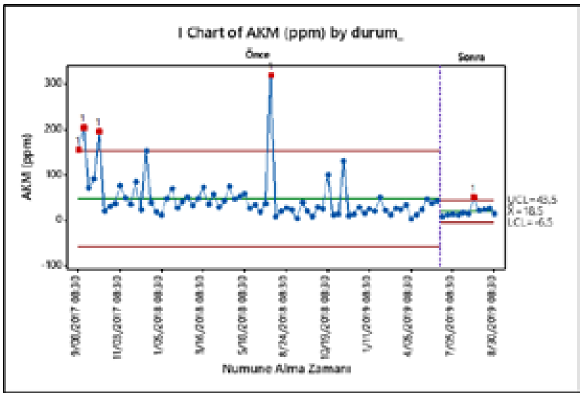

Graphic 3: I Chart of TDS

4. Conclusion

As a result of the work done, the manual and statically managed gas cleaning process has been made dynamic and automatic. Within the scope of industry 4.0 studies, the system has been benefited in terms of digitization and control of the process

Modelling and Digitalization of Mix Slab Applications

İlker AYÇİÇEK, Kübra AKGÜN, Güven SAĞDIÇ, Murat PERÇEM, Burak Emre IŞIK, Arif SAĞBUR, Tayfun KOCABAŞ, A. Mesud ÇAKIR, Fatih ÇELİK, İlyas AÇIKGÖZ

İskenderun Demir ve Çelik A. Ş., Oyak Maden Metalurji Grubu Operasyonel Mükemmellik Direktörlüğü

Turkey

Abstract

In the continuous casting process, cost optimization is provided by producing different qualities in tundish. During production of different grades in the same tundish, slabs called mix slabs. The head-end chemical analyzes of these slabs are different from each other. This difference is one of the most important factors affecting the final properties of the product. In order to bring these slabs into production, a certain algorithm must be designed and this algorithm must be known before production. Based on this need, it is necessary to model the final properties of the product with head-end chemical analyzes and hot rolling mill parameters of mix slabs. With the linear regression model, the final mechanical strength values of the product were modeled by entering slab chemical analyzes and predefined hot rolled parameters into the system. After teaching the system about the rules of how the applications will be given after deviating from the order of the product, the system gives the user the output quality of the mix slabs.

1. Introduction

In 2018, 96.4% of world crude steel production is produced by continuous casting method in 2018 [1]. Yield is the one of the most important issue in continuous casting process. Tundish is related equipment in continuous casting in the aspect of yield. More than 30 heats can be cast in one tundish. At this point, another problem comes up against steel producers. Are there orders with excess tonnage production? With this scope, different steel qualities are generally produced in a single tundish. In this process, mix slabs are produced and using this slabs is a problem in steel factories that produce steel with continuous casting method.

After producing mix slab, these slabs must be used according to slab chemical composition. As nature of producing of these slabs, slab chemical composition is not homogeneous as normal produced slab. Therefore, application of these slabs must require a model and decision making system. These system must be independent from human decision.

2. Method

To establish a decision making system, a model is needed to model the final properties of the material. Final properties of material refers to mechanical properties of steel coil in this work. For making model approximately 70000 test results is uploaded in Minitab. Outputs of model are yield strength and tensile strength of steel coil. Inputs of model are chemical compositions of slab, final thickness of coils and process parameters of hot strip mill. Using linear regression analysis is used for modelling mechanical properties of material.

Before modelling, assumption is head of slab analysis is first heat analysis and tail of slab analysis second heat analysis. Meanwhile, after modelling our system knows mechanical properties of coil before coil is hot rolled. Therefore, system knows how assign slab proper quality. Assignment rules are uploaded to system to assign slab. Assignment rules are; if yield strength/tensile strength difference between head and tail of coil bigger than 7 kg/mm^2 ; slab will be scrap; bigger than 4 kg/mm^2 and less than 7 kg/mm^2 is second grade; less than 4 kg/mm^2 prime quality. Before establish this system qualities were produced in İsdemir grouped in 60 different group and mix slabs were assigned according to these groups and matrix of these groups. This matrix had 3600 cells. In this work, with modelling and decision making system and of course with rules, new matrix is established for each qualities. In İsdemir nearly 400 different slab qualities and matrix will be 160000 cells.

3. Results and Discussion

Two different linear regression models are established. Yield strength and tensile strength are modelling successfully. Model strength are related to the R^2 values. R^2 values of models are 91,97 % and 95,37 % respectively. Formulas of these equations are not given in this paper however of course models derive a equation like; $y= a*x1+b*x2+c*x3$. In these equation a, b, and c letters shows the coefficient of inputs(x1, x2, x3). After modelling and rules that given system, a coil produced from mix slab have 3 different mechanical properties results, for tail, middle and head of slab. After that decision making system evaluate these values, assign slab proper qualities.

These all results are metallurgical and statistical works in this study. On the other hand, establishing these king of system, a factory has mix slab result matrix with high resolution, actually full resolution. This gives a capability to Production Planning Units to plan a tundish with high productivity.

4. Conclusion

After this work, İsdemir has a mix slab matrix with high resolution. Mix slab are assigned by system and digitalization is done according to model and rules for assing mix slabs. İsdemir has two mechanical model for steel coils. These models are not only used in these work but also used in new quality developments. In addition to this İsdemir Production Planning Unit knows the tundish performance before tundish casted. As a result of this study, an annual return of 268.000 $ was achieved.

References

[1] https://www.worldsteel.org/en/dam/jcr:96d7a585-e6b2-4d63-b943-4cd9ab621a91/World%2520Steel%2520in%2520Figures%25202019.pdf

the European Ceramic Society (ECerS XIII), 23-27 June 2013, Limoges-France, pp. 1042-1046.

[3] W.G. Davenport, M. King, M. Schlesinger and A.K. Biswas, Extractive Metallurgy of Copper, Pergamon, 2002, Oxford, United Kingdom, pp. 12, 34-56.

[4] D. Sherman, D. Brandon, Mechanical Properties and their Relation to Microstructure, Ed. R. Riedel, Handbook of Ceramic Hard Materials, Wiley-VCH, 2000, Weinheim, Germany, pp. 13-34, 45, 345-400.

[5] S. Altinok, Thermal Plasma Synthesis of Boron Carbide, M.Sc. Thesis, Middle East Technical University, 2018, Ankara, Turkey, pp. 34-45.

[6] <http://www.metal-powder.net> Dated: 08.11.2019.

Slab Movement Optimization

Ertan CULHACI, Mahmut KAYHAN, Timur KAYNAK, Ugur OKTAY, Halim SADE, Abdurrahman Mesud ÇAKIR, Fatih ÇELİK
İskenderun Demir ve Çelik A. Ş.
Turkey

Abstract

In this slab movement optimization approach; we focused on lowering excessive handling by homogenizing the stacks and boosting lot-shifting system. The project is implemented and tested in a pilot area of the Iskenderun Iron and Steel Co. (ISDEMIR) Slab Stock Yard.

Due to the (dimensional and steel grade) homogenization of the stacks; improvement in occupational safety, 5S and process safety has become more efficient. Lot shifting between slabs has become easier due to the combination of identical slabs. The effective capacity of the slab yard has been increased. Scheduling of rolling mill programs has become easier.

The results are recorded and compared with the past data.

The average number of slab handlings per day was reduced by more than 30%. Great reduction in dimensional average absolute deviation has been observed. Diversity of steel grades in each stacks has been decreased.

1. Introduction

Isdemir slab yard is a hot slab yard where mainly the slabs are sorted and stacked according to production schedule and charged into slab reheating furnaces. Addition to this main task, slabs are stacked destined to move on scarfing, trimming, shipping, or batching at outside yards. Stacking of different types of slabs with different dimensions and steel grades is a very complex activity for any crane operator.

Heterogeneous stacks like this bring some problems;

- These stacks have risk of collapse.
- The stack cannot be used at full capacity
- When a long-hot slab is stacked on a short slab, it bends and causes problem while charging into reheating furnaces
- With the mix of different manufacture lot number of slabs, the slab excessive handling increases

To solve these problems, an automated optimization model is created and implemented in a pilot area of ISDEMIR slab yard which is pointing the slab to the best point with the parameters, predetermined.

Figure 1. A Stack Formed By Operators Judgment Before the Project

2. Experimental Procedure

To see the homogenization of stacks;

- Annual, mean value of average absolute deviation of slab widths in each stack
- Annual, mean value of average absolute deviation of slab lengths in each stack
- Annual, mean value of number of steel grades in each stack

To see the count of Shuffling

- Annually mean number of slab handlings of each day

These performance indicators are recorded and tracked after implementation of the algorithm.

2.1 The Way System Works

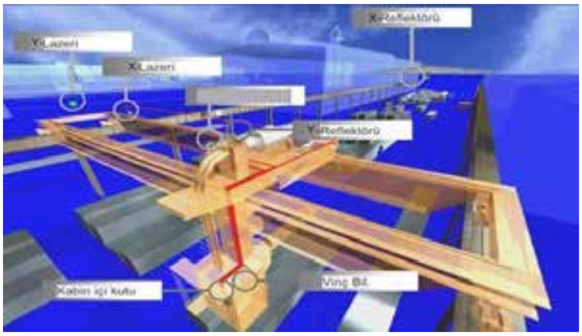

Figure 2. X-Y Lazers on which is being used for virtual mapping

Crane monitoring system includes; X-Y lasers and reflectors, crane system (Level2 application) and Slab Stock Management System (Level-3 application) inside the crane cabin. Slab stock fields are coordinated by dividing them into symbolic addresses in certain x-y value ranges. (See: Figure.2)

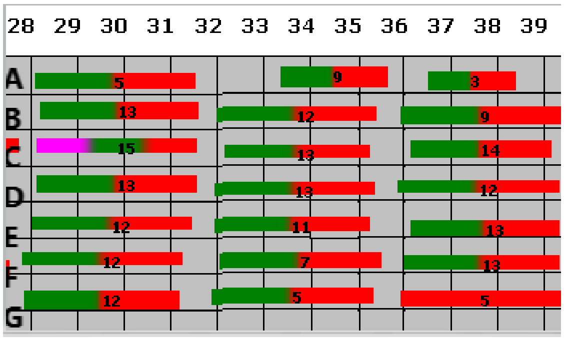

Figure 3. Level3 Virtual Map of a Small Part of The Slab Stock Yard

Slab movements and locations are recorded in the Slab Stock Management System by transmitting the values read from X-Y lasers from Level2 application to Level3 application.

All field registration procedures and crane work order management are performed in Slab Stock Management System.

Slab transfer handling operations were carried out under the control of crane operators. All field information was recorded on a daily basis for this decision mechanism to be realized by the software.

The field changes were examined by performing data analysis on the formed data. Proposal algorithm was supported with operational practices, crane operator feedback and research. Tracking, control and development in the software is facilitated by using the created algorithm with a flow chart.

In order to respond to Level2-Level3 communication in the fastest way and to conclude the analysis on the data in the shortest time, the flow diagram created was processed in database procedures. The suggestion algorithm runs when any slab is picked and destination address is displayed on the Crane Tracking System Level2 Operator Screen.

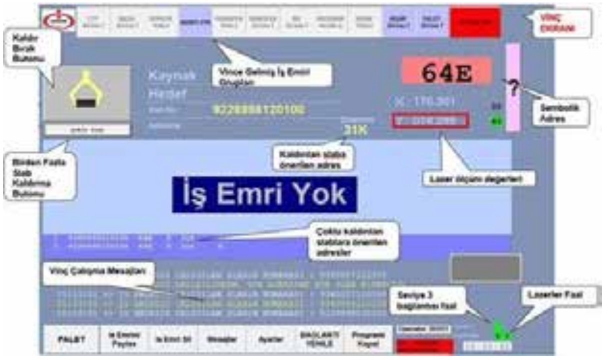

Figure 4. Level2 Operator Screen

3. Results and Discussion

After implementation of the suggestion system at the 17th of May 2019, improvement in the slab stock yard by means of stack homogenization and slab manipulation number are seen visually and numerically.

Figure 5. Pictures, Before and After the Project

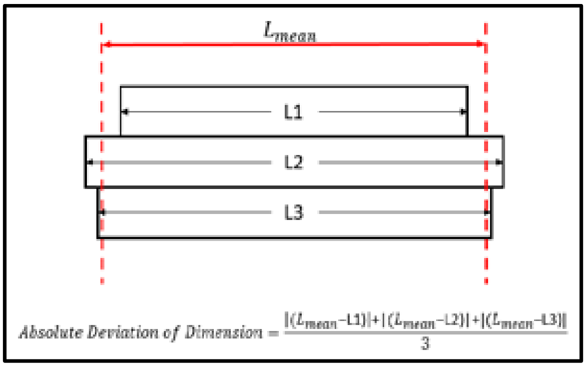

Figure 6. Formula of Average Absolute Deviation of Length For a Stack with 3 Slabs

Average absolute deviation is calculated for each stack by widths and lengths. And the the results showed the general condition of the slab yard.

If each stack had composed with the slab with same length, the average absolute deviation number would be zero. The more the number converges to zero, the more stacks homogenize dimensionally.

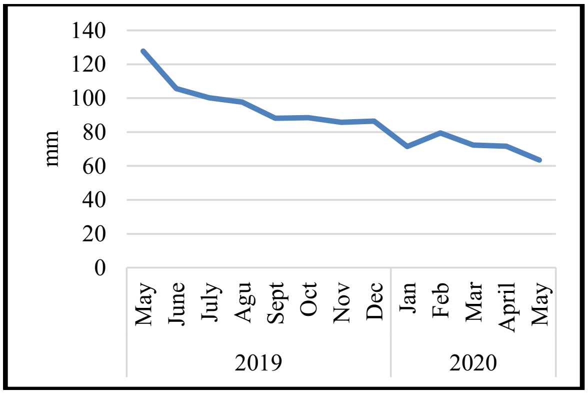

Figure 7. Average absolute deviation of widths for each stack

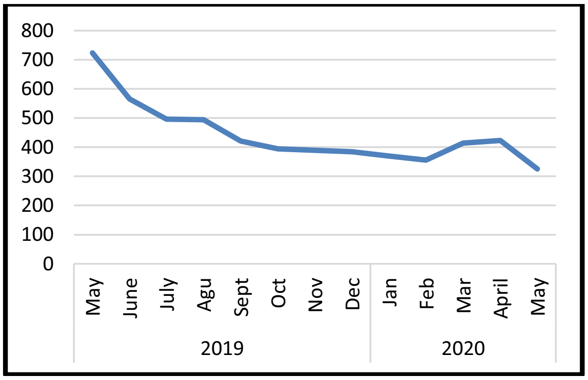

Figure 8. Average absolute deviation of lengths for each stack

As seen in the Figure 7 and Figure 8, great reduction is observed after the project implemented.

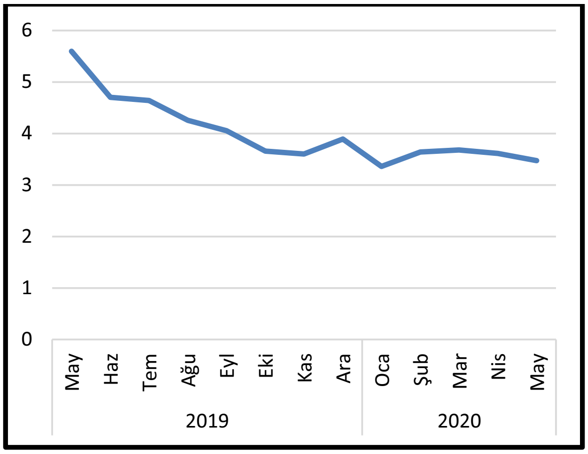

Figure 9. Variety of Steel Grades in Each Stack

Variety of steel grades in each stack is dropped. Same steel grades are stacked together more.

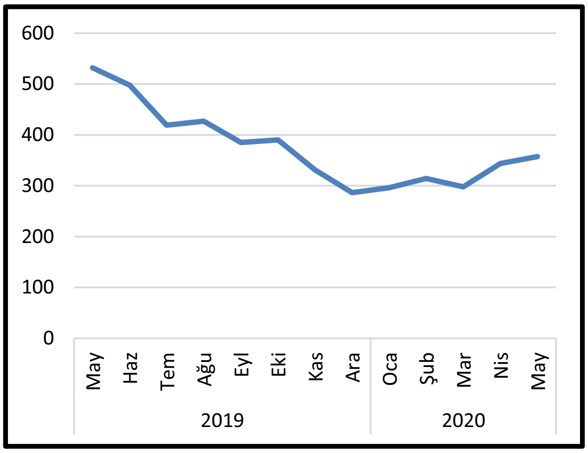

Figure 10. Average Daily Slab Handling Numbers

Average daily slab handlings dropped from around 500 a day to around 300 a day saving more than 300.000TRY a year.

4. Conclusion

Slab handling optimizations are rarely studied and only a few article is published similar to this project. Most of these studies are theoretical and they only focus on coil schedule. But in this unique study, all types of slabs are sorted differently and scheduling of the coil is also supported by embedding inside of the algorithm. The algorithm is implemented to ISDEMIR slab stock yard and tested on the area. The results were achieved only by the implementation of the algorithm without taking any other action, such as fully or partially rearranging any stacks.

A Case Study for Tool Steel Deformation: Crack Investigation of a Cold Work Tool Steel Used for Trimming Operations

Yekta Berk SÜSLÜ[1], Berkay SAVAŞKAN[1,2], Onur ÖZCAN[1], Muammer MUTLU[1], Özgül KELEŞ[2]
[1]Mita Kalıp ve Döküm Sanayii A.Ş., [2]Istanbul Technical University
Turkey

Abstract

High pressure die casting is a major casting method for producing massive amount of aluminum parts in a short time. The combination of repetetive pressure and temperature, dies (moulds) must be durable enough to provide high precision parts. In this manufacturing method, hot work tool steels are used for casting dies and cold work tool steels for trimming moulds. Trimming is an operation for cutting off runners and overflows from a cast part. Trimming mould steels must be hard enough to maintain and have outstanding edge retention ability. To make it possible, several heat treatment processes have to be applied. In this study; a failure analysis is made on a cold work tool steel AISI D2 (1.2379) that was cracked during tempering heat treatment. To obtain possible root causes, several characterization methods were applied to the mould steel. Chemical composition conformance was controlled with optical spectrometer. Specimens from various areas (no crack, crack propogation and crack finish) were metallographically prepared; their microstructures were investigated with optical microscope. Rockwell hardness testing was applied. FESEM analysis was carried out to the crack propogation area. Finally, XRD analysis was applied to check the retained austenite in the steel's structure.

1. Introduction

High pressure die casting is a versatile manufacturing method for aluminum mass production. Enabling relatively faster solidification rates and complex geometry, it has a wide usage area in automobile, defence and white-good industry. This method is carried out via injection of molten aluminum into the steel mould with high speed and following high pressure. With the combination of temperature and pressure, mould steels are exposed to thermomechanical fatigue in each cycle. By this way, chosen steels must be qualified enough to work about 100.000 cycles [1]. In HPDC; hot work tool steels are used for die casting moulds and cold work tool steels for trimming moulds. Trimming operation is the following process for HPDC cast parts to cut off their runners and overflows. In this process, part is placed onto a fixed die-half or fixture and moveable die-half makes vertical move and cuts the part by shearing from its periphery. In trimming operations, steel used must be hard and tough enough to maintain during the process. And have a great edge retention for providing smooth trimming surface. Tempered martensite structure is needed to overcome the compelling process conditions. In this case study, a failure analysis of a 1.2379 cold work tool steel used for the trimming mould was made.

2. Experimental Procedure

Heat treatment process route applied is given in Table 1.

Table 1. Heat treatment process route

Process step	Temperature (°C)	Time (min)
Preheating 1	450	5
Preheating 2	650	45
Preheating 3	850	50
Austenitizing	1050	90
Cooling	800 / 50	90
Tempering 1	530	180
Tempering 2	510	180
Tempering 3	510	180

The crack is observed after 2nd tempering process so 3rd stage of tempering is not applied. Cooling is carried out until the room temperature. Crack is started from a Ø50 mm through hole which is used for fixation. It is observed that the crack progressed in 3 directions. To analyze the failure, 3 locations are selected to investigate; Sample 1 with no crack (far from the crack), Sample 2 from crack propogation and Sample 3 from crack finishing. Crack initiation is at the bottom side of the mould so taking a specimen was not easy and required multiple EDM (Electrical Discharge Machining) stages. This area is omitted to avoid damaging the steel structure. The crack on the mould is given in Figure 1.

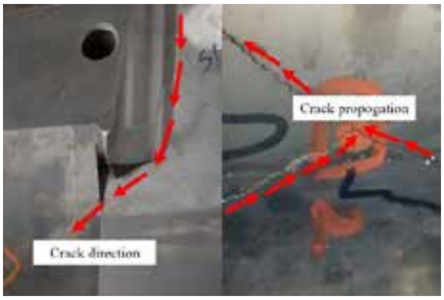

Figure 1. The crack on the mould

Ametek SpectroMaxx optical spectrometer is used for controlling the conformance of the chemical composition. Cut specimens (1, 2 and 3) are metallographically prepared via grinding from 180 mesh to 2500 mesh sandpaper and polished afterwards. Samples are etched with Nital etchant. Optical microsope analysis is carried out with Zeiss Axio. Another crack propogation sample is also morphologically analyzed via Bruker-FESEM. Rockwell C hardness testing is applied to the samples. PANalytical X'Pert PRO XRD is used to obtain the retained austenite in the structure with 45 kV and 40 mA settings (Cu Kα=1.54Å).

3. Results and Discussion

Chemical analysis of the steel is given in Table 2.

Table 2. Chemical composition of the steel (wt%)

	ISO 4957:2018	Steel MDS	Measured
C	1.45 – 1.60	1.48	1.49
Cr	11 - 13	12.44	12.18
Mo	0.7 – 1.00	0.76	0.83
V	0.7 – 1.00	0.79	0.73
Mn	0.2 - 0.6	0.42	0.43
Si	0.10 – 0.60	0.33	0.40
P	max 0.03	0.03	0.04
S	max 0.03	0.02	0.02

Based on optical spectrometer results and ISO 4957:2018 standard, the steel is 1.2379 cold work tool steel. Nital etched microstructures of Sample 1 is given in Figure 2. Tempered martensite can be seen as grayish and primer carbides can be seen as bright white colour which are dispersed in thermomechanical processing direction. Carbide distribution is homogenous in the microstructure. Small micro-voids are observed in the matrix.

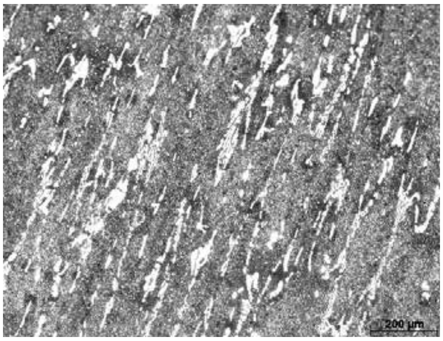

Figure 2. General microstructure of Sample 1

In Figure 3, the crack propagation zone and the crack of Sample 2 is shown. There are dense primary carbide phases at the crack boundary and micro cracks emanating from the main crack continued following these carbides. Added to this, micro-voids are observed and it is seen that these micro-voids helped microcrack propagation. These voids cause the formation of micro cracks in the steel by causing uneven expansion during heat treatment and this can be the cause of microcracks generation.

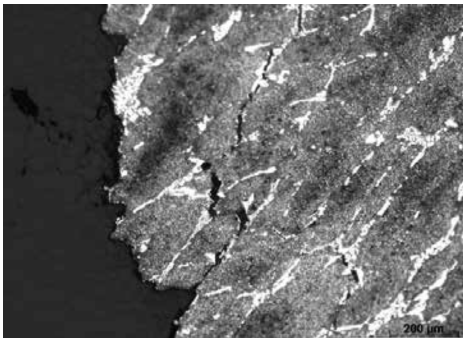

Figure 3. General microstructure of Sample 2

Microstructure of Sample 3 is given in Figure 4. In the region where the main crack ends, it can be seen that the crack continues parallel to the rolling direction. As in the crack propagation zone, dense primary carbide phases are observed at the crack boundaries. However, the presence of micro-voids close to the crack boundaries was detected. It has been observed that the cracks progress, following the relatively harder and brittle carbide phases and continuing through the micro-voids. Microstructural analyses show that micro-voids homogenously distributed among the brittle carbide particles. In some of spesific deformed areas more micro-voids are seen. To obtain the correlation between microstructure and mechanical properties, hardness test is applied. Average Rockwell hardness test results of 5 measurements given in Table 3.

Figure 4. General microstructure of Sample 3

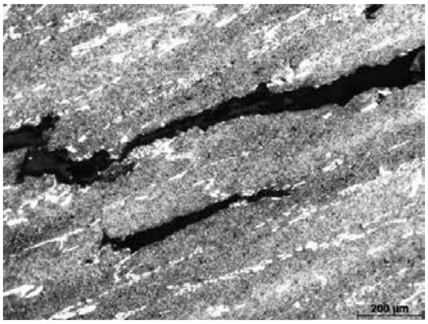

Table 3. Rockwell hardness test results (HRC)

Sample	Area / Hardness (HRC)						
	1	2	3	4	5	Avg.	σ
1	51.8	53.1	52.8	53.6	53.9	53.0	0.8
2	53.2	52.1	52.3	49.7	54.8	52.4	1.8
3	52.2	52.0	53.4	52.0	53.6	52.6	0.8

Despite of cracks and varying microstructure, steel's hardness data are rather homogenous but some differences are seen in each sample. Especially in Sample 2, the difference between the minimum and maximum level is almost 5 HRC. This may caused by deformations or local retained austenites. When all hardness values are evaluated, average hardness is 53 HRC. However, the desired hardness value for trimming tool has to be in the range of 58-60 HRC after tempering heat treatment. This relatively low hardness may caused by the retained austenite in the steel's microstructure due to annealing or tempering. For further observation, back scattered electron image of selected area is given in Figure 5. Spherical phases (large and small) are determined as secondary carbides [2]. Rupture like brittle failure marks can be seen near cracked areas. Crack includes various carbide phases which are enriched with Fe and Cr elements. EDS results are given in Table 4.

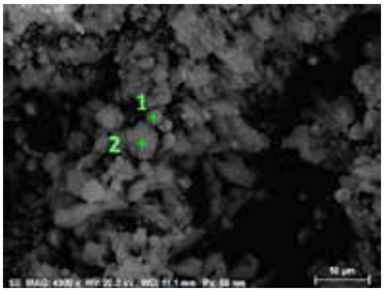

Figure 5. SEM image of Sample 2

Table 4. EDS results of crack area (wt%)

Element / Area	1	2
Fe	38.62	13.86
Cr	16.16	-
O	45.23	86.14

Since the SEM sample is unpolished crack line includes oxide (rust). The shape of the area 2 (fiberous phase) is also in conformance with rust structure of ferrous alloys.

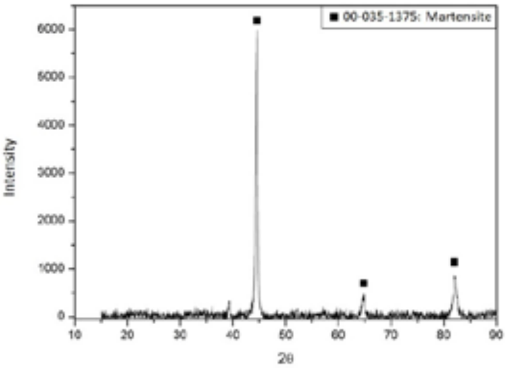

Figure 6. XRD analysis graph

XRD analysis result is given in Figure 6. Martensite phase is obtained (JCPDS-ICDD/00-035-1375). A peak seen at 39° is can not be identified but it is assumed that it can be chromium carbide [3], because martensite peaks and chromium carbide peaks may overlape. About retained austenite, there are no peaks observed at near 50° and 75° peculiarly. Here it can be said that the amount is less than 5% due to the detection range of XRD. Relatively low hardness (app. 53 HRC) can be a result of insufficient tempering stages. As stated, tempering process route includes 3 tempering stages; but when the mould cracked during/after the stage 2, the stage 3 is passed. This passed tempering stage could have an negative effect on the final hardness. Required tempering temperature range is 200°C–550°C to obtain 58-60 HRC for AISI D2 tool steels. Since the temperature range is wide (app. 350°C), tempering can be applied in various ways. Tempering temperature are choosen as 530°C and 510°C twice afterwards. Approximately 530°C is the required tempering temperature for 60 HRC. After this hardness value, there is a breakdown at the same temperatures. Hardness keep decreasing from 550°C – 58 HRC to 600°C – 50 HRC. Since the processing window of tempering is too narrow, tempering in 500°C – 530°C will be safer to prevent decrease in the hardness. Also, recommended temperature is

525°C for 60 HRC. Tempering also have positive effect on transforming retained austenite. The other possible root cause is; obtaining a retained austenite + martensitic structure after regular quenching/cooling stage. Since it is not sub-zero (cryogenic) process, retained austenite must be found in the structure with this transformation: austenite (FCC) – martensite (BCT) + retained austenite (FCC). Cryogenic treatments are applied mostly approximately at -100°C for transforming the martensite up to 99% and even more to prevent residual stress, which is also caused by retained austenite [4]. With cryogenic treatment; toughness, wear resistance and fatigue resistence can be increased. This mechanical improvements can be achieved by controlling the size of carbides. Das et al [5] have claimed that secondary carbide volume can be increased as 11.4% and distribution as 250%. Here, it can be said that coarse and longitudinal primary carbide phases can be distributed more homogenously. According to Li et al [6], 16.9% retained austenite (quenched) can be transformed to 4.1% with the help of cryogenic treatment.

4. Conclusion

A failure analyses were done on a trimming mould crack after 2nd tempering step. And following route causes have determined:

1. Micro-voids observed in the microstructure of the steel. These micro-voids have negative effects during heating and cooling stages of the mould. These defects may result in unstable expansion / shrinkage during heating / cooling stages and lead the crack initiation.
2. Lack of heat treatment step during quenching / cooling operation, lead to undesired crystallographic transformations; having heterogenous carbide sizes and retained austenite.

The possible failure mechanism is that during trimming operations stress applied on to the mould is generated a crack as a result of these microstructural defects causing catastrophic failure.

Acknowledgement

Authors would like to thank Arçelik-Materials Technology Management divison for SEM & EDS analysis, İpek Tunç and Faiz Muaffel for their help in phase analysis.

References

[1] D. Mitrović et al. Engineering Failure Analysis, 109 (2020) 104283.

[2] D. Das, A.K. Dutta, K.K. Ray, Materials Science and Engineering A, 527 (2010) 2182-2193.

[3] M.N. Mohammed et al. Metals, 8.5, (2018) 316.

[4] C.H. Surberg et al., Materials and Manufacturing Processes, 24, (2009) 863-867.

[5] D. Das et al. Wear, 266 (2009) 297-309.

[6] S.H. Li et al., Materials Science and Engineering: A, 605, (2014) 229-235.

The Effect of FeSiMn Usage on Deoxidation at Low Carbon Silicon Restricted Steel Grades

Zafer ÇETİN, Onur KART, Recep TOPAL, Davut ÇELİK, Özcan BAHAROĞLU, Oğuz GÜNDÜZ
Eregli Iron and Steel Works, Co.
Turkey

Abstract

In this study, the effect of FeSiMn addition on aluminum and FeMn (Middle Carbon (M.C)) consumption at low carbon low manganese silicon restricted (%0,03 max.) steel grades was investigated. FactSage 7.3 thermodynamic calculation software was used for thermodynamic equilibrium calculations to determine theoretical FeSiMn usage amount. Also silicon and aluminum level in liquid steel were predicted with thermodynamic simulations. According to calculation results, industrial trials were performed on aimed steel grades. It was observed that, FeSiMn addition decrease aluminum consumption up to 25 kg per heat thanks to the silicon content without exceed the silicon limit on focused steels. Furthermore, cost savings were achieved due to using a lower cost FeSiMn alloy instead of FeMn (M.C).

1. Introduction

At the end of oxygen steelmaking process, steel bath contains 500 to 800 ppm dissolved oxygen. Due to the adverse effect of oxygen, deoxidation is carried out by adding sufficient amount of ferroalloys or special deoxidizer during tapping. Aluminum is the most preferred deoxidizer to make steel fully killed [1,2]. Besides, addition of other ferroalloys as FeMn, FeSi and FeSiMn are support the deoxidation. Due to the relative high cost value of aluminum, the other deoxidizing ferroalloys adding first into the teeming ladle [2,3]. Generally, to prevent carbon and silicon increment in low carbon and silicon limited steel grade FeMn (M.C) is used as manganese source. FeMn (M.C) and FeSiMn alloys have similar C content but currently the unit price of FeSiMn alloy is lower. Therefore, the possibility of using FeSiMn alloy was investigated in this study.

2. Materials and Methods

In thermodynamic modelling, it was determined that free oxygen in liquid steel can be deoxidized with Si in FeSiMn and does not cause any Si increment when achieving Mn target (Fig.1). 120 tone non- deoxidized liquid steel and increasing amounts of manganese up to 200 kg were used in calculations. Industrial trials were performed at 250 heats with using 125kg FeSiMn per 120-tone heat on related steel grades.

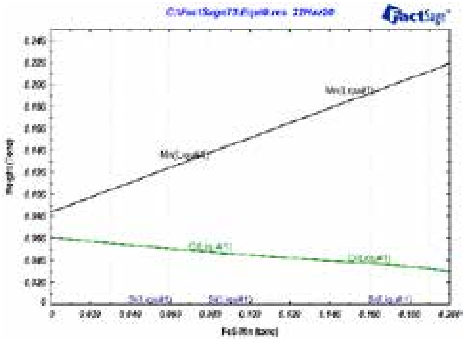

Figure 1. Change of silicon amount with addition of FeSiMn to liquid steel

3. Conclusions

In this study, the effect of FeSiMn usage instead of FeMn (M.C) on silicon restricted low carbon steel grades were evaluated. The results of the study can be summarized as follows:

-Thermodynamic investigations have been carried out for the use of FeSiMn in silicon-limited steel grades and it has been determined that the it is not cause any silicon problem due to the dissolved oxygen in the steel.
-According to thermodynamic examinations, industrial trials were performed in 250 heats with using 125 kg/heat FeSiMn.
-Silicon increment was very limited and not caused any silicon problem in the trials and it was determined that Aluminum consumption is decrease average of 30kg and 100 kg FeMn (M.C) is saved per heat.
-It is determined that a cost advantage of approximately 0,55 USD per ton steel can be achieved due to aluminum and FeMn (M.C) savings.

References

[1] A. Ghosh, Secondary Steelmaking Principles and Applications, Chapter 5, (2001) 103-139.
[2] G. J. W. Kor, P. C. Glaws, The Making, Shaping and Treating of Steel, 11th Edition Steelmaking and Refining Volume, Chapter 11, 677-680.
[3] L. Holappa, Secondary Steelmaking, Treatise on Process Metallurgy: Industrial Processes Volume 3, (2014) 301–345.

The Impact of Additive Aluminum Bullions Upon Recycle of Alloying Elements in Secondary Metallurgy

Mert TURFANDA, Emrecan ZORBA, Oğuzhan SAKARYA, Uğur CENGİZ
Bilecik Demir Çelik San. Tic. A.Ş
Turkey

Abstract

Secondary metallurgy in ladle furnaces being performed for refining of steel bath compositions to ensure and catch chemical % by mass of all alloying elements within tolerances of certain steel grades. The compositions also determines mechanical properties of semi-manufactured drawn billets in CCM and final product of rolled ribbed bars. Steel baths in LF may get prepared not only by adding various amounts of deoxidants as ferrosilicon and ferrosiliconmanganese etc but also by recycling alloying elements from reduction reactions in kinetic balance between liquid steel and slag over the bath. In this study, the potential of alloying elements recovery has been focused and investigated by aliminum bullions as dominant deoxidant in a manner of productivity to set chemical compositions with less consumption of certain deoxidants.

1. Introduction

Steel products in diverse shapes and formsa re entire classified with their chemical composition regarding their application areas in which frequently consumed. Hence, in order to ensure that steel final products always comply with certain quality standarts, ferrosilicon and ferrosilicon (FeSi) and ferrosiliconmanganese (FeSiMn) additives are consumed in a widespread manner. In our meltshop, we put FeSi and FeSiMn addition in use for essential mechanical properties of steel rebars in various diameters.

For this regard of industrial practice with related engineering concepts, we aim at significant decline in consumption of FeSi and FeSiMn additives by change of redox reactions' change in slag batch of metal oxides. It could be possible to enrich steel solution with alloying elements by favour of aliminium high free oxygen affinity while added Aliminium mass in ladles at LF station. Aluminum additions with both shape pressed and bullion stimulate chemaical reactions to reduce metal oxides of additives (MnO, SiO_2) in redox balance.

2. Materials and Methods

Different quantity of pressed aluminium bullions thrown in ladles of several heats in LF after tapping:

- Without Al addition heats No:1 and No:2
- 1 pressed Al bullion (2,65 kg) added in heats No:3 and No:4
- 2 pressed Al bullion (5,30 kg) added in heats No:5 and No:6
- 3 pressed Al bullion (7,95 kg) added in heats No:7 and No:8

After last sampling liquid steel and slag before steel teeming, the results of alloying elements and metal oxides in slag solution are quite comparable.

3. Discussion

Aluminium is apparently predominant deoxidiser in alloying elements as it demonstrates ionic bond attraction with free dissolved oxygen whereas contents of MnO and SiO_2 reduces cations Mn^{2+} and Si^{+4} in steel bath. In order to expand assesment of Al effect about metal oxide reductions, we simply compare composition %MnO and %SiO_2 of collected samples that No.1 and No.2 without Al addition result decrases of 7,3% SiO_2 and 6,2% MnO respectively however No.7 and No.8 with 7,95 kg Al addition come up decreases 12,1% SiO_2 and 9,7% MnO respectively.

In conclusion, pressed aluminium bullions presents conditionally reductive effect on recycling of alloying elements FeSi and FeSiMn additives with convenient parameters like temperature, basicity and viscosity.

4. References

[1] Suguna Soumya Varanasi, Venumadhava Rao More, Anil Kumar Tangudu.: Dey Santanu.: "Slag Modelling for Effective Desulphurization in Ladle Furnace Refining". ",Steel Melt Shop-2, [2]RINL-Visakhapatnam Steel Plant, Visakhapatnam, India."

[2] D.Gosh, V.A. Krishnamurthy, S.R. Sankaranarayanan.: "Applicatıon of Optical Basicity to Viscosity of High Alumina Blast Furnace Slags" "Department of Metallurgical and Materials Engineering, National Institute of Technology Tiruchirappalli, Tiruchirappalli – 620 015, India"

[3] Duffy, J.A., Ingram, M.D.: "Journal of the American Chemical Society,93,1971

The Effect of Different Isolation Practice of Dolomite Steel Ladles on Energy Consumption of Ladle Furnace

Oğuzhan SAKARYA, Mert TURFANDA, Burak EKİN, Uğur CENGİZ, Muammer BİLGİÇ
Bilecik Demir Çelik San. Tic. A.Ş
Turkey

Abstract

Present study is aimed to reduce energy consumption of the Ladle Furnace (LF) as a result of enhancing the isolation level of dolomite ladles. In accordance with this purpose, firstly thickness of isolation layers was improved and then amount of potential energy conservation was calculated by Fourier's Law. The calculated datas compared with the fluctuations of process energy parameters. As a result of that comparison, dolomite ladles achieve great energy efficiency due to low thermal conduction of dolomite refractory bricks, that is 2.05 W/K°m. However, dolomite brick is not the only factor for good isolation and energy efficiency. Thanks to the isolation materials providing better thermal isolation, the spent energy on heating 1°C of the liquid steel in dolomite ladles has been reduced by about 3% and the total amount of potential energy conservation was calculated as approximately 5.2%.

1. Introduction

An important part of the primary energy consumption of modern society is related to the production of basic materials. The steel industry is an energy-consuming industry. Energy costs make up a large portion of steel production costs, which makes energy saving/efficiency investments attractive. However, energy saving is important not only economically, but also due to the need to reduce carbon emissions released into the environment. Energy consumption for steel production can be reduced in a number of ways, but at the heart of these routes is making the whole production process more efficient and avoiding unnecessary resource use. In this context, the sources of energy losses have been examined and it has been decided to improve the isolation level of the ladles in order to make the use of the LF energy more efficient.

2. Materials and Methods

Within the scope of this study, 2 different types of isolation practice were applied to the Dolomite brick ladles. These; *Type 1:* 6 mm Nefalit 16 for wall/bottom, *Type 2:* 10 mm Nefalit 16 and 5 mm Microporous for wall/bottom.

In order to determine the effect of the isolation practices given above configurations on the energy efficiency of the ladle, the amount of energy lost by the ladles and the temperatures transmitted to the surface of the ladle were calculated with the Fourier Law (Equation 1) and compared with the production process data.

$$Q_{\text{loss}} = Q_{\text{loss-wall side}} + Q_{\text{loss-bottom side}} + Q_{\text{loss-radiation}} \qquad (1)$$

3. Conclusion

As a result of this study, the isolation levels of the ladles used in the BDC have been increased by changing the thickness of the isolation materials used. It is calculated that the total energy saving will be approximately 5.2% in the LF with the 2nd type insulated ladles. When we compare the isolation changes and the calculations made with the data of the current production processes, the energy spent to heat the liquid steel 1°C in the LF decrease from 20.23 kWh to 20.03 kWh for 1st type isolation with a 1% decrement ,and 19.62 kWh with a 3% decrement for 2nd type isolation.

20th

INTERNATIONAL
METALLURGY
MATERIALS
CONGRESS
10-12 June
2021

“in Digital Platform”

Ceramics, Glass, Refractory Materials

immc2021

Development of Geopolymer Based Thermal Insulation Material for Industrial Applications

G. Can TATLISU[1,3], Cem ACIKSARI[1,2], Yesim TEKE[2], Cuneyt KARAKAYA[2], Ozge AKARCAY[2], Emre KELES[1,3], Serdar CELEBI[2], Servet TURAN[1,3]

[1]Eskişehir Technical University, [2]TUPRAS R&D Center, [3]Ceramic Research Center

Turkey

1. Introduction

Energy production from renewable energy sources are increasing, it is reported that fossil fuel based sources is still the primary sources of energy output. This causes environmental concerns to be greatly increased due to air pollution and the release of CO_2 into the atmosphere. Therefore, the conservation of the energy in the oil & gas industries, is one of the most significant way of energy saving and emission reduction. Commonly used thermal insulation materials in energy –intensive industries, such as rock, glass and mineral wools, have some disadvantages such as high moisture holding capacity, originating the corrosion under insulation on base metal surface, difficulty in the application for equipment with complex geometry .For this purpose, the geopolymer produced by the chemical activation of industrial solid wastes (fly ash, etc.) is seen as the alternative and green solution for thermal insulation. In this study, it is aimed to develop powder-based alternative and competitive insulation coating material that can be directly applied to the hot metal surfaces (>250°C, etc.) via spraying process.

2. Materials and Methods

The raw materials used to make the geopolymer were: metakaolin from Imersy Metastar 501, Fy Ash from the thermal power plant (ADANA), Hollow glass microspheres (3M), NaOH (12M) and sodium silicate from (Sigma -Aldrich) with composition Na_2O-10%, SiO_2-26%, H2O - 64% by weight. Solid raw materials were firstly mixed to make homogeneously dry solid. Then, the mixture of sodium silicate and NaOH (aq) were added into the solid mixture to prepare uniform slurry at room temperature under slowly mixing conditions. After that, A new framework of hollow microspheres filled fly ash based geopolymer slurry was applied to the hot metal surface (>250°C, etc) via spray deposition technique. The effect of Si/Al, Na/Al, filler/geopolymer matrix ratios and water/geopolymer on the physical, thermal and mechanical properties of insulation coating were investigated. The microstructure of the geopolimer composite materials was determined using a scanning electron microscope (ZEISS SUPRA 50 VP). Thermal conductivity of geopolymer samples was measured with C-THERM TCI and adhesion strength of the coated samples was measured with a POSITEST AT-M .Finally, the thermal and physical stability of the insulation coating was tested for several days under harsh environment.

3. Conclusion

While the filler/geopolymer matrix ratio was increased from 1.0% to 20.0% by weight, the thermal conductivity of the coating decreased down to the values lower than 0.1 W/mK. Even though the thermal conductivity is greatly reduced, the adhesion strength was regrettably diminished as a function of increasing filler ratio in geopolymer matrix. The optimum filler ratio was found to be around 9.0% by weight. A gradual increase in adhesion strength and gelling characteristic of the geopolymer binder was observed when Si/Al mole ratio is increased from 2.0 to 3.0. However, higher Si/Al mole ratio initiated crack formation on the coating surface during the curing under higher temperatures ($T \sim 300$°C). Once Na/Al mole ratio increased from 1.0 to 3.0, the adhesion strength of the insulation slurry at higher pH values was reduced dramatically because of the crystallization of Na rich silicates. The optimum Si/Al mole ratio was between 2.0 and 2.5 whereas Na/Al ratio was approximately 1.5. Added water/geopolymer ratio is also critical for the viscosity, pore characteristic and curing behavior of the final composition. The optimum added water/geopolymer ratio was determined between 0.39 and 0.48 by weight. Results showed that hollow particles filled geopolymer coating material has very low thermal conductivity ($k<0.06$ W/mK) and excellent mechanical properties (Adhesion strength>3.5 MPa). With its high performance, the newly developed fly ash based geopolymer composite will be a promising candidate for thermal insulation coating on hot metal surfaces in energy intensive industries.

Acknowledgement

This study is sponsored by TUPRAS R&D Center under the contract number P1.18AP.02.

Effect of Brazing Parameters on the Microstructural and Mechanical Characteristics of Ceramic Matrix Composite/Titanium Alloy Brazed Joints

Simge TÜLBEZ[1,2], Ziya ESEN[3], Arcan Fehmi DERİCİOĞLU[1]
[1]Middle East Technical University, [2]Roketsan Industries Inc., [3]Çankaya University
Turkey

Abstract

Joining of ceramic matrix composites and metallic components by brazing is an emerging manufacturing technology in which a furnace or a direct heat source is used to join the materials using a brazing filler alloy. Brazing ceramics to metals has received considerable attention in the fields of nuclear reactors, aerospace, automotive and electrical engineering.

In the present study, a ceramic matrix composite (carbon fiber reinforced SiC) and a titanium alloy (Ti6Al4V) were joined using Ag-Cu based filler alloys by vacuum brazing method. In the literature, decreasing the brazing temperature is always recommended due to the advantages such as suppressed interfacial reactions, decreased erosion of substrates and minimum loss of base material properties. For this purpose, the interfacial microstructure and formation mechanism of the brazed joints between the ceramic matrix composite and the titanium alloy were studied for varying brazing temperatures. Brazing of ceramic composite materials to metals becomes feasible and joint strength improves when the ceramic composite surface is pre-metallized. Therefore, Ti was coated on C/SiC composite surfaces as active element in order to enhance the wettability of the substrates and formation of the reaction product layer. In this scope, the interfacial microstructure and formation mechanism of the brazed joints have been studied. Microstructural characterization of the brazed joints was performed using an optical microscope as well as Scanning Electron Microscope (SEM). XRD analyses were conducted to identify phases present in the ceramic matrix composite/titanium alloy joints. Shear tests were conducted for the mechanical characterization of the brazed joints.

1. Introduction

In the present study, brazing of C/SiC composite and Ti6Al4V (TC4) alloy using Cusil® and Cusil-ABA® brazing filler alloys has been investigated, and the interface evolution mechanism of the C/SiC composite/Ag–Cu based filler alloys/ TC4 alloy joints has been analyzed. The aim of this study is to investigate the effects of active brazing on the interface evolution mechanism and mechanical properties of C/SiC composite/TC4 alloy joints. Additionally, in literature, the advantages of decreasing the brazing temperature have been reported as controlled interfacial reactions, reduced erosion of the substrates, minimum loss of base material properties and minimum residual stresses. Therefore, the effect of brazing temperature on the microstructural evolution and mechanical properties of C/SiC composite/TC4 alloy joints have been investigated for both brazing filler alloys. Moreover, brazing of ceramics to metals becomes feasible and joint strength improves when the ceramic composite surface is pre-metallized. Pre-coating of the C/SiC composite surface with pure Ti that forms an active element layer on the C/SiC composite surface creates a wettable surface that strongly bonds the joint surfaces. With the wettable surface, Ti layer coated C/SiC composite joints revealed improved bonding characteristics.

2. Materials and Methods

Experimental studies have been carried out with C/SiC ceramic matrix composite and Ti6Al4V (TC4) alloy. As a brazing filler materials, Cusil® and Cusil-ABA® sheets were used. C/SiC composite surfaces were coated with 200 nm thick Ti layer. Throughout the study, brazing of C/SiC composite and TC4 alloy has been performed by vacuum brazing technique.

3. Conclusion

- For Cusil® brazing filler alloy, insufficient bonding shows that Ti layer coating could not provide enough reactive element for bond formation on the C/SiC composite side.

- For the Cusil ABA® brazing filler alloy, with the help of the Ti layer coating, the joint brazed at 875 °C for 10 min presented the maximum shear strength of ~24 MPa. The interface contains Ti_3SiC_2 and Ti_5Si_3 reaction layer products resulting in strong interfacial bonds and improved joint properties

Synthesis of Nanoceramic Powders and Their Biomedical Applications

Muhammet S. TOPRAK
KTH Royal Institute of Technology
Sweden

Abstract

In recent years, the design and synthesis of functional nanomaterials have attracted significant attention for their disparate and effective applications, in various fields. Contrast media based on nanoparticles (NPs) are used in various biomedical imaging techniques. X-ray fluorescence computed tomography (XF-CT) bio-imaging can provide sensitive and quantitative detection of NPs. X-ray fluorescent NPs, based on Molybdenum, Rhodium and Ruthenium, were synthesized, and employed as contrast agents for XFCT. Recently we showed in a laboratory system that XFCT could use spectrally matched molybdenum oxide (MoOx) based NPs as contrast agents to achieve 200 µm spatial resolution in mice, beyond what can be achieved with other imaging techniques (PET, SPECT, MRI). The specific x-ray fluorescence signal allowed imaging of the MoOx NPs in a time-series. Our attempts of in-vivo imaging has shown a significant difference on NP residence time in different regions.

Understanding the behavior and fate of NPs in biological systems is still a challenge as they will have a biodistribution and in-vivo uptake controlled by their size and surface. NPs will also suffer from critical modification immediately after they come in contact with biological media. We report on the development of MoOx nanoprobes, their stability in biological media using various characterization techniques. Cytotoxicity of these materials have been evaluated on different cell lines, and eventually silica shell was introduced for improved biocompatibility. Furthermore, the NPs were localized in the intracellular environment with confocal imaging, by detecting the fluorescence through the doped commercial fluorophore (Cy5.5 dye), demonstrating their dual-mode function. In fact, as macrophages constitute an important part of the immune defence, the possibility of localizing NPs is relevant to understand their interactions with cells. The hybrid NPs were tested in situ with XFCT bio-imaging on a dead mouse, managing to detect three different core-shell NPs simultaneously. The experiment highlighted the multiplexing property of the designed architecture. Finally, core-shell NPs with Molybdenum core were injected into mice, showing a more homogenous biodistribution than the core NPs alone, while preventing unwanted uptake in the lungs. The combination of optical and X-ray fluorescence properties in a unique hybrid nanomaterial architecture leads to an efficient macroscopic and microscopic imaging tool.

Reactive Hydrothermal Liquid-Phase Densification (rHLPD) - Low Temperature Densification Concept: A Case Study of $BaTiO_3$

Levent KARACASULU, Melike TOKKAN, Umut ADEM, Cekdar VAKIFAHMETOGLU
Izmir Institute of Technology
Turkey

Abstract

Reactive hydrothermal liquid-phase densification (rHLPD), different low temperature concept, was demonstrated as a case study. The ceramics produced from TiO_2 pellets subjected to hydrothermal process with the addition of the reaction solution were characterized not only by their structural properties but also by their electrical properties. Densified samples at low reaction temperatures showed promising electrical properties without additional annealing.

1. Introduction

Recently, different sintering concepts have been introduced that allow the densification of ceramics at temperatures below 400°C which are broadly called as cold sintering techniques. Among them, reactive hydrothermal liquid-phase densification (rHLPD) process consists of an infiltration, hydrothermal reaction, and subsequent crystallization [1]. In this study, $BaTiO_3$ ceramics, as a case model, were produced via rHLPD process having different densification concept from the other cold sintering techniques.

2. Materials and Methods

In this study, to produce highly dense $BaTiO_3$ ceramics, prepared green TiO_2 pellets were subjected to hydrothermal process with the addition of the reaction solution (aqueous $Ba(OH)_2.8H_2O$ solution) at 180°C and 240°C up to 72 h. The bulk densities were measured by Archimedes' method. The produced ceramics were analyzed using SEM, XRD, and TEM. They were characterized not only by their structural properties but also by their electrical properties such as dielectric, ferroelectric, and piezoelectric behaviors.

3. Conclusion

The increase of both reaction time and temperature under hydrothermal conditions by rHLPD process resulted in enhanced densification of the produced ceramics. Despite the low reaction temperatures, $BaTiO_3$ samples having densification reaching about 90% demonstrated acceptable electrical properties ($d_{33} = 84$ pC/N) without additional annealing.

References

[1] C. Vakifahmetoglu and L. Karacasulu, Current Opinion in Solid State and Materials Science, 24(1), (2020) p. 100807.

Hydrothermal Synthesis of Zinc Tin Oxide (Zn_2SnO_4) Particles for High Purity Sputtering Targets

Cem ACIKSARI[1,2], Umut SAVACI[1], Emel OZEL[1], Servet TURAN[1], Ender SUVACI[1]
[1]Eskişehir Technical University, [2]TUPRAS R&D Center
Turkey

1. Introduction

Metal oxide based electronic materials have been currently attractive for various applications such as optoelectronic devices, data storage devices, display technologies, high performance gas sensors due to their superior and unique properties. In today's electronic world, one of the most common applications of metal oxide materials is display panel technologies used in electronic devices like smartphones, computers and TVs. The active layer of TFTs (thin film transistor), which is one of the most significant components of the panel screen, belongs to Indium Gallium Zinc Oxide (IGZO) as amorphous oxide semiconductors (AOS). Although a-IGZO has superior performance in TFTs, higher content of Indium (In) and Gallium (Ga) is pushing up the cost of the final product and the supply of raw materials of In and Ga reserves poses a significant risk due to scarcity. Therefore, the other alternative oxides are needed to research. Zinc Stannate (ZTO) is one of the significant alternative compositions to replace by ITO because of its high abundancy in Earth's crust, relatively low cost, non-toxic nature and having reasonable optical and electrical properties. TFTs active layers as AOS are mainly composed of thin films generally prepared via sputtering technique. To produce high quality film the oxide target material used in sputtering should be high purity (> 3N5 grade), almost dense (> 95% TD) and having homogeneous phase and microstructure. Desired target properties are controlled by the quality of as-synthesized powder. Thus, the aim of this study is to develop a fundamental understanding of the production of high purity, controllable physical and electrical properties of oxide-based target material from hydrothermally synthesized nano particles to be used in the production of ZTO-based thin films with sputter technique for use in electronic industry.

2. Materials and Methods

In this study, zinc nitrate ($Zn(NO_3)_2 \cdot 6H_2O$, Sigma–Aldrich) and tin tetrachloride ($SnCl_4 \cdot 5H_2O$, Sigma–Aldrich) salts were used as zinc and tin sources. Zinc nitrate and tin tetrachloride were dissolved into distilled water to form two transparent solutions, and then, the two solutions were mixed together. An ammonium hydroxide (NH_4OH) solution was added dropwise into the Zn–Sn mixture. The Zn–Sn mixture was charged into a pressure vessel for the hydrothermal reaction, which was conducted at varying temperatures from 160 to 220° C for 24 h under autogenous pressure. The product was washed with distilled water and dried in an oven at 90 ◦C over a period of 1-3 days after the hydrothermal reaction. Zn_2SnO_4 based ceramic target was prepared from hydrothermally synthesized Zn_2SnO_4 powder by pressing at 200MPa in a cylindrical die and sintering under different conditions.

3. Conclusion

ZTO (Zn_2SnO_4) powders were successfully synthesized via hydrothermal method at 220°C for 24h. The effect of synthesis parameters such as initial cation concentration ratio (Zn^{2+}:Sn^{4+}), solution pH, synthesis temperature and time on the particle formation and growth mechanism and yield and stability diagram were investigated under hydrothermal conditions. Furthermore, the particle characteristics such as particle size and distribution, particle morphology during Zn_2SnO_4 formation were discussed as a function of synthesis parameters. Synthesis of Zn_2SnO_4 particles via hydrothermal method showed the high elemental purity (>99.9 wt%, i.e), smaller particle size (<100 nm, i.e), narrow particle size distribution, high surface area (>20 m^2/g) and equaixed particles with cubic morphology. In addition to that, hydrothermal synthesized Zn_2SnO_4 particles were sintered at relatively lower temperature for achieving desired density (~95% TD). The as-sintered ceramic target had homogeneous microstructure and small grain size (~1.5 µm).

Acknowledgment

The author would like to thank TUBITAK under the program of BIDEB 2211-C-National Doctoral Research Scholarship for the financial support. This study is also sponsored by Eskisehir Technical University.

Open and Partially Closed Porosity SiOC Ceramics

Tugce SEMERCI[1], Murilo Daniel de Mello INNOCENTINI[2], Gian Domenico SORARU[3], Cekdar VAKIFAHMETOGLU[1]
[1]Izmir Institute of Technology, [2]University of Ribeirão Preto (UNAERP), [3]Università di Trento
[1]Turkey, [2]Brazil, [3]Italy

Abstract

The so-called polymer derived ceramics (PDCs) are produced from preceramic polymers (PPs) and comprises mainly Si-based ceramics such as SiOC, SiC, SiCN and SiCBN, etc. Polysiloxanes are the most common ones among all PPs because they are economic and easy to handle in an ambient atmosphere with no special care. In the current work, porous SiOC ceramics were produced by using commercial polysiloxanes with both hollow and dense struts by changing the curing conditions during process and they were characterized in detail by various techniques.

1. Introduction

Porous ceramics have a broad range of applications such as filter (molten metals, diesel particulates, gases, etc), thermal insulator and catalyst for the chemical processes, etc. The three most commonly employed methods to form porous ceramics are: replica, direct foaming and sacrificial templating. In the replica method, synthetic/natural templates are infiltrated by ceramic slurry/precursor and squeezed until all solution is impregnated followed by drying. Then, templates are removed by burn-out and porous ceramics are formed as a negative or positive replica of the original template.

2. Materials and Methods

In this work, porous SiOC ceramics have been produced by the replica method by using commercial polysiloxanes. Three different siloxane blends were prepared and open and partially closed polyurethane foams were impregnated by these blends, followed by curing and pyrolysis under Ar flow at 1000 °C by using alumina tube furnace. All formed SiOC ceramic foams were characterized in depth by techniques such as SEM, XRD, BET, FTIR, texture analyzer and air permeation tests.

3. Conclusion

Microstructural features of SiOC ceramic foams were analyzed and they showed higher than 95% total porosity. Effect of PDMS percent in the structure was characterized by N_2 sorption analysis and it was observed that mesopores were formed in the foam surfaces and specific surface area was increased due to the decomposition of PDMS. Compressive strengths and air permeability measurements were analyzed for all SiOC ceramic foams.

Materials Recovery and Reuse for the 21st Century: A Call for Action and the Need for a Paradigm Change

Diran APELIAN
University of California
USA

Abstract

The concept of circularity has been a keystone of civilization. Ironically, the field of materials science and engineering has devoted much of its focus on the development of new materials and processes without much thought as to how these will be recovered and reused at end of life. Moreover, the design process for the manufacture of components has led to the production of many goods that cannot be repaired nor serviced. In this keynote presentation, we will review and assess the situation with data that reveals the severity of the problem. This will be followed with solution pathways and specific recommendations to change the paradigm for a sustainable future.

Investigation of the Effect of Low Cost Graphene on the Mechanical and Thermal Properties of the SiAlON Based Ceramics

Emre KELES[1,3], Cuneyt KARAKAYA[2], Cem ACIKSARI[1,2], Umut SAVACI[1,3], Servet TURAN[1,3]
[1]Eskişehir Technical University, [2]TUPRAS, [3]Ceramic Research Center
Turkey

1. Introduction

SiAlON ceramics are currently used in cutting tool applications especially machining hard materials such as high alloyed cast iron, aviation grade metals and its composites due to their superior mechanical and wear properties. The main disadvantages of SiAlON ceramics are their low thermal conductivity and fracture toughness. The increase of heat on the surface of the cutting tool during machining of the base material may cause some catastrophic failures in the material due to the low thermal conductivity. The cutting performance and the service time of the SiAlON ceramic tools can be improved by increasing the thermal conductivity and friction characteristic of the material. The aim of the study is to investigate the effect of low cost manufactured graphene on the thermal, mechanical and wear properties of SiAlON ceramics.

2. Materials and Methods

Graphene was produced by the Coleman method. Graphene dispersion was prepared by adding graphite to 500 mL CTAB solution in a flask. Then, ultrasonication tip was dipped in to the flask and it was sonicated for hours with 1 % amplitude until the desired concentration was obtained. Surfactant stabilized graphene was used as a raw material without any purification prior to adding into SiAlON matrix. Then, SiAlON powder was prepared. The different amount of graphene (from 0.25 to 1 weight %) were added and mixed in the ball mill at 300 rpm for 2 hours. Graphene-SiAlON mixture was left on the 170°C hot plate until dried and were sieved through 250µm to obtain fine powder. Graphene-SiAlON composites were manufactured by using the Spark Plasma Sintering (SPS) technique at 1775°C and 50MPa.

3.Conclusion

The densities of the samples were measured by using the Archimedes technique. Bulk densities were measured as 3.276 to 3.269 g/cm^3 for the 0 and 1 wt.%, respectively and the theoretical densities were around 99.8 % for all samples. There was not much negative effect of the graphene addition on the densification of SiAlON. Thermal diffusivities were measured at the temperatures between 25 and 700°C with 100°C intervals. It was shown that the thermal diffusivity increased when the graphene amount was increased. Hardness of the SiAlON and Graphene-SiAlON composites were also measured with the Vickers Hardness Test at 5HV. The maximum hardness value were calculated as 16 GPa for SiAlON and the minimum value were 14.5 GPa for the 1 wt.% Graphene-SiAlON composite. According to hardness measurements, hardness decreased from 16 to 14.5 GPa when graphene amount increased. To observe the distribution of the graphene in the ceramic body, SEM and TEM techniques were used and seen that graphene was homogeneously distributed.

$CaCO_3$ Doped AlON Ceramics Fabricated by Reactivxe Spark Plasma Sintering

Demet AYDOGMUS, Samet KAYA, Gultekin GOLLER, Onuralp YUCEL, Filiz SAHIN
Istanbul Technical University
Turkey

Abstract

In this study, polycrystalline aluminum oxynitride (AlON) ceramics doped with different amount of $CaCO_3$ fabricated by reactive spark plasma sintering. α-Al_2O_3 and AlN as starting materials with a composition of 64.3 mol% and 35.7 mol%, respectively. 0.1-0.3-0.5 wt.% $CaCO_3$ doped samples were produced in the temperature range of 1550-1635ºC for 30-40 min holding time at 20/60 MPa uniaxial pressure under nitrogen atmosphere. h-BN spray was applied on the surface of graphite sheets that was in contact with the powder. The effects of different sintering conditions (heating regime, molding condition) with varying amount of $CaCO_3$ on phase composition, densification, microstructure and mechanical properties were systematically investigated. In addition, the effects of applying different heating regime and different molding conditions on carbon contamination in the sintered samples were also discussed in this study.

1. Introduction

Polycrystalline aluminum oxynitride (AlON) ceramics has attracted much attention in recent years with their low density (3.71 g/cm^3), high elastic modulus (320 GPa) and high melting point (2165ºC) besides their superior mechanical and optical properties [1]. Due to mentioned attractive properties of AlON ceramics, they are mostly used in applications such as abrasives, armour materials and missile domes [2], [3].

The transparency of AlON ceramics largely depends on their microstructural properties. Since secondary and/or residual phases, inclusions or pores in the structure make light scattering areas and as a result, the transparency is badly affected. In addition, if AlON, which has a high symmetry cubic structure, has small grains, there will be more grain boundaries in the structure and the grain boundaries also cause light scattering. Highly dense and single phase structure with large grains (approx. 50 µm) should be obtained in order to obtain high transparency [4].

In recent years, various methods have been applied to obtain AlON ceramics including pressureless sintering, hot pressing and hot isostatic pressing. Among these methods, spark plasma sintering (SPS) method has attracted attention by allowing the rapid compaction of highly dense ceramics at relatively lower temperatures with shorter holding times compared to conventional methods [5], [6]. In order to fabricate transparent AlON ceramics, long duration times and high sintering temperatures are required. Therefore SPS is a cost-effective way comparing with conventional sintering processes.

Usually sintering additives are used for enhancing the sintering behavior of AlON ceramics and most studied ones are Y_2O_3, La_2O_3 and MgO in the literature [7]–[10].

In this study, it was aimed to investigate the effects of different sintering conditions (molding condition and heating regime) on AlON phase formation, densification, microstructure and mechanical properties of $CaCO_3$ doped AlON ceramics fabricated by reactive spark plasma sintering method. For this purpose, α-Al_2O_3 and AlN were reacted with varying amount (0.1, 0.3, 0.5 wt.%) of $CaCO_3$ by SPS. In order to minimize the graphite-powder contact in the graphite mold, all the graphite sheets used in this study were h-BN sprayed.

2. Experimental Procedure

High purity α-Al_2O_3 (Inframat Advanced Materials) with an average particle size of 100 nm and high purity AlN (Grade E, Tokuyama Soda Ltd.) with an average particle size of 1 µm were used as starting powders. High purity $CaCO_3$ (Merck GmbH) was used as an additive. The flowchart of the experimental studies was given in Figure 1.

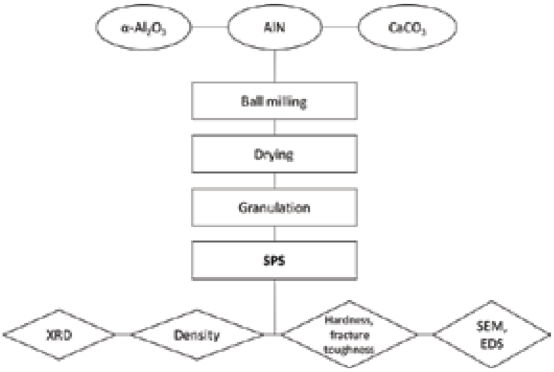

Figure 1. Flow Chart of Experimental Studies.

0.1-0.3-0.5 wt.% $CaCO_3$ doped powder mixtures having the molar ratio of Al_2O_3/AlN=64.3/35.7 were weighed and ball milled with ethanol for 24 hours using 10 mm diameter Al_2O_3 ball media. The majority of the ethanol was evaporated by means of a heated magnetic stirrer. The mixed slurry was then dried in an oven at 120ºC and granulated by sieving to 212 µm. As-prepared powder mixtures were loaded into a circular graphite mold having inner diameter of 50 mm. Sintering was conducted with a spark plasma sintering machine

(SPS-7.40MK-VII, SPS Syntex Inc). The experimental parameters of samples were given in Table 1.

Table 1. Experimental parameters and conditions.

Sample	$CaCO_3$ (wt.%)	SPS Temperature (°C)	Holding Time (min)	Pressure (MPa)	Heating Regime	Mold Condition
1	0.1	1550	30	20-60	50ºC/min	h-BN sprayed graphite foil on top-bottom-side
2	0.1	1575	30	20-60	50ºC/min	
3	0.1	1625	30	20-60	Fast heating*	
4	0.3	1635	30	40-60	Fast heating*	
5	0.3	1600	30	40-60	50ºC/min	
6	0.5	1560	30	40-60	50ºC/min	
7	0.5	1560	40	40-60	50ºC/min	
8	0.5	1560	30	40-60	Slow heating**	
9	0.5	1600	30	40-60	Slow heating**	h-BN sprayed graphite foil on top-bottom
10	0.5	1635	30	40-60	Slow heating**	

*Fast heating regime: 150ºC/min until 1400ºC and 20ºC/min until SPS temperature.

**Slow heating regime: from room temp.to 600ºC 50ºC/min, 25ºC/min until 1000ºC, 15ºC/min until 1400ºC and 8ºC/min until SPS temperature.

The SPS temperature was varied between 1550ºC and 1635ºC with holding time of 30 to 40 min. All experiments were carried out under nitrogen atmosphere. Gradual pressure was applied in all experiments. The pressure was low (20 MPa or 40 MPa) during heating process and initial part of the sintering and then increased to 60 MPa in the last 20 min. of sintering. 10 samples having 50 mm diameter and 2 mm thickness were produced in this study. The graphite foil placed between the mold and the powder to be sintered was applied on the top, bottom and side surfaces of the powder in the first 8 samples, while in the last 2 samples, graphite foil was not placed on the side surfaces. Thus, it was aimed to reduce carbon contamination from graphite foil. h-BN spray was applied on the graphite foil used in this study in order to prevent direct contact between the graphite and the powder to be sintered.

The graphite foil was scraped and also sand blasting was applied to remove remaining graphite on the sample. The crystalline phase analyses were performed by XRD (PANalytical X'pert Pro, equipped with an accelerator) in the 2Θ range of 10-90º by using CuKα radiation. The bulk densities of the sintered samples were measured by using Archimedes principle. The microstructural evaluation was carried out with a scanning electron microscopy (FESEM; JSM 7000 F, JEOL Ltd.). Vickers micro hardness and fracture toughness measurements were carried out by indentation technique with micro hardness tester (VHMOT, Leica Corp.) by applying at least 10 indentations for each sample.

3. Results and Discussion

XRD patterns of samples were given in Figure 2, 3, 4 and 5.

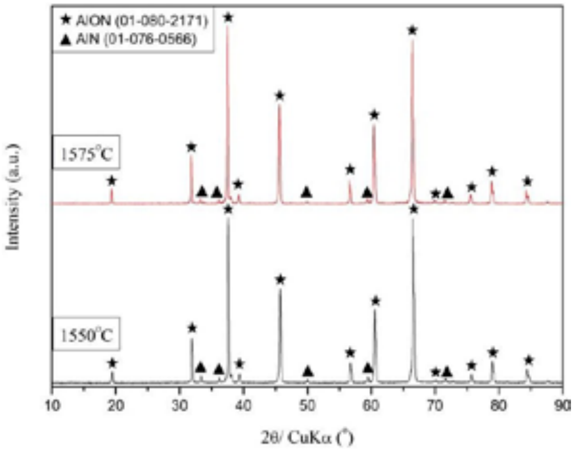

Figure 2. XRD patterns of Sample 1 and 2.

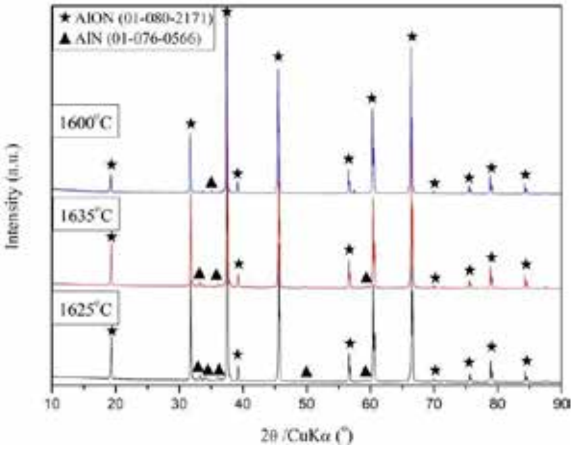

Figure 3. XRD patterns of Sample 3, 4 and 5.

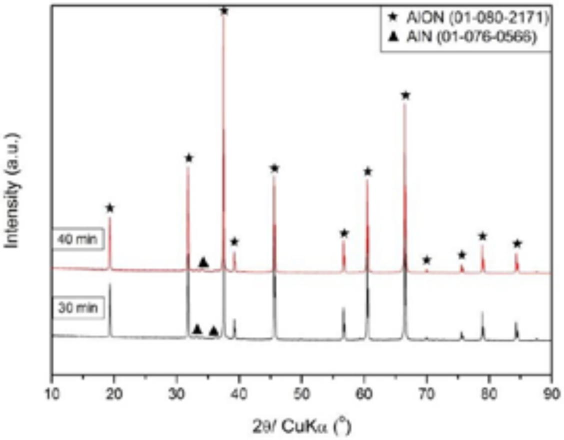

Figure 4. XRD patterns of Sample 6 and 7.

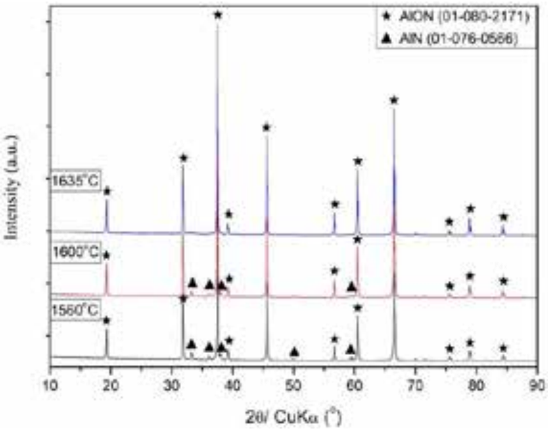

Figure 5. XRD patterns of Sample 8, 9 and 10.

A significant amount of unreacted AlN phase was detected besides AlON phase in the XRD phase analysis of samples containing 0.1 and 0.3 wt.% of $CaCO_3$. The results of Rietveld Analysis of these samples were given in Table 2.

Table 2. The Rietveld Analyses of Samples 1 to 5.

Sample	$CaCO_3$ (wt.%)	SPS Temperature (ºC)	Pressure (MPa)	AlN Phase (%)	AlON Phase (%)
1	0.1	1550	20-60	5.5	94.5
2	0.1	1575	20-60	4.2	95.8
3	0.1	1625	20-60	3.8	96.2
4	0.3	1635	40-60	3.3	96.7
5	0.3	1600	40-60	1.9	98.1

XRD analyses of the samples containing 0.5 wt.% $CaCO_3$ and SPSed at 1560ºC with a constant heating rate of 50ºC/min at different holding times indicated that when the holding time was increased from 30 minutes to 40 minutes, the presence of AlN phase was still present in the structure. However, the intensity of the peaks of the AlN phase decreased in 40 min holding time. Since the problem of carbon contamination could not be solved at a constant heating rate of 50ºC/min, subsequent experiments were carried out by applying a slow heating regime and without using graphite foil on the inner lateral surfaces (side) of the graphite mold. As a result of the increase in sintering temperature by 40ºC, there was no significant decrease in the peak intensities of the residual AlN phase in samples SPSed at 1560ºC and 1600ºC with the same parameters. When the SPS temperature was increased to 1635ºC, 100% AlON formation was obtained. The results of Rietveld Analysis of the samples containing 0.5 wt.% $CaCO_3$ were given in Table 3.

Table 3. The Rietveld Analyses of Samples 6 to 10.

Sample	$CaCO_3$ (wt.%)	SPS Temperature (ºC)	Holding time (min)	AlN Phase (%)	AlON Phase (%)
6	0.1	1560	30	2.7	97.3
7	0.1	1560	40	0.9	99.1
8	0.1	1560	30	3.5	96.5
9	0.3	1600	30	2.9	97.1
10	0.3	1635	30	-	100

The density values of samples obtained according to Archimedes principle. The measured density values of samples containing 0.1-0.3-0.5 wt.% $CaCO_3$ produced with different sintering parameters and mold conditions were given in Table 4.

Table 4. The measured density values of the samples.

Sample	$CaCO_3$ (wt.%)	SPS Temperature (ºC)	Measured density (g/cm^3)
1	0.1	1550	3,65±0,01
2	0.1	1575	3,66±0,01
3	0.1	1625	3,66±0,02
4	0.3	1635	3,66±0,01
5	0.3	1600	3,68±0,01
6	0.5	1560	3,68±0,02
7	0.5	1560	3,70±0,02
8	0.5	1560	3,64±0,03
9	0.5	1600	3,65±0,01
10	0.5	1635	3,68±0,03

While the highest density value was obtained in the sample SPSed at 1560ºC for 40 minutes with a constant heating rate of 50ºC/min, the transparency could not be obtained since the carbon contamination could not be removed and 100% AlON formation could not be achieved in the sample. The relative density of the sample, at which 100% AlON formation was obtained and SPSed at 1635ºC containing 0.5 wt.% $CaCO_3$ with slow heating regime for 30 minutes, was calculated as 99.14%.

Micro hardness and fracture toughness values of the samples were given in Table 5.

The single phase AlON sample doped with 0.5 wt.%CaCO3 and SPSed at 1635ºC under slow heating, has a hardness value of 15.91 ± 0.32 GPa and a fracture toughness value of 2.83 ± 0.30 MPa.m$^{1/2}$. These values are consistent with the theoretical values of AlON ceramics.

Table 5. The micro hardness and fracture toughness values of the samples.

Sample	$CaCO_3$ (wt.%)	SPS Temperature (ºC)	Micro Hardness (GPa)	Fracture toughness ($MPa.m^{1/2}$)
1	0.1	1550	15.60±0.34	3.46±0.27
2	0.1	1575	16.05±0.18	3.51±0.26
3	0.1	1625	15.46±0.21	2.75±0.19
4	0.3	1635	14.89±0.26	2.80±0.18
5	0.3	1600	15.73±0.19	2.50±0.24
6	0.5	1560	15.84±0.19	2.41±0.23
7	0.5	1560	15.81±0.28	3.03±0.50
8	0.5	1560	14.66±0.41	2.95±0.21
9	0.5	1600	14.41±0.35	2.87±0.14
10	0.5	1635	15.91±0.32	2.83±0.30

Figure 6 showed the fracture surface SEM images of the sample, SPSed at 1635ºC by applying 40/60 MPa gradual pressure with slow heating regime containing 0.5% $CaCO_3$. Average particle size of the sample with 100% AlON phase formation was determined as 13-14 µm which was not sufficient to obtain transparency in this sample.

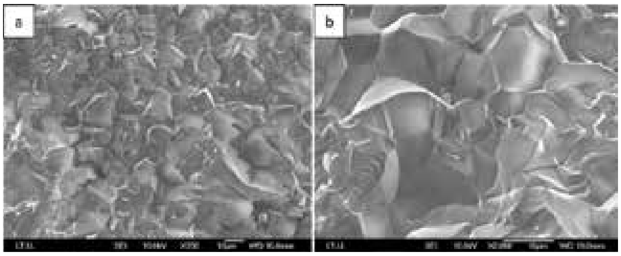

Figure 6. Fracture surface SEM images of Sample 10 a) 750X and b) 2000X.

The EDS mapping image and the elemental analysis result of the sample 10 were given in Figure 7 and Table 6.

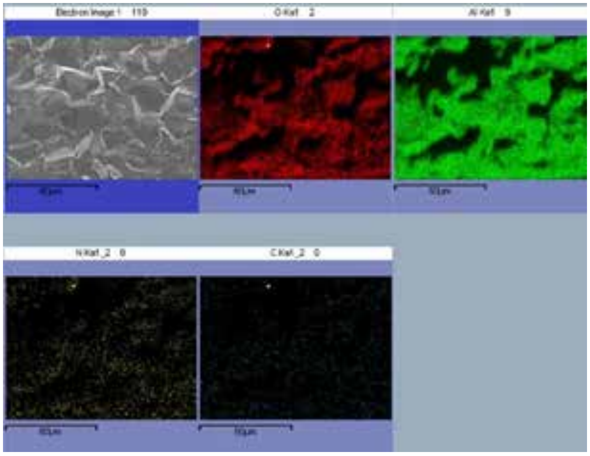

Figure 7. EDS mapping image of Sample 10.

Table 6. The elemental analysis results of Sample 10.

Element	Wt.%	Atomic %
C	2.89	4.73
N	6.53	9.15
O	40.38	49.57
Al	50.21	36.55
Total	100	100

As a result of EDS mapping analysis, carbon dispersion throughout the structure was observed.

4. Conclusion

0.1-0.3-0.5 wt.% $CaCO_3$ doped AlON ceramics with 50 mm in diameter and 2 mm in thickness were produced by using reactive spark plasma sintering method.

Single-phase AlON structure was obtained in the 0.5 wt% $CaCO_3$ doped sample SPSed by applying slow heating regime at 1635ºC for 30 minutes at 40/60 MPa gradual pressure under nitrogen atmosphere. The relative density of this sample was 99.14%, and as a result of the microstructure studies, it was determined that the average particle size was around 14 µm.

Based on these results, it was concluded that in order to obtain transparency, a higher pressure should be applied to produce samples with very high density (> 99.5%) and high grain size (> 50 µm), as well as to eliminate the problem of carbon contamination.

Acknowledgement

This study was financially supported by the Scientific and Technological Research Council of Turkey (TÜBİTAK), Bilateral Project No: 217M905.

References

[1] N. D. Corbin, “Aluminum oxynitride spinel: A review,” *J. Eur. Ceram. Soc.*, vol. 5, no. 3, pp. 143–154, 1989, doi: 10.1016/0955-2219(89)90030-7.

[2] A. M. Tsabit, M. D. Kim, and D. H. Yoon, “Effects of various rare-earth additives on the sintering and transmittance of γ-AlON,” *J. Eur. Ceram. Soc.*, vol. 40, no. 8, pp. 3235–3243, 2020, doi: 10.1016/j.jeurceramsoc.2020.03.027.

[3] Z. Feng, J. Qi, and T. Lu, “Highly-transparent AlON ceramic fabricated by tape-casting and pressureless sintering method,” *J. Eur. Ceram. Soc.*, vol. 40, no. 4, pp.1168–1173,2020, doi:10.1016/j.jeurceramsoc.2019.11.065.

[4] Z. Xiao *et al.*, “Materials development and potential applications of transparent ceramics: A review,” *Mater. Sci. Eng. R Reports*, vol. 139, no. August 2019, p. 100518, 2020, doi: 10.1016/j.mser.2019.100518.

[5] Y. Shan, X. Wei, X. Sun, E. Torresani, E. A. Olevsky, and J. Xu, “Effect of heating rate on properties of transparent aluminium oxynitride sintered by spark plasma sintering,” *J. Am. Ceram. Soc.*, vol. 102, no. 2, pp. 1–12, 2018, doi: 10.1111/jace.16030.

[6] Y. Shan, X. Wei, X. Sun, J. Xu, Q. Qin, and E. A. Olevsky, “Highly infrared transparent spark plasma sintered AlON ceramics,” *J. Mater. Res.*, vol. 32, no. 17, pp. 3279–3285, 2017, doi: 10.1557/jmr.2017.96.

[7] H. Guo, X. Mao, J. Zhang, R. Tian, and S. Wang, “Densification of AlON ceramics doped with Y2O3-La2O3-MnO additives at lower sintering temperature,” *Ceram. Int.*, vol. 45, no. 4, pp. 5080–5086, 2019, doi:

10.1016/j.ceramint.2018.11.210.

[8] X. Li, J. Luo, Z. Feng, S. Zhou, and J. Huang, "In-situ hot pressing sintering behaviors of Y2O3- La2O3 co-doped AlON ceramic," *Ceram. Int.*, vol. 42, no. 15, pp. 17382–17386, 2016, doi: 10.1016/j.ceramint.2016.08.037.

[9] L. Liu *et al.*, "Uniform and fine Mg-γ-AlON powders prepared from MgAl2O4: A promising precursor material for highly-transparent Mg-γ- AlON ceramics," *J. Eur. Ceram. Soc.*, vol. 39, no. 4, pp. 928–933, 2019, doi: 10.1016/j.jeurceramsoc.2018.10.028.

[10] Q. Chen, Y. Wang, J. Qi, and H. Wang, "A contrast of carbothermal reduction synthesis of MgAlON and AlON powders for transparent ceramics," *J. Alloys Compd.*, vol. 791, pp. 856–863, 2019, doi: 10.1016/j.jallcom.2019.03.387.

TiC Synthesis from Oxide Raw Materials Through Self-Propagating High-Temperature Synthesis

Tuğçe ERGÜL, Umay ÇINARLI, Mehmet BUĞDAYCI, Ahmet TURAN
Yalova University
Turkey

Abstract

Titanium carbide (TiC) has very remarkable properties such as high resistance to chemical corrosion, stability at high temperatures, high hardness and wear resistance with good conductivity for electricity. Combustion synthesis (self-propagating high-temperature synthesis, SHS) is one of its production methods resulting in nano-size powders with high purity. The main advantage of SHS method is the low energy consumption for synthesis in comparison to other techniques e.g. carbothermic synthesis [1]. In the present study, synthesis conditions of TiC from oxide raw materials (TiO_2, Mg, and C) were investigated.

1. Introduction

Titanium carbide is a ceramic powder which is one of the hardest natural carbides and, it is used in cermets and advanced ceramic tools. Titanium carbide is produced through carbothermic reduction, chemical vapor deposition, direct carburization, mechanical alloying, and self-propagating high temperature synthesis (SHS) methods [2]. Between the methods in question, SHS results in the formation of high purity and nano-size products because of extremely short reaction times. In this process, TiC is produced with less external energy requirement.

2. Materials and Methods

In the present study, synthesis conditions of TiC from oxide raw materials (TiO_2, Mg, and C) were investigated. Raw materials were mixed at different stoichiometric ratios; up to 3.0x for C and from 0.9x to 1.2x for Mg. After SHS experiments, an HCl leaching step was conducted to purify TiC and to extract Mg-based impurities of the products out. Following leaching conditions were applied: solid weight of 10 g, solid/liquid ratio of 1/10 and duration of 60 minutes at room temperature. Liquid phase consisted of 23 mL distilled water and 77 mL 37%HCl. Filter cakes were dried at 105 °C for 150 minutes. Dried filter cakes were weighed and, mass loss values, after leaching, were recorded. For the characterization of products, XRD, SEM-EDS and particle size measurement techniques were used.

$$TiO_2 + C + 2Mg \rightarrow TiC + 2MgO \qquad (1)$$

Before the experimental studies, thermochemical simulation studies were carried out by means of HSC Chemistry 6.1 software.

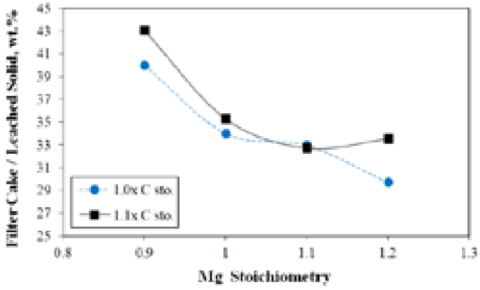

Figure 1. Weight change of filter cakes after HCl leaching in the SHS experiments conducted under air atmosphere

3. Conclusion

Self propagating high temperature synthesis (SHS) is applicable and is a fast process for producing titanium carbide. Application in simple reactors are the main advantage of this process.

References

[1] S. S. Kiparisov, Y. V. Levinskill, O. V. Padalko, A. P. Petrov, I. P. Deulina, Properties of Titanium Carbide Powders Produced from Titanium and Titanium Alloy Swarf.

[2] R. Tomoshige, Y. Kakoki, K. Imamura, A. Chiba, Effect on addition of titanium diboride to titanium carbide produced by the SHS:shock consolidation method, Journal of Materials Processing Technology, Volume 85 (1999), pp. 105–108.

Fabrication of High Density Alumina Ceramics from Nanopowders through Colloidal Processing

Hüseyin Utkucan KAYACI, Simge ÇINAR
Middle East Technical University
Turkey

1. Introduction

Utilizing nanopowders in production of fully dense materials with fine grain structures is highly adventageous, particularly where high mechanical properties are desired. Besides, recently developed techniques, such as additive manufacturing may require high solids content suspensions. Despite the advantages of slurry based processing of oxide ceramics, production of nano-structured high density bodies is still a challenge. The main limitation in colloidal processing of nanopowders is their unexpectedly high suspension viscosities. High viscosities restrict the maximum achievable solids content, which, in turn, limit the structural integrity and the density of green body when consolidated. Furthermore, because of the smaller interparticle distance in highly loaded suspensions, nanopowders tend to agglomerate fast, which creates another challenge in terms of the homogeneous distribution of powders in their suspensions and green bodies. In this study, various approaches for nanopowder suspension formulations were discussed and their effect on the particle packing, green body formation and sintering process were investigated.

2. Materials and Methods

2.1 Materials

Alumina powder with high purity (≥99.5%) and phase distribution of $\gamma/\delta \approx 70:30$ was used as main powder. The powder had a density of 3.67 g/cm^3 and BET specific surface area of 38.8 m^2/g. Its average particle size of 42 nm was calculated as its equivalent spherical particle diameter from BET specific surface area. A commercially available alumina powder (Premalox 0.3 DA) was as α seed. The powder had a density of 3.98 g/cm^3 and was in fully α-phase. NaCl, D-fructose (99%), L-(+)-ascorbic acid (99%) were used as additives. Ultrapure water with the resistivity of 18.2 MΩ cm was used for all suspensions.

2.2 Methods

NaCl and D-fructose or ascorbic acid were added to the ultrapure water. Required amounts of NaCl were estimated in molar quantity of solution and different molarities were studied. However, required amount of D-Fructose or ascorbic acid was determined 4 wt.% or 1 wt.% for D-fructose or ascorbic acid, respectively. Alumina powder as a volume percentage of the suspension was slowly and carefully added into the solution. In studies where the seed α-Al_2O_3 powder was used, volume of the seed powder was taken into account in sample preparation. The suspensions were slip casted into cylindrical polymeric molds. Dried green bodies of alumina were put into furnace and heated to 550 °C with a heating rate of 5 °C/min for an hour to remove organic contents. Then, bodies were further heated to 1000 °C with the same heating rate again. After reaching 1000 °C, heating rate was increased to 10 °C/min. Samples were heated up to 1600 °C and kept at that temperature for 2h. After finishing sintering step ends, samples were left in the furnace to cool down to room temperature.

3. Conclusion

In this study, effects of various approaches and formulations on nanopowder packing and its sinterability was investigated. Suspensions with solids content up to 35-40 vol.% were obtained. When these suspensions were slip cast, the green body densities as high as 58% could be obtained. When sintered, the structures with relative densities up to 96% could be achieved and that can be further increased to 99% using α-Al_2O_3 seed powder during sintering. As a result, high density alumina ceramics could successfully be fabricated from nanopowders.

Synthesis of Magnetic Bioactive Glass

Cansu TAŞAR, Batur ERCAN
Middle East Technical University
Turkey

Abstract
Magnetization of bio-glasses (BG) to target tissues is challenging. To identify the optimal magnetite content for BG, samples having various amounts of magnetic phase were prepared. Magnetic bioactive glasses were fabricated by sol-gel technique and calcined for two hours at 500 ˚C. Samples were named according to magnetite content (wt%) as 10%Fe_3O_4-BG, 20%Fe_3O_4-BG, 30%Fe_3O_4-BG. SEM and XRD investigations were completed on Fe_3O_4-BG particles. Biological results revealed that samples were not toxic upon their interaction with bone cells.

1. Introduction

Bioactive glasses (especially silicate based) have been intensively used in orthopedic applications due to their ability to form apatite upon contact with the physiological fluids. In the last decade, the idea of coupling bioactivity and magnetism for the same material to target specific tissues for drug delivery applications captured significant attention. Thus, this study focused on fabrication of magnetic bioactive glasses for orthopedic applications.

2. Materials and Methods

To prepare Fe_3O_4 nanoparticles, co-precipitation method was used. $FeCl_2.6H_2O$ (Iron (II) chloride hexahydrate) and $FeCl_3.6H_2O$ (Iron (III) chloride hexahydrate) were mixed in 1:2 molar ratio in concentrated HCl solution. Then, prepared acidic solution was injected into to the 1.5M NaOH basic solution at 80˚C. Bioactive glass composition (wt%) was designed as Si:P:Ca:Na 35:9:18:38. For (10-30) %Fe_3O_4-BG synthesis, Fe_3O_4 nanoparticles were used at the beginning of the sol-gel process. Then, 5.8ml TEOS (Tetraethyl orthosilicate, ≥99.0%) and 0.5ml TEP (Triethyl phosphate, ≥99.0%) were included dropwise, respectively. Afterwards, 2.33g sodium nitride ($NaNO_3$) and 3.575g calcium nitride ($CaNO_3.4H_2O$) was added slowly until a clear solution was obtained. Finally, samples were heat treated for two hours at 500 ˚C. Samples were characterized with SEM and XRD to assess their physical and chemical properties. Biological properties of the sample were assessed with interacting them with human bone cells.

3. Results

Magnetization of bioactive glass was observed to change with weight percentages of the magnetic phase. As indicated in the Fig. 1, three samples were prepared according to the magnetic phase content (10%Fe_3O_4-BG, 20%Fe_3O_4-BG, 30%Fe_3O_4-BG). When the magnetite content increases, so did magnetization of the particles. Heat treatment led to decrease in the magnetization behavior of each glass sample due to oxidation of the magnetic phase. 10% Fe_3O_4 was found to be the minimum necessary magnetic phase concentration for bioactive glass to exhibit magnetic properties. XRD results revealed that particles had $CaSiO_3$, SiO_2 and Fe_3O_4 phases. However, the effective magnetization can be reached by around 30% magnetic phase inside the bioactive glasses. Bone cells were observed to proliferate *in vitro* upon treating them with magnetic bioactive glass.

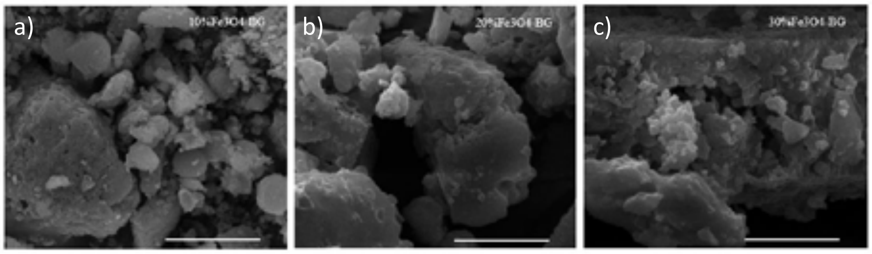

Fig. 1 SEM images of a) 10%, b) 20% and c) 30% Fe_3O_4-BG particles (scale bars are 30 μm)

4. Conclusion

In this research, bioactive glass particles having various concentrations of Fe_3O_4 were successfully synthesized. The samples exhibited magnetic properties. Future work will focus on altering the particle properties and further assessing bone cell functions *in vitro* for drug delivery applications.

Acknowledgements
This work was financially supported by The Scientific and Technological Research Council of Turkey (Grant no: 117M187).

Relationship Between Surface Roughness and Adherence Perfomance of Cast Iron Enamel Coatings

Aykut AK[1,2], Nurullah ÇÖPOĞLU[1,2], Yasin Bozkurt YILMAZ[1,2], Tamer CENGİZ[2], Buğra ÇİÇEK[1]
[1]Yıldız Technical University, [2]Gizemfrit
Turkey

Abstract

Enamel coatings are a type of inorganic coating used to improve and protect the metallic surfaces. The coatings required to adhere well to the substrate metal to provide the expected performance over time. The adherence mechanism of enamel coatings is examined under 4 headings: chemical, mechanical, electrolytic and dendritic. In addition, the oxide layer on the adherence mechanism in cast irons depends on many parameters such as mechanical locking, cast iron composition, furnace atmosphere and the ability of the enamel to spread. In this study, the effects of surface roughness, on the adherence mechanism of casting enamels were investigated.

1. Introduction

Vitreous enamel coating technology(VECT) is an inorganic coating technique that provides high mechanical and chemical resistance, high temperature durability as well as aesthetic properties comes from its glass-ceramic nature. VECT is used in many applications such as; cookware, boilers, architectural applications, turbin blades and cast goods. Enamel has been widely adopted on steel, cast iron and aluminum alloys substrates with different application methods such as dipping, wet/electrostatic spraying, and electrophoretic enameling[1].

One of the main requirement in the enameling process is to provide good adhesion between the enamel and the metallic surface. Unlike other enamel-metal adhesion, cast iron-enamel composition has two main difficulties. First of them, since cast iron has a high coefficient of thermal expansion, enamel to be applied on its surface is expected to have the same coefficient [2]. The second one, the cast iron contains a high proportion of graphitic carbon, so adhesion with enamel decreases and the problem of carbon boiling arises between enamel-cast iron interface during the sintering process [5][6]. These problems decrease the coating performance with local ruptures. By changing the enamel composition, both the thermal expansion coefficient can be intervened and the temperature of the sintering can be lowered [5]. In order to increase thermal expansion, enamel composion should contain less Silicon dioxide(SiO_2) and Aluminium oxide(Al_2O_3) and more Boron trioxide(B_2O_3), Zinc oxide(ZnO), Barium oxide(BaO), and fluoride according to the the surface enamels for steel[7]. At low sintering temperature such as 750°C, the enamel will expand less and interfere the gas outlet, by this way, good adhesion occurs between enamel and cast iron[6].

The theory of adherence can be divided into two main brances: chemical and mechanical theories. In detail, electrolytic and dendritic theories can be added to them [8][9]. Chemical or oxide layer theory comprises four reaction that change the enamel-metal interface structure: dissolution, redox, interdiffusion and precipitation [8]. Chemical reactions are simply bonding phenomena based on electron exchange or association between the atoms of enamel and the metallic surface at the presence of electronic structure.

In the electrolytic hypothesis, cobalt (Co) or nickel (Ni) in the vitreous enamel precipitated when it contact with iron base and form a short-circuited local cell in which iron is the anode [10]. The positive electricity(current) shuttle between iron and cobalt through the melt. As a result of these reactions, iron dissolved from metallic surface to the interface solution area and by this way, surface becomes roughened and oxides of enamels bond theirselfs into the holes [10][8].

According to the dendritic theory, during cooling in liquid in the enamel-metal interface, metallic precipitations are formed. By means of these deposits, dentritic arms are grow from metal to enamel and enamel is attached to the metallic surface [8] [9] [10].

When it comes to mechanical bonding theory, National Bureau of Standards(NBS), Washington, DC, has approved a good correlation between roughness of enamel-iron interface and the adherence index in an air atmosphere [11]. However, according to the other investigations, however, surface roughness can not be the only one that complately responsible for the adhesion. In some experiments, weak adhesion has been observed on very rough interfaces, and some of them shown the very good adhesion between metal and enamel without surface roughening [8][10][11]. Nevertheless, none of the these theories describes exactly how adherence mechanism are formed. Moreover, even at some points, the presence of one could refute the other ones [8]. In this study, it is aimed to investigate effects of sandblasting surface activation technique on adherence mechanism of vitreous enamel coating by parameters of EN 10209:2013 standard, optic image and SEM analysis.

2. Experimental Procedure

2.1. Preparation of Enamel Specimen

Enamel quality grey cast iron was used as the metallic substrate in this study. Enamel coating process can be divided into three major steps. First step is enamel slurry preparation. Second Step is coating by spraying method. Last step comprises the thermal treatments of the enamel coating. The first step has two processes, consisting the frit casting and milling with additives. The studied cast iron enamel frit compositions were produced in the GizemFrit R&D Center (Sakarya, Turkey) with the composition listed in Table 1.

Table 1. X-Ray Fluorescence (XRF) and Atomic Absorption Spectroscopy(AAS) results of prepared frit

	Oxides	**Wt.%**
R_2O	Na_2O, K_2O, Li_2O	11.36
RO	CaO, MgO, ZnO, NiO, CoO	10.02
R_2O_3	Fe_2O_3, Cr_2O_3, Sb_2O_3, Al_2O_3, B_2O_3	20.49
RO_2	SiO_2, TiO_2,	56.57
RO_3	MoO_3	0.54
R	F	1.02
Total		**100.00**

The produced frits are milled in the ball mill with the additives and then sieved through 60 mesh sieves to obtain homogeneous and fine-grained powder. Depending on the type of frit, wt.40-50% water is added into the powder to obtain enamel slurry.

At the second step, cast irons supplied with dimension of 100x100x5mm. The surfaces of cast irons were sandblasted with SiO_2 sand which has 470 µm average particle size. In this study, seven experiment has been made with two different pressure and three different times. Sandblasting pressure adjusted to 6 Bar and 3 Bar. For every pressure, cast iron surface was exposed to sandblasting for 1 min, 2.5 min, and 5 min as listed in Table 3. Also, in one experiment, half of the cast iron surface was sandblasted at 3 Bar pressure for 2.5 min while the other half was left without sanding as it came out of production to see effect of sandblasting. The specimens named as stated at Table 2.

Table 2. Time and pressure parameters for cast iron specimens.

	1 Min	2.5 Min	5 Min
3 Bar	**3B-1**	**3B-2**	**3B-5**
6 Bar	**6B-1**	**6B-2**	**6B-5**
		Untreated	

Enamel suspensions were applied by wet spraying technique. The samples were dried in a oven for 5 min at 320 °C to eliminate CO, CO_2, H_2O gases since these gases can create undesired pores in the enamel coating during firing process. Firing process has been done in a laboratory type furnace (Protherm - PLF110) at 770 °C for 12 min.

2.2. Characterization

In accordance with EN 10209, the enamel is tested by falling the steel bar from 750 mm high with a diameter of 22 mm and weight of 1.5 kg. The amount of enamel which is adhered to the substrate after punch is used for evaluation of adherence level from class 1 to 5. Class 1 states an excellent adherence and class 5 states poor adherence. After the impact test, If the metallic surface appears and enamel layer detach from the metal, this adhesion is get involved to class 5. If the surface of the metal completely covered by enamel, this adhesion is get involved to class 1. The punched area by impact test was inspected by Optical Microscope(Olympus LC30 - SZ61TR) with working area of 10x10mm at x2 magnification.

Microstructure of the interface between enamel and cast iron investigated by JEOL JSM-6060 Scanning Electron Microscope(SEM) with the acceleration voltage of 15 kV and the working distance of 14 mm at x250 magnification. Also, interface composition was analyzed by EDS (IXRFEDS-2004)

Surface roughness was measured by Time TR200 Surface Roughness Tester with display range between 0.005 and 40 µm.

3. Results and Discussion

3.1. Adherence Perfomance Results

After sandblasting the cast iron surfaces at different times and pressure, the surface roughness was measured as in Table 4.

The roughness of the surface of the cast iron that came directly out of production without any treatment was measured as an average of 1.291µm. This value could change according to the quality of the cast.

Table 4. Surface roughness values for different cast iron specimens. Ra refers to average roughness of a surface, Rz refers to the difference between the tallest "peak" and the deepest "valley" in the surface.

Specimen No	**Ra(μm)**	**Rz(μm)**
Untreated	1.291	6.960
3B-1	3.840	22.850
3B-2	4.860	26.080
3B-5	4.934	27.130
6B-1	4.391	22.260
6B-2	5.660	28.230
6B-5	6.110	30.450

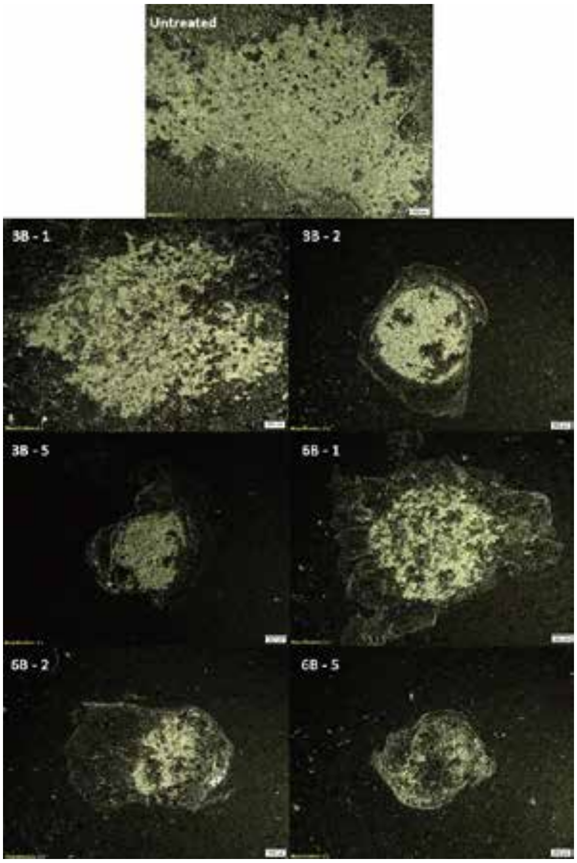

Figure 1. Optic Microscope images of punched areas after the Impact Test.

The surface roughness increased approximately 3 times with 1 min sandblasting at 3 Bar pressure. For longer periods, the roughness increase continued with sandblasting time, but the roughness increasing rate decreased.

The roughness value of the surface, which was sandblasted at 6 Bar pressure increased 3.4 times at the end of 1 min sandblasting according to untreated surface. There was a 29% increase in roughness with 2.5 min of sandblasting in 6 bars compared to 1 min of sandblasting. Roughness reached its highest value in sandblasting at 6 bars for 5 min. When we inspect the Rz values, it increased the highest "pit" depth with the increase of pressure. While the highest pit depth at 3 Bar pressure is 25.35 on average, this value is 26.98 at 6 Bar.

Figure 2. Macro image of enamel surface of cast iron specimen(Left side of specimen was sandblasted at 3 Bar for 2.5 min. Right side of specimen was left untreated).

The impact test results shown in Figure 1 were compared under the microscope with the same magnification from the same distance. The coating applied to the untreated surface was largely detached and the gray metallic surface appeared. In the 3B-1, experiment carried out at 3 bar pressure, the width of the coating area, which was removed from the sandblasted surface for 1 min, was similar to that of non-sandblasted, but there was an increase in the amount of adhering coating. Along with the increasing time, the amount of detached coating decreased. Punched area sandblasted at 6 Bar for 1 min gave a similar appearance to the sandblasted at 3 Bar, but the damaged area was relatively less. The coating that is sandblasted for 2.5 min at 6 bars has almost halved compared to the sandblasted for 1 min, and the metal that has been sandblasted for 5 min has become almost invisible.

The visual results of the impact test are directly proportional to the increase in surface roughness. Increased surface roughness also increases the surface area on which the enamel adheres. Thus, adhesion also increases. In addition, when the enamel surfaces were examined with the naked eye, it was determined that blister defect appeared on the untreated surface. In order to see this error clearly, in one experiment made with half of a cast iron surface sandblasted while half of it was left untreated. In the experiment, the extent to which sandblasting affects the enamel surface quality is exhibited in Figure 2. While the blister defect is clearly visible on the right side of the specimen in the image, the defect disappeared on the sandblasted side of the same specimen.

Accordingly, it can be deduced that the sandblasting affects the enamel surface quality.

3.2. Enamel-Metallic Surface Interface Characterization

When the SEM images of the interface are examined, it can seen in Figure 3 that the intersections of the surfaces subjected to different blasting times have different topography. Vitreous frit powder, which has softened by firing, entered the rough surface on cast iron and filled the voids.

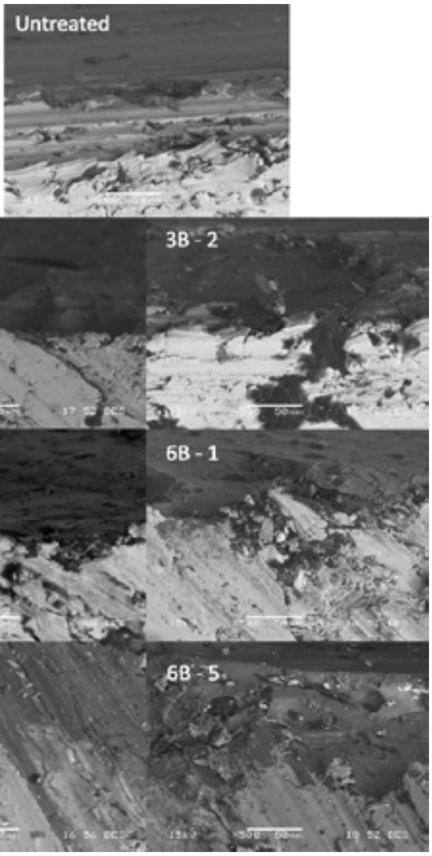

Figure 3. Cross-Section SEM images of enamel specimens.

SEM images show the level of mechanical adhesions that occur when these blanks are filled. Also, It can seen in Figure 3 that there is no roughness on the untreated surface and therefore mechanical adhesion is very low. Although there was not much fluctuation in the intersection of the surface of 3B-1, the fluctuation of the sandblasted surface of 6B-5 was quite high.

The roughness of the surface 6B-1 was less than the sandblasted surface of 3B-2 and 3B-5. The SEM images of interface confirm the impact test results.

4. Conclusion

According to the results obtained from the study, an increase in the roughness of surface of Graphitic Cast Iron has a beneficial effect for adherence mechanism of the enamel coating as a result of raising area of interface. Also, untreated cast iron surface causes blister defect on the enamel surface. This error can be eliminated with any type of sandblasting over 2.5 min sandblasting at 3 Bar pressure.

References

[1] A. I. Andrews, *Porcelain enamels: The preparation, application, and properties of enamels*, Second. Garrard Press, 1961.

[2] H. T. ANGUS, *Cast Iron: Physical and Engineering Properties*, Second Edi. London-Boston: British Cast Iron Research Association, 1976.

[3] R. Elliott, *Cast Iron Technology*, First Edit. London-Boston: Butterworth & Co., 1988.

[4] H. F. Staley, "ENAMELS FOR CAST IRON.1," *J. Am. Ceram. Soc.*, vol. 1, no. 10, pp. 703–709, Oct. 1918.

[5] D. Song *et al.*, "Development of High-Performance Enamel Coating on Grey Iron by Low-Temperature Sintering," *Materials (Basel).*, vol. 11, no. 11, p. 2183, Nov. 2018.

[6] D. Wang, "Effect of crystallization on the property of hard enamel coating on steel substrate," *Appl. Surf. Sci.*, vol. 255, no. 8, pp. 4640–4645, Feb. 2009.

[7] N. I. Min'ko and T. A. Matveeva, "GLASS ENAMELS FOR STEEL AND CAST-IRON ARTICLES (Review)," *Glas. Ceram.*, vol. 56, pp. 11–12, 1999.

[8] L. Samiee, H. Sarpoolaky, and A. Mirhabibi, "Microstructure and adherence of cobalt containing and cobalt free enamels to low carbon steel," *Mater. Sci. Eng. A*, vol. 458, no. 1–2, pp. 88–95, Jun. 2007.

[9] D. M. Stefanescu, *Science and Engineering of Casting Solidification*, Second. Columbus, OH: Springer Science+Business Media, LLC, 2009.

[10] B. W. KING, H. P. TRIPP, and W. H. DUCKWORTH, "Nature of Adherence of Porcelain Enamels to Metals," *J. Am. Ceram. Soc.*, vol. 42, no. 11, pp. 504–525, 1959.

[11] J. C. RICHMOND, D. G. MOORE, H. B. KIRKPATRICK, and W. N. HARRISON, "Relation Between Roughness of Interface and Adherence of Porcelain Enamel to Steel," *J. Am. Ceram. Soc.*, vol. 36, no. 12, pp. 410–416, 1953.

The Investigation of Permanent Linear Change (PLC) Properties of Monolithic Refractories

Oğuzhan SAKARYA, Mert TURFANDA, Emrecan ZORBA, Uğur CENGİZ
Bilecik Demir Çelik San. Tic. A.Ş
Turkey

Abstract

Continuous improvement activities in the performance of refractory materials are required due to cost optimization studies in iron and steel production. At the same time, the use of monolithic refractories such as self-castable, forging mortars and adhesive mixtures in iron & steel production has increased.

Knowing the thermomechanical properties, sintering parameters and degradation of monolithic refractories used in induction furnaces, one of the innovative melting systems, is important in terms of determining their suitability for use conditions. Within the scope of this project, calcined alumina is produced by Bilecik Demir Çelik *(BDÇ)* has been added to the spinel-containing alumina-based monolithic neutral lining material used in different amounts in the induction furnace lining material. Permanent linear change *(PLC)* parameter, which directly affects the physical and thermomechanical properties of samples with and without calcined alumina, has been examined and interpreted on a laboratory scale.

1. Introduction

In plants producing iron & steel, it is necessary to use refractory materials at every step of the process and these materials have to be developed due to their limited performance. In induction melting recycling plants, self-castable amorphous *(monolithic)* refractories are used for furnace lining.

The amorphous refractories, whose usage is increasing day by day, are classified as ramming mortars, casting mortars, gunning mortars, plastering and knitting mortars according to the application method. The application method in this grouping is directly related to the particle size distribution of the mortars, the particle size and the type of binder. As with induction furnace linings, some mortars are applied as granules without binders, they are knitted with vibration technique, compressed and sintered in place. Monolithic refractories, also called amorphous, are used in hard working areas, thin thicknesses, complex constructions. It is also suitable for use as a repair mortar due to its more economical structure and easy and durable adhesion on the refractory. The increase in scrap prices in the iron & steel industry, the increase in refractory raw material prices and energy costs made it compulsory to use new types of refractories and to develop new knitting techniques in steel production plants.

Self-castable *(monolithic)* refractories must have certain rheological properties and fluid behavior for easy operability. In the design of refractory materials, the following characteristics determine their mechanical behavior.

- Refractoriness
- High temperature resistance
- Creep
- Thermal shock resistance
- Permanent linear change

Refractoriness is the temperature at which refractory materials soften or melt, high temperature strength; it is the resistance value against loads applied at high temperatures, creep behavior; plastic deformation caused by continuous forces to which materials are exposed at constant temperature, thermal shock resistance; It is the resistance of refractories against sudden temperature changes, permanent linear change; linear expansion and / or shrinkage that occurs when it is lowered to its initial temperature after heating [1].

The grain size distribution plays an important role in these features and behaviors. The grain size distributions of these substances have a significant effect on operability. For example; The specific surface area of the calcined alumina requires water; grain structure, size distribution and surface activity in fluidity; grain size in the density of the matrix; crystal strength at high temperatures; The effect of the liquid phase on the wetting angle, in the hardening time and high temperature properties, has a significant role in the liquid phase sintering. Control of the aggregates of the refractory structure consisting of matrices and aggregates is of great importance in controlling these properties. Aggregates are coarse particles in refractories. These coarse particles play an important role in controlling many properties of refractories.

1.2. Alumina Refractories

Alumina refractories are refractories containing high amounts of alumina and small amounts of other materials. Alumina material has a melting temperature of 2050° C. It can maintain its high chemical stability at high temperatures. It is also a hard material with a value of 9 on the mohs hardness scale and a material that can show high resistance to thermal shocks.

Alumina shows high chemical resistance against both acids and bases. It is a type of material that can be used up to 1840°C operating temperature that meets the needs of refractory materials with these properties [7,8]. Refractory properties of alumina refractories increase as the amount of alumina increases. Refractories containing high alumina can also be composite refractories with good properties such as alumina-MgO, alumina-spinel ($MgAl_2O_4$).

1.3. Al_2O_3 - MgO Spinel Refractories

The general formula of spinels is AB_2O_4. Industrially used spinels; aluminates ($MgAl_2O_4$) are ferrites ($MgFe_2O_4$) and chromites ($MgCr_2O_4$). Magnesium aluminate spinel is considered to be an excellent material for refractory products due to its superior mechanical, chemical and thermal properties at high temperature. Spinel is produced artificially. Because naturally there is very little in nature. Magnesium aluminate spinel ($MgAl_2O_4$) has a melting temperature of 2135ºC and a density of 3,58gr/cm^3. When magnesium aluminate spinel, $MgAl_2O_4$, or spinel for short, is used with magnesia, it has thermal expansion mismatch and reduces the thermal expansion coefficient of the composition. Therefore, the thermal shock resistance of refractory products containing this raw material is very good. Moreover, when used in conjunction with magnesia, it leads to improved impact resistance and increased slag corrosion resistance [2, 3].

1.3. Spinel Formation Mechanism

MgO-Al_2O_3 phase diagram is presented in Figure 1. Stoichiometric $MgAl_2O_4$ contains 28.2% MgO by weight and 71.8% Al_2O_3. The MgO-Al_2O_3 phase diagram contains two eutectic points and an intermediate phase $MgO.Al_2O_3$. The solubility of the two components in each other is trace amounts. The MgO-Al_2O_3 system can be considered as two different phase diagrams. The first is the MgO-$MgO.Al_2O_3$ system, the second is the $MgO.Al_2O_3$-Al_2O_3 system. $MgAl_2O_4$ shows a wide range of stoichiometry and is the only phase formed up to a temperature of 1650°C [4, 5, 6].

At this temperature, the solubility of MgO and Al_2O_3 in $MgAl_2O_4$ is 2% and 6%, respectively. When the temperature rises above 1700°C, the resolutions increase to 3% and 10% respectively. When the temperature of 2000°C is reached, solid solutions are between 40 and 80%. Naturally, $MgAl_2O_4$ (spinel) structure is very rare [7].

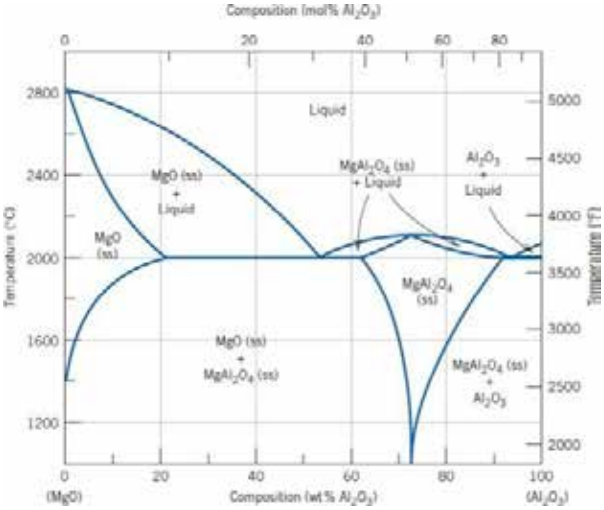

Figure 1. MgO-Al_2O_3 phase diagram

The density of the components during the synthesis of spinelin from periclase (MgO) and corundum (Al_2O_3)

Equation 1.

$$\frac{1}{\rho} = \frac{Al_2O_3\ wt\%}{\rho\ Al_2O_3} + \frac{MgO\ wt\%}{\rho\ MgO} = \frac{0.72}{3.99} + \frac{0.28}{3.58} \rightarrow \rho = 3{,}87\ g/cm^3$$

$$\Delta V = \frac{3{,}87}{3{,}58} \approx 8{,}1\%$$

8.1% volume expansion is linearly equal to 2.6% linear expansion. The formal representation of the expansion is presented in Figure 2.

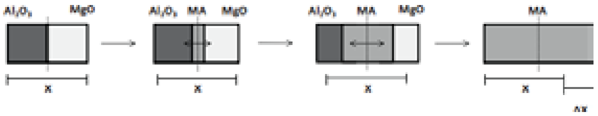

Figure 2. Representation of volumetric expansion occurring during spinel formation.

In order to overcome the expansion in the solid state synthesis of the spinel for refractory materials, double-stage sintering is carried out. However, since this double-stage sintering process increases the cost of spinel production, many studies have been carried out for the refractory applications to synthesize the spinel at the desired density in one step. In a study they carried out, Kanai and his colleagues conducted a thermal expansion study at temperatures above 900°C, where the spinel formation started to occur with various mixtures of MgO/Al_2O_3 with a grain size of approximately 0.5 µm. In the study conducted, they first encountered shrinkage at temperatures above 1300°C. They observed the highest expansion of approximately 5% in trials with mixtures of stoichiometric ratios. The high densities formed in this way prevent the formation of dense spinel structure [8]. Wagner explained spinel synthesis at high temperatures with solid state reactions from corundum and periclase as presented in Figure 3 [9].

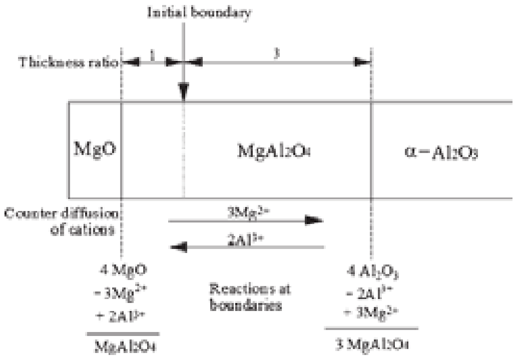

Figure 3. Wagner mechanism

According to Wagner, at points where components are in contact, as presented in Figure 3, oxygen ions remain constant while mutual diffusion of cations occurs. While $3Mg^{+2}$ cations diffuse to the alumina side to ensure load balance, $2Al^{+3}$ cations diffuse to the magnesia side. The $2Al^{+3}$ cation that diffuses at the MgO/spinel boundary forms a $MgAl_2O_4$, while the 3Mg cation that diffuses at the Al_2O_3 / Spinel boundary forms three $MgAl_2O_4$. As a result, the spinel ratio on the Al_2O_3 and MgO sides is 3: 1.
If the Wagner mechanism was absolutely correct, the R value indicating the amount of spinel formed on the Al_2O_3 and MgO sides and the Al_2O_3 and MgO sides would always be 3.

However, as Wagner's theoretically stated, in non-perfect applications, the R value increases depending on the ratio of the components and the sintering temperature. It was formulated by R value in MgO. $MgAl_2O_3$ composition as R = 3. $(7n + 1)\ (3n + 5)$ [4]. Yamaguchi et al. Reported that the R value ranged from 4.1 to 4.6, regardless of whether the components were single crystal or multi crystalline, in the temperature range of 1495-1595°C. However, the factors affecting the R value are not limited to these only. Another factor affecting the R value is the transport of MgO vapor. Saturated MgO vapor is found at 1527°C with MgO and Spinel at $2.5x10^{-5}$ and $6.2x10^{-7}$ Pa pressures, respectively. This shows that MgO molecules can evaporate and settle on alumina grains to form spinels [10].

If the surfaces where alumina and magnesia grains are in contact with each other are rough, MgO vapor will diffuse into the voids caused by roughness and will only cause spinel formation on the alumina side, this will cause an increase in R value. In this study by Nagakawa et al., R value was observed as 5.6 at 1535°C in rough contact points. According to the switch, if only MgO diffuses to the alumina side, the R value is equal to infinity. However, in fact, there are three different contact types in the compressed powder structure: Al_2O_3-Al_2O_3, MgO-Al_2O_3, MgO-MgO [11,12].

Expansion is provided in Figure 4 where an Al_2O_3 grain is in contact with a MgO grain under suitable conditions.

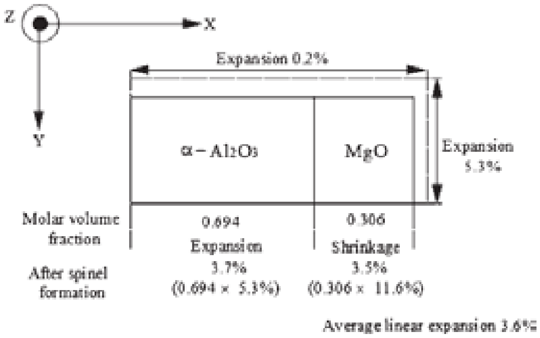

Figure 4. Expansion and shrinkage in contact with an alumina and a magnesia grain under suitable conditions.

When the alumina and MgO molar ratios are 1: 1, spinel formation is completed without alumina or magnesia increase or insufficiency. According to the Wagner mechanism, when four MgO is spent on the MgO side during the spinel formation, one $MgAl_2O_4$ and three Al_2O_3 on the Al_2O_3 side form three $MgAl_2O_4$. While the volume change on the MgO side is proportional to 0.884, it becomes 1.167 on the Al_2O_3 side. Pulling on the MgO side, expansion on the Al_2O_3

side. In the stoichiometric system, the Al_2O_3/MgO molar volume ratios would be 0.694/0.306. After the spinel formation, as shown in Figure 4, the volume after shrinking in the direction of diffusion in the direction of diffusion becomes 0,271 Al_2O_3, the volume after expansion is 0,731, the total volume is 1,002 and a volume expansion of 0,2% occurs. If there is isotropic expansion on the alumina side in other directions, 5.3% expansion occurs. The increase in R value causes an increase in the expansion. In Table 1, volumetric and linear expansion values occurring on the alumina side depending on the R value are given [4, 12].

Table 1. Expansion values due to R value

	Expansion type	
R	**Volumetric (%)**	**Lineer (%)**
3	16,7	5,3
4	24,4	7,6
5	29,7	9
6	33,4	10,1
∞	55,6	15,9

Spinel formation also depends on the quality of the component raw materials. Physical water in chemical raw materials, amount of chemical water, hydroxyl groups, impurities such as CaO, SiO_2, Na_2O, grain size distribution and compression density, firing temperature, sintering time etc. It is affected by many parameters such as [4].

1.4. Permanent Linear Change

Permanent linear change *(PLC)* is a factor used to evaluate the suitability of refractories in the range of service temperature limits. Refractory materials can be subjected to allotropic form changes, chemical and sintering reactions, phase transformation, liquid phase formation, mineral formation, expansion and / or contraction when heated. These heat treatments can cause volume expansion or reduction. After cooling to room temperature, the material will probably be larger or smaller than the original dimensions. This linear change that occurs when the material is lowered to its initial temperature after heating is defined as permanent linear expansion.

PLC is an important refractory behavior that goes through a certain temperature-time process and is a very important parameter especially for the refractory lining design of induction furnaces. While calculating the experimental process of this design, it should be adhered to sector factors such as volumetric stability and high temperature expansion-shrinkage behavior of the material, its performance in the furnace, the manufacturability and production continuity.

2. Experimental Procedure

Neutral lining compositions, in which different samples are formed, are prepared according to the flow chart indicated in Figure 5. The mixture prepared in each step is protected from externally polluting effects. Attention has been paid to the parameters of the created samples, the amount of printed material and the applied pressure. Samples are added to calcined alumina, and these codes are named as K1, K2, K3, K4 and K5 in different% additions.

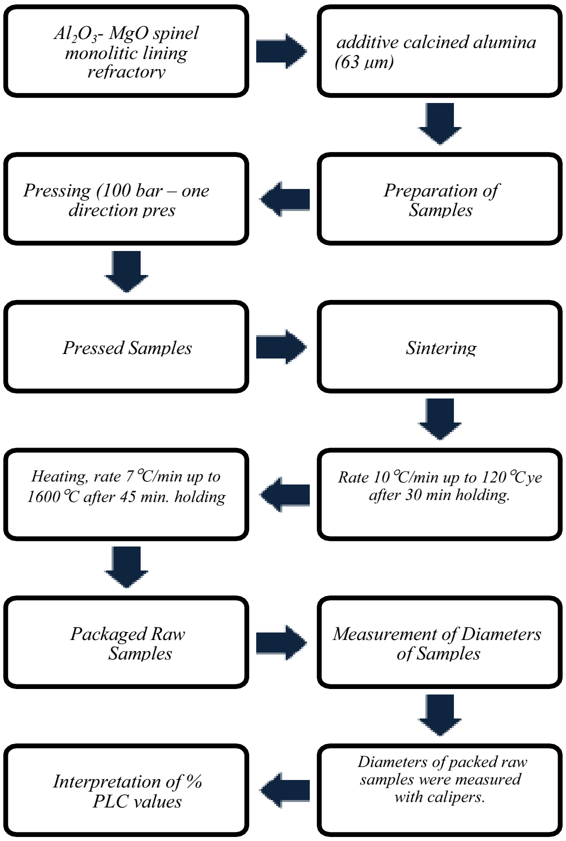

Figure 5. Al_2O_3 - MgO spinel monolithic lining production flow chart

Figure 6. The dimensions of the sintered samples indicated were measured with the help of calipers and permanent linear size changes (%PLC) were calculated after sintering as stated in Equation 2.

Equation 2.

$$PLC = \frac{After\ firing\ Diameter - Initial\ Diameter}{Initial\ Diameter} x100$$

Figure 6. Packaged raw samples

3. Results and Discussion

3.1. Measurement of Diameters of Samples

Permanent linear dimensional changes (PLC) of % 5 after sintering are indicated in Figure 7.

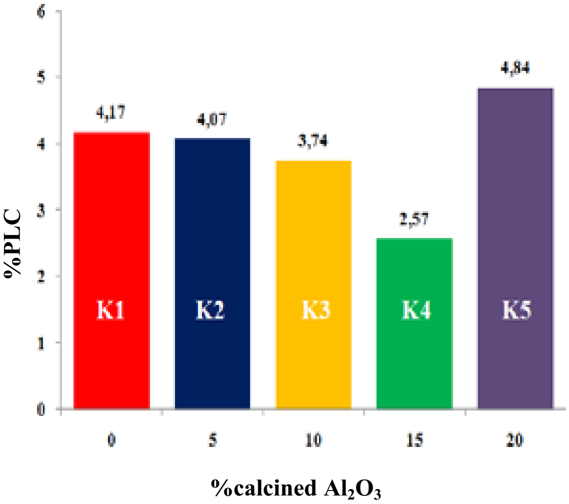

Figure 7.% PLC values of packed raw samples

4. Conclusion

The orientation towards induction furnaces in the iron and steel industry has also caused a significant expansion in the market of castable mortars. Within the scope of this study, PLC parameter directly affecting the design process of the induction furnace lining material, which is open for development, was controlled by adding different amounts of calcined alumina to the main product used in BDC.

PLC represents a combination of dimensional changes due to sintering shrinkage and volume expansion encountered during spinel formation. Due to differences in the density of the MgO, Al_2O_3 and $MgAl_2O_4$ phase, an increase in volume occurs during the thermal synthesis of the spinel. The magnitude of this expansion is governed by the grain size of the MgO and Al_2O_3 components. Thus, PLC can be controlled and monitored by adjustments in particle size distribution. The results obtained are important for understanding the thermo-mechanical behavior of the neutral liner of the induction furnace. If the volumetric change occurring during spinel formation is combined with the effect of thermal/mechanical shocks, crack formation is accelerated.

Therefore, volumetric stability is an important parameter to prevent crack formation in the furnace lining besides its stable refractory thickness. For this reason, 8.1% volume increase during spinel formation should be at minimum level.

As stated in this study, it is a K4 (15% calcined alumina added) sample suitable for hearth lining wear. The% PLC change of K4 sample was calculated as 2.57 by experiments. The fine-grained structure of calcined alumina improves the packaging properties of the grains. Porosity amount decreases and volume weight increases. Fine grains fill the gaps in the structure

At the same time, the alumina-based spinel refractory is 85-90% by weight Al_2O_3 in the composition, optimal for this type of spinels. High amount of alumina increases spinel bond formation and strength. Increased spinel phase helps heal thermal shock resistance. Because MgO and Al_2O_3 react at high temperature to form spinels in place. The spinel phase formed significantly affects the penetration of the slag into the refractory, significantly increasing the life of the refractor. The reason for this is that alumina-rich spinels have a large concentration of cation cavities and FeO, Fe_2O_3 and MnO in the slag are located in these cavities. Therefore, the slag is prevented from advancing in the refractory [13].

References

[1] Refractories Handbook, June (1994). The Technical Association of Refractories, Japan, 1-240.

[2] Duncan G.R. (1985) Electric Furnace Steelmaking (syf 161-166). Chelsea, MI, USA: Iron and Steel Society, Inc, Book Crafters, Inc.

[3] Refractory failure in induction furnaces can be limited. https://www.thefreelibrary.com/Refractory+failure+in+induction+furnaces+can+be+limited.a010913837 (Erişim Tarihi 02.02.2017)

[4] Ganesh, I. (2013). A review on magnesium aluminate ($MgAl_2O_4$) spinel: synthesis, processing and applications, International Materials Reviews, 58(2), 63-112.

[5] Alper, A. M., McNally, R. N., Ribbe, P. H., Doman, R. C. (1962). The System MgO-$MgAl_2O_4$, J. Am. Ceram. Soc, 45(6), 263-268.

[6] Viechnıckı, D., Schmıd, F., McCauley, J. W. (1974). Liquidus-Solidus Determinations in the System $MgAl_2O_4$-Al_2O_3. J. Am. Ceram. Soc., 57 (1), 47–48.

[7] O'Driscoll, M., (1997). ''Fused Spinel—Monolithics Market Future,'' IM Fused Miner. Rev., Özel Sayı, 36–46.

[8] Kanai, T., Nakagawa, Z., Ohya, Y., Hasegawa, M., Hamano, K., (1988). Effect of composition on sintering and bending strength of spinel ceramics, Res. Lab. Eng. Mater. Tokyo Inst. Technol, 13, 75.

[9] Wagner, C., Z. (1936) Physik. Chem., B34, 309–316.

[10] Yamaguchi, G., Shirasuka, K., Munekata, M. (1971). Some Aspects of Solid State Reaction of Spinel Formation in the System MgO-Al_2O_3. Journal of the Ceramic Association, Japan 79, 906, 64-69.

[11] Wagner, C., Z. (1936) Physik. Chem., B34, 309–316.

[12] Nakagawa Z. E., Enomoto N., Yi I. S., Asano K. (1995). Proc. UNITECR '95 Cong., Tokyo, Japan, November 1995, Technical Association of Refractories, 379–386.

[13] Ganesh, I., Teja, K. A., Thiyagarajan, N., Johnson, R., Reddy, B.M. (2005). Formation and Densification Behavior of Magnesium Aluminate Spinel: The Influence of CaO and Moisture in the Precursor. J. Am. Ceram. Soc., 8(10), 27

20th
INTERNATIONAL
METALLURGY
MATERIALS
CONGRESS
10-12 June
2021
“in Digital Platform”

Biomaterials

immc2021

Anodization of 316L Stainless Steel for Implant Applications

Yaşar Kemal ERDOĞAN, Batur ERCAN
Middle East Technical University
Turkey

Abstract

316L stainless steel (SS) surfaces were modified via anodization to form nanopit structures with aim of improving its corrosion resistance, bone cell adhesion, proliferation and enhance its bioactivity. Surface characterization studies revealed that nanopit structures were composed of Fe_2O_3 and Cr_2O_3. The *in vitro* results showed that nanopit surfaces enhanced bone cell proliferation. Thus, we concluded that fabrication of nanostructures on 316L SS surfaces is a promising way to enhance bone cell functions for implant applications.

1. Introduction

316L stainless steel (SS) has been used as an implant material in orthopedics due to its corrosion resistance, high mechanical strength and low price. However, bare 316L stainless steel experience problems in clinical applications, *i.e.* corrosion of metal in the body, nickel releases to the surrounding tissues and bare 316L SS implant do not effectively support cell adhesion and proliferation. Anodization is an electrochemical process to grow a uniform oxide layer on valve metals. Anodization, due to its simplicity, reliability, high controllability and low cost, is a powerful method for large-scale surface modification. In this study, we aim to obtain nanostructured surface features on 316L stainless steels to investigate its effect in orthopedic applications.

2. Materials and Methods

Anodization was carried out in ethylene glycol monobutly ether electrolyte containing 7.5% perchloric acid under 25V for 30 min and 70V for 90 sec. After anodization, samples were annealed in vacuum furnace at different temperatures (450–600 °C) for 1 hour. Anodized surfaces were characterized with SEM (Scanning Electron Microscopy), XPS (X-ray photoelectron spectroscopy), AFM (Atomic Force Microscopy) and water contact angle tests. For cell culture experiments, human osteoblast cells (ATCC® CRL11372™) were seeded at a density of 10,000 cells/cm^2 on each sample at standard cell culture conditions at 37°C temperature and 5% CO_2. Cellular densities were obtained via MTT test assay up to 5 days of culture.

3. Conclusion

25 nm and 200 nm diameter nanopit structured on 316L SS via anodization. AFM root mean square roughness (rms) value for the non-anodized sample was found to be 1.2 nm, while 25 nm and 200 nm surfaces had 1.8 nm and 17.2 nm, respectively. While 25 nm and 200 nm surfaces had contact angles of 93.1° and 96.3°, respectively, non-anodized surface had 57.3° contact angle. In addition, HT450 of 200 nm and HT600 of 200 nm surfaces had contact angles of 84.9° and 60.1°, respectively. Anodized surfaces mainly composed of Fe_2O_3 and Cr_2O_3 while the amount of MoO_3 peak increased upon heat treatment. Importantly, the anodized surfaces do not contain any nickel oxide peaks. In addition, anodized surfaces significantly enhanced osteoblast adhesion and proliferation compared to non-anodized samples. The highest cellular density was observed for annealed 316L SS having 200 nm feature size. The results demonstrate promise for the use of anodized 316L SS for implant applications.

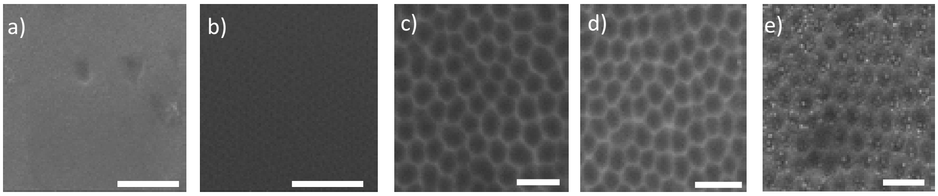

Fig. SEM images of a) non-anodized and anodized samples having b) 25nm, c) 200 nm d) HT450 of 200nm and e) HT600 of 200 nm diameter nanopits (scale bars are 1 µm).

Acknowledge

The authors would like to thank The Scientific and Technological Research Council of Turkey (Grant no: 118M652) and Middle East Technical University Research Funds (GAP-308-2020-10110) for providing financial support.

Polylactic Acid / Calcium Sulfate Composite Production for Bone Tissue Engineering

Ayşe KAPLAN[1,2], Cem Bülent ÜSTÜNDAĞ[2]
[1]Yıldız Technical University, [2]Alvimedica Medical Technologies
Turkey

Abstract

In this study, we are aimed to produce composite materials by using injection molding technology in the treatment of bone tissue deficiencies. Tissue scaffolding was produced using biocompatible and biodegradable polymer and ceramic powder which is a composite material. With the injection molding technology, bone tissue can be produced quickly and in accordance with the patient's morphology. With the double screw extruder system in controlled temperature and pressure, it is possible to produce Polylactic Acid (PLA) granules and Calcium Sulphate (CS) powder nearly homogeneous composite granules. Thanks to the composite granule created by granule-fed injection molding, the desired 3D printing can be obtained.

1. Introduction

Bone tissue engineering is an important research area that aims to support or replace tissue deficiencies caused by traumatic injuries, bone replacement, congenital bone diseases, and osteoma (bone tumor) during the recovery period. Compared to today's treatment methods, the bone tissue scaffold should be both mechanical and structural support by providing physiological and chemical harmony with the targeted tissue and surrounding tissues [1], [2]. For this reason, the material used must be in a porous structure that promotes bone regeneration, biocompatible, bioactive, and compatible with bone cells. Especially desired porous structure and the role of supporting growth was provided with the polymer-ceramic composites in bone tissues. The scaffold must have a porous structure suitable for vascularization in order to the real bone tissues to adapt and grow and proliferate within the scaffold. Therefore, biomimetic material selection and 3D design should be considered in artificial bone tissue scaffolds [3]. PLA has a suitable mechanical structure, a biodegradable feature, and formed with ease of processing. Also, CS has the absence of inflammatory response and osteoinductive property [4], [5].

2. Materials and Methods

PLA-CS Masterbatch Synthesis: Calcium sulfate powder and PLA granules were mixed via twin-screw extruder *Injection Molding of Composite Material:* PLA-CS composite material was produced by using the masterbatch with the injection molding technology. *Evaluation of PLA-CS Composite Material:* The PLA-CS biocomposite material was characterized by thermogravimetric, characteristic mechanical and chemical features analysis (TGA), Differential Scanning Calorimetry (DSC), and FT-IR. The morphology of the composite used was evaluated by SEM and the obtained composite materials are tested to the amount of adhesion with bone cells.

3. Result

CS and PLA were mixed to obtain the composite masterbatch by the extruder. The CS/PLA material was fabricated by using extrusion. In the study of Du et al., researchers observed that Tg of PLA was found 50 ˚C during heating up to 220 ˚C. However, in our research, we found that Tg of PLA was approximately 58 ˚C and we heated up to 250 ˚C. According to our DSC for natural PLA we found an endothermic transition peak as 150 approximately. In another research, in DSC analyses for the PLA/HA composite as three phases were found 53.5 ˚C at the beginning of glass transition, 97 ˚C for cold crystallization, and 146.8 and 154.9 ˚C for melting [6]. In our experiment for the CS/PLA composite, we observed the beginning of glass transition as 59.34 ˚C, cold crystallization as approximately 112 ˚C, and melting as 148.41 ˚C. By that experiment, we can assume that HA has similar properties with CS powder [7].

The FTIR analysis of calcium sulfate powder is shown in Figure 1.a. The bands interested in the stretching vibration of the O-H groups were detected between 3700 and 3500 cm^{-1}. The bending vibrations of the O-H bond in the water molecule were correlated with the wavenumbers at 1723 and 1628 cm^{-1}. The characteristic bands appointed to the vibrations of the S-O bonds in SO_4^{2-} shown at wavenumbers 1142 cm^{-1} and 655-602 cm^{-1}, stretching and bending respectively. PLA (Figure 1.b) represents characteristic stretching frequencies for -OH, C=O, $-CH_3$ asymmetric, $-CH_3$ symmetric, and C–O, between 3750 and 3300, 1746, 2996, 2947, and 1122 cm^{-1}, respectively. Bending frequencies for $-CH_3$ asymmetric and $-CH_3$ symmetric have been identified at 1450 and 1363 cm^{-1}, respectively. It has been observed that it has the desired load carrying performance in the applied mechanical tests. The tensile strength of the PLA and CS/PLA was observed that 63.4

MPa and 50.3 MPa respectively. In addition, SEM images show that the material is mixed in an almost homogeneous structure. Finally, it has a positive adhesion with bone cells and its interaction with the material.

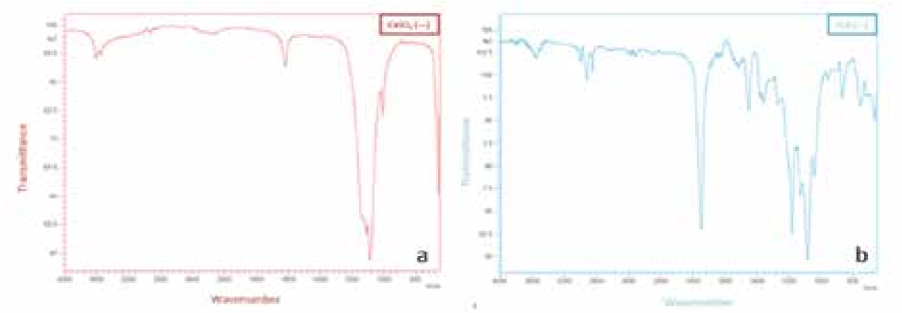

Figure 1: FT-IR spectrum of CS (a), PLA(b.

4. Conclusion

By fabricating bio-composite masterbatch using PLA and CS to use in bone tissue defects, we used to feed granule in an injection molding method according to our designed scaffold in similar mechanical properties like natural bone. We successfully produced our first homogenous bio-composite granule consisting of CS.

References

[1] A. R. Amini, C. T. Laurencin, ve S. P. Nukavarapu, “Bone Tissue Engineering: Recent Advances and Challenges”, *Crit. Rev. Biomed. Eng.*, c. 40, sy 5, ss. 363-408, 2012.

[2] R. Dimitriou, E. Jones, D. McGonagle, ve P. V. Giannoudis, “Bone regeneration: current concepts and future directions”, *BMC Med.*, c. 9, sy 1, s. 66, May. 2011, doi: 10.1186/1741-7015-9-66.

[3] “Bone Substitutes, Grafts and Cement | SpringerLink”. https://link.springer.com/chapter/10.1007/978-3-642-54604-4_29 (erişim Oca. 05, 2021).

[4] K. Maji, “Biomaterials for Bone Tissue Engineering: Recent Advances and Challenges”, içinde *Orthopedic Biomaterials : Progress in Biology, Manufacturing, and Industry Perspectives*, B. Li ve T. Webster, Ed. Cham: Springer International Publishing, 2018, ss. 429-452.

[5] S. K. Lan Levengood *vd.*, “Multiscale osteointegration as a new paradigm for the design of calcium phosphate scaffolds for bone regeneration”, *Biomaterials*, c. 31, sy 13, ss. 3552-3563, May. 2010, doi: 10.1016/j.biomaterials.2010.01.052.

[6] “Fabrication and characterization of fully biodegradable natural fiber-reinforced poly(lactic acid) composites - ScienceDirect”. https://www.sciencedirect.com/science/article/abs/pii/S1359836813005258 (erişim Nis. 09, 2021).

[7] A. Celli ve M. Scandola, “Thermal properties and physical ageing of poly (l-lactic acid)”, *Polymer*, c. 33, sy 13, ss. 2699-2703, Oca. 1992, doi: 10.1016/0032-3861(92)90440-8.

Effect of GTA Vapor Crosslinking Time and Temperature on the Physico-Chemical Properties of Electrospun Gelatin Scaffolds

Aslıhan CALHAN[1,2], Mustafa SENGOR[1], Oguzhan GUNDUZ[1]
[1]Marmara University, [2]Yildiz Technical University
Turkey

Abstract

In this study, gelatin B nanofibers were obtained via electrospinning method. Process parameters were flow rate (0.2 ml/min), electrode distance (10 cm), voltage (23.4 kV) and the temperature (23°C). Crosslinking of gelatin nanofibers was carried out by evaporating 2 ml GTA of 25% GTA aqueous solution. The fibers were exposed to GTA vapor for pre-defined durations and temperature values. Therefore, both effect of vapor crosslinking time and temperature on mechanical performance of gelatin fibers were investigated. The crosslinking time was in the range of 1h-24h at room temperature and the crosslinking temperature was changed in the range of 23°C - 60°C for a fixed time length. SEM, FTIR, DSC analysis was performed on crosslinked and non-crosslinked fibers. According to the results, it is observed that as the crosslinking time increased peak intensity at 3200 cm^{-1} were relatively increased compared to the non-crosslinked case. Sharp decomposition temperature (~225 ^{o}C) in thermographs were indicative for the effect of crosslinking temperature. Morphologies of the nanofibers had changed dramatically with time at room temperature. An interesting fact was found as temperature increased fiber morphology was preserved. At room temperature for 2 hours long crosslinking had a result of deformed flattened fiber surface while 60 ^{o}C fibers had nearly perfect fiber morphologies. Based on these results, it can be concluded that 60 ^{o}C and 2h is one of the best options for gelatin crosslinking.

1. Introduction

Gelatin is a biopolymer which is derived from thermal hydrolysis of collagen in the presence of dilute acids. Gelatin is a protein abundant in animal skin and bones has the natural cell binding motifs like arginine-glycine-aspartic acid (RGD) that is favorable for cell activities[1]. However, gelatin is rarely used alone due to low mechanical stability in body fluid, and thus needs to be enhanced with crosslinking process for medicine and wound dressing applications. When crosslinked, gelatin forms hydrogels and fiber clusters that will be used as scaffolds, due to its availability, intrinsic presence of cell-adhesive motifs, in vivo degradability, and variability.

Glutaraldehyde (GTA) has been used extensively as a golden rule crosslinking agent for collagen-based biomedical materials due to provided high efficiency collagen stabilization, availability and cost-efficiency.

Schiff base is synthesized from amine and carbonyl groups by nucleophilic addition to generate an imine group. It is biodegradable by hydrolysis, and the stability of these bonds decreases as the pH decreasing. Therefore, it is very appropriate for use in the field of biomedical and tissue engineering[2]. The glutaraldehyde crosslinking process occurs due to the bonds created between the amine groups of the gelatin and the hydroxyl groups of the glutaraldehyde, which results in the formation of a Shiff base.

Bigi et al. [3], investigated the mechanical, thermal, swelling and release properties of glutaraldehyde (GTA) crosslinked gelatin films have been investigated in order to verify the infuence of GTA concentration on the stability of the films. The data suggest that the use of GTA at low concentration, which is desiderable to prevent toxicity, allows to modulate the physico-chemical properties of gelatin films, in order to obtain stable materials with a wide range of possible biomedical applications. Campiglio et. al [4], evaluated the effect on fiber morphology of common cross-linking protocols was analyzed, and different strategies to improve the final morphology (including alternative solvents, cross-linker concentration, mechanical constraint, and evaporation conditions). Their studies suggest among the most widely used strategies proposed for the stabilization of collagenous materials (i.e., EDC/NHS, GTA vapor, GTA solution, genipin and others), the use of cross-linking solutions has been proved to be more effective than the employment of vapors, light and heat to stabilize nanofibers substrates[4]. However GTA toxicity poses a risk for biocompatibility, it has also been shown that this can be reduced by decreasing the concentration of GTA in the solution that generates the vapor, and/or by an efficient removal of unreacted GTA left in the material after the crosslinking treatment[5]. Therefore suitable amount GTA vapor can be used instead of GTA solution for crosslinking. Different methods are reported over GTA vapor crosslinking effect on gelatin nanofibers. However there is no study in the literature investigating both temperature and time effects with GTA vapor.

In this study, gelatin B nanofibers were obtained via electrospinning method. The fibers were exposed to GTA vapor for pre-defined durations and temperature values. Therefore, both effect of vapor crosslinking time and temperature on mechanical performance of gelatin fibers were investigated.

2. Experimental Procedure

2.1. Fabrication of gelatin fiber

To prepare the electrospinning solution Gelatin type B from bovine skin was dissolve by %10 wt in water, acetic acid and ethyl acetate solution by ratio acetic acid:ethyl acetate = 3:2 regarding the study in Song et al. (2008)[6]. In this study, an experimental setup is used consisted of a total of 6 piece syringes each one is 1 ml. Therefore, the fibers were obtained thicker at less time. Process parameters were flow rate (0.2 ml/min), electrode distance (10 cm), voltage (23.4 kV) and the temperature (23°C).

2.2. Crosslinking mechanism

Among the chemical crosslinking agents, GTA has been widely used as a crosslinking agent due to the low cost and excellent crosslinking capacity. But it has cytotoxicity effects. Therefore in this study 2 ml GTA was used of 25% GTA aqueous solution. The nanofibers were exposed to GTA vapor for pre-defined durations and temperature values. Therefore, both effect of vapor crosslinking time and temperature on mechanical performance of gelatin nanofibers were investigated. The crosslinking time was in the range of 1h-24h at room temperature and the crosslinking temperature was changed in the range of 23°C - 60°C for a fixed time length.

2.3. Charaterization

Morphological characterization of gelatin nanofibers was examined by an SEM (MA-EVO10, ZEISS). DSC was used for determining of thermal characterization of gelatin fibers by a Shimadzu DSC-60 Plus machine. The temperature range of the device ranges from 25 °C to 300 °C, and this temperature range was used in this study with a heating rate of 10 °C/min. FT-IR was used for determining of the functional groups in the gelatin fiber.

3. Results and Discussion

3.1 Morphology of the gelatin fiber mesh

The morphology of non-crosslinked fiber and GTA vapor crosslinked were presented in Fig.1. Effect of temperature and time on the fiber morphology were revealed. From Fig 1. (a-d) shows 4 different crosslinking time at room temepratures, Fig 1. (b), (e-f) shows the effect of temperature and Fig1 g presents pristine gelatin nanofibers. As gelatin fibers is very sensitive to moisture, while crosslinking with GTA vapor it damages the outer layer of the mesh[7]. When the nanofibers crosslinked, water is emerged, and this water causes degradation of gelatin and morphology of gelatin nanofiber transforms as in Fig.1.

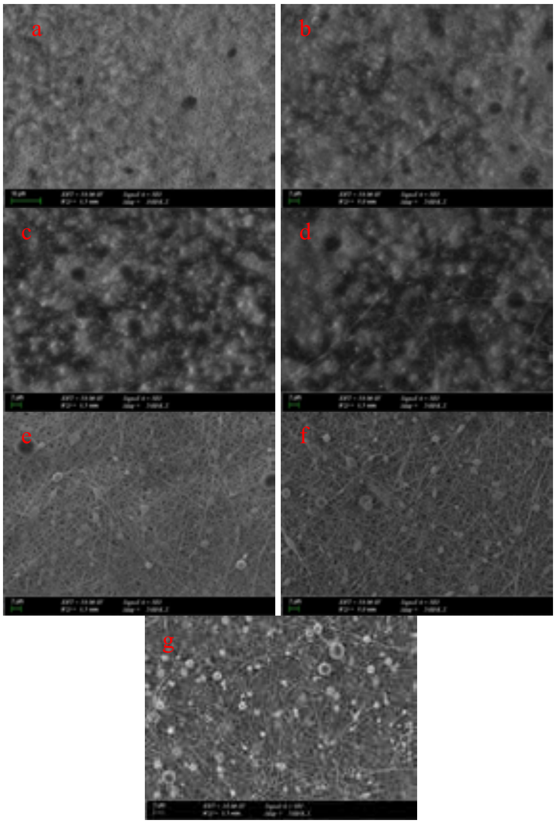

Figure 1. SEM morphologies of gelatin nanofibers a) 1h-RT; b) 2h-RT; c) 12h-RT; d) 24h-RT; e) 2h-37°C; f) 2h-60°C; g) noncrosslinked gelatin fiber

Morphologies of the nanofibers had changed dramatically with time at room temperature. An interesting fact was found as temperature increased; fiber morphology was preserved. At room temperature for 2 hours long crosslinking had a result of deformed flattened fiber surface while 60°C fibers had nearly perfect fiber morphologies. This is due to the Schiff base reaction had resulted in one H_2O molecule which is responsible for the flattened fibers[8]. At higher temperatures higher kinetic energy levels resulted in prompt evaporation of the water molecules, thereby preventing flattening of the gelatin fibers.

3.2. FTIR Analysis

Representative IR spectra (Fig. 2) of gelati nanofibers and gelatin fibers cross-linked by GTA vapor were analyzed. According to the results, it is observed that as the crosslinking time increased peak intensity at 3200 cm-1 were relatively increased compared to the non-crosslinked case. The spectrum of gelatin sample shows characteristic peaks at around 3,304 cm^{-1} for amide A (N–H stretching vibration), 1,640 cm^{-1} for amide I (C = O stretch), 1,539 cm^{-1} for amide II (C–N stretching and N–H bending), and 1,240 cm^{-1} for amide III (N–H in phase bending and C–N stretching vibration)[9].

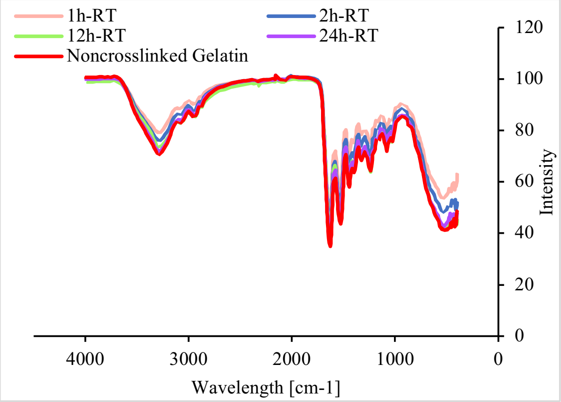

a)

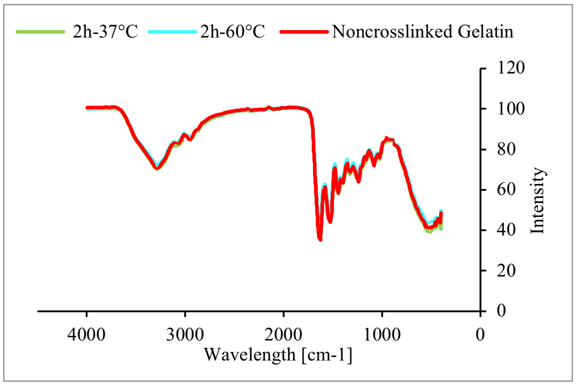

b)

Figure 2. FTIR peaks gelatin nanofibers a) GTA vapor crosslinking effect at different time; b) GTA vapor crosslinking effect at different temperature

3.3 DSC Analysis

Fig. 3 shows the DSC thermograms of crosslinked gelatin electrospun fibers before and after the crosslinking. It is well recognized that the raw gelatin powder shows the appearance of an endothermic peak at approximately 220°C, which is known to correspond to the decomposition temperature of gelatin [6] Sharp decomposition temperature (~225 °C) in thermographs were indicative for the effect of crosslinking temperature. In 2h-37 °C and 2h-60 °C there were no observable sharp transition zones. Ghorani et al.[10] observed that in their studies glass transition region of the electrospun gelatin nanofibers occurred at lower temperature, and the endothermic region for the electrospun nanofibers was limited from 60 °C to 120 °C, with an onset temperature (Tg) at 86.5 °C[10]. Similarly, endothermic region for the electrospun nanofibers was 55 °C to 110 °C in this work . The thermal behavior can be attributed to the bound water content in gelatin samples, and the amorphous structure of nanofibers because of the low degree of helical conformation[11].

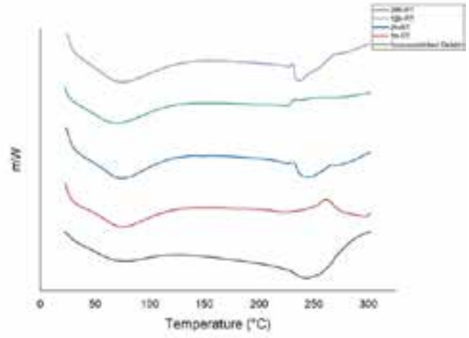

a)

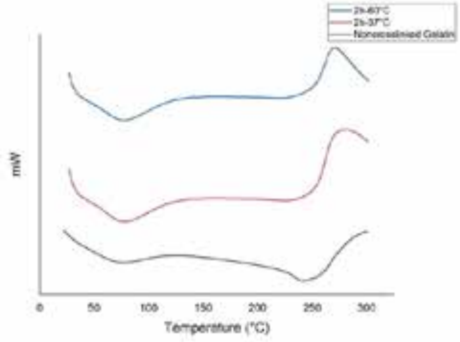

b)

Figure 3. DSC thermographs of GTA crosslinked gelatin nanofiber a) GTA vapor crosslinking effect at different time; b) GTA vapor crosslinking effect at different temperature

Conclusion

In conclusion, the gelatin fibers were produced by electrospinning method. Both effect of vapor crosslinking time and temperature on mechanical performance of gelatin fibers were investigated. Morphologies of the nanofibers had changed dramatically with time at room temperature. An interesting fact was found as temperature increased fiber morphology was preserved. At room temperature for 2 hours long crosslinking had a result of deformed flattened fiber surface while 60 ºC fibers had nearly perfect fiber morphologies. Based on these results, it can be concluded that 60 ºC and 2h is one of the best options for gelatin crosslinking. Based on these results, it can be concluded that 60 ºC and 2h is one of the best options for gelatin crosslinking. Studies of crosslinking gelatin with glutaraldehyde vapor can be improved. Gelatin when crosslinked, it is promising for wound dressing applications with its unique properties.

References

[1] K. Deshmukh, M. Basheer Ahamed, R. R. Deshmukh, S. K. Khadheer Pasha, P. R. Bhagat, and K. Chidambaram, “3 - Biopolymer Composites With High Dielectric Performance: Interface Engineering,” Biopolymer Composites in Electronics, Elsevier, 2017, pp. 39, 27–128.

[2] Y. Li, C. Liu, Y. Tan, K. Xu, C. Lu, and P. Wang, Carbohydr. Polym., 110 (2014) 87–94.

[3] A. Bigi, G. Cojazzi, S. Panzavolta, K. Rubini, N. Roveri, Biomaterials,. 22 (2001) 763–768.

[4] C. E. Campiglio, S. Ponzini, P. De Stefano, G. Ortoleva, L. Vignati, and L. Draghi, Polymers., 12 (2020) 1–15.

[5] S. R. Gomes, G. Rodrigues, G. G. Martins, C. M. R. Henriques, and J. C. Silva, Mater. Sci. Eng. C, 33 (2013) 1219–1227.

[6] J. H. Song, H. E. Kim, and H. W. Kim, J. Mater. Sci. Mater. Med., 19 (2008) 95–102.

[7] A. Laha, C. S. Sharma, and S. Majumdar, Mater. Today Proc., 3 (2016) 3484–349.

[8] C. Bayram, X. Jiang, M. Gultekinoglu, S. Ozturk, K. Ulubayram, and M. Edirisinghe, Macromol. Mater. Eng., 304 (2019) 1–9.

[9] S. Mohammadzadehmoghadam and Y. Dong, Front. Mater., 6 (2019).

[10] B. Ghorani, B. Emadzadeh, H. Rezaeinia, and S. J. Russell, Food Hydrocoll., 104 (2020) 105740.

[11] C. S. Ki, D. H. Baek, K. D. Gang, K. H. Lee, I. C. Um, and Y. H. Park, Polymer (Guildf), 46 (2005) 5094–5102.

3D Silk Fibroin Scaffolds for Tissue Engineering Applications

Melisa KAFALI, Batur ERCAN
Middle East Technical University
Turkey

Abstract

Silk fibroin (SF) gained attention in tissue engineering applications owing to its unique properties including biocompatibility, high strength and ability to control its porous structure. The aim of this study was to fabricate 3D SF scaffolds having an optimum porous structure to provide sufficient mechanical properties while allowing proliferation of cells for enhanced tissue regeneration. To achieve this, effect of various fabrication parameters on SF scaffold characteristics, mainly the pore morphology and pore size, on mechanical and biological properties was investigated. Specifically, dissolution time of raw SF in salt solution, dialysis temperature, freezing rate and freezing temperature of SF solutions were optimized for detailed scaffold characterization.

1. Introduction

Biomedical applications require 3D scaffolds as they provide porous structure for enhanced cell-scaffold interactions. However, the use of scaffolds in tissue engineering was limited due to their insufficient mechanical properties. Therefore, an optimum porous architecture would provide both cell attachment and mechanical stability under condition. Among the various types of materials, SF captured significant interest due to its unique properties and ability to promote cellular functions. Importantly, SF had the ability to fine tune its porous architecture through the alteration of fabrication parameters. Among these fabrication routes to obtain SF scaffolds, a commonly used technique is freeze drying. This study investigated the effects of scaffold fabrication parameters on SF scaffolds.

2. Materials and Methods

SF was extracted from silk cocoons inside boiled 0.02M sodium carbonate solution. Extracted SF was dissolved in 11M lithium bromide solution for 4 and 48h. After that, prepared fibroin solution was dialyzed against distilled water for 3 days at 4, 20 and 37^{o}C and centrifuged to remove remaining impurities. Afterwards, SF solution was frozen in freezer (-20 and -80^{o}C) or liquid nitrogen (-196^{o}C) and lyophilized to obtain porous structure. Pore size and morphology of the samples were characterized using scanning electron microscopy.

3. Results

Altering the dissolution times (4 and 48h) and dialysis temperatures (4, 20 and 37°C) altered molecular weight of SF, and thus influenced the mechanical properties of SF scaffolds. For example, the 4h/4°C scaffolds had higher mechanical strength than the 48h/37°C scaffolds. On the other hand, freezing rate and freezing temperature combinations were used to obtain different pore sizes and morphologies, which were confirmed by using SEM images (Fig. 1). Biological tests are showed that cells were viable and proliferating on all scaffolds.

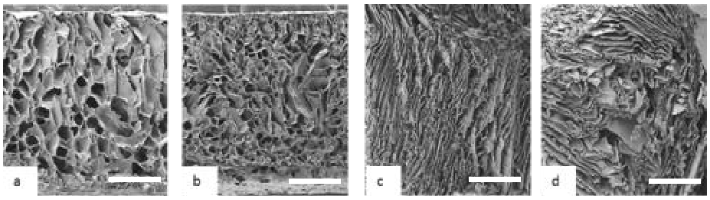

Fig1. SEM images of SF scaffold a) frozen at (-20°C) without isopropanol, b) frozen at (-20°C) with isopropanol, c) frozen at (-80°C) without isopropanol, d) frozen at (-80°C) with isopropanol (scale bars are 1 µm).

4. Conclusion

It was observed that altering fabrication parameters were changing pore morphology and mechanical properties. SF scaffolds providing enhanced cellular interactions together with sufficient mechanical properties were fabricated through a well-designed porous architecture.

Acknowledgements

This work was financially supported by The Scientific and Technological Research Council of Turkey (Grant no:117M754).

20th

INTERNATIONAL
METALLURGY
MATERIALS
CONGRESS
10-12 June
2021

“in Digital Platform”

Nanomaterials

immc2021

Chemically Processed Inorganic Nanostructures for Energy and Health Applications

Sanjay MATHUR
University of Cologne
Germany

Abstract

Chemical nanotechnologies have played, in the past few decades a major role in the convergence of life, physical and engineering sciences leading not only to simple collaboration among the disciplines but to a paradigm shift based on true disciplinary integration. The successful synthesis, modification and assembly of nanobuilding units such as nanocrystals and wires of different materials have demonstrated the importance of chemical influence in materials synthesis, and have generated great expectations for the future. Implications of chemistry as an innovation motor are now visible for knowledge leap forward in various sectors such as materials engineering for energy, health and security. Materials chemistry mostly housed at the universities and academic research institutions has delivered tremendous knowledge leap in the domain of functional materials but in the absence of proper validation of new materials for possible device application, their commercial uptake is severely limited.

Inorganic nanostructures offer new opportunities in materials engineering due to their improved intrinsic properties resulting from the reduction of microstructural features, which also allows engineering the interfacial properties. This talk will present how chemically grown nanoparticles, nanowires and nanocomposites of different metal oxides can be transformed into integrated advanced material technologies. Examples will include application of superparamagnetic iron oxide nanoparticles for magnetic resonance imaging (MRI) and drug delivery applications, vapour phase synthesis and electrospinning of nanowires for application as electrode materials and in PEC water splitting reactions. New sensing concept based on the integration and correlation of complementary functionalities originating from multiple junctions in a singular nanostructure to palliate the current issues in gas sensor technologies such as low power consumption, low operating temperature and cost effective production will be elaborated. Finally, the current challenges of integration of nanomaterials in existing device concepts will be discussed.

Preparation and Photocatalytic Activity of Solar Light Sensitive g-C_3N_4/TiO_2 Heterojunction Nanocomposites

Pelin GÜNDOĞMUŞ[1], Jongee PARK[2], Abdullah ÖZTÜRK[1]
[1]Middle East Technical University, [2]Atılım University
Turkey

Abstract

The solar light sensitive g-C_3N_4/TiO_2 heterojunction nanocomposites were prepared in one step hydrothermal process by growing TiO_2 nanoparticles on the surfaces of g-C_3N_4 particles. The g-C_3N_4 content of the composites varied from 20 to 90 wt%. The composite containing 80 wt% g-C_3N_4 was additionally subjected to a regulated heat treatment at different temperatures in the range from 350 to 500 ºC for 1 h to improve the photocatalytic activity. XRD, FESEM, and DRS characterization techniques were applied to identify the crystalline phases present, to examine morphology developed, and to determine band gap energy of the composites. The Methylene Blue (MB) degradation tests were performed to evaluate the photocatalytic activity of the powders under solar light illumination using a UV-vis spectrophotometer. Results were compared with the results of the phase pure TiO_2 and phase pure g-C_3N_4 powders. The g-C_3N_4/TiO_2 heterojunction photocatalysts exhibited better photocatalytic activity for the degradation of MB than both TiO_2 and g-C_3N_4 powders. The improvement in photocatalytic activity was attributed to the generation of reactive oxidation species induced by photogenerated electrons and to the reduced recombination rate for electron-hole pairs.

1. Introduction

TiO_2 is one of the most widely used photocatalysts among all semiconductors due to its abundancy, non-toxicity, chemical stability, easy availability, and low cost [1-3]. Despite its desirable peculiarities, TiO_2 has large band gap that makes TiO_2 only active in UV region at a wavelength smaller than 388 nm [4]. In order to improve the photocatalytic activity of TiO_2, construction of heterojunction with another semiconductor has been shown very effective. In heterojunction systems, the separation of photogenerated electron/hole (e^-/h^+) pairs is encouraged through charge transfers between the two semiconductors [5]. Different narrow band gap semiconductors including ZnO, WO_3, SnO_2, and Fe_2O_3 were tried for heterojunction construction with TiO_2 [6]. Recently, carbon-based materials like graphene [7], carbon nanotube [8], and graphitic carbon nitride (g-C_3N_4) were utilized to construct heterojunction with TiO_2. g-C_3N_4 has lower band gap (2.7 eV) than TiO_2, which provides a good absorption in the visible light range [9]. Also, g-C_3N_4 has suitable band position (−1.3 to +1.4 eV) that matches to the band-edge region of TiO_2 [10]. g-C_3N_4/TiO_2 heterojunction increases the separation duration of e^-/h^+ pairs and enhances the visible light photocatalytic activity of TiO_2 at extended wavelength range [11,12]. Additionally, g-C_3N_4/TiO_2 heterojunction provides the formation of the mesoporous structure that creates more open sites to improve photocatalytic activity [10].

Even though there are few studies on the synthesis of g-C_3N_4/TiO_2 heterojunction photocatalysts by the hydrothermal method, more research is needed to understand the hydrothermal evolution of these composites better since these composites have both scientific and technological interest for wastewater treatment. The hydrothermal synthesis conditions affect the interfacial interaction of g-C_3N_4 and TiO_2 in the structure [13] which in turn improve the photocatalytic activity in special photocatalytic applications.

The purpose of this study was to prepare solar light sensitive g-C_3N_4/TiO_2 heterojunction photocatalysts by one step hydrothermal process and to compare their photocatalytic activity with the photocatalytic activities of TiO_2 and g-C_3N_4 powders.

2. Experimental Procedure

2.1. Preparation of g-C_3N_4/TiO_2 composites

First, melamine powder (2,4,6-Triamino-1,3,5-triazine, Aldrich, 99%) was heated to 550 °C for 4 h, and then cooled to room temperature at a cooling rate of 2 °C/min. The resultant material was ground using mortar with pestle to get g-C_3N_4 powder.

For the preparation of g-C_3N_4/TiO_2 composites, predetermined amount of g-C_3N_4 was mixed with 118 ml Deionized (DI) water and sonicated for 30 min. After that, 8.33 ml Nitric acid (HNO_3, Aldrich 70%), and 6.67 ml of Titanium tetraisopropoxide (TTIP, Aldrich 97%) was added into suspension during magnetic stirring for

30 min. Finally, the suspension was transferred into the Teflon-lined autoclave to allow the reactions at 110 °C in autogenous pressure for 1 h. After the hydrothermal reaction, the products were washed with DI water, dried at 80 °C for 24 h and ground using mortar with pestle to get g-C_3N_4/TiO_2 powder.

The synthesized composites were named as TCN-XX, where XX represents the weight percent of g-C_3N_4. Heat-treated composites were named as TCN-80-YYY, where the last three digits correspond to heat treatment temperature in ºC.

2.2. Characterization of g-C_3N_4/TiO_2 composites

Crystallographic phases in the powders were identified at a scanning rate of 2º/min between 10 and 65º using an X-Ray Diffractometer (Bruker, D/MAK/B). Morphologies of the powders were analyzed by Field Emission Scanning Electron Microscope (FESEM, Nova, Nanosem). Elemental analysis was done by Energy Dispersive Spectroscopy (EDS, JEOL Ltd).

2.3. Band-gap Analysis and Photocatalytic Activity Measurement

Band gap measurements of the powders were done by diffuse reflectance spectra (DRS). Tauc's transformation formula (Eq.1) was applied to calculate band gap values.

$$(\alpha h\nu)^2 = A(h\nu - \mathrm{Eg}) \tag{1}$$

where α, $h\nu$, A, Eg are a constant, photon energy, absorption coefficient, and band gap energy.

Photocatalytic activities of the synthesized composites were evaluated by Methylene Blue (MB) degradation test under solar light illumination using UV-Vis spectrophotometer. MB solution was prepared by dissolving MB powder in DI water to obtain a concentration of 10 mg/l. Then, 100 mg of the synthesized powder was added into the MB solution. The solution was stirred first in the dark, then under 500-watt Xenon lamp for 60, 120, and 180 min. The MB degradation values were calculated using Eq. 2.

$$\text{Degradation \%} = (C_o - C)/C_o * 100 \tag{2}$$

where C_o and C are the concentrations of MB at initial and at different irradiation times, respectively.

3. Results and Discussion

3.1. X-Ray Diffraction (XRD) Analysis

The XRD patterns of the g-C_3N_4/TiO_2 nanocomposites synthesized as well as the g-C_3N_4 and TiO_2 powders are shown in Figure 1. The diffraction peaks at 2θ of 25.4°, 37.6°, 48°, and 54° correspond to anatase TiO_2 planes of 101, 004, 200, and 105, respectively. The peak at 30.8° belongs to 121 plane of brookite phase of TiO_2. Therefore, synthesized TiO_2 was named as pristine TiO_2. The peaks detected in the XRD pattern of g-C_3N_4 at 13.0° and 27.4°were for the 100 and 002 planes of the g-C_3N_4, respectively. All synthesized composites have both anatase and g-C_3N_4 peaks irrespective of their g-C_3N_4 content. See Figure 1 a. Similar results were reported by Wang et al. [14].

The XRD patterns of the TCN-80 composites heat-treated at various temperatures are shown in Figure 1 b. The main characteristic peaks of anatase and g-C_3N_4 are detected in the patterns of the composites heat-treated at different temperatures. The intensity of the g-C_3N_4 peaks decreases with increasing heat-treatment temperature because of the decomposition of the g-C_3N_4 that decomposes until 700 °C [15]. Structure of g-C_3N_4/TiO_2 nanocomposites remained unchanged until 450 ºC as shown in Figure 1 b.

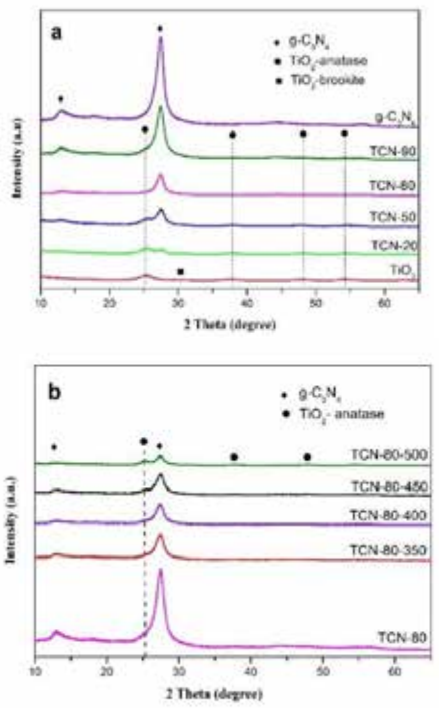

Figure 1. XRD patterns of a) the synthesized powders, b) TCN-80 composites heat-treated at different temperatures.

3.2. Morphological and Elemental Analysis

Figure 2 a, b, c shows the FESEM images of pristine TiO_2, pristine g-C_3N_4, and TCN-80 composites. The morphology of TiO_2 nanoparticles are in spherical agglomerates. The morphology of g-C_3N_4 has a layered structure that stacked with each other. TCN-80 composite includes thin sheet layers of g-C_3N_4 particles covered by TiO_2 nanoparticles.

Figure 2 d shows the EDS spectrum of the TCN-80 composite that consists of Carbon (C), nitrogen (N), Titanium (Ti), and Oxygen (O). This data confirms that there is an interfacial connection between g-C_3N_4 and TiO_2 [16] and confirms the development of g-C_3N_4/TiO_2 composite rather than existence of the two as a mixture.

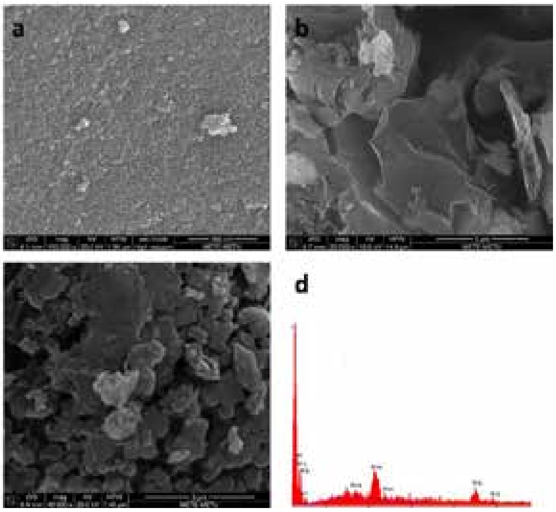

Figure 2. SEM images of (a) pristine TiO_2, (b) pristine g-C_3N_4, (c) TCN-80 composite, d) EDS spectrum of TCN-80 composite.

3.3. Diffuse Reflectance Spectra (DRS) Analysis

The absorbance versus wavelength plots for the powders are shown in Figure 3. The absorbance edge values of the TCN composites are between those of g-C_3N_4 (486.04 nm) and TiO_2 (439 nm). When the absorption characteristics of the TCN composites are compared with those of TiO_2, an extension in the visible light region was noticed because of the composite formation. The band gap energy (Eg) values of the pristine TiO_2 powder is 3.08 eV while that of the pristine g-C_3N_4 powder is 2.7 eV. As expected, Eg value of TCN-80 composite (2.8 eV) has a value between the values of g-C_3N_4 and TiO_2. The band gap measurements suggest that, harvesting light ability of TiO_2 is enhanced by the g-C_3N_4/TiO_2 composite formation. TCN-80-400 composite had almost the same band gap value with TCN-80 composite. This finding suggests that the application of a regulated heat treatment to TCN-80 composite had no major effect on Eg.

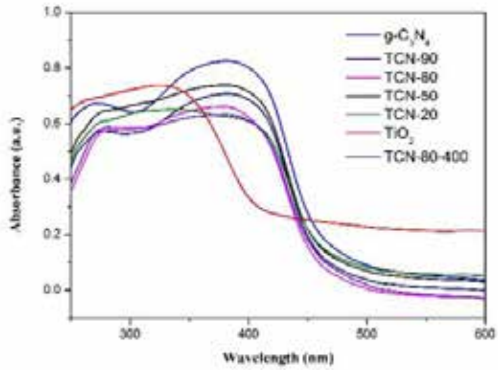

Figure 3. UV-vis diffuse reflectance spectra for the powders synthesized.

3.4 Photocatalytic Activity

The photocatalytic MB degradation plots of the TCN composites, the synthesized pristine powders, together with pure MB solution (blank), and the commercially available TiO_2 powder (P25) were shown in Figure 4. All of the TCN composites showed the photocatalytic degradation ability. Blank sample had almost no absorption and degradation of MB. The MB degradation ability of the TCN composites increases in the order of TCN-20, TCN-90, TCN-50, and TCN-80. TCN-80 exhibited the best photocatalytic activity after 180 min UV/Vis illumination. It degraded 79.7% of the initial MB molecules under 180 min solar light illuminations. In TCN-90 composite, TiO_2 content was not enough to construct a proper heterojunction between the g-C_3N_4 and TiO_2 powders. The findings suggest the optimal wt% g-C_3N_4/TiO_2 ratio is 80/20. Similar results were reported by Pany et al. and Sun et al. [17,18].

It is obvious that the photocatalytic activity of TiO_2 was improved through the heterojunction construction. TiO_2 had the highest absorption in the dark but, the MB degradation of TiO_2 was trivial in solar light because of the short supply of UV light from the solar simulator. TCN-80 composite and P25 powder had almost the same MB degradation. See Figure 4 b. Heat treatment affected the photocatalytic activity of TCN-80 composite positively as shown in Figure 4 c. With increasing heat treatment temperature photocatalytic activity increased until temperature reached to 450 °C. TCN-80-400 composite had the best photocatalytic activity among all powders. It degraded all MB molecules under 180 min of solar light illumination.

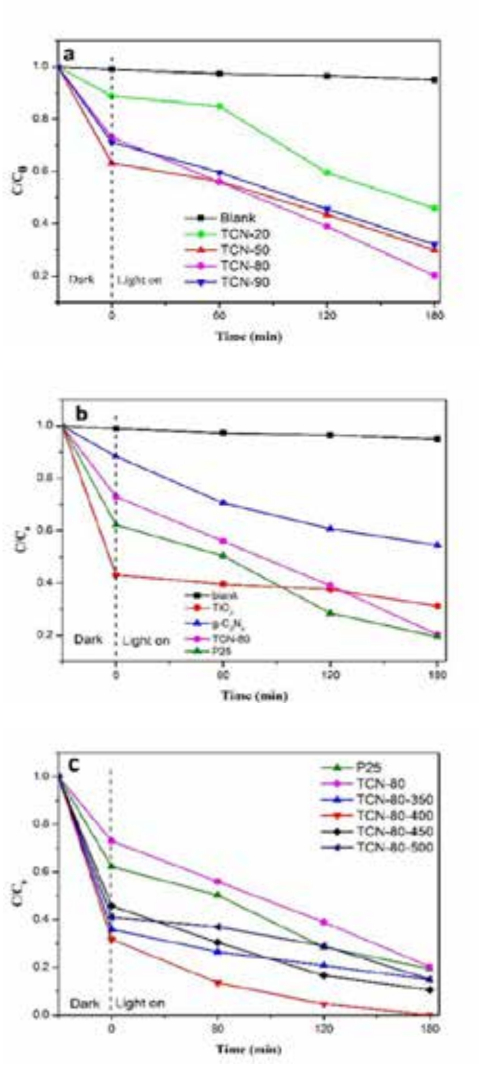

Figure 4. Photocatalytic MB degradation plots for the synthesized powders.

4. Conclusions

1. g-C_3N_4/TiO_2 composites were successfully synthesized by one-step hydrothermal process.
2. The optimum g-C_3N_4/TiO_2 ratio for the photocatalytic properties is 80/20.
3. The mechanism for the heterojunction construction is the deposition of TiO_2 nanoparticles on the surfaces of g-C_3N_4 particles during the hydrothermal synthesis.
4. Heat treatment at 400 ºC for 1 h improves the photocatalytic efficiency. The composite containing 80 wt% g-C_3N_4 subsequently heat treated at 400 ºC for 1 h exhibits the best photocatalytic activity. It degrades all MB molecules in 180 min of solar light illumination.
5. Through heterojunction construction, the photocatalytic activity range of TiO_2 enhances in the visible range since the band gap of TiO_2 decreases and absorption edge increases.

Acknowledgment

The authors thank Middle East Technical University (METU) for the partial financial support through project number YLT-404-2018-3751.

References

[1] P. Gündoğmuş, J. Park, and A. Öztürk, Ceram. Int. doi.org/10.1016/j.ceramint.2020.05.241.
[2] R. Kaplan, B. Erjavec, G. Drazıc, J. Grdadolnik, A. Pintar, Appl. Catal. B Environ. 181 (2016) 465–474.
[3] S. Ouyang, Y. Bi, N. Umezawa, J. Ye, H. Tong, M. Oshikiri, Adv. Mater. 24 (2011) 229–251.
[4] J. Li, Y. Liu, H. Li, and C. Chen, J. Photochem. Photobiol. A Chem. 317 (2016) 151–160.
[5] A. Tang, Y. Jia, S. Zhang, Q. Yu, X. Zhang, Catal. Commun. 50 (2014) 1–4.
[6] N. Abbas, G.N. Shao, M.S. Haider, S.M. Imran, S.S. Park, H.T. Kim, J. Ind. Eng. Chem. 39 (2016) 112–120.
[7] A. Nikokavoura, C. Trapalis, Appl. Surf. Sci., 430 (2018) 18–52.
[8] A. T. Kuvarega, R. W. M. Krause, B. B. Mamba, Nanotechnol. Sustain. Dev. First Ed., 2 (2014) 73–88.
[9] Q. Gao, L. Duan, X. Zhang, I. Kamiya, W. Lü, Superlattices Microstruct. 109 (2017) 860–868.
[10] H. Tang, S. Chang, L. Jiang, G. Tang, and W. Liang, Ceram. Int. 42 (2016) 18443–18452.
[11] G. D. Shen, Y. P. Pu, Y. F. Cui, and P. P. Jing, Ceram. Int. 43 (2017) S664–S670.
[12] I. Koltsov, J. Wojnarowicz, and J. Smalc-koziorowska, Molecules, 24(5) (2019) 874.
[13] X. Chen, J. Wei, R. Hou, Y. Liang, Z. Xie, Y. Zhu, X. Zhang, H. Wang, Appl. Catal. B Environ. 188 (2016) 342–350.
[14] Y. Wang, W. Yang, X. Chen, J. Wang, and Y. Zhu, Appl. Catal. B Environ., 220 (2018) 337–347
[15] G. Dong, Y. Zhang, Q. Pan, and J. Qiu, J. Photochem. Photobiol. C Photochem. Rev., 20 (2014) 33–50.
[16] R. A. Senthil, J. Theerthagiri, A. Selvi, and J. Madhavan, Opt. Mater. (Amst)., 64 (2017) 533–539.
[17] S. Pany, K. M. Parida, Phys. Chem. Chem. Phys. 17 (2015) 8070–8077.
[18] Z. Sun, C. Li, G. Yao, S. Zheng, Mater. Des. 94 (2016) 403-409.

Novel Synthesis of Boron Containing TiO_2 Nanostructures with Variable Morphologies by Sol-Gel and Hydrothermal Processing

Cansu NOBERİ[1], Cengiz KAYA[2]
[1]İstanbul Gelişim University, [2]Sabancı University
Turkey

Abstract

Boron doped TiO_2 nanoparticles were synthesized using sol-gel method. Afterwards those nanoparticles were used as precursors to synthesize B doped TiO_2 nanotubes via hydrothermal method. The structure and phase content of both nanoparticles and nanotubes were characterized in detail using TEM, XRD and FEG SEM. Antimicrobial and anticancer activities of the particles and nanotubes were also investigated. It was shown that the proposed combined technique was successful to obtain B doped TiO_2 nanoparticles and nanotubes at low temperature and they were effective materials for antibacterial and anticancer applications.

1. Introduction

In the past several decades, much attention is being paid to TiO_2 nanostructures because of their unique properties including photocatalytic and antimicrobial activities. Doping of TiO_2 with nonmetal elements, such as boron can be used to improve its photocatalytic activities [1,2]. Boron is also wide known antimicrobial agent so that the addition of boron also enhances the antimicrobial activity of TiO_2 nanostructures as well [3].

2. Materials and Methods

Boron doped TiO_2 nanostructures were prepared by both sol-gel and hydrothermal methods described in the following. As a first step B-TiO_2 nanoparticles were synthesized using sol-gel. After that using those nanoparticles as starting material, B-TiO_2 nanotubes were synthesized hydrothermally. In order to prepare boron dopped TiO_2 nanoparticles titanium isopropoxide (TTIP), 2-propanol (C_3H_8O), boric acid (H_3BO_3) and amorphous boron (in nano scale) were used as precursors. The amount of boric acid and amorphous boron was chosen in order to have app. 10wt.% boron in final B-TiO_2 nanostructures. The percentage of boron was chosen very carefully based on the data published in literature [1]. The final step of the experimental part that included obtaining pure TiO_2 nanoparticles [4,5] and nanotubes [6] were conducted based on the techniques described in our previous works.

3. Conclusion

It was shown that the proposed combined technique involving sol-gel and hydrothermal processing is a powerful tool to obtain B dopped TiO_2 nanostructures and nanotubes at low temperature. It was shown that the size of the both structures was smaller than 100 nm. It was also proved that boron atoms were located inside the TiO_2 lattice due to its radius (too small to replace Ti or O so that they stay interstitial position inside the lattice). Antileishmanial and anticancer tests revealed that B-TiO_2 nanotubes have shown superior effects.

References

[1] A. Zaleska, J.W. Sobczak, E. Grabowska and J. Hupka, Applied Catalysis B:Environmental, 78 (2008) 32-100.
[2] J.H. Jeong, D.W. Jung, E.W. Shin and E.S. Oh, Journal of Alloys and Compounds, 604 (2014) 226-232.
[3] Y. Wang, X. Xue and H. Yang, Chinese Journal of Chemical Engineering, 22 (2014) 474-479.
[4] C. Noberi, A.C. Zaman, C.B. Ustundag, F. Kaya and C. Kaya, Materials Letters, 67 (2012) 113-116.
[5] C. Noberi, F. Kaya and C. Kaya, Ceramics International, 42 (2016) 17202-17209.
[6] C. Noberi and C. Kaya, Materials Discovery, 9 (2017) 23-29

Characterization of Cellulose Nanocrystals Produced via Acid Hydrolysis Method

Burcu SARI, Cevdet KAYNAK
Middle East Technical University
Turkey

Abstract
Cellulose is the most abundant natural polymer on Earth that could be used in the production of many eco-friendly items in the form of macro-, micro- and nano-structure. The main purpose of this study was to obtain cellulose nanocrystal (CNC) structures from the microcrystalline cellulose (MCC) structure by sulfuric acid hydrolysis method.

1.Introduction

The increasing awareness about global environmental problems along with ecological sustainability and waste management has increased the effort of developing new green materials and methods. Today, various traditional materials that have been used in several applications are being substituted by new eco-friendly and lightweight materials. For the development of biocomposites, cellulose nanocrystal (CNC) structures are being significant reinforcement materials due to not only their physical and chemical properties but also their biodegradability, renewability, sustainability, abundance, high biocompatibility. Although there are other techniques, one of the chemical methods for the production of CNC is using acid hydrolysis technique. In this method, amorphous regions of the cellulose microfibrils are eliminated by introducing acid attacks by controlling the parameters of acid concentration, temperature, mixing rate, reaction time, and the amount of raw cellulose.

2. Materials and Methods

The starting raw cellulose for the production of cellulose nanocrystal (CNC) structures was Microcrystalline Cellulose (MCC) material (Sigma-Aldrich) with a diameter and length of 12-15 µm and 35-50 µm, respectively. Cellulose nanocrystals were synthesized from MCC by sulfuric acid hydrolysis (64wt/wt%) at 45℃ for 120 min with continuous stirring. Suspensions were centrifuged at 5000 rpm for 3*5 min. Dialysis against distilled water is then performed for a week to remove any free acid molecules from the suspension. In order to obtain colloidal cellulose nanocrystals, suspensions were sonicated (Bandelin Sonoplus 3200) for 15 min at 30% output control while cooling in an ice bath to avoid overheating. The pH of the suspensions was normally around 6.5. For certain improvements, the pH of the CNC suspensions was also adjusted to 9.5 by adding a buffer solution having NaOH. Finally, freeze-drying (Christ, Alpha 2-4 LDplus) was applied to obtain powders of CNC. Morphologies of CNC structures obtained in this technique were evaluated by using SEM investigation (Figure 1).

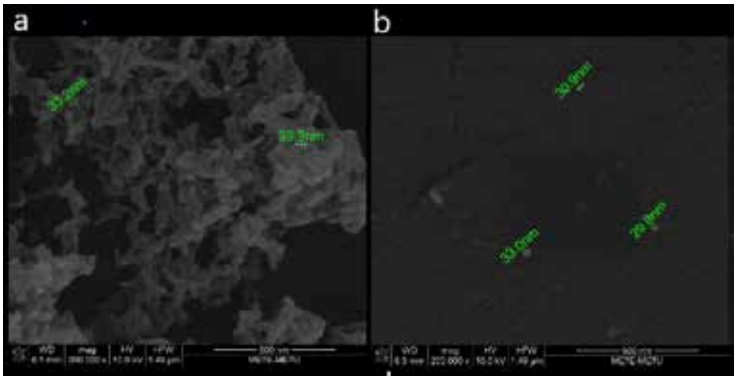

Figure 1. SEM images showing the morphology of CNC structures obtained from the suspensions having a pH of (a) 6.5 and (b) 9.5.

3.Conclusion

It was concluded that thermally stabilized cellulose nanocrystal (CNC) structures could be obtained from the microcrystalline cellulose (MCC) structure by the sulfuric acid hydrolysis method.

Novel Advanced Automotive Graphene Nanocomposites: Challenges and Future Perspectives

Ahmed ELMARAKBI
Northumbria University
United Kingdom

Abstract

The automotive industry is widely viewed as being the industry in which the greatest volume of advanced composite materials will be used in the future to produce light vehicles. Nowadays, several advanced materials are widely used in automotive industry. Because of its multifunctional properties and promising applications, many expectations in composite materials are related to graphene. However, no application of graphene-based materials is currently marketed in the automotive sector. Therefore, research activities are under development to study the potentiality of these systems and all the value's chain of automotive needs to be involved in this effort. One of most challenge aim is the economic impact of the innovative structures on the vehicle market, all the value's chain have to address their effort to get the final cost of the innovative products as low as possible.

The present initiative provides a summary overview on graphene related materials (GRMs) for automotive applications and investigates efficient ways to integrate graphene as polymer reinforcements within composite materials for energy-efficient and safe vehicles (EESVs).

The idea is based on the concept-oriented lightweight design aiming of combination of light structures with novel multifunctional materials.

For such a purpose, GRMs are addressed with respect to some challenging factors, for instance the large scale production of graphene or the non-existence of constitutive material models for high performance structural applications like crashworthiness. Therefore, accurate material models need to be developed to support simulation of structural design for these vehicles. A focus on the hierarchical modelling of GRMs with an emphasis on the multiscale constitutive behaviours of each material phase is elaborated in the framework of the Graphene Flagship to well understand such limitations for a full applicability of graphene. It is anticipated that this initiative will advance innovative lightweight graphene nanocomposites and their related modelling, designing, manufacturing, and joining capabilities suitable for automotive industry which requires unique levels of affordability, mechanical performance, green environmental impact and energy efficiency. This leads to complete understanding of the new graphene nanocomposites and their applicability in high-volume production scenarios.

Synthesis of Metallic Striped and Janus Particles

Mert ULUSEL, Ozan ŞAHİN, Orçun DİNÇER, Bayram YILDIZ, Simge ÇINAR
Middle East Technical University
Turkey

Abstract

Janus particles are colloidal particles with distinct properties on opposite sides and are an emerging class of materials. Based on these distinct properties, metallic Janus particles may respond to external stimuli, such as light, electric field or magnetic field, and thus can be used as smart materials in broad range of applications in the fields of biotechnology, energy, chemistry and so on. Despite their immense potential, the currently available synthesis methods for anisotropic particles are mostly bottom up approaches, not scalable, and mostly applicable to polymers. In this study, a novel scalable technique to synthesize metallic Janus particles was reported. In the synthesis, liquid eutectic alloy droplets, undercooled by 150 °C, were first produced by droplet emulsion technique. Then, the particles are exposed to various heat treatment procedures. Optimization of the temperature, the exposure time and the cooling rate led to the formation of regular and double-sided Janus particles, which is a distinct morphology. This process was scaled up in order to produce at least 10 grams of particles in one batch. The surface and optical properties of the synthesized Janus particles were also characterized, and compared with that of eutectic particles.

1. Introduction

Anisotropic particles attract a great deal of interest due to their differing optical properties and response to applied light, magnetic and electric fields with respect to isotropic particles. Plasmon response of particles to light is strongly dependent on the morphology and nanostructure, which can be employed to produce photocatalytic materials and sensors[1]. Under magnetic fields, anisotropic particles consisting of ferromagnetic or paramagnetic components can be made to rotate, resulting in propulsion, making it possible to use them as colloidal motors and self assembling them into predictable shapes [2]. Despite the promising application areas, in order to produce and characterize anisotropic particles, sufficient amounts need to be produced. The common method used is particle-embedding and surface-modification [3], which is costly and time consuming. Droplet emulsion technique can be used to fabricate large amounts of particles per batch [4]. The particles' surface, produced by breaking up the bulk starting material with shear force, rapidly oxidize [5], preventing heterogeneous nucleation, as the catalytic sites are restricted to only a few particles [6]. The undercooled particles can then be used as a starting point for the fabrication of various particle morphologies. Heat treatment can be applied to large amounts of particles in contrast to the aforementioned methods. As the phase distribution is dependent on solidification parameters, by changing those parameters, different particle morphologies can be promoted.

2.Materials & Methods

Particles are produced with droplet emulsion technique. Diethylene glycol is used as a medium to produce undercooled particles. Eutectic Bismuth-Tin is used. The reaction takes place at 160°C (±10°C). After the reaction, the particles are washed with ethanol via centrifugation and the particles are stored in ethanol. Heat treatment is done using drying oven in open atmosphere. SEM, UV-Vis, DSC, and XRD are used in order to characterize the particles.

3. Conclusion

Undercooled particles can reliably be produced with droplet emulsion technique, with an undercooling of 150°C. At -11.5°C, the particles solidify with regular eutectic morphology. As a result of the optimization of solidification kinetics, the striped morphology and Janus morphologies can be obtained. The process is highly repeatable and can be applied to suspensions with large amounts of particles. Optical characterization shows surface plasmon resonance in striped particles, which is not present in their undercooled or regular eutectic counterparts.

Acknowledgment

This work was supported by The Scientific and Technological Research Council of Turkey under Grant no. 119M306.

References

[1] J. Reguera, D. Jiménez De Aberasturi, N. Winckelmans, J. Langer, S. Bals, and L. M. Liz-Marzán, Faraday Discuss., 191, (2016) 47–59.
[2] O. Güell, F. Sagués, and P. Tierno, Adv. Mater., 23 (2011) 3674–3679.
[3] C. C. Lin, C. W. Liao, Y. C. Chao, and C. Kuo, ACS Appl. Mater. Interfaces, 2 (2010) 3185–3191.
[4] I. D. Tevis, L. B. Newcomb, and M. Thuo, Langmuir, 30 (2014)14308–14313.
[5] Q. Zhang et al, Mater. Chem. A, 2 (2014) 11065–11072.
[6] J. H. Perepezko, J. L. Sebright, P. G. Höckel, and G. Wilde Mater. Sci. Eng. A, 326 (2002) 144–153.

Morphological Evolution of Boron Carbide Particles: Sol-Gel Synthesized Highly Crystalline B_4C Whiskers

Suna AVCIOĞLU, Figen KAYA, Cengiz KAYA
Yıldız Technical University
Turkey

Abstract

1. Introduction

Mesoporous high aspect ratio boron carbide (B_4C) whiskers are a strong candidate for energy applications such as batteries, supercapacitors, and fuel cells. Boron carbide (B_4C) whiskers can also be used as fillers in composite materials to improve both mechanical properties and nuclear shielding performance. In this study, a novel modified sol-gel technique to produce boron carbide (B_4C) whiskers is presented. The evolution of boron carbide particle morphology was investigated, and the growth behaviour of the particles was tailored by controlling processing conditions.

2. Materials and Methods

Preceramic polymeric gels were fabricated by using boric acid, glycerin, and tartaric acid as starting materials. Pyrolysis of gels was carried out in a muffle furnace by two different heating cycle. Final heat treatment on pyrolyzed processors was applied at 1500℃in the Ar atmosphere. The phase composition of synthesized powders was characterized by X-ray diffraction analysis (XRD). The morphology of the particles was examined by scanning electron microscopy (SEM) and high-resolution field emission scanning electron microscopy (HR-FESEM) techniques.

3. Conclusion

The results indicate that boron carbide (B_4C) particles with high crystallinity, and without residual carbon and/or boron oxide content were obtained by both designed production routes. However, a considerable difference was observed in boron carbide particle morphology. Boron carbide particles with polyhedral-equiaxed morphology in average particle size of 2-5µm were fabricated by the first heat treatment route. In addition to the polyhedral-equiaxed particles, boron carbide fibres (50-100µm length) and whiskers (5-20µm) were also formed via second route.

Acknowledgements

The authors are grateful for the financial support from The Scientific and Technological Research Council of Turkey (TUBITAK) under the contract number of 120M651.

Solid Solution Strenghtening in Amorphous-Crystalline Metallic Composites

Sevda FATHIPOUR[1], Amir MOTALLEBZADEH[2], Özgür DUYGULU[3], Sezer ÖZERİNÇ[1]
[1]Middle East Technical University, [2]Koç University, [3]TÜBİTAK Marmara Research Center
Turkey

Abstract

This study investigates the solid solution strengthening effects in confined crystalline layers. For this purpose, we considered Cu-$Cu_{50}Nb_{50}$ and $Cu_{90}Nb_{10}$-$Cu_{50}Nb_{50}$ thin films with alternating amorphous-crystalline layers. The results show that the addition of a small amount of Nb to Cu layers increases the yield strength considerably. Decreasing the layer thickness provides further strengthening. Our findings demonstrate the effectiveness of alloying route at improving the strength of nanostructured metals.

1. Introduction

Nanolayered metals are structures composed of alternating layers of metals with layer thicknesses below 1 µm. The outstanding mechanical properties of these materials make them attractive for a wide range of structural applications [1]. However, most studies in the literature have so far focused on nanolayers composed of pure metals [2]. Industrial applications almost always require alloyed forms of metals, as alloying additions usually improve the mechanical properties and thermal stability. Therefore, there is a need to understand the mechanical behavior of alloyed nanolayers. This study aims to fill this gap in the literature by the experimental characterization of Cu-CuNb system.

2. Materials and Methods

We prepared Cu-$Cu_{50}Nb_{50}$ and $Cu_{90}Nb_{10}$-$Cu_{50}Nb_{50}$ nanolayered films using magnetron sputtering. Layer thickness varied in the range of 10-100 nm. X-Ray diffraction characterized the microstructure of the specimens and nanoindentation measurements probed the mechanical properties.

3. Results

In all samples, $Cu_{50}Nb_{50}$ layers are in amorphous form. On the other hand, both Cu and $Cu_{90}Nb_{10}$ layers are nanocrystalline. Figure 1 shows the nanoindentation hardness of layered samples and the monolithic counterparts. Hardness increases with decreasing layer thickness for both sets of samples. Alloying additions considerably improve the hardness, and the extent of this improvement decreases with decreasing layer thickness.

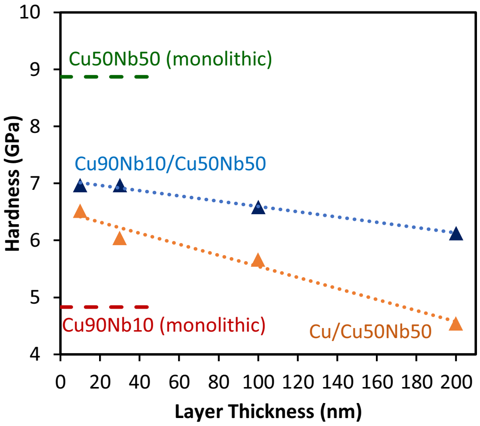

Figure 1. Variation of hardness with layer thickness for monolithic and nanolayered samples. All samples have a total thickness of 1 µm.

4. Conclusions

The results show that alloying is a powerful approach for improving the strength of nanolayered composites. Future studies will focus on the effect of different alloying additions and their size effects.

Acknowledgements

This research is supported by the Scientific and Technological Research Council of Turkey—CAREER Award #116M429 and METU-BAP Project #08-11-2016-072. We thank METU Central Laboratory, Koç University KUYTAM, and Bilkent University UNAM for their support in characterization measurements.

References

[[1] N.A. Mara, D. Bhattacharyya, P. Dickerson, R.G. Hoagland, A. Misra, Deformability of ultrahigh strength 5nm Cu/Nb nanolayered composites, Appl. Phys. Lett. 92 (2008) 231901. https://doi.org/10.1063/1.2938921.
[2] J. Wang, Q. Zhou, S. Shao, A. Misra, Strength and plasticity of nanolaminated materials, Mater. Res. Lett. 5 (2017) 1–19. https://doi.org/10.1080/21663831.2016.1225321.

20th
INTERNATIONAL
METALLURGY
MATERIALS
CONGRESS
10-12 June
2021
"in Digital Platform"

Mechanical Metallurgy

immc2021

Addressing Fundamental Problems in Metallurgy via First Principles Models: Point Defects, Surface Chemistry, and Initial Stages of Precipitation

S. Pamir ALPAY
University of Connecticut
USA

Abstract

Recent materials genomics or informatics initiatives seek to accelerate materials discovery through the use of computations across length and time scales, supported by judicious experimental work. Such efforts typically start at the atomistic level to describe fundamental phenomena related to electronic and/or atomic interactions. Here, we will examine three applications of first principles and ab initio thermodynamics based methods in understanding point defect stabilities and chemistry in Ti, surface structure of Ti in the presence of oxygen, hydrogen, and nitrogen, and the initial stages of Guinier-Preston zone formation in Al-Cu and Al-Ag alloys. In addition to these three classical metallurgical problems, we apply similar quantum mechanical tools to describe solid solution strengthening in Al alloys. We will show in this talk that a careful application of atomistic models can be an invaluable tool in customizing, or entirely replacing, existing metallic alloys, polymers, and ceramics which were developed based on trial-and-error approaches in the past century.

Simulation of the Friction Coeefficent Effect on Wire Drawing Proses

Sevim Gökçe ESEN[1], Zeynep Şeyma SERDAROĞLU[1], Osman ÇULHA[2]
[1]Çelik Halat ve Tel Sanayii A.Ş, [2]Manisa Celal Bayar University
Turkey

Abstract

Using of simulation solutions in manufacturing has become widespread in recent years. Use of simulation in steel industry has increased due to the advantages of parameter selection in production, time and cost saving in tests and experimental designs. In this study, friction coefficient used in simulation of wire drawing operation which is the process of cold plastic deformation and experimental studies in determining this the friction are given. The effects of the lubricant and phosphate coating used in the wire drawing process on the drawing force have been verified by matching them in the experimental studies and numerical simulation.

1. Introduction

Wire drawing; a piece of thick cross-section is passed through the drawing die, reduction process. Generally speaking, any material that may deform under the minimum conditions necessary for wire drawing may be subjected to the drawing process [1]. Circular cross-section wire is come across in the areas of conductor wires, musical instruments and packaging industry, especially steel industry and welding industry. A rod of steel is pulled through a hole in a forming tool that has a smaller diameter than the rod [2,3]. The forming tool, which is called the wiredrawing die, is designed in such a way that the rod is not 'shaved' but is plastically deformed such that its diameter is reduced to the same diameter as the hole in the die without any metal being removed [4,5]. There are multiple parameters that control the effectiveness of wire drawing. Friction is a critical factor that directly affects the pulling force, mechanical properties, and the temperature formed during deformation. Lubricant (dry or liquid) and surface coating (phosphate and borax) is used in order to make controlled wire drawing by reducing the friction between the die and the wire. The lubricant used facilitates wire drawing, prevents the temperature from rising and can prevent damage called chevron cracks.

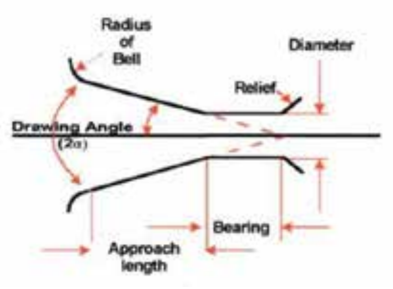

Figure 1. Schematic view of wiredrawing die

Numerical simulation methods are widely used today in industrial applications. Another area where simulation has been used recently is steel wire production. In this way, parameters affecting the wire drawing process and product performance can be predicted. In simulation of wire drawing process, friction coefficient information should be given to the program as well as known parameters such as process speed, die geometry, chemical composition of the wire rod and heat transmission coefficients. In this study, the effects of lubricants and surface coatings used in wire drawing on friction were investigated. Accordingly, the force curve obtained in the experiments carried out in the laboratory environment was simulated and the friction coefficient corresponding to the force was determined.

2. Experimental Procedure

An experimental study has been programmed on the tensile test in order to express the wire drawing process numerically and to determine the force formed between the wire and the die. Accordingly, a die was placed on the immobile jaw of the Zwick Roell Z250 tensile test and wire drawing was performed with the mobile side.

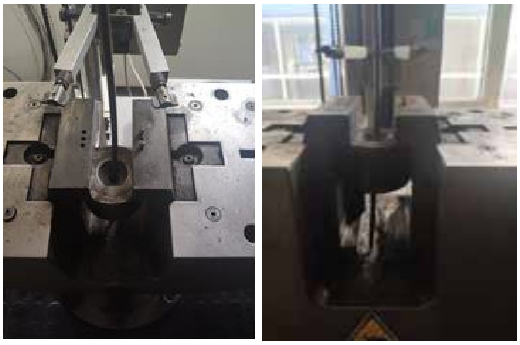

Figure 2. Experimental setup for determination of tensile force in laboratory conditions

In the study, 5.50 mm wire rod with 0.45% carbon content was reduced to 4.77 mm diameter for wire drawing (reduction: 24.78%). In the wire drawing process carried out in the tensile tester, the machine speed was chosen as 0.006 m/s. In the experimental work set up to determine the friction effect, wire drawing was performed in different surface (phosphate and phosphate-borax) and lubricant (dry, liquid and non-lubricant) conditions. The force values obtained in the tensile test according to the type of surface and lubricant as a result of the experimental studies are given in Table 1. However, an example of the force-displacement curve obtained as a result of the drawing process is shown in Figure 3.

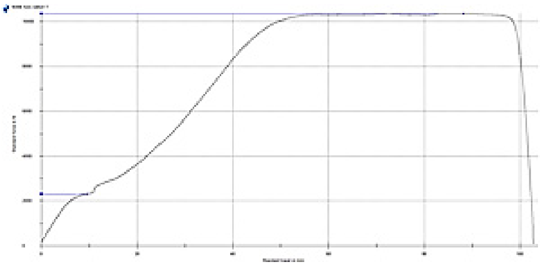

Figure 3. The force - displacement curve obtained in the experimental application performed by the tensile test

Thus, the friction coefficient on which the tensile force generated between the wire and the die will be obtained is determined on the simufact forming software.

Table 1. Experimental working conditions

Surface Conditions	Type of Lubricant	Force (kN)
Phosphated	No Lubrication	10.93
Phosphated	Dry Lubricant	9.89
Phosphated	Liquid Lubricant	10.40
Phosphated + Borax	No Lubrication	9.65
Phosphated + Borax	Dry Lubricant	9.83
Phosphated + Borax	Liquid Lubricant	10.08

The area under the immobile jaw of the tensile testing machine is 10 cm, this distance was taken into account as the displacement length in the wire drawing trial. In the process simulation, a hydraulic press that defines the wire with a speed of 0.006 m/s was described. Heat parameters used in process simulation are given in Table 2 for die and wire. All of the variable parameters required for simulation were selected to reflect the tensile test and the effect of the friction coefficient was examined.

Table 3. Heat parameters used in simulation

	Initial Die Temperature (^{0}C)	Heat Transfer Coefficient Environment W/(m^2.K)	Heat Transfer Coefficient to Workpiece W/(m^2.K)
Die	20	50	20000
Wire Rod	20	50	-

WC-Co drawing die used was defined as non-deformable but heat conducting die and 2D drawing was shown in Figure 4. Carbide dimensions for the selected die were selected as specified in ISO 1684 standards.

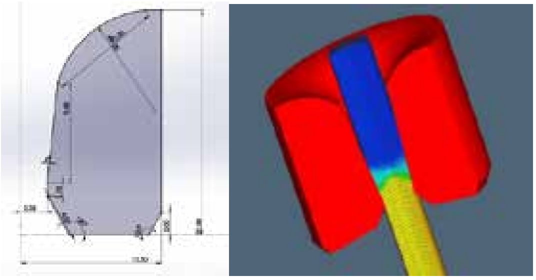

Figure 4. 2D technical drawing of 4.77 mm drawing die

3. Results and Discussion

Different friction coefficients were tested in the simulation to provide the force values obtained as a result of the wire drawing process performed using a tensile testing machine. In addition to entering different friction coefficients to achieve the pulling force obtained in experimental studies, the effect of friction effect on shaping and mechanical properties was also investigated. Simulation images of different friction coefficient values are shown in Figure 5.

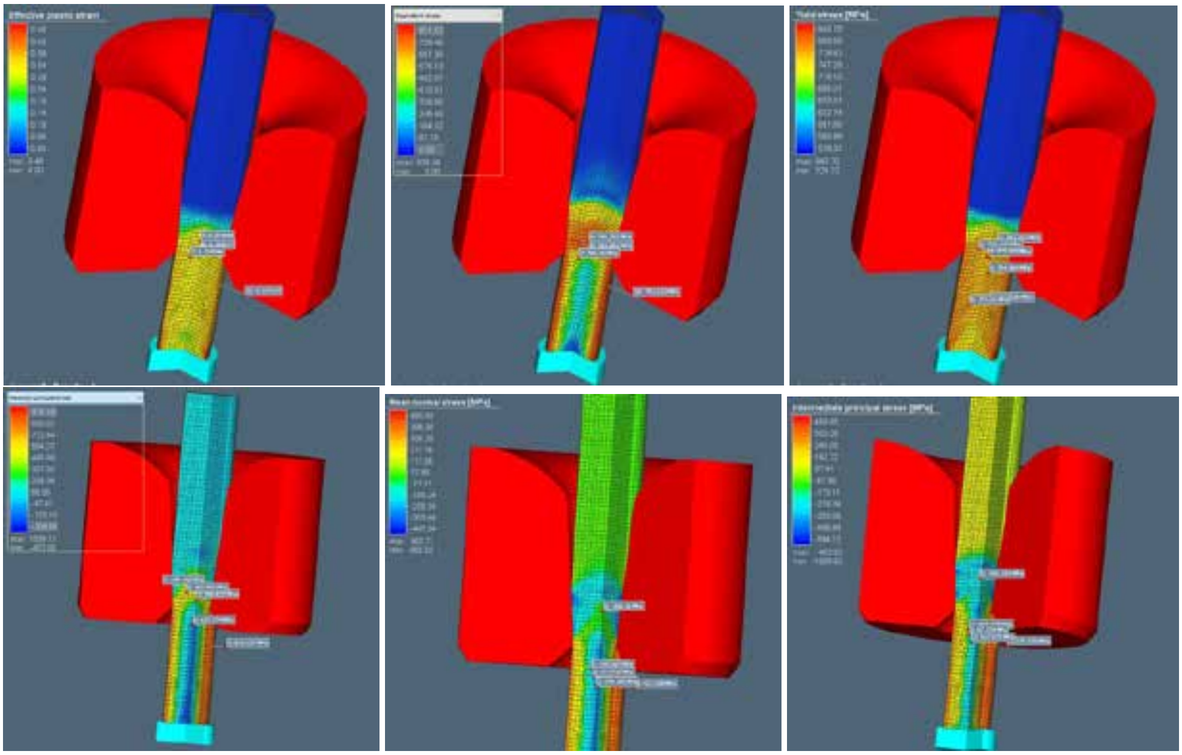

Figure 5. Mechanical results obtained by simulation of different friction environments

Friction environments and Coulomb friction coefficients providing the forces obtained by the tensile test are given in the Table 4. The force graph obtained in the simulation used is shown in Figure 6. Symmetrically visible values in the red and blue colors on the graph result from the vector representation of the force value for the die and wire.

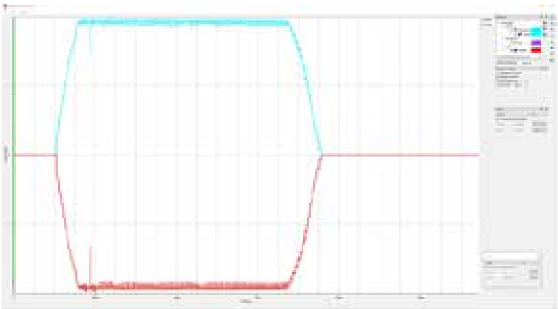

Figure 6. Change in force due to displacement when the Coulomb friction coefficient is 0.30

Table 4. Coulomb friction coefficients found by simulation

Surface Conditions	Type of Lubricant	Force (kN)	Coulomb Friction Coefficient
Phosphated	No Lubrication	10.93	0.30
Phosphated	Dry Lubricant	9.89	0.24
Phosphated	Liquid Lubricant	10.40	0.28
Phosphated + Borax	No Lubrication	9.65	0.20
Phosphated + Borax	Dry Lubricant	9.83	0.23
Phosphated + Borax	Liquid Lubricant	10.08	0.26

The change of the mechanical properties obtained in the simulation according to the friction coefficient is given in Table 5. When the plastic strain and yield stress values are controlled, the friction coefficient increases and the outer surface strength increases in the material (Figure 7). It is seen that the stress on the wire surface in contact with the die does not match the stress value on the wire center.

Although the tension and temperature formed in the wire surface and center are different, the increase between the coefficient of friction and the mechanical properties of the wire is clearly visible.

Table 5. Friction coefficient and wire properties relationship according to simulation

Coulomb Friction Coefficient	Effective Plastic Strain (MPa)	Equivalent Stress (MPa)	Friction Stress (MPa)
0.30	0.36	804.306	190.866
0.24	0.34	796.270	157.615
0.28	0.35	799.306	184.239
0.20	0.28	784.331	100.248
0.23	0.32	790.364	149.563
0.26	0.34	797.425	164.254

In the simulated process, it starts to contact with the die angle of 5.50 mm wire rod and reach its final diameter in the region called bearing zone. Contact between the die and the wire causes stress, temperature and property changes on the wire surface.

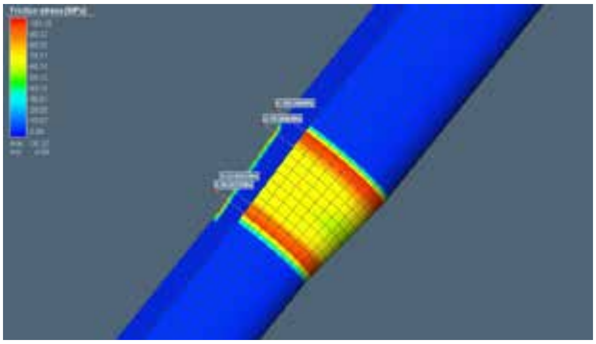

Figure 7. Stress on the wire surface during contact with the die

4. Conclusions

Tension caused by surface contact and pressure occurs between the drawing die and wire rod used in wire drawing. In order to control the tension caused by the contact between the wire surface and the die, the coating and the lubricant are used in the process. Within the scope of this study, it is aimed to determine the friction coefficient formed between the drawing die and the wire rod used in wire drawing in different surface coatings and lubrication conditions. Experimental study was carried out under tensile test conditions for a numerically expressed wire drawing process. Verification of the forces obtained as a result of the tensile test performed in the simulation program. Different friction conditions were tried to obtain the same force / displacement values. Therefore, all parameters except the friction coefficient were selected as fixed according to the tensile test in the simulation. As a result of simulations, friction coefficient values were determined with respect to coating and lubrication. The friction coefficient values obtained as a result of the experiment were found to be very high and did not reflect the wire drawing process carried out under mass production conditions. Because the force curves were performed on a tensile testing machine at a limited displacement and at the speed reported in the TS EN ISO 6892-1 standard. During the wire drawing process performed under these conditions, the die didn't heat up and the lubricant activated temperatures could not be obtained. In the processes defined for simulation, the only variable affecting the force is considered to be the friction coefficient. Studies on determination of friction coefficient values in mass production conditions are continuing within the scope of the project.

Acknowledgment

The authors would like to thank Çelik Halat ve Tel Sanayii A.Ş for opening up all its possibilities for experimental studies and the creation of process conditions. All of the design and experimental studies carried out within the scope of this study were financially supported by TÜBİTAK with project number TEYDEB 3190515.

References

[1] Ünseren M., Tel çekme matrisleri üzerine bir araştırma, Süleyman Demirel Universty, Master tesis, 2006.

[2] Chaudhary A., Kumar R., Aneja A., Rectification of Problem in Wire Drawing By Lean Way, International journal of emerging technology and advanced engineering, vol. 4, Issue1, 2014

[3] Rubio E.M., Camacho A. M., Sevilla L., Sebastian M. A., Calculation of the forward tension in drawing processes, Journal of materials processing technology, 162-163, 2005.

[4] Shemenski, R. M., M. A. Foster, and J. Walters. "Finite Element Analysis of Die Geometry for Drawing Steel Wire," Conference Proceedings, 74th Wire & Cable Technical Symposium, pp. 42–55, Cleveland, Ohio, The Wire Association International, Inc., Guilford, Connecticut, 2002.

[5] Wright, R. N. Workability in Extrusion and Wire Drawing, in Workability Testing Techniques, ed. G. E. Dieter, p. 255, ASM International, Materials Park, Ohio, 1984.

Effect of Manganese and Titanium and Heat Treatment on Microstructure and Friction Behavior of Hadfield Steel

Ugur GUROL[1], Ozan COBAN[2,3], Suleyman Can KURNAZ[1]
[1]Sakarya University, [2]İstanbul Gedik University, [3]İstanbul Technical University
Turkey

Abstract

In this study, the effect of manganese and titanium addition along with the effect of heat treatment on the microstructure, wear resistance and other mechanical properties of Hadfield steels were investigated. The results indicated that increasing Mn content led an increase in wear resistance. In addition, while solution annealing reduced the wear resistance in titanium-free alloys, the wear resistance increased significantly with heat treatment in titanium-containing alloys. Moreover, 0.05% Ti addition in solution annealed alloys increased the wear resistance 21.6% at low friction loads and 36.8% at high friction loads. However, increased Ti content from 0.05 % to 0.10 decreased the wear resistance at high friction loads due to Ti(CN) segregation. These results showed that optimized Ti content provided superior wear resistance alloys operating under high friction load conditions.

1. Introduction

Hadfield steels are most commonly used as wear materials due to their excellent wear resistance [1]. This steel with small changes in its chemical composition or heat treatment, is widely used in various fields of industry such as in mining, earthmoving, quarrying, oil-well drilling, steel-making, cement clay products, rail-roading, dredging, naval, lumbering excavators and crushers [2-4]. Therefore, optimization of ultimate tensile, impact toughness and wear resistance of the high manganese steel is a key factor to increase the service life of critical engineering components.

2. Experimental Study

An industrial-scale induction furnace with a maximum capacity of 3000 kg was used to manufacture the specimens. Chemical analysis was performed by the ARL optical emission spectrometer according to the ASTM E2209 standard. Heat treatments were performed at 1100^0C with 3 hours duration and by quenching in water. Optical microscope and a scanning electron microscope equipped with energy disperse spectrometry were used on microstructural characterization. The ball-on-disc wear test was carried out at room temperature with a 10 mm diameter alumina ball as the counter body. The weight loss of each sample was measured under 2.5N, 5N, 10N and 15N normal loads at 0.2 ms^{-1} sliding speed with 500 m sliding distance.

3. Conclusions

The solution annealing heat treatment was able to dissolve all carbides into austenite matris. This process increased the wear rate in Ti-free alloys while it slightly decreased the wear rate in Ti-containing alloys. Increase on Mn content increased the wear resistance, however, the 21% Mn addition led to decrease in ultimate tensile, elongation and impact toughness properties. 0.05% Ti addition with solution annealing provided an increase in tensile strength of 7%, elongation of 9% and decrease in impact toughness of 22%. This also led an increase in the wear resistance of 21.6% at low friction loads and 36.8% at high friction loads. Increasing the Ti content from 0.05% to 0.10% decreased ultimate tensile, elongation and also wear resistance at high friction loads due to segregation of Ti(CN) particles instead of homogeneous dispersion. Consequently, it can be impressed that optimized 0.05% titanium added Hadfield steels show superior performance under high wear load conditions.

4. References

[1] R. Dalai et al., Effect of thermo-mechanical processing on the low impact abrasion and low stress sliding wear resistance of austenitic high manganese steels, Wear, 420–421 (2019) 176–183.
[2] B. Bal, A study of different microstructural effects on the strain hardening behavior of Hadfield steel, Int. J. Steel Struct., 18 (1) (2018) 13-23.
[3] N. D. Nam et al., Investigation of phase transformation mechanism of high manganese steel Mn15Cr2 heat-treated by subzero temperature process, Int. J. Sci. Eng. Res., 7 (4) (2016) 1527-1530.
[4] A. K. Srivastava, K. Das, Microstructural characterization of Hadfield austenitic manganese steel, J. Mater. Sci., 43 (2008) 5654–5658

Determination of Die Geometry Effect on Mechanical Properties of Wire by Numerical Simulation Method

Sevim Gökçe ESEN[1], Osman ÇULHA[2]
[1]Çelik Halat ve Tel Sanayii A.Ş, [2]Manisa Celal Bayar University
Turkey

Abstract

Among the parameters that control the effectiveness of wire drawing, the most critical one is the geometry of the drawing die. While the die geometry determines the wire diameter and reduction ratio, it also controls the steps such as friction, heat, processing speed and drawing force between the wire and the die. In this paper, the effect of change of die angle and bearing length on the wire properties is analyzed by simulation. The simulation made in this paper shows that drawing forces are strongly influenced by variation of certain process parameter such as die angle.

1. Introduction

Wire drawing is a metalworking process used to reduce the cross-section of a wire by pulling the wire through a single, or series of, drawing die(s) [1]. There are more than one effective parameter in the production of high carbon steel wires used in safety and high strength applications, especially steel wire ropes, spring wires and prestressed concrete strands. A wire rod of steel is pulled through a hole in a forming tool that has a smaller diameter than the rod [2,3]. The forming tool, which is called the wire drawing die, is designed in such a way that the wire rod is not 'shaved' but is plastically deformed such that its diameter is reduced to the same diameter as the hole in the die without any metal being removed [4,5]. The most important factor in wire drawing is die geometry. The sectional view and zones of the wire drawing die are shown in Figure 1. The approach angle from the drawing die sections is important to ensure lubricant flow. With the movement of the wire, the lubricant used in the process is directed towards the die angle and the friction force is reduced. It is critical in the wire drawing process for die angle, lubricant applying on the surface of the wire, and obtaining the final diameter and properties [5]. The selection of the die angle to be used varies depending on the reduction. The die angle is critical for spreading the deformation on the wire surface to an extensive area, not the point, the friction force and the distribution of stresses. Another critical region is the die section called the bearing zone. In here, the wire reaches the final diameter and uniform surface distribution. Dimensions are selected according to the diameter of the drawing die to increase the service life by extending the die wear period.

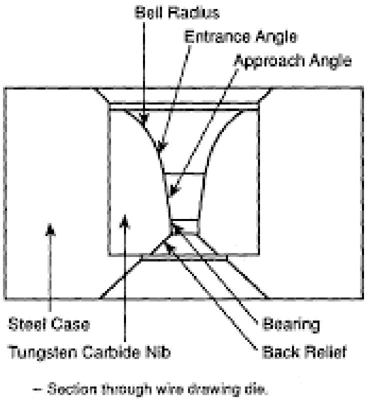

Figure 1. Technical view of wiredrawing die

The most ideal method to examine the effects of the dies used in wire drawing on the wire properties and the process is numerical simulation methods. In this way, appropriate die and drawing process design will be made without high trial costs. In this study, the effects of the bearing zone and die angle variables affecting wire drawing on wire properties were investigated. By investigating the effects of different die angle and bearing dimensions on the wire, it is aimed to determine the appropriate die geometry for the known wire. Thus, the effects of drawing die geometry on the product can be expressed numerically in the given wire drawing processes.

2. Experimental Procedure

All of the experimental studies consist of simulation of the drawing die and wire rod properties used in wire drawing with ideal wire drawing process. The parameters defined for the simulation related to the wire drawing process were chosen to represent the actual production conditions of the wires. Steel with a diameter of 5.50 mm with 0.45% carbon composition specified as C45 in material data for drawing. The wire rod, which was 5.50 mm in the wire drawing defined in the simulation, underwent 24.78% reduction and turned into a diameter of 4.77 mm.

For the simulation of the wire drawing process, a hydraulic press providing a single direction movement with a speed of 1500 mm/s is defined. Wire rod with an initial length of 50 mm was moved at 70 mm displacement.

It is known that tension and temperature distribution, high importance in wire drawing. To express the temperature and friction controlling lubricant in the process, the Coulomb friction coefficient (μ) is defined as 0.15. The heat parameters between the die and the wire are given in Table 1.

Table 1. Heat parameters used in simulation

	Initial Die Temperature (^{o}C)	Heat Transfer Coefficient Environment W/(m^2.K)	Heat Transfer Coefficient to Workpiece W/(m^2.K)
Die	20	50	20000
Wire Rod	20	50	-

In the process of defining the die geometry, which is the purpose of the simulation and study, the drawing die 2D technical drawings were carried out with different die angle and bearing dimensions (Figure 2).

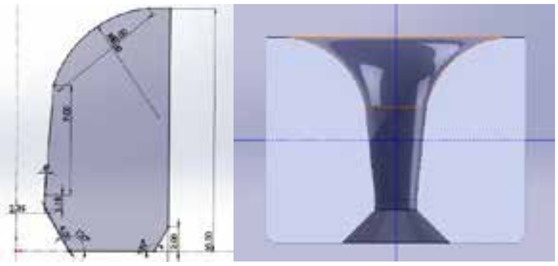

Figure 2. Technical drawing examples of die section

Selected angle and length dimensions are given in Table 2. Trial matrix with three different values, bearing length 15%, 25% and 40% of the diameter, die angle 8^{o}, 10^{o}, 12^{o} and 14^{o}.

Table 2. Trial matrix for die geometry analysis

	Die Angle (^{o})			
Bearing Length (%)	8	10	12	14
15	BL 15 D 8	BL 15 D 10	BL 15 D 12	BL 15 D 14
25	BL 25 D 8	BL 25 D 10	BL 25 D 12	BL 25 D 14
40	BL 40 D 8	BL 40 D 10	BL 40 D12	BL 40 D 14

Drawing die material WC-Co was selected and determined as a non-deformable but heat conducted die in simulation.

As a result of the simulation, the properties and process parameters of the product for each angle and bearing lengths were compared. Especially the stresses on central and surface of the wire, the temperature between the die and the wire, the friction force and the pressure are ideal criteria for die geometry selection.

3. Results and Discussion

Simulations were performed using different die geometries; all of the other process variables defined for the simulation were fixed. Simulations were carried out with different geometry dies according to the experimental matrix designed. Simulation images of effective plastic strain properties of matrices formed by 8 degree and 14 degree die angles are shown in Figure 3.

As a result of the experiments carried out, the tension values on the wire product have been controlled, as well as the contact pressure, friction and temperature values between the die and the work piece. The results representing the mechanical properties on wire of the simulated geometry matrices are shown in Table 3. According to the simulation results, the different die angle directly changes the shape and position of the contact point with the wire surface. Considering to the selected reduction ratio, ideal results in terms of contact area stress values and temperature values during contact were obtained in a 12 degrees die angle and 25% bearing length. If the die angle is chosen from smaller values, the wire and die starts to contact early and is exposed to deformation for a long time. The increase in the angle value, induce the contact time between the wire and the die are low but severe deformation occurs.

Table 3. Effects of die geometry change on wire drawing process and product

Properties	**BL15 D8**	**BL25 D8**	**BL40 D8**	**BL15 D10**	**BL25 D10**	**BL40 D10**	**BL15 D12**	**BL25 D12**	**BL40 D12**	**BL15 D14**	**BL25 D14**	**BL40 D14**
Effective plastic strain (MPa)	0.4715	0.4821	0.4743	0.4869	0.4801	0.4833	0.4978	0.4936	0.4902	0.5216	0.5092	0.4957
Equivalent stress (MPa)	814.40	805.62	799.54	823.42	810.09	801.06	842.45	816.30	790.74	836.24	816.49	767.43
Temperature (^{o}C)	133.90	129.89	132.88	137.68	136.27	137.36	135.54	134.64	134.67	142.37	144.37	149.10
Friction stress (MPa)	77.45	77.96	77.32	74.73	73.86	74.67	80.38	79.82	79.96	77.83	76.43	77.47
Contact pressure (MPa)	516.37	519.78	515.51	498.21	532.42	531.19	535.90	532.15	533.11	538.91	536.23	539.82

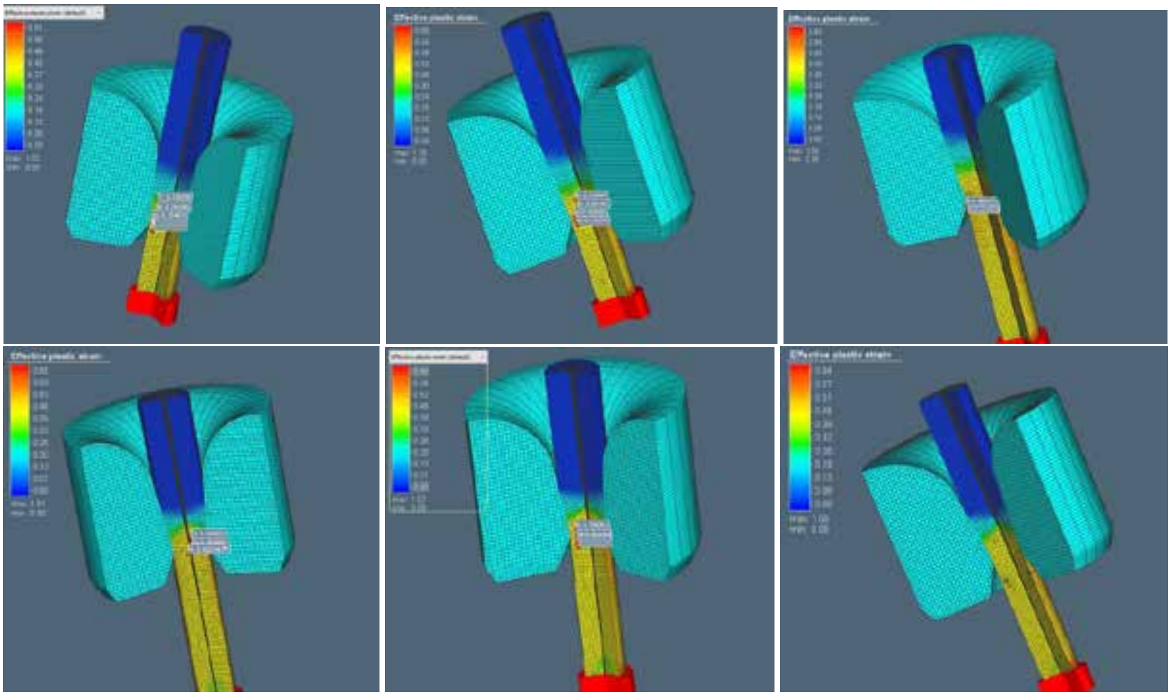

Figure 5. Effective plastic strain images of a) Bearing length 15%, die angle 8^{o} b) Bearing length 25%, die angle 8^{o} c) Bearing length 40%, die angle 8^{o} d) Bearing length 15%, die angle 14^{o} e) Bearing length 25%, die angle 14^{o} f) Bearing length 40%, die angle 14^{o}

In the simulation results, the visuals of the angle and bearing length effects in contact pressure type are shown in Figure 6. Figure 6a and 6b represent the simulation of two different angles with bearing lengths of 25%. It is understood that the contact length is long and the contact pressure is higher in the 8 degrees die angle. In the centre and on the outer surface of the wire are diverged due to temperature and contact pressure. The diameter reached in the die angle region is corrected at the bearing zone and the tension is distributed. The length of the bearing, which is larger than 15% of the diameter, has a positive effect in the way that the tension on the wire reduces the difference between the center and the surface.

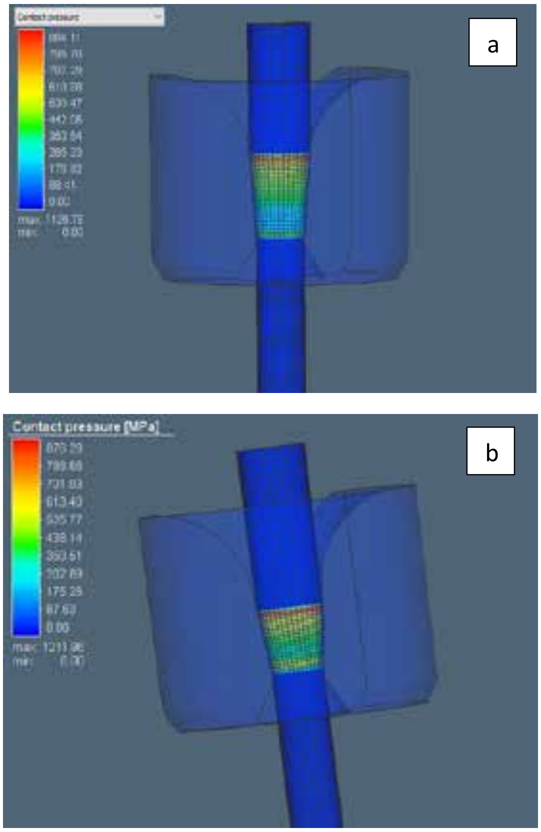

Figure 6. a) die angle 8º and bearing length 25% b) die angle 12º bearing length 25%

4. Conclusions

The effects of die angle and bearing lengths, which are important geometry factors on wire and wire drawing, were investigated. A wire rod of 5.50 mm 0.45% carbon composition was passed through a die and turned into a 4.77 mm wire. For the effects of die geometry, a simulation matrix of 8º,10º,12º and 14º die angles and 15%, 25% and 40% bearing lengths has been created. Ideal geometry is determined by analyzing the parameters such as stresses occurring at the center and surface of the wire obtained as a result of simulation, pressure and temperature at the contact point. In the simulations carried out, it was observed that the contact pressure and the contact surface were large for the die with a die angle of 8 degrees. At 14 degrees die angle, the contact surface is too short and causes an increase in contact pressure. It has been determined that the ideal die angle for the selected reduction ratio can be 10 and 12 degrees. Compared to bearing lengths at the same angle value, 15% and 40% lengths cause high strain difference in wire center and outside of die geometries. Compared with this respect, the wire drawing process carried out with a 12 degrees die angle and 25% bearing length for the selected starting and ending diameters gave the best results.

Acknowledgment

The authors would like to thank Çelik Halat ve Tel Sanayii A.Ş for opening up all its possibilities for experimental studies and the creation of process conditions. All of the design and experimental studies carried out within the scope of this study were financially supported by TÜBİTAK with project number TEYDEB 3190515.

References

[1] Muskalski Z., Wiewiorowska S., The Theoretical Analysis of Wire Drawing Process for Hydrodynamic Friction Conditions, Metallurgy and Mining Industry, 2011, Vol.3, No.74-78

[2] Rubio E.M., Camacho A. M., Sevilla L., Sebastian M. A., Calculation of the forward tension in drawing processes, Journal of materials processing technology, 162-163, 2005.

[3] Shemenski, R. M., M. A. Foster, and J. Walters. "Finite Element Analysis of Die Geometry for Drawing Steel Wire," Conference Proceedings, 74th Wire & Cable Technical Symposium, pp. 42–55, Cleveland, Ohio, The Wire Association International, Inc., Guilford, Connecticut, 2002.

[4] Jo H. H., Lee S. K., Kim M. A., Kim B. M., Pass schedule design system in the dry wire-drawing process of high carbon steel, Proceedings of the Institution of Mechanical Engineers Part B Journal of Engineering Manufacture, 2002, Vol 216, 365-373

[5] Muskalski Z., Selected problems from the high-carbon steel wire drawing theory and technology, Archives of Metallurgy and Materials, 2014, Vol.59, Issue 2, 527-535

20th
INTERNATIONAL
METALLURGY
MATERIALS
CONGRESS
10-12 June
2021
“in Digital Platform”

Advanced Alloys and Processes for Aerospace

immc2021

Mechanical Behavior and Failure Modes of Hybrid Jointed Lap Shear Joints

Tansu GÖYNÜK[1,2], Uğur Can UYSAL[1], Duygu KARAÇAL[1,2], Cengiz Kayahan ÖZLAV[1]
[1]Roketsan A.Ş., [2]Middle East Technical University
Turkey

Abstract

Blind rivet joint is a method to joint two components in the area where needs. Nowadays, rivet joint commonly used in aerospace industry due to the good clam-up, lightweight and providing better corrosion resistance. Highly concentrated load transfer at rivet points causes a very high stress concentration at these points. Therefore, by using an adhesive layer to the connection, these drawbacks were overcome in a hybrid joint [1,2]. EN AW6013 T6 aluminum alloy sheets with the thickness of 2mm riveted by 15-7 Ph stainless steel stem and 5056 aluminum alloy sleeve flush head rivets by applying epoxy and silicone adhesives between the joints. In the present work, the effect of number of rivets, array of the rivets, and test temperature on the mechanical performance of the joints was examined by tensile tests. Also to provide seal and load distribution, effect of applying adhesive between the joint layers was studied. Test matrices were created by using design of experiment techniques. In addition, a fractographic analysis was conducted to characterize the failure modes of the lap joints by using optical microscopy. Results of the tensile tests were confirmed by appropriate hand calculations. All results were analyzed by using Minitab program.

1. Introduction

Blind rivets are permanently installed fasteners. Nowadays, blind rivets provide a wide variety of benefits, such as speed of installation, versatility, simplicity and cost. Different from many other mechanical fasteners, blind rivets cannot be under-torqued, over-torqued or set loose. Blind rivets prevent these errors thanks to its unique design and function [3].

For joining, one of the most significant requirements is the joint strength. However, for aerospace applications stiffness, the damage tolerance and the weight of the joint should also be considered [4]. Adhesive bonding meet all of these requirements. If the adhesive bonding is used with riveting, a quicker and easier joint production will obtained. At the same time the joint will have higher damage tolerance and more uniform stress distrubution in combined joint techniques. The combination of rivet joining and adhesives is called hybrid joining. Hybrid joining combines the properties of two different joining techniques in order to obtain a joint with enhancing properties such as joint rigidity, sealing ability, alternating fatique strength etc. with respect to simple joints [5].

In aerospace applications, to obtain a lighter structure [6], and it is rather common to meet joints where a strong and stiff steel is coupled with a lighter aluminium.

2. Experimental Procedure

3 group of experiments were conducted to analyze the effect of number, array of the rivets, applying adhesive and test temperature on the mechanical properties of the joints. For hybrid joined specimens, before applying adhesive surface of aluminium sheets were cleaned with alcohol and then adhesives gently applied to the both side of the test sheets, the sheets were alligned with the help of the cleko and riveting was done with suitable rivet guns shown in the Figure 1.

Figure 1 Assembly of the hybrid joints

Geometry of the test specimens are shown in the Figure 2.

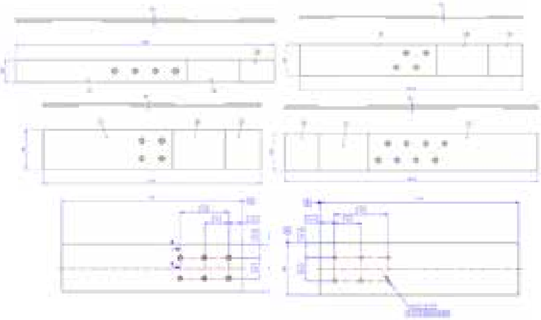

Figure 2 Geometry of the test specimens

Additional parts were added to the both ends of the sample where test specimens placed in the jaws of the test device with the help of glue to arange the axial load of the specimen. All tests were conducted with 5 mm/min strain rate with Instron 550R tensile test machine as seen in

Figure 3. For high temperature tests, specimens were conditioned for 20 minutes before the testing.

Figure 3 Sample placement on the test machine

Tests were grouped into 3 as shown in Table 1. Different set of parameters were tested in each group. Effect of test temperature and array of the rivets on the joint was studied in Group 1 tests. Group 2 tests showed how number of rivet and array of the rivets on joint influenced the mechanical properties of joints. Group 3 tests involved effect of adhesive application and test temperature on lap joints.

Table 1 Test Groups Constants and Parameters

	Constants	Parameters
Group 1	Rivet diameter (4mm)	Test Temperature (25°C and 120°C)
	Number of rivet at joint (4)	Array of rivets (single column, zigzaged)
	No adhesive	
Group 2	Rivet diameter (3,2mm)	Number of rivet at joint (4,6)
	No adhesive	Array of rivets (single column,double column, zigzaged)
	Test Temperature (25 °C)	
Group 3	Array of rivets (zigzaged)	Adhesive application (epocast, loctite, no adhesive)
	Rivet diameter (4mm)	Test Temperature (25°C and 150°C)
	Number of rivet at joint (8)	

3. Results and Discussion

Before testing of hybrid jointed specimens, Aluminum 6013 T6 materials tensile tests were done according to ASTM E8M. Adhesively bonded lap shear tests without riveting were conducted according to ASTM D1002 for epoxy and silicone adhesives without riveting. Test results and specimen photos after tests were showed in the Table 2 and Figure 4.

Table 2 Raw Material and Lap joint Tests of Adhesives

Materials	Max. Load @25°C (kN)	Max. Load @120°C (kN)
EN AW 6013 T6	3,92	3,77
Lap shear tests of epoxy adhesive	6,28	5,75
Lap shear tests of silicone adhesive	0,65	0,50

Figure 4 Raw material and adhesive lap joints test specimens after tensile tests

3.1. Group 1 Tests

According to tensile testing, Group 1 test results are tabulated in the Table 3. Tabulated results are the average of the three times repeated tensile test data. Single rivet's strength in the catalogue is 3,18 kN for 4 mm rivet. Average of load per rivet was lower than the room temperature test results and it was well accord with the test results which were conducted at 120 °C. There was a test error for the load per rivet results however, maximum load results were reasonable.

Table 3 Group 1 Test Results

Rivet Array	Test Temperature (°C)	Max. Load(kN)	Load per Rivet(kN)	Failure Type
Zigzaged	25	14,32	2,38	Rivet
Single Column	25	13,56	2,26	Rivet
Zigzaged	120	14,24	3,50	Rivet
Single Column	120	12,53	3,10	Rivet

Failure type of Group 1 tests was all rivet based fracture. Optical and scanning electron microscopy images of the fractured rivet were given in the Figure 5. Scanning electron microscope fractography for failure analysis showed a ductile fracture with fibrous appearance. Also from optical microscope image, formation of cup and cone type fracture view where maximum shear stress reached, was an another evidence for ductile fracture.

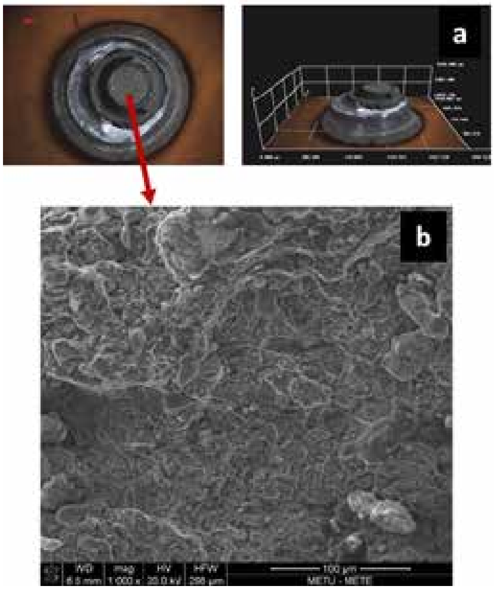

Figure 5 a. Optical microscopy image of fractured rivet surface **b.** Scanning electron microscopy image of fractured rivet surface

To understand the effect of test temperature and array of the rivets on maximum load, interaction plot of them was drawn in Minitab and showed in the Figure 6. As it can be seen from the interaction plot, zigzaged array of riveted joints with 4 rivets had higher strength than single column arangement of them. Also, with increasing test temperature from room temperature to 120°C, maximum load of the joints decreased.

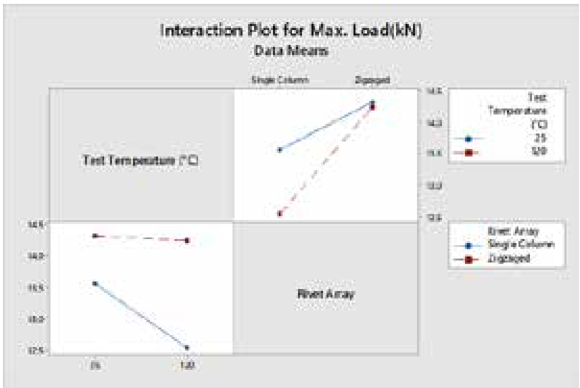

Figure 6. Interaction plot for maximum load of joints

3.2. Group 2 Tests

Group 2 tests were conducted to analyze the effect of array of the rivets which are double column, single column and zigzaged configurations and number of rivet on the mechanical property of the joint. Table 4 consists the result of the Group 2 tests. Single rivet strength on the catalogue is 2.36 kN for 3,2 mm diameter rivet, and average load per rivet was proper with catalogue value.

Table 4 Group 2 Test Results

Rivet Array	Rivet Number	Max.Load(kN)	Load per Rivet(kN)	Failure Type
Double Column	6	14,47	2,40	Rivet
Single Column	6	14,62	2,42	Rivet
Single Column	4	9,85	2,40	Rivet
Zigzaged	4	9,86	2,46	Rivet
Zigzaged	6	14,89	2,46	Rivet
Double Column	4	9,70	2,40	Rivet

All test specimens were failed from the rivets as it can be seen from the Figure 7 which includes optical and scanning electron microscopy of the fractured surfaces of rivets. According to fractured surface of 15-7 Ph stainless steel stem material showed ductile fractured surface with apparent dimples.

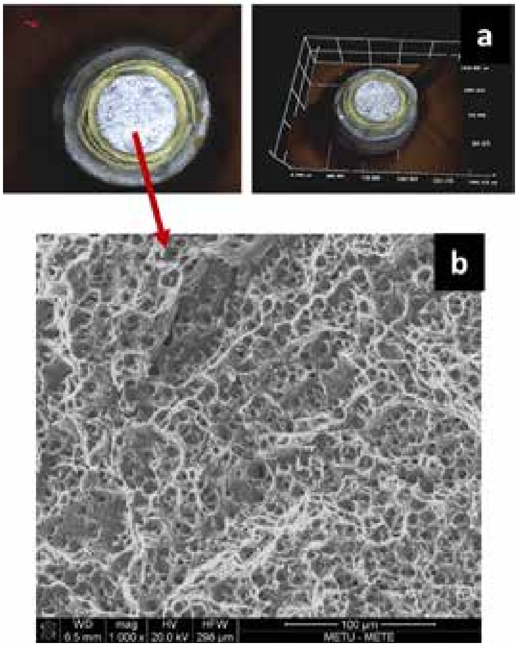

Figure 7 a. Optical microscopy image of fractured rivet surface **b.** Scanning electron microscopy image of fractured rivet surface

Interaction plot for the Group 2 test was shown in the Figure 8. From this graph, differences between test results with respect to different rivet array and rivet number can be seen. Array of the rivets was almost no effect on the mechanical properties whatever the rivet number of the joints for Group 2 tests. Rivet array was seen an important parameter for Group 1 tests however for small diameter rivet this was not effective. Also, with increasing rivet number maximum load for the joints increased.

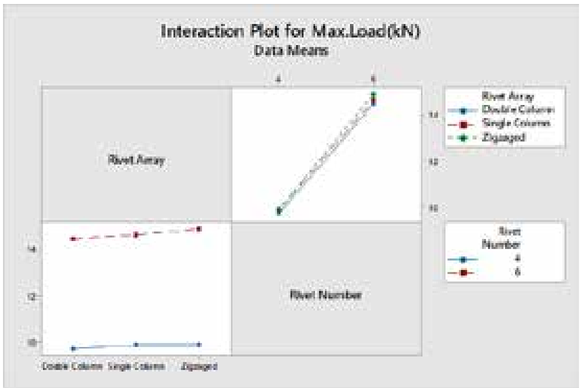

Figure 8. Interaction plot for maximum load of the joints

3.3. Group 3 Tests

Group 3 test results were tabulated in the Table 5. Single rivet's strength in the catalogue is 3,18 kN for 4mm diameter rivets. This is the exact data for lap joints without adhesive application. However, when adhesive applied to the surface of the joints, this value together with maximum load was increased. As expected, adhesive application increased overall strength of joint and distributed the load effectively.

Table 5 Group 3 Test Results

Test Temperature (°C)	Adhesive Application	Max. Load(kN)	Load per Rivet(kN)	Fail Type
25	No Adhesive	25,83	3,20	Metal Sheet
150	No aAdhesive	23,97	3,00	Metal Sheet
150	Epoxy Adhesive	23,56	2,94	Metal Sheet
25	Epoxy Adhesive	27,76	3,40	Metal Sheet
25	Silicone Adhesive	25,53	3,19	Metal Sheet
150	Silicone Adhesive	24,23	3,00	Metal Sheet

All the joints were failured from the metal sheet for Group 3 tests. Rivets maintained its unity without any damage. Optical microscopy and scanning electron microscopy images of the fractured aluminum surface and test specimens after the tensile testing were shown in the Figure 9. Ductile fracture was observed for Aluminum 6013 sheet material in the SEM image.

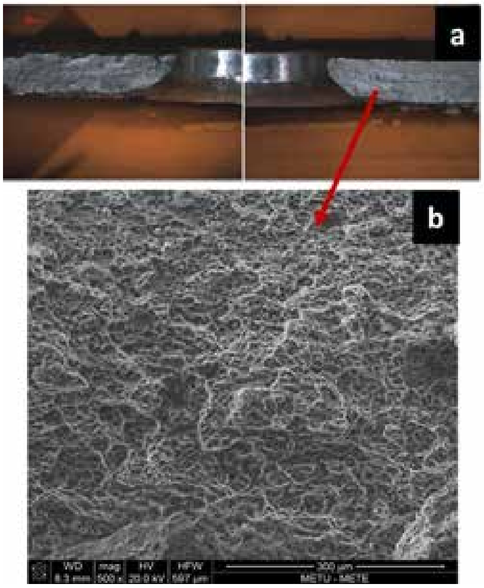

Figure 9 a. Optical microscopy image of fractured metal sheet surface **b.** Scanning electron microscopy image of fractured rivet surface

To see the effect of the adhesive application and test temperature on the tensile strength of the joints, interaction plot for maximum load was shown in the Figure 10. Epoxy based adhesive increased the maximum load of the specimens at room temperature, however this adhesive was the most affected by the increasing temperature. Silicone based adhesive application had almost no effect on the strength of the joints. In addition, with increasing test temperature, maximum load of both joints decreased.

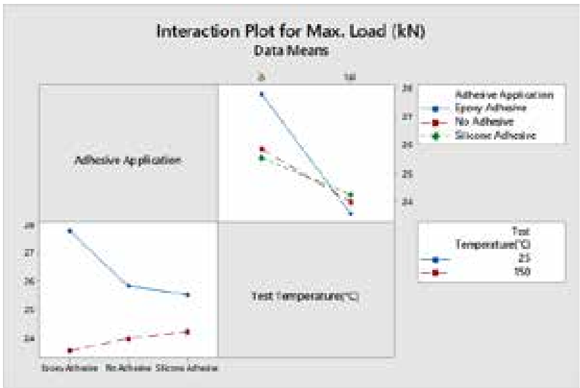

Figure 10. Interaction plot for maximum load of the joints

4. Conclusion

The physical response of the single lap joints of riveted test specimens subjected to tensile test was studied for different number and array of the rivets, adhesive application and test temperature.

Group 1 Tests

- Failure observed in rivets.
- The strength of the joint was decreased with increasing test temperature and single column arrangement of the rivets.
- Effect of test temperature was not much pronounced for Group 1 tests because of lack of adhesives between the joints.
- Fracture surface of the rivet was ductile fracture.

Group 2 Tests

- Failure observed in rivets.
- The strength of the joint was increased with increasing number of rivets of the joints and rivet array for this group of tests was insignificant.
- Fracture surface of the rivet was ductile fracture with dimples.

Group 3 Tests

- Failure observed from aluminum metal sheet.
- The strength of the joint was increased by using epoxy based adhesives and decreasing test temperature as expected. Test temperature was very effective on the epoxy based adhesive.
- Test temperature was much more pronounced for Group 3 tests because temperature decreased adhesive’s strength more seriously.
- Fracture surface of the rivet was ductile fracture with fibrous apperance.

Ultimately, increasing rivet number and rivet diameter, decreasing temperature, using a strong adhesives like epoxy based adhesives, decreasing temperature and using a zigzaged rivet array increased the joint strength. Additionally, applying an adhesive between the joints provided load distribution, impermeability and tightness.

References

[1] Y.B. Wang and G.K. Zhang, Aircraft assembly technology. Beijing, China: National Defense Industry Press, 1990.

[2] F. Moroni, A. Pirondi, Technology of Rivet: Adhesive Joints, Adv Struct Mater (2011) 6: 79–108, DOI: 10.1007/8611_2010_37

[3] C. Lei, Y. Bi, J. Li and Y. Ke, Effect of riveting parameters on the quality of riveted aircraft structures with slug rivet, Advances in Mechanical Engineering 2017, Vol. 9(11) 1–12

[4] C-P. Fung and J. Smart, An experimental and numerical analysis of riveted single lap joints, Proc Instn Mech Engrs Vol 208

[5] T. Balawender, T. Sadowskı, M. Knec, Technologıcal Problems And Experımental Investıgatıon Of Hybrıd: Clınched – Adhesıvely Bonded Joınt, Archıves Of Metallurgy And Materıals, Vol. 56, Issue 2, 2011

[6] N. Senguttuvan, J.Lillymercy, Joint Strength Analysis of Single Lap Joint In Glass Fiber Composite Material, International Journal of Applied Engineering Research ISSN 0973-4562 Volume 10, Number 7 (2015) pp. 16535-1654

Effect of Heat Treatment on Microstructure and Mechanical Properties of Additively Manufactured 18Ni300 Maraging Steels

İbrahim AYDIN[1], Aydın YAĞMUR[2], Süha TİRKEŞ[1], C. Hakan GÜR[1]
[1]Middle East Technical University, [2]EOS GmbH Electro Optical Systems
[1]Turkey, [2]Germany

Abstract

Recently, additive manufacturing of maraging steels has gained importance as an alternative to the traditional manufacturing techniques for aerospace components. In this study, various procedures were conducted to find optimum homogenization and aging treatment parameters for 18Ni300 parts that were additively manufactured via Selective Laser Melting (SLM).

1. Introduction

Production of engineering components having superior mechanical properties and high dimensional stability is very important, especially in aerospace and aircraft industries. Additive manufacturing (AM) has many advantages compared to traditional methods in terms of physical and mechanical properties; in some cases, also cost. Many studies related to the optimization of AM parameters and heat treatments have been done in AM of complex-shaped engineering components with desired properties. Due to the different microstructural features of the additively manufactured parts, optimization of heat treatment processes becomes a critical issue.

2. Materials and Methods

The specimens were additively manufactured from the gas atomized powder of 18Ni300 maraging steel via the SLM technique with 40 µm layer thickness, 250 W laser power, 150 mm/s laser speed and hatch distance of 0.1 mm. The production parameters and building direction were kept constant to minimize their effects on mechanical properties. N_2(g) was used in order to prohibit the oxidation of alloy elements during production. A series of heat treatments, including solution treatment, direct aging and solution + aging treatments have been conducted on the specimens. The specimens were aged at 490°C for different times to obtain the optimum aging time to achieve the desired microstructure and mechanical properties. All heat-treated specimens were quenched in air. The microstructure, micro-hardness and tensile properties were investigated.

3. Conclusions

(1) The parts manufactured by SLM have fine cellular structure and coarse grains. After aging treatment, the grain boundaries of the lath martensite become very blurry, and Ni, Mo and Ti dissolved in the matrix by forming tiny Ni_3Mo, Fe_2Mo and Ni_3Ti particles. Moreover, after solution treatment, the reverse transformation of martensite to austenite takes place and cellular structure disappears.
(2) Due to the disappearance of the cellular structure and the formation of precipitates, the mechanical properties change significantly with the heat treatment parameters. The hardness drops from 370 HV to 323 HV after solution treatment, whereas it rises to 614 HV after aging. The ultimate tensile strength drops from 1206 MPa to 920 MPa after solution treatment, whereas it increases significantly up to 2168 MPa after aging.

Acknowledgement: The authors gratefully appreciate to sample support from the EOS, Germany.

References

[1] ASM International, “Classification and Designation of Carbon and Low-Alloy Steels,” ASM Handbook, Vol. 1 Prop. Sel. Irons, Steels, High-Performance Alloy., vol. 1, no. c, pp. 140–149, 1990.

[2] E. Yasa, K. Kempen, J. P. Kruth, L. Thijs, and H. J. Van, “Microstructure and mechanical properties of maraging steel 300 after selective laser melting,” in *21st Annual International Solid Freeform Fabrication Symposium - An Additive Manufacturing Conference, SFF 2010*, 2010, pp. 383–396.

Advanced Braze Repair of Nickel Base Superalloys for Gas Turbine Applications

Kazım ÖZBAYSAL
Siemens Energy Inc
USA

ABSTRACT

Advanced gas turbine engines are subjected to high loads, high temperatures and extreme environments. During engine operation, the most severe damage occurs on the hot section components of the gas turbine. These components are made from advanced nickel and cobalt base superalloys. The high cost of manufacturing these components necessitates many of them to be repaired and put back into the service. Therefore, development of advanced repair materials as well as new repair processes that would provide near base material properties is required. This paper summarizes development of Nickel-Chromium-Titanium near ternary eutectic braze alloy which provides near base metal properties when used on advanced nickel base superalloy joining and braze repair. Metallurgical structure of the repaired gas turbine blades and vanes as well as the mechanical properties show that this new braze material is capable of supplying creep, low cycle fatigue, hold time fatigue and tensile properties that are equivalent to base metal properties.

1. INTRODUCTION

Gas turbine engines contain some of the most advanced materials and processing methods available to metallurgists. In a gas turbine, compressor section of the engine is made from the forged materials. In the case of aero gas turbines, fan and compressor materials include titanium alloys for specific strength as well as aluminum and polymer-based materials and/or composite materials. Land based gas turbines compressor materials are mostly forged stainless steel since they do not have a weight issue. The compressor section blades are generally under HCF loading.

Combustion section materials are usually cast nickel and cobalt base material. They are usually coated with a MCrAlY bond coat and TBC for high temperature exposure. Most expensive and complex components of the gas turbines are turbine blade and vanes. Blades are made of nickel base super alloys and vanes are made of cobalt or nickel base alloys. Turbine blades and vanes are exposed to high temperature and therefore they are under creep and thermomechanical fatigue loading. A representative Siemens Energy Inc. 8000H advanced gas turbine engine is shown in Figure 1.

Due to different deformation mechanisms and loading acting on the turbine blades (creep and thermomechanical loading) versus (slip and HCF) on the compressor blades, turbine blades are made from cast materials with large grain size. Advanced gas turbine stage one blades are made of directionally solidified or single crystal material to increase creep rupture capability. Vanes do not experience the heavy cyclic or creep loads as blades; therefore, most are made of equiaxed cast nickel or cobalt base materials. High γ' Ni_3(Al, Ti) nickel base superalloys alloys are used in the most advanced gas turbine hot sections. Because of their high manufacturing cost, turbine blade and vane repair is critical to any industrial or aero gas turbine engine business [1].

Advanced gas turbine engine stage one and stage two turbine blades and vanes are coated with an oxidation resistant MCrAlY bond coat and a TBC [2]. Both components have complicated cooling hole designs to lower the temperature of the blade and to benefit from the TBC coating. Because of exposure to high temperature, these components are damaged during operation and the repair of them becomes a critical business. The damage is in the form of TMF cracks, erosion, oxidation, coating loss or creep rupture cracks.

Creep rupture and TMF cracks may be repaired by welding, brazing or may be simple blending depending on the type of the damage. High γ' superalloys contain large amount of Al and to some extent Ti to attain near 60-70% γ' in their metallurgical structure for maximum creep resistance [3]. Because of the high γ' content, it is very difficult to weld repair them (Fig.2) [4]. The difficulty arises when the grain boundary melting temperature of the component is exceeded during welding and resulting in grain boundary cracking during solidification. This type of cracking is one of the main obstacles for effective weld repair of high γ' alloys.

Braze repair becomes a second option to repair these components since during brazing only the braze material is melted and the incipient melting temperature of the component is not exceeded. A further improvement of brazing is also called diffusion brazing where isothermal solidification of the braze material occurs at the brazing temperature of the base metal. The disadvantage of brazing is the repair location composition is diluted with braze material during the process and will result in some change of mechanical, oxidation and corrosion properties. Most common braze material for Ni and Co base gas turbine material contain B and Si melting point depressants. These form borides and other compounds that are hard and brittle and reduce TMF, LCF and rupture ductility. However, they work extremely well for stationary components such as vanes where mechanical property requirements are less demanding than rotating components [5].

A turbine blade repair must be capable of meeting tensile, LCF, TMF and rupture capability. This work is aimed to create a braze repair alloy without forming brittle compounds and with tensile, LCF and rupture capability at or near base material properties.

2. EXPERIMENTAL PROCEDURE

2.a. Braze Alloy Development

The braze alloy development is specifically for high γ' alloy 247. Composition of Alloy 247 is given in table 1. Ni-Cr-Ti ternary eutectic alloy was selected as the core braze repair material. Composition of the braze alloy is Ni-15-25%Cr-15-25%Ti by wt%. The braze alloy was manufactured in powder form by gas atomization technique by Praxair with a size range of <20 micrometers. Alloy 247 powder was also manufactured by Praxair and its size range was approximately 40 micrometers. PSP shapes which were made of base alloy/braze alloy mixture were manufactured by AIM corporation in Cincinnati OH.

Cr	Co	Ti	Al	W	Mo	Ta	C	Hf	Ni
8.3	9.3	0.8	5.4	9.5	0.5	3.2	0.1	1.4	Bal

Table 1. Composition of base metal alloy 247 used in this investigation.

2.b. FIC Cleaning

FIC cleaning was established by utilizing HF gas in a vacuum. All field return components and mechanical test specimens were FIC cleaned prior to brazing. FIC cleaning parameters are company proprietary and will not be disclosed. However, the process is capable of cleaning all oxides from the crack and other surfaces and provide a brazeable surface with no oxides.

2.c. Braze Trials

Braze trials were conducted in a vacuum furnace at a 5x10^-5 torr or better pressure at Siemens Energy Metallurgical Laboratories in Orlando FL or Charlotte NC. Brazing temperature is above 1225°C. Brazing time is 1-12 hours.

2.d. HIP Operation

A HIP cycle was applied to all braze samples and braze repaired components. HIP cycle is above 1200°C for 1-4 hours under high purity Argon pressure (99.9999%Ar) of with greater than 10 ksi pressure. Cooling from this temperature was by argon quench and equivalent to vacuum argon quench in a solution treat cycle. Therefore, HIP treatment and the cooling rate from HIP temperature satisfied the solution treatment requirement for alloy 247. Therefore, HIP operation is used as solution treatment cycle.

2.e. Heat Treatment

Heat treatment after HIP operation involved primary and secondary ageing where both coarse and fine γ' was formed. A high temperature age cycle between 1070°C-1090°C for 2 to 4 hours was applied to all the samples and components for coarse γ'. This was followed by a low temperature age cycle between 860°C-890°C for 16 to 20 hours for fine γ' precipitation.

2.f. Tensile Testing

In all tensile specimens, braze portion of the specimen was located in the middle of the gage section of the tensile specimen. Tensile properties were tested from room temperature up to 1200°C. Tensile tests were conducted using a Tinius Olson machine.

2.g. LCF Testing

Similar to tensile specimens, braze portion of the specimen was located in the middle of the gage section of the LCF specimen. LCF tests were conducted at 850°C under strain control conditions. 850°C test temperature was selected as typical for row 1 turbine blades.

2.h. Metallography

The braze samples were sectioned and mounted using standard metallographic procedures. The mounted samples were ground, polished and then etched using Kalling's agent. The specimens were examined with stereo and optical microscopy.

3. RESULTS and DISCUSSION

3.a. Results

Cracks on service return turbine blades are generally TMF origin. The width of these cracks may be as narrow as 25 micrometers or less. A narrow gap crack is defined as a crack with a width less than 75 micrometers in this study. Many of the turbine blade cracks are larger than 75 micrometers and even exceeding 500 micrometers width in many occasions. Typical service cracks for a representative Siemens Energy Stage 1 blade after FIC cleaning is shown in Figure 3. These are TMF cracks caused by the thermal expansion and contraction during engine start and shutdowns. A metallographic cross section of these cracks is shown on Figure 4. Repairing these cracks is the objective of this work.

Braze alloy development started by evaluating the Ni-Cr-Ti ternary phase diagram at the Ni rich corner as shown in Figure 5 [7]. The ternary eutectic temperature of this eutectic is near 1225C and the composition of the eutectic is approximately Ni-15-25%Cr-15-25%Cr by wt.%. The near Ni-Cr-Ti eutectic of this composition was manufactured in the powder form. A metallographic section of a narrow gap braze with this alloy is shown in Fig.6. a. In this example, base metal (alloy 247) powder was mixed with the eutectic braze powder. This mixture was placed on the top surface of the previously cut EDM notch. EDM notch was 50 micrometers wide was after FIC clean and prior to braze operation. The braze had the fluidity to flow into the narrow gap and resulted in complete repair of the EDM notch. Ti in the braze alloy is a reactive element. Therefore, mixing the braze alloy with the base metal alloy powder prior to placement on the base metal is necessary to prevent erosion on the base metal surface.

Compared to narrow gap repair in Fig. 6.a, filling and repairing a wide gap crack is completely different. If the braze alloy is allowed to flow in and fill a wide gap crack by itself, undesired compounds would form and reduce the mechanical properties as will be discussed in the discussion section. Wide gap cracks are therefore filled with base metal powder first and braze filler metal is placed on top. The assembly is heated to the braze temperature. Braze alloy melts and infiltrates the sintered powder in the cavity (crack) resulting in wide gap repair. A metallographic section of the wide gap braze is shown in Figure 6.b. It is noted that erosion and eta phase (arrowed needle phase at top) formation occurred at the top surface. Both defects were eliminated during application to component by adjusting the fraction of the braze at the top surface as will be discussed later in this section.

Braze cycles for both NGB and WGB are shown in Figure 7. Brazing temperature is above 1225°C and duration is 1-12 hours for both braze types. The reason for long braze times is to allow diffusion of Ti into the surrounding surfaces for NGB and into both surrounding surfaces and base metal powder for WGB. One of the disadvantages of Ni-Cr-Ti braze material is it contains between 15-25% Ti [6,7]. Ni base superalloys typically contain less than 5.0% Ti to prevent formation of eta phase and/or other compounds that are detrimental to mechanical and corrosion properties of the component. Eta phase is needle shape and will reduce LCF capability if formed in the braze section. This phase will be discussed later. Braze temperature, braze duration and fraction of braze in the braze joint therefore becomes critical to prevent the formation eta phase. A braze duration longer than 1 hour homogenizes the braze structure and together with appropriate braze fraction, eta phase formation is prevented.

When repairing a service returned turbine blade component it is therefore advantageous to open all visible TMF cracks, FIC the surface oxides from the crack surfaces and fill them with base metal powder prior to braze repair. This method increases the surface area that the braze alloy interacts with and allows diffusion of the low melting point element (Ti in this case) into the surrounding base metal powder. Figure 8 shows such a process. In Figure 8.a. TMF cracks on a typical row 1 turbine blade platform are opened and FIC cleaned. After the crack opening and FIC, cracks are filled with base alloy powder (alloy 247), then the base metal/braze alloy mixture is placed on top of the crack surface and the braze operation is carried out (8.b). Fig. 8.c. shows a metallographic cross section of the repaired TMF cracks where all cracks were filled. The porosity seen in the Fig 8.c. is acceptable for the application. Regardless, these pores are closed during HIP operation. A representative process is also shown in Fig. 9 for equiaxed grain turbine blade.

The use of this new braze metallic alloy is not limited to crack filling. In the gas turbine industry, use of PSPs are common to build up eroded portions of the components. PSPs are also used for section replacement. Such a section replacement process is shown in Figure 10 for turbine blade tip replacement. Turbine blade with a sectioned tip and its corresponding PSP and attachment tip is shown in Fig 10.a. and the brazed blade tip section is shown in in Fig.10.b.

A metallographic cross section of the section replacement is shown in Fig 10.c. Braze joint is free of undesired metallurgical phases, voids and most importantly free of cracks. A section replacement of alloy 247 is very difficult if not impossible by welding. This new braze material and its PSP produces section replacements interfaces with desired metallurgical characterizes.

Tensile and LCF specimens were prepared according to ASTM standards. Braze joints were in the middle of the gage section. Braze joints for all specimens were 800 micrometers wide, prefilled with alloy 247 and braze material was placed on top prior to braze. They were all brazed at 1250°C/12 hrs. Tensile properties of the braze repairs are shown in Figure 11. The values of Y and X axes are removed since they are Siemens Energy Inc proprietary data. In all test specimens, braze joints did not contain any eta phase or unwanted metallurgical phases. Braze tensile properties are extremely good and matching to base metal properties. LCF capability is the most important property for turbine blade section replacement. This property is usually used to assess the TMF capability of a turbine material. LCF tests were carried out 850°C under strain control conditions and shown in 13. LCF capability at 850°C is extremely good matching the base metal properties.

3.b. Discussion

Development of a new repair material for weld and braze repair requires several important criteria to be met. First is the requirement to meet tensile properties. This is followed by other mechanical properties such as HCF, LCF and creep rupture properties. For gas turbine components, a row 1 turbine blade braze repair alloy must meet the required tensile, LCF and rupture properties because it is a rotating component. Stationary components such as vanes have less stringent requirements. Row 1 turbine blades and vanes are subjected to extreme temperatures during engine operation. Furthermore, temperature distribution on a given component is not uniform during engine operation. As shown in Figure 3 high temperature exposure areas are platform and airfoil tip surface which results in the formation of TMF cracks.

The metallurgical approach used in this work to develop a new braze alloy is such that its composition would not deviate significantly from the base metal to meet corrosion and oxidation properties. A second consideration is that during braze, undesired compounds that are ionic bonded would not form. Compounds such as borides, silicates, oxides and carbides are inherently hard and brittle. Therefore, if they are not spherical, small and do not have fine distribution in the braze repair location they will lower the LCF capability of the repair. Boron and silicon base braze joints have low LCF and rupture capability due to boride and silicate formation when they form continuously [5].

In this investigation, all visible cracks were opened, then cleaned with FIC process and filled with base alloy powder prior to braze repairing of turbine components. In the case of mechanical property specimens, after FIC, base alloy powder first placed into an EDM groove. Braze powder/base alloy powder mix was placed on top surface and braze infiltrated the base alloy powder in the EDM groove area. The advantage of this process is that liquid braze is in contact with a large base alloy powder surface area during brazing. When the braze duration is kept between 1-12 hours, diffusion occurs between the braze and base metal and some degree of homogenization is established in the braze joints. Therefore, this braze operation is called diffusion braze. Boron and silicon braze process also utilize the same diffusion braze concept. In the case of boron braze, diffusion time may be kept short because diffusing element boron is an interstitial and has high diffusivity.

The disadvantage of boron braze is that B does not have any solubility in Ni and hard boride particles nucleate during brazing. If they are continuous LCF is lowered considerably since LCF is ductility dependent. The advantage of the braze material presented here is that the melting point depressant is Ti and it has up to 5% solubility in Ni. This means that as a first approximation, alloy 247 will absorb Ti up to its solubility limit without forming any harmful compounds. Eta phase, which is hexagonal Ni_3Ti phase is known to have low ductility [8] and is undesired in superalloys. Therefore, one of the aims of this investigation is to prevent the formation of eta phase by mixing or infiltrating braze material with the base metal powder such that eta phase would not form. In this respect, the braze alloy developed in this work is specifically for alloy 247 (0.8%Ti), a low Ti superalloy. Brazing a high Ti wt.% superalloy such as GTD 111 (4.9%Ti) would not be feasible with this braze material since the GTD111 is already near the solubility limit of Ti in Ni. A second advantage of this braze alloy is Ti is a γ' former. Since γ' is the primary strengthening precipitate in Ni base superalloys, common available braze alloys that use B, Si, Zr, and Hf as melting point depressants dilute the braze joint and will reduce the amount of γ' for strengthening the repair area. This is not the case if Ti is the melting point depressant.

Formation of eta phase is prevented by using the appropriate base metal/braze metal proportion. Fig 6.a shows that small amount of needle shaped eta phase formed at the top braze rich surface of the base metal after braze infiltration but is absent in the braze joint. No eta phase was observed in the infiltrated portion of the remaining braze joint. This issue was later solved by reducing the amount of braze proportion on top surface and needle shaped eta phase formation was prevented (Figures 8.c., 9.b. and 9.c.). A braze PSP that is used for section replacement shown in Figure 10.c also free of eta phase with excellent mechanical properties when proper fraction of braze used.

In addition to the fraction of braze in the repaired area, MPD is important for mechanical and chemical properties. The most important element in this braze alloy Ti which is the MPD. Ti is a strong γ' former. γ' is a stoichiometric intermetallic compound with a formula $Ni_3(Al, Ti)$. By utilizing Ti as the MPD in the braze material dilution of the braze joint and reduction of γ' fraction is prevented. Other available braze material for nickel base superalloys, that use MPD such as B, Si, Hf, Zr do not have this advantage. Provided that solubility limit of Ti in the base metal is not exceeded and eta phase formation is prevented, Ni-Cr-Ti braze material is one of the braze alloys best suited for carrying LCF and rupture loads.

Ultimate tensile strength of the WGB repair and its comparison to base alloy 247 is shown in Figure 11. WGB repair properties are at or near base material strength at any test temperature. LCF properties of the braze joint deserves some detailed discussion. LCF properties are sensitive to defects in the braze joints. A braze joint is practically a casting joint and therefore contains solidification shrinkage voids. These voids would reduce the LCF properties of the braze joint. Therefore, a HIP operation was necessary to close these voids. All mechanical properties presented in this work were after HIP operation. The LCF capability of WGB joint is comparable to base alloy 247 at the operating conditions (Fig.12)., rupture life of the braze joint is lower than base metal at 850°C.

4. CONCLUSIONS

1. Ni-Cr-Ti ternary eutectic can be used as braze repair material for low Ti wt% (<1.0wt%) nickel base superalloys.
2. The ternary eutectic alloy is capable of repairing wide gap cracks with tensile strength equivalent to base alloy 247.
3. LCF properties of braze repair joints are at or near base metal properties for the blade operation conditions.
4. Section replacement with Ni-Cr-Ti eutectic alloy successful without formation of any undesired metallurgical compounds.

REFERENCES

[1] H.L Bernstein, Proceedings of the 27th Turbomachinery Symposium pg. 199, 1998

[2] H.L. Bernstein, Proceedings of the 28th Turbomachinery Symposium, pg.179, 1999.

[3] J. N. Dupont, J. C Lippold, S.D. Kiser, , “Welding Metallurgy and Weldability of Nickel Base Superalloys’, 2009 by John Wiley & Sons, Inc, pg. 157

[4] K. Ozbaysal, US Patent Application Publication, US 2015/0050157 1, Feb 19, 2015.

[5] X. Huang and W. Miglietti, Journal of Engineering for Gas Turbines and Power, Jan 2012, Vol. 134, pg. 010801-1

[6] K. Ozbaysal, US Patent 10,335,878, 2011, July 2, 2019

[7] K. Ozbaysal, US Patent 9,573,228; Feb. 21, 2017

[8] G.K. Bouse, Superalloys 1996, pg 163. Edited by R. D. Kissinger, D. J. Deye, D. L. Anton, A. D. C&l, M. V. Nathal, T. M. Pollock, and D.A. Woodford, The Minerals, Metals &Materials Society, 1996

NOMENCLATURE

DS	Directionally Solidifieda
EDM	Electric Discharge Machine
FIC	Fluoride Ion Clean
HIP	Hot Isostatic Pressure
LCF	Low Cycle Fatigue
NGB	Narrow Gap Braze
UTS	Ultimate Tensile Strength
TBC	Thermal Barrier Coating
TMF	Thermo Mechanical Fatigue
WGB	Wide Gap Braze

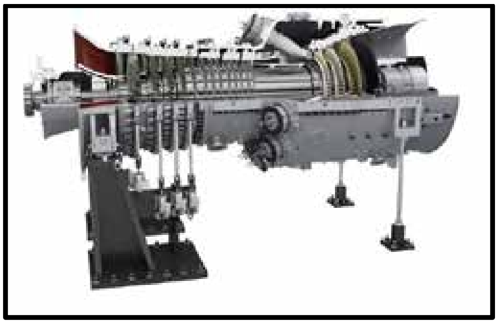

Figure 1. Siemens 8000H Industrial Gas Turbine Engine.

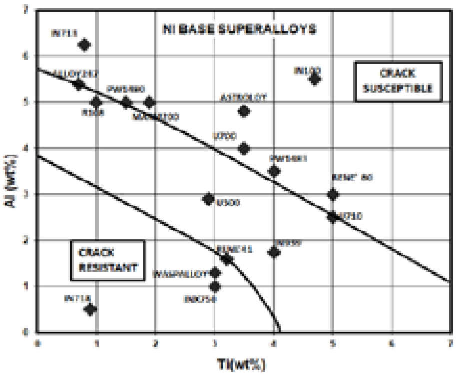

Figure 2. Weldability of Ni base superalloys as a function of Al and Ti content. [4]

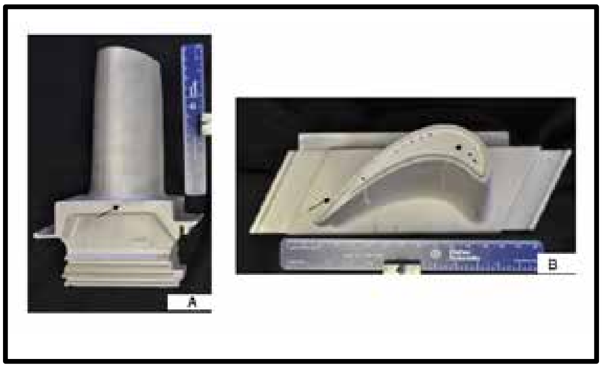

Figure 3. Representative Siemens Energy Inc. Row 1 Equiaxed Turbine blade. Platform cracks in (A) and tip cracks in (B), arrowed.

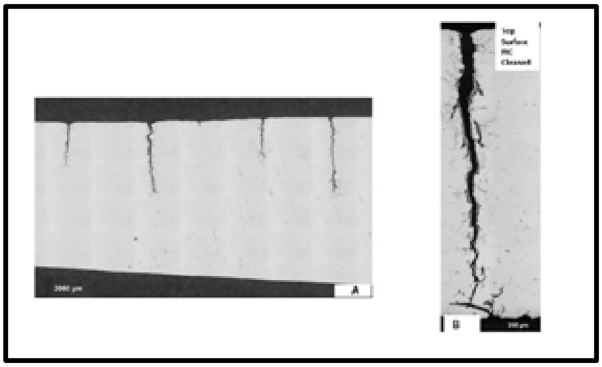

Figure 4. Typical TMF cracks on Siemens R1 turbine blade platform surface after FIC Clean in (A) and high magnification in (B).

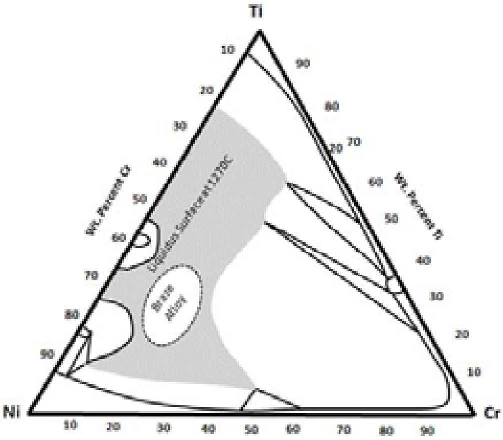

Figure 5. Ni-Cr-Ti Liquidus surface at 1270°C and Braze Alloy Development area (from [7]).

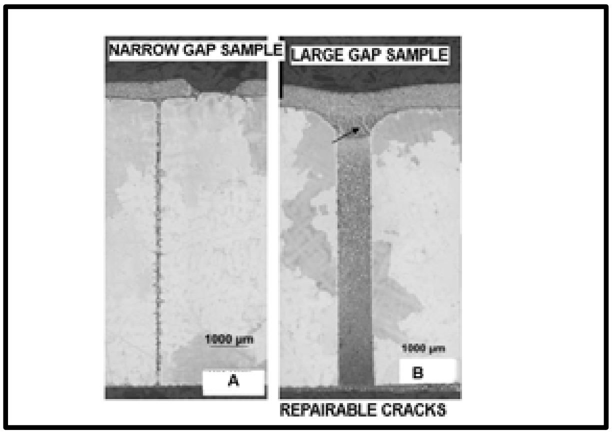

Figure 6. Narrow Gap Braze Repair on a EDM Notch of < 50micron in (A) and Wide Gap Braze Repair on EDM notch of >800micron. Erosion and Eta phase is Is arrowed in (B)

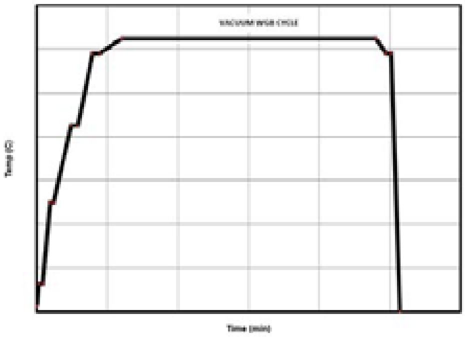

Figure 7. Braze cycle for NGB and WGB for Ni-Cr-Ti eutectic braze alloys on Alloy 247 base metal.

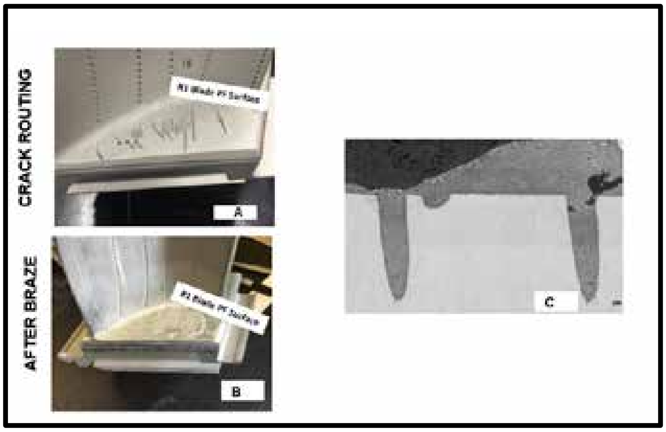

Figure 8. A FIC cleaned DS Siemens R1 Turbine Blade with PF TMF cracks opened in (A), braze Repaired in (B) with PF and cross section in (C).

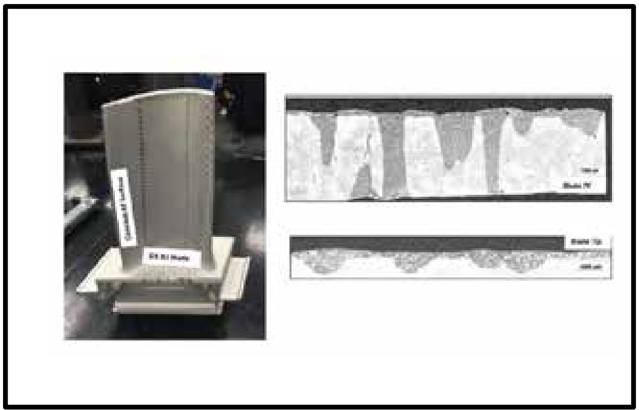

Figure 9. A FIC cleaned Equiaxed Siemens R1 Turbine Blade with PF and AF TMF cracks opened in (A) and metallographic cross section in (B).

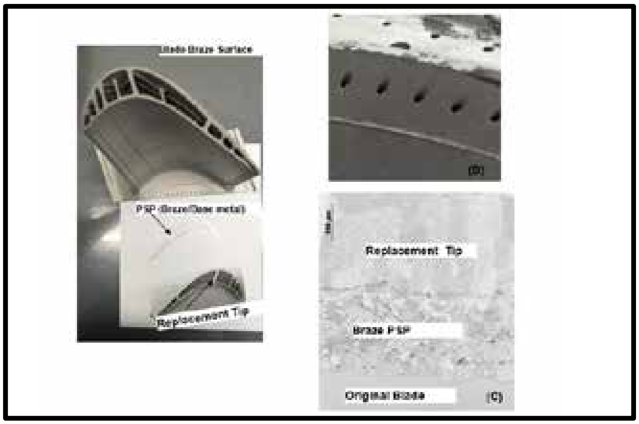

Figure 10. Blade Tip Replacement and Upgrading with Ni-Cr-Ti braze PSP. Upgrade tip and PSP prior to braze in (A), after braze but prior to blending in (B) and metallographic cross section in (C). Scale bars are removed in A and B

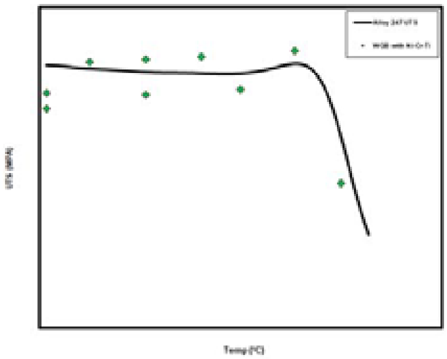

Figure 11. Ultimate tensile strength of WGB joint as a function of temperature.

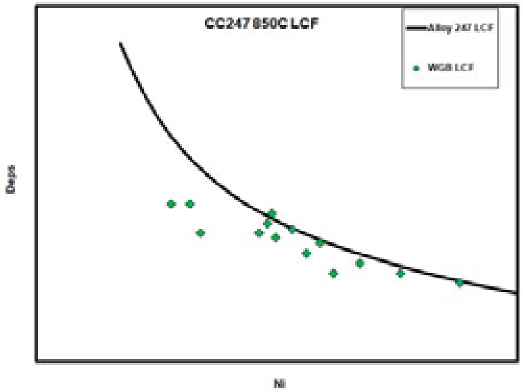

Figure 12. LCF capability of WGB repair with Ni-Cr-Ti Eutectic at 850°C and its comparison to base metal Alloy 247 at 850°C.

The Effect of Recycled Powder Characteristics on the Properties of Additively Manufactured 17-4 PH Stainless Steel

Ece KAHRAMAN[1], Mertcan BAŞKAN[1], Gökhan ÇELİK[1], Mert KELEŞ[1], Andaç ÖZSOY[1], Orkun ÖNEM[1], Bilgehan ÖGEL[2]

[1]Roketsan A.S., [2]Middle East Technical University

Turkey

Abstract

The method in which each layer is formed and the sort of material being produced are two important factors that classify AM systems and technologies. Selective laser melting (SLM) which is a type of powder bed fusion process annihilates several disadvantages of conventional manufacturing techniques by providing a fast production rate for the complex geometries without any need to use expensive tools. By selectively fusing metallic powder using a high-energy laser beam it produces parts in a typically inert atmosphere [1]. One of the most commonly used type of precipitation hardening (PH) stainless steel (SS) is 17-4 PH SS because it provides a combination of high tensile strength, high toughness and high corrosion resistance [2,3]. These properties made the 17-4 PH SS suitable for aerospace applications such as impellers and structural parts in which SLM is an appropriate way for production especially taking into account their complex geometries. Microstructure and mechanical properties of the metal alloy parts fabricated by SLM could be very divergent than those fabricated using conventional methods. In a SLM process, the quality of the final part depends on the quality of the feedstock. Powders' spherical shape degenerates and satellites are formed after several usage of the powders, which decrease the apparent density and flowability. In SLM, in order to obtain more sustainable and cost effective operation, it is prevalent to reuse the powder in successive cycles of the route. However, reutilization of the powder needs to be examined in more detail. In this study, powders of 17-4 PH SS were characterized by means of powder chemistry, size and shape to determine the effect of recycling powders on the SLM process. For this purpose, several production methods were investigated in order to gain maximum efficiency from powders without any loss of mechanical property.

1. Introduction

Additive manufacturing (AM) is officially described as "the process of joining materials to make objects from 3D model data, usually layer upon layer, as opposed to subtractive manufacturing technologies" by the American Society for Testing and Materials (ASTM) [4]. SLM is an additive manufacturing technique that pertains to the powder bed fusion group and allows the manufacturing of complicated and functional metallic parts. In this process, highly focused laser beam is used to selectively melt the metal powder accumulated in very thin layers (e.g. 50 µm) over the build platform. The powder partakes achieving competitive mechanical properties, analogous to other powder metallurgy processes. In order to find out the connection between the quality of manufactured parts and several process parameters, intensive research has been performed. Less regard has been paid to other significant factors like powder characteristics, material contamination and powder reuse. SLM permits reuse of non-consumed powder material leading to a more cost-effective and sustainable process and this is one of the most significant advantage of the SLM process. The powder which is not melted for joining in a component is gathered in a receptacle below the build chamber during the SLM process. However, due to heat exposure, the unused powder particles can become welded and agglomerations are formed. As a result, Particle Size Distribution (PSD) increases and this could impact the flow behavior. Also, risk of contamination due to gas pick-up exists. (Nitrogen and oxygen or moisture) [5]. Based on this subject, several studies are carried out. For example, Zapico et al. conducted a study with 17-4 PH SS powder [6]. In this study, a morphological analysis of a large sample of particles was accomplished by means of microscope image processing techniques that indicated significant changes in the powder after 20 reuses that could negatively affect the mechanical properties of the final manufactured parts . Santecchia et al. studied characterization of different metal powders and they found that after 10 times reusing of 17-4 PH SS powders, similar ultimate tensile strength value was obtained but failure strain of print 10 parts decreased by nearly 7% [7]. In this study, powders of 17-4 PH SS were characterized by means of powder chemistry, size and shape to determine the effect of recycling powders on the SLM process.

2. Experimental Procedure

Within the scope of the study, 17-4 PH SS powder, known to have a D10 value of 15µm and a D90 value of 45µm, was used. 3 different samples were prepared before starting the experiments. Sample 1 consists entirely of unused powder. Sample 2 contains 50% used and 50% unused powder. Sample 3 contains fully used powder. These samples were characterized via different techniques. Also, productions were carried out with the reduced built volume unit of the SLM machine to see the difference in tensile properties between unused and used powder. There are two important details that are needed to remark. It is not known how many times "the used" powder is used and sampling techniques specified in the standards were not applied during experiments. Performed experiments can be listed as follows.

- TGA Study
- Density Determination with Pycnometer
- Determination of Powder Size by Laser Scattering Method
- Determination of Powder Size and Shape by Dynamic Image Analysis
- Determination of Surface Area by BET Analysis
- Scanning Electron Microscope (SEM) Examinations
- Tensile Test

3. Results and Discussion

3.1. Density Determination with Pycnometer

Table 1 Density Determination with Gas Pycnometer

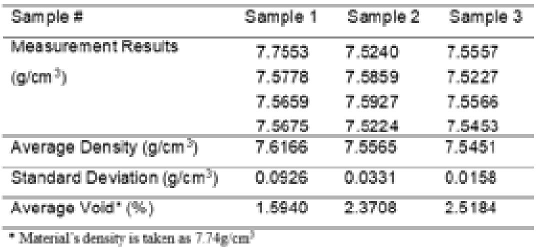

Sample #	Sample 1	Sample 2	Sample 3
Measurement Results (g/cm³)	7.7553 7.5778 7.5659 7.5675	7.5240 7.5859 7.5927 7.5224	7.5557 7.5227 7.5566 7.5453
Average Density (g/cm³)	7.6166	7.5565	7.5451
Standard Deviation (g/cm³)	0.0926	0.0331	0.0158
Average Void* (%)	1.5940	2.3708	2.5184

* Material's density is taken as 7.74g/cm³

The results show that the void volume is the highest and the density is the lowest in sample 3. This indicates that the presence of powders that have been removed from the sphericity and distorted in the used powder. The pycnometry equipment void data from used powder is critical for additive manufacturing. Gaps formed during the spreading will also pose a risk of remaining voids for the final product.

3.2. Determination of Powder Size by Laser Scattering Method

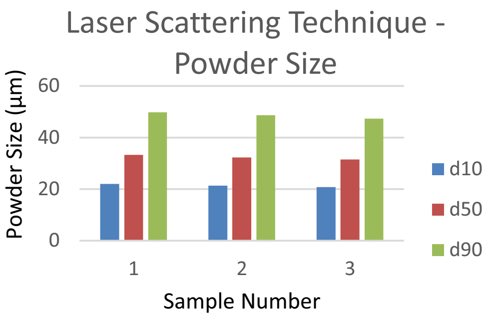

Figure 1 Particle Size Distribution of Powders (Mastersizer)

In Figure 1, the results of the tests with the MasterSizer2000 equipment are included. Particle size distribution D10, D50, and D90 corresponding to the percentages 10%, 50%, and 90% of particles under the reported particle size. Within the scope of the study, 17-4 PH SS powder, known to have a D10 value of 15µm and a D90 value of 45µm, was used. The results obtained seem to be consistent with the size of the 17-4 PH SS metal powder used. Since equivalent diameter method is used, the sphere is accepted regardless of the shape of the particle. So, no data on particle shape have been collected.

3.3. Determination of Powder Size and Shape by Dynamic Image Analysis

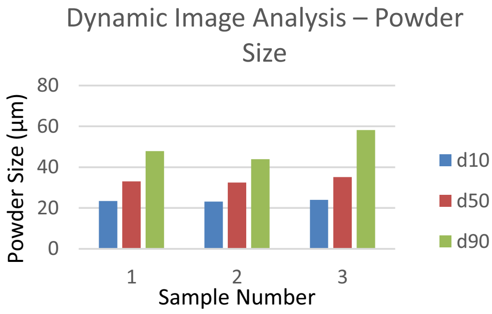

Figure 2 Particle Size Distribution of Powders (Camsizer)

The results in Figure 1 and the results in Figure 2 are parallel to each other. In addition, the data obtained by both different methods (Laser and dynamic measurement based methods) show that the ratio of used and unused powder mixture in the samples has no effect on the particle size. Sphericity is a measure of how closely the shape of an object resembles that of a perfect sphere. The sphericity of a sphere is unity by definition and, any particle which is not a sphere will have sphericity less than 1.

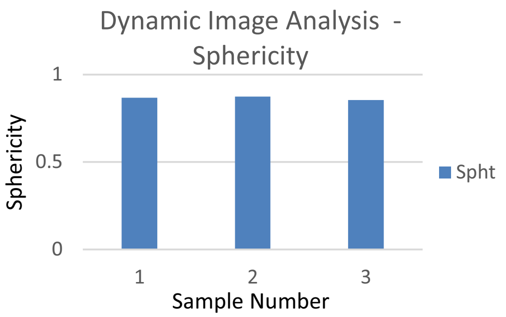

Figure 3 Sphericity Parameters of Powders

The parameters related to powder sphericity were highest in sample 2 and lowest in sample 3.

3.4. Determination of Surface Area by BET Analysis

The results obtained are shown in Table 2.

Table 2 BET Analysis Results

Sample #	1	2	3
Surface Area (m^2/g)	0.234	0.109	0.098

As the amount of used powder increased, a decrease in surface area was observed. According to the BET analysis, the specific surface area increases as the amount of unused powder increases. According to the data obtained from the powder size determination methods, no significant change is observed between the powder sizes of the samples. Thus, the surface area difference can be explained by the surface roughness or agglomeration of powders. The surface area will decrease as the agglomeration increases. In scanning electron microscope, investigations were made with low voltage known to be sensitive to surface morphology, and no obvious difference was observed between the surface roughness. However, aggregation is observed in sample 3. This is consistent with the BET analysis.

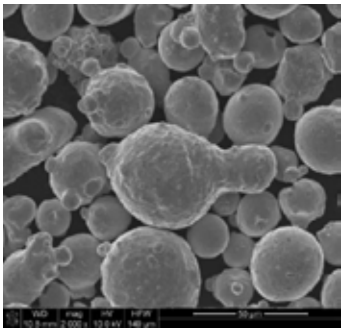

Figure 4 SEM Image of Sample 3

3.5. Scanning Electron Microscope (SEM) Examinations

The images obtained are shown in Figure 5,6 and 7.

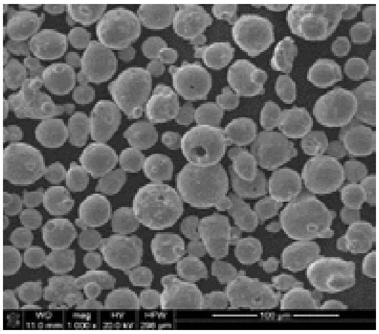

Figure 5 SEM Image of Sample 1

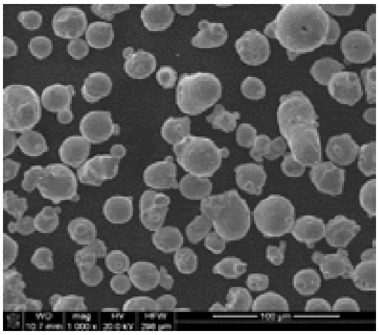

Figure 6 SEM Image of Sample 2

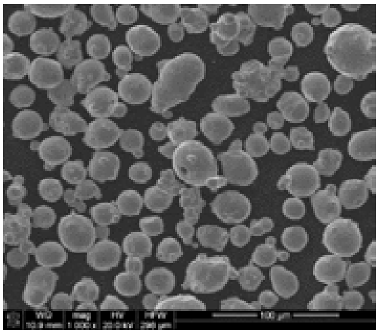

Figure 7 SEM Image of Sample 3

In the images obtained, pores open to the surface in the powder in all samples are visible. These errors are thought to come from the atomization process which is a process to manufacture high quality metal powders. The effects of these errors on the process will also be examined. Apart from this, there was no clear difference between the samples.

3.6. Tensile Test

Result are given in Figure 8.

Production	Coupon Number	Tensile stress at Yield (Offset 0.2 %) (MPa)	Tensile Stress at Maximum Load (MPa)	Tensile strain at Break (Standard) (%)
100% Unused Powder	1	855	896	6,7
	2	776	903	5
	3	770	900	5,5
	4	840	900	4,8
	5	831	905	6,4
	Avg	**814,4**	**900,8**	**5,68**
100% Reused Powder	1	751	904	5,8
	2	780	908	5,5
	3	825	903	5,3
	Avg	**785,3**	**905**	**5,53**

Figure 8 Tensile Test Results

As it can be seen from figure 8, yield strength is slightly higher in parts produced with unused powder than that of used powder. This result is expected considering the increase in particle size and agglomeration formation as powder is used.

4. Conclusion

In this study, powders of 17-4 PH SS were characterized by means of powder chemistry, size and shape to determine the effect of recycling powders on the SLM process. Samples used throughout the study are 17-4 PH SS powders known to be 15-45µm in size, supplied for use in additive manufacturing. Used powders in samples 2 and 3 are powders used in additive manufacturing productions. Reuse of powders did not cause a change in their morphology. However, changes can be observed in productions progressing with the same powder. According to the results of pycnometry, the lowest density was observed in the used sample. It was evaluated that the voids in the sample may cause porosities after production. Data collected from laser-based measurements and data collected with dynamic image processing equipment show that the powder size distribution in all three samples remains unchanged. In the BET analysis, the decrease in the surface area in sample 3 indicates agglomeration of powder. According to the tensile test results, the yield strength of the parts produced with completely used powders was slightly lower than the parts produced with virgin powder.

References

[1] Gibson, I., Rosen, D.W. and Stucker, B. (2010). Additive Manufacturing Technologies. Springer. New York, NY.

[2] Smith, W.F. (1981). Structure and Properties of Engineering Alloys. McGraw-Hill Book. New York, NY.

[3] Lin, X., Cao, Y., Wu, X., Yang, H., Chen, J. and Huang, W. (2012). Microstructure and mechanical properties of laser forming repaired 17-4PH stainless steel. Materials Science and Engineering. 553. 80-88.

[4] Mahmoudi, M., Elwany, A. (2017). Mechanical Properties and Microstructural Characterization of Selective Laser Melted 17-4 PH Stainless Steel. Rapid Prototyping Journal. 23(2). 280-294.

[5] Cordova, L., Campos, M. and Tinga, T. (2019). Revealing the Effects of Powder Reuse for Selective Laser Melting by Powder Characterization. JOM. 71(3).1062-1072.

[6] Zapico, P., Giganto, S., Barreiro, J. and Martinez-Pellitero, S. (2020). Characterisation of 17-4 PH Metallic Powder Recycling to Optimise the Performance of the Selective Laser Melting Process. JMR&T. 9(2). 1273-1285.

[7] Santecchia, E., Spiragelli, A. and Cabibbo, M. (2020). Material Reuse in Laser Powder Bed Fusion: Side Effects of the Laser—Metal Powder Interaction. Metals. 10 (341).

Process Parameter Optimization for Wire and Arc Additive Manufacturing (WAAM) of 316LSi Steel

Mertcan BAŞKAN, Erkan Buğra TÜREYEN, Gökhan CAN, Mert KELEŞ, Ece KAHRAMAN, Orkun Umur ÖNEM, Oğuzhan YILMAZ
Roketsan
Turkey

Abstract

Additive manufacturing (AM) is a fabrication method which enables creation of three-dimensional parts layer by layer, according to a CAD model specifically prepared and imported to the system. AM methods can be divided into many subgroups with respect to raw material type, feedstock form, heat source etc. From these methods, Wire and Arc Additive Manufacturing (WAAM) has become a more popular topic both on academic and industrial applications in recent years. The advantages of WAAM include high deposition rate, lower capital cost with respect to other additive manufacturing techniques and lower scrap material when compared to the conventional manufacturing methods even for large components. However, WAAM has high number of process variables which requires a detailed parameter optimization and process control in order to obtain parts with desired properties. In this study, the effects of wire feed speed and travel speed were investigated by the help of statistical design of experimental tools and analyzed in terms of single bead geometry, micro hardness and microstructure for 316LSi steel material. Then, using the optimized process parameter set, a wall formed by horizontally overlapping weld beads was built and tensile characteristics was determined. Obtained results revealed higher tensile properties when compared with forged counterpart of the same material in both longitudinal and transverse directions and specimen exhibited isotropic tensile behavior.

1. Introduction

Additive manufacturing (AM) has become a versatile production method in recent years with the benefits of low material waste, improved production times and capability of production complex shapes. AM is a production method in which parts are built by deposition of corresponding raw material layer by layer according to the shape of the part. Although AM technologies can be classified in various ways, ASTM categorized AM methods as binder jetting, directed energy deposition, material extrusion, material jetting, powder bed fusion sheet lamination and vat photopolymerization [1]. Among these methods, wire and arc additive manufacturing (WAAM) technique, which is a subcategory of directed energy deposition processes which will be the main focus of this study.

WAAM method has become attractive in both industry and academic studies. Various materials like steels [2], superalloys [3], titanium alloys [4] and refractory metals [5] are used in WAAM technique. Since there are many process parameters in WAAM, many studies are based how to control them. For instance, Ge et al. studied the preheating to decrease thermal stresses and tried to minimize the change the mechanical properties upon layers of 2Cr13 steels [6]. Ou et al. conducted a detailed characterization and modeling study and achieved the modeling the fusion zone and solidification characteristics with apparent cooling rates [7]. Another study is about the development of toolpath geometries for overlapping regions and complex shapes. For instance, Yilmaz et al. developed an algorithm which calculates optimal distance between adjacent beads in real time, using image acquisition methods [8].

In this study, WAAM process parameters are optimized in terms of bead geometry, wetting characteristics and precipitation morphology. Then, with the optimized parameter set, a sample Wall geometry is produced and the mechanical properties are investigated.

2. Experimental Procedure

A specially designed robotic WAAM/welding system with a two-axis positioner was used for the experimental application of the WAAM process. Fronius CMT (Cold Metal Transfer) welding machine was chosen in order to reach the properties similar or better than the conventional GMAW welded or cast parts [9]. Figure 1 shows the experimental setup which consists of KUKA's high accuracy 6 axis industrial robot which is commonly used in welding applications for its effective controllability and precision.

The experimental procedure was designed in order to optimize the main parameters of the process which are wire feed speed (WFS) and travel speed (TS). These parameters regulate the heat input which is critical in controlling the weld properties and therefore the

WAAM process. Among these parameters, WFS and TS are determined to be the part of Taguchi experimental design with 4, 5, 6, 7 m/min and 20, 35, 50 cm/min values consecutively. Workshop experiments were conducted with 1.2mm 316LSi stainless steel wire. Current and voltage values were automatically assigned with the use of CMT method.

Figure 1. Experimental WAAM system: an industrial robot and a two-axis positioner.

Single weld beads with each parameter set is characterized in terms of bead geometry by measuring the basic geometrical properties of the resultant shape. Width (w), height of weld (hw) and depth of weld (hb) values are measured for comparison as also bottom borders of the beads are visualized in Figure 2.

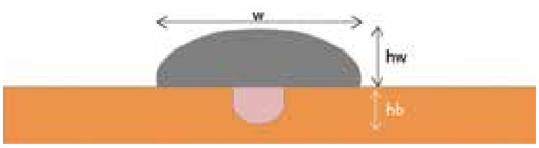

Figure 2. Measured w, hw and hb values from the single weld bead geometries

Metallographic sample preparation procedure was started by conventional grinding and polishing operations and followed by electroetching in 10 vol% chromic acid solution with an applied voltage of 8 V for 10 seconds.

3. Results and Discussion

3.1. Characterization of Single Layer Structures

Characterization of single layer structures gives critical information about the geometry of the beads. Thick layers which have good wetting and adhesion is desired for WAAM processes. Table 1 shows the critical dimensions of the single weld beads. From the dimensions in the results section, hw is a measure of deposition height whereas hb is related with adhesion. The width of the beads, w, is the indication of wetting, as the w increase, the wetting angle decrease and good wetting between the weld bead and substrate is achieved.

Table 1. Designed parameters and measured single bead parameters

Parameters			Results			
#	**WFS**	**TS**	**hw**	**hb**	**w**	**HI**
1	5	35	3.35	0.62	6.03	257
2	4	20	4.05	0.42	7.41	401
3	7	35	3.91	0.96	9.08	420
4	6	50	3.11	0.58	6.40	201
5	5	50	2.96	0.55	5.27	192
6	4	35	3.18	0.50	5.35	183
7	6	35	3.58	0.94	8.31	342
8	4	50	2.67	0.38	3.69	144
9	6	20	4.84	1.02	10.32	610
10	5	20	4.32	0.83	9.25	490
11	7	50	3.39	0.74	6.67	261
12	7	20	4.98	1.39	11.08	690

Note: The unit for WFS is m/min; TS is cm/min; hw, hb, w are mm and Heat Input (HI) is J/mm

Since WAAM is a manufacturing process in an additive manner, bead height (hw) is the most important geometric property mentioned in results section in Table 1. Therefore, from these geometric parameters, the relationship between hw and process parameters is summarized in Figure 3. Deposited material on a specific point increases bead height (hw) because volumetric material flow through the wire feeder continues with the same rate even though the TS is accelerated.

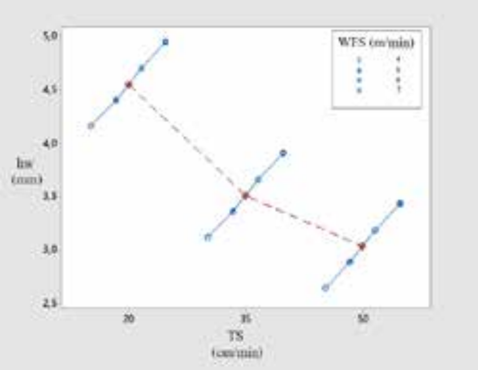

Figure 3. hw dependence on WFS and TS

The geometrical considerations are not sufficient for process parameter selection solely. **Error! Reference source not found.** represents the adhesion at the weld bead-substrate interface under optical microscope. Although the interaction between weld beads is much more critical than that of bead-substrate interface in WAAM studies, it is assumed that they will have similar behavior and the parameter set to be used in wall studies is selected by reckoning latter case. In **Error! Reference source not found.**(a), the fusion layer under the cap is very thin except the penetration on the arc direction. This is a typical behavior for the samples applied low heat input. Also, the wetting angle is near 90°, which means the bead do not wet the substrate properly. This may also cause interlayer or cracking problem for multilayer samples. Hence, these type of samples are eliminated for wall studies due to the possible lack of fusion and interlayer problems. **Error! Reference source not found.**(b) illustrates this behavior for the samples applied moderate heat input. The fusion line under the cap has significant thickness which yields a good interface strength and less lack of fusion problems. The wetting angle is smaller than 90°, which is desired case for WAAM studies. When heat input is more increased, as in **Error! Reference source not found.**(c), the fusion occurred much more deeply with the expense of process speed. However, unlike welding processes, there is no benefit of such deep penetrations by increasing total heat input in WAAM applications. Apart from that, the wetting angle is greater than 90°, which is also not desired due to possible interlayer problems such as delamination, cracks and porosities. The sample 7 seems to be optimum combination of fusion characteristics, wetting properties and process times in single bead experiments.

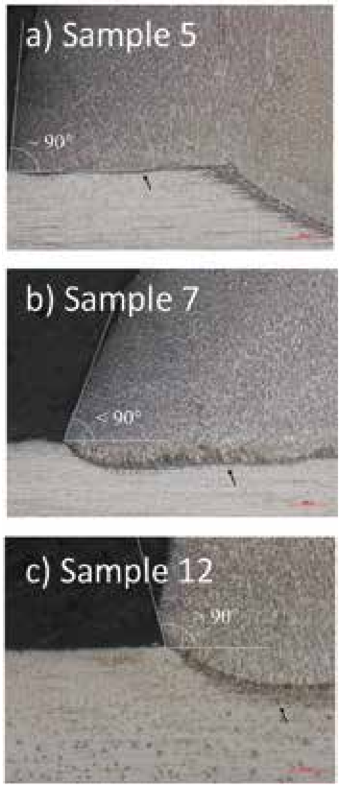

Figure 4 Bead-substrate interface of samples (a) 5, (b) 7 and (c) 12

3.2. Characterization of Multilayer Structures

In this part of the study, the precipitation analysis under electron microscope is conducted and the mechanical properties of WAAM structures are determined by tensile tests.

Figure 5 reveals the morphology of the precipitates under SEM with the EDS analyses conducted on a line. Figure 5(a) represents the precipitate morphology of a sample with application of lower heat input. In this case, the precipitates tend to form a network on the austenite matrix. Since many precipitates formed in stainless steel are known as brittle intermetallics, this type of morphology may cause a catastrophic failure and should be avoided. In Figure 5(b), on the other hand, the sample of moderate heat input is represented with sample 7. In this case, the precipitates do not form a brittle intermetallic network and remain discrete. This will prevent the crack propagation and loss of ductility.

The line analyses show that both samples exhibit similar compositional changes between austenite matrix and precipitates. However, since the difference between them is quite small, it is not clear to identify the exact composition by line analysis and EDS analyses from each phase must be conducted.

(a) Sample 5

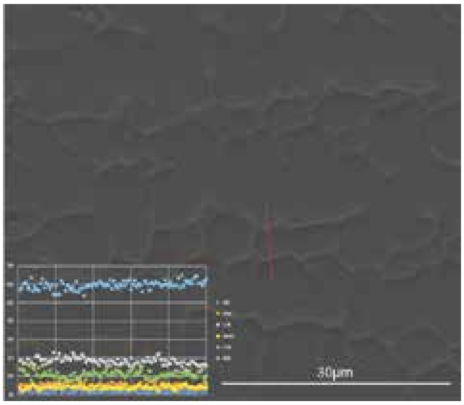

(b) Sample 7

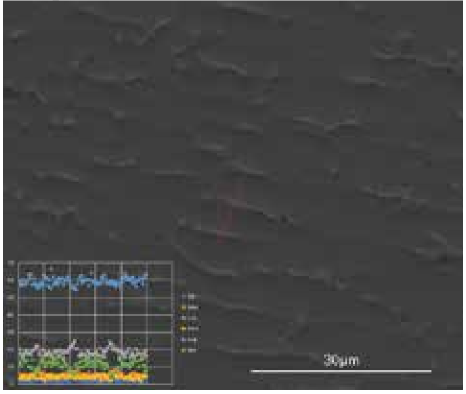

Figure 5. Precipitates in samples (a) 5 and (b) 7.

Table 2 summarizes the results of EDS analysis under SEM as well as the composition of 316LSi material given in the literature. First of all, overall composition of the matrix and the referenced material is very close to each other. Secondly, the precipitates in sample 5 and 7 have similar compositions which can be inferred that the process parameters and applied heat input during the process do not alter the composition of precipitates. When the composition of matrix and precipitate is compared, the latter is enriched by Mo and Cr. It means that the vicinity of these precipitates must be depleted from these elements. It is known that Cr and Mo are the alloying elements which provide corrosion resistance to stainless steel, therefore the vicinity of these precipitates become vulnerable to intergranular corrosion.

Table 2. Compositional analysis

	316LSi	Matrix	Prec_5	Prec_7
Si	0.8	0.8	1.2	1.0
Mo	2.5	3.2	4.5	5.3
Cr	18.5	18.0	23.1	23.3
Mn	1.8	1.9	1.7	1.3
Fe	64.2	63.8	63.0	62.9
Ni	12.2	12.3	6.5	6.2

According to the results obtained from the single bead studies and multilayer metallographic analysis, optimized values are determined to be parameter set 7 and this parameter set is used for making a wall by WAAM to determine the mechanical properties. The wall is made up of 18 layers with a total of 12cm height and tensile test specimens were extracted from these walls in both longitudinal and transverse direction. In this context, the terms longitudinal direction and transverse direction is used for the direction parallel and perpendicular to the welding direction, respectively.

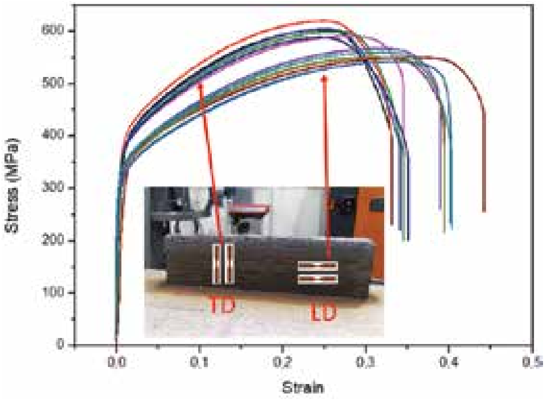

Figure 6. Tensile test results

Figure 6 shows the tensile test results of the wall with the parameters sample 7. First of all, the yield strength of both longitudinal and transverse direction are determined as nearly 300 MPa and they are very close to each other meaning that isotropic structure is achieved in terms of tensile properties. On the other hand, the elongations are greater in longitudinal samples. No premature failure is observed throughout the specimens. Secondly, Portevin Le-Chatelier effect, which is an indication of the interaction between solute atoms and dislocations, is observed in the samples tested in longitudinal direction. All samples in longitudinal direction exhibit serrated flow during plastic deformation range of tensile test. This is a sort of instability and may be prevented by homogenization heat treatment but it is the behind the scope of this study.

4. Conclusions

In this study, the effects of process parameters on the single and multi-bead structures are investigated. After the investigations in terms of geometrical, adherence and metallographic properties, a wall was produced with the optimized parameter set in order to determine the mechanical properties. With the optimized parameters, namely, WFS of 6 m/min and TS of 35 cm/min, a homogenous wall structure was achieved in terms of better mechanical properties. The yield strength is obtained as 300 MPa in both longitudinal and transverse direction of the wall.

Acknowledgement
This research is supported by Scientific and Technical Research Council of Turkey (TUBITAK) under 2244 program, through project No: 118C097.

References

[1] M. Dinovitzer, X. Chen, J. Laliberte, X. Huang, H. Frei, Additive Manufacturing, 26 (2019) 138-146.
[2] O. Yılmaz, A. Ugla, The International Journal of Advanced Manufacturing Technology, 89 (2017) 13-25.
[3] X.Xu, J. Ding, S. Ganguly, S. Williams, Journal of Materials Processing Tech., 265 (2019) 201-209.
[4] J. Wang, X. Lin et al., Journal of Alloys and Compounds, 768 (2018) 97-113.
[5] C. Marinelli et al., Journal of Nuclear Materials, 522 (2019) 45-53.
[6] J. Ge, J. Lin, Y. Lei, H. Fu, Materials Science & Engineering A, 715 (2018) 144-153.
[7] W. Ou et al., International Journal of Heat and Mass Transfer, 127 (2018) 1084-1094.
[8] O. Yılmaz, A. Ugla, Arabian Journal for Science and Engineering, 42 (2017) 4701–4711.
[9] J.L. Prado-Cerqueira, J.L. Diéguez, A.M. Camacho, Procedia Manufacturing, 13 (2017) 895-902.

Comparison of Mechanical and Microstructural Properties of AISI321 Alloy after ESR and ESR+VAR Processes

Sertaç ALPTEKİN, Ömür Can ODABAŞ, Kaan DEMİRALAY, Lütfi YAKUT, Bülent BAHADIR, Havva KAZDAL ZEYTİN

Materials Institute of Marmara Research Center of The Scientific and Technological Research Council of Turkey

Turkey

Abstract

In this study, fabrication of AISI321 austenitic stainless steel was aimed by using Electro slag Remelting (ESR) and Vacuum Arc Remelting (VAR) furnaces. AISI321 electrodes were produced by using Vacuum Oxygen Degassing (VOD) furnace for remelting processes. First experimental group includes just remelting of AISI321 in ESR furnace without any heat treatment application. The second group was remelted in VAR furnace after the ESR process. After remelting processes no heat treatment was also applied on the second group. Samples were extracted from 8 different regions from ingots obtained from both experimental groups. Metallurgical investigations were carried out by applying sample preparation processes for metallographic sample preparation and mechanical testing to remelted samples. Tensile experiments were carried out at room temperature using parameters 120N preload, 0,0067 s^{-1} strain rate in Zwick Z600 device. Effects of ESR and ESR+VAR applications were investigated on AISI321 alloy, both microstructural and mechanical properties.

1. Introduction

AISI 321, popular member of austenitic stainless steel family for aerospace industry, provides superior performance even at between 425 and 800ºC by its microstructure balanced with titanium. In addition to having high-temperature oxidation resistance as well as resistant to intergranular crack thanks to its structure that prevents chromium carbide precipitation [1,2,3,4]. Especially jet engine applications, AISI321 meets the mechanical requirements of strict technical specifications at elevated temperatures. For specialty steel and alloys producing, researchers conscious of the shortcomings of the conventional methods of ingot casting. Undesirable characteristics of conventionally cast ingots such as axial unsoundness, segregation, coarse crystal structure, high non-metallic inclusion content, higher gas content, and porosity affect mechanical properties. To improve product performance especially alloy steels intended for critical applications, consumable electrode remelting processes are often applied. Two methods widely used for this purpose are Vacuum arc remelting (VAR) and Electroslag remelting (ESR) [5,6].

Table 1. Composition of AISI321 grade stainless steel in weight percentage [7]

C	**Mn**	**P**	**S**	**Si**
max. 0,08	max. 2,0	max. 0,045	max. 0,030	max. 0,75
Cr	**Ni**	**N**	**Ti**	**Fe**
17,0-19,0	9,0-12,0	max. 0,10	5x%C+N-0,70	bal.

Both ESR and VAR furnaces use high ampere during remelting process with different power sources. While alternative current (AC) source is used in ESR, source of VAR furnace is direct current (DC). Also, electrode is remelted under vacuum in VAR furnace but electroflux or slag is used in ESR process. Therefore, different elements is refined in ESR and VAR furnaces. Elements with high vapor pressure like Lead, Bismuth, Manganese and Cupper and gaseous elements as Hydrogen, Nitrogen and Oxygen can be removed by evaporation during VAR process. However, in ESR process, elements with high oxygen affinity, Aluminum, Titanium, Sulphur etc. is refined by using proper slag. To prevent removal of desired elements like Al and Ti used in alloys that improves mechanical strength, chosen of suitable slag is very significant due to composition of the alloy. [8,9]

In the end of both processes, remelted ingots have lower impurities, and macro- and micro-segregations than conventional melting methods. However, ESR and VAR processes are slightly different in homogeneity and cleanliness level. While ESR process shows good performance on cleanliness and segregation level, performance of VAR process is better than ESR process [9, 10]. Therefore, especially in aerospace application VAR uses as the final step after ESR for refining but some other applications, like off-shore and chemical, the last process becomes ESR.[9]

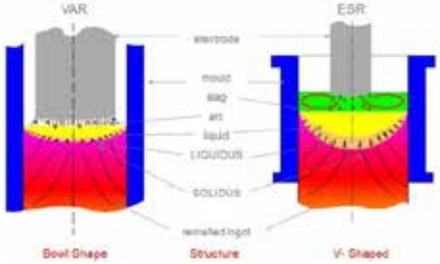

Figure 1. Schematic of remelting processes[9]

There are a lot of studies on properties of remelted steels and stainless steels in literature whereas any studies on remelted AISI321 stainless steel could not found. So in this study, focusing on examination and comparison of metallurgical properties of AISI321 was the main purpose after two different remelting techniques, ESR and VAR.

2. Experimental Procedure

In the experimental set, first AISI321 electrodes were casted in Vacuum Oxygen Decarburization (VOD) furnace by AKDAŞ Casting Industry. Then, two ingots were remelted in Electro Slag Remelting (ESR) furnace (ALD Vacuum Technologies GmbH) by using electroflux with composition of 38% CaF_2, 30% Al_2O_3, 26% CaO and 2,5% MgO. After ESR process, one of the ingots remelted in Vacuum Arc Remelting (VAR) furnace (ALD Vacuum Technologies GmbH) under vacuum of 10^{-3} mbar. In both ESR and VAR processes, working ampere was 6 kA but different melt rates, 1,5 and 2,0 kg/min.

Figure 2. Schematic diagram of remelting stage of ESR and VAR processes

2.1. Chemical analysis

To determine the changes in composition after remelting processes, carbon and sulfur were analyzed for both VOD, ESR and ESR+VAR samples via Horiba EMIA-820V Carbon/Sulfur analyzer. Also, Eltra ONH 2000 was used for nitrogen and oxygen analysis.

2.2. Sample preperation

After remelting processes, both two ingots were cut as a disk shape from start phase and last stages of melting phase (**Figure 2**). Four specimens, which were located from center to surface (**Figure 3**), were cut and prepared for microstructural examination. Traditional methods for metallographic examination were applied, and samples were examined after polishing. Electrolytic etching method was applied on sample in solution of glycerin (25 ml glycerin + 15 ml HCl + 10 ml HNO_3). Both polished and etched samples were examined under Olympus BX53M optical microscope and by using JEOL 6510-LV JSM Scanning Electron Microscope (SEM) etched samples were analyzed with EDS (Oxford Instrument).

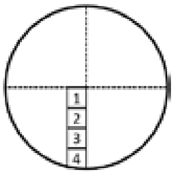

Figure 3. Specimens for the microstructural examination

2.3. Hardness testing

Brinell Hardness testing were applied on five different regions of the same four samples with 2,5 diameter ball under 31 kg load according to ASTM E10 by using EMCO-TEST M5C 030 universal hardness testing equipment.

2.4. Tensile testing

For tensile testing both ESR and ESR+VAR ingots were cut as cylindrical shape from the same regions. Then five samples were taken out from the two regions that means samples were extracted in total 8 different region from the remelted ingots. Tensile testing were carried out under 120N preload with 0,0067 s^{-1} strain rate at room temperature in Zwick Z600 device according to ASTM E8.

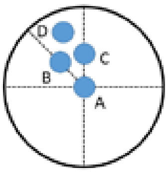

Figure 4. Sections of tensile test specimens taken from remelted ingots

3. Results and Discussion

3.1. Chemical composition

Results of Carbon, Sulfur, Nitrogen and Oxygen analysis were given in **Table 2**. As can be seen from the results, Sulfur was refined during ESR process. Amount of Nitrogen and Oxygen was decreased because of the vacuum in VAR furnace but there was no removal of Sulfur. In addition, after both two processes, Carbon was not removed from the alloy and amount of carbon did not changed.

Table 2. Results of C-S analysis in percentage and N-O analysis in ppm

	C (%)	S (%)	N (ppm)	O (ppm)
After VOD	0,0415	0,0025	56,705	14,960
After ESR	0,0440	0,0005	95,504	19,280
After ESR+VAR	0,0439	0,0002	87,525	7,675

3.2. Microstructure

After sample preparation, three different phases were observed in both start and melting regions of ESR and ESR+VAR samples as seen **Figure 5.e**. One of them had gold color and rectangular shape (Phase1). The second one had dark grey color (Phase2) while the third one were seen black color (Phase3). Both Phase2 and 3 have looked like lying on grain boundaries. Both start and melting regions of ESR and ESR+VAR samples were very similar to each other, and microstructures of both ESR and ESR+VAR samples had no big differences.

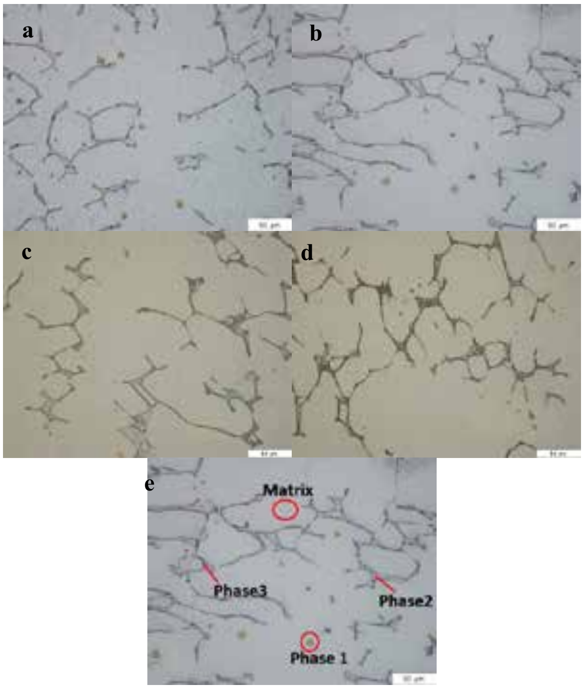

Figure 5. Etched images of specimens from start **(a)** and melting **(b)** regions of ESR ingot, and start **(c)** and melting **(d)** regions of ESR+VAR ingot, **(e)** phases

According to the EDS analysis result of both ESR and ESR+VAR samples, matrix were most probably austenite with Fe, Cr and Ni due to compatibility with composition of AISI321 (**Table 1**) as expected. Phase1 had consists of mainly Ti and N after both ESR and VAR so it could be Titanium Nitride as observed by Liu and his colleagues (2020) [11]. Also, Phase1 had typical appearance of Titanium Nitride which is cold colored and rectangular shaped (**Figure 5**) [12]. However, ESR+VAR samples contained 0,11% Titanium Nitride in start region and 0,13% in melting region while start and melting region had 0,25% and 0,20% after ESR. The reason of this differences was lower N content of VAR sample due to refining ability. Phase2 of ESR and ESR+VAR samples were rich in Cr and Fe like delta ferrite which is produced during solidification due to high Cr content of the alloy [12]. Furthermore, Phase3 might be an intermetallic phase mainly consists of Fe, Cr and Ti, after ESR process and there was no big change in composition after VAR process.

After SEM analysis, delta ferrite content were calculated under optical microscope and compared with Schaeffler diagram (**Figure 6**). First to determine the percent of delta ferrite of AISI321 from the diagram, Cr and Ni equivalent were calculated as 19,06% and 13,11% by using Eq1 and Eq2. Equivalent values have shown that delta ferrite should be 2-4% according to the Schaeffler diagram. Distribution of delta ferrite was determined 3,6% and 4,2% in start and melting phase of ESR ingot. On the other hand, after VAR process samples had 6,2% and 7,7% in start and melting region. These results proved homogenization effect both ESR and VAR processes but delta ferrite percent increased after VAR process.

$$Cr_{(eq)}=\%\,Cr+\%Mo+\%1.5Si+0,5\%Nb \qquad (1)$$
$$Ni_{(eq)}=\%Ni+0,5\%Mn+30\%C+30\%N \qquad (2)$$

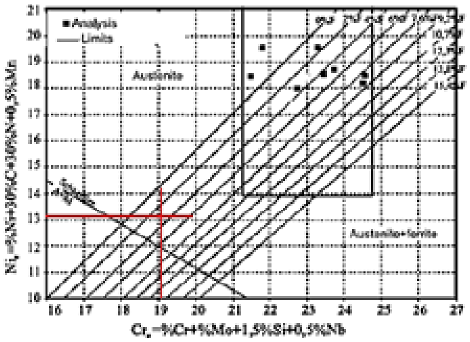

Figure 6. Schaeffler diagram [13]

3.3. Hardness

Hardness values taken from melting regions of both process routes were given at **Table 3**. Comparasion of Brinell hardness values for each sample, melting phase values were higher than start phases due to higher delta ferrite content. Reason of this difference between two regions might be slower cooling rate in start phase. Moreover, after VAR hardness of samples enhanced according to ESR samples for both two regions because of increased amount of delta ferrite.

Table 3. Average results of Brinell hardness testing after ESR and ESR+VAR processes

	After ESR		**After ESR+VAR**	
Sec	**Start phase**	**Melting phase**	**Start phase**	**Melting phase**
1	89,42	97,90	92,20	108,60
2	92,30	93,40	95,40	111,30
3	92,38	102,66	97,40	108,30
4	94,80	95,62	90,90	98,70
Avg	92,2±2	97,4±4	94±3	106,7±6

3.4. Tensile testing

According to the tensile test results given in Table 4, although elongation and yield strength of ESR+VAR samples had more homogeneous distribution and higher % reduction in area than ESR samples, ESR samples had higher yield and tensile strength, and were elongated more than VAR specimens. Elongation, yield and tensile strength results were parallel to test results of 4340 steel reported by Prengamon (1975) [6] except % reduction area. For 4340 steel, cross-section area of ESR sample has more reduced than that of VAR sample.

In addition, as expected there was no significant differences between start and melting phase of both process routes because both ESR and VAR processes provides more homogeneous structure due to direct and controlled solidification. [8]

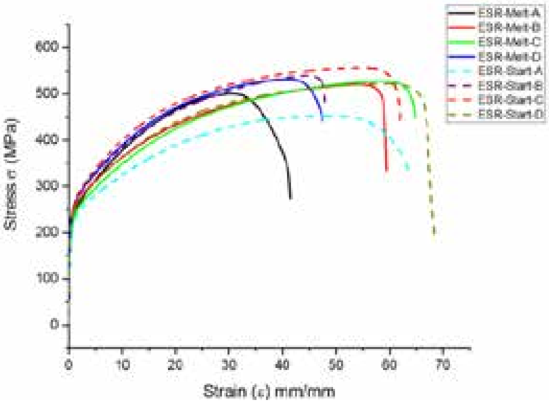

Figure 7. Stress-Strain curves for ESR samples

As shown at **Figure 7** max UTS value was obtained from start region of ESR process (ESR Start-C) and maximum elongation was obtained from D section of ESR start region.

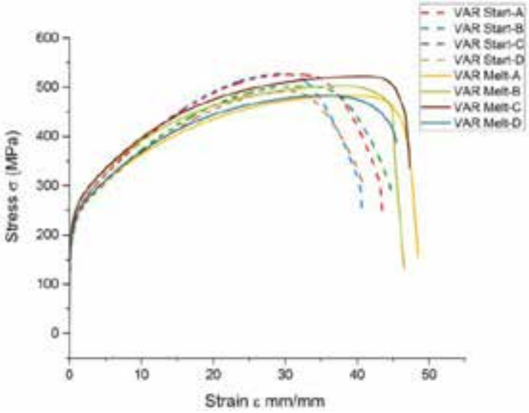

Figure 8. Stress-Strain curves for ESR+VAR samples.

As shown at **Figure 8** Maximum UTS value was obtained from start phase of VAR process (VAR Start-B) and maximum elongation was obtained from melted phase of VAR process (VAR Melt-A).

Table 4. Yield strength, tensile strength, % elongation and % reduction in area results of tensile testing

After ESR								
	Start Phase				Melting Phase			
Sec	$R_{0.2}$ (MPa)	R_e (MPa)	ε (%)	RA (%)	$R_{0.2}$ (MPa)	R_e (MPa)	ε (%)	RA (%)
A	187	452	63,3	70,2	189	500	41,2	73,2
B	217	539	47,8	50,4	201	520	59,3	54,7
C	218	556	61,7	55,0	188	527	64,4	53,6
D	208	521	68,3	51,8	213	531	47,3	64,2
Avg	207,5±14	517,0±46	60,0±9	56,9±12	197,8±12	519,5±14	53,0±11	61,0±9
After ESR +VAR								
	Start Phase				Melting Phase			
Sec	$R_{0.2}$ (MPa)	R_e (MPa)	ε (%)	RA (%)	$R_{0.2}$ (MPa)	R_e (MPa)	ε (%)	RA (%)
A	188	526	43,2	74,9	194	483	48,3	61,9
B	198	527	40,4	61,8	201	503	46,5	60,0
C	190	502	44,3	70,3	210	522	47,1	58,6
D	185	492	40,4	70,5	187	483	45,2	70,5
Avg	190,0±6	512,0±18	42,0±2	69,0±6	198,0±10	497,8±19	46,8±1	62,8±5

4. Conclusion

In conclusion, as a result of comparison of two different remelting routes of AISI321 were;

- There was no microstructural differences in own regions of ESR and ESR+VAR processes.
- Microstructures of ESR and ESR+VAR samples consisted of similar phases but in different amounts.
- After VAR process amount of Titanium Nitride phase decreased according to ESR samples due to nitrogen refining during VAR process.
- Hardness of ESR+VAR samples were higher than ESR samples because of higher amount of delta ferrite.
- Also, melting regions of both processes was harder than start regions due to same reason.
- After ESR process, strength and elongation values were better than after VAR process due to lower brittle delta ferrite content.

For the future studies, detected phases in microstructures are going to be analyzed by XRD for phase determination, and comparison of microstructure and mechanical properties of as-cast, remelted and forged AISI321 ingots is going to be examined.

Acknowledgement

For supports and helps to all colleagues from Critical Metallic Materials Group of Materials Institute of TUBITAK Marmara Research Center, and project partners; TUSAŞ Engine Industry (TEI) and AKDAŞ Casting Industry & Trade Company and for financial support Presidency of Defence Industries of Turkish Republic.

References

[1] K. S. Guan, X. D. Xu, Y. Y. Zhang, and Z. W. Wang, Eng. Fail. Anal., 12 (2005) 623–633.

[2] G. Bhat, “Evaluation of the mechanical properties of a Electroslag Refained Iron Alloy,” Pittsburgh, 1976.

[3] Ugima, “Ugima®4541,” 2013. http://ugitech.com/uploads/ugitransfer/docs/GED_2410.pdf (accessed Apr. 29, 2020).

[4] Sandmeyer, “Specification Sheet : Alloy321/321H,” 2014.https://www.sandmeyersteel.com/images/Alloy321-SpecSheet.pdf (accessed Apr. 29, 2020).

[5] L. Thomas, A Comparison of The Microstructure and Mechanical Properties of 300-M Steel Manufactured by The Vacuum Arc Remelt and The Electroslag Remelt Processes, M.Sc. Thesis, University of California, 2011, USA

[6] M. Prengamon, “VAR and ESR: Do They Measure Up,” *DTIC Doc.*, 1975. pp. 2, 22.

[7] ASTM International, “A240/A240M – 12: Standard Specification for Chromium and Chromium-Nickel Stainless Steel Plate, Sheet, and Strip for Pressure Vessels and for General Applications 1,” *ASTM Int.*, 2012.

[8] R. C. Reed, The Superalloys fundamentals and applications. 2006.

[9] H. Scholz *et al.*, “STATE OF THE ART IN VAR AND ESR PROCESSES – A COMPARISON Harald Scholz, Ulrich Biebricher, Henrik Franz – ALD Vacuum Technologies, Hanau, Germany Alberto Paderni, Paolo Bettoni – ASO Siderurgica, Ospitaletto, Italy.”

[10] M. J. Donachie and S. J. Donachie, Superalloys: A Technical Guide. ASM International, 2008,

[11] Y. Liu, X. Wang, G. Li, X. Huang, Q. Wang, and B. Li, J. Mater. Res. Technol., 9 (2020) 1619–1630.

[12] ASM Metal Handbook Vol.9 Metallography and Microsturcture. ASM International, 1998.

[13] S. A. Gigović-Gekić, M. Oruč, and S. M. Gojić, “Determination of the content of delta ferrite in austenitic stainless steel nitronic 60, 15th International Research/Expert Conference Trends in the Development of Machinery and Associated Technology, 2011, pp. 157-160.

Improving the Thermal Stability of Laser Clad NiCrBSi Coatings

Natalia SOBOLEVA, Aleksey MAKAROV, Irina MALYGINA
Ural Branch of the Russian Academy of Sciences
Russia

Abstract

For laser clad NiCrBSi coatings, a significant decrease in hardness and wear resistance was found when heated to 900...950 °C. However, annealing at temperatures of 1000...1075 °C contributes to a sharp improvement in properties to levels corresponding or even exceeding the characteristics of the original coating formed by laser cladding. The structure formed in the process of annealing and subsequent cooling is thermally stable and, as a result, has increased hardness and wear resistance when heated up to the annealing temperature.

1. Introduction

Coatings made of wear-resistant NiCrBSi alloys are widely used to improve the quality of various products, including those operated under conditions of significant heating (rolls and roller tables in hot rolling mills, hot-press dies, walls of crystallizers of continuous casting machines, parts of heat exchangers, turbines, solid fuel boilers, etc.). However, heating to temperatures of 800...950 °C causes a softening of NiCrBSi coatings and a noticeable decrease in wear resistance [1]. In this regard, an important task is to find ways to improve the thermal stability of the structure and properties of NiCrBSi alloys.

2. Materials and Methods

NiCrBSi powder (wt.%: 16.0 Cr; 3.5 B; 4.0 Si; 0.80 C; ≤5 Fe; the rest is Ni) was used for cladding on a steel substrate in two passes. CO_2 continuous wave laser was used with the following parameters: wavelength 10.6 µm, power 1.4...1.6 kW, scanning speed 160...180 mm/min, laser beam shape 6.0×1.5 mm, powder feeding rate 2.9...4.9 g/min, carrier gas argon. The clad samples were post-treated by heating up in a range of 200...1050°C with subsequent cooling in air and in the furnaces.

3. Results

Annealing at temperatures of 1000...1075 °C contributes to a sharp improvement in properties to levels corresponding or even exceeding the characteristics of the original coating formed by laser cladding. This is due to the formation in the process of annealing and subsequent cooling of the high-strength wear-resistant frame of large chromium carbides and borides. The formed structure is thermally stable and, as a result, has increased hardness and abrasive wear resistance when heated up to the annealing temperature [2]. A decrease in the cooling rate from the annealing temperature can further significantly improve the wear resistance of the alloy. High-temperature annealing of the coating reduces by 1.8 times the wear intensity under sliding friction at sliding speeds of 6.1 and 9.3 m/s when the temperature of frictional heating of the surface layer reaches ~900 °C and above. The structure with large chromium borides and carbides formed as a result of annealing limits the development of the processes of heat seizure and plastic edging. It provides an increase in the frictional heat resistance of the NiCrBSi alloy.

4. Conclusion

Based on the discovered effect of increasing the mechanical and tribological characteristics of laser clad NiCrBSi coatings as a result of annealing, a new approach is proposed to improve the thermal stability of NiCrBSi alloys to temperatures of 1000 °C or more, including coating formation and subsequent high-temperature annealing at temperatures of 1000...1075 °C (RF patent No. 2492980). The proposed new approach expands opportunities for a high-temperature use of NiCrBSi alloys.

Acknowledgment

This work was financially supported by the Russian Science Foundation, project no. 19-79-00031.

References

[1] A. Makarov, N. Soboleva, I. Malygina and A. Osintseva, Metal Science and Heat Treatment, 57 (2015) 161-168.
[2] A. Makarov, N. Soboleva, I. Malygina and E. Kharanzhevskiy, Journal of Crystal Growth, 525 (2019) 125200.

Development of Fire-Resistant Wrought Mg-Zn- Y-Ca Alloys for Civil Aircraft Applications

Önder TUNA[1,2], Halil DEMİRTAŞ[1,2], Deniz Sultan AYDIN[1], Özgür DUYGULU[1], Havva KAZDAL ZEYTİN[1], Metin USTA[1,2], Youngkil JUNG[3], Wonseok YANG[3], Hyun Kyu LIM[3]

[1]TUBITAK MAM, Materials Institute, [2]Gebze Technical University, [3]Korea Institute of Industrial Technology (KITECH)

[1,2]Turkey, [3]Korea

Abstract

The use of magnesium alloys in civil aircraft has been banned to minimize the risk of passengers. Recently, the application of magnesium alloys to aircraft parts has been actively studied due to the development of fire-resistant magnesium alloys. In 2015, the Federal Aviation Administration (FAA) approved the use of magnesium alloys that meet FAA's flammability regulations by changing the regulations that prohibit the use of magnesium alloys in civil aircraft. Therefore, it is necessary to develop and study fire-resistant magnesium alloys which can satisfy the flammability regulation of FAA. In the present study, fire resistant wrought magnesium ZWX (Mg-Zn-Y-Ca) alloy system has been studied.

Introduction

The magnesium alloys have the lowest density among the structural alloys. High specific strength and stiffness, good castability and machining properties, good energy absorbance capacity, electromagnetic shielding property, effective heat dissipation makes magnesium alloys as one of the top candidates [1]. It is sixth most abundant metal and eighth element on the earth. Moreover, it is recyclable. Mg-Zn-Y alloys system attracted great interest from researchers [2]. The main aim of this study is to provide the use of light materials in civil aviation in order to reduce the consumption of fuel and energy, protect the limited fuel reserves and reduce to amount of CO2 gas emission which accelerates global warming. In this study, it is aimed to develop magnesium sheet alloys with high fire resistance in billet and sheet form for civil aviation.

Materials and Methods

Fire resistant wrought magnesium ZWX (Mg-Zn-Y-Ca) alloy system has been studied. By changing the element ratios of Zn and Y elements and by adding Ca element in different ratios, 10 different magnesium alloys were developed by gravity casting. Warm rolling was applied on six different alloys and 1 mm thick magnesium alloy sheets were achieved. Extrusion was performed on four different alloys and 8 mm diameter rods have been developed. Heat treatments such as homogenization, annealing and aging were also performed. The effect of Zn, Y and especially Ca on microstructure, mechanical properties and ignition temperature were investigated. Ignition tests were performed using differential thermal analysis (DTA) and also furnace heating. Calculation of fractional change of different phases were done by using JMatPro7 simulation software. Before and after all processes, detailed characterization studies such as x-ray diffraction (XRD), optical microscopy (OM) examinations, scanning electron microscopy (SEM) examinations and transmission electron microscopy (TEM) examinations were performed. Mechanical properties of the samples were determined by micro hardness and tensile tests.

Conclusion

As a result of microstructural examinations, it was observed that the addition of calcium partially reduced the grain size. It is observed that the addition of calcium significantly increases the ignition temperature of the alloys and the ignition temperature increased to above 915 °C. In extrusion alloys, UTS value has been reached to over 330 MPa and elongation value has been reached to 15-27%. For rolled alloys, UTS values were in between 280-330 MPa with elongation values of 5-26 %. These results indicate that these alloys have great potential in civil aircraft applications.

References

[1] Q. Tan, A. Atrens, N. Mo and M.X. Zhang, Oxidation of magnesium alloys at elevated temperatures in air: A review, Corrosion Science 112 (2016) 734-759.

[2] N. Tahreen and D.L. Chen, A Critical Review of Mg-Zn-Y Series Alloys Containing I,W and LPSO Phases, Advanced Engineering Materials 2016, 18, No.12.

The Effect of Heat Treatment on the Fracture and Micro-Mechanical Behavior of the Selective Laser Melted AlSi10mg

Ahmet Alptuğ TANRIKULU[1], Hakan YAVAŞ[1], Sertaç ALTINOK[1,2], Burcu ARSLAN HAMAT[1,2], Gülten KAFADAR[1,2], Mustafa GÜDEN[3]

[1]Turkish Aerospace Industries Inc., [2]Middle East Technical University, [3]İzmir Institute of Technology

Turkey

Abstract

Additive manufacturing (AM) can allow the production of intricate geometries in a single step, without requiring too many secondary processes which decrease the total production time and cost. While the use of AM-based innovative design solutions is limited in the aerospace industry where the material quality monitoring during processing and service is very strict, mainly due to very complex microstructure of the parts produced with AM. Since, the microstructure solely determines the physical and mechanical properties, it must be fully understood and controlled in order to standardize AM-produced parts for the aerospace industry.

1. Introduction

AM technologies delivers design engineers more space for their imagination and ensure complex and smart geometries. On the contrary it limits the analysis engineers since this technology is not fully understood and challenging to simulate. Moreover, the lack of standardization of AM as a manufacturing technology especially in aerospace industry make it complicate to apply this technology for real part and process applications. Heat treatment (HT) application for post processes is very important for aluminum alloys as the complementary process of the manufacturing. Since the microstructure of AMed metals are more complicated and instable compared to conventional manufactured metals post heat treatment applications should be well defined and correlate with mechanical properties for real aerospace applications.

2. Materials and Metals

All AMed coupons are fabricated in Selective Laser Melting (SLM) process by a proper energy density level. AlSi10Mg aluminum alloy is selected for material since its accessibility in the AM market. Fatigue testing applied to coupons acc. ASTM E466-15 standard and continuous radius sample dimensions selected for the tests. Microstructure of the fracture surface evaluated for crack initiation regions and fatigue properties in order to correlate mechanical behavior with microstructure.

3. Conclusion

Fatigue properties according to different HT applications were examined and the optimum HT application were investigated for the components that are exposed to cyclic loading conditions during service lifetime. Fracture surfaces of fatigue samples provides for HT effect on material.

Acknowledgement

Authors would like to inform that this study is financed fully by TUBİTAK in the scope of TÜBİTAK 1515 Frontier R&D laboratory support program. Authors also would like to record their appreciation to institutions which are Additive Manufacturing Technology Application and Research Center (EKTAM) for manufacturing processes, METU Welding Technology and NDT Research/Application Center (WTNDT) for testing applications and Bilkent University National Nanotechnology Research Center for SEM applications. In order to learn for more details about the project, please apply/refer to Turkish Aerospace Inc.

Validation of Important Simulation Parameters to Predict Porosity Defects in ALSI12 Casting

Muharrem AKKAYA[1], Nuri DURLU[1], M. Akif ŞAHİN[2], M. Bülent ÖZER[2], Yiğit TAŞÇIOĞLU[3]
[1]TOBB University of Economics and Technology, [2]Middle East Technical University,
[3]TED University

Turkey

Abstract
In this study, important simulation parameters were examined to understand their effects on porosity prediction after casting. Examined parameters include initial mold temperature, critical solid fraction, coherency, and shrinkage rate. Simulations with initial mold temperatures at 25°C, 300°C, and 700°C were run. An optimum parameter set was found for critical solid fraction, fraction of solid at coherency, and shrinkage rate parameters. FLOW-3D® CAST simulation software was used to model the filling and solidification of the alloy during casting. Stainless steel tube was used as a mold to validate the simulation results. Casting experiments conducted with 0.165 kg AlSi12 alloy at 710°C. Obtained specimens were sectioned to compare the macroporosity distribution with simulation results. The comparison of simulation results and experimental work showed that porosity formation is highly affected by initial mold temperature, critical solid fraction, and shrinkage rate parameters.

1. Introduction

Metal casting involves a range of dynamic physical processes which is difficult to predict. Numerical simulation tools are broadly used to describe the physics involved like the flow of molten metal, heat transfer, and solidification. They also help to reduce the cost and time spent during mold design and validation by keeping the process in a computer environment. Furthermore, a better understanding of the parameters affecting the defects that occur in a casting process is possible by computer tools.

Along with the industry, researchers were also utilized numerical simulation tools in casting for design optimization. Several researchers offered improvements on the existing permanent mold designs to improve the mechanical properties of gravity die casting[1–3]. However, primary importance in design optimization studies, where a numerical simulation is employed, is to enter the material properties and simulation parameters accurately. These can either be obtained from literature or determined by validation experiments.

In this study, FLOW-3D® CAST (Version 5.0; 2019; https://www.flow3d.com; Flow Science, Inc.) numerical simulation software was used to examine the important simulation parameters. The goal of the study is to obtain a set of parameters affecting the porosity prediction in AlSi12 casting by validating the simulation results with experiments.

2. Experimental Procedure

A simple geometry that does not have sprues, runners, and feeders, will reduce the complexity of the problem, especially in the filling simulations. Also, it will give the advantage of easily and quickly conduct experiments and validate simulation results. A stainless steel tube was considered as a relatively inexpensive mold that only requires a stopper piece and threading to become a gravity die casting mold. It was possible to easily heat the mold to elevated temperatures with a coil heater. The stainless steel tube mold and heater coil are given in Figure 1.

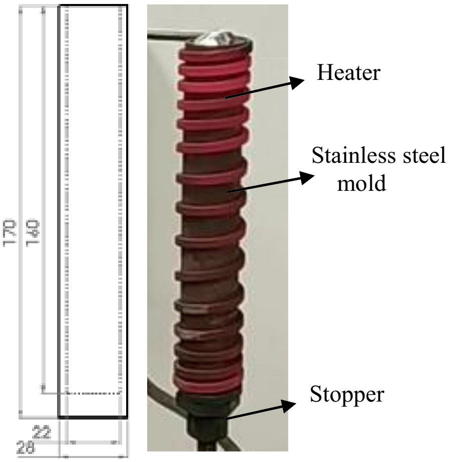

Figure 1. Stainless steel mold and heater coil.

AlSi12 alloy was chosen as casting material because of its extensive use in the automotive and defense industry. Also, it was one of the easiest alloys to find material properties that are critical for an accurate simulation. As a low cost and available material, 4140 steel was selected as mold material instead of high-grade mold steels commonly used in the industry.

Experiments were conducted by preheating the mold up to 700°C. An electric furnace was employed to melt the alloy. The pouring temperature was 710°C.

2.1. Material properties

A critical factor for an accurate casting simulation is the material properties. FLOW-3D® CAST comes with a database of materials for casting and mold materials. But for the best accuracy, some of the material properties like density, solidus and liquidus temperatures were determined experimentally. Other parameters were employed from the literature.

During casting, heat is transferred from the liquid metal to the mold so that the solidification can take place. The crucial factor which affect the solution of heat transfer equations is the thermophysical properties of casting and mold material [4]. The material properties obtained from the literature were given in Table 1.

Table 1. Thermophysical Properties of AlSi12alloy.

	Liquid	**Solidified**
Density *[kg/m^3]*	2600	2700
Specific heat *[J/kg/°C]*[5]	Tabular	963
Thermal Conductivity *[W/m/°C]*[6]	Tabular	178
Thermal expansion coefficient *[1/°C]*[7]	2,2e-05	2,2e-05

2.2. Solidification parameters

Critical solid fraction (CSF) and fraction of solid at coherency (FSC) parameters are used in the solidification model to determine the drag and viscosity. A solid fraction value between FSC and CSF values indicates that flow is in the mushy zone. In this region, the drag is a function of solid fraction. When the solid fraction exceeds CSF value then drag becomes infinite which means the motion of liquid/solid mixture is blocked[8]. The relationship between the fluid motion, solid fraction, and drag is expressed schematically in Figure 2.

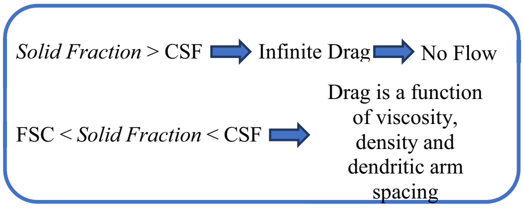

Figure 2. The relationship between the fluid motion, solid fraction, and drag.

Shrinkage adjustment parameter is a multiplication coefficient for volume change during solidification. If this value is greater than unity more shrinkage takes place than computed from the density difference between the solid and liquid phases. Since this parameter plays an important role in the amount and location of the porosity caused by volume change, it was validated through experiments by sectioning and examining the macroporosity locations.

3. Results and Discussion

Different initial mold temperatures and solidification parameters were simulated for a better understanding of the software and the casting material. The effect of initial mold temperatures on porosity formation was agreeable to common casting knowledge. Results of the solidification parameter runs were validated through experiments by comparing sectioned specimens.

3.1. Initial mold temperature

The effect of initial mold temperature on porosity formation examined by a simulation series with the mold pre-heated to 25°C, 300°C, and 700°C.

The black spheres that appear in the filling simulation results, given in Figure 3, represent the entrained air during filling. Entrained air is one of the main reasons for the formation of porosities during casting.

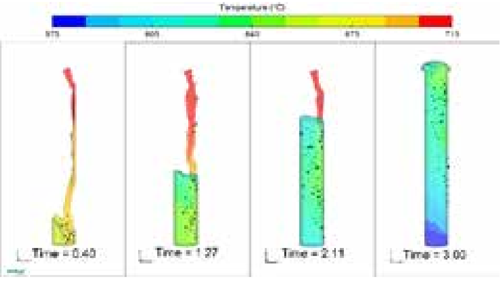

Figure 3. Filling simulation results with respect to time.

The solidification time is shown by the color scale in Figure 4.a-b-c. In the 25°C case, solidification occurs quickly and starts from the inner surface of the mold homogenously. When the mold temperature was 300°C solidification starts from the bottom of the mold and ends up at the top by lasting approximately 180 seconds. However, in the 700°C pre-heated case, the last solidified middle section of the metal stays as liquid up to 800 seconds.

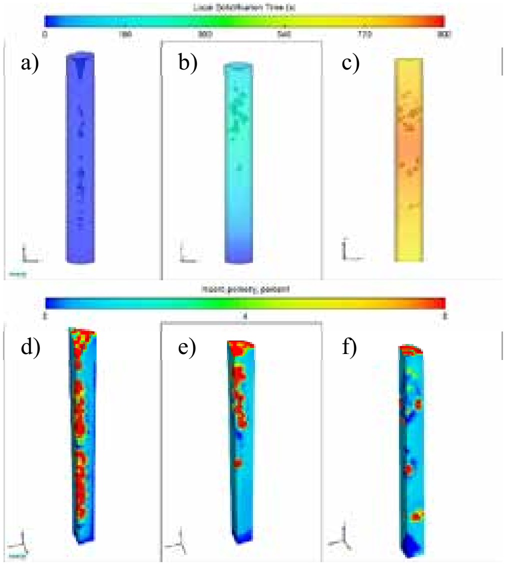

(I) (II) (III)

Figure 4. Solidification time and porosity distribution with respect to mold temperature (I) 25°C (a and d) (II) 300°C (b and e) and (III) 700°C (c and f)

To better observe the porosity distribution 4.d-e-f shows ¼ of the casting as sectioned. It is well known that porosity occurs in the last solidified portion of the casting. For a cold-wall cylindrical mold, porosity is expected to occur in the center region. Because the melt near the relatively cold mold walls quickly starts to solidify. During solidification high-temperature liquid in the center of the casting is absorbed to accommodate the shrinkage caused by the volume change. Thus, a porosity region occurs in the center. In the 25°C case, the simulation was able to predict the porosity in the expected region. Again, in the 300°C pre-heat case, porosity formed at the last solidified region for the same reason. Since, in the 700°C pre-heat case, the solidification rate is uniform throughout the casting, porosity formed relatively uniform in the radial and longitudinal axes of the mold.

3.2. Critical solid fraction

Literature review and simulation studies showed that CSF and shrinkage rate parameters are highly related to the location and the number of porosity in the casting[9–11]. Simulation results for CSF = 0.5, 0.8, 1(Shrinkage Adjustment Parameter = 1) are given in Figure 5. Comparing the experiment and simulations, a CSF value between 0.8 and 1 is proper to meet the location of the porosity.

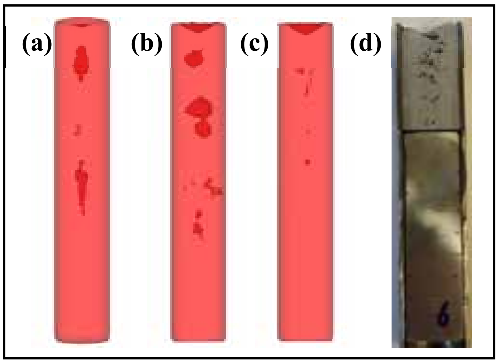

Figure 5. Simulation results with different CSF values (a to c) and sectioned specimen (d) . CSF is (a) 0.5, (b) 0.8, (c) 1, (d) experiment.

3.3. Shrinkage adjustment parameter

A shrinkage adjustment parameter range can be determined by holding CSF constant. Results for the shrinkage adjustment parameter runs are given in Figure 6. It is concluded that a value between 2-3 for the shrinkage adjustment creates excessive shrinkage. So a range between 1-2 is most reasonable.

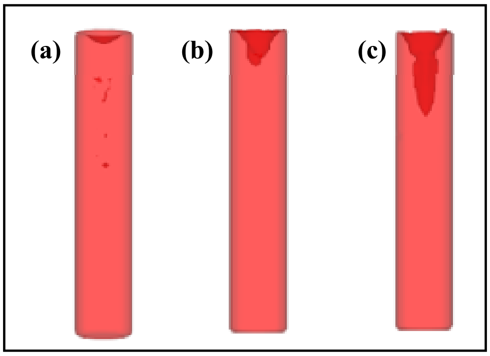

Figure 6. Simulation results with different shrinkage adjusment parameter, (a) 1, (b) 2, and (c) 3.

3.4. Fraction of solid at coherency

The fraction of solid at coherency is another important parameter affecting the defect formation during solidification. Coherency point is defined as the fraction of melt that starts to act as a coherent structure. Figure 7 shows simulation results of FSC point parameter taken as 0.2, 0.5 and 0.75 respectively.

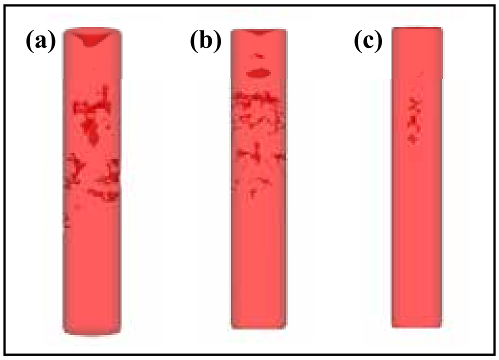

Figure 7. Simulation results with different FSC values. The FSC is (a) 0.2, (b) 0.5, (c) 0.75.

By further tuning these parameters together with refined mesh, a parameter set is obtained as 1.1, 0.35 and 0.9 respectively for shrinkage adjustment, FSC, and CSF. With an additional refinement in the mesh size, the model was able to predict the porosities on the surface of the casting. The simulation results are given in Figure 8.

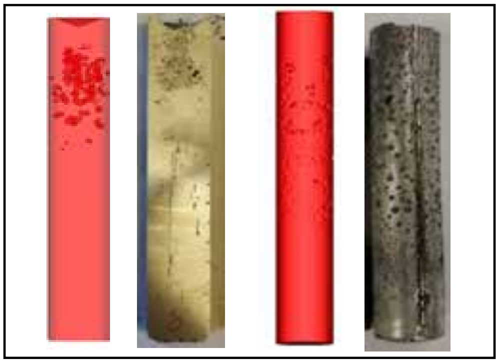

Figure 8. Validation of parameter set and a comparison of the surface porosity with refined mesh.

4. Conclusion

Initial mold temperature, critical solid fraction, the fraction of solid at coherency, and shrinkage adjustment parameters were defined as important simulation parameters to predict porosity formation of gravity die casting of AlSi12 alloy. A value range was determined for parameters by validating simulation results through casting experiments. Short simulation run times and quickly conducted experiments were achieved thanks to the selection of very simple mold geometry.

Acknowledgements

This research is financially supported by TUBITAK (The Scientific and Technological Research Council of Turkey) 1003 Program under grant 315M438. We would like to acknowledge Azim Turan from IOG Engineering for his helps in the use of FLOW-3D® CAST program at the initial stages of this work.

References

[1] Wang, Y., Schwam, D., Neff, D. V., Chen, C.-J., and Zhu, X., Metall. Mater. Trans. A, 43(3) (2012) pp. 1048–1059.

[2] Timelli, G., Capuzzi, S., and Bonollo, F., Metall. Mater. Trans. B, 46(1) (2015) pp. 473–484.

[3] Birsan, G., Ashtari, P., and Shankar, S., Int. J. Cast Met. Res., 24(6) (2011) pp. 378–384.

[4] Hines, J. A., Metall. Mater. Trans. B, 35(2) (2004) pp. 299–311.

[5] Rauta, V., On the effect of heat and metallurgical treatments on the thermal conductivity of cast aluminium alloys, PhD Thesis, Aalto University, 2015, Helsinki, Finland.

[6] Brandt, R., and Neuer, G., Int. J. Thermophys., 28(5) (2007) pp. 1429–1446.

[7] Stadler, F., Antrekowitsch, H., Fragner, W., Kaufmann, H., Pinatel, E. R., and Uggowitzer, P. J., Mater. Sci. Eng. A, 560 (2013) pp. 481–491.

[8] "Flow Science, Inc., Santa Fe, NM, USA. 'FLOW-3D® Cast Help Documentation.' (2018) [Online]. Accessed on: March, 3, 2020."

[9] Kayikci, R., Colak, M., Sirin, S., Kocaman, E., and Akar, N., Mater. Tehnol., 49(5) (2015) pp. 797–800.

[10] Akar, N., Kayikci, R., and Kisaoğlu, K., (2014) pp. 83–89.

[11] Barkhudarov, M. R., "Computer Modelling of Solidification of Pure Metals and Alloys," PhD Thesis, The University of Sheffield, 1995, Sheffield, England.

The Effect of Casting Temperature and Withdrawal Rate on Laue Misorientation in CMSX-4 SLS Single Crystal Turbine Blade Production

Serra BAYRAM, Ecem ANNAŞLI, Furkan Ferhat BONCUK, Sertaç ALPTEKİN, Lütfi YAKUT, Ömür Can ODABAŞ, Havva KAZDAL ZEYTİN

TUBITAK Marmara Research Center

Turkey

Abstract

CMSX-4 SLS is a single crystal castable nickel-based super alloy widely used in the aerospace industry because it exhibits high mechanical properties such as creep resistance in high temperature applications. One of the most important parameters in single crystal materials is the misorientation of dendrites. This parameter, also called Laue misorientation, is of vital importance. The angle of deviation (alpha angle) from the solidification direction is the Laue misorientation angle and should be of the minimum extent. Because as the deflection angle increases, the mechanical properties are seriously affected negatively. In this study, two main parameters affecting Laue misorientation were examined. These are casting temperature and withdrawal rate. The effect of withdrawal rate of 3 mm/min, 4.3 mm/min and 5 mm/min on the alpha angle was examined at casting temperatures of 1540 °C and 1560 °C degrees. The effect of different withdrawal rates on the alpha angle at 1560 °C constant casting temperature was also investigated.

1. Introduction

CMSX-4 SLS alloy is a second-generation nickel-base single-crystal super alloy containing wt. %3 percent (wt.) rhenium (Re) and 70 percent volume fraction of the coherent γ′ precipitate strengthening phase [1,2,3]. It stands out with its creep resistance and high strength. Rhenium (Re) addition does not only benefit creep and mechanical fatigue strength but also known to benefit oxidation, hot corrosion and coating performance [4,5]. This alloy is used in the hot areas of gas turbines in the aviation field, especially in turbine blades and turbine discs, areas exposed to high temperatures [6].

The most basic method for defining the orientation in single crystal castings is the Laue method. The Laue method provides information about the structure of a 1.5 mm area. If a molybdenum X-ray source (tube) is used, Laue diffraction should be done on polished and chemically etched surfaces. Laue scatter indexing is performed using the lattice parameters of the phase under study [7]. Testing details indicated in ASTM E82 standard. The maximum alpha angle value generally valid in the aviation industry is 15 degrees, and the blades whose alpha angle exceeds this value are classified as scrap [8,9].

Onyszko et. al. (2010) carried out the study that the alpha angle was measured by dividing the blade into the cross-sectional areas. The sections they used are shown in **Figure *1*** [10]. They state that Laue misorientation measurement can be made from many areas of the turbine blade. The deviation of dendrites formed in this way depending on the height can be controlled.

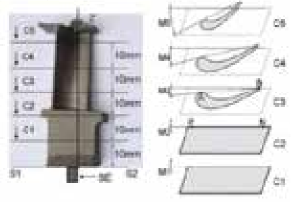

Figure 1. Diagram of cutting of single-crystal blades: C1, C2, C3, C4 and C5 section.

2. Experimental Procedure

In this study, CMSX-4 SLS nickel-based super alloy is used as an alloy. Casting was made by Bridgman method in ALD VIM-IC 10 vacuum induction furnace.

Initially, castings were made in fixed blade geometry at temperatures of 1540 °C and 1560 °C degrees at 3 mm/min, 4.3 mm/min and 5 mm/min withdrawal rates. 3 different withdrawal rates were applied for each casting temperature. Afterwards, castings were made at a fixed casting temperature of 1560 °C at 3 mm / min, 3.5 mm / min, 4.3 mm / min and 5 mm / min withdrawal rates, and alpha angle was measured by Laue XRD method.

Misorientation measurements were made on the cast parts with the Laue XRD method in the Proto Manufacturing Laue-COS device was used for measurement.

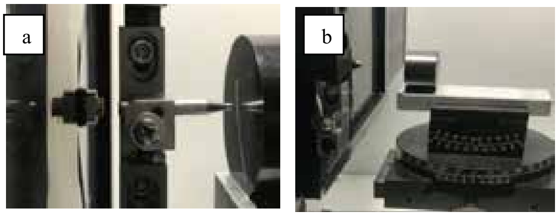

Figure 2. a) accurate positioning of the sample with the detector needle b) removing the needle and making it ready for analysis

Measurement was made with 40 kV voltage and 30 mA current in Laue XRD device. The measured deflection angles (alpha angle) are recorded. The dendrite orientation patterns of the cast parts are placed on the single crystal silicon references pattern and the alpha angle is determined.

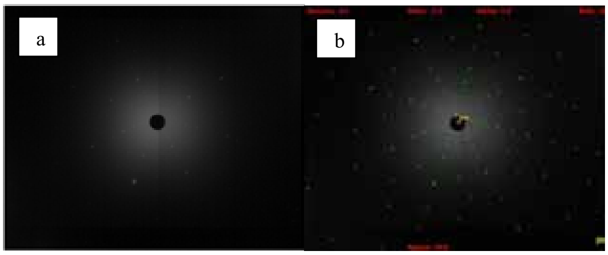

Figure 3. Laue XRD analysis visual of samples a) pattern traces of the sample b) Deflection angle values obtained by placing reference positions on the sample and its appearance

3. Results and Discussion

The graph below shows the effect of different casting temperatures and different withdrawal rates on alpha deflection angle. The alpha angle is similar at a casting temperature of 1540 °C degrees and withdrawal rates of 3 mm/min, 4.3 mm/min and 5 mm/min. Especially the withdrawal rates of 4.3 mm/min and 5 mm/min are almost the same (8.41 and 8.48, respectively). In addition, it was observed that as the casting temperature increased, the alpha angle values corresponding to all withdrawal rates decreased. The biggest reduction is in the withdrawal rates of 5 mm / min and the alpha angle is 3.5. It is clear that the casting temperature of 1560°C degrees is more optimum in terms of alpha than the casting temperature of 1540°C degrees.

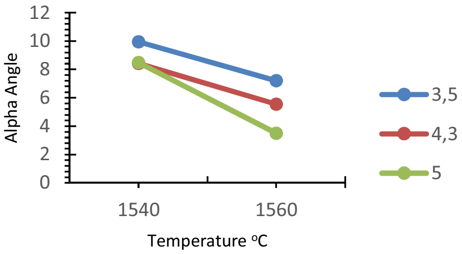

Diagram 1. Effect of Withdrawal Rate and Casting Temperature on Alpha Angle

The alpha angle values for withdrawal rates of 3 mm/min, 3.5 mm/min, 4.3 mm/min and 5 mm/min at a casting temperature of 1560 °C degrees are given in the graph below. Looking at the graph, the alpha angle value decreases dramatically while the withdrawal rate increases at the optimum casting temperature of 1560 °C degrees. Based on the alpha value at a casting temperature of 1560 °C degrees, the optimum withdrawal rate can be said as 5 mm/min.

Kubiak et. al. (2015) examined that the effect of different withdrawal rates up to 1-5 mm/min on the alpha angle in study The Unidirectional Crystallization of Metals and Alloys (Turbine Blades). According to the study, as the withdrawal rate increases (closer to 5 mm/min), the alpha angle decreases [4]. Obviously, the data obtained in our study confirm their conclusions.

Table 1. Effect of Withdrawal Rate (mm/min) on Alpha Angle at 1560 °C Casting Temperature

Withdrawal Rate (mm/min)	Alpha Angle (°)
3	7.53
3.5	7.20
4.3	5.55
5	3.50

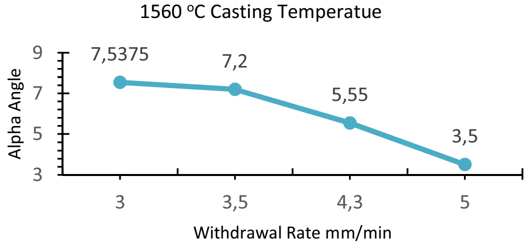

Diagram 2. Effect of Different Withdrawal Rate on Alpha Angle at 1560 °C Degree Casting Temperature

4. Conclusion

In this study, the effect of casting temperature and withdrawal rate on alpha angle on single crystal CMSX-4 SLS turbine blade material was investigated. Measurements were made using the Laue XRD method.

At a casting temperature of 1540 °C degrees, the alpha angle values are similar at withdrawal rates of 3 mm/min, 4.3 mm/min and 5 mm/min. When the casting temperature is increased from 1540 °C degrees to 1560 °C degrees, the alpha angle values decrease for three different withdrawal rates. In addition, when the withdrawal rate of 5 mm/min, the decrease in alpha angle value is more than the others. For this reason, the effect of withdrawal rates on alpha angle values at a fixed casting temperature of 1560 °C degrees was investigated separately.

In 4 different withdrawal rates studies conducted at a fixed casting temperature of 1560 °C degrees, it is clearly seen that as the withdrawal rates increases, the alpha angle value decreases and the lowest value was found at 5 mm / min withdrawal rate as alpha angle 3,5°. As a result, to determine optimum casting temperature for CMSX-4 SLS single crystal turbine blade production, Laue misorientation angle (alpha) is a parameter effect the scrap ratio. Temperature and withdrawal rate should be adjusted to optimum levels. In this study, as a result of the experiments, the optimum temperature was determined as 1560 °C degrees and the optimum withdrawal rate is 5 mm/min. However, in addition to this, there are many final parameters affected by casting temperature and withdrawal rates, and the production process should be considered in every aspect.

References

[1] Reed, R. C., *The Superalloy, Fundamentals and Applications*. 2006: Cambridge University Press, UK

[2] K. Harris, G.L. Erickson, S.L. Sikkenga et al.: *Superalloys*., 1992, vol. 9, pp. 297-306

[3] T.M. Pollock T. Sammy: *J. Propul. Power*, 2006, vol. 22, pp. 361-74

[4] Liu, G., et al., *Influence of withdrawal rate on the microstructure of Ni-base single-crystal superalloys containing Re and Ru.* Journal of Alloys and Compounds, 2011. **509**(19): p 2257-2262.

[5] Li, J. R., et al. "Effect of low angle boundaries on the mechanical properties of single crystal superalloy DD6" *Superalloy* (2008): 443-451

[6] M. Mclean, Phil. Trans. Royal Soc. London. A351 (1995) 419.

[7] Clay, K., Jackson, J. D., Quested, P. N., & Morrell, R. (2009). Improving single-crystal orientation determination for advanced nickel-based alloys.

[8] G. A. Whittaker, Mater. Sci. Technol. 2, 436 (1986).

[9] J. D. Livingston, H. E. Cline, E. F. Koch, and R. R. Russell, Acta Metall. 18, 399 (1970).

[10] Onyszko, A., Bogdanowicz, W., Kubiak, K., & Sieniawski, J. (2010). X-ray topography and crystal orientation study of a nickel-based CMSX-4 superalloy single crystal. *Crystal Research and Technology*, *45*(12), 1326-1332.

Effect of Post-Processing Heat Treatment on the Mechanical Properties of Inconel 718 Fabricated by Selective Laser Melting (SLM)

Seren OZER[1,2], G. Mert BILGIN[1], Ziya ESEN[3], Arcan F. DERICIOGLU[1]

[1]Middle East Technical University, [2]Atılım University, [3]Çankaya University

Turkey

Abstract

In the present study, the effect of the building direction and post-processing heat treatments on the microstructure and high-temperature mechanical properties of SLM processed Inconel 718 alloys have been investigated. The results showed that the mechanical properties of the Inconel 718 alloy were strongly influenced by the post-processing heat treatments. In addition, both the yield strength (YS) and ultimate tensile strength (UTS) of the Inconel 718 alloy decreased at elevated temperatures, mainly due to the dissolution of the strengthening γ'' precipitates and the formation of the δ phase in the matrix.

1. Introduction

Inconel 718 alloy is one of the key materials for many engineering applications owing to its outstanding properties such as excellent creep and fatigue resistance, high temperature strength as well as good hot corrosion and oxidation resistance. This alloy is mainly used in the production of high-pressure compressor blades, discs, casings and other high temperature components which require long working periods at service temperatures exceeding 700 °C [1]. Selective laser melting (SLM) is an additive manufacturing method that allows complex shaped Inconel 718 parts to be produced in a single step from a three-dimensional computer-aided drawing (CAD) which cannot be machined by traditional manufacturing techniques. However, some undesirable features may result in the microstructure of the as-fabricated parts due to the high temperature gradient and fast solidification rate resulting from the SLM process [2,3]. Therefore, post-processing heat treatments are essential to eliminate these aspects in the as-fabricated parts to enhance the high temperature mechanical properties of the Inconel 718 alloy so that it can satisfy the requirements of the demanding working conditions.

2. Materials and Methods

Inconel 718 samples were fabricated by SLM method in two different building directions such that their longitudinal axes were either parallel or perpendicular to the building platform. Subsequently, all samples were solutionized at 1040 °C for 2 h and then air-cooled. After solutionizing, aging treatments were performed at 700 °C for different soaking times (5 to 34 h). Characterization of the samples was performed by scanning electron microscopy (SEM), electron back scattered diffraction (EBSD), transmission electron microscopy (TEM) and X-ray diffraction (XRD) methods. The samples were also subjected to tensile tests both at room temperature and at elevated temperatures up to 900 °C to study the temperature dependence of the mechanical properties of as-fabricated and heat-treated Inconel 718 alloys.

3. Conclusions

For both as-fabricated and heat-treated samples, the texture of the samples was mainly concentrated in (001) plane for both building directions, which reveals the maximum heat flow, and hence easy grain growth direction. The tensile test results performed at room temperature revealed that post-processing heat treatment can significantly increase both YS and UTS values while reducing the elongation (%EL) at failure for both building directions owing to the formation of strengthening γ'' and/or γ' precipitates in the matrix, which serve as barriers to dislocation motion. However, both the YS and UTS of the age hardened Inconel 718 alloy decreased when the tensile test was performed at high temperatures, mainly because of the dissolution of the strengthening γ'' precipitates and the formation of the δ phase in the matrix.

References

[1] S. Ozer. (2020). Effect of Post-Processing Heat Treatment on the Mechanical Properties of Inconel 718 Fabricated by Selective Laser Melting (SLM), Middle East Technical University.

[2] S. Raghavan et al. (2017). Effect of different heat treatments on the microstructure and mechanical properties in selective laser melted INCONEL 718 alloy. Materials and Manufacturing Processes, 32(14), 1588-1595.

[3] V. A. Popovich et al. (2017). Impact of heat treatment on mechanical behaviour of Inconel 718 processed with tailored microstructure by selective laser melting. Materials & Design, 131, 12-22.

Optimizing the Heat Treatment Parameters of Additively Manufactured IN718 Components

Tuğçe KALELİ[1], Aydın YAĞMUR[2], Süha TİRKEŞ[1], C. Hakan GÜR[1]
[1]Middle East Technical University, [2]EOS GmbH Electro Optical Systems
[1]Turkey, [2]Germany

Abstract

Ni-based superalloys have gained importance in aerospace and energy industries due to their excellent mechanical properties at elevated temperatures. Conventional manufacturing methods such as casting and forging create defects having adverse effects on the service performance. Moreover, microstructures of cast and wrought products contain brittle phases, which negatively affect the machinability. In recent years, additive manufacturing techniques have been developed for production of Ni-based superalloy components having extremely complex shapes and/or functionally graded layers. This study focusses on optimization of the heat treatment procedure for the IN718 parts additively manufactured by selective laser melting. The relationships between microstructure and mechanical properties will also be investigated.

1. Introduction

For building complex shapes from IN718, traditional production methods are not preferred due its low machinability. Additive manufacturing (AM) has various advantages, such as easy manufacture of complex-shaped components, improved production-development cycle and cost-saving by optimizing material usage [1]. Selective Laser Melting (SLM) is usually preferred AM technique however it may create some problems due to residual stress, micro segregation, and existence of non-equilibrium phases. Heat treatment processes are required to control of microstructure and to achieve desired mechanical properties.

2. Materials and Methods

The specimens were produced from the gas atomized powder of IN718 by SLM with 40 µm layer thickness, 250 W laser power, 150 mm/s laser speed and hatch distance of 0.1 mm. The production parameters and building direction were kept constant to minimize their effects on mechanical properties. N_2(gas) was used to prohibit the oxidation of alloy elements during the production. The standard heat treatments, i.e. direct age (DA), solutionizing and direct age (STA), homogenization and STA were applied to the specimens. The microstructure, micro hardness and tensile properties of the specimens were investigated.

3. Conclusions

a) The microstructure of IN718 manufactured by SLM is remarkably different from those of as-cast and wrought conditions. Initial microstructure affects the phase transformation kinetics during heat treatments. Homogenization temperature of the specimen produced by SLM is higher than that of conventionally produced one.
b) Elongated grain morphology along the build direction and the melt pool boundaries are still observed after DA while they are not observed after STA. Partial precipitation of γ’ and γ’’ phases had occurred, and remaining Laves phase was observed after DA. However, STA provides fully developed precipitation of γ’ and γ’’ phases.
c) STA significantly improves hardness and tensile strength of the specimens in comparison to the as-processed ones.

Acknowledgement: The authors gratefully appreciate to sample support from the EOS, Germany.

References

[1] E. Hosseini, V.A. Popovich, A review of mechanical properties of additively manufactured Inconel 718, Additive Manufacturing, 30, 100877, 2019, 18 pp.

[2] D. Zhang, W. Niu, X. Cao, Z. Liu, Effect of standard heat treatment on the microstructure and mechanical properties of selective laser melting manufactured Inconel 718 superalloy, Mater. Sci. Eng.: A 644 (2015) 32–40.

An Investigation on the Effect of Reuse and Recycling on Powder Characteristics in Electron Beam Melting

Evren YASA[1], Mutlu KARAŞOĞLU[2], Evren TAN[3], Berkay GÜMÜŞ[3], Emrecan SOYLEMEZ[4], Kuntay AKTAŞ[5]

[1]Eskişehir Osmangazi University, [2]Eskişehir Technical University, [3]Aselsan Elektronik Sanayi ve Ticaret A.Ş., [4]Istanbul Technical University, [5]Btech Innovation

Turkey

Abstract

Degradation of powder feedstock characteristics in Electron Beam Melting (EBM) may have detrimental effect on the final performance of the produced components. The ability to reuse the powder in EBM as well as other powder bed fusion processes for metals is a very critical advantage for cost-effectiveness. However, ensuring that the degradation of powder characteristics do not significantly and unexpectedly alter the part performance while producing structural components, is even more critical where high process reliability is required. EBM is generally considered as an additive manufacturing process with high reliability on the material properties. Yet, very high preheating temperatures up to 700°C during the process may have an effect on the material composition due to formation of oxide inclusions leading to fusion defects and detrimental mechanical properties in the built components. Moreover, the variation of the powder particle size distribution and particle morphology needs to be investigated on process outputs such as porosity. This study presents a detailed comparison between virgin powders from different suppliers and the non-consumed Ti-6Al-4V powder for the EBM process to understand whether the change in material characteristics due to reuse and recycling are statistically different than the variability in between suppliers. The powder characteristics that are under investigation are particle size distribution, material composition, flow rate and particle morphology.

1. Introduction

Electron Beam Melting (EBM) is one of the most commonly used Additive Manufacturing (AM) technologies in biomedical and aerospace applications. The process is realized at a relatively high pre-heating temperature and in vacuum due to employing an electron beam, and this leads to many advantages for this powder fusion process such as good mechanical properties including fatigue and very low levels of contamination. One of the main advantages of this process, like other AM processes, is the low buy-to-fly ratio which is very critical with expensive materials. This ratio defines the amount of scrap material and it is ideal to have a value close to 1. EBM and other AM methodologies are based on material addition rather than subtracting material to achieve the final geometry. A part in EBM is produced in a powder bed and the surrounding sintered powder is recycled and reused. However, degradation of powder characteristics may have detrimental effect on the part performance and this needs to be characterized so that a reuse strategy can be adapted by EBM users depending on the expected quality requirements.

One of the important powder characteristics is its cleanliness. Oxygen pickup of Ti6Al4V is very critically deteriorating its mechanical properties. In the study of Persenot et al., it was demonstrated that fatigue resistance of the samples produced from recycled powder was 20% lower than virgin counterparts on account of increased oxygen content [1]. It is determined by Arcam that oxygen pickup of powder is due to the presence of water vapor in the EBM build chamber. In a study by Draper et al., it was shown that reused powder had oxygen above 0.20 wt.% beyond the Arcam specifications (0.12%) as well as ASTM F2924 (0.20%) [2]. In another study by Petrovic and Ninerola, the same conclusion is supported by the fact that the oxygen content increases from an initial value of 0.17 wt% to a final value of 0.22 wt% at the 26th build. After 15 builds, the oxygen content already exceeds the ASTM F2924 limit which is 0.20 wt%. Moreover, it is underlined that the recyclability limit which was given as 12 in this study, depends on the initial oxygen content which was 0.14 wt% [3]. This is also evident from the study of Tang et al. where an initial oxygen content of 0.08 wt% led to a possible reuse of 21 times before reaching 0.19 wt% [4]. Besides oxygen, the other impurity source elements including, nitrogen, hydrogen and carbon should be taken into consideration for recyclability. Mohammadhosseini et al. reported that oxygen, nitrogen, hydrogen, and carbon content of Ti6Al4V was increased to 0.33%, 0.03%, 0.03%, and 0.02% respectively, subsequent to 90 builds [5]. In this study, it was also shown that the powder became less spherical and a narrower particle size distribution was obtained with increasing reuse times. Eliminating the satellites and humidity in the powder due to reuse increased the flow rate [4].

The shape morphology of the powder particles can significantly be affected by strongly reusing as shown in Figure 1 [6]. Some of the defects already exist in the virgin powder such as presence of satellites or super-balls. The main reasons for the damage caused to the powder are mainly due to sieving and mechanical damage [7]. It is concluded by Popov et al. that the deterioration of the powder morphology may lead to bad flow characteristics in contrast to the findings by Tang et al. [4]. Regarding the mechanical properties, it is shown that the raise in the oxygen content leads to higher strength while lowering the ductility [7].

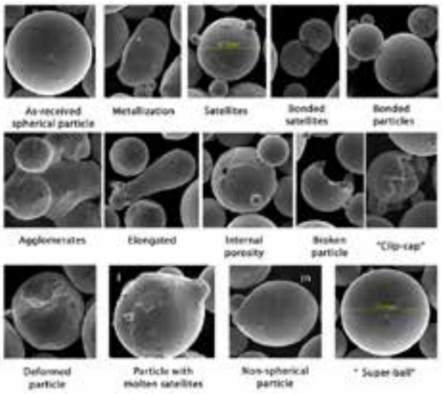

Figure 1: Various defects caused by recycling in a strongly recycled powder [6]

Complex thermal cycles during EBM process may also influence microstructure of the recycled powder. In the study of Sun et al., microstructures of recycled Ti6Al4V powder particles were altered from α′ martensitic to α+β two phase structure which is different from α′ martensite structured virgin powder [8]. Hunter et al. showed that porosity amount of recovered powder was nearly twofold higher compared to virgin powder [9]. Excessive porosity may diminish the mechanical performance of build parts by forming stress concentration areas. This study aims to understand the change of significant powder characteristics for Ti6Al4V powder suitable for EBM processing with increased number or reuse and recycling iterations as well as the effect of the powder supplier.

2. Experimental Procedure

Three type of powders suitable for the EBM processing provided by Arcam and Tekna were investigated in this study. As Table 1 shows, two specimens were virgin Ti6Al4V powders while the third one from Arcam was used and recycled in 18 builds without adding any fresh powder to the mix. In order to understand the effect of re-use and recycling as well as the provider, the following tests were accomplished on these three samples. First of all, flow tests according to ASTM B-213 standard using the Hall Flowmeter Funnel were carried out [10]. Then, the samples were investigated under Scanning Electron Microscope to reveal the particle morphology as well as to understand if any mechanical damage on the powder particles can be observed. Moreover, particle size distribution of three samples was obtained using laser diffraction method per ASTM B-822 standard [11]. Since oxygen was considered to be the most quickly changing element to fail the material composition, elemental analysis to measure the oxygen levels of these samples was carried out. All given values of measurements are taken as an average of 3 measurement of different samples from the same specimen.

Table 1: Various specimens used in this study

#	Provider	Status
1	ARCAM	Virgin
2	TEKNA	Virgin
3	ARCAM	Used for 18 times

3. Results and Discussion

The flow tests carried out using a Hall Flowmeter Funnel gave the following results as shown in Table 2. The obtained flow rates given in [s / 50 g] indicate the flowability of the virgin powder is enhanced after 18 times of reuse and recycling of about 7.5% while the Specimen-2 (Tekna) shows a worse flow behavior in comparison to Specimen-1 (Arcam) both being virgin powders.

In order to understand the change of the flow rate of the powder samples after re-use and recycling, their morphology has been observed using a Scanning Electron Microscope. As depicted in Figure 2, all samples show almost perfectly spherical powder particles at different magnifications (100x and 250x). All powder specimens show some degree of satellite formations. This is even more clear in

Figure 3 where the powders are magnified 1000 times clearly pointing bonded satellites. As depicted, 18 times re-used and recycled Specimen-3 shows mechanical damage deteriorating the sphericity to some extent. This is mainly due to the fracture of necks in between the powder particles during the blasting process. Moreover, SEM images reveal that the powder particles remain spherical and well-defined even after 18 times of recycling.

Table 2: Flow rate results per ASTM B213

#	Specimen	Flow Rate (s/50 g)
1	ARCAM – Virgin	24.85
2	TEKNA – Virgin	25.58
3	ARCAM -18T re-used and recycled	23.09

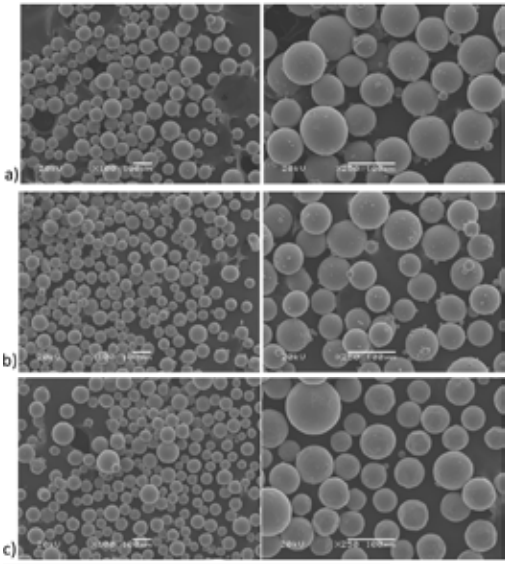

Figure 2: SEM images of three samples
a) Specimen-1 – Arcam virgin powder
b) Specimen-2 – Tekna virgin powder c) Specimen-3 – Arcam 18 times reused powder

The powder particle size distribution (PSD) is another important factor determining the coating characteristics of powder bed fusion process powders. The obtained PSDs for three specimens are given in Table 3. As the measured values in the table show, the particle size distribution of the virgin powder from both suppliers are very close. Moreover, the particle size distribution seems to be narrower for the re-used and recycled powder (specimen 3). This can be attributed to more satellites being attached to the particles as well as elimination of the small particles in the post-processing while large particles are removed from the powder during sieving with a mesh size of 105 µm and powder recycling in the PRS. The evolution of the PSD eliminating large particles when recycled is more evident in Figure 4.

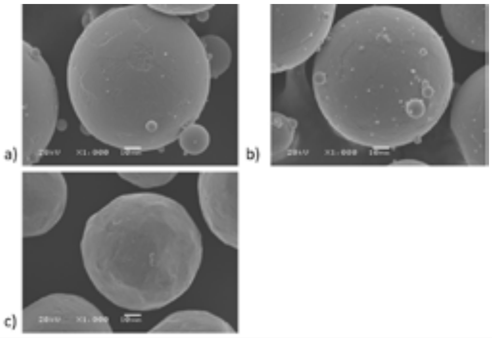

Figure 3: SEM images of three samples at a higher magnification (1000x) a) Specimen#1 – Arcam virgin powder b) Specimen#2 – Tekna virgin powder c) Specimen#3 – Arcam 18 times reused

Table 3: Particle Size Distribution of the samples

#	Specimen	D10 [µm]	D50 [µm]	D90 [µm]
1	ARCAM Virgin	51.12	73.30	105.07
2	TEKNA Virgin	53.20	73.96	103.15
3	ARCAM- 18T re-used and recycled	47.16	67.72	97.57

Figure 4: PSD of three samples

The final measurements were realized by elemental analysis of the samples in order to detect the oxygen amount. Oxygen is a critical element for titanium alloys leading to unexpected brittle fracture if it exceeds a critical threshold. For Ti6Al4V, ASTM F2924 standard dictates a maximum of 0.2 wt.% of oxygen so that the metal powder is free from detrimental amounts of inclusions and impurities. The results obtained with three samples are shown in Table 4. The virgin powders from both suppliers conform to the standard being lower than 0.2%. Specimen-2 from Tekna includes almost half of the oxygen amount that Specimen-1 has from Arcam. The initial oxygen levels are actually critical because this determines the maximum number of re-use and recycling iterations. If the starting O_2 level is closer to 0.2%, then it is possible to re-use this powder for less number of times compared to a lower starting O_2 value. As an example, as shown in [3], when the initial oxygen content is about 0.14%, then it takes only 12 times to exceed the limit of 0.2%. As demonstrated with Specimen-3, the oxygen level has increased to 0.18% from 0.11% for only 18 re-use and recycling iterations without adding any virgin powder. If a linear regression is assumed between the re-use times and oxygen amount, it can be calculated that after approximately 5 additional cycles, the level of oxygen in the re-used powder will not conform to the specification putting a threshold of 0,2%. The linear regression constant is also very close the one obtained in a study by Arcam referenced in [3]. For Specimen-2, using the same linear regression, it is estimated to take at least 39 cycles to reach the threshold showing the importance of the oxygen level of the virgin powder on the number of re-use and recycling iterations.

Table 4: Oxygen levels of three samples

#	Specimen	Average wt.%
1	ARCAM Virgin	0.114
2	TEKNA Virgin	0.052
3	ARCAM 18T re-used and recycled	0.181

4. Conclusion

Since AM has a very important advantage of presenting lower buy-to-fly ratios, it is very important to rely on the recycled powder while powder characteristics play a very critical role on the performance of the produced parts in the EBM process. The established maximum level of recyclability in this study is limited to 18. As a result of this study, it can be concluded that the oxygen content is the factor limiting the recyclability level. Especially, it is very important to have a very low level of oxygen in the virgin powder so that the number of recycling iterations can be maximized. Moreover, from the SEM images, it is understood that re-use and recycling of the Ti6Al4V powder leads to some deformations due to mechanical fracture of the sintered necks in between particles but this is not very dominant after 18 times. The spherical morphology seems to be not very much affected. The particle size distribution from virgin powders were very similar and it was observed that after reuse for 18 times, the distribution becomes narrower eliminating large and small particles from the powder. Regarding the flow rate, the measurements show that the used powder flow better than the virgin powders. This is actually not in line with the other results. Oxygen pickup is expected to decrease the powder flowability [3]. Moreover, the distorted spherical morphology of the powder particles should normally decrease the flowability rather than enhancing it. Thus, as a future work, the flowability of the powders will be studied with other flow characteristics such as Hausner ratio. Lastly, it is important to note that different suppliers may tune their powder properties differently but still conforming to the powder specifications. Especially, the oxygen content of the virgin powder is a critical parameter to be strictly controlled to maximize the number of recycling iterations.

Acknowledgment

This study has been prepared in the scope of a project entitled as “Development of a Productive and Cost-Efficient Process Chain for Electron Beam Melting” and with a project number of 218M717 funded by TUBITAK under ARDEB 1003 program.

References

1. T. Persenot, J.-Y. Buffiere, E. Maire, R. Dendievel, G. Martin, Fatigue properties of EBM as-built and chemically etched thin parts, Procedia Structural Integrity 7 (2017) 158-165.
2. Draper SL, Lerch BA, Telesman J, Martin RE, Locci IE, Garg A, et al. Materials characterization of electron beam melted Ti-6Al-4V. 2016.
3. Petrovic V, Niñerola VPR. Powder recyclability in electron beam melting for aeronautical use. Aircraft Engineering and Aerospace Technology: An International Journal. 2015;87(2):147-55.
4. Tang H, Qian M, Liu N, Zhang X, Yang G, Wang J. Effect of powder reuse times on additive manufacturing of Ti-6Al-4V by selective electron beam meltİng. Jom. 2015;67(3):555-63.
5. A. Mohammadhosseini, D. Fraser, S. Masood, M. Jahedi, A study of morphology of titanium powder used in electron beam melting, Applied Mechanics and Materials, Trans Tech Publ, 2014, pp. 160-163.
6. Katz-Demyanetz, Alexander & Bamberger, Menachem & Garkun, Andrey & Popov, Vladimir. (2018). Effect of powder recycling in Electron Beam Melting. 10.13140/RG.2.2.20237.59369.
7. Popov VV, Katz-Demyanetz A, Garkun A, Bamberger M, The Effect of Powder Recycling on the Mechanical Properties and Microstructure of Electron Beam Melted Ti-6Al-4V specimens, Additive Manufacturing (2018), https://doi.org/10.1016/j.addma.2018.06.003
8. Y. Sun, M. Aindow, R.J. Hebert, The effect of recycling on the oxygen distribution in Ti-6Al-4V powder for additive manufacturing, Materials at High Temperatures 35(1-3) (2018) 217-224.
9. L.W. Hunter, D. Brackett, N. Brierley, J. Yang, M.M. Attallah, Assessment of trapped powder removal and inspection strategies for powder bed fusion techniques, The International Journal of Advanced Manufacturing Technology 106(9) (2020) 4521-4532.
10. ASTM B-213 Standard Test Methods for Flow Rate of Metal Powders Using the Hall Flowmeter Funnel.
11. ASTM B-822 Standard Test Method for Particle Size Distribution of Metal Powders and Related Compounds by Light Scattering.
12. ASTM F2924-14 Standard Specification for Additive Manufacturing Titanium-6 Aluminum-4 Vanadium with Powder Bed Fusion.

Structural and Mechanical Characterization of Scale-Up FeCoCrNiCux, High Entropy Alloys (HEAs)

Z. Anıl ERDAL[1], Gökhan POLAT[1,2], Doğuhan SARITÜRK[1], Y. Eren KALAY[1]
[1]Middle East Technical University, [2]Necmettin Erbakan University
Turkey

Abstract

FeCoCrNiCu$_x$ (x in atomic ratio,x: 0.3,0.6,1) high entropy alloys (HEA) were produced from industrial raw materials that contain various impurity elements, i.e., Al, Si, and C in large quantities using induction melting. HEAs were also produced from pure elements in order to compare with scale-up counterparts in terms of mechanical and structural properties. These alloys were cast into compressed steel molds to prepare mechanical test samples. Structural characterization was performed with X-ray diffraction (XRD) and scanning electron microscopy (SEM). Hardness and compression tests were performed to reveal basic mechanical behavior. Cr_7C_3 phases were present in impure FeCoCrNi alloy beside FCC main phase. On the other hand, the pure specimen had only the FCC phase. The addition of Cu in different proportions to the primary alloy did not affect the change of crystal structure for both pure and impure alloys. It is indicated that the effect of Cr_7C_3 secondary phase, which is the reinforcement phase in the alloys, caused a significant increase in compression test results as well as hardness results. Impure FeCoCrNi alloy, which has 2125 MPa maximum compressive strength with 25% compressive strain at fracture, is the strongest one among produced alloys.

1. Introduction

Conventionally, alloy systems consist of one main element with a small amount of alloying elements added to enhance the properties or processability of the material. Since the amounts of the added elements are considerably lower than the amount of the main element, the structural and mechanical properties of the alloys to be obtained are limited. In this respect, “high entropy alloys (HEA)” have been proposed as a new concept, which refers to alloys that include many elements in almost equal proportions. The main reason for the popularity of HEAs is the stretching the fundamental rules to create metallic alloys such as increment of the number of the main element in an alloy system can lead to the formation of intermetallic compounds and complicated microstructures, which could cause brittleness and processing problems. However, studies conducted by Yeh et al. [1], [2] show that alloys with five or more principal elements that have the concentrations between 5 and 35 at% can be obtained without the formation of intermetallic phases. This new class of alloys is called as high entropy alloys (HEAs) due to higher mixing entropies of their liquid or random solid solution compared to the conventional alloy systems [3]. HEAs form face-centered cubic (FCC), body-centered cubic (BCC) and/or hexagonal close-packed (HCP) solid solutions rather than many complex phases. HEAs have various properties such as high strength/hardness, wear resistance, exceptional high-temperature strength, good structural stability, good corrosion and oxidation resistance, fatigue resistance, and excellent magnetic properties due to the unique multi principal element composition [3-5]. One of the commonly studied types of HEA is FeCoCrNi alloy system having FCC crystal structure, and this alloy is generally produced from highly pure (>99.9% purity) raw materials. A study conducted by He et all. [6] show that FeCoCrNi has 165 MPa yield strength, 400 MPa tensile strength with 68% elongation by using the drop-casting method. However, in order to improve the mechanical properties of the alloy, powder metallurgy (P/M) method was implemented by Liu et al. [7]. According to their study, powder metallurgy (P/M) route consists of mechanical alloying and consolidation operation used in order to obtain improved strength and ductility. A study performed by Liu et al. also demonstrates that gas atomization and hot extrusion processes can be applied to produce scale-up HEAs to get high mechanical properties. According to this study, 359 MPa yield strength, 712.5 MPa ultimate tensile strength with 56% elongation were obtained. Indeed, the most remarkable point for this study is the preparation of large-sized HEAs to obtain higher mechanical properties.

However, one of the drawbacks of P/M method is the price of the powders as the quality of the powders is directly related to the powder processing. In addition, P/M method is a time-consuming process that takes 40-60 h. for alloying and homogenization processes [7].

The present study aims to investigate the structural and mechanical properties of FeCoCrNiCu$_x$ (x:0, 0.3, 0.6, 1) alloy produced by using impure elements and compare with produced pure alloys.

2. Experimental Procedure

Commercial grade raw materials were used to produce impure FeCoCrNiCu$_x$ (x: 0, 0.3, 0.6, 1) HEAs. The chemical composition of the elements used in the experiments is shown in Table 1. Equiatomic amount of raw materials are weighted to produce the alloy. FeCr was used as Fe and Cr source. Additional low carbon steel (99.8 Fe wt. %) was used to balance the atomic ratio of Fe and Cr in FeCr. The other raw materials were used as received.

Table 1. Chemical compositions of the raw materials

Raw Metarials	**Composition (wt.%)**						
	Fe	**Cr**	**Co**	**Ni**	**Al**	**Si**	**Cu**
FeCr	25.5	72	-	-	0.5	2	
Ni	-	-	-	99.5	0.5	-	
Co	-	-	99	-	0.5	0.5	
Cu	0.07						99.3

All impure specimens were produced by using Indutherm MC+15 induction casting machine. Argon was blown into the chamber, and then the vacuum process was applied via a vacuum pump. This cycle was repeated three times to prevent production problems such as oxidation. The casting process was carried out under vacuum sealing to 10-1-10-2 mbar. All raw materials were put into the ceramic crucible. Then, the crucible was placed in the induction coil. After the melting process was completed, the molten alloy was poured into the cylindrical copper mold with 5 mm diameter.

Pure samples were produced by using Edmund Buhler MAM-1 arc melting machine. Small pieces of samples were cut from that alloy, ground, polished, and etched with aqua regia. The phases present in the alloy were examined by Rigaku D/Max 2200PC/Ultima X-ray diffractometer (XRD). In order to perform microstructural characterization, scanning electron microscopy (SEM) with FEI Nova NanoSEM 430 was used. Vickers test was done with 4.903 N load to investigate the hardness of the HEAs. 6 measurements were taken from a different region of the sample. The average of them was indicated as the hardness of the material. Cylindrical compression test specimens with dimensions of 5mm diameter and 10 mm height were prepared. The test was performed with Instron tensile test device with a capacity of 10 tons. Strain rate of $10^{-4}s^{-1}$ was used for the compression test.

3. Results and Discussion

Figures 1 (a) and (b) show the XRD profiles of as-cast impure FeCoCrNiCux and pure FeCoCrNiCu$_x$ (x: 0,0.3,0,6 and 1) alloys. According to the results, the main alloy, pure FeCoCrNi HEA, has FCC crystal structure. On the other hand, impure FeCoCrNi HEA includes Cr_7C_3 phase with FCC phase. This is due to the fact that carbon (C) impurities originated from FeCr. Moreover, low alloy carbon steel that we used for the production of this alloy promotes the formation of Cr_7C_3 phases. The addition of Cu in different proportions to the main alloy has no effect on the change of crystal structure for both pure and impure alloys. The reason is that atomic radius of Fe, Co, Cr, Ni and Cu (1.411Å, 1.385Å, 1.423Å, 1.377 Å and 1.413 Å, respectively) is pretty close to each other [8].

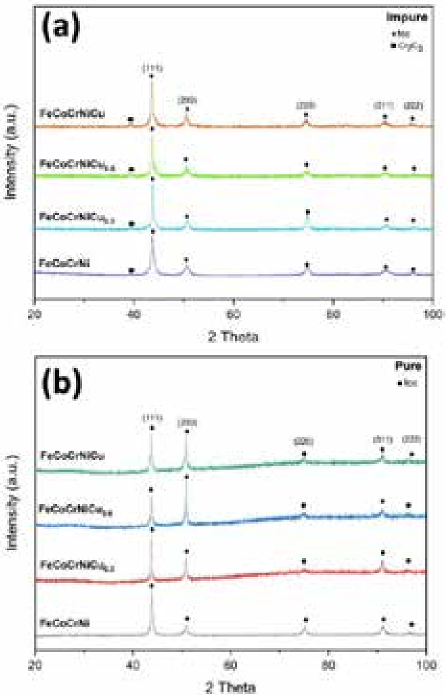

Figure 1. X-ray diffraction pattern of the pure and impure FeCoCrNiCu$_x$ HEAs

Figure 2 and 3 shows the microstructures of impure and pure FeCoCrNiCu$_x$ alloys under SEM. The microstructures of pure and impure $Cu_{0.3}$, $Cu_{0.6}$, and $Cu_{1.0}$ have dendrite and interdendritic structure.

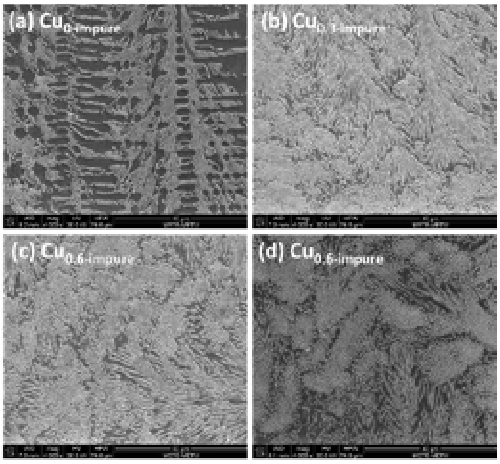

Figure 2. SEM images of the impure FeCoCrNiCu$_x$ HEA

The chemical compositions of dendritic (D) and interdendritic (ID) regions of FeCoCrNiCu$_x$ alloys are given in Table 2. Homogeneous chemical distribution of other constituent elements, Fe, Co, Cr, and Ni in the dendrite regions, was observed for pure Cu$_{0.3}$, Cu$_{0.6,}$ and Cu$_{1.0}$ alloys. However, there is no homogeneous chemical distribution in the interdendritic regions, and Cu is very rich in these regions. When the impure Cu$_{0.3}$, Cu$_{0.6,}$ and Cu$_{1.0}$ alloys are examined, the dendrite and interdendritic structures became different from the pure ones. The majority of the structure consists of an interdendritic structure. In impure FeCoCrNiCu$_x$ alloys, Cu is rich in interdendritic regions in contrast to the main alloy. It is seen that the field density of the interdendritic regions (bright fields for impure alloys, dark fields for pure alloys) significantly increased with the addition of Cu. Since the amount of Cu increases in the alloy, the amount of Cu precipitation increases gradually. The reason for this case is that the bonding force described as mixing enthalpy ΔH^{mix} (kJ mol^{-1}) of Cu with other constituent elements is weaker than the other Fe, Co, Ni, and Cr [9].

Table 2. EDS analysis (at.%) of the dendrite and interdendritic structure of as-cast impure and pure FeCoCrNiCu$_x$ alloys

	Impure								Pure					
	FeCoCrNi		$Cu_{0.3}$		$Cu_{0.6}$		$Cu_{1.0}$		$Cu_{0.3}$		$Cu_{0.6}$		$Cu_{1.0}$	
	ID	D	ID	D	ID	D	ID	D	ID	D	ID	D	ID	D
Fe	24.9	27.7	7.8	20.9	8.4	20.1	8.4	20.9	7.9	22.9	9.2	21.9	7.7	22.5
Co	21.9	28.3	8.6	19.7	6.50	18.6	9.8	19.7	11.2	21.1	7.6	22.0	10.1	22.6
Cr	36.6	12.3	3.4	37.9	2.9	41.5	2.4	27.9	1.9	22.1	2.3	23.5	2.5	23.3
Ni	16.4	30.6	22.7	14.4	23.1	12.0	16.8	23.1	20.9	23.0	19.6	21.6	17.5	21.2
Cu			57.0	6.9	57.6	7.0	62.5	7.91	57.4	11.7	61.6	9.8	66.2	10.3
Si		0.90	0.49		1.31		0.11							

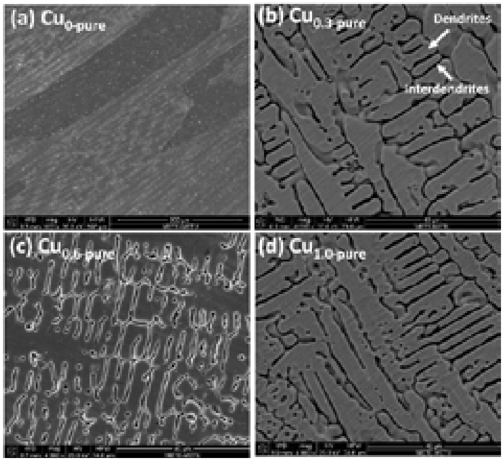

Figure 3. SEM images of the pure FeCoCrNiCu$_x$ HEA

Figure 4 shows the change in Vickers hardness value of pure and impure alloys as a function of Cu content. The hardness of the pure FeCoCrNi alloy is 166 (±7) HV. However, the hardness value of the impure alloy is increased to 379 (±6) HV due to the reinforcement effect of Cr_7C_3 secondary phase. The addition of Cu into the main alloy did not cause a significant change in the hardness of the alloys as it did not affect the crystal structure. The hardness values of the pure Cu$_{0.3}$, Cu$_{0.6}$, and Cu$_{1.0}$ alloys are 160 (±3), 158 (±4), and 164 (±2) HV, respectively. The hardness values of the impure alloys are 376 (±8), 377.(±6), and 382 (± 6) HV, respectively.

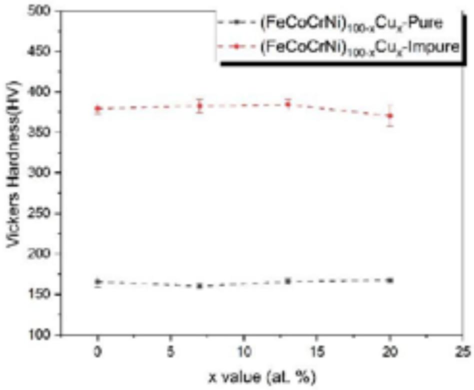

Figure 4. Vickers hardness results of pure and impure FeCoCrNiCu$_x$ (x:0,0.3,0.6 and 1) alloys as a function of Cu content (Dashed lines are drawn for eye-tracking)

The results obtained from the compression test graph of the impure main alloy, Cu$_{0.3}$, Cu$_{0.6,}$ and Cu$_{1.0}$ alloys are shown in Figure 5. It is indicated that the effect of Cr_7C_3 secondary phase, which is the reinforcement phase in the alloys, caused a significant increase in compression test results as well as hardness results. Yield strength values of the impure primary alloy, $Cu_{0.3}$, $Cu_{0.6,}$ and $Cu_{1.0}$ alloys are 1020, 930,925, and 945 MPa, maximum compressive strength values of them are 2125, 1805, 1806 and 1973 MPa respectively. The obtained strength values of the alloys are very close to each other due to the similarity of crystal structures and microstructures. Besides these strength values, all alloys exhibit a significant amount of ductility. The percent compressive strain at fracture for the main alloy, $Cu_{0.3}$, $Cu_{0.6,}$ and $Cu_{1.0}$ are calculated as 25%, 22.1 %, 22.8 %, and 25.9 %, respectively.

The pure main alloy, $Cu_{0.3}$, $Cu_{0.6,}$ and $Cu_{1.0}$ alloys, are started to undergo strain hardening, which is defined as the increment of stress level to produce additional plastic deformation after a certain stress level since they are quite ductile materials. The specimens of these alloys did not fracture after the test. Barreling is the formation of a convex surface on the outside of the specimen. The reason for the barreling is due to the friction between the contact surfaces of the compression sample and the anvils. This deformation behavior shows that the applied stress is not uniaxial compression. Therefore, the results which are not representative are not introduced in this study. However, it can be interpreted that the barreled alloys show similar mechanical properties

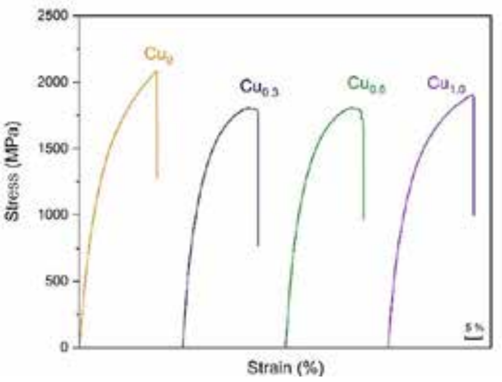

Figure 5. Compression test of the impure $FeCoCrNiCu_x$ HEAs

4. Conclusion and Future Works

In this study, the structural and mechanical properties of impure and pure $FeCoCrNiCu_x$ (x: 0, 0.3, 0.6, 1) alloys were investigated. The properties of pure and impure alloys were also compared in accordance with the amount of Cu. The impure alloys were produced by the induction melting method, while the pure alloys were produced by the arc-melting method. X-ray diffraction (XRD) for determining the crystal structure, scanning electron microscopy (SEM) for observing the resulting microstructures were used. Hardness and compression tests were applied for the mechanical characterization of the alloys.

The addition of Cu in different proportions to the main alloy had no effect on the change of crystal structure for both pure and impure alloys. There was no significant change in the microstructure of Cu containing alloys as in the XRD results. Microstructures of pure and impure $Cu_{0.3}$, $Cu_{0.6,}$ and $Cu_{1.0}$ alloys consist of dendritic structure. The addition of Cu does not have a remarkable effect on the compression test results of the impure alloys.

5. Acknowledgments

This project was supported by METU-BAP under contract number YLT-308-2018-3689.

6. References

[1] Huang, Kuo-Hsiung, and J. W. Yeh. "A study on the multicomponent alloy systems containing equal-mole elements." Hsinchu: National Tsing Hua University (1996).

[2] Yeh, J-W., et al. "Nanostructured high-entropy alloys with multiple principal elements: novel alloy design concepts and outcomes." Advanced Engineering Materials 6.5 (2004): 299-303.

[3] M.-H. Tsai and J.-W. Yeh, “High-Entropy Alloys: A Critical Review,” Mater. Res. Lett., vol. 2, no.3, pp. 107–123, 2014.

[4] Hsu, Chin-You, et al. "Wear resistance and high-temperature compression strength of Fcc $CuCoNiCrAl_{0.5}$ Fe alloy with boron addition." Metallurgical and Materials Transactions A 35.5 (2004): 1465-1469.

[5] Hemphill, Michael Alexander, et al. "Fatigue behavior of $Al_{0.5}$ CoCrCuFeNi high entropy alloys." Acta Materialia 60.16 (2012): 5723-5734.

[6] He, J. Y., Wang, H., Huang, H. L., Xu, X. D., Chen, M. W., Wu, Y., ... & Lu, Z. P. (2016). A precipitation-hardened high-entropy alloy with outstanding tensile properties. Acta Materialia, 102, 187-196.

[7] Chen, Zhen, et al. "Effects of Co and Ti on microstructure and mechanical behavior of Al0. 75FeNiCrCo high entropy alloy prepared by mechanical alloying and spark plasma sintering." Materials Science and Engineering: A 648 (2015): 217-224.

[8] Lihl, F., and H. Ebel. "WB Pearson, a Handbook of lattice spacings and structures of metals and alloys." (1967).

[9] Takeuchi, Akira, and Akihisa Inoue. "Calculations of mixing enthalpy and mismatch entropy for ternary amorphous alloys." Materials transactions, JIM 41.11 (2000): 1372-1378.

Effect of Sintering Parameters on MoTiNbFeCr High Entropy Alloy (HEA) Produced by Mechanical Alloying (MA)

Gökhan POLAT, M. Fatih BAŞ, Hasan KOTAN
Necmettin Erbakan University
Turkey

Abstract
In this project, high entropy alloys (HEAs) were produced and characterized by using mechanical alloying (MA) and arc melting systems. Firstly, MoTiNbFeCr HEA, which has the elements with high melting points to obtain high thermal stability, was designed using thermo-physical calculations and Thermo-Calc software and produced by MA method. Also, the samples were annealed at 800 °C and 1150 °C to reveal the phase transformations in the HEA. The samples were characterized by density and hardness tests, X-Ray Diffraction (XRD), Scanning Electron Microscope (SEM) analyses. As a result, it was observed that the MoTiNbFeCr HEA has a dual-phase in the nano grain structure after MA. It was determined that the grain size increases upon annealing and body-centered cubic (BCC) and C14 phases phase become prominent and the amount of the phases significantly affects the hardness of the HEA.

1. Introduction

Conventional alloy systems are based on one or two principal elements that minor alloying elements are added to improve the properties of the alloys. Due to the limited number of elements on the periodic table, it restricts the combination of these elements to produce new alloy systems and improve their properties. In this manner, a new alloy system which is called as High Entropy Alloys (HEAs) was first proposed in 1995 that there is no such a restriction in this new alloys system. HEAs contain at least five principal elements with 5-35 at. % for each element that let us study in a wide range to produce new alloys. Although HEAs were first proposed in 1995, it has been started in 2004 by Yeh at al. Recently, there are many studies on mechanical, magnetic, and thermal properties of HEAs [1].

Basically, HEA term is based on the highest configurational entropy (S_{conf}) of the alloy system containing at least five principal elements. However, the traditional alloy systems depend principally on one or two main components with the addition of small amounts of alloying elements to improve the properties or processability of the material [2]. The studies conducted by Yeh et al. [3,4] show that alloys with five or more principal elements and the concentrations between 5 and 35 at. % can be obtained without the formation of intermetallic phases. Solid solution phases usually have higher entropy compared to intermetallics that can significantly decrease the Gibbs free energy of the system [5]. Therefore, the HEAs generally form face-centered cubic (FCC) and/or body-centered cubic (BCC) structures rather than many complex phases. Moreover, hexagonal close-packed (HCP) structure, nano-sized precipitated and amorphous phases can be observed in HEAs [6–9].

In this study, a novel MoTiNbFeCr HEA was designed using thermo-physical calculations. The phase diagram of the HEA was consrtıcted by Thermo-Calc software. The HEA was produced by mechanical alloying (MA) and sintered at different conditions. The experimental and simulation results were compared in terms of structure and sintering conditions.

2. Experimental Procedure

The MoTiNbFeCr HEA was designed based on the following thermo-physical calculations [10]:

$$\frac{S_{conf}}{R} = -\sum_{i=1}^{N} c_i \ln c_i \qquad \text{Eq. 1}$$

$$\frac{S_{conf}}{R} = \ln N \qquad \text{Eq. 2}$$

where c_i the concentration of i^{th} element in the alloy. ΔH_{mix}, δ and $\bar{r}$ for an alloy system were calculated based on the following equations [10]:

$$\Delta H_{mix} = 4x \sum_{j \neq i}^{N} \sum_{i=1}^{N} \Delta H_{ij} c_i c_j \qquad \text{Eq. 3}$$

$$\delta = 100x \sqrt{\sum_{i=1}^{N} c_i}\,(1 - \frac{r_i}{r})^2 \qquad \text{Eq. 4}$$

$$\bar{r} = -\sum_{i=1}^{N} c_i \, r_i \qquad \text{Eq. 5}$$

where r_i is the radius of i^{th} element and $\bar{r}$ is the average value for all the atoms in the alloy.

Valance electron concentration (VEC) of the multicomponent HEA systems is used to estimate the resultant crystal structure. VEC is calculated according to the following equation [11]:

$$\mathrm{VEC} = \sum c_i \, \mathrm{VEC}_i \qquad \text{Eq. 6}$$

In addition to these parameters, Yang et al. defined a new parameter which is Ω [12].

$$\Omega = \frac{T_m \Delta S_{mix}}{|\Delta H|} \qquad \text{Eq. 7}$$

The hypothetical value of T_m is calculated according to the rule of the mixture, as shown below [12]:

$$T_m = \sum_{i=1}^{n} c_i \, (T_m)_i \qquad \text{Eq. 8}$$

The phase diagram of the HEA was constructed using Thermo-Calc (version 2019a) software employing a TCHEA (v 2.1) database.

The designed HEA was produced by mechanical alloying by SPEX 8000D high energy ball milling from high purity (>99.5%) powders. The as-milled samples were annealed at different temperatıre and periods to investigate the effect of sintering conditions.

The structural characterization was performed by X-ray diffraction (XRD) using Cu-Kα radiation. Also, the hardness of the samples was investigated using Vickers hardness test.

3. Results and Discussion

Thermo-physical parameters of MoTiNbFeCr HEA, which was designed to be produced, are given in Table 1. The density value of this alloy was calculated to be 7.63 gr/cm^3 according to the rule of mixture. This value is very close to the density of the steel parts due to the elements used with a high density such as Mo, Nb, Fe and Cr. However, since the density value does not play a critical role in the alloy design, this value is an acceptable value in the present study.

The atomic size difference is critical for the formation of the HEA, and thus, it is expected to be less than 6.6 % is indicated in the previous studies. This value was calculated to be 5 for MoTiNbFeCr HEA that it provides the theoretical expectations. In addition, ΔH_{mix} value was calculated as -9.28 kJ/mol, the value of which should be between 22 kJ/mol<ΔH_{mix}<5 kJ/mol as indicated in the literature. Another critical design parameter is the ΔS_{conf} value of the alloy mixture. Theoretically, this value must be greater than or equal to 13.30 kJ/mol.K to define the alloy as HEA [10,11]. The ΔS_{conf} value of the MoTiNbFeCr HEA was calculated to be 13.38 kJ/mol.K and it is sufficient to meet the requirement. In addition, the Ω value was calculated as 3.32 and is greater than the theoretical HEA formation lower limit criterion of 1.1 [13]. The values calculated are in the range of HEA formation parameters. However, the type of the final crystal structure cannot be estimated based on these parameters. Therefore, an additional parameter, which is VEC, is used to estimate the crystal structure. It is shown in the previous studies that, when the VEC value 8.00. On the other hand, if the VEC has a value between 6.87-8.00, the expected crystal structure will be a mixture of BCC and FCC [14]. The VEC value of the MoTiNbFeCr HEA calculated to be 5.8, suggesting BCC crystal structure theoretically.

Table 1. Thermophysical calculations of MoTiNbFeCr HEA

Denisty (g/cm^3)	δ (%)	ΔH_{mix} (kj/mol)	VEC	ΔS_{conf} (kj/mol.K)	T_m (K)	Ω	Crystal Structure
7.63	6.11	-9.28	5.8	13.38	2300	3.32	BCC

Mo, Ti, Nb, Fe and Cr powders with high purity (>99.9%) were used to produce the HEA. The powders were mixed with equ-atomic ratio and XRD analysis was performed before and after mechanical alloying. The XRD patterns of the samples are given in Figure 1.

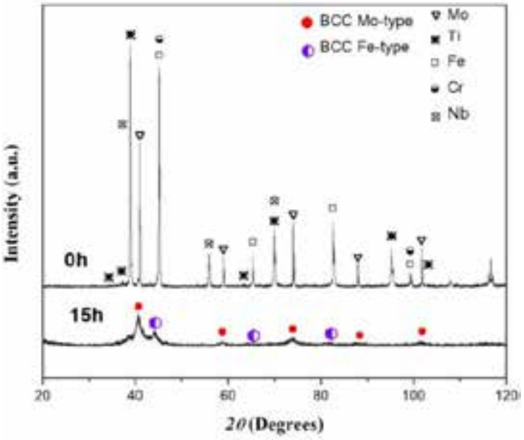

Figure 1. XRD patterns of unmilled powder mixtures and 15 h mechanically alloyed MoTiNbFeCr HEA

The XRD patterns of the powders mixture show individual diffraction lines of the pure Mo, Ti, Nb, Fe and Cr powders before mechanical alloying (0 h). However, after 15 h mechanical alloying, the individual elemental diffraction transforms to the diffraction lines of an alloy consist of BCC-1 and BCC-2 phases. The diffraction lines of these phases correspond to pure Fe and Mo elements, and thus, BCC-1 and BCC-2 phases were labeled as Fe-type and Mo-type phases, respectively.

It is seen in Figure 1 that BCC structure after 15 h mechanical alloying has broad peaks suggesting an alloy with a nano-structure as compared to the elemental powders. This result indicates that the mechanically alloyed samples have very small grains based on the Scherrer equation [15]. Therefore, a nano-structured MoTiNbFeCr HEA with dual BCC solid solution formed after 15 h mechanical alloying. Heat treatments at 800 °C and 1150 °C for 2 h and 4 h, respectively, in a protective atmosphere, were performed on the mechanically alloyed samples to reveal its phase transformation. XRD patterns of the heat-treated samples are shown in Figure 2.

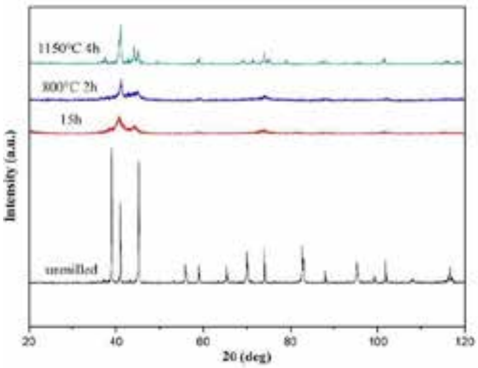

Figure 2. XRD patterns of heat-treated MoTiNbFeCr HEA and unmilled powder mixture

The XRD pattern of annealed samples at 800 °C for 2 h (Figure 2) shows that the peak positions remained the same with the as-milled sample. This result suggests that the structure preserves its basic BCC phases without phase transformation. However, considering the broadening of the peaks, the annealed samples have sharper peaks as compared to the as-milled samples due to grain growth.

The XRD patterns of annealing at 1150 °C for 4 h indicate that peak intensities increase, and the broadening decreases as compared to annealing at 800 °C for 2 h. In addition, it is seen that additional peaks with small intensities, which are relatively invisible at 800 °C 2 h annealing, increase after 1150 °C 4 h annealing. This can be explained by the phase diagram of MoTiNbFeCr HEA constructed with the help of Thermo-Calc software, as shown in Figure 3. The phase diagram of the HEA shows that it has BCC, C14 and $NiTi_2$ phases at room temperature. The theoretical ratio of the $NiTi_2$ phases obtained from the phase diagram is very low that it is neglected for the assumptions and the main BCC and C14 phases are taken into account at room temperature. The comparison of XRD parents (Figure 1) and Thermo-Calc results (Figure 3) reveal that the pattern indicated as Mo-type corresponds to the C14 phase, while Fe type matches with the BCC phase. When this alloy is annealed at 800 °C and above, it is seen that the $NiTi_2$ phase, the amount of which is very low in the structure, completely disappears and the structure transforms into BCC and C14 phases. The heat treatments also confirm that these phases co-exist in the microstructure. However, it is seen that the peak intensities of the BCC phase become stronger due to the high-temperature annealing with longer periods. These results are very close to 50 % vol. BCC + 50 % vol. C14 phase ratio calculated by point equilibrium in Thermo-Calc, suggesting an equilibrium in the microstructure.

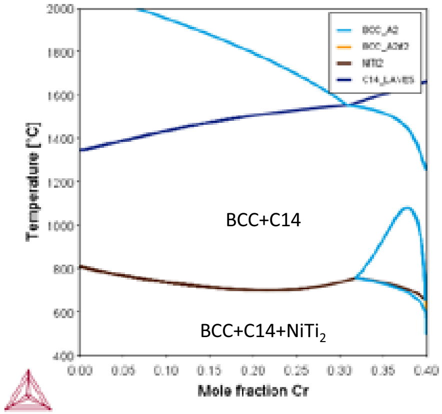

Figure 3. Phase diagram of MoTiNbFeCr HEA constructed by Thermo-Calc software

Microhardness tests were applied to the samples in order to examine the effect of heat treatments on the mechanical properties of the samples. The hardness values of MoTiNbFeCr HEA after mechanical alloying, annealing at 800 °C for 2 h and 1150 °C for 4h are 1192±71 HV, 1443±7 HV and 1165±48 HV, respectively, as shown in Figure 4.

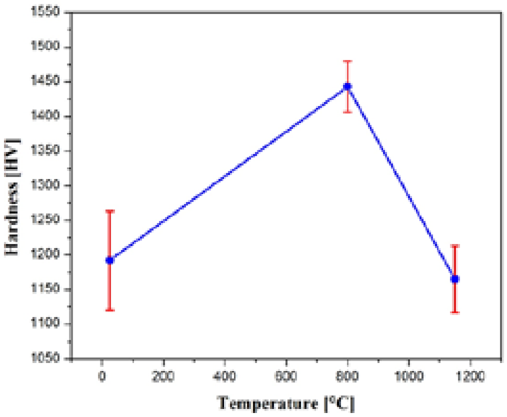

Figure 4. Hardness values of as-milled and annealed MoTiNbFeCr HEA at 800 °C-2 h and 1150 °C-4h

As seen in Figure 4, the hardness value was significantly increased when the samples were annealed at 800 °C for 2 h as compared to the as-milled samples. It is shown in XRD phase analysis (Figure 2) and Thermo-Calc results (Figure 3) that the samples have BCC and C14 phases in the microstructure at room and the corresponding annealing temperatures. The XRD results (Figure 2) show that the equilibrium phases at room temperature and annealing at 800 °C are the same and the main difference between the samples are the broadening values of the peaks due to the increasing grains size upon annealing. Larger grain sizes also increase the hardness value of the samples based on the Hall-Patch equation. Therefore, as a result of grain growth, the hardness increased from 1192±71 HV to 1443±37 HV after annealing at 800 ° C for 2 h. However, it is seen in Figure 4 that the hardness of the samples decreases to 1165±48 HV after annealing at 1150 °C for 4 h as compared to the samples annealed at 800 ° C for 2 h. The XRD and Thermo-Calc results reveal that the relative amounts of the BCC phases increased over C14 phases when the samples were annealed at 1150 °C for 4 h along with the increasing grain size. This can be interpreted that the hardness of the BCC phases is lower than the C14 phases that cause an overall decrease in the hardness.

4. Conclusion

In this study, MoTiNbFeCr HEA was designed based on the thermo-physical calculations and the phase diagram was constructed using Thermo-Calc software. The samples were produced by mechanical alloying and they were annealed at 800 °C for 2h and 1150 °C for 4h. The simulation and experimental results showed that the samples consist of BCC and C14 phases at both room and high temperatures. However, the grain sizes and the amount of the phases were changed after annealing processes. It was observed that nano-sized samples transformed into a microstructure with larger grains after annealing at 800 °C for 2h, and the increasing grain was also increased the hardness. However, the hardness of the samples was decreased after annealing at 1150 °C for 4h due to the increasing amount of relatively soft BCC phases.

Acknowledgment

This work is financially supported by the Necmettin Erbakan Scientific Research Projects Coordination (BAP) under grant no. 181219015.

References

[1] M.-H. Tsai, J.-W. Yeh, Mater. Res. Lett. 2 (2014) 107–123.
[2] J.W. Yeh, Ann. Chim. Sci. Des Mater. 31 (2006) 633–648.
[3] K.-H. Huang, J.W. Yeh, A study on the multicomponent alloy systems containing equal-mole elements, National Tsing Hua University, 1996
[4] J.W. Yeh, S.K. Chen, S.J. Lin, J.Y. Gan, T.S. Chin, T.T. Shun, C.H. Tsau, S.Y. Chang, Adv. Eng. Mater. 6 (2004) 299-303+274.
[5] Y. Zhang, S.G. Ma, J.W. Qiao, Metall. Mater. Trans. A Phys. Metall. Mater. Sci. 43 (2012) 2625–2630.
[6] S. Guo, Q. Hu, C. Ng, C.T. Liu, Intermetallics. 41 (2013) 96–103.
[7] K.M. Youssef, A.J. Zaddach, C. Niu, D.L. Irving, C.C. Koch, Mater. Res. Lett. 3 (2015) 95–99.
[8] O.N. Senkov, S. V. Senkova, C. Woodward, Acta Mater. 68 (2014) 214–228.
[9] J.W. Yeh, Jom. 65 (2013) 1759–1771.
[10] A. Takeuchi, K. Amiya, T. Wada, K. Yubuta, W. Zhang, A. Makino, Entropy. 15 (2013) 3810–3821.
[11] D.B. Miracle, O.N. Senkov, Acta Mater. 122 (2017) 448–511.
[12] X. Yang, Y. Zhang, Mater. Chem. Phys. 132 (2012) 233–238.
[13] X. Yang, Y. Zhang, Mater. Chem. Phys. 132 (2012) 233–238.
[14] S. Guo, C. Ng, J. Lu, C.T. Liu, J. Appl. Phys. 109 (2011)
[15] C.C. Koch, R.O. Scattergood, H. Kotan, M. Saber, Mater. Sci. Forum. 753 (2013) 341–344.

High-Temperature Gas Sensing Materials for Combustion Process Monitoring

Bilge SARUHAN[1], Roussin Lontio FOMEKONG[1,2]
[1]German Aerospace Center, [2]University of Yaounde
[1]Germany, [2]Cameroon

Abstract
This work reports the high-temperature gas sensor developments achieved using M^{3+}-dopants to TiO_2, Rh-dopant to $BaTiO_3$ through resistive sensing. Good sensor signals are achieved to NO/NO_2 at temperatures up to 900°C.

1. Introduction

High temperature gas sensor materials are required for detection of emission and for monitoring of engine efficiency in combustion systems such as gas turbines of aircrafts and power plants and at cement plants [1]. Such sensors have to operate at elevated temperatures (>500°C) with a reasonable sensitivity in coexistence of multiple gases and high humidity. Good sensing properties are difficult to achieve under high temperature gas environment by using simple semiconducting metal oxides. Literature focuses on cost effective metal oxide based gas sensors operate mostly at temperatures <400 °C with only a few exceptions above 400 °C [2]. Thus, the development of innovative sensor materials is required for achievement of excellent high temperature sensing performance towards NOx. High-temperature NOx-sensing is an increasing requirement for combustion processes. TiO_2 is one of the semiconducting oxides that are capable of operating at and above 600 °C [3]. However, TiO_2 is a high resistive n-type semiconductor with relatively poor conductivity for sensing oxidative gases such as NO_2. This disadvantage can be prevailed through addition of low valence dopants to alter its electronic structure [4]. Another strategy is to use catalytically doped perovskite based titanium compounds such as $BaTiO_3$. This context reports the sensor developments achieved using Cr- and Al-doped TiO_2, Rh-doped $BaTiO_3$, as resistive sensors.

2. Materials and methods

For the synthesis of doped TiO_2 layers onto the interdigited Pt-circuits (previously deposited by screen-printing), PVD-Sputtering process was utilized, while Rh-doped $BaTiO_3$ was synthesized by oxalate assisted co-precipitation method followed by calcination. The as prepared powders were deposited as thick films using a simple drop-coating method followed by a heat treatment at 900 °C under H_2 for 30 min on alumina substrates that were previously fitted with interdigitated electrodes.

Microstructure and morphology analysis of the sensing materials in terms of porosity, grain size and surface condition were done by means of FE-SEM (Carl Zeiss NTS Ultra 55). The phase analysis of the sensing materials was carried out by x-ray diffraction, using a SIEMENS D5000 X-ray Diffractometer.

The sensor measurements were carried out in a specially constructed apparatus consisting of a tube furnace and a custom-built quartz glass reactor providing a thermocouple directed at the specimen. The electrical measurements were performed by using a Keithley 2635A Sourcemeter.

3. Conclusions

Nanoparticles of Rh-doped $BaTiO_3$ gas sensors show excellent NO sensing properties even at temperatures up to 900 °C under 5-10% relative humidity. Al-doped TiO_2 sensor layers exhibited very promising results for sensing NO_2 selectively at temperatures exceeding 500 °C. Cr-doped TiO_2-NT sensor layers yield a stable and selective response towards NO_2 at test temperatures as high as 500 °C. The response and recovery times of Cr-doped TiO_2-NT layer are a factor of three shorter than that of the undoped TiO_2-NTs sensor layer. Cr-doping reduces the cross-sensitivity significantly towards CO and the sensor becomes more NO_2-selective to the gas mixtures containing CO plus NO_2 at concentrations higher than 100 ppm.

References

[1] N.O. Savage, S.A. Akbar, P.K. Dutta, Sens. Actuators B, 72 (2001) 239-248.
[2] A. Dey, Mater. Sci. Eng. B 229 (2018) 206–217.
[3] J. Esmaeilzadeh, E. Marzbanrad, C. Zamani, B. Raissi, Sens. Actuators B 161 (2012) 401-405
[4] Y. Gönüllü, A. A. Haidry and B. Saruhan, Sens. Actuators B 217 (2015) 78-87.

20th

INTERNATIONAL
METALLURGY
MATERIALS
CONGRESS
10-12 June
2021
“in Digital Platform”

Surface Treatment and Heat Treatment

immc2021

Modification of Nitride Layer Applied on the Surface of DIN 1.2344 Hot Work Tool Steel with Boron

Yaşar AKÇA[1], Gökhan ÖZER[1], Ahmet KARAASLAN[2]
[1]Fatih Sultan Mehmet Vakıf University, [2]Yıldız Technical University
Turkey

Abstract

In the aluminum extrusion sector, DIN 1.2344 hot work tool steel is mostly preferred due to the price and performance outputs of the molds used in the manufacture of profiles. In order to protect the aluminum from the tribological effects, the most nitration application is made due to the ease of application (applicable to all geometries) and the cost of the steel. Recently, alternative surface coatings have started to work due to reasons such as increased measurement sensitivity and excellent surface performance expectations in profiles. Among these, boron coatings come to the fore due to both their excellent surface performance and ease of application. The application of boron coatings 900 ° C and above, high coating thickness, and related surface deterioration problems occur. In this study, boron application is made on the surface of DIN 1.2344 steel, which has been previously nitrided, and a boron-nitride layer that can work in aluminum extrusion dies in the structure was created. Coatings are characterized by light microscopy, scanning electron microscope, and XRD. According to the results of this study, it has been shown that a more resistant and darker surface coating can be obtained against the tribological effects of aluminum.

1. Introduction

The Turkish Aluminium Industry is the leading motivator for the initiation of this program. The Turkish aluminium industry has shown significant growth over the last decades and achieved growth rates exceeding 5% annual growth. The Turkish Aluminium sector consists of over 18.000 companies with manufacturing and sub-contractors, employs approximately 300.000 people with revenue of $4 billion and investment potential of $20 billion; consisting of 27% extrusion, 20% sheet, 9% secondary aluminium, 7% aluminium foil, 3% primary aluminium 3%. According to Turkey's 11th Development Plan, the aluminium export target was projected as $8 billion. However, in IMMIB's (Istanbul Mineral and Metals Exporters Association) export report, 2018, the export revenues were only $2.99 billion in total. The aluminium manufacturing industry of Turkey, with more than 250 manufacturing companies, has now been established as a manufacturing base for the automotive, construction, and high tech industries and consumers of Europe, the Middle East, Eastern Europe, and North America. Turkish companies export around 60% of their products all over the world, but mainly to European countries. Hot work tool steels are extensively used in extrusion to ensure that aluminum products have the desired shape and quality. DIN 1.2344 hot work tool steel is preferred due to the advantage of the price/performance of hot inner tool steel [1-5]. Due to the tribological effect of aluminum on steel, the surface life of the extrusion dies, and the surface quality of the profiles is increased by surface modification of the dies. Nitride (N) coatings are widely preferred for this purpose. The reason for the preference of nitrocellulose treatment is that it is fast, inexpensive, and applicable to all kinds of dies. The average lifetime of nitriding coatings on extrusion dies 3 tons or 2 kilometers of production. Coatings applied by alternative methods such as PVD and CVD in the manufacturing sector have begun to be preferred in order to increase the lifetime of the dies, especially the dies that require high surface smoothness. However, these coatings are not preferred extensively because they are either expensive, insufficient by means of the desired yield or cannot be applied to every die [6].

2. Tribology in Extrusion Dies

Tribology is a science and technology branch that examines the subjects of friction, wear, and lubrication as literally [7]. In aluminum extrusion, tribological formations (friction and wear) in the mold channel are affected by many factors such as temperature increase in the mold, geometry, and shape of the mold, the length of the mold channel and the channel surface, the properties of the mold steel and the extrusion material. Since the rise in temperature in the mold channel directly affects other factors, temperature is of primary importance in mold wear or friction conditions. The most preferred method for increasing the service life and profile surface quality of the mold steel is the nitration process. The boronizing process is still being studied due to its superior performance (high surface hardness and excellent abrasion resistance), high commercialization capability, and abundant local resources.

3. Boron Coating

Boronizing is a thermo-chemical surface hardening process, which is the process of obtaining a layer of boron on the surface by spreading the boron element to the metal surface at high temperature. Any boron compound can be used as a boron donor. The method can be applied in solid, liquid, and gaseous media. The most useful method is the boronizing box technique and is similar to carburization. Box boronizing technique is simple and economical compared to other boronizing methods [8], [9], [10].

3.1. Boron Nitride Coatings

Boron Nitride is available in two different phases: hexagonal boron nitride and cubic boron nitride. Hexagonal boron nitride (h-BN) is a material with low friction coefficient, insulating, thermal conductivity, and lubricant. On the other hand, cubic boron nitride (c-BN) is a suitable coating material due to its superior mechanical and chemical properties. It has high hardness, low friction coefficient, good thermal conductivity, high electrical and wear resistance, and chemical stability at high temperatures. Because of these properties, especially cubic boron nitride coatings are mostly preferred in cutting tools. These coatings are usually applied by PVD and CVD or equivalent methods [11].

4. Experimental Studies

4.1. Materials Used in Experiments

TQ1 coded (AISI H13) hot work tool steel used in experiments and test works was supplied from the authorized dealer of KIND & CO, 2 meters long, and 120 mm in diameter. The chemical composition of TQ1 steel is given in Table 1.

Table 1. The chemical composition of TQ1 steel[5].

Materials	C	Si	Mn	P	S	Cr	Mo	V
TQ1 (H13)	0.3	0.3	0.4	<0.02	<0.003	5.2	1.9	0.55

A 20 mm diameter cylinder block was removed for the samples used in the experiments. Six cubic samples of 20x20x20 mm were extracted from the cylinder block by wire erosion method (Figure 1).

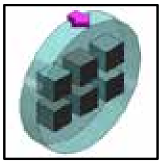

Figure 1. Schematic drawing showing the positions of the cube samples extracted from the TQ1 cylinder block with wire erosion method in dimensions of 20x20x20 mm.

The samples were then prepared metallographically. Gas nitriding to the samples and mold under vacuum has been done in Alper Isil Islem Sanayi ve Ticaret AS. Gas nitriding was done according to the company's own procedure. A sealed box is made of 316L stainless steel for the piping of the test samples. As boron agent, boron donor powder of BORTEC company with grain size below 1000 µm (EKABOR 2) was used. The chemical structures of these powders generally consist of 90% SiC, 5% B_4C, and 5% KBF_4 chemical composition. This agent has the ability to replace N atoms. All samples are arranged to be covered with a boron agent to detect the geometric form interaction. Alumina (Al_2O_3) powder is laid on the floor, side surfaces, and top of the box to prevent interaction between the can and boron powder. The layout of the samples into the box is given schematically in Figure 2. After the contents of the box were prepared, the cover made of 316L stainless steel was closed by the welding method.

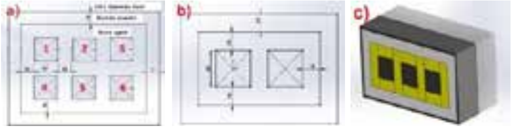

Figure 2. Scheme of placing sealed containers and samples prepared from 316L stainless steel, a) top, b) side, c) three-dimensional view.

Protherm brand furnace at Yıldız Technical University, Metallurgical and Materials Engineering Department was used for the heat treatment of the test samples. Samples were gradually heated to 1030 °C and were waited for a certain period of time according to the diffusion kinetics formula ($D = D0.e^{-Q/RT}$).

5. Results and Discussion

When the boron structures were examined, it was seen that they grew in a colonial structure towards the matrix, and the growth structure was appropriate with the literature studies (Figures 3 and 4) [12, 13].

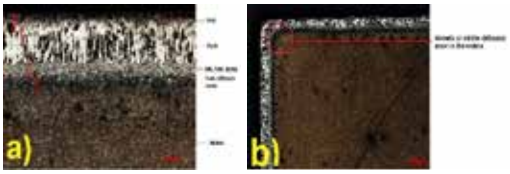

Figure 3. Light microscopy image of a boron nitride coated sample (a), light metal microscope image of a boron nitride coated sample (b).

In imaging and measurement studies performed in the light microscope in samples, it was measured that there was a maximum increase of 10% thickness in the corners. It is determined that the increase in thickness is towards the matrix, as seen in Figure 3a.

As emphasized in the literature studies, it has been stated that the shape of the part is effective in nitride processes, and its thickness increases, especially in the corners [43]. As seen in Figure 3b, it was determined that BN and FeN regions spread towards the matrix while boron coating thickness was constant.

Coating thicknesses obtained in experimental studies were found to be similar in all samples. In the literature studies, it was emphasized that when the boiling time at 1000 °C and the layer thickness is examined, the thickness of the boron layer is above 350 µm [13]. In the experimental study, as seen in Table 2, the thickness of the boron nitride layer was found to be an average of 173 µm. The thickness of the FeB and Fe_2B phases was measured as an average of 117 µm.

Table 2. 1 Measurement values of the phases formed in samples with boron nitride coating.

Sample Code	FeB (µm)	Fe_2B (µm)	Transition Zone BN (µm)	Transition Zone FeN (µm)	Total Thickness (µm)
2	33	85	31	26	175
3	31	89	30	24	174
5	31	87	31	27	176
6	29	82	32	25	168
Avarage Thickness (µm)	31	86	31	26	173

In SEM studies, it was determined that the Fe_2B phase grew in a colonial structure from the main matrix to the surface and bonded with the matrix (Figure 4). The differentiation of color structures can be interpreted depending on the chemical composition of the base material used and the relationship between temperature and duration in the study [14-17].

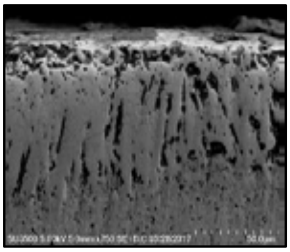

Figure 4. SEM image of boron nitride coated sample.

The hardness of boron nitride coatings was measured with the Shimadzu G21D tester. Hardness measurements were applied to etched samples, and the nitride transition zone was made at intervals of 15 µm. The determined microhardness measurement average results are given in Figure 5.

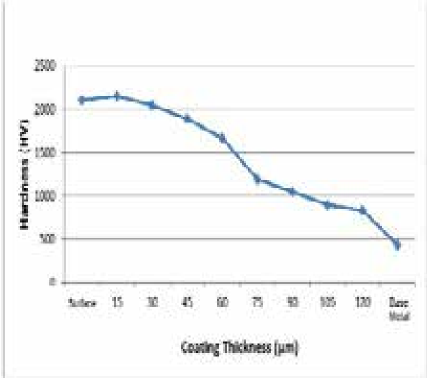

Figure 5. Graph of microhardness ($HV_{0.1}$) changes in boron nitride coated samples depending on the distance.

Microhardness values obtained in the samples are expected hardness values. Hardness values decrease significantly from the end of the columns towards the matrix. This is because the boron atoms emit outside the columns towards the matrix and form solid solution hardening.

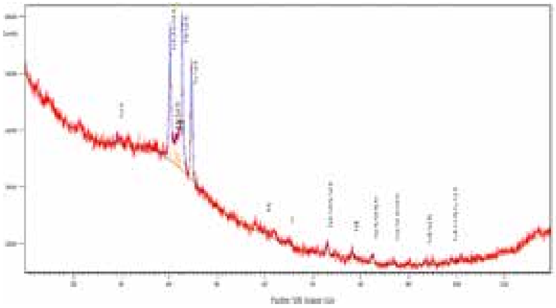

Figure 6. XRD result

FeB and Fe_2B phases and BN transition regions, which are expected to occur in the structure, were also detected in X-ray diffraction analysis (Figure 6). Literature studies show that the Fe_2B and FeB phases are formed respectively, and the Fe_2B phase grows from the surface to the inner parts [8], [14-18]. In the literature studies, it was stated that the Fe_3B phase could occur together with the Fe_2B phase as well as temperature-time interaction [15].

Conclusion

In experimental studies on samples made of H13 (1.2344) hot work tool steel:

- When the light microscope images of boron coating were examined, it was determined that the layer thickness was homogeneous across the surface. In light microscopy images, phases and transition regions can be clearly revealed.
- In the samples used in the study, H13 hot work tool steel with standard boron treatment was applied and 200 HV more hardness than standard gas nitriding was obtained. In addition, it was seen that the hardness changes in the coating are similar to the literature.
- When the boronizing time-layer thickness is taken into consideration; While the average boron layer thickness was determined above 350 µm at 1000 °C, it was emphasized that this thickness value was 110 µm on average in the samples where gas nitration was applied previously. In this study, the thinness of the boron coating layer applied on the nitride layer also reduced the fragile behavior of this layer in practice.
- When XRD outputs are examined, FeB, Fe_2B, BN, FeN, Fe_2N, and Fe_4N phases are determined. Especially the presence of Iron-Nitride phases shows that N loss does not occur due to high temperatures.
- As a result of the application of boron nitride carried out in the current study, it was observed that the main matrix hardness value decreased. However, it was understood that this decrease in hardness would not affect the use of steel.
- Due to these results, boron application on nitration can be studied in aluminum extrusion dies.

References

[1]http://www.aluminyumsanayi.com/aluminyumprofilgenel.htm>Dated:17.01.2017.

[2]K.M. Demirci, “Dünya Alüminyum Ticaretinde Türkiye’nin Yeri,” Metalurji Dergisi, 161 (2010) 17–29.

[3]M. Yılmaz, “Alüminyum Sektör Değerlendirmesi,” Metalurji Dergisi, 177 (2015) 23–29.

[4]Türkiye Alüminyum İstatistiksel Verileri, Türkiye Alüminyum Sanayicileri Derneği, 2016, İstanbul.

[5]<http://www.kindco.de/en/pdf/downloadsprospekte/tq1_gb.pdf>Dated: 11.02.2017.

[6]P.K. Saha, Çeviri: E. Keleşoğlu, Y. Erarslan, Alüminyum Ekstrüzyon Teknolojisi, Birinci Basım, Ege Basım, 2005, İstanbul.

[7]Saha, P. K., WEAR 218 (2018) 178-190.

[8]K. Ã. Genel, Vacuum (2006) 80 451-457.

[9]Borocaot Surface Treatment (2010) 9 8-9.

[10]<http://www.chemicalelements.com/elements/al.html#isotopes>Dates:17.01.2017.

[11]A.Günen, C.Çarboğa, B.Kurt, N.Orhan, Borlama İşleminde Kullanılan Bor Tozu ve Tane Boyutunun Kapalama Tabakası Üzerine Etkisi, Nevşehir Üniversitesi Fen Bilimleri Enstitüsü Dergisi (2013) 2 12-19.

[12]<http://www.alper.com.tr/hizmetler/isilislem/nitrasyon.html>Dates:24.04.2017.

[13]İ.Özbek, (2000). Borlama Yöntemiyle (AISI M50, AISI M2) Yüksek Hız Çeliklerinin ve W1 Çeliğinin Yüzey Performanslarının Geliştirilmesi, Doktora Tezi, Sakarya Üniversitesi Fen Bilimleri Enstitüsü, Sakarya.

[14]W.W.Thedja, B.K. Müller, D.Ruppin, Tribological Process on the Die Land Area During Extrusion of AA6063 Alloy, Beşinci Uluslararası Alüminyum Extruzyon Teknolojileri Semineri, 19-22 Mayıs 1992, Chicago.

[15]Ş. Şen, (1998). Termokimyasal Borlama İşlemiyle AISI 5140, AISI 4140 ve AISI 4340 Çeliklerinin Yüzey Performanslarının Geliştirilmesi, Doktora Tezi, Sakarya Üniversitesi Fen Bilimleri Enstitüsü, Sakarya.

[16]V.I. Dybkov, W. Lengauer, K. Barmak (2005). Journal of Alloys and Compounds, (2005) 398 113-122.

[17]A. Amulevicius, M. Balciunien, B. Petretis, R. Pileckis, Thin Solid Films, (1993) 229 192-195

[18]M.Tabur, (2008). Bor Karbür Kaplanmış Aısı 8620 Ve Hardox 400 Çeliklerinin Abrasiv Aşınma Davranışlarının İncelenmesi, Doktora Tezi, Gazi Üniversitesi Fen Bilimleri Enstitüsü, Ankara.

A Novel Technique for Phase Homogenization in CRTD-Bor: Periodically Interrupted Current

**Oğuz Kağan COŞKUN, Mehtap ARSLAN, Mehran KARIMZADEKHOEI,
Güldem KARTAL ŞİRELİ, Servet TİMUR**
İstanbul Technical University
Turkey

Abstract
Boriding is a type of diffusion coating that results in extremely high surface hardness. In case of steel substrates, boron atoms diffuse to form a diffusion layer consisting of a dual FeB and Fe_2B. Although FeB is known for being a very hard phase, its being brittle makes it undesirable for mechanical and tribological applications. As a result, single homogeneous Fe_2B layer is more desired than a dual phase. Using pulse current, one simultaneous process is used to obtain single phase boride layer via molten salt electrolysis process, developed by our research group, CRTD-BOR. The industrially accepted single phase crackless Fe_2B layer is obtained at the process conditions of 1/8 duty cycle, 200 mA/cm^2 and 950^{o}C.

1. Introduction

Besides the well-known usages such as batteries, fuel cells, thermal energy and nuclear energy applications, an encouraging application of molten salts is to electrodeposit a metal onto the substrate material so that enhanced surface properties, such as increased hardness and wear resistance or anti-corrosion behavior can be obtained [1]. Compared to aqueous solutions, molten salt electrolytes show dominance in aspects like possibility of a higher current density- consequently, a higher production rate- and a better adhesion of deposited species on the substrate surface [2,3]. Among the surface modification possibilities of substrates, molten salts can also be used for the diffusion coatings of substrates by elements such as boron, silicon and nitrogen [1]. Diffusion coating is that a layer does not form on the surface of the substrate, but deposited atoms diffuse into the surface of the substrate under thermal effects forming intermetallic compounds and/or solid solutions [1].

Boriding is a type of diffusion coating that results in extremely high surface hardness (between 1450 and 2000 HV), in which boron atoms diffuse into the work piece to form a range of metal borides, namely MeB and Me_2B [4]. Even though pack boriding – a cementation based process – needs very long processing time and produces solid wastes and gaseous emissions, it is highly preferred by industry among the other boriding methods such as paste boriding, plasma boriding and fluidized bed boriding [5,6]. One option being cementation based-processes, the alternative is electrolytic deposition of species from molten salts which is more controlled than conventional cementation based processes such as pack boriding, in terms of deposition and diffusion rate, as independently controlling cathode current density and temperature is possible [7]. In this context, CRTD-Bor [8] is an environmentally friendly (utilizing a green electrolyte consisting of borax and sodium carbonate), fast and cheap solution of industrial boriding requirements, a technique developed by our research group.

As the name “Cathodic Reduction Thermal Diffusion” implies, CRTD-Bor consists of the following steps:

i. Deposition of boron via series of cathodic reactions
ii. The diffusion of boron into the interstitial sides of the substrate to form intermetallic compounds and/or solid solution.

In case of steel substrates, boron atoms diffuse to form a diffusion layer consisting of a dual FeB and Fe_2B structure, the phase ratio depending on the diffusion parameters. Although FeB is known for being a very hard phase, its being brittle makes it undesirable for mechanical and tribological applications [9]. Furthermore, due to the differences in thermal expansion coefficients of the two phases, micro and macro cracking parallel to the borided surface layers may be observed [10-13]. As a result, single homogeneous Fe_2B layer is more desired than a dual FeB-Fe_2B layer. There are several methodologies concerning to obtain a single Fe_2B boride layer at the surface of the substrate, namely (I) using thinner boriding agents [14], (ii) thermal cycling [15], (iii) dilution of boron concentration of powder mixtures of pack boriding [16]. Alternative to these long and labor-intense procedures, a process called phase homogenization is developed by Kartal and her colleges [17]. With this extra step to CRTD-Bor, cathodic polarization is cut after electrochemical boriding, and the substrate is left in the molten salt for sometimes to allow phase transformations so that a single and homogeneous Fe_2B layer is obtained.

Many times pulse current application is related to (i) increasing the limiting current density, (ii) depositing with desired composition, and structure (iii) reducing the additive requirement, and finally (iv) elimination of thickness build up in areas where current density is high [18-19]. In this study, periodically interrupted current is applied such that the two successive process, where boron atoms are deposited on the surface while the current is on, and the system goes into phase homogenization or diffusion mode when the current is interrupted thanks to the thermal effects, and effect of parameters such as duty cycle and process time on the structure and thickness of borided layer are investigated.

2. Experimental procedure

2.1. Materials and Methods

A rectangular-shaped low carbon steel specimen with the chemical composition is prepared for each experiment. Before each and every experiment, all specimens were polished with SiC emery paper up to 800-grit size to control surface roughness. Then the samples were ultrasonically cleaned in acetone and dried in air. The electrolyte composition of CRT-Bor is 90% borax and 10% sodium carbonate. The graphite crucible was used as node and the steel specimens were the cathodes. A medium frequency induction furnace is used to heat the system. A home-made pulse current generator circuit is designed and employed. The cell was monitored and recorded by using a DAQ Card. The experimental setup is given in Figure 1. Experimental conditions are given in Table 1.

2.2. Characterization of samples

After each and every experiment, the specimens were withdrawn from the electrolyte and left to cool in air. The frozen remnants of electrolyte on the substrate surface were washed away in boiling water. The thickness and morphology of grown boride layers were investigated in cross-section Scanning Electron Microscopy (SEM-JEOL JSM 5410) and optical microscope (OM-Nikon Eclipse L150). The thicknesses were measured for 5 different locations including valleys and hills of the boride layers. The structure of borided samples was determined by thin-film X-ray diffraction (Phillips Model PW3710) using CuKα radiation (10 kV – 10 mA) and a glancing angle of 2°.

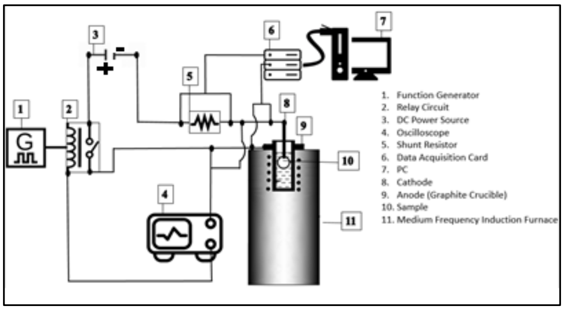

Figure 1 : Experimental Setup

Table 1 : Experimental conditions

Specimen Code	**1**	**2**	**3**	**4**	**5**	**6**
Duty Cycle	1/2	1/3	1/4	1/3	1/4	1/8
Total Process Time	5 min	5 min	5 min	20 min	20 min	25 min
Current Density [mA/cm²]	200	200	200	200	200	200
T	950ºC	950ºC	950ºC	950ºC	950ºC	950ºC

3. Results and Discussion

Figure 2 shows the thin-film XRD results of specimens prepared at 950ºC, 200 mA/cm^2 for 5 minute total process duration. It is understood that electrolysis with 1/2 duty cycle results in dual phase formation even for 5 minutes; on the other hand, single Fe_2B structure is formed after electrolysis with 1/3 and 1/4 duty cycle.

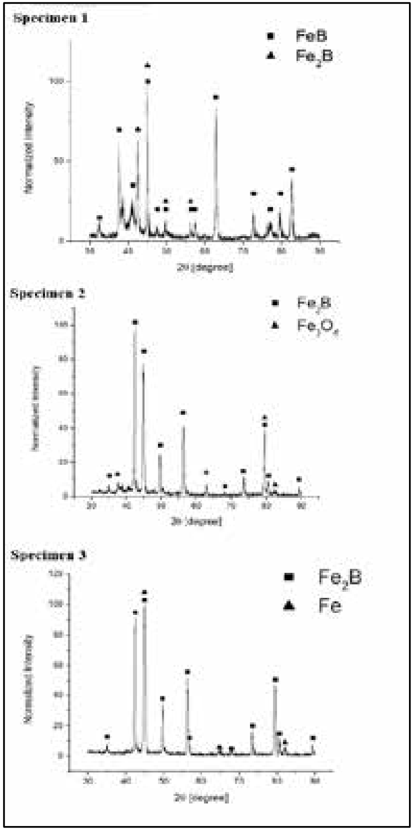

Figure 2 : The thin film X-ray diffractograms. [950ºC, 200 mA/cm^2, duty cycle 1/2, 1/3, 1/4, 5 min]

The cross-sectional SEM examination revealed that boride layers show very tooth-like structure. The thicknesses of the three of these specimens are 17.42 µm, 16.64 µm, and 10.2 µm. As the duty cycle decreases from 1/2 to 1/4, the time for boron reduction on the surface decreases, thus the decreased boride layer thicknesses. In specimen 2, it can be seen that there is a crack formation all the way parallel to the borided layer and also some oxide formation is caught on XRD results. Furthermore, since Specimen 3 has a low boride thickness layer, XRD peaks of Fe atoms can be observed. The cross-sectional views are given in Figure2.

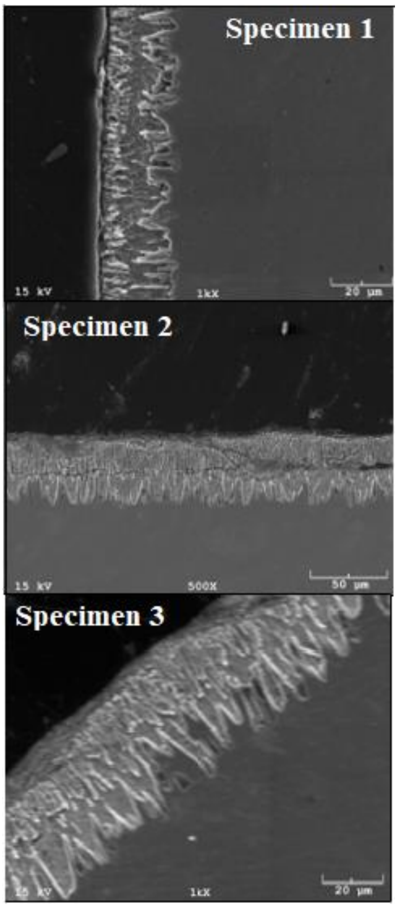

Figure 3 : Cross-sectional SEM investigation of Specimen 1,2 and 3. [950ºC, 200 mA/cm^2, duty cycle 1/2, 1/3, ¼, 5 min]

Increasing total process time from 5 minutes to 20 minutes for duty cycles 1/3 and 1/4 changed the structure of the borided layer in a way that duty cycle 1/3 started to consist of single FeB structure and ¼ became dual phase. The thin film XRD results of Specimens 4 and 5 are given in Figure 4. The cross-sectional SEM examination given in Figure 5 revealed that the borided layers show very tooth-like morphology with the averaged layer thicknesses 38.28 µm and 25.12 µm, respectively. As t_{on} decreases in the total process duration, the observed layer thicknesses decrease accordingly; on the other hand, it allows dual phase structure to transform into single Fe_2B layer. This observation is confirmed with 1/8 duty cycle for even 25 minute total process time. The thin-film XRD result and the cross sectional SEM examination is given in Figure 6.

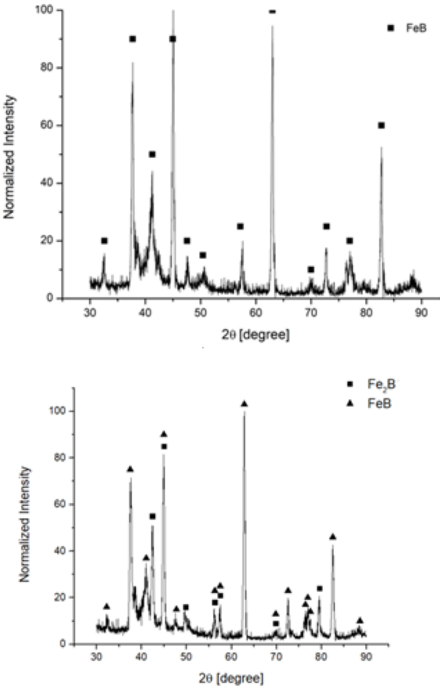

Figure 4 : The thin film X-ray diffractograms of Specimen 4 and 5. [950ºC, 200 mA/cm^2, duty cycle 1/3 and 1/4, 20 min]

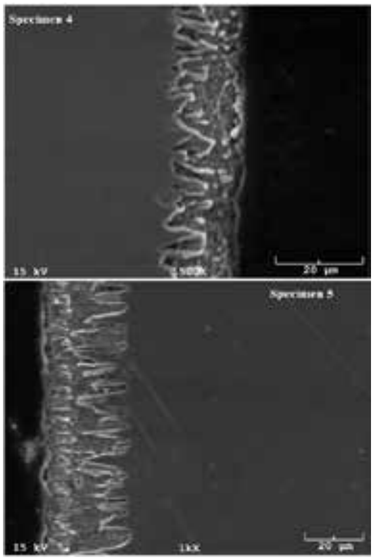

Figure 5 : Cross-sectional SEM investigation [950ºC, 200 mA/cm^2, duty cycle 1/3 and 1/4, 20 min]

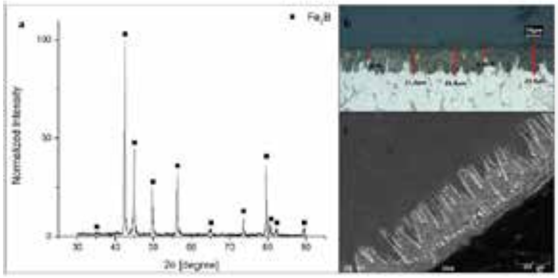

Figure 6 : (a) The thin-film X-ray diffractogram, (b) Optical microscope thickness measurements, and (c) Cross sectional SEM investigation of Specimen *6*

4. Conclusion

In the content of this study, the possibility of applying periodically interrupted current on borided layers produced via CRTD-Bor were investigated in terms of phase homogenization, structure, layer thickness and morphology of boride layers. It seems as the amount boron deposition and total process time increase, the layer thicknesses increase accordingly; while, the phase of boride layers goes from single Fe_2B to a dual phase, and a single FeB structure. The industrially accepted single phase and crackles Fe_2B layer is obtained at the process condition of 1/8 duty cycle, 200 mA/cm^2, 950ºC and 25 minutes.

References

[1]. K. Matiašovsky, P. Fellner, and M. C. Ž. Lubyová, “Electrolytic metal coating in molten salts,” vol. 41, no. iv, 1987.

[2]. Galopin, M., & Daniel, J. S. (1975). Molten salts in metal treating: Present uses and future trends. Electrodeposition and Surface Treatment, 3(1), 1-31.

[3]. Sethi, R. S. (1979). Electrocoating from molten salts. Journal of Applied Electrochemistry, 9(4), 411-426.

[4]. G. Kartal, S. Timur, and C. Arslan, “Effects of process current density and temperature on electrochemical boriding of steel in molten salts,” J. Electron. Mater., vol. 34, no. 12, pp. 1538–1542, 2005.

[5]. Matuschka, A. (1980). Boronizing. Hanser., Sinha, S. K. (2002).

[6]. ASM International Handbook. ASM International, Metals Park, OH.

[7]. G. K. Sireli, “Molten Salt Baths: Electrochemical Boriding,” Encycl. Iron, Steel, Their Alloy., no. January 2015, pp. 2284–2300, 2016.

[8]. Timur, S., Kartal, G., Eryilmaz, O. L., & Erdemir, A. (2015). U.S. Patent No. 8,951,402. Washington, DC: U.S. Patent and Trademark Office

[9]. G. Kartal Sireli, A. S. Bora, and S. Timur, “Evaluating the mechanical behavior of electrochemically borided low-carbon steel,” Surf. Coatings Technol., vol. 381, no. November 2019, p. 125177, 2020.

[10]. M. Rile, Met. Sci. Heat Treat. 16 (1974) 836.

[11]. S. Taktak, S. Tasgetiren, J. Mater. Eng. Perform. 15 (2006) 570.

[12]. E.I. Zhluktenko, R.G. Rakitskaya, E.S. Makritskii, V.Ya. Chel'tsov, Met. Sci. Heat Treat. 19 (1977) 8.

[13]. B.V. Badushkin, B.Z. Polyakov, Met. Sci. Heat Treat. 15 (1973) 577.

[14]. M. Keddam, Appl. Surf. Sci. 253 (2006) 757.

[15]. P. Goapalakrishnan, P. Shankar, M. Palaniappa, S.S. Ramakrishnan, Metall. Mater. Trans. A 33A (2002) 1475.

[16]. T.W. Spence, M.M. Makhlouf, J. Mater. Process Tech. 168 (2005) 127.

[17]. G. Kartal, S. Timur, V. Sista, O. L. Eryilmaz, and A. Erdemir, “The growth of single Fe2B phase on low carbon steel via phase homogenization in electrochemical boriding (PHEB),” Surf. Coatings Technol., vol. 206, no. 7, pp. 2005–2011, 2011.

[18]. N. Rybakova, “„ Production of Titanium Diboride Coatings by,” 2011.

[19]. M. S. Chandrasekar and M. Pushpavanam, “Pulse and pulse reverse plating — Conceptual , advantages and applications,” vol. 53, pp. 3313–3322, 2008.

Development of Chrome-Free Etching for Electroless Coating of Polymeric Materials

Mehtap ARSLAN, Oguz Kagan COSKUN, Guldem KARTAL SIRELİ, Servet TIMUR
İstanbul Technical University
Turkey

Abstract

This study involves development of chrome free etching of polymeric materials for electroless coating and the purpose is to change the etchant type in etching which must be conducted before electroless coating. The importance of development of chrome free etchants is raising day by day because of the cancerogenic and environmentally hazardous nature of chromic acid. In the content of this study, alternative etchant types were tried to etch the surfaces of polymeric substrates. In the light of this, three types of etchants were utilized to etch the surface, namely to form micro holes and/or chemically distorted areas on the surface of the polymeric specimens. These environmentally friendly etchants were crypted as Type1, Type2 and Type3. Each of them is complex formers and contains amine groups. As substrate material, ABS (acrylonitrile butadiene styrene) materials were selected. The polymeric specimens were exposed to pretreatment methods (degreasing, neutralizing, chrome-free etching, sensitization and activation). The cleaned surfaces were etched to form active sides for furthers steps and these etched surfaces were characterized by optical microscope and 3D optic profilometer. As a consequence of these characterizations, it is observed that although the etching mechanisms of Type1, Type2 and Type3 etchants are different from chromic acid etching, the targeted chemical distortions and/or holes could be formed. After etching step, sensitization and activation sections were conducted to etched surfaces to create chemically active sides by means of acidic $SnCl_2$ and $PdCl_2$ solutions. The prepared polymers were plugged into electroless nickel bath to make the surface metallized. At the end of this study, metal coated polymeric materials having the same physical properties with the materials prepared by traditional method in industry, were obtained without being exposed to the hazards of the chromic acid.

1. Introduction

Polymeric materials are coated with metals for decorative or non-decorative (technical) purposes. The driving force of metallizing of polymeric materials is automotive industry and there exists also high demand in electrical industry and house-hold sector [1-3]. One of the most used methods for metallizing of polymers is electroless coating. In order to utilize from electroless coating, the non-conductive surface of polymeric materials should be turned into catalytic form [4-6]. For this purpose, a sequence of pretreatment methods is applied. Among these pretreatment steps, etching has the crucial role and in industry chromic acid (300 – 380 g/L) is used as etchant [1,7]. However, chromic acid is a chemical having extremely harmful nature for both environment and human health [8,9]. In open literature, some studies have been reported to develop chrome-free etching, as an environmental-friendly approach. Han et al. use HNO_3, H_2SO_4 and $NiSO_4$ for 20 minutes, at 50, 60, 70 ˚C respectively for etching and after etching, they applied NaOH 1-methyl-2 pyrroline and 2-Butoxy ethanol to make the surface rough [10]. Gan et all. use $KMnO_4$ and H_2SO_4 mixture in the etching step and coats the PET fabrics electroless method [11]. Wang et all. use the mixture of MnO_4 and H_2SO_4 solutions at 70 ˚C for 20 minutes to etch the ABS surface and then he neutralizes the surface by using $H_2C_2O_4{\cdot}H_2O$ and sulfuric acid at 50˚C for 3 minutes [12]. Gui et all. apply acetic acid solution at 90 ˚C for 30 minutes to etch the surface of PA12 [13]. Hiroshi et all. use sputtering method and the Pt/Pd catalyst is sputtered on the surface of the honeycomb structured PS film after that the electroless coating is applied [14]. Lijeri et all. have a new environmentally friendly solution to take the place of the chromic acid and they can coat ABS surfaces without using chromic acid [15]. Bruce P. has a patent of etching the polyarylene, polyethers, polycarbonate or polyhydroxyethers with N,N dimethylformamide, pyridine, and its compounds [16]. Teixeira et al. uses the mixture of H_2SO_4 and H_2O_2 in different concentrations to etch ABS [17]. Zhang et al. use molecular grafting method to coat ABS with electroless coating [18]. Zarnoch et all. have a patent on etching of aromatic polymers by using nitriding solution (the mixture of HNO_3 and H_2SO_4) firstly and then applying hydroxlating solution like ammonium hydroxide [19]. Pearson at all. have a patent on etching the plastic surfaces by applying the method in which the bath contains Mn(II) solution with 9 M of H_2SO_4 and 15 M of H_3PO_4. After applying current Mn(II) ions turn into Mn(III) ions. These ions form a sulfate complex. By using this complex, the surface of the polymers is etched [20]

Among the other polymeric materials ABS is considered as the best choice for coating since the dispersion of the butadiene group in acrylonitrile-styrene is homogeneous and it gives reaction and dissolves with the presence of concentrated oxidative solutions such as chromic acid [8]

Present study focused on development of new etchants which are safer to use and can be more applicable in many types of polymeric materials as compared to chromic acid. In the light of that aim, three types of novel etchants were developed to etch the surface of ABS (acrilonitril butadiene styrene).

2. Experimental procedure

ABS polymer specimens were provided by Ecoplas firm with the dimensions of 130 mm in length, 60 mm in width and 3 mm in height. Before electroless coating, degreasing, neutralizing, etching (chrome-free), sensitization and activation steps were conducted respectively.

In degreasing and neutralizing steps, specimens were cleaned with 0.1 M of NaOH solution in an ultrasonic cleaner for 15 minutes. The cleaned surfaces were rinsed and neutralized into 0.1 M HCl solution and the specimens were rinsed with distilled water. Then, three solutions named as Type 1-3 were prepared to etch the specimen surfaces. After 10 minutes etching of each specimen, the surfaces were rinsed with distilled water. In sensitization and activation step, the conventional two-step immersing method was utilized. During acidic $SnCl_2$ solution preparation, 10g/L $SnCl_2$ was used with 3.5% HCl in distilled water. The operation temperature was arranged to 45˚C. The etched specimens were immersed into the solution and waited for 10 minutes. During this process, Sn (II) ions were adsorbed on the holes formed during the etching step. After sensitization, the specimens were immersed into an acidic palladium solution consisting of 1g/L $PdCl_2$ with 1% HCl in distilled water. The process was conducted at 45 ˚C for 10 minutes. The reduction of Pd ions are clearly seen in this step. Obtained surface, after all, is catalytic and ready to be coated by autocatalytic way. Finally, in the coating step, a commercial electroless nickel was supplied from AutoTech company and the bath was prepared in given ratios. The pH of the bath kept between 9-10 by using an ammoniac solution. The activated catalytic surfaces were immersed into coating bath after seconds chemical reduction of Ni ions was started, as shown in Figure 1. The bath temperature was fixed at 28 ˚C and coating was conducted about 3 minutes. Surface topography of the etched surfaces was investigated by using optical microscope and 3D optical profilometer. Furthermore, in order to compare the physical appearance of the coatings, images were taken from constant distance and angle to an object (model plane). Upon considering the depth of the taken images, brightness of the coatings etched with three different etchants was compared.

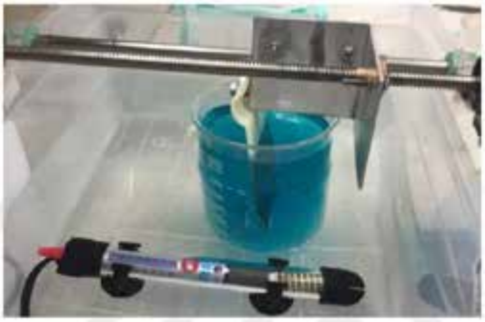

Figure 1. Electroless Ni coating of ABS specimen

3. Results and Discussion

In Figure 2, optical micrographs of the surfaces of ABS specimens before and afer etching with chromic acid and developed chrome-free etchants namely Type 1-3 are presented. As it can be seen in these micrographs when the surfaces etched with etchants Type 1-3 are compared with the surface of the reference specimen, it is clearly seen that the etchants interact with butadiene group of ABS and it results in hole formation.

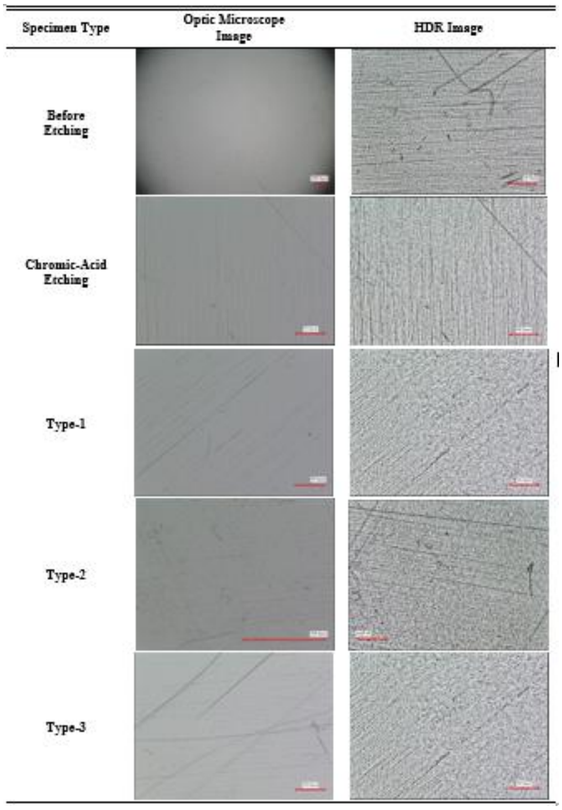

Figure 2. The micrographs belong to reference (before etching) and etched ABS surface with chromic acid and developed novel chrome-free etchants (Type 1-3)

The surface topography images of etched ABS specimens are given in Figure 3. In chromic acid etching wide holes are created on the surface of the substrate.

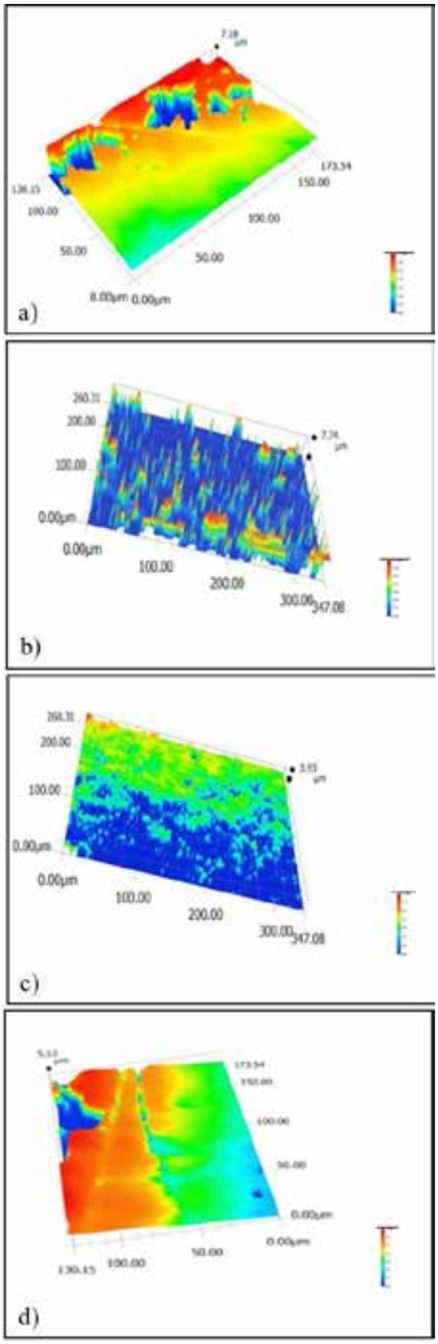

Figure 3. 3D optical profilometer images of the etched ABS samples with (a) chromic acid, (b) Type 1, (c) Type 2 and (d) Type 3.

It is expected behavior, hence chromic acid attacks the butadiene group of ABS. On the other hand, Type 1 and Type 2 etchants have totally different etching mechanisms when they are compared to chromic acid. In Type 1 etching, instead of creating big and wide holes, small pits are formed. However, the depth of the created holes and pits is the same. In Type 2 etching, the mechanism is solving the hills on the surface of the substrate material, because Type 2 etchant is an organic solution like polymeric substrate. Since they have both organic structures, the attraction between them based on solving. While solving the hills, Type 2 creates new active areas where the adsortion and reduction take place for further steps. In Type 3, there is no difference in etching mechanism when it is compared to chromic acid etching.

The brightness and colour features of the typical coatings obtained after experiments with constant and repeated conditions are given in Figure 4.

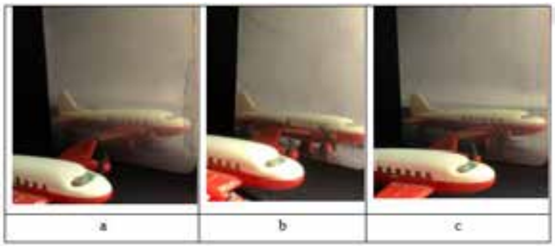

Figure 4. Visuals of brightness and colour properties of electroless Ni plated ABS specimens followed by standard (a) Type 1, (b) Type 2 and (c) Type 3 etching [28 C, 250g/l Ni, pH 9-10, 3 min]

In order to check the durability of the etchants used in this study, after 15 and 30 days of preparation of Type1 etchant the same experiments were repeated. As can be seen in Figure 5, there is no change in the coating quality even the Type 1 etchant is not freshly used. After 30th day experiment, it was understood that there is no effect on time in etchant life they can be used repeatedly like chromic acid. Since the all types of etchants used in this study exhibited similar durability, only the visuals of specimens etched by Type 1 is given.

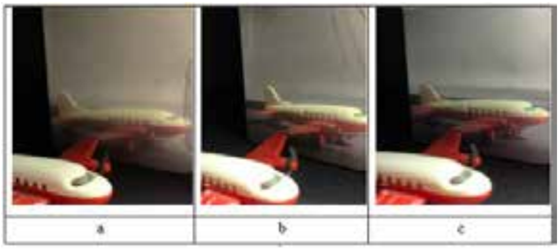

Figure 5. Visuals of brightness and colour properties of coated ABS specimens etched with Type 1 etchant (a) in fresh condition, (b) after 15 days and (c) after 30 days of preparation.

4. Conclusion

In the content of this study ABS polymers were used for the development of chrome-free etching for polymeric materials. For the alternative chemicals to chromic acid three types of etchants were studied. The criteria of this selection was the quality of the coating formed on the substrate surface. The experiments were started with chromic acid etching to check whether the coating bath and the substrate materials are working or not. The results of the examinations can be summarized as follows;

- The novel chrome-free etchants successfully led hole formation and/or chemical distortion on the surface of ABS.
- ABS were coated with electroless Ni coating by three novel chrome-free etchants.
- The effect of the etchant freshness was controlled 15 and 30 day periods and it was observed that there is no change in coating quality with changing in freshness of the etchants.
- In the light of observations and obtained results, it can be said the coating quality in the physical manner is the same with the coatings obtained by chromic acid etching.

This study proved that metal coated ABS polymers, having the same physical properties with the materials prepared by traditional method in industry, can be obtained without being exposed to the hazards of the chromic acid.

Acknowledgment
Authors would like to thank İTÜ BAP office for contributions for the project with a number of MYL-2018-41830. Also Torun Bakır, Ecoplas and AutoTech companies were acknowledged for their support.

References

[1] Garcia, A., Berthelot, T., Viel, P., Mesnage, A., Jégou, P., Nekelson, F., ... & Palacin, S. (2010). ABS polymer electroless plating through a one-step poly (acrylic acid) covalent grafting. ACS applied materials & interfaces, 2(4), 1177-1183
[2] Nigam, S., Mahapatra, S. S., & Patel, S. K. (2017). Fabrication and study of properties in metallized ABS plastic. Integrated Ferroelectrics, 185(1), 16-21.
[3] Tsuji, K., Maeda, T., & Hotta, A. (2015). Polymer Surface Modifications by Coating. In Printing on Polymers: Fundamentals and Applications (pp. 143-160). Elsevier Inc.
[4] Tarditi, A. M., Bosko, M. L., & Cornaglia, L. M. (2017). 3.1 Electroless Plating of Pd Binary and Ternary Alloys and Surface Characteristics for Application in Hydrogen Separation.
[5] Sha, W., Wu, X., & Keong, K. G. (2011). Electroless copper and nickelphosphorus plating: processing, characterisation and modelling. Elsevier.
[6] Roy, M. (2017). Protective Hard Coatings for Tribological Applications. In Materials Under Extreme Conditions (pp. 259-292). Elsevier.
[7] Barker, B. D. (1981). Electroless deposition of metals. Surface technology, 12(1), 77- 88.
[8] Hajdu, J. (1990). Surface preparation for electroless nickel plating. Electroless plating: fundamentals and applications, 193-206.
[9] Toxicology of Chromic Acid. (n.d). Retrieved October 25, 2019, from https://www.nlm.nih.gov/toxnet/index.html
[10] Han, X., Wang, G., He, Y., Wang, Y., Qiao, Y., & Zhang, L. (2018). Surfacemodification of ABS with Cr^{6+} free etching process in the electrolessplating. Journal of Adhesion Science and Technology, 32(22), 2481-2493.
[11] Gan, X., Wu, Y., Liu, L., Shen, B., & Hu, W. (2007). Electroless copper plating on PET fabrics using hypophosphite as reducing agent. Surface and Coatings Technology, 201(16-17), 7018-7023.
[12] Xu, W., Zhuang, M., & Cheng, Z. (2016). Environmentally friendly copper metallization of ABS by Cu-catalysed electroless process. Rare Metal Materials and Engineering, 45(7), 1709-1713.
[13] Gui, C., Chen, Z., Yao, C., & Yang, G. (2018). Preparation of nickel/PA12 composite particles by defect-induced electroless plating for use in SLS processing. Scientific reports, 8(1), 13407.
[14] Yabu, H., Hirai, Y., & Shimomura, M. (2006). Electroless plating of honeycomb and pincushion polymer films prepared by selforganization. Langmuir, 22(23), 9760-9764.
[15] Ijeri, V., Shah, K., & Bane, S. (2014). Chromium-free etching and palladiumfree plating of plastics. NASF Surf. Tech. White Pepers, 78(12), 1-8.
[16] Barth, B. P. (1970). U.S. Patent No. 3,518,067. Washington, DC: U.S. Patent andTrademark Office.
[17] Teixeira, L. A. C., & Santini, M. C. (2005). Surface conditioning of ABS for metallization without the use of chromium baths. Journal of materials processing technology, 170(1-2), 37-41.
[18] Zhang, H., Kang, Z., Sang, J., & Hirahara, H. (2018). Surface metallization of ABS plastics for nickel plating by molecules grafted method. Surface and Coatings Technology, 340, 8-16.
[19] Zarnoch, K. P. (1993). U.S. Patent No. 5,180,639. Washington, DC: U.S. Patent and Trademark Office.
[20] Pearson, T., & Robinson, C. (2019). U.S. Patent No. 10,280,367. Washington, DC: U.S. Patent and Trademark Office.

New Surfaces by Direct Laser Interference Patterning: Optimal Functional Properties due to Fast and Precise Micro-Nano Structuring

Frank MUCKLICH
Saarland University
Germany

Abstract

In the course of evolution, the material surfaces in living nature have often achieved their impressive perfect functionalization through optimized geometric microstructures. Whether e.g. wetting, friction or color effects, very different but periodic microstructures lead to the optimum performance. For this reason it is astonishing that we are still satisfied with the definition of roughness for our technical surfaces of components. Instead, we should make targeted use of the additional degrees of freedom of microstructural and microtopographic surfaces and the resulting possibilities of newly optimized functionality for the very wide variety of our technical surfaces.

Through the advanced use of pulsed laser radiation available today from the nanosecond range down to the ultra-short pulse range, we can exploit a variety of materials science processes to realize microstructural and microtopographic structuring for practically all types of materials. Direct Laser Interference Patterning (DLIP) plays a key role in the fast, geometrically precise but also extremely flexible realization. The talk will discuss ideal-typical examples that address a wide range of potential applications from e.g. extremely low-friction tribology to antimicrobial efficiency and drastically increased reliability of electrical contacts etc.

Effects of Multistep Surface Preparation of PU on Surface Properties of Metallic Coatings

Büşra ÜNLÜ[1,2], Yahya ÖZ[2], Metehan ERDOĞAN[3], İshak KARAKAYA[1]
[1]Middle East Technical University, [2]Turkish Aerospace, [3]Ankara Yıldırım Beyazıt University
Turkey

Abstract

Electroless and electrolytic plating of several materials such as Cu, Ni, Cr, Ag, Au, Zn etc. is applied for several applications. Electrolytic plating on a polymeric substrate is important for composite tool manufacturing in the aerospace industry. The polymeric substrate metallized in this study was electrically conductive in the range of semiconductor materials, highly dense, durable at high temperatures (up to 220°C) and had a low coefficient of thermal expansion. The metallization process consisted of multisteps that are carried out by degreasing, etching, sensitization with Sn^{+2} ions and activation by reducing Pd^{+2} ions to Pd. The activated surface was immersed into the electroless nickel plating bath after the surface metallization process and then directly plated electrolytically. Metallized surfaces were characterized after electrochemical nickel plating at different current densities and surface morphology, roughness as well as physical properties of the coatings were investigated. Results showed that increasing current density adversely affects the surface morphology and metallization processes enhance the surface conductivity of the foam.

Introduction

The main purpose of this study was to enable the way of manufacturing Ni composite lay-up tools via an electroforming method onto a PU surface. It is very important to create know-how and to define the mechanism of this process, which is significant for the aerospace industry for the purpose of bringing it into mass production on a large scale because understanding the background information facilitates intervention at the right time during ongoing production. The originality of this study is the application of a metallization process to prepare PU as mandrel for the electrolytic production of a Ni lay-up tool.

Materials and Methods

Surface preparation processes of polymeric substrates are playing a crucial role for metallization processes. Therefore, the important perquisite of the electrolytic and/or electroless Ni plating is an appropriate catalytic surface. Thus, Sn sensitization, Pd activation, electroless Ni plating in two different solutions and electrolytic Ni plating was appplied on PU surface. Microstructural (SEM, XRD, XPS, surface roughness analysis) and electrical characterization (PPMS analysis) were conducted at each step of metallization process.

$$Sn^{+2} + Pd^{+2} \longrightarrow Pd^{0} + Sn^{+4} \tag{1}$$

Conclusion

The highest electrical conductivity was obtained when acidic bath was used in electroless Ni plating. Additionally, Sn sensitization, Pd activation and electroless Ni plating in the acidic electrolyte was necessary steps before the electrolytic Ni plating on PU substrate.

The Future of Extractive Metallurgy

Fathi HABASHI
Laval University
Canada

Abstract

While pyrometallurgy is most suitable for treating high grade oxide ores, hydrometallurgy is suitable for low grade oxide ores and for sulfide concentrates. Electrometallurgy is presently dominated by the production of aluminum, the electrorefining of copper, and the electrowinning of zinc. It has been also successful in the electrowinning of copper from solution obtained by leaching-solvent extraction. However, if the copper industry shifts from smelting to pressure leaching then electrowinning will dominate the area of aqueous electrometallurgy. At present all data point out to pressure leaching as the eminent route for treating copper sulfide concentrates in the twenty first century. This technology now used for treating zinc sulfide and refractory gold concentrates, alleviates pollution problems by SO_2. The electrometallurgy of aluminum research is undergoing a fundamental change using insoluble electrode instead of carbon electrode.

Using Laser Ultrasonics to Study Austenite Grain Growth Kinetics of Carburizing Steels

Kemal DAVUT[1], **Rasim Köksal ERTAN**[2], **Yasin DEMİRKOL**[2], **Caner ŞİMŞİR**[3]
[1]Atılım University, [2]Simultura Malzeme Teknolojileri, [3]Middle East Technical University
Turkey

Abstract
In this study, austenite grain growth kinetics of 2 different commercial carburizing steel grades (AISI 5116 and AISI 9310) have been measured in-situ by laser-ultrasonics using the attenuation spectra. Laser-ultrasonics is a technology that enables non-contact ultrasonic measurements that can be used on metals heated up to their melting temperature; thus making it ideal for in-situ measurements. The investigated steel grades exhibit different grain growth kinetics. The austenite grain size determined via laser ultrasonics agree within 10% error with the metallographic analysis.

1. Introduction

Carburizing treatments involve longer holdings at the austenite region, which can produce a range of different prior-austenite grain sizes (PAGS) depending on the growth behavior. The PAGS influences hardenability, final phase fraction and hence the final mechanical properties as well as the tempering behavior. Although modern carburizing furnaces allow carburizing at higher temperatures to reduce the carburizing time, excessive austenite grain growth is still a limiting factor for most of the currently available carburizing steels. Controlling the formation of desired austenitic structure during carburizing treatment is particularly important and difficult; since it transforms during subsequent cooling steps.

2. Materials and Methods

In this study, grain growth kinetics of 2 different commercial carburizing steel grades, namely AISI 5116 and AISI9310 has been monitored. Using Gleeble 3500 Thermo-Mechanical Simulator, the specimens were heated to 900, 950 and 1000^{o}C at a rate of 10^{o}C/s and hold there for 15 minutes. During this isothermal holding the growth of austenite grains has been measured in-situ by laser ultrasonics (LUMet) attached to the Gleeble 3500 system. A frequency doubled Nd:YAG laser having 532 nm wavelength, 6 ns pulse duration was used for generation and a frequency stabilized Nd:YAG pulsed laser having 1064 µm wavelength, 90 µs pulse duration was used for detection of ultrasonic pulses. The attenuation spectra of the ultrasonic pulse, collected at a rate of 10 Hz was used to determine the change in grain size of austenite grains. After the heat treatments the specimens were subjected to metallographic examination using optical and scanning electron microscopes. The prior austenite grains were revealed using Bechet-Beaujard's etch method and by Kohn method. Lastly the average size of prior austenite grains were determined using Heyn intercept method per ASTM E112 standard.

3. Conclusions

The grain growth kinetics of carburizing steels can be monitored in-situ by laser ultrasonics (Gleeble 3500 system equipped with LUMet). The system can detect the change in austenite grain size. However; laser ultrasonics have a limited accuracy for grain growths below 5 µm. Moreover, this technique requires the knowledge of the the grain size of firstly formed austenite grains. Nevertheless, by taking the grain size of initially formed austenite grains as 5 µm, the grain size of austenite after 15 minute long treatments was determined. The results of laser ultrasonics agree within 10% error with metallographic analysis. This error range is within the precision of both techniques.

Acknowledgements
Republic of Turkey, Directorate of Strategy and Budgetary is gratefully acknowledged for the use of facilities of Metal Forming Center of Excellence. The authors thank ESTAŞ A.Ş. for supplying the carburizing steel samples.

Influence of Methane Content on Control of Carburizing

M. Tarik BOYRAZ, Heinrich KLUMPER-WESTKAMP, Matthias STEINBACHER
Leibniz-Institut für Werkstofforientierte Technologien
Germany

Abstract

The successful control of the gas carburizing process depends on the accurate prediction of carbon concentration depth profile. When controlling carburization process, there are different procedures with regard to the consideration of the carburization reactions. The main carburizing reactions are Boudouard reaction, heterogeneous Water-gas reaction and Methane reaction. In most industrial applications, influence of the Methane reaction is ignored and usually only one of the first two reactions is used for control of carburizing atmosphere and carbon potential. The ignorance of Methane reaction in control of gas carburizing contributes to impermissible deviations in the treatment results.

In this research, various groups of experiments were designed to investigate the influences of methanol/nitrogen ratio, treatment temperature and carbon potential on formation of residual methane in furnace atmosphere. Additionally, a control model that takes methane influence on furnace atmosphere and carbon potential into account, is assessed and implemented to enable better control of the carburizing process. This is achieved through closely interlinked experimental and theoretical studies. In the theoretical part, the carburization simulation is expanded by taking the methane reaction into account. The experimental verification is done by adding various amounts of methane to nitrogen-methanol based carrier gas and analyzing chemical composition of the furnace atmosphere.

The results of this research show that decrease in the treatment temperature, increase in the methanol/nitrogen ratio and the carbon potential lead to increase in the residual methane content in furnace atmosphere. Furthermore, this research proves that the Methane reaction at steel surface influences carbon potential and carbon depth profile significantly. Ignoring the effect of methane reaction results leads to deviation in the predicted carbon potential and the carbon depth profile.

1. Introduction

Gas carburizing is one of the oldest heat treatments used for surface hardening. Nonetheless, it experiences certain challenges associated with the process control.

The predominant carburizing reactions are the Boudouard reaction and the heterogeneous Water-gas reaction. In industrial applications, usually only one of the two reactions is used for process control by recording CO and CO_2 contents according to the Boudouard reaction or by recording the partial pressure ratio pH_2O/pH_2 with simultaneous knowledge of the CO content according to the heterogeneous water gas reaction.

The furnace atmosphere typically consist of a carrier gas and a hydrocarbon. The dissociation of the carrier gas and the hydrocarbon results in a residual methane formation. This residual methane react and dissociate on steel surface. The carbon activity of this Methane reaction is significantly higher than other two reactions. However, since the methane reaction occurs very slowly, it is not usually taken into account in process control.

In the furnace atmosphere, when the residual methane content is over 1 vol.%, the carburizing can no longer be carried out accurately without considering the effect of methane reaction. Such an increase in the methane content can occur due to low treatment temperatures, high carbon potentials, and/or batches with high surface areas.

Aim of this research is to improve the understanding of trends that lead to higher residual methane formation and implement a control model that takes Methane reaction influence on furnace atmosphere and carbon potential into account to enable better and reproducible control of the carburizing process.

2. Experimental Procedure

2.1. Theory

The methanol can be cracked in the furnace atmosphere, to form a blend of nitrogen and methanol as carrier gas, with a composition of 15-25 vol.% CO, 35-45 vol.% H_2, balanced by N_2 and small amounts of CO_2, H_2O and CH_4. An enrichment gas such as C_3H_8 reacts with CO_2 and H_2O in furnace atmosphere to increase carbon activity. The products of this reaction are CO, H_2 and also CH_4.

The main carburizing reactions at the steel surface are Boudouard reaction (1), the heterogeneous Water-gas reaction (2) and the Methane reaction (3) as given below.

$$2CO \rightarrow [C] + CO_2 \tag{1}$$
$$CO + H_2 \rightarrow [C] + H_2O \tag{2}$$
$$CH_4 \rightarrow [C] + 2H_2 \tag{3}$$

The carbon mass flow density J for the given reactions (1) - (3) at the surface can be described by the following equation [1]

$$J = \rho \ \sum_{v=1}^{n} \beta_v \left(a_{g_v} - a_s\right) \ \left(\frac{g}{cm^2}.s\right) \tag{4}$$

where β_v is

$$\beta_v = \frac{k_v}{a_s^m} \qquad (cm/s) \tag{5}$$

ρ is density of the steel, n is the total number of reactions, v is the reaction number, β_v is the carbon transfer coefficient, a_{g_v} is the carbon activity of the gas, a_s is the carbon activity at the steel surface and k_v is reaction rate coefficient. m = 0 or 1 depending on reaction type [1].

The carbon activity for carburizing reactions (1) - (3) can be calculated by the following three equations respectively [2]

$$\lg a_{g1} = \lg (p_{2CO}/p_{CO2}) + 8817/T - 9{,}071 \tag{6}$$

$$\lg a_{g2} = \lg (p_{CO} \cdot p_{H2}/p_{H2O}) + 7100/T - 7{,}496 \tag{7}$$

$$\lg a_{g3} = \lg (p_{CH4}/p_{2H2}) - 4791/T + 5{,}789 \tag{8}$$

in which a_g is the carbon activity of the reaction, p is partial pressure and T is the treatment temperature in Kelvin. In most carburizing applications, the carbon activity of the Boudouard reaction or heterogeneous Water-gas reaction is accepted as the carbon activity of the furnace atmosphere a_g. This activity is used to calculate and control the carbon potential C_p of the furnace atmosphere by using the following equation [2]

$$\lg a_g = \frac{2300}{T} - 2.21 + 0.15\, C_p + \lg C_p \tag{9}$$

Furthermore, the same activity is also used to calculate the carbon mass flow J as given in following equation [3]

$$J = \rho * \beta * \left(a_g - a_s\right) \tag{10}$$

where carbon transfer coefficient β is [4]

$$\beta = 0.00018 * p_{CO} * p_{H2} - (p_{CO} * p_{H2}/65.78)^2 \tag{11}$$

This widely employed method to predict carbon level and carbon mass flow can be named as One Parameter Model since only carbon activity of one reaction is used. Even though methane reaction has higher activity than the other two reactions, its effect on carburizing atmosphere is ignored. Additionally, the carbon transfer coefficient equation is also insensitive to changes in amount of methane content. These problems in the One Parameter Model cause significant deviations in expected carburizing results of carburizing processes with high methane content.

R. Collin et al. developed the Multi Parameter Model to take each carburizing reactions effect into account for carbon potential and carbon mass flow prediction. The reaction rate coefficients based on Multi Parameter Model for reactions (1) - (3) are given in following equations respectively [5].

$$k_1 = 184 * \left(\frac{p_{CO2}}{p_{CO}}\right)^{-0.3} * p_{CO2} * exp\left(-\frac{22400}{T}\right) \tag{12}$$

$$k_2 = (4.75 * 10^5 * exp\left(-\frac{27150}{T}\right) * \frac{p_{H2O}}{\sqrt{p_{H2}}})/(1 + 5.6 * 10^6 * exp\left(-\frac{12900}{T}\right) * \frac{p_{H2O}}{\sqrt{p_{H2}}}) \tag{13}$$

$$k_3 = 1.96 * 10^{-2} * p_{H2}^{\frac{3}{2}} * exp\left(\frac{-17600}{T}\right) \tag{14}$$

In the Multi Parameter Model, each carburizing reaction has an independent carbon transfer coefficient. These coefficients for reactions (1) - (3) are given in following equations respectively [5].

$$\beta_1 = \frac{k_1}{a_{g1}} \tag{15}$$

$$\beta_2 = k_2 \tag{16}$$

$$\beta_3 = \frac{k_3}{a_{g3}} \tag{17}$$

The contribution of each reaction to total carbon mass flow is considered independently in the Multi Parameter Model as given in following equation [5].

$$J = \rho . \left[\beta_1\left(a_{g1} - a_s\right) + \beta_2\left(a_{g2} - a_s\right) + \beta_3\left(a_{g3} - a_s\right)\right] \tag{18}$$

When furnace atmosphere and steel surface are in equilibrium, the mass flow defined in Equation (18) is equal to zero. The carbon activity of furnace atmosphere and related carbon potential can be calculated by using this equilibrium.

2.2. Program

A program is written in MATLAB 2018a to predict carbon potential and carbon depth profile using the One Parameter and the Multi Parameter Models. Treatment duration, temperature, composition of furnace atmosphere and alloy composition were used as input. A number of node points were defined through steel surface to simplify the calculations.

The mass flow through steel J_i was calculated by the general equation given below [6]

$$J_i = -D_i * \frac{c_i}{a_i} * \frac{da_i}{dx} \tag{19}$$

where

$$D = 0.484 * \exp\left(\frac{-155000}{R.T}\right). \exp\ \left(\frac{(570000 - 320.T) * x_C}{R.T}\right) \tag{20}$$

i is the nod point number, c_i is the carbon composition, a_i is the carbon activity, D is the carbon diffusion coefficient, dx is the distance between node points, da_i is the difference in activity between node points and R is the universal gas constant. Based on Equation (19), carbon content at each node point at different time steps can be calculated by using the following equation

$$c_{t-1}^{t+1} = c_{i-1}^{t} - \frac{dt}{dx}(J_i^t - J_{i-1}^t) \qquad (21)$$

where t is the corresponding time step and dt is the difference between defined time steps.

2.3. Laboratory Experiments

In this research, SOLO 202 CTB 3/3/3 11CG furnace with a 300x300x300 mm^3 chamber size was used in all the carburizing experiments. The composition of CO, H_2, CO_2 and CH_4 gases in furnace atmosphere were analyzed with an ABB gas analysator. The H_2O content of the atmosphere was analyzed hourly with a MESA dew point analyzer.

The first group of experiment was designed to investigate the effect of dissociated methanol/nitrogen ratio on residual methane content as given in Table1.

Table 1. The First Experiment Group Parameters.

CH_3OH/N_2 Flow Ratio	N_2 Flow (ℓ/h)	Temperature (°C)	Carbon Potential (Ma.%)	Duration (h)
0.3	450	930	1	4
2.2	200	930	1	4
16.7	50	930	1	4

The second group of experiments was designed to investigate the effect of treatment temperature and carbon potential on residual methane content in furnace atmosphere as shown in Table 2 below.

Table 2. The Second Experiment Group Parameters.

CH_3OH Flow (ℓ/h)	N_2 Flow (ℓ/h)	Temperature (°C)	Carbon Potential (Ma.%)	Duration (h)
0.26	200	930	1.1	4
0.26	200	890	1.1	4
0.26	200	850	1.1	4
0.26	200	930	0.8	4
0.26	200	890	0.8	4
0.26	200	850	0.8	4

In a third group of experiments, various amounts of methane was added to nitrogen-methanol based carrier gas to investigate the effect of methane content on carbon depth profile of steel samples as given in Table 3 below.

Table 3. Third Experiment Group Parameters.

CH_3OH Flow (ℓ/h)	N_2 Flow (ℓ/h)	Temperature (°C)	CH_4 Addition (ℓ/h)	Duration (h)
0.26	200	930	0	7
0.26	200	930	10	7
0.26	200	930	20	7
0.26	200	930	30	7

The cylindrical C15 low carbon steel samples were only used in the third group of experiments. The samples had an identical height of 1 cm and diameter of 2.5 cm. The chemical composition of C15 samples were analyzed with spark optical emission spectroscopy before and after carburizing. The chemical composition before carburizing is given in Table 4 below.

Table 4: The Chemical Composition of C15 in Ma.%.

C	Si	Mn	Cr	Ni	Cu	Fe
0.15	0.30	0.51	0.122	0.09	0.16	Rest

3. Results

The carburizing experiment results show that methanol/nitrogen flow ratio, treatment temperature and carbon potential have a strong influence on the amount of residual methane content in furnace atmosphere.

The increase in methanol/nitrogen flow ratio resulted in increase of residual methane content since the amount of methanol to dissociate in furnace atmosphere was increased as shown in Figure 1.

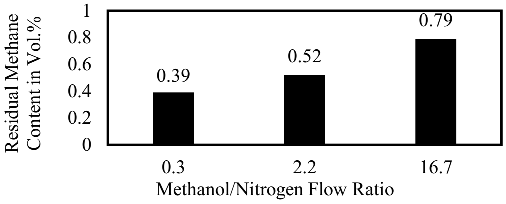

Figure 1. The residual methane content in furnace atmosphere at various methanol/nitrogen rates.

The amounts of measured residual methane content at various treatment temperatures and carbon potentials (Table 2) is shown in Figure 2 below.

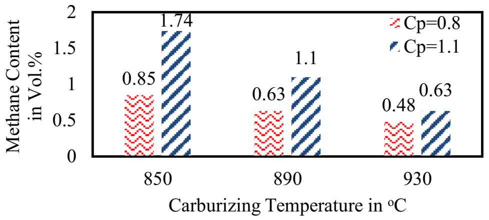

Figure 2. The residual methane content in furnace atmosphere at various temperatures and carbon potentials.

The decrease in treatment temperature, increased the residual methane content formed during the methanol and propane dissociation. Furthermore, to increase the carbon potential, the amount of supplied propane was increased. This leaded to an increase of the amount of residual methane formed during propane dissociation.

To understand the effect of methane content on predicted carbon depth profile, various amounts of methane were added to methanol/nitrogen based carrier gas and the composition of furnace atmosphere was analyzed as given in Table 5.

Table 5: The Composition of Furnace Atmospheres After Various Amounts of CH_4 Addition.

CH_4 addition (l/h)	H_2 (Vol.%)	CO (Vol.%)	CO_2 (Vol.%)	CH_4 (Vol.%)	H_2O (Vol.%)
0	34.64	21.09	1.19	0.13	1.78
10	35.70	21.64	0.76	0.49	1.28
20	37.14	21.28	0.46	0.81	0.76
30	38.94	22.93	0.28	1.08	0.38

The comparison of measured and predicted carbon depth profiles with the One Parameter and the Multi Parameter Models for carburized C15 samples are given in Figure 3 and 4.

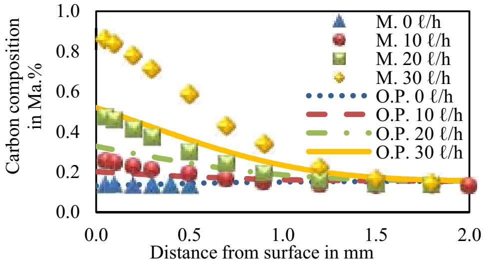

Figure 3. Measured (M.) and predicted carbon contents by using the One Parameter Model (O.P.) for C15 samples carburized with various methane additions.

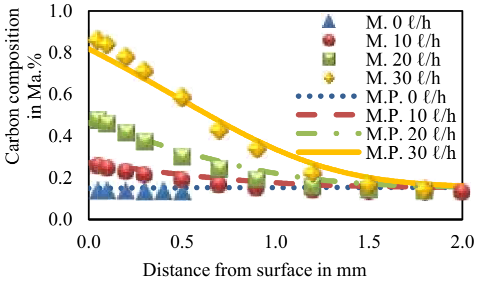

Figure 4. Measured (M.) and predicted carbon contents by using the Multi Parameter Model (M.P) for C15 samples carburized with various methane additions.

Figure 3 shows that the difference between measured and predicted carbon depth profiles using the One Parameter Model increases proportionally with the amount of methane addition since the One Parameter Model does not consider the effect of methane reaction. On the other hand, Figure 4 shows that the predicted carbon depth profile using the Multi Parameter Model shows better compatibility with the measured carbon depth profile even at high methane additions.

Furthermore, the estimated carbon potentials of furnace atmospheres by these models were compared with the measured carbon contents of carburized C15 steel surface in Figure 5.

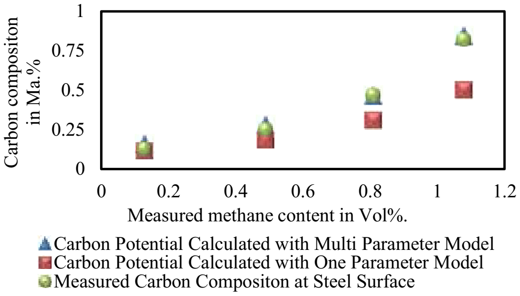

Figure 5. The predicted carbon potentials using the One Parameter and the Multi Parameter Models compared to the measured carbon contents at C15 steel surface.

The Figure 5 shows that the One Parameter Model fails to estimate carbon potential correctly at methane contents over 0.6 Vol.% . Contrarily, the predicted carbon potentials using the Multi Parameter Model found to quite be accurate even at high methane addition contents.

3.1. Conclusion

The increase in methanol/nitrogen ratio, carbon potential and decrease in treatment temperature leads to higher residual methane contents in carburizing atmosphere. The results show that actually combination of these trends may lead a residual methane content almost up to 2 vol.%.

When the residual methane amount is over 0.6 vol.%, the One Parameter Model fails to predict the carbon potential and the carbon depth profile since it ignores the effect of methane reaction. However, the Multi Parameter Model proved to be more accurate at predicting both carbon potential and carbon depth profile specifically for carburizing treatments performed at high methane contents.

Acknowledgment

The IGF Project (AiF 20327) of the Arbeitsgemeinschaft Wärmebehandlung und Werkstofftechnik e.V. (AWT) was funded by the Arbeitsgemeinschaft industrieller Forschungsvereinigungen. The authors are grateful for the financial support. We further wish to thank the Expert Committee FA 20 of AWT for scientific support and supervision of the project.

References

[1] R. Collin, S. Gunnarson and D. Thulin, J. Iron Steel Institute, 10 (1970) 785-789.
[2] U. Wyss, Grundlagen des Einsatzhärtens, HTM Härterei-Technische Mitteilungen, 45 (1990) 44–56.
[3] DIN 17022 Teil 3: Wärmebehandlung von Eisenwerkstoffen; Verfahren der Wärmebehandlung; Einsatzhärten, (1989).
[4] F. Neumann and U. Wyss, Härterei-Techn. Mitt. 25 (1970) 253-268.
[5] R. Collin, The Metals Society, Proc. Heat Treatment 73, (1973) 121.

Investigating the Optimal Parameters of Electro Spark Deposition Coating Method on Inconel 718 with Aluminum

Ahmet KAVUKCU, Kemal KORKMAZ
Gebze Technical University
Turkey

Abstract

Nickel-based superalloys have been used in numerous high-temperature applications where both mechanical strength and oxidation resistance are required. Nevertheless, these superalloys like Inconel 718 are required to be improved by surface modification in aggressive environments. Electro Spark Deposition (ESD) is an efficient and applicable coating method by using electrical sparks between the cathode and anode. Aluminum coatings are generally applied to different types of materials where corrosion and oxidation resistance were required. Therefore, ESD is a significant technique for coating Inconel 718 superalloys with aluminum to improve surface quality with respect to corrosion and oxidation resistance.

Optimal coating parameters of the ESD technique were investigated to develop surface and microstructural properties of Inconel 718 by coating aluminum. Samples have been coated by increasing the current amplitude range from 25A to 300A. Afterward, microstructural characterizations were evaluated by taking into consideration of mass change, phase transformations, surface roughness and thickness comparatively.

1. Introduction

Nickel-based superalloys that are generally used for high temperature parts have been developed to fulfill the requirement of oxidation and corrosion resistance. Inconel 718 alloy is the most widely used nickel-based superalloy in aircraft industry due to its good tensile, fatigue, creep and rupture strength together with ease to fabricate. [1], [2]. There are various types of surface coating techniques such as thermal oxidation, ion implantation, chemical and physical vapor deposition. On the other hand, the electro spark deposition (ESD) process offers some unique advantages relative to other surface modification techniques [3].

In this study, the ESD method was applied to carry out a compact layer Aluminum (Al) on the Inconel 718 substrates and to investigate optimal parameters of ESD by determination the microstructural characterization between substrate and coating layer.

2. Materials and Methods

Inconel 718 rod were cut the dimension of 8 mm diameter and 8 mm thickness. Treating electrode were cut plate-like shape with the dimension of 4 × 4 mm^2 from pure aluminum. Applied amplitude of current are between 25A and 300A using electrical pulses with energy from 0.042 Joule to 0.51 Joule. Inter-electrodes voltage was arranged constantly 17 V with the rectangle impulse form.

Elitron 16 coating machine was used for Electro-Spark Deposition. Structural analysis of the substrate and surface coating were made by using surface roughness analyzer (SJ Mitutoyo Corporation), optical microscope (Leica DM750M), scanning electron microscope (SEM, Philips XL30 SFEG) and X-ray diffractometer (Bruker D-8 Advance X-Ray Device).

3. Conclusion

In this study, results coming from quantitative and qualitative have been indicated followings below.

- Applied 25A amplitude of current have exhibited more sustainable and proper coating surface.
- Most convenient surface roughness has been obtained by decreasing current and frequency.
- Ni-Al phases has been acquired mostly by increasing energy of electrical sparks.

References

[1] H. Qi, Review of INCONEL 718 Alloy: Its History, Properties, Processing and Developing Substitutes, J. Mater. Eng., 2 (2012), pp. 92-100

[2] E. Akca, A. Gursel, Review on Superalloys and IN718 Nickel-Based INCONEL Superalloy Periodicals Eng. Natural Sci., 3 (2015), pp. 15-27

[3] R. N., Sheldon, G. L.: J. Vac. Sci. Technol., 4, 1986, p. 2470.

The Effect of Destabilization Holding Time on the Tribological Behaviour of a Hypoeutectic High Chromium Cast Iron Alloy

U. Pranav NAYAK[1], María Agustina GUITAR[1], Valentin PESNEL[3], Frank MUCKLICH[1,2]
[1]Saarland University, [2]Materials Engineering Center Saarland (MECS),
[3]EEIGM, Université de Lorraine
[1,2]Germany, [3]France

1. Introduction

The excellent abrasion resistance of high chromium cast irons (HCCIs) stems from the dispersion of hard M_7C_3 eutectic carbides (EC) dispersed in a modifiable austenitic matrix. The implementation of proper heat treatments on the cast material can ensure a further improvement in the wear resistance owing to the precipitation of secondary carbides (SC) and the associated transformation of the matrix from austenite to martensite. In the present work, an attempt has been made to derive a mutual relationship between the wear resistance, with, the volume fraction of retained austenite, the stereological characteristics of SC and the matrix hardness, with increasing destabilization holding time.

2. Materials and Methods

The HCCI alloy used in this study had a bulk composition (wt. %) of 2.53% C, 26.6% Cr, 0.66% Mn, 0.26% Ni, 0.24% Mo and 0.37% Si. In addition to the as-cast sample, two samples were subjected to a destabilization treatment at 980 °C for 30 (Q_30) and 90 (Q_90) minutes followed by air cooling and later embedded for metallographic preparation. The polished samples were etched with Vilella's reagent for general microstructural revelation, and a modified Murakami's reagent to analyse the precipitated SC in the HT samples.

Microstructural observations were carried out using optical and scanning electron microscopy (SEM). The backscattered electron (BSE) micrographs obtained from SEM were used in determining the stereological characteristics (size, volume fraction) of the SC using the image analysis software, ImageJ. Furthermore, the retained austenite (RA) content was computed using the software, MAUD from the diffractograms obtained using X-ray diffractometry (XRD). The matrix hardness was calculated using the Vickers hardness method and finally, wear tests were conducted on the samples using a pin-on-disk tribometer in a linear reciprocating motion for 2000 cycles under a constant load of 20N to determine the wear volume loss (WVL) and subsequently, the wear rate (WR).

3. Conclusions

Microstructural observations revealed the precipitation of SC and a predominately martensitic matrix in the HT samples. The increase in the SC size and volume fraction was associated to the increase in destabilization holding time. The matrix hardness of the HT samples increased by about 125% compared to the AC sample, owing to the presence of the SC and a martensitic matrix although, there was no significant rise between the HT samples. Moreover, a corresponding decrease of retained austenite (RA) from about 7% (Q_30) to about 5% (Q_90) was observed. The decrease in RA is attributable to the increased SC precipitation, resulting in a reduction in austenite stability and its corresponding transformation to martensite upon cooling.

The microstructural changes that ensued as a result of the HT were also reflected in the wear volume loss (WVL) and subsequently, the wear rate (WR). The WVL and WR decreased by about 35% in the HT samples compared to the AC sample. Amongst the Q_30 and Q_90 sample, there was no substantial change in the WVL or the WR. In fact, the WVL and the WR increased slightly with increased holding time although, statistically insignificant. This suggests the role of RA in preventing a decrement despite the Q_30 sample having a smaller SC size and fraction and, a lower matrix hardness compared to its Q_90 counterpart.

Acknowledgement

The authors would like to thank Martin Duarte from Tubacero S.A. for providing the materials. Additionally, UP Nayak is grateful to DAAD for the financial support.

Influence of Heat Treatment of 1.4462 and 1.4501 Duplex Stainless Steels on Microstructure and Wear Resistance

Gülüzar YALÇINER[1], Rıdvan GECÜ[1], Alptekin KISASÖZ[2], Ahmet KARAASLAN[1]
[1]Yıldız Technical University, [2]Kırklareli University

Turkey

Abstract

In this study, the effects of heat treatment of duplex stainless steel types on microstructure and wear resistance were examined. The alteration of the sigma phase ratio in the microstructure was measured and it was determined how the wear resistance changed according to the sigma phase ratio in the microstructure.

1. Introduction

Duplex stainless steels (DSSs) consisting of ferrite and austenite phases in an equal amount have been largely used in the oil and gas industry because of their corrosion resistance and high mechanical properties [1-5]. DSSs are vulnerable to secondary phase formation such as sigma phase at high temperatures and the sigma negatively affects the mechanical, corrosion and tribological properties of the material [6–8].

2. Materials and Methods

1.4462 and 1.4501 DSSs were used in experimental studies. The heat treatment was done at 850 °C for 20 minutes followed by water quenching for both samples. Optical microscopy analysis and wear tests were carried out in order to examine heat-treated samples.

3. Conclusion

Dark, grey and light regions indicate secondary phases, ferrite (δ) and austenite (γ), respectively (Fig. 1). This microstructure affects mechanical properties of the alloys. The ratio of sigma phase formed in 1.4501 DSS was higher than that of 1.4462 DSS. The results showed that the wear resistance of 1.4501 alloy was quite lower than 1.4462 alloy due to its higher sigma phase ratio.

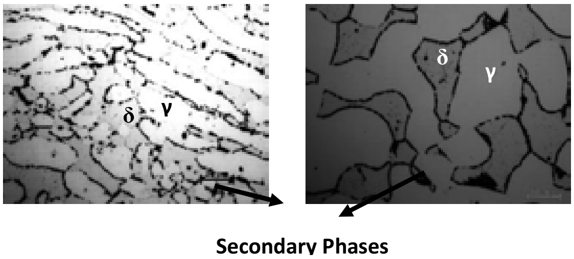

Figure 1. Microstructure of the heat – treated samples a) medium alloy duplex stainless steel b) super duplex stainless steel.

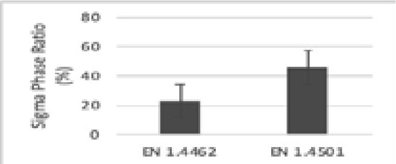

Figure 2. Sigma phase ratios of samples after the heat-treated.

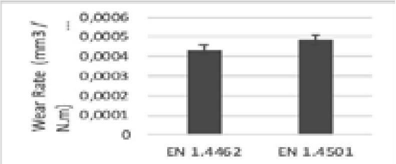

Figure 3. Wear rate results of alloys.

References

[1] A. Kisasoz, S. Gurel, and A. Karaaslan, Metals Science and Heat Treatment, 57 (2016) 544–547.
[2] A. Kisasoz and A. Karaaslan, Materials Testing, 56 (2014) 795–799.
[3] K. H. Lo, C. H. Shek, and J. K. L. Lai, Materials Science and Engineering Reports, 65 (2009) 39–104.
[4] P. Podany, M. Kover, and J. Dlouhy, IOP Conference Series Materials Science and Engineering, 103 (2015) 1.
[5] E. A. Melo and R. Magnabosco, Metallurgical and Materials Transactions A, 48 (2017) 5273–5284.
[6] T.H. Chen and J.R. Yang, Materials Science and Engineering A, 311 (2001) 28-41.
[7] A. R. Akisanya, U. Obi, and N. C. Renton, Materials Science and Engineering A, 535 (2012), 281–289.
[8] H. Sieurin and R. Sandström, Materials Science and Engineering A, 444 (2007) 271-276

Microstructural Characterization of Ferritic Nitro Carburized Layer on the Gray Cast Iron Brake Discs

Ekrem ALTUNCU[1], Recep AKYÜZ[2], Ozan DEMİRDALMIŞ[3], Bilgi ÇENGELLİ[4]
[1]Sakarya University of App. Sci., [2]Tofas Automotive, [3]Kale Balata, [4]Bodycote Istaş
Turkey

Abstract

Surface engineering is a technically attractive and economically viable method aimed at improving the superficial layer of metallic parts. Ferritic Nitro Carburizing (FNC) is a process in which nitrogen and carbon are diffused into ferrous material, producing hard white layer called compound layer, which improves corrosion and wear performance. Gaseous ferritic nitrocarburizing is also known as controlled nitrocarburizing. It is a widely accepted thermo chemical surface treatment process that results in smaller distortion compared to carburizing and carbonitriding processes. Because the process is carried out at temperatures below 650 °C, retention of core properties and good dimensional control are achieved. This is because of the low processing temperature, which reduces thermal stresses and avoids phase transitions in ferro based alloys. FNC compound layer hardness values will typically range from 55 to 65 HRC depending on the base material being treated. Cast iron brake discs require a protective surface layer against wear, corrosion and brake dust problems. In this study, metallurgical characterization and micro hardness measurements were performed on FNC (Corr-I-Dur®) applied cast iron disc. The average compound layer thickness for 24 hours are measured as <20 µm. This compound increases the corrosion resistance of base materials.Hardness level on the surface can be increased by creating a white hard compund layer. It has been verified that FNC treatment improves the surface resistance and heat resistance performance, helping brake performance improvement other than corrosion performance.

Keywords: Brake Disc, Ferritic Nitro Carburizing, Wear, Corrosion

1.Introduction

A disc brake system consists of a cast iron disc rotor which rotates together with the wheel and a stationary brake caliper assembled with brake pads. Automobile manufacturers prefer using disc brakes in order toachieve enhanced riding experience and increasedsafety. Disc brakes offer shorter braking distances independent from the road conditions, thereby ensuring the safety of the occupants. Increasing awareness of safety and environmetal regulationsis primarily driving the growth of the automotive disc brakes market globally which is in turn resulting in rising demand for better surface technologies in brake systems. Brake discs are manufactured in accordance with the IATF16949 automotive standard. Ideal braking performance is the result of a direct interaction between suitable composition of brake pads and suitable surface and material of brake discs [1]. The automotive industry is constantly in need of new materials and developments in order to sustain their fast-developing business. New standards and regulations that will emerge in few years' time concerning PM emissions from automobile brake wear are certain to force the automotive industries to actively seek approaches for minimizing or eliminating particle emissions. Brake discs with various surface and/or heat treatments, can guaranteesuperior braking behaviour compared to conventionally manufactured parts.

Brake disc is a crucial part of the automotive braking system which slows down the vehicle by converting kinetic energy into thermal energy, and consequently increases the temperature of the disc friction surfaces. Gray cast iron is the most commonly used brake disc material due to its high damping capability and desirable thermophysical properties. However, the poor corrosion resistance of cast iron leading to brake judder, high weight contributing to increased fuel consumption, and brake wear emissions in the form of brake dust and particulate matter are some of the major disadvantages of cast iron disc. The most notable advantage of cast iron over other materials is its combination of high melting point and thermal conductivity, which provides excellent thermal stability, apart from cost-effectiveness. Over the years, several types of surface coatings (hard chrome plating, PEO, PTA, laser cladding, thermal spraying) and heat treatments have been applied against wear and corrosion problems and some of these have also been considered for automotive brake disc applications [2].

Ferritic-nitrocarburizing (FNC) processing is becoming a more common alternative to many coating processes that require improved mechanical properties and resistance to corrosion and wear, often on plain-carbon low-alloy steels and cast iron. The addition of nitrogen (N_2) and carbon into the steel or cast iron structure improves corrosion resistance and mechanical properties of the steel component by forming nitrides, carbonitrides and even carbides with iron. These compounds are stable at room temperature, preventing or delaying the formation of corrosion in atmospheric conditions. This thermochemical process creates a shallow surface layer of epsilon iron nitride compound that typically has a hardness ranging between 55-65 HRC. This compound increases the base materials resistance to corrosion. Typical processing temperatures range from 525 ^{o}C to 650 ^{o}C. Common applications include cam, gear, dies, brake discs, hydraulic rods [3-9]. In this study, microstructural investigations were carried out on cast iron discs with FNC treatment. The FNC treated and untreated discs' performances are compared.

2. Experimental Study

The material used in the experimental work was a gray cast iron DIN1561: GG20 type produced in industrial foundry. The standard chemical composition of the material studied is reported in Table 1. FNC process (Corr-I-Dur®) was performed at low temperatures at Bodycote Istaş Gebze plant (Fig.1). The gas nitriding process parameters, such as nitriding time, nitriding temperature, and nitriding potential, have great influence on the forming of nitriding layer. The nitriding process parameters are mainly determined by experience in practical engineering applications. In the present work, a series of gas FNC experiments on grey cast iron specimens were conducted below 650 °C. The nitrocarburizing process consists of three principal steps: heating, diffusion at the nitrocarburizing temperature (550-590 °C) and cooling. Pre-heating to accelerate the nitrocarburizing process and post-oxidation to improve corrosion resistance are optional steps. Process cycles can range from one hour up to 24 hours, depending on the application requirements. With this lower operating temperature and no requirement for quenching, there is good dimensional control with FNC compared to other case-hardening processes.

Table 1. Composition of GG20 cast iron

Element	Symbol	%wt
Carbon	C	2.9-3.65
Silicon	Si	1.8-2.9
Manganese	Mn	0.5-0.7
Sulphur	S	0.10 max.
Phosphorus	P	0.30 max.
Iron	Fe	Remain

Micrographic observations of this material revealed that the matrix was pearlitic- ferritic structure with a lamellar graphite (in Fig 2). The perpendicular cross-sections were used for the observation of the microstructure by scanning electron microscope. The microstructure on the cross-section of nitrocarburized samples was analyzed after metallographic preparation and etching with 3% Nital (3% HNO_3 in ethanol). Microhardness profiles were measured on cross-sections, the distance from surface to core on a perpendicular sample. The ferronitrided case depth was calculated from the microhardness profiles as a depth where the hardness. The hardness distribution profile of the resulting layers was established using a microhardness (HV) tester with a load of 100g for a dwell time of 10 s.

Bodycote Istaş Corr-I-Dur® furnace

Fig 1.Brake discs: Untreated (left), FNC treated (right) disc.

3. Results and Dicscussions

In this experimental study, the gray cast iron (GG20) was subjected to FNC treatment, and then the white layer and diffusion layer were characterized under electron microscope. As shown in the Figure 2b, the white layer is formed on the surface which is known as the compound layer. Beneath the compound layer, there is a diffusion zone. Compound layer thickness is directly related to nitriding temperature. With the increase in nitriding temperature and time, the thickness of case depth increases to some degree, whereas the nitrogen concentration on the surface decreases as nitriding temperature increases.

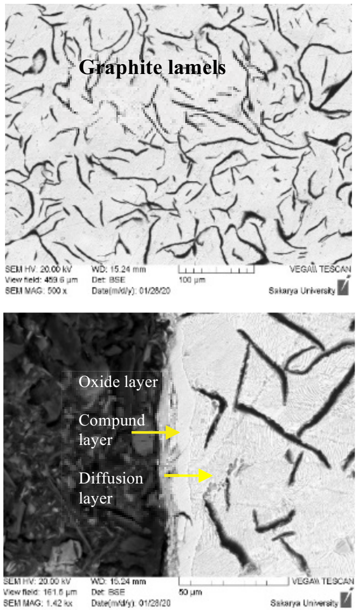

Fig 2. Cast iron microstructure and compound layer

FNC process with post-oxidation is better than other processes with respect to enhanced corrosion performance. The definition of corrosion resistance is typically associated with salt-spray testing. The diffusion of oxygen leaded systematically in over layer a thinner oxide layer (Fe_3O_4) which exhibits extraordinary tribological properties, and corrosion properties. As can be seen in Figure 3, a porous oxide thin layer (3-5µm) is formed on the top surface. This oxide layer translates the color of the part to a dark matte black (Fig 1b). Post-oxidation typically takes place at (450-520°C), with that step of the process ranging up to 60 minutes. As can be seen from Figure 4, compound layer thickness is between 15-20 microns. As can be seen in the EDX analysis, this layer has a very high density of N elements.

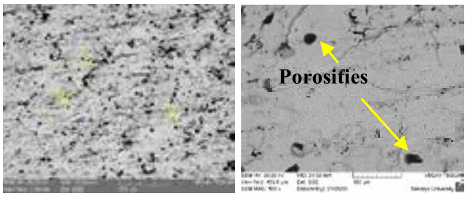

Fig 3. Fe_3O_4 based oxidised porous top layer structure

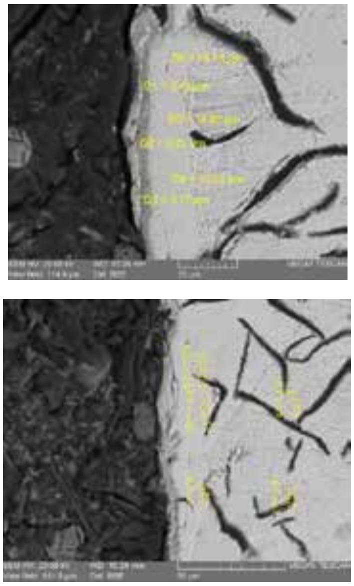

Fig 4. a)Thickness of compund layer section b)Point EDX analysis of compund layer

The tested microhardness values in the depth of 20 and 200 µm are plotted in Fig 5. With the increase in distance from the surface, the hardness decreases to some degree. For 20 µm, the hardness gets its maximum value (625HV0.1).

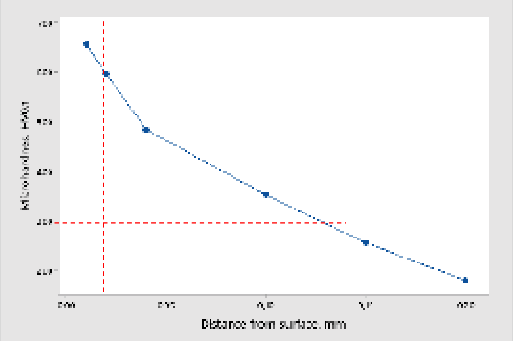

Fig 5. Hardness profile of FNC treated cast iron

Salt spray test was carried out according to the ASTM B117 standard on the test sample removed from the disc. The test was started after the sample was isolated with silicone. Corrosion is observed on the untreated part as soon as the salt spray test begins. However, red corrosion is observed after 120 hours on FNC treated parts.

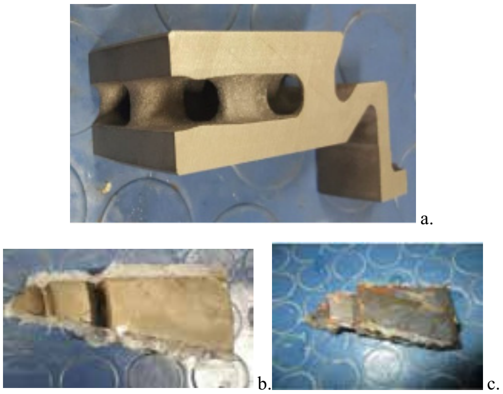

Fig.6. Salt spray corrosion test results
a.section of part b. after 48 hr c. 120 hr.

FNC (Corr-I-Dur®) treated discs and untreated (NP) discs were tested in dynamometer tests and their performances were compared. Pad wear was observed at different test temperatures. The temperature increases with increasing frictional forces between the disc and the pad. Pad exposed for a long time at high temperatures degrades over time and braking performance decreases significantly. Increasing surface resistance with the effect of improvements on the disc surface leads to a controlled friction and wear behavior between the disc-pad. As can be seen in Figure 7, the test results with the FNC treated discindicate a better performance compared to untreated part. It shows controlled wear even at less friction and high temperatures.

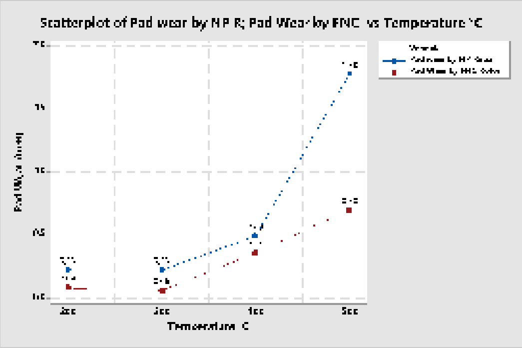

Fig.7. Comparative brake test performances (pad wear)

General Conclusion

Ferritic-nitrocarburizing (FNC) processing is becoming a more common alternative to overlay coating processes that require improved mechanical properties and resistance to corrosion. Ferritic Nitrocarburized (FNC) cast iron brake discs are proposed as a means to improve corrosion resistance, improve brake pad wear, as well as reduce corrosion-induced pulsation of automotive brake discs. With the Corr-I-Dur® process, no distortion was observed on the disc. However, wear on both the disc surface and the pad surface could be reduced. Increasing the surface resistance of the disc is very important in terms of improving the brake disc service life. The FNC treated disc was examined for friction behavior at different temperatures and brake performance remained at standard values even at high temperatures.

Acknowledgements

The authors would like to thank to Bodycote-Istaş Gebze Plant for their support of this study.

References

[1] Rashid, A. Overview of disc brakes and related phenomena-A review. Int. J. Veh. Noise Vib., 10, 257–301,(2014).

[2] Aranke, O.; Algenaid, W.; Awe, S.; Joshi, S. Coatings for Automotive Gray Cast Iron Brake Discs: A Review. Coatings, 9, 552 (2019).

[3] Madhavan Manivannan, Vesselin Stoilov, Derek O. Northwood, Ferritic Nitrocarburizing of SAE 1010 Plain Carbon Steel Parts; SAE Int.J. Mater. Manf. 8(2), (2015).

[4] Torres, J.L., Chuzhoy, L., Burris, K.W., Meng, C. et al., Ferritic NitroCarburizing of Ductile Iron Parts,1st International Surface Engineering Congress and the 13th IFHTSE Congress, USA, October 7-10, (2002).

[5] Andrea Szilágyiné Biró, Trends Of Nitriding Processes, Production Processes and Systems, vol. 6. No. 1. pp. 57-66,(2013).

[6] Frank Czerwinski, Thermochemical Treatment of Metals, Intecopen (2012).

[7] Michael L. Holly, Lisa DeVoe, James Webster, Ferritic Nitrocarburized Brake Rotors SAE Technical Paper 2011-01-0567, (2011).

[8] Valmik Bhavar, Prakash Kattire, Jagdish Sherkar, Digvijay Sheed, RKP Singh, Influence of Medium Used during Ferritic Nitro-Carburizing of AISI H-13 Hot Work Tool Steel, Journal of Materials Science and Engineering A 8 (1-2) 17-24, (2018).

[9] G.Nicoletto, A.Tucci, L.Esposito, Sliding wear behavior of nitrided and nitrocarburized cast irons, Wear, Volume 197, Issues 1–2, 38-44 (1996).

Investigation of Wear Behavior of Vacuum Gas Nitrided Crankshafts

Sayid HAS[1,2], Mehmet YILDIRIM[2], Rabia CENGİZ[1,2], Ali KELEŞ[1,3]
[1]Motus Automotive Inc., [2]Konya Technical University, [3]Dokuz Eylül University
Turkey

Abstract

The cast irons should be subjected to surface treatment before using for automotive parts due to their low surface hardness. Hence, in this study, the crankshafts were manufactured from EN GJS 700-2 cast iron, and then, it subjected to vacuum gas nitriding. Wear behavior was examined via ASTM G77 standard test method. Wear resistance and surface hardness of the crankshaft test sample in increased that after vacuum gas nitriding.

1. Introduction

Crankshafts are one of the key components of an automobile engine. It has been manufacturing from spherical graphite cast irons due to lightness, high-quality and low-cost. Crankshafts have been quenching and tempering to improve mechanical properties [1]. Generally, improve to wear resistance and fatigue strength of crankshafts are applied the surface treatment and one of these is the vacuum gas nitriding method. Vacuum gas nitriding is an important thermochemical method that diffusion of nitrogen into the surface of steels and cast irons [2].

2. Materials and Methods

The crankshafts that used in this study manufactured from spherical graphite cast iron. Firstly, these crankshafts were austenitized and quenched at 935 °C followed by tempered heat treatment at 620 °C. Then, vacuum gas nitriding was carried out at 530 °C for 16 hours that to increase on wears resistance and surface hardness of the polished crankshafts. After the nitriding treatment, the white layer thickness and microstructure of samples examined by an optical microscope. Here, the distribution of hardness of diffusion distance was measured. Following, the wear test was applied to samples according to ASTM G-77 test standard.

3. Conclusion

i. The white average layer thickness was measured to 8,34 µm as shown in the Figure 1.a.
ii. The surface hardness has increased from 335 HV$_{30g}$ to 810 HV$_{30g}$.
iii. Wear resistance determined via wear experiment of samples were characterized and compared. The wear resistance of the crankshafts were increased as can be seen Figure 1.b.

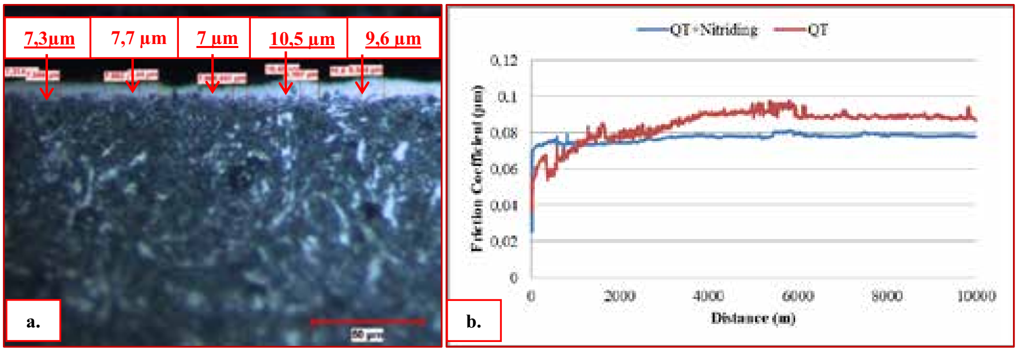

Figure 1. a. Measuring of white layer thickness via optical microscopy, **b.** variation of friction coefficient with distance

References

[1] L. Song, Foundry and Development of Ductile Iron Crankshaft, Institute of Continuing Education, Chongqing College of Electronic Engineering, 2015, 401331, Chongqing, China
[2] P. David, ASM Handbook, Practical Nitriding and Ferritic Nitrocarburizing, 2003

Investigating the Optimal Parameters of Hot-Dip Aluminizing Method on Inconel 718 Superalloy

Ahmet KAVUKCU[1,2], **Faiz MUHAFFEL**[1], **Murat BAYDOĞAN**[1]
[1]Istanbul Technical University, [2]Gebze Technical University
Turkey

Abstract

Nickel-based superalloys have been mostly used in the aviation and aerospace industries. Various types of coating methods are applied to superalloys to provide the requirements of different environmental conditions. Every process has its own advantages and disadvantages concerning applicability and cost. One of the diffusion coating methods commonly used for high-temperature parts is hot-dip aluminizing (HDA). For that purpose, the HDA method is applied to improve surface properties of Inconel 718 Nickel-Based Superalloys. Inconel 718 samples subjected to HDA with different time and temperature processes have been investigated by microstructural and mechanical examination. Specimens are preheated to range from 200°C to 300°C before coating. Afterward, the HDA process has been applied at different temperatures and times between 700°C-800°C and 2-10 min. Additionally, the sample cooling process has been provided with different temperatures by taking into furnace between 200°C-300°C for gradually cooling. Experimental results of microstructural characterization were comparatively evaluated and discussed in respect of different times and temperatures.

1. Introduction

Superalloys have been developed to respond to the request for an alloy that can be used at high temperatures against aggressive environments. Especially, nickel-based superalloys have been commonly used to sustain mechanical strength at high-temperature structural applications [1]. Although nickel-based Inconel 718 superalloy has ability to resist oxidation, various types of coating methods have been applied for many years to improve surface quality where properties of Inconel 718 could become weak in an aggressive atmosphere.

Hot-dip aluminizing (HDA) is a diffusion coating formation process that has been widely used to deposit high-temperature oxidation and corrosion-resistant coatings [2]. HDA has been firstly applied in 1952 for coating nickel-based turbine blades [3].

Recent studies about HDA coating on nickel-based superalloy indicate that there are various methods for using aluminum in the molten bath such as melting Al-Si eutectic alloy in the bath and adding fluxes. [4].

In this study, optimal parameters of preheating, coating, cooling processes the HDA method were investigated by determination of microstructural characterization with respect to coating quality.

2. Experimental Procedure

Inconel 718 rod were cut to the samples that have 15 mm diameter and 8 mm thickness using a water-cooled abrasive cut-off wheel. Sectioned samples were abraded to 400 grit SiC papers and encircled with stainless steel wire for dipping mechanism. After that samples ultrasonically cleaned with HCl for 2 min, dried with ethanol and washed with water. Preheating and cooling were carried out by Protherm PLF 120/5 atmospheric furnace.

Molten bath for hot-dipping was prepared by using commercial pure aluminum fluxed with 40% KCl and 60% NaCl in MF-1000 electrical melting furnace. These samples coated with pure aluminum by the method of HDA. Parameters of the general coating mechanism are given in Table 1. Preheating, coating and cooling processes parameters were investigated by time and temperature. Temperatures ranges are relatively 200-300°C, 700-800°C, 200-300°C for preheating, coating process and cooling with the time range of 2-10 min. The preheating process was carried out for 20 min by holding it in the furnace. Specimens were taken out and coated in the electrical furnace. After coating, samples were immediately put into the heating furnace to complete a different gradual cooling process. Optical microscope images of each process parameter were analyzed step by step. Additionally, the next parameters were determined according to results coming from evaluated analyses. Cumulatively, the effects of all coating processes were investigated and studied to find optimal parameters to carry out excellent surface quality.

Table 1. List of coating process parameters.

	Preheating (°C)	Coating Process		Cooling (°C)
		Temperature (°C)	Time (min)	
1	**200**	**800**	**2**	**x**
2	**200**	**750**	**2**	**x**
3	**300**	**800**	**2**	**x**
4	**300**	**750**	**2**	**x**
5	**x**	**800**	**3**	**200**
6	**x**	**800**	**2**	**300**
7	**200**	**800**	**3**	**200**
8	**200**	**800**	**2**	**200**
9	**300**	**800**	**3**	**300**
10	**300**	**800**	**2**	**300**
11	**x**	**750**	**2**	**x**
12	**x**	**750**	**5**	**x**
13	**x**	**750**	**10**	**x**
14	**x**	**700**	**2**	**x**
15	**x**	**750**	**2**	**Cooled in furnace**

Microhardness measurements were done with Wilson Hardness – Tukon 1102 using a force of 25 g. Structural analysis of the substrate and surface coating were made by using Olympus Light Optical Microscope (LOM), Scanning Electron Microscope (SEM, Philips XL30 SFEG) and X-ray diffractometer (Cu-Kα radiation with a scanning range of 10° to 100°).

3. Results and Discussion

3.1 Microstructure images of optic and scanning electron microscope

Images of as-preheated samples

Optical microscope image of the only as-preheated sample is shown in Figure 1 for specimens numbered 1,2,3,4. In industrial applications, there is an inevitable fact is pure aluminum shrinkage after casting. Shrinkage after casting is not only valid for casting until the part reaches room temperature but also detrimental for coating mechanism of the HDA during solidification.

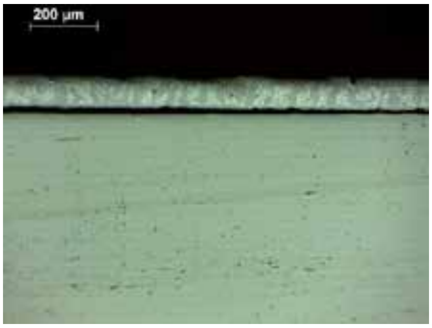

Figure 1. Optical microscope image of only as-preheated samples.

In industrial application, there is an inevitable fact that pure aluminum shrinkage after casting. Shrinkage after casting is not only valid for casting until part reach to room temperature, but also it is harmful for coating mechanism of the HDA [5]. Cavities starting from the edge of coated sample surface were measured to investigate the behavior of the solidification mechanism after coating. Distance between surface and substrate was measured at approximately 15µm. Optimal parameters were studied by using the result of these measurements.

Figure 2 illustrates that images of hot-dip aluminized sample after cooling.

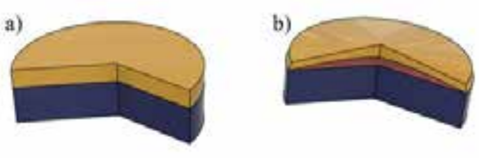

Figure 2. Illustration images of a) post-coating sample and b) cooled sample.

In the edge of samples, there were connection between substrate and coating surface. Therefore, cooling process has become more significant compared to preheating process.

Gradually cooled in furnace samples

Image of sample 5 numbered was shown in Figure 3. On the top of coating, typical shrinkage and gas pores were detected like 6th sample. Non-homogenous surface occurred due to cooling rate of sample. Nevertheless, delamination between substrate and coating does not formed. Minor content of cavities, cracks and pores were expected according to studies about HDA with this parameters [6]. Defects in surface were expected heterogeneously solidified structural micropores, hydrogen cavities owing to shrinkage [5]. Image of gradually cooled sample has not showed optimal characteristics for coating method. This microstructure has not ability reflect requirements of slow cooling. Therefore, cooling in furnace parameters became more desirable than gradual cooling parameters to minimalize these kinds of defects on the top surface.

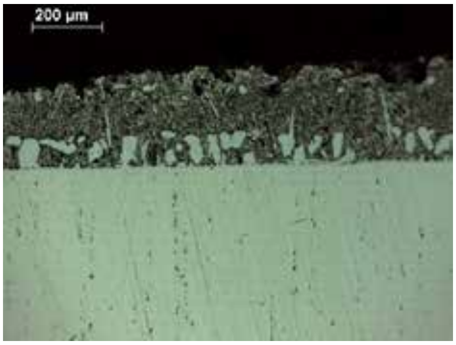

Figure 3. Optical microscope image of gradually-cooled samples.

Preheated and cooled in furnace sample

Figure 4 shows that cross-section image of scanning electron microscope. Smooth and linear interdiffusion zone and homogeneous surface has minor content of defects at the top surface of coating and middle layer compared to other coating of parameters [2].

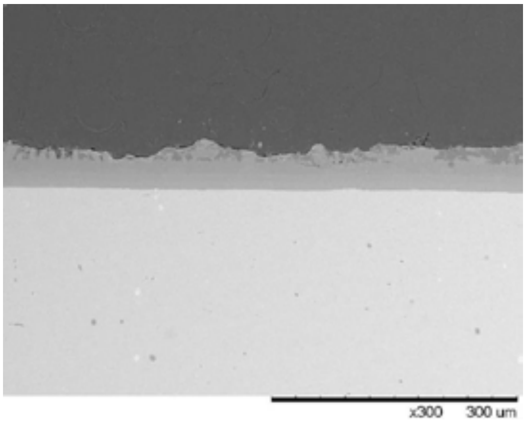

Figure 4. SEM image of optimal HDA sample.

On the other hand, homogeneous elemental distribution in interdiffusion zone proved adequate aluminum reservoir requirements of supported by nickel in the form of $NiAl_3$. Additionally, at top of outer layer defects such as pores and cavities resulting from shrinkage were minor contents. Optimal thickness was obtained approximately 60±7 µm around interdiffusion zone for outward and inward diffusion mechanism. Coating temperature and time perfection did not allow Kirkendall effects due to outward diffusion of Ni, Fe, Cr and Nb [7].

3.2 Hardness measurements

Hardness measurements are given in Figure 5. In the delaminated sample, high value of interdiffusion zone hardness results indicate that diffusion mechanism was carried out by temperature and time before delamination.

In the optimal HDA sample, most of the hardness values that are average of at least ten measurement has tendency to get along with approximate values compared to other types of diffusional coating method.

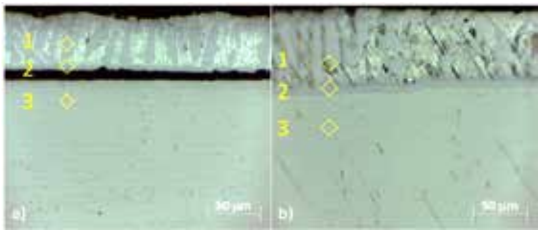

HV 0,025	1	2	3
a) Delaminated sample (only preheated)	82±12	435±23	423±37
b) Optimal HDA sample	79±11	563±32	439±29

Figure 5. Hardness results of delaminated and optimal HDA samples.

3.3 XRD analyses

XRD results are presented in Figure 6. In the bare Inconel 718 XRD pattern solid solution peaks belonging to substrate are clearly shown. Prior to coating, Cr_2O_3 were the primary oxide film to protect oxidation. On the other hand, Cr_2O_3 becomes CrO_3 phase that has volatility above 1000°C.

In the as-aluminized sample, Al_2O_3 peaks were determined due to oxidation of aluminum after coating. Temperature and time led to formation of aluminum reservoir during coating by diffusion as expected [2,3].

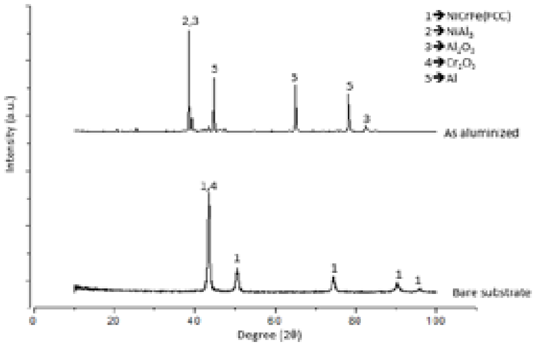

Figure 6. XRD pattern of as-aluminized and bare Inconel 718 substrate.

Phases that enables to form aluminum reservoir for nickel-aluminides were observed. These Ni-Al phases represents that not only diffusion mechanism occur, but also time and temperature parameters are appropriate for coating mechanism. Presence of $NiAl_3$ phases in optimal HDA sample supports that optimal coating process has ability to set up appropriate conditions for diffusion mechanism.

4. Conclusion

Outcomes obtained from result of study are:

- Higher coating temperature and longer holding time has mainly proved that surface and substrate can resist against cracking in interdiffusion zone.
- Samples cooled in furnace showed better surface properties compared to the gradually cooled samples due to low cooling which is efficient way to create perfect condition and balance for diffusion.
- Cooled samples in furnace has exhibited remarkable properties between substrate and surface by having minor content of cavities and pores.
- Quantitative results coming from microstructural analyses thickness of surface coating indicated that preheating process has low efficient compared to cooling processes.

ACKNOWLEDGEMENT

This study was supported by the Istanbul Technical University as scientific research project (Project Nr: MYL-2020-42731).

REFERENCES

[1] R. C. Reed and C. M. F. Rae, “Physical Metallurgy of the Nickel-Based Superalloys,” in *Physical Metallurgy: Fifth Edition*, vol. 1, Elsevier Inc., 2014, pp. 2215–2290.

[2] P. K. Koech and C. J. Wang, “Performance Characteristics of Hot-dip and Plasma Spray Aluminide Coated Nickel-Based Superalloy 718 under Cyclic Oxidation in Water Vapour,” *Medziagotyra*, vol. 25, no. 4, pp. 413–421, Jun. 2019, doi: 10.5755/j01.ms.25.4.21334.

[3] G. W. Goward, “Progress in coatings for gas turbine airfoils,” *Surf. Coatings Technol.*, vol. 108–109, no. 1–3, pp. 73–79, Oct. 1998, doi: 10.1016/S0257-8972(98)00667-7.

[4] S. H. Hwang, J. H. Song, and Y. S. Kim, “Effects of carbon content of carbon steel on its dissolution into a molten aluminum alloy,” *Mater. Sci. Eng. A*, vol. 390, no. 1–2, pp. 437–443, Jan. 2005, doi: 10.1016/j.msea.2004.08.062.

[5] J. P. Anson and J. E. Gruzleski, “Quantitative discrimination between shrinkage and gas microporosity in cast aluminum alloys using spatial data analysis,” *Mater. Charact.*, vol. 43, no. 5, pp. 319–335, Nov. 1999, doi: 10.1016/S1044-5803(99)00059-5.

[6] P. K. Koech and C. J. Wang, “High-Temperature Corrosion Behaviour of Aluminized-Coated and Uncoated Alloy 718 Under Cyclic Oxidation and Corrosion in NaCl Vapour at 750 °C,” *Oxid. Met.*, vol. 90, no. 5–6, pp. 713–735, Dec. 2018, doi: 10.1007/s11085-018-9865-2.

[7] H. Jin Fan *et al.*, “Influence of Surface Diffusion on the Formation of Hollow Nanostructures Induced by the Kirkendall Effect: The Basic Concept,” *NANO Lett.*, vol. 7, no. 4, pp. 993–997, 2007, doi: 10.1021/nl070026p.

[8] C. J. Wang and S. M. Chen, “Microstructure and cyclic oxidation behavior of hot dip aluminized coating on Ni-base superalloy Inconel 718,” *Surf. Coatings Technol.*, vol. 201, no. 7 SPEC. ISS., pp. 3862–3866, Dec. 2006, doi: 10.1016/j.surfcoat.2006.07.242.

IMMC 2021
"in Digital Platform"

20th
INTERNATIONAL
METALLURGY
MATERIALS
CONGRESS
10-12 June
2021
"in Digital Platform"

Non-Ferrous Metals

immc2021

The Outlook of Zinc Mining and Metallurgy

Umut Doğan TURUNÇ[1,2], Cem KAHRUMAN[3]
[1]İstanbul University-Cerrahpaşa, [2]Esan Eczacıbaşı, [3]Bursa Technical University
Turkey

1. Introduction

Zinc is one of the main non-ferrous metals, and the rate of its use has risen rapidly in recent decades. It is currently the fourth most widely consumed metal, after iron, aluminum, and copper. Zinc metal has a range of attractive physical, electro-chemical and chemical properties that enable it to be used in a wide variety of industrial applications. Although these properties have resulted in its use in a wide variety of applications, the primary end use of zinc has been in construction and infrastructure. Moreover, the ending of the cold-war and economic reforms in China resulted in an acceleration in the process of urbanization and industrialization of many of the world's developing economies. Global zinc demand is forecast to 14Mt approximately. Galvanizing is the predominant first use for zinc, accounting for 60% of global usage in all forms. The next largest use of zinc is in the production of die-casting alloys (13%) followed by brass at 11%.

2. Materials and Methods

2017 was likely to be characterised by increased macro uncertainty and risk. The restrictions imposed by refined production enabled the increase in the price of zinc, which reached its highest level for ten years. 2018 was a chaotic year for zinc, with prices falling below 2300 $/ton at a point above 3600 $/ton in early 2018. The most critical issue faced by the zinc market for 2018 - 2019 is the performances of zinc metal production plants and especially zinc smelter plants in China. London Metal Exchange zinc prices have fallen to an average of 1,971 $/ton in March from 2,123 $/ton in February as the coronavirus pandemic impacts global markets beyond Asia. The coronavirus pandemic has necessitated a dramatic change to the base case assumptions for zinc demand in 2020. Analysts assumed that there will be little or no zinc consumption in most of the world’s major economies for 4-8 weeks in the first half of 2020. The collective impact of this assumption is that global zinc demand is forecast to fall by 900kt or 6.8% to 13Mt, its lowest level since 2013. Meanwhile, the coronavirus pandemic has dramatically changed the outlook and it is being expected that this will bring forward some mine closures as well as cuts or delays to projects. We have already seen temporary mine closures to stop the spread of the virus in Australia, Bolivia, Canada, Chile, China and Peru and other countries will take similar action. The impact of coronavirus on zinc demand and market sentiment caused the zinc price to fall from over 2400 $/ton in early-January to below 1800 $/ton for a brief period in March. With governments, central banks and international institutions around the world launching unprecedented packages of measures to mitigate the impact of the looming slowdown, Wood Mackenzie's base case assumption is that economies will start returning to a semblance of normality in the second half of 2020 and that on an annual basis zinc consumption will rebound in 2021, with growth of 7.1% lifting global zinc consumption to 13.9Mt in 2021.

3. Conclusion

Once the global economy starts to recover in 2021, investor sentiment will, it is being believed, result in the price staging a modest recovery from 2020’s lows. However, with high-frequency macro-economic indicators highlighting unprecedented collapses in economic output across the world's major economies in 2020 Q1. The fact that countries are only making tentative moves to emerge from lock-down, 2020 Q2 will be significantly worse. It seems certain that the fall in demand in the coming months will far outweigh mine supply losses. As a result, the Covid-19 pandemic may have rewritten some parts of the script for the market, at least in the short term. Zinc still has new stories to tell.

References

[1] E. Abkhoshk, E. Jorjani, M.S. Al-Harahsheh, F.Rashchi, M.Naazeri (2014), Hydrometallurgy 149, 153-167.
[2] Commodity Market Report (2020), Global Zinc Longterm Outlook 2020 Report, Wood Mackenzie, London, UK, 2-39.
[3] Zinc 5 things to look for in 2018 (2018), Commodity Market Report, Wood Mackenzie, London, UK, 2-4.
[4] Zinc 5 things to look for in 2019 (2019), Commodity Market Report, Wood Mackenzie, London, UK, 1-2.
[5] Glencore slashes zinc mine production (2015), Commodity Market Report, Wood Mackenzie, London, UK, 2-10.
[6] Commodity Market Report (2019), Global Zinc Longterm Outlook 2019 Report, Wood Mackenzie, London, UK, 2-9.
[7] Coronavirus COVID-19 (2020), Metals & Mining Sector Insıghts, McKinsey & Company, London, UK, 1-27.
[8] Zinc Fundamentals in an Out of Favour Environment (2019), BMO Global Commodities Research, BMO, Toronto, Canada, 1 –7.

Solvent Extraction of Lithium from Tuz Lake

Merve ÖZTÜRK[1], Gökhan KADINKIZ[2], Memet PEKGÖZ[2], Bedirhan ERDENER[2], Ş. Samet KAPLAN[1], Nurgul ÇELİK BALCI[1], M. Şeref SÖNMEZ[1]
[1]İstanbul Technical University, [2]General Directorate of Mineral Research and Exploration
Turkey

Abstract
In this study, it was aimed to obtain lithium from Tuz Lake. The main difficulty for producing lithium from Tuz Lake is high Mg/Li ratio. Therefore, experimental studies were carried out primarily to decrease Mg/Li ratio. First, evaporation studies were conducted to decrease the ratio, and then solvent extraction (SX) studies were conducted. Extraction was done by using TBP (Tri-butyl-phosphate), TOPO (Trioctylphosphine oxide), MIBK (Methyl-iso-butyl ketone) system. $FeCl_3$ is also used as co-extractant making Li extraction easier. After SX experiments Mg/Li ratio decreased from 140.32 to 110.34.

1. Introduction

Lithium is one of the most important elements in the earth. Lithium compounds which are lithium carbonate, lithium hydroxide, lithium chloride and butyl lithium are used in many areas such as lithium ion batteries, glass, ceramics, grease, metallurgical industries [1-3]. With the development of the so-called secondary lithium-ion batteries, it has started to be used in mobile phones and laptops. Today, in the World market, approximately 37% of rechargeable batteries are lithium-ion batteries and usage of them is constantly increasing [4].

Considering the energy and carbon footprint, industrial developments and environmental sensitivity, it is important to develop methods that will enable lithium to be obtained efficiently and quickly from primary and secondary sources. Therefore, it should be aimed to produce lithium, which is not produced in our country, from domestic sources. In Turkey, reserves of lithium have been found in some lakes and as an impurity element in boron rich deposits having lower than 40 ppm of Li. On the other hand, Li content of the Tuz Lake reaches up to 325 ppm depending on the water concentration of the lake in certain seasons. Due to the high amount of Mg in Tuz Lake, separation of Mg and Li should be considered as the crucial step for the Li recovery [5]. To extract Li from high Mg-containing brine, some technologies have been developed, including solvent extraction [6], electrodialysis [7], nanofiltration [8], ion exchange and adsorption [9-10].

In the first stage of the study, the effect of evaporation on the concentrations of the ions in lake liquor was investigated. Then, solvent extraction, which has many advantages such as very high extraction efficiency and selectivity of Li, industrially applicable and low cost, is used for the recovery. The typical extraction systems include extractant, diluent and co-extraction agent [11-12]. Tributyl phosphate (TBP) is the most widely used extractant because of the high extraction selectivity. Diluents (kerosene and MIBK) are mainly used to reduce the viscosity and density of extractants, and improve the mass transfer effect. The co-extraction agent plays a key role in terms of increasing both the extraction efficiency and selectivity of Li ions in the extraction system. $FeCl_3$ is the most commonly used co-extraction agent for recovery of Li as seen in both Eq. 1 and Eq. 2 [13-15].

$$FeCl_3 + Cl^- \leftrightarrow FeCl_4 \quad (1)$$
$$Li^+ + FeCl_4^- + nTBP \leftrightarrow LiFeCl_4.nTBP \quad (2)$$

In this work, TBP and $FeCl_3$ were used as an extractant and co-extraction agent, respectively. The volume concentration of TBP, the molar ratio of Fe^{3+} to Li^+ and the O/A phase ratio on extraction performance was studied.

2. Materials and Methods

Lake liquor samples were taken from Kayacık and Cihanbeyli regions of Tuz Lake. Analytically pure TBP (purity > 99%), MIBK (purity > 99%), kerosene and $FeCl_3.6H_2O$ were used in solvent extraction experiments. Chemical analysis were done by using inductively coupled plasma-atomic emission spectroscopy (ICP-AES), while pH measurements were conducted by pH meter.

3. Experimental

Both pH values of liquors and their chemical compositions were given in Table 1 and Table 2, respectively.

It was found that liquors have similar pH values. Mg content of the samples were analysed as 35960 ppm and 25020 ppm, while 273 ppm and 183 ppm Li was detected in Kayacik and Cihanbeyli, respectively.

Table 1. pH data for the samples collected from Tuz Lake.

Region of Tuz Lake liquor	**pH**
Kayacik	7.00
Cihanbeyli	7.16

Table 2. Chemical analysis of Tuz Lake samples (ppm).

Region	**Na**	**K**	**Ca**	**Mg**	**Li**	**B**	**SO_4^{2-}**	**Cl^-**
Kayacik	95560	14320	145	35960	273	347	49400	188770
Cihanbeyli	109060	46930	196	25020	183	230	33970	187370

Accelerated evaporation tests were carried out for two different liquors to investigate concentration change of ions at 70°C. It was conducted for 20, 30, 35, and 40 min under sunlight. Chemical composition of the samples after the evaporation was given in Table 3.

Table 3. Chemical analysis of samples after the evaporation (ppm).

Sample[#]	**Na**	**K**	**Ca**	**Mg**	**Li**	**B**	**$(SO)_4^{2-}$**	**Cl-**	**Mg/Li**
C – 20	44562.5	3750	133.75	10875	77.5	105	15750	92812.5	140.32
C – 30	46700	4812.5	167.5	12987.5	96.25	130	19187.5	100687.5	134.93
C – 35	32675	4537.5	111.25	12050	92.5	122.5	17525	77112.5	130.27
C – 40	36362.5	5362.5	137.5	13650	108.75	145	21375	87150	125.51
K – 20	435625	6575	86.25	17175	131.25	173.75	27612.5	104412.5	130.85
K – 30	43275	7750	116.25	20412.5	152.5	226.25	35837.5	109275	133.85
K – 35	22837.5	5550	77.5	14387.5	110	140	21500	65437.5	130.79
K – 40	33525	8125	107.5	22687.5	170	218.75	37225	97750	133.45

[#] Region abbreviation– Evaporation duration (min)

It was seen that evaporation decreased Mg/Li ratio which was beneficial for SX as seen in Table 3. For samples taken from Cihanbeyli region, Mg/Li ratio decreased from 140.32 to 125.51. However, samples taken from Kayacik region, Mg/Li ratio increased from 130.85 to 133.45 which means evaporation step makes SX more difficult. This may be due to higher Cl^-, and $(SO)_4^{2-}$ concentration in comparison to Kayacik region liquor. Boron was also concentrated while evaporation. As expected, Na, and Ca concentrations decreased.

Solvent extraction experiments were carried out in funnel at room temperature (25 ± 1 °C). Organic phase containing different concentrations of TBP and aqueous phase having different concentrations of Fe^{3+} were used in the single stage extraction experiments. Organic and aqueous phases were mixed at 400 rpm using shaker. Aqueous and organic phase separated after 7 min of extraction. Aqueous phases were prepared for chemical analysis.

In extraction experiments, TBP-kerosene-$FeCl_3$ (TKF) and TBP-MIBK-$FeCl_3$ (TMF) systems were used as an organic phase. For TKF system, 60 % of TBP and 40 % of kerosene, while 40 % of TBP and 60 % of MIBK were used as organic phase for TMF system, respectively. Liquor collected from Cihanbeyli region of Tuz Lake was elected as an aqueous phase considering less Mg ion content. Different organic / aqueous (O/A) ratios were selected for efficiency investigations ranging from 5/1, 1/1 and 1/5. Chemical analysis of the aqueous phases obtained after the extraction was given in Table 4.

Table 4. Chemical analysis of solutions obtained after the extraction with TBP.

	Na	K	Ca	B	Fe	Mg	Li	Mg/Li
TKF 5/1	139350	9900	274	165	35	24450	185	132.16
TKF 1/1	126800	10250	261	215	85	24650	190	129.73
TKF 1/5	137500	10150	252	250	15.5	24750	205	120.73
TMF 5/1	117550	8775	257.5	176.7	5.25	22350	170	131.47
TMF 1/1	112200	9575	252.5	224.5	102	30450	200	152.25
TMF 1/5	128900	9550	270	265	80.7	23725	215	110.34

It was clear from the results that Li was extracted from the lake liquors. On the other hand, Mg content of the solution was still high after the extraction.

4. Conclusion

Two different organic phase mixtures, TBP-kerosene-$FeCl_3$ and TBP-MIBK-$FeCl_3$, were used for the extraction of Li from Tuz Lake. For decreasing Mg/Li ratio, liquors were evaporated, and observed that Cihanbeyli liquor Mg/Li ratio decreased from 140.32 to 125.5. Following to evaporation studies, SX was applied for separation of Mg and Li. After the extraction experiments, it was concluded that TBP-MIBK-$FeCl_3$ was more efficient in terms of decreasing Mg/Li ratio. Further studies are needed for the sufficient Li recovery.

Acknowledgement

The authors would like to thank General Directorate of Mineral Research and Exploration (MTA) for their financial support.

References

[1] Batyrbekov, E.G., Gordienko, Y.N., Ponkratov, Y.V., et al., 2016. Development of the reactor lithium ampoule device for research of spectral-luminescent characteristics of nuclear-excited plasma. Fusion Engineering and Design 204–207.

[2] Lüders, C.V., Zinth, V., Erhard, S.V., et al., 2017. Lithium plating in lithium-ion batteries investigated by voltage relaxation and in situ neutron diffraction. Journal of Power Sources 342, 17–23.

[3] Sun, C., Liu, J., Gong, Y., et al., 2017. Recent advances in all-solid-state rechargeable lithium batteries. Nano Energy 33, 363–386.

[4] Swain, B., 2016a. Recovery and recycling of lithium: a review. Sep. Purif. Technol. 172, 388–403.

[5] Dünyada ve Türkiye'de Lityum, MTA, Haziran 2017.

[6] Xiang, W., Liang, S.K., Zhou, Z.Y., Qin, W., Fei, W.Y., 2016. Extraction of lithium from salt lake brine containing borate anion and high concentration of magnesium. Hydrometallurgy 166, 9–15.

[7] Ji, Z.Y., Chen, Q.B., Yuan, J.S., Liu, J., Zhao, Y.Y., Feng, W.X., 2017. Preliminary study on recovering lithium from high Mg2 +/Li+ ratio brines by electrodialysis. Sep. Purif. Technol. 172, 168–177.

[8] Sun, S.Y., Cai, L.J., Song, X., Yu, J.G., 2015. Separation of magnesium and lithium from brine using a Desal nanofiltration membrane. J. Water Process. Eng. 7, 210–217

[9] Lawagon, C.P., Nisola, G.M., Mun, J.Y., Tron, A., Torrejos, R.E., Seo, J.G., Kim, H., Chung, W.J., 2016. Adsorptive Li+ mining from liquid resources by H2TiO3: Equilibrium, kinetics, thermodynamics, and mechanisms. J. Ind. Eng. Chem. 35, 347–356.

[10] Shi, X.C., Zhou, D.F., Zhang, Z.B., Yu, L.L., Xu, H., Chen, B.Z., Yang, X.Y., 2011. Synthesis and properties of Li1.6Mn1.6O4 and its adsorption application. Hydrometallurgy 110, 99–106.

[11] Zhang, L.C., Li, L.J., Shi, D., Peng, X.W., Song, F.G., Nie, F., Han, W.S., 2018. Recovery of lithium from alkaline brine by solvent extraction with β-diketone. Hydrometall. 175, 35–42.

[12] Zhang, L.C., Shi, D., Li, L.J., Peng, X.W., Song, F.G., Rui, H.M., 2019. Solvent extraction of lithium from ammoniacal solution using thenoyltrifluoroacetone and neutral ligands. J. Mol. Liq. 274, 746–751.

[13] Shi, C.L., Jing, Y., Jia, Y.Z., 2016. Solvent extraction of lithium ions by tri-n-butyl phosphate using a room temperature ionic liquid. J. Mol. Liq. 215, 640–646.

[14] Zhou, Z.Y., Qin, W., Fei, W.Y., 2011. Extraction equilibria of lithium with tributyl phosphate in three diluents. J. Chem. Eng. Data 56, 3518–3522.

[15] Zhou, Z.Y., Qin, W., Liang, S.K., Tan, Y.Z., Fei, W.Y., 2012a. Recovery of lithium using tributyl phosphate in methyl isobutyl ketone and FeCl3. Ind. Eng. Chem. Res. 51, 12926–12932.

The Effects of Calcium Addition and the Thermomechanical Processing on the Corrosion Resistance and Ignition Temperature of Mg Alloys

Halil DEMİRTAŞ[1,2], Önder TUNA[1,2], Özgür DUYGULU[1], Deniz Sultan AYDIN[1], Havva KAZDAL ZEYTİN[1], Metin USTA[1,2]

[1]TUBITAK MAM Materials Institute, [2]Gebze Technical University

Turkey

Abstract

The effects of calcium (Ca) addition and the thermomechanical processing on the corrosion resistance, ignition temperature and the mechanical properties of Mg alloys were investigated. Ca-containing AZ31 (Mg-3Al-1Zn), AM60 (Mg-6Al-1Zn) and WE43 (Mg-4Y-3RE) alloys were cast and subjected to warm rolling and hot extrusion processes after homogenization heat treatment. The corrosion properties were determined via hydrogen evolution and Tafel extrapolation methods in 3,5% NaCl solution. The immersion test results indicated improved corrosion resistance due to alloy composition and the altered microstructure in selected alloys. Continuous heating experiments carried out in dry air-flow revealed that Ca has beneficial effect on the ignition temperature of Mg alloys. Detailed characterization studies such as x-ray diffraction (XRD), optical microscopy (OM) and scanning electron microscopy (SEM) examinations were performed. Mechanical properties of the samples were determined by micro hardness and tensile tests.

1. Introduction

Given their low density, high specific strength and good recycling potential, magnesium alloys are attractive for aviation and automotive industry where lightness is very important [1, 2]. However, the poor corrosion resistance and the high temperature oxidation resistance restrict their extensive use in many applications [3]. In the current work, effects of different amounts of Ca additions and the thermomechanical processes on the microstructure, ignition temperature and electrochemical properties of magnesium alloys were investigated.

2. Materials and Methods

Alloys with Ca synthesized in an induction furnace under protective cover gas (CO_2 + 0.5%SF_6). The Ca additions were carried out at 700-720 ºC; casting temperatures were 730–740 ºC. The chemical compositions are determined via optical emission spectroscopy (OES). As-cast alloys were homogenized at 400 °C for 24 hours. Warm rolling and hot extrusion processes were applied to the heat treated samples. Immersion tests were performed in 3,5% NaCl solution. Each sample was suspended to the bottom of a funnel covered by an inverted silicon caulked burette full of solution. The weight change of samples and the volume of hydrogen gas released as corrosion products were collected and measured for each sample. Electrochemical tests were performed by using VoltaLab PGZ 301 Model Potentiostat / Galvanostat with Tafel extrapolation method. For the ignition tests, electric furnace was used and the ignition temperatures were recorded with a data logger. The microstructural evaluation was done by XRD and SEM techniques. Tensile and micro hardness studies were carried out to determine the mechanical properties of the samples.

3. Conclusion

It has been observed that Ca has beneficial effect on the ignition temperatures of as-cast AZ31 (0.5wt%Ca) AM60 (0.8wt%Ca) and WE43 (1 wt%Ca) alloys with the increase of 200 °C, 150 °C and 30 °C, respectively. On the other hand, homogenization heat treatment and thermomechanical processes showed different effects on the corrosion rates of each alloy system. It has been found that heat treatment and extrusion processes improved the corrosion resistance of AM60 and AM60-Ca alloys significantly. The lowest corrosion rate was determined as 0.27 gr/cm^2/day on heat treated AM60-Ca alloy. On the other hand, increase in corrosion rates were determined on heat treated, warm-rolled and extruded AZ31 and AZ31-Ca alloys. In contrary, a significant decrease in corrosion rate was determined on warm-rolled WE43-Ca alloy (WE43-rolled: 1.84 gr/cm^2/ day, WE43-Ca-rolled: 0.45 gr/cm^2/day). Positive effects of both Ca addition and thermomechanical processes on the mechanical properties of the alloys were determined via micro hardness and tensile tests.

References

[1] K. U. Kainer, The Current State of Technology and Potential for further Development of Magnesium Applications, Magnesium – Alloys and Technology, Wiley-VCH, 2003, Weinheim, Germany, pp 1-23.

[2] D. S. Kumar, C. T. Sasanka, K. Ravindra, K. N. S. Suman, Magnesium and Its Alloys in Automotive Applications: A Review, American Journal of Materials Science and Technology, Columbia Int., 2015, Columbia, USA, pp. 4, 12-30.

[3] B. S. You, W.-W Park, I.-S Chung, Effect of Calcium Additions on The Oxidation Behavior in Magnesium Alloys, Scripta Materialia, Elsevier Ltd., 2000, Oxford, United Kingdom, pp 42, 1089-1094.

Cooling Slope Casting of 7075 Aluminum Alloy with Various Tilt Angles for Thixotropic Feedstock Production

Serhat ACAR, İzel KOCABAŞ, İbrahim TÜTÜK, Ayberk KÖÇKEN, Ali DOLU, Kerem Altuğ GÜLER
Yıldız Technical University
Turkey

Abstract

In this study, the cooling slope casting technique was employed for semi-solid feedstock production with 7075 aluminum alloy. Within the scope of experimental studies, the tilt angle of the cooling slope has been tried to be optimized for designed setup. In this context, castings were made with five different angles between 15° and 75°. As-cast, reheated, and thixoformed specimens were investigated in microstructural and mechanical aspects. According to the findings, it has been observed that castings made with 45° and 60° gave more preferable results than the others, however, the tilt angle of 45° resulted in a slightly finer microstructure.

1. Introduction

Semi-solid forming processes consist of shaping the metallic alloys between solidus and liquidus temperatures [1]. In order to perform these processes, globular grains rather than dendrites should be formed in the microstructure [2]. Production of the feedstocks required for thixoforming can be carried out via different methods. In the cooling slope casting method used in this study, the melted alloy with a low superheat is poured on a plate or through a slope which has a cooling effect into a mold. The elliptical contact zone is formed on the slope following the casting, which supports the subcooling required for the nucleation of α-Al crystals. The first crystals form in the contact zone, are separated from the surface of the slope due to the force of gravity and melt flow inertia (crystal separation mechanism) and carried downward to the slope exit with the flow [3]. Due to the effects of the resulting shear forces and the rapid cooling, feedstocks with equiaxed microstructure are produced. The method is quite simple and the equipment requirements are minimal. However, various parameters such as casting temperature, length and tilt angle of the slope, and water cooling may affect the properties of the final products [4].

2. Materials and Methods

The casting stage of the 7075 specimens was carried out by employing a copper cooling slope with a length of 650 mm. The casting temperature was selected as 645 °C which is 10 °C above the liquidus temperature of the alloy. Low superheated liquid metal was cast into a steel mold with the tilt angles of 15°, 30°, 45°, 60°, and 75°. Cylindrical feedstocks of 120 mm height and 30 mm diameter obtained for each casting angle were quenched in water after reheating at 615 ° C for 40 minutes. Another set of feedstocks was subjected to the same reheating process on a steel mold and formed at the semi-solid state with a pressure of 150 bar via a hydraulic press. All specimens were ground, polished, and etched with Keller solution. Following the microstructural observations, grain size and shape factor calculations were made to examine microstructures quantitatively. Brinell hardness tests and density measurements were also carried out on semi-solid shaped specimens.

3. Conclusions

The following conclusions were reached according to the obtained results;
1) The feedstock production for thixoforming was successfully applied by the cooling slope casting method.
2) Low casting efficiency due to excessive interaction with slope and coarse microstructure caused by the insufficient shear forces were obtained in casting with 15° of tilt angle.
3) Although it is observed that the microstructural properties obtained in castings made with 75° of tilt angle is quite sound, porous feedstocks were obtained due to the created turbulence with high tilt angle.
4) Tilt angles of 45° and 60° were observed to be preferable tilt angles by means of all evaluations.

4. References

[1] H. V. Atkinson, Mater Sci Technol, 26 (2010) 1401–1413.
[2] S. Gencalp, N. Saklakoglu, Mater Manuf Process, 25 (2010) 943–947.
[3] Z. Guo, J. Mi, S. Xiong, P.S. Grant, J Comput Phys, 257 (2014) 278–297.
[4] I.S.-E. El-Mahallawi, T.S. Mahmoud, A.M. Gaafer, F.H. Mahmoud, Mater Res, 18 (2015) 170–176.

Effect of Sn Alloying Element Addition on Microstructural Change in Al-Mg-Si Alloys

Osman Halil ÇELİK, Mehmet Buğra GÜNER, Görkem ÖZÇELİK
ASAŞ Alüminyum A.Ş.
Turkey

Abstract
For investigating the effect of tin addition on microstructure in Al-Mg-Si aluminum alloys, standard 6082 aluminum alloy is selected due to its usage of especially in railway industry. Direct chill casting method was used to produced 14 inches billets in ASAŞ Aluminum's prototype casting facility. After billet production, homogenization heat treatment applied at 530 °C for 6 hours to minimize the segregation and stabilize the precipitates distribution. Samples were taken from the billets both before and after homogenization process. Microstructural investigation was conducted with optical microscope and SEM to understand change between Sn added 6082 and standard alloy.

1. Introduction

Demand for lowering the weights is growing rapidly due to aim of energy consumption for many major industries such as automobile, aerospace, railway. In this respect high strength aluminum alloys are used as main alternative to relatively heavier steel components. 6082 alloy as a flexible option with satisfactory specific strength and elongation properties is preferred by many railway (subway, tram and fast train) companies. Heavy extruded profiles are mainly used in railway industry, that produced with extrusion technique. Extrusion process is solid state diffusion when hollow profiles were produced. Cracks or vacancies can be occurred while longitudinal welding in the extrusion die bearings. Scrap profiles rate can be up to 70% by changing of profiles' weight per meter.

2. Materials and Methods

In this study tin alloying element that has low melting temperature (231 °C) was added to 6082 aluminum alloy to compare the chance of microstructure to improve the solid state bonding mechanisms' first step of casted billets.

Table 1. Chemical composition of direct chill casted 6082 alloys

Alloy	Si (%)	Fe (%)	Cu (%)	Mn (%)	Mg (%)	Zn (%)	Cr (%)	Ti (%)	Sn (%)
6082	0.982	0.194	0.014	0.472	0.798	0.014	0.162	0.030	
6082+Sn	0.979	0.301	0.012	0.401	0.564	0.012	0.123	0.033	0.538

Table 2. Optical and SEM micrographs of 6082 aluminum alloys

Method	6082 BH	6082 AF	6082+Sn BH	6082+Sn AH
Optical	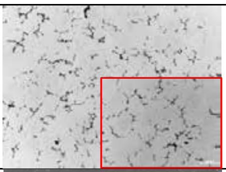	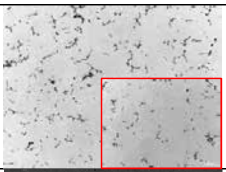	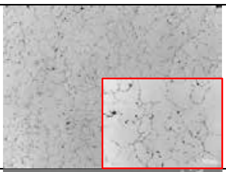	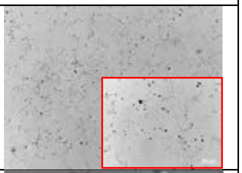
SEM	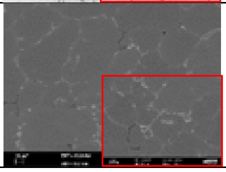		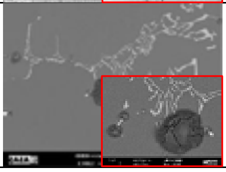	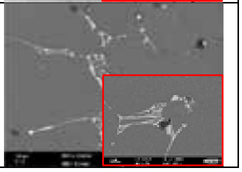

3. Conclusion

According to optical and SEM micrographs, high tin element addition in 6082 aluminum alloy precipitate directly as element and also damage the matrix like crack problem. It is observed that cracks are closed more than before after homogenization process. For our opinion, tin was melted and seal the cracks during homogenization. Therefore, it is a fact that tin can be used to seal the longitudinal welding cracks during extrusion process.

Behaviour of Al_2O_3 and Al_4C_3 Particles during Sedimentation and Gas Purging Processes in Aluminium Melts

Mertol GOKELMA[1], Bernd FRIEDRICH[2], Gabriella TRANELL[3]
[1]Izmir Institute of Technology, [2]RWTH Aachen University,
[3]Norwegian University of Science and Technology
[1]Turkey, [2]Germany, [3]Norway

Abstract

The quality requirements of high-tech aluminium products are increasing. The melt quality is mainly affected by non-metallic inclusions in different size and chemistries. Oxides, carbides, nitrides and borides are the main non-metallic inclusions found in aluminium melts. Oxide and carbides are formed during the entire production chain due to the contact with air, moisture and carbonaceous species. Sedimentation is a widely applied method to remove particles and the settling characteristic of inclusions affects the removability and the final melt quality accordingly. A similar removal mechanism (with an opposite direction to the sedimentation) is observed during gas purging as a side effect besides the removal of dissolved elements. This paper presents a study on behaviour of oxide and carbide particles during sedimentation and gas purging. The settling of particles is analytically investigated by using Stokes law and experimentally by LiMCA (Liquid Metal Cleanliness Analyzer) and an optical microscope. The removal of Al_4C_3 particles during flotation with different gas mixtures and the interaction between carbide particles and Al_2O_3 films during the melt treatment processes were also studied by using an optical microscope and gas chromatography analysis to detect the Al_4C_3 concentration.

1. Introduction

Non-metallic inclusions are an important quality criteria in wrought alloys. Inclusions may harm mechanical properties crucially especially for the products with low wall thicknesses. Filtration and sedimentation are used to remove inclusions from aluminium melts.

Filtration efficiency is strongly dependent on the cleanliness of the melt and the filter type. CFF filter are commonly used and the filtration efficiency is drastaclially decreasing with the decreasing size of the inclusions. On the other hand, the filtration efficiency will increase if particles agglomerate and form large clusters.

Sedimentation works based on the density difference between the inclusion and the melt. However, the similar size versus efficiency problem can be observed during sedimentation as well. Large particles and clusters will be removed easier than the fine particles during sedimentation.

Gas purging is used to remove dissolved hydrogen and other elements such as alkalis work partly as an inclusion removal method by the side effect so called flotation. The inclusion behaviour and interactions become important phenomena to asses and improve the recyclability in all methods.

This work focuses on the recent developments in the field of sedimentation and gas purging with a special focus on oxides and carbides and their interactions.

2. Materials and Methods

80 kg aluminium melt in a crucible furnace was used for the sedimentation trials. Inclusion detection was performed via LiMCA (Liquid Metal Cleanliness Analyzer) unit and the assessment was done via post processing of the measurement data as well as a mathematical modelling. In addition, gas purging/flotation trials were performed in a resistance heating furnace with a volume of 1 lt. The concentration and interactions of carbide and oxides were studied via gas chromatography (GC) and a Scanning Electron Microscope (SEM).

3. Conclusions

- Most of the inclusions in aluminium melts have Re>0.15 due to their small size
- Settling velocity of inclusions clearly increases with the increasing sphericity
- Melt velocity has a large effect on sedimentation, especially for particles having a large surface or small diameters. This points out the importance of temperature control and design of holding furnaces in order to reduce the melt flow due to the thermal convection during particle settling.
- A strong clustering tendency between aluminium carbide particles and oxide films was observed. The attachment of particles on films promoted the removal of carbides via sedimentation on the oxide film.

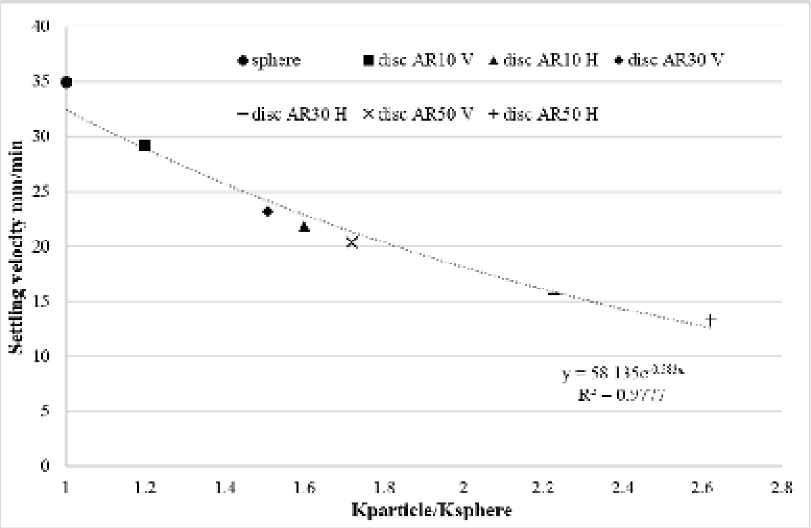

Figure 1: Shape factor effect on the settling velocity

Characterization of the Semi-Continuous Casted AlSi Alloy Microstructure in Function of Solidification Parameters

Agota KAZUP, Viktor KARPATI, Balazs GASCI, Greta GERGELY, Zoltan GACSI
University of Miskolc
Hungary

Abstract

By Indutherm CC3000 semi-continuous casting equipment different types of Al alloys were casted in a laboratory, inter alia AlSi12 was produced, while casting parameters: secondary water-cooling, pulling speed and pulling pause function were being changed. Solidified microstructures were analysed using quantitative method with an image analysing software. Theme of our presentation is characterization of semi-continuous casted AlSi alloy microstructure in function of solidification parameters.

1. Introduction

AlSi12 alloy is used as a solder too, because of its low melting point and right value of strength [1, 2]. The solder raw ingot is produced with semi-continuous casting method, and through covering solder technology heater/cooler systems are fabricated [3]. The aims of our research were to observe the effect of casting parameters, like secondary cooling and casting speed to the microstructure, because it is affected significantly by technology environment [4]. Furthermore microstructure has large importance to the material attribution (processing, end product) [5]. The AlSi12 alloy is corresponding if microstructure is homogeneous, the alloy forms with the other materials during covering solder process and melts easily in the furnace.

2. Materials and Methods

During our research we characterized the microstructure of AlSi12 alloy, measured the size and quantity of primary phase, furthermore the size and shape of silicon phases in the texture. We worked out the sample analysis and measurement methodology for these. Investigations were carried out with optical and stereology microscopes, measurements were done with Leica QWin image analyser software. Based on results we clarified the relationship between the semi-continuous casting parameters of molten metal and solidifying microstructure.

3. Conclusions

(a) We guessed an image transformer algorithm, which using to separate the primary and the eutectic part of α-phases, furthermore separate the primary and the eutectic part of silicon. (b) We assessed the powerful and favourable effect of secondary cooling to the microstructure, because intensive cooling causes finer and homogeneous microstructure. (c) Homogeneous structure is verified also through the cross-section of the ingot if casting speed was decreased. (d) During casting process we proved so that using of pause function has positive effect to the structure. (e) Consequently, we state that lower casting speed without secondary cooling or its contrary case can be used to reach more homogeneous microstructure.

Acknowledgement

In this paper the published research is supported by the ÚNKP-19-2 New National Excellence Program of the Ministry for Innovation and Technology and the EFOP-3.6.1-16-2016-00011 „Rejuvenating and Renewing University – Innovative Knowledge City – part of the University of Miskolc intelligent specialization aided institutional development” project – in the Szechenyi 2020 – by the assistance of European Union, realized by the European Social Fund co-financing.

References

[1] Z. Niu et al.: Effects of germanium additions on microstructures and properties of Al−Si filler metals for brazing aluminum, Trans. Nonferrous Met. Soc. China 26 (2016) p. 775-782
[2] X. Chen et al.: Interfacial structure and formation mechanism of ultrasonic-assisted brazed joint of SiC ceramics with Al-12Si filler metals in air, Journal of Materials Science & Technology 33 (2017) p. 492-498
[3] Markovits T.: Alumíniumötvözetek CO_2 lézeres forrasztása, PhD értekezés, Budapest (2004) p. 5-26
[4] R. Nadella et al.: Macrosegregation in direct-chill casting of aluminium alloys, Progress in Materials Science 53 (2008) p. 421-480
[5] L.Y. Zhang et al.: Effect of cooling rate on solidified microstructure and mechanical properties of aluminium-A356 alloy, journal of materials processing technology 207 (2008) p. 107-111

High Temperature Deformation Behavior of NiCoCrAlY Alloy

Makoto HASEGAWA, Yuji KUBOTA, Nozomi TAKAHASHI
Yokohama National University
Japan

Abstract

Change of microstructure and texture of NiCoCrAlY alloy is experimentally investigated under high temperature deformation. Due to the work-softening type true stress – true strain curve and increase of grain size with decreasing Zener-Hollomon parameter (Z value) indicates the occurrence of dynamic recrystallization. As for γ' phase, independent of Z value, texture was not developed due to the twin boundary formation during the grain boundary migration. Regarding the β phase, texture developed with decreasing Z value by the grain boundary migration. However, in the lowest Z value, texture was not developed by the grain boundary sliding during deformation.

1. Introduction

NiCoCrAlY alloy has been used as an alloy to protect Ni-base superalloy from oxidation and corrosion. In the classification based on entropy, the NiCoCrAlY alloy is positioned as a high entropy or medium entropy alloy. There are reports that high entropy alloys are excellent in environmental resistance as well as mechanical properties. For NiCoCrAlY alloys that are excellent in environment resistance and can be classified as high entropy alloys, there is a possibility that they may exhibit excellent mechanical properties as well. However, there are few such reports. Further, the possibility of microstructure control in the alloys is still open question. In this study, high temperature compressive deformation was performed on NiCoCrAlY alloy, and deformation behavior, microstructure and texture formation were experimentally investigated.

2. Materials and Methods

NiCoCrAlY alloy was produced by sintering of the compacted NiCoCrAlY powders. The compacted material was sintered in vacuum at 1523 K for 10 hours. A cylindrical specimen with a diameter of 6mm and a height of 9 mm or a diameter of 8 mm and a height of 12 mm was cut by machining. Uniaxial compression tests were carried out at various temperatures ranging from 1073 K to 1473 K with true strain rates from $5.0 \times 10^{-2} s^{-1}$ to $1.0 \times 10^{-4} s^{-1}$. After the deformation up to ε= -1.0 or -1.8 in true strain, the specimen was cooled immediately by blowing N_2 gas. Microstructure observation and EBSD analysis were performed at the polished cross-section of the specimens. Texture measurement was performed by XRD using Cu-Kα radiation.

3. Conclusion

NiCoCrAlY alloy was composed of γ' and β phases. True stress – true strain curves at various deformation condition indicate so-called work softening type. Deformation under low Z condition, the average grain size in γ' and β phases became large, while after deformation under high Z conditions, the grain size became rather small. From the features of the true stress – true strain curve and the change of the grain size in each phase, it is concluded that dynamic recrystallization (DRX) has occurred during high temperature deformation. The orientation of the DRX grains went toward the stable orientation of compressive deformation (<101> in the γ′ phase and <111> in the β phase). In case of γ′ phase, fraction of twin boundary to the total length of high angle grain boundary increased with decreasing Z value. However, in the case of b phase, the fraction of twin boundary was about 5% independent of Z value. Independent of Z value, the texture was not developed, and the maximum pole density was about 2~3 in case of γ' phase due to the twin boundary formation during the grain boundary migration under DRX by bulging mechanism. Regarding the β phase, texture developed with decreasing Z value by the grain boundary migration. However, in the lowest Z value, the texture became weak due to the grain boundary sliding during deformation.

Structural and Mechanical Characterization of $Al_{35}Ti_{35}V_{20}Cr_5Mn_5$ Lightweight High Entropy Alloy (LWHEA)

Gökhan POLAT[1,2], Ziya Anıl ERDAL[1], Yusuf Eren KALAY[1]
[1]Middle East Technical University, [2]Necmettin Erbakan University
Turkey

Abstract

High entropy alloys (HEAs) is a promising novel class of metallic materials that shows superior mechanical, electrical and magnetic properties and also and thermal stability. The type and amount of the candidate elements used to produce HEAs are very critical to achieve the goals with lower density values. In this study, a novel $Al_{35}Ti_{35}V_{20}Cr_5Mn_5$ lightweight high entropy alloy (LWHEA) was produced with a density of 4.34 gr/cm^3. The specific combination was chosen between 5 to 35 at. % for each element and the phases and thermos-physical properties were simulated using empirical calculations and Vienna Ab initio Simulation Package (VASP). The designed LWHEA was produced using arc melting set-up with suction casting technique and the simulation results were validated experimentally. The samples were investigated structurally in detail using X-ray diffraction (XRD) and scanning electron microscopy (SEM) techniques. Also, compression test was performed on the samples to reveal the mechanical properties. The correlation of structural and mechanical analyses showed that the formation of B2 phase makes the LWHEA hard but brittle with very low ductility. This project is being supported by TUBITAK, under project number 216M058.

1. Introduction

Conventional alloy systems are based on one or two main components. The properties such as mechanical, electrical, magnetic, corrosion can be improved by the addition of minor alloying elements to the main component. That being said, such alloying strategy restricts the researchers to increase the alloy configuration and forcing them to study only in the regions close to the edge or corner of the multicomponent systems. However, there is less knowledge about the center of phase diagrams of multicomponent systems. In this manner, high entropy alloys (HEAs) concept, which was first proposed in 2004, makes it possible to study the center part of the phase diagrams of multicomponent systems. HEA concept introduces a new area to produce novel alloys with unique properties that cannot be achieved by conventional alloy systems. HEAs are basically defined as a new type of solid solution that contains at least five or more principal elements with a composition between 5-35 at. % for each element. These alloy systems are located at the center or close to the center of the phase diagram that it increases the configurational entropy to its maximum. Thus, these HEAs are also called equiatomic or near equiatomic alloys. Due to their higher configurational entropy (S_{conf}), stable single or dual solid solution phases without any intermetallic can be produced, maintaining the phase stability even at elevated temperatures [1]–[4].

In this study, a combination Al, Ti, V, Cr, Mn, elements were used to design a lightweight high entropy alloy (LWHEA) with low density, high strength and ductility as compared to density (~7.86 gr/cm^3) and mechanical properties steel parts used in the industry. Thermo-physical calculations, Vienna Ab initio Simulation Package (VASP) software were used to design the LWHEA. The LWHEA was produced by copper-hearth arc-melter and suction casting in cylindrical shapes with 4 mm diameters and structural and mechanical investigations were performed on the samples.

2. Experimental Procedure

The LWHEA was designed based on the thermos-physical parameters pointed out in the literature. Firstly, S_{conf} was calculated using an equation proposed by Takeuchi et al. [5]:

$$\frac{S_{conf}}{R} = -\sum_{i=1}^{N} c_i \ln c_i \qquad \text{Eq. 1}$$

$$\frac{S_{conf}}{R} = \ln N \qquad \text{Eq. 2}$$

where c_i the concentration of i^{th} element in the alloy. ΔH_{mix}, δ and $\bar{r}$ for an alloy system were calculated based on the following equations [5]:

$$\Delta H_{mix} = 4x \sum_{j \neq i}^{N} \sum_{i=1}^{N} \Delta H_{ij} c_i c_j \qquad \text{Eq. 3}$$

$$\delta = 100x \sqrt{\sum_{i=1}^{N} c_i} \, (1 - \frac{r_i}{r})^2 \qquad \text{Eq. 4}$$

$$\bar{r} = -\sum_{i=1}^{N} c_i \, r_i \qquad \text{Eq. 5}$$

where r_i is the radius of i^{th} element and $\bar{r}$ is the average value for all the atoms in the system. By using these equations the most suitable composition for the formation of a specific HEA can be determined manually with thermodynamic calculations.

Valance electron concentration (VEC) of the multicomponent HEA systems was used to estimate the resultant crystal structure ant it was calculated according to the following equation [6]:

$$\mathrm{VEC} = \sum c_i \, \mathrm{VEC}_i \qquad \text{Eq. 6}$$

In addition to these parameters, Yang et al. defined a new parameter which is Ω [8].

$$\Omega = \frac{T_m \Delta S_{mix}}{|\Delta H|} \qquad \text{Eq. 7}$$

In this equation, T_m is an effective term due to the formation of phases near the melting temperature of the alloys that it is adopted to entropy term. The hypothetical value of Tm is calculated according to the rule of the mixture, as shown below [8]:

$$T_m = \sum_{i=1}^{n} c_i \, (T_m)_i \qquad \text{Eq. 8}$$

Vienna Ab initio Simulation Package (VASP), along with Molecular dynamics (MD) module, was used to determine the properties of the final crystal structures of the designed alloys by thermo-physical calculations.

The designed and simulated HEA ingots were prepared from high purity elements (>99.5%). The alloy mixture was melted in vacuum arc melter at least 3 times to ensure the chemical homogeneity. The homogeneous ingots were cast into 4 mm diameter copper molds with the help of suction casting.

The crystal structure of the samples was identified by X-ray diffraction (XRD). Scanning electron microscope (SEM) micrographs were used to determine morphology and distributions of the phases in the microstructure. Compression tests were performed according to ASTM E9-09 standard with INSTRON 5582 universal testing machine at 10^{-4} s^{-1} strain rate.

3. Results and Discussion

The LWHEAs consist of Al, Ti, V, Cr, and Mn were chosen in terms of density and thermos-physical properties to produce LWHEAs with a single/dual solid solution. Our previous simulations and results showed that AlTiVCrMn LWHEA has a single solid solution with a BCC crystal structure with a density of 5.34 g/cm^3. Therefore, this LWHEA is termed as LWHEA due to its unique structure. Also, the atomic amounts of Al, Ti, V, Cr, and Mn were changed to have a lower density value under HEA formation criteria. Thus, $Al_{35}Ti_{35}V_{20}Cr_5Mn_5$ LWHEA was designed with a density of 4.34 g/cm^3. Thermo-physical calculation results of the LWHEA are given in Table 1. All the results are in the limit parameters [9] to form a solid solution for HEAs. The VEC values of the HEAs are critical to estimate the final crystal strcutıre. Guo et al. [7] showed that when VEC of the HEAs is equal or higher than 8, lower than 6.87 FCC and BCC crystal structure is expected, respectively. In the gap of 6.67 and 8 for VEC, HEAs will have FCC+BCC composite crystal structure.VEC value of the $Al_{35}Ti_{35}V_{20}Cr_5Mn_5$ LWHEA is 5.9 that suggesting BCC crystal structure.

Table 1. Thermo-physical calculations of $Al_{35}Ti_{35}V_{20}Cr_5Mn_5$ LWHEA

Density (g/cm3)	δ (%)	ΔH_{mix} (kJ/mol)	VEC	ΔS_{mix} (kJ/mol.K)	T_m (K)	Expected Crystal Structure
4.34	3.96	-22.92	4.1	11.28	1618	BCC

VASP simulations of $Al_{35}Ti_{35}V_{20}Cr_5Mn_5$ LWHEA are shown in Figure 1. VASP along with molecular dynamics (MD) module is used in MedeA interface for the simulation. The initial temperature of the simulation was chosen just above the melting points of the LWHEA and it was solidified to room temperature (298 K). Final atom positions were revealed for the LWHEA and the XRD pattern was simulated based on these atom positions. The simulated XRD pattern of LWHEA is given in Figure 1 (c). It is seen in the figure that the final crystal structure of the LWHEAs is BCC. These results well agree with the phases predicted from thermophysical results (Table 1).

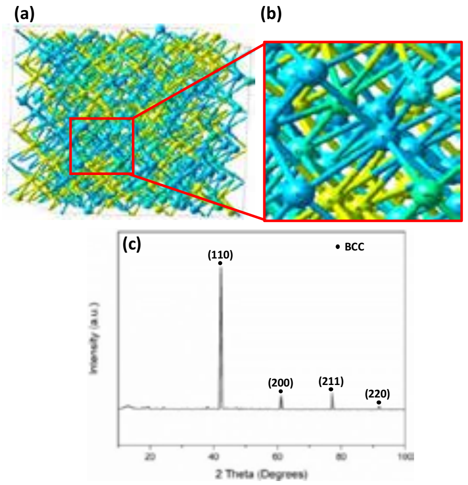

Figure 1. VASP simulation of $Al_{35}Ti_{35}V_{20}Cr_5Mn_5$ LWHEA; a) 4x4x4 simulation box, b) Zoom-in view of BCC crystal structure, c) Simulated XRD pattern based on atom positions obtained from VASP simulation

XRD patterns of $Al_{35}Ti_{35}V_{20}Cr_5Mn_5$, LWHEA is seen in Figure 2. Thes LWHEA has a BCC phase without any secondary phases. Also, the LWHEA has a lattice parameter of 3.033 Å, that the experimental lattice parameter is very close to the theoretical one obtained from the VASP simulation (Figure 1).

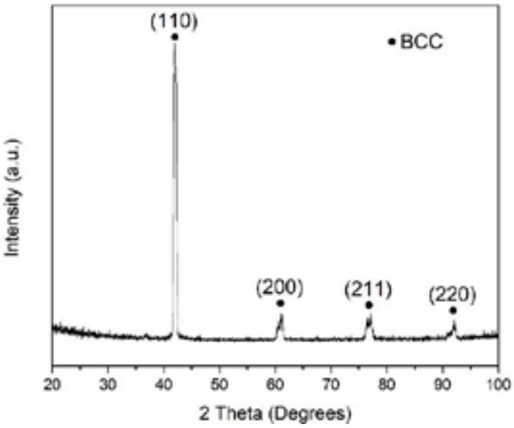

Figure 2. XRD pattern of $Al_{35}Ti_{35}V_{20}Cr_5Mn_5$ LWHEA

SEM and OM images of as-cast $Al_{35}Ti_{35}V_{20}Cr_5Mn_5$, LWHEAs cast into 4 mm water-cooled copper mold are shown in Figure 3. It is seen in the images that the LWHEA has a dendritic microstructure in the as-cast condition. It is known that these types of materials have a brittle structure in as-cast state and ductility of the alloys can be improved by heat treatment processes [10].

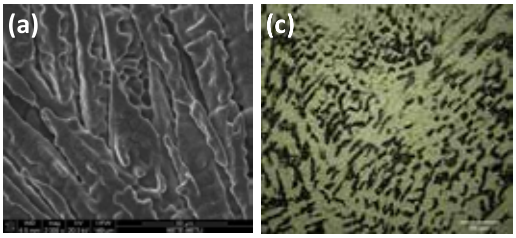

Figure 3. a) SEM (2000x), b) OM (500x) images of $Al_{35}Ti_{35}V_{20}Cr_5Mn_5$ LWHEA

The compression stress-strain curves of the $Al_{35}Ti_{35}V_{20}Cr_5Mn_5$ LWHEA is given in Figure 4. The LWHEA has a maximum stress value of 387 MPa and an elastic modulus of 28 GPa. It is seen in the figure that the LWHEA has a limited ductility and a brittle behavior. The brittleness of the sample was attributed to the presence of B2 (ordered BCC) phases, as seen in the literature [11].

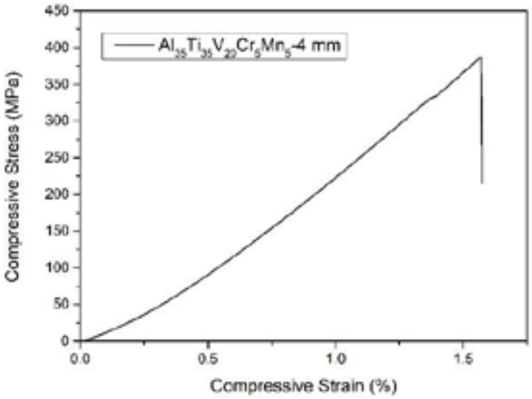

Figure 4. Compression stress-strain curve of $Al_{35}Ti_{35}V_{20}Cr_5Mn_5$ LWHEA

Fracture surfaces of $Al_{35}Ti_{35}V_{20}Cr_5Mn_5$ LWHEA after the compression test is seen in Figure 5. It is shown in the figure that the $Al_{35}Ti_{35}V_{20}Cr_5Mn_5$ LWHEA has a transgranular brittle fracture (cleavage). When the fracture surfaces are investigated in detail, river patterns are seen in $Al_{35}Ti_{35}V_{20}Cr_5Mn_5$ LWHEA that cracking started from the grain boundaries. These characteristic fracture surfaces are also seen in BCC containing AlCoCrCuFeNi HEAs. Ghassemali et al. [12] observed transgranular crack propagation throughout the BCC grains in dual-phase AlCoCrFeNi HEA. A similar trend is also pointed out by Roy et al. [13]. The transgranular fracture behavior is attributed to the BCC grains in the matrix and at the grain boundary interrupted as an obstacle for the crack propagation [12]. Therefore, the fractography of $Al_{35}Ti_{35}V_{20}Cr_5Mn_5$ LWHEA shows higher strength in the inter-grains as compared to the grains that causing a transgranular fracture.

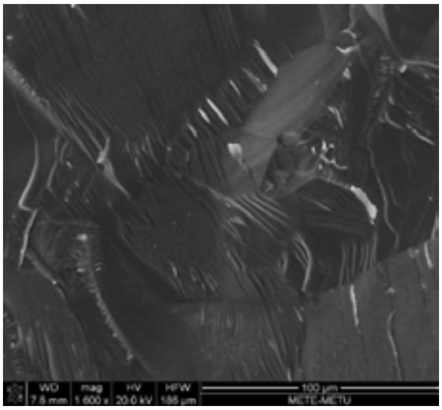

Figure 5. The fracture surface of $Al_{35}Ti_{35}V_{20}Cr_5Mn_5$ LWHEA after compression test

4. Conclusion

In this study, $Al_{35}Ti_{35}V_{20}Cr_5Mn_5$ LWHEA was designed by thermos-physical calculations and Vienna Ab initio Simulation Package (VASP). The primary alloy design criterion was to produce an LWHEA, including low-density elements such as Al and Ti. The LWHEA was produced by arc-melter and cast to 4 mm water-cooled cylindrical copper molds to investigate their structural and mechanical properties. A lower density value was obtained in $Al_{35}Ti_{35}V_{20}Cr_5Mn_5$ LWHEA with a value of 4.34 g/cm^3. The LWHEA has a maximum strength of around 400 MPA with a limited ductility that attributed the presence of brittle B2 phases in the microstructure.

Acknowledgment

This work is financially supported by the Scientific and Technological Research Council of Turkey (TUBITAK) under grant no. 216M058.

References

[1] M.-H. Tsai and J.-W. Yeh, "High-Entropy Alloys: A Critical Review," *Mater. Res. Lett.*, vol. 2, no. 3, pp. 107–123, 2014.

[2] C. Hsu, J. Yeh, S. Chen, and T. Shun, "Wear resistance and high-temperature compression strength of Fcc CuCoNiCrAl0.5Fe alloy with boron addition," *Metall. Mater. Trans. A*, vol. 35, no. 5, pp. 1465–1469, 2004.

[3] J. W. Yeh, "Recent progress in high-entropy alloys," *Ann. Chim. Sci. des Mater.*, vol. 31, no. 6, pp. 633–648, 2006.

[4] J. W. Yeh *et al.*, "Nanostructured high-entropy alloys with multiple principal elements: Novel alloy design concepts and outcomes," *Adv. Eng. Mater.*, vol. 6, no. 5, pp. 299-303+274, 2004.

[5] A. Takeuchi, K. Amiya, T. Wada, K. Yubuta, W. Zhang, and A. Makino, "Entropies in alloy design for high-entropy and bulk glassy alloys," *Entropy*, vol. 15, no. 9, pp. 3810–3821, 2013.

[6] D. B. Miracle and O. N. Senkov, "A critical review of high entropy alloys and related concepts," *Acta Mater.*, vol. 122, pp. 448–511, 2017.

[7] S. Guo, C. Ng, J. Lu, and C. T. Liu, "Effect of valence electron concentration on stability of fcc or bcc phase in high entropy alloys," *J. Appl. Phys.*, vol. 109, no. 10, 2011.

[8] X. Yang and Y. Zhang, "Prediction of high-entropy stabilized solid-solution in multicomponent alloys," *Mater. Chem. Phys.*, vol. 132, no. 2–3, pp. 233–238, 2012.

[9] S. Guo and C. T. Liu, "Phase stability in high entropy alloys: Formation of solid-solution phase or amorphous phase," *Prog. Nat. Sci. Mater. Int.*, vol. 21, no. 6, pp. 433–446, 2011.

[10] V. Soni, O. N. Senkov, B. Gwalani, D. B. Miracle, and R. Banerjee, "Microstructural Design for Improving Ductility of An Initially Brittle Refractory High Entropy Alloy," *Sci. Rep.*, vol. 8, no. 1, pp. 1–10, 2018.

[11] G. Polat, Z. A. Erdal, and Y. E. Kalay, "Design of Novel Non-equiatomic Cu-Ni-Al-Ti Composite Medium-Entropy Alloys," *J. Mater. Eng. Perform.*, 2020.

[12] E. Ghassemali, R. Sonkusare, K. Biswas, and N. P. Gurao, "In-situ study of crack initiation and propagation in a dual phase AlCoCrFeNi high entropy alloy," *J. Alloys Compd.*, vol. 710, pp. 539–546, 2017.

[13] U. Roy, H. Roy, H. Daoud, U. Glatzel, and K. K. Ray, "Fracture toughness and fracture micromechanism in a cast AlCoCrCuFeNi high entropy alloy system," *Mater. Lett.*, vol. 132, pp. 186–189, 2014.

Effect of CuAg0.1 Wire Rod Solidification on Continuous Extrusion Process

Zeynep SİREL, Murat ÖNEY, Orçun ZIĞINDERE, Mehmet Ali AKOY
Sarkuysan Elektrolitik Bakır Sanayi ve Ticaret A.Ş.
Turkey

Abstract

Copper-silver alloy products are frequently used in industry due to their high conductivity and durability for applications which need to run in high temperatures.

The aim of this study is to investigate the effect of solidification behavior of copper-silver alloys which are produced in upwards continuous casting on downstream process products. In this research, CuAg0.1 wire rods are conventionally produced in upwards continuous casting with different production parameters. Afterwards, they were extruded to round profiles in continuous extrusion process.

According to the result of inspections, it is concluded that there are remarkable variations in the intensity of oxides between these extruded products. It is observed that the effect of solidification mechanisms in casting process leads to important changes in oxide distributions of final extruded products.

1. Introduction

Copper and copper alloys are preferred because of their superior electrical and thermal conductivity, strength, ductility and excellent corrosion resistance. These properties enable copper to be more suitable for wire drawing, tube forming and many other machinable applications. The performance of copper can be developed to be applied in many areas by alloying. More than 400 copper alloys offer unique advantages according to the application area such as connectors, commutators, catenary wires, springs, etc… [1]

Addition of silver to copper enhances strength without sacrifice in electrical conductivity. Silver content level improves softening temperature and creep behavior of copper. Copper-silver alloys are preferred in many applications because of superior mechanical and electrical properties [2] According to TS EN 1977:2013 standard [3], CuAg0.1 alloys should contain 0.08-0.12% silver. This alloy is used for catenary wires in high speed railway applications. With the increase of the train speed, wear resistance of overhead catenary system wires becomes much more crucial. CuAg0.1 alloy contact wires should be used for the speeds up to 250 km/hour.

Upwards continuous casting is a conventional copper wire rod production process developed within the Finnish Outokumpu Group towards the late of 60's [4]. In this process, the surface of the melted copper is covered with charcoal in the melting furnace and with flake graphite in the holding furnace to prevent oxidation. Graphite cover and die also enables the reduction of oxygen and improves the mechanical and electrical properties of the wire rod. According to the ASTM B170-99 standard [5], the oxygen level of the Cu-OF copper should be less than 5 ppm. A graphite die and a copper mold are used where water is circulated inside of the copper mold for cooling (Figure 1). Through the effect of the metallostatic pressure the wire rod is solidified and drawn in the opposite direction of gravity. Peripherally solidification of copper wire rod is crucial for the following processes to obtain stable behavior.

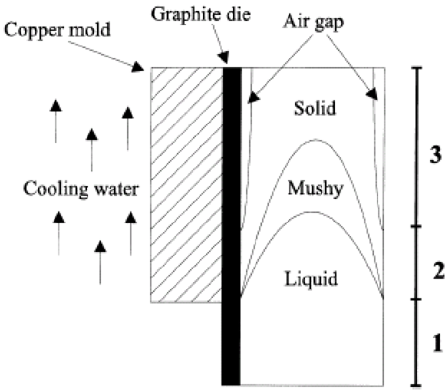

Figure 1. Interface between casting and mold [6]

Continuous extrusion process was invented by UKAEA (United Kingdom Atomic Energy Authority) Springfield laboratories in 70's. With continuous extrusion method, production of complex shaped products is available with low cost and energy savings. Continuous extrusion machinery consists of a rotative grooved wheel, a shoe that fits to the groove, an abutment to restrain the material, die and die chamber (Figure 2). In continuous extrusion process 8 - 35 mm diameter copper wire rods are used as inlet material. When the inlet material enters to the groove of the wheel, rotating wheel forces the inlet material to the abutment, the material flows to the die and extrudes according to the final shape of the die. With the effect of the friction force, without heating, the temperature of the inside of the die chamber is increased above 500 °C for copper [7] [8] [9].

In continuous extrusion process, some defects inside or outside of the final product may be encountered. Controlling the continuous extrusion process parameters and the quality of the inlet material is essential. In this process, dirt or oil on the surface of the inlet material, worn out tooling and non-uniform metal flow cause discontinuity inside of the final product. These areas become weaker and risk of cracks or breaks is increased in the following processes like bending [8] [10].

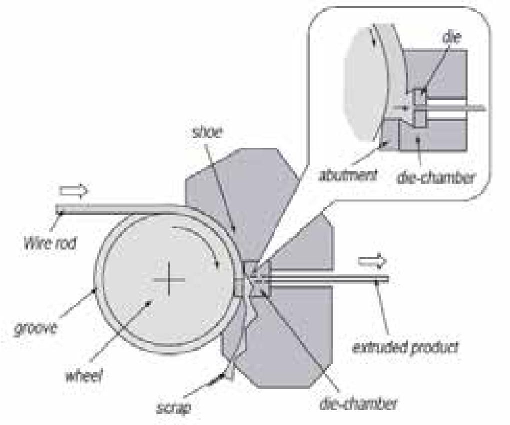

Figure 2. Continuous extrusion process [8]

2. Experimental Procedure

In this study, CuAg0.1 alloy wire rod was produced with upwards continuous casting method, utilizing a graphite crucible.

The diameter of cast CuAg0.1 wire rod is 20 mm. In two production trials, different casting parameters were applied to observe the solidification mechanism of wire rods. For each trial, two simultaneously cast wire rods were produced. In Trial 1, sample S1 and S2 were produced at upwards casting speed 60% higher than Trial 2, where sample S3 and S4 were produced.

Chemical compositions were controlled with ARL 4460 model Optic Emission Spectroscopy (Table 1). Tensile tests were done with Otto-Wolpert-Werke U10 model machine and electrical conductivity tests were done with HIOKI 3545 model conductivity bridge (Table 2). Metallographic specimen preparation was done for the samples that were taken from each trial. Sectioning and cutting from perpendicular to the casting direction, grinding, polishing and etching steps were done. The cross sections of the samples are depicted in Figure 3.

Table 1. Chemical composition of the CuAg0.1 wire rods

Element	EN 1977:2013 Standard	S1	S2	S3	S4
Cu %	Rem.	99.9023	99.9097	99.9122	99.9070
Ag %	0.08-0.12	0.09645	0.08907	0.08654	0.09158
Bi %	0.0005	0.00004	0.00004	0.00004	0.00005
Others%	0.0065	0.00126	0.00116	0.00120	0.00139

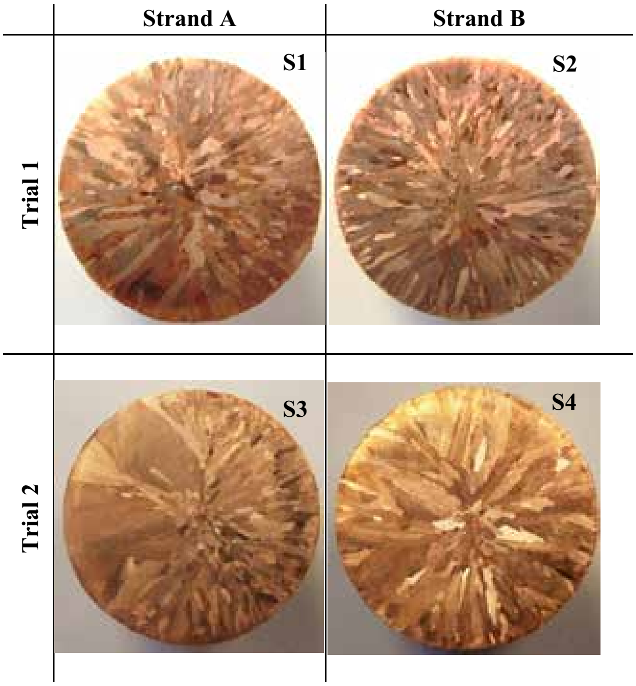

Figure 3. Cross sections of the as-cast CuAg0.1 wire rods

Cast wire rods are extruded to 17.3 mm diameter round profiles. Mechanical and electrical tests were conducted. Test results are given in Table 2. The samples were metallographically prepared with the same manner as wire rod preparation. Afterwards, the samples were inspected in detail with Thermo Fisher

Scientific Prisma E model Scanning Electron Microscope (SEM) and Energy Dispersive Spectroscopy (EDS), shown in Figure 4. Problematic areas are shown in Figure 5.

Table 2. Mechanical and electrical test results of 20 mm diameter CuAg0.1 wire rods and 17.3 mm extruded profiles

Condition	**As Cast (20 mm)**				**Extruded (17.3 mm)**	
Sample	**S1**	**S2**	**S3**	**S4**	**ES1**	**ES3**
Tensile Strength (N/mm^2)	199.6	203.2	188.9	176.9	242.9	243.0
Elongation (%) (A_{200})	43.2	40.8	37	37	51	47.5
Conductivity ($m/\Omega mm^2$)	58.61	58.80	58.87	58.85	58.65	58.56

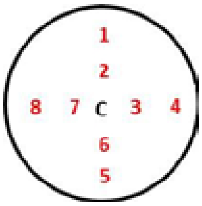

a) Schematic view of profile cross section and inspection zones

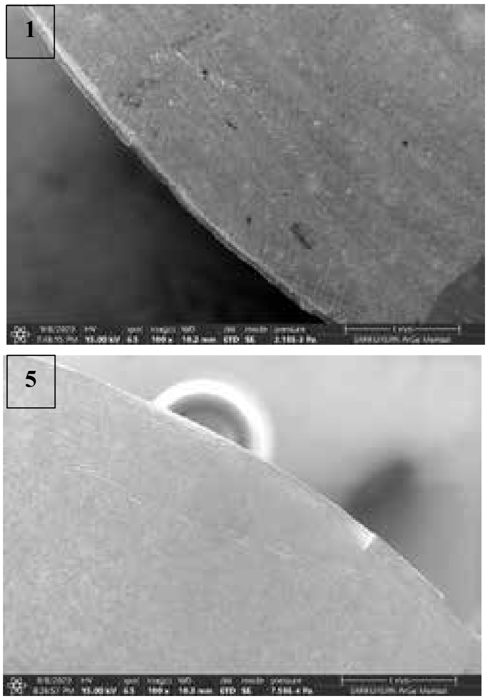

b) SEM photographs of ES1 cross section

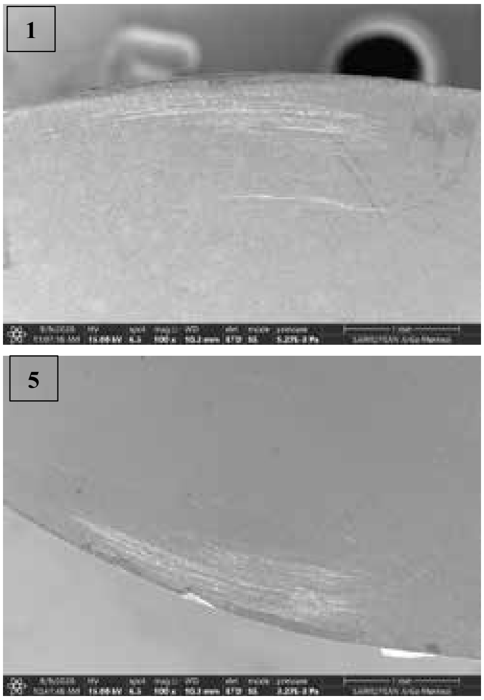

c) SEM photographs of ES3cross section

Figure 4. The SEM photographs of extruded profile cross sections

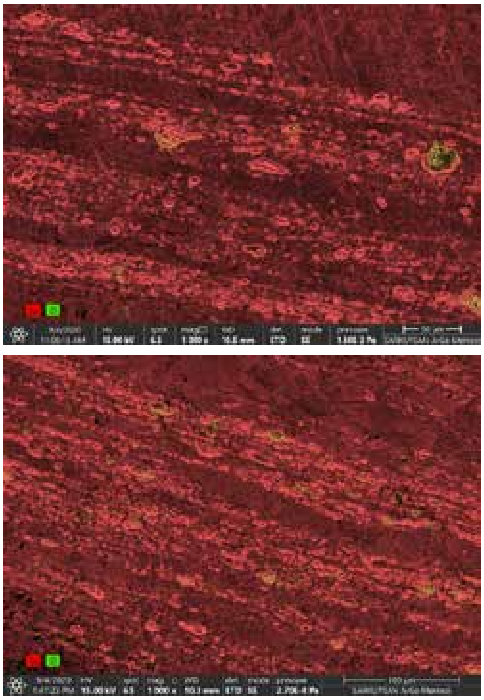

Figure 5. The ColorSEM photographs of ES3 cross section

3. Results and Discussion

The cross sections of samples were inspected in order to observe the effects of different casting parameters on the solidification structure. Solidification center of the samples are almost centered as seen in Figure 3. Solidification conditions are same in Strand A and B. Thus grain sizes are similar to each other in Trial 1.

Grain sizes of the S3 and S4 are larger than S1 and S2 (Figure 3). The cause of this situation is the difference of the casting speed between the Trial 1 and Trial 2. When the upwards casting speed is slower, the heat flux decreases and the grains can grow easily.

Although the production parameters are completely same with each other, the solidification structures of the S3 and S4 are different, where the die used for the S3 was worn out. Grain size distribution of the S3 is not homogeneous because of the non-uniform circumferential heat flux, affected by surface imperfections of the casting die.

According to the SEM results, in the extruded profiles arc shaped oxide clusters are detected in two opposite directions. The arc lengths of oxide clusters in ES1 are 3.2 and 5.2 mm and their footprint area is 1.54 mm^2, which is 0.6% of total cross-section. On the other hand the arc lengths of oxide clusters in ES3 are 4.2 and 3.7 mm and their footprint area 2.79 mm^2 (1.2% of total cross-section). This means that ES3 contains 81% more defect than ES1.

In the continuous extrusion process, inhomogeneous solidification structure of the inlet wire rod is undesirable because of the non-equivalent local material flow and deformation. This significantly increased the oxide intensity in the profile of ES3 in continuous extrusion process. Using worn out die created non-uniform heat flux in S3 and thus the intensity of the oxides in ES3 is dramatically more than ES1.

4. Conclusion

Continuous extrusion defects are caused by surface imperfections and contamination, extrusion practices, tooling and non-uniform metal flow.

This study proves that grain size inhomogeneity of the inlet material also affects internal defects to a degree of about 81% more than a homogeneous structure. This is caused by disruption of the metal flow during extrusion, where grain distribution inhomogeneity is attributed to cooling heat flux fluctuations caused by cooling die wear in the continuous casting process.

No adverse effect of silver alloying was detected, as the silver content was inside the solid solution range.

Acknowledgements

This study was done in Sarkuysan A.Ş., Gebze Plant. We thank Sinan Selvi, Uğur Ilgaz, Furkan Aytekin, Murat Demir, Cem Vural, Zeki Örenç for providing support on casting and extrusion trials.

References

[1]<https://copperalliance.org.uk/about-copper/copper-alloys/> Dated: 03.09.2020

[2] D. Chapman, High Conductivity Copper for Electrical Engineering, Copper Development Association, Publication No 122, February 2016

[3] TS EN 1977:2013 Standard Copper and Copper Alloys- Copper Drawing Stock (Wire Rod)

[4] <https://upcast.com/upcast-original-upcast-story/> Dated: 31.10.2019

[5] ASTM B170-99 Standard Specification for Oxygen-Free Electrolytic Copper-Refinery Shapes

[6] K. Harkki and J. Miettinen, Mathematical Modeling of Copper and Brass Upcasting, Metallurgical and Materials Transactions B, Volume 30B, February 1999-75

[7] K. Khawaja, L. Seneviratne, Sensing & Control of Conform™ Extrusion Gap Between Wheel and Tooling Plates, 2001 IEE/ASME International Conference on Advanced Intelligent Mechatronics Proceedings, 8-12 July 2001, Como- Italy

[8] T. Tonogi, K. Okazato, S. Tsukada, Precise Extrusion Technology by Conform Process for Irregular Sectional Copper, Hitachi Cable Review No.21, August 2002

[9] C. Etherington, Conform – A New Concept for the Continuous Extrusion Forming of Metals, Journal of Engineering for Industry, August 1974

[10] J. Palan, J.V. Taboada, T. Kubina, L. Malecek, J. Hodek, Continuous Extrusion of Commercially Pure Titanium Grade.4, Journal of Achievements in Materials and Manufacturing Engineering, Volume 69, Issue 1, March 2015

20th
INTERNATIONAL
METALLURGY
MATERIALS
CONGRESS
10-12 June
2021
"in Digital Platform"

Corrosion and Wear

immc2021

The Effects of Nitriding and TiCrN Coating by Cathodic Arc PVD Method on DIN1.2379 Cold Work Steel Substrate

Seda ATAŞ BAKDEMİR[1], M. Cenk TÜRKÜZ[2], Elif UZUN KART[3], Serdar SALMAN[1]

[1]National Defence University, Naval Academy, [2]Titanit Ultra Hard PVD Coating Company, [3]Marmara University

Turkey

Abstract

In this work the influence of the number of layers and nitriding process was studied on the mechanical and tribological properties of multilayer TiCrN coating deposited on DIN 1.2379 cold work steel subsrate by cathodic arc deposition. By X-ray diffraction (XRD), a cubic crystal structure centered on the faces (FCC) was observed for all coatings. Atomic force microscopy determined that by nitrided layer, the roughness of coating decreased. By indentation it was found that the hardness (H) increases due to nitrided layer. By reciprocating wear test at 15N load, no change in the coefficient of friction was observed which was related to hardness and the roughness. According to the SEM /EDS results of the wear scar, oxide residues formed due to abrasive wear were not found in coated samples.

1. Introduction

In the last years, there has been an increasing demand for industrial surface treatments which can modify the surface properties of different materials. Thin film coatings are a strong candidate to minimize damage to a large number of industrial components exposed to various wear mechanisms thanks to their high adhesion, hardness and toughness [1]. In addition to thin film coatings, chemical diffusion processes can also improve surface properties. Nitriding one of the chemical processes, involves nitrogen delivery to the substrate by diffusion. Alloy nitrides formed by nitrogen diffusion increase the hardness. Due to the nitration process takes place between 450-590 °C, no phase transformation occurs [2]. The use of duplex process with higher thickness multilayer coatings is an approach to increase the load bearing capacity and adhesion of the coating [3]. In the present study, multilayered TiCrN films were deposited on the DIN 1.2379 cold work steel substrates (with nitrided and non-nitrided) by cathodic arc deposition method. The mechanical and anti-wear properties were investigated.

2. Experimental Procedure

DIN 1.2379 cold work steel substrates with a dimension of 35×35×5 mm^3 were polished, ultrasonically cleaned and dried by air. The chemical composition of the 1.2379 steel is given in the Table 1.

Table 1. Chemical composition of the DIN 1.2379 (wt%)

C	Mn	Si	Cr	V	Mo	Fe
1.45-1.60	0.20-0.60	0.10-0.60	11.00-13.00	0.70-1.10	0.70-1.00	Balance

Treatments were realized in a gas nitriding furnace which was preheated to 450 °C where the ambient air consists of ammonia and nitrogen gas mixture. The temperature was set to 530°C during the active nitriding process. Titanium (99.6%) or chromium (99.8%) targets were placed face to face was where N2 gas was introduced to deposit films. During deposition, the Ti and Cr targets were supplied by two different power supplies.While both targets were evaporated simultaneously to produce TiCrN thin film, CrN interlayers were used to obtain a multilayer coating. Tribometer (UTS 10/20) with a ball-on-flat reciprocating module device was operated to determine the wear behaviour of the samples and to obtain the

Numune	Rockwell C Indentation
Nitrided	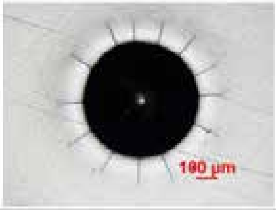
Multilayer Coating	
Nitrided + Multilayer Coating	

Figure 1. Rockwell C indentation.

friction coefficient values. Alumina balls with a diameter of 6 mm were used at wear test. Scanning electron microscopy (SEM) and EDS analyses was used to investigate the surface and wear scar morphologies and elemental analysis X-ray diffractometer (Bruker D8 Advance) was used to determine the crystalline phase of the films with Cu Kα radiation (1.542 Å). The adhesion strength of films was evaluated by a Rockwell C indentation test with a load of 150 kgf. The surface microhardness of the films was examined with a ultra microhardness tester (Fisher HP100) using an applied load of 30 mN. Morphological changes and wear mechanisms formations were observed by optical microscope and AFM analysis. Wear volumes of the wear scars were evaluated with scanning of the all wear scar surface by an optical profilometer (Sensofar).

3. Results and Discussion

The total thickness of multilayer TiCrN was measured by calotest as 4.8 µm. The nitration layer thickness was determined as 75-90 µm by examining with the optical microscope after the sample cros section was etched with 5% nital.

The Rockwell C indentation optic microscope images are given Figure 1. The results of the adhesion strength quality test showed limited spherical cracks around the indentation in a non-nitrided multilayer TiCrN coating, indicating that the films showed the best HF1 value. In the Rockwell C indentation of the only nitrided and nitrided + multilayer TiCrN sample, small size cracks known as the egg shell effect are observed.

The nitration layer, which has a hard and low toughness, causes this effect. However, this crack level around the indentation is acceptable because there is no layer delamination [4]. Adhesion quality of nitrided + multilayered TiCrN coating is HF2.

The hardness volue of all sample are given Table 2. The hardness of 2970,1 HV as well as a hardness of 3177,9 HV were obtained for the monolayers of multilayer TiCrN and nitrided + multilayer TiCrN respectively. The nitrided + multilayer TiCrN showed betters properties due to physical structure that is produced by the increase in the number of interlayer (by CrN layers), which causes an obstacle to the movement of dislocations [5].

Table 2. Hardness (HV) of nitrided, multilayer TiCrN and nitrided multilayer TiCrN.

Sample Name	Hardness (HV)
Nitrided	756,4
Multilayer Coating	2970,1
Nitrided + Multilayer Coating	3177,9

Figure 2 shows the diffraction patterns for the multilayer and nitrided multilayer coatings deposited on substrates where diffraction peaks were obtained located in the crystallographic planes (111) (200), (220) and (222). The wide range of XRD peak widths indicates that the coating is highly crystalline structure. The TiCrN film exhibited a similar XRD pattern as those of TiN or CrN. It is the α-Fe phase in the orientation (110) which has the highest intensity in the XRD phase analysis pattern of the nitrided sample. In addition to the ferrite phase, low-intensity peaks of the ε-Fe_3N and γ-Fe_4N phases forming the white layer were observed [6]. To study the surface morphology of the samples numerically, the atomic force microscopy (AFM) technique was used. The surface roughness values obtained in coated samples are two times higher than the nitrided sample (Figure 3). The reason for the high surface roughness are the droplet pieces formed on the surface during the coating process. Droplet particles are also seen in optical microscope and AFM images.

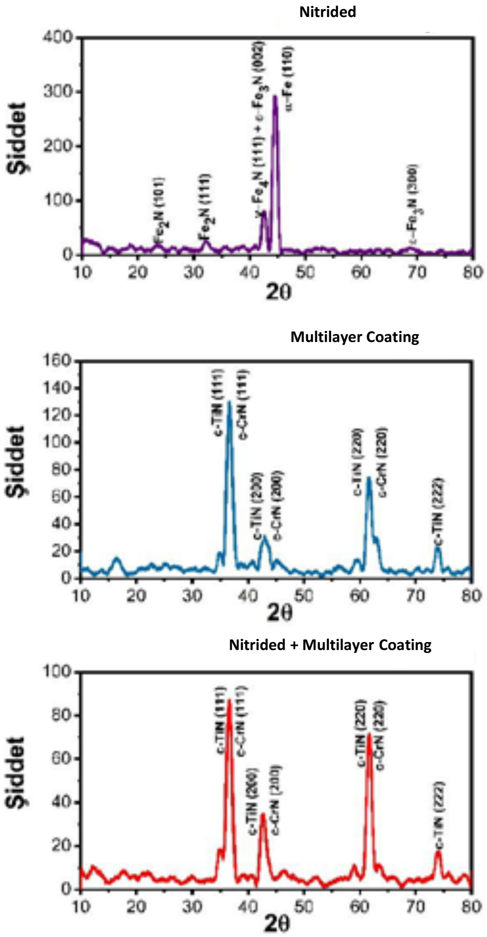

Figure 2. The XRD patterns of the nitrided, multilayer TiCrN and nitrided multilayer TiCrN.

In Figure 4, the friction of coefficient values obtained by the wear test of the samples are shown depending on the sliding distance. For nitrided and non-nitrited coated samples, the friction coefficient values are very close to each other (0.16-0.18), but lower than the nitrated sample (0.8). The COFs of coated samples are steady through sliding distance, this indicates that the wear test took place in the first TiCrN layer. Figure 4 also shows the wear rates of all samples. The wear rate supports the behavior of the friction coefficients. The lowest wear rate belongs to the multilayer TiCrN sample.(7.79 x10^{-8} mm^3 / N.m) The coating on nitrided sample (1.19x10^{-7} mm^3 / N.m) shows higher wear rate because of the white layer forming the brittle structure. Figure 2 shows the SEM eds results of the wear scars performed at 15N load. Abrasive wear lines are high dense in the nitrided sample. Although the amount of nitrided sample (10.35 %). increases with respect to EDS results, the amount of oxygen in coated samples is 3.59-3.92%. The dominant elements in the wear marks are Ti, Cr and N.

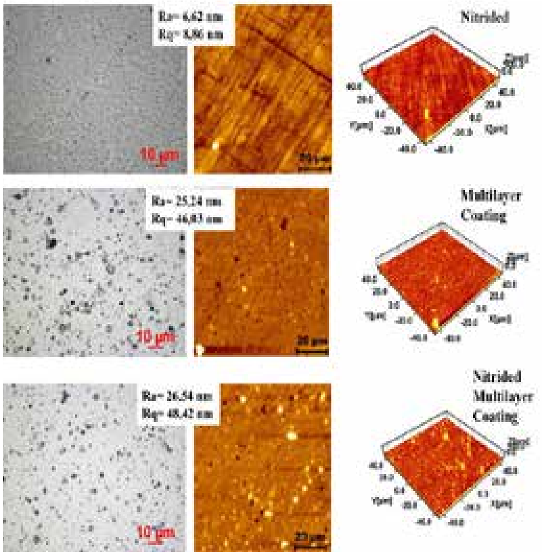

Figure 3. AFM analyses and roughness surface of nitrided, multilayer TiCrN and nitrided multilayer TiCrN.

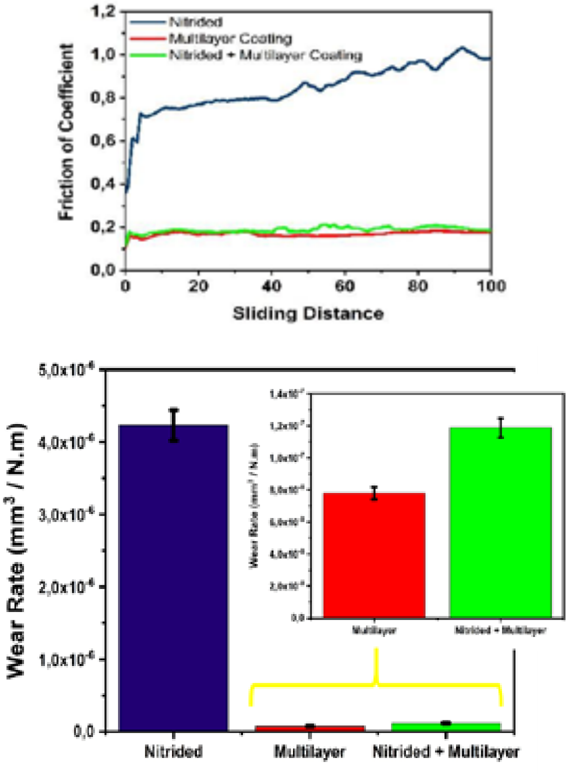

Figure 4. The COFs and wear rate of nitrided, multilayer TiCrN and nitrided multilayer TiCrN.

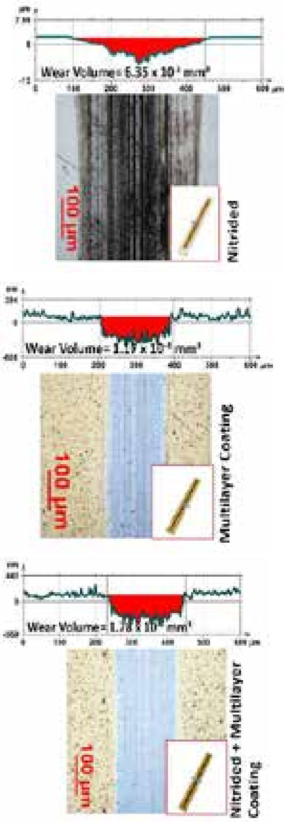

Figure 5. The optical microscope image wear scar and wear volume of the nitrided, multilayer TiCrN and nitrided multilayer TiCrN.

Figure 6 shows the wear volumes and graphics of all samples. In addition, according to the maximum trace depths obtained from the graphs, the lowest depths are in the nitration sample with 0.52 µm. (max. depths of multilayer sample 0.57 µm.)

4. Conclusion

In the present study, the multilayer TiCrN, and nitrided multilayer TiCrN films were deposited DIN 1.2379 cold work steel substrates by the CAD technique. The mechanical and tribological properties increased as the number of interlayers also increased, since increasing the number of interfaces generated greater impediment to the dislocation movement. Although the TiCrN coating applied on the nitration layer does not improve the friction coefficient and wear volume, the maximum scar depth is lower.

Acknowledgment

The authors thank to the support of the Scientific Research Projects Unit of Marmara University, for the funded project, Project no FEN-C-YLP-120619-0198 and Titanit ultra hard PVD coatings company in Turkey.

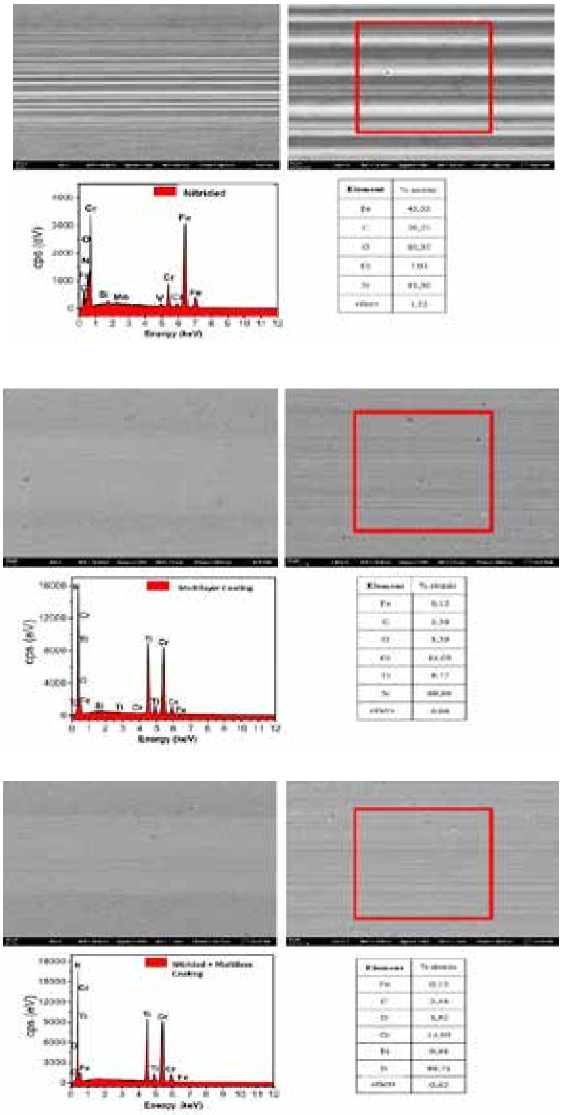

Figure 6. The SEM / EDS analyses wear scar nitrided, multilayer TiCrN and nitrided multilayer TiCrN.

References

[1] <https://www.titanit.com.tr> Dated: 26.05.2019.

[2] A. Arif, S. Akhtar and B. Yilbas, International Journal Surface Science and Engineering, 4 (2010) 396-415.

[3] I. Ebrahimzadeh, F. Ashrafizadeh and B. Sadeghi, Surface Topography: Metrology and Properties, 7 (2019)

[4] S. V. Bhaskar and H. N. Kudalb, Archives of Mechanical Technology and Materials , 37 (2017) 50-57.

[5] C. Ortiz, H. Colorado, W. Aperador and A. Jurado, Tribology in Industry, 41 (2019) 330-343.

[6] Y.-Y. Chang and A. Siddhant , Materials 12 (2019) 795-809.

Development of Wear Resistant Coatings for Drilling Equipments

Emre YAVUZ[1,2], Nuri DURLU[1]
[1]TOBB University of Economics and Technology, [2]Turkish Petroleum Corporation
Turkey

Abstract

In this study abrasive wear resistance of Ni-based claddings containing tungsten carbide (WC) was investigated. AISI 4145 steel samples (4 x 12.7 x 80 mm) were cladded by Gas Metal Arc Welding (GMAW) and Oxyacetylene Arc Welding (OAW). The effect of spherical and crushed carbides on the wear resistance was investigated. The wear resistance of the samples were measured by using abrasion test unit. Mechanical properties (micro hardness of matrix and WC particles) were measured and microstructures of samples (shape and length of WC particles, distribution of WC particles in matrix and discontinuities on the layer) were examined with optical microscopy. The study showed that spherical carbides of 500-1000 µm size led to an increase in average carbide hardness and wear resistance of applied cladding. Moreover it was observed that the WC distribution of the samples cladded with the OAW method was more homogeneous and contained less discontinuities. Laboratory test results were also verified by testing different cladding materials applied to the surface of the stabilizer equipment used in the petroleum industry under field conditions. The sample containing spherical WC particles cladded with OAW method showed better abrasion resistance than other samples.

1. Introduction

Abrasion can be defined as the formation of micro cracks as a result of the interaction between the surfaces exposed to friction and the formation of physical separation with the progress of these cracks. In the oil and gas industry, the formation carries various corrosive and abrasive particles in crude oil and natural gas. These particles accelerate the wear of the drilling equipments and this in turn reduces the lifetime and increase the operational costs. According to the characteristics of the working environment, four types of wear - adhesive, abrasive, corrosive or fatigue - occur. Based on the working environment more than one of these types leads to wear.

Wear affects the drilling and oil/natural gas production costs directly. Daily drilling costs in the oil industry are around $30,000 - $50,000 in on-shore wells and $500,000 - $1,000,000 in off-shore wells [1]. Especially for drilling components that need to be changed periodically during drilling, such as drills and stabilizers, service life affects the overall costs directly. To change any one of these equipments, maneuvering times of 1 to 10 days are required depending on the depth of the well. Hence, selection of wear resistant materials is very important in terms of avoiding losses due wear [2, 3].

Corrosion and abrasion resistant coating processes are applied to the surface in order to prevent the contact of the acid, liquid and gases with low Ph in the oil wells with the material. Depending on the working environment of the material, the thickness of the applied coating can go up to 10 mm thickness from the micrometer level. In cases where abrasive wear is the dominant factor, bulk type coating methods are preferred due to high thickness ratio. In this study, because of their widespread use, gas metal arc welding (GMAW) and oxyacetylene arc welding (OAW) coating methods with various coating materials are examined. Comparison of the wear resistance and microstructure analysis of these coatings are conducted. [4, 5]

The most commonly used carbide type is tungsten carbide (WC / W2C) among hard carbides in areas where aggressive wear is effective in the oil and gas industry. The main reasons for choosing WC / W2C are its high hardness, high thermal conductivity, high plasticity and good weldability compared to other ceramics. [6, 7].

Co, Fe and Ni are used as binder because of their high wetting capabilities in coating hard carbide particles to the surface. In the past Co was used commonly as binder. However due to the oxidation and decrease of abrasion resistance of cobalt at 600 ºC and above temperatures and being an expensive and toxic element, the use of Ni and Fe binders are increasing day by day [8, 9]. Ni binders are widely used in the petroleum industry because of their good ductility, impact resistance and corrosion resistance properties [10]. In a study conducted by Hidouci et al. [11], the properties of Co and Ni binders were compared. In this study, it was determined that the Co matrix is harder than the Ni matrix. However, due to the formation of $\mathbf{M_7C_3}$ carbide in samples coated with Co binder, it was observed that crack formation increased in matrix structure. As a result of these discontinuities, the abrasion resistance of Co matrix was lower than Ni matrix. At the same time, oxidation is encountered in samples coated with Co binders while it is not determined in Ni-binding samples. In similar studies it is stated that WC-Ni composite metals with Ni binders show better corrosion and oxidation resistance as well [12, 13]. Considering these studies and sectoral experiences, Ni binder was preferred in this work. Finally, broken carbide and spherical carbide coating materials were chosen to examine the effect of WC shape on the wear rate. The coatings are applied on 4145H steel, which is widely used in the oil industry because of its good hardenability and weldability properties. Considering that field tests will be carried out in soft and medium hard formation, alloys with WC parts of 500-1000 µm in size are preferred.

In this study, the effect of carbide size, carbide shape and the processing method in wear resistant coatings for drilling equipments is investigated. The final objective is to optimize these factors and develop wear resistant coatings which maximize service life of drilling equipments.

2. Experimental Procedure

The coating alloys specified in Table 1 are selected to be used in experimental and field tests. The size of each sample was prepared in accordance with ASTM G65 standards abrasion tester in the dimensions of 12.7 mm **x** 30mm **x** 80mm. Coatings were applied to the 12.7 x 80 mm side of the sample.

Before the microstructural analysis, the samples were cut in appropriate sizes and polished with 6, 3 and 1 µ diamond particles. Carbide shapes were determined by using images obtained from an optical microscope, the average carbide size was measured and it was determined whether it provides homogeneous distribution in the matrix. Also discontinuities in the coating were analyzed. In addition, before applying abrasion tests, crack and pore inspection was carried out with penetrant liquid in accordance with EN ISO 3452-1 standards.

Brinell hardness measurements (HV 0,1) of the carbide and matrix structures of the prepared samples were made and the average hardness distributions of both carbides and matrix structure were determined.

In first stage of the study, seven samples shown in Table 1 were prepared and microstructural analysis and hardness measurements of these samples were completed. According to the hardness values and WC particle distribution, three samples were chosen for abrasion tests as shown in Table 2. Laboratory and field wear tests were applied to three selected samples.

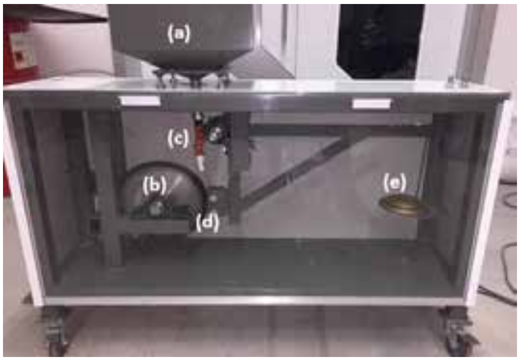

Figure 1. Abrasion Test Unit (ASTM G65 Standard), (a) Sand Unit, (b) Rubber Wheel and Rotary Drum, (c) Sand Sprayer, (d) Test Sample, (e)Weight [14]

The wear tests were conducted in the abrasive test unit manufactured in accordance with the ASTM G 65 standard. Wear tests were carried out under 130 N force for 30 minutes in accordance with ASTM G 65 Procedure-A standard. The surfaces of the coated samples were prepared by grinding them with a homogeneous coating thickness of 4mm and a surface roughness less than 0.8 µm. During the abrasion tests, silica casting sand with AFS (American Foundary Society) 45/50 (280-300 µm grain size) 7 (Mohs Scale) hardness, 2.65 g/cm^3 density and 1785°C melting temperature was used. The flow rate of the sand was set at as 300 gr/min during the tests.

In the tests, the amount of wear was determined using the "weight difference measurement" method, using a balance with a precision of 0.001g. Total amount of wear was determined by weighing each sample before and after the test**.**

Table 1. Samples Covered by GMAW and OAW Methods. Classification of Samples According to Cladding Method, Carbide Shape and Size and Carbide and Matrix Hardnesses.

Sample #	Carbide Type	Electrode / Powder WC Manufacturer	Carbide Size (mm)	Coating Method	Average Hardness of Matrix (HV)	Average Hardness of Carbide (HV)
1	WC-Crushed	A Electrode	0,5-1	GMAW	450	2652
2	WC-Crushed	Carbodurflex	1-2	GMAW	904	1900
3	WC-Spherical	Technodur	0,5-1	OAW	508	2611
4	WC-Crushed	Powder WC-Ni Electrode	0,5-1	GMAW (Pre-heating)	1033	1856
5	WC-Crushed	Powder WC-Ni Electrode	0,5-1	GMAW	871	1681
6	WC-Crushed	A Electrode	0,5-1	OAW	423	2465

Table 2. Classification of Abrasion Test Samples According to Cladding Method and Carbide Shape.

Sample	Coating Method	Average Hardness of Matrix	Average Hardness of Carbide	Carbide Shape
#1 Elect-A	GMAW	450 HV	2652 HV	Crushed
#2 Elect-A	OAW	423 HV	2465 HV	Crushed
#3 Techno	OAW	508 HV	2611 HV	Spherical

Following the laboratory test results, each of the 3 bladed oil drilling equipment-stabilizer blades shown in Figure 2 were coated using the coating methods applied in the abrasion tests in order to verify the results obtained. Each wing of the stabilizer is coated with Electrode-A applied by GMAW method, Electrode-A applied by OAW method and Technodur Electrode applied by OAW method. Surface of the stabilizer before and after the drilling tests was given in Figure 2. During field test, stabilizer remained in the well approximately 84 hours and actively worked for 73 hours. The stabilizer rotated between 110 and 125 rpm and drilled vertically 777 meters of limestone-marl-chert (Hoya) formation and 12 meters of germav (Marn) formation. At the end of the test, the amount of wear on each wing of the stabilizer was measured with the help of a special caliper shown in Figure 2.

Figure 2. Surface of the stabilizer before and after the field tests at TPAO Beşikli-34 well.

3. Results and Discussion

Microstructure analysis and hardness measurements of 7 samples shown in Table 1 were completed in the first stage of the study. According to the carbide particle distributions, detected discontinuities, average carbide and matrix hardnesses and carbide shapes, A-electrode (crushed Tungsten Carbide) applied by GMAW and OAW methods; Technodur electrode (spherical Tungsten Carbide) applied by OAW method, were selected for abrasion tests. Laboratory wear tests were applied for 30 minutes in three steps under a load of 130N. Test results are shown comparatively in Figure 3.

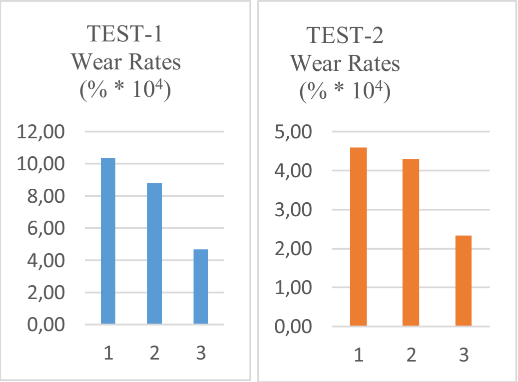

Figure 3. x10^4 % wear rates of samples as a result of 0-60 min and 60-90 wear tests. (1) Electrode-A coated by using GMAW method; (2) Electrode-A coated by using OAW method; (3) Technodur spherical WC electrode coated by using OAW method.

In the abrasion test results, the sample prepared with the OAW method showed higher wear resistance in the abrasion tests, although both the matrix and carbide hardness of the sample applied by GMAW method were higher as seen on Table 2. This was correlated to the plurality of discontinuities in the WC particles and matrix structure of the sample coated by applying GMAW method as seen in the microstructures (a) and (b) of Figure 4.

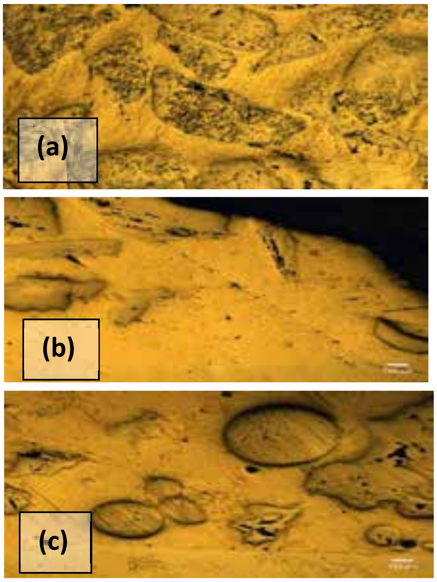

Figure 4. (a) Electrode-A applied by GMAW method, (b) Electrode-A applied by OAW method, (c) Technodur Electrode applied by OAW method.

The third sample which was applied by using OAW method and has spherical WC particles compared with the other two samples as well. The average carbide and matrix hardness of the third sample was measured higher than the second sample which was applied by using OAW method but has crushed WC particles. Abrasion tests have also shown parallel results with hardness measurements, showing that the wear resistance of sample three is higher than that of the other two samples. However, when the microstructure of the third sample is examined, degradation, pore formation and grain growth occurred in WC particles as seen in Figure 4 (c). In addition, the values obtained in hardness measurements were approximately 15% lower than the catalog values of the used electrode. Although third sample showed better wear resistance than the other two samples, it was found that the desired coating could not be obtained. In the penetrant liquid crack examination applied to the prototypes coated for use in field tests, a large number of cracks were detected on the surface as well. When similar studies in the literature are examined, it is thought that the situation occurred due to the high ratio of 70% WC grains in the coating [15 - 19].

Microstructural analysis showed that WC particles precipitate in both coating methods (OAW and GMAW). In the wear test results given in Figure 2, it is seen that the wear rate decreases with the duration of the wear test on the basis of each sample. Abrasion tests also confirm that the WC ratio increases in the deepening layers of the coating. This may be due to the big WC particles (500-1000 µm) and / or the long solidification time of melt binder during welding [20 – 26].

The amount of abrasion in each wing of the stabilizer, which has been field tested in TPC Beşikli-34 well, is shown in Figure 5. As a result of the measurements, it is seen that the wear amount of Electrode-A coating applied with GMAW method is higher than both of the coatings applied with OAW method. When the wear amount of Electrode-A and Technodur electrode samples applied by OAW method are compared, it is seen that Technodur Electrode with spherical carbide particles give better performance ~~results~~. Laboratory wear test results were confirmed with field tests.

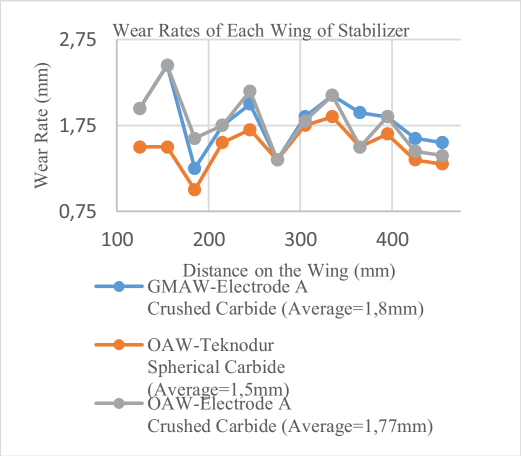

Figure 5. Abrasion Amounts of the Stabilizer Wings Used in Field Tests

4. Conclusion

In this study various coating materials with 70 % WC ratio and Ni binder were applied by GMAW and OAW methods to AISI 4145 steel. Samples were compared by their microstructure, hardness values, discontinuities and wear resistances. Effect of coating method and carbide shape on the wear resistance were examined. In laboratory and field test results, samples cladded by using OAW method gave higher wear resistance than the samples cladded with GMAW method. The sample with spherical carbide particles showed better wear resistance than the sample with crushed carbide particles. In the field tests, it was observed that the crushed carbide Electrode-A applied with OAW wore about 18% more compared to the spherical carbide Technodur electrode applied with OAW.

Acknowledgement

This study was realized with contributions of TOBB University of Economics and Technology and Turkish Petroleum Corporation. A recent support from The Scientific and Technological Research Council of Turkey under the 1002 program (Project Number 120M065) was also acknowledged.

References

1. Turkish Petroleum International Company, Annual Report 2018.
2. Archard J. F., Contact and Rubbing of Flat Surfaces, Journal of Applied Physics 24, 981-988, 1953.
3. Burwell, Jr., J.T., Survey of Possible Wear Mechanisms, Wear, Vol 1, Issue 2, 119-141, 1957
4. Kou, S., Welding Metalurgy, Wiley Interscience Publication, 2003.
5. Smallman, R., Bishop, R., Modern Physical Metallurgy and Materials Engineering, Buttrworth Heinemann Publishing (6th Edition), 1999.
6. Davis, J.R., Hardfacing, weld cladding and dissimilar metal joining in D.L. Olson, T.A. Siewert, S. Liu, G.R. Edwards (Eds.), ASM handbook: Welding Brazing and Soldering, Vol. 6, ASM International, 789–829, 1993.
7. Fernandes, C.M., Senos, A.M.R., Cemented carbide phase diagrams: A Review, Int. J. Refract. Met. Hard Mater. 29, 405–418, 2011.
8. Tarrago, J.M., Ferrari, C., Reig, B., Coureaux, D., Schneider, L., Llanes, L., Mechanics and mechanisms of fatigue in a WC–Ni hard metal and a comparative study with respect to WC–Co hardmetals, Int. J. Fatigue, 70, 252–257, 2015.
9. Antonov, M., Hussainova,I., Pirso, J., Volobueva, O., Assessment of mechanically mixed layer developed during high temperature erosion of cermets, Wear, 263, 878–886, 2007.
10. Moustafa, S.F., Abdel-Hamid, Z., Osama Baheig, G., Hussien, A., Synthesis of WC hard materials using coated powders, Adv. Powder Technology, 22 (5), 596–601, 2011.
11. Hidouci, A., Pelletier, J.M., Ducoin, F.D., El Guerjouma, D.R.., Microstructural and mechanical characteristics of laser coatings, Surface and Coating Technology, 123 (no. 1), 17–23, 2000.
12. Imasato, S., Tokumoto, K., Kitada, T., Properties of ultra-fine grain binderless cemented carbide 'RCCFN', Int J Refract Metals Hard Mater, 13, 305–312, 1995.
13. Gille, G., Bredthauer, J., Gries, B., Advanced and new grades of WC and binder powder: their properties and application, Int J Refract Metals Hard Mater, 18, 87–102, 2000.
14. Işık, Z. M., Gökdağ, İ., Ozaner, O. C., Tekçam, Y., Design and Manufacturing **of** Abrasive Wear Unit, TOBB ETÜ Mechanical Engineering Department Mak498 Senior Design Project, Supervisor, Prof. Dr. Nuri Durlu, 2017.
15. Fernandez, M.R., Garcia, A., Cuetos, J.M., Gonzales, R., Effect of actual WC content on the reciprocating wear of a laser cladding NiCrBSi alloy reinforced with WC, Wear, 324-325, 80-89, 2015.
16. Dubourg, L., Ursescu, D., Hlawka, F., Laser cladding of MMC coatings on aluminium substrate: influence of composition and microstructure on mechanical properties, Wear, 258, 1745–1754, 2005.
17. Zhang, Z., Chen, Y., Zuo, L., The effect of volume fraction of WC particles on wear behavior of in-situ WC/Fe composites by spark plasma sintering, Int J Refractory Metals Hard Mater, 69, 196-208, 2017.
18. Jankauskas, V., Antonov, M., Varnauskas, V., Effect of WC grain size and content on low stress abrasive wear of manual arc welded hardfacings with low-carbon or stainless steel matrix, Wear, 328-329, 378-390, 2015.
19. Weng, Z., Wang, A., Wu, X., Wear resistance of diode laser-clad Ni/WC composite coatings at different temperatures, Surface and Coatings Technology, 304, 283- 292, 2016.
20. Gong, T., Yao, P., Zuo, X., Zhang, Z., Influence of WC carbide particle size on the microstructure and abrasive wear behavior of WC–10Co–4Cr coatings for aircraft landing gear, Wear, 362-363, 135-145, 2016.
21. Saito, H., Iwabuchi, A., Shimizu, T., Effects of Co content and WC grain size on wear of WC cemented carbide, Wear, 261, 126-132, 2006.
22. Tng, X., Li, F., Kuang, M., Effects of WC particle size on the wear resistance of laser surface alloyed medium carbon steel, Applied Surface Science, 258, 3214-3220, 2012.
23. Gao, P., Chen, B., Wang, W., Simultaneous increase of friction coefficient and wear resistance through HVOF sprayed WC-(nano WC-Co), Surface and Coatings Technology, 363, 379-389, 2019.
24. Ning, M., Lei, G., Zhenxiong, C., Wu, H., Fuxing, Y., Improvement on mechanical properties and wear resistance of HVOF sprayed WC-12Co coatings by optimizing feedstock structure, Appl. Surf. Science, 320, 364–371, 2014.
25. Counts, W.A., Braginsky, M.V., Battaile, C.C., Holm, E.A., Predicting the Hall–Petch effect in FCC metals using non-local crystal plasticity, Int. J. Plast., 24, 1243–1263, 2008.
26. Yuan, Y., Wu, H., You, M., Li, Z., Improving wear resistance and friction stability of FeNi matrix coating by insitu multi-carbide WC-TiC via PTA metallurgical reaction, Surface and Coating Technology, 378, 124957, 2019.

Microscale Fracture Toughness Testing on Hard Coatings

Burçin KAYGUSUZ[1], Amir MOTALLEBZADEH[2], Özcan Doğu KARADAYI[3], Kürşat KAZMANLI[4], Sezer ÖZERİNÇ[1]

[1]Middle East Technical University, [2]Koç University,
[3]Ionbond Turkey Yüzey Teknolojileri A.Ş., [4]İstanbul Technical University

Turkey

Abstract

Nitrides such as TiAlN and CrAlN are widely utilized as metal cutting tool coatings for improving the lifetime of the cutting tool. However, the brittle nature of these coatings make them vulnerable to damage and reduce their effectiveness. Fracture toughness is the critical parameter that determines the damage tolerance of hard and brittle coatings. Determining the fracture toughness of such coatings is challenging due to their micron-level thickness. In this work, we present the application of a recently developed microcantilever bending experiment for determining the fracture toughness of nitride coatings.

1. Introduction

Improving the machining performance of cutting tools is critical for improving product quality and decreasing production cost. The application of hard coatings on cutting tools provides an effective solution to this problem. Metal nitrides (MNs) are coatings that are suitable for this purpose, due to their high hardness and elastic modulus [1]. TiAlN is one of the most popular and effective nitride coatings in terms of reducing tool wear. One of the main disadvantages of AlTiN coatings, however, is their brittle nature. The low ductility increases the likelihood of crack formation and subsequent failure. An ideal coating should possess high fracture toughness to minimize this problem. Direct measurements of the fracture toughness of coatings have not been possible until recently due to the small thickness of the coatings. The advancements in micromanufacturing and nanoindentation have enabled direct measurements possible through microcantilever bending experiments [2]. This work demonstrates the application of this technique to TiAlN coatings.

2. Materials and Methods

A lab-scale reactive magnetron sputterer deposited TiAlN coatings of about 2 µm thickness on oxidized silicon substrates. A 30% KOH solution etched the silicon wafer for about 100 minutes, which provided 30 µm-wide free standing regions of the coatings at the edges. In the next step, a focused ion beam (FIB) milled micro-cantilevers of 2 µm thickness, 4 µm width, and 15 µm length. FIB also machined a notch at the base of the cantilever to facilitate the fracture. Figure 1 shows SEM images of some examples of these cantilevers. Finally, a nanoindenter equipped with a diamond Berkovich tip loaded the cantilever up to the point of fracture to determine the fracture toughness of the coatings.

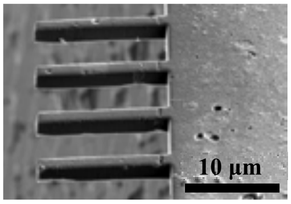

Figure 1. SEM image of some microcantilevers manufactured by focused ion beam.

3. Conclusion

The preliminary results show that the notch dimensions and the cantilever design are critical for the success of the method. Future studies will focus on optimizing these parameters that will enable repeatable measurements.

Acknowledgments

This research is supported by the Scientific and Technological Research Council of Turkey Grant No. #116M429. We thank METU Central Laboratory, Koç University KUYTAM, and Bilkent University UNAM for their support in characterization measurements.

References

1. G. Greczynski, J. Lu, O. Tengstrand, I. Petrov, J.E. Greene, I. Hultman, Scripta Materialia, 2016. 122, p.40-44.
2. D. Di Maio, S.G. Roberts, Journal of Materials Research, 2005. 20, 299-302.

Environmental Impact on the Corrosion Behavior of Marine Grade Steel in the Arabian Sea Conditions - A Comparative Analysis of Field and Laboratory Based Corrosion Tests

Muntazir ABBAS[1], Nigel SIMMS[1], Liyun LAO[1], Owais A. MALIK[2], Luqman ASHRAF[2]
[1]Cranfield University, [2]National University of Science & Technology, PNEC
[1]United Kingdom, [2]Pakistan

Abstract

Corrosion-induced degradation of marine steel structures is highly dependent on the surrounding environmental conditions and so varies significantly around global seawaters. This research has investigated the dependence of corrosion of carbon steel alloy for marine service on seawater composition and climatic conditions typical of the Arabian Sea. Natural and polluted seawater sites in the Arabian Sea were selected for field exposures. In addition, environmental conditions spanning those anticipated for the shipping structures operating in the Arabian Sea have been simulated in laboratory-based experiments by using heated and aerated artificial seawater. Following their exposures, the performance of samples have been investigated using the weight-loss and dimensional metrology methods. High overall corrosion losses were observed in the polluted seawaters than in the natural seawater conditions of Arabian Sea.

1. Introduction

In the marine environment corrosion induced structural degradation accounts for the highest failure incidents in marine/shipping structures despite the application of protective measures such as corrosion resistant paint schemes and cathodic protection measures [1,2]. The rates of corrosion processes in marine grade low carbon steel are highly dependent on the severity of operating and sea environmental conditions; seawater composition and temperature in particular. Variations in these parameters are quite significant across global seawater reservoirs [3]. In addition to the temperature, dissolved oxygen (DO) concentration, salinity level, pH level, water velocity, chlorides, sulphates, microbiological agents, and nutrients in the form of dissolved inorganic nitrogenous (DIN) compounds in the seawater are considered as the influential factors towards corrosion processes in marine assets. Although, the standard ASTM method G1-03 provides a good approximation for the uniform corrosion loss, however, the use of suc data in design maintenance planning may lead to serious consequences by underestimating the real rate of deterioration and failure probabilities.

In this paper, a new corrosion measuring approach based on the 'Dimensional Metrology' (DM) has been used for the first time to investigate the corrosion behaviour of ship grade steel under seawater immersion conditions. Two sites in the Arabian Sea near the southern coast of Karachi have been selected for field corrosion experiments (i.e. a clean open natural seawater site and a pollutant-rich seawater site). In addition, environmental conditions spanning those anticipated for the Arabian Sea have been simulated in the laboratory-based experiments by using artificial seawater followed by a comparative analysis for corrosion loss between the dimensional metrology and standard weight-loss methods. The accumulated corrosion products have been characterized using the scanned electron microscopy/ energy dispersive X-ray spectroscopy (SEM/EDS) and X-ray diffraction (XRD) methods.

2. Experimental Procedure and Methodology

2.1 Material selection and experimental plan

During the corrosion experiments, coupons were immersed in the two sites in the Arabian Sea; clean natural seawater, and pollutant-rich seawater, respectively. In the laboratory-based experiments, influential seawater parameters of Arabian Sea were simulated using artificial seawater. Contrary to the average seawater surface temperatures of the Arabian Sea (27-30 °C), the seawater in the laboratory-based experiments was maintained at ~40 °C, so as to simulate the temperature of slightly heated seawaters flowing in the ship structures operating in these regions. The laboratory based experiments were also repeated at a mean seawater temperature of ~18 °C with water specifications as for the experiments conducted at ~40 °C. Table 1 (a & b) shows the compositions of the steel coupons.

Table 1 Elemental compositions (wt.%) of (a) laboratory coupons (b) field coupons.

C	Mn	Si	P	S	Al	Mo	Fe
0.1	0.34	0.13	1.2	0.006	0.3	0.2	balance

---

*Corresponding author. Email: l.lao@cranfield.ac.uk

(a)

C	Mn	Si	P	Cu	Ni	Cr	Fe
0.06	0.9	0.4	0.01	0.4	0.7	0.7	balance

(b)

Table 2 shows the influential seawater parameters for corrosion process recorded/maintained for all three experimental conditions.

Table 2 Influential seawater parameters at field and laboratory based experiments.

Parameters	Units	Polluted (Field)	Natural (Field)	Artificial seawater
Temperature	°C	27±3	27±3	40±3
DO	mg/L	1±0.3	>3.5	3.4±0.75
pH		6.5±0.5	7.5-8.2	7.5-8.2
Conductivity	mS/m	63± 4.8	50-55	60±4
Velocity	m/s	~ 0.3	~ 0.3	~ 0.3
DIN(Nitrates)	mg/L	1.5±0.2	>0.005	>0.005
Sulphates	mg/L	~ 2900	~1900	~1900

2.2. Dimensional Metrology Method for Corrosion Measurement

The dimensional metrology (DM) approach is purely based on the measurement of dimensions (test coupons) accurately prior and post exposure to the corrosive environment. This uses a contact metrology technique (with digital micrometers) to measure the plate dimensions before exposure. After exposure, again the measurements of plate thickness were taken at the same predetermined positions, as shown in Figure 1.

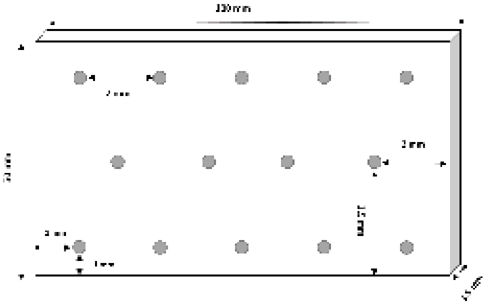

Figure 1 Schematic of DM pattern. Here dots indicate positions of measured prior/post immersion.

After collection of the samples from seawater exposure, the known position and the nearest vicinities were measured for the thickness loss and deepest points. In addition to the DM technique, the standard weight-loss method [4,5] has also been used to calculate corrosion rate/loss and compared to the DM approach. Equations below (1 and 2) refer to the standard weight-loss method.

$$C_R \text{ (mm/yr)} = 87.6 * \left(\frac{\Delta W}{D.A.T}\right) \qquad (1)$$

Where C_R is the corrosion rate, ΔW is the weight difference prior/post immersion (in milligrams), D is the material density in grams/cm^3, A is the sample's exposure surface area in cm^2 and T is the exposure time (hours). Similarly, average corrosion loss is calculated using the following equation:

$$\text{Corrosion loss } (\mu\text{m}) = \frac{\Delta W * 1000}{D.A} \qquad (2)$$

For all field and laboratory based tests, the rust compounds accumulated on the metal surface during the seawater immersion were characterized using SEM/EDS and XRD.

3. Results and Discussion

3.1 Laboratory-based corrosion test results

In the laboratory-based experiments, duplicate coupons were recovered from 20 up to 228 days of immersion. Figure 2 illustrates the average corrosion loss calculated using equation 2 and Figure 3 shows the cumulative distribution function (CDF) of corrosion loss calculated using the DM approach.

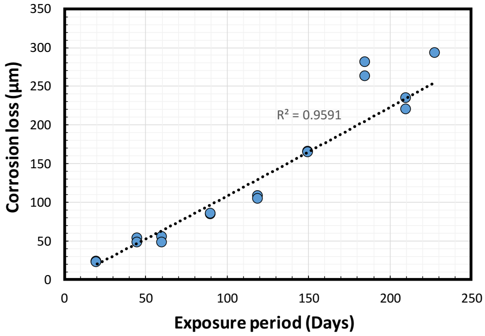

Figure 2 Average corrosion loss calculated using standard weight-loss method (for laboratory corrosion tests carried out at ~40 °C).

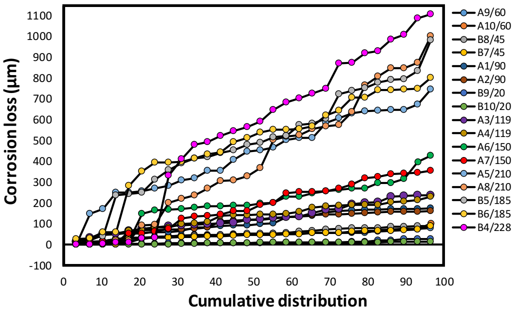

Figure 3 Cumulative distributions of corrosion loss measurements using the DM approach (legends indicates coupon denomination/immersion period in days).

In this DM approach, the greater the number of measured points prior- and post-exposure the more stable are the incremental trends of corrosion. The DM plot (in Fig. 3) provides a comprehensive information on the corrosion phenomena such as mean corrosion depths, deepest pit depths, their percentage above mean value, probability density, CDF, and a definite trend line classifying the corrosion pattern (i.e.

uniform or localised) on either sides of the corroding surfaces (multi-modal pattern of corrosion). Figure 4 demonstrates a comparative analysis for corrosion loss calculated using DM approach and standard weight-loss method. It shows maximum corrosion depth points (orange and blue markers) and mean corrosion depths (green markers) calculated using DM approach; whereas, red and yellow markers represents corrosion losses calculated using standard average weight-loss method.

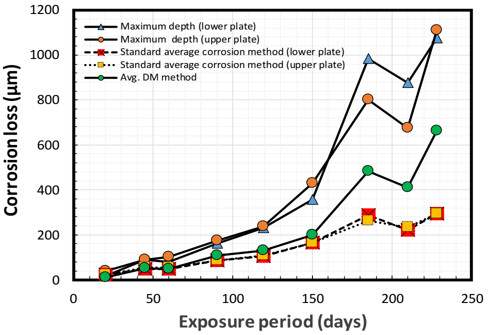

Figure 4 Comparison of corrosion loss parameter calculated using the standard average corrosion method.

In the laboratory experiments, a corrosion test with similar seawater conditions (salinity/conductivity, pH, flow velocity) was repeated at a seawater temperature of 18.6 ± 2.8 °C for 210 days. The experimental results revealed that both the mean corrosion losses and the maximum corrosion depths were around 4 times higher for a seawater temperature of ~40 °C than those observed with a mean temperature of ~18.6 °C.

3.2 Field corrosion test results

Figures 5 and 6 represent the corrosion loss for both seawater sites (clean natural seawater and polluted seawater) in the Arabian Sea calculated using the standard weight-loss and DM methods, respectively.

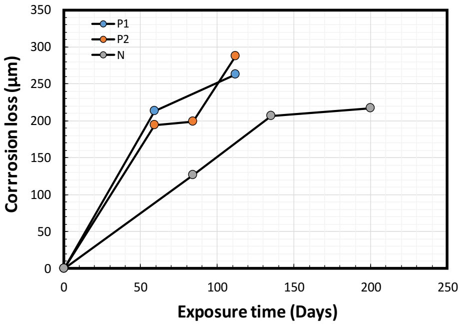

Figure 5 Standard average corrosion loss calculated in the natural seawater (N), and polluted seawaters (P1, P2)

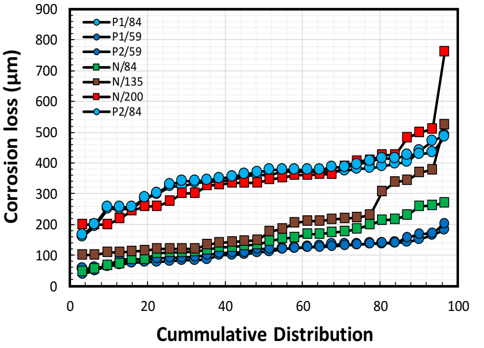

Figure 6 Corrosion loss (DM approach) in natural seawater site (N) and pollutant-rich seawater site (P_1, P_2).

The above graphs indicate considerably higher corrosion losses observed in the pollutant-rich seawaters than in the clean natural seawater.

3.3 Characterization of rust product

Figure 7 illustrates SEM micrographs for the corrosion product accumulated on the steel coupons submerged under the three different seawater conditions (as outlined above). The EDS results show high sulphur (S) content (~2.7 wt.%) in the corrosion product on the coupons in the pollutant-rich seawater site, whereas a lower S content appeared in the corrosion product collected in the natural seawater site (~0.77 wt.%) and an even lower level was found in that formed in the artificial seawaters of laboratory-based conditions (~0.16 wt.%). In the X-ray diffraction (XRD) analysis, the presence of typical rust phases were observed in all environmental conditions. Additionally, aragonite, calcite, other carbonates/calcareous compounds and silicon oxides were also detect in the corrosion layers; predominantly in the polluted and natural seawater.

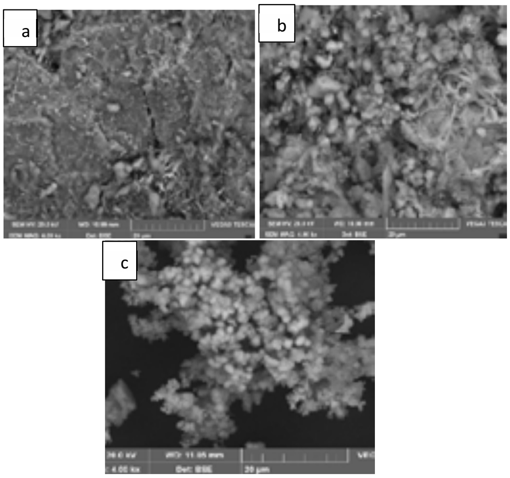

Figure 7 SEM micrographs of corrosion products (Fe/O-rich globules, spongy globules, and distinct phases) formed in: a. natural seawater, b. pollutant-rich seawaters, c. artificial seawater (laboratory).

3.3 Discussion

The rate of corrosion is significantly different between the open natural seawater conditions and the pollutant-rich seawater; despite availability of similar seawater temperature, velocity, salinity level and immersion depth. However, some other influential corrosion accelerating factors, such as DO, DINs and pH level were found to be quite different at both field experimental sites. According to previous studies, DO has a direct relationship to the corrosion rate, with its lower concentration in the pollutant-rich seawater favouring a lower corrosion rate. The difference in the pH level is not very significant between both field experimental sites (6.9-8.2); with the available literature suggesting that pH level ranging between 4-10 does not directly affect the rate of corrosion [6,7]. The potential factor is the presence of high DINs (nitrates) in polluted seawater (1.5 ppm). In addition to the high DIN content, presence of significantly high sulphur can be the contributory factors towards accelerated corrosion rates. The EDS results also confirm the presence of high sulphur contents in the corrosion deposits settled in the polluted seawater site.

The average corrosion rates recorded for the clean natural seawater site (~0.4-0.55 mm/yr.) and that in the simulated laboratory conditions (0.4±0.7 mm/yr.) were quite comparable. Whereas in the polluted seawater sites the average corrosion rates ranged 0.87-1.32 mm/yr. for an exposure period up to112 days. Although known biological activities were not present in the laboratory-based experiments and a difference in the seawater temperature (10 °C) also existed between the field (natural seawaters) and laboratory based experimental conditions. Further, a remarkable corrosion rate difference observed in laboratory tests conducted at 40 °C and 18.6 °C seawater temperature (4 times higher at 40 °C) provide a reason that the corrosion rates in the field environments of Arabian Sea should be significantly higher at a seawater temperature of 40 °C than those recorded in current study at 27-30 °C. As seawater temperatures in the ship tanks, pipelines and equipment (operating in the Arabian Sea) can reach as high as 40 °C. The thickness loss measurements using DM provides a novel approach to collect a useful data set which would otherwise be missing/ underestimated with the conventional procedures.

4 Conclusion and future research avenues

This research study concludes following:

Higher corrosion damage rates were recorded in the polluted seawater site of Arabian Sea than in the natural seawater conditions under similar seawater temperatures (27-30 °C), salinity, flow velocity, and pH level. This is mainly attributed to the presence of high DINs (nitrates) levels.

In EDS analysis, the presence of high sulphur levels were observed in the corrosion product accumulated in the polluted seawaters, which has a vital role particularly during the long-term (anaerobic) phases of corrosion.

As compared to the standard weight-loss method, the dimensional metrology approach provides a superior capability to measure various corrosion damage parameters simultaneously and an opportunity to carry out in-depth statistical analyses/prediction modelling for general as well as localized corrosion.

Under similar environmental conditions and seawater specifications in the laboratory-based experiments, 4 times higher corrosion losses (mean corrosion and maximum depths) were recorded at a seawater temperature of ~40 °C than those observed at a seawater temperature of 18.6 °C. These results revealed that the seawater temperature is the most critical parameter in determining the rate of corrosion of submerged steel structures.

References

[1] Lampe, J.; Hamann, R. Probabilistic model for corrosion degradation of tanker and bulk carrier. *Mar. Struct.* **2018**, *61*, 309–325.

[2] Melchers, R. E. Corrosion uncertainty modelling for steel structures. *J. Constr. Steel Res.* **1999**, *52*, 3–19.

[3] Zayed, A.; Garbatov, Y.; Guedes Soares, C.; Wang, G. Environmental factors affecting the time dependent corrosion wastage of marine structures. *Marit. Transp.* **2005**, *1*, 589–598.

[4] ASTM G1 − 03 Standard practice for preparing , cleaning , and evaluating corrosion test 2017, 1–9.

[5] Fontana, M. G. *Corrosion Engineering*; 3rd ed.; McGraw Hill Book Company: New York, USA, 1987; ISBN 0070214638.

[6] Abbas, M.; Mahmood, S.; Simms, N. Corrosion behaviour of cupronickel 90/10 alloys in Arabian Sea conditions and its effect on maintenance of marine structures. In *Proceedings of the ASME 2019 38th International Conference on Ocean, Offshore and Arctic Engineering OMAE2019*; ASME: Glasgow, Scotland, UK, 2019; pp. 1–9.

[7] Bhandari, J.; Khan, F.; Abbassi, R.; Garaniya, V.; Ojeda, R. Pitting degradation modeling of ocean steel structures using Bayesian Network. *J. Offshore Mech. Arct. Eng.* **2017**, *139*, 051402.

A Predictive Model for Corrosion Under Insulation

Guodong WANG[1], Luyao MEI[1], Prafull SHARMA[2], Hoi YEUNG[1,2], Liyun LAO[1]
[1]Cranfield University, [2]CorrosionRADAR Ltd
United Kingdom

Abstract
Corrosion under insulation (CUI) is one of the critical issues associated with piping system's integrity. The nature of CUI that corrosion occurs beneath the insulation layer makes the phenomenon imperceptible until some significant failure appears. This paper reports a study on the development of a predictive model for CUI in the industry. Aiming at building a robust model, a comprehensive review on the experimentations and corrosion models were performed. An adaptive neural fuzzy inference system (ANFIS) and American Petroleum Institution Recommended Practice (API RP 581) were adopted to the model development. To generate the validation data, a novel test rig which is easy to access for corrosion inspection, and capable of accommodating testing condition sensors and specimen, was designed and set up following ASTM G189. Coupons were used to acquire the corrosion development data. The ANFIS model was trained and validated with use of the datasets collected from literature and the rig tests. The test rig was used to generate the CUI data under representative corrosion conditions. The developed ANFIS-based CUI model was verified using both API RP 581 data and the CUI data generated from the experimentation in this study. Results showed the model can reasonably well predict the corrosion rate.

1. Introduction

Corrosion under insulation (CUI) is a very prevalent problem in piping systems. CUI associated with carbon steel pipes can take place under all types of insulation[1]. CUI is related to two crucial substances, oxygen and moisture, which could be readily available and co-exist with a pipe during its service life [2]. Once corrosion initiates under the insulation, manual inspection often fail to identify this problem in the early stage. Without proper maintenance and monitor, CUI can exaggerate and could finally lead into a disastrous consequence in the economical and safety aspects. Numerous efforts therefore have been put into seeking a solution to avoid such loss, aiming at monitoring and predicting CUI process.

Many models aiming at predicting corrosion rate have been developed. Most of them can be classified into following three categories, simple time-dependent models, probabilistic models and artificial intelligence (AI) tool-based models. Regarding time-dependent models, the two most popular ones probably are the power law model[3] and Soares model[4], both capture the variance of the corrosion rate with time but ignore the effect of the environment. Probabilistic model, based on probability theory such as Bayes theorem, is a powerful tool to make accurate predictions, but it requires a comprehensive and clear cause and effect relationship between the contributors and corrosion loss[5]. AI based model is more effective and versatile compared with the former two as AI tool is employed, therefore has now become a well-recognized tool for making prediction. In a previous study, researchers successfully employed an adaptive neural fuzzy inference system (ANFIS) to improve the reliability based inspection (RBI) activities for CUI[6].

In the study reported in this paper, an ANFIS and modified API RP 581 data were adopted for the model development. In order to develop and validate models, quality data of the corrosion development is vitally important. While acquiring some CUI data via literature survey, for this study a set of dedicated test rig was constructed to perform an experimental study aiming to obtain CUI data. The rigs were designed mainly by following ASTM G189-07, a standard guide for laboratory simulation of CUI [7]. However, the recommended design in ASTM G189-07 makes it impractical to do periodical mass loss measurements without significantly disturb the corrosion development process. In order to resolve this issue, novel features have been implemented in this rig to allow CUI data obtained along the corrosion develops.

2. Experimentation

2.1. CUI Test Rig

The test rig was designed to simulate CUI on the surface of

---

*Corresponding author. Email: l.lao@cranfield.ac.uk cuboid coupons under simulated conditions. The pipe and 4 sets of plain cuboid coupon samples used in the tests were made from the same material, carbon steel Grade S235. Each set has two coupons. A section of mineral wool insulation from ROOKWOOL Ltd. was cut into two parts along axial direction and was placed around the pipe section. All the coupons were placed and fixed on the bottom half insulation. The test solution was pumped into the rig from the inlet holes located on the top (12 o'clock) of the external aluminum jacketing, would flow through the annular space between the pipe and insulation, drain via the outlet holes located on the bottom (6 o'clock), into a container underneath the test section. Inside the pipe, there is a heating coil controlled by a temperature controller to regulate the test temperature. The pipe section was supported appropriately and placed in a dedicated fume hood (Figure 1). Moisture sensor and thermocouple in the annular space were used to monitor the wet and temperature. Cable ties were used to bundle the two half insulation sections together.

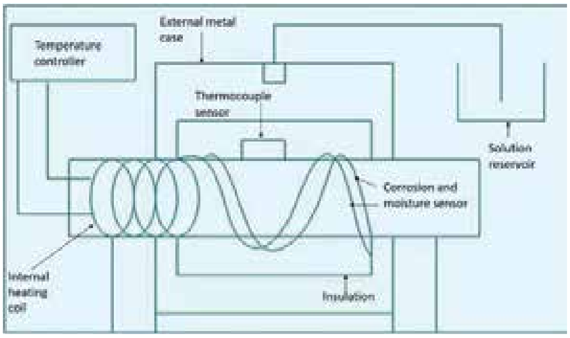

Figure1. Schematic of test rig

2.2. Test Procedure

After rinsing with acetone to remove rust and oil, the dimensions of coupons, approximately 50 mm×25 mm×2.5 mm, were measured by using vernier caliper and micrometre gauge. The mass of these coupons was measured by a Sartorius CP224S balance with an accuracy of 0.01 mg.

The test matrix and the elemental compositions of laboratory test coupons and pipe are detailed in Table 1. The solution feeding pump was set to work 5 minutes every hour and this was proved to be able to keep the insulation layer in annular space constantly wet. The temperature was at 32±1℃ and the fluctuations were due to the ingress and egress of the test solution. To accelerate the corrosion an aqua solution of 3wt% NaCl was used.

Table 1. (a) Laboratory test matrix (b) Elemental compositions (wt%) of laboratory test coupons and pipe.

Coupon Set No.	1	2	3	4
Exposed Days	7	14	21	28

(a)

C	Mn	Si	P	S	N	Fe
0.18	1.4	-	0.04	0.04	0.009	balance

(b)

After the rig was set to run, test solution was pumped into the annular space. Each set of coupons was taken out for measurement according to the schedule specified in Table 1 above. The coupons were cleaned by following the procedure recommended in [8] and the measurement of mass loss due to corrosion was taken. The average corrosion rate was calculated by:

$$CR=3.65 * 10^5 * \Delta m/(\rho A t) \quad (1)$$

where CR is the average corrosion rate (mm/year), Δm is the mass loss during that exposed period (g); ρ is the density of the material (g/cm^3); A is the exposed area of the coupon's , the total surface when the test was initiated (mm^2); and t is the exposed time (day).

2.3. Other Corrosion Data

API RP 581 provides a table showing base corrosion rate under different drivers and temperature, and also a modification equation for the final corrosion rate calculation.

$$C_{rF} = C_{rB} \cdot F_{INS} \cdot F_{CM} \cdot F_{IC} \cdot \max[F_{PS}, F_{IP}] \quad (2)$$

where C_{rF} is the final corrosion rate for each application scenario. F_{INS} is the insulation type factor, F_{CM} is the pipe complexity factor, F_{IC} is the insulation condition factor, F_{PS} is the pipe supports factor and F_{IP} is the pipe's interface with water/soil factor. Modification factors were chosen according to the new test rig mentioned above. To generate enough data for training model, interpolation of the table was carried by Excel. Each driver category then had 60 sets of the final corrosion rate data for training. The simplified table is shown as follows (Table 2).

Table 2. Modified Corrosion Rate (mm/a) data from API RP 581

Temperature (℃)	Final CR as a Function of Driver			
	Air/Dry	Temperate	Marine	Severe
6	0.039	0.119	0.198	0.397
32	0.039	0.119	0.198	0.397
71	0.080	0.198	0.397	0.794
107	0.039	0.039	0.198	0.397

The two input variables of the model are temperature and driver, the output is corrosion rate. In order to improve the prediction accuracy and do a conservative prediction, pipe was set to only experience "temperate" and "severe" surroundings.

2.4. ANFIS Model

The model was trained by the back-propagation algorithm and gradient descent learning algorithm combined hybrid method which can provide better training results[9]. The linguistic variables for the driver input were set as temperate and severe corresponding to 0 and 1 respectively. The temperature was fuzzified into nine categories that can represent the range from -16 to 190 ℃ as M. M. Khan[10] did in his previous work, namely very very low, very low, low, intermediate low, medium, intermediate high, high, very high and very very high. The type of these 11 variables' membership function was all set as the Gaussian type for its smoother transition between different variables. After defining the descriptive variable and membership function type of inputs, data then were submitted to the training system for generating fuzzy inference system using Neuro Fuzzy Designer Tool from MATLAB (Figure 2). Modelling accuracy of the ANFIS model is related to the amount of data used for training, this specific relationship was then evaluated by comparing accuracy indicators between systems generated by different amount of training data (60%, 70%, 80% and 90% respectively).

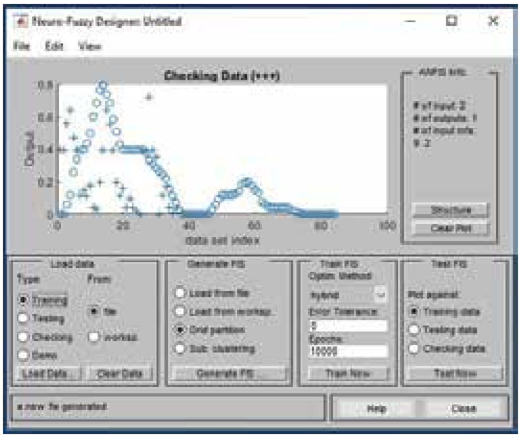

# of input: 2
# of outputs: 1
# of input mfs:
9 2

Optim. Method: hybrid
Error Tolerance: 0
Epochs: 10000

a new fis generated

Figure 2. Loading data to training system

3. Results and Discussions

3.1. Result of CUI Test Rig

The corrosion rate of each set of coupons are detailed in Table 3. The corrosion rate was decreasing with exposure time increased, which is consistent with the trend reported in [11].

Pictures of the coupons used in this CUI test and conditions inside the external jacketing are shown in Figure 3. It is noted that the coupons were heavily corroded due to CUI.

Table 3. Corrosion rates of each coupon set (mm/year)

Coupon Set No.	Corrosion Rate	
1	0.47728	0.46032
2	0.48743	0.46795
3	0.36667	0.39627
4	0.40526	0.40795
Mean	0.42741	

Figure 3. Coupons(left) and pipe(right) inside CUI test rig

3.2. Model

The uncertainty of the model was evaluated by root mean square error (RMSE) and mean absolute error (MAE or MAD). There are 18 rules generated for predicting output (Figure 4). Based on the 120 sets of data, the effect of the training data's percentage on the model's performance is shown in Table 4.

Table 4. Performance of different amount of training data

Data	**60%**	**70%**	**80%**	**90%**
RMSE	0.003527	0.003304	0.004668	0.004285
MAD	0.001387	0.001385	0.001946	0.001802

It is obvious that using 70% of data to generate FIS can get the minimal error, then the one trained by this data set was the final fuzzy inference system for the predictive model. Figure 4 shows the correlation between the predicted corrosion rate and the two input variables using this predictive model.

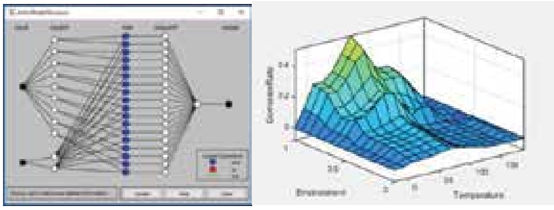

Figure 4. Fuzzy Inference System model and its 3-D function plot

For the evaluation of the model's performance, the comparison with another high accurate prediction model developed by Khan et al [6] was conducted. The uncertainties, in terms of MAD, were on a similar level for both models, as shown in Table5.

Table 5. Accuracy Comparison

Model	Khan's Model [6]	This study
MAD	0.00060	0.00096

The performance difference between ours and Khan's models may due to following two points: 1. Different values of the base corrosion rate (C_{rB}) and final corrosion rate (C_{rF}) selected for training will result in slightly different model. 2. Data selected for training the two model were unlikely the same ones.

Further validation using the results from our test rig was also conducted. As mentioned above, pipe in the rig was experiencing wet sea water surrounding during the test, which means the input of driver will be set as "severe", i.e. 1. The input of temperature was set as 32 ℃ as indicated. Results are shown in Table 6.

Table 6. Validation with measurements from rig

	Test rig	Predictive model
CR (mm/a)	0.42741	0.41700

As it can be seen from the table above, the experimentally calculated corrosion rate was very close to the corrosion rate data predicted by the model.

4. Conclusions

The ANFIS was used to develop a corrosion development model which based on the available API RP 581 database. Inherent toolbox in MATLAB was explored for generating the model.

A novel CUI test rig was developed in this study. Instead of conventional ring specimens, plain cuboid coupons were successfully used for the simulated CUI tests under artificial conditions. Because of the novel design of the test rig, corrosion rate at different exposure time was able to obtain by opening the test rig and taking coupons out for measurements, which could be a considerable advantage compared with the conventional test methods. In addition, the corrosion rates generated by this CUI test rig were consistent with that found in the published literature.

The model was verified using both the API RP 581 data, and further validated using the CUI data generated from the experimentation in this study. Uncertainty assessment result showed the model can reasonably well predict the corrosion rate.

Acknowledgment

This work reported in this paper was sponsored by CorrosionRADAR Ltd.

References

[1] <http://www.insulation.org/io/articles/cui-an-in-depth-analysis/> Dated: 31.03.2020
[2] American Petroleum Institute, API Recommended ractice 581, 2008, Washington, USA, pp. 2-122.
[3] R. E. Melchers and R. B. Petersen, Corrosion Engineering Science Technology, 53(2018) 131–140.
[4] C. G. Soares and Y. Garbatov, Journal of Ship Research, 43(1999) 65-78.
[5] Det, Shan Guan, Veritas, Norske, Jain, Swati, Sánchez, Andrea N, Guan, Shan, Wu, Shanshan, Ayello, Francois, Sridhar, Narasi, Feng, Qingshan and Yan, Bingchuan, Probabilistic assessment of external corrosion rates in buried oil and gas pipelines, NACE - International Corrosion Conference, January 2015, Texas-USA, no. 5529
[6] M. M. Khan, A. A. Mokhtar, and H. Hussin, ARPN Journal of Engineering and Applied. Science, 11(2016) 13325-13330.
[7] ASTM ,Standard Guide for Laboratory Simulation of Corrosion Under Insulation,2008, Pennysylvania, USA pp. 1–11.
[8] Standard Practice for Preparing, Cleaning, and Evaluating Corrosion Test Specimens.， 1985， Pennysylvania, USA, pp. 16-18.
[9] C. Loganathan and K. V Girija, International Journal of Engineering and Science, 2(2013) 6-13.
[10] M. M. Khan, A. A. Mokhtar, and H. Hussin, ARPN Journal of Engineering and Applied. Science, 11(2016) 268-276.
[11] E. Hamzah, M. F. Hussain, Z. Ibrahim, and A. Abdolahi, Arabian Journal for Science and Engineering, 39 (2014)6863–6870.

Corrosion Resistance of Electroless NiB Coatings Synthesized in a Bath Free of Stabilizing Agent

Muslum YUNACTI[1], Alexandre MEGRET[1], Alex MONTAGNE[2], Véronique VITRY[1]
[1]Université de Mons, [2]ENSAM Lille
[1]Belgium, [2]France

Abstract

Electroless Nickel-Boron coatings present attractive properties in terms of mechanical and corrosion resistance, as well as tribology. Therefore, they have been considered as outstanding alternatives to replace hard chromium coatings. There are several components in the plating solution, and one of them is a stabilizing agent, which is used to stabilize the plating bath and regulate the plating rate. However, toxic heavy metals such as Tl and Pb are employed as a stabilizing agent in the commercially available electroless NiB coating baths.

Recent researches have allowed the development of new toxic-heavy-metals-free bath formulations, and one of them is a bath free of stabilizer. It was designed in our laboratory through the adjustment of the complexing agent and pH regulator concentration. The new coating exhibits properties close to those of the conventional electroless NiB coatings. However, the most remarkable feature of this new deposit composition is its much-improved corrosion resistance, which is the object of a thorough investigation in this work.

Keywords: Electroless nickel, Ni-B coating, corrosion, environmentally friendly technology, stabilizers

1. Introduction

Electroless deposition is a process that is the reduction of metal ions by a reducing agent and depositing on an activated substrate without any external current source that makes it different from electroplating. It was comprehensively found in 1954 by Brenner and Riddel. [1-3] One of the main reasons to choose the electroless plating towards the electroplating is that producing a uniform deposit even on the complex shapes, which is not possible in the electroplating processes. [4] Nickel electroless plating is the most used type of electroless plating, thanks to its excellent mechanical, tribological, and corrosion properties. [1,5] There are three different electroless nickel coatings differentiated from their reducing agent: hypophosphite for Ni-P deposits (EN-P), these are the most popular ones, borohydride or dimethylamine borane for Ni-B (EN-B) deposits, and hydrazine for the pure nickel deposits.. [1,6,7]

The bath used for EN-B deposits contains several substances such as nickel ion source, reducing agent, stabilizer, complexing agent, pH adjuster with the particular function, and these substances noticeably affect the properties of the deposits. [1,8,9] Several baths are containing different types and amounts of the complexing agent and stabilizer used for EN-B deposits. Additionally, baths stabilized with thallium or lead-based stabilizer, are extensively used in the industry. [7] On the other hand, these baths are restricted to use by new legislation, besides the use of thallium-based stabilizer is completely banned in the European market. [3] The further restriction in the use of lead increased the requirement of a completely environmentally friendly bath. To this end, the new bath that is stabilizer-free was revealed through the adjustment of the complexing agent and pH regulator in the EN-B bath. [7]

2. Experimental Procedure

Mild steel (St-37) with dimensions 25 mm*25 mm* 1 mm were used as substrates. The substrates were prepared by mechanical grinding with SiC paper of 180, 500, and 1200 grade. Then it followed by degreasing in the acetone solution. The final pre-treatment step was activation by etching in 30% HCl. Then the samples were rinsed with distilled water and immersed in the electroless Ni-B solution.

Plating bath was operated at 95 ± 1 °C, with a pH higher than 13 and with mechanical agitation, in a one-liter cell with controlled heating. The plating bath was composed of sodium borohydride ($NaBH_4$) as a reducing agent, nickel chloride hexahydrate ($NiCl_2.6H_2O$) as a nickel source, ethylenediamine (NH_2-CH_2-NH_2-CH_2) as a complexing agent and sodium hydroxide (NaOH) as a pH adjuster.

Plating thickness and plating rate were determined from the weight gain and observation of the samples by optical microscopy, with a HIROX KH-8700 digital microscope. Glow-discharge optical emission spectroscopy (GD-OES) will be used to determine the composition of the coatings. The roughness was measured with a Zeiss 119 SURFCOM 1400D-3DF apparatus. Hitachi SU8020 SEM was used to observe the surface morphology and cross-section of the samples.

Corrosion characterization was performed by Potentiodynamic polarization in 0.1 M NaCl solution with a Bio-logic SP-50 potentiostat. Salt spray tests were performed in a Q-FOG Cyclic corrosion tester. The neutral salt spray tests were applied according to ASTM B117-07. The tests were conducted for different periods ranging from 0.5 h to 7 days. Then, the corroded surfaces after salt spray testing were observed by image analysis, using the open-source image processing and analysis program *Imagel*.

3. Conclusion

Electroless nickel-boron deposits were produced in a stabilizer-free bath. The stabilizer-free bath composition was optimized based on the thickness and roughness of the deposits. The new deposits showed modified chemical composition, different growth mode, morphology, mechanical, tribological, and corrosion behavior when compared with reference deposits produced in a conventional bath containing Pb as a stabilizer (NiB-Pb). The new coatings exhibit a featureless cross-section, and the surface morphology did not show the cauliflower-like surface texture that is the typical surface morphology of the electroless-nickel boron deposits. NiB-Pb deposits present higher hardness than the new deposits. The most notable results were about corrosion resistance since the protection of the new deposits against corrosion was higher than the one of NiB-Pb deposits.

References

[1] F. Delaunois, V. Vitry. L. Bonin, (2019). Electroless Nickel Plating. Taylor & Francis Group, Mons, 2019

[2] Riedel, W. (1991). Electroless Nickel Plating, Finishing Publication LTD., London, 1989

[3] L. Bonin. Replacement of Lead Stabilizer in Electroless NiB: Baths. Ph.D. Thesis, Faculté Polytechnique de Mons, 2018

[4] L. Bonin, V. Vitry, Mechanical and wear characterization of electroless nickel mono and bilayers and high boron-mid phosphorus electroless nickel duplex coatings, Surface and Coating Technology 307 (2016) 957-962.

[5] P. G. Venkatakrishnan, S. S. Mohamed Nazirudeen, T. S. N. Sankara Narayanan, Electroless Ni-B-P Ternary Alloy Coatings: Preparation and Evaluation of Characteristic Properties, European Journal of Scientific Research ISSN 1450-216X Vol.82 No.4 (2012) 506-514.

[6] J.T. Tijerina, K.A.Camarena, R.T.Sanchez, C.D. Rios, D.M. Cortes, Tribological evaluation of electroless NiB coating on metal-working tool steel, The International Journal of Advanced Manufacturing Technology 103 (2019) 1959-1964.

[7] L. Bonin, C. C. Castro, V.Vitry, A.L. Hantson, F. Delaunois. Optimization of electroless NiB deposition without stabilizer, based on surface roughness and plating rate. Journal of Alloys and Compounds 767 (2018) 276-284.

[8] Bulbul, F. The Effects of Deposition Parameters on Surface Morphology and Crystallographic Orientation of Electroless Ni-B Coatings, Met. Mater. Int., Vol. 17, No. 1 (2011) 67-75.

[9] M.Anik, E. K. Effect of coating bath composition on the properties of electroless nickel–boron films. Surface & Coatings Technology 202 (2008) 1718-1727.

20th
INTERNATIONAL
METALLURGY
MATERIALS
CONGRESS
10-12 June
2021
"in Digital Platform"

Casting

immc2021

Evaluation of a New Eco-Friendly Sodium Silicate-Based Binder System for Chromite Sand Application

Necip ÜNLÜ[1], Ahmet ODABAŞ[2]

[1]Istanbul Technical University, [2]Alazan Casting Chemicals & Industry Metal Inc. Co.

Turkey

Abstract

Many sand systems composed of silica base and many Na-silicate binders have been developed and investigated since over sixty years in the foundry industry. In this study, technological importance of a recently developed Na-silicate binder with a liquid hardener, and its applicability in chromite base mold/core system have been investigated. It has been determined that using Na-silicate binder in chromite base mold/core system results in benefits such as shorter period (10 s) for CO_2 application, sound mold surface without cavity, high temperature strength availability, good gas permeability, long shelf-life at high moisture environment (90 % moisture at 23ºC for 24 h). Further, a casting trial of a high-speed train's brake disc has been performed by using the molds prepared with the chromite/silica sand mixture with the current Na-silicate binder, and the observations have been evaluated. It has been observed that the preparation of molds with the current Na-silicate binder hardened by CO_2 process provides practically odorless and fast process, also outstanding casting quality during the trials.

1. Introduction

Numerous foundries in the world have been focus on both developing and using of eco-friendly sodium silicate base binders since the observation of detrimental outputs such as dermatitis, irritated eyes, skin and mucous membrane, decomposing urea to CO_2 and ammonia, thus, insufferable toxic concentrations originated from resin-type binders (phenol-, urea formaldehyde, phenolic-, and furan) [1-9]. Additionally, usage of sodium silicate has been resulted in advantages such as high strength, and rigidity, good permeability, compatibility with green sand and low cost without producing detrimental gases or vapors [5, 7, 10], many research and development investigations have been performed in the past to develop the mixture system composed of sand and sodium silicate [11-17]. Though there are a many types of molding sands in the casting industry, some unique conditions require the applications of special molding/core sand mixtures. For instance, during the production of large steel casting components the chromite base sand is often used due to the its desirable properties, i.e., high refractoriness above 1750°C, high thermal shock resistance, high compressive strength and thermal conductivity [18-23]. Moreover, it should be noted that the chromite base sand is preferred because of its ability to resist metal penetration by molten steel and oxides [18]. In the current study, the AFS standard green/dry and high-temperature strengths, gas permeability, moldability index tests were made to evaluate a recently developed Na-silicate based binder, and its hardener for chromite base sand mixtures. The effect of relative humidity on the strength was also evaluated. In addition, practically, casting trials of 4140 alloy high-speed train's brake disc were performed, and the final product and obtained molds were inspected in the face of the current binder system.

2. Experimental Procedure

In this research as a main component of the sand mixture, the chromite sand with AFS grain size number of 39.9 was used. As a binder component, a recently developed Na-silicate based solution and its hardener were used [24]. The physicochemical properties of this Na-silicate binder are given in Table 1. For hardening reaction, commercial grade liquefied carbon dioxide gas (>99.99 % purity) was used. Sieve analysis of the sand was performed by using Octagon-200 mark mesh analysis device. The preparation of sand mixture with the current Na-silicate binder was carried out by using a laboratory sand mixer, which has two S-shaped blades mounted on solid steel cone rotating at a speed of 35 rpm. The cylindrical test specimens prepared in accordance with the standard [5, 6] were subjected to curing with CO_2. While applying CO_2 gas to the specimens, a Ridsdale model gas supply apparatus connected to the CO_2 tank was used. CO_2 gas flow rate was adjusted as 10 l/min, and applied only for 10 sec. To determine the dry compressive strength, the specimens were held in the Heraeus model laboratory type-furnace for 2 h at 110ºC. In addition, high temperature strengths were investigated after holding the specimens at 800, 1000 and 1200ºC for 30 min., thus, the extent of decomposition of the Na-silicate binder, referring to the term of shakeout ability [25], was evaluated by using the ratio of gassed to baked strength. Green/dry and high temperature strengths of the prepared AFS standard cylindrical test specimens were determined by using George Fisher model universal sand strength machine, and Instron 1195 machine at a crosshead speed of 0.1 mm/min, respectively. AFS standard gas permeability and moldability index tests were performed.

Table 1. Physicochemical properties of Na-silicate used in the current investigation

Modulus (SiO_2/Na_2O molar ratio)	2.84
Density (20°C) g/cm^3	1.424
Fe_2O_3 max. %	0.021
Baume degree (°Be)	39

The effect of relative humidity on strength of the prepared samples, and their moisture absorbability were determined. The samples were maintained in a controlled conditioning cabin with 90% relative humidity for 24 h at 23°C. Casting trials of 4140 alloy high-speed train's brake disc having 700 mm. in diameter with approximately 150 kg in weight, were performed in Yahyaoglu Steel Casting Inc. Co., Zonguldak, Turkey. The CO_2 hardened sand mixture was composed of the silica sand with the AFS grain size number of 50, the chromite sand with the AFS grain size number 40, and the current Na-silicate binder in 2.0 wt.%. The prepared sand mixture ratio of silica sand to chromite sand was adjusted as 50:50. The manually molding method was applied, melting was carried out by using the induction furnace, and the pouring temperature was 1680°C. Observations taken from the casting trials were evaluated.

3. Results and Discussion

Compression strength test results of the sand mixtures prepared with the current Na-silicate binder in 1.0 wt. %, and its liquid hardener are given in Figure 1. The green compression strength values of the CO_2 hardened and the liquid hardened sand mixtures were determined as 105.62 ± 4.75 psi, and 302.69 ± 15.18 psi, respectively. It has been suggested that the compression strength values to be minimum about 200 psi, and maximum about 1200 psi for the manufacture of cores [26]. Thus, the current sand mixture prepared with the Na-silicate binder in 1.0 wt. %, and its liquid hardener, has provided the appropriate compression strength values for the manufacture of cores. However, the CO_2 hardened chromite sand mixture with the Na-silicate binder in 1.0 wt. %, presented lower strength (105.62 ± 4.75 psi) than 200 psi, indicating the necessity of increment for the amount of Na-silicate binder. As can be seen in Figure 1, the compression strengths of both sand mixtures increased linearly when the applied temperature increased from 110°C through 1200°C. Compression strength values of CO_2 hardened sand mixture at 800°C and 1200°C were determined as 436.90 ± 36.28 psi and 548.67 ± 30.71 psi, respectively. Besides, the sand mixture prepared with the liquid Na-silicate hardener yielded strengths of 789.04 ± 86.88 psi, and 1463.84 ± 160.14 psi at 800°C and 1200°C, respectively. Kunsmann [11] has reported that minimum compression strength of 50 psi is required to prevent erosion and mold deformation in CO_2 hardened mold system at elevated temperatures (815-1150°C), and maximum compression strength must not exceed 600 psi to avoid hot tearing type problems. Current results of high-temperature compression strength showed that the CO_2 hardened chromite sand mixture with the Na-silicate binder in 1.0 wt. %, ensured the requirements for CO_2 hardened sand mold systems. The sand mixture prepared with the liquid Na-silicate hardener would not be preferred due to the exorbitantly high compression strength values at elevated temperatures.

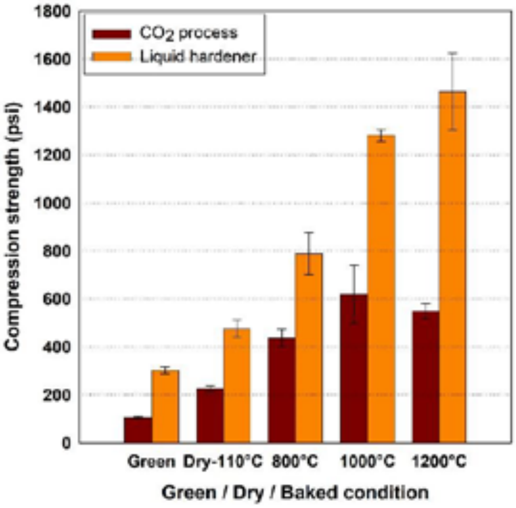

Figure 1. Compression strength data of the sand mixtures prepared with the investigated Na-silicate binder in 2.5 wt. %, and its liquid serter hardener

Gas permeability indicates the venting characteristics of foundry sand [27]. Both the green and baked core/mold must have sufficient gas permeability to avoid the formation of bubbles, blow holes, and expansion defects in the finished casting. The gas permeability values of the CO_2 hardened and the liquid hardened sand mixtures were determined as 280, and 295, respectively. It might be noticed that the obtained high gas permeability with the current Na-silicate binder consistent with the grain fineness number (AFS 39.9) of the base sand. Further, the current findings are congruent with the literature [28] which indicates an acceptable the AFS standard gas permeability range of 130-300 for steel parts over 100 kg. in the sand molding systems having the AFS grain fineness number interval of 38 to 62.

Moldability describes the behavior of molding sand when being rammed into a mold. Moldability index is characterized by the basis that the ramming energy to produce a mold is relative to the force to separate the cohering grains from the uncompact molding sand. Sands having a moldability index higher than 80 present good moldability, besides an index under 20 exhibits relatively tough sand [29]. Moldability index of the CO_2 hardened sand mixture with the Na-silicate binder in 1.0 wt. % was determined as approximately 91. However, the moldability of sand mixture with liquid Na-silicate hardener was determined at five minutes after binder addition to the sand, and an approximately similar moldability index value of 90 was obtained. The investigated Na-silicate binders yield the chromite sand mixtures having good moldability, therefore, provide both filling core/mold boxes with intricated shapes more effectively at a high manufacturing rate, and obtaining strong core/mold surface.

The moisture absorbability has significant importance in the Na-silicate bonded sand systems since the absorbed water molecules spread into the binding interface, thus, causing a decrease in the strength of the sand system [15]. The moisture absorbability and effect of relative humidity on strength of the standard AFS samples were determined after storing in the conditioning cabin with 90% relative humidity for 24 h at 23°C. Average humidity absorbing values of the CO_2 hardened samples, and the samples prepared with Na-silicate liquid hardener were determined as 0.29 %, and 0.48 %, respectively. Due to the effect of 90% of relative humidity for 24 h at 23°C, the compression strength of CO_2 hardened samples with the Na-silicate binder 1.0 wt. %, decreased from the initial strength of 105.62 ± 4.75 psi to 69.51± 15.54 psi, while the compression strength of the samples prepared with Na-silicate liquid hardener decreased from the initial strength of 302.69 ± 15.18 psi to 209.39 ± 37.94 psi. This strength behavior corresponds to the findings of humidity absorbing (%). As a comparison, Jina et al [15] reported that in the humidistat at 98% humidity condition for 24 h, the strength of the sodium silicate bonded sand samples hardened by microwave heating was nearly zero. Though the current CO_2 hardened samples, and the samples prepared with Na-silicate liquid hardener sustained a significant amount of their compression strength values for the 90% humidity condition. Therefore, one may indicate that the current Na-silicate binder maintains its bonding capability even though the chromite sand structure absorbs a significant amount of moisture from the atmosphere, and presenting the opportunity of long shelf-life.

Mold preparation and casting processes of 4140 alloy high-speed train's brake disc were performed in Yahyaoglu Steel Casting Inc. Co., Zonguldak, Turkey. The sand mixture composed of the silica sand, and chromite sand with the current Na-silicate binder in 2.0 wt. %, provided high quality mold surfaces (Figure 2a-c). During casting process along with the molds created using the current binder, the molds were able to withstand extremely high temperature up to 1700°C, also it was observed that the current CO_2 hardened sand mixture with Na-silicate binder system, presented odorless process with the excellent surface finish (Figure 2f). Besides, no any casting defects about mold originated such as penetration, cuts and washes, drops and rat-tails, were observed.

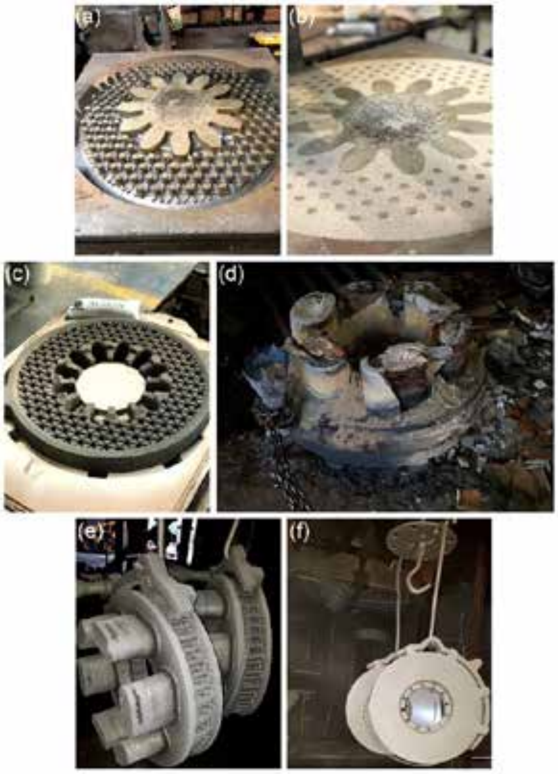

Figure 2. Casting trials of 4140 alloy high-speed train's brake disc (a), (b) core, and (c) mold preparation (d) shakeout (e) casting is ready for shot blasting and (f) after shot blasting

4. Conclusion

In the present study, the chromite sand mixture with the current Na-silicate binder hardened by CO_2 process and the liquid Na-silicate hardener, have been evaluated. Both a shorter time (i.e., 10 s) of the implementation of CO_2 gas, and usage of a lower amount of the current Na-silicate binder in 1.0 wt. % fulfill the requirements effectively for the preparation of mold/core systems. The sand mixtures with the current Na-silicate binder in 1.0 wt. %, and its liquid hardener exhibit the required intervals of compression strength for the manufacture of cores. It has been observed that the sand mixture prepared with CO_2 process might be used in mold systems due to its available high-temperature strength result. Both the CO_2 hardened sand mixture with the current Na-silicate binder in 1.0 wt. %, and the sand mixture prepared with liquid Na-silicate hardener exhibit sufficient gas permeability and good moldability, consequently, it is possible to perform the core making/molding even with intricated shapes effectively at a high manufacturing rate. Under the 90% relative humidity condition for 24 h at 23°C, the compression strength of CO_2 hardened sand samples drops to approximately 34 % of the original strength, while the compression strength of the samples prepared with Na-silicate liquid hardener drop to approximately 30 % of the original strength, indicating excellent storage life. Further, during the casting trial works and at the shakeout, no odors were generated. The molding mixture composed of the current binder system resulted in high quality mold surfaces, and sound final casting.

5. Acknowledgements

Alazan Casting Chemicals & Industry Metal Inc. Co., is gratefully acknowledged for permission to publish this work. Authors are also grateful to Yahyaoglu Steel Casting Inc. Co., Zonguldak, Turkey for their help during the casting trials of this study.

References

[1] Warren D. Recent developments in silicate based foundry processes. The British Foundryman, 1971, 64(12): 52-56.
[2] Czerwinski F, Mir M, Kasprzak W. Application of cores and binders in metalcasting. International Journal of Cast Metal Research, 2015, 28(3): 129-139.
[3] Drożyński D, Bobrowski A, Holtzer M. Influence of the reclaim addition on properties of moulding sands with the geopol binder. Archieves of Foundry Engineering, 2015, 15(1): 138-142.
[4] Gigante G. How can we become a practical green foundry industry?. International Journal of Metalcasting, 2010, 4(3): 7-15.
[5] Parappagoudar M B, Pratihar D K, Datta G L. Neural network-based approaches for forward and reverse mappings of sodium silicate-bonded, carbon dioxide gas hardened moulding sand system. Materials and Manufacturing Processes, 2009, 24(1): 59-67.
[6] Wolf R J, Score R E. Sand core and mold composition and method of making cores and molds therefrom. United States Patent: 2765507, 1951.
[7] Bergna H E. High ratio silicate foundry sand binders. United States Patent: 4316744, 1982.
[8] Boyle M A, Martin C J, Neuner J D. Epoxy resins. Ed. B. Miracle and S.L. Donaldson, Ohio: ASM International, 2001: 78.
[9] Heth J A. Safety and health issues. Ed. S.T. Peters, London: Chapman & Hall, 1998: 832.
[10] Ohdar R K, Pushp P T. Prediction of collapsibility of moulds and cores of CO_2 sands using a neural network. Proceedings of the Institution of Mechanical Engineers, Part B: Journal of Engineering Manufacture, 2003, 217(4):475-487.
[11] Kunsmann H G F. Hot strength and collapsibility of CO_2 sand. AFS Transactions, 1971, 79: 488-492.
[12] Barker S A, Baggett N, Stevenson J, deCourcy D R. Alkali metal silicate binder compositions. United States Patent: 4504314, 1985.
[13] Schumacher W. Applications of the carbon dioxide process in the foundry. AFS Transactions, 1955, 63: 488-492.
[14] Chang H, Chen E L, Lindeke R. Collapsibility of sodiumsilicate cores cured by microwave energy and CO_2 gassing process. AFS Transactions, 1988, 96: 217-222.
[15] Jina W, Zitian F, Xiaolei Z, Di P. Properties of sodium silicate sand hardened by microwave heating, China Foundry, 2009, 6(3): 191-196.
[16] Zaretskiy L. Modified silicate binders new developments and applications. International Journal of Metalcasting, 2016, 10(1): 88-99.
[17] Ünlü N, Odabaş A. Development and evaluation of a new eco-friendly sodium silicate-based binder system. International Journal of Metalcasting, 2018, 12(4): 765-771.
[18] Stec K, Podwórny J, Psiuk B, Kozakiewicz Ł. Determination of chromite sands suitability for use in moulding sands. Archives of Foundry Engineering, 2017, 17(2): 107-110.
[19] Stec K. Determining the content of chrome (VI) in raw materials and post-production waste. Ceramika (Ceramics), 2008, 102: 189. (In Polish)
[20] Stec K, Determination of chromium oxide in the ore and chrome refractory materials containing chromium oxide. Ceramika - Polski Biuletyn Ceramiczny, 2005, 88: 223-245. (In Polish)
[21] Furmanek J. Installing the regeneration of molding and core. Archives of Foundry 2(3): 42-49. (In Polish).
[22] Dańko J, Holtzer M, Dańko R. Problems concerning reclamation of used foundry sands. Polish Journal of Environmental Studies, 2007, 3B(16): 93-102.
[23] Izdebska-Szanda I, Angrecki M, Palma A. Recycling of waste moulding sands with new binders. Archives of Foundry Engineering, 2013, 13(2): 43-48.
[24] Ünlü N. Analysis report for characterization study of casting binders. 26052015, Itunova, 2015.
[25] Moore W H, Gruver W E. Process for improved silicate bonded foundry molds and cores. United States Patent: 2883723, 1959.
[26] Rao T V R. Metal Casting: Principles and Practice. New Age International, 2010.
[27] https://en.wikipedia.org/wiki/Permeability (foundry_sand). Accessed 25 May 2017.
[28] Foseco. The Foseco Foundryman's Handbook. Ed. T.A. Burns, New York, USA: Pergamon Press, 1986:70.
[29] GF Sand Testing Equipment Catalog, George Fischer Limited, Schaffhausen, Switzerland.

The Effect of Nodularizer Type on the Microstructure and Mechanical Properties of EN-GJS-700-2 Nodular Cast Iron

Ali KELEŞ[1], Sayid HAS, Rabia CENGİZ[1], Mehmet YILDIRIM[2], Muhammed KIRICI[1]
[1]Motus Automotive Company, [2]Konya Technical University
Turkey

Abstract

In the scope of this work, the effect of new generation nodularizers on the microstructure and mechanical properties of EN-GJS-700-2 nodular cast irons was investigated in detail. In the amount (area) of graphite in the medium section, in the number of nodules of the thin and the medium section, and the thick section for nodularity was obtained a remarkable increase. While there was a similar increase in tensile and impact tests, there was no significant change in hardness values.

1. Introduction

Ductile irons (DIs) that have a wide range of application fields have superior casting properties and machinability, which enhances production performance and decreases the cost of manufacturing [1]. As for the mechanical properties of DI depends on the general shape, total volume/mm^2, and the number of spheroidal graphite which are located on the microstructure [2]. In this sense, many researchers studied to investigate effects on the graphite morphology of lanthanum and cerium, calcium and magnesium, yttrium and magnesium, bismuth, and rare earth elements. In the scope of this work, the effect of new generation nodularizers as La-FeSiMg on the microstructure and mechanical properties of DIs according to section thickness was investigated in detail.

2. Materials and Methods

The As-cast DI material utilized in this research was produced EN-GJS-700-2 in the form of a stepped block by conventional sand-casting technique. As nodularizer, traditional FeSiMg and new generation La containing FeSiMg were used. The microstructural examination was performed using an optical microscope and mechanical properties were determined by impact, tensile and hardness test. All experiments were carried out at room temperature.

3. Conclusion

In Figure 1-b, Nodularity in the medium and thick sections of the stepped block was achieved increase about by 15 %. While the effect of lanthanum to the number of nodules occurred a 15% increase in thin sections, there was almost constant in medium and thick sections (Figure 1-d). The amount of graphite was increased by 56% in the medium section. Tensile and un-notch impact test in room temperature test results was found that tensile strength and impact toughness has increased for 16, 20 %, respectively (Figure 1-a and Figure 1-c).

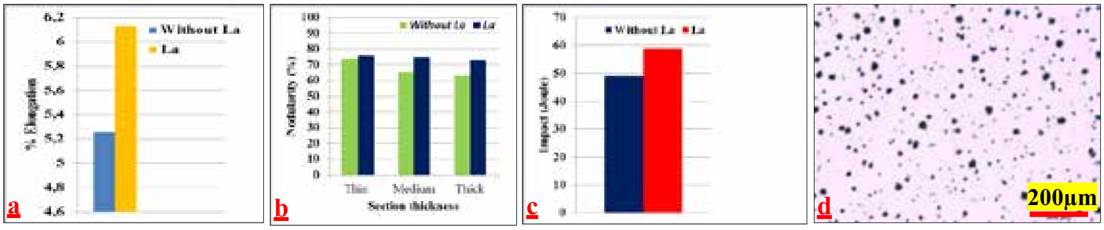

Figure 1 Effect of La-FeSiMg nodularizer on **a.** % elongation, **b.** % nodularity, **c.** un-notch impact toughness, **d.** imagine of OM on 100x magnitude

References

[1] O.O. Oluwole, O.E. Olorunniwo, O.O. Ogundare, P.O. Atanda and O.O. Oridota, Effect of Magnesium and Calcium as Spheroidizers on the Graphite Morphology in Ductile Cast Iron, Journal of Minerals and Materials Characterisation and Engineering, 2007, pp. 6, 1, 25-37.

[2] P. Minnebo, K. Nilsson, and D.Blagoeva, Tensile Compression and Fracture Properties of Thick-Walled Ductile Cast Iron Components, Journal of Materials Engineering and Performance, 2007, pp. 16, 35–45.

Squeeze Pin Application on the HPDC Process for Improving Part Quality

Ekrem ALTUNCU[1], Naci EKMEN[2], Ali OZKAN[2]

[1]Sakarya University of Applied Sciences, Material and Manufacturing Technologies Application And Research Center (SUMAR), [2]Arpek High Pressure Die Casting Company

Turkey

Arpek High Pressure Die Casting Company, Kocaeli, Turkey

Abstract

The high pressure die casting (HPDC) process is usually used to produce aluminum-silicon alloy automotive parts. Die casting is a process where the complex sized parts are casting at high production rates by injecting molten metal into the die under high pressure. The most important advantage of this casting process is the ability of the product to be produced quickly and serially in dimensions close to the final product. In addition, the desired mechanical properties and microstructural properties can be achieved. HPDC is ideally suited to high production rates, and wall thickness can be as little as 1-5 mm. Casting discontinuities can be observed in casting parts due to solidification and process conditions. The die filling phase is highly critical because defects such as air entrapment and shrinkage porosity might occur. Preventing of this kind of defects there could be some options such as use extra pressure on the problematic thick section areas during solidification time. This is called as squeeze pin or core pin application. After the die is quickly filled with molten metal, the sequeeze pin is applied locally to the thick section following the compression pressure. Target of this compression is feed the extra metal and preventing the shrinkage porosity. In HPDC process, castings and dies geometry design, as well as casting parameters, gating and cooling systems, die layout and the heat flow paths can be optimized by using Magmasoft simulation program. Data resulting from them are very valuable information for investigate the problem and make a diagnosis as well as in die design and process parameter optimization as they simulate casting solidification. The main aim of this study; explain the application of the squeeze pin and its effect on the casting part quality. In this study, aluminum alloy compressor part with some sections up to 10 mm thickness is taken as an example. X-ray measurement results and some thick part sections are examined. Casting machine diagrams and some process parameters effect on the squeeze pin is explained and discussed in detail. As a result of this study, it was observed that shrinkage porosity can be reduced significantly with the use of sequeeze pins.

Keywords: Die Casting, Solidification, Shrinkage porosity, Squeeze pin

1. Introduction

The die-casting process involves different stages, but the total cycle time is short and will be between ten seconds and a few minute, typically. The first step in die-casting is the preparation and clamping of both halves of the die. Before clamping, each of the die halves is cleaned and lubricated properly. The two die halves are then attached inside the machine, and securely clamped and closed. At second stage; molten metal, maintained at a set temperature is transferred to a cold chamber and then injected to the die. After transferring the molten metal, it is injected into the die at high pressures. This high pressure holds the molten metal in the die and the metal solidifies inside the die. When the molten metal enters the die cavity, it will start to cool and solidify. After cooling time has passed, the die halves are opened and an ejection mechanism pushes the casting out of the die [1-5].

Quality control and process efficiency are vital for high pressure die casting foundries. Numerous test methods, design changes, process optimization methods, simulations are available in order that OEM can control the extent to which their products meet the requirements of the customers and automotive standards. As technical requirements and quality demands for die cast aluminum alloy parts continue to increase, also the requirements for casting process control technology are increasing. These demands force the die casting companies to use different design concepts and new engineering solutions. Die casting process capability of parts with complex geometries and variable cross-section thicknesses becomes difficult and increases casting quality problems. The wall thickness of aluminum alloy parts produced by die casting method can be up to 15mm. Different solidification rates along the different section (wall thicknesses vary from 3 mm to 15 mm.) of the part, it has been caused internal defects such as shrinkage porosity and are decreased casting quality. Minimum porosity ratio is expected in a high quality and efficient die casting process. Gas porosities can be eliminated or reduced with vacuum systems or airflow design changes. However, shrinkage porosity is directly related to solidification rate. The die casting performance varies depending on the casting temperature, the die temperature, the molten metal flow rate, the filling time, compression pressure, the geometric properties of the part and the limits of the die casting machine. There are many technical restriction to remove shrinkage porosity. For this reason, shrinkage porosity can not be easily eliminate with only design changes. Shrinkage defects generally are located at the last solidified regions and hot spots in the thick sections. After the molten metal is injected into the die, it must have time to solidify and cool. During this time the die cannot be unclamped. Once the metal has completely cooled it takes on its final shape of the casting. Shrinkage porosity occurs when the shrinkage on solidification cannot be compensated. Solidification under high pressure controls the shrinkage. There is a high heat transfer between the molten metal and the die. Due to the liquid metal flow, the thermal balance of the die can change. However, inhomogeneous heat distribution affects the rate of solidification in different sections. The shrinkage is as high as wall thickness is heavy. The causes of this shrinkage defects are different wall thickness, cross section too thick, metal pressure too low, gate too thin for maintenance pressure. Using die casting simulation programs for shrinkage porosity prediction can lead to significant costs reduction thanks to major improvements in material and energy consumption, labour resources, and scraps reduction. In order to control the shrinkage porosity, besides the simulation studies and design changes, additional sequeeze pins can be applied locally during solidification stage [6-12]. In this study, the effects of the sequeeze pin application on the compressor part on the die casting quality were examined.

2. Experimental Procedure

In this study, AlSi10Mg(Fe) alloy used (**Table 1**) which is one of the most commonly used aluminum-silicon alloy in high pressure die casting processes. AlSi10Mg(Fe) is a typical casting alloy (EN AC-43400) with good casting properties and it's typically used for cast parts with thin walls and complex geometry. It offers good strength, hardness and dynamic properties and is therefore also used for parts subject to high loads. A Part of air compressor system (**Figure 1)** was selected to observe effects of squeeze pin application on shrinkage porosity. Wall thickness of part is about 20 mm. This part is one of the most intensely produced parts in mass production. Die casting process parameters were presented at **Table 2**. Experimental investigations were carried out comparatively. Magmasoft program was used in simulation studies and the effect of the sequeeze pin on the solidification was investigated. Afterwards, by applying sequeeze pin under high pressure die casting conditions, the casting parts were imaged by X-ray analysis (YXlon machine). Radioscopy pictures were captured.

Table 1. Chemical composition of casting alloy

Element.	Cu	Zn	Si	Fe	Ti	Ni	Mn	Mg	Al
%	0,1	0,1	9,0-11,0	1,0	0,15	-	0,001 - 0,4	0,2-0,5	remain

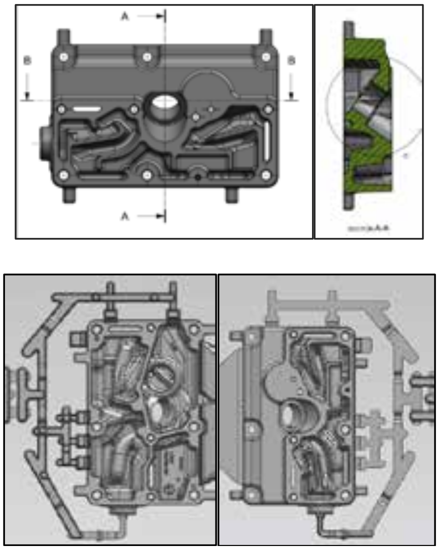

Figure 1. Front and back side of compressor part section with runner and overflow

Table 2. Die Casting process Parameters of Buhler HPDC unit

Injection parameters	Unit	Value
Velocity of metal at gate	m/s	42,8
Plunger velocity	m/s	4,64
Weight After from gate	g	3000
Shot weight	g	5149
Shot sleeve filling rate	%	51
Maximum pressure intensification phase	Bar	778
Die filling time	s	0,12
Density of solid metal (average value)	g/cm³	2,65
Active shot sleeve length	mm	565
Plunger diameter	mm	100

When casting solidification is examined with Magmasoft simulation program, hot spot areas can be clearly observed during solidification analysis. The introduction of liquid metal into the die and subsequent cooling in the die can be simulated. In the figure 4, at the end of a certain solidification time of the part, the liquid region in its thickest section is observed. The last solidified area is the blue colour in **Figure 2**. It is understood that the liquid phase still exists in that area. The probability of having shrinkage porosity in this region, which is the hottest and last solidified during solidification, is quite high. In this region, design improvements and/or sequeeze pin is have to be applied.

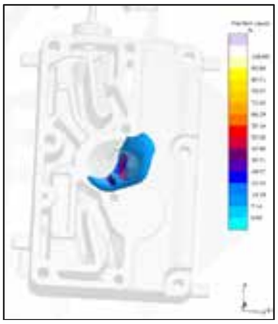

Figure 2. Fraction Liquid of the part Magma Simulation

Squeeze pin was designed (in **Figure 3)** for machining allowance 1 mm at one side. PVD thin film was applied on the pin surface because of the molten metal soldering risk. Hydraulic Cylinder is chosen from AHP Merkel Company as bore diameter 100 mm stroke 20 mm. Temperature of the die could be considered because of the cylinder position on the fix side on the die. Temperature should be min 350 C ° and sealing inside the cylinder should be chosen consider this temperature. Squeeze pin was cooled from inside with water.

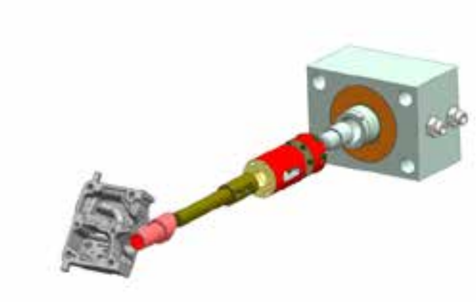

Figure 3. Squeeze Pin Design Concept

3.Results and Discussions

It is necessary to determine the region where the pin will be applied and calculate the appropriate pin design and pressure. Red lined box regions **(Figure 4)** are the die casting internal defect regions. X-ray investigations show that these areas are potential shrinkage porosity regions (Bild 3-6). Red dash lined regions are higher magnification of the X-ray images. As can be seen, the defects mostly appeared in the central last solidified region and in the thickest section. X-ray examinations show that these areas have dense shrinkage porosity. Investigation of the part with x-ray 3 points have defect at the front view of the part. Bild 4 and 5 areas are not suitable. However, Bild 6 is suitable area can be used squeeze pin. Bild 8 and 9 **(Figure 5)** are the other defect areas on the part. X-ray investigations show that these areas also have a shrinkage porosity at the feeder.

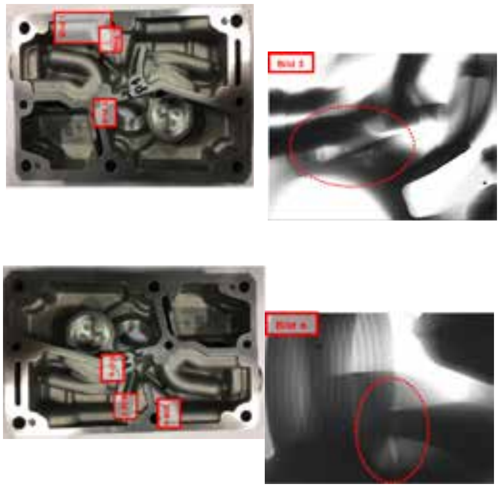

Figure 4. Shrinkage porosity regions on the part

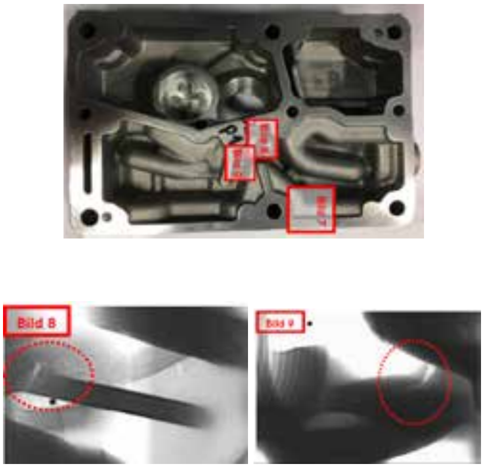

Figure 5. Shrinkage porosity regions on the feeder

Investigation of the simulation study of the current design and improved new design respectively**(Figure 6 and 7)**. Hot spot at the inside of the red rectangular area show that this area need to feed from gate nearly 15-18 second to eliminate shrinkage holes. Investigation of the simulation at the current design show that the region which have shrinkage hole is same the production records. New design simulation results (**Figure7**) show that the porosity is at the region is clearly eliminated. New design /with squeeze pin simulation results for hot spot investigation show that Hot Spot FS time is 12-14 sec. need to eliminate shrinkage porosity.

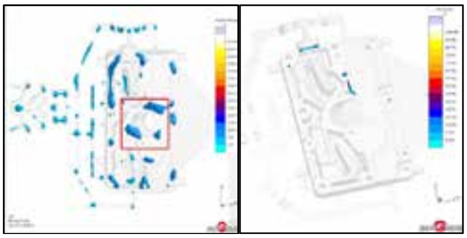

Figure 6. Current design simulation results a)hot spots, b)porosity areas

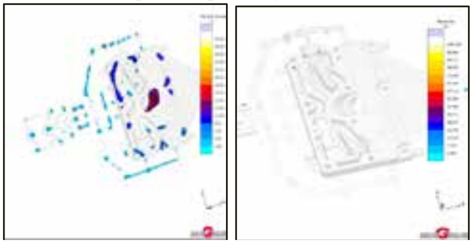

Figure 7. Improved design simulation results a)hot spots b)porosity areas

X-ray investigation with the new improved design **(Figure 8)** show that problematic region Bild 3,6,8 and 9 have less porosity than the previous design.

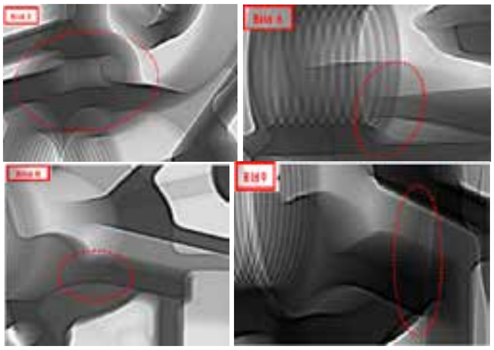

Figure 8. X-Ray images after new design with pin

4. Conclusions

The use of squeeze pins is a practical method of material homogeneity improvement for parts with high risk of shrinkage porosity resulted also from flow and solidification simulations for the high material volume areas. In this study it was found that squeeze pin has a major affect at the thick region which observed shrinkage porosity. Magma simulation results show to us there is no possibility to feed the thick region from gate because of the earlier freezing gate section. Last solidified points are the more potential region for the shrinkage porosity. These areas need to be analyzed with the simulation and to be highlighted. If the last solidified point is near the pin there could be leakage. As a solution the pin can be as a squeeze pin to eliminate the shrinkage. The designer considers this option during design stage. The other important think is the pin activation time. The basic rule is that the gate needs to be solidified before pin was activated. This time can be observe with the simulation .It is nearly 1-4 sec .The x-ray results after the new design verified the simulation results. The problematic area which have shrinkage porosity can be eliminated with the squeeze pin application. The additional pressure coming from the squeeze pins have as a direct effect higher density of alloy.

References

[1] S.M. Dargusch, G. Dour, N. Schauer, C.M. Dinnis, G. Savage, The influence of pressure during solidification of high pressure die cast aluminium telecommunications components. J. Mater. Process. Technol. 180, (2006), 37–43.

[2] T.H. Imvinkelried, H. Homberger, Mould fill simulation to improve the quality of a component. Magnes. Ind. (2001), 39–43.

[3] E.S Kim, K.H.Lee, Y.H. Moon, A feasibility study of the partial squeeze and vacuum die casting process, J. of Materials Processing Technology, 105, (2000), 42-48.

[4] Li, S., Mine, K., Sanakanishi, S. and Anzai, K., Quantitative Prediction Method for Shrinkage Porosity Considering Molten Metal Supply by Pressure in Squeeze Casting, Materials Trans., 48, (2007), 2186-2193.

[5] I.Ohnaka, J.D. Zhu, A. Sugiyama, F.A. Kinoshita, A Method to set process parameters of local squeeze in HPDC, MCWASPXIII, IOP Conf. Series: Mat. Sci.and Eng.33 (2012), 1-8.

[6] S. Biradar, P. T. Borlepwar, Minimization of Shrinkage Porosity in HPDC Process with Local Squeeze Pin Using Flow Simulation, Proceed. Int. Conf. on Intelligent Manuf. and Automation, (2018), 435-443.

[7] P. Vispute, D. Chaudhari, Utilizing Flow Simulation in the Design Phase of a Casting Die to Optimize Design Parameters and Defect Analysis, Materials Today: Proceedings 4(8):9256-9263, 2017.

[8] R. Ashiri, F. Karimzadeh, B. Niroumand, On effect of squeezing pressure on microstructural characteristics, heat treatment response and electrical conductivity of an Al-Si-Mg-Ni-Cu alloy, Mat. Sci. and Tech. 30(10), (2014),1162-1169.

[9] B. Matthew, D. Matthew, Nave, Mark and McKinney, Peter, Squeeze pin implementation in a high pressure die casting, in Proceedings of the 1st Int. Light Metals Technology Conf. CAST, (2003), 239-243

Irregular Eutectic Solidification: Coupled or Uncoupled Growth?

Samira MOHAGHEGHI[1], Shabnam Fadaei CHATROUDI[1], Sabine BOTTIN-ROUSSEAU[2], Silvère AKAMATSU[2], Melis ŞEREFOĞLU[1]

[1]Koç University, [2]Sorbonne Université

Turkey

1. Introduction:

Irregular eutectics are an important class of industrial alloys. The extensive applications of these faceted/nonfaceted alloy systems such as aluminum-silicon alloys and gray cast iron, encourage many efforts to characterize their solidification microstructures. However, many fundamental questions regarding the irregular eutectic solidification dynamics, and, in particular, the growth behavior of the faceted phase, remain open. In this experimental work, we employed *in-situ* directional solidification of a transparent faceted/nonfaceted alloy in order to investigate the dynamics of irregular eutectic growth.

2. Materials and Methods:

Transparent organic alloys are crystalline materials that can be utilized as model systems to observe the solid-liquid interface in real time with a regular optical-microscopy spatial resolution. In the chosen system, namely, the binary Amino-methyl-propanediol/Succinonitrile (AMPD/SCN) alloy, the SCN (AMPD) solid grows with a non-faceted (faceted) solid-liquid interface. Alloy samples close to the eutectic composition were prepared by mixing calibrated amounts of the highly purified AMPD and SCN compounds. Directional solidification of thin (~12µm) AMPD-SCN samples has been performed at various growth velocities V in a fixed temperature gradient. An optical microscope with transmitted light was employed for real-time observation of the solidification front.

3. Results and discussion

Overall, the AMPD solid was observed to grow in the form of thin, fiber-like faceted crystals, and the SCN solid as a nonfaceted crystal with a smooth solid-liquid interface. We identified two distinct directional-solidification regimes in the AMPD-SCN irregular eutectic system as a function of the growth velocity. In low velocity regime, ($V<0.3\mu m/s$), the AMPD crystals were observed to grow more or less individually, with their growing tip at a position far ahead of, thus at a higher temperature than the SCN growth front. In this low-V regime, triple-point junctions at which the SCN, AMPD and liquid phases meet do not equilibrate –this growth mode is therefore called “uncoupled”, in contrast to the coupled growth observed in regular eutectic systems. At higher V values, the temperature difference between the growth fronts of AMPD and SCN crystals was observed to decrease, and coupled growth established locally. In addition, this morphological transition from low to high velocity regime was also accompanied by a dramatic increase in number of AMPD crystals at the solidification front. This results from frequent non-crystallographic branching events at, or close to the triple-point junctions. The reverse transition was observed by decreasing V.

4. Conclusion

The transparent AMPD-SCN alloy is a promising model system to investigate the growth dynamics of irregular, faceted/nonfaceted eutectics by real-time optical microscopy. By varying the directional-solidification velocity, we could characterize a morphological transition from an uncoupled growth regime in which two eutectic phases grow essentially independently, to a coupled-growth mode that is made unsteady by a frequent non-crystallographic branching. Further experiments will be performed in particular to analyze transient regimes and the formation of two-phased, dendrite-like structures. This study also may be inspiring for a better understanding of some microstructures in cast iron ingots.

Acknowledgment

This work is funded by TÜBİTAK 2509 (Grant no: 217M089) and Campus France (PHC BOSPHORUS 39706RE).

3D Numerical Simulation and Experimental Investigation of Pure Tin Solidification Under Natural and Forced Convection

SARI Ibrahim[1,2], HACHANI Lakhdar[1], ZAIDAT Kader[2], FAUTRELLE Yves[2]
[1]Université Amar Telidji-Laghouat, [2]Université Grenoble Alpes
[1]Algeria, [2]France

Abstract

The numerical simulation of the horizontal solidification of pure tin under the natural and forced convection induced by electromagnetic stirring is presented and compared to experimental results obtained by a Benchmark setup so-called AFRODITE, whose description was published earlier in several works [1-5]. The proposed 3D numerical model has shown its effectiveness to predict the effect of EM stirring on the solidification process in terms of: thermal field, dynamic field and finally the shape and localization of solidification front.

Introduction

Many researchers are interested in the solidification process since the last century due to its important routes to produce materials, especially metals and alloys. The condition for the transformation from liquid to solid (phase change process), such as the temperature gradient and the growth rate vary from process to process and in one process also as a function of time and space. For this reason, we need to the numerical simulation when the simulated problems are complex to obtain more pronounced results.

Results

Instantaneous temperature maps presented in Fig. 1 represent the thermal evolution during the solidification process. The maps of pure thermal convection (case I) and forced convection case II (EM stirring) are compared with the experimental results (Exp).

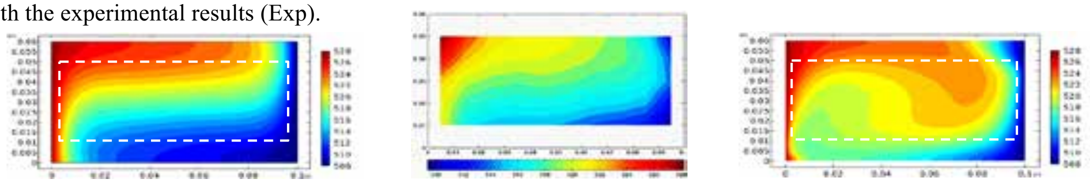

CaseI **Exp** **Case II**

t =7609 s

Fig. 1. Temperature maps at t = 7609 s during the solidification of a pure tin.

Conclusion:

The solidification model has been derived on the basis of an enthalpy formulation based on fixed-grid techniques. With this model, very good comparisons are obtained with the measured thermal fields and front advancing during the solidification process. This implies that the buoyancy convection is correctly taken into account in this 3D simulation. The model used has also shown its effectiveness in predicting the process of tin solidification under forced convection in terms of velocity field, temperature field and morphology of the solidification front.

References

[1] X. Wang, P. Petitpas, C. Garnier, J. P. Paulin and Y. Fautrelle, *A quasi two- dimensional benchmark experiment for the solidification of a tin-lead binary alloy*, C. R. Mecanique, 335 (2007) 336-341.

[2] X. Wang and Y. Fautrelle, *an investigation of the influence of natural convection on tin solidification using a quasi-two-dimensional experimental benchmark*, Int. J. Heat Mass Transfer, 52 (2009) 56245633.

[3] L. Hachani, B. Saadi, X. Wang, A. Nouri, K. Zaidat, A. Belgacem-Bouzida, L. Ayouni-Derouiche, G. Raimondi and Y. Fautrelle, *Experimental analysis of the solidification of Sn-3 wt%Pb alloy under natural convection,* Int. J. Heat Mass Transfer, 55 (2012) 1986-1996.

IMMC 2021
"in Digital Platform"

20th
INTERNATIONAL
METALLURGY
MATERIALS
CONGRESS
10-12 June
2021
"in Digital Platform"

Materials for Energy

immc2021

Design of Materials for Advanced Energy Storage

Cengiz S. ÖZKAN
University of California
USA

Abstract

The global electrochemical energy storage market ranging from electric vehicles and personal electronics to physical grid storage and defense applications demands the development of new classes of materials for fabricating high performance batteries and supercapacitors. I will describe innovative approaches for the design and synthesis of nanostructured materials towards enhanced reversible capacity; superior rate performance and cycling stability; superior gravimetric capacitance; and enhanced energy density and power density. Hierarchical three dimensional (3D) graphene-carbon nanotube hybrid materials called pillared graphene nanostructures (PGN) grown by chemical vapor deposition possess ultra large surface area, tunability, mechanical durability and high conductivity which are appealing to diverse energy storage systems. Integration of nanostructured pseudocapacitive metal oxides to such 3D hierarchical templates provides superior electrochemical performance. Among the high performance capacitor systems developed includes MGM (graphene-MWNT-Manganese oxide) and RGM (graphene-MWNT-Ruthenium oxide) hybrid systems. High specific/areal capacitance and extended operational voltage window provides an exceptionally high energy density and power density. Similar three-dimensional templates are transformed into cone-shaped carbon nanotube clusters decorated with amorphous silicon for lithium ion battery anodes (SCCC), by depositing amorphous silicon onto the mesoporous nano-carbon templates via magnetron sputtering. The seamless connection between silicon decorated CNT cones and the graphene substrate facilitates charge transfer and provides a binder-free technique for preparing lithium ion battery anodes. Lithium ion batteries based on the SCCC architecture demonstrated ultra-fast charging, high reversible capacity and excellent cycling stability. Mildly reduced graphene oxide (mrGO) and silica coated Sulfur particles (SCSP) have been developed as new generation cathode materials, forming the basis for Li–S batteries. During cycling, SCSPs fracture and release active material, and mrGO helps to contain the ruptured particles, thereby reducing the polysulfide shuttling effects and improving the cycling stability. In addition, I will describe the use of computerized tomography (CT) scans for the physical characterization of battery layers and interfaces post cycling. Selected metal oxide (MO2) thin film barrier layers have been developed to further mitigate the polysulfide shuttling effects, and to further enhance the performance and cyclic stability of Li–S batteries. Through analysing the binding energies of Li2Sn adsorbed onto selected MO2 surfaces via density functional theory (DFT) calculations and Molecular dynamics (MD) simulations, we show that the strong Li-O bonds dominate the interactions between Li2Sn and selected MO2 surfaces. Our studies demonstrate that selected MO2 thin film barrier layers could be employed to further enhance Li-S battery performance.

Combinatorial Development of Active Materials for Energy Storge and Conversion

Fatih PİŞKİN[1,3], **Hasan AKYILDIZ**[2], **Tayfur ÖZTÜRK**[3]
[1]Sıtkı Koçman University, [2]Konya Technical University, [3]Middle East Technical University
Turkey

Abstract

Development of active materials in energy storage and conversion, as in similar developments in other fields of materials research, have largely followed Darwinian approach of focusing on one material composition at a time. Combinatorial approach is an alternative method whereby a large number of samples each with a different composition are produced simultaneously and they are then screened in a fast manner to single out the material(s) with best performance. This approach is more efficient in terms both time and effort and yield more fruitful result. In this work, we illustrate this method in several applications in energy storage and conversion, namely the development of hydrogen separation membrane with reduced Pd content, the development of efficient catalysts for ORR as cathode for intermediate temperature solid oxide fuel cells and the development of MnO_2 based cathodes for rechargeable batteries.

1. Introduction

Material development has traditionally followed a Darwinian scheme which involved limited variation at given time and a selection resulting in slow evolution. In the context of material development, this approach requires a careful pre-consideration in altering the material composition and detailed characterization with regard to both the resulting structure and the properties.

Combinatorial approach is an alternative method whereby a large number of samples each with a different composition are produced in a single experiment yielding the so-called material library. These are then screened in a fast manner using a suitable method identifying the compositional field with the required properties. If necessary, the process may be repeated for the second time by re-examining the selected field to pinpoint the exact composition(s).

Here we illustrate this method for three selected applications in the area of energy storage and conversion. First, we will deal with a binary case of development of dual phase- (La, Sr)CoO_3(LSC113) and $(La,Sr)_2CoO_4$ (LSC214) cathode for intermediate temperature solid oxide fuel cells(IT-SOFCs). We will then move to a ternary case involving Pd, Ag and Ni where the aim is to develop hydrogen separation membrane with reduced Pd content. The last example is quaternary involving oxides MnO_2, Cr_2O_3, CuO and Bi_2O_3. Here the aim is to develop layered MnO_2 cathode for alkaline batteries with improved rechargeability and voltage profile.

2. Experimental Procedure

Material library for each application was produced in the form of thin films using sputter deposition. For this purpose, a thin film deposition system was designed for the purpose of combinatorial studies[1]. The system had a vacuum chamber of 125 liter in volume. The chamber is connected to a turbomolecular-rotary pump system which can provide a base pressure in the range of $1x10^{-7}$ - $5x10^{-8}$ Torr. The system had sputter guns placed on a circle with 250 mm in diameter at 60^o intervals. In binary work, the sputter guns could be placed at 180 degrees apart. In ternary, the angle was 120^o, Fig.1. In quaternary, the disposition of sputter guns was the same as ternary, with the addition of the 4th gun at the very middle.

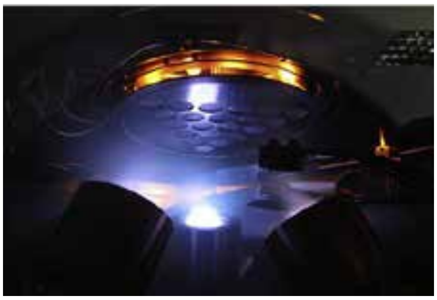

Fig.1 Ternary configuration of sputter guns positioned at 120o. Above the sputter guns there is a substrate magazine housing a total of 21 substrate mimicking the triangular arrangement of the guns underneath.

3. Results and Discussion

3.1 Cathode Development for IT-SOFCs; There is a considerable interest to reduce the operating temperature of solid oxide fuel cells. An operating temperature of about 600 ℃ or so would greatly reduce the problems associated with the conventional SOFC which operate in the temperature range 800-1000 ℃. The main obstacle in development of IT-SOFCs is to find a suitable catalyst for ORR which can be used as cathode. The development of oxides with mixed ionic and electronic conductivity e.g. - (La, Sr) CoO_3(LSC113) has been a major step in this respect. Added to this, there is the discovery that ORR performance can be further improved with dual phase cathode, i.e. when (La, Sr)$_2CoO_4$(LSC214) was added to (La, Sr)CoO_3(LSC113).

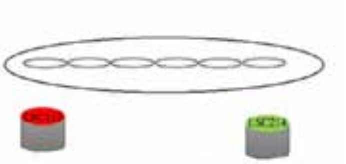

Fig.2 Schematic representation of combinatorial sputter deposition geometry used to obtain a library of thin film cathodes for IT-SOFCs.

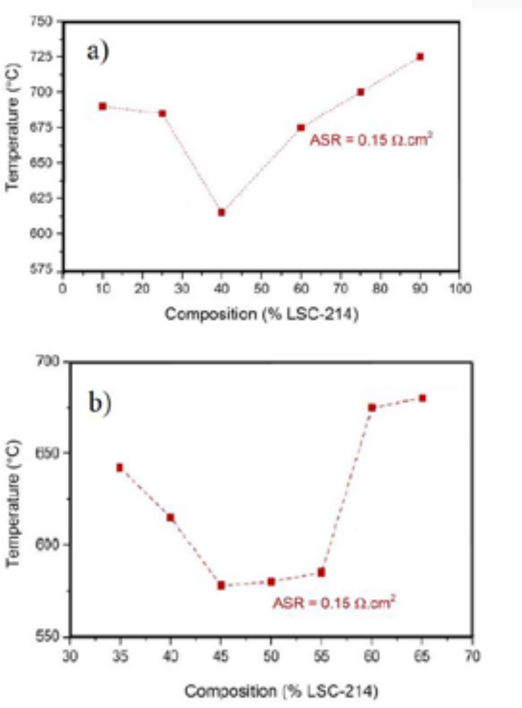

Fig.3 Temperature at constant value of ASR=0.15 Ω.cm^2 as a function of cathode compositions a) first run b) focusing at compositions close to 40% LSC214. - adapted from ref [4].

The object of the combinatorial study was to find the best combination of LSC113-LSC214 dual phase cathode. For this purpose 2” sputter targets were prepared [2,3] and cathode library consisting of 6 thin film compositions were deposited, Fig.2. The library of cathodes were screened with EIS measurement using a symmetric cell from 400 ℃ up to 700 ℃ [2].

Fig.3 is based on area specific resistance value of ASR=0.15 Ω.cm^2. This value provides a useful benchmark for cathode and shows that the temperature at which ASR= 0.15 Ω.cm^2 decreases at mid-composition. Noting that the temperature is minimum with 40% LSC214, combinatorial study was repeated by realigning the sputter targets and a second set of 6 cathode library was produced. Screening yields LSC113-45 % LSC214 as the best dual phase cathode for IT-SOFCs. The temperature at this composition is as low as 575℃ which is quite satisfactory for most purposes. Detailed description of this study can be found in references [2-4] by Sari et al.

3.2 Hydrogen Separation Membrane with Reduced Pd Content; Unlike solid oxide fuel cells which can handle both hydrogen and natural gas, PEM fuel cells uses pure hydrogen as a fuel. Thus, it is necessary to ensure that hydrogen is sufficiently pure so that catalysts used in electrodes were not adversely affected. Hydrogen could be produced in a number of ways. Of these, steam reforming of natural gas or coal is perhaps most common. But there are other methods as well e.g. biomass gasification or waste processing. In all, a mixture of gases is generated from which it is necessary to separate hydrogen. With the availability of low cost renewable energy, hydrogen may also be produced via water electrolysis. The easiest use of this hydrogen is to inject it into natural gas pipeline. It seems that this practice of injecting hydrogen into the natural gas pipeline would become a standard practice in coming decades which makes the mixture of hydrogen and methane a considerable interest. The separation of hydrogen from this mixture is altogether a new area for separation membranes.

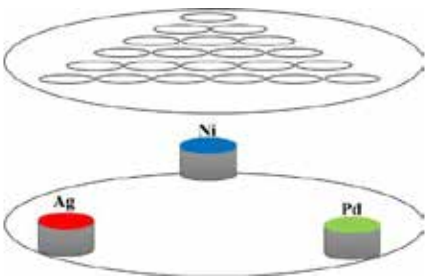

Fig.4 Schematic representation of thin film Pd-Ag-Ni membranes produced via sputter deposition.

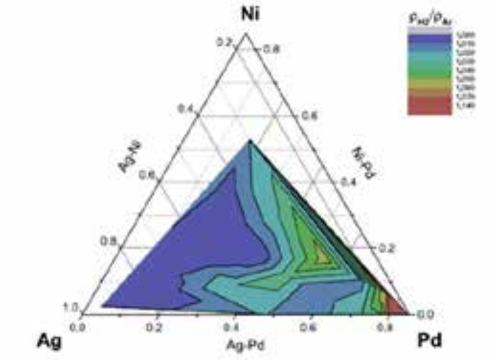

Fig.5 Map of reactivity index ρ_{H2}/ρ_{Ar} in Pd-Ag-Ni ternary diagram. -adapted from ref [1].

Dense metallic membranes are perhaps the most reliable method of hydrogen separation since no other gas can pass through the membrane. $Pd_{77}Ag_{23}$ is the most common composition and functions quite satisfactorily in the temperature range from 300 up to 450 ℃. With the potential widening of the use of separation membranes, it is necessary to develop cost effective membranes. An issue in this respect is the high cost of Pd. Thus, it would be desirable to develop separation membranes with reduced Pd content.

Combinatorial study undertaken in this respect is based on Pd-Ag system but examined a partial replacement of the elements with a third element, namely Ni. Thus, three sputter targets, Pd, Ag and Ni were used in triangular geometry with substrate magazine comprising 21 substrate each 19 mm in diameter.

Ideally each membrane should be screened by measuring its hydrogen permeability. This measurement is not easy. However, it is certain that if a thin film could be used as separation membrane it is necessary that the membrane should dissolve hydrogen. Dissolution of hydrogen in membranes is easy to follow as this leads to changes in its resistivity. Thus, we screened the thin film membranes with 4-point probe measurement both under Ar and H_2 from room temperature up to 400 ℃. We have defined the so-called reactivity index which refers to ρ_{H2}/ρ_{Ar} where ρ_{H2} and ρ_{Ar} are resistivity of the membrane under H_2 and Ar, respectively. Results are reported in Fig.5. It should be noted that there is an extensive compositional field where $\rho_{H2}/\rho_{Ar}=1$. There are three compositions $Pd_{33}Ag_{59}Ni_8$, $Pd_{55}Ag_{28}Ni_{17}$ and $Pd_{76}Ag_{18}Ni_6$ where the reactivity index reaches quite a high value. Foils were prepared with matching compositions by melting and casting followed by rolling to ~ 100 μm in thickness. This has shown that a permeability value of 6.50×10^{-10} mol/m s $Pa^{1/2}$ could be obtained at 400 °C in $Pd_{55}Ag_{28}Ni_{17}$ where Pd content is nearly two thirds of the commercial alloy $Pd_{77}Ag_{23}$. Further details concerning the use of combinatorial approach in the development of separation membranes are given by Piskin et al [1,6,7].

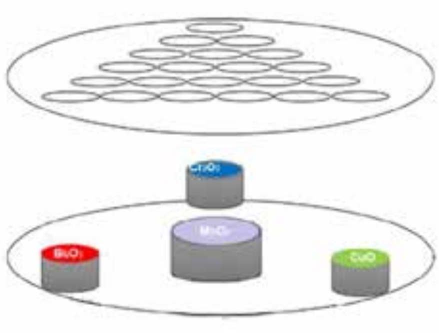

Fig.6 Schematic representation of thin film layered MnO_2 cathodes doped with CuO, Cr_2O_3 and Bi_2O_3.

3.3 MnO_2 based cathodes for rechargeable batteries;

Although considerable progress has been made regarding rechargeable batteries, they are still far from being cost-effective. This is particularly important for grid-energy storage where a huge storage capacity is needed in coming decades. Thus, a drastic reduction is necessary in the cost of batteries so as to allow the desirable penetration of renewable energy into the existing energy system. Zn-MnO_2
batteries satisfy this requirements except for the fact that it is not rechargeable.

Combinatorial study undertaken in this context aims for chemically modifying MnO_2 so that it can be charged and discharged reversibly. γ-MnO_2, the polymorph used in the primary battery, has a very low rechargeability. δ-MnO_2 has a better potential in this respect provided that this layered structure can be stabilized. The combinatorial study currently underway makes use four sputter guns, MnO_2 is central target and other oxides, namely CuO, Bi_2O_3 and Cr_2O_3 are at the periphery which will be used as dopants. The work at the time of writing is in progress and the results will be reported in due course.

4. Conclusion

Combinatorial approach is an alternative to conventional approach of material development where the aim is gradual improvement in materials chemistry. The combinatorial methodology of generating a large number of samples in a single experiment and screening them with a fast method would allow a faster improvement and innovation in material development. In the current paper this is illustrated with three examples of active material development in the area of energy storage and conversion.

Acknowledgment

The work reported in this paper is outcome of projects supported by TUBITAK (104M206, 109M580 114M128 and 118M076) which we gratefully acknowledge. We also acknowledge the support received by DPT/Ministry of Development (BAP-2016K121510) for the provision of laboratory facilities for combinatorial material science

References

[1.] F Pişkin, H Akyıldız, T Öztürk, International Journal of Hydrogen Energy 40 (24), 7553-7558 (2015)
[2.] ZÇ Torunoğlu, D Sarı, O Demircan, YE Kalay, T Öztürk, Y Kuru International Journal of Hydrogen Energy 43 (40), 18642-18649 (2018)
[3.] D Sari, ZC Torunoglu, YE Kalay, T Ozturk Ceramics International 43 (17), 15185-15188 (2018)
[4.] D Sari, F Piskin, ZC Torunoglu, B Yasar, YE Kalay, T Ozturk Solid State Ionics 326, 124-136 (2018)
[5.] D Sari, B Yaşar, F Pişkin, YE Kalay, T Öztürk Journal of The Electrochemical Society 166 (15), F1157 (2019)
[6.] F Pişkin, T Öztürk Journal of Membrane Science 524, 631-636 (2017)
[7.] F Pişkin, T Öztürk Journal of Alloys and Compounds 775, 411-418 (2019)

High Performance and Flexible Supercapacitor Cells for Energy Storage from Renewable Energy Sources

Apurba RAY, Delale KORKUT, Jenny ROTH, Bilge SARUHAN
German Aerospace Center (DLR)
Germany

Abstract

In this work, we report the optimization and fabrication of two different supercapacitor cells: (a) light-weight flexible symmetric solid-state pouch-cell supercapacitors (SCs) that is based on polymer embedded MWCNTs (multiwall carbon nanotubes) and polymer gel electrolytes (PEGs) and (b) Laser-induced interdigital structured graphene electrodes that are covered with PEGs. The cell manufacturing was carried by preparing the electrodes after air brush spray coating on KOH-etched Kapton200RS100 (KP) flexible substrates and by sandwiching with the PEG and a tissue separator. Initial single cell were of 2 x 2 cm square and is capable to be enlarged to 7 x 7 cm square. The flexible cells show satisfactory supercapacitive performance (areal capacitance 2.47 mF cm^{-2} @ 0.1 mA) with high cycle stability. The LIG-interdigital SCs are more suitable for autonomous operation of sensors and actuators delivering capacitance values in the range of μF. cm^{-2}.

1. Introduction

The recent demand on renewable energy that can be harvested from available natural resources like solar, wind, water etc. is growing rapidly. Due to irregular nature of these energy resources the need for peak power energy storage systems (ESSs) are extremely desirable. In order to enable their industrial application, it is required that EESs are high performant, low-cost and lightweight [1]. Among various types of electrochemical ESSs, supercapacitors (SCs) are the most promising candidates as eco-friendly, low-cost, high performance ESSs over batteries and conventional capacitors [2-3]. Recently developments of smart mobile electronic products are strongly demanding eco-friendly, inexpensive and high performance flexible as we as miniaturized SCs devices due lot of significant advantages, setting one of our major research motivations.

2. Device Fabrication and Electrochemical Performances

The active electrode material was produced by mixing 70 wt% aqueous PEDOT-poly(3,4-ethylenedioxythiophene:PSS-poly(styrene sulfonate) solution (Clevious™), 20 wt% MWCNT and 10 wt% PVP-(polyvinylpyrrolidon) and sonicating overnight to get uniform dispersion. This active composite material was coated on a 20 min. KOH-etched KP substrate using air brush spray coating method. The flexible symmetric solid-state pouch-cell SCs were initially manufactured by sandwiching propylene carbonate-PPC-matrix embedded ionic liquid (ethyl-methylimidazolium bis(trifluoromethylsulfonyl)imide-[EMIM][TFSI]) gel electrolyte (PEG) between two composite electrodes. A commercially available tissue paper was used as separator. This flexible solid-state SC exhibits lower charge transfer resistance providing short charge diffusion paths, wide stable potential window (up to 2.0V), large discharge time (areal capacitance 2.47 mF cm^{-2} @ 0.1 mA), high cycling life without any degradation of electrodes. The LIG-interdigital SCs are manufactured by CO_2-laser structuring of Kapton foils and using the PPC embedded [EMIM][TFSI] and $LiClO_4$ PEGs.

3. Conclusion

This work demonstrates that the flexible supercapacitor is a promising candidate and exhibits satisfactory capacitance, cycling stability and capability for component integrated next generation energy storage from renewable energy sources.

Acknowledgment

The financial support provided by the DLR-Space Directory in the frame of the peak power storage project – HySES.

References

[1] A. Ray, A. Roy, S. Saha, M. Ghosh, S. Roy Chowdhury, T. Maiyalagan, S. K. Bhattacharya, S. Das, Langmuir 2019, 35, 8257−8267

[2] A. Ray, A. Roy, M. Ghosh, J. Alberto Ramos-Ramón, S. Saha, U. Pal, S. K. Bhattacharya, S. Das, Applied Surface Science 463 (2019) 513–525

[3] D. P. Dubal, J. G. Kim, Y. Kim, R. Holze, C. D. Lokhande, W. B. Kim, Energy Technology 2014, 2, 325 – 341

On the Surfaces of Complex Oxides

Taner AKBAY[1], John A. KILNER[2,3], Tatsumi ISHIHARA[3]

[1]Yeditepe University, [2]Imperial College London, [3]Kyushu University

[1]Turkey, [2]United Kingdom, [3]Japan

Abstract

Complex oxides attract considerable attention as catalytically active materials for devices such as solid oxide fuel cells and electrolysers. In this work, the importance of the evolution of structure and composition of the outer most surfaces of mixed ionic electronic conducting (MIEC) air electrodes in relation to their activity to oxygen reduction reaction is addressed.

1. Introduction

MIEC oxides with fast surface exchange, high oxide ion conduction, and tunable electronic properties are of interest in variety of applications ranging from catalysts to electrochemical devices. Among those, transition metal oxides with perovskite (ABO_3) and perovskite-related (e.g. A_2BO_4) structures attract attention as electrode materials for devices such as solid oxide fuel cells and electrolysers. Although suitable performance values have already been attained at high temperatures from about 800-900℃, durability improvement and cost reduction requirements of these devices remain to be achieved. One of the ways to fulfill these requirements is to lower operating temperatures of such devices to 500-600℃. For successful operation at low temperatures, one needs to develop a comprehensive understanding of the surface properties of MIEC oxide electrodes.

2. Materials and Methods

Teams at Kyushu University and Imperial College London have access to unique surface specific techniques such as Low Energy Ion Scattering (LEIS) to analyse the outermost atomic layers of complex oxides. [1] As electrochemical device performances are related to changes in the surface composition of the electrodes, it is highly important to comprehend the evolution of electrode surfaces after treatment at specific atmospheres and temperatures. The teams analysed the surfaces of variety of MIEC oxides including $La_{1-x}Sr_xCoO_{3-\delta}$, and $La_2NiO_{4+\delta}$ and found that the AO-termination dominates their surface structures while B-site cations enrich the subsurface layers. In conjunction with this, the effect of the surface domination by less- or not-active A-site cations on oxygen reduction reaction is investigated by using the Density Functional Theory (DFT) calculations. [2]

3. Conclusions

DFT calculations showed that the A-site cation and the associated surface defect structure are highly influential in enhancing the air electrode performances. This finding is obviously very important since B cations are commonly believed as the ones which are catalytically active for oxygen activation and dissociation reactions. It is shown that the defect free LaO-terminated basal planes are energetically favorable for oxygen adsorption and dissociation on $La_2NiO_{4+\delta}$. The activation energies for oxygen dissociation reaction are estimated as in the order of 1.0 eV by using the DFT+U and Climbing Image Nudged Elastic Band (CI-NEB) calculations. The electronic structure calculations clearly demonstrated that the LaO-terminated surface is actually capable of promoting charge transfer from the La atoms to the adsorbed oxygen molecule on the surface. These findings have far reaching implications in fundamental understanding of the interaction of oxygen with surfaces of complex oxides.

Acknowledgement

The support of the WPI-I^{2}CNER sponsored by the Ministry of Education, Culture, Sports, Science and Technology (MEXT) of the Japanese government is highly acknowledged.

References

[1] J. Druce, H. Téllez, M. Burriel, M.D. Sharp, L.J. Fawcett, S.N. Cook, D.S. McPhail, T. Ishihara, H.H. Brongersma, and J.A. Kilner, *Energy & Environmental Science*, 7(11) (2014) 3593-3599.

[2] T. Akbay, A. Staykov, J. Druce, H. Téllez, T. Ishihara, and J.A. Kilner, *Journal of Materials Chemistry A*, 4 (2016) 13113-13124.

Production of Modified Iron Oxide with the Addition of Me (Me: Co,Ni) and Investigation of its Energy Storage Performance

Mehmet Feryat GÜLCAN[1], Billur Deniz KARAHAN[2]
[1]Istanbul Technical University, [2]Istanbul Medipol University
Turkey

Abstract

In this work, two differently modified iron oxide powders have been fabricated via hydrothermal method, by adding metal salts (cobalt chloride (S1), nickel chloride (S2)) into the iron chloride precursor solution. The powders' morphologies and structures have been examined by scanning electron microscopy images and X-ray diffraction data. Their energy band gaps have been calculated based on their absorption spectra. Their electrochemical behaviour in cycling have been discussed considering their galvanostatic test results, cyclic voltammetry curvatures and EIS spectra.

The SEM images demonstrate that S1 has cubic and S2 has bramble-knitted like irregular shaped particles, respectively. XRD analysis depicts the prevalence of hematite structure in both samples and displays no additional peaks related to ferrite or binary oxides formations that include Co and Ni. Both samples have been galvanostatically tested and reveal higher 1st discharge capacities (S1 and S2 deliver 1402 and 1243 mAh/g, respecitvely) than that of the pure iron oxide. To further improve the capacity retention of both electrodes, 10 vol% vinylene carbonate (VC) is added into the standard electrolyte. The results highlight the positive effect of the VC addition onto the electrodes' performances.

1. Introduction

Greenhouse gas (GHG) emissions have been dramatically increased over years following the rapid growth of industries and populations [1]. Nowadays, in order to reduce GHG emissions and achieve a sustainable Earth, people and researchers have turned to the use of environmentally friendly energy sources instead of fossil fuels. At this point, the storage of green energy is defined as a remarkable problem along with its production. Among alternative energy storage technologies, lithium-ion batteries have gained a privileged importance due to their light weight, high energy and power densities [2].

Lithium-ion batteries (LIBs) have had an increasing market share from the first day they were commercialized until today. This situation increases the importance of studies on improving the performance of LIBs. Reviews show that from 1990 to 2020, amount of publication on LIBs have been increased over years [3-4]. Many of these articles are focused on the design and production of suitable anode material that can replace graphite. At this point, following the article published by Poizot et al [4] the use of transition metal oxides as anodes has become a remarkable topic.

Considering the alternative transition metals, iron oxides shine out owing to their high first discharge capacities (≥1000 mAh/g), non- toxicity, high abundance on Earth, economic processing cost and improved safety.

Iron oxide react with lithium according to Equation 1 as stated by Larcher et al [5].

$$N - Fe_2O_3 \xrightarrow{monophasic} \alpha - LiFe_2O_3 \xrightarrow{biphasic} cubic\ Li_2Fe_2O_3 \xrightarrow{biphasic} Fe^0 + Li_2O \qquad (1)$$

Although the iron oxide material has many advantages, it exhibits a short cycle life when it is used as an anode material in LIBs, due to its low conductivity and high volumetric change happened upon its reaction with Li. Thus, to improve their cycle performances different approaches have been proposed: dimension reduction, composite formation, doping - functionalization, morphology control, coating - encapsulation and electrolyte modification [2].

In this study, we aim to analyze two cases that have not been discussed in the literature before: examination of the structural and morphological properties of the modified iron oxide powders obtained by the addition of Co (S1) and Ni (S2) containing salts in the precursor solution, during hydrothermal synthesis; analysis of VC addition's effect on the electrochemical performances of these powders (S1 and S2) when they are used as anodes for LIB. Such powders have been characterized structurally, morphologically and compositionally by using XRD, SEM and EDS. Spectrophotometry has been used to calculate their energy band gaps. And finally, galvanostatic tests, CV and EIS tests have been applied on both S1 and S2 powders to evaluate their electrochemical behavior as an anode material in LIBs.

2. Experiment

$FeCl_3$ has been purchased from Sigma Aldrich (8.03945.0500). Nickel chloride, cobalt chloride, sodium hydroxide (NaOH) and deionized water are technical grade. Before the hydrothermal synthesis 0.02 M solution is prepared by mixing iron chloride and metal chloride. The mol ratio of iron over metal is adjested as 5:1. pH of the solution is adjusted to 10, by using 6 M NaOH. Then, 200 ml of the solution is transferred into a Teflon coated autoclave (200 ml). Hydrothermal operation has been performed at 180˚C for 90 min. After synthesis, the powders have been separated from the solution by filtration and cleansed several times with ethanol and deionized water via centrifuge. The powders are dried in air atmosphere at 100˚C for 12 hours.

Morphological analysis and elemental analysis are made by field-emission scanning electron microscopy (Zeiss Gemini 500) and energy dispersive X-ray spectroscopy (EDS, Bruker). Structural analysis is performed with a scan rate of 5˚/min between 20-90˚ by X-ray diffractometer (PANalytical X'Pert PRO). To determine the bond type in the powders, Fourier Transform Infrared Spectrocopy (FTIR) has been applied between 4000-400 cm^{-1} by Perkin Elmer Spectrum two. The absorbance spectrum of both samples (S1, S2) have been collected by Molecular Devices SpectraMax i3 between 230-800 nm in 3 nm step.

Finally, modified iron oxide electrodes are prepared by mixing 80 wt% active material, 10wt% carbon black and 10 wt% polyvinylidene fluoride (PVDF) with n-methylpyrrolidone (NMP). Then Dr. Blade method is used to laminate the slurry onto Cu foil. After vacuum dried (70˚C overnight), the foil is punched and CR2032 coin-type half cells are assembled in the glovebox (MBraun,Labmaster) to evaluate the lithium ions storage abilities of the powders. A Merck solution made of 1 M $LiFP_6$ in EC:DMC (1:1) is used as the electrolyte and Celgard 2400 is used as the separator. Galvanostatic tests are performed between 1 mV-3 V under a current load of 50 mA/g. Cyclic voltammetry (CV) measurement has been done between 1 mV-3 V with a scan rate of 0.1 mV/s. And electrochemical impedance spectroscopy (EIS) has been obtained at 1 mV, in the frequency range 100 kHz- 0.01 Hz, using 0.1 mA rms perturbation signal, via Gamry Interface1000E. To further enhance the capacity retention of both electrodes, 10% vol. VC (Sigma-Alrich vinylene carbonate (BCBH5910V)) is added into the standard electrolyte and galvanostatic tests are repeated in the above- mentioned conditions.

3. Result and Discussion

As seen in Figs 1a-b, S1 has cubic and S2 has bramble-knitted like irregular morphology. This fact agrees with Teng et al [6]'s study where they state that Co presents as $Co(OH)_3$ in the case of $CoCl_3$ precursor at pH:10, and hydrothermal treatment transforms $Co(OH)_3$ into Co_3O_4 with cubic morphology [6]. On the other hand, in case of $NiCl_2$ existence in the solution, bramble-knitted like particles are formed as a result of hydrothermal reaction, as explained by Ma et al [7].

This result clearly reveals that although there is predominantly iron chloride in the precursor solution, the presence of other transition elements (Co (S1) and Ni (S2)) in trace amounts affects the physical properties of the powder by adjusting the nucleation and growth mechanism of the powder, during the hydrothermal reaction. This inference is in line with Mishra et al.'s studies outcomes [8].

The amounts of Co and Ni in the S1 and S2 powders are determined by EDS: 6.3%at. Co and 5.34%at. Ni are found in S1 and S2, respectively.

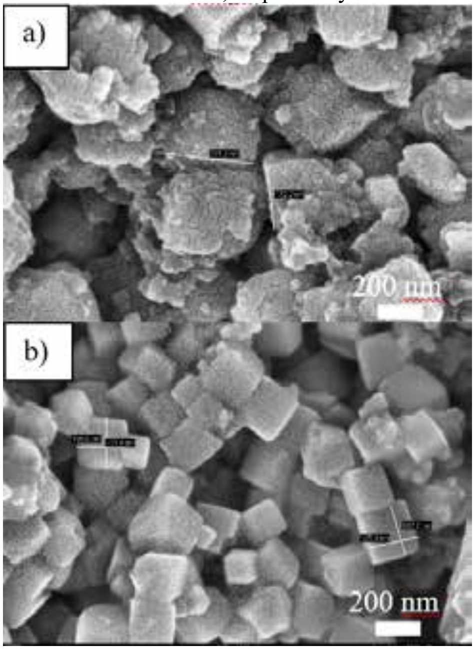

Figure 1. SEM analysis of doped iron oxide a) nickel b) cobalt

Then, the structural investigation demonstrates that all the peaks seen in the XRD data (Figure 2.a) of S1 and S2 samples match with hematite (JCPDS: 01-089-0596). No peaks are observed regarding the presence of intermetallics/binary oxides or ferrites formation including Ni and Co atoms. This situation can be explained as that Co (Radius 0.75 Å) and Ni atoms (Radius 0.69 Å) can be found by replacing iron in the hematite crystalline structure, since they have similar radii and properties to Fe atoms (Radius 0.64 Å). A scrutiny look reveals a shifting in the peak position. Such a peak shifting is mostly related to chemical composition changes or strain formation in the crystalline structure, as stated by Cullity [9].

FTIR analysis (Figure 2.b) shows that S1 and S2 have similar results. Peaks at ~570 and ~490 belong to Fe-O bonding and others refer to water [10-11]. The fact that no peaks related to different formation is noted, agrees with XRD result.

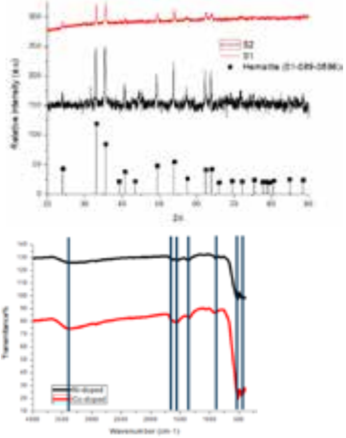

a)

b)

Figure 2. a) XRD patterns of co and ni doped particles b) FTIR line for co and ni doped

Then, the absorbance spectra (Fig. 3.a) of both samples show that S1 has narrow energy band gap than that of S2. Smaller particle size [12] or increase in lattice strain [13] could be a reason for that (Figs.3b,c)

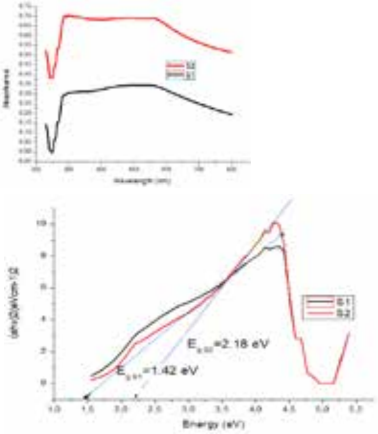

a)

b)

Figure 3. a) Absorbance graph of S1 and S2 b)band gap of S1 and S2

To discuss the lithiation mechanism of S1 and S2, CV curves are examined (Figs. 4.a-b). Both samples have characteristic peaks related transition metal reduction at 0.6, 1V and 1.5V in the 1st cathodic scan. The cathodic peak at 0.8V is believed to be related to SEI (solid electrolyte interface) formation. Then in anodic site, two peaks are noted around 1.5 and 1.75 V related to the oxidation of metals [14]. The comparison of the first cycle CV curve to the subsequent cycles demonstrates that in the first cycle an irreversible reaction happens on both electrodes. SEI formation (solid electrolyte interface) and possible morphological changes happen in lithiation/delithiation could explain this change.

It is possible to explain the lithiation mechanism of both samples by using Aziam et al [15]'s proposal: (Equation 2), Me stands for Co (S1) and Ni (S2);

$$Me_xFe_{2-x}O_3 + Li \leftrightarrow Li_2O + Me^0 + Fe^0 \qquad (2)$$

Then, to evaluate the performances of S1 and S2 as anode materials for LIBs, both samples have been tested galvanostatically. S1 depicts 1400 mAh/g and S2 demonstrates 1243 mAh/g as the first discharge capacities, when tested between 1mV-3V. According to capacity voltage graph (Figure 5.a-d) plateaus are noted around 1.5 V, 1 V and 0.8 V related to the insertion of lithium ion into the anode [5] and the SEI formation [14], respectively.

To further improve the capacity retention of both samples, 10 vol.% vinylene carbonate (VC) is added into the standard electrolyte. The results highlight the positive effect of the VC addition onto the electrodes' performances over the first 10 cycle. In case of VC addition, first discharge capacity is found to be lower in both cases, but the retention is remarkably improved as agreed with McNultit et al [16]'s study. More stable SEI formation on each electrode surface could explain this improvement.

For further investigation of electrode performance, EIS is also applied when coin cells are assembled with standard electrolyte. EIS spectrum of the samples (Fig. 6a) demonstrate that S1 has lower charge transfer resistance than S2. Park et al [17] claims that narrower band gap increases surface electronic properties, which positively affects electron transport, eventually.

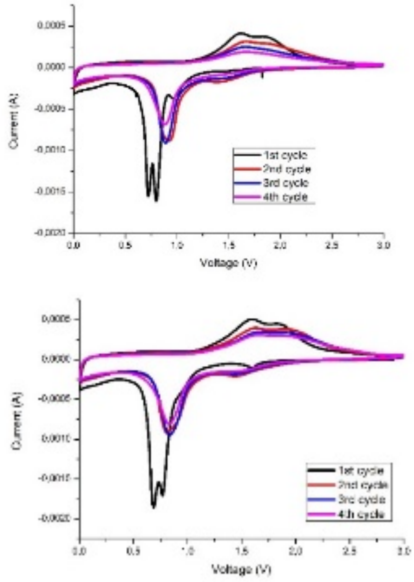

a)

b)

Figure 4. CV graphs of iron oxide a) cobalt b) nickel

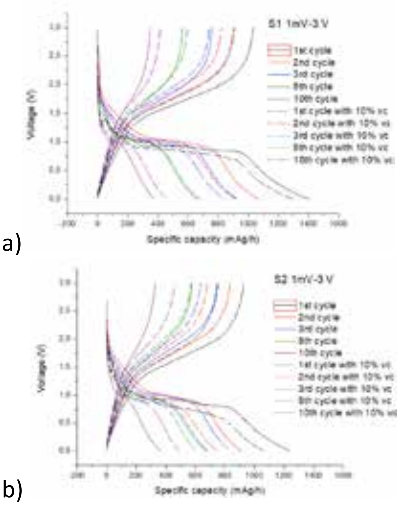

Figure 5. Capacity-voltage graphs with standard electrolyte and the electrolyte with 10 vol.% VC: a) S1 between 1 mV-3 V b) S2 between 1 mV-3 V

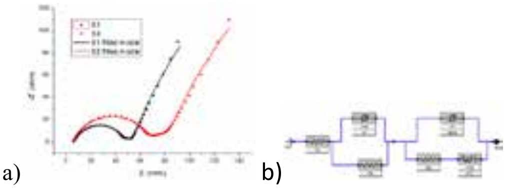

Figure 6. a)EIS result of S1 & S2 b) Equivalent circuit model

4. Conclusion

Modified iron oxide powders have been produced via hydrothermal method, by mixing metal chloride salts with iron chloride solution before the synthesis reaction. No further heat treatment is applied after the synthesis. EDS analysis verifies the existence of Co (6.3%at.) in S1 and Ni (5.34%at.) in S2. XRD analysis shows that there is no additional peak related to intermetallics / binary oxides of ferrite formation that include Co and Ni. SEM images depict that trace amount of Co or Ni existence in the precursor solution affects the nucleation and growth mechanism hence the properties of the powder, eventually. Absorbance spectrum justifies this fact and exhibits that S1 has lower energy band gap.

Then the galvanostatic tests display that S1 has larger discharge capacity than S2.

Finally, to further improve the capacity retention of the electrodes, 10vol% vinylene carbonate (VC) is added into the standard electrolyte. The results highlight the positive effect of the VC onto the electrodes' performances.

In order to understand the exact positions of Co and Ni atoms in the iron oxide crystal structure, detailed characterizations are recommended for future studies.

Acknowledgement

We would like to thank Prof. Dr. Sebahattin Gürmen, Prof. Dr. Özgül Keleş, Prof. Dr. M. Kürşat Kazmanlı, Dr. Selim Ertürk, Assoc. Prof. Dr. Yasemin Yüksel Durmaz, Assoc. Prof. Dr. Sultan Sibel Erdem and Ayşegül Demiral for their supports in characterizations.

References

[1] Andres, R. J., Fielding, D. J., Marland, G., Boden, T. A., Kumar, N., & Kearney, A. T. (1999). Carbon dioxide emissions from fossil- fuel use, 1751–1950. Tellus B, 51(4), 759-765.

[2] Nitta, Naoki, et al. "Li-ion battery materials: present and future." Materials today 18.5 (2015): 252-264.

[3] Marom, R., Amalraj, S. F., Leifer, N., Jacob, D., & Aurbach, D. (2011). A review of advanced and practical lithium battery materials. Journal of Materials Chemistry, 21(27), 9938-9954.

[4] Poizot, P. L. S. G., Laruelle, S., Grugeon, S., Dupont, L., & Tarascon, J. M. (2000). Nano-sized transition-metal oxides as negative-electrode materials for lithium-ion batteries. Nature, 407(6803), 496-499.

[5] Larcher, D., Masquelier, C., Bonnin, D., Chabre, Y., Masson, V., Leriche, J. B., & Tarascon, J. M. (2003). Effect of Particle Size on Lithium Intercalation into α Fe2 O 3. Journal of the Electrochemical Society, 150(1), A133-A139.

[6] Teng, Y., Yamamoto, S., Kusano, Y., Azuma, M., & Shimakawa, Y. (2010). One-pot hydrothermal synthesis of uniformly cubic Co3O4 nanocrystals. Materials Letters, 64(3), 239–242. doi:10.1016/j.matlet.2009.10.039

[7] Ma, Y., Yang, M., & Jin, X. (2020). Formation mechanisms for hierarchical nickel hydroxide microstructures hydrothermally prepared with different nickel salt precursors. Colloids and Surfaces A: Physicochemical and Engineering Aspects, 588, 124374.

[8] Mishra, R., Goswami, M., Dixit, A., & Krishnan, M. (2016). Study on thermophysical properties and phase evolution in Nd doped Li2O-Al2O3-SiO2 glass nucleated by multiple nucleating agents. Journal of Non-Crystalline Solids, 447, 66-73.

[9] Cullity, B. D. (1956). Elements of X-ray Diffraction. Addison-Wesley Publishing.

[10] F. Wang, X.F. Qin, Y.F. Meng, Z.L. Guo, L.X. Yang & Y.F. Ming (2013).Hydrothermal synthesis and characterization of α-Fe2O3 nanoparticles. Materials science in semiconductor processing, 16(3), 802-806.

[11] Z. Jing & S. Wu (2004). Synthesis and bending vibration of water molecules (of monodisperse hematite nanoparticles modified by surfactants via hydrothermal approach. Materials Letters, 58(27-28), 3637-3640.

[12] Deotale, Anjali Jain; Nandedkar, R.V. (2016). Correlation between Particle Size, Strain and Band Gap of Iron Oxide Nanoparticles. Materials Today: Proceedings, 3(6), 2069–2076. doi:10.1016/j.matpr.2016.04.110

[13] Nair, S. S., Mathews, M., & Anantharaman, M. R. (2005). Evidence for blueshift by weak exciton confinement and tuning of bandgap in superparamagnetic nanocomposites. Chemical physics letters, 406(4-6), 398-403.

[14] Zhang, P., Guo, Z. P., & Liu, H. K. (2010). Submicron-sized cube-like α-Fe2O3 agglomerates as an anode material for Li-ion batteries. Electrochimica acta, 55(28), 8521-8526.

[15] Aziam, H., Tamraoui, Y., Ma, L., Amine, R., Wu, T., Manoun, B., Xu, G.L., Amine, K., Alami, J. & Saadoune, I. (2018). Mechanism of the first lithiation/delithiation process in the anode material CoFeOPO4@ C for Li-ion batteries. The Journal of Physical Chemistry C, 122(13), 7139-7148.

[16] McNulty, D., Geaney, H., & O'Dwyer, C. (2017). Carbon-coated honeycomb Ni-Mn-Co-O inverse opal: A high capacity ternary transition metal oxide anode for Li-ion batteries. Scientific reports, 7(1), 1-13.

[17] Park, H., Wu, H. B., Song, T., Lou, X. W., & Paik, U. (2015). Porosity- controlled TiNb2O7 microspheres with partial nitridation as a practical negative electrode for high- power lithium- ion batteries. Advanced Energy Materials, 5(8), 1401945.

Nickel Cobalt Aluminum Oxide (NCA) Cathode Production for Lithium-Ion Battery

Dila SIVLIN, Ozgul KELES
Istanbul Technical University
Turkey

ABSTRACT

The world understands the importance of energy storage devices. In a few years, more than ten battery factories only in Europe will be able to produce various designs of lithium-ion batteries. Cathode materials are one of the most essential and pricy components of these devices. The co-precipitation method is the most effective and commercial way to bring cathode materials alive in batteries. Ammonia –NH_3- is used as a chelating agent in this process, however, the toxicity and not being able to form a complex between NH_3 and Al create several problems especially in lithium nickel cobalt aluminum oxide cathode (NCA) production. To investigate and to find an alternative solution to these problems, in this paper, citric acid is used as a chelating agent in NCA cathode production.

INTRODUCTION

With the popularity and the success of Tesla Motors, car producers finally realize the importance of electric vehicles. It is also realized that the most important and indispensable part of these vehicles is batteries. Hence, many countries and the car producers in Europe have started their investments, not later than 2024, Europe will be able to provide approximately 500 GWh of energy per year [1]. In his manner, the production of the battery components which are anode, cathode, separator, and electrolyte becomes essential. Especially cathode material production is critical because cathode materials are the limiting component of the battery [2]. Battery performance, quality and life strictly depend on the cathode material. Since 1990 the first commercialization of lithium-ion batteries, cathodes used in the cells changed according to the specific area. The first commercialized batteries include $LiCoO_2$, however, cobalt toxicity and price, the relatively low practical capacity of $LiCoO_2$ limited its usage in high energy applications [3]. $LiMn_2O_4$ gained significant attention because the abundance of manganese is higher than cobalt thus the price is lower than cobalt. However, this material suffers from phase transformation during cycling and this affects its performance [4]. $LiNiO_2$ was the promising cathode due to its high theoretical capacity, yet, high Ni content causes diffusion of Ni^{2+} ion to Li^{+} sites and deteriorate battery performance [5]. As an alternative lithium nickel cobalt aluminum oxide ($LiNi_xCo_yAl_{1-x-y}O_2$-NCA) and lithium nickel cobalt manganese oxide ($LiNi_xCo_yMn_{1-x-y}O_2$-NMC) cathodes have been developed. These materials show better performance (approximately 200 mAh/g first discharge capacity and 98-95% capacity retention after 100 cycles) and structural stability [6]. NCA cathodes are currently used in Tesla Model S electric vehicles due to their safety.

Today, the co-precipitation method is the most effective way to produce lithium-ion battery cathodes, it provides control of the particle shape, size, and chemistry thanks to the complex formation between chelating agents and metal ions. The traditional co-precipitation method includes ammonia as a chelating agent. Despite its toxicity ammonia forms complexes with transition metals. However, in NCA production, although nickel and cobalt ions can form complexes, aluminum ions can not be chelated with ammonia [7]. This causes flocculation in the solution and the elemental distribution of the particles have deteriorated [7]. In addition to this problem, ammonia also causes a huge amount of wastewater. Storage and purifying of this wastewater increase the cathode production cost. To sustain battery production cleaner, alternative, non-toxic chelating agents must be investigated. This paper aims to investigate citric acid adaptation to the coprecipitation method and analyzing the electrochemical performance of resulting cathode materials.

EXPERIMENTAL

All precursors were purchased from commercial suppliers and used without further purification. 1 M stoichiometric transition metal solution (Ni/Co/Al= 0.8/0.15/0.05), 2 M NH_3 solution, and 2 M NaOH solution is continuously fed to the reaction tank for NH_3-NCA production. 1 M stoichiometric transition metal solution (Ni/Co/Al= 0.8/0.15/0.05), 0.5 M citric acid (CA) solution, and 4 M NaOH solution is continuously fed to the reaction tank for CA-NCA production. For both samples mixing rate, pH, temperature, and reaction time are kept constant. Finally, the resulting mixture was filtered and washed repeatedly with distilled water. The product dried at 120°C for 24 h to obtain hydroxide precursor. 1 mole of hydroxide precursor is mixed with 1.05 mole $LiOH.H_2O$ and 2 step calcination process was performed. First, the mixture was pre-heated at 550°C to eliminate organic substances and then calcinated at 750°C for crystallization. The crystal structure of metal hydroxide and oxide materials were identified by powder X-ray diffraction (XRD Cu Kα=1.54Å) analysis with 2θ range from 10°-80° at a scan rate of $2°min^{-1}$ and 0.02° step size. The particle morphology and composition of the precursor and active material were examined by using a field-emission scanning electron microscope (FESEM, Zeiss Gemini 500).

The slurry that contains 10% PVDF, 10% C black, and 80% active material are dispersed in NMP solvent and cast on aluminum foil followed by vacuum drying at 80°C for 8-10 hours. The electrochemical performances of the cathodes were evaluated by CR2032 coin half cells. NCA cathodes were used as working electrodes, lithium foil was used as a reference electrode, Celgard 2300 was used as a separator, and (1.0 M LiPF6 (lithium hexafluorophosphate) in EC (ethylene carbonate):DMC (dimethyl carbonate) (1:1 in volume)) electrolyte. Galvanostatic tests were performed between 3.0-4.3 V with a C/10 current rate using Neware Battery test system. Rate tests were also performed in the same voltage range with different current densities.

RESULTS AND DISCUSSIONS

XRD results of both hydroxide and oxide samples are given in Fig.1. In both hydroxide samples α and β $Ni(OH)_2$ peaks are observed. Ideally, only β $Ni(OH)_2$ phase forms in co-precipitation. Although NCA production was performed in N_2 atmosphere, a small amount of oxygen may involve the coprecipitation process and causes α-$Ni(OH)_2$ formation.

Table 1. Lattice parameters of the cathode materials

Sample Code	I_{006}/I_{104}	c/a	Chi^2
NH_3-NCA	1.18	4.96	1.98
CA-NCA	1.28	4.94	3.02

Crystal parameters of the oxide samples were determined by the Rietveld method and Table 1 shows analysis and lattice parameters. Samples contain no impurity peak and both α and β $Ni(OH)_2$ transformed desired material. I_{006}/I_{104} ratios of the cathodes which show cation mixing degree are found to be 1.18 and 1.28 for NH_3-NCA and CA-NCA samples, respectively. This ratio should be higher than 1.2 and it could be claimed that usage of citric acid has a positive effect in forming a more stable crystal structure. Because citric acid forms complex with all three metals, thus crystal structure may contain fewer defects as a result more stable crystal was obtained when citric acid was used as a chelating agent [7,8].

Fig.2. shows SEM images of the samples before and after the heat treatment step. The primary particle morphology of the NH_3-NCA sample is needle-like, in the CA-NCA sample this needle-like shape disappeared. Primary particle morphology is directly related to the chelating agent type and ratio. Yue et al. have shown chelating agent ratio changes the growth direction of the crystal as a result of morphology [8]. With a citric acid ratio optimization needle-like primary particles can be obtained.

Fig.3. shows the electrochemical performance of the cathode materials. First discharge capacities are found to be 173.78 mAh/g and 162.80 mAh/g for NH3-NCA and CA-NCA,

respectively. After 100 cycles, the capacity retentions of the cathodes are found to be 55.26% and 70.29% for NH_3-NCA and CA-NCA, respectively.

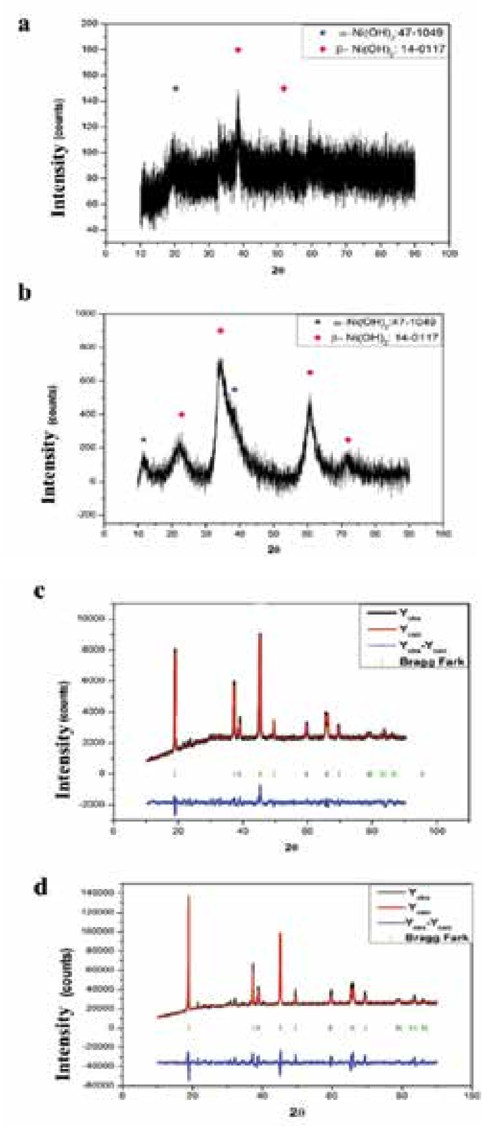

Figure 1. XRD Analysis of the cathode materials (a. NH3-NCA Before Heat Treatment b. CA-NCA Before Heat Treatment c. NH3-NCA After Heat Treatment d. CA-NCA After Heat Treatment)

NCA cathode produced by using citric acid as a chelating agent has better cycling performance compared to the NH_3-NCA. It is known that electrochemical performance strictly depends on crystal stability, since the NH_3-NCA cathode has a higher cation mixing degree, during cycling its crystal could not protect its stability and ends up with inadequate electrochemical performance.

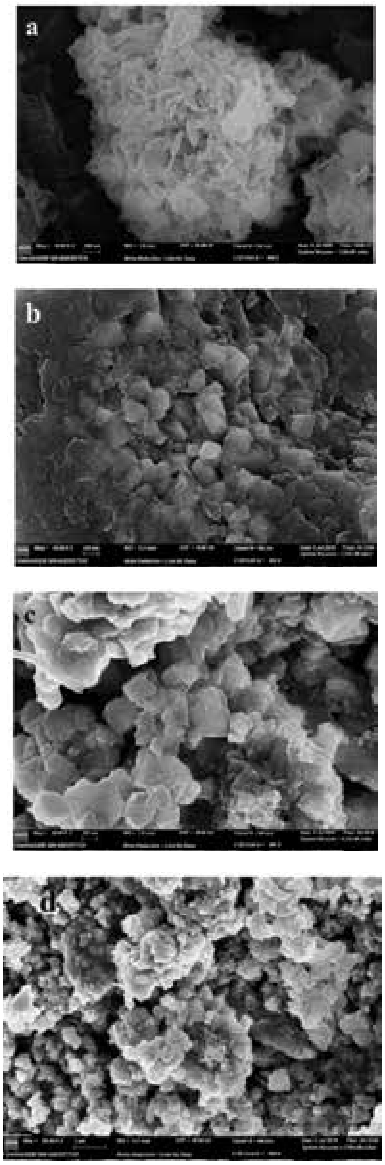

Figure 2. SEM images of the cathode materials (a. NH3-NCA Before Heat Treatment b. CA-NCA Before Heat Treatment c. NH3-NCA After Heat Treatment d. CA-NCA After Heat Treatment)

The same trend is observed in the rate performance of the cathodes. CA-NCA sample has superior performance compared to the NH_3-NCA sample. Its structural stability was good enough to be able to endure at high current rates.

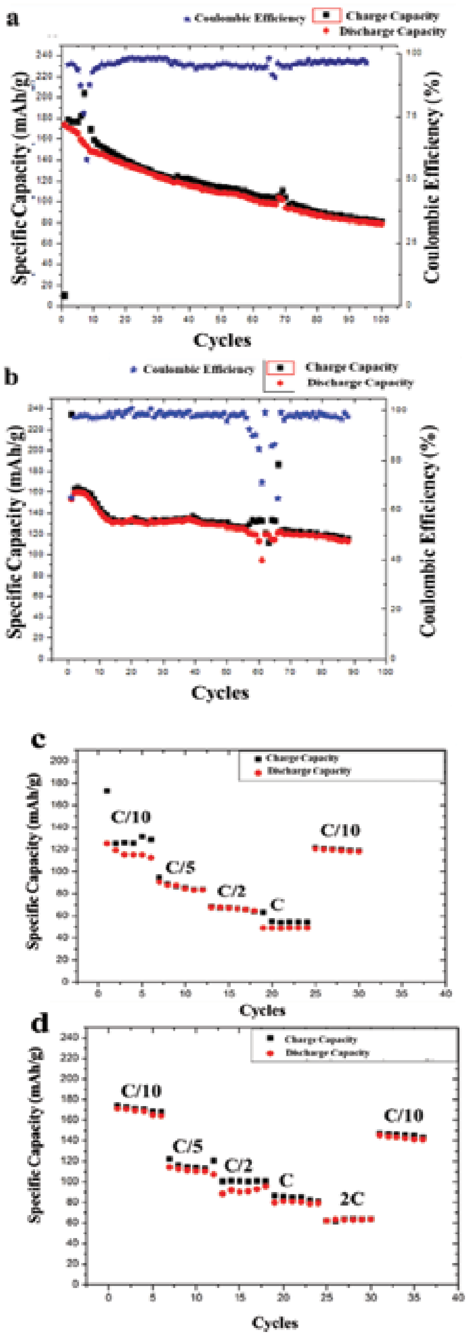

Figure 3. Electrochemical Performance of the cathode materials (a. NH3-NCA100 cycles performance b. CA-NCA 100 cycles performance c. NH3-NCA rate test performance d. CA-NCA rate test performance

CONCLUSION

In this paper, NCA cathode materials are produced with different chelating agents by the co-precipitation method. The crystal structure of the CA-NCA cathode is more stable and desirable compared to the NH_3-NCA cathode. Thanks to this stability CA-NCA cathode has better electrochemical performance compared to the NH_3-NCA cathode. Even further improvement, the citric acid molar ratio optimization study will be performed for a more accurate understanding.

ACKNOWLEDGEMENT

The authors appreciates to ITU for financial support in 33996 BAP Project. And, thank Medipol Regenerative and Restorative Medicine Research Center for SEM analysis.

REFERENCES

[1] https://www.pv-magazine.com/2019/07/04/recharging-economies-ev-battery-manufacturing-outlook-for-<europe/

[2] D. Sivlin, O. Keles, Effect of Sonication Power on Al_2O_3 Coated $LiNi_{0.5}Mn_{0.3}Co_{0.2}O_2$ Cathode Material for LIB, 147th The Minerals, Materials and Metals Society (TMS), Energy Technology 2018, 10-14 March 2018, Phoenix-USA, pp. 515-522.

[3] J. Li, R. Klöpsch, M.C. Stan, S. Nowak, M. Kunze, M. Winter, S. Passerini, Synthesis and electrochemical performance of the high voltage cathode material $Li[Li_{0.2}Mn_{0.56}Ni_{0.16}Co_{0.08}]O_2$ with improved rate capability, Journal of Power Sources, 196(2011), 4821-4825.

[4] A. Yamada, M. Tanaka, Jahn-Teller Structural Phase Transition Around 280K in $LiMn_2O_4$, Materials Research Bulletin, 30(6), 715-721.

[5] G. Hu, W. Liu, Z. Peng, K. Du, Y. Cao, Synthesis and electrochemical properties of $LiNi_{0.8}Co_{0.15}Al_{0.05}O_2$ prepared from the precursor $Ni_{0.8}Co_{0.15}Al_{0.05}OOH$, Journal of Power Source, 198(2012), 258-263.

[6] R. Zhao, J. Miao, W. Ian, Z. Wu, M. Hung, D. Lv, R. Zeng, G. Shi, H. Chen, Synthesis of layered materials by ultrasonic/microwave-assisted coprecipitation method: A case study of $LiNi_{0.5}Co_{0.2}Mn_{0.3}O_2$, Sustainable Materials and Technologies, 17(2018).

[7] H. Z. Zhang, C. Liu, D. W. Song, L. Q. Zhang, L. J. Bie, A new synthesis strategy towards enhancing the structure and cycle stabilities of the $LiNi_{0.80}Co_{0.15}Al_{0.05}O_2$ cathode material, Journal of Materials Chemistry A, 5, 835-841.

[8] Y. Yue, X. Shengming, X. Ming, H. Yinghe, H. Guoyong, Y. Youcai, Growth mechanisims for spherical mixed hydroxide agglomerates prepared by co-precipitation method: A case of $Ni_{1/3}Co_{1/3}Mn_{1/3}(OH)_2$, Journal of Alloys and Compounds, 619, 846-853.

Investigation of the Performance of Colloidal $LiFePO_4$ Particles in Suspension Flow Battery

Bayram YILDIZ[1], **Yasemin AŞKAR**[1], **Elif COŞKUN**[1], **Bora MAVİŞ**[2], **Simge ÇINAR**[1]
[1]Middle East Technical University, [2]Hacettepe University
Turkey

Abstract

In this study, colloidal $LiFePO_4$ particles were synthesized through solvothermal route. Effect of solvothermal method parameters on formation of colloidal $LiFePO_4$ was investigated. Post-processing treatments were found effective to obtain non-aggregated colloidal particles. The rheological behavior of aqueous suspensions including electroactive material was examined in terms of salt, electroactive material concentration and carbon content. A three-electrode systems was used to analyze electrochemical performance of aqueous $LiFePO_4$ suspensions.

1. Introduction

Electrochemical energy storage appliances have remarkable importance to balance the inconsistent and fluctuating nature of renewable energy sources. Among various systems, redox flow batteries are propitious for large scale energy storage because of their unique conformation which allows independent design of power and energy units, thus offers scalability and cost effectiveness. Utilization of suspensions involving electroactive materials instead of dissolved species within electrolyte seems to be one of the most promising ways to raise the energy density up to 20-fold when compared to that of commercial vanadium based RFBs [1]. However, currently, suspension flow batteries are suffering from the extremely high viscosities of highly loaded electroactive suspensions and are not feasible. In order to design an efficient and practicable suspension flow battery system, the viscosity of suspensions should be reduced. Here, we propose the use of colloidal particles in order to obtain less viscous and more stable suspensions. To this end, typical solvothermal technique was employed to synthesize colloidal $LiFePO_4$ particles with adjustment of reaction parameters. The effects of reaction conditions on particle size, morphology and structure were studied. We have also revealed that post-processing conditions are critical to obtain colloidal $LiFePO_4$ particles. Influence of the solids loading and electrolytes on the flow behavior of aqueous $LiFePO_4$ suspensions were investigated. Electrochemical performance of $LiFePO_4$ suspension were characterized using a three-electrode design.

2. Materials and Methods

$LiFePO_4$ was synthesized with typical solvothermal method using LiOH, H_3PO_4 and $FeSO_4.7H_2O$ as precursors. The effects of reaction parameters, namely temperature, duration, stoichiometric ratio of precursors, on the formation, size and morphology of $LiFePO_4$ particles were studied. In addition, post reaction treatments, i.e. washing procedure, were examined to understand the influence on aggregation state of obtained particles. The crystal structure and morphology of synthesized particles were analyzed by X-ray diffraction and scanning electron microscopy. Particle size distribution and stability of suspensions were determined via dynamic light scattering. Effects of electroactive material amount and conducting additive on the rheological behavior of suspensions were investigated via rheometer. Moreover, the influence of electrolytes on the stability and the flow characteristics of aqueous $LiFePO_4$ suspensions was examined. Electrochemical behavior of aqueous $LiFePO_4$ suspensions was characterized using a three-electrode cell.

3. Conclusion

The reaction parameters and the post-reaction treatments have found to be effective on formation of pure and non-aggregated $LiFePO_4$ powder. Rheological measurements have demonstrated aggregation state of particles has importance for obtaining stable dispersions and consistent flow behavior. Increasing salt concentration in electrolyte has been found to be effective on zeta potential and particle size distribution of aqueous $LiFePO_4$ powders. The use of non-aggregated powders has a potential to improve electrochemical performance and the durability of suspension flow batteries.

References

[1] M. Duduta, B. Ho, V. C. Wood, P. Limthongkul, V. E. Brunini, W. C. Carter, and Y. M. Chiang, Advanced Energy Materials, 1(4) (2011) 511-516.

Graphene Alternative 2D Materials: Mxene

Mesut Ramazan EKİCİ, Ahmet ATASOY
Sakarya University of Applied Science
Turkey

Abstract:
For a variety of applications with outstanding electronic, mechanical and optical properties related to 2D materials in the past decade many studies have been done. In electronic devices and electric vehicles the most used rechargeable batteries and super capacitors, rapidly developing and increasing in modern society the most important electrochemical energy storage devices. Two-dimensional Ti_3C_2 MXene, It is prepared by a combination of Ti_3SiC_2 powder abrasion with Hydrochloric Acid (HCl) or Hydrofluoric Acid (HF). The surface terminations such as the -O, -OH, -F group on the MXene widely affect its properties. Number of MXene and MXene layers, checking the spacing between layers features are largely adjustable. Surface finishes affect the MXene's capacitance. This improvement in performance for better conductivity and faster transport of electrons higher carbon content and aqueous electrolyte it is attributed to the wider surface area for greater access to the electrode. MAX phase Ti_3SiC_2 powder and MXene phase $Ti_3C_2T_x$ powder, X-ray diffraction (XRD), Scanning Electron Microscope (SEM & FESEM) and Brunauer-Emmett-Teller (BET) theory analyzed.

1. Introduction

Complex layered phases, known as MAX phases (eg, $M_{n+1}AXn$, where M: early transition metal, A: group A element, X: C and / or N, n = 1, 2, 3), for material design and process it is an exciting model system. When layers A are selectively scraped from MAX phases, To highlight the parallel relationship with MAX phases and graphene A new type of 2D material is created, called MXene [1-4]. Since their discovery in 2011, MXenes has for composition variations and feature adjustments it is rapidly being established as a new class of 2D materials with remarkable possibilities. As one of the MAX triple compounds, Ti_3SiC_2 has received much more attention recently[4-9]. It is a unique combination of metal and ceramic-like properties[2]. Ti_3SiC_2 is the most studied MAX triple compound[4-9]. MXenes has the chemical formula $M_{n+1}AX_n$ (M = Sc, Ti, V, Cr, Zr, Nb, Mo, Hf, Ta; X = C) Two-dimensional (2D) transition metal is a new class of carbide and nitrites[1-8]. Recently synthesized by wear of MAX phases, these 2D systems are named as MXene since they subtract 'A' elements from MAX phases and are structurally similar[9]. Ti_3SiC_2's Ti - C bonds with relatively weak Ti - Si bonds layered structure that is quite strong, are traces of unusual feature combinations[1]. Experimentally, MXene's are transparent conductors[9-12], field-effect transistors[9], super capacitors[6,10,13], Li-ion batteries[6,9], electromagnetic interface screensavers[9,14], filling in polymeric composites[9,15-16], water purifier[5,9,17], double sensitive surfaces[9], substrate suitable for paints[9,13], catalyst[7,9], for methane storage promising materials[9], also ceramic biomaterials with high photothermal conversion efficiency for cancer treatment studies are carried out in many fields[7,9,17-18]. Theoretically, for hydrogen, catalytic and photocatalytic reactions[16-17] alongside new potential materials Many applications have been proposed for MXene in electronic[6-13], magnetic[7-8,14,18], optical[9-10,18-19], thermoelectric[9] and sensing devices[7].

2. Experimental procedures

Starting powder Forsman Scientific (Beijing) Co., Ltd. from the company. MAX phase Ti_3SiC_2 starting powder is 98% (<2% TiC) purity and 200 mesh size. 1 gram Ti_3SiC_2 powder in plastic beaker it was slowly added to 10 ml of acid solutions in the beaker. While preparing the acid solution 50% deionized water was used as a 50% acid (HCl or HF) solution[20-25]. The created solution is under fume hood with magnetic stirrer set at 750 rpm stir for 2, 16 and 48 hours. Samples are expressed in acid and mixing times used (such as HCl-2, HF-2, HCl-16). Teflon Magnetic Fish (PTFE) was placed into the beaker for mixing. After mixing solution and powder the beaker was taken into the centrifuge tube. The NF 200 Model was subjected to 5-minute processes at a speed of 3500 rpm in the centrifuge. After centrifuging, the supernatant was placed in separate containers in the upper part. For the supernatant portion without emptying the centrifuge tube pH measurements were made with Mettler Toledo brand pH meter. Centrifugation was continued at 5 minutes until the pH value was between 5-6. After the pH reaches a value between 5-6, the supernatant in the centrifuge tube is discharged. The part that remained under the centrifuge was placed in a glass beaker. Centrifuge tubes were cleaned with ethanol and the residue was taken in a glass beaker.

Figure 1: Production Phases from MAX Phase to MXene.

40 ml of ethanol was added to the glass beaker. It was left for 48 hours to allow the dust to settle on the bottom of the glass beaker. The remaining ethanol was then drained with the Eppendorf pipette. 5 ml of ethanol was added again and left for 24 hours. Afterwards, the clay (mud) in which the dust was found collapsed to the bottom of the beaker. Vacuum filtering process was carried out for 1 hour in order to filter the clay (clay) powder and separate it from the liquid. After the vacuum filtering process, the dried powder was left in the oven for 4 hours in order to easily remove the dust remaining from the filter paper. Summary of the MXene production phase is shown in Figure 1. RIGAKU D-MAX-2200 model X-Ray Diffraction, Field Emission Scanning Electron microscope (FESEM) in Micromeritics ASAP2020 Brunauer-Emmett-Teller (BET) theory analyzes were made. ZEISS-supra 40 vp / gemini scanning Electron Microscope (SEM) was used for micro and nano size analyzes. Prior to SEM, powders were coated with 80% Gold and 20% Palladium with the Quorum Q150R ES coating device.

3. Results and Discussion

pH change of MXene phase $Ti_3C_2T_x$ powder after centrifugation increases logarithmically. There is a proportional change between mixing time with HCl and HF, the time elapsed for the centrifuge. As the mixing time increases, the time it takes for the pH value to reach a value between 5-6 increases. (Figure 2).

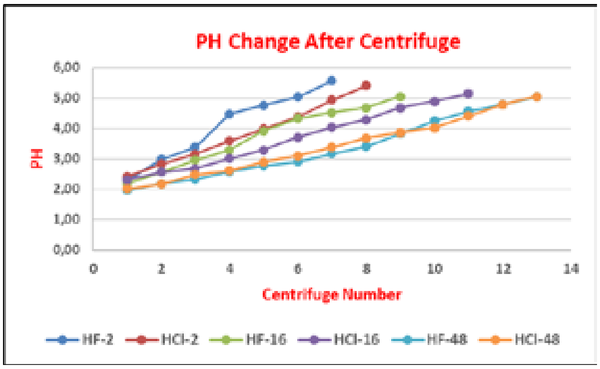

Figure 2: pH value change over time after centrifugation.

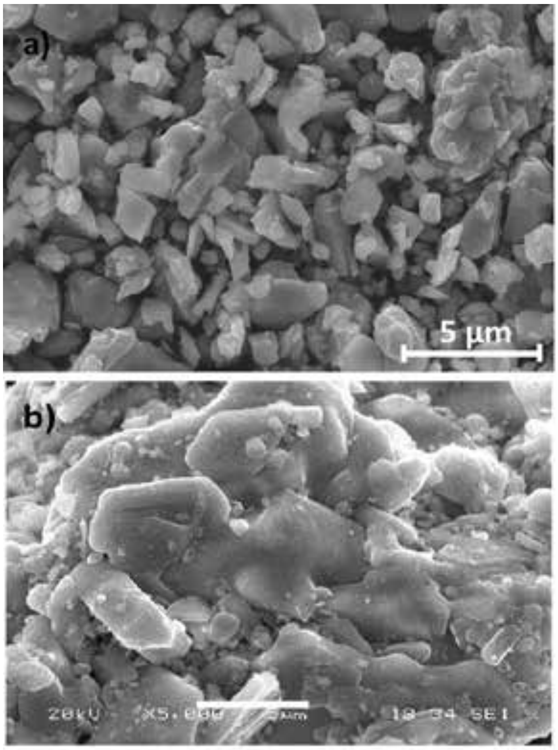

Figure 3: MAX Phase Ti_3SiC_2 Powder a) FE-SEM images b) SEM images.

FE-SEM and SEM images of MAX phase starting powder Ti3SiC2 powder before mixing with acids can be seen (Figure 3). It is understood from the analyzes that the powder undergoes physical and chemical changes after mixing with acids for different periods of time.

SEM images of powders obtained by mechanical stripping of MAX Phase Ti_3SiC_2 starting powder with Hydrochloric Acid (HCl) for 2, 16 and 48 hours are shown in Figure 4. As the mixing time increases, the effects of physical and chemical changes can be easily seen. The starting powder is transformed into a layered structure by showing physical and chemical changes [8,17,26].

SEM images of the powders obtained by the mechanical peeling of the starting powder with Hydrofluoric Acid (HF) for 2, 16 and 48 hours are shown in Figure 5. In Ti_3SiC_2, Ti_3C_2 layers (structural according to the dual TiC phase where C is in the octahedral sites) are combined with the atomic layers of Si which act as mirror planes. Si-Ti bonds are very weak, and covalent Ti-C bonds are much stronger. Ti_3SiC_2 displays unusual mechanical properties and chemical stability at high temperatures [21-22,26].

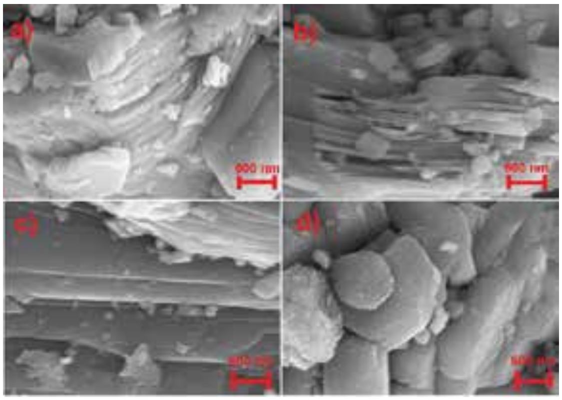

Figure 4: Starting powder of MAX Phase Ti_3SiC_2 Powder (a), 2 hours (b), 16 hours (c) and 48 hours (d) SEM images of the powder obtained by mechanical peeling of Hydrochloric Acid (HCl).

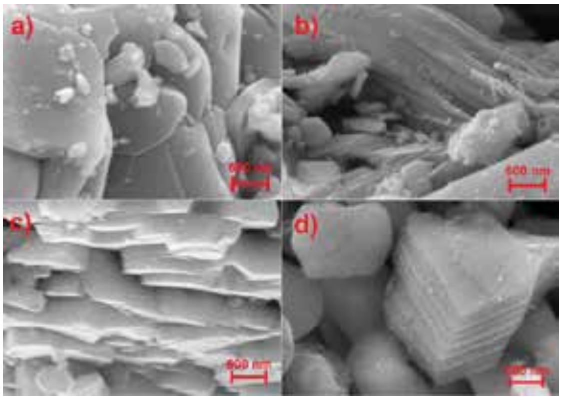

Figure 5: Starting powder of MAX Phase Ti_3SiC_2 Powder (a), 2 hours (b), 16 hours (c) and 48 hours (d) SEM images of the powder obtained by mechanical peeling of Hydrofluoric Acid (HF).

In the analysis of the layered structure in the transformation of Mene, the difference of silicon between the layers can be seen easily. After mixing with acids, silicon reacts and is expected to move away or decrease from the environment. It is understood from SEM / EDX analysis (Figure 6) that the amount of silicon decreases in case of conversion to MXene when the process is performed. Although the Ti_3SiC_2 powder with MAX Phase has more Ti_3SiC_2 phase in the XRD image (Figure 7), Ti_3O and TiO phases were also found.

XRD images of powders obtained by mechanical stripping of MAX phase Ti_3SiC_2 starting powder with HCl and HF for 2, 16 and 48 hours are shown in Figure 8. After mixing with hydrofluoric acid, the peaks on the XRD graph shift to the right. MXene refers to the change in structure. In HF, after the process, the layer gap of the starting powders and c cage parameter increases. After the silicon is etched, stratification occurs and the layer gap increases. It shows that with increasing time in the HF process, d-distances increase. Observed peaks shifting to higher angles for HF-16 and HF-48 can be attributed to the diffusion of Si atoms present in the solution into the structure of the resulting TiC. In fact, the atomic radius of Si is lower than for Ti [27-29].

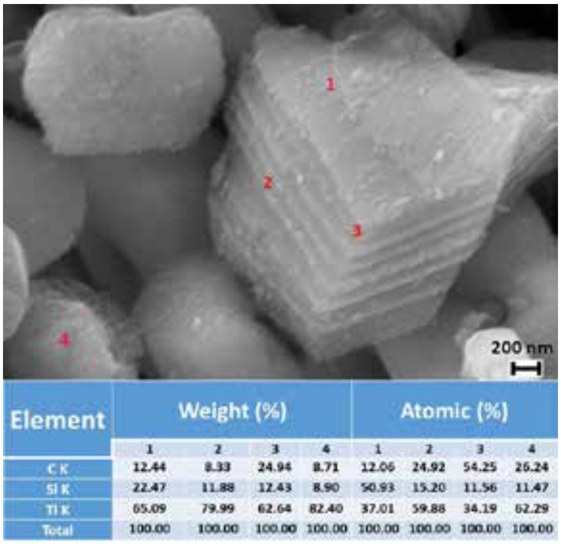

Element	Weight (%)				Atomic (%)			
	1	2	3	4	1	2	3	4
C K	12.44	8.33	24.94	8.71	12.06	24.92	54.25	26.24
Si K	22.47	11.88	12.43	8.90	50.93	15.20	11.56	11.47
Ti K	65.09	79.99	62.64	82.40	37.01	59.88	34.19	62.29
Total	100.00	100.00	100.00	100.00	100.00	100.00	100.00	100.00

Figure 6: SEM/EDX Analysis of powder obtained by mechanical peeling of MAX Phase Ti_3SiC_2 Powder for 48 hours Hydrofluoric Acid (HF).

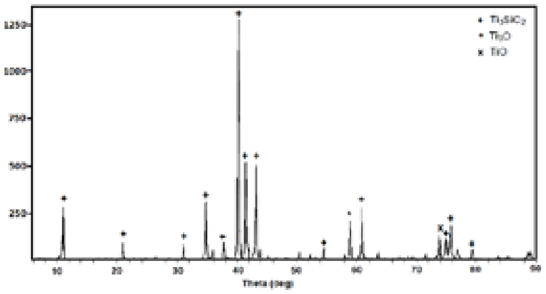

Figure 7: MAX Phase Ti_3SiC_2 Powder XRD images.

It is clear that by dipping the starting powder into the HF solution, Ti_3SiC_2 breaks and its layered structure disappears. In addition, the chemical composition of the HF-48 powder is analyzed by EDX (Figure 6). In accordance with the XRD pattern, it is seen that the 48-hour HF treatment leads to a reduction in the amount of Si. According to the XRD template of Ti_3SiC_2 powder treated with HF, TiC is the most important impurity of the prepared Ti_3SiC_2. In this regard, it can be considered that the thermal expansion coefficient of TiC is lower than for Ti_3SiC_2, and the prepared powder has residual tension.

Therefore, the presence of residual stresses accelerates chemical activity and separation of the Si layer. In summary, it can be said that the presence of TiC in the prepared powder can be given as a possible cause of the low resistance of Ti_3SiC_2 to HF treatment [27-29].

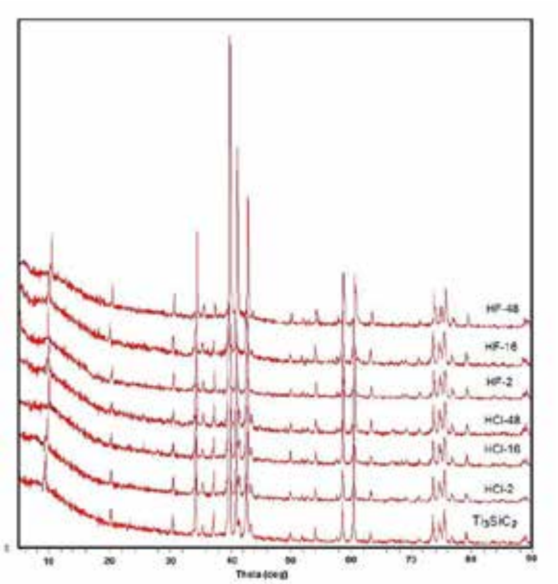

Figure 8: MAX Phase Ti_3SiC_2 Powder, With Hydrochloric Acid (HCl) and Hydrofluoric Acid (HF) XRD image of powders formed by mixing for 2, 16 and 48 hours.

It was carried out using a Micromeritics ASAP 2020 device at 77 K after exporting N2 for 48 hours under vacuum at 200 ° C. The powders formed by mixing Ti3SiC2 Powder, Hydrochloric Acid (HCl) and Hydrofluoric Acid (HF) for 48 hours with multi-point analysis method were analyzed with Brunauer-Emmett-Teller (BET) (Table 1). Total pore volumes were calculated as 0.8957 m2g-1 of P / Po = Ti3SiC2 Powder, while 3,5778 m2g-1 of HCl-48 was calculated as 2.4581 m2g-1 in HF-48. Pore size distributions were obtained from the desorption branch using the Barrette Joynere Halenda (BJH) model.

Table 1: Brunauer - Emmett - Teller (BET) analysis of powders formed by mixing MAX Phase Ti_3SiC_2 Powder, Hydrochloric Acid (HCl) and Hydrofluoric Acid (HF) for 48 hours.

Summary Report	Ti_3SiC_2	HCl-48	HF-48
Single point surface area at p/p° (m²/g)	0,8957	3,5778	2,4581
BET Surface Area (m²/g)	0,9337	3,6341	2,5694
Langmuir Surface Area (m²/g)	1,2978	4,9408	3,5748
t-Plot Micropore Area (m²/g)	0,1307	1,0904	0,1792
t-Plot External Surface Area (m²/g)	0,8031	2,5436	2,3902

4- Conclusions

In this study, after immersion of MAX phase Ti_3SiC_2 powder in HCl and HF solution, it was investigated in phase and morphology. The HCl and HF used change the physical and chemical structure of the Ti_3SiC_2 powder. A new structure is formed by breaking the weak bonds between Ti-Si and removing the silicon from the environment.There is a ratio between the mixing time with acids and the pH measured in the centrifugation process. In the conversion of MAX phase Ti_3SiC_2 powder into layered Ti_3SiT_x structure in MXene structure, it was seen that the best solution was obtained after mixing with HF. It has been found that mixing $T_{i3}SiC_2$ powder with HF for 48 hours is more effective in transforming it into graphene-like MXene. The MXene structure changes as a result of different terminations of MAX phase powders, mixing at different times and at different temperatures. For new researchers, MAX and MXene structures have a wide range of work and research opportunities.

References:

[1] M. Peng, X. Shi, Z. Zhu, M. Wang, Q. Zhang, Facile synthesis of Ti_3SiC_2 powder by high energy ball-milling and vacuum pressureless heat-treating process from Ti-TiC-SiC-Al powder mixtures, Ceramics International, 38 (2012) 2027-2033.

[2] X. He, Y. Baia, Y. Li, C. Zhub, X. Konga, In situ synthesis and mechanical properties of bulk Ti_3SiC_2/TiC composites by SHS/PHIP, Materials Science and Engineering A, 527 (2010) 4554-4559.

[3] M. Kurtoğlu, M. Naguib, Y. Gogotsi, M.W. Barsoum, First principles study of two-dimensional early transition metal carbides, MRS Communications, 2 (2012) 133-137.

[4] P. Eklund, J. Rosen, P.O. Å. Persson, Layered ternary $M_{n+1}AX_n$phases and their 2D derivative MXene: an overview from a thin-film perspective, Journal of Physics D: Applied Physics, 50 (2017) 113001.

[5] A. Atasoy, E. Saka, Ti_3SiC_2 MAX Phase from TiC-Si-Ti Mixture”, Bilge International Journal of Science and Technology Research, 2 (2018) (Special issue), 25-31.

[6] X. Zhang, Z. Zhang, Z. Zhou, MXene-based materials for electrochemical energy storage, Journal of Energy Chemistry, 27 (2018) 73-85.

[7] S. Venkateshalu, A.N. Grace, MXenes-A new class of 2D layered materials: Synthesis, properties, applicationsas supercapacitor electrode and beyond, Applied Materials Today, 18 (2020) 100509.

[8] M. Alhabeb, K. Maleski, T.S. Mathis, A. Sarycheva, C.B. Hatter, S. Uzun, A. Levitt, Y. Gogotsi, Selective Etching of Silicon from Ti_3SiC_2 (MAX) To Obtain 2D Titanium Carbide (MXene), Angew. Chem. Int. Ed.,57 (2018) 5444-5448.

[9] M. Khazaei, A. Ranjbar, M. Arai, T. Sasaki, S. Yunoki, Electronic properties and applications of MXenes:a

theoretical review, Journal of Materials Chemistry C, 5 (2017) 2488.

[10] J. Li, A. Levitt, N. Kurra, K. Juan, N. Noriega, X. Xiao, X. Wang, H. Wang, H..N. Alshareef, Y. Gogotsi, MXene-conducting polymer electrochromic microsupercapacitors, Energy Storage Materials, 20 (2019) 455-461.

[11] P. Eklund, M. Beckers, U. Jansson, H. Högberg, L. Hultman, The $M_{n+1}AX_n$ phases: Materials science and thin-film processing, Thin Solid Films,518 (2010)1851-1878.

[12] K. Kozak, M. M. Bućko, L. Chlubny, J. Lis, G. Antoua, T. Chotard, Influence of composition and grain size on the damage evolution in MAX phases investigated by acoustic emission, Materials Science & Engineering A,743 (2019) 114-122.

[13] H. Li, Y. Hou, F. Wang, M.R. Lohe, X. Zhuang, L. Niu, X. Feng, Flexible All-Solid-State Supercapacitors with High Volumetric Capacitances Boosted by Solution Processable MXene and Electrochemically Exfoliated Graphene, University of Chinese Academy of Sciences, Adv. Energy Mater., Volume7, Issue4 (2017) 1601847 https://doi.org/10.1002/aenm.201601847.

[14] M.S. Cao, Y.Z. Cai, P. He, J.C. Shu, W.Q. Cao, J. Yuan, 2D MXenes: Electromagnetic property for microwave absorption and electromagnetic interference shielding, Chemical Engineering Journal, 359 (2019)1265-1302.

[15] C. B. Hatter, J. Shah, B. Anasori, Y. Gogotsi, Micromechanical response of two-dimensional transition metal carbonitride (MXene) reinforced epoxy composites, Composites Part B, 182 (2020) 107603.

[16] M. Naguib, Two-Dimensional Nanocrystals Produced by Exfoliation of Ti(3)AlC(2), Linköping University Post Print, 2011, Linköping, İsveç.

[17] K. Rasool, R. P. Pandey, P. A. Rasheed, S. Buczek, Y. Gogotsi, K. A. Mahmoud, Water treatment and environmental remediation applications of twodimensional metal carbides (MXenes), Materials Today Volume 30 (2019).

[18] Y. Wang, W. Feng, Y. Chen, Chemistry of two-dimensional MXene nanosheets in theranostic nanomedicine, Chinese Chemical Letters, Volume 31, Issue 4, (2020) 937-946, https://doi.org/10.1016/j.cclet.2019.11.016.

[19] L. Zhang, W. Su, H. Shu, T. Lü, L. Fu, K. Song, X. Huang, J. Yu, C.T. Lin, Y. Tang, Tuning the photoluminescence of large Ti_3C_2Tx MXene flakes, Ceramics International, 45 (2019) 11468-11474.

[20] R. Li, L. Zhang, L. Shi, P. Wang, MXene Ti_3C_2: An Effective 2D Light-to-Heat Conversion Material, ACS Nano, 11, 4 (2017) 3752-3759, http://dx.doi.org/10.1021/acsnano.6b08415.

[21] G. Cui, X. Zehng, X. Lv, Q. Jia, W. Xie, G. Gu, Synthesis and microwave absorption of Ti_3C_2Tx MXene with diverse reactant concentration, reaction time, and reaction temperature, Ceramics International, 45 (2019) 23600-23610.

[22] X. Zhang, Y. Liu, S. Dong, J. Yang, X. Liu, Flexible electrode based on multi-scaled MXene ($Ti_3C_2T_x$) for supercapacitors, Journal of Alloys and Compounds, 790 (2019) 517-523.

[23] X. Wang, K. Sun, K. Li, X. Li, Y. Gogotsi, $Ti_3C_2T_x$/PEDOT:PSS hybrid materials for room-temperature methanol sensor,
Chinese Chemical Letters, Volume 31, Issue 4 (2020) 1018-1021 https://doi.org/10.1016/j.cclet.2019.11.031 .

[24] M.N. Abdelmalak , MXenes: A New Family of Two-Dimensional Materials and its Application as Electrodes for Li-ion Batteries, Doctor of Philosophy, Submitted to the Facultyof Drexel University, 2014, Philadelphia, USA.

[25] C. Ren, Interaction of Ions with Two-Dimensional Transition Metal Carbide (MXene) Films,Doctor of Philosophy,Submitted to the Faculty Drexel University, 2017, Philadelphia, USA .

[26] Z. Sun, J. Zhou, D. Music, R. Ahuja, J.M. Schneider, Phase stability of Ti_3SiC_2 at Elevated Temperatures, Scripta Materialia,(2006) 54,105-107.

[27] H. Aghamohammadi, H., Heidarpour, A.,Jamshidi, R., The phase and morphological evolution of Ti3SiC2 MAX phase powder after HF treatment, Ceramics International, (2018) 44,17992-18000.

[28] G. Lv, J. Wang, Z. Shi, L. Fan, Intercalation and delamination of two dimensional MXene (Ti3C2Tx) and application in sodium-ion batteries, Materials Letters (2018) 219, 45-50.

[29] O. Salim, K.A., Mahmoud, K.K. Pant, R.K. Joshi, Introduction to MXenes: synthesis and characteristics, Materials Today Chemistry (2019), 14, 100191.

Recent Development in 2D Metal Carbides and Nitrides (MXenes) for Energy Storage

Müslüm DEMİR
Osmaniye Korkut Ata University
Turkey

The new family of 2D transition metal carbides, carbonitrides and nitrides (collectively named as MXenes) has extended rapidly in the past several years after the discovery of Ti2C. The materials have unique properties including surface terminations, such as hydroxyl, oxygen or fluorine, which inform hydrophilicity to their surfaces. Since 2011, more than 22 different MXenes have been synthesized by selective etching of many atomic layers from their layered precursors MAX phases. The availability of solid solutions, the control of surface terminations and a recent discovery of multi-transition-metal layered MXenes suggest the potential for synthesis of certain new structures. The adaptable chemistry of MXenes leads the tuning of properties for applications including energy storage technology, hydrogen storage technology, adsorptive environmental application, electromagnetic interference shielding, water treatment, gas- and biosensors, and chemical catalysis. In this talk, we present the synthesis, structure and physical and chemical properties of MXenes. Additionally, energy storage applications including Li-ion batteries, supercapacitors and an outlook for future research will be given.

1. Introduction

Recently, energy has become very popular topic in the nature. Due to the limitation of fossil fuels resources, renewable energy such as solar and wind energy attract great attention. However, wind and solar energies are suffered from sustainability because the energy supply is based on environment and weather conditions. Thus, Electrochemical energy storage technology including Li-ion batteries (LIBs), Li-S batteries (LISs) and supercapacitors are reflected to be alternative methods to store renewable energy supply. However, today’s battery the performance could not meet the developing demand for scale-up energy storage. In order to overcome abovementioned issue, scientists and industry specialist are seeking novel materials with advance performance in the energy storage technology. Since the discovery of single layer of graphite called two-dimensional (2D) graphene in 2004 [1], many 2D materials have been intensively investigated in detailed because they have unique physical, chemical, mechanical and electrochemical properties. Examples of 2D materials are hexagonal BN[1],[2] silicene [3] germanane [4] transition metal dichalcogenides (TMDs) [5] and phosphorene [6],[7] were also successfully produced in laboratories. Especially, the high surface area to volume ratio and actual surface areas of 2D materials result in high energy density and large mobility ensuring making very strong candidates for ESD. In the last decade, a new class of 2D early transition metal carbides, nitrides or carbonitrides, also known as MXene, have been synthesized by selectively etching the “A” elements from their three-dimensional (3D) MAX phases [8], [9] , [10], [11]. The chemical order of MAX phase is consists of Mn+1AXn (n = 1, 2 or 3), which are early transition metal “M”, carbon and/or nitrogen and “X” main group element “A”, along with having layered hexagonal architecture. Until 2020, over 80 types of MXene have been reported and the number MXene studies are still growing.

Justification of MXene is about the strong M–X bonds, and low M-A bond the "A" are further chemically active. Therefore, it is likely to selectively react "A" layers from the 3D MAX phase, producing a novel 2D materials, which are named as MXene. There are many application of MXene including in catalysts, photothermal conversion, ion sieving, topological insulators, field-effect transistors and hydrogen evolution reactions see Figure 1. .

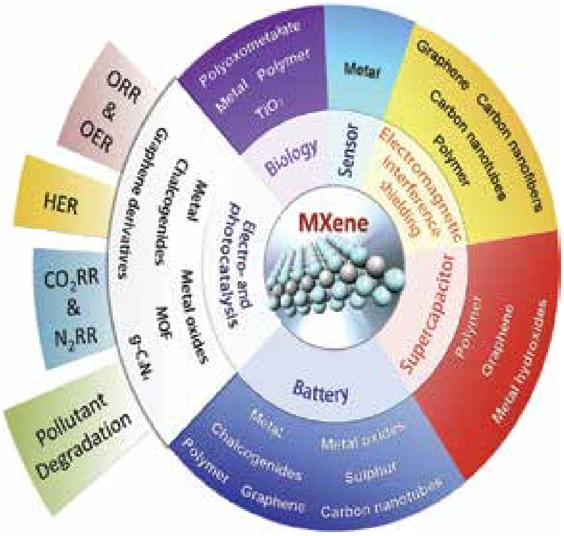

It is taken from reference [12]

Meanwhile, as abovementioned properties, MXene shows excellent performance in electrochemical energy storage including batteries and supercapacitors. Several review papers are published to summarize the properties, preparation and possible applications please see them for details. [13], [14], [15], [16] etc. On the other hand, we herein reviewed the recent breakthroughs of MXenes in energy storage technology. In the present review, the latest reports are in detail investigated to promote the advance development of MXene for batteries and capacitors.

MXene Preparation

Other review papers are in details discussed optimum preparation of the MXene sheets . In short, Al-containing MAX phases can be etched by hydrofluoric acid (HF) to form 2D MXene. . For example,

First, Ti3AlC2 (2.0 g) was gradually added to 40 mL of 40% HF solutions and then the reaction mixture was mixed using a stirrer at 60 °C for 18 h. Second, the solids in the solution were gathered by centrifuging, washed with double distilled water, and lyophilized. During the synthesis, the subsequent reaction mechanism was followed:

$$\mathrm{Ti3AlC2 + 3HF \rightarrow Ti3C2 + AlF3 + 3/2H2} \quad (1)$$

$$\mathrm{Ti3C2 + 2H2O \rightarrow Ti3C2(OH)2 + H2} \quad (2)$$

$$\mathrm{Ti3C2 + 2HF \rightarrow Ti3C2F2 + H2} \quad (3)$$

The etching conditions (HF concentration and time) that were necessary to change a given MAX phase differ extensively, depending on the temperature and particle size.please see figure 2 for details.

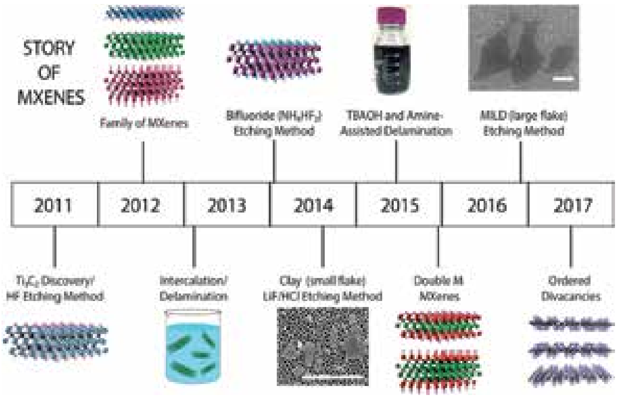

It is taken from reference [17]

MXene for Batteries

Secondary lithium-ion batteries are widely employed in energy storage technology. The LIB holds a great cyclability, elevated rate capacity and high lithium storage capacity all of which depend on the properties of the electrode materials in LIB's. Graphite is the great candidate anode component, but it has problems from a low specific capacity of 372 mAh/g and low rate capability. Inhere, a lot investigation attempts have opened the growth of novel anode materials in LIBs including MXene.

MXene for Supercapacitors

Muslum Demir is an assistant professor at Osmaniye Korkutata University, Osmaniye, Turkey. He was received his Ph.D. in Prof. Ram Gupta's lab at Virginia Commonwealth University (Virginia, USA) 2017. He received his M.S. in Chemistry from Rutgers University (USA) in 2013 and his B.S. in Chemistry from Cukurova University (Turkey) in 2008. His research focused on the development of biomass-derived carbon materials for energy storage and conversion applications. He has published more than 10 peer-reviewed papers and attended prestigious conferences such as ACS, AICHE and ECS meetings.

Corresponding author: Muslum Demir, muslumdemir@osmaniye.edu.tr tel:+90328 825 1818

References

1. Steiner, D.; Mittendorfer, F.; Bertel, E., Quasiliquid Layer Promotes Hexagonal Boron Nitride (h-BN) Single-Domain Growth: h-BN on Pt(110). *Acs Nano* **2019,** *13* (6), 7083-7090.
2. Wang, X. S.; Hossein, M.; Wei, Z. M.; Xie, L. M., Growth of two-dimensional materials on hexagonal boron nitride (h-BN). *Nanotechnology* **2019,** *30* (3).
3. Drissi, L. B.; Ouarrad, H.; Ramadan, F. Z.; Fritzsche, W., Graphene and silicene quantum dots for nanomedical diagnostics. *Rsc Adv* **2020,** *10* (2), 801-811.
4. Rosli, N. F.; Rohaizad, N.; Sturala, J.; Fisher, A. C.; Webster, R. D.; Pumera, M., Siloxene, Germanane, and Methylgermanane: Functionalized 2D Materials of Group 14 for Electrochemical Applications. *Adv Funct Mater* **2020,** *30* (21).
5. (a) Rosati, R.; Perea-Causin, R.; Brem, S.; Malic, E., Negative effective excitonic diffusion in monolayer transition metal dichalcogenides. *Nanoscale* **2020,** *12* (1), 356-363; (b) Choi, W.; Akhtar, I.; Kang, D.; Lee, Y. J.; Jung, J.; Kim, Y. H.; Lee, C. H.; Hwang, D. J.; Seo, Y., Optoelectronics of Multijunction Heterostructures of Transition Metal Dichalcogenides. *Nano Letters* **2020,** *20* (3), 1934-1943; (c) Murthy, A. A.; Stanev, T. K.; dos Reis, R.; Hao, S. Q.; Wolverton, C.; Stern, N. P.; Dravid, V. P., Direct Visualization of Electric-Field-Induced Structural Dynamics in Monolayer Transition Metal Dichalcogenides. *Acs Nano* **2020,** *14* (2), 1569-1576.
6. Ghambarian, M.; Azizi, Z.; Ghashghaee, M., Remarkable improvement in phosgene detection with a defect-engineered phosphorene sensor: first-principles calculations. *Phys Chem Chem Phys* **2020,** *22* (17), 9677-9684.
7. Henry, L.; Svitlyk, V.; Mezouar, M.; Sifre, D.; Garbarino, G.; Ceppatelli, M.; Serrano-Ruiz, M.; Peruzzini, M.; Datchi, F., Anisotropic thermal expansion of black phosphorus from nanoscale dynamics of phosphorene layers. *Nanoscale* **2020,** *12* (7), 4491-4497.
8. Kalambate, P. K.; Gadhari, N. S.; Li, X.; Rao, Z. X.; Navale, S. T.; Shen, Y.; Patil, V. R.; Huang, Y. H., Recent advances in MXene-based electrochemical sensors and biosensors. *Trac-Trend Anal Chem* **2019,** *120*.
9. Yu, H.; Wang, Y. H.; Jing, Y.; Ma, J. M.; Du, C. F.; Yan, Q. Y., Surface Modified MXene-Based Nanocomposites for Electrochemical Energy Conversion and Storage. *Small* **2019,** *15* (25).
10. Sun, Y. L.; Meng, X.; Dall'Agnese, Y.; Dall'Agnese, C.; Duan, S. N.; Gao, Y.; Chen, G.; Wang, X. F., 2D MXenes as Co-catalysts in Photocatalysis: Synthetic Methods. *Nano-Micro Lett* **2019,** *11* (1).
11. Zhang, C. F.; Nicolosi, V., Graphene and MXene-based transparent conductive electrodes and supercapacitors. *Energy Storage Mater* **2019,** *16*, 102-125.
12. Peng, J. H.; Chen, X. Z.; Ong, W. J.; Zhao, X. J.; Li, N., Surface and Heterointerface Engineering of 2D MXenes and Their Nanocomposites: Insights into Electro- and Photocatalysis. *Chem-Us* **2019,** *5* (1), 18-50.
13. Hu, J. J.; Cheng, Y. J.; Zhang, X. Z., Recent advances in nanomaterials for enhanced photothermal therapy of tumors. *Nanoscale* **2018,** *10* (48), 22657-22672.
14. Mukherjee, S.; Ren, Z. K.; Singh, G., Beyond Graphene Anode Materials for Emerging Metal Ion

Batteries and Supercapacitors. *Nano-Micro Lett* **2018,** *10* (4).
15. Ding, J.; Hu, W. B.; Paek, E.; Mitlin, D., Review of Hybrid Ion Capacitors: From Aqueous to Lithium to Sodium. *Chemical Reviews* **2018,** *118* (14), 6457-6498.
16. Xiong, D. B.; Li, X. F.; Bai, Z. M.; Lu, S. G., Recent Advances in Layered Ti3C2Tx MXene for Electrochemical Energy Storage. *Small* **2018,** *14* (17).
17. Alhabeb, M.; Maleski, K.; Anasori, B.; Lelyukh, P.; Clark, L.; Sin, S.; Gogotsi, Y., Guidelines for Synthesis and Processing of Two-Dimensional Titanium Carbide (Ti3C2TX MXene). *Chemistry of Materials* **2017,** *29* (18), 7633-7644.

Improved Ionic Conductivity in NASICON-Type Ce^{3+} Doped $LiZr_2(PO_4)_3$ for Li-Ion Batteries

Farah LAMARA, Nedjemeddine BOUNAR
University of Jijel
Algeria

Abstract

Ce^{3+} doped $LiZr_2(PO_4)_3$ has been synthesized by sol-gel method . The influence of substitution of Ce^{3+} for Zr^{4+} on the ionic conductivity, morphology, and structure of the parent compound $LiZr_2(PO_4)_3$ (LZP) is investigated. Their structures $Li_{1+x}Zr_{2-x}Ce_x(PO_4)_3$ (x = 0 - 0.2) solid electrolytes were determined from X-ray powder diffraction method (XRD) using Rietveld analysis. Rietveld refinement of powder x-ray diffraction data reveals that the Ce^{3+} substitution stabilizes the LZP in the highly conducting rhombohedral R-3c phase at room temperature. Ce^{3+} substituted LZP display enhanced ionic conductivity, showing the highest ionic conductivity of 0.67 x 10^{-4} S/cm at room temperature for the composition $Li_{1.1}Zr_{1.9}Ce_{0.1}(PO_4)_3$. Also investigated is the increase of LZP conductivity with another aliovalent substituent, Cu2 +, whose ionic radius is close to Zr^{4+} (0.72 Å).Further, the activation energy falls from 0.51 eV for the parent LZP to 0.44 eV for x = 0.1 Ce^{3+} substituted LZP. Lithium-ion transference number obtained by direct current polarization for $Li_{1.1}Zr_{1.9}Ce_{0.1}(PO_4)_3$ is 0.87, confirming the strong ionic conducting existence of the solid electrolyte.

1. Introduction

Rechargeable lithium-air battery is a promising power for electric vehicles, because its theoretical energy density is much higher than that of traditional batteries and the cost of materials is lower [1, 2]. Up to now, the two types of lithium-air batteries widely studied and reported by researcher are non-aqueous lithium-air battery and aqueous lithium-air battery respectively. Although the energy density of the lithium-air battery in the aqueous system is lower than that of the non-aqueous battery, it can overcome the defects of the non-aqueous lithium-air battery, such as the corrosion of Li metal by the water and carbon dioxide in the open air environment, the precipitate of the reaction products with high resistance in the discharge process and the high polarization of the Li_2O_2. In the lithium-air battery of aqueous system, due to the violent reflection of the lithium metal in the water solution, a solid electrolyte of lithium ion conductor is needed as the protective layer to isolate the lithium electrode from the aqueous electrolyte and the external environment [3,5]. Although several groups have reported broad range of inorganic solid electrolytes, the development of solid electrolyte membranes with good ionic conductivity and chemical stability in aqueous solutions (as in the case of hybrid Li-air batteries) having wide pH range is challenging [6, 7]. Ever since NASICON was first prepared by Goodenough and Hong in1976 [8], its unusual structure has attracted the interest of a number of researchers with regards to its preparation, properties and potential applications .This structure is characterized by corner sharing PO_4 tetrahedra and ZrO_6 octahedra that create a 3-D network of channels through which lithium ions can be transported [9]. Morespecifically,twoZrO_6 octahedra are separated by three PO_4 tetrahedra ,with which they share corner oxygen atoms and two distinct of Li sites : a Li1site located between two octahedra on the c-axis, and a Li2 site located midway between two Li1sites along the a-axis [10]. Aliovalent substituted-$LiTi_2(PO_4)_3$ and $LiGe_2(PO_4)_3$ solid electrolytes exhibit impressive ionic conductivity (>10-4 S/cm) [11,12]. However, the Ti^{4+} and Ge4+ ions in these materials are getting reduced against lithium metal or lithiated graphite anode, which limits their application in lithium batteries [13].High ionic conductivity is the most important property for solid-electrolytes in rechargeable battery technologies. The ionic conductivity in the range of ~ 10-5 S/cm is sufficient for the solid electrolytes to be used thin film micro-batteries since the device current densities are very low [14].Substitution of Zr^{4+} cations in LZP with ions of different radii and valence states tunes the hopping tunnel size for Li+ ions, leading to enhanced Li ion mobility .This paper explores the effects of substitution of Ce^{3+} (ionic radii: 1.03 Å) for Zr^{4+} (ionic radii: 0.72 Å), in LZP on the Structure and ionic conductivity .

2. Experimental Procedure

$LiZr_{2-x}Mx(PO_4)_3$ [M = Ce^{3+} for Zr^{4+}; x = 0, 0.05, 0.1 and 0.2] compounds were synthesized via sol-gel method using ciritic acid as a chelating agent. All precursors such as LiCOOCH3, Ce2O3/COOCH3, ZrO2, and NH4H2PO4 were dispersed in an aqueosus citric acid solution in stochiometric ratio except LiCOOCH3(12 % excess). To this solution, ethylene glycol having molar ratio of 1:1 to citric acid was added and stirred for 16 h at 90°C.The premixed final solution was kept at 200°C for 16 h for gelation. The gel obtained was then heat treated at 600°C and 1100°C for 10 h (heating/cooling rate: 7°C/min) .The powders obtained were pressed at 20t into cylindrical pellets with 3 mm thick and 10 mm diameter. Pellets were sintered at 1250°C for 20 h in air at a heating/cooling rate of 5°C/min to obtain the solid electrolytes. The X-ray diffraction patterns were recorded at room temperature with a D8-Advance Diffractometer of Bruker AXS (CuKa radiation) equipped with a curved graphite monochromator in the secondary beam. The data were collected in the 10°-70°(2θ) range in steps of 0.02° and a counting time of 16 s per step. The refinement of the structure by the Rietveld method was performed using the TOPAS 3.0 software .The surface morphologies of the pellets were observed with scanning electron microscopy on a PHILIPS XL 30 apparatus. For conductivity measurements, the either side of pellet's surface was sputtered with gold. Li/pellet/Au cells were used for cyclic voltammetry measurements. Solid electrolyte pellets coated with gold on either side of its surface was used for the determination of lithium-ion transference number by direct current polarization method. Impedance measurements were done from room temperature up to 423 (K); a Hewlett Packard 4284 (A) apparatus was used, in a frequency range from 20 (Hz) to 1 (MHz) and with an oscillating voltage of 100 (mV).

3.Results and Discussion

Figure1.shows the powder X-ray diffraction (XRD) patterns obtained for various compositions of $Li_{1+x}Zr_{2-x}Ce_x(PO_4)_3$ [x = 0 , 0.05 , 0.1 , 0.2] at room temperature. The X-ray Bragg peaks in all these patterns could be indexed to a NASICON type rhombohedral structure R-3c.

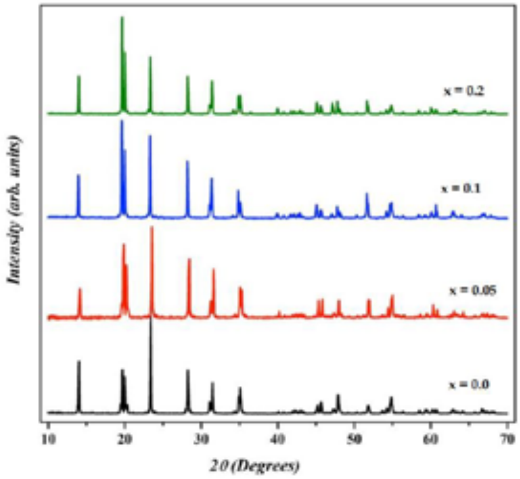

Figure 1. Powder X-ray patterns for $Li_{1+x}Zr_{2-x}Ce_x(PO_4)_3$ samples

The structural refinements were carried out with a polynomial function for the background , pseudo-voigt function for the peak shape; the other refined parameters include scale factor , lattice parameters, atomic coordinates and isotropic thermal parameters. The unit cell parameters determination was obtained by full pattern decomposition according to the Lebail method. Starting structural parameters for Rietveld refinement were taken from the usual NASICON data in the R-3c space group. The zirconium and cerium cations were assumed to be randomly distributed over the same crystallographic site, with the respective occupancies corresponding to the nominal composition . For example, the final Rietveld plot for the composition x = 0.1 is presented in Figure 2.The unit cell parameters for the compound $LiZr_2(PO_4)_3$ (x = 0) are in good agreement with those reported in previous works [15].

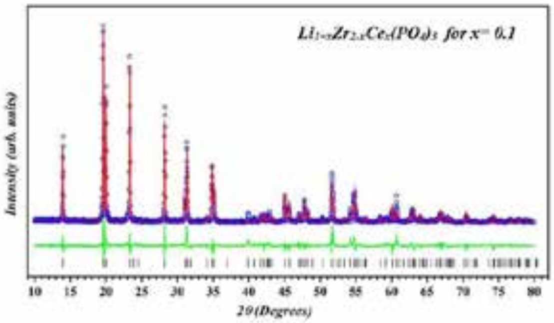

Figure 2. Rietveld refinement of powder XRD patterns for $Li_{1+x}Zr_{2-x}Ce_x(PO_4)_3$ with x= 0.1

Figure 3 displays the effect of cerium content on the lattice constants of $Li_{1+x}Zr_{2-x}Ce_x(PO_4)_3$ (LZCeP).A gradual increment in the lattice constants (a&c) and cell volume (V) with increase in x is seen. Increase in lattice parameters with x could be attributed to the size difference between Ce^{3+} and Zr^{4+} cations. As ionic radii of Ce^{3+} (1.03 Å) is considerably larger than that of Zr^{4+} (0.72 Å), the incorporation of larger Ce^{3+} into the lattice would lead to an expansion in the unit-cell [16].

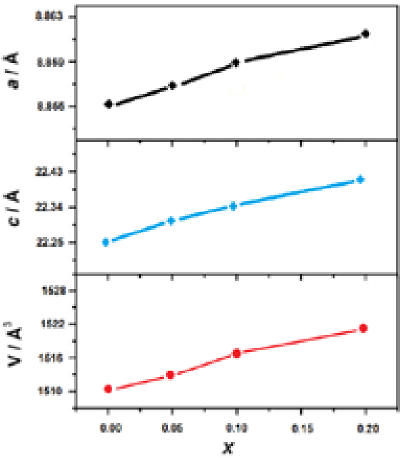

Figure 3. Evolution of the unit cell constants vs. x for $Li_{1+x}Zr_{2-x}Ce_x(PO_4)_3$

Alamo et al. have reported the stabilization of rhombohedral phase at room temperature in LZP powders synthesized at 1250 °C via solgel route [17]. However, our attempts to synthesize LZP powders at various calcination temperatures between 1100 °C to 1300 °C, invariably resulted in c-1 and R-3c mixed phase. Rhombohedral α-$LiZr_2(PO_4)_3$ phase is known to be stable above 70 °C and transforms into a triclinic α' modification below that temperature [18]. Doping with aliovalent cations is known to change the structural phase transition temperature in various inorganic compounds by varying the structural distortion levels. Rhombohedral to triclinic structural transition in LZP is due to the movement of Li to the 4-fold-oxygen coordinated M″ position which lies midway between M′1 and M′2 sites of rhombohedral R-3c NASICON structure Figure3. Substitution of smaller Zr^{4+} by larger Ce^{3+} changes the distortion of MO_6 octahedra and could facilitate the disordered distribution of Li1 and Li2 around the 6-fold coordinated M′1site [19]. Furthermore, increase in Ce^{3+} content (x) is accompanied by the increase in the number of Li atoms in unit cell for charge balancing. This leads to more Li^+ occupying hitherto empty M′ sites and resultant higher symmetry.

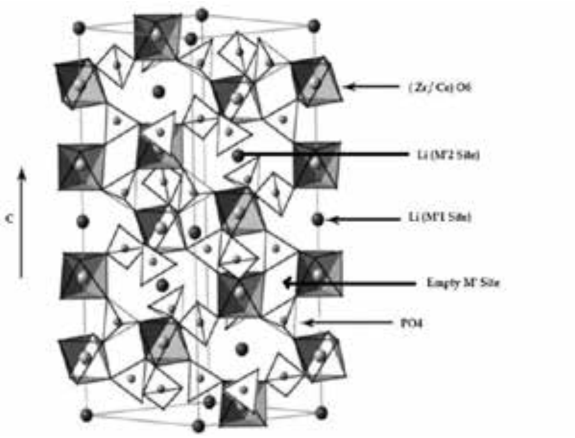

Figure 3. Schematic representation of the LiZr2(PO4)3 with rhombohedral NASICON-type structure.

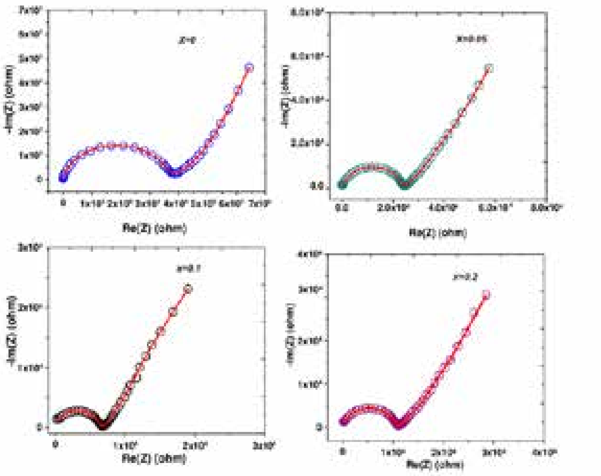

Figure 5. Representative Nyquist impedance plots of LZCeP (x=0, 0.05, 0.1, 0.2) recorded at 30 °C. Scattered open symbols are measured data and the solid red lines are fitted data.

Figure 4 shows the SEM images recorded for the sintered pellets of $Li_{1+x}Zr_{2-x}Ce_x(PO_4)_3$ for different values of x. Grains of various sizes with significant inter-grain pores are seen for $LiZr_2(PO_4)_3$ (x=0) pellet sintered at 1250 °C for 20 h. The maximum relative density obtained for the LZP pellet is ~85%.

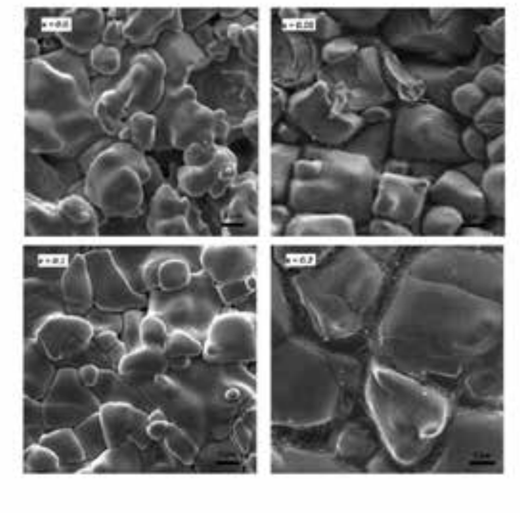

Figure 3. SEM images of surface microstructure for $Li_{1+x}Zr_{2-x}Ce_x(PO_4)_3$ ceramics sintered for 15 h.

There is a noticeable decrease in inter-grain pores and an increase in average grain size in Ce^{3+} doped pellets. Decrease in pores there by significant improvement in the relative density was observed upon substitution of Ce^{3+} for Zr^{4+} with composition $Li_{1.1}Zr_{1.9}Ce_{0.1}(PO_4)_3$ i.e. x = 0.1 and estimated to have a density of ~ 95%.

There is a considerable degree of increment in average grain size as well as decrease in pores thereby significant improvement in the relative density was observed upon substitution of Ce^{3+} for Zr^{4+}. For x = 0.2, grains are significantly bigger and a grain boundary phase is noticeable though presence of such phase was not detected in XRD analysis. The relative density of pellet initially increases from 85% to 95% on doping (for the x = 0 to 0.1), but decreases to 92% when x = 0.2.Presence of larger grain boundaries could be responsible for the slight reduction in relative density for x = 0.2 [20].

Typical Nyquist impedance plots for LZCeP (for x=0 - 0.2) measured at 30 °C are shown in Figure 5. The Nyquist plots show a single semicircular arc at higher frequency region and a tail at a lower frequency region for all samples. The impedance characteristics of polycrystalline materials are expected to be composed of grains, grain boundaries and sample-electrode interfaces [21]. Tail observed at lower frequency side represents the impedance response due to the blocking electrode, a characteristic feature expected for ionic conductors [22,23].Typical capacitance values (10^{-11} to 10^{-10} F) estimated from semicircular arcs presented in Figure 6 suggest that the high frequency response stems from bulk of samples.

As only a single depressed semicircle is observed for all samples, deconvolution of grain and grain boundary conductivities is not possible. Bulk (grain + grain boundary) electrical conductivity was calculated from the bulk resistivity, which is derived by fitting the complex impedance data to an equivalent circuit model $(Q_BR_B)Q_{ELE}$ (shown as an inset in Figure 6 ; here R_B and Q_B represent the resistance and constant phase element associated with the bulk of the sample respectively and Q_{ELE} is the constant phase element of blocking electrodes .

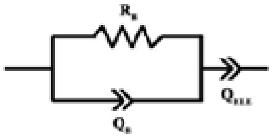

Figure 6. Equivalent circuit model $(Q_BR_B)Q_{ELE}$

The bulk conductivity is calculated from the R_B and sample dimensions by using the equation , $\sigma = (R_b \times \frac{t}{A})$ (where t and A: thickness and surface area of the sample, respectively). The total conductivity values at 30°C for all the compositions of LZCeP (x=0, 0.05, 0.1, 0.2) are provided in Table 1. LZP (x=0) compound exhibits bulk conductivity of 8.67 x 10^{-7} S/cm at 30°C .

Table 1. Chemical analysis of the Material (wt%)

Sample	x = 0.0	x = 0.05	x = 0.1	x = 0.2
σ_{RT} S/cm)	8.67 x 10^{-7}	3.24 x 10^{-6}	6.32 x 10^{-5}	4.85 x 10^{-5}
E_a (eV)	0.55 ± 0.01	0.50 ± 0.01	0.44 ± 0.01	0.48 ± 0.01

LZP (x=0) compound exhibits bulk conductivity of 8.67 x 10^{-7} S/cm at 30°C. For Ce^{3+} incorporated LZP, the bulk conductivity increases to 6.32 x 10^{-5} S/cm for x = 0.1 and decreases to 4.85 x 10^{-5} S/cm for x = 0.2 at 30°C (RT).

Figure 7 shows the temperature dependences of bulk conductivity and activation energy of LZCeP solid electrolytes with various x values. The temperature dependences of conductivity plot between ln(σ) vs.1000/T was fitted and adheres a linear relationship with temperature. Substitution of trivalent Ce^{3+} for tetravalent Zr^{4+} introduces one extra Li+ in the unit cell and thus an improved ionic conductivity is anticipated in LZCeP (for x = 0.1). Further, the change in grain boundaries causes a small drop in the ionic conductivity when x = 0.2 as seen in Figure 5 [24].

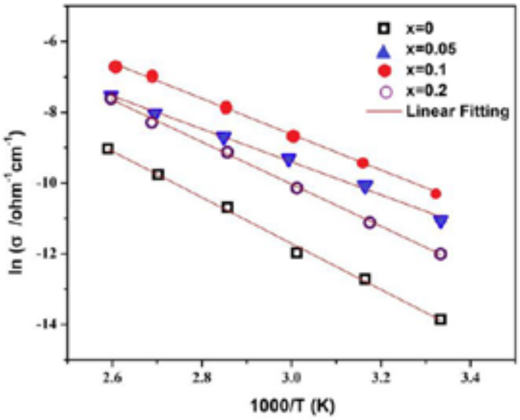

Figure 7. Temperature dependence of conductivity of $Li_{1+x}Zr_{2-x}Ce_x(PO_4)_3$.
Solid lines are linear fit to Arrhenius equation.

The electrical conductivity of $Li_{1.1}Zr_{1.9}Ce_{0.1}(PO_4)$ was calculated from the current obtained by appling a DC voltage of 500 mV as shown in Figure 8 . Initially, there is a rapid decay of the direct current, which attains steady state over time. The measured current over time reaches steady-state is only because of electrons and holes as Au electrodes coated on either side of the pellet block Li ions [25,26]. The electronic conductivity was calculated to be ~10^{-8} S/cm (cf. ionic conductivity is ~10^{-5} S/cm) and the transference number is close to 1. This demonstrates the ionic conducting nature of the Ce^{3+} substituted LZP.

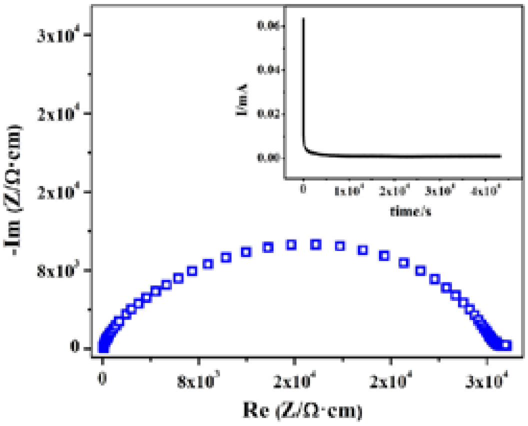

Figure 7. Impedance plots recorded at room temperature for $Li_{1.1}Zr_{1.9}Ce_{0.1}(PO_4)_3$ using metallic lithium electrodes.
Inset shows the DC polarization curve for
$Au/Li_{1.1}Zr_{1.9}Ce_{0.1}(PO_4)_3/Au$
cell under an applied voltage of 500 mV.

In order to evaluate the electrochemical stability for $Li_{1.1}Zr_{1.9}Ce_{0.1}(PO_4)_3$, cyclic voltammetry was performed in the cell confugration of Li / $Li_{1.1}Zr_{1.9}Ce_{0.1}(PO_4)$ /Au. The cyclic voltammograms recorded for the cells at different anodic cut-off potentials are shown in Figure 8. The voltammograms reveal that the $Li_{1.1}Zr_{1.9}Ce_{0.1}(PO_4)$ has electrochemical stability up to ~ 4.0 V vs. Li and starts showing additional degradation peaks when scanned up to 5.0 V. Peaks appearing at the cathodic potentials due to the formation of Au-Li alloy and Li stripping from the alloy [27] validate the Li ion conducting nature of $Li_{1.1}Zr_{1.9}Ce_{0.1}(PO_4)$ at room temperature.

Conclusion

In summary, we successfully synthesized $Li_{1+x}Zr_{2-x}Ce_x(PO_4)_3$ samples with x= 0, 0.05, 0.1, and 0.2 by a sol-gel route.XRD patterns of the solid electrolytes show stabilization of pure rhombohedral R-3c phase for both LZP and Ce^{3+} substituted LZP at room temperature and increased the room temperature ionic conductivity from 8.67 x 10^{-7} S/cm for LZP to 6.32 x 10^{-5} S/cm for sample with x=0.1. DC polarization measurement proves that the transference number of solid electrolytes is close to 1 and the electrolytes are ion conductors with negligible electronic conductivity. The cyclic voltammetry data reveal that the LZCeP (x=0.1) exhibits an electrochemical stability window of up to ~ 4.0 V vs. Li.

References

[1] B. Dunn, H. Kamath, J.-M. Tarascon, Science 334 (6058) (2011) 928.

[2] S.J. Visco, E. Nimon, in: J. Garche (Ed.), Encyclopedia f Electrochemical Power Sources, Elsevier, Amsterdam (2009)376–383.

[3] G. Girishkumar, B.McCloskey, A.C. Luntz, S. Swanson,W.Wilcke, J. Phys. Chem. Lett.1 (14) (2010) 2193.

[4] Y. Shao, F. Ding, J. Xiao, J. Zhang, W. Xu, S. Park, Adv. Funct. Mater. 23 (8) (2013) 987.

[5] X. Wang, Y. Hou, Y. Zhu, Y. Wu, R. Holze, An Aqueous Rechargeable Lithium Battery Using Coated Li Metal as Anode, Sci. Rep., 3 (2013) 1 – 5.

[6] P. Knauth, Inorganic solid Li ion conductors: An overview, Solid State Ionics, 180 (2009) 911 – 916.

[7] N. Kamaya, K. Homma, Y. Yamakawa, M. Hirayama, R. Kanno, M. Yonemura, T. Kamiyama, Y. Kato, S. Hama, K. Kawamoto, A. Mitsui, A lithium superionic conductor, Nat. Mater. 10 (2011) 682 – 686.

[8]J.W.Fergus,Iontransportinsodiumionconductingsolidelectrolytes,Solid StateIon.227(2012)102–112.

[9] P.Yadav, M.C.Bhatnagar, Structural studies of NASICON material o fdifferent compositions by sol–gel method, Ceram. Int.38(2012)1731–1735.

[10] L. Wang,R.V.Kumar,AnewSO2 gas sensor based on an Mg2þ conducting solid electrolyte,J.Electroanal.Chem.543(2003)109–114.

[11] E. Kazakevičius, A. Určinskas, A. Kežionis, A. Dindune, Z. Kanepe, J. Ronis, Electrical properties of Li1.3Ge1.4Ti0.3Al0.3(PO4)3 superionic ceramics, Electrochim. Acta 51 (2006) 6199 – 6202.

[12] H.S. Jadhav, R.S. Kalubarme, A.H. Jadhav, J.G. Seo, Highly stable bilayer of LiPON and B2O3 added Li1.5Al0.5Ge1.5(PO4)3 solid electrolytes for non-aqueous rechargeable Li-O_2 batteries, Electrochim. Acta 199 (2016) 126 – 132.

[13] S. Hasegawa, N. Imanishi, T. Zhang, J. Xie, A. Hirano, Y. Takeda, O. Yamamoto, Study on lithium/air secondary batteries—Stability of NASICON-type lithium ion conducting glass– ceramics with water, J. Power Sources 189 (2009) 371 – 377.

[14] E. Quartarone, P. Mustarelli, Electrolytes for solid-state lithium rechargeable batteries: recent advances and perspectives, Chem. Soc. Rev. 40 (2011) 2525 – 2540.

[15] F. Sudreau, D. Petit, J.P. Boilot, J. Solid State Chem. 83 (1) (1989) 78.

[16] R.D. Shannon, Acta Crystallogr. 32 (1976) 751.

[17] J. Alamo, J.L. Rodrigo, Solid State Ionics 32–33 (Part 1) (1989) 70 0.

[18] M. Catti, A. Comotti, S. Di Blas, Chem. Mater. 15 (8) (2003) 1628.

[19] M. Catti, S. Stramare, R. Ibberson, Solid State Ionics 123 (1–4) (1999) 173.

[20] H. Xie, Y. Li, J. B. Goodenough, NASICON-type $Li_{1+2x}Zr_{2-x}Ca_x(PO_4)_3$ with high ionic conductivity at room temperature, RSC Adv. 1 (2011) 1728-1731.

[21] J.T.S. Irvine, D.C. Sinclair, A.R. West, Adv. Mater. 2 (3) (1990) 132.

[22] H. Xie, Y. Li, J.B. Goodenough, RSC Adv. 1 (9) (2011) 1728.

[23] R. Murugan, V. Thangadurai, W. Weppner, Angew. Chem. Int. Ed. 46 (41) (2007) 7778.

[24] R. D. Shannon, Revised effective ionic radii and systematic studies of interatomic distances in halides and chalcogenides, Acta Cryst. 32 (1976) 751 – 767.

[25] V. Thangadurai, W. Weppner, Determination of the Sodium Ion Transference Number of the Dion−Jacobson-Type Layered Perovskite NaCa2Nb3O10 Using ac Impedance and dc Methods, Chem. Mater. 14 (2002) 1136 – 1143.

[26] V. Thangadurai, W. Weppner, Li6ALa2Ta2O12 (A = Sr, Ba): Novel Garnet-Like Oxides for Fast Lithium Ion Conduction, Adv. Func. Mater. 15 (2005) 107 – 112.

[27] M. Kotobuki, K. Kanamura, Ceramics International, 39 (2013) 6481 – 6487.

IMMC 2021
"in Digital Platform"

20th
INTERNATIONAL
METALLURGY
MATERIALS
CONGRESS
10-12 June
2021
"in Digital Platform"

Advanced Alloys and Processes for Aerospace

immc2021

Effect of Cold Rolling on the Shape Memory Behavior of Ni Rich NiTiHf High Temperature Shape Memory Alloy

H. Onat TUGRUL, Ogulcan AKGUL, Mustafa S. VELIPASAOGLU, Benat KOCKAR

Hacettepe University

Turkey

1. Introduction

Shape memory alloys are promising actuator replacements in aerospace industry due to their higher work-output to weight ratio via shape changing ability with phase transformation. Nickel Titanium is the most studied shape memory alloy with highest strain recovery values, between 50°C -100°C temperature interval [1]. Since operational temperatures for aerospace applications are higher due to extreme conditions, High Temperature Shape Memory Alloys (HTSMA's) with transformation temperatures above 100°C, have gained attention for the last two decades. Among all, NiTiHf alloys have higher strength with reasonable toughness and Ni rich NiTiHf alloys are suitable for precipitation hardening which also enables tailoring of transformation temperatures [1,2]. In this work, effect of cold rolling on precipitation hardened Ni50.3Ti29.7Hf20 HTSMAs' functional loading capacity is presented using isobaric testing.

2. Materials and Methods

NiTiHf billet is cast from pure elements in vacum induction melting and as cast billet is solutionized at 1050 °C for 2h under high purity argon atmosphere. Flat samples having 45 mm length and 1 mm thickness are cut by Wire ElectroDischarge Machining (WEDM) equipment for cold tolling operation. Cold rolled samples are mechanically deformed using a laboratory sized rolling machine to 5% deformation (CR5) and 10% deformation (CR10). All samples are aged for 3 hours at 550°C as optimal aging condition [2] and tensile test specimens are cut with WEDM from the cold rolled flat samples.

Isobaric tests are conducted using universal tensile-compression machine which was modified in house. The samples are heated above the austenite finish temperatures, loaded to the predetermined stress magnitude and cooled down below the martensite finish temperatures. Heating is controlled with resistive heaters attached on grips and constant cooling is applied on the grips using waterflow through copper tubes wrapped on the remaining part of the sample grips. For control of heating-cooling, industrial Autonics controller is used so that heating and cooling rates remain as 10°C per minute. Grips and the samples are covered with thermal blankets to stabilize the heat loss. Strain values are measured by an Epsilon high temperature extansometer mounted on samples. Temperature values are collected by a J type 1 mm thick thermocouple mounted on the middle of the gauge section of the samples.

3. Conclusion

Solutionized (S) specimen showed the highest transformation strain in any loading condition but failed under 400 MPa during loading. Solutionized and Aged (S-A) sample presented the second highest tranformation strain which was successfully loaded up to 500 MPa. On the other hand, Cold Rolled samples have lower transformation strains and broader thermal hysteresis. Contrary to expectation, CR5 sample failed under 500 MPa loading while CR10 sample failed at 700 MPa loading. Increasing deformation percentage increased martensite start to martensite finish range and recoverable strain of CR10 was less than half of the recoverable strain of solutionized and aged sample. Isobaric tests have shown that cold rolling is suppressing tranformation strains such that even at higher stress magnitudes transformation and actuation strain values of Cold Rolled Samples are about half of the values of Solutionized-Aged sample.

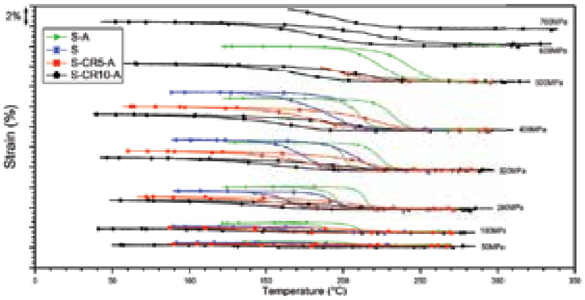

Figure 1. Isobaric Test Results Comparison

References

[1] J. Ma, I. Karaman and R.D. Noebe, International Materials Reviews, 55 (2010), 257-315

[2] H.E. Karaca, S. M. Saghaian, G. Ded, H. Tobe, B. Basaran, H. J. Maier, R.D. Noebe and Y. I Chumlyakov, Acta Materialia, 61 (2013), 7422-7431

The Effect of Lattice Periodicity on the Compression Behavior of the E-Beam Melted Bcc-Like Ti6Al4V Lattices

Alican Tuncay ALPKAYA[1], Burak HIZLI[1], Burcu ARSLAN HAMAT[2], Hakan YAVAŞ[2], Ahmet Alptuğ TANRIKULU[2], Mustafa GÜDEN[1]
[1]İzmir Institute of Technology, [2]Turkish Aerospace Industries
Turkey

Abstract

Experimental and numerical studies were performed to determine the constitutive equation of an EBM-produced Ti6Al4V alloy. The determined equation was then used to model a BCC-like lattice structure with different number of cells and strut diameter to verify the fidelity of the determined equation. The effect of the number of cells on the crushing behavior was determined both experimentally and numerically.

1. Introduction

The research on additively manufactured (AM) metallic alloy parts has increased in aerospace and biomedical industries where material performance is of primary importance [1]. Additive manufacturing has the capabilities of manufacturing parts in near-net shape almost with no geometrical constraints and reduces pro- and post- processing steps significantly. Now with this, intricate lattice structures suitable for impact load mitigation can be constructed easily. Both selective laser melting (SLM) and electron beam melting (EBM) are available methods for AM metallic alloys parts, while the latter is advantageous due to its faster manufacturing capabilities with low residual stresses [2]. The use of accurate material constitutive equations for AM-processed structures is of primary concern to correctly predict the deformation behavior particularly under varying loading rates. Currently, both 316L and Ti6Al4V (Ti64) are widely investigated alloys for industrial applications. There have been studies on the determination of the constitutive equations of SLM-manufactured Ti64 such as ref [3]. One problem regarding the extraction of constitutive relations is the difficulty in testing EBM-fabricated alloys, as they are inherently very brittle. Because of this, the results of the numerical mechanical models on EBM-fabricated Ti64 alloys showed significant divergence although the samples tested were produced using similar processing parameters. In this study, experimental and numerical studies were performed to determine the constitutive equation of an EBM-produced Ti6Al alloys. For that, compression and tension tests on the samples varying in sizes were conducted at a quasi-static strain rate of 10^{-3} s^{-1}. The determined equation was then used to model BCC-like lattice structures constructed with varying number of cells to verify the fidelity of the equation. The effect of the number of cells on the crushing behavior was determined both experimentally and numerically.

2. Experimental and numerical model

BCC-like lattice structures were designed via CATIA v6 and manufactured using Ti64 (ELI) powder (30-110 μm) in 27 unit cells with 1 mm constant strut diameter and 5 mm strut length and 8, 27, 64 and 125 unit cells with 2 mm constant strut diameter and 10 mm strut length in an Arcam Q20+ EBM printer. The powder bed tray was heated to 650°C during entire production. The processing parameters used were the parameter set by the producer. The first lattice structure was used to verify the constitutive equation derived and the second was to determine the effect of number of cells and strut size on the crushing behavior. The position of lattice in the 3D printer in x, y and z-axis is schematically shown in Fig. 1(a). The building direction is the z-axis. All lattices were processed with 2 mm-thick face sheets along y-axis, (Fig. 1(a)). The compression tests were performed parallel to y-axis. The fabricated 2 mm diameter strut lattices were 20x24x20 mm, 30x34x30 mm, 40x44x40 mm and 50x54x50 mm (in z, x and y-direction) and 1 mm strut lattices with 27 cells were 15x19x15 mm. Cylindrical Ti64 samples were also produced using the same processing parameters with lattices for mechanical tests. The untested and tested Ti64 samples were epoxy mounted, grinded and then polished down to 0.25 µm using diamond solutions. Vickers Hardness tests were performed on the polished surfaces of mounted samples in a Shimadzu Micro Vickers Hardness Tester under 4.9 N for 10 ms. The density of EBM-produced samples (5 repeating measurements) was determined by the Archimedes method.

Quasi-static uniaxial tension tests were performed on EBM-fabricated dog-bone shaped Ti64 tension test samples machined in accord with ASTM-E8/E8M-16. These test samples were machined from EBM-fabricated Ti64 bars, 7 mm and 5 in diameter and 80 mm in length. The long axes of bars were the building direction (z-axis). The tensile test specimens were machined from these bars in 5 mm diameter 25 mm gage length. Compression test samples having 0.8, 1, 2 and 3 length to diameter ratios (L/D) but a constant diameter of 6 mm were machined from EBM-fabricated Ti64 bars in 7 mm diameter. Both tension and compression tests were performed in a displacement-controlled SHIMADZU AG-250 kN test machine at 1x10^{-3}, 1x10^{-2} and 1x10^{-1} s^{-1}. At least, two tests were performed for each group of samples at a specified strain rate. A video extensometer was used measure the displacement in the tension and compression tests. The determined true stress-strain curves were fitted with the simplified Johnson and Cook (JC) stress equation given as,

$$\sigma = [A + B\varepsilon^n]\left[1 + c\ln\left(\frac{\dot{\varepsilon}}{\dot{\varepsilon}_0}\right)\right] \tag{1}$$

where, σ is the equivalent stress, ε equivalent plastic strain, $\dot{\varepsilon}$ and $\dot{\varepsilon}_0$ are sequentially the strain rate and reference strain rate and *A, B, C* and *n* are the constants. The compression tests on lattices was performed in the y-axis at 1x10^{-3} s^{-1}.

The quasi-static uniaxial compression tests of lattices were modelled in the LS-DYNA at the same strain rate with the experiments, 1x10^{-3} s^{-1}. The schematic of a lattice model composing of 64 cells is shown in Fig. 1(b). Tool-steel top and bottom compression test platens of the test machine were modelled using 500 constant stress solid elements (8x8 mm) and MAT_020_RIGID material model (E=210 GPa, ρ=7800 kg m^{-3} and υ=0.33). 3D lattice models were constructed using 190000, 560000, 1280000 and 2800000 one-point nodal pressure tetrahedron (0.74 mm long) elements with a constant element density of 0.4 mm and the MAT_098_SIMPLIFIED_JOHNSON_COOK (J-C) flow stress model. Flanagan-Belytschko stiffness form was further used in order to take into account the hourglass effect. The contact between lattices and the compression test platens was defined by the AUTOMATIC_SURFACE_TO_SURFACE, while the ERODING_SINGLE_SURFACE contact was used for the contact between struts. There are 3 edges in the model as depicted in Fig. 2: (i) cell edge (where 4 struts meet), (ii) cell surface edge (where two struts meet) and (iii) cell face sheet edge (where two struts meet at the face sheet). The static and dynamic friction coefficients in the models were taken 0.3 and 0.2, respectively. In order to model the quasi-static deformation in the LS-DYNA, mass scaling was implemented by using the CONTROL_TIMESTEP card. Lastly, an erosion criterion of PSFAIL (effective plastic strain at failure) determined nearly 0.4 from the compression tests at 1x10^{-3} s^{-1} was used to model the failure of struts. The strut diameters of the as-fabricated-Ti64 lattices were noted to vary locally. In 1 mm-diameter strut lattices, the smallest diameter measured was 0.97 mm and the thickest one is 1.628 mm. In the 2 mm-diameter strut lattices, the smallest diameter was 1.89 mm and the thickest one was 2.2 mm. The strut diameters were altered in the models with the measured thinnest section.

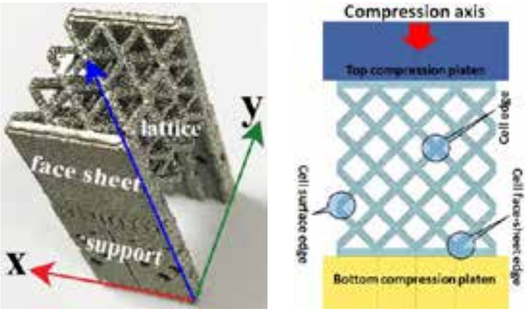

Figure 1. (a) 1 mm strut diameter lattice with 27-cell and (b) the compression test model

3. Results and Discussion

The average density of tensile test EBM-Ti64 was determined 4317±0.017 kg m^{-3} and the average porosity 2.6473±0.377% by taking the density of bulk Ti64 4429 kg m^{-3} determined by the Archimedes method. The hardness across (through z-axis) varies between 366 and 380 HV until about a distance of 17 mm from the base plate of the used 3D-printer. After about 17 mm, the hardness decreases to an average value of 355 HV. The hardness measurements through diameter also confirm a high hardness value near the base plate with an average value of 345 HV, which is slightly lower than the average hardness in the x-y plane when the height is higher than 17 mm. The hardness values show an anisotropy between x-y plane and z-direction. The anisotropy was found as much as 33 MPa at a 17 mm distance or more from the base plate. Therefore, the lattices were produced with the supports having a length of 17 mm. The compressive strengths and failure strains were affected by the sample L/D ratio. As the L/D ratio decreased from 3 to 0.8, both the maximum stress and failure strain increased. The proportional limit is determined 935 MPa at aspect ratio one. Tensile true-stress strain curves of EBM-Ti64 and Ti64 rod (conventional) are shown in Fig. 2 together with the compression stress-strain curve of EBM-Ti64 at 1x10^{-3} s^{-1}. EBM-Ti64 shows a relatively brittle tensile behavior, fracturing at low strains (0.015-0.036) without showing necking, while conventional Ti64 samples fracture at larger strains after necking at 0.08 strain. The failure stresses of EBM-Ti64 and conventional-Ti64 are however similar, 1090 MPa. The compressive flow stresses are slightly higher than tensile flow stresses. Both the tensile and compressive stress-strain curves shown in Fig. 2 are further fitted with Eqn. 1. The yield strength (A) in Eqn. 1 was determined from the tensile test on 5 mm-diameter test samples at 1x10^{-3} s^{-1} as 825 MPa. The determined JC equation parameters are tabulated in Table 1 for both tension and compression, while the parameters determined from tension tests were used in the modelling compression of lattices. The value of *c* was determined from the compression tests performed at different quasi-static strain rates. The compression flow stresses at 0.05 strain was used to extract strain rate sensitivity parameter as the heating effect at the highest strain rate is the lowest at this strain level.

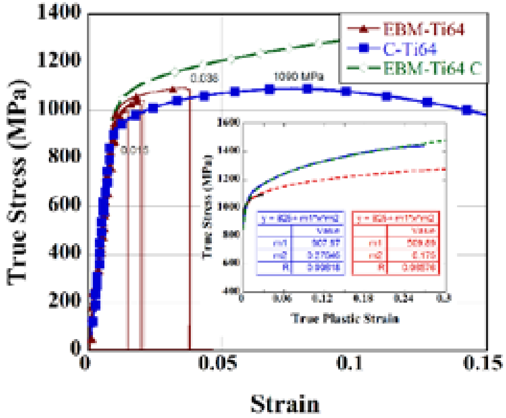

Figure 2. Tensile and compression true stress-true strain curve of EBM-produced and conventional Ti64

Table 1. JC parameters of EBM-produced Ti64

	A (MPa)	B (MPa)	n	c	E (GPa)	υ	ρ (kg m^{-3})
T	825	510	0.175		107	0.31	4350
C	825	910	0.275	0.016			

The experimental and numerical compression stress-strain curves of 1 mm-diameter strut lattices with 27-cell are shown in Fig. 3 together with the experimental and numerical pictures of the deformed lattice cells at various strains. As is seen in Fig. 3, both experimental and numerical lattice cells crush sequentially and progressively starting from either near the top and bottom sections as marked with arrows. The stress localization on the cell edges are also clearly seen in Fig. 3, reaching a maximum stress of 1256 MPa on these cell edges (red sections), corresponding to a stress of 0.4 erosion strain in the JC flow stress model. The initial peak stress in the stress-strain curves in Fig. 3 is taken as the collapse stress. The densification strain was determined by the intercept method. Although, the experimental and numerical collapse stresses are similar, the numerical sample densifies at a larger strain. The experimental compression stress-strain curves of three tests of 2 mm-diameter strut lattices with 27-cell are shown in Fig. 4. The deformation mode of 2 mm-diameter strut cells is very similar to the deformation mode of 1 mm-diameter strut cells: sequential progressive layer crushing. A large difference between the numerical and experimental stresses is noted in 2 mm-diameter strut lattices following the initial peak stress. The experimental cell collapse in 2 mm strut lattices also starts in the third layer from top, but the collapse of this layer results in the fracture of cell edges in layers above as shown by arrows in Fig. 4. While no cell edge fracture is seen in the numerically deformed lattice structure and the third layer fully densifies at 0.3 strain as shown in Fig. 3. The facture of cell edges leads to reduced collapse stresses in 2 mm strut lattices after the initial collapse stress. This also shows that the erosion parameter of 0.4 strain is much lower in 2 mm strut diameter lattices.

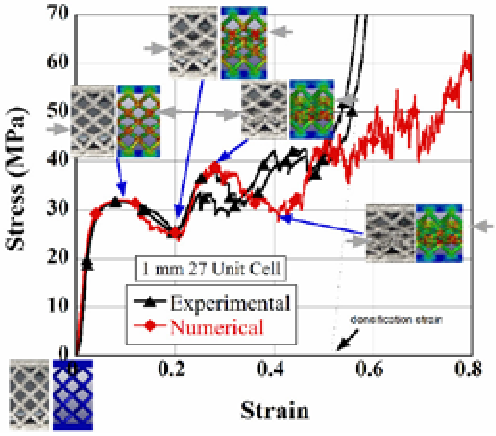

Figure 3. Experimental and numerical compression stress-strain curves of 1 mm strut diameter 27-cell lattices (diameter was taken 0.97 mm)

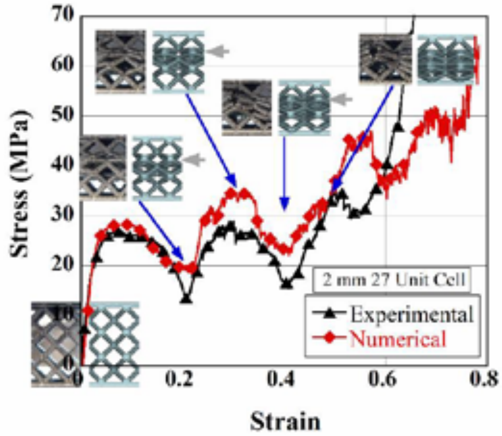

Figure 4. Experimental and numerical compression stress-strain curves of 2 mm strut diameter 27-cell lattices (diameter was taken 1.89 mm)

The experimental compression stress-strain curves of 2 mm strut lattices (with 8, 27, 64 and 125 cells) is shown in Fig. 5. As is seen in the same figure, both collapse stress and densification strain decrease with increasing number cells.

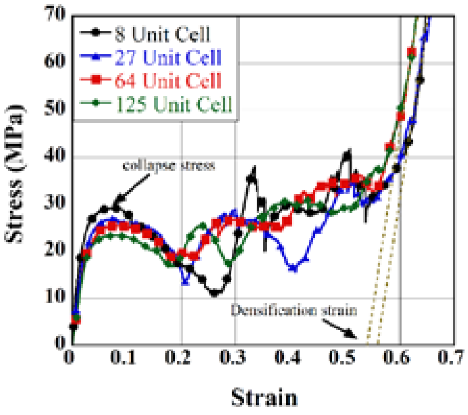

Figure 5. Experimental compression stress-strain curves of 2 mm strut lattices

Fig. 6 shows the experimental and numerical variation of collapse stress and densification strain of 2 mm strut lattices with the volume of test sample. In the same graph, the collapse stress and densification strain of the models without face sheets (NFS) and 1 mm strut lattices are also shown for comparison. Both with and without face sheet model lattices show a constant collapse after 64-cell (4 cells/edge) cells and densification strain after 27-cell. The inclusion of face sheets decreases the collapse stresses at the number of cells lower than this critical number of cells while face sheets have reverse effect. This is resulted from the difference in the layer deformation sequence between the lattices with and without face sheet. As seen in the inset of Fig. 6, the layer crushing starts from the end layers of without face-sheet lattices, while it starts at the mid-layer when face-sheet included. The experimental collapse stresses however continue to decrease after 64-cell. Brittle foams show a size dependent fracture strength, following the Weibull distribution [4]. Larger the size of samples, higher the probability of the existence of larger pores. The experimental collapse stress (σ_c) is fitted with the following equation

$$\sigma_c = C(\frac{V_o}{V})^{1/m} \qquad (2)$$

where, C is a constant, V and V_o are the volume of lattice and the characteristic volume and m is the Weibull modulus. The resultant Weibull modulus is found 12.53 as shown in Fig. 6, In order to validate the Weibull modulus further, the collapse stress of 1 mm lattices is predicted. The predicted collapse stress is 31.51 MPa, which is very similar with the measured experimental average stress of 31.63 MPa. A similar Weibull modulus for an Al foam was previously reported as 8.9 [5]. It was also reported that for size independent modulus of EBM-BCC lattices 1000-cell were required [6]. This study also supports this, when the extrapolation in Fig. 6 is extended to 1000-cell. This result is contrary to the previously determined 5 and 6-cell/edge for size independent properties of Al foams [7]. Finally, the differences between the experimental and numerical results are due to the process-induced porosities in the EBM-fabricated Ti64 lattices, leading to a facture following the Weibull distribution.

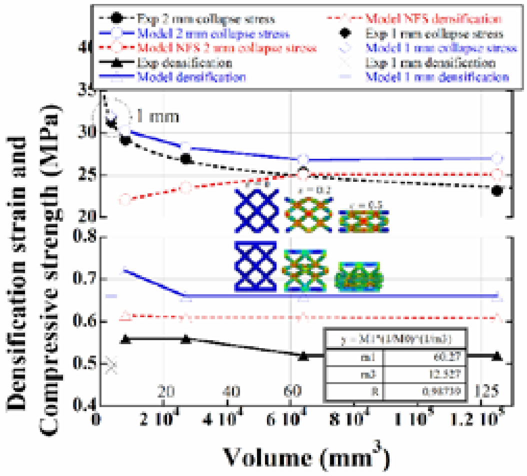

Figure 6. Experimental and numerical collapse stress and densification variation

4. Conclusions

The effect of lattice periodicity on the additively manufactured metal structures was determined experimentally and numerically. Numerically, 4-cell/edge was shown for size independent collapse stress, while experimentally it was more than 5-cell edge. This was ascribed to the presence of porosities in EBM-fabricated Ti64 lattices.

References

[1] J. Parthasarathy, B. Starly, S. Raman, Journal of Manufacturing Processes, 13 (2011) 160-170.
[2] S. Liu, Y.C. Shin, Materials & Design, 164 (2019) 107552.
[3] P. Li, Materials Science and Engineering: A, 622 (2015) 114-120.
[4] W. Weibull, Journal of applied mechanics, 18 (1951) 293-297.
[5] J.S. Blazy, A. Marie-Louise, S. Forest, Y. Chastel, A. Pineau, A. Awade, C. Grolleron, F. Moussy, International Journal of Mechanical Sciences, 46 (2004) 217-244.
[6] I. Maskery, A.O. Aremu, M. Simonelli, C. Tuck, R.D. Wildman, I.A. Ashcroft, R.J.M. Hague, Experimental Mechanics, 55 (2015) 1261-1272.
[7] E.W. Andrews, G. Gioux, P. Onck, L.J. Gibson, International Journal of Mechanical Sciences, 43 (2001) 701-713.

In Situ High Temperature Characterization of 3D-Printed Ti-6Al-4V Alloy

F. R. KASCHEL[1], R. K. VIJAYARAGHAVAN[2], P. McNALLY[2], D. P. DOWLING[1], M. CELIKIN[1]
[1]University College Dublin, [2]Dublin City University
Ireland

1. Introduction

Additive manufacturing is being increasingly used in the fabrication of Ti-6Al-4V parts to combine excellent mechanical properties and biocompatibility with high precision. However, a post-thermal treatment is generally required to obtain sufficient mechanical performance. This study investigates the structural evolution (α' martensite phase decomposition) during the heat treatment of 3D-printed Ti-6Al-4V alloy. The changes in crystal lattice and lattice strain were investigated up to 1000˚C using in situ high temperature X-ray diffraction (XRD). This investigation provides a deeper understanding on the mechanism of phase transformation through martensitic decomposition, as well as on the influence of post-thermal treatment conditions on the crystal structure.

2. Materials & Methods

Additively manufactured Ti64 test samples were produced using the production scale powder bed system, Renishaw RenAM 500M equipment. Stress relaxation and structural evolution were studied via in situ high temperature x-ray diffraction (XRD) using a triple-axis Jordan Valley Bede D1 high resolution XRD system with a Cu-Ka (λ=1.5405 A) radiation source operated at 45 kV and 40 mA. The Bede D1 system was equipped with an Anton Paar DHS 1100 heating stage which allowed in situ temperature dependent measurements in vacuum ($\leq 10^{-5}$ Pa). Samples were heated at a rate of 200°C/min, with a dwell time of 15 minutes before performing a scan at a temperature range of 25 – 1000 °C. XRD peaks were analysed using OriginPro software.

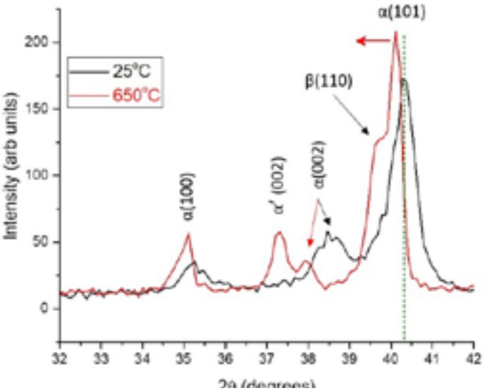

Figure 1 - In situ XRD patterns of the Ti64 as-built sample, obtained after heating to 650°C illustrating the peak splitting and shifting phenomena and the formation of β phase at elevated temperatures.

3. Conclusions

In situ XRD analysis indicated stress relaxation without phase transformation at a temperature range of 25 to 400°C. Above 400°C, martensitic decomposition was initiated and occurred in a step-wise manner. Equilibrium and α-martensitic phases co-exist as α-martensite gradually decomposes. Lattice parameters (*a* and *c*) of the hcp crystal increased linearly between 500 - 700°C causing the crystal structure to fully transform in to α (equilibrium) and β (equilibrium) at 700°C. Heating above this temperature caused a further expansion of the crystal lattice, while maintaining the c/a ratio.

Nature Inspired Macro-Atomistic Design Approach in Additive Manufacturing

Hakan YAVAŞ[1], A. Alptuğ TANRIKULU[1], Alican Tuncay ALPKAYA[2], Mustafa GÜDEN[2]
[1]Turkish Aerospace Industries Inc., [2]İzmir Institute of Technology
Turkey

Abstract

In this study, we propose a guideline to design novel crystal lattices with superior mechanical properties based on predictive simulations and experimental studies to be used in future space applications. A combination of various lattice structures prepared by additive manufacturing technologies emerges as the revolutionary way to enhance simultaneously strength, toughness, and hardness while keeping strength to weight ratio at minimum. We will fully harvest the potential of simulations to predict lattice dynamics and its mechanical properties together with state of the art fabrication methods and mechanical/microstructural characterization at different length-scales. We will be able to produce truly lattice structures with strut geometry, where control of a single strut element is vital to reach structural limits. We will use few pre-selected lattice structures as model examples; however, our ambition is not just to prepare any particular unit cell geometries, but to provide clear evidence that our design concept formulates the basis applicable to a large variety of structural satellite parts. Furthermore, a unique design approach will be implemented into the additive manufacturing flow using crystal plasticity mimicking approach.

Introduction

We will first show how to investigate the design of AM concept via studying mimicry of natural crystal lattices then we will prepare a design guideline that is specific for the AM. As it is well-known that a crystal is composed of atoms arranged in an ordered manner with defined symmetry operations of a unit cell. A single crystal is consisting of unit cells of the same type and orientation but most crystalline materials consist of many grains that are different from their neighbors (polycrystals). Those various geometries and also other intrinsic and extrinsic defects such as dislocations control the deformation kinetics of the materials. Our micro/sub-micron scale materials design route, the mimicry of crystal microstructure of metals on a macroscopic scale by constructing lattices consists of an ordered arrangement of nodes (analogous to atoms) connected by rods (like atomic bonds) by using a computer-aided design package via AM. The deformation behavior of lattices and generated geometries can be modified through the iterative design of the lattice unit cells, giving access to the unprecedented mechanical properties, such high-strength and negative Poisson's ratio. However, work on such materials architectures has focused only on a few small systems or single orientation lattices so a further detailed investigation is needed. Inspiring from nature it is possible to develop damage-tolerant materials architectures by designing strengthening mechanisms analogous to the crystal plasticity. The exploration space for Design for AM (DAM) will firstly focus on the basic crystal lattices implementation on the macro-scale. The selected Bravais lattices are simple-cubic, face-centered cubic (fcc), body-centered cubic (bcc) and hexagonal-close packed (hcp) separately. For example, for the case of the fcc structure, one can easily visualize its formation via Thomson tetrahedron. All in all, we will represent a unique guideline to approach a multivariant design approach to implement next-generation hybrid lattice structures in AM.

Materials and Methods

Parts and representative test samples were built by EBM Q20 plus and Concept Laser SLM machines separately. Several different alloy compositions; i.e. $AlSi_{10}Mg$, 316L stainless steel and Ti-6Al-4V (Tekna Inc., France) alloys were used as starting powder. For each lattice combinations, strut geometries and lattice structures were designed according to geometrical baseline studies. The test samples were oriented at different angles (0-90) to investigate the effects of building envelope and laser-e-beam parameters on lattice deformation kinetics The effects of lattice geometries, strut type and size, part size, surface processing (machining, polishing), and mechanical properties were tested. Characterization studies were done in detail to obtain a relation between the microstructures and mechanical properties.

Conclusion

The exploration space for Design for AM (DAM) will firstly focus on the basic crystal lattices implementation on the macro-scale. The selected Bravais lattices are simple-cubic, face-centered cubic (fcc), body-centered cubic (bcc) and hexagonal-close packed (hcp) separately. For each selected lattice structures detailed mechanical, structural and microstructural tests were done to figure out their future applications in satellite secondary mechanical structures. All in all, we will represent a unique guideline to approach a multivariant design approach to implement next-generation hybrid lattice structures in AM for the space heritage materials a

Acknowledgment This research is part of the TÜBİTAK 1515 Frontier R&D laboratory support programme and is fully financed by TÜBİTAK. In order to learn for more details about the project, please apply/refer to Turkish Aerospace Inc. We thank Bilkent University UNAM for contributing to the microstructural characterization and METU Welding Technology and Non-Destructive Testing Research/Application Center for contribution in the mechanical tests.

Advances in Thermal Barrier Coatings: Current Status and Future Perspectives

Makoto HASEGAWA
Yokohama National University
Japan

Abstract

The turbine inlet temperature (TIT) has been increasing year by year, and currently, a system having a TIT exceeding 1873 K is operating. In the systems with such a TIT, superalloy of the turbine blade has already exceeded its melting point. For this reason, sophisticated and complicated cooling systems are provided to protect components. One of them is called air film cooling, and complicated processing techniques such as air holes formation and so on for components have been developed. Another cooling technique is thermal barrier coatings (TBCs). TBCs are applied to almost all aircraft jet engines and to all high-efficiency, high-temperature turbines for power generation systems. Although TBCs are a well-established technology, research and development to improve its performance, such as heat shielding, durability and lifetime, is still active. Here, the history of research on TBCs and recent technological trends will be introduced. In addition, the degradation, damage and delamination behavior of TBCs will be mentioned. Furthermore, a quantitative evaluation method for delamination resistance and an attempt to improve the delamination toughness of TBCs will be discussed.

Investigation of the Effect of Chemical Vapor Aluminizing Process Time and Heat Treatment on Nickel Aluminide Coating

Ahmet Arda İNCEYER[1],[2], Gökhan GÜVEN[2], Kaan DEMİRALAY[2], Havva KAZDAL ZEYTİN[2], Metin USTA[1],[2]

[1]Gebze Technical University, [2]Materials Institute of Marmara Research Center of The Scientific and Technological Research Council of Turkey

Turkey

1. Introduction

Nowadays, turbine entry temperature of aero-engine is increased up to 1400°C which is higher than the melting point of single crystal nickel-based superalloys (SCNBS). Therefore, the application of thermal barrier coating is inevitable for providing thermal protection of SCNBS [1]. TBCs consist of ceramic top layer, thermally grown oxide layer and bond coat layer (NiAl-nickel aluminide). Chemical vapor aluminizing (CVA) is the most attractive process for NiAl bond coat production. NiAl bond coat is produced under three different conditions with CVA technique which are high temperature-high activity (HTHA), low temperature-high activity (LTHA), high temperature-low activity (HTLA). However, HTHA coating is an attractive process as desired β-NiAl phase can be obtained in a single treatment without requiring any additional heat treatment (HT) process [2]. Therefore, this study aims to examine the effect of HTHA CVA process time and HT process on the microstructure, type of formed phases and hardness of the nickel aluminide coating on CMSX-4 in this study.

2. Materials and Methods

SCNBS CMSX-4 was used for base metal. CVA process was carried out for 4 and 6 hours at 1070°C to produce NiAl bond coat. After CVA processes, HT processes of 4 and 6 hours CVA coatings were performed in CVD reactor at 1050°C for 2 hours. The gas flow Ar and HCl was done during the process. Al-Cr (50 wt% Al – 50 wt% Cr) granules were used for Al source. After the coating and HT processes were completed, NiAl coatings were systematically characterized by SEM (scanning electron microscope, Philips XL30S FEG), XRD (X-ray diffraction, Rigaku Smartlab), EDS, Vickers hardness analyze techniques.

3. Conclusion

The following conclusions can be drawn from this study:
(1) The microstructures of HTHA aluminide coatings consist of the inter-diffusion zone (IDZ) and additive layer (AL). The IDZ layers of 4 and 6 hours CVA coatings include topologically close-packet (TCP) precipitates.
(2) XRD analyzes showed that the main phase of the AL of 4 hours CVA coating is δ-Ni_2Al_3. δ-Ni_2Al_3 phase transforms into β-NiAl with HT process. However, the main phase of the AL of 6 hours CVA coating is β-NiAl before and after HT process. β-NiAl phase formed during 6 hours CVA coating process is stable.
(3) Phase transformation from δ-Ni_2Al_3 to β-NiAl phase decreases the hardness of the AL of 4 hours CVA coating. The hardness values of the IDZ layers of all NiAl coatings is higher than $1000HV_{10}$ due to the presence of TCP phases.

Acknowledgment

Thanks for the supports to all colleagues from Critical Metallic Materials Group of Materials Institute of TUBITAK Marmara Research Center.

References

[1] X. Peng, Metallic Coatings for High-Temperature Oxidation Resistance, Ed. H. Xu and H. Guo, Thermal Barrier Coatings, Woodhead Publishing., 2008 Cambridge, England, pp. 53-74.

[2] H. Rafiee, S. Rastegari, H. Arabi, and M. Mojaddami, Iran. J. Mater. Sci. Eng., 2010, 7(4), 42–49.

Investigation of High Temperature Oxidation Behavior of Additively Manufactured in 939 Alloy

Batuhan BAŞBOZKURT, Cevat SARIOĞLU
Marmara University
Turkey

Abstract
It was aimed to investigate the high temperature oxidation behavior of IN 939 produced by selective laser melting technique and compared to conventionally produced as cast samples. Oxidation tests were carried out at 800, 900 and 1000°C. Weight gain results showed that all samples followed a parabolic oxidation behavior and there was no spallation at 800 and 900°C. 3D samples especially with heat treatment, showed remarkably comparable oxidation performance compared to as cast samples. XRD measurements were also done to reveal oxidation products. Surface morphologies were investigated using stereomicroscope and SEM.

1. Introduction

IN 939 is a high corrosion resistant nickel-based superalloy that is used in land-based gas turbines as blade and vane[1]. It was developed as a high corrosion resistant and strong material, capable of operating temperatures around 850°C for long periods of time[2].

The chemical composition of the IN 939 is as follows, Ni-22.5%Cr-19%Co2%W-1%Nb1.4%Ta-3.7%Ti-1.9%Al-0.15%C-0.1%Zr-0.01%B[3], [4]. The high chromium content makes IN 939 a superior corrosion resistant superalloy, among others. In fact, it has superior corrosion resistance compared with IN 738LC which has 16%Cr and comparable stress rupture properties[5].

IN 939 has been produced by conventional casting methods and used for industrial gas turbines as blades and vanes, also has been discussed to be employed in large structures of aerospace gas turbine engines[6]. However, conventional techniques have limitations when it comes to complex geometries and machining of nickel-based superalloys is very hard since it causes rapid work hardening which is not desirable[7]. Therefore, the search for new manufacturing techniques have raised and consequently adapting additive manufacturing (AM) techniques to produce nickel-based superalloys has been in focus lately.

2. Experimental Procedure

2.1. Samples preparation

IN 939 samples were produced both by casting and SLM method were supplied from TEI (Tusaş Engine Industries). Half of the samples were subjected to a heat treatment such as solution heat treatment at 1160°C± 14°C for 4 hours ± 15 minutes then cooling with a rate faster than air cool, followed by aging at 845°C± 8°C for 16 hours± 30 minutes followed by air cooling. Heat treatments were carried out according to AMS 2774, AMS 2773 (general furnace atmospheres) and AMS 2769 standard (vacuum).

Before oxidation tests, all surfaces were grinded using 180, 320, 500 and 800 grit SiC abrasive paper and then cleaned with ethanol in an ultrasonic cleaner for 15 minutes.

2.2. Oxidation tests

samples were weighed using 0.1mg accuracy phoenix ASN-224 laboratory balance. After weighing, geometrical measurements were done on all samples using a digital micrometer gauge for defining the surface areas. 3 different temperatures were chosen for oxidation tests 800°C, 900°C, 1000°C. Porcelain crucibles were used for 800 and 900°C tests where for 1000°C tests, alumina crucibles were preferred. Samples were arranged resting against the wall of the crucible. Oxidation times were set as 1, 3, 5, 7, 9, 11, 13, 15, 17, 19, 21, 23h…etc. This is because when the times are added on top of each other, it gives the square of a number, making it easier to reveal the oxidation kinetics.

To reveal the composition of oxidation products on the surface of samples XRD analysis were conducted using a Bruker D2 Phaser X-Ray diffractometer which uses Cu-Kα radiation (1.54060 Å), 30 kV voltage and 10 mA current

3. Results and Discussion

Weight change regime of all IN 939 samples after oxidation at 800°C are shown in figure 1. As cast (AC) sample resulted in less amount of mass gain. 3D and heat treated as cast (HT AC) samples exhibited similar curves whereas heat treated 3D sample seems to gain slightly less weight after 239 hours of oxidation.

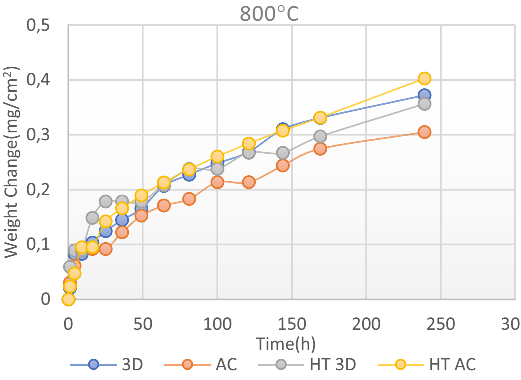

Figure 1 Oxidation weight change results at 800°C

Figure 2 shows the weight change graph of at 900°C. Amount of weight gain increased when the temperature increased as expected. Mass gain numbers stayed between 0.3 to 0.4 mg/cm^2 for 800°C whereas at 900°C it increased to 1.13 to 1.36 mg/cm^2. At 1000C weight gain numbers reached up to 2.17mg/cm^2 for 3D IN939. Figure 3 shows weight changes at 1000°C.

Mass change behavior of selective laser melted IN939 and heat treated as cast (HT AC) IN939 seemed to be close whereas heat treated 3D (HT 3D) sample had less mass gain at all temperatures compared to those two.

As can be seen from figure 3, after 36 hours, three of the samples exhibited a dramatic mass loss due to spallation of oxide scales. However, HT 3D sample resisted up to 64 hours before spallation took place.

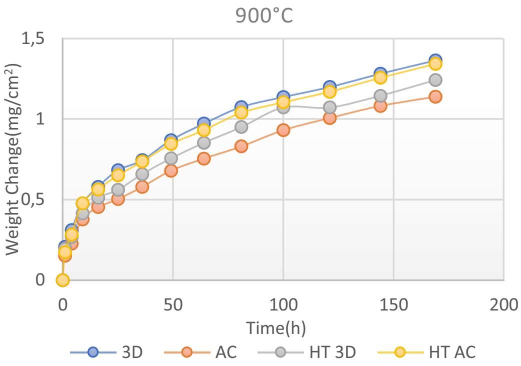

Figure 2 Oxidation weight change results at 900°C

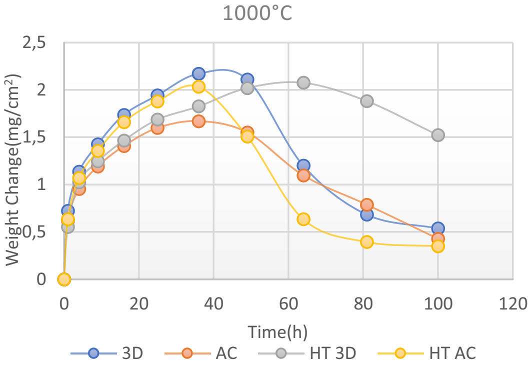

Figure 3 Oxidation weight change results at 1000°C

After oxidation at 800, 900 and 1000°C, XRD measurements were taken to be able to discuss the oxide products which formed on the surfaces of IN939 samples.

Figure 5 shows the XRD measurements of 3D IN939 samples without heat treatment after oxidation at 800, 900 and 1000°C for 239, 169 and 100 hours, respectively. Chromium oxide (Cr_2O_3) was the most dominant phase detected which was expected. Other than Cr_2O_3, the oxide scale was consisted of TiO_2 in the rutile structure and aluminum nickel (Ni_3Al). The titanium oxide phase can be attributed to the titanium diffusion through Cr_2O_3 scale during oxidation. Ni_3Al phase is the γ’ (gamma prime) phase that can be seen in microstructure of several nickel-based superalloys.

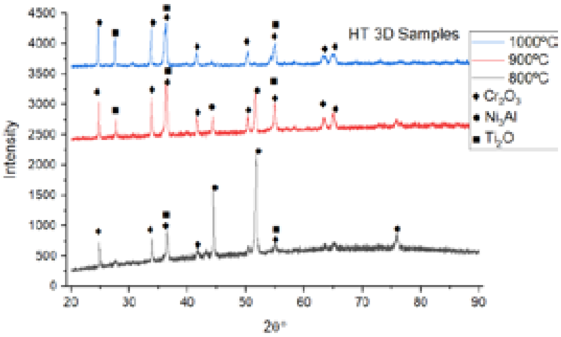

Figure 4 XRD results of HT 3D samples

As the temperature rises the Ni_3Al starts to disappear which can be related to increase of oxide scale since this phase is the gamma prime phase from substrate.

Figure 4 shows the XRD measurements taken for HT 3D IN939 after oxidation at 800, 900 and, 1000°C for 239,169 and 100hours, respectively. It could be easily pointed out that Cr_2O_3 is again the dominant peak which proves the point that a chromium oxide protective layer was occurred on the surface of samples. As the temperature increase, the peaks of oxide products increase as well. Again, the Ni_3Al gamma prime peaks should be coming from substrate hence as the scale thickens these peaks disappear.

Figures 6 shows XRD results of as cast IN939 samples oxidized at 800, 900 and 1000°C. Although most of the peaks are similar, for 1000°C samples there was additional one peak at around 30 degree which seems to be $NiCr_2O_4$. Litz et al.[8] showed that after oxidation at 1100°C the spalled parts of the oxide scale of IN939 were consisted of Cr_2O_3, TiO_2 and $NiCr_2O_4$ which agrees with our results.

Figures 7 show XRD measurements of heat-treated as cast IN939 samples after oxidation at 900 and 1000°C, respectively. Results show that samples are rich in Cr_2O_3 and TiO_2. There seems to be a small amount of $NiCr_2O_4$ for 1000°C which might be attributed to small amounts of spallation since $NiCr_2O_4$ peaks are only visible for 1000°C.

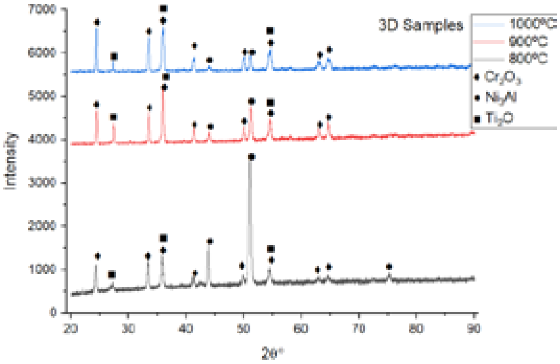

Figure 5 XRD results of 3D samples

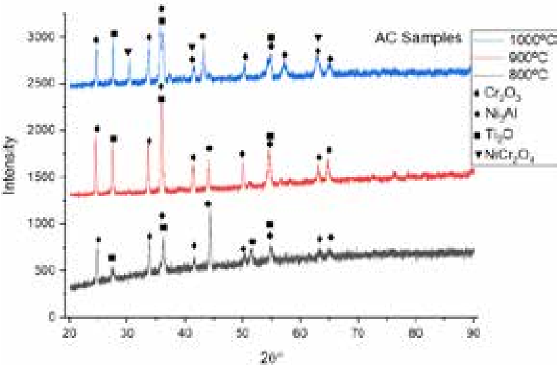

Figure 6 XRD samples of AC samples

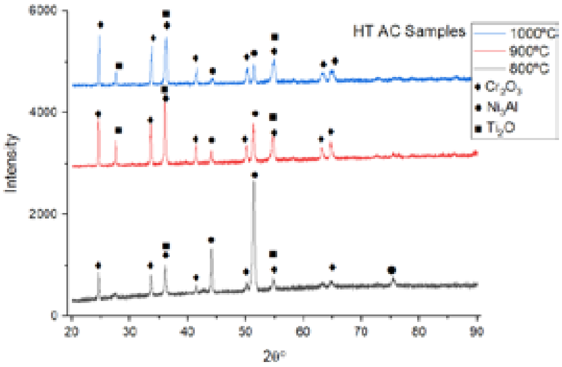

Figure 7 XRD results of HT AC samples

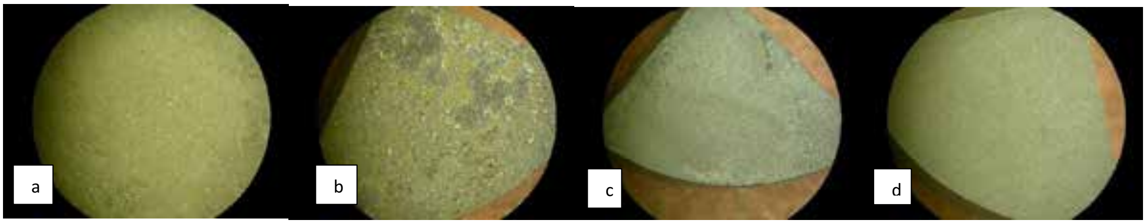

Figure 8 Stereo images of a) 3D, b) AC, c) HT3D, d) HTAC surfaces after 100 hours of oxidation at 1000°C

4.Conclusion

- At 800, 900 and 1000°C oxidation experiments, IN 939 samples obeyed a parabolic rate of oxidation.
- In terms of weight gain trends, heat treated as cast (HT AC) samples and 3D samples showed very similar behavior.
- Heat treated 3D samples were lower in weight gain compared to HT AC and 3D samples at all temperatures.
- Spallation did not occur at 800 and 900°C oxidation tests however at 1000°C after 49 hours of oxidation visible spallation occurred for all specimens.
- XRD results showed that a Cr_2O_3 dominant oxide scale formation is the case for all specimens.
- Cr_2O_3, TiO_2 (in rutile form) was the oxidation products found for all samples and $NiCr_2O_4$ were the oxide product that was found for AC sample at 1000°C.
- Spallation behavior seemed significantly better than other samples for HT 3D IN939.

5.References

[1] M. Abedini, M. R. Jahangiri, and P. Karimi, “Oxidation and Hot Corrosion Behaviors of Service-Exposed and Heat-Treated Gas Turbine Vanes Made of IN939 Alloy,” *Oxidation of Metals*, vol. 90, no. 3–4, 2018, doi: 10.1007/s11085-018-9847-4.

[2] S. W. K. Shaw, “RESPONSE OF IN-939 TO PROCESS VARIATIONS.,” 1980, doi: 10.7449/1980/superalloys_1980_275_284.

[3] ASM, “ASM handbook Volume 2 - Properties and selection: Nonferrous alloys and special-purpose materials,” *ASM Metals Handbook*, vol. 2, 1993.

[4] S. W. K. Shaw, “IN-939: A CORROSION-RESISTANT ALLOY FOR INDUSTRIAL AND MARINE TURBINE BLADES.,” *Met Prog*, vol. 115, no. 3, 1979.

[5] T. B. Gibbons and R. Stickler, “IN939: METALLURGY, PROPERTIES AND PERFORMANCE.,” 1982, doi: 10.1007/978-94-009-7907-9_15.

[6] G. Sjöberg *et al.*, “Evaluation of the IN 939 alloy for large aircraft engine structures,” 2004, doi: 10.7449/2004/superalloys_2004_441_450.

[7] M. C. Karia, M. A. Popat, and K. B. Sangani, “Selective laser melting of Inconel super alloy-a review,” in *AIP Conference Proceedings*, 2017, vol. 1859, doi: 10.1063/1.4990166.

[8] J. Litz, A. Rahmel, M. Schorr, and J. Weiss, “Scale formation on the Ni-base superalloys IN 939 and IN 738 LC,” *Oxidation of Metals*, vol. 32, no. 3–4, 1989, doi: 10.1007/BF00664797.

20th

INTERNATIONAL
METALLURGY
MATERIALS
CONGRESS
10-12 June
2021

“in Digital Platform”

Welding Metallurgy

immc2021

Creep Cracking Mechanisms of Welded Joints for Cr-Mo Heat-Resistant Pressure Vessel Steels

Cong WANG
Northeastern University
China

Abstract

Recently, in order to reduce CO_2 emissions and meet environmental obligations, improved thermal efficiency of power plant, from 35% to 45%, has been the main driver for the development of pressure vessel steels. Cr-Mo heat-resistant steels, also commonly known as creep strength enhanced ferritic steels, has been extensively employed in thermal power-generating applications as header, superheater, and reheater due to superior thermal conductivity, low thermal expansion coefficient, and excellent resistance to thermal fatigue. However, the mechanical properties of the as-received steels can be significantly influenced by the welding thermal cycle induced phase transformation and microstructure evolution, which can lead to catastrophic failure in operation conditions. Consequently, it is important to elucidate creep cracking mechanisms and ensure the overall performance of the final product.

It is found that the creep behavior in terms of creep rupture strength and minimum creep rate of the welded joints of these steels is controlled by that of the intercritical heat-affected zone (ICHAZ). A soft zone in ICHAZ of the welded joints accelerates the formation of creep cavities and results in the creep cracking, which indicated that solute depletion has significance influence on the degradation of the hardness and creep strength.

Investigation of Microstructure and Mechanical Properties of Ferritic Stainless Steels Processed with Laser Welding

Günseli GÜÇ, Onuralp YÜCEL
Istanbul Technical University
Turkey

Abstract

Laser beam welding is widely used in industrial applications in the joining of materials due to the advantages provides and is a suitable fusion welding for automation. In this study, butt-welding of ferritic stainless steel sheets of different grades was performed by solid state disk laser welding in continuous wave mode. Welding parameters were determined as 1300 Watt power, 6 m/min speed and argon gas was used as shielding gas. Welding parameters were kept constant in order to compare ferritic stainless steel sheets. 430, 430Ti and 441 grade ferritic stainless steel sheets were used from different manufacturers. The elemental content of each ferritic stainless steel sheet was determined by chemical analysis. Metallographic examinations, microhardness measurement, SEM-EDS analysis, tensile tests, bending tests and cupping tests were carried out with laser welded sheet samples. In addition to these, original 430, 430Ti and 441 grade ferritic stainless steel sheets were also subjected to tensile and cupping tests for comparing the mechanical properties after laser welding.

1. Introduction

Ferritic stainless steels are widely used in railway transportation equipment, mining, automobile, household appliances and machinery industries due to their properties such as superior corrosion resistance, strength, toughness, and intermediate welding ability. In addition, the use of ferritic stainless steels creates a more economical alternative to austenitic stainless steels [1,2].

Stainless steels can be properly joined by all welding methods with some limitations. Different chemical compositions and characteristics of stainless steels affect the mechanical and physical properties in welding and may cause weld defects and problems in terms of weldability. These defects are also important in terms of affecting the service life of the structures joined by welding. These characteristics can be listed as low heat conduction coefficient, high coefficient of thermal expansion and high electrical conductivity, sensitivity to cold forming, grain growth, carbide formation, structural changes observed in welding such as sigma phase and delta ferrite, and sensitivity to corrosion [3]. Because of low heat conduction and high expansion properties, the heat input should be low in order to prevent distortion during welding [4].

Weldability in ferritic stainless steels is considerably better than martensitic stainless steels. One of the major problems encountered in the welding process in ferritic stainless steels is their extreme tendency to grain coarsening when the temperature of 1150ºC is exceeded. During welding, a part of heat affected zone reaches a temperature above 1150ºC and causes grain growth in the heated area. Since no austenite-ferrite transformation occurs in ferritic stainless steels, the grains cannot be reduced by heat treatment. Ferritic stainless steels become brittle when they become coarse grained and as a result their impact strength decreases [5].

Another problem that may be encountered in ferritic stainless steels is excessive sensitivity to intergranular corrosion in HAZ (heat affected zone) region. This problem is encountered especially in unstabilized types containing high chromium and carbon. It occurs during high speed cooling at temperatures above 900ºC. Compared to the austenitic structure, chromium carbide precipitation occurs at higher rates in the ferritic structure. They are therefore susceptible to intergranular corrosion in areas adjacent to the weld seam. Welded joints made with stabilized 17% chromium ferritic stainless steels can be made resistant to intergranular corrosion if they are annealed at 750ºC immediately after welding. In addition to the this, if they are stabilized with titanium or niobium alloy elements, welded joints are resistant to intergranular corrosion without heat treatment. Moreover, martensite formation can be seen at grain boundaries in some ferritic stainless steels and it causes brittleness [4-6].

Advantages of laser welding over other welding methods are; depending on the material and laser power, reaching high welding speeds above 10 m/min, low heat input and as a result, little or no distortion, strong, reliable welding seam and high speed manufacturing, the weld seam is narrow and the depth/width ratio is high, the HAZ region is small due to cooling at high speed and the base material is almost not affected, possibility of welding in places where conventional welding cannot be applied, flexible, easy and fast welding process, compliance with automation, being an industrial process open to continuous production and obtaining very good results in different materials in welding processes [7].

Lasers can be classified as gas, solid state, semiconductor diode and liquid lasers according to the active material used in creating the laser beam. Industrial uses of solid-state lasers have increased significantly with Nd (neodymium): YAG (yttrium aluminum garnet ($Y_3Al_5O_{12}$)) lasers developed. In solid-state laser systems, in general, the crystal in the form of a cylindrical rod is fixed in a metal container after the two ends are polished and coated with an anti-reflective agent. Special flash lamps and reflective mirrors are placed in this container, considering the method to be used as a stimulator. Laser beams with a wavelength of 1064 nm can be produced with the Nd: YAG crystal excited from its outer surface with high energy service light. The most important problem of this type of laser is the heat between the inner and outer surfaces of the excited crystal. It is the occurrence of thermal stresses with the effect of differences. The amount and quality of laser beam that the crystalline structure can emit is affected by these thermal stresses. In recent studies as a solution to this problem, it has been evaluated that the crystalline form used to produce laser beams is a long and thin fiber or a thin disk instead of a cylindrical structure, and as a result of these studies, fiber and disk lasers with much higher beam quality and efficiency have been developed. In such crystals, unlike the rod form, since the distance between the excited surface and the inner parts of the crystal is below a few hundred microns, no significant thermal stress occurs in the crystal. This allows the crystal to be used more efficiently [8].

In this study, it was aimed to investigate the suitability of different ferritic stainless steels to be joined by laser welding method. To determine weldability of 430, 430Ti and 441 ferritic stainless steels, the sheets was joined by solid state disk laser welding in continuous wave mode and chemical analysis, metallographic examinations, microhardness measurement, SEM-EDS analysis, tensile tests, bending tests and cupping tests were carried out.

2. Experimental Procedure

In this study, 0.5 mm thickness of 430, 430Ti and 441 grades ferritic stainless steel sheets were used. Chemical analysis of 430, 430Ti and 441 stainless steel sheet samples were made in optical emission spectrometer.

For microstructural examinations of the base metal and the weld zone, the samples extracted in appropriate sizes are cold molded over their large surfaces. Sanding and polishing processes were carried out respectively by standard metallographic methods. After polishing, electrolytic etching process was performed in 30 seconds at 12V DC using 10% oxalic acid solution ($H_2C_2O_4$).

Tensile testing of the samples was carried out with test samples taken from welded and unwelded plates. The change in the strength values of stainless steel sheets before and after welding was examined.

The bending test of the samples was done in a 3-point bending apparatus. In the bending tests where the support and mandrel diameters are 5 mm, the distance between the supports was applied as 25 mm. Test samples were prepared in 50 mm length and 20 mm width.

In the microhardness measurement, samples polished by standard metallographic methods were used. In the experiments where the standard Vickers tip and 500 g load were used, microhardness measurements were carried out at regular intervals in the weld zone and the area up to about 2 mm on both sides of the weld zone.

The results regarding the formability of unwelded sheet metal samples and welded samples by cupping tests were compared. The samples are 95 mm wide and prepared in a way that the weld seam remains in the middle.

In the SEM-EDS examinations, the Zeiss Supra 55VP scanning electron microscope was used. SEM images of 430, 430Ti and 441 welded metal plates were taken from the weld regions and elementally Cr, Ti, Nb, C, N ratios were examined by EDS analysis.

The samples were first made into tangible by taking bakelite, and then the surface was prepared with 320, 500, 800, 1200 and 2500 sandpaper and polished in 3 and 1 micron polishing felts, respectively. The polished samples were etched with 15 ml of HCl, 6 ml of HNO_3 and 100 ml of H_2O solution. Since the bakelites were insulating, the surface was coated with gold and put into the electron device chamber for imaging.

3. Results and Discussion

The results of the chemical analysis of different quality stainless steel samples used in the thesis are given in Table 1. Unlike 430 grade, 430Ti grade contains 0.38% Ti. The 441 grade contains 0.373% Nb in addition to the Ti alloying element it contains at a rate of 0.164%.

Table 1. Chemical analysis of 430, 430Ti and 441 (wt%)

Element	430	430Ti	441
C	0,039	0,012	0,009
Mn	0,54	0,33	0,31
P	0,001	0,001	<0,001
S	<0,0005	<0,0005	<0,0005
Si	0,31	0,34	0,51
Cr	17	16,84	18,32
Mo	<0,0050	0,02	0,02
Cu	0,004	0,103	0,09
Ti	0,001	0,38	0,164
Nb	0,004	0,01	0,373
W	0,12	0,16	0,15
Ni	0,11	0,24	0,42

In the optical microstructure images of the samples prepared for microstructural examinations, the weld zone and the region of approximately 200 μm on both sides of the weld zone were displayed. It was observed that the weld zone in all samples consisted of elongated grains and microstructure images of 430, 430Ti and 441 samples are given in Figure 1. The interface between weld zone and base metal is flat and has no apparent heat-affected zone observed except for the 430 stainless steel sample. However, in the 430 stainless steel sample, on both sides of the weld zone consisting of elongated grains, an HAZ of about 100 μm in size with coaxial grains was observed.

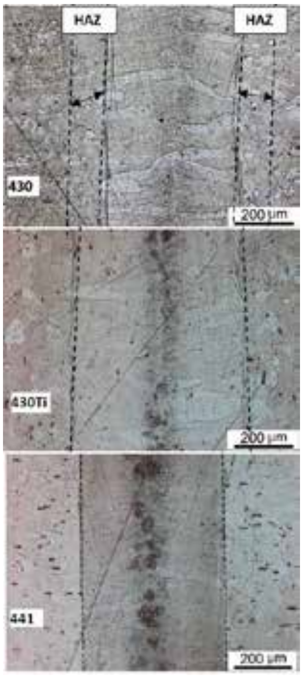

Figure 1. Microstructures of the weld zone of 430,430Ti and 441 ferritic stainless steels

After the tensile tests of the samples prepared from welded and unwelded plates, the rupture zones of the tensile samples were checked. In welded samples of 430 grade ferritic stainless steel, rupture occurred in the weld zone. This indicates that the weld quality is poor compared to other samples. In 430Ti and 441 samples, rupture occurred in the base metal zone. Test results are given in Table 2.

Table 2. Tensile test results of 430, 430Ti and 441

Sample	Tensile Strength (N/mm²)		Yield Strength (N/mm²)		Elongation %	
	Welded	Unwelded	Welded	Unwelded	Welded	Unwelded
430	479,92	476,28	333,16	314,99	18,40	26,28
430Ti	433,09	446,61	315,97	312,87	27,73	30,57
441	471,98	480,70	301,36	313,72	30,85	29,79

At the end of the bending tests, cracking was not observed in the welding area of the 430, 430Ti and 441 ferritic stainless steel samples. Average flexural strengths were determined as 9.8, 10.8 and 9.6 MPa for 430, 430Ti and 441, respectively. The highest flexural strength was measured at 11 MPa in the 430Ti sample.

The highest microhardness value of 430 stainless steel sample was observed as 187 HV in the region close to HAZ. At the welding center, the microhardness was measured as 166 HV. In the 430Ti stainless steel sample, the highest microhardness measurement was observed in the weld seam with 211 HV. The highest microhardness value in the 441 grade stainless steel sample was observed as 223 HV in the base metal region. Microhardness was measured as 202 HV at the welding center. In the study performed by Niklas Sommer et al. with laser welded 430 and 430Ti welded sheets, high hardness values were found in the range of 290-325 HV in the weld area of 430 samples and the martensite formation observed at the grain boundaries resulted in an increase in hardness values. Moreover, similar to the results we obtained in the weld seam of the 430Ti sample, the hardness values were measured in the range of 200 - 210 HV and it was determined that it decreased towards the base metal [9]. In this study, martensite formation was not observed in the microstructure of the 430 welded samples as well as in the 430Ti and 441 welded sheet samples.

After the cupping tests of the samples prepared from welded and unwelded plates in Erichsen cupping device, the tear regions and the amount of deformation of the samples were compared and controlled. The least change was detected in 430Ti samples with a decrease rate of 4%. Deformation values decreased by 19% and 10% in the 430 and 441 samples, respectively. The effect of the weld has been observed mostly in 430 ferritic stainless steel samples.

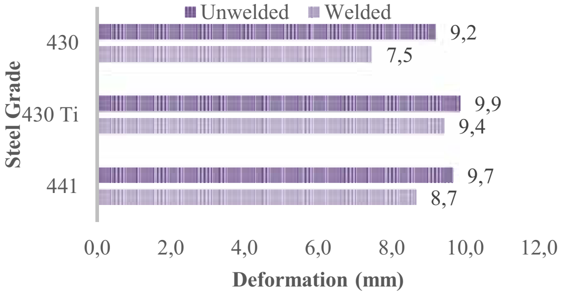

Figure 2. Cupping test results

Various EDS scans have been conducted including point, line and mapping on welding zone of the samples prepared for SEM examination.

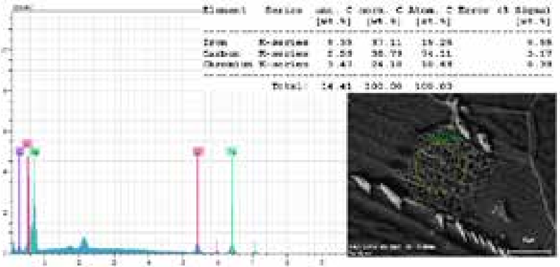

Figure 3. EDS analysis of precipitates in 430 sample

SEM and EDS analysis of the samples were carried out on the base metal, HAZ and weld zones, and thin and long precipitate structures were observed in the weld zone of 430 ferritic stainless steels. In EDS line and mapping analyzes, it is seen that the % C ratio increased in these structures and the precipitates were interpreted as carbides. Multi-point analysis was made with EDS in the welding area and precipitates predicted to be chromium carbide in the structure were observed in Figure 3.

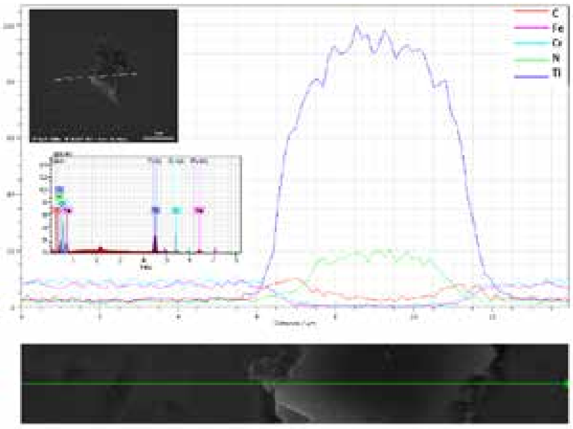

Figure 4. EDS analysis of precipitate in 430Ti sample

In the welding zone of 430Ti ferritic stainless steel, precipitation was observed in the grains. As a result of EDS line analysis on the precipitate, the precipitate was interpreted as titanium carbonitride precipitate in Figure 4.

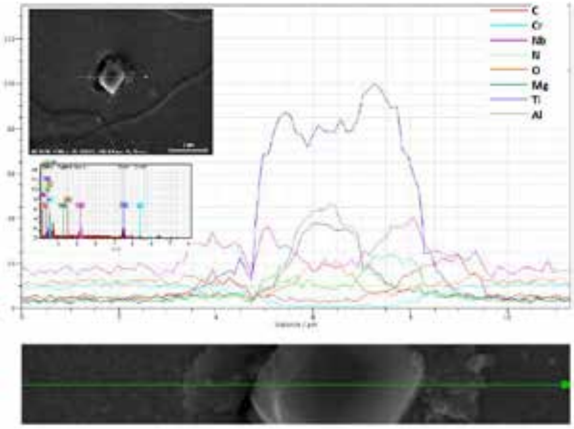

Figure 5. EDS analysis of precipitate in 441 sample

Similarly, in the weld zone of 441 ferritic stainless steel, transgranular precipitation was observed in Figure 5. As a result of the line and mapping analysis made on the precipitate, the (Ti, Nb) (N, C) whose main composition consists of Ti, N, C and Nb elements was interpreted as composite precipitate. Al, Mg and O elements have also been detected in the core of the precipitate that predicted to be aluminum and magnesium oxide inclusions.

4. Conclusion

The structure and property relationships of ferritic stainless sheets joined by laser welding were examined by microstructure studies and measurement of their mechanical properties, and the results were compared and interpreted. Laser welding process was performed under argon gas by using Trudisk device in continuous wave mode with 1300 Watt power, 6 m/min speed, keeping welding parameters constant. As a result, adequate welding quality could not be achieved in 430 ferritic stainless steel samples, and it was observed that the welding ability was insufficient compared to 430Ti and 441 ferritic stainless steel sheet samples. It has shown that Ti and Nb alloying elements positively affect weldability.

Acknowledgment

The research for this project was financially supported by the Scientific and Technological Research Council of Turkey (TÜBİTAK), project No: 3180968.

References

[1] Shao, Y., Li, X., Ma, J., Liu, C. & Yan Z., Microstructure Formation of Low-Carbon Ferritic Stainless Steel during High Temperature Plastic Deformation. Metals, 9(4) (2019), 463.

[2] Mohandas, T., Reddya G. M. & Naveed, M., A Comparative Evaluation Of Gas Tungsten and Shielded Metal Arc Welds of A ``Ferritic" Stainless. Journal of Materials Processing Technology, 94 (1999), 133-140.

[3] Baylan, O., Elektrik Ark Kaynak Yöntemiyle Birleştirilen Östenitik-Martenzitik Farklı Paslanmaz Çeliklerin Kaynaklı Bağlantılarında, Mikroyapı ile Özellikler Arasında İlişkinin Araştırılması. (Yüksek Lisans Tezi). Z.K.Ü. Karabük Teknik Eğitim Fakültesi, 2003, Zonguldak.

[4] Aran, A. & Temel, M., Paslanmaz Çeliklerin Üretimi, Kullanımı, Standartları (2.bs.), 2004, Sarıtaş Teknik Yayın No:1, Acar Matbaacılık A.Ş., Istanbul, Turkey.

[5] Kaluç, E., Tülbentçi, K., Paslanmaz Çelikler ve Kaynaklanabilirliği, Seminer Notları, 1998, Kocaeli.

[6] Lippold, J. C. & Kotecki, D. J., Welding Metallurgy and Weldability of Stainless Steels, Wiley, 2005, New Jersey.

[7] Çelen, S., Paslanmaz Çeliklerin Lazer Kaynağında Kaynak Parametrelerinin Bağlantının Dayanım ve Korozyon Özelliklerine Etkisinin İncelenmesi. (Yüksek lisans tezi). Dokuz Eylül Üniversitesi, Fen Bilimleri Enstitüsü, 2006, Izmir, Turkey.

[8] Koechner, W. & Bass, M., Solid-State Lasers, Springer-Verlag, 2003, New York.

[9] Sommer, N., Kryukov, I., Wolf, C., Wiegand, M, Kahlmeyer M. & Böhm S., On the Intergranular Corrosion Properties of Thin Ferritic Stainless Steel SheetsWelded by Fiber-Laser. Metals, 10(8) (2020), 1088.

Calculating Effectiveness Of Filler Metals in Reducing Solidification Cracking Susceptibility of AZ31 Mg Alloy

Tayfun SOYSAL
Igdir University
Turkey

Abstract
AZ31 magnesium alloy is susceptible to solidification cracking. A simple crack susceptibility index, the maximum $|dT/d(f_S)^{1/2}|$, was used with a commercial thermodynamic software to predict the crack susceptibility of AZ31 magnesium welds made with and without filler metal. The filler metals made out of AZ61 and AZ92 magnesium alloys were studied in terms of effectiveness to reduce susceptibility of AZ31 magnesium alloy to solidification cracking.

1. Introduction

Magnesium (Mg) alloys have been drawing attention for their low density and high strength and used for light weight applications, especially replacing some of the components in the transportation vehicles to save fuel. The research in welding of Mg alloys have recently gained a rapid acceleration to bring solutions to the difficulties in welding of Mg alloys. One of the difficulties is solidification cracking. Solidification cracking is directly related to weldability of Mg alloys, and it must be addressed to improve the weldability.

Recently, Kou [1] has studied the solidification cracking with his simple crack susceptibility index which is based on his criterion for cracking during solidification [2]. During solidification of alloys in welding, he considered columnar dendritic grains, which are typical in welding, to explain how solidification cracking occurs. The grains are separated by the tensile strains caused by the solidification shrinkage, e.g. 4.2 % for Mg, and the thermal contractions as the grains grow and grain boundary liquid feeds through the channel between the grains during solidification. If the tensile strain rate exceeds both the grain growth rate and the liquid feeding rate, solidification cracking occurs. Kou [1] related the grain growth to his cracking index, that is, maximum $|dT/d(f_S)^{1/2}|$, and predicted crack susceptibility of aluminum alloys by proposing smaller the index, lower the crack susceptibility is. This susceptibility index has successfully been applied to aluminum, magnesium, and nickel-based alloys and verified by transverse motion weldability test [3-5]. In this study, the susceptibility index will be used to investigate the filler metal effect of two commercially available filler metals AZ61 and AZ92 Mg alloys on the solidification cracking susceptibility of the most commonly used AZ31 Mg alloy.

2. Materials and Methods

Crack susceptibility predictions were made based on the simple crack susceptibility index, the maximum $|dT/d(f_S)^{1/2}|$. Crack susceptibility of AZ31 was firstly calculated without filler metal, then, it was assumed to be welded with the commercial Mg filler metals AZ61 and AZ92 with 20% base metal dilution in the weld metal, that is, the weld metal is composed of 80% filler metal and 20% workpiece. T vs $(f_S)^{1/2}$ curves of the workpiece and the welds were plotted using a commercial thermodynamic software using the chemical compositions of them as inputs. Scheil solidification model was used for the calculations. The maximum $|dT/d(f_S)^{1/2}|$ of the curves were calculated using the slope function of MS Excel for a data point including two data points ahead of the data point in the calculations.

3. Conclusions

Solidification cracking susceptibility predictions of the AZ31 Mg welds were made based on the simple crack susceptibility index, the maximum $|dT/d(f_S)^{1/2}|$, which was calculated using a commercial thermodynamic software. The filler metals AZ61 and AZ92 Mg alloys were found to reduce susceptibility of AZ31 Mg alloy to solidification cracking but the filler metal AZ92 Mg alloy was little bit more effective than the filler metal AZ61 Mg alloy at the crack susceptibility reduction. The predictions were explained using a recently proposed criterion for cracking during solidification.

References

[1] S. Kou, Welding Journal, 94 (2015) 374-s to 388-s.
[2] S. Kou, Acta Materialia, 88 (2015) 366-374.
[3] T. Soysal and S. Kou, Acta Materialia. 143 (2018) 181-197.
[4] K. Liu and S. Kou, Science and Technology of Welding and Joining, 25 (2020) 251-257.
[5] C. Xia and S. Kou, Science and Technology of Welding and Joining, 25 (2020) 690-697.

20th
INTERNATIONAL
METALLURGY
MATERIALS
CONGRESS
10-12 June
2021
“in Digital Platform”

Composite and Polymer Materials

immc2021

Polymeric Composites with Novel 2D Nanofillers Mxenes

Mária OMASTOVA
Polymer Institute Slovak Academy of Sciences
Slovakia

Abstract

Considerable research efforts have been devoted in recent decade to new types of materials, two-dimensional (2D) nanomaterials. 2D nanoparticles such as graphene, MoS2 and the others are currently the most intensive studied materials with great potential for future applications. MXenes are a new class of 2D inorganic materials, first described in 2011. Different MXenes are prepared from different MAX phases of the formula Mn+1AXn, where M is the most common transition metal, A is an element of the 13 or 14 group of the periodic table of elements, X is usually C and/or N. By etching of the A layers from MAX phase, MXene are formed. The surface of etched MXenes contains functional group e.g., -O, -F, -OH, leads negatively charged surface. Polymeric composites used MXene as fillers can reach interesting properties and started to be topic of intensive research.

In our work MAX phase Ti3AlC2, particle size 40 µm was used for MXene preparation. MXene Ti3C2 was prepared by selectively etching the aluminium layer out of the Ti3AlC2 MAX phase in LiF+HCl solution. X-ray photoelectron spectroscopy (XPS) analysis confirmed etching the aluminium layer out of the Ti3AlC2 MAX phase. The intensity of Al signal decreased from 12.9 at.% to 0 at.%. Results also showed cleaning MXene from oxidized parts, which are in precursor MAX phase in a larger amount, 23.8 at. % signal for oxygen in oxide form.

As polymeric matrices poly(methylmethacrylate) (PMMA) Plexiglas® 7N and waterborne epoxy resins were used for preparation of composites by solution casting method. Polymeric composites with various amount of MXenes from 1.0 wt.% to 10.0 wt.% were prepared. Electrical properties composite were measured by Broadband Dielectric Spectrometer (BDS). BDS measurements showed increasing of conductivity with increasing content of MXene in polymeric composites. Experimental condition of MAX phase etching and methods of MXene preparation significantly influence the final electrical conductivity of this filler. The higher the MXene conductivity, the higher the final conductivity of polymeric composites. Prepared composites showed good electrical properties, therefore they can be used for further application.

Simultaneous Activation of Multiple Toughening Mechanisms: Interleaving Layered Composites with Blends of Thermoplastic Polymers

Melike KILIÇOĞLU[1], Erhan BAT[2], Güngör GÜNDÜZ[2], Bora MAVİŞ[1]
[1]Hacettepe University, [2]Middle East Technical University
Turkey

Abstract

In this study, it was shown that by blending PCL and PA6 on the fiber level, a concerted action of distinct toughening mechanisms can be attained at the interface of layered carbon fiber reinforced polymer composites. When only PA6 was used in the interleaved interfaces debonding from the epoxy matrix results in peeling of layers without much resistance in mode I. In PCL only cases, a 50% increase in $G_{IC\text{-}ini}$ and a 28% increase in $G_{IC\text{-}prop}$ were observed, due to the plasticizing effect of PCL in the interlayer epoxy. Synchronous activation of debonding and bridging was only possible at a level of phase separation that permits PCL zones to form an interpenetrating network with the epoxy and function as "bridge pillars" upon melting during curing. PA6 was also crystallized in its stiffer phase at this PCL level. With 69% and 59% improvements in $G_{IC\text{-}ini}$ and $G_{IC\text{-}prop}$ values, respectively, 60/40 blend showed the best performance compared to the pristine interfaces. Melting of the phase separated regions in 40/60 blend resulted in the loss of cross-sectional integrity of fibers. In this blend, the mode I resistance of interleaved interface against crack initiation and propagation was even lower than that of the unmodified interface.

1. Introduction

Use of electrospun thermoplastic veils in the layered composite interfaces as homopolymers or as their physical mixtures have been shown to improve the interlaminar toughness of the composites [1]. Distinct toughening mechanisms were observed to be activated by the individual fiber types used in the physical mixtures that were examined in the previous studies. Nevertheless, in simultaneously spun polymer fiber mixtures [2] or stacked layers of mixed polymers [3], the individual polymers interact with the propagating crack rather independently from each other. Therefore, in this study the idea of blending two polymers in the fiber level was investigated.

2. Materials and Methods

Three fibrous veils of PA6:PCL blends (80:20, 60:40 and 40:60) were prepared by electrospinning and hot-pressed in the mid-layer with carbon fiber – epoxy based prepregs. Double Cantilever Beam (DCB) tests were performed to determine the improvements in interface toughness in Mode I crack growth. The phase separation tendencies of the blends were examined by Differential Scanning Calorimetry (DSC).

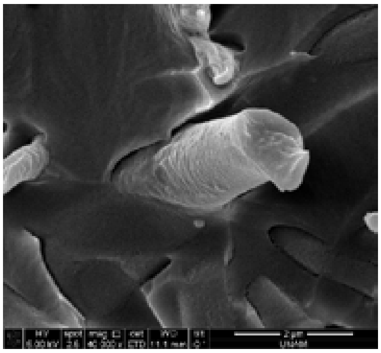

Figure 1. A fiber strained and fractured after partial debonding in PA6:PCL (60:40) blend modified interface.

3. Conclusion

Phase separation tendencies in the fibrous blends can be used to activate diverse toughening mechanisms simultaneously. The fiber level blending can be used in design of composites with better damage tolerance.

Acknowledgment

The authors acknowledge use of the services and facilities of UNAM-National Nanotechnology Research Center at Bilkent University and the financial support from TÜBİTAK (Project No: 214M110).

References

[1] R. Palazzetti, A. Zucchelli, Composite Structures, 182 (2017) 711-727.
[2] F. Bovicelli, H. Saghafi, T.M. Brugo, J. Belcari, A. Zucchelli, G. Minak, Procedia Materials Science, 3 (2014) 1316-1321.
[3] H. Saghafi, A. Zucchelli, R. Palazzetti, G. Minak, Composite Structures, 109 (2014) 41-47.

Fabrication and Compressive Behaviour of B_4C Reinforced Al Foam

Bilgehan Cem TURAN, Mevlüt GÜRBÜZ
Ondokuz Mayıs University
Turkey

Abstract

In this study; boron carbide (B_4C) reinforced aluminum (Al) matrix composite foam specimens have been produced by using the powder metallurgy method, and the change of physical and mechanical properties in the Al matrix composite foams depending on the B4C reinforcement has been examined. For this purpose, pure Al powders with grain sizes ranging in 7-15 µm and urea (70% by volume) with sizes ranging in 1-2 mm were mixed, pressed, and sintered. Then, with the same properties, pure Al powder, urea (70% by volume) and B_4C (1%, 3%, 5%, 7%, 9%, 11% by weight) with an average grain size of 3.5 µm were mixed and B_4C reinforced Al matrix composite foam samples were obtained at the same conditions and all of the samples obtained were subjected to compression tests. From the results of the compression tests, the yield strength of pure Al foam samples has been observed between 4.5 MPa and 5.25 MPa; the yield strength of B_4C reinforced Al matrix composite foam samples has been observed in the range of 7.25 MPa and 12 MPa at highest. Crystal structure and microstructure of the composite foams were confirmed by X-ray diffraction and scanning electron microscopy.

1. Introduction

Al is quite popular and has got a very important place among metal foams because of its properties such as low density (2.7 g/cm3), low melting temperature (660°C), easy formability, high corrosion resistance, high electrical and thermal conductivity and especially when processed as aluminum matrix alloy or composite having higher mechanical properties than other metals. Due to its physical and mechanical properties, there are many applications in various sectors such as; automotive, aerospace and aviation, rail system vehicles, construction industry, defense industry, etc. and R&D activities for these sectors are continuing increasingly day by day [1]. B4C is a ceramic material due to its featured properties such as; high Young modulus (450 GPa), low density (2,52 g/cm3), extraordinarily high hardness (3000HV) [2] and because of these properties, B4C has been drawing attention for many years in many industrial sectors such as; defense industry and ballistic applications [3], [4].

Metallic foams are such materials that draw attention especially for the last two decades because of their physical and mechanical properties such as; low relative density, high impact absorption capability, being capable of sound and heat conductive or insulator depending on pore morphology [5]. For that reason, obtaining Al matrix B4C reinforced composite foams and optimizing mechanical and physical properties coming from Al, B4C, and foams physical morphology may result in obtaining an advantageous composite foam material. That is why in this study, Al matrix B4C reinforced composite foam materials have been obtained by using powder metallurgy method and mechanical and physical properties of the composite foam samples have been examined by the changing ratio in addition of B4C (1%, 3%, 5%, 7%, 9%, 11% by weight). For determining mechanical properties all samples have subjected to compressive tests and from obtained results yield strength and toughness have been the selective parameters.

2. Experimental Procedure

2.1. Materyal

In this study, as the matrix material, aluminum powder which has got %99 purity and grain sizes ranging in 7-15 µm; urea which has got %98.5 purity and grain size ranging in 1-2 mm as pore obtaining material and B_4C as the reinforcement material which has got 3.5 µm average grain size has been used.

2.2 Method

Boron carbide (B_4C) reinforced aluminum (Al) matrix composite foam specimens have obtained by using powder metallurgy method which consists of these stages; mixing powders by ball mill, filtering, drying, sieving, mixing powder with urea, pressing, sintering and subjecting to mechanical and chemical tests.

At first step, B_4C and Al powders have been added into ethanol and mixed by ball mill to get a homogenous mixture of powders. After that, the mixture of ethanol and powders filtered in drying oven at 50ºC for 24 hours to remove ethanol and drying powders. Next, powders have been sieved to resolve the clumping caused by filtering and drying. The mixture of powders has been mixed with urea grains with a ratio of 70%(vol.) urea and 30(vol.) powder. The mixture of powder-urea has been pressed and shaped by uniaxial hydraulic press by applying 250 MPa. The green samples have been kept in water for 3 hours at 80ºC for dissolving urea, subsequently dried in drying oven at 50ºC for 6 hours. The dried green samples sintered at 645ºC for 3 hours and after that, the specimens have been subjected to physical, mechanical and chemical tests.

3. Results and Discussion

3.1. Evaluation of Density and Porosity Test Results

In this section, the results of relative density (ρ_{rd}) and porosity (P) of pure Al foam and B4C reinforced Al matrix composite foam have been evaluated. The formula of relative density is Eq (1); and the formula of porosity is Eq (2).

$$\rho_{\mathrm{rd}} = 1 - \left(\frac{\rho}{\rho_{\mathrm{Al}}}\right) \quad (1)$$

$$P = \left(1 - \left(\frac{\rho}{\rho_{\mathrm{Al}}}\right)\right).100 \quad (2)$$

In these formulas, ρ is density (g/cm^3) of foam samples, ρ_{Al} is density of Al (2.7 g/cm^3). Figure 1 gives the density and porosity of samples.

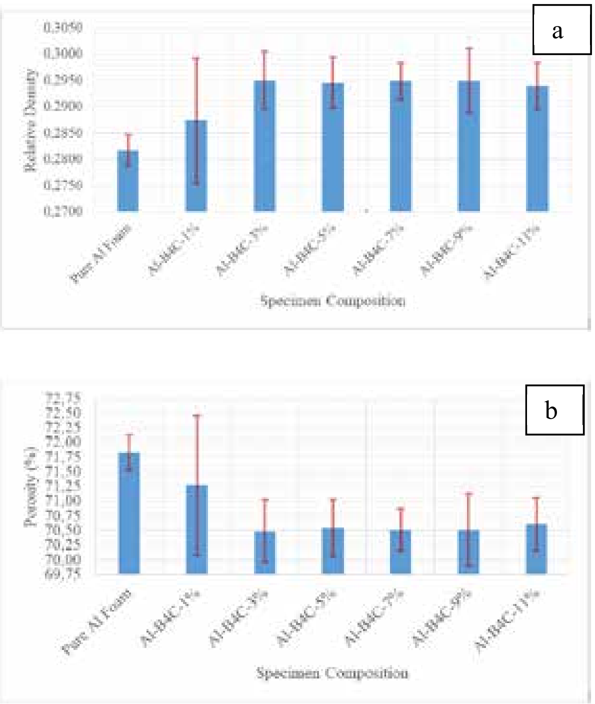

Figure 1. Variation of density and porosity with B_4C addition

3.2. Evaluation of Compression Test Results

For compression tests (Figure 2), at least five specimens of each specimen composition have been subjected to tests and the variation of yield strength results depending on B_4C addition can be seen in Figure 3. From the results, it is observed that; while yield strength of pure Al foam specimens is ranging in 4.5-5.25 MPa; 7% (by weight) B_4C reinforced Al composite foam specimens yield strength are ranging in 7.25-12 MPa which is the highest range in among all specimen compositions. 9% and 11% (by weight) B4C reinforced Al composite foam specimens have lower yield strength than Al-B4C-7% because it is possible that, as the ratio of B4C increases the higher chance of clumping becomes possible.

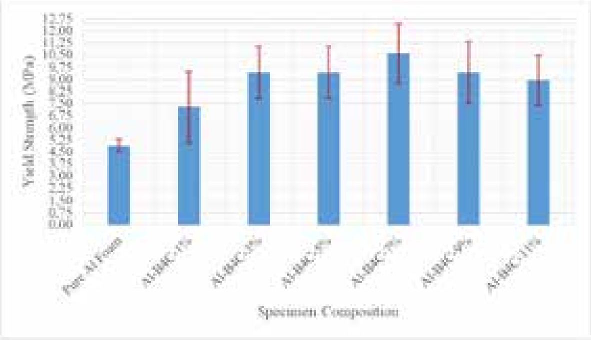

Figure 2. Variation of yield strength with B_4C addition

4. Conclusion

In this study, to improve impact absorption capacity of Al foams which is a very important parameter for Al foams; B_4C reinforced (1%, 3%, 5%, 7%, 9%, 11% by weight) Al composite foam specimens have been obtained by powder metallurgy method and subjected to physical, mechanical and chemical tests. From the obtained results, as the addition of B_4C increases the yield strength of specimens also increases until reaching 7% (by weight) B_4C addition. More than 7% (by weight) B_4C addition increases the possibility of clumping of B_4C in microscale and it reduces the mechanical properties of the foam. So, the optimum B_4C reinforcement composition is 7% (by weight) addition of B_4C to Al matrix composite foam materials.

References

[1] M. C. Santos, A. R. Machado, W. F. Sales, M. A. S. Barrozo, and E. O. Ezugwu, “Machining of aluminum alloys: a review,” *Int. J. Adv. Manuf. Technol.*, vol. 86, no. 9–12, pp. 3067–3080, 2016.

[2] P. Feinle and H. Knoch, “Product Development with SiC and B4C Ceramics,” in *3rd European Symposium on Engineering Ceramics*, F. L. Riley, Ed. Dordrecht: Springer Netherlands, 1991, pp. 51–67.

[3] M. Garcia-Avila, M. Portanova, and A. Rabiei, “Ballistic performance of composite metal foams,” *Compos. Struct.*, vol. 125, pp. 202–211, 2015.

[4] M. Garcia-Avila, M. Portanova, and A. Rabiei, “Ballistic Performance of a Composite Metal Foam-ceramic Armor System,” *Procedia Mater. Sci.*, vol. 4, no. 2010, pp. 151–156, 2014.

[5] J. Banhart, “Light-metal foams - History of innovation and technological challenges,” *Adv. Eng. Mater.*, vol. 15, no. 3, pp. 82–111, 2013.

Development of Resistance Welding Process for Fiber-Reinforced Thermoplastic Matrix Composites: Experimental Analysis and Multiphysics Modeling

Elvan ATEŞ[1], Oğuzhan BAŞ[1], Mete BAKIR[1,2], Fahrettin ÖZTÜRK[1,2]
[1]Ankara Yıldırım Beyazıt Üniversitesi, [2]Türk Havacılık ve Uzay Sanayii A.Ş.
Turkey

Abstract

Structural materials which have high mechanical strength, as well as low costs and recycling capability, are generally preferred in the aerospace industry. Having these attributes, thermoplastic composites, enabling high strength to density ratios, design flexibilities, and corrosion resistance are considered to be the next generation of aerostructure materials. Thermoplastic composites can be conveniently melted and reshaped under certain process temperatures and pressures. In this respect, the research efforts have been directed towards the manufacturing and joining schemes of these materials. In this study, it is targeted to optimize the melt-joining problems by using different process parameters for woven carbon fiber-reinforced polyphenylene sulfide matrix (CF/PPS) composites. As a result, optimum process parameters for the resistance welding method are determined. Depending on the degree of adhesion, the effective cohesion forces between the heating element and composites, and the lap shear strength tests are examined, and appropriate adhesion quality is achieved.

1. Introduction

Aerospace industries constantly demand performance increases from both commercial and military air vehicles. Therefore, the development of new structural materials is an imminent challenge falling under this purpose. Structural materials have high specific stiffness and dimensional stability for the concerning aerospace applications. For many years, based on the importance of thermoplastic composites, up-scale projects such as TAPAS-1 and TAPAS-2 have been carried out by major aerospace companies, to realize lower fuel consumption and costs. The aerospace industry urges thermoplastic composites which are lightweight and affordable, so thermoplastic composites have progressively become more advantageous in this field. Thermoplastic composites are those that can be re-melted and reshaped under certain process temperatures and high-pressure. In this way, thermoplastic composite materials can potentially replace metals and thermoset composites while having exceptional features in terms of material performance, processing conditions, and assembly flexibility. Today, manufacturing methods, assembly techniques, assembly process steps, and the effective role of molten polymer material on the assembly process are among the main research thrusts. The conventional mechanical joining methods exert stresses during the drilling operations that may degenerate the material structural integrity, which can directly reflect on the overall strength properties. Within the scope of this work, the resistance welding process, a favorable alternative to mechanical joining methods at mechanical assembly stages, is examined.

The resistance welding scheme is a joining technique with low process cost and less labor intensity for thermoplastic composite materials. The resistance welding method requires a heating element that is placed between the two parts to be joined and the joining is achieved by the effects of increasing the temperature and applied pressure between the mating parts. The welding current is applied to generate heat energy over the heating element. The heating zone forms on the surface of the parts facing the heat transfer element, wherein pseudo-isothermal conditions are ensured by the use of insulating materials. The pressure was applied via insulating materials to enhance the area of adhesion surfaces. A three-dimensional heat transfer model was developed for the adhesion surface to solve for the temperature, electrical current, and applied pressure, which are the main parameters of the resistance welding process. Under the process flow model required for resistance welding conditions, the optimum value ranges were determined for the dwell time and applied pressure. In this context, temperature distributions formed in composite materials were compared with the literature and time-stamped calculations of the molten polymer content under welding application are conducted.

In this study, multi-physics simulations were performed to formulate the thermal behavior of the material. Then, experimental joining tests were carried out using a laboratory-scale resistance welding setup. The phase change analysis wasc performed by coherently simulating and experimenting the resistance welding technique to determine molten polymer content during the joining process, which is not fully understood in the literature. Lap shear strength tests were conducted to validate the simulation results.

2. Experimental Procedure

The 5-harness satin CF/PPS (Toray Cetex® TC1100) material used in this experiment was acquired from Toray Advanced Composites (the Netherlands). The test samples have a width of 25 mm, length of 100 mm, and thickness of 2.5mm per the ASTM D1002. A plain woven AISI 304-L stainless steel mesh, with a wire diameter of 0.04 mm, and a thickness of 0.08 mm was used as the heating element. The heating element wire mesh has 45 mm x 12.5 mm dimensions. The insulator was made of stainless-steel block which has 5 mm thickness and 25 mm x 12.5mm dimensions. It provided about 0.1 MPa pressure to the composite samples.

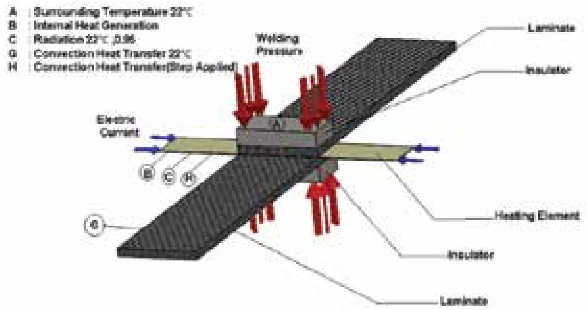

Figure 1. Schematic set-up for the resistance welding process.

The three-dimensional solid model of the resistance welding configuration used in the Multiphysics analysis was shown in Figure 1. The pressure, which is one of the basic parameters, was kept constant at 0.1MPa, and the current and time parameter values were controlled by experimental design methodology. The values of 12A-15A-18A for current and 30s-60s for the time were determined based on the studies in the literature, respectively [1 - 4]. One of the main objectives of the study was to determine the parameter values to be applied in the experimental setup by determining the temperature distribution in different layup directions affecting the composite material in the analysis environment. The designed solid model was then transferred to the ANSYS Workbench analysis software through third-party .step file systems. The material properties of the composite structure were determined and adapted to the geometry. Then, the loads and boundary conditions to which the mesh structure was exposed are defined in the finite element method for the composite structure. Thus, all requirements for analysis were defined as the finite element solver system. After the solution was obtained, the thermal results of the composite material were examined.

Experiments were performed to investigate the weldability of thermoplastic composites. The welding process parameters are dwell time, supplied electrical current, and applied pressure, which they were controlled for the optimum bonding strength. The bonding strength is related to the temperature and the main source of temperature is electrical energy. The temperature of the laminate parts started to increase because the energy is supplied by the internal heat generation of the heating element. Time and current affect the interlayer temperature which initiates the phase transition in the course of the welding process. After reaching the phase transition temperature, the laminates were cooled while the applied pressure was kept. Insulator provided the pressure to the samples, so the apparent bonding quality was increased. The current is a variable electrothermal power on the thermoplastic composites since affecting the weld quality and resin strength. It is positively affected by increasing of given power from Joule's law. On the other hand, it was negatively changed by decreasing of clamping distance on temperature distribution [5]. The resistance is increased by the inverse proportion of the wire diameter and direct proportion of wire length, according to the resistivity equation. So, the energy consumption is affected negatively. Figure 1 shows the experimental setup.

2.1. Transient heat transfer

The symmetrical model was used in the heat transfer analysis of the resistance welding system to determine the boundary conditions. The heat transfer element makes direct contact with composite materials. This refers to the conductive heat transfer defined for the analysis.

$$\rho \cdot C_p \cdot \frac{\partial T}{\partial t} = \dot{q} + k_{xx} \cdot \frac{\partial^2 T}{\partial x^2} + 2k_{xy} \cdot \frac{\partial^2 T}{\partial x \partial y} + k_{yy} \cdot \frac{\partial^2 T}{\partial y^2} \tag{1}$$

$$\dot{q} = \frac{U \cdot I}{V} \tag{2}$$

Where $\dot{q}$ is the heat generation rate of using heating element $[\frac{W}{m^3}]$, V is the volume of material, U is the voltage $[V]$, I is the current $[A]$, k is thermal conductivity $[\frac{W}{m \cdot K}]$, ρ is the density of material $[\frac{kg}{m^3}]$, c_p is heat capacity $[\frac{J}{kg \cdot K}]$.

The main source of heat energy was electrical power. The heating element which passes the electricity transforms electrical energy to heat energy. Heat is transferred to the thermoplastic composite materials by the facing surface boundaries. The transformed electrical energy is controlled through the welding time, current, and pressure. These are also defined as main welding parameters in this experiment. The current passing through the wire creates a special power density depending on the variable parameters of the materials. Power is directly related to the current and resistance. The current is constant, so the change in power level is due to resistance. Resistance is dependent on temperature.

$$P = I^2 . R \tag{3}$$

However, in this case, it was focused to calculate on x-direction for heat transfer analysis. The analysis of heat transfer of thermoplastic composite laminate was calculated in one dimensional because of the direction of heat vectors.

$$\frac{\partial}{\partial x}\left(k \cdot \frac{\partial T}{\partial x}\right) + \dot{q} = \rho \cdot c \cdot \frac{\partial T}{\partial t} \tag{5}$$

The determination of boundary conditions was identified due to the method of heat transfer and the effective experiment process. In the heat transfer model, the surrounding temperature was identified as 22 °C, the convection heat transfer model was used for the heating element, composite materials, and insulator since the cooling process depends on the surrounding conditions. The conduction, convection, and radiation heat transfer models were identified on the heating element. One of the main reasons is that the heat generation was created on the heating element. Besides, the coupling temperature was identified to the connecting parts which are located between samples-heating elements and samples-insulators. Boundary conditions/assumptions were created to determine the energy value by comparing the conduction-conduction model and conduction-convection.

Heat generation on the heating element essentially driven by the supplied current and resistivity of materials. Likewise, the length of the heating element and its contact regions affects the efficiency of heat generation. The produced energy by the current can be effectively multiplied by the ratio between the contact region and the length of the heating element, so the value of heat energy is decreasing. On the other hand, the convection model was obtained between the component surface and the ambient conditions. In general, air properties, which are dependent on time, were used in the convection analysis. Besides, the boundary conditions were set as the convection and ambient radiation conditions. After applying for the heat transfer with boundary conditions, the change in the material form was examined by phase change. Adding or removing energy (heat, electrical, etc.) to a system causes a phase change in the welding processes. In the first-order phase transition, the transient substance has a more characteristic feature than changes in discontinuity. If the material in solid form becomes liquid, its density property is different for the solid phase and liquid phase. Therefore, this is characterized as a distinct phase change feature. Although heat energy is supplied to a substance at a certain rate, the temperature change during the phase change phase remains constant or nearly constant. Heat energy is absorbed by changes in the molecular structure of the substance. The energy required for the substance to change the phase is called latent heat. Latent heat is related using the enthalpy property which varies with temperature. Therefore, a thermal phase change analysis is non-linear.

$$H = \int \rho \,.\, c \,.\, dT \tag{6}$$

where H is the enthalpy, ρ is related to density, c is specific heat and dT is changing of temperature.

2.2. Lap shear test

The lap shear test was performed to determine the bonding strength and quality of the joined parts. The sample geometries were defined according to the ASTM standard that is subject to the welding process. The shear stress was obtained with the joined material lap shear tests. Bonding strength and adhesion quality of the obtained material was measured by shear stress. The lap shear test was performed by an Instron-Bluehill3 universal test system. At the end of the test, the adhesive-cohesive rate of the material was examined under ultrasonic microscopy under ultraviolet light. The high cohesive adhesion rate means that the welding quality was high so that the two parts were bonded together in better quality.

3. Results and Discussion

Through the resistance welding experiments applied to the CF/PPS thermoplastic composites, the optimum process parameters were found for the supplied current, dwell time, and applied pressure parameters. As a result of the given optimum values, the heat movement in the material was examined, and the optimum molten material thickness required for effective bonding was calculated. The currents of 12A-15A-18A passed over the heating element kept supplied for the 30 and 60 s. The generated power during these periods was integrated into the heat transfer model. The heat transfer model in resistance welding includes heat transfer modes of conduction, convection, and radiation. Thus, the analysis processes were adapted to the actual experimental setup. The accuracy of the analysis processes was verified by comparing them with the results obtained through the experimental setup. In this sense, the lap shear strength values on the junction surface of composite materials become essential.

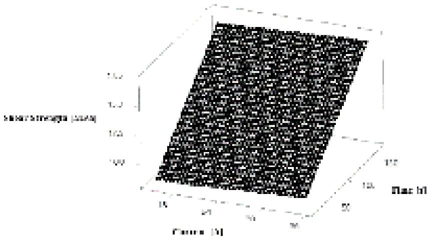

Figure 2. Response surface analysis for CF/PPS composite.

In the literature [1 - 4], thermal expansion values of similar thermoplastic composite materials were examined, and the design of experiment analysis was carried out about these values. Figure 2 shows the response surface analysis graph that was created with the values obtained from the literature. In this context, the current values were simulated concerning time values of 30 and 60 s, and optimum contents of molten material were examined. The electric current of 12A was supplied in two different time intervals of 30 and 60 s on the material in the experimental setup. At this current, the material could not reach the melting point and the phase change was not observed. The electric current given at 15A was applied in two different time intervals on the material in the experimental setup. According to the simulation results, the maximum temperature reached 361.9 °C, wherein the melting point of 280 °C, the phase change was observed on the CF/PPS material. This temperature provides enough activation energy to combine CF/PPS composite parts. As a result, the quality of adhesion and the amount of melting for 15A - 30 s parameters were examined, and optimum parameters were determined. The electric current given at 18 A was applied in two different time intervals, the 30 and 60 s, on the material in the experimental setup. According to the simulation results, the maximum temperature reached 470. 6°C, while the melting point was 280 °C, and phase change was observed on the material. However, the degradation temperature value of CF/PPS material was around 450 °C. The degradation temperature value determines the degradation of the material and above this temperature, the material loses its mechanical and thermal properties. As a result, degradation will occur in the material structure at parameters 18A - 30 s and 18A - 60 s has been identified. Following the different parameters, the temperature-time graph in Figure 3 was obtained with the cooling phase naturally. I. Fernandes Villages et al. [5] obtained a graph which likewise compares the numerical modeling with the experimental results. The aforementioned studies consist of experimental data obtained with different current values. Based on these studies, our graph that was observed analytically matches the actual graph obtained experimentally. The time-dependent graphs of the ratio of the volume of molten polymer to the composite part volume during the heating phase were shown in Figure 4 and the relationship between the start of the phase transition versus the applied electrical power is shown in Figure 5. Accordingly, while high electrical power means that phase transition will start faster, due to material properties, mechanical and thermal properties may cause a degradation mechanism. For this reason, electrical-thermal efficiency properties are also emphasized in this resistance welding study.

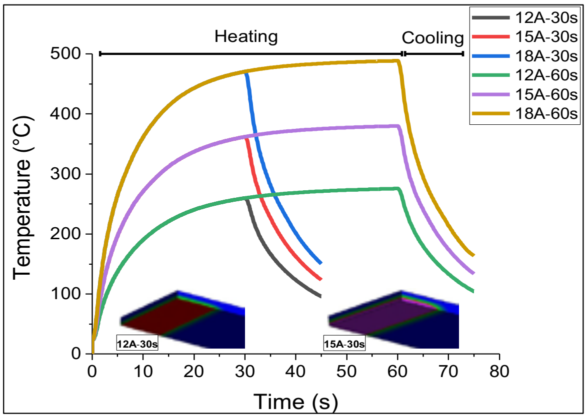

Figure 3. Comparing different parameter values chart for 12A, 15A,18A with 30 and 60 s.

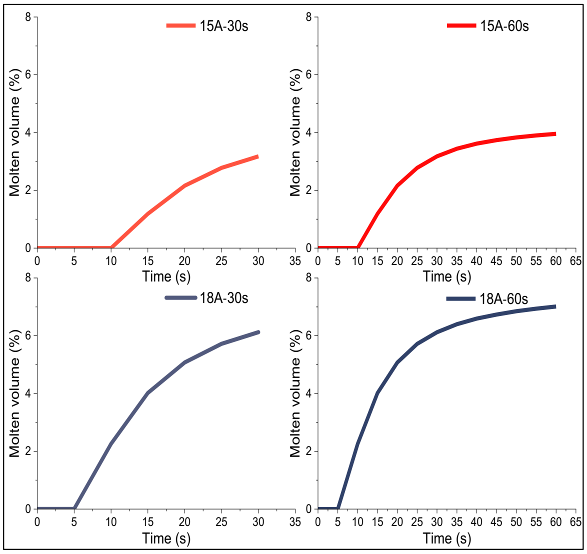

Figure 4. Melting volume fraction-time graph under the specified conditions.

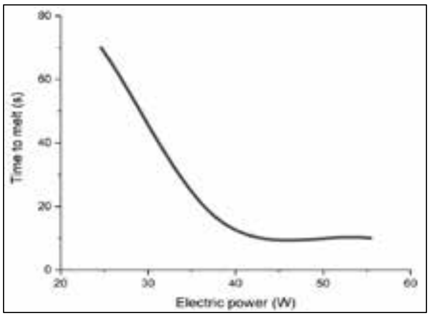

Figure 5. Relationship of the time to start melting with electric power.

According to the applied current, certain different adhesion qualities were observed on the material. Interlaminar Shear Strength (ILSS) tests were carried out to measure the degree of adhesion quality. The values obtained as a result of the ILSS test were compared with the strength values of engineering materials. The fracture condition and adhesion quality of the broken pieces obtained after the lap shear tests were observed under ultraviolet lights. The stress-strain graph was created with the data obtained from the test results. In the simulation results obtained, the effect of different parameter levels on the adhesion quality has emerged. Experiments were carried out depending on the design of experiment methods and simulation results. Experiments were carried out using sample sets of experiments for 15A-30s values, which were the optimum joining parameters.

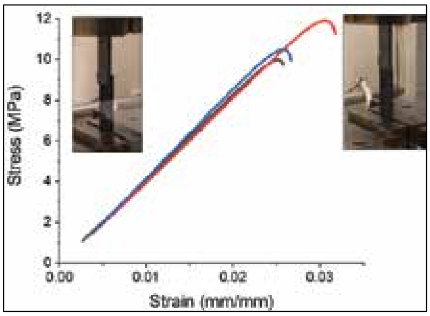

Figure 6. Stress-strain graph for 15A-30s experiment.

4. Conclusion

In this work, the supplied current, the applied pressure, and dwell time parameters controlling the resistance welding were investigated. In line with the information obtained from the prior literature, electrical, thermal, and mechanical models were integrated into the analysis. In the thermal-electric model, the heating element that efficiently affects the fiber structure of the thermoplastic composite material is defined as 304L steel. The behavior of the heating element used and the CF/PPS material during the heat transfer was analyzed. Conduction, convection, and radiation heat transfer methods affecting the test apparatus parts throughout the heat transfer have been scientifically studied and negligible factors have been investigated with scientific approaches.

It was concluded that the method can be used effectively and suitable in combining samples with carbon fiber polyphenylene sulfide material, which is a thermoplastic composite material. It is a great advantage that the method is a flexible manufacturing method, especially in production situations where the part length is varied, such as the aerospace industry.

References

[1] L. C. M. Barbosa and S. D. B. de Souza, "Fractographic Study of Welded Joints of Carbon Fiber/PPS Composites Tested in Lap Shear," 2018.
[2] C. Ageorges and L. Ye, "Experimental investigation of the resistance welding for thermoplastic-matrix composites. Part I: Heating element and heat transfer.," Elsevier, 1999.
[3] S. D. B. de Souza, A. B. R. M. Abrahao, M. L. Costa, J. M. F. Marlet, L. R. O. Hein and E. C. Botelho, "Experimental Investigation of Processing Welding Parameters for PPS/Carbon Fiber Laminates for Aeronautical Applications," Trans Tech Publications, Sao Paulo, 2016.
[4] D. Stavrov and H. E. Bersee, "Resistance Welding of Thermoplastic Composites-An Overview," Elsevier, 2005.
[5] H. Shi, I. Fernandes-Villegas, and H. E. Bersee, "Modelling of Heat Transfer and Consolidation for Thermoplastic Composites Resistance Welding," The Netherlands, 2018.

Recovered Carbon Blacks for Enviromentally Friendly EPDM Based Sealing Systems

Yusuf GÜNER, Yasemin DURMUŞ, Ali Erkin KUTLU
Standard Profil Automotive A.S.
Turkey

Abstract

The purpose of this study is that developing environmentally friendly EPDM based sealing system. For this aim, two types of recovered carbon black which were produced pyrolysis method and conventional carbon black N550 were used. Therefore, rheological and mechanical characteristics were compared. In conclusion, it was observed that Mooney viscosities were decreased, scorch times were increased, particularly for recovered carbon black containing compounds. Mechanical properties except tear strength and elongation at break for RCB2 declined. However, combination of recovered carbon black and N550 carbon black containing compounds gave promising results.

1. Introduction

EPDM (Ethylene Propylene Diene Monomers) is one of the elastomers which is wide spready used for outdoor applications such as rubber sealing profiles on vehicles since it has great resistance to ozone, oxidation, weathering and chemicals with high fatigue resistance [1,2]. Rubber compounding of EPDM includes many ingredients, one of the most consumed one carbon black which produced by using natural resources as feedstock which are highly polluting and costly. Thus, using recovered carbon black instead of or with conventional CB could be a way to produce environmentally friendly products [3]. Pyrolysis is a method which is a thermochemical decomposition of organic materials mostly waste tires under non-oxidative environment at elevated temperatures (from 400ºC to 800ºC) in order to obtain recovered carbon black (RCB) [4]. Providing implementation of RCB for industrial rubber production, not only environmentally friendly products could be achieved but also waste disposable polymeric substances could be recycled.

2. Experimental

2.1. Materials

Ethylene propylene diene rubber (EPDM) was used as polymer matrix which has Mooney Viscosity (ASTM D1646) ML 1+4, at 125°C of 70, ethylene content 50 wt% and ethylidenenorbornene level (ENB) 4-5 wt%. Recovered carbon black was provided commercially. The specification of recovered carbon black and N550 could be seen in **Table 1**. All other rubber compounds ingredients such as carbon black, steric acids, zinc oxides, accelerators...etc were commercial grades.

Table 1. Specifications of Recovered Carbon Blacks and N550 Carbon Black

	RCB1	**RCB2**	**N550**
CTAB (m^2/g)	65±5	66±5	43±5
OAN ($cm^3/100g$)	62±5	61±5	121±5
Ash (%)	unknown	unknown	0.45

2.2. Sample Preparation

Rubber blends were prepared by using laboratory grade 1.5 L internal mixer. The formulations could be seen in **Table 2**. As labelled EPDM REF, contains entirely conventional carbon black, N550. EPDM RCB1 compounds includes completely recovered carbon black 1. Similarly, EPDM RC2 contains recovered carbon black 2. EPDM COMP1 contains 50:50 loading ratio N550:RCB1. Likewise, EPDM COMP2 contains 50:50 loading ratio N550:RCB2. EPDM COMP3 and EPDM COMP4 were prepared, respectively according to 75:25 and 25:75 filling ratio of N550:RCB2., Mixing process was single passed. EPDM matrix was masticated for a minute; then; recovered carbon blacks and/or conventional carbon black with oil and small chemicals were added and formed the masterbatches. In the next step, curing system and Sulphur content were added and mixed for three minutes. Finally, rubber compounds were cooled and shaped by using the laboratory scale mill. The rubber compounds were waited for 24 hours in room temperature before vulcanization process.

2.3. Curing Characteristics

Curing characteristics of samples were determined by using Alpha Moving Die Rheometer at 180ºC for

Table 2. Formulations of Compounds

	EPDM REF	EPDM RCB1	EPDM RCB2	EPDM COMP1	EPDM COMP2	EPDM COMP3	EPDM COMP4
EPDM	100	100	100	100	100	100	100
CB	164			82	82	123	41
RCB 1		164		82			
RCB 2			164		82	41	123
Oil	103	103	103	103	103	103	103
Whiting	77	77	77	77	77	77	77
Small Chemicals	15	15	15	15	15	15	15
S+ Accelerators	8	8	8	8	8	8	8

2.5 minutes. Mooney viscosity (1+4 min) was obtained at 100 °C and Mooney scorch (1+20 min) was attained at 121°C. All rheological tests were conducted according to ASTM D 1646 standard.

2.4. Compression Molding

Rubber samples were prepared by using laboratory scale hydraulic press. The samples were placed into the mold as rectangular shaped and cured at 180°C for five minutes. It is necessary to point out that disk shaped samples were cured at 180°C for ten minutes. The cured samples were stored at room temperature before testing.

2.5. Mechanical Properties

Shore A hardness tests were carried out by using disk shaped samples according to DIN ISO 7619-1 standards. Stress-stain properties by determined by dumb bell-shaped samples with dimensions 2 mm thickness and 20 mm gauge length according to DIN 53504 standard. Tear strength was obtained trousers shaped samples by using DIN ISO 34-1 Method A standard. Additionally, compression sets were carried out by followed ISO 815-1 standard.

3. Results and Discussions

3.1. Curing Characteristics

Vulcanization parameters which are minimum torque (M_L), maximum torque (M_H), differences between them (M_H- M_L) could be see in **Figure 1**. M_L connects to viscosity of uncured rubber. Also, green strength of compound which is related to physical crosslinking between polymer chains could affect minimum torque. It was observed that the ref compound which filled with conventional CB N550 had the highest M_L, 1.85 Ib-in. Moreover, it was seen that recovered CB1 and CB2 containing compounds had 1,26 Ib-in and 1.42 Ib-in, respectively. It is essential to point out that recovered CB containing compounds had lower M_L when compared to rest of compounds. The reason of this situation is that nature of it, its dispersion ability could be low or it contains higher ash content. M_H showed similar trend with M_L. Furthermore, increase in torque which refers difference between M_H and M_L depends on crosslinking of compounds [5]. Based on this consideration, it could be concluded that the highest crosslinked density possessed to N550 carbon black compound, 11,07, the lowest one belonged to RCB2 compound which was 9.02. Degree of crosslink affects several factors but, in that case, it could be related functionality of carbon blacks. Because recovered carbon blacks are obtained pyrolysis process, they could contain some impurities or inorganic matters which affects vulcanization reaction in negative way [5].

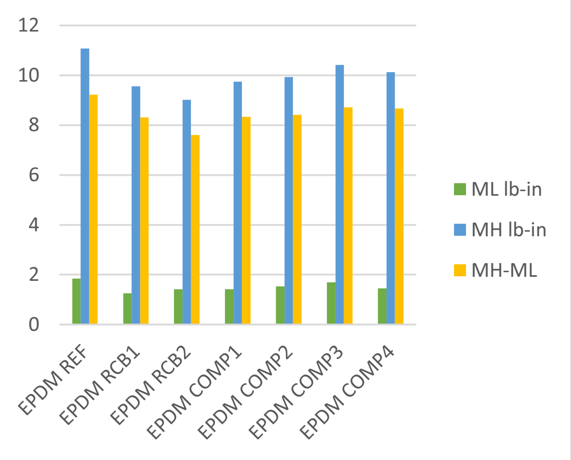

Figure. 1. Vulcanization Properties of Compounds

Mooney viscosity and scorch time of compounds could be seen in **Figure 2** and **Figure 3**. It was clearly observed that Mooney viscosity and scorch time were different from N550 CB containing compound which are critic parameters for extrusion production. The reference compound was 65.80 MU; however, 43.90 MU and 45.60 MU for RCB1 and RCB2, respectively. As amount of RCB decreases, the viscosity also increases. This dramatic decrease could arise from oil absorption ability of recovered CB. Oil absorption of recovered carbon black oil was lower when compared to conventional carbon black. Thus, less oil absorption by carbon black caused lower viscosity. Less physical crosslink due to nature of RCBs could also lead lower viscosity.

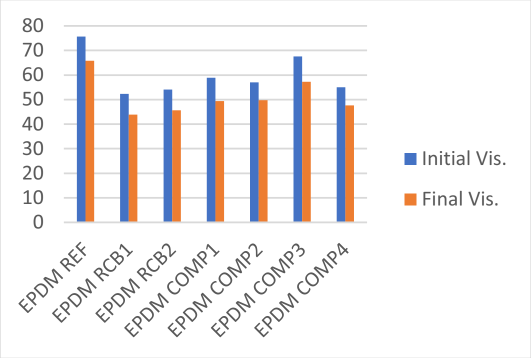

Figure. 2. Mooney Viscosity of Compounds

Following figure shows scorch time of compounds (**Fig. 3**). It was observed that recovered carbon black had significant effect on scorch time. EPDM REF compound had 5.92; however, RCB1 and RCB2 had 11.18 and 11.99 minutes, respectively. EPDM COMP1 and EPDM COMP2 compounds contained half amount of conventional carbon black. It was seen obviously, as content of RCB decreases, the scorch time narrowed considerably.

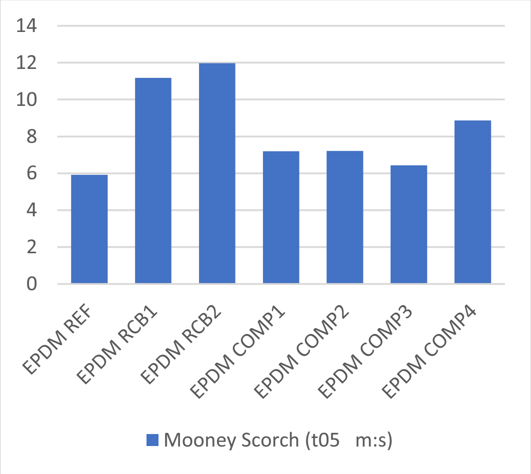

Figure. 3. Scorch Time of Compounds

3.2. Mechanical Properties

Figure 4 displays Shore A hardness of compounds. Reference compound had 72 ShA hardness but recovered CB compounds had 63ShA. As amount of recovered RCB1-2 increases, hardness decreases which could be related to surface area of carbon blacks. It is a fact that surface area of CB increases, the interaction between polymer chains and carbon black also increases; thus, mobility of chains decreases [5]. As a result, hardness of compound could be boosted as surface area of carbon black loading to the compound.

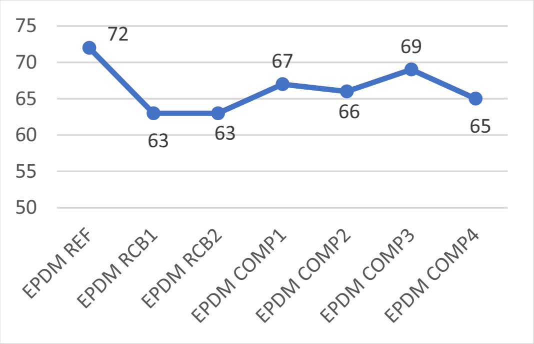

Figure. 4. Hardness of Compounds

Following figure shows tensile strength and tear strength of compound (**Figure 5**). As considering tensile strength, RCB 1 and RCB2 amount increases in the compounds, tensile strength decreases which could be related to reinforcing effect of CB. Tear strength; however, similar for all compounds except RCB2 carbon black compounds. Surprisingly, an increase from 6.10 N/mm (EPDM REF) to 7.76 N/mm (EPDM COMP1) was observed.

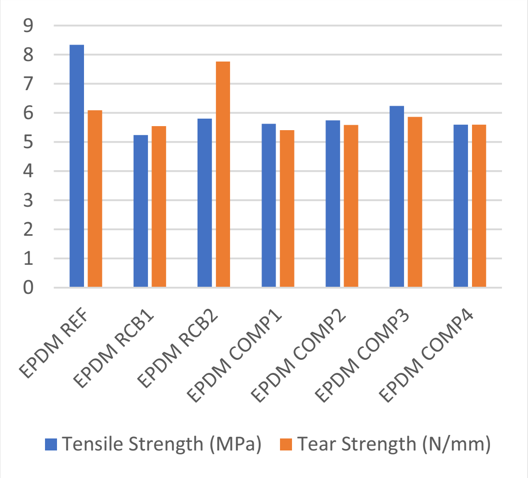

Fig. 5. Tensile and Tear Strength of Compounds

Elongation at break of compounds could be seen in **Figure 6**. It is important to point out that conventional carbon black N550 combine with recovered carbon black, elongation at breaks were declined.

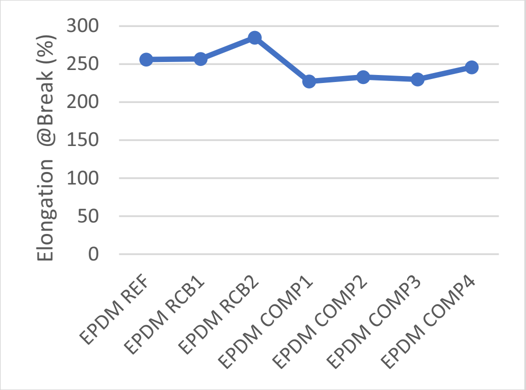

Figure. 6. Elongation at Break of Compounds

Modulus of compounds which could be associated with M_H-M_L and crosslink density. That means as recovered carbon blacks loading increases in the compounds, crosslink densities could be declined as mentioned in **3.1. Section.** It refers as crosslink density decreases in a compound, modulus also decreases. In this study, the highest modulus was observed N550 containing compound, the lowest one was for RCB2 compound.

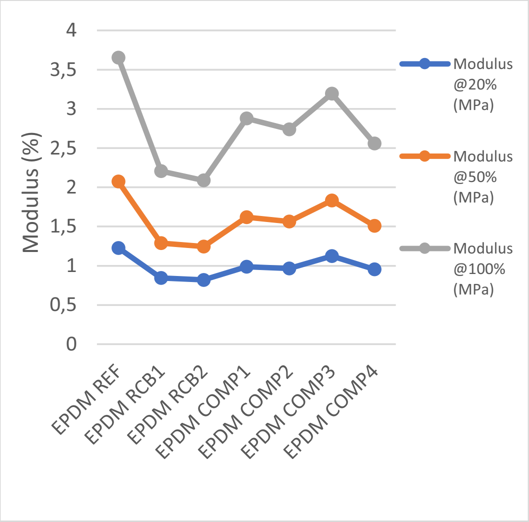

Figure 7. Modulus (20%, 50%, 100%) of Compounds

Compression set results of compounds could be seen in **Figure 8**. It was concluded that although combination with N550 and RCB1-2 containing compounds had higher compression set, there was not considerable change.

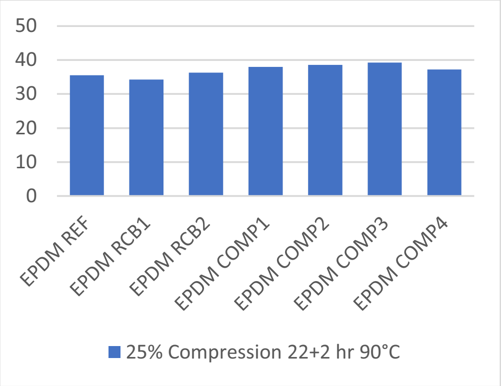

Figure 8. Compression Sets of Compounds

4. Conclusions

In this work, rheological and mechanical properties of EPDM rubber compounds with recovered carbon black and/or conventional carbon black N550 loading for vehicle sealing system application was studied. It was concluded that recovered carbon black had detrimental effect on rheological features. Mooney viscosity decreases and scorch time increases significantly. However, promising mechanical results were obtained when compared to N550 containing compound. Thus, it could be possible to produce extrudable environmentally friendly sealing systems in the future.

References

[1] Gamlin, C., Dutta, N., Roy-Choudhury, N., Kehoe, D., & Matisons, J. (2001). Influence of ethylene–propylene ratio on the thermal degradation behaviour of EPDM elastomers. Thermochimica acta, 367, 185-193.

[2] Dijkhuis, K. A., Noordermeer, J. W., & Dierkes, W. K. (2009). The relationship between crosslink system, network structure and material properties of carbon black reinforced EPDM. *European Polymer Journal*, *45*(11), 3302-3312.

[3] Zhong, R., Xu, J., Hui, D., Bhosale, S. S., & Hong, R. (2020). Pyrolytic preparation and modification of carbon black recovered from waste tyres. *Waste Management & Research*, *38*(1), 35-43.

[4] Moulin, L., Da Silva, S., Bounaceur, A., Herblot, M., & Soudais, Y. (2017). Assessment of recovered carbon black obtained by waste tires steam water thermolysis: an industrial application. *Waste and Biomass Valorization*, *8*(8), 2757-2770.

[5] Sagar, M., Nibedita, K., Manohar, N., Kumar, K. R., Suchismita, S., Pradnyesh, A., ... & Jayaramudu, J. (2018). A potential utilization of end-of-life tyres as recycled carbon black in EPDM rubber. *Waste Management*, *74*, 110-122.

Spark Plasma Sintering and Characterization of B_4C- TiB_2 Composites

Leyla YANMAZ[1], S. Ege PARIM[2], Gültekin GÖLLER[1], Onuralp YÜCEL[1], Filiz Çınar ŞAHİN[1]
[1]Istanbul Technical University, [2]Gebze Technical University
Turkey

Abstract

Boron carbide (B_4C) is an advanced structural material with high melting point, low density, high hardness, high neutron absorption capability, chemical stability and good impact and wear resistance. It is widely used in industrial cutting-grinding tools, nuclear reactors, wear resistant components, abrasive materials and lightweight armors. However, there are limitations due to its strong covalently bonded structure which causes limited sinterability at low temperatures without use of additives. B_4C-TiB_2 ceramic composites are promising materials ensuring sinterability and good mechanical properties of B_4C. In this study, B_4C-TiB_2 composites in square geometry with the varying amounts of TiB_2 (0, 5, 10, 15 vol. %) were prepared by spark plasma sintering at 1540°C with pressure of 50 MPa in vacuum environment. The effects of TiB_2 addition and square geometry on the densification, hardness and fracture toughness were investigated.

1. Introduction

Boron carbide is one of the hardest materials after diamond and cubic boron nitride, which has high melting point, low density, good chemical and physical stability, high neutron absorption cross section, high compression strength and high wear resistance [1, 2]. However, sintering of boron carbide has some limitations due to its crystal structure and strong covalent bonds. In addition, low fracture toughness of the material is a disadvantage for some structural applications. In order to overcome these limitations and increase the sinterability of boron carbide, additives including oxides, carbides, nitrides and borides are used widely [1-4]. Due to its significant properties titanium diboride (TiB_2) is commonly used as an additive for sintering of boron carbide. It helps to increase fracture toughness and contributes the densification of boron carbide [5-10]. Uygun et al. [11] produced B_4C-TiB_2 composites by spark plasma sintering and composites having 5, 10, 15 and 20 vol.% TiB_2 were prepared. Sintering was performed at 1760°C under 40 MPa for 5 minutes. They found that with the increasing amount of TiB_2, relative density of the samples were increased.

The aim of this study is to manufacture highly dense and B_4C-TiB_2 composites in square cross section by using spark plasma sintering (SPS) method and reduce property difference between edge and center of the square shaped composites. The effect of TiB_2 was investigated terms of to the density, hardness and fracture toughness.

2. Experimental Procedure

In this study, commercial B_4C (Grade HS, d_{50}=0.8 µm, H. C. Stack GmbH&Co., Germany) and TiB_2 (Grade D, d_{50}=3-6 µm, H. C. Stack GmbH&Co., Germany) powders were used. Powder mixtures of B_4C-TiB_2 were prepared using ball milling. After milling, powder mixtures were dried, screened and loaded into a graphite die having 50x50x5 mm dimensions. B_4C-TiB_2 composites with 0, 5, 10, 15 vol.% TiB_2 were spark plasma sintered with SPS-7.40MK-VII, SPS Syntex Inc. apparatus at 1540°C under vacuum atmosphere with pressure of 50 MPa for 7 minutes holding time. In order to obtain a homogenously densified sample, B_4C-15 vol.% TiB_2 composite was produced at the same sintering conditions for 9 minutes holding time. The spark plasma sintered samples were sand blasted to remove graphite foil layers and then cut into 9 pieces and labeled as center, edge and corner accordingly to understand the densification of the square-shaped sample. XRD phase analysis was conducted in the 2θ range of 10-90° with CuKα radiation (XRD Miniflex, Rigaku Corp.). Density of the samples were measured using Archimede's principle and relative densities were calculated using rule of mixtures for composites. Samples were ground and polished to 0.25µm finish. The microhardness and fracture toughness measurements were done using Vicker's indentation method (Struers Duramin A300).

3. Results and Discussion

XRD results of B_4C-TiB_2 composites are given in Figure 1. It can be seen that when the amount of TiB_2 addition increased, the intensity of TiB_2 peaks increased.

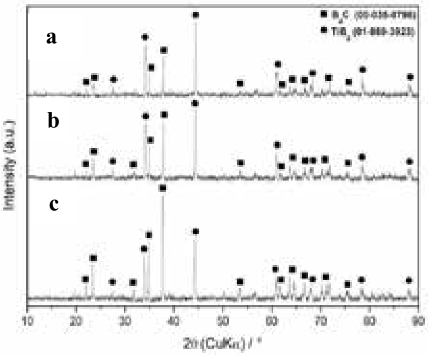

Figure 1. XRD analysis of spark plasma sintered **(a)** B_4C-15 vol.% TiB_2 **(b)** B_4C-10 vol.% TiB_2 **(c)** B_4C-15 vol.% TiB_2 composites.

The relative density values of B_4C-TiB_2 composites with 0, 5, 10, 15 vol.% TiB_2 are shown in Figure 2.

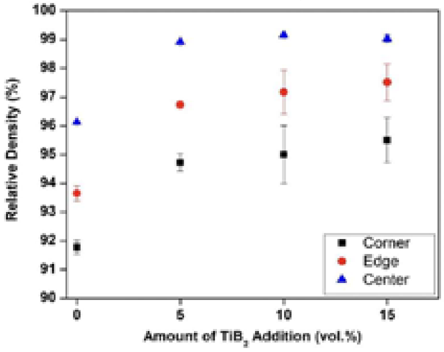

Figure 2. Relative density values of B_4C-TiB_2 composites sintered at 1540°C by applying 50 MPa pressure for 7 minutes holding time.

Relative densities of B_4C-TiB_2 composites sintered at 1540°C under 50 MPa for 7 minutes having 0, 5, 10 and 15 vol.% TiB_2 were measured as 96.13%, 98.92%, 99.16%, 99.03% for centers, 91.78%, 94.73%, 95.00%, 95.50% for corners and 93.65%, 96.73%, 97.17%, 97.51% for edges, respectively. There is no significant difference in relative densities of 10 vol.% and 15 vol.% TiB_2 containing composites. In addition, relative densities of edges and corners increased significantly with increasing amount of TiB_2 compared to monolithic B_4C. This increment in relative densities of composites can be attributed to improvement in densification behavior of boron carbide with addition of TiB_2. It can be seen that there is a density difference between center, edges and corners of the samples. Therefore, holding time of B_4C-15 vol.% TiB_2 composite production was extended to 9 minutes to be able to produce more homogenous sample. According to Figure 3, it was observed that the increase in holding time causes a slight increase in relative density from 95.50% to 96.52%, from 97.51% to 98.13%, and from 99.03% to 99.23% for corners, edges and center, respectively. As a result, more homogeneous sample was obtained for 9 minutes holding time.

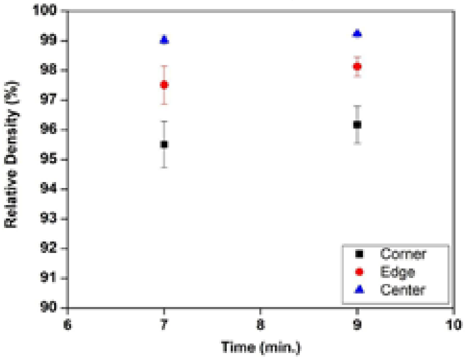

Figure 3. Relative density values of B_4C – 15 vol.% TiB_2 composites sintered at 1540 °C by applying 50 MPa pressure for 7 - 9 minutes holding time.

Hardness values of B_4C-TiB_2 composites containing 0, 5, 10, 15 vol.% TiB_2 were measured as 30.42±0.94 GPa, 30.26±0.68 GPa, 30.42±0.41 GPa and 30.78±0.32 GPa, respectively, as shown in Figure 4. The highest hardness value was measured as 31.00±0.38 GPa for B_4C-15 vol. % TiB_2 composite which is sintered for 9 minutes holding time. The reason for the increase in hardness value can be caused by increase in holding time which leads to higher densification of B_4C and decrease in amount of porosity.

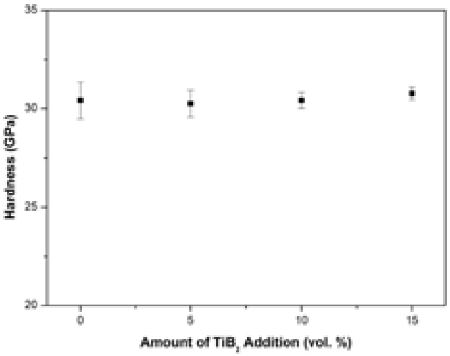

Figure 4. Hardness values of B_4C - TiB_2 composites sintered at 1540 °C by applying 50 MPa pressure for 7 minutes holding time.

Fracture toughness values for B_4C-TiB_2 composites containing 0, 5, 10, 15 vol.% TiB_2 were measured as 3.97±0.07 MPa.m$^{1/2,}$ 4.24±0.17 MPa.m$^{1/2}$, 4.39±0.13 MPa. m$^{1/2}$ and 4.72±0.10 MPa. m$^{1/2}$, respectively, as shown in Figure 5. The highest fracture toughness value was measured as 4.97±0.44 MPa. m$^{1/2}$ for B_4C-15 vol.% TiB_2 composite which was sintered for 9 minutes holding time. The mechanism of increase in fracture toughness can be explained by thermal mismatch between TiB_2 and B_4C. Since, TiB_2 has a higher thermal expansion coefficient than B_4C, it creates tensile stresses at the interface between B_4C-TiB_2 during cooling from sintering temperature to room temperature. As a result of these tensions, microcracks at the interface absorb the energy of the crack by stopping or changing the direction of the crack in the matrix and causes an increase the fracture toughness [12].

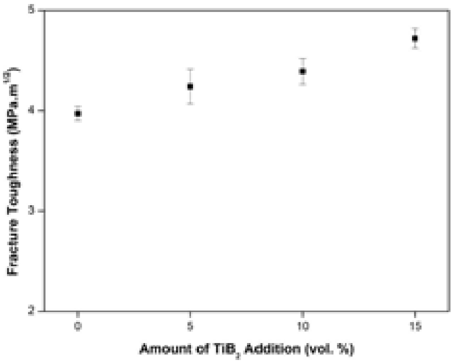

Figure 5. Fracture toughness values of B_4C - TiB_2 composites sintered at 1540 °C by applying 50 MPa pressure for 7 minutes holding time.

4. Conclusion

In this study, monolithic boron carbide (B_4C) and B_4C -TiB_2 composites having 5, 10 and 15 vol.% TiB_2 were produced in square shape with 50 mm length, 50 mm width and 5 mm thickness using spark plasma sintering method at 1540°C under 50 MPa pressure for 7 minutes holding time.

The relative density of B_4C (center) is increased from 96.13% to 98.12, 99.16 and 99.03 % with 5, 10, 15 vol. % TiB_2 addition, respectively. With the increasing amount of TiB_2, density of the composites increased accordingly. However, there was a difference between densities of center, edges and corners. B_4C-15 vol.% TiB_2 composite was spark plasma sintered for 9 minutes holding time to overcome this difference in properties. The relative density of corners, edges and center converged slightly and measured as 96.52%, 98.13%, and 99.23%, respectively.

The highest hardness value was measured as 31.00±0.38 GPa for 9 minutes sintered B_4C-15 vol.% TiB_2 composite.

Addition of TiB_2 increased the fracture toughness of B_4C from 3.97 MPa.m$^{1/2}$ to 4.72 MPa.m$^{1/2}$. The highest fracture toughness was found as 4.97 MPa.m$^{1/2}$ for B_4C-15 vol.% TiB_2 composite sintered for 9 minutes.

References

[1] F. Thevenot, “Boron Carbide A Comprehensive Review,” *Journal of th European Ceramic Society*, vol. 1, no. 4, pp. 205–225, 1990.

[2] A. K. Suri, C. Subramanian, J. K. Sonber, and T. S. R. C. Murthy, Synthesis and consolidation of boron carbide: a review, vol. 55, no. 1. 2010.

[3] M. Asadikiya, C. Zhang, C. Rudolf, B. Boesl, A. Agarwal, and Y. Zhong, “The effect of sintering parameters on spark plasma sintering of B4C,” Ceramics International, vol. 43, no. 14, pp. 11182–11188, 2017.

[4] F. C. Sahin et al., “Spark plasma sintering of B4C-SiC composites,” Solid State Sciences, vol. 14, no. 11–12, pp. 1660–1663, 2012.

[5] H. O. Pierson, “Applications of Refractory Carbides and Nitrides,” Handbook of Refractory Carbides and Nitrides, pp. 309–326, 1996.

[6] F. C. Sahin and S. A. Yesilcubuk, “B 4 C-TiB 2 Composites via Reactive Hot Pressing,” pp. 277–284, 2009.

[7] M. Saeedi Heydari and H. R. Baharvandi, “Comparing the effects of different sintering methods for ceramics on the physical and mechanical properties of B4C-TiB2 nanocomposites,” International Journal of Refractory Metals and Hard Materials, vol. 51, pp. 224–232, 2015.

[8] L. Nikzad, R. Licheri, T. Ebadzadeh, R. Orrù, and G. Cao, “Effect of ball milling on reactive spark plasma sintering of B4C-TiB2 composites,” Ceramics International, vol. 38, no. 8, pp. 6469–6480, 2012.

[9] L. Nikzad, R. Orrù, R. Licheri, and G. Cao, “Fabrication and formation mechanism of B 4 C - TiB 2 composite by reactive spark plasma sintering using unmilled and mechanically activated reactants,” Journal of the American Ceramic Society, vol. 95, no. 11, pp. 3463–3471, 2012.

[10] C. Xu, Y. Cai, K. Flodström, Z. Li, S. Esmaeilzadeh, and G. J. Zhang, “Spark plasma sintering of B4C ceramics: The effects of milling medium and TiB2 addition,” International Journal of Refractory Metals and Hard Materials, vol. 30, no. 1, pp. 139–144, 2012.

[11] B. Uygun, G. Göller, Y. Onuralp, and F. Ç. Şahin, “Production and Characterization of Boron Carbide – Titanium Diboride Ceramics by Spark Plasma Sintering Method,” Advances in Science and Technology, vol. 63, no. Volume 63, pp. 68–73, 2010.

[12] V. V Skorokhod and V. D. Krstic, “Processing, Microstructure, And Mechanical Properties Of B4C-TiB2 Particulate Sintered Composites. II. Fracture and Mechanical Properties,” *Powder Metall. Met. Ceram.*, vol. 39, no. 9, pp. 99–107, 2000.

The Effect of B_4C Amount on the Wear Properties of Al-B_4C Composites Obtained by High Energy Ball Milling

Sezgin YAŞA, Ahmet KABİL, Burak BİROL
Yıldız Technical University
Turkey

Abstract

Boron carbide which has a high hardness and friction strength is a well reinforcement material for aluminum composites to be able to improve its properties. In this study various amounts of B_4C (0, 5, 10 and 15%) particles and 2% of stearic acid as PCA were added to Al powders with commercial purity. Then these mixtures were ball milled with 5 hrs using a planetary ball mill under vacuum conditions. The ball to powder weight ratio and rotational speed were 10:1 and 400 rpm, respectively. 3 g of ball milled powder mixture were pressed under 720 MPa with a metal mold having a diameter of 14 mm. Following this green samples were sintered at 600 °C under Ar atmosphere for 60 mins. The properties of the products were investigated by SEM, Brinell hardness, and apparent density measurements. Additionally the wear rates of the samples were obtained by using a Pin-on disc wear testing device. According to the results, the particles were homogeneously dispersed and low amounts of porosity were observed also the density measurements prove this result. Because B_4C has a specific weight very close to pure aluminum (2,52 gr/cm^3), no significant difference between the samples were encountered. Moreover increasing B_4C amount increases the wear resistance of the composite samples. On the contrary it was found that hardness values decreases with the increasing amount of reinforcement ratio.

1. Introduction

In the last century, great advances have been made in the field of material science in parallel with the developments in science and industry. Industries such as aero-space and defense where material performance is ahead of material cost play a leading role in the development of new material groups. Metal matrix composites (MMC) are materials created by adding ceramic reinforcements such as Al_2O_3, B_4C, SiC to metal matrices such as Al, Mg. Although MMCs were originally developed for these sectors, today their production methods have diversified and their usage has become widespread with the decrease in material cost [1], [2].

Metal matrix composite materials offer superior physical and mechanical properties such as high specific strength and specific rigidity, high hardness and wear resistance, low thermal expansion and coefficient of friction, high thermal conductivity and energy absorption ability [3].

Metal matrix composite material production methods are categorized into three main groups as solid state processes, liquid state processes and semi-solid state processes. Depending on the production method, the rate of reinforcement, the type of reinforcement and the interface properties vary and significant differences are observed in the material properties depending on this change [4], [5].

The powder metallurgy method includes the steps of mixing the reinforcement and matrix particles, pressing the powder mixture in the desired geometry, and sintering the compacted material. One of the most important factors affecting the properties of the final material produced is the homogeneous distribution of the reinforcing particles in the matrix. The ratio of the reinforcement particle size to the matrix particle size is an important parameter so that the reinforcement particles can be distributed uniformly within the matrix. If the matrix particle size is larger than the reinforcement, the reinforcements fill the gaps between the large particles and agglomerate in these regions. The ratio of reinforcement / matrix size to close to 1 was determined to be ideal ratio for the homogeneous distribution of reinforcing particles [4-10].

B_4C is the third hardest material known after diamond and cubic boron nitride. Besides its hardness, its properties such as low density, chemical stability and high melting degree make B_4C attractive in its use as a reinforcing material [11], [12].

High energy ball milling process provides homogeneous mixing of reinforcement and matrix powders as well as reducing the grain size [13].

2. Experimental Procedure

In the present study, to investigate the B_4C addition to the aluminum matrix, aluminum powder and B_4C powder obtained from ESK Ceramics were used as raw materials. The chemical composition of the aluminum powder was determined with Hillger Optic Emission Spectrometer and given in Table 1.

Table 1. Chemical analysis of the Al powder (wt%)

Fe	Si	Cu	Mg	Al
1.50	0.339	0.103	0.285	97.773

The particle size of aluminum and B_4C are <45 µm and 60-100 µm, respectively. Powder mixtures were prepared with 0, 5, 10 and 15% B_4C reinforcement, 2% of PCA (stearic acid) ratio. Powder mixtures were than ball milled in a vacuum atmosphere by using a planetary ball mill for 5 hr. The parameters of the ball milling process were selected as; ball to powder ratio 10:1 and rotational speed of 400 rpm. 20% of the balls used in the ball mill were selected as 8 millimeters and 80% were selected as 5 millimeters in diameter. 3 gr of the powder blends were than pressed under 720 MPa with using a hydraulic press. Compacts, with a 14 mm diameter were then removed from the metal mold and sintered at 600 °C under Ar atmosphere for 60 mins in an atmosphere controlled tube furnace given in Figure 1.

Figure 1. Atmosphere controlled tube furnace

After sintering process, density measurements were conducted using Archimedes Principle. After that, hardness values of the specimens were measured with using Brinell hardness method. Wear characteristics of the produced composites materials were performed by using Pin-on disc wear testing device given in Figure 2.

Figure 2. Pin-on disc wear test machine

Wear test conducted under conditions of; 0,05 m/s sliding speed and 10 N load. Pin material was 100Cr6 steel ball with a diameter of 10 mm and 840 HV. As a result of the wear testing, wear rate values were obtained. In order to investigate the microstructural features of the composites and wear track surface, SEM examination of the specimens were done.

3. Results and Discussion

As a result of the density measurements, the density of the samples without reinforcement, containing 5%, 10% and 15% B_4C was found to be 2,56, 2,58, 2,58 and 2,62 gr / cm^3, respectively..

Figure 3. shows the change of hardness according to the amount of boron carbide added by weight..

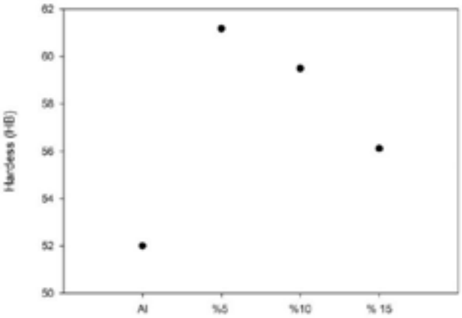

Figure 3. Variation of hardness with B_4C addition

An increase of approximately 18% in hardness was observed in the 5% reinforced sample compared to the non-reinforced sample. This increase in hardness was less in samples with 10% and 15% reinforcement. In reinforced samples, a decrease in hardness was observed with increasing reinforcement rate. Depending on the sintering temperature and duration, chemical bonding between the reinforcement and the matrix did not occur, and the reinforcing particles are thought to be held only mechanically by the matrix. Therefore, the hardness value decreases because the reinforcement / matrix interface increases spatially with the reinforcement ratio and this interface is weaker than the reinforcement or matrix.

The wear rates obtained as a result of the pin-on disc wear test are shown in Figure 4.

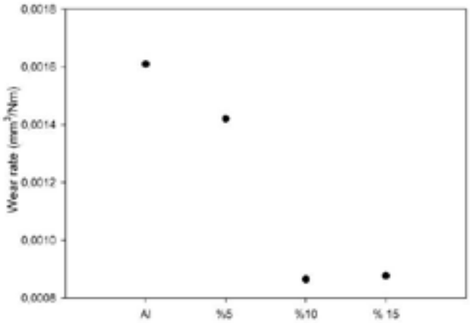

Figure 4. Variation of wear rate with B_4C addition

The rate of wear is observed to decreases with increasing reinforcement rate. With the increase of the reinforcement rate, the harder and friction resistant B_4C reinforcement particles prevent the surface from abrasion, allowing less material removal.

Figure 5, shows SEM images of the wear surfaces.

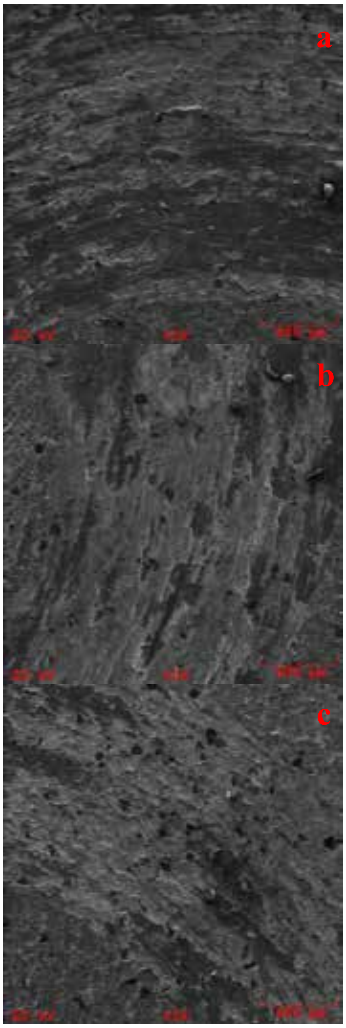

Figure 5. SEM image of wear surfaces (a: %5 B_4C, b: %10 B_4C, c: %15 B_4C)

As can be seen in Figure 5a, the wear region has been deformed and plastered on the aluminum surface and covered the B_4C particles. When we examine the SEM image of the B_4C reinforced sample (Figure 5.b), it is seen that the reinforcement particles prevent the matrix from undergoing plastic deformation. Finally, B_4C particles were easily observed on the surface of the 15% reinforced sample and the plastering of aluminum was largely prevented.

Figure 6 is SEM images showing microstructures of samples containing 5%, 10% and 15% B_4C.

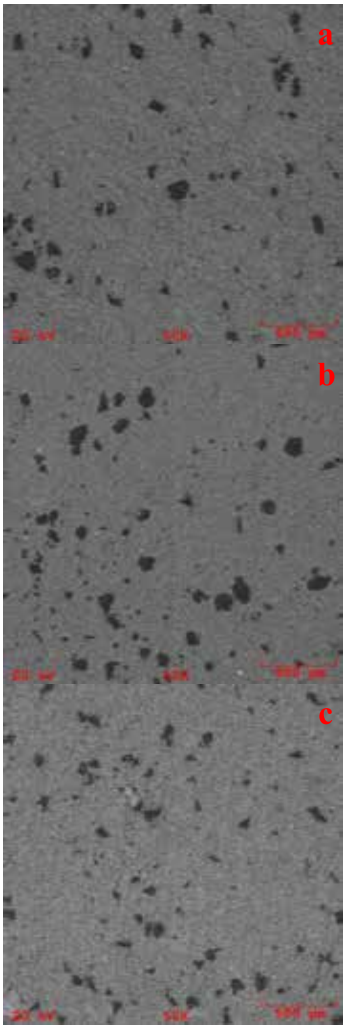

Figure 6. SEM images of the composites (a: %5 B_4C, b: %10 B_4C, c: %15 B_4C)

When the images were examined, it was seen that the B_4C particles were partially dispersed homogeneously. Regions containing no reinforcement and where the reinforcement particles were agglomerated were observed. These heterogeneous zones are thought to have a negative impact on the hardness and wear properties of the material

4. Conclusion

- As a result of the study, aluminum matrix composite materials containing B4C in different proportions were produced using a high energy ball mill and an atmosphere controlled furnace.
- The hardness of the composite materials produced is observed to be higher compared to non-reinforced aluminum, but the hardness decreases with increasing reinforcement rate.
- Except for 15%, wear rate values decreased in parallel with the increasing reinforcement rate.
- In the SEM examination, the matrix's plastic deformation was prevented as the reinforcement rate increased.
- Stronger formation of the interface can be achieved by changing the sintering time and temperature.
- Secondary processes such as forging and rolling can improve the material properties thanks to the homogeneous distribution of the reinforcements.

References

[1] D. Miracle, “Metal matrix composites – From science to technological significance”, Composites Science and Technology, 65 (2005) 2526-2540.

[2] I. Ibrahım, A. Mohamed and E. Lavernia, “Particulate Reinforced Metal Matrix Composites-a review,” Journal of Materials Science, 26 (1991) 1137-1156.

[3] M. Surappa, “Aluminum Matrix Composites: Challenges and Opportunities,” Sadhana, 28 (2003) 319-334.

[4] S. Jayalakshmi and M. Gupta, Metallic Amorphous Alloy Reinforcements in Light Metal Matrices, Singapore, 2015, Springer.

[5] N. Chawla and K. Chawla, Metal Matrix Composites, New York, 2006, Springer.

[6] A. Cuevas, E. Becerril, M. Martinez and J. Ruiz, Metal Matrix Composites Wetting and Infiltration, 2018, Springer.

[7] S. Suresh, A. Mortensen and A. Needleman, Fundamentals of Metal Matrix Composites, 1993, Butterworth-Heinemann.

[8] F. Campbell, Structural Composite Materials, 2010, ASM International.

[9] J.B. Fogagnolo, F. Velasco, M.H. Robert, J.M. Torralba, “Effect of mechanical alloying on the morphology, microstructure and properties of aluminium matrix composite powders” Materials Science and Engineering A, 342 (2003) 131-143.

[10] M. Khakbiz and F. Akhlaghi, “Synthesis and structural characterization of Al–B4C nano-composite powders by mechanical alloying”, Journal of Alloys and Compounds, 479 (2009) 334–341.

[11] I. Topcu, H.O. Gulsoy, N. Kadioglu and A.N. Gulluoglu, “Processing and mechanical properties of B_4C reinforced Al matrix composites”, Journal of Alloys and Compounds, 482 (2009) 516–521.

[12] A.Baradeswaran and A.Elaya Perumal, “Influence of B_4C on the tribological and mechanical properties of Al 7075–B_4C composites” Composites: Part B, 54 (2013) 146–152.

[13] R. Zhenga, X. Hao, Y. Yuan, Z. Wang, K. Ameyama and C. Ma., “Effect of high volume fraction of B4C particles on the microstructure and mechanical properties of aluminum alloy based composites” Journal of Alloys and Compounds, 576 (2013) 291–298.

Production and Characterization of Graphene Reinforced Al-10Si Matrix Composites via Powder Metallurgy

Berk ŞENYURT[1], Nazlı AKÇAMLI[1], Duygu AĞAOĞULLARI[2], Hasan GÖKÇE[2]
[1]Bursa Technical University, [2]Istanbul Technical University
Turkey

1. Introduction

Aluminum and its alloys are highly demanded materials for the automotive and aerospace industries due to their remarkable light weight-high strength properties. Reinforcing agents such as different hard ceramic compounds and carbon structures enable to further improving the strength properties of these light-weight alloys for special applications. Graphene is an important potential reinforcing agent for aluminum matrix composites (ACMs) with its remarkable mechanical properties [1-3].

2. Materials and Method

In this study, graphene nanoplatelets (GNPs, up to 5 wt.%) reinforced Al-10Si matrix composites are fabricated via powder metallurgical processing route. Al, Si powders and GNPs are mechanically alloyed (MA'ed) at 1200 rpm for 0, 2 and 6 hours in a stainless steel milling medium under Ar atmosphere. The MA'ed powders are consolidated via powder metallurgical route including uniaxial pressing at 500 MPa and pressureless sintering at 565 °C for 2 h under Ar atmosphere.

The effects of MA time and GNPs amount on the microstructural and mechanical properties are investigated. Microstructural characterization and phase analysis of the as-blended and MA'ed powders and bulk samples are performed via X-Ray diffraction (XRD) and scanning electron microscopy (SEM) techniques. Additionally, physical, mechanical and tribological characterization of the bulk samples are performed via Archimedes density, microhardness and reciprocating wear tests. As a result, the optimum conditions for production of GNPs reinforced Al-Si matrix composites are determined.

3. Results

Only Al and Si phases are determined and Al_4C_3 phase formation is not observed in XRD patterns of the sintered samples (Fig. 1a). This shows that graphene preserves its stability after the mechanical alloying and sintering processes. Relative densities of sintered samples MA'ed for different durations are determined as between 94.44% to 96.82%. The hardness value of the Al10Si composite prepared from the 6 hours of MA'ed powders increased to 171.67 HV from 105.75 HV by the addition of 5 wt.% GNP.

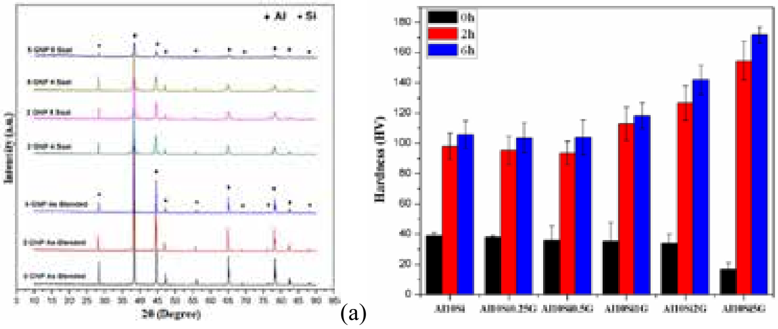

(a) (b)

Fig.1 (a) XRD patterns and (b) hardness values of Al10Si-xGNP (x: 0-5 wt.%) composites.

References

1. Lawrance, C. A., Suresh Prabhu P. 2015. "Al 6061-TiB2 metal matrix composite synthesized with different reaction holding times by in-situ method", International Journal of Composite Materials, 5 (5), 97-101.

2. Woo, K. D., Zhang, D. L. 2004. "Fabrication of Al–7wt%Si–0.4wt%Mg/SiC nanocomposite powders and bulk nanocomposites by high energy ball milling and powder metallurgy", Current Applied Physics, 4 (2-4), 175-178.

3. Pérez-Bustamante, R., Pérez-Bustamante, F., Estrada-Guel, I., Licea-Jiménez, L., Miki-Yoshida, M., Martínez-Sánchez, R. 2013, "Effect of milling time and CNT concentration on hardness of CNT/Al2024 composites produced by mechanical alloying", Materials Characterization, 75, 13-19.

Development of Novel Production Method for LaFeSi Based Materials and Its Room Temperature Magnetic Properties

Semih ATEŞ[1], Doğaç TARI[1], Şerzat SAFALTIN[1], Sebahattin GÜRMEN[1], Öznur KARAAĞAÇ[2], Hakan KÖÇKAR[2]
[1]Istanbul Technical University, [2]Balıkesir University
Turkey

Abstract

Lanthanide group metals are among the current applied – research materials technologies due to the chemical, optical and magnetic properties as a result of unique electronic structures. These are used in wide range from direct – consumption technologies such as MR devices, LED systems, catalyst materials, to green energy systems for instance wind turbines, photovoltaics, magnetic refrigerators. On the other hand, rare earth metals are high cost materials because of their production route. This study aimed to develop Hydrogen Reduction (HR) Method from Lanthanide Oxalate powders to produce LaFeSi based materials instead of conventional production techniques. According to pre – experimental analyses (DSC – TG, numerical thermodynamics) reduction temperatures were determined. LaFeSi based powder materials were produced in one step with HR method at different reduction temperatures. The structural properties of powders were analyzed with XRD and SEM. The VSM analyses were done to observe final magnetic properties in accordance with magnetic applications of final materials.

1. Introduction

Rare earth metals constitute the basics of indispensable material systems of today's critical technologies (LCD screens, MRI devices, refrigerators, super magnets, etc.) in terms of their application – based properties that they have shown outside of the traditional metals. In high – tech device manufacturers that works for critical technological devices, most of the time uses pure metallic powders to get the final material. In the most general sense, producers are focused on final properties and performance of these materials instead of production technique and supplies. When this situation is evaluated in terms of green engineering approaches, production method should be reevaluated and improved as well as researching importance of material performance. According to magnetic materials, LaFeSi based materials are in the novel functional magnetic materials family. If they are to be further specified, they are included in the magnetocaloric material group which are used as a new – gen refrigeration systems [1]. After the discovery that the cooling response created by Gd metal with the effect of magnetism is applicable in cooling systems, these properties of rare earth metals are started to be investigated. LaFeSi based materials show large values of magnetic entropy changes while they have cubic $NaZn_{13}$ – type structure. Because of this, they used in magnetic refrigeration systems [2]. Magnetocaloric materials are given at Figure 1. $NaZn_{13}$-type crystal structure of LaFeSi is given at Figure 2. To obtain LaFeSi based alloy, arc or induction melting are used as conventional production method and pure metallic powder forms of each components are used as starting materials [3]. In accordance with philosophy of green technologies, the magnetic behavior of these materials at room temperature should be examined for refrigeration systems that used in daily life and essentials for homes [4].

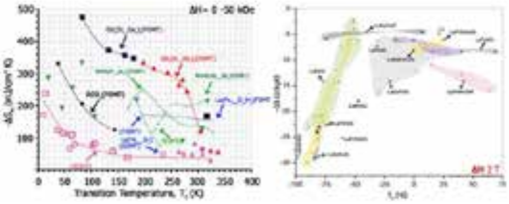

Figure 1. Magnetocaloric propeties, (left) material groups [5], (right) LaFeSi materials.

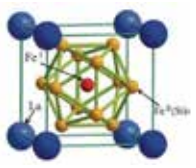

Figure 2. $NaZn_{13}$-type structure of LaFeSi material

In the light of relation between production method – structure – properties – performance, the magnetic properties of LaFeSi based materials can be directly control with the parameters of the production method. Recent studies show that when La is partially replaced by the rare earth element Ce, magnetic and magnetocaloric properties of these materials are enhanced [6].

This work mainly focusses on to develop a Hydrogen Reduction (HR) method for LaFeSi based materials. Oxalate forms of La, Ce and Fe were used as a raw material for this novel production technique. Thus, it is ensured that energy and raw material consumption loads of conventional production methods of LaFeSi based materials are prevented. $La_{0,7}Ce_{0,3}Fe_{11.8}Si_{1.2}$ nominal composition at $NaZn_{13}$-type crystal structure was produced in single step with HR at different *($T_{red.}$ = 700°C, 800°C, 900°C)* reduction temperatures. Hence, reduction temperature effect on final product and magnetic properties of produced materials were be investigated.

2. Experimental Procedure

Lanthanum oxalate ($La_2(C_2O_4)_3$), Cerium oxalate ($Ce_2(C_2O_4)$) and Iron oxalate ($Fe(C_2O4)$), silicon dioxide (SiO_2) powders mixture used as a raw material to obtain aimed material composition. The powder mixture was heated up to desired temperature under N_2 atmosphere (inert) and then exposed to reduction by H_2 (reducing agent). The overall experimental procedure is given at Figure 3.

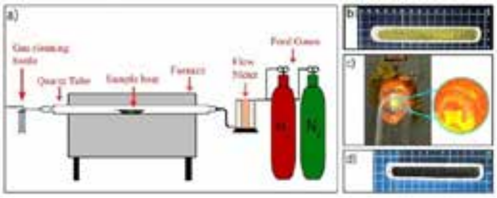

Figure 3. a) Components of HR system, b) Powder mixture before reduction, c) Inside of furnace, d) Powder mixture after reduction.

Before adjusting the reduction temperature, DSC – TG analyses were done to observe thermal properties of starting powder mixture and numerical Gibbs Free Energy calculations (for reducing oxalate compounds to elemental forms of metals) were investigated. XRD studies were done to observe produced material phases. Finally, magnetic properties of materials that were produced with different reduction temperatures were examined with VSM at Nano – Magnetic Materials Research Group at Balıkesir University.

2.1. Pre – experimental Studies

To observing the thermal behaviors of starting powders that includes $La_2(C_2O_4)_3$, $Ce_2(C_2O_4)_3$, FeC_2O_4 and SiO_2 powder mixture, DSC – TG study was done 0°C – 1000°C at inert (N_2) atmosphere. Thermal analyze is given at Figure 4.

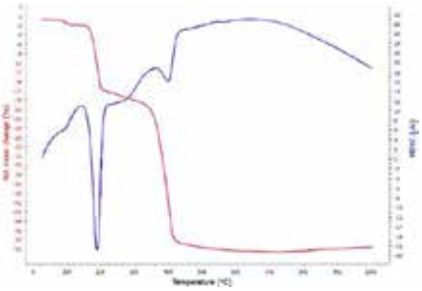

Figure 4. DSC – TG analyze of raw material of HR

According to DSC – TG analyze, starting powder mixture lost its hydrate bases completely after 417°C. At 185°C sharp endothermal peak is observed for mixture. According to literature works to examine thermal decomposition temperatures and steps of Lanthanum Oxalate and Cerium Oxalate (see [7], [8]), oxide forms of these metals were observed after 600°C and 270°C respectively. For Iron Oxalate, the metal – oxide form can be obtained above 535°C (see [9]). Thus, this sharp peak obviously stands for the process of dehydration. The second sharp endothermal peak also stands for the carbon release of oxalate base as carbon monoxide form. The other endothermal peak is broader and continuous. At these inert conditions, it should be referring for reducing to metal – oxide form of each component. Also, numerical Gibbs Free Energy calculation is given at Figure 5 was done.

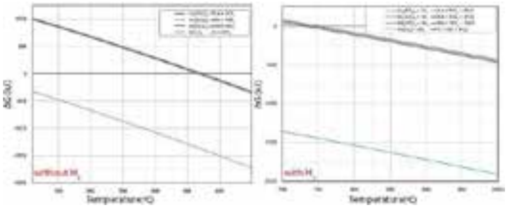

Figure 5. Numerical free energy calculation results of –oxalate to metallic form, (left) in vacuum, (right) with H_2

According to free energy calculations of given reactions, it can be clearly seen that after ~750°C, oxalate powders can be reducing to metallic form with Hydrogen.

2.2. Hydrogen Reduction

In the aim of to produce $La_{0.7}Ce_{0.3}Fe_{11.8}Si_{1.2}$ nominal composition, $La_2(C_2O_4)_3.10H_2O$; $Ce_2(C_2O_4).10H_2O$; $Fe(C_2O_4).2H_2O$ and SiO_2 were mixed and then added to crucible boat. After mixing the powder, HR was carried out in 700°C, 800°C, 900°C reduction temperatures, 2 hours reduction duration, the schematic of HR process is shown in Figure 6 and its parameters were given at Table 1. After reduction, samples were cooled in inert atmosphere to room temperatures (not time dependent).

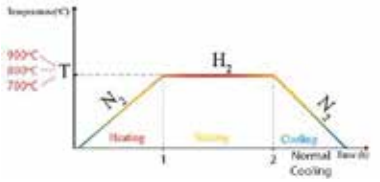

Figure 6. Schematic of HR process

Table 1. HR process parameters

Parameters	**Values**
Heating duration, atmosphere	1 hour, N_2
Reduction duration, atmosphere	2 hour, H_2
Reduction temperature	700°C, 800°C, 900°C
Cooling duration, atmosphere	- , N_2

3. Results and Discussion

Since the reduction from silicon source in raw materials is not thermodynamically possible, therefore silicon source constitutes a bottleneck for this novel production approach. In our recent studies for LaFeSi based magnetocaloric material production from oxalate powders with HR technique, raw materials that were prepared with pure silicon and silicon dioxide both of them showed the Si containing phases (see [10]). Thus, SiO_2 can be used as a raw material to produce LaFeSi based phases. After reduction process each final magnetocaloric powder materials were studied with X – ray diffraction method and analyzed according to $NaZn_{13}$ crystal structure. Before aimed phase examination, effect of temperature on final phase comparison is shown at Figure 7. XRD data were fitted with polynomial approach at $R^2 = 0.8762$. According to comparative analyze, $2\Theta = 28^o$ (observed at 700°C product) was not observed for 800°C and 900°C products. Also, as it can be seen in that raw XRD result of 700°C product had noisy regions and could not generate characteristic peak pattern. However, after reduction at 800°C and 900°C a characteristic peak patterns were observed (specially for $2\Theta = 35^o, 37^o$).

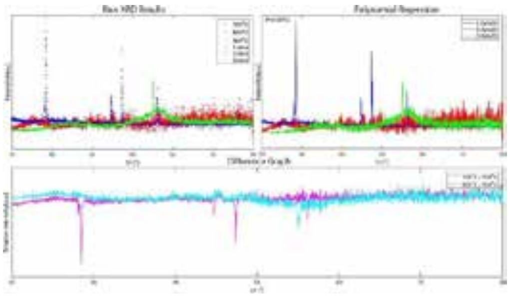

Figure 7. XRD results of final products that produced with HR at reduction temperatures: 700°C (red), 800°C (green), 900°C (blue) reduction temperature, difference of 900°C – 800°C (cyan), 900° – 700°C (pink)

$NaZn_{13}$ structure examination results on XRD data is given at Figure 8.

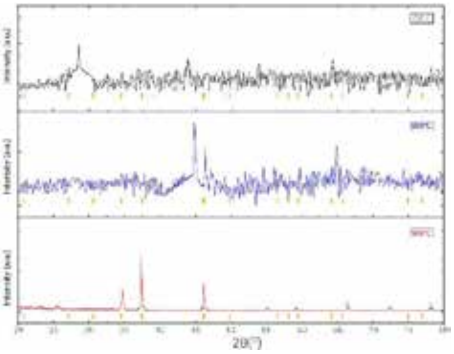

Figure 8. XRD results of final powder products that were produced with reduction at 700°C (black), 800°C (blue), 900°C (red), $NaZn_{13}$ structure pattern (orange)

According to these results the early highest peak that seen in 700°C product, is related with SiO_2 phase, and there is not clear $NaZn_{13}$ crystal pattern like peak occurred in that temperature. Also the XRD result is very noisy and characteristic peaks cannot have analyzed clearly. Material that produced with reduction at 800°C showed an intensive peak at near $2\Theta = 45^o$ which is related to α – Fe. This peak is shifted slightly right at 900°C product. Most of $NaZn_{13}$-type crystal structure pattern peaks were found to be compatible at 900°C product. Also, 700°C and 800°C products has lost of minor peaks. According to conventional methods, after cooling of arc/induction melted alloys are annealed at least 7 days to recover minor phases.

HR process was applied on powder mixture that was in crucible, most likely; particles were distributed in homogenously. Morphology of final products was examined with SEM, is given at Figure 9. According to SEM results, particle sizes (only focused location) lowered with increasing reduction temperature.

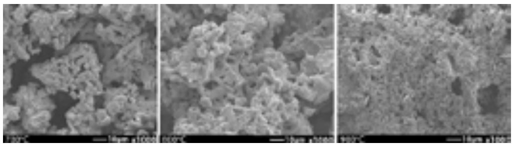

Figure 9. SEM images of powders after reduction at 700^{o}C (left), 800^{o}C (middle), 900^{o}C (right).

Magnetic properties of produced magnetocaloric materials were examined with vibrating sample magnetometer at room temperature under 2T. Results graphs of products were shown at Figure 10.

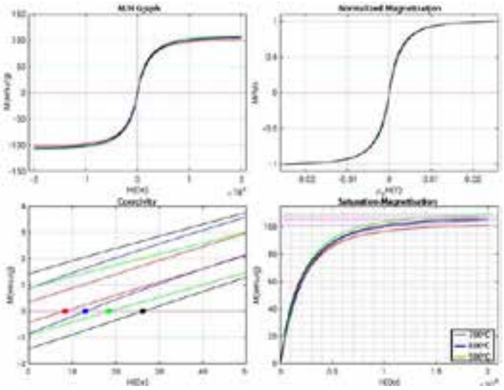

Figure 10. VSM results of final powders after reduction at 700^{o}C(red), 800^{o}C(blue), 900^{o}C(green).

Saturation magnetization properties of materials were increased with increasing reduction temperature. Highest saturation magnetization and coercivity; 108.64 emu/g, 18.25 Oe was observed for magnetocaloric material that was produced at 900^{o}C reduction temperature.

4. Conclusion

LaFeSi based materials can be altering the refrigeration systems by their energy efficient, non-coolant systems as well as environmental friendly production techniques should be developed. In this context, Hydrogen reduction technique were developed to altering the conventional production methods of LaFeSi based magnetocaloric materials. Oxalate compounds of Lanthanum, Cerium and Iron were used as raw materials instead of pure metallic powder components. In this novel production method; 700^{o}C, 800^{o}C and 900^{o}C which were determined according to pre – experimental studies, reduction temperatures were applied to observe temperature effect on final products. According to structural characterization results, reduction at 900^{o}C was enough to obtain smallest particle sized $La_{0.7}Ce_{0.3}Fe_{11.8}Si_{1.2}$ nominal composition and its $NaZn_{13}$-type crystal structure. Moreover, increasing temperature increased the magnetic properties (saturation magnetization and coercivity) of LaFeSi based magnetocaloric materials. Also, in further studies; annealing will be done to clean minor phases to observe exact effect of reduction temperature on final phases.

Acknowledgment

This research has been funded by Turkish Scientific and Technological Research Council (TUBITAK) with a grant number TUBITAK-218M904.

References

[1] A. Zhukov and Arcady Zhukov, *Novel Functional Magnetic Materials Fundamentals and Applications*. 2017.

[2] P. Kumaran, V. Giridharan, R. Gokulakrishnan, and M. Hariharan, “A Review of Room Temperature Magnetocaloric Materials for Home Appliance,” *Int.J.Pure Appl.Math.*,vol. 119, no. 16, pp. 2053–2059, 2018.

[3] K. A. Gschneidner and V. K. Pecharsky, “Magnetocaloric Materials,” *Annu.Rev.Mater. Sci.*, vol. 30, no. 1, pp. 387–429, Aug. 2000.

[4] H. Szymczak and R. Szymczak, “Magnetocaloric effect. Physics and applications,” *Mater.Sci. - Pol.*, vol. 26, no. 4, pp. 807–814, 2008.

[5] J. Lyubina, “Magnetocaloric Materials,” in *Springer Series in Materials Science*, vol. 231, 2016, pp. 115–186.

[6] L. Mu, J. Huang, W. Zhang, C. Liu, G. Wang, and Z. Zhao, “Influence of partial substitution of cerium for lanthanum on magnetocaloric properties of La1–xCexFe11.44Si1.56 and their hydrides,” *J. Rare Earths*, vol. 32, no. 12, pp. 1135–1139, Dec. 2014.

[7] G. Zhan, J. Yu, Z. Xu, f. Zhou, and R. Chi, “Kinetics of thermal decomposition of lanthanum oxalate hydrate,” *Trans. Nonf. Met. Soc. China*, vol. 22, no. 4, pp. 925–934, Apr. 2012.

[8] Almeida L De, Grandjean S, Vigier N, and Patisson F, “New insights on the thermal decomposition of lanthanide (III) and actinide (III) oxalates : from neodymium and cerium to plutonium,” *Eur.J.Inorg.Chem*, vol. 31, pp. 4986–4999, 2012.

[9] M. Hermanek, R. Zboril, M. Mashlan, L. MacHala, and O. Schneeweiss, “Thermal behaviour of iron(II) oxalate dihydrate in the atmosphere of its conversion gases,” *J. Mater. Chem.*, vol. 16, no. 13, pp. 1273–1280, 2006.

[10] S. Ateş, Ö. Karaağaç, H. Köçkar, and S. Gürmen, “LaFeSi Based Magnetocaloirc Material Production by Hydrogen Reduction Method from Their Oxalate Powders and Production Optimization,” in *proceeding book and metallurgy conference 2019*, 2019, pp. 162–165.

Liquid Crystal Self-Assembly: A Route for Anisotropic Composites

Selin SENGUL, Emre BUKUSOGLU
Middle East Technical University
Turkey

Abstract
Liquid crystals can be used to template the polymerization of the mesogenic molecules to synthesize materials with anisotropy. In this study, we present our progress towards the synthesis of polymeric microparticles with pre-defined ordering and chemical patches.

1. Introduction

Liquid crystals (LCs) are phases of matter which possess long range orientation ordering while maintaining their fluidic properties. Studies in the literature have shown that LCs can be used to template the self-assembly of the molecular and colloidal species through defect localizations[1] and elastic force directed, anisotropic assemblies[2,3]. Such species include amphiphiles[1], nanoparticles[4], microparticles[5–7] with diverse chemical functionalities. Recent progress has shown that polymeric materials with well-defined anisotropy can be synthesized through templated polymerization of the LCs and can be shaped in the form of microscopic particles.[8] We presents our efforts to synthesize microparticles with chemical patches in motivation towards the synthesis of composite microparticles with pre-defined shapes and chemical patches.

2. Materials and Methods

4-cyano-4'-pentylbiphenyl (5CB) or E7, room temperature thermotropic nematic LCs were used as received. 4-(3-acryloyoxypropyloxy) benzoic acid 2-methyl-1,4-phenylene ester (RM257) were used as reactive monomer. For templated polymerization, 20% or 25% mixtures of RM257 were prepared in 5CB with the addition of photoinitiator and co-solvent, toluene. After mixing, co-solvent was evaporated under vacuum. 2 µL of either 5CB or RM257/5CB mixture was emulsified in ultrapure water (or solutions with pH= 3 or 5) using a vortex mixer to obtain droplet diameters around 1-10 µm. Silica nanoparticles with diameter of ~100 nm were synthesized using Stöber method and functionalized with either DMOAP or mixed monolayers of DMOAP and carboxylate terminated silanes.[9] Functionalized nanoparticles were also added in the emulsion medium and vortexed to enhance the adsorption to the interfaces of droplets. RM257 was polymerized with UV-light and the particles were obtained after extraction of the unreacted parts using ethanol. The characterizations of the particles were performed using polarized optical microscopy and electron microscopy to determine the configurations of LCs, surface roughness of the polymeric particles and the positioning of the particles at the interfaces of the LC droplets.

3. Conclusion

We found concentration- and nanoparticle surface functionality-dependent configurations of 5CB droplets that highlights the formation of a heterogenous, “patchy” LC-water interfaces upon adsorption of the nanoparticles. The findings of this study will provide a basis for future studies motivated towards synthesis of composite particles with pre-designed nanostructures.

Acknowledgements
This work was supported by the The Scientific and Technological Research Council of Turkey under Award No. 219M068.

References

[1] X. Wang, D.S. Miller, E. Bukusoglu, J.J. de Pablo and N.L. Abbott, Nat. Mater. 15 (2016) 106–112.
[2] I. Musevic, M. Skarabot, U. Tkalec, M. Ravnik and S. Zumer, Science. 313 (2006) 954–958.
[3] C.P. Lapointe, T.G. Mason and I.I. Smalyukh, Science. 326 (2009) 1083–1086.
[4] M. Rahimi, T.F. Roberts, J.C. Armas-Pérez, X. Wang, E. Bukusoglu, N.L. Abbott and J.J. de Pablo, Proc. Natl. Acad. Sci. U. S. A. 112 (2015) 5297–5302.
[5] F. Mondiot, X. Wang, J.J. de Pablo and N.L. Abbott, J. Am. Chem. Soc. 135 (2013) 9972–9975.
[6] E. Bukusoglu, X. Wang, Y. Zhou, J.A. Martínez-González, M. Rahimi, Q. Wang, J.J. de Pablo,and N.L. Abbott, Soft Matter. 12 (2016) 8781–8789.
[7] X. Wang, D.S. Miller, J.J. de Pablo and N.L. Abbott, Soft Matter. 10 (2014) 8821.
[8] B. Akdeniz and E. Bukusoglu, , Langmuir. 35 (2019) 13126–13134.
[9] W. Stöber, A. Fink and E. Bohn, J. Colloid Interface Sci. 26 (1968) 62–69.

Development and Characterization of SAC305 Alloy Matrix Composites

Zoltán GYOKER, Gréta GERGELY, Zoltán GACSI
University of Miskolc
Hungary

Abstract

The most crucial properties of the solder in microelectronics are the good wetting, strong bonding and low electrical resistance. Aim of our scientific work was to improve the mechanical and wetting properties of commercially available lead-free solders. Surface modified ceramic particles were added to lead-free SAC305 solder paste to form composites. The mechanical properties of the composite joint were tested by microhardness measurement and shear test, while the microstructure and the IML were examined by PFIB-SEM.

1. Introduction

In the microelectronics the parts are fastened to PCB by reflow soldering, which simultaneously provides mechanical and electrical connection [1]. According to the the miniaturization of modern electronic devices, the new requirements with traditional materials are becoming more and more difficult to achieve, so the development of lead-free solders has started, for instance by composites (associated materials). In composite fabrication process, the wetting between the matrix and the particle has great importance and can be influenced by the lattice type [2,3].

2. Materials and Methods

During our scientific work we used a special experimental FR-4 PCB and SMD components. SAC305 solder paste (96.5 wt% Sn, 3.0 wt% Ag, 0.5 wt% Cu Type 4) was applied as base material. β-SiC with average particle size of 2 µm and 20 µm were mixed with the solder paste. To improve the poor wettability between the SAC solder and SiC particles, we used a three-step electroless Ni and Cu coating technology to form a nano layer on the surface of SiC. After reflow soldering, the microstructure and IMC of the solder joint were examined with SEM and image analysis. We also examined the interface between the matrix and particles with PFIB-SEM (Fig.1). The mechanical properties of solder composites were investigated by shear test.

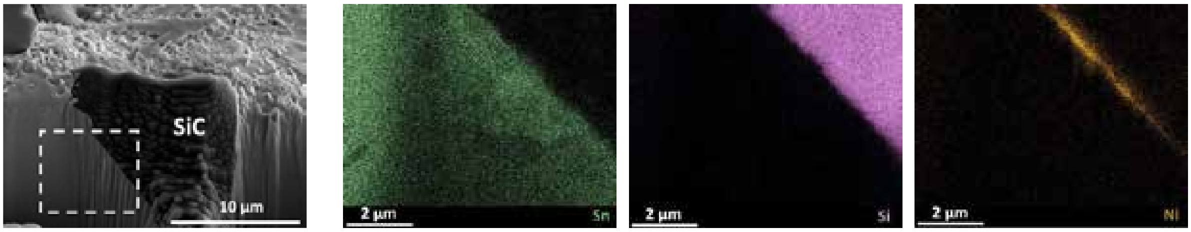

Figure 1. The elemental analysis of solder-SiC(Ni) interfatce after PFIB SEM cross-section milling

3. Conclusions

After our successful metal coating experiments, reflow soldering was applied with the application of special PCB. The solder composite joints were investigated, and the following conclusions were made: 1. The ceramic particle and the metallic coating have an IML-decreasing effect and an modify the IMCs (which were investigated by image analysis). 2. The metallic coating improves the distribution of ceramic particles in the matrix. The distribution of SiC becomes more homogeneous due to the metal coat. 3. Based on the shear force measured during the PCB shear test, the metallic coating has a clear reinforcing effect.

Acknowledgement

The described study was carried out as part of the GINOP-2.3.2-15-2016-00027 “Sustainable operation of the workshop of excellence for the research and development of crystalline and amorphous nanostructured materials” project implemented in the framework of the Szechenyi 2020 program. The realization of this project is supported by the European Union.

References

[1] Lei Nie, Michael Pecht, Richard Ciocci, Regulations and market trends in lead-free and halogen-free electronics, Circuit World 33 (2) (2007) 4–9.
[2] Z. Gyökér, G. Gergely, D. Koncz Horváth, E. Bodnár, Z. Gácsi, Role of reinforcement surface treatment on the SnAg3Cu0.5 microelectronic joints, Appl.Surface Sci. 475 (2019) 982–985
[3] T.P.D. Rajan, R.M. Pillai and B.C. Pai, Reinforcement coatings and interfaces in aluminium metal matrix composites Journal of Material Science, Vol. 33 (1998) 3491-3503..

20th

INTERNATIONAL
METALLURGY
MATERIALS
CONGRESS
10-12 June
2021
“in Digital Platform”

Recycling and Sustainability

immc2021

Retrofitting and Recycling Approaches on Aluminium Industry with Computer Aided Engineering and Physical Simulations to Sustain Circular Economy within Retrofeed Project

Zeynep Tutku ÖZEN[1], Tolga DEMİRKIRAN[1], Görkem ÖZÇELİK[1], Hasan Basri TAŞKIN[1], Akın OBALI[2], Kadir KÖSOĞLU[2], Deniz ÜRK[2], Aleksandra KIEDRZYNSKA[3], Beata GLOT[3], Jaroslaw HERCOG[3]

[1]ASAŞ Alüminyum A.Ş., [2]Sistem Teknik Endüstriyel Fırınlar Ltd.,
[3]Institute of Power Engineering

[1,2]Turkey, [3]Poland

Abstract

Many techno-economic studies have been made to propose integrated, modular and energy efficient solutions in the World.. RETROFEED is a European Commission funded Project within the scope of Horizon 2020 program. The main objective of RETROFEED is to enable the use of variable, bio-based and circular feedstock in process industries by physical and digital tranformations of process equipment and adaptation of novel technologies. Validation of RETROFEED solutions in aluminium industry were carried out to use lacquered scrap in aluminium melting processes and increase energy efficiency of the current furnace

1. Introduction

Recycling is one of the vital topics to create sustainable and energy efficient processes. In aluminium industry, secondary material usage is very important as primary production of aluminium requires a lot of energy. To increase raw material type one can use painted or lacquered scraps in aluminium production. Lacquered scrap contains generally 2-5% percent of impurities. As lacquered scrap re-melting causes increased metal oxidation and gaseous emissions, process equipment and conditions must be retrofitted.

2. Materials and Methods

.In order to analyse current system and apply changes without committing process equipment to become out of service during trials, digital twin of the reverberatory type aluminium melting furnace has been studied with ANSYS TWIN BUILDER. Also, combustion processes and gas flows were analysed with ANSYS FLUENT. To simulate, lacquered scrap melting, painted process scraps were analysed in a tip-up furnace. Materials fed to furnace were changing between 100-1300 grams. Tip furnace temperature has been set to 535°C and increased up to 600°C in 7-67 minutes in an uncontrolled atmosphere. Materials temperatures were measured with a thermocouple which are ranging from 470°C to 510°C.

3. Conclusion

According to CFD results, optimal burner head design is confirmed with the integration of oxygen lance to increase burning quality. It is expected to increase energy efficiency of current aluminium melting furnace by 22% at least for the real time trials. According to painted scrap roasting trials it is observed that the paint starts to evaporate after 300°C. Paint particles separation can be observed after 525°C and 540°C. As a result, the heating system must be designed to reach at least 540°C. Pyrolysis time must be set to 30 minutes in the developed de-lacquering system for 500 kg materials. Controlled atmosphere tests and dross formation boundaries studies are ongoing to improve the process.

Acknowledgement

This work was performed in the framework of the RETROFEED Project (Implementation of a Smart RETROfitting Framework in the Process Industry towards its Operation with Variable, Biobased and Circular FEEDstock). This project has received funding from the European Union's Horizon 2020 research and innovation programme under grant agreement N.869939. It is a pleasure to thank all of the RETROFEED Project partners for their intensive support to this study.

New Regulation Estimation for Efficient and Environmentally Friendly Lamp Recycling in Turkey

S. Samet KAPLAN[1], M. Şeref SÖNMEZ[1], Zeynep AKKAYA[2], Elif KARA[2], Mustafa ÇETİN[2]
[1]İstanbul Technical University, [2]AGİD, Aydınlatma Gereçleri İmalatçıları Derneği
Turkey

Abstract
This study outlines the management of end-of-life fluorescent lamps, the recycling or reprocessing technologies and policies in Turkey. The mercury-containing lamp recycling initiatives currently available in the worldwide were examined. Manufacturers and importers are the main parties responsible for the recycling, and disposal of the spent fluorescent lamps in Turkey. In view of the situation in Turkey this paper discusses the implementation of new regulations in Turkey in terms of efficient lamp collection and recycling.

1. Introduction

Considering its toxicity, persistence, bioaccumulation, and environmental mobility; mercury as a main component of a fluorescent lamp is a contaminant of concern in the waste stream. The name "fluorescent lamp" is derived from the fact that the inner surface of the fluorescent lamp tubes are coated with fluorescent materials (mainly as calcium hydrogen phosphate), where both ends of the tube are filled with tungsten filaments that act as electrode coils either double wounded or triple-wounded, and the filaments are coated with electron-radiating materials (nickel, strontium, calcium oxides) [1]. Mercury emits ultraviolet energy, which is absorbed by the phosphor-coated glass tube. There are several types of MCLs: fluorescent bulbs, including compact fluorescent light (CFL) bulbs, long tubes, circle and U-shaped lamps, and high intensity discharge (HID) bulbs [2]. The fluorescent lamp recycling sector is growing considerably in Europe due to increasingly strict regulations aimed at inciting the consumption of low energy light bulbs and their end-of-life management [3].

2. New Regulation Estimation

The end-of-life lamp recycling process consists of removing the aluminium cap and lead-containing glass on both ends of the straight tube by cutting and subsequently blowing off the fluorescent powder contained therein, collecting the mercury vapour and the powder, and distilling the powder to recover mercury [1]. This study aimed the related knowledge of the management of end-of-life lamps, the recycling or reprocessing technologies and policies in the World, and subsequent policies can then be taken into effect to reduce the environmental impact of fluorescent lamps in Turkey. The regulations are required for all producers to join a compliance scheme, which manages the process on their behalf, and schemes such as AGİD – which works on behalf of the lighting industry. Under the regulations, the producer may fund the collection, recycling and any environmentally friendly disposal. However, it is the end user that has ultimate responsibility for making sure the product is recycled when it reaches end of life.

3. Conclusion

This study focused on the most prominent methods that are used in the world for the recycling of end of-life lamps. It was aimed to design national lamp recycling management system for Turkey. The position of lamp stakeholders in recycling as well as refund system for the efficient lamp recycling were discussed.

References

[1] C.H. Lee, S.R. Popuri, Y.H. Peng, S.S. Fang, K.L. Lin, K.S. Fan, T.C. Chang, J Mater Cycles Waste Manag (2015) 17:312–323.
[2] G.T.R Silveria, S.Y. Chang, Waste Management & Research 29, 6 (2011) 656–668.
[3] F. Zimmermen, M.T. Lecler, F. Clerc, A. Chollot, E. Silvente, J. Grosjean, Waste Management 34 (2014) 1257–1263.

Design of Laboratory Type Electric Arc Furnace and Production of Copper Alloy From E-Waste

Rıdvan ORMAN, Barış DARYAL, Oğuz Kağan COŞKUN, Mehtap ARSLAN, Servet İbrahim TİMUR

İstanbul Technical University

Turkey

Abstract:

The increasing amount of e-waste is important for environmental pollution and economic importance due to its precious and heavy metals content. For metal recovery from e-wastes pyrometallurgy is preferred, especially DC Arc Plasma systems which allow the harmless disposal of combustion gases. In this study, the design and manufacture of a laboratory type electric arc furnace with 6kW DC power supply has been completed which is capable of 2 kg ladle and working autonomously in continuous arc cycle. A gas collection and flushing system was added to the furnace to collect the possible gas output during the arc melting process.

After installing the system, the working regime was established by successfully melting of different metallic scrap such as copper, aluminum and steel. An electronic control circuit is used to perform a fast and precise electrode movement for continuous arc cycle. The average arc voltage can be adjusted by regulating the electronic board coding which were calculated as 17V during melting experiments and temperatures over 1700 °C were achieved in the ladle by arc formation.

Copper (CuFeAlSn) alloys have been synthetically produced in different compositions by using the waste PCB (without disassembly) and metal scraps in EAF. The leaching behavior of the alloys was observed by sulfuric acid (nitric acid and hydrogen peroxide used as oxidant).

Synthetically produced alloy mainly has copper-rich matrix and iron-rich phases. Cu, Fe, Al, Sn, Zn, Cr, Pb containing alloy and Ca, Al, Si containing slag were obtained from melting of the shredded waste PCB and copper scraps as a collector metal. The intermetallic structures consisting of Cu-Al, Fe-Al, Cu-Sn, Cu-Fe-Al phases and inhomogeneous distribution of these via XRD and SEM-EDS analyses. Finally, 82.46% Cu dissolution efficiency in stoichiometric HNO_3 + 1M H_2SO_4, 66.41% stoichiometric H_2O_2 + 2M H_2SO_4 and complete dissolution in 4M H_2SO_4 + stoichiometric HNO_3 were achieved in 60 minutes.

1. Introduction

The amount of e-waste is known to increase at an incredible rate worldwide. These scraps (motherboards, relays, capacitors, integrated circuits etc.) are important for environmental pollution as they consist of a complex structure including both organic and heavy metals [1]. Moreover, they have an economic importance due to their metallic content which is almost 10 times of the grade of metals in the ore that consisting of Cu, precious metals (Au, Ag) and platinum group metals [2]. Therefore, big investments are made for e-wastes and there are many experimental studies about their recovery and disposal.

There are a variety of methods for the recovery of e-waste, which can be grouped as physical, hydrometallurgical and pyrometallurgical methods [2, 3]. Physical separation processes are mostly applied as pre-enrichment process. Hydrometallurgical methods are frequently preferred in small-scale factories due to low investment costs. However, the complexity of e-waste containing refractory oxides (silica and alumina), polymeric, metallic and toxic contents makes it difficult to apply hydrometallurgical methods [4]. Pyro-hydrometallurgical methods have been integrated into a system in the most widely applied industrial processes such as Umicore, Noranda, Aurubis [5, 6].

In the last 20 years, the use of traditional pyrometallurgical methods, especially the DC Arc Plasma systems which allow the harmless disposal of combustion gases, has increased for metal recovery from e-wastes [7, 8]. E-wastes are charged to the arc furnace with copper and lime/silica. While organic components such as dioxin, furan are destroyed in plasma/arc environment, precious metals turn into copper alloy and toxic heavy metals turn into inert glassy structure [7, 9]. Copper ingot is refined by hydrometallurgical techniques for purification [9, 10]. Depending on the power source and the design, electric arc furnaces are used for many different purposes, especially for the smelting of iron and steel scrap and the recovery of non-ferrous metals. They have been widely used in the recovery of precious metals from catalytic converters, batteries and e-wastes, since the early 2000s [7, 8].

Within the scope of this study, the design and manufacture of a laboratory type electric arc furnace (LT-EAF) with a 6kW (30V-200A) DC power supply has been completed which is capable of working autonomously with continuous arc cycle at the upper limits of 160A and 30V. A gas collection and flushing system was added to the furnace to collect the possible gas output during the arc melting process. As a result of this study, a furnace with a capacity of 2 kg was constructed.

2. Experimental Procedure

There are different methods for calculation of arc lengths given in the literature [11, 12] and the general behavior of electric arc (see Fig. 1) was defined by Browne in 1955 [13]. The diameter (d, cm) of graphite electrodes can be found by the formula (1) [14]:

$$d = \sqrt[3]{(0,406 * I^2 * \delta)/K} \qquad (1)$$

K is a coefficient ($2.1*10^4$ W/cm^2) and δ is electrode resistivity at 500°C, 10 ohm.mm^2/m for graphite.

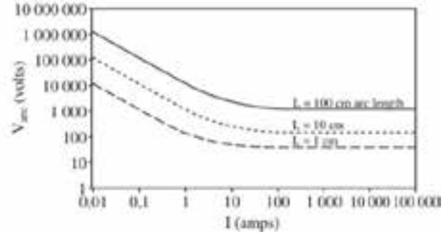

Figure 1. Arc lenght in open-air, V_{ark}= f(I_{ark}) [11].

Diameter of graphite electrode selected as 18 mm according to upper current limit (160A) and formula (1). Contolling of movement of electrode up/down is important in an EAF, especially in a small scale furnace, because it is difficult to achieve continuous arc. An electronic circuit board is used to perform a fast and precise electrode movement for continuous arc cycle. DC motor movement is controlled according to voltage changes monitored by electronic board and cathode position is being adjusted.

After installing of the system, the working regime was established by successfully melting of different metallic scrap such as copper, aluminum, steel and tin (100g charges). Then, the process of pyrometallurgically producing copper alloy from shredded waste PCB has been studied in electric arc furnace and copper (CuFeAlSn) alloys have been synthetically produced in different compositions.

The leaching behavior of these alloys was observed by sulfuric acid with oxidizing agents (HNO_3, H_2O_2). Leaching conditions were 10 g/L solid/liquid ratio, 500 rpm stirring rate, 60 minutes, 25 and 80°C, molarity (1, 2, 3 and 4M) of H_2SO_4.

The study were concluded by characterization of leaching solutions and produced alloys.

3. Results and Discussion

During the copper melting experiments, where the continuous arc cycle is captured and melting is achieved completely, the most efficient voltage range without arc breakage has been determined. Some voltage breaks may occur due to material charging. In the melting process, it was observed that the arc was harmonically formed and the potential change in the system was approximately at 8-24V levels during the production of synthetic copper (CuFeAlSn) alloy is shown in Fig. 1 and of alloy produced from waste PCB in Fig. 5.

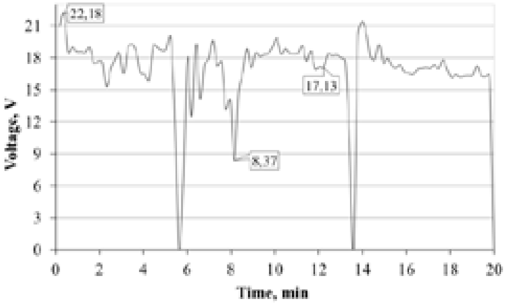

Figure 2. Voltage changes during producing CuFeAlSn [69.3% Cu + 24.7% Fe + 4% Al + 2% Sn].

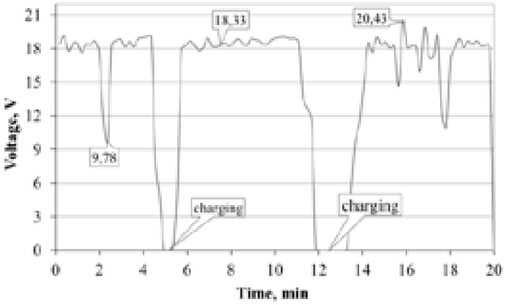

Figure 3. Voltage changes while producing alloy from waste PCB [55.6% Cu + 44.4% shredded waste PCB].

SEM image and micrograph obtained from synthetic copper (CuFeAlSn) alloy are shown in Fig. 4.

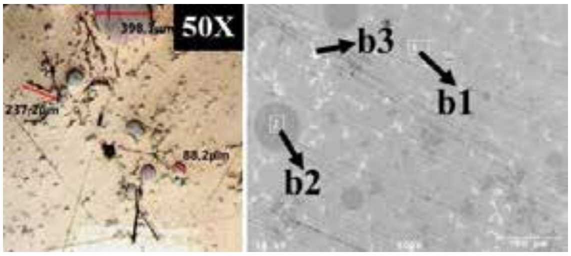

Figure 4. Micrograph and SEM image of synthetic CuFeAlSn alloy [69.3% Cu+24.7% Fe+4% Al+2% Sn].

Examination by EDS (Table 1) revealed that synthetic CuFeAlSn alloy has Cu-rich matrix [91.4% Cu + 2.5% Fe + 6% Al] in b1 zone, Fe-rich spheres [4.69% Cu + 92.3% Fe + 1.9% Al] in b2 zone and white points including Sn [77.4% Cu + 1.05% Fe + 2.6% Al + 18.7% Sn] in b3 zone.

Table 1. EDS CuFeAlSn alaşımının EDS analizi sonuçları.

Zone	Cu (wt.%)	Fe (wt.%)	Al (wt.%)	Sn (wt.%)
b1	91.48	2.51	6.00	-
b2	4.69	92.38	2.92	-
b3	77.46	1.05	2.68	18.79

XRD pattern shows that $Cu_{41}Sn_{11}$, Al_2Fe, Fe and AlCu intermetallic phases were obtained from synthetic CuFeAlSn alloy (Fig. 5).

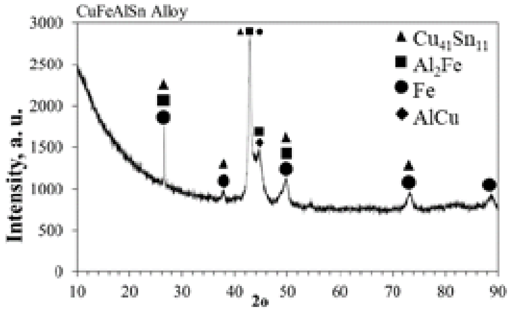

Figure 5. XRD pattern of synthetic CuFeAlSn alloy.

When production of synthetic copper alloy which represents the approximate composition of waste PCB achieved, the smelting experiments of waste PCB were conducted. Chemical analysis results of alloy and slag from waste PCB is shown at Table 2.

Table 2. Chemical analysis results of alloy and slag from waste PCB [55.6% Cu + 44.4% shredded waste PCB].

Alloy [wt.%]					
Cu	**Fe**	**Al**	**Sn**	**Zn**	**Pb**
82.76	2.11	4.5	6.8	1.1	2.74
Slag [wt.%]					
Cu	**Ca**	**Al**	**Si**	**Balans**	
2.4	9.45	14.34	9.86	63.95	

Addition of copper as collecting metal led to produce a copper-based alloy from smelting of waste PCB in LT-EAF. SEM image and micrograph of copper alloy produced from waste PCB are shown in Fig. 6.

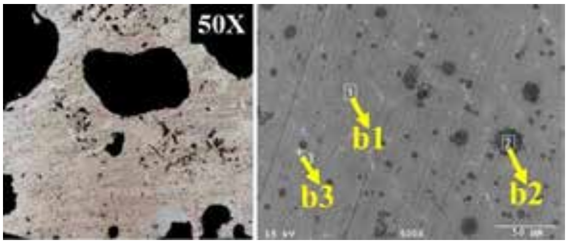

Figure 6. a) optic microscopy and b) SEM of produced alloy [55.6% Cu + 44.4% shredded waste PCB].

Table 3. EDS results of produced alloy from waste PCB [55.6% Cu + 44.4% shredded waste PCB].

Zone	wt.%						
	Cu	**Fe**	**Al**	**Sn**	**Si**	**Pb**	**Cr**
b1	81.95	0.93	7.187	4.47	5.45	-	-
b2	6.203	79.40	0.173	0.53	11.76	-	%1.99
b3	35.17	2.00	0.418	34.83	1.35	26.22	-

Examination by EDS (Table 3) revealed that produced alloy from waste PCB has same phases as synthetic CuFeAlSn alloy which are Cu-rich matrix, Fe-rich spheres with Cu, Fe, Al, Sn and Pb containing zone.

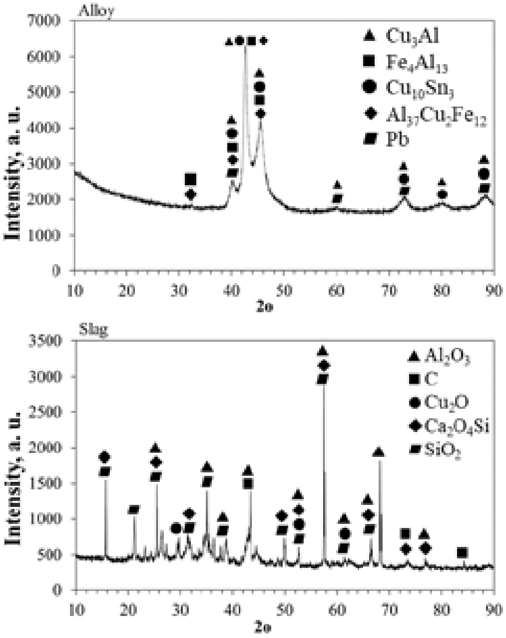

Figure 7. XRD pattern of a) alloy and b) slag produced from waste PCB [55.6% Cu + 44.4% shredded waste PCB].

XRD patterns in Fig. 7 show that Cu_3Al, Fe_4Al_{13}, $Cu_{10}Sn_3$, Pb and $Al_{37}Cu_2Fe_{12}$ phases were obtained in alloy produced from waste PCB and Al_2O_3, C(graphite) Cu_2O, Ca_2O_4Si and SiO_2 phases were obtained in slag.

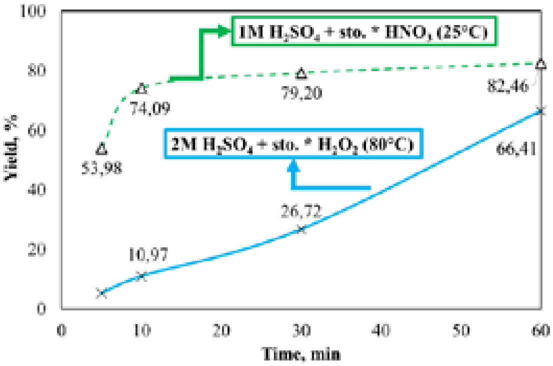

Figure 8. Cu dissolution behavior in H_2SO_4 with different oxidants [500 rpm, 10 g/L, 60 min].

When the leaching behavior of alloys was examined, in 60 minutes, 82.46% Cu dissolution efficiency were achieved for stoichiometric addition of HNO_3 as oxidant to 1M H_2SO_4 and 66.41% yield for stoichiometric H_2O_2 addition to 2M H_2SO_4. In the same way, it was determined that the alloy was dissolved 100% in 4M H_2SO_4 + stoichiometric HNO_3 solution.

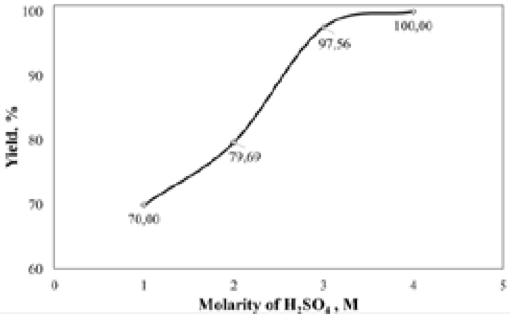

Figure 9. The effect of H_2SO_4 molarity on leaching o Cu alloy [25°C, stoichiometric addition of HNO_3, 500 rpm, 10 g/L, 60 min].

4. Conclusion

During the furnace experiments, temperatures over 1700 °C were achieved in the ladle by arc formation. Thereby melting of waste PCB at once without disassembly and melting of different metals was observed and achieved. The average arc voltage value was around 18V when mixture of copper, iron, tin and aluminum charge was melted. The average arc voltage can be adjusted by regulating the electronic circuit board coding.

Within the scope of this study; synthetic alloys produced by melting Cu, Fe, Al, Sn charge which is representing the alloy to be possibly formed by melting the printed circuit board scrap. They could be brought into the intermetallic structure and the production of targeted copper alloy was obtained successfully.

Alloy produced with Cu, Fe, Al charge has copper-rich Cu-Al matrix phase and iron-rich Fe-Al phase in spheres. A third phase containing Sn was formed in the alloy produced by adding tin to the Cu, Fe, Al charge. At the end of waste PCB melting experiments, Cu, Fe, Al, Sn, Zn, Cr, Pb containing alloy and Ca, Al, Si containing slag were obtained as a result of the melting of the shredded waste PCB by the addition of copper scraps as a collector metal. Finally; three different phases consist of Cu matrix, Fe rich spheres and Sn containing white regions were produced in CuFeAlSn alloys produced from waste PCB.

It was determined that the inhomogeneously distributed intermetallic structures are consisting of Cu-Al, Fe-Al, Cu-Sn, Cu-Fe-Al phases via the micrographs obtained from SEM-EDS and XRD analyses.

References

[1] D. Mmereki, B. Li, A. Baldwin and L. Hong, "The Generation, Composition, Collection, Treatment and Disposal System, and Impact of E-Waste," in E-Waste in Transition-From Pollution to Resource, InTech, 2016, pp. 65-93.

[2] M. Kaya, "Recovery of Metals from Electronic Waste by Physical and Chemical Recycling Process," World Academy of Sci., Eng. and Technology, International Journal of Chemical and Molecular Engineering, vol. 10, no. 2, pp. 259-270, 2016.

[3] E. Y. L. Sum, "The Recovery of Metals from Electronic Scrap," JOM, pp. 53-61, April 1991.

[4] H. M. Veit and A. M. Bernardes, Electronic Waste Recycling Techniques, Vols. Topics in Mining, Metallurgy and Materials Eng., C. P. Bergmann, Ed., London: Springer International Publishing, 2015.

[5] A. Khaliq, M. A. Rhamdhani, G. Brooks and S. Masood, "Perspective, Metal Extraction Processes for Electronic Waste and Existing Industrial Routes: A Review and Australian," Resources, vol. 3, pp. 152-179, 2014.

[6] A. Gurgul, W. Szczepaniak and M. Zabłocka-Malicka, "Incineration, pyrolysis and gasification of electronic waste," in E3S Web of Conferences, 2017.

[7] M. Hull, "Tetronics: plasma processing holds key to consistent nanopowders," Powder Metallurgy, vol. 45, no. 1, pp. 8-9, 2002.

[8] E. Hsu, K. Barmak, A. C. Westabd and A. A. Park, "Advancements in the treatment and processing of electronic waste with sustainability: a review of metal extraction and recovery technologies," Green Chemistry, vol. 21, no. 5, pp. 919-936, 2019.

[9] T. P. Johnson, "Recovery of Valuable Base Metals From Secondary Materials Using DC Plasma Smelting".

[10] T. Johson, "Prospectors: The Next Generation," The Chemical Engineer, no. 874, pp. 28-31, April 2014.

[11] A. Vignes, "Electric Melting and Smelting Furnaces," in Extractive Metallurgy 3: Processing Operations and Routes, ISTE Ltd. London and John Wiley & Sons, Inc. New York, 2011, pp. 217-263.

[12] T. J. E. Miller and A. R. Oltrogge, "Reactive Compensation and The Electric Arc Furnace," in Reactive Power Control in Electric Systems, New York, John Wiley and Sons, 1982, pp. 299-331.

[13] T. R. Curr, "The High Current D.C. Arc in Extractive Metallurgy," in The Julian Szekelyy Memorial Symposium on Materials Proc., Massachusetts, 1997.

[14] F. Edneral, Electrometallurgy of Steel and Ferro-alloys, Moscow.: MIR Publishers, 1979, pp. 1-87.

An Overview of Pyrometallurgical Concepts for Recycling of Metals from Waste Electrical and Electronic Equipment

Mertol GÖKELMA, Alireza HABİBZADE
Izmir Institute of Technology
Turkey

Abstract

In the last decades, the electrical and electronic equipment has become one of the fastest-growing global waste mainly due to the rapid population increase, continuous technological innovations, and decreasing the life cycle of the most electronic devices. The environmental threats caused by the disposal and incineration of electronic waste have raised high alerts and concerns. Besides, WEEE is an important secondary source of critical raw materials (CRM) which are essential in the development of novel high-tech applications. For example discarded printed circuit boards (PCBs) contain high amounts of copper (Cu), gold (Au), silver (Ag), aluminium (Al), zinc (Zn), and nickel (Ni) and permanent magnets contain a significant amount of rare earth elements (REE). As all these electronic and electrical waste possess richness in the metal values it would be worth recovering the metal content as efficient as possible and protect the environment from the pollution. The infrastructure to collect and pick up PCBs and other electronic waste materials from consumers is still in a developing phase in Turkey. In this study, an overview of the recycling of WEEE and preliminary lab-scale trials completed by the pyrometallurgical routes for recovering the precious metals are presented. Finally, recommendatory strategies and processes are discussed.

1. Introduction

According to the WEEE directive 2002/96/EG, the PCBs are in the sixth category of ten [1]. Electronic scrap roughly consists of 15-30% plastics, 40-50% ceramics and 20-30% metals like copper, aluminium and iron. [2] The metallic fraction in printed circuits boards (PCBs) consists of approximately 16% copper, 4% tin-lead, 3% iron and ferrite, 2% nickel, 0.05% silver, 0.03% gold, 0.01% palladium. [3-4]

Precious metals (e.g. Au, Ag, Pd…) represent today one of the major concern in recycling of WEEE not only due to its economic importance but also for its risk of supply e.g. palladium (Pd).

After collecting, the mechanical pre-processing has the biggest impact in the recycling rate of the base metals as well as precious metals. The metals which end up in the “wrong” fraction will hinder its recovery. Data suggest that for precious metals the recovery of silver is only 11.5%, for gold is 25.6% and for palladium is 25.6%. In the case of Copper, iron and aluminum, the estimated recovery is about 60%, 95.6% and 75% respectively [5]

After general mechanical pre-processing, chemical processes will be used to recovery of WEEE. These processes includes pyrolysis and pyrometallurgical processes for non-metallic fraction of E-waste. WEEE is processed via pyrometallurgical and hydrometallurgical routes. Pyrometallurgy is the most traditional and standard treatment process where hydrometallurgy is a recent advancement [6]. Pyrometallurgy involves incineration, smelting in plasma arc or blast furnaces, drossing, sintering, melting, and gas-phase reactions at high temperatures [7].

2. Current Procedures

Presently, WEEE recycling is dominated by pyrometallurgical routes [8]. Pyrometallurgical routes are similar to mechanical or hydrometallurgical processes with the steps of liberation, separation/upgrading, and purification. WEEE is mainly treated in smelters instead of mechanical processing [9]. Various metallurgical processes such as oxidation, reduction, vulcanization, melting, matte forming, slag forming, and fumes of nonferrous metal compounds can occur during the smelting process [10].

All pyrometallurgical treatments of WEEE have in common the need of an energy source to reach high temperatures, turbulences to increase the slag-metal interaction, good settling of the metal phase for good slag-metal separation, good slag properties to increase the process efficiency and casting behaviour [11].Top Blown Rotary Converter (TBRC) serves one of the most flexible pyrometallurgical recycling method in terms of variety of input material and successful process control [11]. This method reaches high recovery efficiencies for copper containing precious metals in the alloy. Some alternative processes are shown in Table 1.

Table 1: Overview of selected pyrometallurgical procedures used for WEEE recycling

	Elements in the Scraps	Recovered Elements	Procedures	Efficiency (%)	T (°C)	Ref
WEEE metallic fraction & PCB	Cu, Pb, Sn, Ni, Ag, Au, Al, Fe, Si, Br, Cr,…	Cu Al Zn	Pyrolysis Vacuum metallurgy	98 93 96	500-700	[5]
PCB	Cu, Sn, Pb, Fe, Ni, Cr, Mo, Ag, Au, Pd	Cu Fe Ni Ag Au Pd	Pyrolysis Combustion - Reduction Melting (crucible furnace)	99 56 87 85 79 89	600-1500	New N16
WEEE metallic fraction	Cu, Fe, Pb, Zn, Au, Ag, Pt, Pd, Ni	Cu	Noranda Smelting Process	99	1250	[13]
PCB	Cu, Cd, Zn, Bi, Pb, Sn	Cu Zn Cd Pb Bi	Removal and separation of this Cu, Cd, Zn, Pb, Bi By vacuum metallurgy	91-98 up to 97 up to 99 87 87	600-850	20 21 22

Pyrolysis can be used for a good separation of organincs and the metal value prior to the pyrometallurgical processing. Vacuum metallurgy can be used if metals like Zn, Cd, Pb and Bi. Both processes add an extra cost however they may be useful if the process is economically feasible.

3. Conclusions

- A thermal or mechanical treatment is needed prior to melting due to the large number of organics in the electronic scraps. Thermal pre-treatment procedures are more costly, but it is possible to produce bio-coke hence a new energy source.
- TBRC is suitable for such recycling applications which is processed with flexible parameters. On the other hand WEEE charge in furnaces where primary copper concentrates are processes, such as Noranda Process, may impact the parameters by changing the liquidous temperature of the slag because of Alumina and Chromium addition.

4. References

[1] J. Huisman, F. Magalini, R. Kuehr, C. Maurer: 2008 Review of Directive 2002/96 on Waste Electrical and Electronic Equipment (WEEE) –Final report, p 228-256, 2008.
[2] Chancerel, P., Rotter, S., 2009. Recycling-oriented characterization of small waste electrical and electronic equipment. Waste Management 29, 2336-2352.
[3] Canal Marques, A., Cabrera, J-M., de Fraga Malfatti, C., 2013. Printed circuit boards: A review on the perspective of sustainability. Journal of Environmental Management 131, 298- 306.
[4] Chen, M., Wang, J., Chen, H., Ogunseitan, O. A., Zhang, M., Zang, H., Hu, J., 2013. Electronic Waste Dissasembly with industrial Waste Heat. Environmental Science and Technology 47, 12409-12416.
[5] Diaz, F; Florez S.; Friedrich, B., 2015. High recovery recycling route of WEEE: The potential of pyrolysis. IME Process Metallurgy and Metal Recycling, RWTH Aachen University.
[6] S. Ramanayaka, S. Keerthanan & M.Vithanage, 2019. Handbook of Electronic Waste Management, chapter 2, 1st Edition.

[7] Hsu, E., Barmak, K., West, A.C., Park, A.H.A., 2019. Advancements in the treatment and processing of electronic waste with sustainability: a review of metal extraction and recovery technologies. Green Chem. 21 (5), 919936.
[8] Khaliq, A., Rhamdhani, M., Brooks, G., Masood, S., 2014. Metal extraction processes for electronic waste and existing industrial routes: a review and australian perspective. Resources 3 (1), 152179.
[9] Cui, J., Zhang, L., 2008. Metallurgical recovery of metals from electronic waste: a review. J. Hazard. Mater. 158 (23), 228256.
[10] Ma, E., 2019. Recovery of waste printed circuit boards through pyrometallurgy. Electron. Waste Manag. Treat. Technol. 247267.
[11] D. Latacz, F. Diaz, A. Birich, B. Flerus, B. Friedrich, 2020. WEEE Recycling at IME – RWTH Aachen: From Basic Metal Recovery to Resource Efficiency. World of Metallurgy – ERZMETALL 73 (2020) No. 3.
[12]
[13] A. Lennartsson F. Engström, C. Samuelsson, B. Björkman, J. Pettersson, Large-Scale WEEE Recycling Integrated in an Ore-Based Cu-Extraction System, Journal of Sustainable Metallurgy (2018) 4:222–232
[14]
[15]
[16]

White Dross Benefication by Pyrometallurgical Methods

İlayda Elif ÖNER, Buse Tuğçe POLAT, Selçuk KAN, Kağan BENZEŞİK, Onuralp YÜCEL
İstanbul Technical University
Turkey

Abstract

Experiments have been designed and applied in order to evaluate non-metallic residues (NMRs) by pyrometallurgical method and to use the enriched product as high purity aluminium oxide. Within the scope of the research, aluminum white dross was calcinated at 1000 °C, 1100 °C and 1150 °C, and samples taken from the rotary furnace after different periods were examined by X-ray and chemical analysis methods.

1. Introduction

Aluminum is the third most common element in the earth's crust after oxygen and silicon. Aluminum is the most commonly produced and used non-ferrous metal due to its superior properties such as light weight, high corrosion resistance and high strength values. For this reason, the application areas of aluminum are expanding day by day. The main uses of aluminum can be listed as construction, electronics, automotive, aviation, railways and packaging industry. Although aluminum is a common material in terms of availability, energy consumption is high in production processes. Increasing demand and high energy consumption make secondary aluminum production and recycling a necessity [1].

Aluminum production is divided into two sub-categories: primary aluminum production and secondary aluminum production. In primary production, aluminum is extracted from its ores (mostly bauxite) by pyrometallurgical or hydrometallurgical methods. On the other hand, aluminum process scraps (dross, salt cake etc.) and used aluminum products (cans etc.) are used as raw materials in secondary production. Aluminum can be recycled many times without losing its mechanical properties. In addition to this feature, secondary aluminum production not only reduces energy consumption, but also minimizes environmental concerns. Secondary aluminum production requires 5% less energy and emits 5% less greenhouse gases than primary production [2]. The most commonly used method for secondary production is the melting process with salt slag containing low amounts of fluoride, sodium and potassium in reverber or rotary furnaces. These slags have two main functions: to minimize oxidation losses during the process and to facilitate the separation of aluminum from non-metallic impurities.

Recycling methods may differ depending on the metallic aluminum or alumina concentration of the waste product. Wastes from primary aluminum production are called white dross. It consists of a high proportion of aluminum oxide and can contain 15% to 70% recyclable metallic aluminum. Wastes from secondary aluminum production are called black dross and typically contain aluminum oxide and oxides of aluminum alloys and often contain between 12% and 18% recyclable aluminum [3].

Most common treatment practice for such non-metallic products is landfilling. Recycling these non-metallic residues instead of landfilling not only helps preserve raw material reserves but also provides many economic and environmental benefits. AlN in aluminum dross, turns into alumina and ammonium gas in contact with humidity as shown in Reaction 1.1, it is harmful to the environment when landfilled. This situation prevents the formation of oxygen and ammonium gas in the atmosphere when moisture is removed by reaching high temperatures in an oxidizing environment as seen in Reaction 1.2 [4].

$$2AlN + 3\,H_2O \rightarrow NH_3 + Al\,(OH)_3 \qquad (1.1)$$

$$2AlN + 3/2\,O_2 \rightarrow Al_2O_3 + N_2 \qquad (1.2)$$

In this study, the FactSage program was used to determine the temperatures at which the experiments will be performed for the removal of salts from the white slag in the rotary kiln and the impurity removal of other impurities. Evaporation temperatures of NaCl and KCl salts under atmospheric pressure have been calculated as approximately 1400 ° C.

The acquisition of aluminum from white and black dross and salt cakes has recently begun to attract the attention of researchers. These current researches are concentrated on obtaining high purity aluminum oxide by hydro and pyrometallurgical methods from NMRs. In this study, it is aimed to recover high purity alumina from white dross by pyrometallurgical method.

2. Experimental

2.1. Raw Materials

Prior to calcination experiments, raw materials are characterized by using sieving analysis, X-ray diffraction analysis and chemical analysis. The results are given as Table 1 and Figure 2.

Table 1. Raw material chemical analysis results

	Al dross

Al_2O_3	68.83
$Al_{(Me)}$	9.27
N	5.47
K_2O	2.49
SiO_2	1.11
Na_2O	0.66
Fe_2O_3	0.54
MgO	0.15

Sieve analysis details are summarized in the Table 2 and related graphic is given for aluminium dross in Figure 1.

Table 2. Particle size of raw aluminium dross

Mesh Size (μm)	Weight(g)
-45	6,38
45	52.02
106	32,2
250	9,4
Total	100

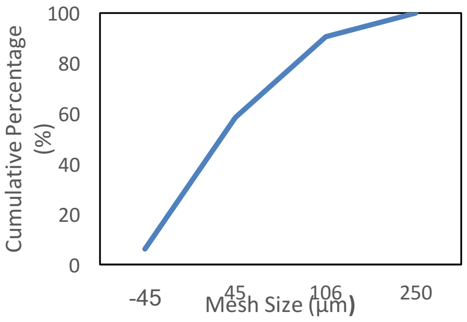

Figure 1.Cumulative Sieving Analysis of Aluminium Dross

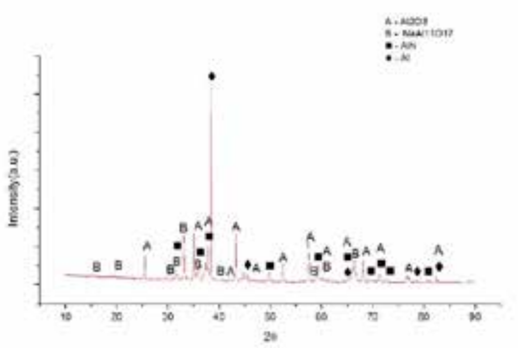

Figure 2. XRD pattern of raw aluminium dross

2.2. Procedure

After raw material analysis, calcination is done at a rotary furnace. The schematic of used a both open-end laboratory scale rotary furnace which is illustrated in Figure 3.

Reaction zone is in a tube which is designed to hold the temperature stable during experiment. The tube can be easily changed with using hand-operated pump which is connected to hydraulic mechanism. The maximum temperature that can be heated up to is 1400°C utilizing via SiC resistances. The rotation is applied by the gears on side and rotation speed can be adjusted between 0-10 rot/min. In this study speed is set to 1 rot/min.

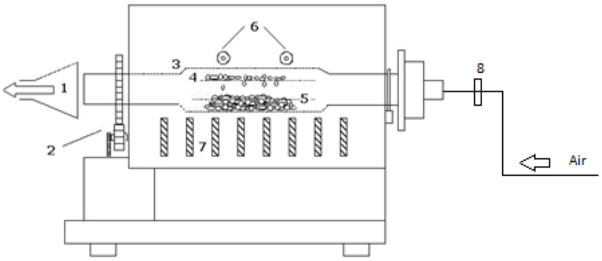

Figure 3.Rotary kiln (1-Gas and powder collector, 2-Gear, 3-Stainless steel reaction tube, 4-Mixing wing, 5-Charge materials, 6-Thermocouples, 7-SiC resistances, 8-Flowmeter)

Three experiments aimed to find out optimum temperature and duration. The furnace is heated up to 1000°C which named as RF I, 1100°C named as RF II and 1150°C named as RF III and charged with 1000 g of non-metallic residue. In the first hour, 4 samples are taken out every 15 minutes and in the second hour 4 samples are taken out every 30 minutes by using the scoop. Therefore, 8 samples are taken out in total and weight. Before and after calcination pictures of white dross are given in Figure 4.

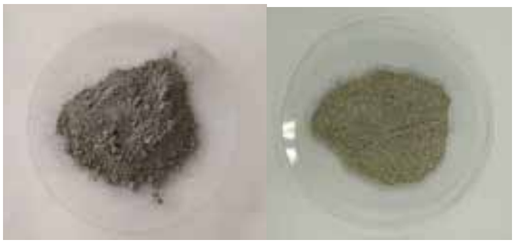

Figure 4. Raw and calcinated aluminium white dross at 1000°C

3. Results and Discussion

After experiments are being done, related results are obtained through chemical analysis and X-ray diffraction (XRD) analysis. The aim is to obtain desired chemical composition which eliminated such impurities as well as different phases.

The results from Rotary Furnace I experiment are given in Table 3, 4 and Figure 5.

Table 3. Chemical analysis results of Al dross residue and calcined white dross at 1000°C, 2 h.

	Al dross	**RFI 120**
Al_2O_3	68.83	88.17
$Al_{(Me)}$	9.27	2.2
N	5.47	0.84
K_2O	2.49	1.29

SiO_2	1.11	1.17
Na_2O	0.66	0.27
Fe_2O_3	0.54	1.37
MgO	0.15	0.10

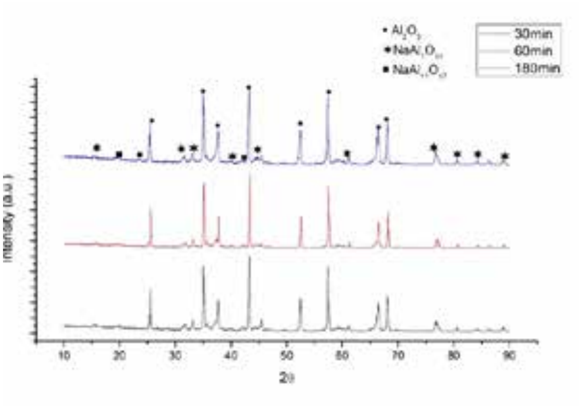

Figure 5. XRD patterns of 30, 60 and 180 min of calcined aluminium white dross at 1000°C.

Table 4. Existing phases of calcined aluminium white dross at 1000° for 30, 60 and 180 m.

Sample	Al_2O_3	$NaAl_7O_{11}$	$NaAl_{11}O_{17}$
RF I 30	+	+	+
RF I 60	+	+	+
RF I 180	+	+	+

Results of experiments with similar conditions at 1100°C are given in Figure 6 and Table 5.

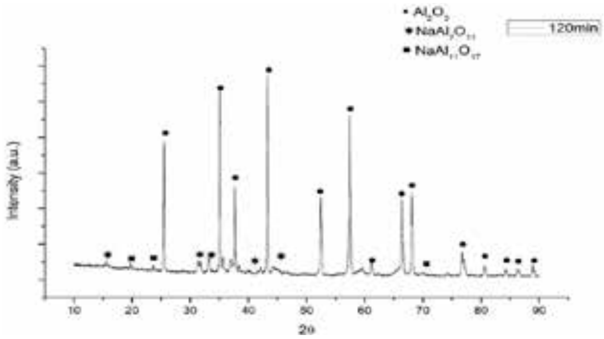

Figure 6. XRD analyses patterns of calcinated samples at 1100°C for 120 min.

Table 5. Existing phases of calcinated aluminium white dross residue at 1100°C for 120 min.

Sample	**Al_2O_3**	**$NaAl_7O_{11}$**	**$NaAl_{11}O_{17}$**
RF II 120	+	+	+

The calcination experiments continued at 1150 °C as the obtained results showed that the increasing temperature was very effective in removal of N. The obtained results are given at Table 6, 7 and Figure 7.

Table 6. Chemical analysis of calcinated white dross residue at 1150°C for 2 hours.

	Al dross	**RFIII 120**
Al_2O_3	68.83	94.67
$Al_{(Me)}$	9.27	0.73
N	5.47	0.25
K_2O	2.49	0.83
SiO_2	1.11	0.96
Na_2O	0.66	0.22
Fe_2O_3	0.54	0.59
MgO	0.15	0.23

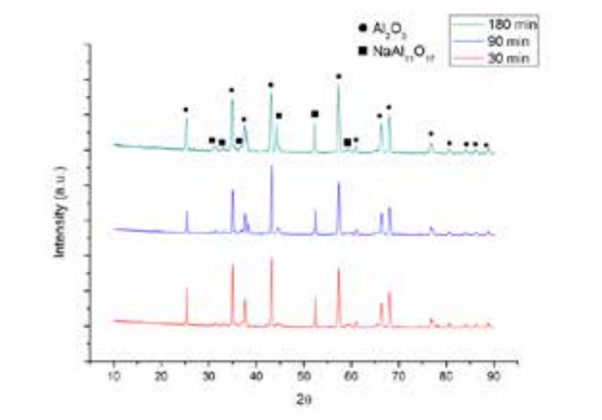

Figure 7. XRD analyses patterns of calcinated samples at 1150°C for 30 min, 90 min and 180 min.

Table 7. Existing phases of calcined aluminium white dross at 1150°C.

Sample	Al_2O_3	$NaAl_{11}O_{17}$
RF III 30’	+	+
RF III 90’	+	+
RF III 180’	+	+

As result of the experiments, it is seen that with increasing temperatures and holding time, decreasing amount of N from 5,47% to 0,25% and decreasing amount of metallic aluminium (Al_{Me}) from 9,27% to 0,73% is possible. Thus, the risks that may arise due to the chemical content of the material are eliminated when it is stored for disposal or reuse.

4. Conclusion

In this study, optimum parameters which temperature and duration are determined after a literature research. By eliminating N and O from non-metallic source, 2 hours of calcination at 1150, 95% of purity has been reached according to XRD and chemical analysis.

References

[1] Eminoğlu, S., Aytaş, S., Ayhan, S. and Varır, A. (2011). Alüminyum Isil MetalürjisiAtikYönetimi (AlüminyumSektörü) RehberDokümani.

[2] Tsakiridis, P. (2012). Aluminium salt slag characterization and utilization – A review. Journal of Hazardous Materials, 217-218, pp.1-10.

[3] G. J. Kulik and J. C. Daley, "Aluminum Dross Processing in the 90's", J. H. L. van Linden, D. L. Stewart, Jr, and Y Sahai (eds.), Second International Symposium– Recycling of Metals and Engineered Materials, Warrendale PA, TMS, 1990. p. 427.

[4] Breault, R. et al, 1995. PROCESS FOR THE PREPARATION OF CALCIUM ALUMINATES FROM ALUMINIUM DROSS RESOURCES. 5,407,459

Production of Mo_2FeB_2-Fe Composites by Using Mill Scale via Self Propagating High-Temperature Synthesis

Bora DERİN, Buse YILMAZ, Faruk KAYA
İstanbul Technical University
Turkey

Abstract

In this study, intermetallic-matrix composites (IMC) containing Mo_2FeB_2 ternary boride reinforcement were produced by self-propagating high-temperature synthesis (SHS). The raw materials were selected as molybdenum trioxide (MoO_3), boron trioxide (B_2O_3), mill scale from the continuous steel casting process, and aluminum. Before the experiments, thermochemical calculations were conducted with FactSage software to determine precursor amount, the composition of the as-cast alloy and the adiabatic temperature of the combustion reaction. A detailed examination on the as-cast structures was made by X-ray fluorescence (XRF), X-ray diffraction (XRD), scanning electron microscopy (SEM/EDS) and microhardness test methods, respectively.

1. Introduction

The changes in industrial needs and advances in technology have brought more attention to the composites which possess great advantages at certain engineering applications. Recently, a wide variety of advanced composite materials have been produced with different element additions and different production methods [1,2]. Owing to its high abrasion resistance, high hardness, high thermal shock resistance and high melting point, Mo_2FeB_2 has been investigated for use as refractory materials, cutting tools and wear resistant parts [3,4]. In the literature, reaction boronizing sintering, vacuum sintering, and two-step sintering were successfully used for the synthesis of Mo_2FeB_2 [3,4]. However, these methods also have some disadvantages such as high energy requirements, high raw material costs, the need of several production steps, and grain growth during sintering. Therefore, in this study, the production of Mo_2FeB_2-Fe composites was aimed by non-centrifugal SHS method from oxides which is considered as a low cost, fast and easy method [5]. In order to contribute to recycling, the mill scale was used as iron source.

2. Materials and methods

The reactants were selected as 98% pure B_2O_3, 3% Fe containing MoO_3, mill-scale, and 99.9% pure aluminum. Prior to the SHS experiments, thermochemical modeling studies were done by using FactSage to calculate the precursor amounts and adiabatic temperature of the reaction. Then, the powders were weighed and dried at 110 °C for 30 min in a drying oven. After thoroughly mixing the powders for 45 min, the SHS process was realized in a Cu crucible.

3. Results and Conclusion

According to the XRD and SEM results, the ternary Mo_2FeB_2 reinforcement phase was successfully produced in a metallic Fe matrix together with binary boride phases such as MoB and Fe_2B. Increased mill-scale amount induced the transformation of binary MoB phase into ternary Mo_2FeB_2 reinforcement phase in Fe matrix. Vickers hardness tests results were in the range of 1163 ± 60 $HV_{0.5}$ and 1591 ± 26 $HV_{0.5}$. Wear loss, wear rate and coefficient of friction values were revealed by reciprocating sliding abrasion tests. It was observed that the wear resistance was proportional to the hardness of the composites.

References

[1] X. Yuan, G. Liu, H. Jin and K. Chen, In situ synthesis of TiC reinforced metal matrix composite (MMC) coating by self-propagating high temperature synthesis (SHS), Journal of Alloys and Compounds, 509, (2011) 1301-1303.
[2] Y. Nishida, Introduction to Metal Matrix Composites Fabrication and Recycling. Springer, 2013.
[3] X. Ren, L. Yu, Y. Liu, H. Li, J. Wu and Z. Liu, Effects of extra boron addition on the liquid-state sintering process and properties of hard Mo_2FeB_2 based cermets, Journal of Refractory Metals and Hard Materials, 61, (2016) 207-214.
[4] H. Yu, W. Liu, P. Feng and Y. Zeng, Synthesis and microstructure evolution during vacuum sintering of Mo_2FeB_2 based cermets, Journal of Refractory Metals and Hard Materials, 45, (2014) 48-52.
[5] S.C.Tjong and Z.Y. Ma, Microstructural and mechanical characteristics of in situ metal matrix composites, Materials Science and Engineering, 29, (2000) 49-113.

Industrial Study on the Recovery of Platinum Group Metals from the Catalytic Converter

H. Hande CEBECİ[1,3], Berk GÜLÖRTEN[3], Mahmut KARADAŞ[3], Safiye TANRIVERDİ[2,3]
[1]Yıldız Technical University, [2]Istanbul University – Cerrahpaşa, [3]Proses Rafinasyon ve Metal Geri Kazanım Makina Sistemleri San. ve Tic. Ltd. Şti
Turkey

Abstract

The scrap auto catalytic converter is a valuable source of platinum group metals, so it is important to have it recycled in order to recover precious metals. In order to increase environmental awareness, to produce more with less pollution and to contribute to the economy, platinum group metals should be recovered from scrapped catalytic converters In the recovery of these metals; While particle size and temperature are effective in roasting process, solid / liquid ratio, temperature and time are one of the important parameters during leaching.

1. Introduction

Catalytic converters have honeycomb-shaped structures with a large surface area, consisting of ceramic (magnesium-aluminum silicate) or metal. Catalytic converters installed in a car exhaust pipe can convert more than 90% of HC, CO and NO contained in an engine into less harmful carbon dioxide, nitrogen and water vapor. Catalytic converters include Platinum, Rhodium and Palladium. These metals do not react with exhaust gases and act as catalysts., 360 kg of soil and rock must be processed, while the same amount can be recovered from a catalytic converter with an average weight of 1,5 kg. According to these data, recycling costs are much lower than the production costs from mining.[1]

2. Materials and Methods

In this study, the steps of catalytic converter recycling were investigated in the production of PGM metal from catalytic converter by acid leaching. In this study effect of time, temperature, and S/L ratio on leaching efficiency are investigated . The increase of the level of each effective tends to increase the leaching efficiency of platinum and palladium. The optimum dissolution of platinum, palladium and rhodium by acid leaching is at a time of 120 minutes, temperature 100°C, and solid/liquid ratio 1/20. Recovery of platinum, palladium and rhodium was possible by the precipitation using at almost 65°C for 1 hour. The chemical analysis of the acid leaching solution is given in table 1. The XRF result of the catalytic converter after acid leaching is given in table 2.[2]

Table 1. Chemical analysis of the Acid leaching solution (wt. %).

Pt	Pd	Rh
159,6	306,5	33,70

Table 2. XRF result of the Catalytic converter after acid leaching (ppm).

Pt	Pd	Rh
0,253	8,56	2,59

3. Conclusion

These studies are show that recovery efficiency of platinum was 99.8%, while recovery efficiency of palladium was 97.3% and rhodium 92.8%.

Reference

[1] Rumpold, R., Antrekowitsch, J., “Recyclıng of Platınum Group Metals from Automotıve Catalysts by an Acidic Leachıng Process”, University of Leoben

[2] Hammadi, M. Q., Yassen, R. S., Abid, K. N., 2017, “Recovery of Platinum and Palladium from Scrap Automotive Catalytic Converters”, Al-Khwarizmi Engineering Journal, 13, 131-141

Leaching of Spent Ni-W Hydrodesulphurization Catalyst in H_2SO_4 Solution

Aycan DEMIR, Aycan ISCAN, Ahmet Orkun KALPAKLI, Mert ZORAGA, Sedat ILHAN
Istanbul University-Cerrahpaşa
Turkey

1. Introduction

Hydrodesulphurization (HDS) catalysts are widely used for the removal of sulfur in hydro-treating processes of crude oil. After a certain operation time HDS catalysts are deactivated gradually and discarded as hazardous waste [1, 2]. Spent catalyst includes different amount of Al, Si, Mo, Ni, W, V, C and S depending on the type of catalyst. Therefore recovery of valuable metals from catalyst is important from the economic and environmental point of view. Although different methods have been proposed for the recovery of valuable metals from spent catalysts, one of the most promising methods is leaching in acid solutions after oxidative roasting step for the removal of S and C. In this work, the effects of temperature, H_2SO_4 concentration, stirring speed, milling and solid to liquid ratio on the leaching of spent Ni-W catalyst were investigated.

2. Materials and Methods

Spent HDS catalyst used in this work was obtained from a refinery in Turkey. Spent HDS catalyst was roasted at 500 °C prior to leaching experiments. Roasted spent catalysts includes mainly Al, Si, Mo, W, Ni and V. H_2SO_4 solutions were prepared using high purity H_2SO_4 solution (Merck, 97 %). Leaching experiments were performed in a water heated, jacketed borosilicate glass reactor system (HWS DN 100). 1 L of 0.5-2 M H_2SO_4 solutions, temperature range of 25-70 °C, stirring speed of 100-300 rpm, unmilled and milled sample, reaction time of 5-180 min and solid to liquid ratio of 5-100 g/L were used for the determination of leaching behavior of spent Ni-W catalyst.

3. Conclusion

XRF analysis showed that roasted catalyst contains 37 % SiO_2, 32 % Al_2O_3, 22 % WO_3, 5,7 % NiO, % 1 MoO_3 and 0,56 % V.

Milling has no significant effect on the leaching rate of spent Ni-W HDS catalyst.

Stirring speed of 300 rpm was found to be optimum stirring speed. Increasing temperature increased the leaching rate of W, Ni, Mo, V and Al.

While increasing H_2SO_4 concentration increased leaching rate of Ni, Mo, V and Al, leaching rate of W decreased with increasing acid concentration.

Extraction rate of elements obtained in optimum leaching conditions, in which 23 % of W, 99 % of Ni, 92 % of Mo, 98 % of V and 43 % of Al were extracted, are shown in Figure 1.

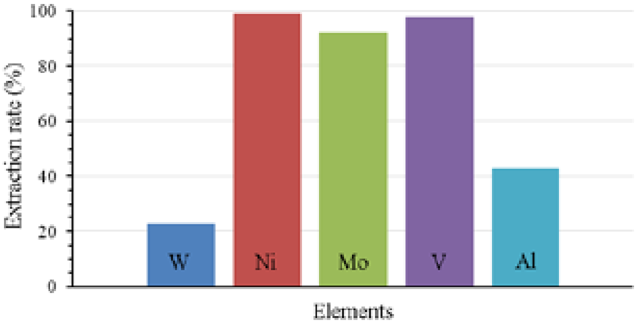

Figure 1: Extraction rate of elements obtained in the optimum leaching conditions. (2 M H_2SO_4, 70 °C and 300 rpm)

References

[1] P. Dufresne, Applied Catalysis A: General, 322, (2007), 67-75.

[2] U. EPA, Hazardous Waste Management System; Identification and Listing of Hazardous Waste: Spent Catalysts from Dual-Purpose Petroleum Hydroprocessing Reactors, E. PROTECTION, et al., Editors. 2001, Federal Register pp. 35379-35384.

Liberation and Extraction of Valuable Components From Li-ion Battery Waste via Supercritical Carbon Dioxide System

Yuanpeng FU[1,2], Burçak EBİN[2]
[1]China University of Mining and Technology, [2]Chalmers University of Technology
[1]China, [2]Sweden

Abstract

Considering the issues of global metal resources shortage and potentially hazardous effects on the environment, it is necessary to promote approaches to recycle the major components of the spent LIBs. As an emerging technology, supercritical carbon dioxide (SC CO_2) process has been introduced as a method for metals recovery from WEEE and separate its constituent materials by removing the polymers. In this study, SC CO_2 combined with a co-solvent dimethyl sulfoxide was adapted to recover valuable components from spent LIBs. It is confirmed effective for the liberation of the cathode materials as well as the extraction of organic binders under the optimal processing pressure, temperature, and time. The research revealed that technology is a multifunctional recovery method that can be customized for material recycling processes from battery waste.

1. Introduction

The rapid development of energy storage systems due to the booming of portable electronic devices, electrical vehicles, and renewable energy sources causes a burst demand of lithium-ion batteries (LIBs), which results in a large number of spent LIBs to be recovered. SC CO_2 is a good low-cost solvent without any secondary pollution and non-flammable advantages such as low viscosity, a high mass transport coefficient, high diffusivity, and high solubility of organics, which is beneficial for the dissolution of organic and metals. Therefore, SC CO_2 system was used to liberate and extract valuable components from LIBs.

2. Materials and Methods

The spent aluminum laminated Li-ion batteries (ALBs) used in this study were provided by Volvo Cars, Sweden, and the reagent DMSO (analytically pure) was purchased from Sigma-Aldrich, Ltd. CO_2 (purity 99.998%) was used for extraction experiments. In this study, SC CO_2 combined with a co-solvent dimethyl sulfoxide was adapted to recover valuable components from spent LIBs.

3. Conclusion

The results indicate that pure PVDF dissolves completely using supercritical CO_2- DMSO system under the optimum conditions. To practically put it into actual material, the method is effective to liberate cathode material and aluminum foil under the treatment of SC CO_2 fluid. Compared with the previous recycling process, this method was found to be efficient, low energy consumption, and environmentally friendly.

Thermodynamic and Experimental Study of the Fluoride Recovery from Spent Pot Lining Recycling Process by Precipitation of Calcium Fluoride

Anna Mas HERRADOR[1,2], Jonas SCHUSTER[1], Yuanpeng FU[1,3], Martina PETRANIKOVA[1], Burçak EBİN[1]

[1]Chalmers University of Technology, [2]Universitat Politècnica de Catalunya,
[3]China University of Mining and Technology

[1]Sweden, [2]Spain, [3]China

Abstract

Spent Pot Lining (SPL) is a hazardous waste generated in the primary production of aluminum. The current waste treatment approach is hazardous waste storage or incineration. This work is focused on the thermodynamic study to predict the behavior of a stream coming from an SPL recycling process by introducing calcium salts in order to obtain a precipitated product of interest such as CaF_2. The thermodynamic of the reaction chemistry was investigated by HSC Chemistry software and the subsequent verification of these results in an experimental way.

1. Introduction

After steel, aluminium (Al) is the most highly produced metal and the most produced non-ferrous metal [1]. Worldwide aluminium production in 2019 was approximately 63.7 million tonnes [2]. Aluminium is produced from bauxite ore by mineral pretreatment followed by molten-salt electrolysis [3]. The waste material resulting from removing the electrolytic cell in primary aluminium production is called Spent Pot Lining (SPL). A typical figure would be 22 kg of SPL produced per tonne of aluminium, although it would be between 20 and 50 [3].

SPL is typically a mix of all cell lining materials. However, SPL consists of two fractions. The portion above the collector bars is often referred to as the first cut and contains mainly a carbonaceous cathode. It typically consists of a relatively homogeneous and very hard mix of materials including carbon, fluorine, and a small amount of cyanide. The first cut forms about 55% of the total weight of the SPL and constitutes the hazardous fraction due to high leachable fluoride and cyanide contents SPL is considered to be toxic due to its high concentration of fluorides and cyanides, which are corrosive and reactive with water. The fraction below the collector bar or second cut is essentially composed of refractory brick (insulating and firebricks). These insulating materials are used to minimize heat loss through the pot walls. The second cut is typically less homogeneous than the first cut and contains lower levels of cyanide and fluorine. Aluminium, silica, and sometimes iron are also present [3]. It is estimated that more than 50% of the SPL generated annually is stored indefinitely or deposited in a landfill [5]. In 2018, approximately 1.6 million tonnes of SPL was generated from the production of primary aluminium [6].

There are several approaches for SPL recovery including using as an additive material in different industries or direct recycling, which is limited. One of the first industries to use SPL is the cement industry, to improve firing conditions, but there are restrictions on the sodium content allowed. The mineral wool, iron (as an additive), and steel (as a substitute for fluorite) industry also use SPL. The problem with these uses is that only relatively small amounts of SPL may be used, to avoid complication in the process [7]. All these approaches necessitate separation of the main components carbon, brick, and fluorides. Considering the recycling of SPL, pyrometallurgical, or hydrometallurgical processes are applied but the industrialization of these process technologies is limited. In the case of hydrometallurgical treatment, the destruction of cyanides, and the recycling of carbon, brick, cryolite, and fluoride are the main goals of a process. The most developed and upscaled process involving chemical conversion to valuable products is the Low-Caustic Leaching and Liming (LCL&L) developed by Rio Tinto Alcan, Québec. This plant has a capacity to treat 80,000 tonnes of SPL annually [5-8].

Precipitation is considered a simple and cost-efficient method of removing fluoride from aqueous streams leading to the recovery of a valuable product such as fluorite. Fluorite (CaF_2) is one of 27 critical raw materials for the European Union (EU) because the risks of supply shortages and their impact on the economy are high. Almost 810,000 tonnes of fluorite is consumed industrially in Europe. The main uses are in the metallurgical, ceramic, and chemical industries [9]. Moreover, CaF_2 is especially added to sodium cryolite in the amount of 3-5 wt% mainly to reduce the temperature of the liquid electrolyte in the primary aluminum production. Therefore, the separation of calcium fluoride from SPL has an important value in the aluminum production process, as a product to be reused.

In this study, thermodynamic of the CaF_2 precipitation reactions were investigated from the process water of a recently proposed SPL recycling technology. Additionally, the precipitation process was simulated, and experimentally studied from an artificial solution.

2. Method

A reaction model was built according to the main and possible side chemical reactions taking into account the calculated chemical composition of the SPL first cut material after detoxification and caustic leaching stages, which covers the processing of 5 kg SPL per hour corresponding to the pilot-scale process. HSC Chemistry 9 software developed by Outotec was used for the thermodynamic study of the process stage for $Ca(OH)_2$ addition as precipitating agents. The calculated input flow data of the leachate for precipitation unit contains dissolved NaOH, NaF, and $NaAl(OH)_4$ with amounts

The reagents used to prepare the artificial sample (NaOH, NaF, $Ca(OH)_2$ and $Al(OH)_3$) have been purchased from Sigma- Aldrich, Ltd. $Ca(OH)_2$ has 96% purity and contains max. 3% $CaCO_3$.The precipitation reactions were carried out at room temperature and with constant agitation for 3 hours by using a magnetic stirring plate at 500 ppm. After 20 hours, the precipitate is separated by centrifugation using an OHAUS Frontier FC5714 Multi-Pro centrifuge and left to dry in the laboratory oven at 40ºC.

The pH evolution of the solution was measured by a visual comparison of the Dosatest pH test strips. A Perkin Elmer Spectrum Two FTIR Spectrometer and an X-ray diffractometer Siemens (XRD, D8 ADVANCE, Bruker) with Cu Kα radiation (35KV and 30mA) were used to detect the composition of the precipitate.

3. Results and Discussion

The input flow for the fluoride precipitation unit is defined by the pre-treatment of the SPL material. The pre-treatment modeling of the recycling process contains reactive leaching and detoxification stages. The input stream has the following composition.

Table 1. Input flow that was used in thermodynamic modeling of the precipitation unit.

Input flow	
Mass flow	51.161 kg/h
Volume	49.235 L/h
H_2O	49.944 kg/h
$NaOH_{(a)}$	106 g/h
$NaF_{(a)}$	206.12 g/h
$NaAl(OH)_4$	123 g/h

The Gibbs free energy and reaction equilibrium constants of the following chemical reactions as a function of temperature from 0 to 90°C were calculated and results are given in Figure 1.

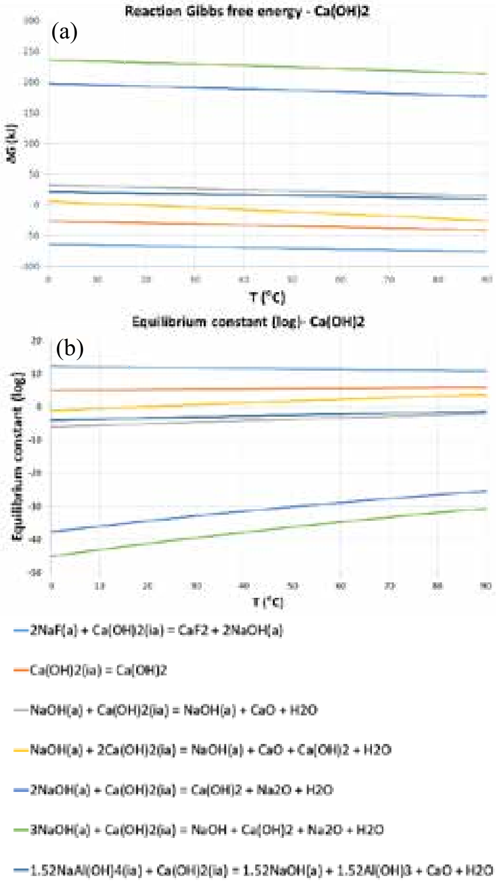

Figure 1. (a) Gibbs free energy and (b) reaction equilibrium constant changes by the temperature of possible reactions for precipitation unit in suggested SPL recycling process.

Considering the Gibbs free energies and reaction constant values, NaF can spontaneously react with $Ca(OH)_2$ to form CaF_2. On the other hand, precipitation of the $Ca(OH)_2$ is a possibility due to the side reactions. The equilibrium composition of precipitation using $Ca(OH)_2$ as a precipitation agent was investigated at 25°C as shown in Figure 2. The reaction system designed as add amount mode which means that 1 mol $Ca(OH)_2$ was added step by step in total 50 stages.

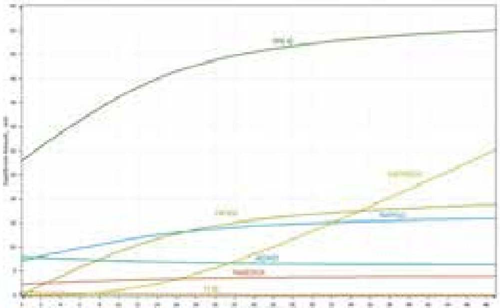

Figure 2: Equilibrium amount of each component according to the added amount of $Ca(OH)_2$ in the precipitation system.

In the precipitation system, CaF_2 generation does not reach a clear stagnation point, but the slope of the curve is reduced by an increased amount of $Ca(OH)_2$ feeding. Although $Ca(OH)_2$ is dominantly consumed by precipitation reactions in the low dosing amounts, solid $Ca(OH)_2$ starts linearly increase when the CaF_2 formation approach to the saturation. The thermodynamic simulation of the precipitation indicates that high purity CaF_2 can be precipitated in a low recovery efficiency zone. Increasing recovery efficiency reduces the purity of the precipitate due to co-precipitates, specifically calcium salts.

An artificial solution to simulate the SPL recycling process precipitation unit was prepared in chemical composition given in Table 2. $Ca(OH)_2$ (0.2022 g) was fed into the solution in the powder form. The pH of the solution was measured as 14 and 0.2461 g precipitate was obtained after 20 h.

Table 2. Chemical composition of 50 ml artificial input solution.

Species	Amount (g)
NaOH	0.1478
NaF	0.3391
$Al(OH)_3$	0.0814

It is important to mention that the solubility limit of $Ca(OH)_2$ in water is 1.73 g/L at 20°C. Used precipitation agent amount exceeds the solubility limit in the experiments, but it is lower than the theoretically required amount to recover all fluoride from the solution. It was assumed that all fed $Ca(OH)_2$ can be used by time due to consumption in the precipitation reaction. The calculated yield of precipitation reaction is around 78 wt% considering the F^- the amount in the solution and all precipitate is CaF_2.

On the other, when the yield is calculated using the full consumption of the precipitation agent, it is 115 wt%. This means that precipitate is not pure CaF_2, and it can contain impurities. The crystalline structure of the precipitate was characterized by XRD. Figure 3 presents the XRD pattern of the precipitate.

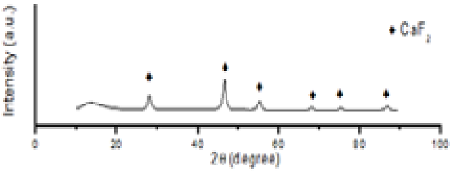

Figure 3. XRD pattern of the precipitate.

The XRD pattern of the precipitate is corresponding face centered cubic crystal structured calcium fluoride (space group Fm-3m, PDF Card No: 01-087-0971). Crystalline structured impurity such as $Ca(OH)_2$ was not detected, but a smaller amount of impurity or amorphous impurities still can be in the precipitate sample.

High purity CaF_2 is used to manufacture optical components such as windows and lenses for spectroscopy applications due to their transparent properties over a broad range from ultraviolet (UV) to infrared (IR) frequencies. Thus, FTIR analysis is a useful methodology to detect the purity of the prepared CaF_2 precipitate. Figure 4 shows the FTIR spectrum (transmittance view) of the precipitate sample and pure CaF_2. The peaks at around 1450, 1000 and 850 cm^{-1} belong to different vibration modes C-O of carbonate groups CO_3^{2-}. The result indicates that precipitate contains $CaCO_3$ impurity which originates as an impurity in $Ca(OH)_2$. Since the solubility of $CaCO_3$ is limited (0.013 g/L at 25°C), the impurity amount in the precipitation agent exceeds the solubility limit of the experimental condition.

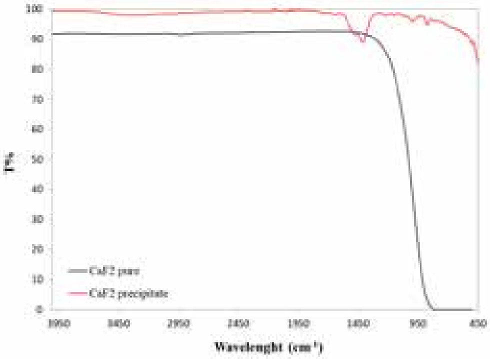

Figure 4. FTIR spectrum of precipitate and pure CaF_2.

The result reveals that the recovery of fluoride in the form of CaF_2 by precipitation reactions using

$Ca(OH)_2$ is an efficient approach. However, the purity of the final product is limited due to $CaCO_3$ impurity.

4. Conclusion

Fluorite (CaF_2) is one of the raw materials that present risks of shortage for the EU. On the other hand, Spent Pot Lining (SPL) from primary aluminium production is a hazardous waste due to its content of fluorides and cyanides. This research proposes a process stage for the recovery of CaF_2 by precipitation reactions for an innovative SPL recycling process, which is also including leaching and reactive detoxification stages prior to precipitation.

The thermodynamic of CaF_2 precipitation and side reactions from the SPL recycling process water was investigated. Theoretical calculations reveal that high purity CaF_2 can be obtained only in low recovery efficiency due to possible co-precipitation reactions and limited solubility of precipitation agent. Subsequent experimental research is confirmed the successful recovery of CaF_2 using $Ca(OH)_2$ as a precipitation agent. However, the purity of the final product is affected by the $CaCO_3$ impurity level of the agent.

Acknowledgment

This project "Closing the loop of the Spent Pot-line (SPL) in Al smelting process" is a KIC Added Value Activity (KAVA) project funded by the European Institute of Innovation and Technology (EIT) Raw Materials (Project No: 17141). This body of the European Union receives support from the European Union's Horizon 2020 research and innovation program.

References

[1] British Geological Survey, World Mineral Production 2014-2018, (2020).

[2] The International Aluminium Institute, "World Aluminium — Primary Aluminium Production," 2020. [Online]. Available: http://www.world-aluminium.org/statistics/primary-aluminium-production/#data. [Accessed: 19-Apr-2020].

[3] D. Brough and H. Jouhara, International Journal of Thermofluids, 1-2 (2020) 100007.

[4] N. I. Poulimenou, I. Giannopoulou, and D. Panias, Mater. Manuf. Process., 30/12 (2015) 1403–1407.

[5] G. Holywell and R. Breault, *JOM*, 65/11 (2013) 1441–1451.

[6] P. Nunez Sustainable Spent Pot Line Management Guidance. In: Tomsett A. (eds) Light Metals 2020. The Minerals, Metals & Materials Series. Springer, pp 1225-1230.

[7] T. J. Robshaw, K. Bonser, G. Coxhill, R. Dawson, and M. D. Ogden, Waste and Biomass Valorization, (2020).

[8] Z. N. Shi, W. Li, X. W. Hu, B. J. Ren, B. L. Gao, and Z. W. Wang, Trans. Nonferrous Met. Soc. China, 22 (2012) 222–227.

[9] European Commission, Communication from the Commission to the European Parliament, the Council, the European Economic and Social Committee and the Committee of the Regions on the 2017 list of Critical Raw Materials for the EU, Brussels, September 2017.

Recovery of Valuable Metals from Waste Lithium-Ion Batteries by Metallurgical Routes

Sepehr ABTAHI[1], Kağan BENZEŞİK[1], Ahmet TURAN[2], Onuralp YÜCEL[1]
[1]Istanbul Technical University, [2]Yalova University
Turkey

Introduction

Lithium-ion batteries (LIBs) are widely used in mobile phones, laptops, new energy vehicles and other fields because of their advantages of being clean energy, having a long service life, high energy density and high operational safety. In this work, the objective is to develop a selective process for the recovery of valuable metals (Li, Co, Ni, Cu, and Mn) from spent LIBs through pyrometallurgy and hydrometallurgical leaching.

Materials and Methods

Through a literature review, two different methods were selected: (1) First method is hydrometallurgical leaching with HCl acid, which was applied on LIBs having 3200 mA current and (2) through pyrometallurgy by smelting and roasting the material in the induction and ash furnaces.

Results

As for the hydrometallurgical path, separated electrode materials (112.3 g) taken from the LIBs were put in a beaker to be leached in hydrochloric acid solution (50%) with distilled water (50%) by vol. for 2 hours at an average temperature of 85.5 ºC. For an accurate result, after heating for 2 hours and filtering, the solid cake containing the electrodes was separated and dried in a drying oven for 12 hours. An atomic absorption spectrometry (AAS) analysis was made on the samples taken at different periods (30 min., 60 min. and 120 min.) which it was observed that the samples contain [@30 min: Mn: 0.76 (mg/L); Cu: 0.23 (mg/L); Ni: 0.018 (mg/L); and Co: 0.039 (mg/L)], [@60 min: Mn: 1.460 (mg/L); Cu: 0.542 (mg/L); Ni: 0.03054 (mg/L); and Co: 0.0686 (mg/L], and [@2 hours: Mn: 2.399 (mg/L); Cu: 0.771 (mg/L); Ni: 0.05574 (mg/L); and Co: 0.0914 (mg/L)] by having different diluting factors. Meanwhile, in the pyrometallurgical path, samples of electrodes (30g) were roasted at incremental temperatures from 700 ºC to 1500 ºC in different furnaces for periods from 1 hour up to 3 hours. A summary of the x-ray fluorescence (XRF) analysis of the calcined samples at different tempratures are given in the Table 1.

Table 1 – XRF analysis of the samples at different tempratures

<table>
<tr><th rowspan="2">Experiment</th><th colspan="2">Metal Mode</th><th colspan="2">Oxide Mode</th></tr>
<tr><th>Anode</th><th>Cathode</th><th>Anode</th><th>Cathode</th></tr>
<tr><td>1400 C (Direct)
30 minutes
30 grams
Induction furnace</td><td>Cu = 95.24
Mn = 0.96
Fe = 0.62</td><td>Mn = 81.83
Ni = 10.06
Co = 5.89</td><td>Cu = 8.65
Mn = 0.258
Fe = 0.169</td><td>Mn = 61.96
Ni = 6.19
Co = 3.51</td></tr>
<tr><td>1200 C (Direct)
3 hours
30 grams
Ash furnace</td><td colspan="2">Mn=82.73
Cu = 10.84
Ni = 3.51
Co = 2.32</td><td colspan="2">Mn = 47.57
Cu = 8.89
Ni = 0.81
Co = 0.81</td></tr>
<tr><td>1150 C (Direct)
3 hours
30 grams
Ash furnace</td><td colspan="2">Mn = 74.56
Cu = 22.05
Ni = 1.37
Co = 1.24</td><td colspan="2">Mn = 46
Cu = 9.08
Ni = 0.61
Co =0.61</td></tr>
<tr><td>1150 C (Indirect)
3 hours
30 grams
Ash furnace + Muffle furnace</td><td colspan="2">Mn = 60.81
Cu = 34.74
Ni = 2.36
Co = 1.81</td><td colspan="2">Mn = 33.31
Cu = 11.61
Ni = 0.90
Co = 0.63</td></tr>
</table>

Conclusion

From the obtained results, it is conceived that the main elements that were extracted from the Li-ion Batteries in the selected batch were Mn, Cu, Ni, and Co. Hence in this work, it was concluded that increasing the temperature rapidly to a certain degree between 1250 – 1350 ºC will allow a direct metallic formation of the valuable elements to be left behind in the crucible. Equally important, to prevent any adhesive behavior between the sample and the ceramic crucible and to have a fully smelted sample, flux materials silica (silicon dioxide) and borax (sodium borate) were used. This is an ongoing project and, further experiments will take place to utilize the process to allow an efficient recovery for Li-ion battery wastes.

References:

[1] - Ma, Yayun, et al. "A Promising Selective Recovery Process of Valuable Metals from Spent Lithium Ion Batteries via Reduction Roasting and Ammonia Leaching." Journal of Hazardous Materials, vol. 402, Jan. 2021, p. 123491. ScienceDirect, doi:10.1016/j.jhazmat.2020.123491.

[2] - Zhao, Yanlan, et al. "Regeneration and Reutilization of Cathode Materials from Spent Lithium-Ion Batteries." Chemical Engineering Journal, vol. 383, Mar. 2020, p. 123089. ScienceDirect, doi:10.1016/j.cej.2019.123089.

[3] - Arshad, F., Li, L., Amin, K., Fan, E., Manurkar, N., Ahmad, A., … Chen, R. (2020). A Comprehensive Review of Advancement in Recycling Anode and Electrolyte from Spent Lithium Ion Batteries. ACS Sustainable Chemistry & Engineering. doi:10.1021/acssuschemeng.0c04940

[4] - Zhang, Jialiang, et al. "Efficient and Economical Recovery of Lithium, Cobalt, Nickel, Manganese from Cathode Scrap of Spent Lithium-Ion Batteries." Journal of Cleaner Production, vol. 204, Dec. 2018, pp. 437–46. ScienceDirect, doi:10.1016/j.jclepro.2018.09.033.

Indium Recovery from Model Leach Solutions by Solvent Extraction

Doğaç TARI[1], Semih ATEŞ[1], Burçak EBİN[2], Sebahattin GÜRMEN[1]
[1]İstanbul Technical University, [2]Chalmers University of Technology
[1]Turkey, [2]Sweden

Abstract

Indium is an essential part of liquid crystal displays (LCD). As consumption of these technologies increase, indium usage also increases. Waste LCDs are a rapidly growing problem involving critical metal indium and extraction from ITO thin film form is usually done with leaching. Even though leaching efficiencies are high, leaching is not a selective method to recover indium. This represents the problem of indium mixing with impurities in leach solution. In this study, we designed a solvent extraction process to extract indium from synthetic leach solutions, modelled after our previous studies and literature research. Model leach solution was prepared with most abundant elements (In, Sn, Al, Fe, Zn, Cu) dissolved in 1M H_2SO_4 solution. D2EHPA diluted in kerosene was used as the extractant. Different D2EHPA concentrations, shaking durations and O/A ratios were tested for extraction process. 1M HCl was chosen as stripping agent, which was tested with different shaking times and O/A ratios. As a result, indium was separated from tin, the biggest impurity in leach solutions.

1. Introduction

Indium is classified as a critical metal [1]. Its supply presents potential bottlenecks. LCDs are indispensable parts of our lives as the most popular screen technology in the world [2]. Indium is an essential part of LCDs and more than 70% of indium consumption worldwide is attributed to ITO manufacturing [3]. LCD-ITO situation makes recycling of indium an important obstacle to overcome [4]. Some of main problems are low indium amount in LCDs and impurity presence in LCD structure. In our study, the aim was to optimize solvent extraction process to separate indium from impurities.

2. Materials and Methods

Synthetic solution was prepared by dissolving respective sulfate salts of In, Sn, Al, Fe, Zn and Cu in 1M H_2SO_4 solution. Composition of starting sulfate media can be seen on Table 1. Experiments were conducted in separation funnels without additional heating and cooling. For extraction, 0.1M, 0.25M and 0.5M D2EHPA dissolved in Kerosene were used at O/A ratios of 2/1, 1/1 and 2/3. 5 and 10 minutes of shaking time were used. For stripping, 1M HCl was used at O/A ratios of 1/1, 5 minutes shaking, for 3 steps. Afterwards, O/A ratio of 2/1 was also tested for 5, 10 and 15 minutes of shaking.

Table 1: Concentrations of elements in synthetic model solution.

Metal	Indium	Tin	Aluminum	Zinc	Iron	Copper
Concentrations (mg/L)	517.52	59.34	5.94	11.7	32.3	13.04

3. Conclusion

0.1M of D2EHPA was not enough to extract all of indium for O/A=1/1 and 5 minutes shaking. However, 0.25M and 0.5M D2EHPA had almost perfect indium extraction percentages for same O/A ratio and shaking time. Indium stripping with 1M HCl was successfully increased by multiple steps, while still keeping impurity levels in check. Especially tin extraction was lower than 2% for all D2EHPA concentrations and shaking times. Increasing shaking time from 5 to 15 minutes also increased indium stripping percentage. Increasing shaking times and step count increased impurity concentrations in extremely small amounts.

References

[1] L. Rocchetti, A. Amato, V. Fonti, F. Vegliò, F. Beolchini, Chemical Engineering Transactions, 43 (2015), 1987-1992.
[2] J. Ruan, Y. Guo, Q. Qiao, Procedia Environmental Sciences, 16 (2012), 545-551.
[3] J. Ylä-Mella, E. Pongrácz, Resources, 5 (2016), 34.
[4] L. Ciacci, T. Werner, I. Vassura, F. Passarini, Journal of Industrial Ecology, 23 (2019), 426-437.

20th
INTERNATIONAL
METALLURGY
MATERIALS
CONGRESS
10-12 June
2021
“in Digital Platform”

POSTERS

immc2021

Air Hardened Bainitic Forging Steel

İ. İsmail İrfan AYHAN[1], Caner GÜNEY[1], N. Başak DÜRGER[1], Emre ALAN[1], Ersoy ERİŞİR[2,3]
[1]ÇEMTAŞ R&D Center, [2]Kocaeli University, [3]OBER R&D
Turkey

Abstract

This paper reports the design and properties of new bainitic steel, CARGEM B1200. Results show that the steel have bainitic microstructure with some retained austenite and M/A phases. According to mechanical test results, 1200 MPa tensile strength, >12% elongation and >20 J toughness can be obtained with proper amounts of Ti – Mo – Cr alloying and optimized heat treatment cycles.

1. Introduction

In recent decades there has been an increased emphasis on the development of new steel alloys for forging steel, although combination of high strength and good toughness properties have been achieved by quenched and tempered (Q&T) steels. Age hardening Ferritic-Pearlitic (AFP) steels can be produced with air cooling after forging. However, AFP steels have tensile strength about 1000 MPa with acceptable ductility/toughness values. On the other hand, newly developed bainitic forging steels made possible to achieve high strength (>1150 MPa) and toughness properties with lower process costs compared with Q&T steels. In this work, ÇEMTAŞ has developed air-hardened carbide free bainitic steel alloy for automotive parts with high strength >1150MPa) and moderate ductility.

2. Materials and Methods

The newly developed bainitic steel used in this study is CARGEM B1200 produced by ÇEMTAŞ. All specimens were austenitized at 1250 °C at induction furnace and forged to 30 mm diameter rods from 37 mm hot rolled billets. Still air cooling (1°C/s) was applied followed by forging. The mechanical properties and microstructural evolution were investigated in as-rolled and as-forged conditions. Tensile tests were carried out on a universal test machine of 400 kN load capacity. Longitudinal impact toughness was measured on Charpy V(2mm)-notched samples at room temperature. For microstructural observations specimens were ground and polished using standardized techniques. %2 Nital etching solution was used to reveal the microstructure by light microscopy. SEM analysis was carried out on Zeiss Model (EVO50) operating at 20 kV. Quantitative X-Ray analysis (Stresstech, Cr radiation) and EBSD analysis were applied to determine the fraction of retained austenite. From XRD measurements the fraction of retained austenite was calculated from the intensities of (200), (220) austenite peaks and (200), (211) planes of ferrite. Continuous cooling diagram (CCT) was calculated assuming austenite grain size ASTM 5 at 1200 °C by using JmatPro Software. Deformation CCT diagram was constructed by Baehr deformation dilatometer on the basis of dilatometric tests. Specimens with a section of 5mm diameter and 10 mm were used. In order to physically simulate the hot forging process, samples were hold at 1200 °C for 10 min and followed by compression deformation at 0,3 true strain with a deformation rate of 1 /s.

3. Conclusion

Carbide free bainitic structure was achieved successfully by air cooling after forging. The structure was mostly bainitic with some retained austenite and M/A constituents. Retained austenite amount is 17 vol. %. CARGEM B1200 steel showed high strength (1200MPa). The homogeneous bainitic structure can be guaranteed at cooling rates between 0,15 and 8°C/s. The results showed that designed steel is promising candidate for many forging parts with different dimensions.

Acknowledgment

This study was supported by TUBITAK (Grant No: 3180102). The authors wish to acknowledge the contributions of KANCA A.Ş. and DELPHI.

The Site and Phase Preferences of Mo Element in a Model Ni-Al-Mo Superalloy

Rasim ERİŞ, M. Vedat AKDENİZ, Amdulla O. MEKHRABOV
Middle East Technical University
Turkey

Abstract

It is well accepted that the superior mechanical properties of Ni-based superalloys can be further enhanced by alloying element addition which leads to formation of coherently distributed γ'-Ni_3Al precipitates within γ-Ni matrix. Depending on the site and phase preferences of alloying elements, novel types of these materials can be developed. The current study aims to reveal site and phase preferences of X = Mo element via first-principles calculations and energy-dispersive X-ray spectroscopy (EDS) technique. To conclude, X = Mo atoms prefer to occupy Al sites of γ' precipitates and participate into γ matrix.

1. Introduction

Ni-based superalloys having excellent mechanical properties and oxidation-corrosion resistance at high temperatures are used in many application areas such as turbine blades, nuclear reactors and power plants. In these materials, $L1_2$-type ordered γ'-Ni_3Al precipitates are coherently distributed in FCC-type disordered γ-Ni matrix phase. The site preference of X = Mo element atoms in γ'-Ni_3Al-Mo precipitates can be revealed via theoretical first-principles calculations. In addition, the phase substitution behaviour of X = Mo element can be determined as:

$$\kappa_{Mo} = \frac{c_{Mo}^{\gamma'}}{c_{Mo}^{\gamma}} \qquad (1)$$

where κ_{Mo} is the partitioning coefficient Mo element, $c_{Mo}^{\gamma'}$ and c_{Mo}^{γ} are the concentrations of Mo metal in γ' and γ phases, respectively.

2. Materials and Methods

The site occupancy tendencies of alloying X elements in γ'-Ni_3Al-X precipitates at 0 K can be determined by applying anti-site formation-based formalism. Depending on the sign and magnitudes of $E_{Ni \rightarrow Al}^{X}$ parameters, the site substitution preferences of alloying X elements can be classified into three groups:

- 1st group: $E_{Ni \rightarrow Al}^{X} < 0$, X elements preferably substitute for Al sites;
- 2nd group: $E_{Ni \rightarrow Al}^{X} > H_{Ni_{Al}} + H_{Al_{Ni}} = 1.04$ eV, X elements tend to occupy Ni sites;
- 3rd group: $0 < E_{Ni \rightarrow Al}^{X} < H_{Ni_{Al}} + H_{Al_{Ni}} = 1.04$ eV, X elements may substitute for both Al and Ni sites.

Phase preference of X = Mo element in $Ni_{80}Al_{15}Mo_5$ alloys can be determined by using field emission gun model of scanning electron microscope (FESEM) equipped with an energy-dispersive X-ray spectroscope (EDS).

3. Conclusion

X = Mo atoms preferentially occupy Al sites of γ'-Ni_3Al-Mo precipitates since $E_{Ni \rightarrow Al}^{Mo} = -1.13$ eV. Furthermore, X = Mo atoms tend to become enriched in γ matrix (i.e. $\kappa_{Mo} \approx 0.85$) and promote solid solution strengthening.

Acknowledgement

The Scientific & Technological Research Council of Turkey (TUBITAK) is acknowledged for the scholarship programme for graduate students (2211).

Numerical Simulation and Experimental Analysis of the Dynamic Behaviour of Ternary Metal Alloy (Ga-In-Sn) Flow Driven by Tubular Electromagnetic Stirrer

Brahim HIBA[1], Lakhdar HACHANI[1], Abdallah NOURI[1], Kader ZAIDAT[2], Yves FAUTRELLE[2]
[1]Université Amar Telidji de Laghouat, [2]SIMAP-EPM PHELMA, University of Grenoble Alpes
[1]Algeria, [2]France

Abstract

In this work, we present a multiphysics computational study of a traveling magnetic field (TMF) and its application to control the dynamics behaviour of the selected metallic alloy (Ga-In-Sn). The results are obtained by a 3D numerical simulation of a tubular inductor (Bitter electromagnet) using COMSOL software and consolidated with experimental characterization. The built model allows us to carry out some numerical experiments in order to discern the ability of the proposed tubular inductor to generate and control a travelling magnetic field, which in turn, creates a controlled movement in the liquid Ga-In-Sn metallic alloy in a crucible box.

1.Introduction

In the process of solidification, hydrodynamic motions in the liquid phase are always present [1-3]. These motions have an effect on the solidification process and the quality of the final crystal [4-5]. The use of electromagnetic stirring in order to isolate and control the phenomena due to these motions in liquid metals is a very relevant solution and technically possible [6]. Indeed, our work will be focused on predictive 3D numerical simulation backed by an experimental investigation, of the different possibilities of control of melt dynamic behaviour by means of the travelling magnetic field on a laboratory scale.

2. Materials and Methods

This study examines both numerically and experimentally a liquid Ga-In-Sn metal flow generated by a travelling magnetic field. The built model allows us to carry out some numerical experiments in order to discern the ability of the proposed tubular inductor to generate and control a traveling magnetic field, which in turn, creates a controlled movement in the liquid charge. It's about an electromagnetic stirring without the contamination of liquid metal by other materials and this only by acting on the electromagnetics forces configurations. the ternary liquid metal (Ga In Sn) at room temperature is enclosed in a crucible which the dimensions are: radius R = 2.5 cm, height H = 30 cm. We place the crucible inside a tubular inductor has six windings supplied with three-phase currents at network frequency f_0 = 50 Hz. Its height is H_{IN} = 18 cm.

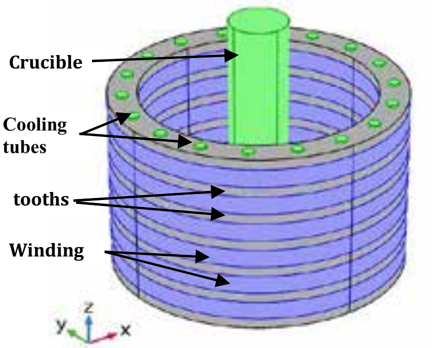

Figure 1: Schematic of the studied system

3. Conclusion

The electromagnetically driven flow in ternary alloy (Ga-In-Sn) in a cylindrical crucible was numerically investigated. A 3-D numerical model was established to investigate the effect of the travelling magnetic field on the driven flow behaviour of the melt at room temperature. An electromagnetic stirrer was proposed. The optimized Tubular form of the inductor was designed to generate different modes of a traveling magnetic field. Each mode of TMF gives its a particular flow driven. This control of the flow driven of melt allows us a batter control of the dynamic behaviour and the proposal of some technical solutions in order to avoid some undesired effect related to the hydrodynamic motions in the liquid phase

[1] HACHANI L., SAADI B., WANG X.D., NOURI A., ZAIDAT K., BELGACEM-BOUZIDA A., AYOUNI-DEROUICHE L., RAIMONDI G., FAUTRELLE Y., Experimental Analysis of the Solidification of Sn-3wt.%Pb Alloy Under Natural Convection, , *International. Journal of Heat Mass Transfer* Vol 55 (7–8) 1986–1996. 2012.

[2] HACHANI L., ZAIDAT K., SAADI B., WANG X-D., FAUTRELLE Y., Solidification of Sn-Pb Alloys: Experiments on the Influence of the Initial Concentration, *International Journal of Thermal Sciences* Vol 91, 34-48. 2015.

[3] HACHANI L., ZAIDAT K., FAUTRELLE Y., Multiscale Statistical Analysis of the Tin-Lead Alloy Solidification Process, *International Journal of Thermal Sciences* Vol 110, 186-205. 2016.

[4] WANG X.D., FAUTRELLE Y., ETAY J., MOREAU R., A Periodically Reversed Fow Driven by a Modulated Traveling Magnetic Feld. Part I: Experiments with Ga-In-Sn, *Metall. Mater. Trans.* B 40 (1) 82–90. 2009.

[5] B. WILLERS, S. ECKERT, U. MICHEL, I. HAASE and G. ZOUHAR, The Columnar to Equiaxed Transition in Pb-Sn Alloys Affected by Electromagnetically Driven Convection, *Materials Science and Engineering A*, 402 (1-2) (2005) 55-65.

[6] R. MOREAU: Magnetohydrodynamics, *Kluwer Academic Publishers, Dordrecht, Netherlands*, (1990), pp. 250-51.

The Effect of Heat Input on Mechanical Properties of Trip Steels in MAG Welding

Gökhan ERİAN[1], Adem KURT[2]
[1]Turkish Accreditation Agency, [2]Gazi Univ.
Turkey

ABSTRACT

The effect of heat input on mechanical properties in MAG welding was investigated in a TRIP Steels. To control the effectiveness of the developed procedure, all the plates were single pass welded and thermal cycle at different points situated at the surface of the welded plates were performed. In the experimental part, thermal cycle profiles were obtained by taking temperature measurements at 1-2-3-5 mm distance from the weld zone using 4-channel K—Type thermocouples at the different welding speeds. Mechanical tests were performed in accordance with ISO / IEC 17025 standard and microstructural investigation were also conducted. The results were discussed in details to evaluate the effect of heat input on thermal cycle profiles of welded TRIP Steel plates as a function of welding speed.

1. INTRODUCTION

The story of TRIP steels before being used in the automotive industry started in the 1930s. Scheil et al. stated that the martensite transformation of austenite cannot be expressed only by the thermal change of atoms, the transformation must have a special mechanism [1]. In the 1950s Patel and Cohen stated that the transformation of austenite from martensite may be supported by shear stresses, but this transformation can be supported by components of the normal tension in the tensile or compressive direction, and vice versa. They examined the effect of applied stress on M_S temperature and they generally, declared that the higher the martensitic transformation takes place over the M_S temperature, the required amount of tension has increased in the correct proportion [2]. Meta-stable austenitic steels alloys with completely austenitic matrix at room temperature showed martensitic transformation due to applied stress. This phenomenon named as Transformation Induced Plasticity (TRIP) and TRIP effect officially became part of literature after Zackay et al. patented this issue on November 22, 1966 [3]. By the 1960s, industry's main goal was to reduce the amount of nickel in meta-stable austenitic steels and reduce the cost, as well as obtain similar and even better mechanical properties. In these nickel-reduced alloys, austenite could be stabilized with manganese. These alloys having Mn content up to 30 wt. % were referred to as high-manganese (HMnSi) TRIP steels [4].

In 1972 Miller applied heat treatment called Austenite Reverted Transformation – ART to an alloy consisting of 5.7 wt. % Mn, 0.11 wt. % C, 0.26 wt. % Si, 0.10 wt. % Cr, 0.025 wt. % Mo, 0.012 wt. % S and these alloys called as Medium Manganese (MMnSi) TRIP steels [5]. MMnSi TRIP alloys having Mn content less than 12 wt. % also have less amount of Al and Si compared to HMnSi TRIP alloys. By ART annealing process conducted between A_1 and A_3 temperature for the alloy, austenite get enriched in C and Mn. Due to these characteristics of ART annealing final microstructure of MMnSi TRIP steels consists of ferrite and austenite phase[4].

More economical ways were sought due to the amount of alloy elements used in Fe-Ni alloys and meta-stable austenitic steels and the high production process costs. By the 1980s, Matsumura announced Low Carbon (LC) TRIP steels with total elongation up to 30% and ultimate tensile strength (UTS) more than 1000MPa. LC TRIP steels having chemical composition of Fe-0.4C-1.5Si-0.8Mn are also not fully austenitic; their microstructure consists of retained austenite, ferrite and bainite [6]. Later considering the weldability issue, carbon content decreased to 0.2 wt.%. Commercial LC TRIP steels used in automotive industry prepared according to VDA 239-100 and EN 10338 standards; such as TRIP690 and TRIP780.

For automotive and light truck weldments, properties of lap joint weldments such as; weld throat geometry, weld toe size are given on AWS-D8.8M [7]. There are several studies reported in the literature for lap joint MAG welding of TRIP steels. During these studies welding parameter such as, welding current, voltage, heat input, welding speed plays key role for obtaining the thermal cycle profile. Studies on DP790 single lap joints with plate thickness of 1.6mm, revealed that fracture occurs at the weld throat or weld heel. It is also reported that weld porosity was frequently observed [8]. Studies conducted for TRIP780GI Steel with different welding speed from 58 cm.min^{-1} to 150cm.min^{-1} revealed that peak temperature obtained at a specific point obtained with thermocouple, increases with increasing heat input [9][10]. HAZ width of GMAW application to TRIP steels with heat input of 0.16 to 0.34 kJ.mm^{-1} was found between 3.8 to 5mm [11]. Lap joints TRIP steel weldments using ER70-03 welding filler showed less UTS compared to base metal. This is attributed to the fact that thermal cycle during GMAW of TRIP steel, decreases the TRIP effect due to decrease in the retained austenite [12]. GMAW applications on A516-Grade 70 carbon steel with ER309LSi welding electrode at pure Argon protective gas environment revealed that as a function of heat input, martensite bands on austenitic weld metal matrix exists [13].

The aim of this study is to determine the effect of heat input on the thermal cycle and mechanical properties of TRIP800 steel lap joint weldments with different welding speeds using ER309LSi electrode.

2. EXPERIMENTAL PROCEDURE

In this study, effect of heat input and the resultant thermal cycle on mechanical properties in MAG welding was investigated in a TRIP800 Steels. TRIP800 steel used as a base material has yield strength (YS) of 496MPa, UTS of 840MPa and total elongation (TE) of %32. Selected material thickness is 1.5mm. The chemical composition of the plates is as given in Table 1. Schematic view of test pieces prepared in the size of 170 x 150 x 1.5 mm is given in Figure 1. K-type thermocouples were placed 1mm, 2mm, 3mm, and 5mm away from the end of TRIP800 steel plate respectively. Plates were clamped from both sides in order to avoid angular distortion as a result of heat input. Heat input values for different welding speeds and welding parameters are given in Table 2.

Table 1. Chemical composition (wt. %) of TRIP800 steel

C	Si	Mn	P	S	Cr
0.21	1.66	1.71	0.0096	0.0042	0.0216
Ni	**Cu**	**Al**	**Mo**	**V**	**Nb**
0.0239	0.0095	0.0464	0.0075	0.0038	0.0009

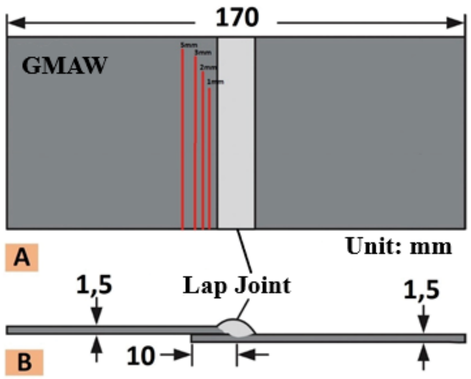

Figure 1. Schematic layout of K-type thermocouples in GMAW application

Table 2. Welding parameters and heat input

Code	72cm.min^{-1}	102cm.min^{-1}	150cm.min^{-1}
U(V)	18	19	20
I(A)	141	166	211
V(cm min^{-1})	72	102	150
WFS (m min^{-1})	3.5	4.5	6.5
h (efficiency)	0.8	0.8	0.8
E	0.212	0.186	0.169
Q(kJ mm^{-1})	0.169	0.148	0.135
Tp	25	22	22
F2	0.9	0.9	0.9
F3	0.67	0.67	0.67
d(mm)	1.5	1.5	1.5
$\Delta t_{8/5}$ thin plate (sec) (Calculated)	12.9	9.9	8.2
$\Delta t_{8/5}$ thin plate (sec) (measured)	12.4	9.7	-
Measured Peak Temp (^{0}C)	920.2	870.2	770.3

WFS: Wire Feed Speed; LWS: Linear Weld Speed; E: Line energy; E = (I *x* U) / Weld speed
Q: Effective Line Energy

$$\Delta t_{8/5} - (4300 \quad 4.3.T_p).10^5.\frac{Q^2}{d^2}.\left(\frac{1}{(500-T_p)^2} \quad \frac{1}{(800-T_p)^2}\right).F_2 \qquad (1)$$

The lap joints were produced by using Metal Active Gas (MAG) welding process using ER309LSi electrode with a protective environment of 82%Ar and %18 CO_2 gas mixture. $\Delta t_{8/5}$ values were calculated using the equation 1 for thin plate weldments. During experimental procedure tests were conducted by laboratory accredited from TS EN ISO/IEC 17025. Vickers Hardness measurements were conducted according to TS EN ISO 6507-1 Metallic materials - Vickers hardness test - Part 1: Test method and tensile tests were conducted according to TS EN ISO 6892-1 Metallic materials - Tensile testing - Part 1: Method of test at room temperature (ISO 6892-1:2016). Chemical composition is determined according to ASTM E 415 Standard Test Method for Analysis of Carbon and Low-Alloy Steel by Spark Atomic Emission Spectrometry. Measurement uncertainty determined for hardness testing was ±4HV and for tensile testing was ±12,81 MPa. For metallographic examination of HAZ region and Base metal first 4% Picral and HCl solution then 10% Metabisulfite solution applied to samples. For weld metal examination, separate set of samples prepared and electro—etched with 40%NaOH solution.

3. RESULTS AND DISCUSSION

Thermal cycle analysis results are given in Figure 2 for welding speed of 72 cm.min^{-1}, 102 cm.min^{-1} and 150 cm.min^{-1} respectively. $\Delta t_{8/5}$ values using thermal cycle profiles and $\Delta t_{8/5}$ values calculated using the equation 1 were given in Table 2. $\Delta t_{8/5}$ value for welding speed of 150cm.min^{-1} could not be calculated. Because for that heat input peak temperature obtained from K-type thermocouple 1mm away from edge of the TRIP800 steel plate did not reach 800^{0}C. Peak temperatures of 920.2^{0}C, 870.2^{0}C and 770.3^{0}C were obtained from K-type thermocouples were placed 1 mm away from edge of steel plates for welding speed of 72 cm.min^{-1}. 102 cm.min^{-1} and 150 cm.min^{-1} respectively. For High-Si TRIP steel containing 0.2 wt. % C, A_{e1} and A_{e3} were calculated as 716 ℃ and 854 ℃ respectively [14]. For welding speed of 72 cm.min^{-1} and 102 cm.min^{-1} complete austenitization occurred at 1mm away from end of the steel plates. However, for welding speed of 150 cm.min^{-1} material was partially austenitized.

Figure 3 shows HV0.5 Vickers micro hardness measurements obtained from samples with welding speed of 72 cm.min^{-1}, 102 cm.min^{-1} and 150 cm.min^{-1} respectively. For each specimen micro hardness measurements taken from weld centerline to 1.5mm were collected from the weld metal. Starting from 1.5mm away from weld centerline to 5mm measurements were obtained in order of fusion line, course grained HAZ, fine grained HAZ, subcritical HAZ and weld metal.

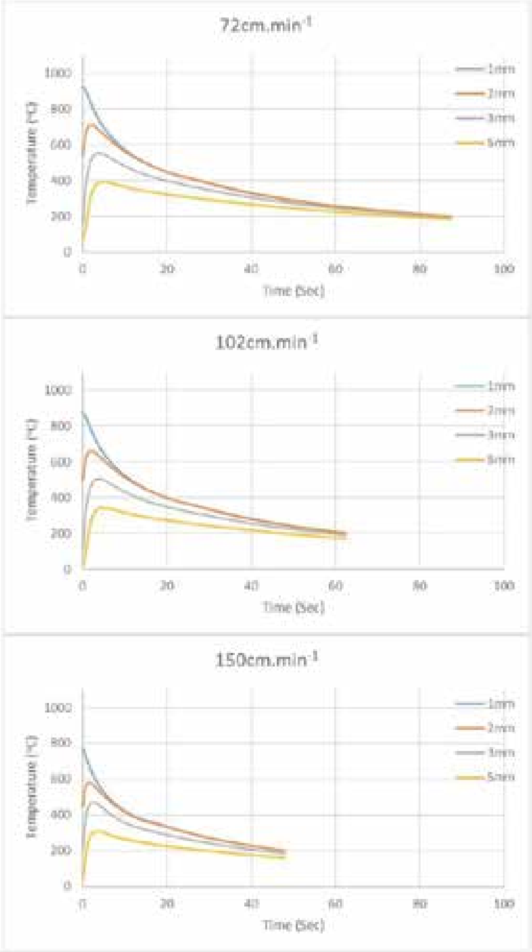

Figure 2. Thermal cycle analysis results for welding speed of 72cm.min^{-1}. 102cm.min^{-1} and 150cm.min^{-1}

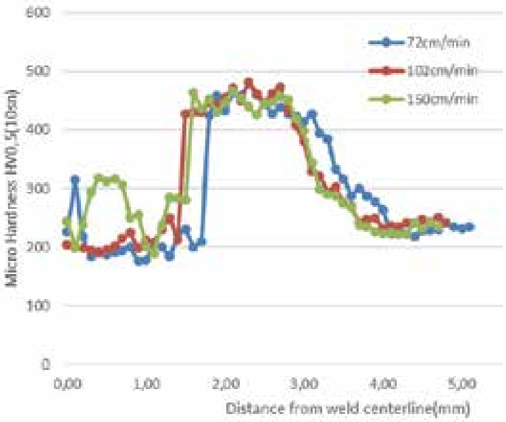

Figure 3. Micro hardness measurements according to different welding speeds in GMAW application

Figure 4. Dark field optical microscope image of the TRIP 800 steel weld metal with welding speed of 150 cm.min^{-1}

It is clearly noticeable that sample with welding speed of 150cm.min^{-1} has higher weld metal hardness compared to others. This is due to martensite band formations on the austenitic weld metal as seen on dark field optical microscope image given at figure 4. Weldments with the speed of 150cm.min^{-1} had austenite, ferrite and martensite on weld metal microstructure. However, weldments with speed of 72 cm.min^{-1}, 102 cm.min^{-1} generally had ferrite and austenite at their weld metal composition. Base metal hardness was determined as 237 HV0.5. Microstructural investigation revealed that HAZ width of the specimens measured as 2.6 mm, 2.3 mm and 2.2 mm for the welding speeds of 72 cm.min^{-1}, 102 cm.min^{-1} and 150 cm.min^{-1} respectively.

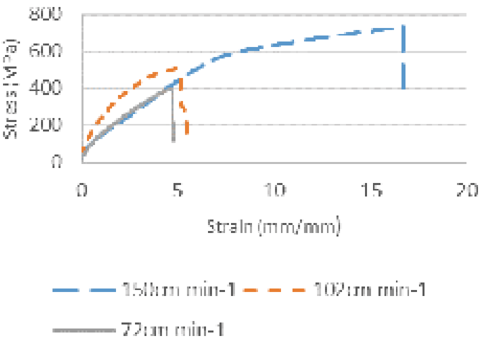

Figure 5. Stress vs. Strain Diagram of Weldments with welding speeds of 72 cm.min^{-1}. 102 cm.min^{-1} and 150 cm.min^{-1}

High-Si TRIP800 steel base metal used in this project had a yield strength of 483MPa, tensile strength of 839MPa and total elongation of 31.5%. Tensile test results of weldments with welding speed of 72cm.min^{-1}, 102 cm.min^{-1} and 150 cm.min^{-1} were given respectively in Figure 5. It is easily noticed that total elongation values and tensile strength of weldments with speed of 72 cm.min^{-1} and 102 cm.min^{-1} decreased dramatically. Fracture occurred at the weld metal for weldments with speed of 72 cm. min^{-1} and 102 cm.min^{-1}. Macro examination revealed that for weldment with the highest welding speed (150cm.min-1) and lowest heat input, weldments fractured from the section of HAZ close to weld metal as seen in Figure 6. Exposure of the macro photo in figure 6 was set high in order to show the difference between weld metal and parent metal.

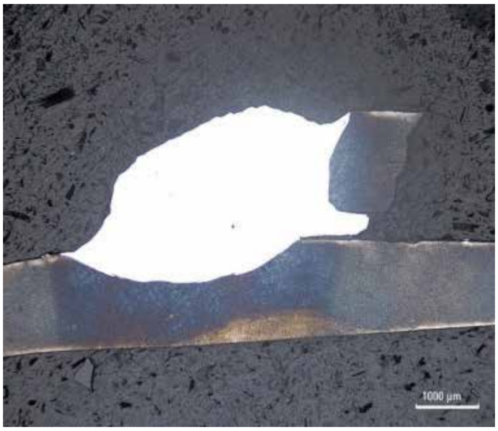

Figure 6. Fractured sample of weldment with speed of 150cm.min^{-1}

4. CONCLUSIONS

This paper presents the effect of successive heat inputs on the mechanical properties of TRIP800 steel. In this projects as welding speed increases heat input due to welding operation decreases. Decreased heat input is beneficial to the mechanical properties. None of the welded TRIP800 steel sample fractured from the base metal. Tensile test samples with the welding speed of 72 cm.min^{-1} and 102 cm.min^{-1} fractured from weld metal. However tensile test samples with the welding speed of 150cm.min^{-1} fractured from the section of the HAZ close to base metal. Considering the mechanical tests and metallography examinations of the samples, it is concluded that TRIP effect had successfully been achieved for the weldments with welding speed of 150 cm.min^{-1}.

Acknowlegements:
The authors wants to express their thanks to Taner Cangül for supplying TRIP800 grade steel samples.

REFERENCES

[1] E. Scheil. Über die Umwandlung des Austenits in Martensit in Eisen- Nickellegierungen unter Belastung. Z. Anorg. Allg. Chem.. 207 (1932) 21-40.
[2] J.R. Patel. M. Cohen. Criterion for the action of applied stress in the martensitic transformation. Acta Metallurgica. Volume 1. Issue 5. (1953) 31-538.
[3] V. Zackay and E. Parker. US patent No. 3488231. class 148-12 (c. 12d 7/13). issued November 22. 1966.

published January 6. 1970. French patent lqo. 1550475. class C22c.
[4] B. Wolfgang, G. Xiaofei, M. Yan, The TRIP Effect and Its Application in Cold Formable Sheet Steels. steel research international. 88. (2017).
[5] R.L. Miller. Ultrafine-grained microstructures and mechanical properties of alloy steels. MT 3. (1972). 905–912.
[6] O. Matsumura, Y. Sakuma, H. Takechi. Enhancement of Elongation by Retained Austenite in Intercritical Annealed 0.4C-1.5Si-O.8Mn Steel. Transactions of the Iron and Steel Institute of Japan. Volume 27. Issue 7. (1987) 570-579.
[7] AWS D8.8M. Specification for Automotive Weld Quality—Arc Welding Welding of Steel; American Welding Society (AWS): Miami. FL. USA. 2014
[8] H. Kang, A. Khosrovaneh, T. Link, J. Bonnen, The Effect of Welding Dimensional Variability on the Fatigue Life of Gas Metal Arc Welded Joints. SAE Int. J. Mater. Manuf. 4(1) (2011) 298-313.
[9] J. Bonnen, R. Mandapati, H. Kang, R. Iyengar, Durability of Advanced High Strength Steel Gas Metal Arc Welds. SAE Int. J. Mater. Manf. 2(1) (2009) 155-171.
[10] R. Iyengar, J. Bonnen, E. Young, D. Maatz, Influence of Weld Process Parameters on the Geometric Variability of the Gas-Metal Arc Welds. SAE Technical Paper (2009)2009-01-1549.
[11] S. Keeler. M. Kimchi. P.J. Mooney: Advanced High Strength Steel Application Guidelines (Version 6. 2017) Retrieved May 26. 2018. from World Auto Steel
[12] Z. Feng et al., Characterization of Thermo Mechanical Behaviors of Advanced High Strength Steels (AHSS): Task 2 Weldability and Performance Evaluations of AHSS Parts for Automotive Structures." 2006 Annual Progress Report. U.S. DOE Automotive Lightweighting Materials Program (2006).
[13] M. Rowe, T. Nelson, J. Lippold, Hydrogen-Induced Cracking along the Fusion Boundary of Dissimilar Metal Welds. Welding Journal - WELD J. Volume:78, Issue:2 (1999) 31-37.
[14] L. Guo, Modelling of Microstructure in TRIP-Assisted steels, M.Sc. Thesis, Pohang University of Science and Technology, 2007, Pohang, Korea, pp. 24-27.

Invar Anomaly of Cu-Doped Fe64Ni36 Alloys

Ebru GEZGİN[1], Melike Nur ENGELOĞLU[1], Aslı ÇAKIR[1], Uğur Can ÖZÖĞÜT[1], Tolga TAVŞANOĞLU[1], Mehmet ACET[2]
[1]Muğla Sıtkı Koçman University, [2]Duisburg-Essen University
[1]Turkey, [2]Germany

Abstract

In this work, we investigated the effect of Cu-doping on the invar property of $Fe_{64}Ni_{36}$ alloy. Scanning electron microscopy, x-ray diffraction and temperature dependent elastic measurements were performed to understand the effect of Cu-doping.

1. Introduction

$Fe_{64}Ni_{36}$ compound is known as invar alloy with the emerging property of low thermal expansion coefficient around room temperature. Invar alloys exhibit great dimensional stability over a temperature range due to the volume magneto-striction [1-2]. Application of these alloys can be extended to semiconductors, tv monitors, motor valves, thermostats, shadow-mask frames, aerospace and cryogenic transport. These applications are generally where the dimensional stability is needed.

2. Materials and Methods

$Fe_{64}Ni_{36}$ and $Fe_{64}Ni_{36-x}Cu_x$ alloys with x=2.8 and 6.1 at% were produced in an arc furnace using high purity elements (99.9%). For homogenization, the samples were annealed under Ar at 1073 K in sealed quartz tubes for 5 days. To verify the sample homogeneity, EDX spectra were collected from three different areas. The compositions were found to be homogeneous to within 0.05% for all samples. Scanning electron microscopy (SEM) images were obtained on polished and subsequently etched specimens and they are given in figure 1. X-ray diffraction (XRD) measurements were carried out in the 2θ range $20° \leq 2\theta \leq 120°$ using a Cu K_α x-ray source and obtained results are given in figure 2. The impulse excitation technique (IET) was used for the elastic modulus measurements. Temperature dependent elastic behavior of the alloys are given in figure 3.

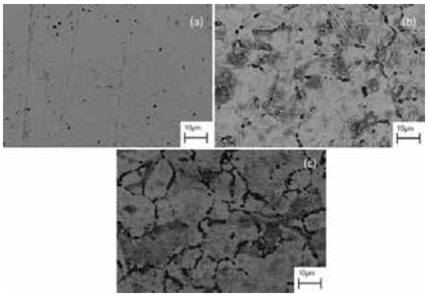

Figure 1. SEM images of pure invar (a) and Cu-doped alloys for x=2.8 (b) and x=6.1 (c).

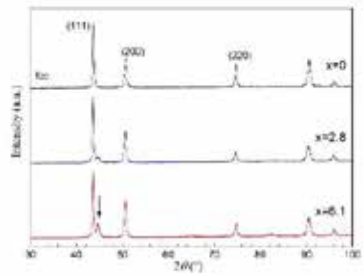

Figure 2. XRD measurements of Cu-doped and pure invar alloys.

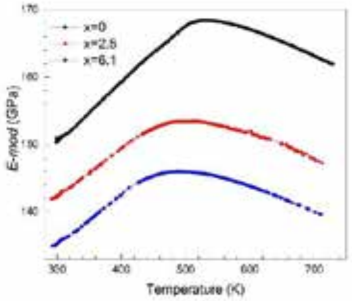

Figure 3. Temperature dependent elastic modulus measurements of Cu-doped and pure invar alloys.

3. Conclusion

The current work deals with the effect of Cu-doping on the invar anomaly of $Fe_{64}Ni_{36}$ alloy. As seen from XRD measurements, the x= 0 data, the non-doped invar alloy exhibits characteristic peaks of the fcc structure. However, Cu-doping leads to the appearance of a bcc structure as seen in the data for x = 2.8 and x = 6.1 at %. From the SEM image of $Fe_{64}Ni_{36}$ (a) we can detect grains of the fcc structure. SEM images of Cu-doped invar alloys in (b) and (c) show the $Fe_{64}Ni_{36}$ structure and precipitates corresponding to bcc phase in accordance with XRD results. The E-mod results show a decrease below T_c (Curie temperature) that is the region of the invar anomalies being observable in both pure and Cu-doped invar alloys. Additionally, the increasing amount of copper, the decreasing Curie temperature but the invar property still observable in Cu-doped alloys.

References

[1] Guillaume, C. E. Compt. Rend. Acad. Sci. 1897, 125, 235-238.
[2] Wassermann, E. F.; Acet, M. Magnetism and Structure in Functional Materials; Springer, Berlin, Hiedelberg, 2005.

Effect of Electro-Discharge Machining (EDM) on the Microstructure of Selective Laser Melting Processed 17-4 PH Stainless Steels

Andac OZSOY[1,2], Mert KELES[2], Ziya ESEN[3], Arcan F. DERICIOGLU[1]
[1]Middle East Technical University, [2]Roketsan Industries Inc., [3]Çankaya University
Turkey

Abstract

In this study, microstructural changes in SLM processed 17-4 Precipitation Hardening (17-4 PH) stainless steel parts have been observed in two different conditions, namely in as-built and solution heat treated. Heat-affected zone microstructures on the surfaces cut by EDM were compared to those of unaffected zones in 17-4 PH parts under the same two conditions.

1. Introduction

In the last decade, Selective Laser Melting (SLM) has gained remarkable importance in metal industry enabling the production of complex-shaped metal parts with mechanical properties similar to those of the conventionally-produced metallic components. The most common method for removal of the parts from the baseplate or building plate used in metal additive manufacturing is Electro-Discharge Machining (EDM), where an arc is generated between a conducting wire and the part in a dielectric medium to remove the part. However, EDM is known to create a heat-affected zone in the material due to the arc generated between the wire and parts.

2. Materials and Methods

17-4 PH stainless steel was utilized as the material for Selective Laser Melting. As-built and solution heat treated (45 min at 1240 °C and 45 min at 1100 °C followed by air cooling) specimens were examined. EDM was applied on one surface of each specimen. Specimens were then polished, etched and observed under optical microscope. Figure 1 shows microstructural features at EDM-processed surfaces.

Figure 1. Microstructure of a) as-built and b) solution heat treated specimen after EDM cutting.

3. Conclusion

Microstructural observations of SLM processed 17-4 PH stainless steel specimens have been made after EDM. It has seen that the as-built specimen has not been affected by the EDM. However, microstructural changes have occurred after EDM in the case of solution heat treated material. Therefore, it has been concluded that any heat treatment operation must be applied after EDM cutting operations to prevent phase changes and possible subsequent mechanical failure.

Effect of Submerged Arc Welding on High Temperature Tensile Properties of P91 Type Steel

Junaid ASLAM, Caner BATIGÜN, C. Hakan GÜR
Middle East Technical University
Turkey

Abstract

There have been research efforts to increase the efficiency of power plants by improving creep-resistant steels having stable mechanical properties at elevated temperatures. The components operating at temperatures between 575°C and 650°C are usually made of P91 (9Cr-1Mo) steel. The application of welding techniques creates a risk of reduction in high-temperature strength and creep resistance, particularly in the heat-affected zone of the weldments. In this study, the effect of the shielded metal arc welding (SMAW) on the high temperature tensile properties of P91 type steel plates was investigated.

Keywords: P91 steel, shielded metal arc welding, high temperature tensile properties

1. Introduction

P91 steels with optimum addition of some precipitate forming elements such as B, Mn, Ni, N, Nb, V, Cr, and Al have the excellent potential to provide higher strength at elevated temperatures [1]. To obtain the better mechanical properties, P91 steels undergo the normalizing and tempering [2]. Welding is a major joining process for the fabrication of steam generator components made of P91 type steels. Formation of heterogeneous microstructure in the heat affected zone during weld thermal cycle leads to a strength gradient across the weld joints. It is known that the fine grain heat affected zone attains the most weakened region in the weldments. Since evaluation of elevated temperature tensile properties is a preliminary step towards characterization of materials performance for high temperature applications [3], the effect of SMAW on the high temperature tensile properties of P91 type steel plates was investigated in this study.

2. Materials and Methods

The 30mm x 70mm plates, extracted from the P91 pipes having 186 mm outside diameter, were joined by SMAW using the E9015-B91H4R electrode in accordance with the AWS A5.5/A5.5M; and then, post-weld heat treatment (780°C/2h) was applied. The specimens were prepared by cutting the weld in the transverse direction. Following radiographic inspection, metallographic investigation and hardness measurement, tensile tests were performed at 20°C, 660°C, and 700°C.

3. Results and Conclusions

The initial material has a tempered-martensite microstructure with an average hardness of 336 HV0.1. The results of the tensile tests at 20°C, 660°C, and 700°C give UTS values of 728 MPa, 208 MPa, and 160 MPa; and % elongation in length values of 21, 25, and 28. The failure mode of all specimens is purely ductile, as characterized by the occurrence of dimples with voids. Fracture surface of the 700°C-tensile test specimen shows the existence of some secondary cracks.

Acknowledgment: The authors acknowledge the Magmaweld for the support of welding consumables.

References

[1] M. Peter, Evolution of microstructure and mechanical properties of the heat-affected zone in B-containing 9% chromium steels, Ph.D. Thesis, July 2007, Graz University of Technology, Austria Graz
[2] C. Pandey, A. Giri, M.M. Mahapatra; Effect of normalizing temperature on microstructural stability and mechanical properties of creep strength enhanced ferritic P91 steel, Materials Science and Engineering A, 657 (2016) 173-184
[3] B.K. Choudhary, J. Christopher, Influence of temperature and strain rate on tensile deformation and fracture behaviour of boron added P91 steel, International Journal of Pressure Vessels and Piping, 171 (2019) 153-161

Production and Characterization of Mg and WE43 Infiltrated Ti6Al7Nb Matrix Composites

Ezgi BÜTEV ÖCAL[1], Ziya ESEN[2], Arcan F. DERİCİOĞLU[1]
[1]Middle East Technical University, [2]Çankaya University
Turkey

Abstract

In the scope of this study, newly designed biomedical Ti6Al7Nb-Mg and Ti6Al7Nb-WE43 composites have been successfully produced by a pressureless infiltration method in which liquid Mg or WE43 magnesium alloy were filled in the pores of the porous Ti6Al7Nb alloy. These composites display both bioinert and biodegradable characteristics where porous Ti6Al7Nb acts as the bioinert scaffold while infiltrated magnesium or its alloy constitutes the biodegradable part responsible for promoting bone growth. A Na-rich coating was deposited on the pore surfaces of the Ti6Al7Nb by hydrothermal method prior to the infiltration step. Na-rich coating layer not only enhanced the bioactivity of the titanium alloy surfaces but also decreased the galvanic corrosion effect between the titanium alloy and the magnesium during in-vitro tests.

1. Introduction

This study covers the production of Ti6Al7Nb-Mg and Ti6Al7Nb-WE43 alloy composites by pressureless infiltration method and determination of their corrosion behaviors using electrochemical techniques. Additionally, bioactivities of composites with and without Na-rich coating have been compared by immersing them in simulated body fluid (SBF).

2. Materials and Methods

Ti6Al7Nb alloy powders of 20 µm particle size were utilized as starting materials for the production of porous samples. Mg and WE43 alloy chips (Changchun Institute of Applied Chemistry, China) were used in the pressureless infiltration process at 800 °C. Prior to composite production, porous Ti6Al7Nb alloy was manufactured using a loose powder sintering method, which has been conducted at 1000 °C for 90 min. In addition, Na-rich coating was deposited on the pore surfaces of the Ti6Al7Nb by hydrothermal method before the infiltration step. Samples were immersed in 5 M NaOH solution at 60 °C for 24h. Corrosion behavior of Ti6Al7Nb-Mg and Ti6Al7Nb-WE43 composites were determined by potentiodynamic polarization tests. Furthermore, the apatite formation abilities of composites have been predicted by in vitro tests in SBF.

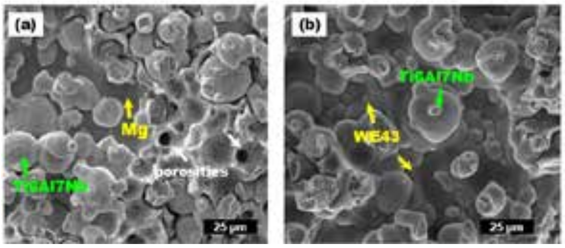

Figure 1. (a) Ti6Al7Nb-Na-Mg and (b) Ti6Al7Nb-Na-AZ91 composites.

3. Conclusions

Both Ti6Al7Nb-Mg and Ti6Al7Nb- WE43 composites have been successfully manufactured through the use of liquid infiltration method. Ti6Al7Nb-WE43 composite possessed higher degradation rate in SBF compared to Ti6Al7Nb-Mg composites. Formation of Na-rich coating resulted in an increase in the corrosion resistance of composites by forming an insulating layer between the porous titanium alloy and the infiltrated magnesium alloy. Therefore, the galvanic corrosion effect between Ti6Al7Nb and Mg or We43 alloy was diminished.

Acknowledgment

This study is financially supported by TUBİTAK through the project 118M791.

Hydration Efficiency of Metallic-Ion Incorporated Calcium Phosphate Cement Bone Analogs

Bersu BASTUG AZER, Caner DURUCAN

Middle East Technical University

Turkey

Abstract

Calcium phosphate cements (CPCs) are promising hard bone tissue healing substances. For improving their therapeutic properties different metallic ions are used. In this study, Se has been incorporated to α-tricalcium phosphate (α-TCP) and it was mixed with water in order to obtain Se-incorporated calcium-deficient hydroxyapatite (CDHAp) cement. The effect of Se-doping in different amount and the hydration kinetics of cement conversion reaction were investigated in details by different techniques. 2 wt.% Se doping is critical limit for obtaining only α-TCP and for improving the hydration kinetics of cement conversion reaction from α-TCP to CDHAp.

1. Introduction

Bone cements are self-setting, injectable or moldable systems allowing filling irregular shape bone defects. CPCs are formed by mixing a liquid phase with a combination of one or more CaP(s). It first forms a paste, and then hardens within the body which makes it a good candidate for clinical applications. Between the two end products which are brushite and apatite cements, HAp cements are desired because of their resemblance to mineral component of bone. α-TCP cements are the most promising HAp cements. Although CPCs have many advantages, they have some limitations, which are their poor mechanical properties because of their ceramic origin, their low reaction kinetics and lack of their therapeutic property. In order to enhance their therapeutic property some metallic ions (Ag, Sr, Si, Se, etc.) are added to CPCs. In this study, Se^{4+} ion was incorporated to α-TCP particles and the effect of addition of this metallic ion on the cement-type conversion was investigated as the first time.

2. Materials and Methods

Pure α-TCP was synthesized by the solid-state reaction of $CaCO_3$ and custom synthesized $CaHPO_4$ with the following reaction. For Se-incorporation different amounts of Na_2SeO_3, was used to obtain $CaHPO_4$:Se. Equation 1 was also used with $CaHPO_4$:Se to synthesize α-TCP:Se. The cement-type setting was performed in Isothermal Calorimetry by exposing pure α-TCP and α-TCP:Se powders with DI water. The hydration was done at 37°C for 48 h with a solid to liquid weight ratio of 1:2.

$$CaCO_3(s) + 2CaHPO_4(s) \rightarrow Ca_3(PO_4)_2(s) + CO_2(g) + H_2O(g) \quad (1)$$

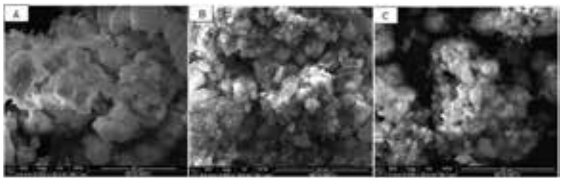

Figure 1. The SEM micrographs of CDHAp products obtained by hydration of (A) pure α-TCP, (B) α-TCP:Se:low (C) α-TCP:Se:high

3. Conclusion

It was seen that Se-incorporation occurs at a limited extent lower than the theoretical values. Higher amount of Se addition results in the formation of HAp together with α-TCP. Cement-type conversion from α-TCP to CDHAp completely occurred with Se incorporation, however, overall setting occurs by a different mechanistic way, with a single heat event. Therefore, it can be said that Se incorporation may give a synergetic effect. The optimum amount of Se favoring hydration kinetics in obtaining phase pure reactants and products seem to less than 2 wt. %.

Production and Characterization of Si3N4 Reinforced Ti6Al4V Composites

Erdem SAYIN, Mevlüt GÜRBÜZ
Ondokuz Mayıs University
Turkey

Abstract

Ti6Al4V (Ti64) alloys are widely used in industries such as the aerospace, defense, biomedical, automotive and aerospace industries because of their low density, high strength, fracture toughness, good corrosion resistance and biocompatibility. However, higher properties for alloys are needed depending on the developing industrial areas. In this area, production in composite form is very important. In recent years, nitride-based particulate reinforced composites have been started to be studied, but grain growth is not prevented by conventional sintering. In this study, the composite material was produced by powder metallurgy method using Ti64 powder (<-43μm) and Si_3N_4 powder (<1μm) 1.3.5.7% by weight of Si_3N_4 was reinforced in the Ti64 matrix. According to the results, the density decreased as the amount of Si_3N_4 increased. The best density value was found in 96% for 1% Si_3N_4 reinforced composite material. An increase of hardness was performed up to 5% reinforced sample which decreased above this content. While the hardness value of pure Ti64 is 408 HV, the high hardness value was measured in 634 HV with 5% Si_3N_4 doped sample. It was observed from the crystal structure (XRD) and microstructure analysis (SEM) that the Si_3N_4 supplement was homogeneously distributed in the Ti64 matrix.

1. Introduction

It is of great importance to use materials developed and developed in different ways depending on the developing technology in today's world. One of these materials is Ti6Al4V alloy, which is of great importance in some sectors. The importance of Ti6Al4V comes from having good mechanical properties such as low density, superior corrosion resistance and high strength. Therefore, the Ti6Al4V alloy alone accounts for 60% of all titanium and titanium alloys produced in the world. The aviation industry alone uses 80% of the ti6al4v alloy produced. After the aviation industry, the automotive and biomedical industries mostly use the Ti6Al4V alloy. Due to the fact that it is so preferred, many studies are carried out to improve the mechanical properties of the Ti6Al4V alloy. [1-3]

When manufacturing composite materials, many parameters such as the type of reinforcement and matrix material, the amount of reinforcement, and the grain size of the materials used cause changes in mechanical and microstructure properties. When the production studies of Si3N4 reinforced composite materials in the literature are examined, this situation clearly emerges. Monticelli et al, 2009, examined the corrosion behavior of the Ti6Al4V alloy and Si_3N_4 / TiN (SN / TiN) composite material. Tests have shown that most of the corrosion damage in the two materials is caused by mechanical wear. In addition, SN / TiN composite material showed better wear behavior than Ti6Al4V material. Mechanical wear and corrosion damage to the materials has reached the range of 70-78% for the SN / TiN composite and 95-96% for the Ti6Al4V alloy. This shows that the composite material has a positive effect on wear and corrosion behavior.[4] Kgoete et al., In their 2018 study, produced a composite material with spark plasma sintering method by adding a mixture of three different ratios of Si_3N_4 and TiN reinforcement material to the Ti6Al4V matrix material. Spark plasma sintering method was applied under 50 Mpa for 6 minutes at 1000 ^{o}C. Mechanical and microstructural properties of the prepared samples were examined. It was observed that the hardness value reached 585.73 HV, intermediate phases such as $TiSi_2$ did not occur in the microstructure and the corrosion resistance increased with Si_3N_4 reinforcement.[5] Kgoete et al, 2018, examined the microstructure, corrosion and thermal stability of the Si_3N_4 supplement on Ti6Al4V. Kompozit numuneler 1000 ^{o}C spark plazma sinterleme yöntemi ile 6 dakika boyunca 50 MPa basınç altında üretildi. Composite samples with three different Si_3N_4 ratios were produced. These contain 5%, 10%, 15% Si_3N_4. Considering the results obtained, Si_3N_4 reinforcement has a critical effect on the hardness, microstructure, corrosion and thermal stability of the composite sample. [3]

In this study, Si_3N_4 reinforced Ti6Al4V matrix composite material was produced by using powder metallurgy method. Reinforcement rates were used in 4 different ratios such as 1% Si3N4 by weight, 3% Si_3N_4 by 5% Si_3N_4, and 7% by Si_3N_4. Density, hardness, compression, abrasion resistance and microstructure tests were performed on composites with Ti6Al4V matrix. The mechanical and microstructure properties of the varying Si_3N_4 reinforcement ratios on the Ti6Al4V matrix will be examined.

2. Experimental Procedure

2.1. Materyal

In this study, Ti6Al4V (Nanography, ≤43 μm) was used as matrix material and Si_3N_4 (UBE Industries Japan, ≤0.8 μm) was used as reinforcement material. The aim of this study is to investigate the production of Ti6Al4V matrix composite material and the effect of Si3N4 reinforcement on Ti6Al4V matrix. Table 1 shows the Si_3N_4 ratios reinforced to the

Ti6Al4V matrix composite material and how each sample is coded.

Table 1. Si_3N_4 reinforcement rates and sample code

Reinforcement rates	Sample code
Ti6Al4V	Ti64
Ti6Al4V+1 Si_3N_4	Ti64-1SN
Ti6Al4V+3 Si_3N_4	Ti64-3SN
Ti6Al4V+5 Si_3N_4	Ti64-5SN
Ti6Al4V+7 Si_3N_4	Ti64-7SN

2.2 Method

Si3N4 supplement powders in the ratio of 1.3.5.7% were mixed together with Ti6Al4V in ethyl alcohol medium. The mixed composite powders were mixed in the ultrasonic homogenizer for 15 minutes and in the ball mill rotating at 800 rpm for 20 minutes to dissolve the pellets and mix homogeneously. Filtering and drying were performed to remove ethyl alcohol from the composite powder mixture. To shape the composite powder, 1200 Mpa pressure was applied in the steel mold. After forming, the samples were sintered under argon gas in the high temperature furnace. Since Ti6Al4V alloy is a material that oxidizes very fast, the tube was vacuumed before argon gas flow was provided. Figure 1 shows the powder metallurgy production flow chart.

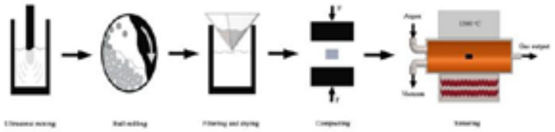

Figure 1. Flow chart showing Si_3N_4 reinforced composite material production

Results and Discussion

Figure 2 a-b gives the density and hardness plot of the composites. As given density is reduced with ceramic content. The best hardness value is observed for wt. 5% ceramic particle.

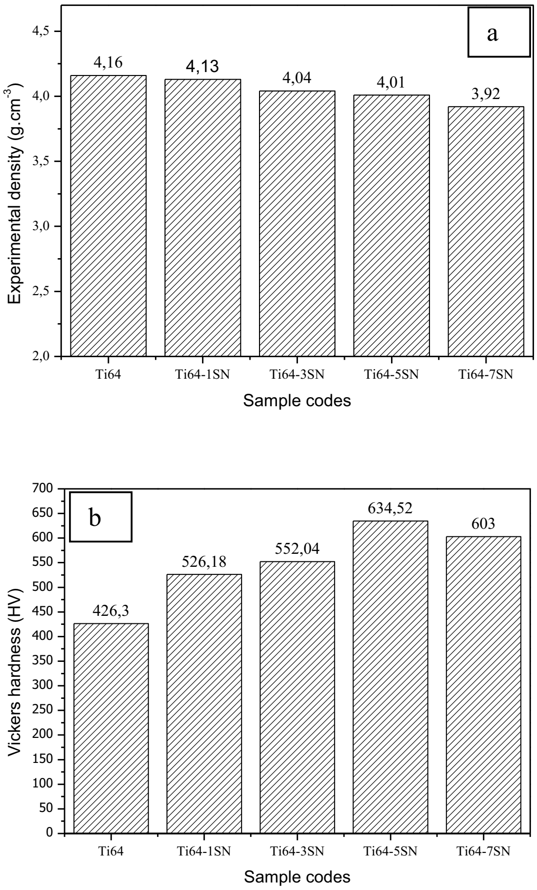

Figure 2. Density and hardness measurement of composites

Figure 3a-b presents the compressive and wear behavior of composites. The maximum compressive behavior is observed for wt.1% ceramic particles. The wear behavior is much better as hardness results for for wt.1% silicon nitride.

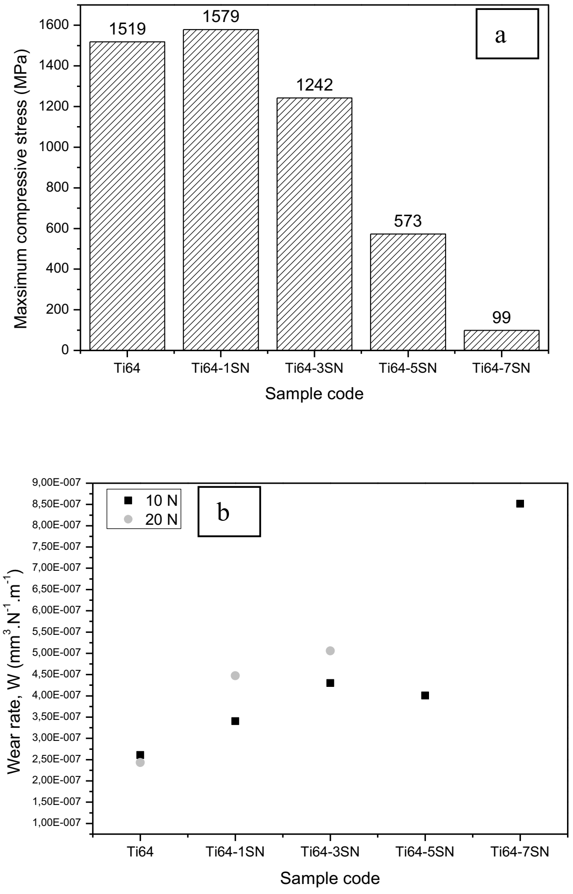

Figure 3. Compressive and wear rate behavior composites

4. Conclusion

In this study, the composite material was produced by powder metallurgy method using Ti64 powder (<-43µm) and Si_3N_4 powder (<1µm) 1.3.5.7% by weight of Si_3N_4 was reinforced in the Ti64 matrix. According to the results, the density decreased as the amount of Si_3N_4 increased. The best density value was found in 96% for 1% Si_3N_4 reinforced composite material. An increase of hardness was performed up to 5% reinforced sample which decreased above this content. While the hardness value of pure Ti64 is 408 HV, the high hardness value was measured in 634 HV with 5% Si_3N_4 doped sample. It was observed from the crystal structure (XRD) and microstructure analysis (SEM) that the Si_3N_4 supplement was homogeneously distributed in the Ti64 matrix.

References

[1] C.M. Şenel, M. Gürbüz, E. Koç, Grafen Takvİyelİ Alümİnyum Matrİslİ Yenİ Nesİl Kompozİtler, Mühendis ve Makina Dergisi, 56 (2015) 669.

[2] R. Boyer, G. Welsch, E.W. Collins, Materials Properties Handbook: Titanium Alloys, Materials Park, ASM International, USA, 2007.

[3] F.M. Kgoete, A.P.I. Popoola, O.S.I. Fayomi, I.D. Adebiyi, Influence of Si3N4 on Ti-6Al-4V via spark plasma sintering: Microstructure, corrosion and thermal stability, Journal of Alloys and Compounds, 763 (2018) 322-328.

[4] C. Monticelli, F. Zucchi, A. Tampieri, Triboelectrochemical behaviour of a Si3N4–TiN ceramic composite and a titanium alloy commonly used in biomedical applications, Wear, 266 (2009) 327-336.

[5] F.M. Kgoete, A.P.I. Popoola, O.S.I. Fayomi, I.D. Adebiyi, Spark plasma sintered Ti-6Al-4V-Si3N4-TiN ternary composites: Effect of combined microsized Si3N4 and TiN addition on microstructure and mechanical properties for aerospace application, Journal of Alloys and Compounds, 769 (2018) 817-823.

Setting of $CaSO_4$ Based Bone Cements in the Presence of Eggshell Membrane Protein

Şule KARAGÜLLEOĞLU, M. Utku YILDIRIM, Bora MAVİŞ
Hacettepe University
Turkey

Abstract

Use of $CaSO_4$ (CS) based cements in bone and dental defect repairs is growing. Although their compressive strength is about one fourth of that of calcium phosphate-based cements, the setting reactions and the resorption rates can be controlled with better precision. Also, eggshell membrane protein (ESMP) is a natural extract that is based on a widely available waste material world-wide and has been proven to have an appreciable level of bioactivity [1]. It can be predicted that both the bioactivity and mechanical properties of CS cements can be increased by use of ESMP. In this study, incorporation of ESMP in CS based cements will be presented.

1. Introduction

CS has been investigated in many clinical applications for use in repairing bone defects. Two CS phases, namely calcium sulphate dihydrate (CSD) and hemihydrate (CSH) have unique advantages. CSD alone has limited mechanical properties, moldability and resorption, but can reduce the setting times significantly. CSH, on the other hand, is complementary for the drawbacks observed in CSD. In combination, these phases serve as optimum biomedical platforms for certain applications [2]. While water is an effective and simple setting agent for both CS phases, solubility of ESMP in water is limited. Nevertheless, solubility of ESMP can be increased in the presence of some ions or organic molecules. Here, we present the effects of use of; (i) such agents in increasing the solubility of ESMP in water, and ESMP setting solutions on the (ii) phase transitions observed during setting reactions and (iii) mechanical properties of the cements.

2. Materials and Methods

CS's were prepared by mixing K_2SO_4 and $Ca(NO_3)_2{\cdot}4H_2O$ in aqueous medium at temperatures between 80-90ºC. ESMP was extracted from membranes by treating them in acidic solutions. The simplest method of mixing ESMP with the cement would be by dissolving ESMP in the setting solution. Solubility of ESMP in water was increased in the presence of some of $CaCl_2$ and/or urea. Mechanical test samples were prepared according to ASTM D695-15 and compressive strength of the cements were determined. The phase changes in the setting reaction was followed by X-ray powder diffraction (XRD) analyses.

3. Conclusion

With increased solubility of ESMP in setting solutions, it was observed that the mechanical strength can be increased. This increase was accompanied with a phase transformation from CSH to CSD. ESMP was found to be a promising ingredient that can be used in the setting solutions of CS bone cements for increasing mechanical strength and potentially bioactivity.

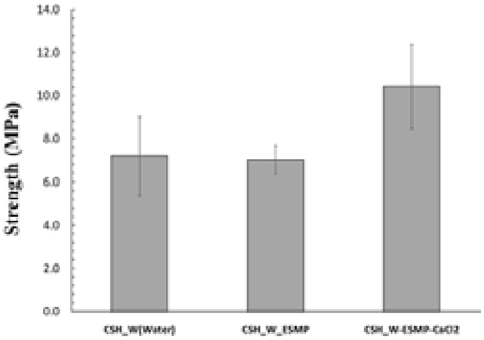

Figure 1. Compressive strengths of CS's after setting with different setting solutions

Acknowledgment

The authors acknowledge use of the services and facilities of UNAM-National Nanotechnology Research Center at Bilkent University and are indebted to Assoc. Prof. Dr. Benat Koçkar and Halil Onat Tuğrul for providing their generous assistance in the conduction of mechanical tests.

References

1. M.M. Pillai, T. Akshaya, V. Elakkiya, J. Gopinathan, K.S. Sahanand, B.D. Rai, A. Bhattacharyya, R. Selvakumar, RSC Advances, 5 (2015) 76019-76025.
2. Z. Chen, H. Liu, X. Liu, X. Lian, Z. Guo, H.-J. Jiang, F.-Z. Cui, Materials Science and Engineering: C, 33 (2013) 1048-1053.

Investigation of Natural Hydroxyapatite Originated from Salmon Fish Bone Wastes

Merve BAS[1], Sibel DAGLILAR[1], Nilgun KUSKONMAZ[1], Cevriye KALKANDELEN[2], Oguzhan GUNDUZ[3]

[1]Yıldız Technical University, [2]Istanbul University- Cerrahpasa, [3]Marmara university

Turkey

Abstract

Hydroxyapatite (HA), which is chemically similar to the bone and hard tissue mineral component of mammals, is a bioceramic material that is frequently preferred for the change and reconstruction of damaged bone tissue in the body due to its high bioactivity and biocompatibility properties. It can be obtained synthetically in laboratory environment or from natural sources. In this study, waste Salmon fish bones, which are natural resources, were preferred for the production of bioceramic materials. Salmon bones were subjected to calcination at 800 °C for 3 hours after they were cleaned from soft tissue residues and dried. The material is powdered and sintered at different temperatures. The properties of the material obtained and samples sintered at different temperatures were analyzed by Fourier transform infrared spectroscopy (FTIR), X-ray diffraction (XRD) and *in vitro* MTT cytotoxicity tests. From the results of the analysis, it was concluded that HA was successfully produced from salmon fish bones, which is a natural source. In this study, an environmentally friendly, low production cost and uncomplicated method is provided to obtain bioceramic material from waste salmon fish bones.

1. Introduction

Bioceramic materials are needed in many applications such as regeneration and restructuring of damaged tissues in the body and coating of metallic biomaterials. The material placed in the damaged area must provide integrity structurally and morphologically with the natural tissue [1]. Hydroxyapatite (HA), which is found in the inorganic structure of bone and tooth enamel, is a calcium phosphate (CaP) component, it is a highly preferred bioceramic material in biomedical applications thanks to its high bioactivity and biocompatibility properties. Hexagonal crystal structure hydroxyapatite $Ca_{10}(PO_4)_6(OH)_2$ has chemical formula and stoichiometric Ca / P molar ratio is 1.67 [2]. CaP ceramics are prepared by many methods using synthetic raw materials. However, producing Cap ceramics with these methods are time-consuming, complex and costly techniques.

Apart from many synthetic chemical ways, it is also possible to obtain HA from natural sources. It is quite common to use bovine and pig bones to obtain hydroxyapatite [3]. In addition, many natural resources such as fish bones, eggshells and seashells are natural materials that can be used in the same scope and there are researches on this subject [4] [5].

In this study, waste salmon bones which are natural resources for HA production were evaluated. HA was obtained from fish bones by calcination method and analyzed by sintering at different temperatures.

2. Experimental Procedure

Waste Salmon fish bones were collected from various places and boiled in 100 °C water for 1 hour to separate them from meat and skin parts. This process has been repeated several times. The bones were thoroughly washed under running pure water and dried to prevent degradation during holding. Bones were calcined for 3 hours at 800 °C in a custom-made oven. The grinding process for pulverizing the material obtained was carried out in a planetary mill using alumina balls for 2 hours at 150 rpm, and then the powders were sieved using a 63 µm sieve. Powders were sintered in Nabertherm LHT 02/17 oven at 1000, 1100, 1200 and 1300 °C for 4 hours to examine the effect of sintering temperature on the material. XRD, FTIR and MTT cytotoxicity analyzes of HA and sintered samples obtained from salmon bones (sHA) were performed. Figure 1 shows schematically obtaining HA from fish bones.

X-ray diffraction (XRD) patterns of powder samples were analyzed by CuKα radiation. Data were acquired in the range of 10-90° (2θ) using a 0.02° step size. For the quantitative analysis of crystal phases, Rietveld Analysis method was used in the High Score Plus program. Fourier transform infrared spectrometer (FTIR, JASCO FT / IR-4700) analyzes were performed in the $450 cm^{-1} – 4000 cm^{-1}$ wavelength range in order to examine the chemical structure of the samples. The FTIR spectrum of Commercial HA (CHA, Sigma Aldrich) was used to compare the results. MTT cytotoxicity test was performed with SBF to determine whether toxic substances are released from the materials.

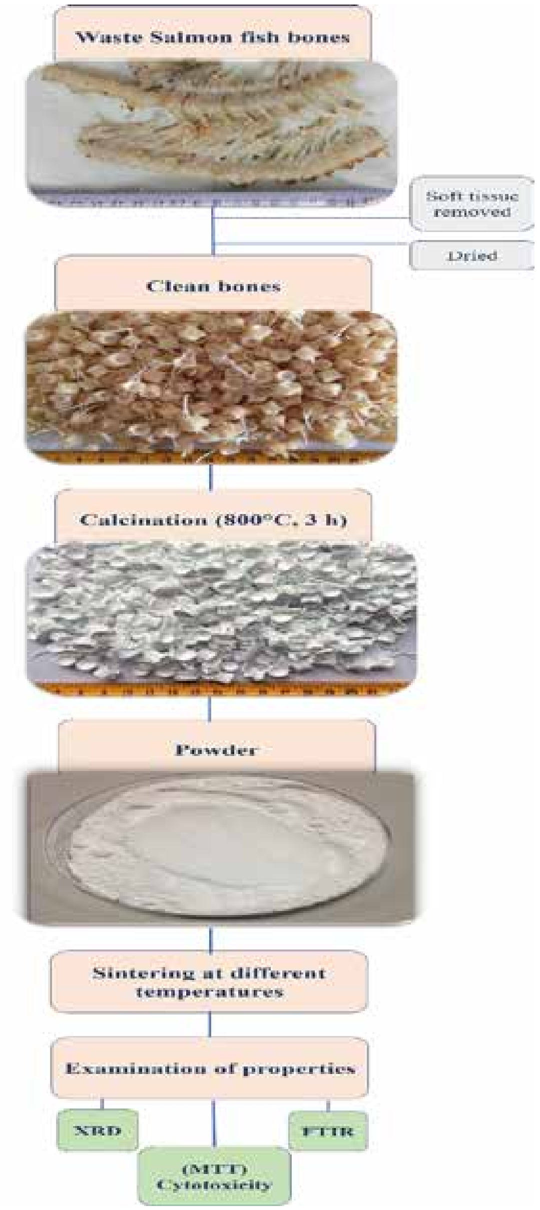

Figure 1. Hydroxyapatite from natural source salmon fish bones

3. Results and Discussion

Figure 2 shows FTIR spectra of raw Salmon bone (fish bone) and sintered samples. The fish bones were seen to have a C-H stretching absorption peak around 2924 cm^{-1} - 2875 cm^{-1}. It is observed that the PO_4^{-3} peaks determining the HA structure are weak due to the presence of organic structures in raw salmon bone. On the other hand, amide peaks expressing the organic structure are clearly seen. Characteristic bands for amide groups appeared at 1627 cm^{-1}, 1549 cm^{-1} and 1237 cm^{-1} [6]. These bands have been associated with characteristic functional organic groups such as collagen, protein and fat found in raw bones. After calcination at 800 °C, all these peaks have almost disappeared [7]. It was observed that organic materials were removed from the structure by calcination process. In the spectra, bands corresponding to hydroxyl (O-H) vibration groups were determined at 629, 631 and 3570 cm^{-1}. The O-H band seen at 3570 cm^{-1} is thought to be due to the moisture absorption of the CHA in the powder sample. As the sintering temperature increased, the presence of O-H bands decreased. sHA's bands corresponding to OH^- and PO_4^{-3} at peaks of about 550, 570, 1010 and 1026 cm^{-1} are shown in the FTIR spectrum. Additionally, bands of 560, 597, 629, 960, 1011 and 1084 cm^{-1} were seen that fit the reference HA spectrum. It was observed that the FTIR results of the samples obtained were consistent with the FTIR results of the CHA powders.

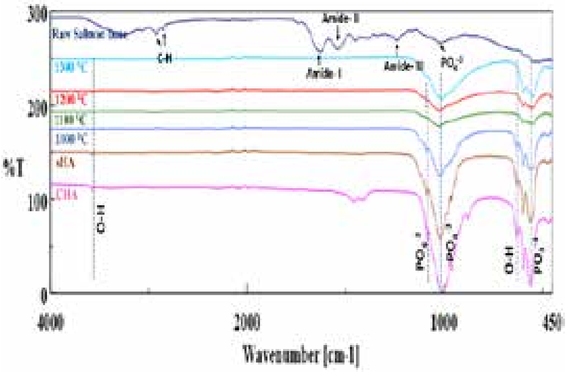

Figure 2. FTIR spectra of; raw salmon bone, sHA, CHA and samples sintered at different temperatures

In Figure 3, XRD analysis of pure sHA and sintered sHA samples at different temperatures samples are shown. Typical HA and Tricalcium phosphate (TCP) crystal structures were seen in the XRD results. In pure sHA and sintered samples, the TCP phase remained stable and the amount of the phase increased with increasing temperature. Rietveld Analysis showed that this phase corresponds to the code number 98-008-2984 JCPDS. The same analysis program showed two HA phases with JCPDS card numbers 98-005-2691 and 98-007-7966. As the result of the analysis, as the temperature increases, HA continues to exist in different phases. It has been observed that crystallinity increases when pure sHA is sintered. Figure 4 shows the XRD analysis of CHA [8]. The XRD analysis of sHA was found to be consistent with the XRD JCPDS index of CHA.

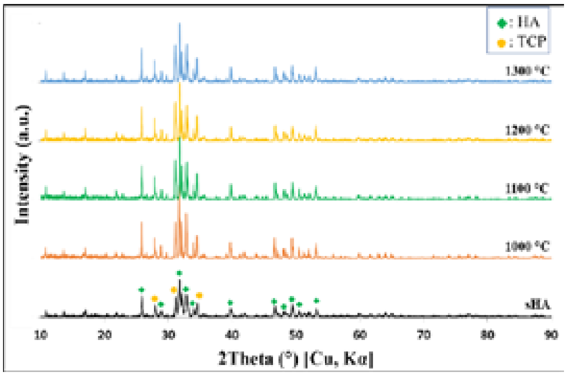

Figure 3. XRD patterns of sHA samples

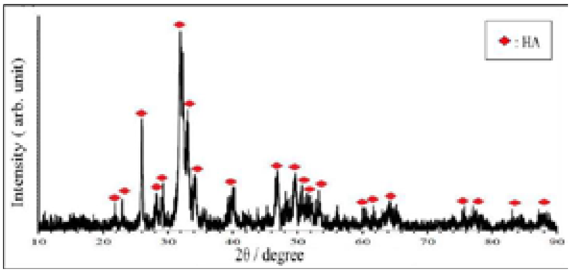

Fig 4. XRD pattern of CHA [8]

Figure 5 shows the cytotoxicity (MTT) results of pure sHA and sintered sHAs after 1 day, 3 days and 7 days, and it was determined that the samples were not cytotoxic when compared with the control group. While no change in cell proliferation was observed in the first day samples, in the third day study sHA-1000°C increased cell proliferation but was ineffective on the other samples. In the seventh day study, sHA-1300°C gave the best result. Statistically significant results were indicated by (*) and the p-value was calculated as p<0,05. *In vitro* MTT cytotoxicity test, sHA and sintered samples are thought to have appropriate cytocompatibility and may contribute to developments in biomedical applications.

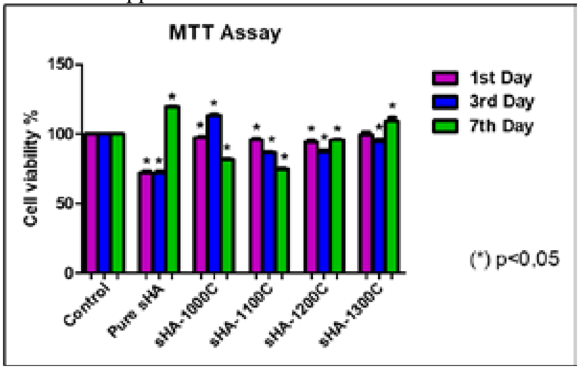

Figure 5. The cytotoxic effects of sHA samples on viability of Saos-2 cells in different days obtained by MTT assay

4. Conclusion

Salmon bones seen as waste were evaluated to obtain bioceramic material and the effect of different sintering temperatures was investigated. The XRD analysis of the samples showed that CHA was consistent with the XRD JCPDS index. FTIR spectra showed that organic compounds and carbonate were no longer present in the calcined structure at 800 °C. Similar bands were seen when compared with CHA. In the MTT results made by comparing it with the control group, it was determined that the samples have appropriate cytocompatibility. From the analysis results, it was concluded that HA, a material with high added value, was successfully produced from salmon fish bones, a natural resource.

Acknowledgment

References

[1] B. Stevens, Y. Yang, A. Mohandas, B. Stucker, and K. T. Nguyen, "A review of materials, fabrication methods, and strategies used to enhance bone regeneration in engineered bone tissues," *J. Biomed. Mater. Res. - Part B Appl. Biomater.*, vol. 85, no. 2, pp. 573–582, 2008, doi: 10.1002/jbm.b.30962.

[2] S. M. Best, A. E. Porter, E. S. Thian, and J. Huang, "Bioceramics: Past, present and for the future," *J. Eur. Ceram. Soc.*, vol. 28, no. 7, pp. 1319–1327, 2008, doi: 10.1016/j.jeurceramsoc.2007.12.001.

[3] J. Lamsihar Manalu, B. Soegijono, and D. J. Indrani, "Characterization of Hydroxyapatite Derived from Bovine Bone," *Asian J. Appl. Sci.*, vol. 03, no. August, pp. 2321–0893, 2015.

[4] A. M. Sofronia, R. Baies, E. M. Anghel, C. A. Marinescu, and S. Tanasescu, "Thermal and structural characterization of synthetic and natural nanocrystalline hydroxyapatite," *Mater. Sci. Eng. C*, vol. 43, pp. 153–163, 2014, doi: 10.1016/j.msec.2014.07.023.

[5] S. W. Lee *et al.*, "Comparative Study of hydroxyapatite prepared from seashells and eggshells as a bone graft material," *Tissue Eng. Regen. Med.*, vol. 11, no. 2, pp. 113–120, 2014, doi: 10.1007/s13770-014-0056-1.

[6] T. Riaz *et al.*, "FTIR analysis of natural and synthetic collagen," *Appl. Spectrosc. Rev.*, vol. 53, no. 9, pp. 703–746, 2018, doi: 10.1080/05704928.2018.1426595.

[7] Q. Zhu *et al.*, "The preparation and characterization of HA/β-TCP biphasic ceramics from fish bones," *Ceram. Int.*, vol. 43, no. 15, pp. 12213–12220, 2017, doi: 10.1016/j.ceramint.2017.06.082.

[8] Demirkol, N, 2013, *Koyun hidroksiapatit esaslı kompozitlerin üretimi ve karakterizasyonu,* Doktora Tezi, İstanbul Teknik Üniversitesi , Fen Bilimleri Enstitüsü.

Hydroxyapatite Production in Solution Combustion Synthesis Using Different Fuels

Deniz ALTAN ALTINBAŞ[1], Şevki Samet KAPLAN[1], Sadia ILYAS[2], M. Şeref SÖNMEZ[1]

[1]Istanbul Technical University, [2]Jeonbuk National University

[1]Turkey, [2]Korea

Abstract

In this paper, hydroxyapatite ($Ca_{10}(PO_4)_6(OH)_2$) production by solution combustion synthesis (SCS) was investigated. Calcium nitrate tetrahydrate and diammonium hydrogen phosphate were used as calcium and phosphate sources. Different fuel types (glycine, urea, maleic acid, and ethylene glycol) were investigated to observe powder production performance. SCS reactions were carried out under 1.67 Ca/P molar ratio, 1 fuel to oxidizer ratio, and 500 ^{o}C furnace temperature. Produced powders were then calcined at 900 and 1100 ^{o}C for 2 hours. Because of promising production performance according to Rietveld analysis, maleic acid was used for SCS reaction with different fuel to oxidizer ratios from 1.5 to 3 to reach optimum hydroxyapatite production rate.

1. Introduction

Hydroxyapatite (HA) is one of the most widely used calcium phosphate bioceramics for bone replacement because it is the main mineral component of natural bones and teeth [1]. High biocompatibility, osteoconductivity, and bioactivity are important properties of HA, therefore it is used for coating metallic implants, repair of bone defects, and bone augmentation applications. To produce HA powder, many processes are used. These processes include the sol-gel method, aqueous precipitation, hydrothermal processes, and solid-state reactions [2]. In recent times, there has been a growing interest in HA production with self-propagated solution combustion synthesis (SCS) that has emerged as a simple, versatile, and cost-effective method [3]. In this paper, the production of HA with the solution combustion synthesis (SCS) method was investigated.

2. Materials and Methods

In this study, $Ca(NO_3)_2.4H_2O$ and $(NH_4)2HPO_4$ at 1.67 Ca/P ratios, and urea ($CO(NH_2)_2$) were mixed in water using a magnetic stirrer at a speed of 500 rpm for 30 minutes. The fuel to oxidizer ratio was kept as 1. Besides, 5-6 ml of HNO_3 was added while stirring to dissolve the precipitates. The final solution pH was around 1. To initiation of SCS, the mixed solution was put into the 500 °C preheated furnace for 30-40 minutes. Produced powders were then calcined at 900 and 1100 $^{\circ}$C for 2 hours. The same steps were investigated with glycine, ethylene glycol, and maleic acid with the same conditions. After these experiments, maleic acid was used with different fuel to oxidizer ratios (1.5, 2, 2.5, and 3).

3. Conclusion

According to the XRD analysis results, HA and β-tricalcium phosphate were the main phases for all experiments with different fuels. The ratio of HA to β-tricalcium phosphate increased with increased calcination temperature for all fuels, according to the Rietveld analysis. However, amounts of HA phases were not very satisfactory for all cases, but a higher amount of HA powder was observed with urea and maleic acid than ethylene glycol and glycine. Because of its promising production performance, maleic acid was used for SCS reactions.

References

[1] Sasikumar, S., & Vijayaraghavan, R. (2008). Solution combustion synthesis of bioceramic calcium phosphates by single and mixed fuels—a comparative study. *Ceramics International*, *34*(6), 1373-1379.

[2] Wu, S. C., Hsu, H. C., Hsu, S. K., Tseng, C. P., & Ho, W. F. (2019). Effects of calcination on synthesis of hydroxyapatite derived from oyster shell powders. *Journal of the Australian Ceramic Society*, *55*(4), 1051-1058.

[3] Kavitha, M., Subramanian, R., Narayanan, R., & Udhayabanu, V. (2014). Solution combustion synthesis and characterization of strontium substituted hydroxyapatite nanocrystals. *Powder technology*, *253*, 129-137.

The Operational and Quality Effects of Dynamic Superheat Control During the Continuous Casting Process

İsa KESKİN, Sergen Ali KAT
Heraeus Electro-Nite Turkey, Ekinciler Demir Çelik A.Ş.
Turkey

Abstract

Excessive heating of the steel above the liquidus temperature leads to such defects as columnar structures in cast ingots, central porosity, axial segregation, and heightened susceptibility to crack formation; It can also cause break outs or even strand losses. In this study, via Castemp and Castip systems, the liquid steel temperature in 20 tons of tundish will dynamically controlled; The effects of superheat control on operation, quality and productivity will be determined.

1. Introduction

Currently almost 90-95% of steel production is being made with continuous casting process. Maintaining the required temperature during the Continuous casting process is one of the most crucial challenges for steelmakers. Moreover, due to melting and casting a steel grade successfully, it is sufficient to determine the liquidus temperature, which is the temperature at which the steel will begin to solidify at equilibrium on cooling. During the tundish process, the freezing risks can be increased when enough superheat is not maintained.

Ekinciler Demir Çelik, prior to the installation of the CasTemp Superheat system, controlled casting speed with the superheat of the steel in the tundish. The liquidus value used to calculate the superheat was provided via an equation that used optical emission spectroscopic chemical analysis of a metal coupon sample as an input. This method has drawbacks but remains the industry standard at many casters around the globe. Liquidus calculated with an equation can and has been proven to be inaccurate. Indeed it is the accuracy of the existing liquidus equation that should be first questioned, particularly in some cases in its response to carbon and silicon. Accurate superheat control is a key factor to successful and efficient management of a continuous casting machine. Heraeus Electro-Nite recently installed the new CasTemp SuperHeat system at Ekinciler Demir Çelik caster # 2. The system pairs a through wall tundish thermocouple, CasTemp, with a top immersion disposable liquidus sensor, CasTip. The data generated by the system has allowed the steelmaker to begin looking at improving their process in the following ways: Increasing casting speeds, reducing ladle arrival temperatures, improving their soft reduction process and providing the opportunity to automate casting speed control. On top of these benefits the system has also led to a reduction of temperature related casting problems including break-outs, freeze-offs and some surface defects.

2. Materials and Methods

CasTemp

The type B thermocouple in the CasTemp sensor generates an analog DC millivolt signal. The mV value is converted to a digital temperature value by the CasTemp Wireless instrument and transmitted wirelessly to a receiving station.

CasTip

CasTip is a direct reading liquidus temperature sensor which measures the thermal solidification profile of a captured metal sample. It is optimized for use in a tundish, and uses thermocouple technology to deliver a stable liquidus arrest plateau. Latent heat released during solidification provides an arrest in the cooling curve at a value which corresponds to the equilibrium liquidus despite the non-equilibrium cooling conditions. The CasTip liquidus sensor is immersed into the tundish steel bath utilizing a hand pole fitted with a CasTip wireless QUBE transmitter that sends the liquidus temp data to the CasTemp Wireless receiving station. There the data are integrated into the CasTemp Superheat software, combined with plant inputs and live CasTemp temperature measurements to calculate superheat and forward predict end of ladle superheat.

Figure 1: CasTemp Superheat instrument display.

3. Conclusion

Via stabilized tundish temperature, the tundish capacity utilization was maximized. (In the case of high steel temperature in tundish, the steel level is being decreased in order to decrease ferrostatic pressure and casting speed. Moreover working with low steel level in tundish causes to refractory erosions and decreases tundish life.)

Figure 2 shows that after CASTEMP and CASTIP initiation, the time loss due to break outs decreased 30% and average casting speed increased 12%. Furthermore the macro analysis of billets demonstrate that the billets casted by lower superheat have less central defects and blow holes than higher superheat casted ones. Consequently plant experts made a decision that with controlling the tundish temperature continuously and dynamic superheat maintaining the casting speed could be increased without affecting the process parameters and final product quality negatively.

Trial	Break Outs (Sum)	Break Outs(Per Day)	Time Loss Due To Break Outs(Mins)	Time Loss Due To Break Outs(Per Day)	Casting Speed (Mt/Min.)
Before Castemp	565	2,1	11743	43,5	2,42
After Castemp	25	1,6	481	30,1	2,7

Figure 2: Plant data summary via CASTEMP utilization

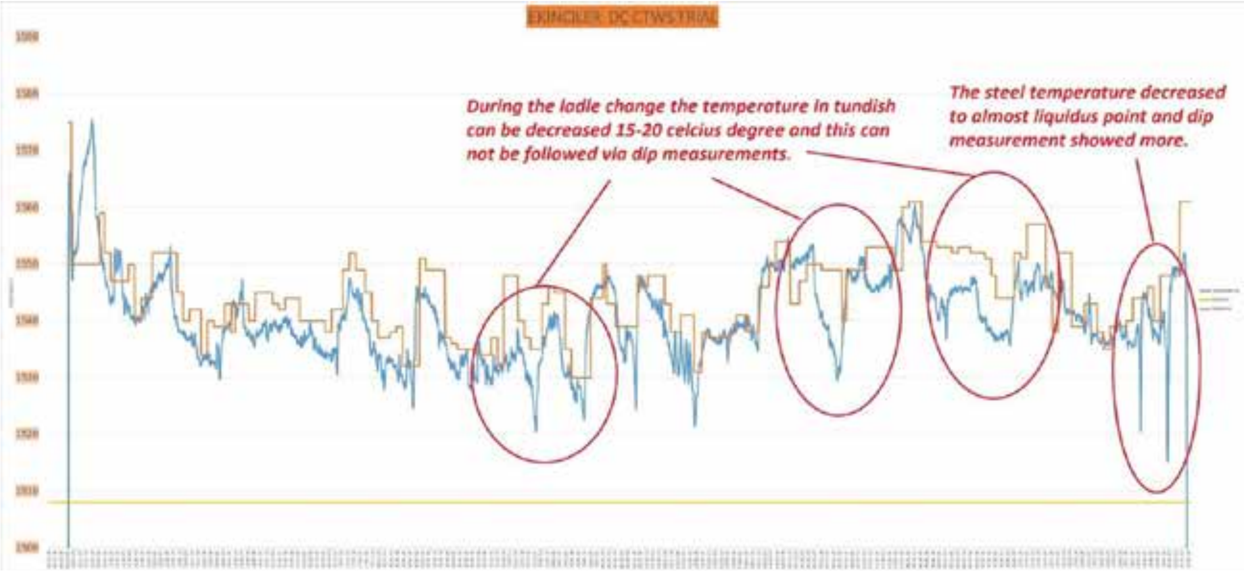

Figure 3: The temperature traces during one tundish sequence. Blue lines (Castemp) - Orange lines(Dip measurements)

Optimization of High Pressure Die Casting Parameters for the Minimization of Porosities in Aluminium AlSi9Cu3 Casting Parts

Leyla ŞİMŞEK[1],[2], Ahmet TURAN[2], M.Cahit ENSARİ[2]
[1]Kırpart Inc., [2]Yalova University
Turkey

Abstract

Aluminium alloys have a high usage rate particularly in aviation, defence and automotive industries where weight reduction is extremely important. Aluminium-silicon alloy casting parts, which were produced by high pressure die casting method (HPDC), generally contain porosity in different proportions and sizes due to the discharge problems of gases trapped during the rapid injection of molten metal into the mold cavity. In this study, it was aimed to determine the optimum casting parameters to minimize porosity formation for the HPDC of AlSi9Cu3 alloys in the form of automotive oil pan parts. The DOE (design of experiment) method was used to determine the production parameters to investigate as molten metal temperature, stroke rate and stroke distance.

1. Introduction

Verran et al. (2006), investigated the effects of the first and second phase velocities and the third phase, which was the compression phase, in the HPDC process. In addition, casting simulations were done. According to the results obtained, the increase of the first phase and the second phase velocities increased the rate of porosity whilst the increase in the third phase pressure value decreased porosity formation [1].

2. Experimental Studies, Results and Discussion

Porosity, cold shut , leakage and assembly hole positions (T4 and T5) were determined (Table 1) and investigated. A total of 170 pieces were casted with the DOE designed under the specified conditions. The articles were characterized through post-casting cold shut control, post-casting dimensional control (CMM), post-casting, porosity ratio and leakage tests after machining. As a result of evaluations, optimum parameters were determined as following; the metal temperature of 680 °C, the pressure of 320 bar, the machine speed of 5 m/seconds and the stroke distance of 550 cm.

Table 1. Investigated experimental conditions.

Parameters	Min.	Mid.	Max.	Parameters	Min.	Mid.	Max.
Metal temperature, °C	680	690	700	**Pressure, bar**	300	310	320
Machine speed, mm/sec.	5	5.5	6	**Stroke distance, cm**	450	500	550

Acknowledgment

The authors are pleased to acknowledge the financial support for this research from Yalova University, Scientific Research Projects Department under grant number 2019/YL/0003.

References

[1] Verran G.O., Mendes R.P.K. ve Rossi M. A. Influence of Injection Parameters on Defects Formation in Die Casting Al12Si1,3Cu: Experimental Results and Numeric Simulation. Journal of metarials Processing Technology, 179, 190195, 2006.

Hardness and Microstructural Evaluation of the Graphene Reinforced Al Composites Using Waste Beverage Cans

Özgür YILMAZ, Mevlüt GÜRBÜZ

Ondokuz Mayıs University

Turkey

Abstract

Aluminum is widely used in sectors such as automotive, aviation, and defense industry due to its lightness, easy workability, high strength and oxidation resistance when used in alloys or composites. In general, aluminum matrix composites are produced by powder metallurgy or liquid phase methods, and the stir casting method, which is one of the liquid phase methods, is both simpler and less costly than powder metallurgy. Beverage cans where aluminum is used most commonly are recycled, and when used as a matrix material in composite material production, the production cost is significantly reduced and environmental pollution. Within the scope of this study, graphene reinforced aluminum matrix composites were produced with the casting method. Experimental samples were obtained from these composites and hardness, density, abrasion test; X-ray diffraction (XRD) and scanning electron microscopy (SEM) analyzes were performed. According to obtained the results, the hardness value increased from 70.1 HV to 78,84 HV with wt. %0,05 graphene reinforcement. With increasing graphene content, the hardness of composites was deteriorated. According to SEM analysis, the graphene nanoflakes is homogeneously distributed in the matrix for low concentration graphene.

1. Introduction

Since the end of the 20th century, technological developments in the automotive, aerospace and aviation sectors have been increasing rapidly. Due to technological developments, the conventional materials used in these sectors cannot compensate the intended mechanical properties and performance[1]. Production and use of composite materials with higher hardness, tensile and compressive strength, abrasion and corrosion resistance and low density have become widespread instead of metals, alloys, ceramic and polymer materials. Studies on the production of composite materials, production methods and improve their mechanical properties are increasing rapidly [2-5]

Composite materials are divided into three types according to type of matrix used: metal, ceramic and polymer matrix composites. Metal-matrix composite (MMC) materials are highly preferred in engineering materials due to their enhanced mechanical and thermal properties, lightness and easy formability. Metals and alloys such as Al, Mg, Ni, Cu, Ti, Fe are commonly used as matrix materials in the production of MMC materials. Al and its alloys are the most used matrix material in metal matrix composites due to their lightness, high mechanical and physical properties in industries such as automotive, space and aviation [6-8]. The reinforcement material is as important as the matrix material in improving the properties of composites. As reinforcing materials; SiC, Si_3N_4, Al_2O_3, B_4C, MgO, W, C, TiC, TiB_2 and carbon based reinforcements, such are graphite, carbon nanotube, fullerene and graphene, are widely used. Graphene is an almost two dimensional single layer of graphite structure consists of honeycomb braided carbon atoms. It has superior properties due to the graphene structure which has been used as reinforcement component after 2008. Production of graphene reinforced composites has become important due to properties of high lubricity, flexibility, durability and thinness in recent years [9].

In the production of metal matrix composite (MMC) materials; the characteristics of the composite material to be produced, the use of matrix and reinforcement elements has led to the development of different techniques. Depending on whether the matrix is liquid or solid, the most commonly used methods of MMC production are powder metallurgy or liquid metal mixing method. Stir casting is preferred for the production of composite materials containing large grain size and low rates of reinforcements. Stir casting is a more economical and simpler method than powder metallurgy [10-12].

Wang et al. (2012) produced 0.3% by weight of graphene nano partially reinforced aluminum composite with powder metallurgy method and determined that the tensile strength of the composite increased by 62% compared to the non-reinforced Al matrix [13]. Rashad et al. (2014) investigated the effects of graphene nano-layered aluminum composite and graphene nano-particle addition on mechanical properties by using powder metallurgy and then hot extrusion method. It was observed that the tensile strength and hardness of pure aluminum increased and the compressive strength decreased as a result of 0,3% by weight of graphene reinforcement [14].

Yan vd (2014) produced graphene nanofibre reinforced aluminum alloys with powder metallurgy. Composite samples were obtained with reinforcements of 0.15% and 0.5% by weight. Tensile strength and yield strength increased with the increase of the reinforcement rate. Most importantly, as with most other MMCs, ductility has not decreased with the addition of reinforcement [7]. Jagadish (2015) in this study; in the composites produced by the powder metallurgy method used Al-2024 alloy as matrix and graphene at rates of 0.25, 0.5, 0.75 and 1% by weight as reinforcement. With the addition of graphene reinforcement, the hardness value decreased and the lowest hardness value was observed in 5% graphene reinforcement. It was determined decreased of impact strength and increased the bending strength with the increase of weight ratio of the graphene[15].

Gao et al. (2016) produced aluminum composites with a graphene reinforcement of 0.1, 0.3 and 0.5% by weight by powder metallurgy. When the graphene content is 0.3% of produced composites, the tensile strength is maximized. In addition to that, by increasing graphene addition ratio, fracture behavior of graphene reinforced aluminum matrix composite became brittle from ductile [16].

Gürbüz vd (2017), Powder metallurgy method by adding 0.1%, 0.3, 0.5% by weight of graphene powder into aluminum powder; the effect of graphene on microstructure and mechanical properties was investigated. Different times and temperatures were studied to examine the effect of sintering time and sintering temperature. The highest density value was 0.1% with GNP contribution. The hardness value increased from 38 to 57 HV. The best result was achieved when the sintering temperature was 630 ° C and the sintering time was 180 minutes [17].

Yang et al. (2018) produced aluminum metal matrix composite materials with graphene reinforcement by casting method. 0.54% by weight of graphene is added to aluminum powder. Al and GNP powders are granulated in a ball mill and then melted. This melt was poured by pressure filtration method. After solidification at room temperature, hot extrusion was applied to the samples at 450 ° C. And then annealing was carried out at 400 ° C for 2 hours. Tests were performed before and after extrusion of sample. According to this; the increase in yield and tensile strength before hot extrusion was measured as 116% and 45%, respectively. The increase in yield and tensile strength after hot extrusion was 228% and 93%, respectively[18].

Dasari et al. (2018) produced graphene oxide (GO) reinforce aluminum metal matrix composite by powder metallurgy. They made a graphene contribution of 0.05%, 0.1% and 0.2% by weight of into 35 µm particle size aluminum powder microstructure and hardness measurements were performed to the produced composites by using SEM, XRD and EDX analyzes. According to the results obtained; the highest increase in hardness value was observed in 0.2% by weight GO reinforced aluminum composite.[19]. Venkatesan and Xavior studied the mechanical properties of graphene reinforced aluminum matrix composites produced by stir casting. Optimal results in graphene reinforcement at 0.33%, 0.55% and 0.77% was reached 0.33% graphene ratio [20]. Depending on technological developments; reducing the use of natural resources and prevention of environmental pollution, environmental protection has become the primary issue in recent years. Recycling waste materials is important in terms of environmental pollution and protection. Today, aluminum is produced from primarily ore and secondarily scrap aluminum. Recycling beverage cans, which is one of the most common product made of aluminum, has a significant share in terms of environmental protection [21].

The most important feature of the study is the use of waste aluminum beverage cans for MMC material matrix. Using waste beverage cans both waste beverage will be recycled and composite material will be produced at cheaper cost compared to other composite material production methods. The original aspect of the study is the production of lightweight and highly mechanical composites from waste aluminum using high lubricating, mechanical and thermal properties of graphene, which is widely used in recent years. We purpose that fabrication and characterization of Graphene reinforced (0,05-0,75 wt. %) aluminum matrix composites from waste beverage cans. The effect of reinforcement ratio on the density, hardness, compressive and tensile strength of the composites were evaluated in detail.

2. Experimental Procedure

2.1. Materyal

In this study, instead of primary aluminum materials or aluminum powders, liquid aluminum obtained from casting of waste beverage cans have been used for the matrix material and graphene with 5-8 nm thickness and 10 µm radius have been used as the reinforcement, for the production of the composite. Graphene reinforced aluminum composites with %0.05, %0.15, %0.30, %0.45, %0.60 and %0.75 ratios by weight have been produced by stir casting method.

2.2 Method

The matrix material of the composite is prepared for the first step. In order to do that, waste beverage cans have been casted at the temperature 850°C and obtained aluminum ingots. Each ingots weight and graphene reinforcement addition have been measured based on ratios by weight (%0.05, %0.15, %0.30, %0.45, %0.60 and %0.75). Stir casting set-up has been used for producing composite material. While the temperature of furnace was between 700°C-750°C, aluminum ingots have been placed in crucible. After the aluminum has been melted, in order to increase wettability of graphene and obtain coherent interface, the temperature of furnace has been decreased to 630°C-650°C. After that, the liquid has been mixed at 400 rpm for five minutes by a mechanical mixer. At the next step, the temperature has been increased to 700±10°C and the mixing process has been continued for two more minutes to obtain a homogeneous mixture. Before the ingredient has been poured into the mold which was heated to 400°C-450°C, the dross was removed from the surface of the liquid. At last, after waiting at the room temperature for the solidification of the mold, the mold has been removed from the casting mold. A schematic representation of the method used is given in Figure 1. The specimens prepared have been coded as seen at Table 1.

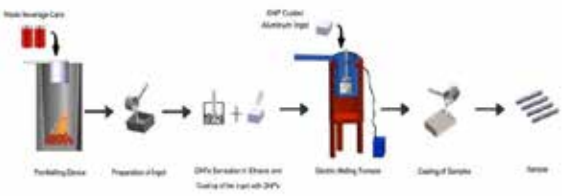

Figure 1. Production stages of composite materials

3.Results and Discussion

2.1. Hardness

Vickers hardness values of unreinforced and graphene reinforced composite materials produced by mixing casting method are given in Figure 2. With the addition of graphene, the hardness values of the composite materials increased from 70,81 HV to 78,84 HV.

The highest hardness value was measured in 0,05% by weight of graphene reinforcement. It is observed that the hardness value decreases with increasing graphene reinforcement rate. It is thought that after 0.05% by weight of graphene reinforcement into the matrix, the graphene tends to agglomerate and cause a decrease in hardness. Theoretically, the hardness increase can be explained with the rule of mixtures by Eq.2 [23].

$$H_c = H_m f_m + H_r f_r \qquad (1)$$

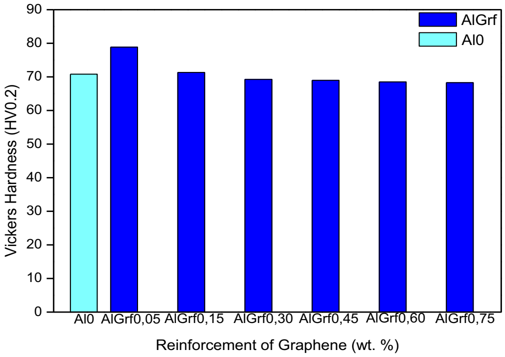

Figure 2. Hardness Change with Graphene Reinforcement Ratio Increase

2.2. Characterization of the composites

Table 2 gives the EDX analyses of the fabricated aluminum alloy ingot from waste aluminum which includes the Si, Mg, Mn instead of Al. These alloying elements positively affect the mechanical properties of the composites.

Table 1. EDX analyses of pure beverage cans and casted aluminum alloy

	Al	Si	Mg	Mn
Pure Beverage Cans (wt.%)	94.72	3.62	0.78	0.88
Casted Samples (wt.%)	93.85	4.18	0.76	1.21

The SEM images of Al-Grf composites are represented in Fig.3. As given in the figure, Grf particles between 0,05-0,75 wt.% are homogeneously distributed in matrix. Also, aluminum grain and graphene particles have good interphase. The dispersion of the particles is deteriorated above 0,75 wt.% graphene content due to the excess amount which led to nonhomogeneous particle agglomeration.

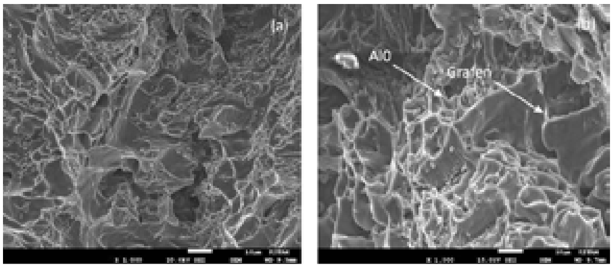

Figure 3. Broken surface images of non-reinforced and graphene-reinforced Al composites: (a) Al0, (b) AlGrf0.05

Also, The XRD patterns of graphene reinforced aluminum composites are given in Fig. 4. As clearly seen, all diffractions possess the pure Al and graphene. In addition, second phases such as aluminum carbide (Al_4C_3) peak is not detected for all Al-graphene samples due to the low temperature casting which is not activate to react Al with C.

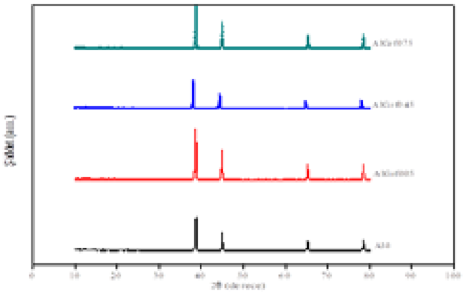

Figure 4. XRD weave patterns of graphene-reinforced Al matrix composites

4. Conclusion

From the results, the hardness value increased from 70.1 HV to 78,84 HV with wt. %0,05 graphene reinforcement. With increasing graphene content, the hardness of composites was reduced due to easy sliding between the particles. According to SEM analysis, the graphene nanoflakes is homogeneously distributed in the matrix for low concentration graphene.

References

[1]Öztop B. and Gürbüz M. "Investigation of Properties of Composites Produced by Reinforcement Graphene Matrix Obtained from Waste Aluminium," International Journal of Multidisciplinary Studies and Innovative Technologies, vol. 1, no. 1, pp. 4-8, 2017.

[2] Erdoğan M. "The Production of steel fibre reinforced aluminium composite material and investigation of its mechanical properties experimentally," Master Thesis, Department of Mechanical Engineering, Dumlupınar University, Kütahya, 2005.

[3]Işık E. "The production of Al-12Si matrix composite reinforced with SiC particles by powder metallurgy and analysis of the wear behaviour," Master Thesis, Department of Mechanical Engineering, Gazi University, Ankara, 2014.

[4]Bağcı C. "Production of silicon nitride (Si3N4) type technological ceramic material from sepiolite and its characterization," Doctorate Thesis, Department of Metal Education, Gazi University, Ankara, 2007.

[5]Mindivan H. "The investigation of tribological behavior in

silicon carbide (SiC) reinforced aluminum matrix composites," Doctorate Thesis, Departman of Mechanical Engineering, İstanbul Technical University, İstanbul, 2007.

[6]Y. Seçkin, Introduction to Composite Materials. Ankara: Seçkin Publisher, 2006.

[7]Yan S.J., Zhang X.Y., Yang C., et al. "Investigation aluminum alloy reinforced by graphene nanoflakes," MaterialsScience&EngineeringA, vol. 612, pp. 440-444, 2014.

[8]Latief F.H. and Sherif E.M. "Effects of sintering temperature and graphite addition on the mechanical properties of aluminum," Journal of Industrial and Engineering Chemistry, vol. 18, pp. 2129-2134, 2012.

[9]Şenel M.C., Gürbüz, M. and Koç, E, "Graphene Reinforced Aluminum Matrix New Generation Composites," Engineer and Machine, vol. 56, no. 669, pp. 36-47, 2015.

[10]Surappa M.K. "Aluminum matrix composites: Challenges and opportunities," Sadhana, vol. 28, no. 1-2, pp. 319-334, 2003.

[11]Sur G., Şahin Y. and Gökkaya H. "Production of aluminum based particle reinforced composites by molten metal mixing and pressure casting," Gazi University Journal of Faculty of Engineering and Architecture, vol. 20, no. 2, pp. 233-238, 2005.

[12]Hashim J., Looney L. and Hashmi M.S.J. "Metal matrix composites: production by the stir casting method," Journal of Materials Processing Technology, vol. 92-93, pp. 1-7, 1999.

[13]Wang J., Li Z., Genlian Fan, et al. "Reinforcement with graphene nanosheets in aluminum matrix composites," Scripta Materialia, vol. 66, pp. 594-597, 2012.

[14]Rashad M., Pan F., Tang A and Asif M. "Effect of Graphene Nanoplatelets addition on mechanical properties of pure aluminum using a semi-powder method," Progress in Natural Science: Materials International, vol. 24, pp. 101-108, 2014.

[15]Jagadish B.S. "Synthesis and Characterisation of Aluminium 2024 and Graphene Metal Matrix Composites by Powder Metallurgy Means," SSRG International Journal of Mechanical Engineering (SSRG – IJME), vol. 2, no. 7, pp. 13-17, 2015.

[16]Gao X., Yue H., Guo E., et al. "Preparation and tensile properties of homogeneously dispersed graphene reinforced aluminum matrix composites," Materials and Design, vol. 94, pp. 54-60, 2016.

[17]Şenel M.C., Gürbüz, M. and Koç, E "The effect of sintering time, temperature, and graphene addition on the hardness and microstructure of aluminum composites," Journal Of Composite Materials, vol. 52, no. 4, pp. 553-563, 2018.

[18]Yang W., Zhao Q., Xin L., Qiao J., Zou J., Shao P., Yu Z., Zhang Q. and Wu G. "Microstructure and mechanical properties of graphene nanoplates reinforced pure Al matrix composites prepared by pressure infiltration method," Journal of Alloys and Compounds, vol. 732, pp. 748-758, 2018.

[19]Dasari B.L., Morshed M., Nouri J.M., Brabazon D., Naher S. "Mechanical properties of graphene oxide reinforced aluminium matrix composites," Composites Part B, vol. 145, pp. 136-144, 2018.

[20]Venkatesan S. and Xavior M.A. "Mechanical behaviour of Aluminium metal matrix composite reinforced with graphene particulate by stir casting method," Journal of Chemical and Pharmaceutical Sciences, vol. 10, no. 1, pp. 55-59, 2017.

[21]Gürbüz M. "Effect of cold treatment on mechanical properties of aluminum made from waste beverage cans," Dokuz Eylul University Faculty of Engineering Journal of Science and Engineering vol. 20, no. 58, 2018.

[22]Şenel M.C., Gürbüz, M. and Koç, E "Investigation of the Mechanical Properties of Al-Si3N4 Metal Matrix Composites Produced by Powder Metallurgy Method," Engineer and Machinery, vol. 59, no. 693, pp. 33-46, 2018.

[23]Şenel M.C., Gürbüz, M. and Koç, E "Mechanical and tribological behaviours of aluminium matrix composites reinforced by graphene nanoplatelets," Materials Science and Technology, 2018.

[24]Hu Z., Tong G., Nian Q., Xu R., et al. "Laser sintered single layer graphene oxide reinforced titanium matrix nanocomposites," Composites Part B: Engineering, vol. 93, pp. 352-359, 2016.

An Analytical Approach to Fortification Walls of Ephesos Lysimakhos

Cansu NOBERİ, Fırat BARANAYDIN
İstanbul Gelişim Üniversitesi
Turkey

Abstract

Throughout the Ancient Age, Ephesos was the capital city of the Kingdom of Arzawa and later led 12 Ionic cities. In addition, during the Hellenistic Period, Ephesos was one of the favorite cities of Lysimakhos. Afterwards, in Roman Era, the city was also a capital city of the Asia States and during the Byzantine Period it was hosted for the important people of Christianity. When the commander of Alexander the Great rebuilding the city in its new site, he was surrounded it with fortification walls. Furthermore, he was built sentry castles for the attracts that might come to the city. Archeology can be date the fortification structures built on Pion, Koresos and Ayasuluk to the same period. However, we do not have precise data on the materials and construction processes of these structures. In order to overcome those kind of obscurity, number of characterization analysis were carried out.

1.Introduction

Ephesos has hosted many civilizations due to its harbor, fertile lands and a climate suitable for life, and for these features have caused struggles through the city. These struggles continued from the Hellenistic period to the Byzantine era (1) and caused destruction most of the symbolic buildings in and around the city. However, functional structures have been used for a long time without being destroyed. Those include roads, bridges, water structures and systems, and fortification systems (2). While the localization of Ephesos city by Lysimakhos, the fortifications built in Pion and Koresos mountains around the city and the fortifications built on Ayasuluk Hill were also used in the following periods. However, archaeological excavation results, which are not sufficient for today, keep the knowledge about those fortification structures at a basic level. This particular study aiming to reveal that Lysimakhos made these structures simultaneously during the development activities, using basic characterization methods both including electron microscopy and X-Ray Diffraction methods in the light of archeology data. As a result, it has been confirmed that the stone material used in the construction of the fortifications was brought from the same ore (quarry).

2.Materials and Methods

It can be seen that Ayasuluk Hill has a homogeneous structure in terms of the stone material used in the unearthed part of the Lysimakhos walls of the Hellenistic period. Taking 3 samples in the masonry, in which a single type of stone was used and processed in the same size and form, was found suitable for minimum intervention to the structure. 3 samples were taken from the Hellenistic fortifications in Pion mountain like Ayasuluk fortifications. In the Hellenistic fortifications, which are close to 3 km long on Koresos mountain, it was found sufficient to take 3 samples from different points due to the similar properties as other materials. In addition, 3 samples were taken from the ancient quarries on Pion Mountain. As a result all the experiments were conducted onto 12 samples which have been taken different location of the area.

3.Conclusion

Due to all characterization investigation it can be said that all samples that have been taken from all those fortification walls were belong to the same ore. Those informations were supported the archeological ones so that it has proven that there is an organic bond between the zoning activities nad fortification building system of the ancient city of Ephesus during the Hellenistic period

Referances

1- Ladstätter 2012, 13.

2-Baranaydın 2016

A Preliminary Study on TiO_2 Coating Deposited on the AISI 2205 by High Energy Ball Milling

Serhat ACAR[1], Burak BİROL[1], Alptekin KISASÖZ[2]
[1]Yıldız Technical University, [2]Kırklareli University
Turkey

Abstract

Titanium dioxide (TiO_2), which is a hard and corrosion resistant oxide, is used for coating stainless steels and other biomedical metals in order to improve pitting corrosion resistance. Generally, TiO_2 based coatings can be produced by various methods like sol-gel and vapor deposition. Moreover, particulates can be deposited with mechanical activation. SPEX is one of the methods that produced coating with mechanical activation and leads to formation of higher process energy for production of homogenous coatings. In this study, titanium dioxide particulates were coated on the AISI 2205 duplex stainless steels by high energy ball milling. Milling process was carried out for 2, 5 and 10 hours. Coated samples were sintered at 500˚C for an hour. Sintered samples were characterized by scanning electron microscopy (SEM), surface roughness and corrosion tests.

1. Introduction

Duplex stainless steels (DSSs) consist of an equal amount of ferrite and austenite phases, and DSSs combine the physical and mechanical properties of these phases. Ferrite phase provides mechanical strength and pitting corrosion resistance as well as austenite phase provides ductility and general corrosion resistance. This dual-phase structure widens the usage of DSSs in many areas such as offshore applications, transportation, petrochemical and shipbuilding industries compared to austenitic stainless steels [1-4]. Moreover, researches are carried out to expand the usage of DSSs and to increase corrosion resistance, biocompatibility and wear properties in various aggressive environments [5, 6].

Titanium dioxide (TiO_2) based coatings are one of the most common coatings applied to stainless steels, and such coatings are especially applied to austenitic stainless steels. TiO_2 coatings exhibit desired wear properties, biocompatibility and corrosion resistance. Also, researches revealed that a small amount of TiO_2 in the coatings causes changes in surface energy and it affects the bacterial adhesion [7-11].

TiO_2 based coatings can be produced by various techniques like mechanical alloying and electrochemical techniques. Mechanical alloying provides the homogenous distribution of the fine particulate. Also, high energy ball milling, one of the mechanical alloying techniques, produces a strong mechanical energy transfer to base material and powder and this phenomenon enables to produce fully dense coating with superior mechanical properties [12-15].

In this study, production of TiO_2 coating on AISI 2205 DSS was investigated. Also, effect of milling time was examined, and SEM (Scanning Electron Microscopy), EDS (Energy Dispersive Spectroscopy) and electrochemical corrosion tests were carried out in order to determine properties of produced samples.

2. Experimental Procedure

In order to examine the coating properties of the TiO_2 on AISI 2205 with SPEX milling, AISI 2205 duplex stainless steel cubes (a = 11±0.5 mm) as base and commercial grade TiO_2 (<20 µm) powder as the coating material were selected. The steel cube and the TiO_2 powder (3 g) were ball milled in a high energy Retsch MM200 milling machine. The ball size, ball/powder ratio and mill frequency were selected as 8 mm, 10:1 and 25 Hz, respectively. The ball milling process was conducted for 2, 5 and 10 hours and the process were paused for 5 minutes at each 30 mins to avoid increasing the temperature of the system and raw materials. Then the samples were sintered at 500 °C for an hour in a Protherm PLF/110 furnace under atmospheric conditions.

The properties of the obtained coatings were analyzed by SEM (Hitachi SU3500), EDS (Oxford Instrument) and surface roughness analyze by profilometer (Mahr Perthometer S2). Additionally, corrosion tests were conducted by using an Ivium Compactstat potentiostat in 3.5 wt.% NaCl solution at 24°C with a scanning rate of 0.5 mV/s. The reference electrode of the corrosion test cell was a Ag/AgCl electrode. A platinum counter electrode with a surface area of 400 mm^2. The test sample was connected as the working electrode and a reacting surface area was adjusted as 100 mm^2.

3. Results and Discussion

The SEM-micrographs of the samples are given in Figure 1.

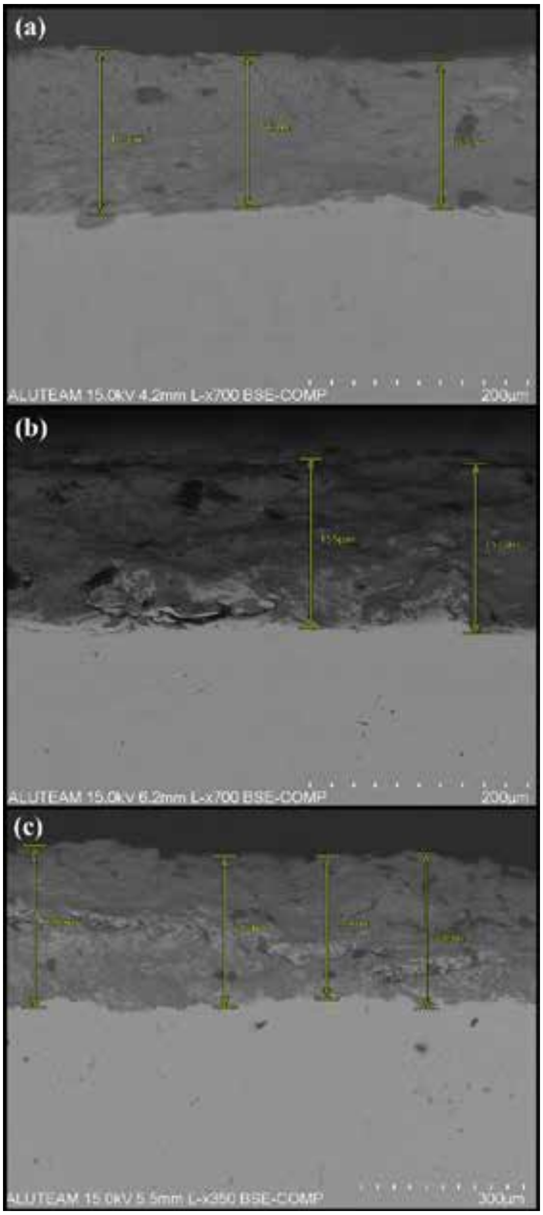

Figure 1. SEM micrographs of the samples ball milled for (a) 2h, (b) 5h and (c) 10h.

According to the SEM micrographs of the samples, the average coating thickness of the samples are 144, 156 and 283 µm, respectively. This result shows that accumulation of the coating powder on the metal surface increases with the increasing ball milling time. From this point of view, a relatively homogeneous coating is observed.

Additionally, EDS analyzes and line spectrums of the produced samples were investigated. One of these EDS analyzes (2 h ball milled sample) is given in Figure 2.

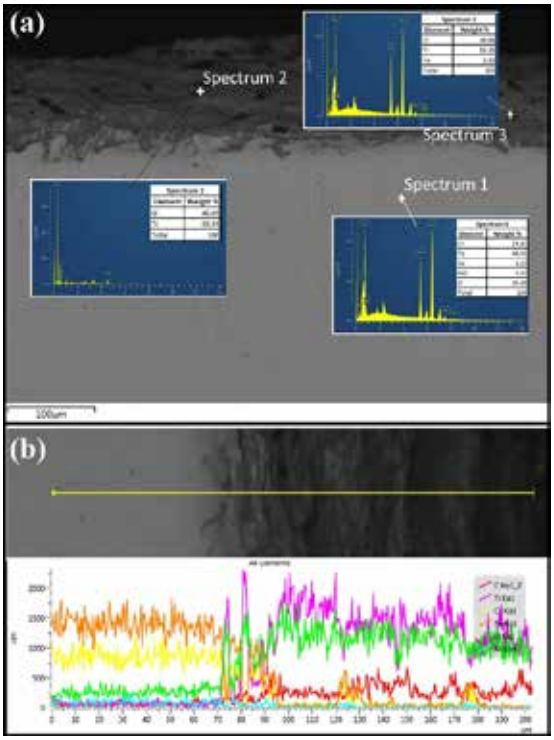

Figure 2. EDS (a) point spectrum and analysis and (b) line spectrum for 2h ball milled sample.

Regarding to the EDS analyzes it was observed that the metallic phase analysis gives the exact composition of the AISI 2205 steel (Figure 2 (a) Spectrum 1), also the coating (Figure 2 (a), Spectrum 2) has the composition of Ti and O atoms, as expected. On the other hand, in Figure 2 (b) the linear spectrum shows that from 0 to 70 µm the spectrum shows only the composition of steel. There is a transition area where both steel and TiO_2 compositions are met between 70th and 90th µm. TiO_2 is the dominant phase after the 90th µm. Especially the transition area, where both TiO_2 and metallic phases occur, shows that the coating powder firstly accumulates on the notches on the metal surface. These notches occur during the impaction of the ball milling process and let fine powders to compress with the help of the ball impactions. This transition area plays an important role on the coating process, because it works as a bridge between the metallic phase and ceramic coating. Otherwise it would be impossible to coat the ceramic phase on a flat metallic surface.

On the other hand, slight amounts of Fe and C is observed at the coating phase. Also, in the analysis of the dark area in the coating phase (Figure 2 (a), Spectrum 3) 6% Fe is encountered. So, this can be explained by the wear of the balls and the vial. The particles that splits from both the vial and the balls scatter through the TiO_2 powder and accumulate with the powder on the metallic surface. To eliminate this problem, PCAs (Process Controlling Agents) like stearic acid, methanol, etc. may be used.

Moreover, roughness tests were also conducted to determine properties of the coating. The Ra value of the samples that were milled for 2, 5 and 10 h were 4.2, 3.8 and 4.9 µm, respectively. Although the values are close, there is a slight difference that can be explained through compaction phenomenon. When both coating thickness and roughness values are taken into account, it is observed that the coating thickness of the 5h ball milled sample is not higher than the 2h sample, whereas its roughness is less. Also, the 10 h sample has both higher thickness and roughness values than the other samples. Therefore, it can be deduced that there is a relationship between the coating thickness and roughness, in other words milling time and roughness. At the early stages of the ball milling process the powders begin to accumulate but not in a very compact manner, but in time the accumulated powders will compress and new particles will begin to accumulate on the compressed surface. During the compressing stage the roughness lower where more accumulation occurs, the roughness increase.

The potentiodynamic polarization curves and experimental results of the AISI 2205 Steel, 2h and 10 h ball milled samples after corrosion tests are given in Figure 3 and Table 1.

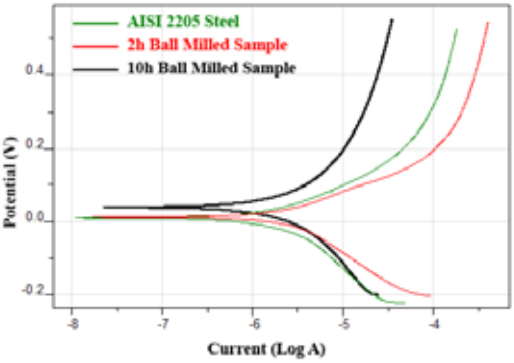

Figure 3. Potentiodynamic polarization curves of the AISI 2205 steel, 2h and 10h milled samples

Table 1. Potentiodynamic polarization curves of the AISI 2205 steel, 2h and 10h milled samples

Sample	E corr (V)	I corr ($A/10^{-6}$ cm^2)	Corrosion Rate (mm/y)
AISI 2205	0.0094	1.88	0.02009
2h Milled S.	0.0131	1.81	0.01935
10h Milled S.	0.0521	1.62	0.01737

Due to Table 1, corrosion resistance (E_{corr}) increases with the increasing ball milling time, also corrosion rate and I_{corr}, which indicates the kinetics of the corrosion, decreases. Nevertheless, the corrosion rates don't decrease proportionally with the increasing corrosion resistance, as expected. The reason of this case can be explained by the discontinuities on the coating phase.

Although the coating seems homogeneous and has low roughness values, this homogeneity is areal and some cracks on the overall sample surfaces are observed.

4. Conclusions

In the present study, it was aimed to physically coat an AISI 2205 duplex stainless steel with TiO_2 powder by high energy ball milling following a fixed sintering process. According to the experimental results the following conclusions were obtained.

1. At fixed milling parameters (25 Hz, 3 g TiO_2, 8 mm steel balls and 10:1 ball: powder ratio) increasing milling time increases the coating thickness.
2. To be able to physically accumulate TiO_2 powder on the metallic phase, there should be some physical deformations, so that ceramic phase will hold on these notches and play a bridge between the metallic and ceramic phase.
3. Roughness varies with the increasing milling time. Increasing milling time means increasing coating thickness and increasing coating thickness requires more time to compress and form a compact coating.
4. According to the corrosion tests, the corrosion resistance increases with the increasing coating thickness. However, corrosion rates do not change proportionally as expected. This can be explained by the discontinuing coating phase.

According to the experimental results ball milling may be a proper coating method however the inhomogeneity and discontinuities on the coating phase lower the success of this method. On the other hand, these problems can be eliminated by changing the milling parameters (milling time, ball to mill ratio, ball size, etc.) and/or sintering parameters (temperature, regime, etc.) or by adding some metallic phases (metallic Ti powder, etc.) to the TiO% powder in order to make stronger bonds between the metallic and the ceramic phases. Therefore for the future studies it is planned to study these parameters and investigate their effects on the coating properties.

References

[1] M. Pohl, O. Storz, T. Glogowski, Materials Characterization, 58 (2007) 65-71.
[2] J.O. Nilsson, Materials Science and Technology, 8 (1992) 685-700.
[3] C Hsieh, W. Wu, ISRN Metallurgy, 4 (2012) 1-16.
[4] A. Kısasöz, S. Gürel, A. Karaaslan, Metal Science and Heat Treatment, 57 (2016) 544-547.
[5] A. Rokanopoulou, P. Skarvelis, G. D. Papadimitriou, Surface and Coatings Technology, 289 (2016) 144-149.
[6] P. NithinRaj, Nithin Sivadas, K. Sekar, M. A. Joseph, Materials Today, 22 (2020)2172-2178.
[7] A. S. Hammood, M. A. S. Mahdi, L. Thair, H. Haddad, Materials Research Express, 6 (2019) 1-13.

[8] L. Skowronski, A. A. Wachowiak, K. Zdunek, M. Trzcinski, M. K. Naparty, Thin Solid Films, 627 (2017) 1-8.
[9] T. Verdier, M. Coutand, A. Bertron, C. Roques, Coatings 4 (2014) 670-686.
[10] S. Zhang, X. Liang, G. M. Gadd, Q. Zhao, Applied Surface Science, 490 (2019) 231-241.
[11] E. Zalnezhad, A. M. S. Hamouda, G. Faraji, S. Shamshirband, Ceramics International, 41 (2015), 2785-2793.
[12] H. Zoz, D. Ernst, H. Weiss, M. Magini, C. Powell, C. Suryanarayana, F. H. Froes, Metall, 50 (2000) 575-579.
[13] J. Lv, W. Guo, T. Liang, M. Yang, Materials Chemistry and Physics, 197 (2017) 79-86.
[14] V. Cannillo, L. Lusvarghi, A. Sola, Journal of the European Ceramic Society, 11 (2018) 2161-2169.
[15] S. Miszczak, B. Pietrzyk, Ceramics International, 6 (2015) 7461-7465.

Evaluation of Glass Waste in Ceramic Glazes

Fatma GÖL[1], Ali YILMAZ[1], Selin ŞİMŞEK[1], Emre KAÇAR[1], Zeynep Gizem SARITAŞ[1], Çiğdem TÜRE[1], Melek ARSLAN[1], Fatih ŞEN[1,2]

[1]Keramika Ceramics, Ünsa Mining, Tourism, Energy, Ceramics, Forest Products, Electricity Production Industry, [2]Dumlupınar University

Turkey

Abstract

With the technological developments taking place in the world, the rapidly growing economy and with it urbanization, industrialization and population increase cause a significant increase in the amount of waste. Considering the limited natural resources, the social, economic and environmental effects of recycling come to the fore. In this study, the use of glass waste instead of frit used in glaze compositions in the ceramic industry was evaluated. Ceramic tableware glaze recipes were formulated using 3%, 5% and 8% glass waste by weight. After adding glass waste into the standard glaze, the whiteness, brightness, L a b values, glaze flows, harkort test results, final water absorption values of the test glazes were compared. The results indicated the feasibility of using 3% glass waste in the production of ceramic tableware.

1.Introduction

Pine; It has physical and chemical properties such as transparency, sealing, mechanical, chemical and thermal resistance, so it is widely used. Because of these properties, it can be remelted and used without losing its physical or chemical properties. Reusing glass wastes and transforming them into products helps to reduce ceramic raw material costs.

In this study, waste glasses were added to glaze compositions and 12 different glaze recipes were studied. Transparent, opaque and matt ceramic glazes were prepared with glass waste added at different rates. Later, these glazes were applied to ceramic biscuit surfaces. After the firing process of the products obtained, the whiteness, brightness, heat resistance and glaze flow of the final products were checked.

2. Materials and Methods

Glass waste used in the study was obtained from the relevant glass companies. Test glazes prepared with glass waste were tested for 3 different types of glaze as transparent, opaque and matte, and a total of 12 formulations were prepared. The glass waste used in the study was used instead of frit in the glaze formulation at 3%, 5% and 8% by weight.

Test glazes were applied on the ceramic biscuit using the dipping method. The glazed products were fired in the Roller oven in the temperature range of 1050-1200 ºC for 2 hours. After the glaze surfaces were examined, L a b values were measured. The final water absorption and collateral tests of the products were made and the flows of the glazes were determined.

	Transparent Production	3%	5%	8%
L	86,66	86,4	86,62	87,98
a	2,27	2,35	2,07	2,35
b	10,9	10,92	10,57	10,32
ΔE		0,41	0,49	1,25

Table 1. Transparent glaze L * a * b data

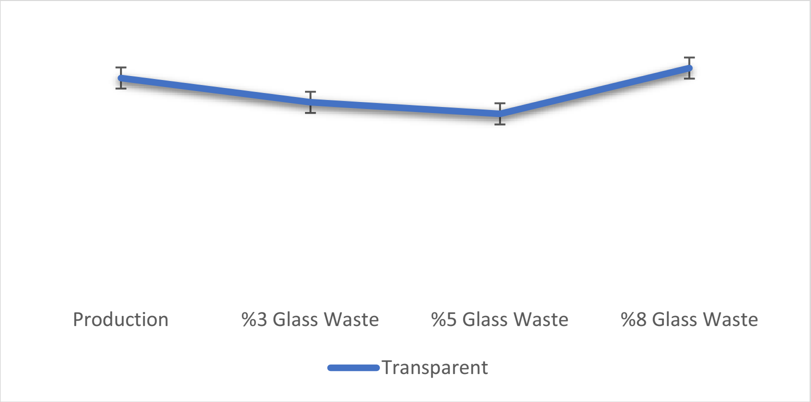

Figure 1. Transparent glaze water absorption test data

3. Conclusions

As a result of this study; The reuse of glass waste and its effect on ceramic glazes were studied. Glass waste; trs, opaque and matt ceramic tableware glazes were added at the rate of 8% - 5% - 3%. It has been determined that 3% to 8% gain has been achieved in glaze costs. As the glass waste rate increases, it has been determined that the product strength decreases as a result of the harcort test. The ideal rate for the harcort test is 3%. Color tones remained at standard values. The closest L * a * b value is 3%. The ideal usage rate for the production of ceramic tableware has been determined as 3% glass waste. A positive effect of 3% glass waste addition on final water absorption values was observed. This will help increase the life of the product. The results of the experiments showed that 3%, 5%, 8% glass wastes can be used in the production of ceramic tableware. Physical and chemical tests were applied to the glaze compositions obtained. As a result, the properties of the 3% glass waste added glaze were observed to be similar to those of the standard glaze.

Acknowledgment

We would like to thank the KERAMIKA FAMILY for providing us financial support and opportunity during this work. We would like to express our thanks KERAMIKA General Manager Mr. Emin YÜCE for always supporting us.

Enhancing the Ductility of 3D-Printed Polylactic Acid

Burçin KAYGUSUZ, Sezer ÖZERİNÇ
Middle East Technical University
Turkey

Abstract
Polylactic acid (PLA) is one of the most commonly used filament materials in fused deposition modeling (FDM) 3D printing. However, PLA is a relatively brittle material, which is a major disadvantage for the printing of load-bearing structures. In this study, we investigated the performance of a commercial PLA/PHA filament with improved ductility. The specimens printed at the nozzle temperature of 220°C provided elongation at failure exceeding 200%, demonstrating more than an order of magnitude improvement compared to pure PLA. The results show that PLA/PHA is a very promising polymer blend for applications requiring high ductility.

1. Introduction

FDM has become one of the most popular techniques for the manufacturing of plastic components in relatively low quantities[1]. One of the most commonly used raw materials in FDM is polylactic acid (PLA). PLA has a higher strength than many common polymers such as polystyrene, polypropylene, and polyethylene terephthalate[2]. On the other hand, PLA has a relatively low ductility of about 5% elongation at fracture, which results in low damage tolerance. Previous studies on injection molded PLA/PHA blends showed that the addition of about 10 wt.% PHA improves the tensile ductility of PLA considerably. In this work, we investigate a similar route of utilizing PLA/PHA blends for improving the ductility of printed parts, a topic that has not been investigated so far.

2. Materials and Methods

An Ultimaker 2+ FDM 3D printer printed the dog-bone shaped tensile test specimens according to the ASTM D638-4 standard. The filament material is a PLA/PHA blend filament (90:10 wt.%), purchased from Colorfabb (Netherlands). We considered nozzle temperatures in the range of 190°C–260°C and prepared 5 identical specimens for each condition. A Z250 Zwick/Roell universal testing machine mechanically tested the specimens and an Ultima IV Rigaku X-ray diffractometer analyzed the microstructure using $\theta - 2\theta$ geometry in the 2θ range of 0–40°. For comparison purposes, a set of pure PLA specimens were also printed and tested.

3. Results and Discussion

The addition of PHA to PLA dramatically improves the ductility for the nozzle temperatures in the range of 200 – 240°C. The greatest improvement takes place for the nozzle temperature of 220°C, resulting in an elongation at fracture exceeding 200%. At a low nozzle temperature of 190°C, premature failure takes places due to poor bonding between the printed lines. On the other hand, 260°C specimens also fail in a brittle fashion, which we attribute to the partial decomposition of the polymer at this temperature. The increase in the ductility is accompanied with a reduction in tensile strength, on the order of 20%, compared to pure PLA parts.

4. Conclusions

The result demonstrate that the utilization of a PLA/PHA blend instead of pure PLA can improve the ductility of printed parts dramatically, at the expense of slightly reduced tensile strength. Therefore, PLA/PHA blend filament is a promising material for applications that require high damage tolerance, such as the printing of load-bearing components.

References

1. Mohamed, O.A., Masood, S.H. and Bhowmik, J.L., 2015, Advances in Manufacturing, 3, 42-53.
2. Carrasco, F., Pagès, P., Gámez-Pérez, J., Santana, O. O. , 2010, Polymer Degradation and Stability, 95, 116-125.
3. Bugnicourt, E., Cinelli, P., Lazzeri, A. and Alvarez, V. A., 2014, Express Polymer. Letters, 8, 791-808.

Synthesis of Barium Strontium Titanate (BST) Ceramics for Tunable Polymer Matrix Composite Substrates

Nazlı ÖZKARAGÖZ, Başar SÜER, Arcan F. DERİCİOĞLU
Middle East Technical University
Turkey

Abstract
This study is about one of the ferroelectric materials, Barium Strontium Titanate (BST), which exhibits tunable dielectric properties under varying applied bias voltage at wide frequency ranges. BST has high dielectric constant at about its Curie temperature. Compared to other materials, BST has a relatively high Curie temperature value, which is not suitable for some specific working conditions. Therefore, by changing the Ba content of BST, Curie temperature approaches to room temperature. Besides the challenge about the working temperature, BST is a ceramic material brittle in nature limiting its usage especially in conformal areas. To overcome this limitation BST dispersed polymer matrix composites can be utilized instead of monolithic BST ceramics because of their superior processability and flexibility.

1. Introduction

In recent years, demand for new generation tunable materials has increased. Tunable in this context means the control over the dielectric constant of the material via an applied external voltage. Tunability is provided by ferroelectric materials. Ferroelectric materials are affected by an applied electrical field and polarization occurs. Above Curie temperature, ferroelectric materials become paraelectric where they are not affected by the electrical field. One of the ferroelectric materials which is used in tunable applications is Barium Strontium Titanate (BST). BST has perovskite structure which provides strong dependency of dielectric constant on electric field. By changing Ba content of BST, Curie temperature drops to around room temperature where the material reveals highest dielectric constant and becomes available for applications including radar and communication systems operating at room temperature [1]. Consequently, BST is a good choice for microwave applications, yet flexible substrates available for conformal applications cannot be provided by BST. For this reason, BST/polymer composites having high dielectric constant and low loss tangent which also reveal easy processability and desirable flexibility are being developed [2]. In these composites BST particle size, particle distribution and particle loading are critical parameters effective on the tunability performance.

2. Materials and Methods

In this study, during the production of the BST particles two different mixing methods, namely conventional mixing and centrifugal mixing, were used. Barium carbonate, strontium carbonate and titanium dioxide were mixed at a specific proportion. The mixture was pressed as pellets which was subsequently calcined at different temperatures from 900 to 1100 °C for 7 h and sintered at 1100 °C for 5 h. Followingly, sintered material was crushed using mortar and pestle. As for the polymeric matrix of the composites polystyrene (PS) was chosen as a preliminary material. After dissolving PS in a solvent, BST particles were added to polymeric solution and mixed using magnetic stirrer. This mixed solution was cast as thin films on glass substrate by tape casting. Chemical analysis, XRD and scanning electron microscopy were used for the characterization of the BST particles. Free-space measurement method has been used to measure the dielectric constant and loss tangent of the resulting BST/polymer composites in 2-18 GHz frequency range.

3. Conclusion

BST is a good candidate for microwave applications, where tunability on the dielectric properties of this ferroelectric ceramic can be achieved by an applied bias voltage. As monolithic BST films are not applicable at conformal applications, BST particle dispersed polymer matrix composite substrates can be used in such applications. Chemical composition of the BST particles as well as their size, loading and distribution are key parameters for controlling the tunability of the resulting composites.

References

[1] J. Xu,W. Menesklou, E. Ivers-Tiffée, “Processing and properties of BST thin films for tunable microwave devices,” Journal of the European Ceramic Society ,Vol.24, Issue 6, Pages 1735-1739, 2004.
[2] E. Hajisaeid, M. Haghzadeh, M. Shone, P. Mooney, A. Panwar, C. Barry, J. Mead, C. Armiento, A. Akyurtlu, “Printed tunable frequency selective surface on a developed flexible functionalized ceramic-polymer based substrate,” IEEE International Symposium on Phased Array Systems and Technology (PAST), 1-5, 2016.

Production and Characterization of B_4C Reinforced Al-8.5Si-3.5Cu Matrix Composites via Powder Metallurgy

Berk ŞENYURT, Nazlı AKÇAMLI
Bursa Technical University
Turkey

1. Introduction

Aluminum and its alloys are very critical materials for the automotive and aerospace industries due to their unique combination of light weight and high strength properties. On the other hand, their applications remain limited because of their low strength and wear resistance properties. To improve aluminum alloys' mechanical properties, several reinforcements such as carbides, borides, etc. were added to the aluminum matrix. Boron carbide's extremely high hardness and low density make it very suitable reinforcement agent for the Al matrix composites which are designed as military armors and light weight aircraft bodies [1-3].

2. Materials and Method

In this study, B_4C reinforced (0, 5, 7.5 and 10 % wt.) Al-8.5Si-3.5Cu alloy matrix composites were produced via powder metallurgical route. Al, Si, Cu and B_4C powders were mechanically alloyed for different durations up to 7 h in a planetary ball mill using WC milling medium under Ar atmosphere. The MA'ed powders are transformed into bulk structures via a sequential process of uniaxial pressing at 500 MPa and pressureless sintering at 555 °C for 2 h under Ar atmosphere. The effects of MA time and B_4C amount on the microstructural and mechanical properties were investigated.

Microstructural characterization and phase analysis of the as-blended, MA'ed powders and bulk specimens were carried out by X-Ray diffraction (XRD) and scanning electron microscopy (SEM) techniques. Additionally, characterization of the sintered samples in terms of physical, mechanical and tribological properties were performed with Archimedes density, microhardness and reciprocating wear tests. As a result, the optimum conditions for fabrication of B_4C reinforced Al-Si-Cu matrix composites were determined.

3. Results

According to XRD analysis (Fig. 1a), B_4C particles remained stable after mechanical alloying for 7h and sintering process. Archimedes densities of 7 hours MA'ed composites reinforced with 0, 5, 7.5, 10 B_4C are determined respectively as 95.22%, 98.70%, 98.47% and 99.1%. The hardness value of 7 hours MA'ed sample increased to 167 HV from 110.9 HV by the addition of 10 wt.% B_4C (Fig. 1b). Homogenous distribution of the B_4C particles and Al_2Cu intermetallic phase are observed in Al matrix in via SEM-EDX analysis.

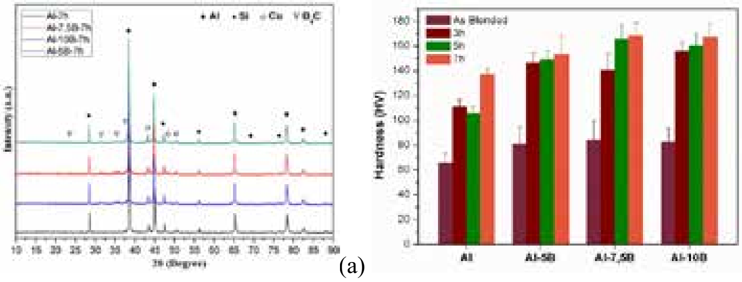

(a) (b)

Fig 1. (a) XRD patterns and (b) hardness values of Al-8.8Si-3.5Cu-xB_4C (x: 0, 5, 7.5, 10 wt.%) composites.

References

1. Azimi, A., Shokuhfar, A., Nejadseyfi, O. 2015. "Mechanically alloyed Al7075–TiC nanocomposite: Powder processing, consolidation and mechanical strength", Materials & Design, 66, 137-141.
2. 18. Woo, K. D., Zhang, D. L. 2004. "Fabrication of Al–7wt%Si–0.4wt%Mg/SiC nanocomposite powders and bulk nanocomposites by high energy ball milling and powder metallurgy", Current Applied Physics, 4 (2-4), 175-178.
3. Javad, M., Isfahani, N., Payami, F., Asadi, M., & Asghar, A. 2019. Investigation of the effect of boron carbide nanoparticles on the structural, electrical and mechanical properties of Al-B4C nanocomposites. Journal of Alloys and Compounds, 797, 1348–1358.

Electrostatic Flocking of Small-Sized Flocks

M. Utku YILDIRIM[1], Erhan BAT[2], Bora MAVİŞ[1]
[1]Hacettepe University, [2]Middle East Technical University
Turkey

Abstract
This study is performed to investigate the experimental setup and process parameters required to position the short flocks perpendicular to the carbon fiber prepregs. The conductivity of the epoxy is much lower than the water-based adhesives used in the textile industry. Low conductivity requires the parameters to be more precisely adjusted for the vertical positioning of the flocks. In order to increase the vertical alignment of shorter flocks and control their surface density; applied voltage, application time and distances of the flock reservoir and the target to a grid placed in between them were varied.

1. Introduction

Electrostatic flocking has been shown to be a promising technique in advanced applications like interfacial toughening of layered composites. Although shorter flocks were more effective in increasing interfacial toughness, in these focused studies, the shortest flocks used have not been less than 1.3 and 0.6 mm for N66 and polyester flocks, respectively [1]. Moreover, the effect of areal density of the flocks on mechanical properties have not been studied in depth. On the other hand, the z-pinning effect of flocks in bridging a crack can be expected to improve as the flock feature sizes would approach the sizes of the “hills and troughs” of the prepregs used. In contrary to the generally sought high values for densities in commodity item coatings, a well-controlled areal density of flocks in these high end applications can be critical. For testing these hypotheses, the knowledge of electrostatic flocking of flocks with small feature sizes is essential. Previous studies show that positioning short flocks vertically is more difficult than taller [2]. Here, we focus on the effect of experimental parameters that can possibly affect the density and vertical alignment of shorter flocks on carbon fiber prepregs.

2. Materials and Methods

The predetermined static voltage was applied to a metal grid between the two grounded plates. The flocks placed on the bottom plate were carried perpendicularly to the top plate where an epoxy matrix carbon fiber prepreg was placed. The effects of the distance between metal grid and grounded plates, variable voltage values and its application time on flock areal density and vertical alignment were studied. 0.6 mm and 0.4 mm long N66 flocks were used as the examples of the shortest flocks that could be provided from the commercial vendors.

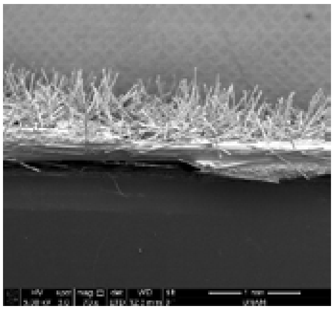

Figure 1. 0.6 mm N66 flocks on carbon fiber prepreg

3. Conclusion

The distance from the metal grid to which the voltage is applied, should be precisely adjusted to allow enough time for the flocks to reach vertical position (i.e. parallel to the electrical field lines) while travelling in the electrical field towards the target. The smallest value of the distance depends on the specific flock size. The combined factor, field intensity, which can be represented as V/cm, was found to be more effective compared to electrical field application time, on flock density. The improvements in the vertical alignment and the homogeneity of the areal density of the shorter flocks (0.4 mm versus 0.6 mm) on the prepregs are remarkable.

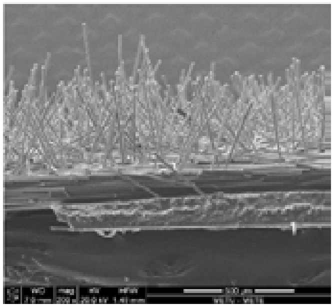

Figure 2. 0.4 mm N66 flocks on carbonfiber prepreg

Acknowledgment
The authors acknowledge use of the services and facilities of UNAM-National Nanotechnology Research Center at Bilkent University and the financial support from TÜBİTAK (Project No: 214M110) and Hacettepe University (Project No: FYL-2020-18719).

References

1. Kim, Y.K. and A. Lewis, Journal of Advanced Materials -Covina, 2017.
2. Yu, Z., S. Wei, and J. Guo, Journal of Materials Science: Materials in Electronics, 2019.

Hollow Glass Microsphere and Glass Bead-Polyamide 12 Composites Production by Selective Laser Sintering Method

Burçin ÖZBAY[1,2], İ. Ersin SERHATLI[2], M. Enes BULDUK[1]
[1]Fatih Sultan Mehmet Vakif University, [2]Istanbul Technical University
Turkey

Abstract

Selective Laser Sintering (SLS) is one of an Additive Manufacturing (AM) method, which is still a developing technique for many different areas, such as aerospace, automotive applications, and medical materials. However, density reduction is a critical issue in terms of the automotive and aerospace industries to reduce CO_2 emission and also to increase fuel effectiveness. Therefore, hollow glass microsphere's density decrease effect was investigated and compared with the same amount of glass bead (filled glass microsphere) filled polymer composite structures. This research covers the production and characterization of hollow glass microsphere and glass bead added Polyamide 12 polymer composites production by SLS-AM technique. Density measurements and also tensile, flexural, and impact properties of all produced structures were investigated. Performed density measurement results demonstrated that the density of 20 % of hollow glass microsphere filled sintered samples have been significantly reduced up to 20 % according to neat PA 12. On the other hand, 20 % of glass bead filled composites showed approximately 14 % higher density than neat PA 12.

1. Introduction

Selective laser sintering (SLS) is a powder bed fusion (PBF) additive manufacturing (AM) technique that uses high-energy beams (laser beams, electron beams, or an infrared panel heater) to melt polymer particles by a layer-by-layer procedure to design and create 3D solid models [1-3].

The “Sintering Window” is one of the most essential criteria of the availability of a polymer powder in the laser sintering (LS). The “Sintering Window” covers the area between the starting point of the crystallization temperature (Tc onset) and the starting point of the melting temperature (Tm onset). And it changes according to polymer type, the type and amount of the additive used in the polymer. The differential scanning calorimetry (DSC) evaluation of polymers enables the determination of the temperatures/temperature ranges that can be selected in LS process [4], [5]. Figure 1 shows an exemplary sintering window area in a DSC thermogram.

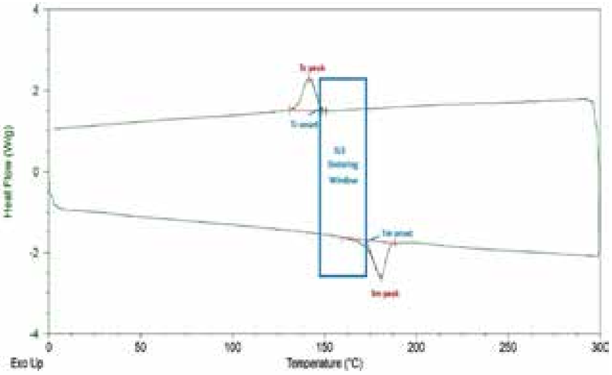

Figure 1. DSC Thermogram- Laser Sintering (LS) temperature range as “Sintering Window”

The most commonly used thermoplastic polymers in this method are polyamides (mainly PA 12, followed by PA 11, PA 6), and some of the following and non-polyamide polymers (Polystyrene (PS), Polypropylene (PP), Polyethylene (PE), Thermoplastic Polyurethane (TPU), etc). Besides, to create polymer composite structures via SLS method, filled glass spheres (glass beads), silicon carbide, aluminum powder, hydroxyapatite, nano-level inorganic fillers such as nano-silica, nano-size clay, nano-Al2O3, etc. could be used [3], [6-8].

According to the literature review, several studies can be found about filled polymers in SLS technique [9-11]. However, the production of density reduced SLS parts, which are filled with hollow glass microspheres and a comparison between glass bead filled ones, have not been under research before. One of our study was related to how different amounts of hollow glass microsphere effect PA 12 polymer composites in terms of physical and mechanical properties

[12]. However, this study has been covered that the comparison of the same amount of glass bead filled PA 12 polymer composite with HGM filled PA 12 composite in terms of mechanical features and density data. The results were compared according to the physical and mechanical properties of all sintered samples.

2. Experimental Procedure

Polyamide 12 (PA2200, *EOS GmbH*) was used as the polymer matrix in this work. As glass additives, Hollow Glass Microsphere (HGM) iM16K from *3M^{TM,}* and Glass Bead (GB) 3000 CP03 from *Potters Industries* were used. EOS P 110 (EOS GmbH) SLS production machine with 100 microns of layer height was used.

In this laser sintering method Energy Density (ED) calculation were done with below formula [13], where ED, P, v, h, d is energy density (J/mm^2), laser power (W), laser beam speed (mm/s), scan spacing (mm), respectively.

$$ED = \frac{P}{v\,.h} \tag{1}$$

SLS production of unfilled PA 12 was done with EOS default parameters, which can be seen in Table 1, and the processing temperature was 170 °C. On the other hand, SLS processing parameters of 20 % of HGM and GB filled polymer composites were detected as below (in Table 1) after several laser parameter determination experimental trials, which include energy density values that are changing from 0.020 J/mm^2 to 0.100 J/mm^2. At this point, several parameter determination trials were needed while HGM and GB addition crystallization temperatures are increasing because of the additives act as a nucleus in the polymer matrix. In addition, the processing temperature was defined as 176 °C for composites according to thermal analysis results and also experimental trials from 170 °C to 178 °C.

Table 1. Selective laser sintering process parameters

Material	Building Chamber Temperature (°C)	Laser Power (mm/s)	Scan Speed (mm/s)	Hatch Distance (mm)	Energy Density (ED) (J/mm^2)
PA 12	170	21	2500	0.25	0.0336
PA 12-20% GB	176	21	1787	0.25	0.0470
PA 12-20% HGM	176	21	1787	0.25	0.0470

2.1. Processing and characterization

Firstly, thermal analysis (Differential Scanning Calorimetry (DSC) was done to detect the processing temperature ranges, which calls as "Sintering Window". After that, optimum process temperatures and process parameters were determined with several parameter determination trials, and tensile, 3-point bending flexural test and notched charpy impact test specimens were manufactured for all different compositions and for PA 12 itself. Additionally, the density measurement samples of polymer and polymer composite samples were produced.

To characterize the used polymer powder and additives and observe cross-sectional areas of manufactured composite samples after mechanical tests, Scanning Electron Microscopy (SEM) was used.

3. Results and Discussion

According to optimized processing values, polymer composites were manufactured, and the physical and mechanical tests were performed at related international standards [14-16]. From Figure 2 to Figure 5, tensile test, 3-point bending test, notched charpy impact test, and density measurement results can be seen with their standard deviation values, respectively.

The tensile test results can be seen in Figure 2. Unfilled PA 12 samples showed 48.07 MPa of average maximum tensile stress, 1.66 GPa of tensile modulus, and 28.99 % of maximum elongation at break value. While maximum tensile stress results were lower than unfilled PA 12, E-modulus values increase with GB and HGM addition.

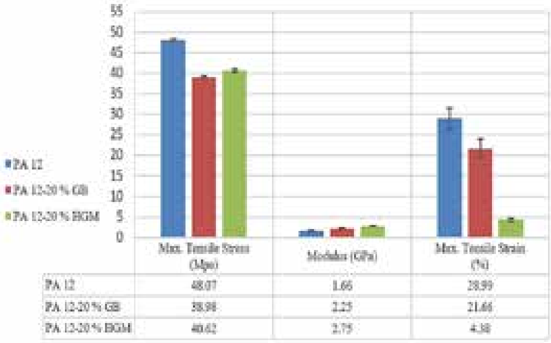

Figure 2. Tensile test results

Figure 3 shows 3 Point bending flexural test results of unfilled and filled PA 12 structures. PA 12 had 1.68 GPa, 67.58 MPa, and 7.70 % of flexural modulus, maximum flexural stress, and maximum flexural strain, respectively. By the addition of GB, flexural values were not changed much. In comparison, HGM added to the polymer, especially flexural modulus increases significantly, and maximum strain value decreases.

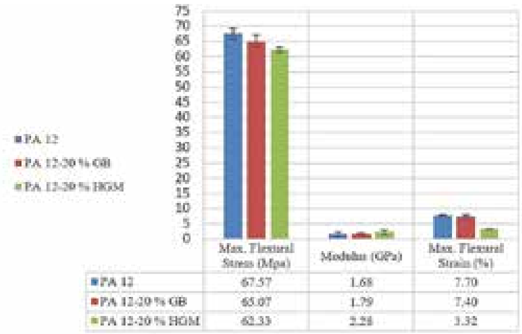

Figure 3. 3 Point bending flexural test results

In Figure 4, notched charpy impact test result can be found. While the result of PA 12 itself was 7.66 kJ/m^2, with GB addition the impact strength value reached to 11.80 kJ/m^2, and decreased at 4.70 kJ/m^2 with HGM addition.

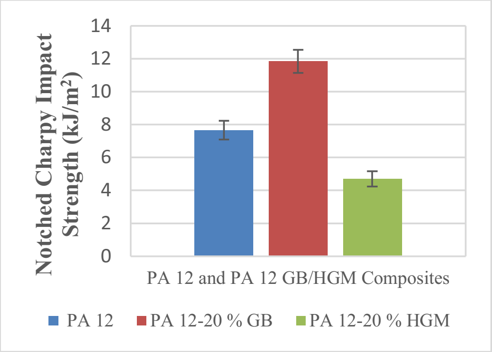

Figure 4. Notched charpy impact strength test results

Figure 5 illustrates the density measurement results of PA 12 and polymer composites. The density of PA 12 sintered samples was 1.01 g/cm^3. By the addition of GB the density increased to 1.15 g/cm^3; in contrast, by the addition of the same amount of HGM, it reduced to 0.80 g/cm^3.

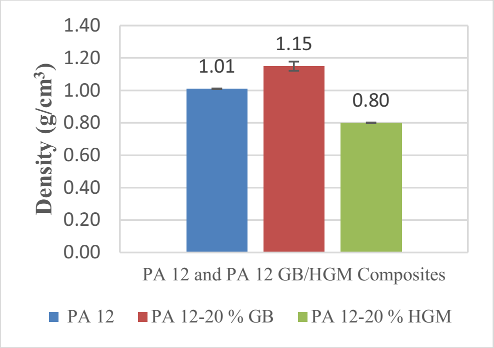

Figure 5. Density measurements

The below figures demonstrate SEM images of cross-sectional areas of GB and HGM filled composite structures after mechanical tests. According to SEM observations, it can be said that HGM had a more homogeneous mixture and better interface connection with the polymer matrix.

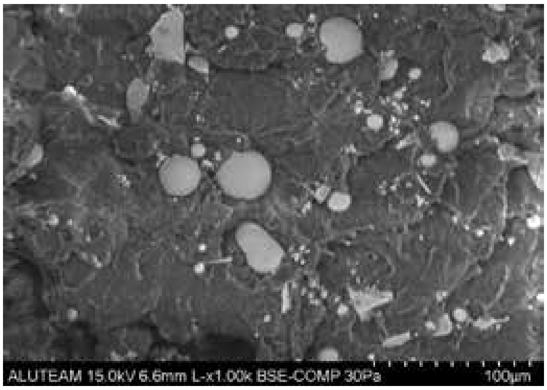

Figure 6. SEM Image of 20 % GB filled PA 12 composite

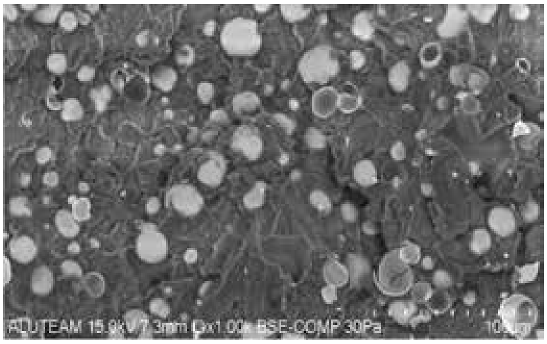

Figure 7. SEM Image of 20 % HGM filled PA 12 composite

4. Conclusion

In this research the effects of GB (filled glass microsphere (glass bead)) and HGM (hollow glass microsphere) on PA 12 polymer matrix were investigated in terms of density values and mechanical test results of produced samples by SLS-AM method.

According to performed mechanical tests maximum tensile stress results of composites were lower than unfilled PA 12, E-modulus values increase by the addition of GB and HGM. In addition, when GB added to PA 12 matrix flexural values were close to unfilled PA 12 itself. However, by HGM addition E-modulus, therefore, stiffness of the structure was increased, while maximum flexural strain was decreased.

When density measurement results were investigated, it can be inferred that HGM addition saved a 20 % density reduction to the structure. On the other hand, the same amount of GB addition increased the density of the structure by almost 14 %.

However, SEM observations showed that HGM had a better connection with the polymer matrix. The reason for the reduction in tensile stress results may be because of a weak interface connection between GB additive and PA 12 matrix. Besides, the reduction at some mechanical results of HGM added polymer composites may be due to the hollow featured structure of glass microspheres.

All in all, HGM added polymer composites production by SLS additive manufacturing technique, which has a great potential to especially aerospace and automotive industries thanks to their high amount of density reduction ability.

Acknowledgment

Fatih Sultan Mehmet Vakif University, Aluminum Test Training and Research Center is supported by Istanbul Development Agency (ISTKA).

References

[1] ISO/ASTM 52900:2015 (2015). Additive Manufacturing General Principles, Terminology. International Organization for Standardization (ISO).

[2] A. M. Forster, Materials Testing Standards for Additive Manufacturing of Polymer Materials: State of the Art and Standards Applicability, National Institute of Standards and Technology, 2015, Gaithersburg, United States.

[3] J. R. C. Dizon, Jr. A. H. Espera, Q. Chena, R. C. Advincula, Mechanical Characterization of 3D-Printed Polymers, Additive Manufacturing, 20 (2018) 44-67.

[4] M. Schmid, Laser sintering with plastics technology, processes, and materials, Hanser Publications, 2018, Cincinnati, United States.

[5] M. Schmid, K. Wegener, Additive manufacturing: Polymers Applicable for Laser Sintering (LS), International Conference on Manufacturing Engineering and Materials, (ICMEM 2016), 6-10 June 2016, Nový Smokovec-Slovakia, pp. 457-464.

[6] S. Kumar, Selective Laser Sintering: Recent Advances, Journal of Laser Applications, 607 (2010) 1-8.

[7] C. Yan, L. Hao, L. Xu, Y. Shi, Preparation, Characterization and Processing of Carbon Fiber/Polyamide-12 Composites for Selective Laser Sintering, Composites Science and Technology, 71 (2011) 1834-1841.

[8] A. A. Mousa, The Effects of Content and Surface Modification of Filler on the Mechanical Properties of Selective Laser Sintered Polyamide12 Composites, Jordan Journal of Mechanical and Industrial Engineering, 8 (2014) 265-274.

[9] W. Jing, C. Hui, W. Qiong, L. Hongbo, L. Zhanjun, Surface Modification of Carbon Fibers and The Selective Laser Sintering of Modified Carbon Fiber/Nylon 12 Composite Powder, Materials and Design, 116 (2017) 253-260.

[10] P. K. Jain, P. M. Pandey, P. V. M. Rao, Selective Laser Sintering of Clay-Reinforced Polyamide, Polymer Composites, 31 (2010), 732-743.

[11] S. Negi, R. K. Sharma, S. Dhiman, Experimental Investigation of SLS Process for Flexural Strength Improvement of PA-3200GF Parts, Materials and Manufacturing Processes, 30 (2015), 643-653.

[12] B. Özbay, İ. E. Serhatlı, M. E. Bulduk, Manufacturing and Characterization of Filled Polyamide 12 Composite Structure by Selective Laser Sintering Method, 5th Edition of International Conference on Polymer Science and Technology, 10-11 June 2019, Berlin-Germany, pp. 26.

[13] S. A. Aldahsh, Development of A New Composite Powder Material of Cement Additive with Polyamide 12 for Selective Laser Sintering, PhD Thesis, 2011, Cardiff University, Cardiff, United Kingdom.

[14] ISO 527-2:2012 (2012). Plastics-Determination of tensile properties-Part 2: Test conditions for molding and extrusion plastics. International Organization for Standardization (ISO).

[15] ISO 178:2019 (2019). Plastics-Determination of flexural properties. International Organization for Standardization (ISO).

[16] ISO 179-1:2010 (2010). Plastics-Determination of Charpy impact properties-Part 1: Non-instrumented impact test. International Organization for Standardization (ISO).

Corrosion and Wear Resistance of Aluminum Bronze Increased by Heat Treatment

Aleattin KULAKLI, Talip ÇİTRAK, Serdar TOZKOPARAN, Aydın Barış ŞİMŞİR, Edanur KASAP
Sağlam Metal A.Ş.
Turkey

Abstract

In this study we investigated the effect of heat treatment on the properties of nickel-containing aluminum bronze (CuAl10Ni5Fe4 alloy). The alloy was produced by melting scrap in a metal induction furnace, pouring molten metal into a mold made of steel and applying hot forging processes. In order to examine the effect of heat treatment on the phase structure of the alloys, microstructural examination was also conducted. Micro hardness was measured using the relevant test devices. Potentiodynamic corrosion tests were performed in a neutral NaCl solution in order to determine the corrosion rates of the forged and heat-treated alloys. Furthermore, wear behavior of alloys under 10 N and 40 N loads was investigated. General results suggest that solution and aging treatment contribute to improvement in the corrosion and wear resistance of the CuAl10Ni5Fe4 alloy.

1. Introduction

Aluminum bronze is very useful in a great number of engineering structures with a variety of the alloy finding its applications in different industries [1]. Aluminum bronze contains 5 to 12% Al as its primary alloy element. The iron, nickel and manganese additions enable this alloy to be used commercially [2]. Nickel aluminum bronze casting alloys are increasingly used in areas where high strength, high impact properties and good corrosion resistance are required [3]. The addition of nickel increases the alloy's strength without diminishing its excellent ductility, toughness and corrosion resistance. These alloys are mainly used in valve seats, piston tips, marine engine shafts, valve guides, pump shafts and aircraft components [4].

Typical as-cast microstructures are seen in Figure 1 and show light etching areas of copper-rich solid solution or α-phase, some dark etching regions of "retained β", and intermetallic "κ" phases. The large dendritic precipitate (Figure 1(b)) is κ, the smaller dendritic precipitates with dimensions of 5 to 10 µm are κ_{II}, and the finely dispersed particles, <1 µm diameter, located in α-grains, are κ_{IV}. The lamellar intermetallic phase is κ_{III} [5].

Depending on the application, the alloy is subjected to various heat treatments such as annealing, solution or aging in order to achieve different levels of hardness and microstructure in the alloy [6, 7].

In this study the properties of the CuAl10Ni5Fe4 alloy in forged and heat-treated condition was investigated. The alloy was produced through melting of metal scrap in an induction furnace, pouring the melt into a mold made of steel. After casting, the ingot was subjected to hot forging, solution treatment, quenching and aging. The microstructure of the samples was investigated in order to visualize the phase structures of the alloys.

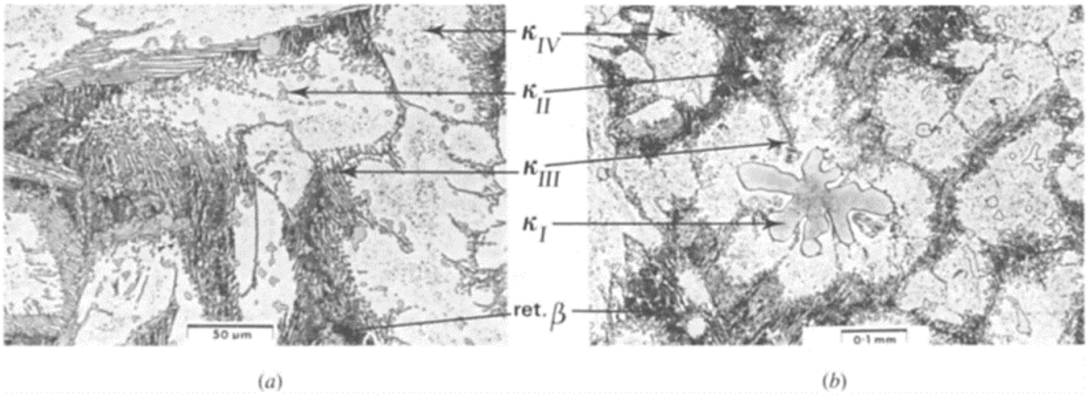

(a) (b)

Figure 1. The as-cast microstructure of (*a*) Alloy 1 and (*b*) Alloy 2. The phases and their distribution are similar in both alloys, except that Alloy 2 (with the higher Fe content) contains large κ_I particles [5].

Hardness values were evaluated by utilizing the relevant test devices. A potentiodynamic corrosion test was conducted in a neutral NaCl solution in order to measure the corrosion resistance of the forged and heat-treated samples. Also, wear resistances of the alloys under loads of 10 N and 40 N were measured at room temperature.

2. Experimental Procedure

The chemical composition of the aluminum bronze casting that was studied is given in Table 1. A standard CuAl10Ni5Fe3 alloy (C63000) was used as the reference material.

Table 1. Chemical composition of the cast aluminum bronze

Sample	Chemical composition (wt %)				
	Cu%	Al%	Ni%	Fe%	Mn%
Alloy	81	9.89	5.10	3.0	0.87

Charge weighting 10 kg were melt in a 15 kg capacity induction furnace and poured into a cylindrical shaped cast iron mold. The major body of the ingot was hot forged into bars with a cross-section of 40 mm x 24 mm (held at 800 °C for 1 h before the forging). Forged samples were solution treated at 800 °C for 1.5 hours and aged at 500 °C for 2 hours.

Micro hardness values of all the samples (as-cast, forged and aged) were measured through Vickers indentation. The hardness measurement was performed using a Future-Tech FM800E micro hardness tester under a load of 1000 gf which was applied for 10 seconds. Furthermore, microstructural investigations to the as-cast, hot forged, solution treated and aged materials were carried out via an optical microscope (Nikon Eclipse MA100) after polishing and chemically etching the samples. The samples were chemically etched in micro scale by immersion in 100 ml pure water containing 50 ml HCl, 10 ml HNO_3 and 10 g $FeCl_3$. Potentiodynamic corrosion tests were performed to determine the corrosion rates of the forged alloys in a neutral NaCl solution. In addition to the corrosion experiments, the samples were subjected to wear test at room temperature under loads of 10 N and 40 N. Test parameters were determined as 20 mm, 500 m and 120 mm/s for impingement distance, sliding distance and sliding velocity respectively while a 6 mm diameter ball made of 1040 steel was used as the abrasive material.

3. Experimental Results

In this section, results derived from each type of characterization process are presented with brief comments.

3.1. Microstructural Investigations

As-cast microstructure of the alloy, the photograph of which is given in Figure 2(a), represents the typical microstructure described in many studies about a nickel containing aluminum bronze. Copper-rich α (alpha) solid solution phase, martensitic β (beta) phase and some intermetallic κ (kappa) phases (fine κ_{III} and black spherical κ_{IV}) were identified in this microstructure [6]. On the other hand, as-cast microstructures of the alloys are expected to get considerably finer as a result of the forging. The forged alloy (Figure 2(b)) involves the same α, β and κ phases as in its as-cast condition. Solution treatment and quenching conditions dissolve the κ phase in the eutectoid (expect the globular κ_{II}) and the β phase transforms to the non-equilibrium β^I phase. Upon quenching and aging, fine κ_{IV} precipitates form in the β^I phase. The β^I phase and fine precipitates provide the quenched and aged material with high hardness at low aging temperature. With increasing aging temperature, the size of α grains grows. Slow cooling leads to coarsening of the κ precipitates and to the formation of larger amounts of lamellar κ_{III} precipitates in the eutectoid. The κ phase also precipitates along the α grain boundaries. With increasing α grain size the strength and hardness decrease [3]. The heat-treated microstructure of the alloy, the image of which is given in Figure 2(c), involves spherical α grains and κ phases. SEM and EDS examinations are needed to make the phase analysis more accurate in case of heat treatment. Phase components will be determined in detail by conducting SEM examinations of the alloys in future studies.

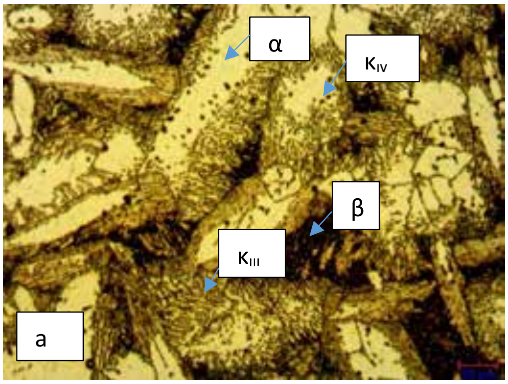

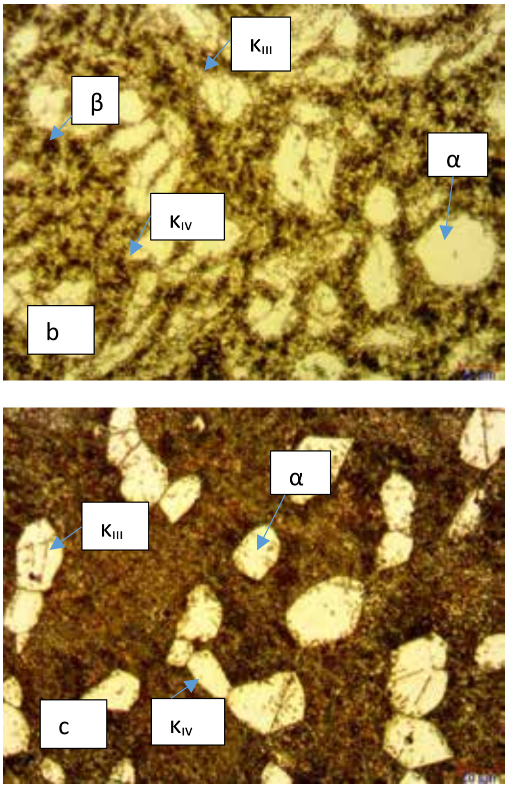

Figure 2. Optical micrographs of (a) as-cast, (b) forged and (c) solution treated and aged (magnification: 500x)

3.2 Hardness Measurements

Results of Vickers micro hardness measurements of as-cast, forged and aged samples of the alloy are presented in Table 2. The hardness values of the alloy were very different, depending on the process conditions. Forging resulted in a significant hardness increase in the alloy. After the aging the hardness decreases compared to forged condition. The decrease is thought to be due to the increase in the α grain size in the microstructure.

Table 2. Vickers micro hardness measurement results of as-cast, forged and aged samples of the alloy

Sample	Average hardness value (HV_{1000})		
	as – cast	forged	Solution treated and aged
Alloy	199.80	256.10	221.93

3.3. Potentiodynamic Corrosion Test

After the completion of the potentiodynamic corrosion test that was conducted in a neutral solution containing 3.5 % NaCl, corrosion rate values of the alloys were calculated as presented in Table 3. Between the forged and aged alloys, the forged alloy exhibited a higher corrosion rate compared to the aged alloy. The heat treatment process decreased the corrosion rate significantly. It is estimated that the reason for the increase of corrosion resistance in the aged condition may be due to the presence of κ phases, which increase the corrosion resistance and decrease β phases that negatively affect the corrosion resistance.

Table 3. Calculated corrosion rates of the forged and aged samples of the alloy

Sample	Corrosion rate, mm/year
Forged alloy	2.62
Solution treated and aged alloy	2.46

3.4. Abrasive Wear Test

Measurement results of the wear test are given in Table 4. Wear area loss of forged and aged alloys under load of 10 N were 0.03 mm² and 0.039 mm², respectively. Between samples, results of alloy wear loss were similar for both process conditions. Wear area loss of forged and aged alloys under load of 40 N were 0.40 mm² and 0.16 mm², respectively. It's clear that the wear resistance of the alloys was increased after aging and under load of 40 N.

Table 4. Measured wear resistances of the forged and aged samples of the alloy

Sample	Wear resistance, mm^2/10 N	Wear resistance, mm^2/40 N
Forged alloy	0.03	0.40
Solution treated and aged alloy	0.039	0.16

4. Conclusions

In this study the hardness, wear and corrosion resistance of forged and aged aluminum bronze (CuAl10Ni5Fe4) was compared. Heat treatment process affected hardness, wear and corrosion resistance significantly. Hardness value decreased at 500 °C in the aged condition. On the other hand, heat treatment increased the wear and corrosion resistance of the aluminum bronze.

REFERENCES

[1] Nwaeju, C. C., Odo, J. C., & Nnuka, E. E., *Effect of niobium addition on the structure and mechanical properties of aluminium bronze (Cu-10% Al) alloy,* International Journal of Research in Advanced Engineering and Technology, 2, 70-75, (2015).

[2] Yuanyuan Li, T. L. NGAI, *Grain refinement and microstructural effects on mechanical and tribological behaviours of Ti and B modified aluminum bronze*, Second Department of Mechanical Engineering, South China University of Technology, Guangzhou, People's Republic of China, Journal of Materials Science 31 (1996) 5333-5338.
[3] E. A. Culpan, G Rose, *Microstructural characterization of cast nickel aluminum bronze*, Admiralty Underwater Weapons Establishment, Portland, Dorset, UK, Journal of Materials Science 13 (1978) 1647-1657.
[4] Peter Slama, Jaromır Dlouhy, Michal Köver, *Influence of heat treatment on the microstructure and mechanical properties of aluminum bronze*, Comtes FHT a.s., Prumyslova 995, 334 41 Dobrany, Czech Republic, ISSN 1580-2949 MTAEC9, 48(4)599(2014).
[5] A. Jahanafrooz, F. Hasan, G. W. Lorimer, and N. Rıdley, *Microstructural Development in Complex Nickel-Aluminum Bronzes*, Metallurgical Transactions A, Volume 14A, October 1983-1951.
[6] Muhammad Kamran Yaseen, Muhammad Mansoor, Haider Ali Ansari, Sajawal Hussain and Saheed Khan, *Effect of heat treatment on tribological characteristics of CuAl10Ni5Fe4 nickel aluminum bronze*, Institute of Industrial Control Systems, P.O. Box 1398, Rawalpindi, Pakistan, Key Engineering Materials, ISSN: 1662-9795, Vol. 778, pp 61-67.
[7] H. Meigh, *Cast and Wrought Aluminum Bronzes Properties, Processes and Structure*, Copper Development Association, 2002, Hanover, USA.

Fabrication of Colloidal and Conductive $LiFePO_4$ Particles for Suspension Flow Batteries

Yasemin AŞKAR[1], Bayram YILDIZ[1], Bora MAVİŞ[2], Simge ÇINAR[1]
[1]Middle East Technical University, [2]Hacettepe University
Turkey

Abstract

Carbon coating of electroactive particles is critical for energy storage materials due to its positive effects on electrical conductivity and chemical stability of particles. Even though carbon coating is widely applied for electroactive materials such as $LiFePO_4$ (LFP), homogeneous distribution of the coating over the particles is still a challenge. Achieving the homogeneous dispersion with effective conductivity can be difficult as nanoparticles tend to agglomerate. In this study, LFP particles were coated by carbon via *ex-situ* method. To this end, dispersable LFP powders and cetrimonium bromide (CTAB) were used as the electroactive starting material and as a carbon source, respectively. Interactions between CTAB and LFP particles were optimized in such a way that individual particles can be homogeneously coated by the carbon source. CTAB coated particles were pyrolyzed and the fabricated C-coated particles were analyzed in terms of their morphology, crystal structure, conductivity and dispersion characteristics.

1. Introduction

Demand for the development of Li-ion cathode materials have been increasing because of their high energy storage capacity. LFP stands out among other Li-based electroactive materials due to its high theoretical capacity (170mA/g). LFP has low electronic and ionic conductivity; however, this drawback can commonly be improved by carbon addition in solid state batteries[1]. Suspension flow batteries requires circulation of the highly loaded electroactive material suspension, but this causes an increase in the pump power requirement and result in high operational cost[2]. The studies on the rheological behavior of electroactive suspensions in literature highlighted that the carbon additions to the suspensions severely increase the viscosity of electroactive suspensions. It is known that the dispersion properties of colloidal particles are critical for optimization of suspension flow behavior. In this study, we used the sub-micron size colloidal LFP particles and coated them with carbon using *ex-situ* techniques in order to improve the flow behavior of suspensions. Preserving the dispersion properties of colloidal LFP particles is challenging due to the carbon bridges formed between particles during pyrolysis of the carbon source[3]. Here, we optimized the interactions between LFP particles and the carbon source, thus fabricated colloidal and conductive LFP particles. The effect of C-coating on the rheological behavior of aqueous LFP suspensions was investigated. The quality of the carbon coating and its effect on the suspension battery performance was also discussed.

2. Materials and Methods

Dispersable LFP powders were used as a starting material. In order to coat the particles by ex-situ method, particles were treated with CTAB in ethanol solution. Then, the mixture is centrifuged, subsequently annealed at 500°C under the nitrogen atmosphere. The structure of the synthesized LFP/carbon were analyzed by X-ray diffraction (XRD), scanning electron microscope (SEM) and transmission electron microscope (TEM). Dispersion characteristics of the C-coated LFP powders were analyzed by particles size and zeta potential measurements, and sedimentation analysis. Rheological behavior of their suspensions was also characterized.

3. Conclusion

The carbon coated LFP particles were successfully synthesized by ex-situ method. By control of the interactions between carbon source and the electroactive materials, quality of the C-coating around powders could be optimized. The particles were dispersable in aqueous media. Such powders are promising for use in suspension flow batteries as they reduced the viscosity of electroactive material suspensions.

References

[1] Benoit, C., Franger, S., J. Solid State Electrochem. 12, (2008) 987-993.
[2] M. Duduta, et. al. Adv. Energy Mater., 1.4 (2011) 511-516.
[3] Z. Chen, Y. Qin, K. Amine, and Y.K. Sun, 2010. Journal of Materials Chemistry, 20(36), 7606-7612.

Bimetallic Metal-Organic Frameworks for Wearable Energy Storage Systems

Farzaneh HEKMAT, Husnu Emrah UNALAN
Middle East Technical University
Turkey

Abstract

Wearable supercapacitors using highly porous Ni-Co metal-organic framework@cotton fabric (Ni-Co MOF@CF) electrodes were fabricated. The assembled electrodes showed a remarkable areal specific capacity of 119.74 mC.cm^{-2} with promising cycling stability (88% after 3000 charge-discharge cycles). The capacitive performance of the assembled supercapacitors was preserved even if they were bent or folded.

1. Introduction

In parallel with growing energy demands, developing smart energy systems, which are comprised of both energy harvesting and energy storage systems, seem to be inevitable for portable electronic applications [1]. Having the benfits of not only small band gap, but also highly active sites, bimetallic Ni-Co MOFs seem to be a promising alternative with enhanced capacitive performance compared to mono-metal counterparts [2, 3]. In this work, high-performance, cost-effective wearable electrodes using bimetallic Ni-Co MOFs@CF electrodes were fabricated through one-pot hydrothermal approach.

2. Materials and Methods

The cleaned CFs were directly decorated by Ni-Co MOFs via a one-pot hydrothermal method at a relatively low temperature. Before the hydrothermal process, a 40 ml aqueous solution containing Co, Ni and organic linker was prepared. The prepared bluish solution was then transferred to an autoclave and the cleaned CFs were immersed into the prepared solution. Afterwards, the autoclave was sealed and kept at 120 °C for 16 h. A well-maintained fiber network structure was obtained for Ni-Co-MOF decorated CFs.

Cyclic voltammetry, galvanostatic charge-discharge, and electrochemical impedence spectroscopy (results provided in Figure 1) were conducted to investigate the electrochemical performance of the prepared electrodes in a 3M aqueous KOH electrolyte.

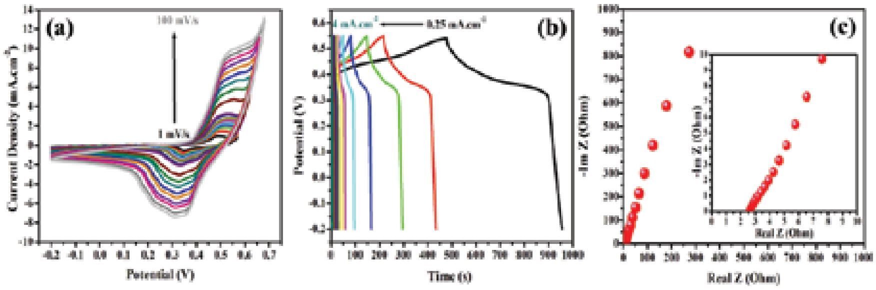

Figure 1. (a) CVs of the prepared electrodes at different scan rates, (b) GCD curves of the prepared electrode at different current densities, and (c) Nyquist plot of prepared electrode. Inset shows the magnified high-frequency range.

3. Conclusion

The fabricated electrodes showed remarkable electrochemical performance in terms of high areal specific capacity, resonable rate capability and remarkable cyclic durability. Results obtained herein, revealed that the fabricated electrodes are promising storage devices for high performance wearable electronics.

Acknowledgment

This work was supported by the Scientific and Technological Research Council of Turkey (TUBITAK) under Grant No. 119M809.

References

[1] Q. Xue *et al.*, *Small* 13 (2017) 45.
[2] Y. Xu *et al.*, *Electrochim. Acta* 285 (2018)192-201.
[3] P. C. Banerjee *et al.*, *ACS Appl. Mater. Interfaces* 7 (2015) 3655-64.

Synthesis of Lithium Iron Phosphate with Controlled Size and Shape

Elif ÇOŞKUN[1], Bayram YILDIZ[1], Yasemin AŞKAR[1], Bora MAVİŞ[2], Simge ÇINAR[1]
[1]Middle East Technical University, [2]Hacettepe University
Turkey

Abstract

Low cost, scalable energy storage will be the key for renewable energy technologies. Flow batteries are very promising for large-scale energy storage due to their scalability and flexibility in design. The size and shape of particles directly affect the rheological behavior and stability of colloidal suspensions. In order to optimize the viscosity of electroactive material suspensions and to improve the performance of suspension flow batteries, here we suggested a procedure to synthesize $LiFePO_4$ particles with controlled size and shape, and investigated the influence of the particle design in rheological behavior of electroactive particle suspensions and the battery performance.

1. Introduction

In recent studies, the development of suspensions instead of dissolved couples to increase the achievable power density per unit volume become important in flow battery research and named as suspension flow batteries. However, high pump power requirements and limited life spans are the reasons why suspension battery systems are not currently applicable. The properties of the suspension such as stability and rheological behavior should be improved to handle these problems. Even though there is an increasing attention to improve the performance of suspension flow batteries in recent literature, the effects of electroactive material properties on the stability, flow behavior, and the electrochemistry are currently overlooked. In this study, we synthesized colloidal $LiFePO_4$ particles. Thorough control over the reaction kinetics allowed us to adjust size and shape of these particles. It is known that lithium-ion transport in $LiFePO_4$ nanoparticles is relatively favorable along the [010] direction[1]. Therefore, controlling the dominant growth direction of $LiFePO_4$ crystallites can be critical for improving electrochemical performance (i.e. it could shorten the path of lithium-ion diffusion)[2]. Preferential growth of the crystal in one specific direction gives rise to the formation unequiaxed crystallites. From the viscosity point of view, on the other hand, the spherical particles commonly lead to lower suspension viscosities when compared to unequiaxed counterparts. Here, we studied the effects of various reaction parameters including the precursor type and concentration, feeding sequence, reaction time, reaction temperature and suspension pH. The chemical, crystallographic, morphological, and surface properties of synthesized particles were characterized. Effects of particle size and the particle shape on the stability and the rheological behavior of electroactive suspensions were examined. The effect of particle structure on the performance of suspension flow batteries and scalability of the developed particle synthesis process was also discussed.

2. Materials and Methods

LFP particles were synthesized using different stoichiometric ratios of lithium, iron, phosphate precursors. Moreover, the reaction kinetics was optimized by altering reaction temperature, reaction time and feeding sequence of precursors. The synthesized particles were characterized in terms of their chemical, physical, crystallographic, morphological and surface properties using X-ray diffraction, scanning electron microscope, transition electron microscope, Brunauer-Emmett-Teller surface area analysis, particle size analysis and zeta potential measurements. The electrochemical behavior of synthesized powders was analyzed and the rheological behavior of LFP particle suspensions was investigated.

3. Conclusion

LFP particles in submicron size range were successfully synthesized. Understanding the reaction kinetics enabled us to control the nucleation and growth mechanisms of LFP powders, thus lead to the synthesis of LFP powders with various size and shapes. As a result of crystallographic analysis of the synthesized powders, the effect of crystal growth directions on the shape of the powders, thus on the rheological behavior of their suspensions and on the battery performance, were revealed.

References

[1]. L. Yang, J. Chen, L. Chen, P. Yang, J. Zhang, A. Li, Y. Wang, Y. Wang, R. Wang, Journal of Materials Science: Materials in Electronics, 27 (2016) 12258-12263

[2]. X. Huang, X. He, C. Jiang, G. Tian, RSC Advances, 4 (2014) 56074-56083

Fractographic and Metallurgical Analysis Investigations of the Failure of HP Turbine Blade

M.A. DJERIDANE[1], M. FERHAT[2], H.A. BENHORMA[2]

[1]Sonatrach-Direction Maintenance Laghouat Company, [2]University of Laghouat

Algeria

Abstract

This paper deals with fracture investigations of High Pressure (HP) gas turbine blade of a 10 MW transportation power plant in Algeria. These blades were made from IN738LC nickel superaloy. The main focus of the paper is the fracture analysis, which took place at the airfoil region at 45 mm from the root of the blade. Two of the fractured blades was retrieved to identify the cause of failure. The investigations included the visual examination, SEM fractography, chemical analysis, hardness measurement, and micro-structural characterization. Transgranular cleavage fractures along with beach marks are observed. The cause of failure is possibly the fatigue. These causes of failure are also underlined in this paper.

1. Introduction

HP turbine blades are found to be more susceptible to failure as compared to the LP section blades. The major causes of failure in gas turbines are fatigue, stress corrosion cracking and corrosion fatigue. The vibration of blade arising from the variable flow of gases induces vibratory stresses and causes fatigue failure. The fatigue failure is further intensified due to corrosion. Vibratory stresses can be reduced by ensuring blade frequencies within a narrow limit and thus avoiding resonant vibration and limiting gas bending stresses.

In this paper the results of the analysis of failed HP turbine blades of a thermal power plant are presented. The unit was commissioned in 1994 and during first overhaul after seventeen years of commissioning, 80 blades from HP rotor were found damaged and replaced. After 69,873 hour of service the unit was forced to shut down because of high level of noise and vibration at the HP zone during operation. On opening the turbine casing, blade from 1st stage HP rotor was found fractured.

2. Materials and Methods

This includes the analysis of gas turbine blade. Analysis contains the visual examination, chemical analysis, hardness measurement, metallographic examination and analysis of fracture surfaces. The blade material was a cast Ni-base superalloy known as *Inconel 738LC*. The turbine has been in service for about 70,000 h and due to the blade failure the turbine engine was damaged severely.

3. Conclusion

The fatigue mechanism as the main cause of several premature failures ofIN738LC alloy hight pressure blades was characterized. Metallurgical and mechanical deviations were found for the blade material without respect to the standards. Instead The catastrophic failure of the blade has occurred by the following sequence:

1. Formation of the non-protective nickel and cobalt oxides.
2. Degradation of the metal beneath the scale.
3. Deepening of the pits at the leading and trailing edges due to the bending stresses.
4. The propagation of crack by the fatigue mechanism because of the vibration of blade in a resonant condition.

4. References

[1] Poursaeidi , M. A.. Failure analysis of a Second stage blade, Engineering failure analysis, 15(2008).

[2] Z. Mazur. Failure analysis of gas turbine blade made of IN 738LC alloy"; Engineering failure, 12(2005).

[3] Jung-Chel Chang, Failure analysis of gas turbine buckets", Engineering failure analysis, 2003, pp 559-567.
[4] N. J. Lourenco, Fatigue failure of a compressor blade", Engineering failure analysis, 2007, pp 1150-1154.
[5] R.C.ReedThe Superalloys: Fundamentals and Applications, Cambridge University Press, 2006.
[6] Boyce, Meherwan P, *Gas Turbine Engineering Handbook* (3rd ed.). Oxford: Elsevier. 2010.

A Study on The Failure Mechanisms of Various Milling Inserts

Nuray Beköz ÜLLEN, Gizem KARABULUT
Istanbul University-Cerrahpaşa
Turkey

Abstract
Machining is a method that stands out among the production techniques to give the desired final shape to metal parts and to ensure perfect connections with each other at their points of use. The most important factor determining the process quality of machining, which is frequently used as a finishing process in production, is the quality of cutting tools. The tools with a limited service life due to factors such as wear and fracture, it creates a significant amount of expenditure. In addition, it is necessary to examine the problems that occur in the inserts due to reasons such as any failure affects the inserts also affects the pieces. Failure mechanisms that occur in inserts should be examined in order to determine tool life, to prevent any problems that may arise in the machined piece and to reduce the additional cost. In the literature, there are generally studies on the failure analysis of a certain factor on a piece. In the present study, the general failures that may be encountered on the inserts during the milling process, the mechanisms that cause failure and the recommendations to prevent this failure were mentioned. Milling inserts that examined in the study were obtained from Bor Cutting Tools Machine Industry Trade Ltd. Co. Examinations on the inserts were made using a Scanning Electron Microscope (SEM). In general in this study were observed different modes of cutting tool failure including plastic deformation, rake face wear, flank wear, chipping, abrasion and breakage.

1. Introduction

In the production of metallic parts, machining is the most widely used manufacturing method to give the final shape [1]. In recent years, with the developments in the industry, the machining sector was also developed. Production quantities have been increased with the improvement of cutting tools and machine tools and development of high speed production techniques, and as a result, the machining sector has gained importance [2]. As a result of the development of technology day by day, the industry also develops and the competition between manufacturers increases. For this reason, it is getting harder for manufacturers to maintain their positions in the sector and retain their customers. Manufacturers need to keep up with innovations and keep their costs under control. Cutting tools are an important expense item in the machining sector. Due to errors in machining parameters or incorrect tool selection, wear occurs on the inserts and breakage occurs due to the progress of these wear. Failures to the inserts are a big problem for manufacturers both due to the tool cost and the poor quality of the workpiece [1-3]. For this reason, it is very important to examine the wear on the inserts for an efficient machining and lower cost. The main purpose in machining processes is that the cutting tool can remove chips at the desired properties with high performance and maximum tool life. Different machining applications require different tool materials. The ideal cutting tool material should have all of the following properties: [4-5]

- resists wear and thermal shock,
- impact resistant,
- harder than the work it is cutting,
- high temperature stability,
- chemically inert to the work material and cutting fluid.

The most important factor affecting the tool life is a failure that occurs on the inserts. Failures occur such as thermal and mechanical fatigue, fracture, wear and plastic deformation in the insert during machining and make the tool unusable. Since failures occurs on cutting tools for various reasons during machining, the inserts loses its cutting feature. Deformations occur on the work-piece surface due to changes caused by failure in the insert surface and the progress of failure causes fractures in the insert and cutting tool. Many failure mechanisms can occur at the inserts. In order to increase the service life of the tools and to maintain the product quality, it is necessary to analysis the failures that occur on the inserts [2-3, 6-7]. For this purpose, there are many failure analysis studies on the inserts used in machining and milling in the literature [8-14]. In the studies carried out, the failure mechanism of a certain factor or an insert type was examined. In this study, it is aimed to support the literature by examining the failures on different inserts. Although the milling is a traditional method, it is still a machining process that is frequently used in the industry. For this reason, the tools used in milling were examined in this study. The tools obtained from Bor Cutting Tools Machine Industry Trade Ltd. Co. and failure analysis were made using a Scanning Electron Microscope. Different types of failure such as plastic deformation, rake and flank wear, chipping, abrasion and fracture were observed at the examined inserts. For the purpose of to prevent the tool wear and to extend the tool life in a fundamental way, an in-depth understanding of the inserts failure mechanisms is firstly required [14]. The failure mechanisms that cause these wears and cracks have been evaluated in compatible with the literature and the wear characteristics have been indicated. Suggestions have been made in order to prevent failures and extend the service life, and it is aimed to contribute to the users and the literature.

2. Experimental Procedure

Due to the large number and variety of failures encountered on cutting tools, the most common failure mechanisms are discussed here. In this study, inserts with various failure mechanisms that have completed their service life are used in the milling process by Bor Cutting Tools Machine Industry Trade Ltd. Co. The whole cutting tools have an ISO designation of SPKN150608. Si_3N_4-based ceramic, PCBN, Al_2O_3-based ceramic, Al_2O_3+TiC coated carbide, and fine-grained grain cemented carbide inserts were used for failure analysis in the study. All inserts were used in a Computer Numerically Controlled (CNC) machining center with a maximum spindle rotational speed of 10,000 rpm and a 15 kW drive motor. Image analysis of the surfaces of cutting inserts with Jeol JSM-5600 Scanning Electron Microscope (SEM) at different magnifications has been made.

3. Failure Analysis of Milling Inserts

There are many studies on failures of cutting tool used in milling [1-3, 6, 8-14]. The difference of this study is that the worn inserts were obtained and analyzed directly from the sector before the inserts were not prepared for study. Figure 1-5 shows SEM images of the failure mechanisms of the inserts used in the machining of different parts that have been used in various milling processes and have completed their service life. Most of the mentioned abrasions were observed because the failure mechanisms were more than one and interacted with each other in all examined inserts.

In Figure 1, flank and crater wear were observed on the surfaces of the tip, PCBN tool after milling. Edge and flank wear are both normal and slow types of tool wear. If the abrasiveness of the workpiece is high, such as with some cast-iron, this wear types will be accelerated [5]. Crater wear occurs behind the cutting edge and usually occurs in the machining of steels. Cratering is often observed in the machining chipping of steels and occurs behind the cutting edge. If the crater was grown large enough to come into contact with the cutting edge, the tool will immediately fail [5, 16].

Generally, the end of tool life is determined by excessive wear of the tool flank and race at conventional cutting speed. Typical tool wear on the rake and flank face using Al_2O_3-based ceramic tool is shown in Figure 2 (a) and (b), respectively. This wear pattern creates wear zones on the side and end flanks of the insert because the surface of the machined workpiece is abrasive [17]. This wear is actually caused by the very high cutting temperature at the rake face [15-16].

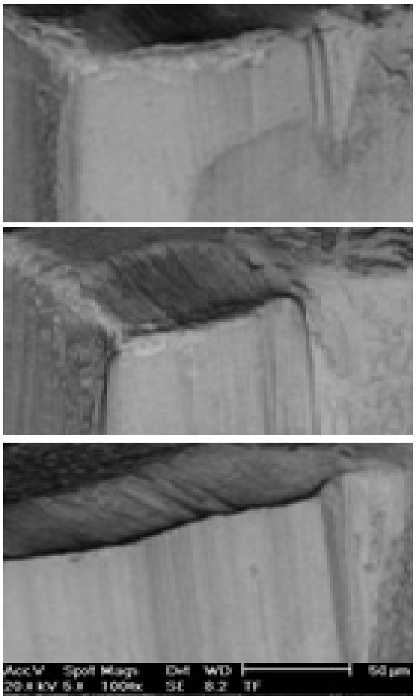

Figure 1. Wear patterns of PCBN tools in continuous milling

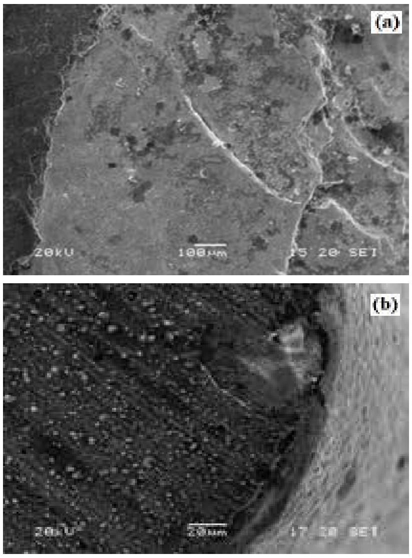

Figure 2. SEM images of worn faces of Al_2O_3-based ceramic tool

The wear mechanism that occurs on the inserts has been determined to be plastic deformation type wear, which is generally the result of a combination of high pressure and temperature [18]. Figure 3 shows abrasion and plastic deformation formation after regional melting at the cutting tip. It is thought that the cause of the wear here is high temperature and pressure. Heat build-up is the main factor causing deformation of a tool or insert. It is difficult to detect deformation without the use of a microscope, but using of a microscope is also very harmful to the machining process. Reducing the cutting speed or using a heat-resistant tool will help to prevent this deformation [5, 16].

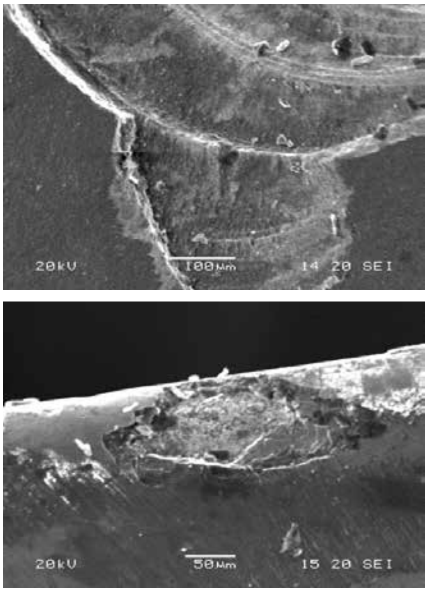

Figure 3. SEM images of worn faces of fine-grained grain cemented carbide inserts

Chipping on tool edge using Al_2O_3+TiC coated carbide tool is shown in Figure 4. Chipping is an unpredictable form of tool defect. Sometimes it starts when a high point on one side breaks. A stronger carbide grade, different edge preparation or change of clearance angle can eliminate chipping [15-16].

In Figure 5, failure mechanisms occurring in the insert are seen as breakage of the insert and built-up edge. The thermal and mechanical shocks are important factors in tool wear morphology. Fracture in tools is usually caused by the combination of the effects of thermal and mechanical stresses in an intermittent cutting process. Thermal cracking can be caused the inserts are subjected to rapid cooling and heating cycles and it can also be caused by interrupted cutting and improper application of cutting fluids [19-20].

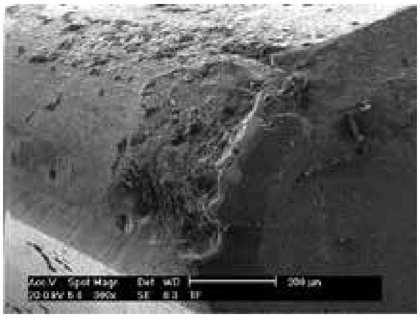

Figure 4. SEM images of worn faces of Al_2O_3+TiC coated carbide tool

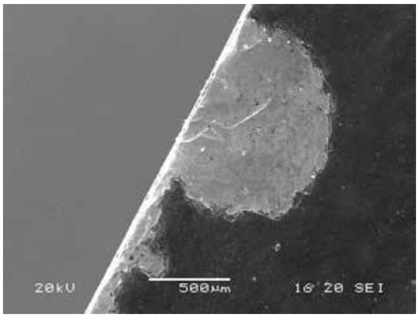

Figure 5. SEM images of worn faces of Si_3N_4-based ceramic inserts

4. Conclusion

All cutting inserts are prone to deterioration quickly, so they have a limited working life. It is not correct to use the blunt inserts with worn surfaces until they break. This is a safety hazard that causes scrap formation, affects tools, parts and therefore production costs and expenses, and also reduces productivity. For this reason, the causes of failure to the insert surfaces in machining should be known and the service life of the tips should be extended by taking the necessary precautions. For these purposes, the inserts used in the milling process, which are frequently preferred in the industry, were examined in this study. In general in this study were observed different modes of cutting tool failure including:

- edge wear and flank wear
- cratering wear
- chipping
- plastic deformation
- mechanical and thermal shocks
- breakage

Changing the hardness of the workpiece material from one point to another within the part, the variation in the cutting tool material, geometry and preparation style, tool holder and workpiece connection and other factors, vibrations caused by the workpiece surface characteristics, chemical effect of the coolant used, speed of the cutting tool directly affect the life.

Acknowledgment

The inserts used in the experimental study were supplied by Bor Cutting Tools Machine Industry Trade Ltd. Co. The authors would like to thank the company for their support in this matter.

References

[1] E. Kuljanic, M. Sortino, TWEM, A Method Based on Cutting Forces Monitoring Tool Wear in Face Milling, International Journal of Machine Tools and Manufacture, 45(1) (2005) 29-34.

[2] İ. Karagöz, Kesici Takım Malzemesi Seçiminin Kesici Takım Kaynaklı Hatalar Üzerindeki Etkisinin İncelenmesi, Kalıp Dünyası Dergisi, 76 (2012) 118-123.

[3] I. Jung, V. Lubich and H.J. Wieland, Tool Failure Causes and Prevention, 6th International tooling conference, 2002, Sweden.

[4] S. R. Maity, P. Chatterjee and S. Chakraborty, Cutting Tool Material Selection Using Grey Complex Proportional Assessment Method, Materials & Design (1980-2015), 36 (2012) 372-378.

[5] F. Klocke, A. Kuchle, Cutting Tool Materials and Tools, In: Manufacturing Processes 1. RWTHedition Springer, Berlin, Heidelberg, pp. 95-196.

[6] H.M. Ertunç, İ. Sevim, Kesici Takimlarin Aşınmasını Gözlemleme Üzerine Yapılan Çalışmalar, Pamukkale Üniversitesi Mühendislik Bilimleri Dergisi, 7(1) (2011) 55-62.

[7] K. Habali, H. Gökkaya, H. Sert, Kesici Takım Kaplama Malzemesi ve Kesme Parametrelerinin AISI 1040 Çeliğinin İşlenmesinde Yüzey Pürüzlülüğüne Etkisinin Deneysel Olarak İncelenmesi, Politeknik Dergisi, 9(1) (2006).

[8] F. Wang, K. Ji, K., and Z. Guo, Microstructural Analysis of Failure Progression for Coated Carbide Tools During High-Speed Milling of Ti-6Al-4V, Wear, 2020, 203356.

[9] X. Zhao, W. Ke, S. Zhang, and W. Zheng, Potential Failure Cause Analysis of Tungsten Carbide End Mills for Titanium Alloy Machining, Engineering Failure Analysis, 66 (2016) 321-327.

[10] L. Liu, Y. Cheng, R. Guan, M. Xu, and T. Wang, Performance evaluation of coated cemented carbide inserts milling 508III steel, International Journal of Nanomanufacturing, 14(2) (2018) 101-114.

[11] K. Monkova, S. Sun, P.P. Monka, S. Hloch, and M. Belan, Durability and Tool Wear Investigation of HSSE-PM Milling Cutters Within Long-Term Tests, Engineering Failure Analysis, 108 (2020) 104348.

[12] J.E. Peters, B. Hoefler, Relationship Between Carbon Chemistry and Thermal Cracking Resistance in Carbide Milling Inserts, International Journal of Refractory Metals and Hard Materials, 11(3) (1992) 159-163.

[13] S. Zhang, X. Ai, J. Li, and X. Fu, Failure Analysis on Clamping Bolt of Milling Cutter for High-Speed Machining, International Journal of Machining and Machinability of Materials, 1(3) (2006) 343-353.

[14] A. Li, J. Zhao, D. Wang, J. Zhao, and Y. Dong, Failure Mechanisms of a PCD Tool in High-Speed Face Milling of Ti–6Al–4V Alloy, The International Journal of Advanced Manufacturing Technology, 67 (2013) 1959-1966.

[15] T.H. Childs, K. Maekawa, T. Obikawa, and Y. Yamane, Metal Machining: Theory and Applications, 2000, Butterworth-Heinemann.

[16] W. A. Knight, G. Boothroyd, Fundamentals of Metal Machining and Machine Tools, 2019, CRC Press.

[17] Z. Q. Liu, X. Ai, H. Zhang, Z. T. Wang and Y. Wan, Wear Patterns and Mechanisms of Cutting Tools in High-Speed Face Milling, Journal of Materials Processing Technology, 129(1-3) (2002) 222-226.

[18] N. B. Üllen, Tornalama İşlemlerinde Çeşitli Kesici Takım Uçlarının Hasar Mekanizmaları, 2nd International Eurasian Conference on Science, Engineering and Technology (EurasianSciEnTech 2020), 7-9 Ekim 2020, Gaziantep- Türkiye, pp. 655-661.

[19] H. Awaji, S.M. Choi and E. Yagi, Mechanisms of Toughening and Strengthening in Ceramic-Based Nanocomposites, Mechanics of Materials, 34(7) (2002) 411–422.

[20] S.X. Song, X. Ai and J. Zhao, Fabrication and Cutting Performance of Al2O3/TiC Nanocomposite Tool Material, Zhongguo Jixie Gongcheng/China Mechanical Engineering, 14(7) (2003) 1523–1526.

Effect of Coating on Surface Integrity of Tools and End Products after Piercing Operation

Fuat Can AĞARER[1], Hatice SANDALLI[1], M. Burak TOPARLİ[2], İ. Etem SAKLAKOĞLU[3]
[1]Norm Somun San. ve Tic. A.Ş., [2]Nedu Bağlantı Elemanları San. ve Tic. A.Ş., [3]Ege Üniversitesi
Turkey

Abstract

Cold forging is an extensively used metal forming technique in many industries due to advantages over other methods including casting and machining. Having said that, tools used in cold forging may experience extreme tribological conditions such as high contact pressure and temperature. These conditions may lead to premature tool wear and tool failure. In addition, surface quality of end products is very dependent on the surface integrity of tools used in cold forging. With the aim of extending tool service life and enhancing end product quality, different surface treatment techniques can be applied on cold forging tools. In this study, TiN coating was applied on piercing punch and its wear performance was observed in the production line. In addition, surface quality of end parts produced by these tools were investigated. It was found that, tools coated with TiN and uncoated reached the limiting punch diameter after 70.000 and 5.000 parts, respectively. It was also revealed that surface integrity of end product is very dependent on surface conditions of cold forging tools.

1. Introduction

Cold forging is one of the metal forming methods preferred thanks to superior surface quality of the end products, improved mechanical properties and suitability for mass production. Owing to its advantages over other metal forming methods, it is extensively used in various engineering applications such as bolt and nut production.

In cold forging, the contact pressure between work-piece and forging tool can reach up to 3000 N/mm^2, relative velocities can reach about 500 mm/s and die temperature may raise up to 600°C [1]. Due to these extreme tribological conditions, forging tools experience wear phenomenon. Tool wear is one of the important type of failure in manufacturing, as it affects both work-piece quality and production efficiency.

In industrial applications, hard thin film coating technologies such as PVD (Physical Vapor Deposition) and CVD (Chemical Vapor Deposition) are employed in coating of forging tools in order to extend their lifetime, to reduce wear and to increase the efficiency of production.

2. Materials and Methods

In this study, effect of TiN coating via PVD on wear of a piercing punch was investigated. A comparison was made between the lifetime of TiN coated and uncoated samples. The wear on piercing punches was monitored by checking diameter with caliper at regular intervals during production and by visual inspections. In addition, surface quality of end products was also investigated with the same intervals.

3. Results and Conclusions

Within the scope of this study, it was revealed that, diameters of punches were decreased due to wear, as expected. After a critical diameter, so-called limiting punch diameter, tear marks were observed during piercing operation, leading to burr in tapping operation. It was found that, TiN coated and uncoated tools reached the limiting punch diameter after 70.000 and 5.000 parts, respectively. Therefore, it was revealed that surface integrity of end products was very dependent on tool wear in terms surface profile and dimensional requirements. The results of this study exposed the importance of hard thin film coating in cold forging processes particularly for piercing operations in terms of tool life and surface integrity of end products.

References

[1] P. Groche, C. Müller and A. Jahn, Tribology Letters, 53 (2014), 599-605.

Microstructure, High Strength and Electrical Conductivity of the Ufg Cu-0.5%Cr-0.2%Zr Alloy Processed by HPT

Igor ALEXANDROV[1], Wei WEI[2], Elena SARKEEVA[1], Vil SITDIKOV[1]
[1]Ufa State Aviation Technical University, [2]Changzhou University
[1]Russia, [2]China

Abstract

The effect of severe plastic deformation (SPD), realized by high pressure torsion (HPT), and subsequent aging on the formation of an ultrafine-grained (UFG) microstructure in the Cu-0.5%Cr-0.2%Zr alloy (wt.%) is investigated. It is shown that as a result of the treatment, a high-strength state can be formed with a tensile strength of ≈ 900 MPa and an electrical conductivity of 70% IACS.

1. Introduction

Cu–Cr–Zr alloys are widely used in various fields of technology due to their inherent properties: high strength, ductility, and electrical conductivity. When using these alloys, for example, for the production of resistance welding electrodes, heat exchangers, railway contact wires, strength, in addition to electrical conductivity, is the most important factor that needs to be considered. It is possible to significantly increase the strength of copper alloys by forming an UFG structure as a result of the use of severe plastic deformation (SPD) methods [1, 2]. High-pressure torsion is the SPD method, which allows to achieve the greatest refinement of the microstructure and, thus, to maximize the strength properties of metallic materials. It was shown in [3, 4] that the use of HPT can reduce the grain size to 10 nm, which results in significant hardening. The use of additional heat treatment after SPD increases both the strength and electrical conductivity of the Cu–Cr–Zr alloys [5-8] due to dispersion hardening. At the same time, dispersed particles can effectively stabilize the UFG structure upon heating [8]. Therefore, the desired combination of properties, increased strength combined with high electrical conductivity, can be obtained by optimizing the microstructure through a combination of deformation and thermal processes.

The aim of this work was to analyze the influence of the phase composition and the exact amount of the volume fraction of precipitates, which will allow us to purposefully control physics-mechanical properties by changing the modes of implementation of SPD processing. In addition, knowing the exact amount of precipitates in the alloy will allow us to estimate the completeness of decay, since the more complete the decay, the cleaner the matrix of the main phase and the higher the electrical conductivity.

2. Experimental Procedure

The copper alloy with chromium and zirconium Cu-0.5%Cr-0.2%Zr (wt.%) was chosen as the material for the studies. In order to obtain a supersaturated solid solution, the as-received rods with a diameter of 20 mm were subjected to high-temperature heat treatment at 1000 °C for 0.5 hours, followed by quenching in a 5% NaCl solution. As a result, the initial state (IS) was formed. Furthermore, the rods were cut into discs 2 mm in thickness and subjected to HPT at room temperature. The disks were deformed under an applied pressure of 6 GPa. The number of revolutions N = 10, which corresponded to the true degree of ~ 157. HPT was carried out in a "hole" with a depth of 0.2 mm. As a result of the HPT, samples of Ø20 mm and a thickness of h = 2 mm were obtained. Aging was carried out in air in an oven SUOL 45 at 450 °C for 1 hour.

To study the microstructure, an optical microscope (OM) OLIMPUS GX51 and a transmission electron microscope (TEM) JEOL 2100 were used. X-ray structural analysis of the samples was performed by diffractometer Rigaku Ultima IV (Bragg-Brentano geometry) using $Cu_{K\alpha}$ monochromatic radiation at the reflected beam (parabolic graphite monochromator). The microhardness of the test samples was measured on a Duramin instrument under a load of 100 g and with a holding time of 10 seconds for the load. Uniaxial tensile tests were carried out on an Instron 8801 small specimen testing machine at room temperature at a speed of 10^{-3} s^{-1}. Samples with dimensions 10×4×4 mm were cut perpendicular to the radial section of the disks. Three samples were tested for each condition. Conductivity studies were carried out at a temperature T=23 °C by an eddy current method on flat samples. The accuracy is ±2%.

All investigations of microstructure and properties were carried out for regions located at a distance equal to half the radius of the disks.

3. Results and Discussion

3.1. Microstructure

The microstructure of the Cu–0.5%Cr–0.2%Zr alloy in the initial state is shown in Figure 1. The general view of the microstructure indicates the formation of a homogeneous and equiaxed coarse-crystalline structure. The average grain size was 140±8 μm.

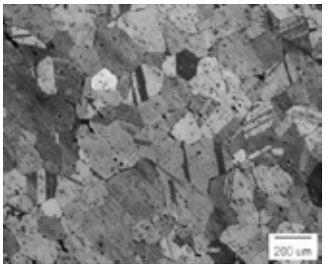

Figure 1. Initial state (IS) microstructure. Optical metallography.

HPT leads to a strong refinement of the initial coarse-grained structure of the IS and the formation of an UFG microstructure (Fig. 2a) with a high dislocation density. The average grain / subgrain size determined by the analysis of dark-field images was 135 ± 40 nm. Also, dispersed particles with an average size of 10 nm, having a predominantly spherical shape, are clearly visible in the microstructure.

As a result of aging, a microstructure is formed, consisting of grains with clearly defined boundaries (Fig. 2b). The striped contrast of grain boundaries indicates their perfection. Improving the microstructure is the result of relaxation processes that are accompanied by grain growth. However, at the same time, grains with blurred boundaries are preserved. The heterogeneity inside some of them indicates the preservation of the stress state. The size of individual grains reaches 340 nm, and the average grain / subgrain size is 140 ± 50 nm. Moreover, part of the grains has a size of 20 - 40 nm. Particles of the second phase are also observed in the microstructure. The average particle size is 10 nm. Particles are located unevenly both in volume and in grain boundaries.

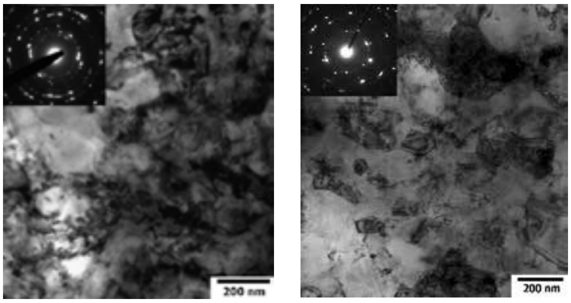

a b

Figure 2. The microstructure of the alloy after: a - HPT; b - HPT + aging. TEM.

The general form of the diffraction patterns in the various states studied is similar and is characterized by a set of the same maxima with Miller indices (111), (200), (220), (311) and (222) corresponding to pure copper (Fig. 3). However, significant differences from the powder diffraction pattern of copper are associated with the formation of various crystallographic texture in the samples [9]. In particular, the intensity ratio of such peaks as (220), (311) and (222) differ markedly.

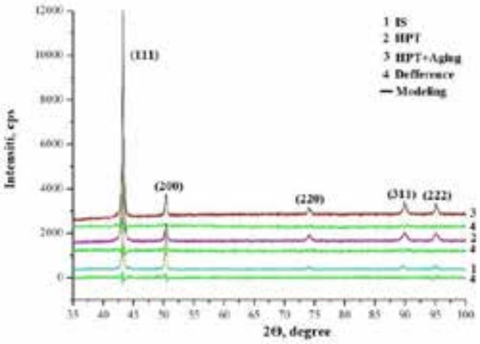

Figure 3. X-ray diffraction patterns of the alloy in various structural states.

The latter indicates the formation of a different crystallographic texture in the IS and after HPT, since all the diffraction patterns were taken from the same surface of the samples. The most detailed analysis of the diffraction patterns showed that HPT leads to a substantial broadening of the diffraction lines (Table 1), which is directly related to the decrease in the size of coherent scattering domains (CSDs), as well as to an increase in the density of introduced defects in the crystal structure. To find the fine structure parameters of the copper alloy, the diffraction patterns were simulated as part of the PM2K program. The calculated diffractograms are shown in Fig. 3 as solid black lines. Fig. 3 also shows the difference curves between the experimental and calculated diffractograms. In this case, the inconsistency R_{wp} factor for the upper diffraction pattern was 6.9%, for the average - 7.1%, and for the lower - 6.2%. These values indicate a high degree of coincidence of diffractograms obtained experimentally and by computer simulation.

As a result of the analysis of the diffraction patterns, it was possible to determine the microstructure parameters of the alloy in the studied states (Table 1). In the initial state, the lattice parameter is 0.36285(3) nm and significantly exceeds the lattice parameter of pure copper (0.3615 nm). The latter is directly related to the presence of impurity atoms in the main matrix. The value of the dislocation density is very small and corresponds to that characteristic for CG copper alloys [1]. Dislocations belong to both the edge and screw types, since the parameter m_{ixp}, equal to proportion of edge dislocations, is closer to 50%. The parameter R_e associated with the arm of the dislocation dipole (effective radius of dislocations) is typical of metals in the CG state [10]. On the other hand, an estimate of the lattice parameter showed that HPT leads to a decrease in the lattice parameter of the alloy to 0.36178(5) nm compared with the initial state. This lattice parameter value is much closer to the lattice parameter of pure copper. As is known, the presence of impurity atoms in a copper matrix leads to an increase in the lattice parameter of copper, as in the case of the initial state. The observed decrease in the lattice parameter towards the lattice parameter of pure copper after HPT indicates the depletion of the matrix, which should lead to the formation of secondary phases. Typical precipitates for this alloy are Cr and Cu_8Zr_3 [11].

Aging at 450 °C of the sample after HPT leads to a further decrease in the lattice parameter, and, consequently, the volume fraction of the secondary phases increases. In general, HPT treatment leads to a decrease in the average size of CSDs by more than 5 times. Aging of the samples slightly increases the size of the CSDs, but at the same time, the strength of the alloy is quite high. The latter, apparently, is associated with the increasing role of dispersion hardening of the alloy. After HPT, the dislocations mainly belong to the edge type, since the m_{ixp} parameter is close to 100% (Table 1). In this case, the effective radius of the dislocations (shoulder of the dislocation dipole) also decreases by about 7 times. However, aging of the UFG samples contributes to an increase in the fraction of edge dislocations and an increase in R_e. The average dislocation density after HPT increases significantly (Table 1), and after aging it decreases slightly.

Table 1. TEM and X-ray microstructure parameters: d_{av} - average grain size, a – lattice parameter, D_{xrd} – CSDs size, ρ – dislocation density, m_{ixp} – proportion of edge dislocations, R_e – effective radius of dislocations

State	d_{av}, µm	a, nm	D_{xrd}, nm	ρ, 10^{15} m^{-2}	m_{ixp}, %	R_e, nm
IS	140±8	0.36285(3)	160	-	46(5)	17
HPT	0.135±0.04	0.36178(5)	33	8.78	94(2)	7
HPT+ Aging	0.14±0.05	0.36171(4)	46	5.86	77(4)	14

A comprehensive study of particles in the alloy by X-ray scattering methods provided important information on their phase composition, size and volume fraction. In order to identify peaks from certain particles in the X-ray diffraction pattern, the detection limit was increased by obtaining X-ray patterns in the transmission mode with increased parallel X-ray beam intensity and a long pulse count per point. Next, we determined the interplane distances d for all reflexes and their intensity I using WPPM (Whole Powder Pattern Modeling) approach [12]. By comparing d and I with those stored in the database (PDF – 2), the phase composition of the precipitates was identified. In quantitative calculations of the volume fraction of precipitates, the same X-ray diffraction patterns were processed using the Rietveld method. This method is considered the most accurate, because it relies on the atomic-structural parameters of the calculated phases. As a result of applying this approach to the studied materials, it was possible to identify their phase composition and volume fraction of precipitates. On the other hand, the application of the modified approach of small-angle X-ray scattering (SAXS), which takes into account not only the shape and structure, but also the spatial distribution of particles, made it possible to establish the size, shape, and distribution of particles in those areas of the foil in which X-ray phase analysis (XFA) was performed. The use of XFA in the case of a copper alloy of the Cu–Cr–Zr system made it possible to reveal a difference in the phase composition of particles in IS and the state subjected to HPT. When refining the diffraction patterns in order to determine the content of precipitates, the phases of pure Cu, Cr, and Cu_8Zr_3 were considered as possible. The types of precipitates detected by the XRD method and their corresponding volume fractions are presented in Table 2. It was found that particles of the Cu_8Zr_3 phase of a spherical shape with an average diameter of ~ 30 nm were observed only after HPT. In IS, in the alloy, spherical precipitates of Cr with an average diameter of ~ 4.3 ± 0.1 µm, and after HPT, the size of spherical precipitates of Cr is smaller and is ~ 2.5 ± 0.2 µm (the size of Cr precipitates was determined from SEM photographs). In this case, the volume fraction of Cr particles after HPT exceeded that characteristic for IS. Consequently, dynamic aging occurs in the HPT process.

Table 2. The types, contents, and sizes of precipitates detected by X-ray scattering in IS and after HPT. Sizes determined by the SAXS method

State	Volume fraction Cr, %	Volume fraction Cr_8Zr_3, %	d_{av} Cr_8Zr_3, nm
IS	0.59	-	-
HPT	0.92	0.62	30

3.2. Tensile properties and electroconductivity

IS is characterized by rather low strength properties Hv = 845 MPa and σ_{uts} = 225 MPa (Table 3), but a high elongation ε of 62%. The electrical conductivity of this state is equal 31 % IACS.

HPT significantly increases the strength values (Hv = 2925 MPa and σ_{uts} = 820 MPa) while maintaining the elongation to failure at a fairly high level (ε = 22%). Such an improvement in the strength characteristics of the alloy as a result of HPT can be explained by a significant decrease in fragment sizes. According to the Hall – Petch equation, a decrease in grain size increases its strength due to the influence of grain boundaries [1, 13-14]. In addition, during HPT, the dislocation density increases significantly (Table 1), which also leads to strain hardening, which increases strength by limiting the ability of dislocations to slip. As recent studies [15] have shown, during SPD dynamic deformation aging is realized, which leads to the formation of precipitates. Precipitates are additional obstacles to the movement of dislocations and further increase the strength characteristics of the alloy.

The electrical conductivity of the HPT state is improved up to 33% IACS. In dispersion-hardened copper alloys, the value of electrical conductivity is primarily determined by the atoms of the alloying elements in the solid solution and is practically independent of the defects that arise during SPD [16].

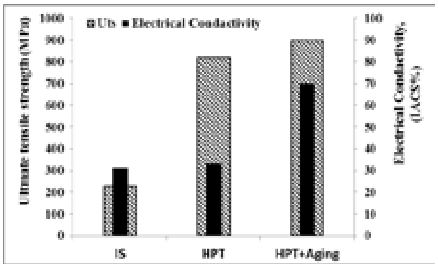

Figure 4. Tensile strength and conductivity of the alloy in various states

Thus, the detected increase in electrical conductivity can be associated with dynamic deformation aging that occurs during the HPT process. This is indicated by a decrease in the lattice parameter (Table 1). However, the still low value of electrical conductivity indicates that the decay process did not go completely and a certain number of atoms of the alloying elements remains in the matrix.

Aging after HPT leads to an additional increase in strength characteristics (Hv = 3290 MPa and σ_{uts} = 900 MPa), while maintaining technological plasticity (ε = 16%). As shown in [17, 18], two competing processes occur during aging: on the one hand, the decomposition of a supersaturated solid solution with the release of dispersed particles and the recovery processes leading to a decrease in the dislocation density. Given a four-fold increase in the strength characteristics of the alloy and data from microstructural studies (a change in the decrease in the lattice parameter and an increase in the volume fraction of particles), it can be assumed that aging significantly increases the contribution of dispersion hardening. In this case, the electrical conductivity of the alloy is significantly restored, up to 70% IACS, which is due to the decomposition of the supersaturated solid solution in the copper matrix and relaxation processes that occur during aging.

Table 3. Mechanical characteristics of different states

State	Hv, MPa	σ_{uts}, MPa	ε, %	IACS, %
IS	845±25	225±5	62±1	31
HPT	2925±150	820±5	22±1	33
HPT+ Aging	3290±110	900±15	16±1	70

4. Conclusion

In this work, we studied the effect of SPD by torsion and subsequent aging on the microstructure, and the mechanical properties of the Cu–Cr–Zr alloy. The main results and conclusions of this study can be summarized as follows:

1. As a result of the HPT of the Cu-0.5%Cr-0.2%Zr alloy, an UFG microstructure is formed with an average grain size / subgrain size of fragments of 135 ± 40 nm. Subsequent aging of the UFG sample has practically no effect on the grain / sub-grain size of 140 ± 50 nm. In this case, the volume fraction of particles increases, their average size decreases. In addition, spherical Cu_8Zr_3 phase particles were observed only after HPT.
2. The strength characteristics of the alloy after HPT and subsequent aging increase by 4 times compared with the initial state, due to a decrease in grain size and dispersion hardening.
3. Aging after HPT significantly increases electrical conductivity up to 70 % IACS. A significant improvement in electrical conductivity can be explained by the decomposition of a supersaturated solid solution in a copper matrix and relaxation of grain boundaries.

Acknowledgment

This work was supported by the Ministry of Education of the Russian Federation, project 0838-2020-0006 Fundamental study of new principles for the creation of promising electromechanical energy converters with characteristics above the world level, with increased efficiency and minimum specific indicators, using new highly efficient electrotechnical materials.

The authors are grateful to be supported by the National Natural Science Foundation of China under grant No. 51561001 and 21476031, the Priority Academic Program Development of Jiangsu Higher Education Institutions (PAPD), the Top-notch Academic Programs Project of Jiangsu Higher Education Institutions (TAPP), and the Science and Technology Project of Changzhou, P. R. China under grant No.CZ20180016 and CE20170028.

References

[1] R.Z. Valiev and I.V. Alexandrov, Bulk nanostructured metal materials: preparation, structure and properties, 2000, Akademkniga, Moscow, pp. 271.

[2] R.Z. Valiev, R.K. Islamgaliev and I.V. Alexandrov, Progress in Mater Sci, 45 (2000) 103-189.

[3] X. Sauvage, P. Jessner, F. Vurpillot and R. Pippan, Scr Mater, 58 (12) (2008) 1125-1128.

[4] A. Bachmaier, G.B. Rathmayr, M. Bartosik, D. Apel, Z. Zhang and R. Pippan, Acta Mater, 69 (2014) 301-313.

[5] A. Vinogradov, V. Patlan, Y. Suzuki, K. Kitagawa and V.I. Kopylov, Acta Mater, 50 (2002) 1639-1651.

[6] E. Sarkeeva, M. Abramova and W. Wei, Defect and Diffusion Forum, 385 (2018) 278-283.

[7] G. Purcek, H. Yanar, O. Saray and I. Karaman, Maier Wear, 311 (2014) 149-158.

[8] D. Shangina, Y. Maksimenkova, N. Bochvar, V. Serebryany, G. Raab, A. Vinogradov, W. Skrotzki and S. Dobatkin Adv. Mater. Res, 922 (2014) 651-656.

[9] R.K. Islamgaliev, V.D. Sitdikov, K.M., Nesterov and D.L. Pankratov, Rev. Adv. Mater. Sci., 39 (2014) 61-68.

[10] J. Gubicza, X–ray line profile analysis in Materials Science, 2014, IGI–Global, Hershey, PA, USA, pp. 359.

[11] V.D. Sitdikov, R.K. Islamgaliev, M.A. Nikitina, G.F. Sitdikova, K. X. Wei, I.V. Alexandrov and W.Wei, Philosophical Magazine, 99 (2019) 73–79.

[12] J. Rigaku, Integrated X–Ray Powder Diffraction Software PDXL, 26(1) 2010 23–27.

[13] N. Hansen, Scr. Mater, 51 (2004) 801-806.

[14] G. Purcek, O. Saray, M.I. Nagimov, A.A. Nazarov, I.M. Safarov, V.N. Danilenko, O.R. Valiakhmetov and R.R. Mulyukov, Philos. Mag., 92 (2012) 690-704.

[15] W. Wei, K.X. Wei, F. Wang, Q.B. Du, I.V. Alexandrov and J. Hu, Mater. Sci. Eng. A., 528 (2011) 1478–1484.

[16] R.G. Chembarisova, E.A. Sarkeeva and I.V. Alexandrov, IOP Conf. Series: Mater. Sci. and Eng. 672 (2019) 012023.

[17] K.V. León, M.A. Muñoz-Morris and D.G. Morris, Mater.Sci. and Eng. A, 536 (2012) 181-189.

[18] N. Gao, E. Huttunen-Saarivirta, T. Tianen and M. Hemmila, Mater. Sci. and Eng. A, 342 (2003) 270-27.

Morphological, Optical and Electrochromic Properties of Vanadium Pentoxide Thin Films Prepared by Ultrasonic Spray Deposition Method

Yusuf TUTEL, Seyma KOC, Mete Batuhan DURUKAN, Serkan KOYLAN,
Husnu Emrah UNALAN
Middle East Technical University
Turkey

1. Introduction

Metal oxide semiconductors have received significant attention due to their unprecedented properties to be used in applications like electronics [1], optoelectronics [2], biosensors [3] and catalysis [4]. Among metal oxides, vanadium pentoxide (V_2O_5) have been utilized in a wide range of applications. It is the most stable phase among other vanadium-oxides with an oxidation state of +5. Among practiced V_2O_5 deposition methods, ultrasonic spray deposition (USD) is highly promising as a low-cost and atmospheric deposition method that can be used to deposit films over large areas. It also allows reproducible deposition of high-purity thin films. In this work, we have investigated morphological, optical and electrochromic properties of V_2O_5 thin films deposited through USD method.

2. Materials and Method

Vanadyl acetylacetonate (VO(acac)2, 98 %, Sigma Aldrich) was dissolved in methanol at a concentration of 0.25M. The V_2O_5 thin films were deposited onto pre-heated FTO/glass substrates (T=110 °C) using Sono-Tek Exacta Coat USD system and then annealed at different temperatures (450-550 °C) for 60 min under ambient conditions.

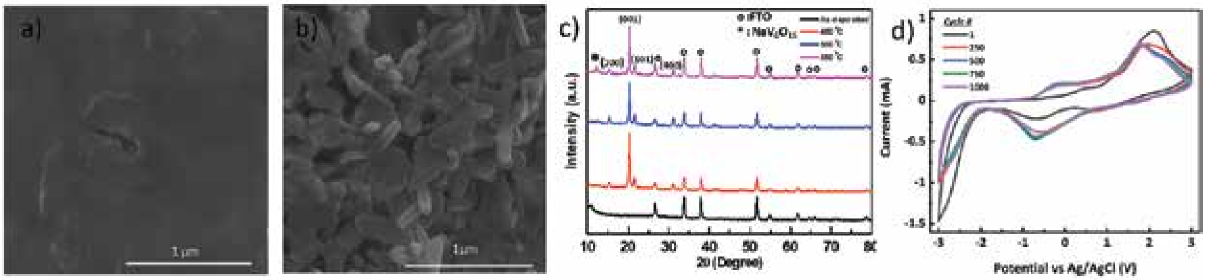

Fig 1. Surface morphologies of (a) as-deposited and (b) 450°C annealed V_2O_5 thin films. (c) XRD patterns of V_2O_5 thin films for different annealing temperatures. (d) Cyclic voltammetry (CV) test results of 450°C annealed V_2O_5 thin films.

The SEM image of as-deposited films (Fig 1 (a)) show characteristic amorphous surface features, while annealed films (Fig 1 (b)) have crystalline structures. XRD patterns proved the amorphous structure of as-deposited films, while annealed films showed orthorhombic structure of V_2O_5 phase (PDF 00-041-1426), provided in Fig 1 (c). Promising cyclic stability up to 1000 cycles was obtained through cyclic voltammetry (Fig 1 (d)).

3. Conclusions

It was demonstrated that the oxidation state of vanadium ions of all deposited films following post deposition annealing was +5. Results presented herein provides a roadmap for the deposition of V_2O_5 through USD method and this work can certainly be extended to other metal oxide systems.

4. References

[1] L. Petti, N. Münzenrieder, C. Vogt, H. Faber, L. Büthe, G. Cantarella, F. Bottacchi, T. D. Anthopoulos and G. Tröster, Applied Physics Letters, 3.2 (2016): 021303.
[2] Y. Xinge, T. J. Marks and A. Facchetti, Nature Materials, 15.4 (2016): 383-396.
[3] S. K. Arya , C. C. Wong, Y. J. Jeon, T. Bansal and M. K Park, Chemical Reviews, 115(11) (2015): 5116-5158.
[4] S. Kevin, The Journal of Physical Chemistry Letters, 4.10 (2013): 1624-1633.

Fabrication of P-type CuI Nanowires Networks for Transparent Flexible Electronics

Alptug CALASIN[1], Aleyna ASCIOGLU[1], Serkan KOYLAN[1], Sensu TUNCA[1], Sahin COSKUN[2], Husnu Emrah UNALAN[1]
[1]Middle East Technical University, [2]Eskisehir Osmangazi University
Turkey

Introduction

The development of novel transparent electronics highly depends on the improvements in transparent semiconductors. Compared to n-type semiconductors, p-type oxide semiconductors are still at their infancy and necessitate further exploration. Unfortunately, high growth temperatures are typically required to obtain p-type conductivity, which imposes a severe problem for flexible electronics. Among the native p-type semiconductors, copper iodide (CuI) with a zinc-blend type crystal structure is highly promising due to its superior chemical stability, wide bandgap, low material cost and deposition temperatures. In this work, nanowires of CuI are fabricated through iodization of copper nanowire networks and their photo response characteristics were measured.

Materials and Methods

In this study, the synthesis of Cu NWs was carried out via hydrothermal method reported elsewhere [1]. In a typical synthesis, a Teflon sealed autoclave was filled with aqueous hexadecylamine, glucose and copper chloride solution and kept overnight at 100 ºC. Following the synthesis, Cu NWs were separated from byproducts through multistep centrifugation. Cu NW networks were then prepared via spray coating. To have solid iodination, the networks were subjected to iodine gas using a handmade setup. A detailed parametric study was conducted to determine the effects of reaction time, temperature and vapor pressure of iodine to obtain complete transformation of Cu NWs into CuI NWs. XRD pattern and scanning electron microscopy (SEM) image of the fabricated CuI nanowire networks are provided in Figures 1 (a) and (b), respectively.

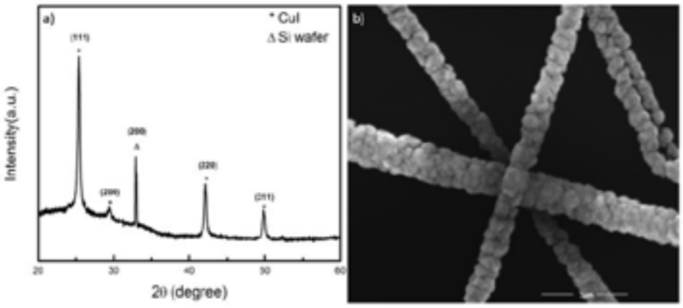

Figure 1 (a) XRD pattern and (b) SEM image of CuI nanowire networks.

The peaks at 25.34º, 29.44 º, 42.27 º and 50.01 º (Figure 1 (a)) correspond to CuI zinc blend structure). The other peak at 32.93 º comes from Si wafer. The preferred direction was (111) which is the highest packed plane in CuI zinc blend structure with minimum surface energy. Therefore, the fastest growth rate is enhanced in that plane. Moreover, as the other peaks are observed together, the polycrystalline structure was formed. The peak situated at 25.34 º is (111) plane. Using Bragg's Law for the peak situated at 25.34 º for (111) plane a d_{111} value of 3.7411 Å was calculated, which was in good agreement with the tabulated d values of CuI. SEM image in Figure 1 (b) shows homogeneous polycrystalline nanowire structures with a nanowire radius between 100-150 nm that is increased from 50 nm(bare Cu nanowire). No cracks and voids were observed on the CuI nanowires. Following the fabrication and materials characterization, CuI nanowire networks were then used as active materials in simple photodetectors.

Conclusions

CuI is a highly promising, transparent p-type semiconductor. In this work a simple room-temperature method was used to fabricate CuI nanowire networks, which were used as active materials in photodetectors.

References

[1] Tigan, D., Genlik, S. P., Imer, B., & Unalan, H. E. (2019). Core/shell copper nanowire networks for transparent thin film heaters. *Nanotechnology*, *30*(32), 325202.

Functionalization of Glass Fiber Woven Fabrics by Transparent Conducting Oxide (TCO) Thin Films and Characterization of Their Electromagnetic Properties

Merve OZDIL, Tilbe BETIN, Caner DURUCAN, Arcan F. DERICIOGLU
Middle East Technical University
Turkey

Abstract

The aim of this study is to fabricate a hybrid type of radar absorbing composite material combining Jaumann and graded type absorber characteristics that can absorb electromagnetic waves between 2-18 GHz. Within the scope of this aim, indium tin oxide (ITO) thin films were coated on glass substrates as well as on glass fiber woven fabric structures by sol-gel method, and the electrical conductivity of this conducting oxide layer was controlled to incorporate electromagnetic (EM) wave absorbing characteristic to glass fiber woven fabrics. The surface functionalized dielectric material will be used as reinforcement in EM wave absorbing polymer matrix composites.

1. Introduction

Transparent conductive oxides (TCOs) draw attention in the field of electromagnetic shielding, since they are electrically conductive, optically transparent and have low absorption of electromagnetic radiation in the range of visible light. There are various types of transparent conductive oxides, and selection of a TCO for a specific application is based on the requirements of the application and its own parameters.

Among all types of TCOs, tin doped indium oxide (ITO) is the most promising one for electromagnetic shielding applications, because it has good substrate adherence, it does not require high temperature to coat, it is chemically and mechanically stable and it is transparent in visible region yet absorbing in ultraviolet and infrared regions. It has intermediate electrical conductivity and cost when compared to other types of electromagnetic shielding materials.

2. Materials and Methods

ITO thin films have been applied to surfaces by sol-gel method. In the sol preparation process, firstly, $In(NO_3)_3.H_2O$ was dissolved in acetylacetone with continuous stirring, and this solution was refluxed at 75 °C for 3 h. Next, $SnCl_4.5H_2O$ was dissolved in 2-propanol, and it is continuously stirred for 2 h. After that these two solutions were mixed at room temperature and stirred for 1 h. Final coating solution was kept for 4 days for ageing purpose. According to this processing route, different solutions with different molarity were prepared, and these solutions were coated on both glass substrates and glass fiber woven fabrics using either dip or spray coating.

3. Conclusion

In order to optimize some parameters that cannot be achieved with glass fiber woven fabrics, soda lime glass substrates were coated with ITO by using dip coating method. First observation was on the effect of number of dipping (passes) on the sheet resistance. A 0.7 molar ITO solution was prepared and substrates were coated with different number of passes. As it is expected when the number of passes increases, thickness of the film also increases. Resulting increase in carrier concentration provides higher electrical conductivity and hence lower sheet resistance as demonstrated in Figure 1.

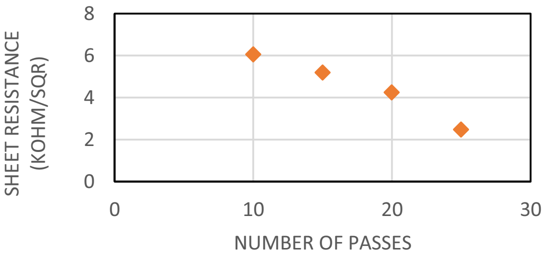

Figure 1. Sheet Resistance vs Number of Passes.

Determination of the Effectiveness of the Conservation Area by Using Nano Particles on Archaic Stones with $CaCO_3$ Content

Halit S. CANOL[1], **Cem B. ÜSTÜNDAĞ**[2], **Rıza G. AKGÜN**[3]
[1]Mimar Sinan Fine Art University, [2]Yıldız Technical University, [3]Maltepe University
Turkey

Abstract

In this scope, methods have been occurred that is the acceleration of chemical redox reactions thanks to the synergy of particular materials (usually semiconductor) and solar light, is one of the most promising tool for the handling of different problems in several areas of applied chemistry, including environmental science . In this study developing on natural stones containing $CaCO_3$; to evaluate the self-cleaning and de-polluting properties of titanium dioxide-based suspension and Silver (Ag) particle. It is planned that a new nano-size protective product will be introduced into the body by activating the potential variability in the metabolism of organisms such as algae, lichen and bacteria which may be harmful for natural stones and by the help of these photocatalyst. To assess compatibility with stone substrates, microstructure analysis, colour and gloss measurements, static contact angle analysis and two different water absorption tests were carried out.

1.Introduction

In this case, some photocatalytic materials have been chosen for bio mediation methods for conservation of natural stone with $CaCO_3$ content. Titanium dioxide (TiO_2) is one of the mostly used photocatalytic material in order to develop innovative materials and solutions in different fields: water and air purification, anti-bacterial and self-sterilizing surfaces, food industry, paintings, paper production, cosmetics and building materials [1–2]. Photocatalysis is not the only photochemical effect of TiO_2 activated by ultraviolet irradiation of solar light. Under UV exposure titanium dioxide becomes super-hydrophilic, thus decreasing water contact angle and creating a uniform water film on treated surfaces [1,3], preventing contact between external dirt and surfaces themselves. The synergy of these two photo-induced properties (photocatalysis and super-hydrophilicity) is the base of self-cleaning ability of TiO_2 [2], since the formation of a water film over treated surfaces and the photocatalytic degradation of pollutants and external agents could make removal of degradation agents easier bringing to a real self-cleaning effect. In additional, Silver ions (Ag^+) and silver nanoparticles (Ag NPs) are well-known components for providing antibacterial activity [4–5], Titanium dioxide (TiO_2) has also been demonstrated to have excellent antibacterial and photocatalytic properties under UV irradiation.

In this paper, development a single-celled green alga on stone surfaces, synthesis of TiO_2 and Ag/ TiO_2 nanoparticles and their characteristic examinations were studied.

2.Experimental Procedure

2.1. Initial Studies to Observe the Development of Micro-Biological Organisms on natural stone content with $CaCO_3$

The development of “Chlorella Vulgaris”, a single-celled green alga species, was first observed on five (5) different types of natural stones with $CaCO_3$ properties. The discrete culture system of Chlorella Vulgaris was created and produced isolated from freshwater deposits in volumes of 100, 200, 500, 1000, 2000 and 4000 ml. The light source of system (150 µmol.m-2. s-1) is placed with horizontally at the distance of 22 cm from behind the cultures. Cultures were applied 16: 8 light / dark period and grown at room temperature at 22-25 ^{0} C. Cultures were obtained evenly distributed in volumes from 4000 ml to 600 ml beakers. Five (5) $CaCO_3$ featured natural stones were placed in each of these beakers. These systems were followed up in weekly periods in 23.9 ^{0}C temperature environment. Developments on samples were followed with UV spectrophotometer.

2.2. Synthesis of Ag, TiO_2 and Ag/TiO_2 Nanoparticles

Synthesis of Ag Nanoparticles

Nano size silver powder synthesis was produced with starting materials which are Silver Nitrate ($AgNO_3$) Sodium Hydroxide (NaOH), Sodium Dodecyl Sulfate ($C_{12}H_{25}SO_4Na$), Hydrazine Hydrate ($N_2H_4.H_2O$). Synthesis has been started with preparation of mixtures that 1 M sodium hydroxide in 300 ml distilled water and a 0.5 M silver nitrate mixture in 500 ml distilled water, separately. After, these two solutions were mixed. The reaction of after mixing is below.

$$2AgNO_3 + 2NaOH \rightarrow Ag_2O + 2NaNO_3 + H_2O$$

After a while it was observed that brown sedimentation formed. After sedimentation formation, the solution was washed 3 times and at this stage, pH value was determined as 10. A new solution was obtained by adding 500 ml of distilled water to the sedimentation. 1 M SDS solution which was prepared with 5 ml distilled water added to this solution. The solution was mixed in a magnetic stirrer until a homogeneous mixture of macro size was obtained and 3 ml of hydrazine hydrate was added dropwise to the solution.

Synthesis of TiO_2 Nanoparticles

In the typical procedure, 6 mL of Titanium (IV)-n-butoxide was first dissolved in 2 mL of isopropyl alcohol, and the solution was subsequently be added dropwise to a solution containing 2.0 mL of nitric acid and 200 mL of distilled H_2O and vigorously stirred at room temperature. White precipitate was formed immediately upon each additional drop. The final mixture was vigorously stirred for 48 h, followed by aging for 48 h at room temperature to produce the TiO_2 sol. The colloidal suspension of the TiO_2 sol-gel will be a white blue colour, semi-transparent, but quite stable for over one month.

Synthesis of Ag/TiO_2 Nanoparticles

For every 10.0 mL of TiO_2 sol-gel, 31, 156, and 780 L of 0.1 M $AgNO_3$ solutions was used to produce theoretical 0.2%, 1.0%, and 5.0% Ag to TiO_2 molar ratios of sols, respectively. The $AgNO_3$ solution was also added dropwise to the TiO_2 sol in a dark container, while being vigorously stirred at room temperature. The suspension was stirred for 30 min before adding excess ascorbic acid (0.1 M) dropwise, where the resulting sol - gel was continuously stirred for another 30 min.

2.3. Characterizations of Ag, TiO_2 and Ag/TiO_2 Nanoparticles

The morphology of the Ag, TiO_2 and Ag/TiO_2 nanoparticles was analysed by a scanning electron microscope (SEM) and contained an energy-dispersive spectroscopy (EDS) spectrometer to characterize the chemical composition. The X-ray diffraction (XRD) patterns were chosen wavelength will be 0.154 nm, which was generated by CuK radiation at 40 kV and 40 mA using a Ni filter.

3.Results and Discussion

The development of "*Chlorella Vulgaris*", a single-celled green alga was development on $CaCO_3$ content stone which has fine quartz grained limestone with low metamorphism grade after five weeks period. "*Chlorella Vulgaris*" development on stone samples shown in Fig.1. Another four surfaces of stone samples with $CaCO_3$ content were not observed *"Chlorella Vulgaris"* in this period. In the studies conducted, five different microbiological organisms were detected on this type of stones [6]. This study has been done to understand that growth of algae on natural stones due to selection of inhibition catalyst materials.

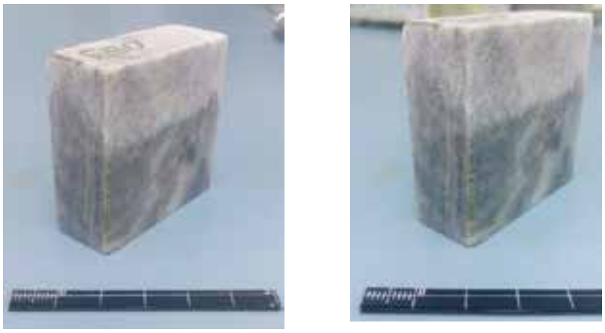

Figure 1. “*Chlorella Vulgaris”* development on $CaCO_3$ content stone with low grade metamorphism

The SEM photographs of the synthesized nano powders were shown in Fig. 2. after the sol gel synthesis process of Ag, TiO_2 and Ag/TiO_2 nanoparticles. The obtained powders are in nano-sized according to SEM images. However Ag nanoparticles are coarser than TiO_2 nanoparticles and all particles are almost equiaxial both Ag, TiO_2 and Ag/TiO_2 nanoparticles.

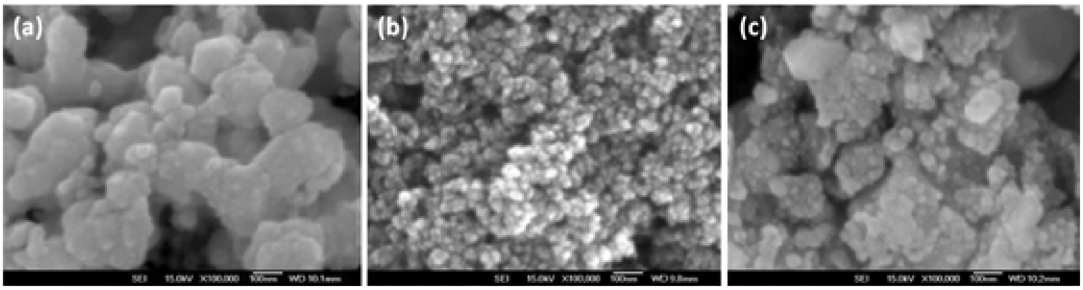

Figure 2. SEM image of synthesized Ag nanoparticles **(a),** TiO_2 nanoparticles (b), and Ag /TiO_2 nanoparticles (c).

SEM-EDS analysis of synthesized Ag /TiO_2 nanoparticles are shown in fig 3. The peaks indicate that the synthesized nano powders has Ti, O, and Ag which corresponds to TiO_2 and silver nano particles.

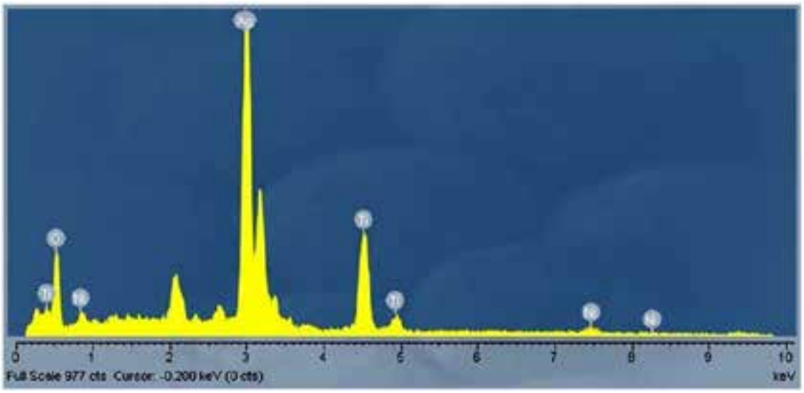

Figure 3. SEM-EDS analysis of synthesized Ag /TiO_2 nanoparticles.

The XRD result are shown in fig. 4 showed that the synthesized powders has anatase phase TiO_2 via sol-gel method and all peaks are indicates anatase phase. All the peaks correspond to anatase phase (JSPDS Card no. 21-1272). And there is no peak indicating the presence of any other peaks than anatase in synthesized TiO_2 nano powders.

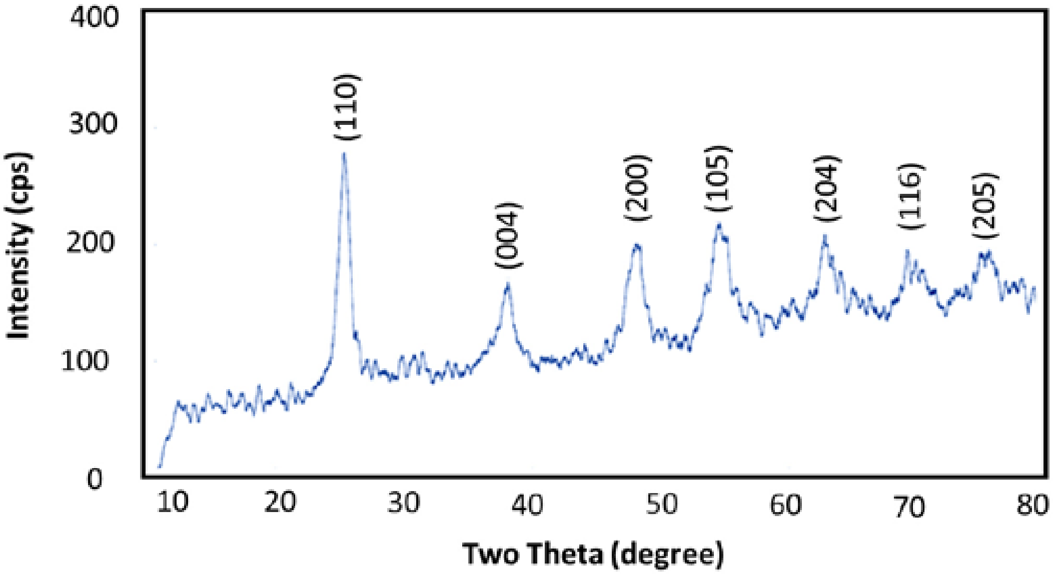

Figure 4. XRD patern of sythesized TiO_2 nanoparticles

Conclusions

"Chlorella Vulgaris" type algae not to hang on to carbonic stone, in this case, another types of microorganisms such as lichens, fungi and bacteria will development on carbonic stones due to choose appropriate interaction photocatalytic materials. TiO_2 and Ag /TiO_2 nanoparticles which obtained will mixed some polymer materials (Fluoroelastomers, silicon based etc.) then apply on stone surfaces that observe photocatalytic effect due to make self-protection coating materials. These coating materials will evaluate with some cultural heritage tests methods such as water repellence, contact angle, vapour permeability and colour determination for durability of these materials. In other hand, photocatalytic properties of TiO_2 and Ag /TiO_2 nano particles will test for self-cleaning effect due to remove detrimental microorganisms on stone surfaces.

[1] Fujishima A, Honda K. Electrochemical photolysis of water at a semiconductor electrode. Nature 1972; 238:37–8.
[2] Chen J, Poon C. Photocatalytic construction and building materials: From fundamentals to applications. Build Environ 2009; 44:1899–906.
[3] Wang R, Hashimoto K, Fujishima A, Chikuni M, Kojima E, Kitamura A, et al. Light-induced amphiphilic surfaces. Nature 1997; 388:431–2.
[4] Rai, M.; Yadav, A.; Gade, A. Silver nanoparticles as a new generation of antimicrobials. Biotechnol. Adv. 2009, 27, 76–83.
[5] Richard, L.D.; Samuel, F.E. The development and functions of silver in water purification and disease control. Catal. Today 1997, 36, 107–114.
[6] Canol, H, Conservation and Restoration of Archaic Stones of Ancient Cities of Euromos and Iasos – Development of New Polymers for the Protection of Archaic Stones, 2018, PhD Thesis, University of Florence.

Characterization of Zirconium-Tantalum Metallic Glass Coatings Produced by Combinatorial Sputtering

Ali Bagheri BEHBOUD[1], Gökhan TARMAN[2], Amir MOTALLEBZADEH[3], Sezer ÖZERİNÇ[1]
[1]Middle East Technical University, [2]TOBB University of Economics and Technology, [3]Koç University
Turkey

Abstract

In this work, we explore the metallic glass forming ability of binary alloys of zirconium and tantalum. We prepared Zr-Ta alloy coatings on a single oxidized silicon substrate by employing the combinatorial sputtering technique. X-ray diffraction characterized the microstructure of the coatings and nanoindentation measurements provided the hardness as a function of composition. High hardness and amorphous structure of the coatings at a wide range of compositions make ZrTa a promising alloy system for various coating applications.

1. Introduction

Metallic glasses are alloys that exhibit an amorphous structure, as opposed to conventional crystalline alloys. Depending on the composition and alloying elements, metallic glasses exhibit desirable properties such as high hardness, wear resistance, corrosion resistance, and biocompatibility [1]. Metallic glasses can also be obtained in thin film form [2], making them a suitable class of materials for various coating applications. In this work, we explore the glass forming ability of binary alloys of zirconium and tantalum, a system that has not been systematically investigated so far. Zirconium and tantalum are two metals with high hardness, corrosion resistance, and biocompatibility, making this binary alloy a promising system for coating design and development.

2. Materials and Methods

We prepared 1.5 μm-thick Zr-Ta alloy coatings on an oxidized single crystal silicon substrate using magnetron sputtering. We employed the combinatorial sputtering technique to get different compositions over a single substrate. We analyzed 13 different compositions of Zr-Ta by cutting the sample into small segments.

2. Results

The results show that the coatings with Zr content in the range of 30–70 at.% are amorphous. When the Zr content is lower, Ta phase exhibited partial crystallization, forming nanoparticles within the amorphous matrix. The hardness of the coatings varied in the range of 6–12 GPa, and hardness increased with increasing Ta content, as shown in Figure 1.

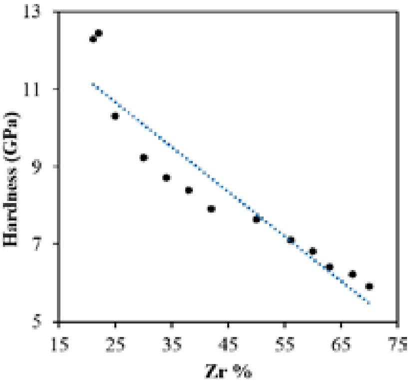

Figure 1. Variation of hardness with Zr composition.

3. Conclusion

The study shows that magnetron sputtering can produce ZrTa metallic glass coatings over a wide range of compositions. The high hardness of the coatings with no grain boundaries provides a powerful model system for the development of corrosion and wear resistant coatings for various applications.

Acknowledgment

This research was supported by the Scientific and Technological Research Council of Turkey, Project #218M219. We thank METU Central Laboratory and Koç University KUYTAM for their support in characterization measurements.

References

[1] W.H. Wang, C. Dong, and C.H. Shek, Mater. Sci. Eng.R, 44 (2004) 45-89 .
[2] J.P. Chu, J.S.C. Jang, J.C. Huang, H.S. Chou, Y. Yang, J.C. Ye, Y.C. Wang, J.W. Lee, F.X. Liu, P.K. Liaw, Y.C. Chen, C.M. Lee, C.L. Li, and C. Rullyani, Thin Solid Films, 520 (2012) 5097-5122.

A Comparative Study in the Economy of the Hydrometallurgical and Pyrometallurgical Copper Extraction from Low-Grade Chalcopyrite Ores

Mohammad MOKMELI[1], Masoumeh Torabi PARIZI[2], Hassan Sahraei PARIZI[2]
[1]University of Tehran, [2]R&D Center of Sarcheshmeh Copper Complex
Iran

Abstract

Chalcopyrite, as the most abundant source of copper, has been traditionally recovered pyrometallurgically, using flotation, smelting and electrorefining processes. The ore treatment is usually limited to the cut-off grade concentration below which the ore cannot be profitably treated. In this study a comparison in pyrometallurgical and hydrometallurgical treatment of low grade (0.23%Cu), high content chalcopyrite (>90%) ore for a treatment rate of 5,000,000 ton ore/year was studied from an economical point of view. Capital cost estimates were made assuming that the current SX and EW facilities in a hydro plant and the current smelting and electrorefining plants in the pyro route have enough free capacity to absorb the upstream outputs. The bio heap and ore dressing plant however, was assumed to be needed to be built. The copper extraction efficiency for the pyro plant was obtained 80% where the hydro plant extraction efficiency is expected to be between 30% to 50%. The operating cost for the pyro plant was calculated 17 times less than the hydro plant, mostly due to the gold, silver and molybdenum credits. The impact of the discount rate was found very significant on the preference of the hydro route over the pyro route despite the high operating cost of the hydro plant. The capital cost of the ore dressing plant can easily make the hydro process more feasible than the pyro process at interest rates higher than 19.7%. At the discount tare of 19.7%, the Net Present Value of the pyro plant at 80% Cu recovery is equal to the NPV of the hydro plant at 30% Cu recovery.

1.Introduction

Chalcopyrite ore, is the most common economic copper mineral to be treated pyrometallurgically through ore dressing, smelting and electrorefining process. Higher copper recovery and byproduct credits of silver, gold and molybdenum were resulted in lower operating cost in the pyrometallugiacal treatment of chalcopyrite ores comparing to the hydrometallurgical treatment of the ore. However, high capital cost, and low flexibility in pyrometallurgical treatment of low-grade ores, limited the treatment of chalcopyrite to the cut-off grade concentrations below which the ore cannot be profitably treated.

In this study, economic feasibility in treatment of 5,000,000 ton/year low grade (0.23%Cu) chalcopyrite ore (>90%) through pyrometallurgical and hydrometallurgical routs were investigated. It is expected that a 100 million tons of low-grade ore, mostly chalcopyrite, is available (rough estimate) at waste dump areas at Sarcheshmeh mine. For this amount, and with treatment of 5,000,000 ton/year, 20 years of operation, in minimum, seems promising.

2. Experimental Procedure

60 tons of low-grade ore was sampled and sent to the pilot plant for crushing and grinding. About 15 tons of the crushed ore was then fed to the ore dressing pilot plant. The average chemical and mineralogical analysis of the ore using XRD and XRF analysis are presented in table 1.

Table 1. Low grade chalcopyrite ore analysis of Sarcheshmeh.

Composition	$CuFeS_2$	FeS_2	CuO	Mo
Value (%)	0.64	8.84	0.01	0.023
Composition	Fe	Cu	Quartz	Microcline
Value (%)	4.39	0.23	18.9	9.5
Composition	Muscovite	Illite	Albite	Clinochlore
Value (%)	30.6	28.6	3.6	3.5

The sample is about 100% chalcopyrite and free of chalcocite and covellite. About 76% of the ore is consisted of clay type gangue. The very high value of illite, in specific, can cause difficulties in floatation and through the froth making process. Despite the high illite content of the ore, the pilot scale flotation tests resulted in production of 22.45% Cu concentrate with the 90.9% total copper recovery. The copper concentrate in the rougher was found 1.75%. The iron recovery in the rougher were 21.4% and 5.9% in the final stage. The molybdenum recovery was also reported as 78.6%. The silicon content of the concentrate was 7.6%. Repetition test was validated the results. 23.3% copper content of the concentrate including 6.3% SiO_2 and final recovery of 87.9% was observed after repetition. As a result, the copper extraction efficiency for the ore dressing plant was chosen 87% in upcoming calculations. The smelting and electrorefining extraction efficiency were reported 93% and 99%. This is equal to the 80% total copper extraction efficiency (87%×93%×99%) from the ore to the final Cu cathode product. In this regard, the annual production rate in a form of copper cathode from a 5,000,000 ton of 0.23% chalcopyrite mineral is equal to 9,212 ton/year cathode.

The operating cost for the pyro process excluding the open pit mining cost, exploration right cost and precious metals and molybdenum credit is about 19,000,000 toman/ton of copper cathode; equal to 1.9 $/t Cu cathode assuming 1$/10,000 toman exchange rate. This value is reduced to 1,117,000 toman/ton of copper cathode with addition of the Au, Ag and Mo credits. This is about one seventieth of the original operating cost. For the pyrometallurgy route, the gold, silver and molybdenum content of the ore are recovered as anode slime as well as molybdenum concentrate at the recovery rates of 0.001% and 0.02% for Au/Ag and Mo, respectively. The operating cost for the hydro process excluding the open pit mining cost and exploration right cost was reported about 17,500,000 toman/ton of copper cathode; equal to 1.75 $/t Cu cathode assuming 1$/10,000 toman exchange rate. The construction of a heap facility is included in this value. This is because the heaps are usually constructed assigning to treat a known amount of ore. Au, Ag and Mo content of the ore are not usually recovered through hydrometallurgical routes and therefore a relevant credit value to it do not reduce the final operating cost. The tax rate is already included in the pyro plant and hydro plant's operating expenses.

The capital cost required for the 5,000,000 ton/year ore dressing plant (including the ore crusher and grinder) is about 1,800,000,000,000 toman, about 180M$. The smelting and electrorefining plants at Sarcheshmeh have a 50,000 and 100,000 tons of free production capacity and therefore a total capital cost assigned for treatment of 5,000,000 ton/year low grade ore is confined to the ore dressing plant. Considering the free capacity of the SX and EW, the capital cost required for the hydro plant is assumed 0 toman.

3. Results and Discussion

The heap leach/SX/EW copper efficiency is very much depends on the heap leach extraction efficiency. The copper extraction efficiency for a low-grade chalcopyrite ore may vary from 20% to 50% for one year [1]. In this study the minimum extraction at which the Net Present Value of hydro plant get equal to the pyro plant is being calculated. As a result, the extraction efficiency of the hydro plant was chosen as a variable. The Net Present Value of the project and its Internal Rate of Return were calculated as a function of different extraction efficiencies for the hydro plant and 80% extraction efficiency for the pyro plant. The economic analysis in this study projects the cash position and return on investment for both hydro and pyro plants and based on the basic assumptions listed in table 2. For both operations to be profitable, the selling price of the copper must exceed the operating costs calculated above and presented in table 2 and also should be below the market price of 5.175US$/kg Cu cathode (LME price, 17 April 2020). The measurement of investment attractiveness for a pyro and hydro plant are presented in this study based on a net present value (NPV) of the projects and their internal rate of return (IRR). The procedure details are presented in special issue of the mineral processing plant design, practice and control proceeding [2-6]. The capital cost for an ore dressing plant is assumed to be invested in 3 years and therefore in three portions: 20% for the engineering and procurement over the first year, 60% for the construction and commissioning expensed over the second year and the final 20% working capital expensed over the third year.

Table 2. Assumptions made in calculation of hydro and pyro plants' NPV and IRR.

Tax rate	25% (deducted from the OPXEX)
Operation duration	20 years
Ore dressing plant construction period	3 years (20% 1st year, 60% 2nd year, 20% 3rd year)
Depreciation	12.5%
Interest rate	Variable (0%, 10%, 18.5%)
Capital cost for the pyro plant	1800 Billion toman
Capital cost for the hydro plant	0 toman
Pyro plant extraction efficiency	80%
Hydro plant extraction efficiency	Variable
Cu cathode market price (LME, 8 April 2019)	5.175US$/kg Cu cathode

At the end of year three, the plant is assumed to reach to the production level of 5,000,000 tons ore treatment. The copper selling price was assumed to be constant over the whole operation period for US$5175/ton (LME price reference, 17 April 2020).

The ore dressing plant's capital cost is depreciated linearly with 12.5% rate over the first eight years. The 25% tax rate is already included in the operating cost. The operating cost was assumed to be constant over 20 years and not inflated. The analysis does not take into account the salvage value of the ore dressing plant after 20 years of operation and the possibility of capital recovery for the portions of working capital.

The overall results for the IRR, project cash position over the life of the project and net present value of the projects at the discounted rates of 0%, 10% and 19.7% for both pyro and hydro plants are presented in figure 1. As can be seen the discount rate has a vital effect on the preference of the hydro plant over the pyro plant. The lower the discounted rate the more feasible the pyro route. For example, in a discount rate of 0%, the NPV of the pyro plant is 9,328 billion toman whereas the hydro plant even at 100% copper extraction efficiency generates 7,879 billion toman revenue. Increasing the discount rate to 10%, lowers the pyro

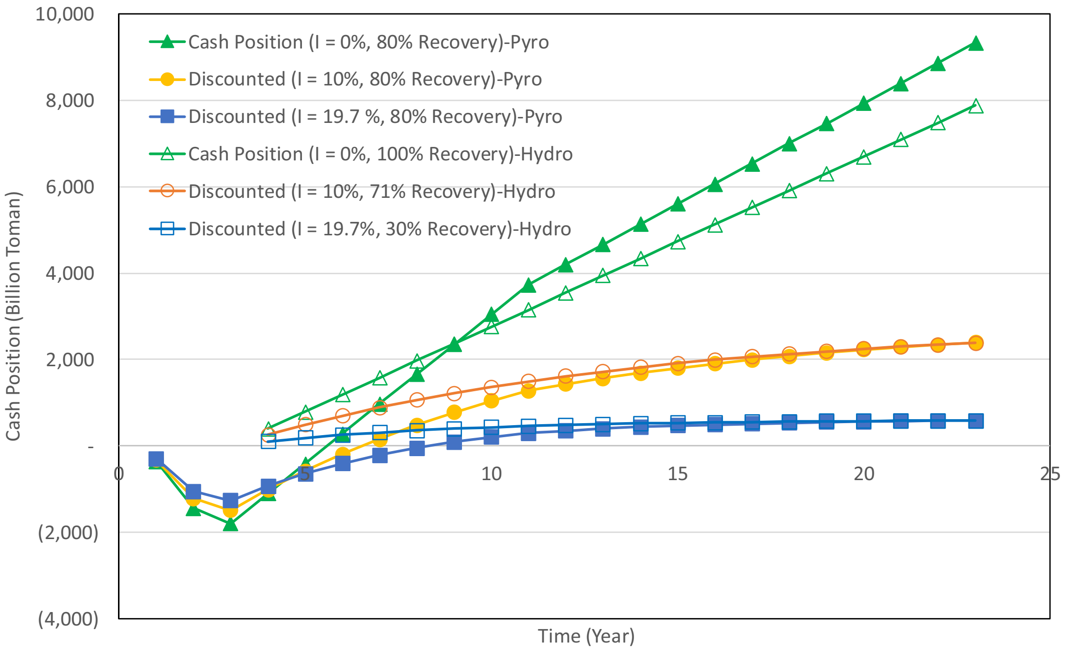

Figure 1. Cash position diagram for the 80% pyro plant and 100%, 71% and 30% hydro plant Cu recovery as a function of discounted rates of 0%, 10% and 19.7%

project's NPV to 2,395 billion toman which is equal to 71% copper extraction efficiency for a hydro plant. The 71% copper extraction efficiency is almost impossible to achieve in bio heaps of low-grade high content chalcopyrite ores. The maximum extraction recovery that was reported is about 50% [1]. This means that at interest rate of 10%, the ore dressing plant is favored economically over the hydro plant. The more reasonable rate at which bio heap leaching of the low-grade high content chalcopyrite ore was reported is 30% over one year of operation [6]. At 30% hydro plant operation the NPV of the plant will be 583 billion toman. For this value the pyro plant generates the similar NPV at 19.7% discounted rate. Considering the fact that 30% recovery is attainable over a year of operation for a low-grade ores and since the 19.7% discount rate is not very appealing investment, the hydro process seems more feasible than the pyro process at this interest rate. This is irrespective to the 17 times higher operating cost of the hydro plant and is due to the high capital cost investment required for the pyro plant. The authors of this work, however, does not recommend the running of hydro plant with just 30% recovery rate due to the waste of other 70% and its environmental consequences. There have been few recent innovations in a pilot scale on bio heap recovery of low-grade chalcopyrite ores [8]. What we are suggesting is to wait or continue researching the subject until one of the solutions for the efficient treatment of the low-grade primary copper ores reaches to commercial scale operation. Long story short, do nothing scenario seems to be the best option for above mentioned scenario.

4. Conclusion

The concentrate made through the operation of the ore dressing pilot plant proves the technical feasibility of producing 22.4% Cu concentrate form a low grade (0.23% Cu) high content (>90%) chalcopyrite ore. The capital cost investment required for the treatment of 5,000,000 ton/year low grade ore makes the pyro route economically feasible at lower interest rates. At the discount rates higher than 19.7%, the NPV of the pyro plant with 80% total extraction efficiency becomes equal to the NPV of a hydro plant with 30% extraction efficiency. For the hydro plant capital investment was not taken into consideration due to the usage of the available free capacity of the hydro plant. Therefore, at interest rates higher than 19.7%, a do-nothing scenario is suggested in treatment of low-grade ores due to the environmental impacts and waste of resources the current low efficient bio heap recoveries are generating.

Acknowledgment:

The authors of this work wish to gratefully acknowledge the National Iranian Copper Industries Company for their support of this work.

References:

[1] J. Scott, B. Johnston, Mineral processing plant design, practice, and control proceedings, SME, 2002, vol 1, 281-310

[2] M. Mokmeli, Hydrometallurgy, 191, (2020) 105, 215

[3] A. L. Mular, Mineral processing plant design, practice and control proceeding, SME, 2002, vol 1, 310-326

[4] D. Halbe, T. J. Smolik, Mineral processing plant design, practice and control proceeding, 2002, SME, vol1, 326-346,

[5] R. Halupka, Mineral processing plant design, practice and control proceeding, SME, 2002, vol 1, 371-383

[6] L. D. Smith, Mineral processing plant design, practice and control proceeding, SME, 2002, vol 1, 346-371

[7] S. Panda, K. Sanjay, L. B. Sukla, N. Pradhan, T. Subbaiah, B. K. Mishra, M. S. R. Prasad, S. K. Ray, Hydrometallurgy, 125–126, (2012), 157–165

[8] D. Dreisinger, Copper 2019 conference, 2019, Vancouver, Canada.

Industrial Study of Tantalum Metal Production from Ore with Alkaline Process

Safiye TANRIVERDİ[1,2], H. Hande CEBECİ[2,3], Cem KAHRUMAN[1]

[1]İstanbul University – Cerrahpaşa, [2]Proses Rafinasyon ve Metal Geri Kazanım Makina Sistemleri San. ve Tic. Ltd. Şti, [3]Yıldız Technical University

Turkey

Abstract

The tantalum metal in the ore is produced as a result of alkali process. This process has been adapted to the industry by achieving successful results with alkaline studies. For the production of Ta from ore, more environmentally alkaline process method has been developed instead of HF studies are done worldwide. Alkali / ore ratio, roasting time and temperature are effective in roasting process, while solid / liquid ratio, mixing speed and temperature are effective in leaching process.

1. Introduction

The production of rare element tantalum from ore is carried out worldwide with systems using HF. Since hydrofluoric acid is an abrasive, piercing and highly poisonous gas, different methods have been sought in the primary production of Ta. In this article, primary production with alkali process has been studied. 6-7% evaporation in HF systems causes serious pollution. To eliminate environmental concerns, large amounts of fluoride-containing wastewater should be treated. Alkaline roasting followed by water leaching processes were started to eliminate fluoride pollution. In alkali roasting studies with KOH and NaOH in the literature, dissolution efficiency was obtained at rates of 95% and 65%, respectively.[1]

2. Materials and Methods

In this study, the steps of alkali roasting and leaching processes were investigated in the production of tantalum metal from ore by alkaline process. The first step is alkaline roasting. With alkaline roasting, tantalum metal is intended to form water-soluble compounds. Alkaline roasting experiments were carried out with potassium hydroxide and sodium hydroxide. Sample was roasted with NaOH for 120 minutes at 600°C. Other sample was roasted with KOH for 90 minutes at 650°C. Then, the roasted sample was leached with water as second step for the transition of tantalum metal to the solution. The chemical analysis of the starting sample is given in table 1. The chemical analysis of the solution after leaching is given in table 2 and table 3.

Table 1. Chemical analysis of the material ore (wt. %).

Fe_2O_3	Nb_2O_5	Ta_2O_5	SnO_2	Al_2O_3	MgO	MnO	SiO_2	TiO_2
10.00	15.76	17.25	10.61	9.12	0.52	7.72	9.52	8.21

Table 2. Chemical analysis of the leaching solution (ppm) after alkali roasting with NaOH

Ta	Sn	Ti	Mn	Si	Fe	Al
36.996	10.501	2.532	12.056	13.565	0.234	22.187

Table 3. Chemical analysis of the leaching solution (ppm) after alkali roasting with KOH

Ta	Sn	Ti	Mn	Si	Fe	Al
59.758	4.216	27.488	13.337	7.554	12.739	25.563

3. Conclusion

The amount of tantalum oxide contained in the starting sample and the amount of tantalum transferred to the leaching solutions were examined. The yield of tantalum in leaching after alkaline roasting with NaOH is about 42%, while it is about 69% with KOH. Alkali roasting with KOH provides tantalum yield higher than NaOH.

Reference

[1] Nguyen, T. H., Lee, M. S., 2018, “A review on the separation of niobium and tantalum by solvent extraction”, Mineral Processing and Extractive Metallurgy Review, doi:10.1080/08827508.2018.1526794.

Effect of Building Direction and Thermo-Hydrogen Processing on the Microstructure and Texture of Electron Beam Melting (EBM) Processed Ti6Al4V Alloy

Merve N. DOĞU[1,3], Ziya ESEN[2], Kemal DAVUT[3,4], Evren TAN[5], Berkay GÜMÜŞ[5], Arcan F. DERİCİOĞLU[1]

[1]Middle East Technical University,[2] Çankaya University, [3]Atılım University,
[4]Metal Forming Center of Excellence, [5]ASELSAN A.Ş.

Turkey

Abstract

The present study investigated the effects of building direction and 2-step Thermo-Hydrogen Processing (THP) on the microstructure and texture of Ti6Al4V alloy parts produced by Electron Beam Melting (EBM). The results showed that regardless of the building direction, microstructure and crystallographic texture of the as-built samples had Widmanstätten structure and columnar β-grains which is parallel to building direction. The main texture component for the α phase was $(10\bar{1}0)$ // building direction, and for β phase (001) // building or heat flow direction. On the other hand, after application of THP, microstructure was refined, and randomized crystallographic texture was obtained.

1. Introduction

Ti6Al4V alloy is one of the most widely used titanium alloys because of its superior properties such as high specific strength, low density and good corrosion resistance [1]. It is generally produced via conventional fabrication techniques, yet additive manufacturing technique offers some advantages such as production of complex shapes in a single step, which is not possible by conventional fabrication techniques, and decreasing scrap metal [2]. EBM is a powder bed metal additive manufacturing technique, and it provides high density (>99%) for the produced complex parts. Although EBM offers various advantages, there are also some drawbacks such as residual stress and high surface roughness [3]. In order to eliminate these drawbacks post-processes, i.e. machining to improve surface quality and heat treatments to eliminate residual stress, should mostly be applied after the production. THP is an alternative heat treatment, and it is used to increase the strength of titanium and titanium alloys produced by casting as well as by powder metallurgical processes via microstructural refinement without deformation [4].

2. Materials and Methods

In the present study, Ti6Al4V alloy parts were produced at three building directions (90º, 45º, 0º) via EBM. After production, 2-step THP (hydrogenation and dehydrogenation) was applied only to samples produced at 90º. In 2-step THP, 650 °C and 700 °C were used as the hydrogenation and dehydrogenation temperatures, respectively. Microstructure of the as-built and heat-treated samples were examined using optical microscope and scanning electron microscope (SEM). In order to investigate texture of the as-built and heat-treated samples, electron backscattered diffraction (EBSD) was used.

3. Conclusions

Microstructure and crystallographic texture of the as-built samples had Widmanstätten structure and columnar β-grains which is parallel to building direction regardless of the building direction. The main texture component for the α phase was $(10\bar{1}0)$ // building direction and for β phase (001) // building or heat flow direction. After the application of 2-step THP, microstructure was refined and crystallographic texture was randomized. The grain boundary misorientation distributions also changed in accordance with the microstructural changes during the 2-step THP.

References

[1] M.N. Doğu, Production of Ti-6Al-4V Alloy by 3D Electron Beam Melting Technique and Development of its Post Treatments, Middle East Technical University, 2019.

[2] M. Fousová, D. Vojtěch, K. Doubrava, M. Daniel, C.F. Lin, Influence of inherent surface and internal defects on mechanical properties of additively manufactured Ti6Al4V alloy: Comparison between selective laser melting and electron beam melting, Materials (Basel). 11 (2018).

[3] H.K. Rafi, N. V. Karthik, H. Gong, T.L. Starr, B.E. Stucker, Microstructures and mechanical properties of Ti6Al4V parts fabricated by selective laser melting and electron beam melting, J. Mater. Eng. Perform. 22 (2013) 3872–3883.

[4] G.M. Bilgin, Z. Esen, Ş.K. Akın, A.F. Dericioglu, Optimization of the mechanical properties of Ti-6Al-4V alloy fabricated by selective laser melting using thermohydrogen processes, Mater. Sci. Eng. A. 700 (2017) 574–582.

Characterization of Interfaces Between Intermetallic Precipitates and Matrix in Some Magnesium Alloys

Uğur Can ÖZÖĞÜT[1], Servet TURAN[2], Ali Arslan KAYA[3]
[1]Muğla Sıtkı Koçman University, [2]Eskişehir Technical University
Turkey

Abstract

This work focusses on the nature and the effect of precipitate/matrix interfaces with the aim of relating it to the damping as well as to the deformation capacity qualitatively. The fundamental property, work function, may be considered as an indicative of the stacking fault energy (SFE) through the predominant bond type in matrix and at the precipitate/matrix interfaces. Therefore, the work function values of different precipitate/matrix interfaces in some magnesium alloys with reference to pure magnesium have been measured and compared. Magnesium alloys with nominal compositions of Mg-10Al-5Ca-2Ba-2Sn, and Mg-2Zn-2Y have been employed as they involve a number of different types of precipitates and therefore interfaces with the magnesium matrix. Work function values at the atmospheric conditions were measured using Kelvin Probe Force Microscope (KPFM), E-Modulus values of each alloy were measured via an impact excitation technique via RFDA (resonance frequency damping analysis).Line analysis on the work function maps showed the difference between each individual intermetallic precipitates and matrix phase. These values compared with the ab-initio SFE values obtained from literature have been incorporated in our interpretations and comments with respect to the SFE values of the alloy systems as well as to the damping and deformation capacities.

1. Introduction

Magnesium and its alloys widely preferred in many enginnering applications due to its light weight among the structural metals. The recent researches show that besides the light weight of magnesium alloys, corrosion resistance and mechanical properties should be enhanced. This improvement is made possible by alloying that mostly in the presence of second phase or precipitates. The characterization of precipitates and matrix interfaces is very crucial to determine the mechanical property of magnesium alloys.

2. Materials and Methods

In this work, magnesium alloys with nominal compositions of Mg-10Al-5Ca-2Ba-2Sn, and Mg-2Zn-2Y are investigated. Work function values at the atmospheric conditions were measured using Kelvin Probe Force Microscope (KPFM), E-Modulus values of each alloy were measured via an impact excitation technique via RFDA (resonance frequency damping analysis).

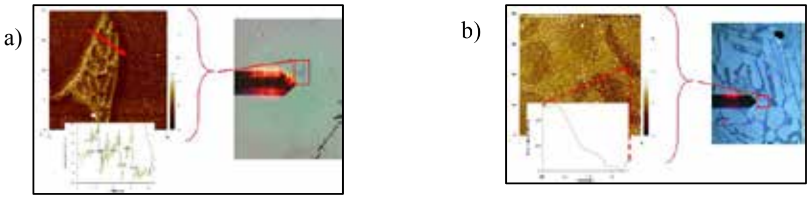

Figure 1. KPFM line analysis of work functions a) Mg-2Zn-2Y, b) Mg-10Al-5Ca-2Ba-2Sn.

3. Conclusion

As a result, E-Modulus values of Mg-10Al-5Ca-2Ba-2Sn, and Mg-2Zn-2Y respectively 42.32 GPa, 53.47 GPa were determined via RFDA. And work functions of these alloys as it shown in the figure above are the same change regime qualitatively of the ab-initio SFE values from literature.

Nanostructured High Entropy Alloys with High Strength

Ö. Gökhan TARMAN[1], M. Yiğit KÖHNETARFUN[1], Amir MOTALLEBZADEH[2], Sezer ÖZERİNÇ[3]
[1]TOBB University of Economics and Technology, [2]Koç University,
[3]Middle East Technical University

Turkey

Abstract

Development of high entropy alloys (HEA) has become a topic of extensive research in recent years due to the excellent properties and great potential of HEAs for structural applications. In this study, we synthesized HEA nanocomposites composed of alternating layers of NbMoTaW and CrCoFeNi. At a layer thickness of 10 nm, the nanocomposite hardness reaches 10.6 GPa. Outstanding strength of the nanolayered structure offers new opportunities for the development of next generation high performance alloys.

1. Introduction

High entropy alloys are promising materials due to their unique properties such as high strength, sluggish diffusion, severe lattice distortion, and cocktail effects [1]. Nanostructured metals is another class of materials that provides outstanding mechanical properties due to grain refinement [2] and large density of interfaces & free surfaces. By combining the idea of nanostructured materials with high entropy alloys, further enhancement in mechanical properties seems possible. We investigated this route by the fabrication of FCC/BCC nanolayered HEA composites.

2. Materials and Methods

We prepared NbMoTaW/CrCoFeNi nanolayered thin film samples by performing magnetron sputtering on oxidized silicon substrates. The layer thicknesses varied in the range of 10 to 200 nm. Both NbMoTaW and CrCoFeNi layers had equiatomic compositions. X-ray diffraction characterized the microstructure and nanoindentation quantified the hardness of the films.

3. Results

Microstructural analyses suggest the presence of FCC and BCC layers. As layer thickness decreases, the average grain size of each phase decreases. On the other hand, hardness monotonically increases with decreasing layer thickness, and reaches its maximum value of 10.6 GPa for the 10 nm layer thickness sample.

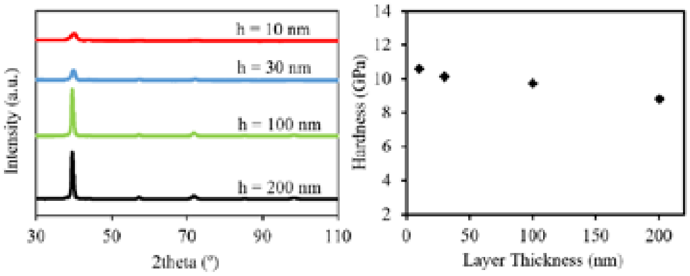

Figure 1. On the left, XRD patterns, on the right, hardness of the nanolayers.

4. Conclusion

The results show that the strength of HEAs can be further improved by employing a nanostructured design. Combining the ideas generated by the nanostructured materials research community with those of HEA research provides a promising route towards the development of novel high performance structural alloys.

Acknowledgments

We would like to thank METU Central Laboratory and Koç University KUYTAM for their support in material characterization.

References

[1] Y. Zhang et al., Progress in Materials Science, 61 (2014) 1-93.
[2] Y. Ma, M. Yang et al., Metals, 9 (2019) 598

Determination of Mixing Ratio of Alloy Materials in Manufacturing of Power Transmission Line Aluminium Alloy Conductor

İ. BİNBUĞA, Ü. UNCU, E. KISTI, H. AYKANAT, İ. GÖK, S. ÖZER

EMTA Conductor &Cable

Turkey

Abstract

As the purpose of this project, in terms of the production method, in bare transmission lines for 6101 and 6201 series aluminum alloying element in which there is less than 2% of the total suitable alloy element, parameters of the production process that are effective on each other have been identified, the optimal alloy ratio has been determined, the delicate balance between conductivity and strength interpreted, the effectiveness of the parameters affecting the dump has been determined and a computer package program has been created from these parameters. As a result of the project, optimum raw material comparison rates and production parameters were determined to provide the required characteristics of the product in a way to minimize raw material costs without experimental production using functional relationships and mathematical models. Thus, more efficient and economical working conditions were provided without test products both in terms of time and cost. Advantage and competitive advantage with regards to time has been achieved. In addition, the efficient operation of personnel and machines was ensured by minimizing work packages resulting from test productions.

1. Introduction

Today, companies meet consumer demands by performing the activities fulfilled during the production process and by producing on time. In order to achieve quality for the first time and to achieve an effective and efficient production, they must also consider test products as cost-reducing. In this context, it is aimed to provide more effective and economical working conditions without test productions with respect to both time and cost. And by writing an interface program with mathematical modeling, this problem has been tried to be eliminated.

2. Materials and Methods

In our study, primarily alloy elements that will be used in the production of 6101 and 6201 series aluminum alloy, which we will produce, was selected. The lower and upper limits of the elements of this alloy are specified as defined in legal regulations or standards. As a percentage, how much was to incorporate, which will affect some production processes as well as production (furnace temperature, furnace temperature, tundish metal temperature, exit temperature of the bar the wheel bar inlet temperature induction, temperature of induction plate bar output temperature, casting speed, coolant temperature, coolant flow rate and pressure, water hardness, and conductivity, temperature and emission flow rate) and quality parameters (strength, % elongation, twisting, winding) electrical conductivity and mechanical properties, surface quality, etc. processes) was determined. Design of test, microstructural analysis of experiment production, conducting tensile and conductivity tests, chemical analysis tests of material were used in determining test production, statistical analysis and regression analysis were used in determining functional relationships (ANOVA analysis) and mathematical modeling (Linear or nonlinear programming), artificial neural networks and sensitivity analysis techniques were used in determining optimal prescription and production parameters.

Our production losses in casting, wire drawing, knitting sections have decreased from 50% to 5% thanks to optimization and mathematical modeling, which are among our main objectives. Our number of test productions decreased by 80% thanks to interface software that provides the required casting parameters for the desired results before the casting process. A 15% reduction was achieved in raw material and energy packaging, which was a result of the decrease in test production. This has led to an increase in production volume. As a result of the increase in production volume, our foreign market share increased by 15%.

3. Conclusion

Test productions have been carried out, determination of parameters affecting production has been completed, priority order of the parameters and upper and lower limits of the alloy materials required for casting were determined and optimal alloy mixture ratio has been experimentally determined. The mathematical model of obtaining the mixture quantity at the desired rate has been determined and some optimization studies have been completed. There is a significant decrease in raw material and energy consumption.

Acknowledgment

‘Alloyed Raw Material Comparison Rate and Production for High Voltage Transmission Line Electrical Cable and Communication Production' have been accepted as TÜBITAK project numbered 3141014.

Determination, Examination and Improvement of Breaking Problems in Wire Drawing Processes of 6101 Series 9,5 mm Diameter Aluminum Alloy Wire Rods

Necati OCAK[1], U. G. UNCU[1], İ. BİNBUĞA[1], S. ASLAN[2], E. DURU[2]

[1]Emta Conductor&Cable, [2]Sakarya University

Turkey

Abstract

The aluminum conductor production phase is formed of continuous casting, plastic deformation and stranding processes. The production starts with the melting of aluminum ingots and casting of raw materials in the continuous casting unit. The 6101 series, which is supplied from the continuous aluminum wire rod production line, continues by cold-drawing the 9.5 mm diameter aluminum alloy wire rod in wire drawing machines and converting into any required diameter wire. Aluminum wires drawn at required diameter and length values and stranded in stranding machines and produced as aluminum conductor.

Various defects may occur during aluminum wire drawing processes. Such damages and defects cause problems in the next step. Wire breaks occurring in aluminum wire drawing process during overhead line conductor manufacturing process are one of the most common and costly challenge faced by the wire industry today. Defects must be well known, identified, improved and using damaged products must be prevented to reduce number of aluminum wire breaks. The purpose of this study is to examine the reasons for failure resulting in breakages with respect to wire drawing process in aluminum conductor production and to improve the casting and wire drawing process activities by finding solutions to such causes. Therefore, more efficient and economical working conditions will be provided both with respect to time and cost. In this sense, wire break problems of 6101 series aluminum alloy wire rods at 9.5 mm diameter encountered during drawing will be examined and wire defects and damage will be analyzed with Scanning Electron Microscopy (SEM) and Energy Dispersion Spectroscopy (EDS), causes of failure will be interpreted and improvement methods will be discussed.

1. Introduction

It is required to transmit and distribute electrical energy from production to consumption regions with high efficiency and minimal loss. Energy Transmission is carried out using overhead lines because high voltage insulation problems. The use of copper and aluminum conductors on overhead lines is common [1].

ACSR type overhead line conductors were known to be the most important line products until 40-50 years ago. However, because these conductors contain a composite structure containing steel and aluminum, their vulnerability to environmental impacts was assessed as the negative effect of these conductors. Today, it reveals galvanic corrosion of different materials used in the same construction due to environmental and climatic conditions. That is why they are not preferred. As a result of using aluminum + galvanized steel wire together, it reduces the service life of the conductor after a minimum of 5 years. Therefore, Al-Mg-Si alloys with improved content are preferred. Not only corrosion, but also conductor breaks are other parameters that affect the life of the conductor [2,3]. Environmental conditions in the use of the conductor and vibrations between the wires affect micro damage caused in the production of aluminum wires and further can cause them to break. Accordingly all the problems that may occur in the manufacturing stages, from the raw materials used to the machines being processed, from the operators to the production methods, should be carefully examined.

In this study, the production of 9.5 mm aluminum alloy wire rod of 6101 series and the breaking problems encountered during wire drawing will be examined and wire defects and damage will be analyzed with Scanning Electron Microscopy (SEM) and Energy Dispersion Spectroscopy (EDS), causes of failure will be interpreted and improvement methods will be discussed.

2. Experimental Procedure

6101 series aluminum alloy wire and wire production was carried out in the premises of EMTA Conductor&Cable in Turkey. The samples to be analyzed were taken from broken wires in wire drawing machines. Wires were also analyzed in Sakarya University Metallurgical Engineering SEM-EDS laboratory.

Aluminum conductor production takes place in 4 stages. These are casting, wire drawing, heat treatment and stranding processes. Aluminum ingots with a minimum purity of 99.8% are used as the main raw material. The chemical properties of the aluminum used were determined by Thermoscientific brand chemical analyzer (Table 1.)

Table 1. Aluminum Ingot Chemical Analysis

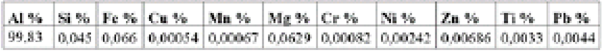

Al %	Si %	Fe %	Cu %	Mn %	Mg %	Cr %	Ni %	Zn %	Ti %	Pb %
99,83	0,045	0,066	0,00054	0,00067	0,0629	0,00082	0,00242	0,00586	0,0033	0,0044

Aluminum ingots are charged to the natural gas-powered melting furnace for melting. The metal, which is melted at about 750°C, is transferred to the tilting furnace at a temperature of 670-730^{0}C by means of a runner. Alloying materials are added from inside the tilting furnace. Homogenization is achieved by mixing liquid metal with the addition of alloying materials. As a result of the transfer of liquid metal from the tilting furnaces, cooling water is supplied to the copper casting mold(wheel) and an aluminum bar with a section area of approximately 2090 mm2 is obtained at a temperature of about 450-500 ° C. The aluminum bar is converted into a 9.5 mm diameter aluminum wire rod in the rolling mill that works with the casting machine. And the aluminium rod is heat treated. Continuous casting line process current diagram is shown Figure 1.

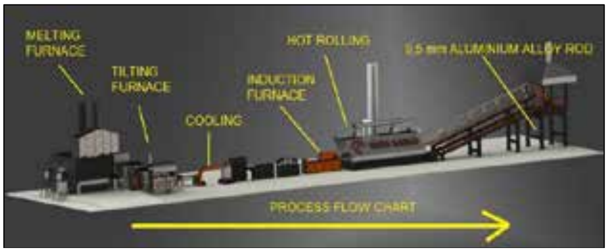

Figure 1. Continuous Casting Flowchart

The 9.5 mm aluminum rod coming from the aluminum continuous casting production line continuously passes through the successive wire drawing lines in the wire drawing machines to achieve the desired diameter. The diameters of each line and successive lines are less than 9.5 mm in diameter. The diameter of the wire decreases as it passes through each die. In the wire drawing process, no material is required to be disposed of, so it is a waste-free process. The volume of the rod is the same if drawn; only the length of the wire is elongated. Wire drawing process current diagram is shown Figure 2 [2,3].

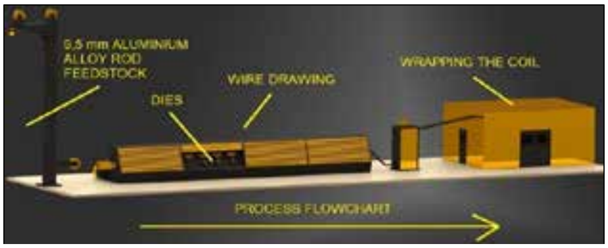

Figure 2. Wire Drawing Process Flowchart

Metals such as aluminum and its alloys, steel, copper are within the cold forming range at room temperature and have the ability to deform significantly without breaking. When the material is cold formed, it becomes stronger. In other words, it increases its strength with cold form change. This is because new dislocations are created by form change, and the movements of new dislocations are becoming more and more difficult, both with each other and with other obstacles. Material hardening as a result of dislocation causes breaks by triggering micro defects (internal voids, oxides etc.) caused by raw material or process within the product). At the same time, the tensile stress should not exceed the yield stress [4].

3. Results and Discussion

Specifications of samples collected from wire drawing machines are shown in Table. 2.

Table 2. Mechanical and electrical properties of the drawn wires

Product Type	Diameter (mm)	IACS (%)	Tensile (MPa)
6101 AA	3,16	55,63	265

The first sample collected during the production of the wire is the tensile break shown in Figure 3. The reason for this type of break is that the wire does not receive enough oil or it cannot resist the pulling force due to absence of lubrication. It breaks like a tensile test. That is, it occurs when the tensile force exceeds the final tensile strength of the wire. Changes in oil concentration and dies prevent wire breaking. In such breaks, a characteristic small crater is found in the fracture formed.

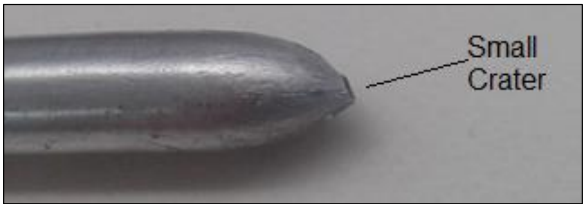

Figure 3. Tensile Breaks

The absence of lubrication can lead to surface defects such as transverse cracks. Surface defects are shown in Figure 4. This is due to the deterioration of lubrication between the die and the aluminum wire. Or it is the cause of die which has completed its life. This type of surface defects affects the embedded oxides, if any, in the next steps, causing the material to break.

Figure 4. Surface Tearing

The wire must have a conical structure. When this angle cannot be provided on the wire, a bulging and distorted structure appears. It is shown in Figure 5. It is understood that die geometry is improper. The problem can be avoided by checking the die system.

Figure 5. Bulging

Crow's feet are V-shaped surface breaks (Figure 6). These are cracks caused by poor lubrication, wrong die usage, and abrasion surface die usage. V signs show the direction of drawing operations. Fractures are usually of the type cut at a 45degree angle. The die can be cleaned, the alignment of the wire in the die can be controlled, abrasive die can be replaced, and the oil flow on all die can be controlled.

Figure 6. Crowsfeet

There is usually a shearing fracture and a shallow hole or cavity on one side of the wire. This void occurs when the inclusion occurs during or after wire break. It can be cleaned better in furnace. Liquid metal should be cleaned from its inclusions. Filtering operations can be done on runner. The hot roll machine can be controlled (Figure 7.).

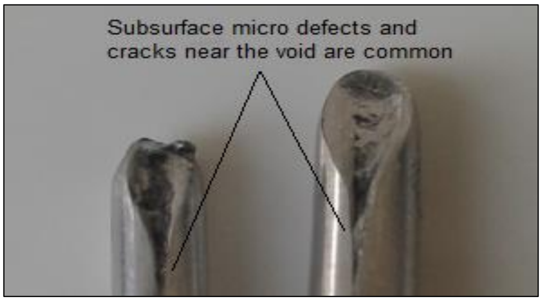

Figure 7. Inclusion Absent

During the melting process, aluminum and aluminum alloying elements (magnesium, silicon, iron, copper, titanium, Boron) are oxidized due to the reaction they enter with atmospheric oxygen. At the end of the melting process the melt oxidizes and contains different solid inclusions. These are contaminants solid pollutants, refractory particles from the furnace, and slag residues. These slags are transferred with liquid metal into aluminum rod. Inclusions should be taken from the melt by proper filtering methods or fluxing before casting to prevent unwanted mechanical and characteristic problems during processing in subsequent processes. A typical slag problem is shown in figure 8.

Figure 8. Slag

In Figure 9 (a), aluminum has a high interest in hydrogen. H_2 absorption of molten metal causes pores in the product. It has a negative effect on the mechanical properties of the material. In order to prevent porosity, gas extraction should be performed by treating atmospheric gases with liquid metal.

In Figure 9 (b), Cuppy wire, oftentimes called central bursting, contains both a cup and a cone end. The wire is extremely brittle near the break. If the break occurs in the rod mill, the cone end always points in the drawing machine, the direction of drawing is reversed. Therefore, the tip of the cup or cone can indicate the direction of the drawing. Cuppy wire may be caused by worn dies, small area reduction, or large reduction angle. However, these internal defects are more of a problem in the presence of internal cavities or oxides.

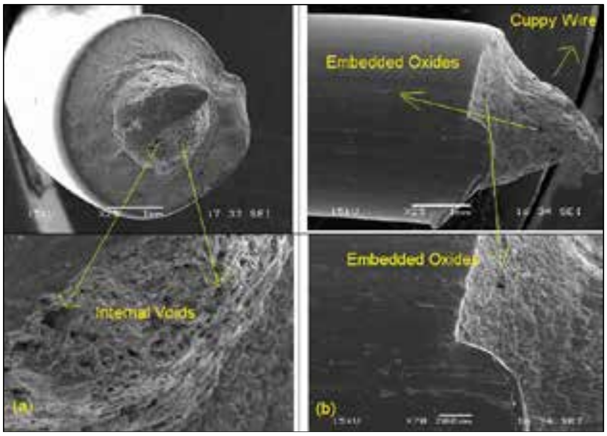

Figure 9. (a) Micro Porosity, (b) Cuppy Wire, Embedded Oxides

Macro porosity in Figure 10 (a), is hollow wire caused by gas, metal shrinkage of casting complications during the casting process. Both ends of the beak contain the internal void. In order to prevent the formation of macro porosity, cooling and temperature control should be done during solidification and the gas content in liquid metal should be reduced

In Figure 10 (b), during continuous casting, solid impurities, inclusions and contaminants in the refractory particles in the furnace are transferred to subsequent processes as inclusions. These are CaO, MgO, SiO2 etc. As they have a hard structure, they can cause breakage in the wire. These pollutants can be prevented from proceeding to the next process with appropriate homogenization, fluxing and filtering methods.

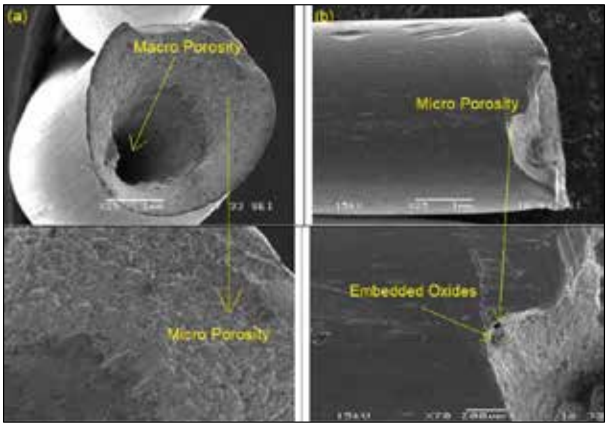

Figure 10 (a) Macro ve micro porosity (b) Embedded Oxides

In Figure 11, Sliver and seams are formed due to improper roll gaps during the rolling process. When the raw material is drawn to the required wire diameter, the strips and seams are the potential source of breakage. The seams and strips are made up of subsurface oxides, which cause the wire to crack and separate. The seams are usually cracks near the center of the wire. The rolling gap settings can be controlled. Guide scratching can be prevented, Drawing application can be controlled.

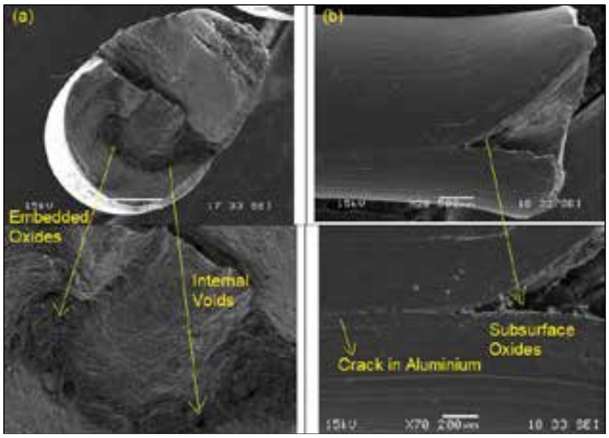

Figure 11 Oxides

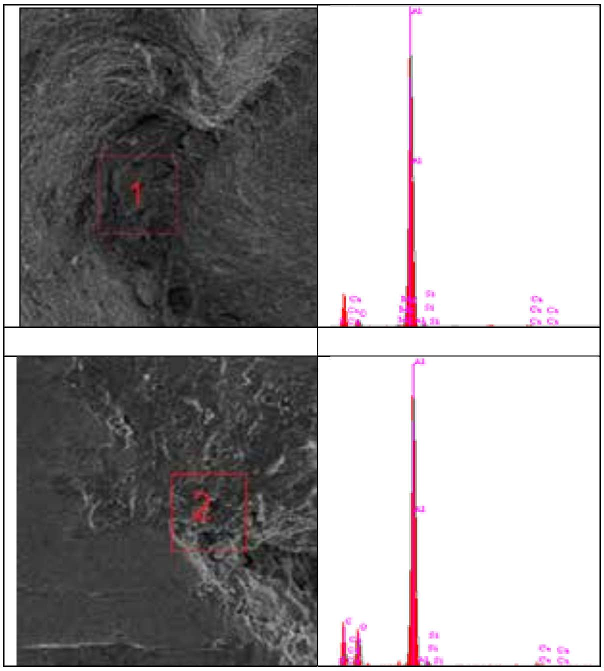

Figure 12. Alloying elements

In Figure 12, the oxide and intermetallics of Al, Mg, Si, Ca, elements form the interstitial compound. There is no metallic bond in intermetallic compounds. That's why, the possibility of breakage during plastic deformation is very high. (As Mg_2Al_3)

4. Conclusion

In this study, different defects were investigated and their causes were explained. The following conclusions can be drawn from this study.

- The use of oil in wire drawing is very important. Non-oil operation can cause damage to wire surfaces. These damages trigger oxides and cavities embedded close to the surface, causing breaks
- The surface quality and geometry of the dies in the wire drawing process affect the properties of the wires. Quality of low surface dies during wire drawing may cause wire surface damage
- In the internal structure analysis of wire breaks, the presence of porosity and oxide structures caused by casting was determined.
- To prevent porosity, temperature and cooling control should be done and the gas content should be reduced.
- During continuous casting, the refractory material particles that come into contact with the aluminum alloy are separated and become inclusions. In addition, oxide and intermetallics of Mg, Si, Ca elements form an interstitial compound in the structure.
- There is no metallic bond in intermetallic compounds. That's why, the possibility of breakage during plastic deformation is very high. These are MgO, CaO, SiO_2 etc. As they have a hard structure, they can cause breakage in the wire. These structures should be checked during melting and alloying of the metal, with proper homogenization and filtering.

References

[1] Electric Electronic Technology, Overhead Energy Lines, Ankara 2011, T.C. Ministry of Education, pp.3-10
[2] Davies,G., Aluminium Alloy [6201, 6101A] Conductors, International Conference on Overhead Line Design and Construction: Theory and Practice (up to 150kV) 28-30 Nov, London UK, 1988, 93-97
[3] Karabay, S., Ertürk A.T., Failure analysis of wire-breaks in aluminum conductor production and investigation of early failure reasons for transmission lines, Engineering Failure Analysis 83 (2018) 47-56
[4] Moharana, B., Breakage Analysis of Aluminum wire rod in Drawing Operation, International Research Journal of Engineering and Technology, Volume: 04 Issue: 12 | Dec-2

Investigation, Development of Parameters Affecting the Technical Properties of ACCC Lisbon Aluminium Conductor and Comparison with ACSR Hawk Conventional Conductor

Necati OCAK[1], U.G. UNCU[1], E. BİLDİK[1], E. KISTI[1], C. DURMAZ[1], Serdar ASLAN[2]
[1]Emta Conductor&Cable, [2]Sakarya University
Turkey

Abstract

Transmission of electricity from generating stations to consumption stations is done by means of overhead line conductors. The selection of conductors used in energy transmission lines is very important. In the choice of conductor to be used, energy losses are aimed to be minimum. Increasing the capacity and efficiency of existing or proposed transmission lines is becoming more important as electricity demand continues to increase. In high voltage transport lines, aluminium conductor steel reinforced (ACSR), commonly referred to as conventional conductors, are used. These conductors are aimed at increasing the current carrying capacity by increasing the dimensions. When the dimensions are increased the weight of the Conductor increases, it tends to sag more at higher temperatures. In order to meet the increasing energy demands, aluminum conductors composite core (ACCC) have been developed in recent years, which combine the increase in efficiency and current carrying capacity with the technology developing according to steel core conductors of the same diameter and weight, allowing more power to be transmitted with less sag. In this study, the mechanical and electrical technical properties (strength, elongation, conductivity) of ACCC Lisbon composite core aluminum conductor, which has been manufactured for the first time in Turkey, will be examined and the improvement works will be explained and within the scope of field applications, the current carrying capacity of the ACSR Hawk conductor line has been increased by approximately 15% in the ACCC Lisbon conductor renovation project without replacing the existing poles, and the sag values have been reduced by approximately 1.5 meters.

1. Introduction

In Turkey, aluminum conductors steel reinforced are generally preferred in power transmission lines. The outer wires in these conductors are high purity aluminum, chosen because of their good conductivity, low weight and low cost. The central wire is steel that serves as the additional carrier to help support the conductor's weight. Steel has higher strength than aluminum, allowing more mechanical stress to be applied to the conductor. Dimensions are increased in these conductors to increase current carrying capacity. It is difficult to give up this feature as it provides steel carrier duty. The current carrying capacity increases when the conductor size is increased. The weight of the conductor increases due to the increase in size. Another negative factor is the sag event, which shortens the life of the conductor line and causes more sag at high temperatures. To eliminate the disadvantages of conventional conductors in order to meet increased energy demands along with the developing technology in recent years, the current carrying capacity of conventional conductors of the same diameter and weight and yield increase as compared to combining more power, less sag, which allows to be transmitted with aluminum conductors composite core that have been developed [1]. Instead of the steel core used in conventional aluminum conductors (ACSR), composite core is used in aluminum conductors (ACCC) with a higher strength and lighter weight. ACCC conductors have an average 40% strength, 70% lighter and 10 times less thermal elongation coefficient than conventional ACSR conductors thanks to composite core [2].

Production of ACCC Lisbon type aluminum conductors composite core for the first time in Turkey, ensuring its development and energy efficiency and producing alternatives are among the priorities of this study. In this project, it is aimed to explain how the mechanical (60-95 MPA, min 20% elongation) and electrical (min 63% IACS) properties of the product are captured in ACCC Lisbon production stages and within the scope of field applications, the comparison of current carrying capacity and sag data between ACCC lisbon conductor which will be used instead of ACSR Hawk conductor will be explained. Conductor production was carried out in EMTA Conductor&Cable Factory and field application was conducted in Uludağ Elektrik Dağıtım A.Ş. facilities.

2. Experimental Procedure

Minimum 99.8% purity aluminum ingots were used as the main raw material. The chemical properties of the aluminum used were determined by Thermoscientific brand chemical analyzer (Table 1.)

Table 1. Aluminum Ingot Analysis

Al %	Si %	Fe %	Cu %	Mn %	Mg %	Cr %	Ni %	Zn %	Ti %	Pb %
99,83	0,045	0,066	0,00054	0,00067	0,0629	0,00082	0,00242	0,00686	0,0033	0,0044

Conventional conductors are conductors that are stranded with round-shaped aluminum wires over round-shaped steel wires. Aluminium conductor composite core are conductors built with trapezoidal shaped aluminum wires on a round shaped carbon fiber core (Figure 1.) [1].

Composite materials are preferred because of their longevity, light weight, high mechanical and chemical strength. These advantages are the main reasons for being used in lines [3].

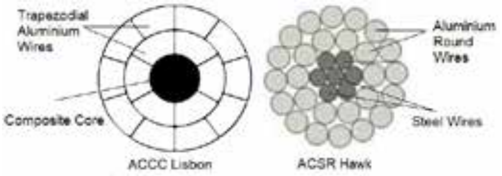

Figure 1. ACCC Lisbon ve ACSR Hawk

The composite core used in power transmission lines consists of fiberglass and carbon fiber. The fiberglass part consists of glass fiber reinforced resin and the carbon fiber part consists of carbon fiber reinforced resin. The composite core is produced by means of a pultrusion process in which carbon and glass fibers are impregnated with resin and drawn from a specially heated mold to complete roughening [3]. The properties of the composite core used are shown in Table 2 below.

Table 2. ACCC Lisbon Composite Core Specifications

Specifications	Output
Nominal Diameter of Composite Core	7.11
Nominal Cross-Sectional Area of Core	39.7
Core Nominal Mass per Unit Length	76
Rated Strength of Composite Core (MPa)	2158
Rated Tensile Load at Failure (kN)	85,7
Final Modulus of Elasticity (GPa)	112.3

Comparison of size of ACCC Lisbon conductor with same diameter as ACSR Hawk is given in Table 3. The ACCC Lisbon conductor contains about 21% more aluminum than the ACSR Hawk conductor of the same diameter. This increases the current carrying capacity of the ACCC Lisbon conductor compared to the ACSR Hawk conductor.

Table 3. ACCC Lisbon-ACSR Hawk Size Comparison

Type	Conductor Diameter (mm)	Core Diameter (mm)	Conductor Cross Section (mm^2)	Core Cross Section (mm^2)
ACSR Hawk	21,8	8,04	281,1	39,5
ACCC Lisbon	21,8	7,11	355,2	39,7

ACCC Lisbon conductor production stages consist of 4 main processes; casting, wire drawing, heat treatment and stranding processes. Aluminum ingots with a minimum purity of 99.8% are used as the main raw material. Aluminum ingots are charged to the natural gas-powered melting furnace for melting. The metal, which is melted at about 750°C, is transferred to the tilting furnace at a temperature of 670-730^{0}C by means of a runner. As a result of the transfer of liquid metal from the tilting furnaces, cooling water is supplied to the copper casting mold(wheel) and an aluminum bar with a section area of approximately 2090 mm2 is obtained at a temperature of about 450-500 ° C. The aluminum bar is converted to a 9.5 mm diameter aluminum wire rod shape in the rolling mill that works with the casting machine. At this stage, strength and elongation tests with the Zwick Roll tensile device and conductivity tests with the Burster resistance meter were conducted. And the aluminium rod is heat treated.

The 9.5 mm aluminum rod coming from the aluminum continuous casting production line continuously passes through the successive wire drawing lines in the wire drawing machines to achieve the desired diameter. The diameters of each line and successive lines are smaller than the input diameter of the material, and the wire diameter shrinks as it passes through each die. The aluminum wires used in traditional conductors are made by passing through round-shaped dies. In ACCC conductors, special trapezoidal die is used to produce trapezoidal wires. Wires are wrapped in coils in drawing machines. Strength and elongation tests were carried out with the tensile device to the wires, and conductivity tests were performed with the resistance meter. If these values are not conforming then wires are sent to heat treatment. The coils are kept in the furnace at the specified degree and time. For each of the coils removed from the oven when time expired tensile strength and elongation tests were made with drawing device and conductivity tests were conducted with resistance meter. Temperature and duration applied in heat treatment applications are very important. The desired mechanical properties can be captured if annealed at the appropriate temperature for the appropriate duration

Aluminum wires wrapped in coils in heat treated standard are sent to stranding machines. Composite core is passed through the center. In order to strand the upper layers, the wires in the coils loaded into the stranding machine are passed through the holes in the machine and wrapped in the rollers by stranding according to the construction of tc he product. After stranding, strength and elongation tests were done with tensile device and conductivity tests with resistance meter.

3.Results and Discussion

The strength and conductivity of aluminum wire rod produced in the casting process is checked. The parameter acting on strength is the casting speed and the content of the aluminum. When the casting speed is slowed down, grain sizes will decrease because aluminum rod produced after forming by hot rolling method is cooled more with emulsion. The material strength will increase as the amount of grain boundaries that prevent dislocation movements with the shrinking grain size increase. When casting speed is increased, the strength of the less cooled aluminum will be low. Resistance, elongation and conductivity tests are performed on each wire rod after casting. Aluminum wire rods are grouped according to the strength, elongation and conductivity values determined by EN 1715-2 standard. (Table 4)

Table 4. EN 1715-2 Mechanical and electrical values

Alloy Designation	Temper	Mechanical Properties			Electrical Properties (temperature:20 C)	
		Tensile Strength		Elongation typical	Resistivity	Conductivity
		Mpa		$A_{100\,mm}$	µΩ.cm	% IACS
		Min	Max	%	Max.	Min.
EN AW -1370 (Al 99,7) and EN AW -1350 (Al 99,7)	H14	115	130	14	2,801	61,5
	H13	105	120	16	2,801	61,5
	H12	95	110	20	2,801	61,5
	H11	80	95	25	2,785	61,9
	O	60	80	40	2,725	63,3

For conductivity, the purity value of the raw material used is the most important parameter affecting conductivity. The raw material used in casting consists of 99.8% pure aluminum ingots. In addition to the purity of aluminum it contains 0.2%

of the other elements in titanium and vanadium particle because of its thinning properties negatively affect the conductivity. It is possible to convert approximately 60-80% of Ti+Cr+V+Zr in liquid aluminum to boron connections by adding AlB3 master alloy. In liquid aluminum, these companion elements are separated from the solution CrB, VB, TiB, ZrB as boron components. These particles can no longer affect the conductivity of aluminum in this state [4].

The elongation value of the wires placed in the stranding machine should be 20% minimum, the conductivity value should be 63% IACS minimum, and the strength value should be in the range of 60-95 MPa (EN 50540). To be able to reach the desired values in aluminum wire before and after stranding among aluminum wire rod groups “O” type shown also in Table 4 with the highest conductivity have been seen as suitable. O type wire rod is obtained after heat treatment to H11 group aluminum wire rod. The recrystallization temperature is approximately 0.5 times the melting temperature [5]. Aluminum melting temperature is 660 ^{0}C. The highest conductivity (63.12% IACS) of the O type wiring rod produced after the heat treatment process of 330 ^{0}C for 5 hours was used for the H11 Group 4 wiring rod (Table 5.)

Tablo 5. O type aluminium rod

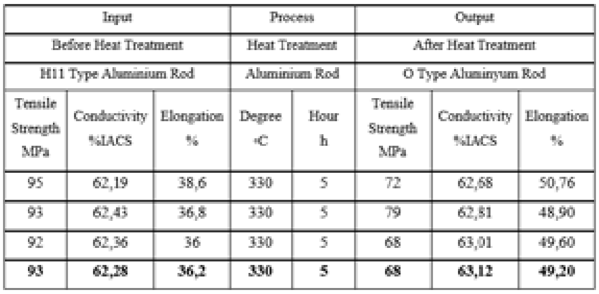

Input			Process		Output		
Before Heat Treatment			Heat Treatment		After Heat Treatment		
H11 Type Aluminium Rod			Aluminium Rod		O Type Aluminyum Rod		
Tensile Strength MPa	Conductivity %IACS	Elongation %	Degree °C	Hour h	Tensile Strength MPa	Conductivity %IACS	Elongation %
95	62,19	38,6	330	5	72	62,68	50,76
93	62,43	36,8	330	5	79	62,81	48,90
92	62,36	36	330	5	68	63,01	49,60
93	**62,28**	**36,2**	**330**	**5**	**68**	**63,12**	**49,20**

With the use of O type 68 MPa, 63.12% IACS and 49.2% elongation, it was observed that the elongation values of the wires before the stranding were below 20% and the strength values were above 95 MPa. With the heat treatment applied to the wires, the elongation before the stranding was increased and the strength and conductivity values were ensured. However, when heat treatment is applied to the wires produced from O-type wire obtained by applying heat treatment to H11 Wire, the strength value provided is close to the lower limit of 60 MPa, which means that this material is a soft product. As the strength value was close to the lower limit, it caused the wires to elongate and decrease in diameter during the bending process of the wires. In tests performed on the sample taken after bending, it was observed that the elongation values of some wires were below 20% (Table 6).

In wire production, H11 type wire rod, which has the highest conductivity after negative results in O type wire rod, was used. In wires produced from wiring rods of H11 Type 93 MPa without heat treatment, 63.76% IACS, with 47.5% elongation, strength, conductivity and elongation values after wire drawing were found to be non-standard. After the heat treatment applied to the wires, the values found were within the standard. However, after the stranding process tests showed that the elongation values for some wires were outside the standards (Table 7**.**)

In some wires, the desired result could not be achieved in elongation values, heat treatment was applied by changing the values. After the heat treatment applied to the wires, the values specified in the standard are ensured. In the tests performed after the stranding process, the problems caused by straining were minimized and values were provided after stranding. In addition, it is determined that the elongation values after heat treatment should be maximum 50% for a single wire to keep the elongation values after stranding. (Table 8.)

Table 6. O type Aluminium Rod Results

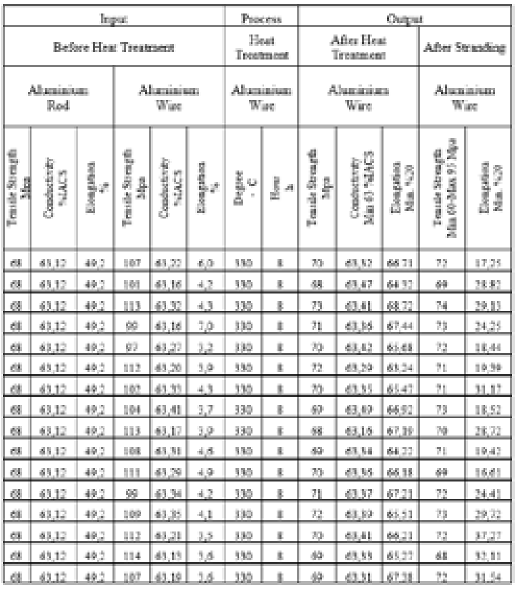

Input						Process		Output				
Before Heat Treatment						Heat Treatment		After Heat Treatment			After Stranding	
Aluminium Rod			Aluminium Wire			Aluminium Wire		Aluminium Wire			Aluminium Wire	
Tensile Strength Mpa	Conductivity %IACS	Elongation %	Tensile Strength Mpa	Conductivity %IACS	Elongation %	Degree °C	Hour h	Tensile Strength Mpa	Conductivity Min 63 %IACS	Elongation Min. %20	Tensile Strength Min 60-Max 95 Mpa	Elongation Min. %20
68	63,12	49,2	107	63,22	6,0	330	8	70	63,52	68,71	72	17,25
68	63,12	49,2	101	63,16	4,2	330	8	68	63,47	64,32	69	28,82
68	63,12	49,2	113	63,32	4,3	330	8	73	63,41	68,72	74	29,13
68	63,12	49,2	99	63,16	7,0	330	8	71	63,36	67,44	73	24,25
68	63,12	49,2	97	63,27	3,2	330	8	70	63,42	65,68	72	18,44
68	63,12	49,2	112	63,20	3,9	330	8	72	63,29	63,24	71	19,39
68	63,12	49,2	102	63,33	4,3	330	8	70	63,35	65,47	71	31,17
68	63,12	49,2	104	63,41	3,7	330	8	69	63,49	66,92	73	18,52
68	63,12	49,2	113	63,17	3,9	330	8	68	63,16	67,39	70	28,72
68	63,12	49,2	108	63,31	4,6	330	8	69	63,34	64,22	71	19,42
68	63,12	49,2	111	63,29	4,9	330	8	70	63,35	66,18	69	16,61
68	63,12	49,2	99	63,34	4,2	330	8	71	63,37	67,21	72	24,41
68	63,12	49,2	109	63,35	4,1	330	8	72	63,39	65,51	73	29,32
68	63,12	49,2	112	63,21	3,5	330	8	70	63,41	66,21	72	37,27
68	63,12	49,2	114	63,15	3,6	330	8	69	63,35	65,27	68	32,11
68	63,12	49,2	107	63,19	3,6	330	8	69	63,31	67,38	72	31,54

Table 7. H11 93 MPa Aluminium Rod Results

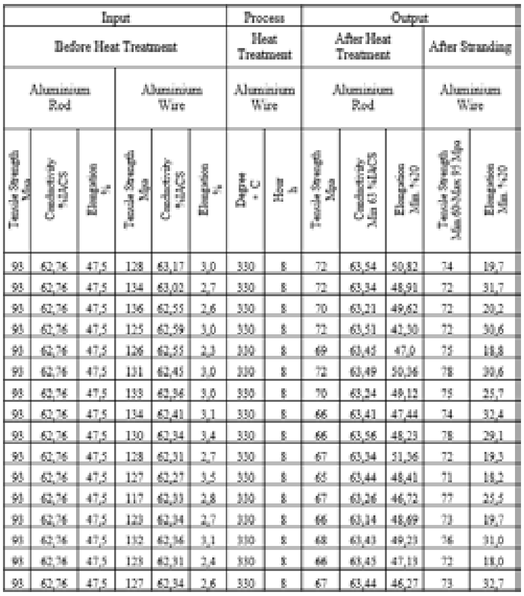

Input						Process		Output				
Before Heat Treatment						Heat Treatment		After Heat Treatment			After Stranding	
Aluminium Rod			Aluminium Wire			Aluminium Wire		Aluminium Rod			Aluminium Wire	
Tensile Strength Mpa	Conductivity %IACS	Elongation %	Tensile Strength Mpa	Conductivity %IACS	Elongation %	Degree °C	Hour h	Tensile Strength Mpa	Conductivity Min 63 %IACS	Elongation Min. %20	Tensile Strength Min 60-Max 95 Mpa	Elongation Min. %20
93	62,76	47,5	128	63,17	3,0	330	8	72	63,54	50,82	74	19,7
93	62,76	47,5	134	63,02	2,7	330	8	72	63,34	48,91	72	31,7
93	62,76	47,5	136	62,55	2,6	330	8	70	63,21	49,62	72	20,2
93	62,76	47,5	125	62,59	3,0	330	8	72	63,51	42,30	72	30,6
93	62,76	47,5	126	62,55	2,3	330	8	69	63,45	47,0	75	18,8
93	62,76	47,5	131	62,45	3,0	330	8	72	63,49	50,36	78	30,6
93	62,76	47,5	133	62,36	3,0	330	8	70	63,24	49,12	75	25,7
93	62,76	47,5	134	62,41	3,1	330	8	66	63,41	47,44	74	32,4
93	62,76	47,5	130	62,34	3,4	330	8	66	63,56	48,23	78	29,1
93	62,76	47,5	128	62,31	2,7	330	8	67	63,34	51,36	72	19,3
93	62,76	47,5	127	62,27	3,5	330	8	65	63,44	48,41	71	18,2
93	62,76	47,5	117	62,33	2,8	330	8	67	63,26	46,72	77	25,5
93	62,76	47,5	123	62,34	2,7	330	8	66	63,14	48,69	73	19,7
93	62,76	47,5	132	62,36	3,1	330	8	68	63,43	49,23	76	31,0
93	62,76	47,5	123	62,31	2,4	330	8	66	63,45	47,13	72	18,0
93	62,76	47,5	127	62,34	2,6	330	8	67	63,44	46,27	73	32,7

The installation process of the finished conductors was carried out in the field. Field measurement parameters in the project for renewal of the 2 km line from ACSR Hawk conductor to

ACCC Lisbon conductor are indicated in Table 9.

Tablo 8. H11 95 MPa Aluminium Rod Results

Input						Process		Output				
Before Heat Treatment						Heat Treatment		After Heat Treatment			After Stranding	
Aluminium Rod			Aluminium Wire			Aluminium Wire		Aluminium Rod			Aluminium Wire	
Tensile Strength Mpa	Conductivity %IACS	Elongation %	Tensile Strength Mpa	Conductivity %IACS	Elongation %	Tensile Strength Mpa	Conductivity %IACS	Tensile Strength Mpa	Conductivity Min 63 %IACS	Elongation Min. %39	Elongation %	Tensile Strength Mpa
95	62,94	51,8	135	62,65	3,8	350	6	74	63,24	47,5	76	29,8
95	62,94	51,8	121	62,58	4,3	350	6	72	63,21	47,5	74	29,7
95	62,94	51,8	135	62,73	3,5	350	6	75	63,34	47,6	77	35,5
95	62,94	51,8	136	62,77	3,3	350	6	76	63,24	43,8	72	30,2
95	62,94	51,8	137	62,70	3,1	350	6	79	63,31	48,0	76	32,3
95	62,94	51,8	134	62,68	3,9	350	6	81	63,34	47,0	74	28,0
95	62,94	51,8	133	62,70	1,8	350	6	79	63,26	48,1	78	28,0
95	62,94	51,8	130	62,61	3,0	350	6	80	63,21	46,0	78	35,0
95	62,94	51,8	136	62,68	3,2	350	6	77	63,19	45,5	76	35,4
95	62,94	51,8	132	62,64	2,7	350	6	76	63,25	48,2	73	34,8
95	62,94	51,8	131	62,70	3,1	350	6	75	63,27	47,3	74	28,4
95	62,94	51,8	132	62,66	3,2	350	6	76	63,30	50,3	74	31,7
95	62,94	51,8	133	62,67	3,0	350	6	77	63,21	45,4	76	31,8
95	62,94	51,8	137	62,69	3,2	350	6	78	63,24	48,4	79	27,0
95	62,94	51,8	133	62,71	2,8	350	6	73	63,21	43,8	74	33,8
95	62,94	51,8	134	62,75	3,2	350	6	74	63,24	48,3	75	25,8

Tablo 9. Facility Measuring Parameters

Measuring parameters	Measuring Range	Measuring Method	Explain
Conductor Sagging	1 time in 2 hours / On site visit	Teodolite Device	Theodolite is the sensitive device that measures the coordinates and vertical / horizontal distances on earth. Calculates the elevation difference of sea level altitude of the current location.
Conductor Current	1 time in 2 hours / On site visit	Transformer	It was measured in amperes with relays in current transformer.

Measurements for the ACSR Hawk were taken prior to the installation of the ACCC Lisbon conductor. The ACCC Lisbon line was established in a short time as 6 days. Therefore, the measurement of the two conductors was evaluated in the same seasonal conditions. Measurements were made in 1 day at intervals of 2 hours. The conductor currents were taken as amperes from the digital display via relays through the current transformer. When the current power is increased the temperature also increases. Current transport measurement results are shown in Table 10.

Table 10. Current Carrying Capacity

		Conductor Type	
Current Capacity (A)	Measuring Time	ACSR Hawk	ACCC Lisbon
Current Capacity (A) 60 °C	10.00 am	492	579
	12.00 pm	497	576
	14.00 pm	501	571
	16.00 pm	498	573
	Average	497	574,75
Current Capacity (A) 80 °C	10.00 am	891	1059
	12.00 pm	903	1044
	14.00 pm	894	1043
	16.00 pm	901	1047
	Average	897,25	1048,25

Current Carrying Capacity More than %15,64

Current Carrying Capacity More than %16,77

According to the ACSR Hawk conductor, the reduction in the sag with the ACCC conductor was recorded at about 1.5 meters. The conductor was measured by theodolite device (Table 11.).

Tablo 4.11. Sag Performance Results

		Conductor Type		
Current Capacity (A)	Sagging Values (m)	ACSR Hawk	ACCC Lisbon	Difference (m)
Current Capacity (A) 60 °C	Upper Sag Value	10,40	12.00	1,60
	Medium Sag Value	8,50	10.00	1,5
	Lower Sag Value	6,50	8.00	1,5
Current Capacity (A) 80 °C	Upper Sag Value	12,5	11,2	1,4
	Medium Sag Value	11,4	9,9	1,5
	Lower Sag Value	9,2	7,8	1,4

4. Conclusion

When the heat treatment results applied to ACCC Lisbon conductor wires produced from O type (60-80 MPa) wire rod are evaluated, the conductivity, elongation and strength values of aluminum wires as a result of the heat treatment are within the standards. However, according to the results of the tests on the ACCC Lisbon conductor and wires at the end of the stranding, it was observed that some of the elongation of the wires came out of the standard values. The reason is that the wires are soft and extend on the machine due to the tension created by the machine brakes and drum in the stranding machines. After the heat treatment applied to ACCC Lisbon conductor wires produced from H11 type (80-95 MPa) wire rod, the values specified in the standard have been provided and the problems caused by the elongation in the stranding machine have been minimized in the tests made after the stranding process due to the increase in strength and the values after stranding have been provided. It has been determined that the maximum elongation value of the wires must be 50% at the end of the heat treatment in order to reach the elongation value of the end of the stranding. The strength of the wire rod to be used should be at least 62% IACS in the range of 80-95 Mpa (N/mm2).

The existing poles of the line were used in the project to increase the capacity of the line. In this way, the costs of the new pole with the new conductor were avoided. At 60°C the ACCC Lisbon conductor has a current carrying capacity of approximately more than 15.64% compared to the ACSR Hawk conductor and at 80°C it has a current carrying capacity of approximately more than 16.77%. Compared to ACSR Hawk conductor the decrease in the ACCC Lisbon conductor sag was recorded as approximately 1.5 meters. Compared to ACSR Hawk, while ACCC Lisbon conductor providing the advantage of capacity expansion in conductor renovation projects, and also takes the lead in sag values.

References

[1] Kıstı, E., 2016. Studies for Producing Aluminum Conductor Composite Core and Increasing Conductivity, p:7

[2] www.emtaaccc.com Dated:16.05.2020.

[3] CTC Global Corporation, 2011. Engineering transmission lines with high capacity low sag ACCC conductors, first edition, pp. 1-270

[4] Mohanty, P. S., Guthrie, R. I. L., and Gruzleski, J.E. 1995. Studies on the Fading Behaviour of AlTi-B Master Alloys and Grain Refinement Mechanism Using Limca. Light Metals. Edited by J. Evans, pp. 859-868.

[5] Savaşkan, T., 2015. Material information and inspection, Palme book, p:396, Trabzon

The Effect of Tin Addition and T6 Heat Treatment on the Mechanical Properties of A356 Aluminum Alloy

Selda HASÇELİK, Işıl KERTİ
Yıldız Technical University
Turkey

In the present work, A356 casting aluminum alloy was used. The production of the A356 aluminum alloy containing 0.05% and 0.1 wt. % Sn was accomplished by the addition of commercial pure Sn powder using an electric resistance furnace in the graphite crucible at a constant temperature of 750 ° C. The as-cast alloy was subjected to T6 heat treatment including 8 h solution at 530 °C followed by water quenching at room temperature, and between 2-12 h ageing at 160 °C. Their effects were studied in terms of microstructure using OM and mechanical properties by hardness measurements. The highest hardness value was measured in A356.0 alloy reinforced with 0.05% Sn and the lowest hardness value was measured in A356.0 alloy without micro alloy.

1. Introduction

In today's competitive environment, higher quality products should be produced at lower costs. In this requirement necessitates development and use of new generation materials in the industry. In many engineering applications in the industry are needed lower density (light), rigid, recyclable, high corrosion resistance and high strength materials. In this context, Aluminum and Magnesium alloys are more preferred. [1-3]

Al-7Si-0.3Mg alloys have been widely used in automobile, aircraft, and defence industries because of their excellent castability, high corrosion resistance, good weldability, low coefficient of thermal expansion and mechanical properties can be improved by ageing . [4-6]. These alloys also have been good tensile strength, fatigue strength and wear resistance. [7].

Various methods are introduced to improve the increase strength such as precipitation hardening, dispersion hardening, reducing the grain size, microalloying, heat teratmant [8,9]. Microalloying is one of the important methods to enhance the mechanical properties of Al-7Si-0.3Mg. Many different elements such as Mn, Ag, Yb, Sn, Sr, Si, Cr, Na, Yb, Sc, Ti, V, B are used for microalloying in aluminum alloys [10-13].

According to binary phase diagram, Al and Sn have mutual solid solubility. The maximum solubility of Sn in Al being about 0.1 wt pct at approximately 627°C, decreasing to reach a probable value of 0.05 to 0.07 pct Sn at the eutectic temperature, and considerably lower values at lower temperatures. When Sn is added A356 alloy, it remove iron and other impurities from solid solution and therefore reducing the volume fraction of iron-rich intermetallics. [5,14,15]

Qıu [14] et al reported that adding 0.5 % Sn to Al−7Si−Mg alloy may prevent the formation Mg_2Si intermetallic phase, but Sn precipitates as Mg_2Sn intermetalic phase between Si/Si and Al/Si intefaces. MOHAMED [15]et al reported that A356.2 alloy with addition of 0.05 % Sn has better mechanical properties compared with other alloys with different Sn contents
VIEIRA et[16] al found that adding 0.5 % Sn to Al−7Si−Mg alloy could improve its flowing behavior, increase the mould-filling capability, and reduce the liquid segregation..

In this study, micro alloying was made by added Sn in different ratios into the A356 aluminium alloy. Following the casting process, the as-cast alloy was subjected to T6 heat treatment including 8 h solution at 530 °C followed by water quenching at room temperature, and between 2-12 h aging at 170 °C. The hardness value and microstructures of these samples were examined. When the results of hardness values are analyzed, it was observed that the highest hardness value was in A356 alloy reinforced with 0.05 wt. % Sn, and the lowest hardness value was in A356 alloy without micro alloying.

2. Materials and Methods

The chemical composition of A356 casting alloy (Al-7Si-0.3Mg) used in the experiments is shown in Table I. Melting was carried out in an electric resistance furnace using graphite crucible at 750 ± 5◦C. 0.05 and 0.1 wt % commercial pure Sn was added in molten A356 mater alloy, respectively. The melt was thoroughly stirred with stainless steel impeller which is covered by boron nitride. The holding time was 15 min for enough incubation of Sn. The molten metal was poured into a metallic mold which was previously heated at 200 ° C.

The samples were applied to the T6 heat treatment. The samples were undergone solution heat treatment using muffle furnace having an open atmosphere for 8 hours. The temperature used for solution heat treatment was 520±2 °C. The samples were rapidly quenched in water at room temperature after completing the solution treatment and were aged at 170 °C for 2-12 hours (Table 2)

Table 1 Chemical Composition of A356 Alloy (Mass Fraction, %)

Alloy	**Si**	**Mg**	**Fe**	**Cu**	**Ti**	**Zn**	**Al**
A356	**6.16**	**0.311**	**0.165**	**0.20**	**0.096**	**0.013**	**bal**

Table 2. Heat Treatment in This Study

Cycle	SOLUTION		QUECHING	AGING	
	Temperature (°C)	Holding time (h)	Temperature (°C)	Temperature (°C)	Holding time (h)
1	530	8	25	-	-
2	530	8	25	170	2
3	530	8	25	170	4
4	530	8	25	170	6
5	530	8	25	170	8
6	530	8	25	170	10
7	530	8	25	170	12

After completing T6 heat treatment, metallographic samples were prepared using the diamond grinders and suspensions. The microstructure was observed using optical microscope. Brinell hardness measurements was used for hardness testing in this study. The hardness measurements were carried out on the as-cast and heat-treated samples employing a steel ball 2,5 mm in diameter, and a load of 62,5 kgp applied for 10 seconds.

3. Conclusion

In this study, three different alloys were obtained which have different ratio Tin was added.

1) Sn-free A356 alloy, 0.05% Sn added A356 and 0.1% Sn added A356 alloyed highest brinell hardness values were obtained different aging times respectively 135 HBN (6h), 137 HBN (12h), 134 HBN (10h).
2) When tin was added to A356, thinner grains were formed and the hardness value increase accordingly. Nonetheless tin amount was over 0.05%, it cause grain roughening and decrease of hardness value with increasing aging time. A356 alloy with added 0.05wt. % Sn was highest hardness value.
3) Addition of Sn into A356 alloy may prevent the formation of Mg_2Si. Mg_2Sn phase has formed instead of Mg_2Si phase.
4) A356 alloy with added 0.05 wt. % Sn has better mechanical property than others.

Acknowledgment

I would like to gratefully thank Prof.Dr. Ahmet Karaaslan for the raw material support for the project. I would also like to thank my valuable thesis supervisor, who supported me during the project.

References

[1] M Özcömert.,2006. Otomotiv Endüstrisinde Alüminyum, İstanbul Ticaret Odası ,OSD, Otomotiv Sanayicileri Derneği, Www.Osd.Org.Tr

[2] Y Şahin,., 2000, Kompozit Malzemelere Giriş,

[3] T. A Başer., Alüminyum Alaşımları Ve Otomotiv Endüstrisinde Kullanımı, Malzeme Bilimi Ve Mühendisliği, Toksan Yedek Parça İmalatı Tic. Ve San. A.Ş., AR-GE Merkezi - ,2013, Bursa, Turkey

[4] Lu S., Du R., Liu J., Chen L., Wu S., Anew Fast Heta Treatment Process for Cast A356 Alloy Motorcycle Wheel Hubs, Huazhong University Of Sience And Technologoy,2017, Wuhan, China

[5] G Yuan., Z Li .,Y Lou., X Zhang . Study On Crystallization And Microstructure For New Series Of Al-Sn-Si Alloys, Guangdong University Of Technology, 2000, Guangzhou, China

[6] D Özyürek., E Kibar., R Yılmaz ,Toz Metalurjisi ile Üretilen A356 Alüminyum Alaşımının Aşınma Davranışlarının İncelenmesi , Karabük University, 2009, Karabük, Turkey

[7] T Tunçay, A356 Alaşımında Cu Miktarının Mikroyapı ve Aşınma Davranışı Üzerine Etkisi, Karabük University, 2016, Karabük, Turkey

[8] A Akdoğan , Alüminyum Ve Alaşımları Ders Notları, Makine Mühendisliği Departmanı, Yıldız Technical University, 2008,İstanbul, Turkey

[9] Z Taş, Yüksek Dayanımlı Düşük Alaşımlı Çeliklerde Metalürjik Mukavemet Artırma Mekanizmaları, M.Sc Thesis, Bozok University, 2012 Yozgat, Turkey.

[10] R.S Rana., R Purohit., S Das, Reviews on the Influences of Alloying Elements on the Microstructure and Mechanical Properties of Aluminum Alloys and Aluminum Alloy Composites, Maula Azad National Institute of Technology, Departmant of Mechanical Engineering, 2012 India.

[11] M Ak,AA206 Alüminyum Döküm Alaşımında Empürite Demirin Mekanik Özelliklere Etkilerinin İncelenmesi, M.Sc Thesis , İstanbulTechnical University, 2012, İstanbul, Turkey.

[12] Y Deng., Z Yin., Kai Zhaoa, J Duana., J Hua.,Effects Of Sc And Zr Microalloying Additions And Aging Time At 120°C On The Corrosion Behaviour Of An Al–Zn–Mg Alloy, Zhenbo Heb School Of Materials Science And Engineering, 2012,Central South University, China

[13] T Gancarz., G Cempura, Characterization of Zn -Al Cast Alloys With Li Addition, Materials and Design 104 (2016)51–59, 2016,Poland.

[14] K Qıu., R Wang., C Peng., N Wang., Z Cai C. Zhang, Effects of Mn and Sn on microstructure of Al−7Si−Mg alloy Modified by Sr and Al−5Ti−B, Central South University,2015,, Changsha, China

[15] A Mohamed., F Samuel., A Samuel., H Doty., S Valtıerra., Influence of Tin Addition on the Microstructure and Mechanical Properties of Al-Si-Cu-Mg and Al-Si-Mg Casting Alloys, Sciences Applique´es Universite´ du Que beca Chicoutimi, 2008, Chicoutimi, Canada

[16] E.A Vieira., A.M Kliauga., M Ferrante. , Microstructural evolution and rheological behaviour of aluminium alloys A356, and A356+ 0.5% Sn designed for thixocasting, Universidade Federal de São Carlos, 2004,São,Carlos, Brazil

Fire Resistant Composite Doors Concepts and Smart Modular Design

Cem MEHMETALİOĞLU, Murat KONAR, Görkem ÖZÇELİK, Zafer ZORLU, Tutku ÖZEN
ASAŞ Alüminyum Sanayi ve Ticaret A.Ş.
Turkey

Abstract

The main objective of the study is the development of innovative doors leaves designs looking for improvements in terms of weight, acoustic attenuation and thermal insulation. The new concept developed suggest that traditional joining processes like welding or bolting could be replaced by other techniques, like adhesives, which would allow a stress reduction in concentration points, so improving the overall performance and potentially simplifying assembly processes.

1. Introduction

According to the EC, rising traffic demand, congestion, security of energy supply and climate change are the major challenges that the railway sector will have to face in the next few decades, which should be addressed through an appropriate research and innovation policy [1]. The Railway Strategic Master Plan defines policy objectives for the railway system of the future such as high capacity, low cost, improved performance and high reliability [2]. The study has the overall aim of reducing train door's weight and develop concepts for permanent structural joining technologies.

2. Materials and Methods

Traditional railway doors are produced with aluminium extrusion technology. The new design has been developed based on aluminium & innovative processes, where the main structural component is a frame made with high-grade aluminium, potentially using bent thin-shell parts or simplified extrusion profiles. In the selected concept the door frame can be manufactured by bending the only sheet of aluminium to get the required shapes and profiles and joined by adhesive. This method is an innovative idea for the rail sector since it has not been implemented previously in the rail systems sector and this shaping is possible with the roll forming method in the serial production process. it is possible to work with thinner cross sections due to high strength with the same costs when the extrusion products use EN AW 6005A T6 instead of EN AW 6060 T6. The average weight of the traditional doors is 18 kg after the final assembly. New design concepts weight has min. 50% weight reduction on this structural part of the door leaf. With the application of insulation materials, the project target of sound and insulation can be reached. The traditional welding process has been eliminated as the concepts of adhesive are used. Adhesive bonding reduces the stress in concentration points. The risk of corrosion has been reduced because of similar material pairs and no thermal degradation.

3. Conclusion

The developed concept in aluminum materials, opens a path for the analysis about the application of different manufacturing processes that would allow the use of different quality-grade aluminum alloys. Those processes and alloys are currently used in other sectors, like aeronautics, but are innovative in the railway sector and they have a high potential for overall performance improvement in terms of weight and cost. The concept developed also suggest that traditional joining processes like welding or bolting could be replaced by other techniques, like adhesives, which would allow a stress reduction in concentration points, so improving the overall performance and potentially simplifying assembly processes.

Acknowledgmet

This study has received funding from the Shift2Rail Joint Undertaking under the European Union's Horizon 2020 research and innovation programme under grant agreement No 777595.

References

[1].<https://ec.europa.eu/transport/modes/rail/shift2rail_en> Dated: 04.02.2021
[2].<https://ec.europa.eu/transport/sites/transport/files/modes/rail/doc/2015-03-31-decisionn4-2015-adoption-s2r-masterplan.pdf> Dated: 04.02.2021

Production and Analysis of Cu and CuNi Nano Particles with Solution Combustion Synthesis

Mustafa Çağrı ALTINBAŞ[1], Şevki Samet KAPLAN[1], Sadia ILYAS[2], M. Şeref SÖNMEZ[1]
[1]Istanbul Technical University, [2]Jeonbuk National University
[1]Turkey, [2]Korea

Abstract

In this paper, metallic Cu and bimetallic CuNi production by solution combustion synthesis were investigated. $Cu(NO_3)_2 . 3H_2O$ and $Ni(NO_3)_2 . 6H_2O$ were used as oxidizers, while urea, maleic acid, and oxalic acid were used as fuels. According to XRD results, metallic Cu observed as the primary peak, and Cu_2O observed as the secondary peak when urea was chosen as fuel for the pure metal production process. In the case of the bimetallic particle production process, XRD peaks give CuNi as the primary peak while NiO was the secondary peak. The main objective of the solution combustion synthesis is to produce nano-scale particles in a cost-effective manner. Analysis so far suggests that a rather simplistic and effective route is achieved.

1. Introduction

Copper and copper-nickel bimetallic nanopowders have vast application areas. Nano copper mainly is used as an efficient catalyst for chemical reactions, anti-microbial agent, electrical conductor, and alloying element. Copper-nickel bimetallic nanoparticles also find a variety of application areas due to their stability. There are many methods that exist to produce nano copper and bimetallic copper-nickel [1]. In this paper, solution combustion synthesis (SCS) method was investigated.

2. Materials and Methods

Solution combustion synthesis is a self-propagating method. Oxidizer, fuel, and the initial temperature are critical parameters for the reaction to occur. The process is a high-temperature redox reaction in nature. Reactions mainly take place between an oxidizer and a fuel [2].

$Cu(NO_3)_2 . 3H_2O$ was chosen as an oxidizer for nano copper production, while $Ni(NO_3)_2 . 6H_2O$ and $Cu(NO_3)_2 . 3H_2O$ were both oxidizers for CuNi nano particle production. Fuels for the SCS process such as urea, oxalic acid, and maleic acid were used in the experiments. Fuel to oxidizer ratio was selected as 2.

3. Conclusion

Copper/copper oxide powder was produced when urea used as fuel. Maleic acid and oxalic acid did not give satisfying results. Since urea was the proper fuel for copper production, it was also used in CuNi bimetallic particle production. XRD results suggested that CuNi bimetallic particles obtained by this process.

References

[1] Din, M. I., & Rehan, R. (2017). Synthesis, characterization, and applications of copper nanoparticles. *Analytical Letters*, *50*(1), 50-62.
[2] Carlos, E., Martins, R., Fortunato, E. M. C., & Branquinho, R. (2020). Solution combustion synthesis: towards a sustainable approach for metal oxides.*Chemistry–A European Journal*.

Evaluation of Determination of Aluminum Wire Rod Surface and Subsurface Defects by Eddy Current Method

Ebru KISTI[1], Necati OCAK[1], U.G. UNCU[1], Yıldız Y. OZBEK[2]

[1]Emta Conductor&Cable, [2]Sakarya University

Turkey

Abstract

Eddy current is one of the most sensitive non-destructive inspection methods especially for the detection of surface defects. It is the most widely used non-destructive inspection method in sectors with many fault criteria (which do not allow even very small cracks), such as the aerospace industry. In this study, the availability of Eddy Current test system will be investigated for the first time in continuous cast aluminum wire rod manufacturing in Turkey. With Eddy Current method, the penetration depth of the eddy current and the parameters affecting this depth will be investigated during manufacturing of 12 mm aluminum wire rod with a minimum purity of 99.7% in the aluminum continuous casting unit. Evaluation of the detection of internal faults and surface defects by Eddy Current tester will be made. Factors affecting the eddy current will be discussed and improvement will be ensured.

1. Introduction

Aluminum is used in many industries nowadays like conductor, plate, sheet and etc. 12 mm aluminum rod (Wire Rod) semi-finished product is produced by processing the using various methods such as extrusion, rolling and casting processes.

In the continuous casting line, the melting furnaces are fed with aluminum ingots. Melted aluminum ingots are taken to the tilting furnace. High thermal resistance and low thermal conductivity refractories are used to take molten aluminum from the tilting furnace to the tundish. Gas removal and filtration processes are applied during the coming phase of molten aluminum from the furnace. The transfer of the liquid metal to the copper wheel is performed, which is adjusted by fixing the level at the tundish. Solidification of liquid metal is achieved by cooling the copper wheel with water by means of nozzles. The aluminum bar from the copper wheel is processed in the rolling unit, producing 12 mm aluminum rod. In the continuous casting line, solidification and forming are performed simultaneously sequentially. The aluminum rod coming out of the rolling unit is wrapped in the basket by passing through the non-destructive testing device that works with the eddy current method. Continuous casting unit workflow is shown in Figure 1. [1].

In aluminum continuous casting units process failures may result in large quantities of defective products during production. That's why it's important to get immediate feedback regarding quality. To prevent expensive raw materials from being scrapped, it is therefore, important to intervene at an early stage in any problem. This is exactly what the eddy current test system does. It acts as an early warning system for defects and other production problems that leave a mark on the product and prevents the use of the defective product at the stages of the part during production and prevents the sale of the defective material.

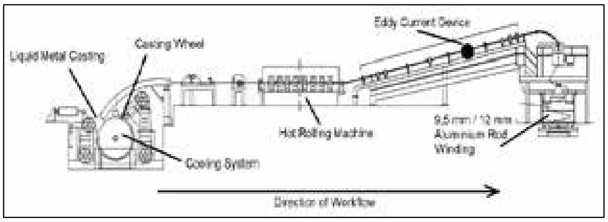

Figure 1. Continuous Casting Workflow

Discontinuities are detected by monitoring the signal outputs obtained from non-destructive inspection device at manufacturing speed. In this way, it is possible to eliminate the defect by interfering with the process at that time in case of identifying potential problems in signal outputs received at manufacturing speed. Parameters such as test frequency, coil diameter etc. directly affects the signal outputs and the manufacturing operator immediately interferes with the casting line according to the feedback information. Therefore, accurate detection of parameters affecting signals is very important. The optimum values will be determined by examining these parameters with controlled experiments.

The defects that occur within the material and cannot be detected by visual control occur during the processing of the materials and the creation of the final product. Due to these defects, the end products are scrapped, resulting in irreversible labor and quality costs. It is therefore very important that discontinuities formed in the material, surface and under surface are detected online in the continuous casting process.

2. Experimental Procedure

Non-destructive inspection is the control of defects in the material without damaging the material. There are various non-destructive inspection methods such as penetrant control, magnetic particle control, ultrasonic control, radiographic control, eddy current control. One of the methods of non-destructive testing is the eddy current methods, based on the electromagnetic theory. This method is one of the most appropriate non-destructive inspection methods for the detection of defects on and below the surface of the material.

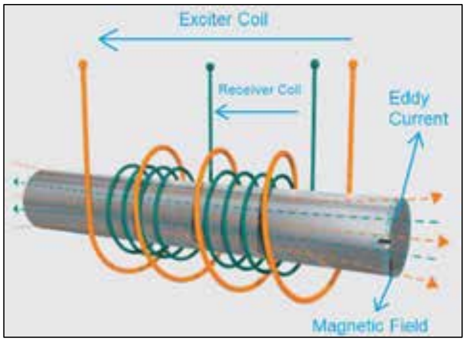

Figure 2. Eddy current and the magnetic field it creates [2]

The non-destructive inspection device has 2 peripheral coils (trigger coil and receiver coil) that are formed by tightly winding the wire. A variable magnetic field (primary magnetic field) is created by passing alternating current (AC) through the trigger coil. When a conductive material is passed through the magnetic field formed by the trigger coil, a voltage is induced within the material. This voltage induced in the conductive material induces a circular eddy current (induction current, Eddy Current) that returns to the point where it begins within the material. Eddy currents flow in planes perpendicular to the magnetic field, inside a closed loop, and form a magnetic field (secondary magnetic field) against the primary magnetic field formed by the triggering coil. This secondary magnetic field formed by eddy currents is detected by the receiving coil. The presence of discontinuities in the material causes changes in the secondary magnetic field formed by eddy currents. When there is a defect in the material, the flow of eddy currents changes and impedance changes are detected by the receiving coil. (Figure 3).

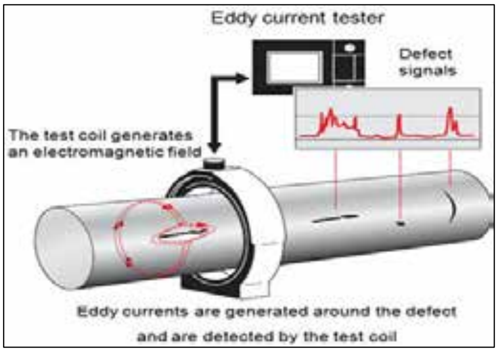

Figure 3. Distribution of eddy current on faulty surface and output signal [3]

The densities of eddy currents radiate at different density within the material. This density is greatest on the surface of the material and decreases exponentially with depth (skin effect.

The density and penetration depth of the eddy currents vary according to the type of metal material and the frequency of the test applied. The increase in frequency causes the depth of penetration to decrease, and the eddy currents gather at the surface [4].

The AC current density, J, decreases exponentially over a conductor, depending on the value on its surface (Js) and its depth (d). The formula is as follows

$$J = J_S\, e^{-d/\delta} \tag{1}$$

δ refers to the penetration of influence. The penetration at which the eddy current density drops to 1 / e or about 37% of the surface density is called the standard penetration depth.

$$\delta = \frac{1}{\sqrt{\sigma\,\pi\,f\mu}} \tag{2}$$

δ : standard penetration depth (m)
f : test frequency (Hz)
σ: electrical conductivity of the test material (m / Ωmm²)
µ: magnetic transition of test material (H/mm)

Eddy currents flow mainly between the conductor's surface and the depth of penetration. Test frequency and material properties to be tested directly affect the depth of penetration (Figure 4.)

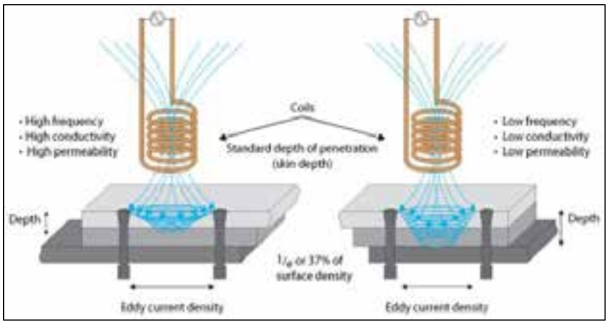

Figure 4. Penetration depth and affecting parameters [4]

The current density induced in the tested material depends on the density of the current-inducing magnetic field. The magnetic field weakens at the distance from the peripheral coil to the surface of the material being tested, resulting in losses in signal strength. The range effect between the peripheral coil and the surface to be controlled is called the filler factor. The filler factor is directly connected to the inner diameter of the coil and the number is the diameter. The fillings factor is found with the following equation.

$$\boldsymbol{\eta} = \left(\frac{D_{testpiece}}{D_{Coil}}\right)^2 \tag{3}$$

η: Filler Factor
$D_{\text{test piece}}$: Test piece diameter
D_{coil} : coil diameter

Aluminum rod products are tested online with the Eddy Current tester. Non-destructive testing device is mounted between the rolling process outlet and the wrapped basket area of the product. The aluminum rod passes through the non-destructive inspection tester with an average speed of 6 m / sec. at a temperature of about 180-220^{0}C. Up-and-down tremors that can be faced during production can produce output signals that can be interpreted as defects. For this reason, non-destructive testing device is integrated into the system on special tables designed to minimize shaking and cooling the coil bed. (Figure 6.)

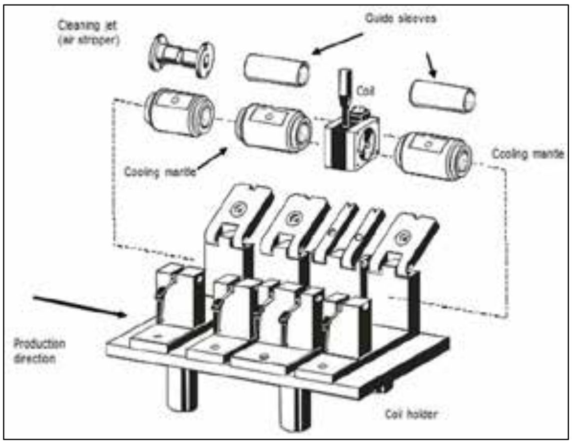

Figure 6. Integrating the test coil into the casting line

3. Results and Discussion:

This study was carried out in the laboratory environment before integrating the system into production. For the analysis of the factors affecting the received signals, sample 12 mm Aluminum wire rod (Figure 7.) with horizontal and spot errors were passed through a non-destructive inspection device and tested in a laboratory environment under controlled conditions.(Figure 8.) In tests performed;

1- Comparison of the return signals received by passing the same test sample through different diameters of the test coil while all other parameters are constant (test frequency, test speed, signal gain etc.) (Change of filler factor).
2- It was aimed to compare the return signals received as a result of different test frequencies application while all other parameters of the same test sample were fixed (coil diameter, test speed, signal gain etc.).

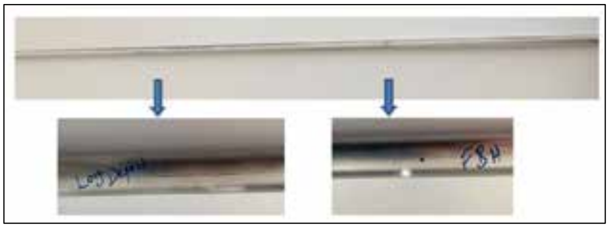

Figure 7. Long defect (LD) and Flat bottom hole (FBH) defects formed on 12 mm aluminum rod wire

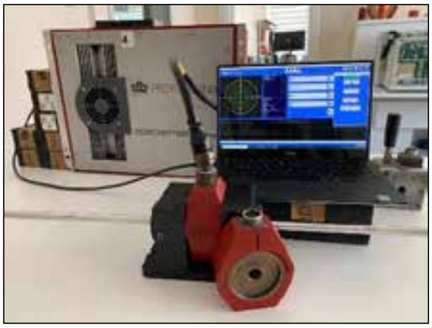

Figure 8.: Experiment layout prepared in laboratory environment using 12 mm aluminum rod, 15 mm and 20 mm coils

3.1. Effects of filler factor on output signal

The ratio of the recognized filler factor between the number and the diameter of the round coil is defined as being between 0.5 and 0.9 according to DIN 54140 standard for typical round coils. By keeping constant range, signal gain, test speed, test frequency values of 12 mm Aluminum rod where flat bottom and point defects occurred and signals obtained from tests with the use of two different coils of 15mm and 20mm are compared.

Coil Diameter: 15 mm Sample Diameter: 12 mm Filler factor: 0,64 (between 0,5 ile 0,9)	Coil Diameter: 20 mm Sample Diameter: 12 mm Filler factor: 0,64 (between 0,5 ile 0,9)

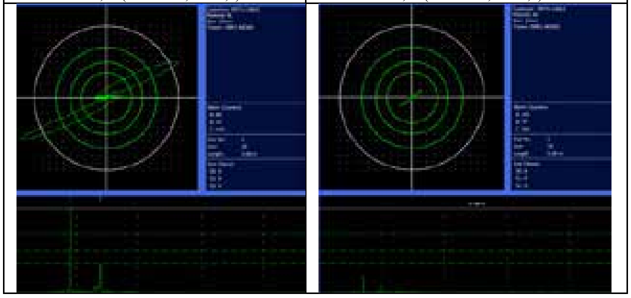

Figure 9. Test Frequency 10 kHz- Test Speed:0,2 m/s

Coil Diameter: 15 mm Sample Diameter: 12 mm Filler factor: 0,64 (between 0,5 ile 0,9)	Coil Diameter: 20 mm Sample Diameter: 12 mm Filler factor: 0,64 (between 0,5 ile 0,9)

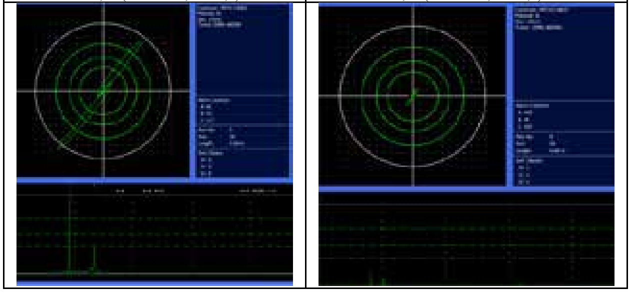

Figure 10. Test Frequency 20 kHz- Test Speed:0,2 m/s

Coil Diameter: 15 mm Sample Diameter: 12 mm Filler factor: 0,64 (between 0,5 ile 0,9)	Coil Diameter: 20 mm Sample Diameter: 12 mm Filler factor: 0,64 (between 0,5 ile 0,9)
	

Figure 11. Test Frequency 50 kHz-Test Speed:0,2 m/s

Coil Diameter: 15 mm Sample Diameter: 12 mm Filler factor: 0,64 (between 0,5 ile 0,9)	Coil Diameter: 20 mm Sample Diameter: 12 mm Filler factor: 0,64 (between 0,5 ile 0,9)
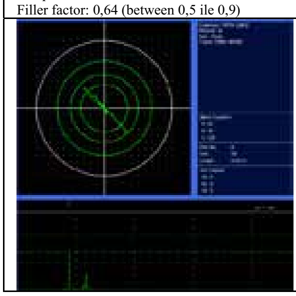	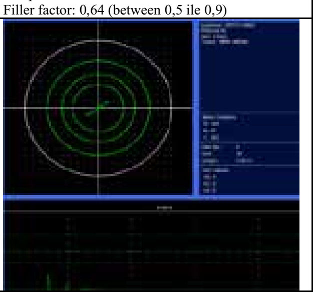

Figure 12. Test Frequency 100 kHz-Test Speed:0,2 m/s

3.2. Effects of Test Frequency on the output signal

The signals obtained from tests conducted for 12 mm aluminum rod at different frequencies were compared by keeping filter range, signal gain, test speed, coil (15 mm) variables constant. it is observed that increasing the test frequency makes only superficial errors of the output signals, where errors deepen, defects are not measured and the output signal weakens

Test Frequency 10 kHz	Test Frequency 20 kHz
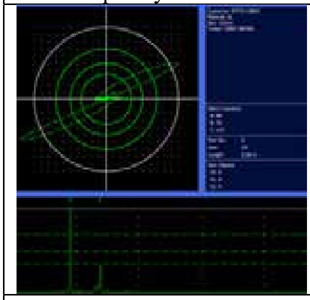	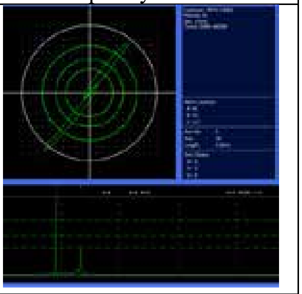
Test Frequency 50 kHz	Test Frequency 100 kHz
	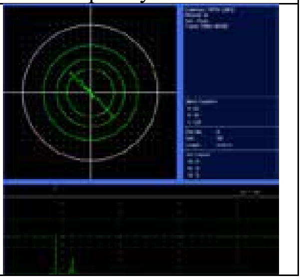

Figure 13. Test Frequency

4. Conclusion

- The diameter of the round coil used in non-destructive testing with eddy currents management must be specified according to the number diameter to be tested. The diameter of the coil used for the diameter of the coil used for the 12 mm aluminum rod is 15 mm. Filler Factor;

  Filling Factory (12 mm aluminum rod) = (12 mm / 15 mm) ^{2} = 0.64

  This ratio is in the range of 0.5 to 0.9 in DIN 54140 standard. The efficiency of the output signal was also observed by controlled experiments in the studies conducted in this range.
- To determine the defect up to the points closest to the center of the 9.5 mm / 12 mm aluminum rod that will be subjected to non-destructive inspection, a frequency value appropriate to the line speed should be selected in order to keep the depth of penetration at maximum. The depth at which eddy currents penetrate a material is influenced by the frequency of the excitation current and the electrical conductivity and magnetic transduction of the sample. Depth of penetration decreases with increased frequency, increased conductivity and magnetic transition. In the examination of these parameters affecting the depth of penetration, 12 mm aluminum rod resistance will increase and reduce conductivity due to increased heat at 180-200^{0} C after casting process. In this case, the penetration depth is expected to be greater than the penetration depth of 20 ^{0} C in the laboratory.
- One of the important factors affecting the depth of influence is frequency. Very high frequencies are used to report very shallow defects in a material. Similarly, lower frequencies should be used to measure defects deeper than the percentage near the material center and to test for high-conductivity, magnetic, or thick materials. In laboratory experiments, it is observed that increasing the test frequency makes only superficial errors of the output signals, where errors deepen, defects are not measured and the output signal weakens. Under-surface defects of the aluminum rod are directly affected by the end product produced using this rod. The 12mm aluminum rod has to operate at low frequencies suitable for line speed in order to detect continuity up to the nearest location to the center.

5. References

[1] Doğan, E., Deformatıon And Re-Crystalızatıon Behavıor Of 1050 And 8006 Alumınum Alloys. P:11-12

[2] https://www.foerstergroup.com/en/usa/technology/eddy-current-testing/ Date.17.06.2020

[3] https://www.pruftechnik.com/tr-TR/ Date: 17.06.2020

[4] Yakupoğlu, A., Perceptıon Of Surface Crackes Wıth The Eddy Current Probe, P:12-13, 22-24

Recovery of Rare Earth Elements (Nd, Gd, and Dy) from Apatite Concentrate, Esfordi Mine-Yazd Province

Ghazale KOHOOLAT, Sina SHAKIBANIA, Mohammad MOKMELI
University of Tehran
Iran

Abstract

Rare earth elements (REEs) comprise critical components of many of our modern-day technological devices and everyday electronics. The increased use of REEs in magnets, modern electronics and a variety of commercial products has led to a shortage of REEs for production purposes. The two major mineral sources of REEs are bastnasite and monazite. However, their production can come from a variety of other minerals, such as xenotime, apatite, yttrofluorite, cerite, and gadolinite. Apatite concentrate can contain up to 0.8 wt. % of rare earth oxides. In the present study, the recovery of rare earth elements of Gd, Dy, and Nd from Esfordi apatite concentrate has been studied. Esfordi mine located at Bafq, Yazd, has one of the largest iron-apatite deposits in Iran. The apatite sample used in this research mainly consisted of Fe (21.89 wt.%), Ca (20.59 wt.%), and P (8.31 wt.%). The concentration of Nd, Gd, and Dy were 1769, 240, and 127 ppm respectively. The total economic value of these elements was estimated 155 US$ per ton of ore assuming 100% recovery. This is higher that the value the phosphate content of the concentrate can generate. The phosphate content of the concentrate is usually treated to produce phosphoric acid/phosphate fertilizer. The residue may be treated to recover rare earth elements. In the first step, the apatite was digested in a concentrated nitric acid solution (5 M). The recovery of Gd, Dy, and Nd were 100%, 87%, and 11% respectively. After leaching, calcium as $Ca(NO_3)_2.4H_2O$ was precipitated by cooling and recrystallization. The solution was then neutralized using ammonia whereby the REEs precipitate mainly as phosphates ($REEPO_4.nH_2O$). At the optimum condition, more than 98% of Dy, 85% of Gd, and 9% of Nd were precipitated and separated from the solution.

1. Introduction

Rare earth elements (REEs) are a group of chemical elements, including the lanthanides, scandium, and yttrium. Despite being relatively abundant in the earth's crust, they rarely occur in concentrated forms, making them economically challenging to recover. REEs are an essential commodity to the global market. Most of REEs production comes from the processing of bastnasite, monazite, ion adsorption clays, xenotime, and loparite. Apatite concentrate, which is produced from the beneficiation of igneous phosphate ores, are one of the most promising sources of REEs, with about 250 million tons of phosphate ore being annually treated in the phosphoric acid and phosphate fertilizer industries [1]. Despite its low rare-earth content, apatite could become an important source of rare earth elements since it is processed in large quantities and is also found all over the world [2]. The quantity of rare earth elements in phosphate sources is estimated to be eight million metric tons of earth oxides (REOs) worldwide [3]. Apatite concentrate can contain up to 0.8 wt. % of REOs [3].

Due to their unique spectroscopic and magnetic properties, REEs are used in a wide variety of products and applications such as permanent magnets, catalysts, rechargeable batteries, mobile phones, plasma televisions, and computer disc drives [4, 5].The demand for REEs is high, and their consumption is projected to even increase more in the near future.

Nitrogen, phosphorous, and potassium (NPK) fertilizers can be produced by digestion of phosphate rock by a concentrated nitric acid solution through the nitrophosphate process (Also known as Odda process) [6, 7, 8]. An integrated separation of rare earth elements in the nitrophosphate process makes the hydrometallurgical process cost of rare earths effective and introduces a new environmentally sound source of REEs. The latter is an important point as the global demand for REEs such as Nd and Dy is predicted to rise by 700% and 2600% in the coming 25 years [4].

The nitrophosphate process starts with the digestion of the phosphate rock in a concentrated nitric acid solution. The digestion of apatite in the nitrophosphate process is performed in a concentrated acid in order to reduce the amount of water in the process [9, 10, 11, 12]. When leaching is conducted by nitric acid, most of the rare earth elements in the apatite ore will dissolve and transfer into the pregnant leach solution (PLS). An important aspect regarding the application of nitric acid is that the dissolution rate of REE is permanently higher with nitric acid compared to other acidic reagents such as sulfuric acid [13, 12]. Furthermore, nitrate solutions are preferable for the extraction and separation of the REEs by solvent extraction [14].

Calcium is a non-nutrient in NPK fertilizer and is considered as a diluent of this fertilizer by increasing its volume. Calcium nitrate tetrahydrate is removed from the digestion solution to increase the nutrient content as well as reaching the appropriate CaO to P_2O_5 ratio in the fertilizer. This is achieved by lowering the temperature of the digestion solution below 0°C until cooling crystallization occurs [7]. At this condition, precipitation of $Ca(NO_3)_2.4H_2O$, the most stable hydrated form of calcium nitrate, happens [15]. The lanthanides can be recovered from the leach solution after crystallization of $Ca(NO_3)_2.4H_2O$ and defluorination, by pH adjustment. The recovery of REEs and their concentration in the obtained precipitate is a function of pH and calcium concentration [13].

In this study, the recovery of the rare earth elements of Gd, Dy, and Nd from Esfordi apatite concentrate has been studied. The selection criteria were the economic value of the first three elements. Esfordi mine, located at Bafq, Yazd, has one of the largest iron-apatite deposits in Iran. The process for recovery of REEs consists of apatite concentrate digestion in concentrated nitric acid solution, precipitation of calcium nitrate, and then precipitation of REEs by pH adjustment. The obtained optimum conditions have been reported in this work.

2. Experimental procedure

2.1. Materials

The apatite concentrate used in this study was obtained from Esfordi mine, Yazd province, Iran. The apatite concentrate was primarily received in a pulverized condition. To determine the chemical composition of the concentrate, a representative sample was analyzed by Inductively Coupled Plasma atomic emission spectroscopy, ICP-OES (Varian-735, United States). The results are represented in Table 1. All the chemicals used in this research were analytical grade. Nitric acid and ammonium hydroxide were purchased from Merck, Germany.

2.2. Experimental procedure

A schematic of the REEs recovering procedure is shown in Figure 2. The recovering procedure consists of a leaching stage, followed by cooling and crystallization, then precipitation of REEs. The leaching experiments were conducted in a 1-L three-neck flat-bottom flask kept at the water bath. Apatite concentrate was mixed with 5 mol/L solution of nitric acid with the solid to liquid ratio of 1:5 g/ml at 60°C for 2 hours on the magnetic stirrer (Alfa D500, Iran). A schematic illustration of the apparatus is shown in Figure 1.

Table 1. Chemical composition of the apatite concentrate

Element	Ca	Fe	P	Si
Conc.	20.59 %	21.89 %	8.31 %	6.33 %
Element	La	Ce	Pr	Sm
Conc.	1233 ppm	3078 ppm	427 ppm	280 ppm
Element	Nd	Dy	Gd	Cl
Conc.	1769 ppm	127 ppm	234 ppm	104 ppm
Element	Mg	Yb	Cl	Y
Conc.	1.74 %	47 ppm	104 ppm	461 ppm

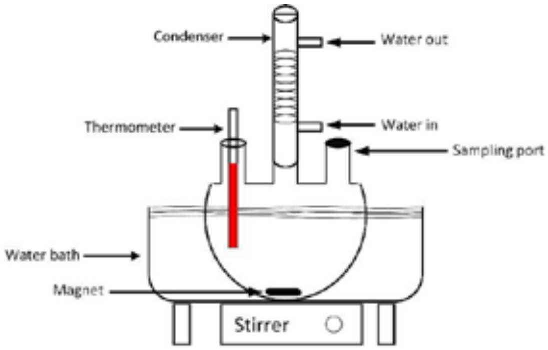

Figure 1. Schematic illustration of the apparatus.

After the leaching, the PLS and leach residue were separated using filter paper. The PLS was kept at -2°C at the fridge for 48 hours to promote the crystallization of calcium as $Ca(NO_3)_2.4H_2O$. Hydrated calcium nitrate was then washed with ethanol. The precipitation of rare earth elements was carried out by partial neutralization by the addition of ammonium hydroxide to the leach solution until the final solution pH reaches to1.4.

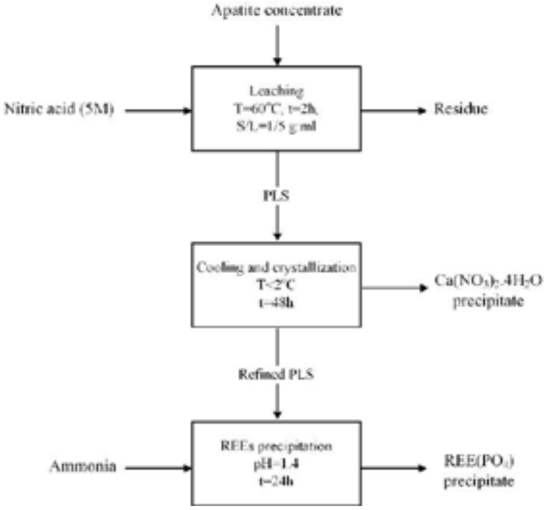

Figure 2. Flowsheet of the recovering procedure of REEs.

3. Results

3.1. Speciation of REEs in NO_3^{2-} and PO_4^{2-} medium

Prior to the interpretation of the results, in order to provide a better understanding of the system, the speciation of the studied REEs in the presence of NO_3^{2-} and PO_4^{3-} is demonstrated in Figure 3, 4 and 5. According to the Eq. 1, apatite can react with nitric acid, which results in the generation of a considerable amount of phosphoric acid.

$$Ca_5(PO_4)_3OH + HNO_3 = CaNO_3 + H_3PO_4 + H_2O \qquad (1)$$

Accordingly, the behavior of the REEs in the presence of nitrate and phosphate has been studied. The speciation diagrams of Gd, Dy, and Nd are presented in Figures 3 to 5. The initial concentrations of the species were based on the relevant concentration of these compounds in the studied work. These figures have been plotted using Medusa speciation software.

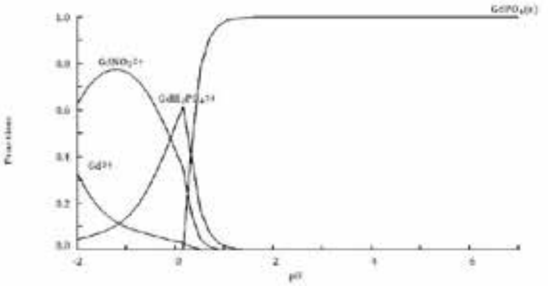

Figure 3. Speciation distribution of Gd ([Gd]=0.3.10-4 M, $[NO_3^{2-}]$ =4 M, $[PO_3^{3-}]$ =3 M, and T=25°C).

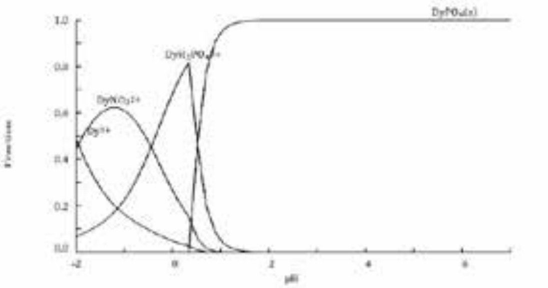

Figure 4. Speciation distribution of Dy ([Dy]=0.3.10-4 M, $[NO_3^{2-}]$ =4 M, $[PO_3^{3-}]$ =3 M, and T=25°C).

According to these figures, Gd, Dy, and Nd are showing similar chemical behavior in the presence of nitrate and phosphate ions. These elements are majorly found as aqueous nitrate complexes in cationic form at pH values below 0. The distribution of the REE species, as a function of pH, can be chosen such that the separation stage being more efficient. According to the figure 2 to 4, the dissolution of the Gd, Dy, and Nd is possible using concentrated nitric acid solutions. The fraction of Nd nitrate complexes at pHs below 0 is relatively higher in comparison to Dy and Gd.

The fraction of phosphate complexes of these elements is an increasing function of pH. As the pH of the solution increases, more nitrate complexes of Gd, Dy, and Nd transforms into phosphate complexes. At pHs above 1, almost all of the Gd, Dy, and Nd precipitate as REEs phosphate. Accordingly, and as will be seen in the precipitation section, precipitation and separation of these elements can be performed by pH adjustment.

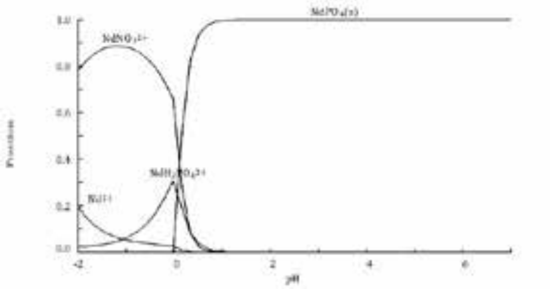

Figure 5. Speciation distribution of Nd ([Nd]=0.3.10-4 M, $[NO_3^{2-}]$ =4 M, $[PO_3^{3-}]$ =3 M, and T=25°C).

3.2. Leaching

The results of the leaching experiments under the optimum condition are summarized in Table 2. The optimum leaching condition was determined to be $[HNO_3]$ = 5M, solid to liquid ratio of 1:5 g/ml, T= 60°C, and leaching time of 2 hours. Under this optimum leaching condition, the extraction percentages of Dy and Gd were at 100 and 87%, respectively. The dissolution percentage of Nd was lower in comparison to Dy and Gd. Only 11% of the Nd in the apatite concentrate was dissolved.

Table 2 Results of leaching experiment under optimum condition ($[HNO_3]$ = 5M, solid to liquid ratio of 1:5 g/ml, T= 60°C, and t= 2 hours)

Element	Dy	Gd	Nd
Dissolution %	100	87	11

3.3. Cooling, crystallization, and precipitation

In order to remove Ca from the PLS, the temperature of the PLS was decreased to -2°C. The PLS was kept at this temperature for 48 hours. The co-precipitation of REEs in the Ca removal stage was determined to be negligible. After partial removal of Ca, the pH of the solution was increased to precipitate REEs in the form of phosphate from the solution. The optimum pH of the precipitation stage was determined to be 1.4. High precipitation percentage of REEs was obtained at the pH of 1.4 after 24 hours. It was calculated that Dy, Gd, Nd were recovered with the percentages of 98, 85, 9, respectively. Precipitation percentages of REEs are shown in Figure 6.

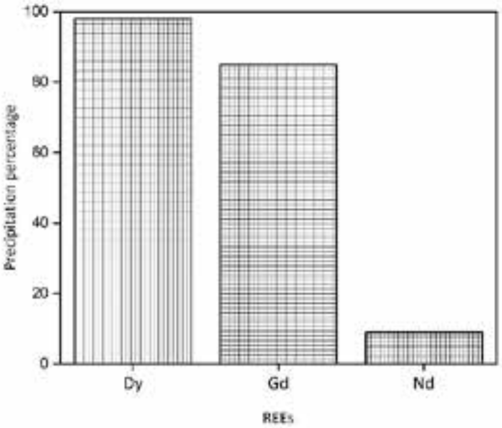

Figure 6. Precipitation percentage [M5] of REEs from purified PLS (pH=1.4, t=24 hours).

4. Conclusion

The recovery of the rare earth elements (Gd, Dy, Nd) from an apatite concentrate has been studied. Under the optimum condition, dissolution percentages of 87% for Gd, 100% for Dy, and 11% for Nd were obtained using 5 M nitric acid. The $Ca(NO_3)_2.4H_2O$ was separated by cooling crystallization. The solution was then neutralized using ammonia, whereby the REEs precipitate mainly as phosphates ($REEPO_4.nH_2O$). The Dy, Gd, Nd were recovered with 98%, 85% and 9%, respectively.

References

[1] Wu, S., Wang, L., Zhao, L., Zhang, P., El-Shall, H., Moudgil, B., Zhang, L., Chemical Engineering Journal,335, (2018), 774-800.

[2] C.K. Gupta and N. Krishnamurthy: Extractive Metallurgy of Rare Earths, CRC Press, New York, 2004.

[3] Gupta, C., Krishnamurthy, N. Extractive Metallurgy of Rare Earth, 2005.

[4] Alonso, E., Sherman, A. M., Wallington, T. J., Everson, M. P., Field, F. R., Roth, R., & Kirchain, R. E. Environmental Science & Technology, 46, (2012), 4684-4684.

[5] Voncken, J. (2016). The Rare Earth Elements. Springer Briefs in Earth Sciences.

[6] Association European Fertilizer Manufacturers, production of NPK fertilizers by the Nitrophosphate Route. Vol. 7. 2000.

[7] Wiesenberger, H., 2002. State-Of-The-Art for the Production of Fertilizers with Regard to the IPPC-Directive (Wien).

[8] Binnemans, K., Jones, P. T., Blanpain, B., Gerven, T. V., & Pontikes, Y. Journal of Cleaner Production, 99, (2015), 17-38.

[9] Bandara, A., & Senanayake, G. Hydrometallurgy, 153, (2015), 179-189.

[10] Sandstöm, Å., Fredriksson, A., 2012. Apatite for Extraction - Leaching of Kiirunavaaraapatite for Simultaneous Production of Fertilizer and REE. International Mineral Processing Congress (IMPC2012). India.

[11] Forsberg, K.M., Mohammadi, M., Ghafarnejad Parto, S., Martinez De La Cruz, J., Rasmuson, Å., 2014. Recovery of REE from an apatite concentrate. 53rd Conference of Metallur gists, Vancouver; Canada.

[12] Aly, M. M., & Mohammed, N. A. Hydrometallurgy, 52, (1999), 199-206.

[13] Habashi, F. Journal of Chemical Technology and Biotechnology. Chemical Technology, 35, (2007), 5-14.

[14] V.I. Kuzmin, G.L. Pashkov, V.G. Lomaev, E.N. Voskresenskaya, and V.N. Kuzmina: Hydrometallurgy, 129, (2012), pp. 1–6.

[15] Paulik, J., Paulik, F., & Arnold, M. Journal of Thermal Analysis, 27, (1983), 409-418.

Production of Alumina-Based Ceramics from Aluminium Black Dross

Umay ÇINARLI, Ahmet TURAN
Yalova University
Turkey

Abstract

Aluminium dross arises due to the high interest of aluminium to oxygen during melting, molten metal transfer and refining processes. It is divided into two sub-groups as black and white with respect to the aluminium content. In this study, it was aimed to determine the optimum conditions for the valorization of black dross with pyrometallurgical and hydrometallurgical processes.

1. Introduction

Aluminium dross consists of metals, salts, oxides and other non metallic substances. It is classified as white and black dross with respect to the aluminium content. White dross has high metallic aluminium content whilst the black dross has low metallic aluminium content. White dross is obtained from the melting of aluminium as a result of primary and secondary production whereas the black dross is a result of the recycling of aluminium with the use of high amount of salt-based flux materials. In this study, the aim is to determine the conditions necessary for the valorization of black dross through processes such as calcination, leaching and sintering [1,2].

2. Materials and Methods

In the first series, the black dross was calcined at five different temperatures (from 700 °C to 1100 °C) to remove halide-based impurities by evaporation and to convert its metallic Al content to Al_2O_3. In the second series, original and calcined black dross samples were leached in different reagents such as HCl, H_2SO_4 and HNO_3 to obtain an alumina-based filter cake as pure as possible. Calcined black dross, which was calcined at 1100 °C for 60 minutes, was leached in H_2SO_4 solution. Obtained alumina-based ceramic powders were compacted under 600 MPa uniaxial pressure and sintered under argon atmosphere for 60 minutes at increasing temperatures up to 1550 °C to observe the use of the produced powder as refractory material. XRD, XRF, chemical analysis, TGA, Vickers hardness measurement and Archimedes density techniques were used to characterize raw materials, produced ceramic powders and compacted ceramics.

3. Conclusion

Various experimental studies have been conducted to observe the effects of different reagents on product quality and recovery efficiency. Calcination experiments at five different temperatures have shown that the conversion of metallic aluminium to alumina increases with increasing temperature. It has been observed that H_2SO_4 is suitable for use in this field in terms of both price and performance. Alumina-based ceramic powders produced under optimized conditions were pressed under 600 MPa pressure and sintered at increasing temperatures up to 1550 °C for 60 minutes. In the sample sintered at 1550 °C, the density value of 3.15 g.cm-3 along with 69.58 HV hardness was measured. In addition, 10.66% weight loss was detected in the sample after sintering because of the evaporation of remaining halide-based compounds.

Acknowledgment

The authors are pleased to acknowledge the financial support for this research from Yalova University, Scientific Research Projects Department under grant number 2019/YL/0002.

References

[1] O. Yücel, E. Car, UCTEA Metallurgy Journal, 175 (2015) 35-43.
[2] K. Tripathy, S Mahalik, C. K. Sarangi, B. C. Tripathy, K. Sanjay, I. N. Bhattacharya, Minerals Engineering, 137 (2019) 181-186.

Production of FeCo from Mill Scale Through Aluminothermic Reduction

Mehmet BUGDAYCI[1], Ahmet TURAN[1], Levent ONCEL[2]
[1]Yalova University, [2]Sinop University
Turkey

Abstract

Mill scale is a waste material that contains 70% iron by mass. It is an oxide layer, and it arises during the hot rolling of steel slab and billets. The use of secondary raw materials is a necessity both to mitigate pressure on primary resources and to decrease the CO_2 emissions in primary production. In the present study, FeCo production from mill scale was investigated through an aluminothermic (metallothermic) production route.

1. Introduction

Annually, 13.5 million metric tons of mill scale is formed around the World. Cobalt is not a commonly used alloying element, but it is used in the alloying of high-speed tool steels, maraging steels, high-fracture toughness steels, high-performance carburizing martensitic stainless steels and martensitic stainless steel hardfacing alloys. Cobalt and other alloying elements are added to the steel structure in the form of ferroalloys. Also, FeCo is a soft magnetic material and because of this feature, it is used in related applications.

2. Experimental Studies, Results and Discussion

The metallothermic reduction was chosen because of its advantages such as minimum energy consumption, completion of the process in a short time and no need for complicated equipment. Before the experiments, the system was thermochemically simulated by means of HSC Chemistry and FactSage software. In the experimental studies, the effects of aluminium, as a reductant, in different stoichiometries on total metal recovery yield were investigated (Figure 1). Samples were characterized by using optical microscopy (Figure 2), X-ray fluorescence (XRF), atomic absorption spectrometry (AAS) techniques and hardness test. It was seen that the highest metal recovery yields were obtained as 81.25% for iron and 93.78% for cobalt in the experiment conducted with the addition of 105% stoichiometric aluminium.

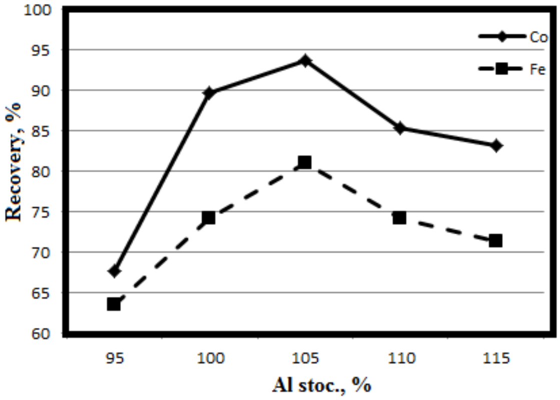

Figure 1. Metal recovery ratios of Fe and Co with increasing aluminium stoichiometry.

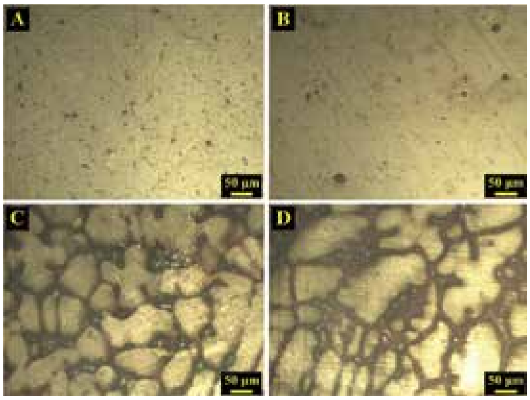

Figure 2. Optical microscopy micrographs of obtained FeCo phases at 200x magnification (A: 95% Al sto., B: 100% Al sto., C: 105% Al sto., D: 110% Al sto.).

Effect of Flash Design on Efficiency in Hot Forging Process

Fulya EYÇİN[1], Tuğçe YAĞCI[2,3], Adem KORKMAZ[2], Serhat BARDAKÇI[3], Osman ÇULHA[2,3]
[1]Tirsan Kardan San. ve Tic. A.Ş., [2]Manisa Celal Bayar University,
[3]Twin R&D Engineering Company

Turkey

Abstract

The effects of flash width and thickness on the forging force are clearly demonstrated in line with qualitative studies. Forging force in hot forging processes with flash; increases with decreasing flash thickness. Increasing the flash thickness and width causes an increase in friction and a decrease in the metal temperature in the flash flow area. As a result of many studies, certain expressions have been developed for flash design based on forged part geometry and part weight. In this way, flash width and thickness information can be obtained by knowing the weight and geometric properties of the part to be hammered. New forging designs of the shaft part have been realized by considering the theories of flash width and thickness of researchers such as Teterin and Tarnovskij, Neuberger and Mockel, Wolf.

In this study, it is aimed to reduce the amount of flash that occur during the production of the flange yoke a cardan shaft. The amount of flash leaking as a result of the process was minimized by the new hot forging with flash. Problems were prevented such as material loss, die pressure problems and internal defects in the workpiece by minimizing the amount of flash. Design, design verification and process development studies were carried out with numerical simulation assisted analysis.

1. Introduction

The forging process generally includes multiple pre-forming processes and a species finishing process [1,2]. Forging processes usually produce little or no scrap and generate the final part geometry in a very short time, usually in one or a few strokes of a press or hammer [3]. The hot forging process is one of the conventional techniques to produce high-duty components used in industries of automotive and aerospace [2,4,5].

Forging with flash process is the most commonly used forming process in industrial applications. In this forging method, the material flow is occurred to fill all the die cavity thanks to movement of dies. The first step of the filling process is the upsetting of the raw material. In the next stage of forming, material flow takes place towards the boundaries of the cavity. Finally, deep cavities are filled and the process is completed [2,4,6].

The development of new generation technological applications plays an important role in increase the potential global competitiveness of different industries as well as many other fields. Thus, computer aided programs that dynamic, learning and interactive were created in virtual environment. As a result of this development, the fact that the digital twin of the product or process is created in the virtual environment has come to the fore in R&D studies. The concept of "*Digital Twin*" was offered as a result of the combination of simulation technology with cyber-physical systems and the internet of things that come into our life by industry 4.0. Digital twins are systems that show the behavior of a real system in a virtual environment. Digital twins enable to identify problems, test new developments, simulate and analyze all planned models. In short, it enables to every product to be physically will obtained to be tested in a virtual environment [7, 8].

From the perspective of Material Science, it is a great advantage for manufacturers to know what properties the product / process will display when its production chain ends or its efficiency before mass production. For this purpose, 2D or 3D simulation programs are used in forming applications. These programs have properties such as lower cost, getting results faster, defining many materials, temperature and friction values and analyzing them with many variables. One of these computer aided application tools is *Simufact Forming* that can simulate many forming processes such as forging, rolling, extrusion, sheet metal forming, heat treatment, mechanical joint and pressure welding. Simufact Forming enable hot, cold and warm forging and die forging processes and offered as well as sub processes to perform such as cooling, cutting, pre-deformation and extrusion processes [9].

2. Experimental Procedure

A new forging operation was carried out in order to achieved the flash reduction in the production of the flange yoke of cardan shaft. The number of operations was decreased and the amount of material used during production were reduced to a minimum by the new forging process. The design of the new forging process and the flange yoke of the cardan shaft was carried out by numerical simulation supported analysis.

The dimensions of the workpiece used in the forging process are 214 mm length and 90 in diameter. In hot forging with flash proses, AISI 1015 (DIN 1.1141) steel material which is the raw material of the forked flange part was used. The chemical composition of AISI 1015 steel used during simulation is given in Table 1.

Table1. The chemical composition of AISI 1015 steel [8].

Element	C	Mn	P	S	Fe
wt.%	0.15	0.45	0.01	0.031	Bal.

The process was carried out in 4 stages that are upsetting, pre-forging, final forging, and ironing. Firstly, upsetting was performed and the sample to be placed between the die ears was brought to appropriate dimensions. Pre-forging process was carried out before the forging process. The production model was realized on the hot forging application model by simufact forming. Mechanic press was used as a press and an amount of friction parameters were defined to the dies. The number of mesh elements was defined on the workpiece to ensure the most accurate results.

The flash that was leaking out was removed from the surface of the sample by the flash cutting process. Then the ironing process was applied and the production model was completed.

At the end of the simulation process, data such as contact pressure, effective plastic strain, material flow, force-displacement were obtained.

3. Results and Discussion

Figure 1 shows the simulation results of plastic stress. When the results are examined, it is observed that the experimental data match the data obtained during simulation. Figure 2 show the simulation results of material flow.

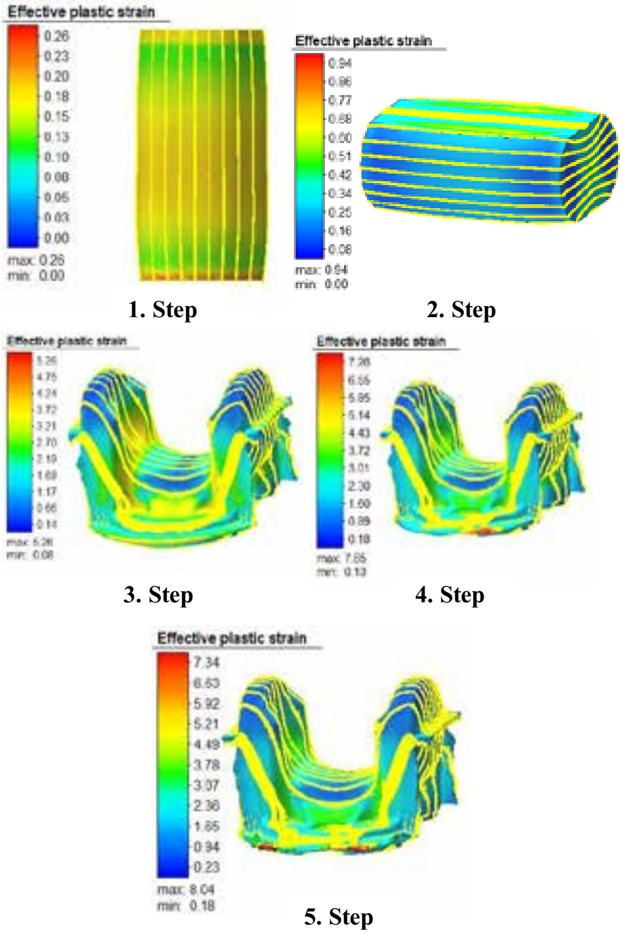

1. Step 2. Step 3. Step 4. Step 5. Step

Figure 1. Simulation results of the effective plastic strain.

Figure 2 show the simulation results of material flow. In addition, the values of the material flow data obtained during the simulation are given in table 2. At the end of the simulation, die cavities were filled with raw material. In addition, workpiece was given a rough form in the first forging process. In the second forging process, the deep cavities of the forging die were filled. Thus, the workpiece was forged without the failure to fill. It was observed that the material flow was at its maximum value especially in the 4th stage. It was observed that the material flow values were close to each other in the first and second stages of the upsetting process. The material flow values are very high in the pre-forging process and the final forging process.

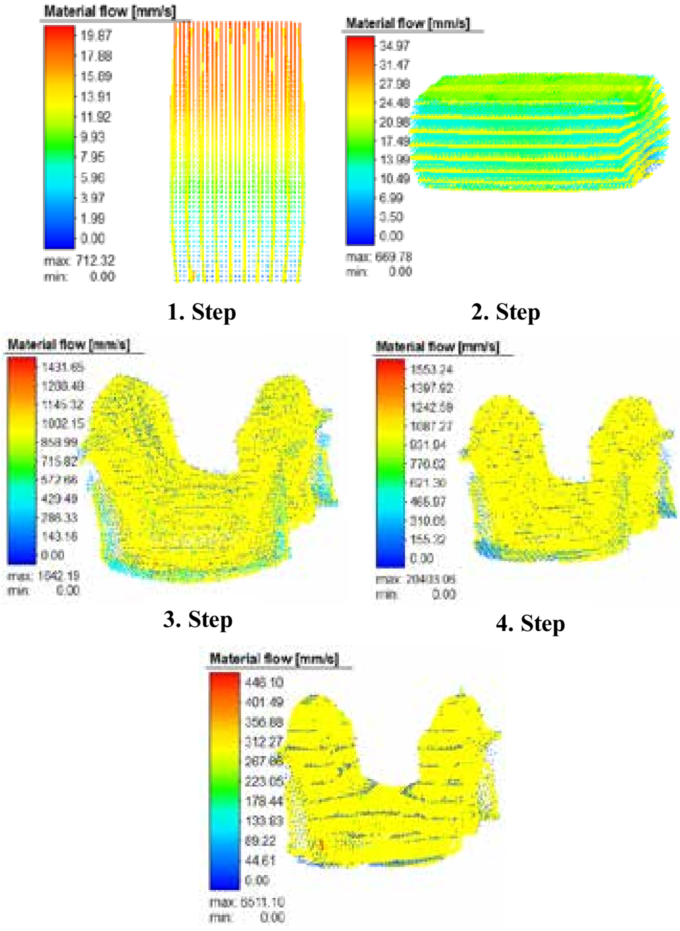

1. Step 2. Step 3. Step 4. Step 5. Step

Figure 2. Simulation results of the material flow.

Table 2. Simulation data of the material flow.

Simulation Step Number	Maximum Flow Rate (mm/s)
1	712.32
2	669.78
3	1642.19
4	20403.06
5	6511.10

The effective stress values formed on the part are given in Figure 3. In addition, Table 3 shows the stress values of the stages. When the results are analyzed, the effective stress values in steps 3 and 4 are almost the same. In steps 3 and 4 where the flange part is formed, the stress value has reached its maximum value. When the simulation data were examined and as seen in the figure, stress value was increased in the bottom region of workpiece contacted with the lower die.

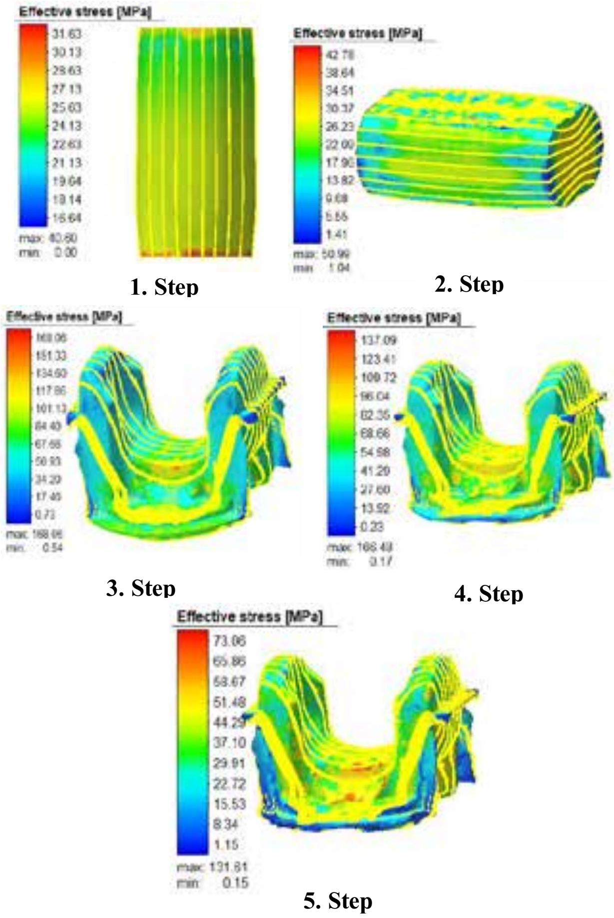

1. Step 2. Step 3. Step 4. Step 5. Step

Figure 3. Simulation result of the effective stress

Table 3. Simulation data of the effective stress values.

Simulation Step Number	Effective Stress (MPa)
1	40.60
2	50.99
3	168.06
4	166.48
5	131.61

Contact pressure values are shown in Figure 4. Data of contact pressure are given in table 4. When results examined, the lowest contact pressure values were observed in step 1. The contact pressure was increase considerably in steps 3 and 4 and was observed to reach its maximum value in step 4.

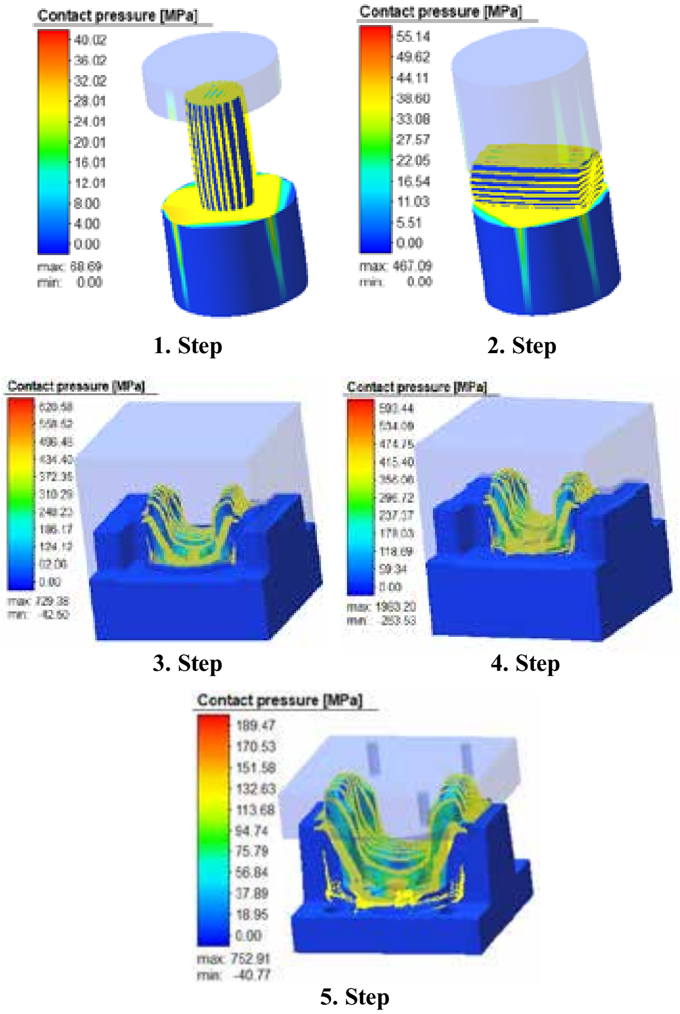

1. Step 2. Step 3. Step 4. Step 5. Step

Figure 4. Simulation result of the contact pressure.

Table 4. Simulation data of the contact pressure values.

Simulation Step Number	Contact Pressure (MPa)
1	68.69
2	467.09
3	729.38
4	1983.20
5	752.91

In addition, force - displacement graphics were obtained as a result of simulation. These graphs (belonging to operation steps 1, 4 and 5) are given in figure 5. In addition, numerical data of the obtained force-displacement graphs are given in table 5. The force - displacement data obtained at the end of the upsetting process is 178 tons for stage 1 and 59 tons for stage 2. Force values have increased in pre-forging and forging processes. While the force value is 1280 tons for stage 3, it is 1182 tons for the stage 4. It was determined that the forging force required for the ironing process is 462 tons.

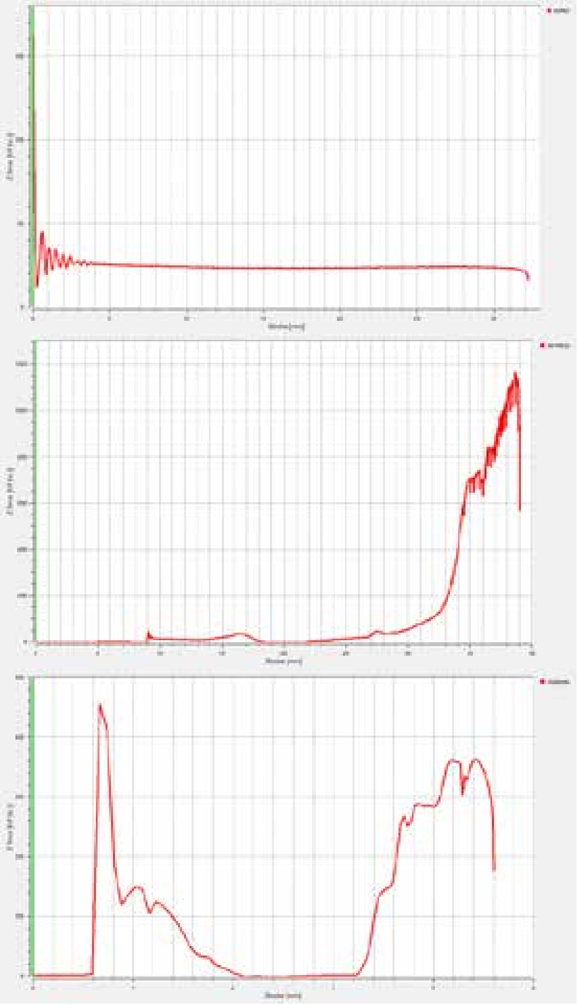

Figure 5. Force-displacement curves of steps 1, 4 and 5.

Table 5. Simulation data of the contact pressure values.

Simulation Step Number	Forging Force Values (tnf)
1	178
2	59
3	1280
4	1182
5	462

4. Conclusion

A new hot forging process was developed for the production of the flange yoke of the cardan shaft. Forging process model were carried out by Simufact Forming software. It was controlled whether this production model is compatible with the reel physical production conditions. The dimensions of the workpiece at the beginning of the process was reduced and the amount of flash flowing out at the end of production was minimized. Material loss was minimized thanks to the reduced amount of flash. It was proved that flash parameters such as flash thickness and width have a positive effect on the flawless production of the workpiece, die life, stresses on the die by finite elements analysis. The new forging process model was aimed to exhibit superior features than the existing forging process. For this reason, the applicability of the forging process was investigated through the simulation program and the results were reported in detail.

References

[1] S. Fujikawa, Application of CAE for hot-forging of automotive components, 98(2): pp. 176-181

[2] Levon ÇAPAN, Metal Forming Handbook, 2010, İstanbul.

[3] T. Altan, G. Ngaile, G. Shen, Cold and hot forging : fundamentals and applications, ASM International, 2005.

[4] Makas, T., General Overview of Hot Forging. 2016.

[5] Y. Liu, Y. Wu, J. Wang, S. Liu, Defect analysis and design optimization on the hot forging of automotive balance shaft based on 3D and 2D simulations, 2018, pp. 2739–2749, doi.org/10.1007/s00170-017-1080-9.

[6] Keife, H., & Ståhlberg, U. The influence of flash design on material flow and tool pressure in closed-die forging: a practical example. Journal of Mechanical Working Technology, 1984, 9(1), pp. 37–52. doi:10.1016/0378-3804(84)90092-5

[7] BIM, “Digital Twin” (2018). <https://assets.new.siemens.com/siemens/assets/api/uuid:610b5974-241d-4321-8ae6-55c6167446bf/version:1562849283/bim-digitwin-ru.pdf>, Dated: 14.06.2020.

[8] Makhatha, M. E., Fatoba, O. S., & Akinlabi, E. T. Effects of rapid solidification on the microstructure and surface analyses of laser-deposited Al-Sn coatings on AISI 1015 steel. The International Journal of Advanced Manufacturing Technology, 2017, 94(1-4), pp. 773–787. doi:10.1007/s00170-017-0876.

[9] <https://www.simufact.com/module-hot forging.html> Dated: 15.06.2020.

Recovery of WC and Co-Based Compunds from Waste Cutting Tools through Hydrometallurgical Route

Hakan KUŞDEMİR[1,2], Ahmet TURAN[3], Onuralp YÜCEL[1]
[1]Istanbul Technical University, [2]Körfez Döküm Sanayi ve Ticaret A.Ş., [3]Yalova University
Turkey

Abstract

Tungsten abundance in the earth crust is less than 0.001% which is very low ratio comparing to industrial metals such as iron, aluminium etc. Tungsten is used especially in wearing applications such as metal cutting tools and mining wearing machines. Comparing to ores, a typical tungsten scrap has more than ten times higher tungsten ratio which makes tungsten recovery more important in terms of economical and environmental concerns. Because of high tungsten concentration, various tungsten recovery methods from scraps are being applied for many years. Moreover, tungsten production methods from ores have numerous chemical enrichment processes that causes economical disadvantages and environmental problems.

On the other hand, cobalt is also assumed as a critical raw material. It is widely used in highly crucial industries such as lithium-ion batteries and superalloys. Earth crust consists of lower than 0.003% cobalt ratio and cobalt is generally obtained as by product of nickel and copper production. Democratic Republic of Congo has appx. 50% of world cobalt reserves. Similar to tungsten, a typical cobalt scrap consists of several times higher metal concentration than its ore. Therefore, cobalt recovery is as important as tungsten recovery.

A typical cutting tool scrap comprises more than 80% W and 6-16 % Co by wt. which make it economically important. Because of high tungsten and cobalt concentrations, the recovery of cutting tools is very critical. There are three main methods to apply to cutting tools for recovery and, they are direct, semi direct and indirect routes. Each one has specific metallurgical process which are pyro, hydro and electrometallurgical process or combination of them.

In the present study, a hydrometallurgical technique was tried to investigate to recover WC and $Co(OH)_2$ from waste ~6wt.% cobalt-containing cutting tools. Leaching operation was applied to grinded waste cutting tools by using HNO_3, H_2SO_4 and HCl. The purpose of leaching experiments was to extract cobalt binder phase out into solution and to obtain a filter cake containing almost pure WC. The highest Co extracting rate (87% by wt.) was obtained in the experiments which were carried out in nitric acid media and, remaining experiments were conducted by using nitric acid. In the second stage of leaching experiments, nitric acid molarities (from 1 M to 6 M), temperature (from 20 °C to 80 °C) and stirring rate (from 600 to 1200 rpm) were investigated for WC-Co powders having different average particle sizes (from <45 µm to <250 µm). A constant solid-liquid ratio of 1:10 was applied for all experiments. By using those leaching experiments, it was achieved that to increase the Co extracting rate greater than 90% with decreasing average solid particle size in the experiment carried out at 20 °C for 2 M acid concentration. After leaching experiments, $Co(OH)_2$ precipitation from pregnant solutions was investigated by the addition of NaOH to the solution. Precipitation parameters were the pH of 7-11 and the temperature of 20-50 °C. The most remarkable aspect of the present study was the investigation of different solid average particle sizes in leaching experiments. Sieve analysis, XRD, XRF, AAS and SEM-EDS methods were used for the characterization of raw materials and products.

Solid State Synthesis of Li_4SiO_4 Using Different Kind Steel Slags as SiO_2 Source

Fatih Kutay METE[1], Kağan BENZEŞİK[1], Ahmet TURAN[2], Onuralp YÜCEL[1]
[1]Istanbul Technical University, [2]Yalova University
Turkey

Abstract

At present, fossil fuel burning accounts for a significant percentage of the world's energy needs and induces a rise in atmospheric carbon dioxide (CO_2), which has been described as a significant contributor to global warming. For several more years, though, fossil fuels will prove to be the primary source of energy. Consequently, the most feasible approach to counteract the associated greenhouse effect is to develop cost-effective and environmentally friendly technology for large scale CO_2 capture and storage before release into the atmosphere. Lithium orthosilicate (Li_4SiO_4) is considered a possible material for capturing carbon dioxide (CO_2) owing to its high capture capability and thermal stability. The main purpose of this study is to optimize lithium orthosilicate synthesis by a solid-state method and to maximize the capture of CO_2 in conjunction with benefiting from slags for waste utilization. This involves the evaluation of the key characteristics of the synthesized material that improve the efficiency of the CO_2 capture. Li_4SiO_4 can be synthesized by the reaction of a homogeneous mixture of lithium carbonate (Li_2CO_3) and silica (SiO_2) in a 2:1 mole ratio. In the present study, blast furnace (BF) and blast oxygen furnace (BOF) were used as silica sources along with Li_2CO_3 to synthesize lithium silicate. Moreover, a pure SiO_2 reagent was also used in the reaction with Li_2CO_3 to be able to compare the results with the slag derived samples. The effect of the process conditions such as synthesis temperatures of 850-950°C and holding times of differentiating 4-10 hours in muffle furnace of the mixed powders have been studied and compared. Conversion rates to lithium silicate were followed and will be optimized. The samples and slags were characterized by x-ray diffraction (XRD) analysis.

1. Introduction

Global warming is an aspect of climate change, referring to the long-term rise of the planet's temperatures. It is caused by increased atmospheric greenhouse gas concentrations, primarily from human activities such as fossil fuel burning in industry, deforestation, and farming. Mostly due to the fossil fuels that people burn, carbon dioxide emissions are increasing. Fossil fuels like coal and oil contain carbon that plants pulled out of the atmosphere through photosynthesis over the span of many millions of years; we are returning that carbon to the atmosphere in just a few hundred years [1]. Global warming occurs when the atmosphere collects carbon dioxide (CO_2) and other air contaminants and greenhouse gases and these gases absorb heat and solar radiation that is bouncing off the surface of the earth. In order to reduce the carbon dioxide content in the atmosphere, many studies have been done. A range of technologies, including absorption, adsorption, membrane gas separation, or gas hydrate technologies, can be used to absorb carbon dioxide directly from the air or industrial sources. New material approaches are being proposed such as lithium orthosilicate (Li_4SiO_4); considered a potential material due to its high capture capacity of carbon dioxide and due to its thermal stability [2].

Lithium orthosilicate (Li_4SiO_4) is one of the lithium silicate ceramics researched for its wide variety of applications such as lithium-ion batteries and CO_2 doping. As this ceramic demonstrates immediate absorption and desorption of CO_2, it has also been proposed as a robust sorbent for CO_2 capture [3].

2. Experimental Procedure

Li_4SiO_4 can be synthesized by the reaction of a homogeneous mixture of lithium carbonate (Li_2CO_3) and silica (SiO_2) in a 2:1 mole ratio. Li_4SiO_4 produced by chemical reaction with solid-state synthesis according to below Eq (1).

$$2Li_2CO_3 + SiO_2 \rightarrow Li_4SiO_4 + CO_2 \qquad (1)$$

In this work, lithium orthosilicate adsorbents have been prepared using two separate slags as silica sources, and the following step was the preparation of the mixture with a mole ratio of 2.1:1 to avoid evaporation of lithium carbonate at high temperatures. Each sample has been mixed for 30 minutes in a turbula mixer to ensure a homogeneous mixture. The mixtures have been put into alumina boats (120x40x15 mm) for calcination and the calcination has been done in a muffle furnace at a temperature range of 850-950°C and durations (holding time) of 4-10h for varying samples. After cooling down under normal conditions, the samples were grinded with an agate mortar in order to shape them into a powder form for XRD analysis.

Two different slags were used, these slags are named; BF (blast furnace) and BOF (blast oxygen furnace). The chemical compositions of slags are given in Table 1 below.

Table 1. Chemical compositions of slags (wt%).

Slag	Fe	SiO_2	CaO	Al_2O_3	MgO
BF	0.36	37.20	39.55	13.14	5.89
BOF	18.43	12.25	48.04	2.12	3.72

3. Results and Discussion

Preliminary results show that the samples made from BOF with the increasing temperatures decrease the formation rate of lithium silicates and these samples tend to have lithium iron oxide phase. According to the XRD results and Rietveld refinement made by HighScore Plus, with the decrease of holding time, the samples from BF slag tend to have more lithium silicate and calcium doped lithium silicates, which improves the CO_2 capture according to other studies made on this topic [4, 5]. The involvement of calcium phases and small quantities of Mg, Fe, and Al in slag-derived lithium silicates may increase both the absorption of CO_2 and the kinetic behavior [6].

Below, the conversion rate chart (Figure 1), XRD results (Figure 2), and experiment list table (Table 2) can be found.

Table 2. Experiment list.

Specimen No #	Temperature / Time	Raw Material
1	950°C / 8h	BF
2	950°C / 4h	BF
3	950°C / 6h	BF
5	950°C / 10h	BF
6	950°C / 10h	BOF
7	850°C / 10h	BF
8	850°C / 10h	BOF
9	850°C / 8h	BF
10	850°C / 8h	BOF

In compliance with the chart (Figure 1), the conversion rate to Li_4SiO_4 are as follows respectively; 0%, 41.7%, 45.3%, and 50.5% respectively for holding times of; 10 hours, 4 hours, 8 hours, and 6 hours. It can be seen that at 950°C and holding time of 6 hours, Li_4SiO_4 conversion rate was found to be 50.5% and this is the highest conversion rate that is realized. In addition, when the conversion rate of both lithium orthosilicate and lithium calcium silicate are considered and summed up, the best conversion rate was obtained at a holding time of 4 hours with a total of 71.4%.

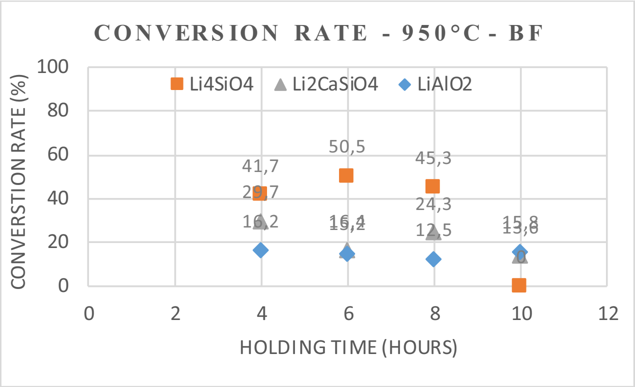

Figure 1. Conversion Rate chart for 950°C samples.

In figure 2, XRD results are shown. Holding time of 10 hours resulted in the formation of calcium phyllo-dodecaalumotetrasilicate ($Al_2CaSi_4O_{27}$), which can be seen by a sharp peak which is represented by the letter F. For the other samples, however, lithium silicate formation has been successfully achieved. The peaks comply with the Rietveld analysis data and show correlation and accuracy. Characteristic peaks of lithium orthosilicate are missing in XRD analysis for the holding time of 10 hours, which is confirmed by the Rietveld analysis as well.

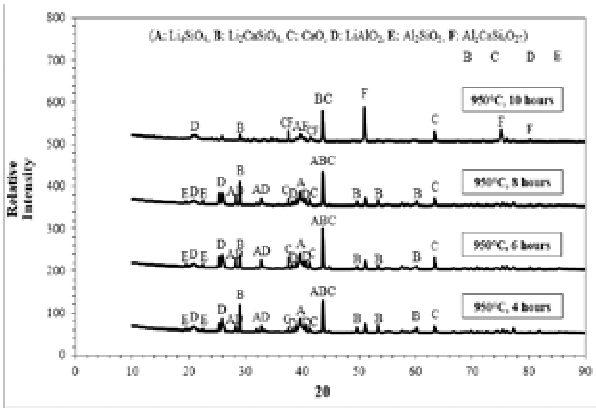

Figure 2. XRD data comparison for 950°C samples with different holding times in muffle furnace.

4. Conclusion

In this study, in addition to lithium orthosilicate production from steel slags in terms of waste utilization, parameters such as temperature and time were examined and the highest conversion rate was reached at 950°C and 4 hours of duration. Since this is an on-going study, the CO_2 capture tests are undone and still awaiting, but from the results gathered, it can be said that samples produced at 850°C and lower holding times will be showing off their capability with higher quality for the upcoming CO_2 capture tests since they have a higher ratio of consisting lithium silicates and calcium doped lithium silicates according to XRD and Rietveld analyses. Moreover, electric arc furnace (EAF) slag derived Li_4SiO_4 will be produced with the same method and the products will be subjected to the same characterization techniques. The most promising slag derived sample is yet to be decided.

References

[1] Climate change: Atmospheric Carbon Dioxide: NOAA Climate.gov. (2020, August 14). Retrieved February, from https://www.climate.gov/news-features/understanding-climate/climate-change-atmospheric-carbon-dioxide

[2] Izquierdo, M. T., Turan, A., García, S., & Maroto-Valer, M. M. (2018). Optimization of Li4SiO4 synthesis conditions by a solid state method for maximum CO2 capture at high temperature. Journal of Materials Chemistry A, 6(7), 3249–3257.

[3] Stefanelli, E., Puccini, M., Vitolo, S., & Seggiani, M. (2020). CO2 sorption kinetic study and modeling on doped-Li4SiO4 under different temperatures and CO2 partial pressures. Chemical Engineering Journal, 379, 122307.

[4] Mandal, D., Jadeja, M. C., & Chougule, B. K. (2015). Synthesis of Lithium Orthosilicate and Fabrication of Pebbles by the Solid-State Reaction Process. Indian Chemical Engineer, 59(1), 21–30.

[5] Vollath, D., Wedemeyer, H., & Günther, E. (1985). Improved methods for fabrication of lithium silicates. Journal of Nuclear Materials, 133–134, 221–225.

[6] Alcántar-Vázquez, B.-C., & Ramírez-Zamora, R.-M. (2020). Lithium silicates synthetized from iron and steel slags as high temperature CO2 adsorbent materials. Adsorption, 26(5), 687–699.

The Influence of Change in Microstructure by Heat Treatment on Drill Quality of Hot Forged AISI 4140 Steel

Nuray BEKÖZ ÜLLEN[1], Tuğba ÖNENÇ[2]
[1]Istanbul University-Cerrahpasa, [2]ULPATEC Air Filter Technology
Turkey

Abstract

Heat treatment is a link between the forging process and machining process, and heat treatment can regulate and control the mechanical properties and machinability of the workpiece through the change of microstructure. In industry, quality, efficiency and cost are the most important components in the manufacturing process. The accurate way to come up with these components depends on the selection of the accurate and suitable production conditions. In this context, AISI 4140 (42CrMo4) steel is one of the most widely used materials in the industry and is used in automotive, aircraft and space fields. Therefore, it is very important to process this steel material effectively and efficiently. AISI 4140 steel in experiments was chosen as reference material due to its extensive applications in many areas. In the present work, the effect of heat treatment on machinability of hot forged AISI 4140 steel in the drilling process was investigated at constant cutting parameters using different drill types (uncoated and TiAlN coated HSS twist drills). For this purpose; the surface roughness, dimensional accuracy, and circular and cylindrical deviations characterizing the hole quality were investigated experimentally. As a result, coated drill compared with uncoated drill gave positive results for each evaluation criterion. A better drill quality was obtained for the heat-treated samples than those of the unheat-treated samples at all conditions.

1. Introduction

Metal cutting is a widely used method in manufacturing technologies and it is mostly applied to all mechanic items. The most important point about the machining method is to produce with the desired quality and appropriate standards by obtaining the lowest costs [1-3]. In industry, quality, efficiency and cost are the most important components in the manufacturing process. The most accurate way to uncover these components depends on improving machinability. AISI 4140 steel is one of the most commercially used quenched and tempered steels. It's a most important feature is that it has a high rate of the martensitic structure as a result of heat treatment by having Cr and Mo elements and it allows some mechanical properties in the structure to coexist, such as strength, ductility, toughness etc. AISI 4140 steels are widely used in many fields such as axles, gears, shafts, turbine engines, automobile and airplane manufacturing, brake rings and arms of turbo generators, ship chains and anchors, railway wheels and shafts, machinery and building elements etc. These parts are regularly processed via machining operations like drilling or turning. Therefore, it is very important to machining this steel material effectively and efficiently [4-6]. Forging technology is commonly used in steel alloy forming process, heat treatment also usually is employed to regulate and control the microstructure and mechanical properties, and the forging part must be machined to increase dimensional accuracy and improve surface integrity. Hence the heat treatment can be an important link between the forging process and machining process. During the hot forging process, the grain structure of the metal is rearranged to make the manufactured part more durable but residual stresses occur. It is necessary to eliminate the residual stresses in order to obtain better and permanent performance of the parts with these superior properties. It is aimed to eliminate residual stresses in the structure by heat treatments in different combinations that we will apply to the parts and to improve the properties of the material such as mechanical strength, machinability, hardness. AISI 4140 steel produced by hot forging is able to impart various properties through different heat treatments and this greatly expands the field of use in the industry [7-12].

The drilling process is one of the most important material removal processes, covering approximately 33% of machining operations [13]. Since drilling application has an important place in machining processes, investigation of its process is very important for the manufacturing industry. There are many problems in drilling applications. The dimensional accuracy, circularity, cylindrical deviation, and the quality of the drilled surfaces are a significant design specification that is known to have considerable influence on mechanical properties such as wear-resistance and fatigue strength. As these indicators are important for obtaining high-quality holes, additional operations such as reaming are necessary [14]. Surface roughness in machining has been found to be influenced in varying amounts by a number of factors such as cutting parameters, cutting fluid, and workpiece hardness. Important properties such as hardness, strength and toughness are greatly influenced by heat treatment processes [15]. Most of the previous investigators examined the effect of heat treatment on the mechanical properties [5-15]. However, only a few researchers have focused on the relationship between heat treatment and surface roughness. From the literature review, it was noticed that design of parameters in drilling of AISI 4140 was observed to be inadequate although a substantial work was performed in the drilling process with various materials. The objective of the study is to examine the surface quality in the drilling process on hot forged AISI 4140 steel, and the effect on the machinability of change in microstructure by various heat treatment was identified.

2. Experimental Procedure

2.1. Material and heat treatment details

The material studied was a hot forged AISI 4140 steel, and the chemical composition of the material is shown in Table 1.

Table 1. Chemical composition of the material (wt%)

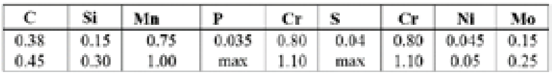

C	Si	Mn	P	Cr	S	Cr	Ni	Mo
0.38 0.45	0.15 0.30	0.75 1.00	0.035 max	0.80 1.10	0.04 max	0.80 1.10	0.045 0.05	0.15 0.25

In this study, the differences in terms of machinability between unheated hot forged parts (HF) and heat-treated groups given in Table 2, were investigated experimentally.

Table 2. Heat treatment applied to the workpieces

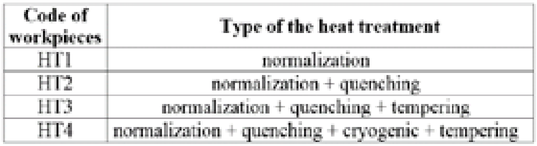

Code of workpieces	Type of the heat treatment
HT1	normalization
HT2	normalization + quenching
HT3	normalization + quenching + tempering
HT4	normalization + quenching + cryogenic + tempering

First of all, normalization heat treatment was applied to all samples. Preheat process was performed before the normalization process. A pre-heat treatment process was done by standing at 450 °C for 40 minutes prior to normalization. The samples were placed in the oven and reached 880 °C after normalization was done in 29 minutes of processing time. The protective atmosphere containing 0.15 carbon was used to prevent oxide layer formation on the sample surfaces during heat treatment. After the normalization process, the samples were given HT2, HT3, and HT4 codes and then tempered with the same parameters and at the same time. In the tempering process, it waited 29 minutes after reached 860 °C process temperature and 0.67 carbon-containing protective atmosphere was used to prevent oxide layer formation on the sample surfaces during heat treatment. The hardening process was achieved by sudden cooling in the oil for 30 minutes at the processing temperature of 70 °C. Normalization and quenching with the same parameters were applied to HT3 coded samples and subsequently subjected to tempering. Tempering was done at 410 °C process temperature. The samples that placed in the heat treatment furnace reached a temperature of 410 °C after 30 minutes and the holding time at this temperature was kept for 120 minutes. During the process, propane gas was fed to the furnace and a protective atmosphere containing 0.67 carbon was used on the purpose of making a heat treatment in which the desired properties are obtained. Samples given HT4 code were applied for normalization, quenching and afterwards cryogenic heat treatment was performed for 2.5 hours at -100 °C.

2.2. Drilling

In this study, the properties characterizing the hole quality such as the surface roughness, dimensional accuracy, circular and cylindrical deviations were investigated experimentally as a function of change in microstructure by heat treatment. Drilling experiments were performed on a commercially available VCM 4824 model CNC milling machine repeating the same cutting parameters in cooling lubricant condition. The drill cut completely through the test piece on each hole. The workpiece was a rectangular block of length 150 mm, width 100 mm and depth 5 mm. The drilling parameters and drill specifications used in the drilling process are given in Table 3.

Table 3. Cutting tool specifications and cutting parameters

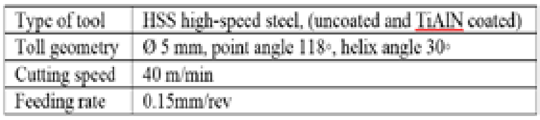

Type of tool	HSS high-speed steel, (uncoated and TiAlN coated)
Toll geometry	Ø 5 mm, point angle 118°, helix angle 30°
Cutting speed	40 m/min
Feeding rate	0.15mm/rev

Characterization of the surface finish of workpiece was carried out using a SJ-201P model Mitutoyo surface roughness measurement device. Coordinate measuring machines (CMMs) are widely used to obtain three-dimensional metrological shape information on a workpiece and to evaluate it. CMMs was used for measuring the hole diameters, circular and cylindrical deviations for the holes obtained from the drilling tests. The machinability properties of different heat-treated materials were compared with each other. The studies made are discussed in comparison with the literature.

3. Results and Discussion

Microstructure and hardness of the material to be machined plays an important part in understanding the characteristics of machined surfaces. The hardness and microstructure properties of the parts to be machined are given in Table 4.

Table 4. Hardness and microstructures of unheated and heat treated parts.

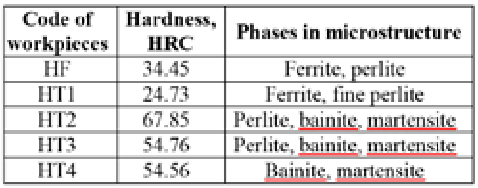

Code of workpieces	Hardness, HRC	Phases in microstructure
HF	34.45	Ferrite, perlite
HT1	24.73	Ferrite, fine perlite
HT2	67.85	Perlite, bainite, martensite
HT3	54.76	Perlite, bainite, martensite
HT4	54.56	Bainite, martensite

Achieving the desired hole quality in drilling processes is one of the most important issues in the manufacturing industry. It is very difficult to ensure the dimensional accuracy and geometric circularity of the hole diameter within the desired tolerances for holes directly drilled by the drilling machine. It is extremely important that this difference should be within acceptable limits. The application type, workpiece properties, cutting parameters and tool properties affect the dimensional accuracy of the hole in drilling operations [14,16]. The accuracy of hole diameter dimension, circular deviation, cylindrical deviation and machined surface quality (average surface roughness) to determine the hole quality were evaluated. The effect of material structure changing by heat treatment and drill types (uncoated and coated) on the surface roughness, results of deviation from diameter, results of circular deviation, results of cylindrical deviation expressing the dimensional accuracy of the hole in drilling operations is given in Figs. 1-4.

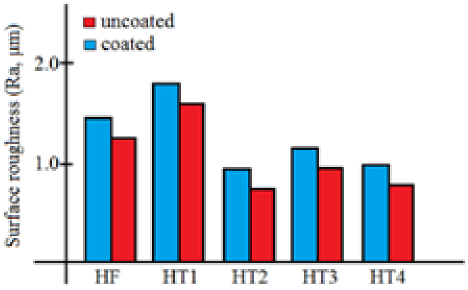

Figure 1. Effect of the heat treatment on the surface roughness

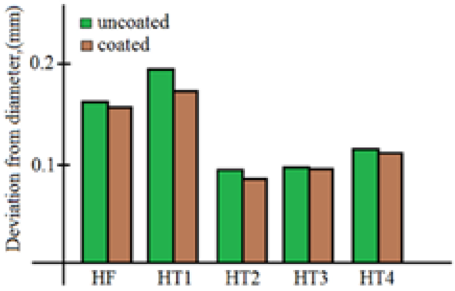

Figure 2. Effect of the heat treatment on the results of deviation from diameter

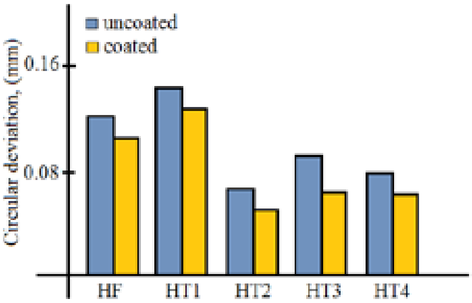

Figure 3. Effect of the heat treatment on the results of circular deviation

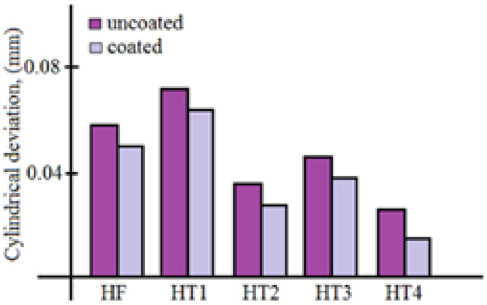

Figure 4. Effect of the heat treatment on the results of cylindrical deviation

When the graphs in Figs. 1-4 compared with each other in terms of coated and uncoated drills, it was observed that applying the coating on the drills affected positively the surface quality. This situation can be referred to the abrasion resistance of the drill and easier chip disability due to low friction coefficient when the coated drill is used. An improvement in drill quality was observed because the increasing temperature by heat energy during the cutting processes made the plastic deformation and chip flow easier [14]. Chip disposal in the drilling process is one of the most serious problems depending on the drilling depth as it causes the chip adhesion to cut tool surface, resulting in poor surface quality, and the cutting tool breakage [16]. Meral et al. [14] stated that the drillability of the workpiece can be easier during the drilling process when the recommended values for the workpiece and the drill materials were not exceeded.

The graphs in Figure 1, the surface roughness of AISI 4140 steel decreases with heat treatment. But, it increased with the normalization process expressed with HT1 due to the decrease in the hardness value. The improvement of the surface roughness for HT2, HT3 and HT4 groups drilled with the coated drill was calculated as 42%, 47% and 28%, respectively. The graph in Figure 2 showed that the deviation from hole diameter was slightly lower than holes drilled by uncoated drill when the coated drill was used. The graph in Figure 3 showed that the heat treatment and drill type were effective parameters on the circular deviation for drilled holes. It is recommended to use the coated drill to obtain the hole dimension within tolerance limits. According to Figure 4, the cylindrical deviation values obtained from coated drill compared to results by uncoated drill was relatively more than impact on surface roughness, and deviation from the diameter and circular deviation. When the graphs in Fig. 1-4 were evaluated, it was seen that the heat treatment was an effective parameter on dimensional accuracy. The heat treatment operations applied have created important differences in the hole quality. Particularly, the holes drilled by coated tools have become more evident. The HT2, HT3 and HT4 heat treatment groups showed a finer-grained and homogeneous martensite morphology, especially HT4 group produced by the cryogenic process. The cryogenic process has improved microstructure strength-ductility properties. The entire structure is converted to martensite with the cryogenic process at low temperatures. In this way, it is possible to increase the toughness without hardness [17-18]. Quenching and normalizing heat treatments were increased the hardness level of the workpieces. Better surface roughness was obtained for the heat-treated samples than those of the unheat-treated samples at all cutting conditions. Most of the previous researchers examined the effect of heat treatment on the mechanical properties. However, only a few researchers have focused on the relationship between heat treatment and surface quality. Dwivedi et al. [19] and Brunzel and Fomin [20] found that heat treatment reduced the surface roughness. Choi et al. [21] indicated that heat treatments improved the quality in terms of microstructures and surface roughness. The results obtained from this study are in good agreement with the previous researcher's works. A significant correlation between the machinability and the hardness determined by the microstructure changing with heat treatment could be determined.

4. Conclusion

In this paper; the influence of microstructure on and machinability was studied through heat-treatment process. The following results are obtained:

- A better drill quality was obtained for the heat-treated samples than those of the unheat-treated samples at all conditions.
- The properties of the heat-treated workpiece microstructure and its high hardness caused the workpiece surface roughness to be reduced.
- For the HT2 group, higher values were obtained in improving the hole quality with both drills.
- Coated tools compared with uncoated tools gave positive results for dimensional accuracy.

Acknowledgment

This work was supported by Scientific Research Projects Coordination Unit of Istanbul University-Cerrahpaşa, Project number FDK-2019-33913.

References

[1] T.H. Lee, Society of Manufacturing Technology Engineers, 20 (2011) 419-426.

[2] S. Demirok, Çelikleri Farklı Sertlik Oranlarında İşlenebilirliklerinin Araştırılması, Gebze Institute of Technology, 2008, Gebze, Turkey.

[3] M. A. Hassan, N. S. Mehat, S. Sharif, R. Daud, S. H. Tomadi and M. S. Reza, Study of the Surface Integrity of AISI 4140 Steel in Wire Electrical Discharge Machining, Proceedings of the International MultiConference of Engineers and Computer Scientists (IMECS 2009), March 18-20, 2009, Hong Kong.

[4] A. Salak, M. Selecká, H. and Danninger, Machinability of Powder Metallurgy Steels, Cambridge Int. Sci. Publishing, 2005, Cambridge.

[5] M.H. Khani Sanij, S.S. Ghasemi, Banadkouki, A.R. Mashreghi and M. Moshrefifar, Materials & Design, 42 (2012) 339-346.

[6] A.H. Meysami, R. Ghasemzadeh, S.H. Seyedein and M.R. Aboutalebi, Materials & Design, 31 (2010) 1570-1575.

[7] E. Kesti, Ç-4140 Çeliğinin, Mikro Yapı ve Mekanik Özelliklerine Su Verme Ortamının Etkilerinin Araştırılması, M.Sc. Thesis, Selçuk University, 2009, Konya, Turkey.

[8] S. Choo, S. Lee, and M.G. Golkovski, Materials Science and Engineering A, 293 (2000), 56–70.

[9] E. Turhan, Islah Celiklerinde Isıl İşlem Parametrelerinin Aşınma Davranışına Etkisi, M.Sc. Thesis, Süleyman Demirel University, 2001, Isparta, Turkey.

[10] R. Kunc and I. Prebil, Materials Science and Engineering A, 345 (2003) 278-285.

[11] X. Zhao, G. Zhao, G. Wang and T. Wang, Journal of Materials Processing Technology, 5682 (2002) 1-8.

[12] J.H. Chuang, L.W. Tsay and C. Chen, International Journal of Fatigue, 20 (1998) 531-536.

[13] H.L. Tonshoff, W. Spintig, W. Konig and A. Neises, Ann. CIRP 43:2 (1994) 551–560.

[14] G. Meral, M. Sarıkaya, H. Dilipak and U. Şeker, Arabian Journal for Science and Engineering, 40:12 (2015) 3709-3722.

[15] F. Al-Qura'n, Contemporary Engineering Sciences, 8 (2009), 355-359.

[16] S. Coromant, Cutting Tool Hand Guide, Sweden, 2008.

[17] A.D. Nembhard, J.K. Sinha and A. Yunusa-Kaltungo, Measurement, 75 (2015) 320-337.

[18] D. Senthilkumar and I. Rajendran, Mater. Manuf. Process, 27:5 (2012) 567-572.

[19] D.K. Diwivedi, A. Sharma and T.V. Rajan, Journal of Materials Processing Technology, 196 (2008) 197-204.

[20] Y. M. Brunzel and I.M. Fomin, Material Science and Heat Treatment, 35 (1993), 3-8.

[21] K. K. Choi, W. J. Nam and Y.S. Lee, Journal of Materials Processing Technology, 201 (2008) 580-584.

Effects of Microalloying Elements on Microstructure and Mechnical Properties of Leaf Sprig Steels

İ. İrfan AYHAN[1], Caner GÜNEY[1], Emre ALAN[1], N. Başak DÜRGER[1],
M. Fatih KAYADEĞİRMENİ[2], Gülbeniz YILDIZ[2], Yakup YÜREKTÜRK[2], Nazlı AKÇAMLI[2]
[1]ÇEMTAŞ Çelik Mak. San. Tic. A. Ş. R&D Center, [2]Bursa Technical University
Turkey

Abstract

51CrV4 is one of the well-known steel grade for producing leaf springs used on vehicles. Chemical composition of 51CrV4 includes 0,10-0,25% vanadium [V] according to DIN EN 10089 standard. Generally, steel producers use various optimum levels of vanadium in order to obtain required mechanical test results as demanded in steel specification. In this study, vanadium content of 51CrV4 leaf spring steel will be reduced to 0,10% as its minimum level, and microalloying elements such as Nb, Ti, B will be added to investigate their effects on microstructural and mechanical properties. JMatPro v.10.2 computational thermodynamic and thermomechanical software will be used to design new microalloyed steel grades. 80x80x140 mm sized laboratory scaled ingots will be produced in predetermined chemical compositions. Optical microscope (OM), scanning electron microscope (SEM) observations and mechanical test results will be compared with standard 51CrV4 steel grade.

1. Introduction

ÇEMTAŞ is able to produce a wide range of quality steel products including various dimensions of hot rolled round bar, spring steel flat bar for automotive and machinery industries and also stabilizer products that produced from round bars. 51CrV4 steel grade has the largest production volume in leaf spring steel flat bar products.

Leaf spring is one of the key parts of suspension system belonging to heavy commercial vehicles like vans, trucks, etc. They are designed as mono or usually at a number of laminated leaves with a gradation in their size and directly attached to the frame of the vehicle. The main purpose of a leaf spring is to provide comfort and safety by absorbing vertical vibrations and impacts caused by the road irregularities. Even though, the recent studies focus on composite material usage on leaf springs for their weight reduction advantage, still today steel is the most popular material due to its higher mechanical properties within lower cost.

High strength values and fatigue life are main requirements for a leaf spring steel. In order to obtain higher performance in service conditions; chemical composition, heat treatment and design parameters need to be chosen properly. Optimization of leaf spring design is the most studied subject among them since the composition and heat treatment parameters of the steel generally restricted by the material's specification. However, addition of microalloying elements plays a crucial role to get desired mechanical properties by precipitation hardening mechanism and optimizing steel microstructure.

In this study, microalloying elements such as Nb, Ti, B will added to 51CrV4 based steel by reducing V content to its minimum level "0,10%" as defined on its specification and their effects to microstructural and mechanical properties will be investigated.

2. Materials and Methods

Alternative chemical compositions including Nb, Ti, B microalloying elements will be designed by using computational thermodynamic and thermomechanical software JMatPro v.10.2. By comparing precitipation diagrams and CCT-TTT curves of designed compositions and reference 51CrV4 grade, three different steel compositions will be decided for laboratory scaled productions.

10 kg scaled vacuum induction melting unit will be used to produce 80x80x140 mm sized steel ingots. The steel ingots will be hot deformed by using a 120 ton capacity press at 1150 °C. Subsequently, quenching and tempering processes will be conducted under the certain parameters defined in the 51CrV4 specification. After deformation and heat treatment processes, microstructure of steels will be investigated by using OM and SEM. Prior austenite grain sizes [PAGBs] will be determined according to ASTM E112 standard. Steel samples will be tested in order to determine tensile strength, impact toughness, hardness, micro hardness and hardenability properties and the results will be compared with the reference 51CrV4 grade.

3. Conclusion

In this study, effects of Nb, Ti, B microalloying elements on 51CrV4 leaf spring steel grade will be investigated by using computational thermodynamic software and laboratory scaled productions. Microstructural and mechanical testing results of newly designed steels will be compared with standard 51CrV4 steel.

Effects of Pre-Heat Treatment on Mechanical and Microstructural Properties of Q&T and Bainitic Steels

İ. İrfan AYHAN[1], Caner GÜNEY[1], Emre ALAN[1], N. Başak DÜRGER[1], Ö. Faruk ŞENSOY[2], Sedanur KARDAŞ[2], Betül ÖZER[2], Nazlı AKÇAMLI, Yakup YÜREKTÜRK[2]
[1]ÇEMTAŞ Çelik Mak. San. Tic. A. Ş. R&D Center, [2]Bursa Technical University
Turkey

Abstract

Quenched and tempered [Q&T] steels and bainitic steels are widely used in parts where high strength, high toughness, high fatigue life are needed in service conditions. In order to obtain improved mechanical properties of these steel grades, modifying initial microstructure by pre-heat treatments has a worthwhile potential. In this study, pre-heat treatment process parameters will be designed by using JMatPro v.10.2. A pre-treatment will be applied to Q&T and bainitic steel samples using these parameters in order to modify the initial microstructure. The effects of pre-treatment to final microstructure and mechanical properties will be presented by comparing with the conventionally heat-treated steels. Microstructural investigations will be performed by using optical microscope (OM) and scanning electron microscope (SEM). Mechanical properties will be determined with tensile, Charpy impact, Jominy hardenability, hardness and microhardness tests.

1. Introduction

Chemical composition and heat treatments are key parameters for improving mechanical properties of steel via modifying the microstructure. It is possible to have different microstructures for same steel composition by changing heat treatment parameters.

The term of heat treatment covers combination of heating and cooling processes of material for obtaining proper microstructure to have desired mechanical properties such as; high strength, high toughness, high ductility, etc. Annealing, normalizing, hardening are the most used heating processes while controlled cooling in air or furnace conditions or rapid cooling process are well known cooling options. Quenching after austenization process results in martensitic microstructure which makes steel very brittle, thus, in order to give desired toughness, a tempering process usually follows the quenching. Bainitic microstructure is obtained after continuous cooling or isothermal heat treatment process where the steel composition has adequate elements to form bainite. Depending on cooling process and including elements, bainitic steels are able to exhibit both high strength and toughness values.

The initial microstructure controls the morphology austenite grains and kinetics of austenization process and thereby final microstructure of steel after cooling. Thus, recent studies are focused on modifying initial microstructure by pre-heat treatments in order to have better results in mechanical properties after subsequent heat treatment.

In this study, effects of modifying microstructure by proper heat treatments of Q&T and bainitic steels on mechanical properties will be investigated. Pre-heat treated, rapid-cooled Q&T steel and controlled air-cooled bainitic steel will be compared with regular heat-treated references by means of tensile strength, toughness, hardness and hardenability.

2. Materials and Methods

The first work-package of the study will consist of deciding Q&T and bainitic steel grades with suitable heat treatment process parameters. JMatPro v.10.2 computational thermodynamic and thermomechanical software will be used to generate CCT/TTT curves, precipitation diagrams and to estimate mechanical properties of selected steel compositions under various heat-treatment conditions.

Before quenching and tempering processes, initial quenching without tempering and initial annealing processes will be applied to Q&T steel grade separately. The temperatures of initial quenching, initial annealing and final tempering will be calculated in the first work-package. In bainitic steel grade, pre-annealing will be applied before regular austenization and controlled air-cooling process. The conditions of pre-annealing will be decided in the same way defined above.

In order to compare the mechanical properties of the pre-heat treated steels with the regular processed reference, tensile test, Charpy impact test, Jominy hardenability test, hardness and micro-hardness measurements will be conducted on the both samples. Microstructures before and after heat-treatments will be investigated by OM and SEM. Prior austenite grain sizes (PAGBs) will be determined according to ASTM E112 standard.

3. Conclusion

In this study, pre-heat treatment will be applied before quenching and tempering process of Q&T steel grade and controlled air cooling process of bainitic steel grade. Effects of pre-heat treatments on final microstructure and mechanical properties will be compared with reference Q&T and bainitic steels that are produced with conventional heat treatment process.

Increasing the Rate of Hot Charging and Reducing Energy Consupmtion by the Hot Rolling Mill Monitoring Screen Approach

Gökhan BİLMEZ, Burak Emre IŞIK, Murat PERÇEM, Uğur OKTAY, Erhan KORKMAZ, Erman KAYA, Yavuz DEMİRCİ
İskenderun Demir ve Çelik A. Ş.
Turkey

Abstract

In the production planning department, production programs are prepared in order to ensure the continuity of hot rolling mill production and prioritize the hot charge production mentality. Scheduling production programs should be created in very precise way to keep the hot charge rate high. In this study, it is explained in the production planning unit of Iskenderun Iron and Steel Company (ISDEMIR) that the hot rolling mill monitoring screen has completed the digitization process and contributed to the reduction of the energy consumption, which is one of the biggest cost component of ISDEMIR.

1. Introduction

In the hot rolling strip mill (ISDEMIR), slabs coming from the continuous casting machine are rolled out to steel plates with a thickness between 1.30 to 22mm. Firstly, the slabs coming from the continuous caster are pre-sorted in the slab yard. As alternative to the first step, the slabs coming from the continuous caster can be sent in a Direct Charge program without any sorting. Before we can start rolling out the slabs, they need to be heated until they reach a temperature of around 1.200° C. This is done in the reheating furnaces of the hot rolling strip mill. Afterwards, the slab is rolled out in several steps. It is conveyed through a reversing roughing mill and a continuous rougher. These reduce the thickness of the slabs to approximately 30mm. In the finishing mill, we reach our final thickness. Before entering the mill, the scale layer is once again removed. The slab then goes through seven adjacent rolling stands. Every stand making the steel strip thinner and longer. When leaving the finishing mill, the thickness, width, profile, flatness and temperature of the strip is measured. Before coiling, the steel is cooled by a low-pressure water beam so that it gets to the correct temperature.

Figure-1 Hot Strip Mill

Mill depreciation and the efficiency related constrains are applied in the scheduling process of the Hot Rolling Strip Mill Facility of ISDEMIR. The total number of constraints correlated to the physical characteristics, grade and order requirements of a slab is 60.

There are 5 distinct program types that are given to the Hot Rolling Strip Mill:

1. Cold Charge (0-300 C^0)
2. Hot Charge (301-600 C^0)
3. Direct Charge (>600 C^0)
4. Direct Charge from the Continuous Casting Machine (>600 C^0)
5. Imperative Cold & Hot Charge programs.

In order to create a Hot Charge and Direct Charge Programs, Continuous Casting Tundish programs should be created in advance. Virtual slabs (Coming from the Continuous Casting) and cold slabs from the stock are used to create a Hot Charge and Direct Charge programs. Cold slabs in the Hot Charge and Direct Charge programs are used to satisfy the various constraints that can not be met just with the virtual hot slabs.

After casting, virtual slabs in the programs are subjected to the matching step. In the matching step, designed virtual slabs are produced and if there is no production flaw, match process concluded, hence virtual slabs becomes real slabs.

To mill the schedules in the Hot Rolling Strip Mill Facility as soon as possible, Program Order Lists are prepared. In figure-2, examples of Direct Charge and Hot Charge program structures can be found.

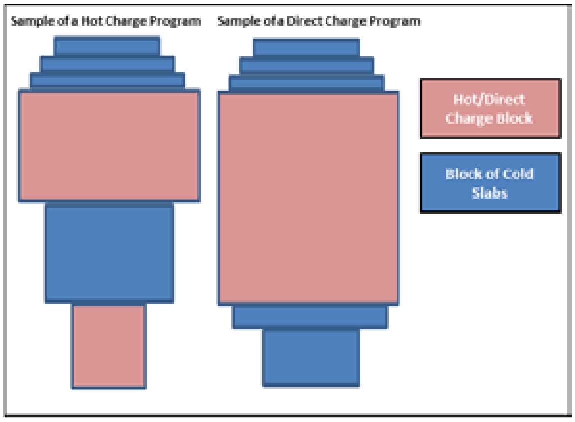

Figure-2 Direct Charge and Hot Charge program structures

2. Experimental Procedure

Order of programs, production statistics, stock statistics, forecast of Hot Charge ratio can be found in Hot Rolling Strip Mill Monitoring Screen (Available in UYS Screen). Hot Rolling Strip Mill Monitoring Screen was created from the integrated efforts of both Software and Production Planning Departments.

1. UYS Screen that provides the order of the virtual slabs (will be produced in the continuous casting machine) arranged by casting and program schedules. Schedulers can find and use necessary virtual slabs in this screen.
2. UYS Screen that provides the forecast of expected process time based on the number of slabs in the programs and the order of the given schedules. Schedulers can arrange the program order in the schedules. Except the currently processed program, all other programs can be rearranged by using this screen.
3. UYS Screen that enables users to monitor vital production statistics and information. Production statistics of the last one hour, yesterday and month can be monitored live in this Screen.
4. In this UYS Screen, *'Area Dispersion-equipment matrix'* based on critic parameters can be tracked live.
5. UYS Screen that enables users to monitor the 24 hour-Forecast of Hot Charge Ratio (Instantly modified after any change with the Order of Programs and production parameters). Also characteristic features of current production and duration of the production halts can be monitored via this Screen.

Figure-3 – Hot Rolling Strip Mill Monitoring Screen

3. Results and Discussion

Hot Strip Mill Monitoring Screen was tested live in november. Encountered defficiencies were overcomed in december by disabling them. At the end of the december, the status of system was managed to set ‘live’. Hot Charge Ratio of 46.37% was increased to 55.78% thanks to this update.

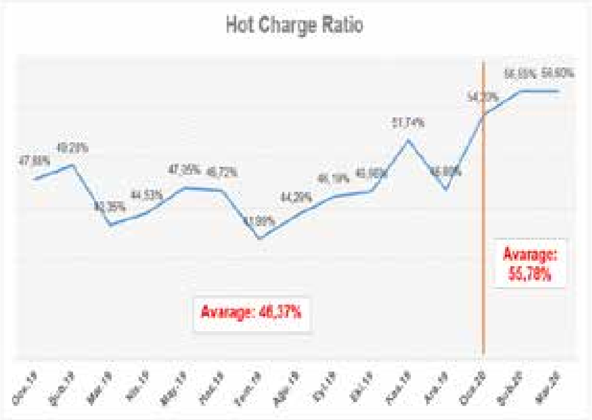

Figure-4 – Hot Charge Ratio Graph

4. Conclusion

Current sector conditions & competitive environment compels firms to minimize the cost of their final products. To achieve the minimal cost in Steel Producing Plants, sending slabs directly to the mills from the continuous casting machine is an essential step. Sending the slabs as soon as possible to prevent cooling saves substantial amount of fuel. In this project, an UYS Screen was developed to display the relevant information of stock, program details and values of Hot Rolling Strip Mill production. Moreover, a model was developed to forecast Hot Charge Value to help the schedulers by providing estimates based on their program creation and selection activities. The software created by Production Planning & IT Departments, was tested and rated as satisfactory in November 2019. In 2020, the software was started to be used by ISDEMIR schedulers. Final Product cost was minimized by achieving significant decrease of fuel consumption as well as increasing the Hot Charge Ratio after the software was utilized.

References

[1] Dong-feng HE1,2, Xiao-nan YU1,2, Jin-bao CHANG3,You-bing XIANG3, Zong-yu XUAN3 Temperature Holding Hood for Hot Charging of Continuous Casting Slab in Tangshan Iron and Steel Company, Journal of Iron and Steel Research, International, 2014, 21 (Supplement 1)

[2] Zhao, Wang, Liu, Wang and Shi (2009), A two-stage Scheduling Method For Hot Rolling and Its Application, Control Engineering Practice, 632-640, Retrieved from www.elsevier.com/locate/conengprac

[3] Casado S., Laguna M., Pacheco J., Puche J.C. Grouping products for the optimization of production processes: A case in the steel manufacturing industry

[4] Ilmer Q., Haeussler S., Missbauer H. Optimal synchronization of the hot rolling stage in steel production IFAC-PapersOnLine, Volume 52, 2019

[5] Mattik, I. (2013), Integrated Scheduling of Continuous Casters and Hot Strip Mills, Springer Gabler Abraham-Lincoln-Straße 46 65189 Wiesbaden Deutschland, Springer Gabler

Increasing the Quality of the Surface with Transformation from Adhesive Scale to Easy to Remove Scale

Koray ARAY, Turgut ARSLAN, Kübra AKGÜN, Gökhan BİLMEZ, Serdar GÜNBAY, Hasan YILDIRIM, Tayfun KOCABAŞ, A. Mesud ÇAKIR, Burcu SOYSAL ATAN, İlyas AÇIKGÖZ
İskenderun Demir ve Çelik A. Ş., Oyak Maden Metalurji Grubu Operasyonel Mükemmellik Direktörlüğü
Turkey

Abstract

Iskenderun Iron and Steel CO.(Isdemir) has a Hot strip mill which has 3.500.000 tons/year capacity. Slabs are annealing in the furnaces and respectively rolling in the roughing mill and finishing mill. During the Rolling, Oxide scale has consisted on the surface and been tried to remove from the surface with helping high pressure water. In this study, transformation from adhesive scale to easy to remove scale is explained with the optimisation of process temperature, type of the rolls and % C content.

1.Introduction

Scale is iron oxide compound consist of at high temperature. It can be 3 different compound depends on the iron, Oxygen content and temperature. These 3 layers are wustite, magnetite and hematite (Figure 1). Wustite is the softest phase that has direct contact with the metal substrate surface, has a minimum O_2 content from the compounds. Amount increases with temperature. Magnetite is the intermediate phase in the scale structure. Hematite is the phase at the farthest of the scale, rich in oxygen and having the hardest structure. It occurs above 900 C. Scale can occur at any temperature above 570 °C (Figure 2).

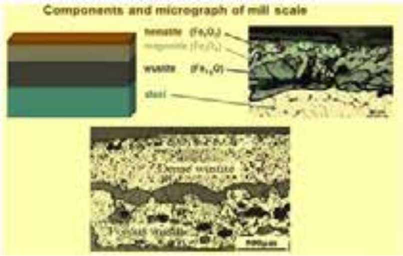

Figure 1. Scale Layers

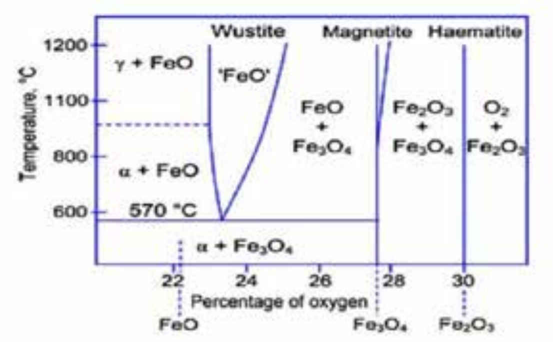

Figure 2. Scale-Temperature

2. Experimental Procedure

There are multiple factors that affect the scale formation mechanism (Figure 3). In order to obtain a perfect surface, all of these parameters must be optimally correct. This study was carried out to prevent scale defects in S235JR quality.

Figure 3. Scale Formation Mechanism

By analyzing data, parameters that affect the defect were tried to be determined. Minitab program was used for analysis studies. In regression analysis, parameters with p-value less than 5% were tried to be found. Some of Minitab results are given below (Figure 4). Scale defects were affected reheating furnace exit temperature, Roughing Mill Exit Temperature, F1 Reduction Ratio, F1 and F2 type rolls, % C content and coiling temperature according to the analyzing data.

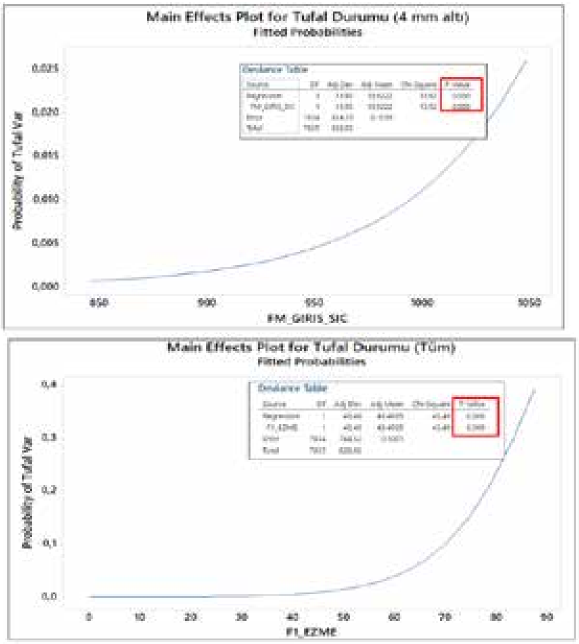

Figure 4. Minitab Analyzes

According to research, even if HSS type rolls are more useful than Hi-Cr type rolls in regards to lifetime and costs, Hi-Cr type rolls has still some of advantages. Generally F1 and F2 reduction ratio are higher than the other rolls in hot strip mill. And rolling strip has approximately above 1000 C on this rolls. It is known that the surfaces of HSS type rollers are softer than Hi-Cr rollers. Hematite can be occur above 900 C and has 1000 HV hardness.(Figure 5) With the changes made, it was aimed to create a softer Wustit and Magnetite phase instead of a hard Hematite phase.

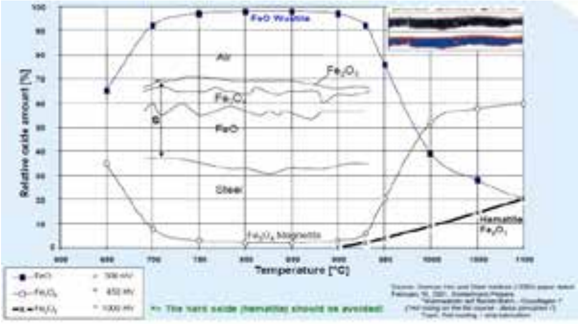

Figure 5. Scale Layers Temperature and Hardness

3. Results and Discussion

Individual changes have been made on the effective parameters. Reheating furnace exit temperature, Roughing Mill Exit Temperature, F1 Reduction Ratio, F1 and F2 type rolls, % C content and coiling temperature has been changed regarding to prevent scale on the surface. After these revisions, approximately 80% improvement was achieved on the scale defects. In addition, with the reduction of the carbon ratio, the casting speed increased by approximately 15% and this caused an increase in the production rate.

With the completion of this project successfully approximately 2 million dollar profit was gained.

4. Conclusion

Reducing process temperatures and changing roller types were successful in scale improvement. Although HSS type roller is cheaper than Hi-Cr roller, other advantages using of Hi-Cr roller have made this price difference situation to be ignored.

References

[1] O. Joos, C. Boher, C. Vergne, C. Gaspard, T. Nylen, F. Rezai-Aria, Assesment of oxide scales influence on wear damage of HSM Work Rolls (2018)

[2] J. Lecomte-Beckers, J. Tchoufang, E. Pirard, P. Breyer, Physical Metallurgy of HSS Material For Hot Rolling Mill Rolls

[3] D.T. Blazevic, Hot Strip Mill Operations Volume 5 Scale, 2005

Power Transformer Fault Diagnosis with Fuzzy Logic Based Oil Dissolved Gas Analysis

Ahmet BEŞKARDEŞ, Serdar YILDIRIM, Emre TOPDEMİR
Iskenderun Iron & Steel Works Company
Turkey

Abstract

Power transformers have a great place and importance in energy transmission systems. Therefore, transformers must work uninterruptedly. Unexpected transformer failure is not desired. Oil-dissolved gas analysis (DGA) is one of the commonly used methods to predict these failures or to determine the root causes of existing failures. In this study, a smart system application developed to detect possible faults in power transformers of Iskenderun Iron & Steel Works Company (ISDEMIR) is explained. In this system, fault diagnosis was made with Roger, Doernenburg, Duval triangle and fuzzy logic methods. Unlike the literature, in fuzzy logic method, a system capable of making multiple diagnoses, whose inputs consist of gas ratios and outputs within regions of the Duval triangle, has been designed. The results are presented comparatively.

1. Introduction

Power transformers perform voltage increasing and decreasing duties in the transmission and distribution of produced electrical energy. Proper operation of power transformers is critical to safe operation of the power system [1], [2], [3]. Early detection of new failures in power transformers is crucial to minimize device damage, economic loss, and adverse effects on reliability [3], [4]. If faults can be detected in advance, maintenance plans can be made accordingly and transformers can work more efficiently. With such planning, the life of a transformer can be increased from 20 to 60 years [4].

Three types of faults generally occur in transformers. These are arc formation, thermal failure, and partial discharge failures in order of importance [4]. While these failures occur, Hydrogen (H_2), Methane (CH_4), Ethane (C_2H_6), Ethylene (C_2H_4), and Acetylene (C_2H_2) gases dissolved in the transformer oil are produced. The emergence and density of each gas indicate a certain type of fault. While H_2 and CH_4 gases are generally formed in partial discharge failure, C_2H_4 and C_2H_6 gases occur in thermal failures and H_2 and C_2H_2 gases occur in arc failure [2], [4], [8]. Accordingly, the quality and quantity of each gas type can be decisive for the failures to be detected and identified [3].

Effective monitoring and diagnostic techniques are required to increase the reliability of the equipment and avoid faults. The dissolved gas analysis (DGA) method is the most frequently used method among these techniques [1], [2]. There are many interpretation techniques for DGA results, but all these techniques rely more on staff experience than on analytical formulation [2]. It is a highly preferred method since DGA can detect transformer failures just at start-up [6]. In the literature, there are many DGA methods such as key gas, Roger ratio Doernenburg, and Duval triangle method and important studies have been done with these methods [5], [7]. These methods, also called traditional methods, may not produce the same result for the same oil sample. These methods have disadvantages such as not being able to find some faults or not being able to identify them when more than one fault [2], [4].

In the interpretation of the results of the DGA, researchers have turned to artificial intelligence applications in order to overcome the disadvantages caused by the failure to identify the fault types in case of more than one fault and invalid diagnoses that may be caused by some DGA data [2], [4]. Fuzzy logic, artificial neural networks, neuro fuzzy system, Dempster-Shafer Theory [3], associative rule mining [9] hyper sphere multi-class support vector machine [10] are some of them.

Imprecision is an important problem in many complex diagnostic procedures. A correct technique and extensive experience are required to overcome this uncertainty and make an effective diagnosis. The evaluation of this information in a specialist system requires a strong model for imprecision and uncertainty. Fuzzy logic is very successful in these issues [1] and very effective results have been developed with this method. Fuzzy logic has been applied to almost all methods in the literature and effective results have been obtained [1], [2], [4], [11], [12]. In some studies, two- or three-stage fuzzy systems were developed and more accurate results were obtained by evaluating the diagnoses of more than one method together [8], [13].

In this study, a smart system application developed to detect possible faults in power transformers belonging to İsdemir is explained. In the developed application, fault diagnosis was made with Roger, Doernenburg, Duval triangle and fuzzy logic methods. Fuzzy logic was developed on the Duval triangle method. Unlike the literature, in fuzzy logic method, a system capable of making multiple diagnoses, whose inputs consist of gas ratios and outputs within regions of the Duval triangle, has been designed.

2. DGA Diagnose Methods

There are many DGA interpretation techniques in the literature such as key gas, IEC, Roger, Doernenburg, and Duval triangle. Of the methods used in this study, Roger [14] and Doernenburg [15] method use the ratios given in Equations 1-5. The fault diagnosis to be made according to the value of these rates is given in Table 1.

$$R_1 = C_2H_2/C_2H_4 \tag{1}$$

$$R_2 = CH_4/H_2 \tag{2}$$

$$R_3 = C_2H_4/C_2H_6 \tag{3}$$

$$R_4 = C_2H_4/CH_4 \tag{4}$$

$$R_5 = C_2H_6/C_2H_2 \tag{5}$$

Table 1. Failure types according to gas rates for Roger and Doernenburg methods [14],[15]

Method/Rate	R1	R2	R3	R4	R5	Diagnose
Roger's Ratio	<0.1	0.1-1	<1	x	x	N
	<0.1	<0.1	<1	x	x	D1
	0.1-3	0.1-1	>3	x	x	D2
	<0.1	0.1-1	1-3	x	x	T1
	<0.1	>1	1-3	x	x	T2
	<0.1	>1	>3	x	x	T3
Doernenburg Ratio	-	<0.1	x	<0.3	>0.4	PD
	>0.75	0.1-1	x	>0.3	<0.4	DHE
	<0.75	>1	x	<0.3	>0.4	TF

Among the abbreviations used in Table 1, N: Normal State, D1: Discharges of Low Energy, D2: Discharges of High Energy, T1: thermal faults of temperature <300 °C, T2=thermal faults of temperature 300 °C<T<700 °C, T3 = thermal faults of temperature > 700 °C, PD: Partial Discharge, DHE: Discharges of High Energy, TF: Thermal Fault.

The Roger and Doernenburg methods are only valid if there is a significant amount of gas used in the proportion, otherwise the method will not be able to identify the type of fault and will give an invalid code error. Therefore, gas ratio methods can be used to identify the type of fault more than detecting it [2].

Duval stated that many DGA results are outside of ratio-based interpretation techniques and cannot be diagnosed using these methods and proposed a triangle for the diagnosis of transformer fault [16], [17]. This method has proven to be accurate and reliable for many years and is often found in highly accurate diagnoses [5]. In the Duval method, based on the visualization of the location of dissolved gases in the triple map, a fault diagnosis is made. The triangle method is shown in Figure 1.

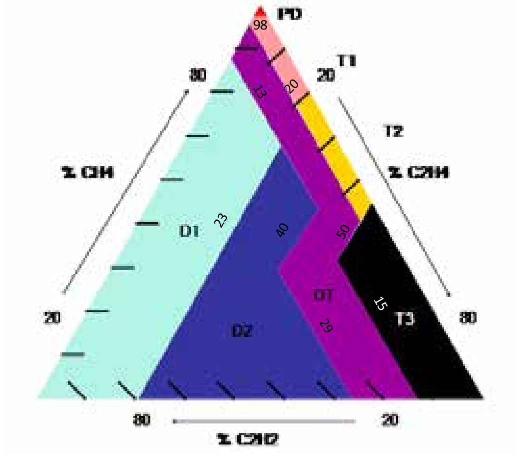

Figure 1. Duval triangle

The coordinates of the Duval triangle shown in Figure 1 are calculated from the DGA results in ppm, according to the following Equations [16]:

$$\%CH_4 = 100 \times \frac{CH_4}{CH_4 + C_2H_4 + C_2H_2} \tag{6}$$

$$\%C_2H_4 = 100 \times \frac{C_2H_4}{CH_4 + C_2H_4 + C_2H_2} \tag{7}$$

$$\%C_2H_2 = 100 \times \frac{C_2H_2}{CH_4 + C_2H_4 + C_2H_2} \tag{8}$$

When interpreting using the Duval triangle method, it should be remembered that the sum of the ratios found above should be equal to 100. Three types of faults can be detected in the Duval triangle, mainly partial discharge, high and low energy arc, and thermal failure. These fault types are shown in Table 2. Since no region is determined for the normal aging condition in the Duval triangle, if this method is applied carelessly, it can be seen as if there is a mistake that is not present. To avoid this problem, dissolved gases must be evaluated for their normality before being interpreted using the Duval triangle [5].

Table 2. Fault definition and boundary zones for Duval triangle method [3]

Fault Type	Fault Definition	CH_4 [%]	C_2H_4 [%]	C_2H_2 [%]
PD	Partial Discharges	98	-	-
D1	Discharges of Low Energy	-	23	13
D2	Discharges of High Energy	-	23-40	13-29
T1	Thermal Faults T < 300 ºC	-	20	4
T2	Thermal Faults 300 ºC<T<700 ºC	-	20-50	4
T3	Thermal Faults T >700 ºC	-	50	15
DT	Thermal and Electrical Faults	-	40-50	4-29

Duval triangle consists only of areas related to fault states, there is no area for normal results. Therefore, this method can only be used to identify the type of fault in case of a faulty transformer, and therefore new faults cannot be detected with this method [2].

3. Fuzzy Logic Model

Fuzzy logic is well suited for systems consisting of nonlinear behaviors where it is difficult to obtain a mathematical model. Fuzzy logic models can offer very effective solutions in situations where the expert's knowledge, experience, and intuition are important, such as finding a transformer error. Fuzzy logic control is an effective way of associating input variables with output variables, determined by the knowledge and experience of a process specialist and using "IF...THEN" statements. In fuzzy logic, input and output variables are defined as continuous functions called membership functions. According to the definition of membership functions, variables are assigned a membership degree. With the determined rules, it can be easily determined in which case and what decision to take. Parts of a fuzzy system are shown in Figure 2.

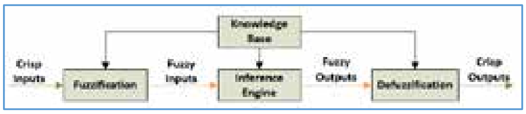

Figure 2. Fuzzy system

The fuzzy system developed in this study is based on the definition of polygonal boundaries in the Duval triangle with smooth transitions instead of precise lines. In the Duval triangle method, the area where the gas rates relative to the intersection point can be determined programmatically by looking at the color defined earlier. Another method is to write rules by looking at the boundaries of the polygons defined in the triangle. Akbari et al. [5] identified polygons in the triangle, determined their coordinates, and formulated the fault state accordingly.

Although the Duval triangle method is a very effective method in the DGA analysis, there is a problem as follows: What will happen if the intersection point of the three ratios is located on the intersection of the polygons? In order to overcome this problem, Akbari and his colleagues considered the intersection point as a circle with a certain radius and determined in which area this circle was located, and made the diagnosis accordingly [5]. In this study, this problem was solved with fuzzy logic. The fuzzy system consists of three inputs and seven outputs as shown in Figure 3. Ten membership functions are defined for each input. A comparison of the membership function that provides a graded definition instead of precise lines is shown in Figure 4.

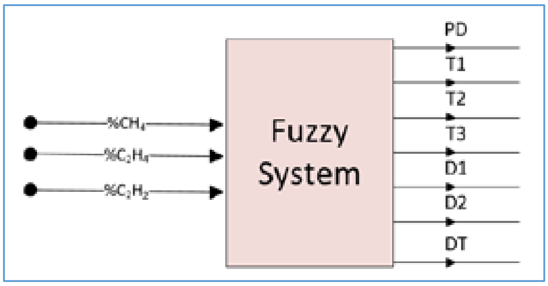

Figure 3. Fuzzy system inputs and outputs

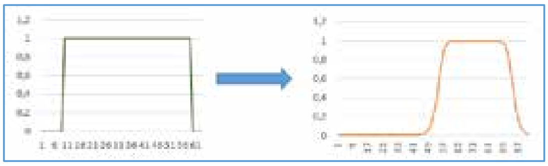

Figure 4. Gradual identification with membership function

Table 3. Fuzzy logic rule table

Rulo No	IF P1	IF P2	IF P3	THEN Fault
1	PD	PD	PD	PD
2	T1	T1	T1	T1
3	T2	T2	T2	T2
4	T3	T3	T3	T3
5	D1	D1	D1	D1
6	D2_1	D2_1	D2_1	D2_1
7	D2_2	D2_2	D2_2	D2_2
8	DT_1	DT_1	DT_1	DT_1
9	DT_2	DT_2	DT_2	DT_2
10	DT_3	DT_3	DT_3	DT_3

The rule table of the developed fuzzy system is shown in Table 3. These rules were created in a practical and simple way thanks to the defined membership functions. The rules described in Table 3 operate as follows: There are ten membership functions defined for each zone for each input. There is a result by subjecting the values of these functions to the operator "AND", that is, taking the minimum value in them. According to this result, the error region (s) are determined. For example, for P1 = 48.89% P2 = 48.89 and P3 = 2.22, 100% T2, 45% T3 and 11% DT are diagnosed.

4. Isdemir Application and Results

This model, developed for İsdemir transformers, diagnoses according to Roger, Doernenburg, Duval triangle, and fuzzy logic-based methods whenever new analysis comes, then report the results and e-mails them. Figure 5 shows the diagnoses produced by Roger, Doernenburg, and Duval triangle methods for the same DGA condition. Figure 6 shows the diagnostics produced by the Duval triangle method and the fuzzy logic-based method in another DGA case.

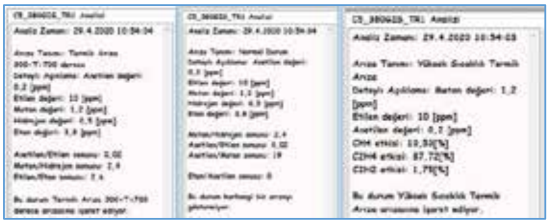

C5_380G25_TR1 Analizi

Analiz Zamanı: 29.4.2020 10:54:03

Arıza Tanımı: Yüksek Sıcaklık Termik Arıza

Detaylı Açıklama: Metan değeri: 1,2 [ppm]

Etilen değeri: 10 [ppm]

Asetilen değeri: 0,2 [ppm]

CH4 etkisi: 10,53[%]

C2H4 etkisi: 87,72[%]

C2H2 etkisi: 1,75[%]

Bu durum Yüksek Sıcaklık Termik Arıza arızasına işaret ediyor.

Figure 5. Diagnostics based on Roger, Doernenburg and Duval triangle methods

As can be seen in Figure 5, the results of the three methods diagnosed by calculating according to different gas rates are different. Therefore, it is useful to consider all diagnoses for safe transformer service.

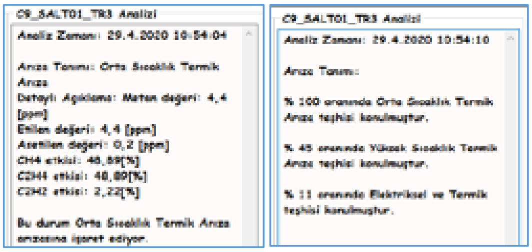

C9_SALT01_TR3 Analizi

Analiz Zamanı: 29.4.2020 10:54:04

Arıza Tanımı: Orta Sıcaklık Termik Arıza

Detaylı Açıklama: Metan değeri: 4,4 [ppm]

Etilen değeri: 4,4 [ppm]

Asetilen değeri: 0,2 [ppm]

CH4 etkisi: 48,89[%]

C2H4 etkisi: 48,89[%]

C2H2 etkisi: 2,22[%]

Bu durum Orta Sıcaklık Termik Arıza arızasına işaret ediyor.

C9_SALT01_TR3 Analizi

Analiz Zamanı: 29.4.2020 10:54:10

Arıza Tanımı:

% 100 oranında Orta Sıcaklık Termik Arıza teşhisi konulmuştur.

% 45 oranında Yüksek Sıcaklık Termik Arıza teşhisi konulmuştur.

% 11 oranında Elektriksel ve Termik teşhisi konulmuştur.

Figure 6. Diagnoses of Duval triangle and fuzzy logic methods for the same analysis results

As seen in Figure 6, Duval triangle for the same analysis values indicated medium temperature thermal faults. The fuzzy logic-based method, on the other hand, reported that partial high-temperature thermal faults and electrical and thermal faults as well as medium-temperature thermal faults.

6. Conclusion

In this study, the application developed to detect possible faults of İsdemir transformers by the DGA method is explained. This app is for diagnoses with Roger, Doernenburg, Duval triangle, and fuzzy logic methods. Although the DGA method is one of the most effective tools in diagnosis, sometimes different methods can give different results. For this, the results of the four different methods are evaluated together and the employees are informed.

The Duval triangle method is the most effective DGA method. However, the fault shown by a point above the cross-sections of polygons in the triangle area is sometimes insufficient or wrong. In this study, the success of the Duval triangle method is tried to be increased by defining these sections more smoothly with fuzzy logic.

The fuzzy logic method is easy to program, it is suitable for a new rule or variable definition and can be used with other methods. In future studies, it will increase the diagnostic ability much more by running other DGA methods on the fuzzy logic basis and completing each other's missing points with an upper model.

References

[1] K. Tomsovic, M. Tapper and T. Ingvarsson, A Fuzzy Information Approach To Integrating Different Transformer Diagnostıc Methods, IEEE Transactions on Power Delivery, 8 (1993)

[2] A. Abu-Siada, S. Hmood and S. Islam, A New Fuzzy Logic Approach for Consistent Interpretation of Dissolved Gas-in-Oil Analysis, IEEE Transactions on Dielectrics and Electrical Insulation, 20 (2013)

[3] T. Kari, W. Gao, D. Zhao, Z. Zhang, W. Mo, Y. Wang and L. Luan, An Integrated Method of ANFIS and Dempster-Shafer Theory for Fault Diagnosis of Power Transformer, IEEE Transactions on Dielectrics and Electrical Insulation, 25 (2018)

[4] F. Atalar, A. Kuntman, Diagnosis of Power Transformers Faults using Fuzzy Logic Method, emo.org.tr

[5] A. Abu-Siada, M. Arshad, and S. Islam, Fuzzy Logic Approach to Identify Transformer Criticality using Dissolved Gas Analysis, IEEE (2010)

[6] S. Köroğlu, A. Demirçalı, M. Yıldız, M. E. Çalı and G. Mıhcı, Diagnosis of Power Transformer Faults with Dissolved Gas Analysis, ELECO International Conference on Electrical and Electronics Engineering, 27 – 29 November 2014, Bursa

[7] I. B. M. Taha, S. S. M. Ghoneim and H. G. Zaine, Improvement of Rogers Four Ratios and IEC Code Methods for Transformer Fault Diagnosis Based on Dissolved Gas Analysis, North American Power Symposium (NAPS) 2015

[8] A. Akbari, A. Setayeshmehr, H. Borsi and E. Gockenbach, A Software Implementation of the Duval Triangle Method, Conference Record of the 1988 IEEE International Symposium 2008

[9] Z. Yang, W. H. Tang, A. Shintemirov and Q. H. Wu, Association Rule Mining-Based Dissolved Gas Analysis for Fault Diagnosis of Power Transformers, IEEE Transactıons on Systems, Man, and Cybernetıcs—Part C: Applications and Reviews, 39 (2009)

[10] H. Shang, J. Xu, Z. Zheng, B. Qi and L. Zhang, A Novel Fault Diagnosis Method for Power Transformer Based on Dissolved Gas Analysis Using Hypersphere Multiclass Support Vector Machine and Improved D–S Evidence Theory, Energies, 12 (2019)

[11] N.A. Muhamad, B.T. Phung and T.R. Blackburn, Comparitive study and analysis of DGA methods for mineral oil using fuzzy logic, The 8th International Power Engineering Conference (IPEC), 2007

[12] H. Ma, Z. Li, P.Ju, J. Han and Limin Zhang, Diagnosis of Power Transformer Faults Based On Fuzzy Three-Ratio Method, International Power Engineering Conference, 2005

[13] S. A. Wani, S. A. Khan, G. Prashal and D. Gupta, Smart Diagnosis of Incipient Faults Using Dissolved Gas Analysis-Based Fault Interpretation Matrix (FIM), Arabian Journal for Science and Engineering

[14] R. R. Rogers, IEEE and IEC Codes to Interpret Incipient Faults in Transformers, Using Gas in Oil Analysis, IEEE Trans. Electr. Insul, Vol EI-13 No 5, (1978)

[15] H. Suna, Y. Huanga and C. Huangb, A Review of Dissolved Gas Analysis in Power Transformers, Energy Procedia 14 (2012) 1220 – 1225

[16] M. Duval, A Review of Faults Detectable by Gas-in-Oil Analysis in Transformers, IEEE Electrical Insulation Magazine (2002)

[17] M. Duval, New Techniques for Dissolved Gas-in-Oil Analysis, IEEE Electrical Insulation Magazine (2003)

Effect of Sintering Conditions on Microstructural and Mechanical Properties of Injection Molded 420 Martensitic Stainless Steel

Lütfi YAKUT[1,2], Sertaç ALPTEKİN[2], H. Özkan GÜLSOY[1]
[1]Marmara University, [2]TUBITAK MRC
Turkey

Abstract

This paper describes the effect of sintering conditions on microstructural and mechanical properties of injection molded AISI-420 martensitic stainless steels. At the initial stage, AISI-420 martensitic stainless steel powders were mixed with a multi-component binder system for preparing feedstock. Then the prepared feedstock was granulated and shaped by injection molding. And then, the shaped samples were subjected to the debinding process. These samples were sintered at different temperatures which is 1250°C and 1350°C, and under different atmosphere which is Ar and H_2. Samples sintered under 1350°C and H_2 atmosphere that gave the highest relative density and better mechanical features. Sintered and heat-treated samples were separately subjected to microstructural and mechanical characterization. Mechanical characterization was performed by hardness measurements and tensile tests.

1. Introduction

Powder injection molding (PIM) is a powder metallurgy process currently used for the production of complicated and near-net-shape parts of high-performance materials. This technique basically combines the advantages of the plastic injection molding with the versatility of the traditional powder metallurgy, producing highly complex part of small size, tight tolerance, and low production cost. The process overcomes the shape limitation of traditional powder compaction, the cost of machining, the productivity limits of isostatic pressing and slip casting, and the defect and tolerance limitations of conventional casting [1–4]. A well processed powder injection molded materials are indistinguishable when its compared with cast and wrought materials. The PIM consist of 4 main steps that first mixing of the material powders and organic binders, second injection molding process, third debinding (solvent and thermal) and fourth is sintering. In some cases, secondary operations may possible if it is need it [5-6].

Among the stainless steels, AISI-420 has useful properties including high strength, hardness, and corrosion resistance when its heat treated [7] that makes it suitable choice for wear applications [8]. Properties of AISI-420 can change via heat treatments Even though there are some experimental studies regarding different sintering temperatures and atmospheres on stainless steels [9], there are not information in literature on PIM AISI-420 SS, more detailed information is not available in literature [10].

The aim of this study is investigate the effect of different sintering temperature and different sintering atmosphere on final properties of powder injection molded AISI-420 samples. Metallographic techniques were employed to sintered tensile bars to investigate sintering conditions. Following that mechanical properties including hardness and tensile tests were investigated. Powder morphology, molded, debinded, sintered and heat-treated samples were analyzed under scanning electron microscope (SEM).

2. Experimental Procedure

In this study, the AISI-420 stainless steel powder's chemical composition is given under the **Table 1**. Particle size distribution indicated under the **Table 2Hata! Başvuru kaynağı bulunamadı.**. Morphology of powder observed by using SEM that showed on **Fig. 1** It shows all powders spherical in shapes.

To prepare the feedstock carnauba wax (CW), paraffin wax (PW), polypropylene (PP) and stearic acid (SA) were used as multi-component binder system which is needs to mixed with stainless steel powders. That multi-component binder system consists of PW (69 %wt), CW (20 %wt), PP (10 %wt) and SA (1 %wt). In order to observe rheological data of feedstocks, powder samples were prepared with 62.5 % vol. of metal powders. In order to mix the powders and binders homogenously, special made blade mixer was used. It was mixed at 180°C for 45 mins. Which makes it more homogenous mixture. Cooled feedstocks were granulated by hand so that to measure rheological behavior of 62.5 %vol. AISI 420 ss powders. It is measured by rotational rheometer Physica MCR51 (Anton Paar. Austria) at shear rates from 10 to 1.000 s^{-1} at temperatures 120-170 °C. The value of viscosity is given by the shear stress divided by the shear rate.

Cooled feedstock was also used to create standard tensile test samples by using special designed injection molding machine for this research that Injection happened to have green parts under 12.5 MPa, at 180 °C for 20 seconds. Mold temperature were carried out at 35 °C. The geometry of feedstock is molded according to MPIF-35 standard.

Table 1. Chemical composition of AISI-420 powder

	Elements(wt.%)	
	AISI-420 MPIF Standart	AISI-420 (Sandvik-Ospray)
Fe	Bal.	Bal.
Nb	--	NA
Mo	--	NA
Cr	12-14	12.8
Ni	--	--
Mn	<1.0	0.72
Si	<1.0	0.79
P	<0.04	0.012
C	>0.15	0.3
S	<0.03	0.01
O	--	0.04
N	--	0.09

Table 2. Powder characteristics of AISI-420 powder

Item	AISI-420 SS
Vendor	Osprey Co.
Production method	Gas atomized, N
Shape	Spherical
Particle size (µm) D_{10}	4.30
Particle size (µm) D_{50}	12.55
Particle size (µm) D_{90}	26.64
Tap density, g/cm^3	4.70

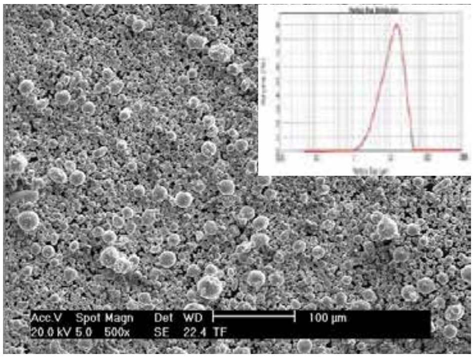

Fig. 1. Scanning electron micrograph of AISI-420 powder

Debinding process were applied to green parts so that to have brown parts. It was carried out in two steps that includes solvent and thermal debinding. Green parts first kept in solvent at 60 °C for 4 hours in hexane. Followed by thermal debinding at 600 °C with heat ramp of 1.8 °C/min. Debinded samples first pre-sintered at 900 °C with heat ramp 4°C/min. for 1 h under pure Ar and H_2 separately. The samples were sintered in an atmosphere controlled vertical recrystallized alumina tube furnace. The sintering cycle applied to the samples was as follows; samples were heated to 1200 ºC at a rate of 10 ºC/min and held at 1200 ºC for 5 min., then the samples were heated to various sintering temperatures of 1250 ºC and 1350 ºC at a rate 5 ºC/min and they were held at each temperature for 1 hour in Ar and H_2 separately. Solution heat treatment was chosen for the samples to change the properties and it was carried out under Ar atmosphere at 1030 °C for 1 hour, followed by air quench and aging treatment at 440 °C for 1 hour then cooled in air.

Densities of sintered and heat treated tensile test samples carried out according to Archimedes method. For metallography process, samples were cut from tensile bars, mounted, ground and polished with 0.3 µm and 0.5 µm surface finishing standard procedures. A Kalling's reagent was used to etch the samples for optical metallography. Samples observed by optical microscope. All tensile tests were performed using Zwick-Z250 mechanical tester at constant crosshead speed of 25.4 mm/min (25 mm gauge length). The hardness tests were performed using an Instron-Wolpert Dia Testor 7551 at HRC scale. An average of five values of all mechanical measurements was reported. The fractures were examined using a scanning electron microscope (FEI-Srion).

3. Results and Discussion

The rheological data of feedstock on viscosity is given under **Fig. 2** that shows viscosity can change through the changes on shear rate and temperature. It is also depending on powder type. Values on higher temperature shows lower viscosity. The lower viscosity, the easier to inject your feedstock through the complex shapes of molds. The reason that viscosity decreased following increase on temperature that the viscosity of the polymer binders that used is decreased while temperature is increasing [1,2]. It is known that for successful injection molding process viscosity is expected under 100 Pa.s [6].

Sintered density of the samples showed on **Fig. 3** that it clearly shows higher sintering temperature lead higher density on samples. Also, samples sintered under H_2 atmosphere has higher density then samples sintered under Ar. It is well known that sintering temperature has great effect on density [1,5,11,12]. Comparing the atmosphere, H_2 showed higher density then in Ar. The main point of that difference is that H_2 atmosphere reduces the oxide surfaces from samples even there is not much and H_2 atmosphere has slightly better heat conductivity. Therefore, it increased the density [9]. Picture of Molded and thermal debinded samples showed on **Fig. 4** taken by SEM. The **Fig. 4** shows that on molded samples binders were connecting the powders properly. Debinded SEM pictures shows binders avoided from the samples and there is only AISI-420 powders.

Metallographic procedures were carried out for both different temperature and different atmosphere samples. Pictures of polished samples are shown in that at lower sintering temperature surface of samples were more pores. By increasing the temperature to 1350 °C, the pore quantity become less than before. With the increased sintering temperature, the formation of inter-particle neck has increased, and as a natural consequence, the pore amount has decreased while the density values have increased. H_2 also decreased the quantity of pores. The heat conductivity of H_2 increased the sintering behavior. Etched pictures of samples are shown in **Table 1** that at 1250 °C all samples show a high amount of pores and insufficient sintered particles however, with the increase of sintering temperature, it is seen that the pores in the microstructure are mostly closed, the grains grow and sintering develops. When, the effect of the sintering atmosphere on the microstructure was evaluated, it was observed that sintering developed especially due to the high thermal conductivity coefficient of the H_2 atmosphere and oxide reduction.

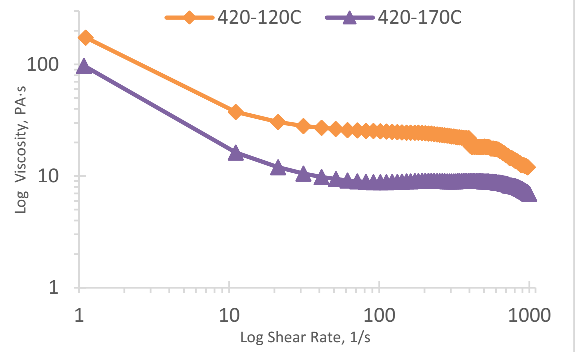

Fig. 2. Temperature-dependent viscosity versus shear Rate of AISI-420 feedstock

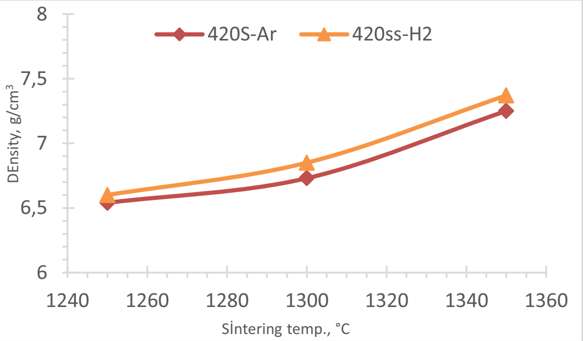

Fig. 3. Sintered density of the samples sintered at different temperatures and atmosphere

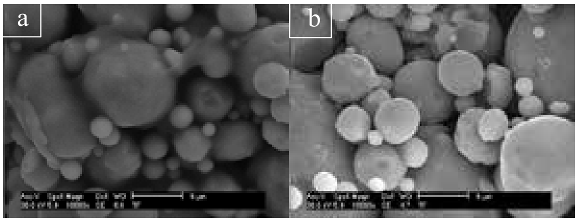

Fig. 4. SEM images of a) molded and b) thermal debinded samples

Table 1. Polished and etched pictures of different temperature and atmosphere

		Sintering Temperature, ºC	
		1250	1350
Atmosphere	Ar	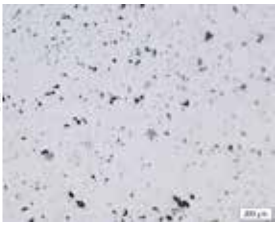	
	H_2	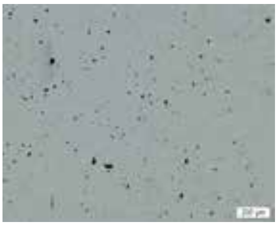	
	Ar		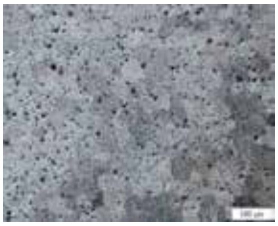
	H_2	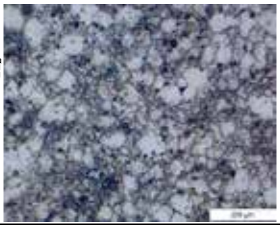	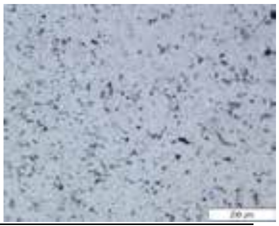

Mechanical properties are shown in **Fig. 5.Hata! Başvuru kaynağı bulunamadı.** that having different atmosphere at 1250 °C doesn't changes properties much. However, not only at 1350 °C samples but also under H_2 atmosphere it increased the mechanical properties slightly. At the same time, due to the increasing sintering temperature, it has been an important mechanism in the development of mechanical properties in increasing density values and decreasing pore. The presence of martensite plates formed in the grains with the heat treatment effect led to the development of mechanical properties significantly [13,14].

Mechanical properties of AISI-420 samples under different atmosphere at 1350 °C are given in **Table 2.** that it also shows that all properties slightly increased by increasing the temperature and under H_2 atmosphere.

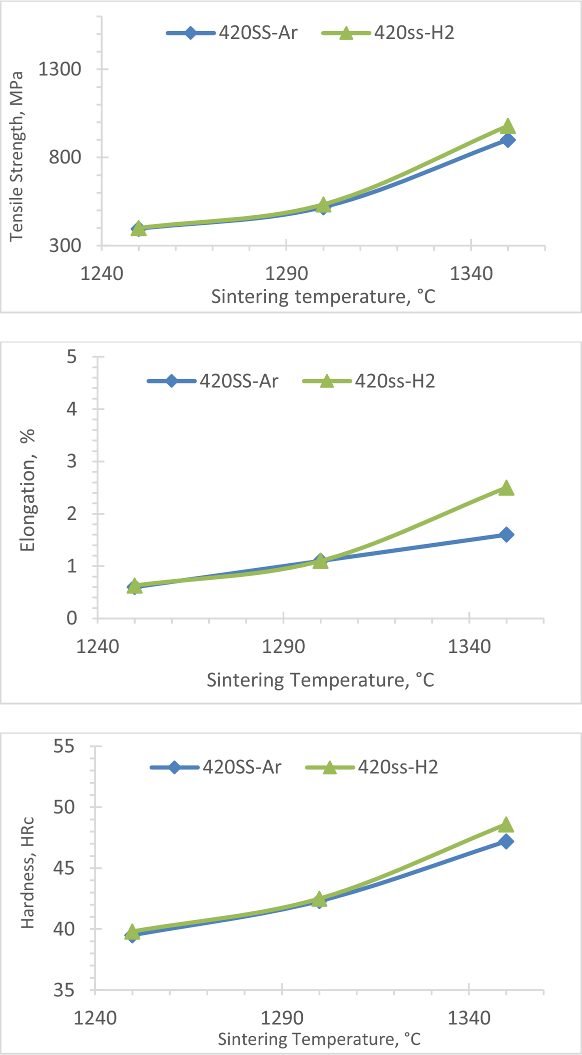

Fig. 5. Mechanical properties of samples at different temperature and atmosphere

Fractography SEM pictures of the samples for different temperature and atmosphere are shown in Table 3. that it shows at low temperatures on fracture surfaces has pitted surfaces and pores. However, by increasing the temperature it increased the sintering temperature meanwhile decreasing pitted surfaces and pores. It also shows crater type fracture which is called ductile fracture [15].

		Density g/cm^3	Relative Density g/cm^3	Tensile Strength MPa	Elongation %	Hardness HRC
Atmosp	Ar	7,25	95,39	901	1,6	47,2
	H_2	7,37	96,97	980	2,5	48,6

Table 2. Mechanical properties under a different atmosphere at 1350 °C

		Density g/cm^3	Relative Density g/cm^3	Tensile Strength MPa	Elongation %	Hardness HRC
Atmosp	Ar	7,25	95,39	901	1,6	47,2
	H_2	7,37	96,97	980	2,5	48,6

Table 3. SEM pictures of samples under different temperatures and atmosphere

Sintering Temperature, ºC

1250 1350

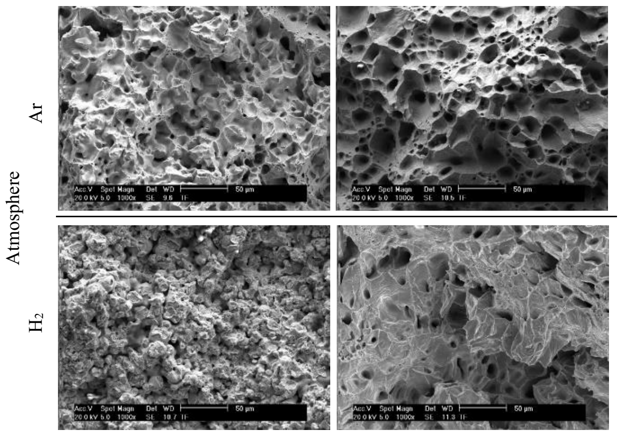

4. Conclusion

In this study, AISI-420 stainless steel powders manufactured by the PIM process to have samples and different temperature and atmosphere applied to investigate microstructural, sintering behavior and mechanical properties. This study also showed that by increasing on sintering temperature from 1250°C to 1350°C, density from 6,54 g/cm^3 to 7,25 g/cm^3, tensile strength from 396 MPa to 901 MPa, elongation from %0,6 to %1,6 and hardness from 39,5 HRC to 47,2 HRC properties of AIS-420 samples are increased. Following same temperatures but using the H_2 atmosphere instead of Ar for sintering, it also increased density from 6,54 g/cm^3 to 7,37 g/cm^3, tensile strength from 400 MPa to 980 MPa, elongation from %0,63 to %2,5 and hardness from 39,8 HRC to 48,6 HRC. It is clearly evidence that increasing the temperature and using H_2 instead of Ar, increased the mechanical properties and sintering behaviors slightly.

Acknowledgement

The authors are grateful to Marmara University (Project No.: FEN-C-YLP-121218-0618) and Sandvik Osprey Ltd. for their financial support and the provision of laboratory facilities.

References

[1] R. M. G. and A. Bose, *Injection molding of metals and ceramics*. 1997.
[2] R. M. German, *Powder injection molding*. 1990.
[3] H. O. Gulsoy, "Mater. Sci. Tech.", c. 24, sayı 12, ss. 1484–1491, 2008.
[4] S. Gulsoy, H.O. Özgün, Özgür. Bilketay, "PowderinjectionmoldingofStellite6powder:Sintering, microstructuralandmechanicalproperties", *ELSEVIER*, c. 651, ss. 914–924, 2016.
[5] D. Li, H. Hou, L. Liang, ve K. Lee, "Powder injection molding 440C stainless steel", *Int. J. Adv. Manuf. Technol.*, c. 49, sayı 1–4, ss. 105–110, 2010.
[6] Enneti RK., Onbattuvelli VP., Gulsoy O., Kate KH., Atre SV., "Handbook of metal injection molding, Powder-binder formulation and compound manufacture in metal injection molding (MIM)", *Woodhead Publ. Ltd.*, ss. 57–88, 2020.
[7] E. G. A.J. Coleman, K. Murray, M. Kerns, T.A. Tingskog, B. Sanford, "Properties of MIM AISI 420 via Pre-alloyed and Master Alloy Routes". 2013.
[8] C. E. P. A. F. CANDEL ´ARIA, "Influence of the heat treatment on the corrosion resistance of the martensitic stainless steel type AISI 420", *J. Mater. Sci. Lett.*, c. 22, ss. 1151–1153, 2003.
[9] Koseski RP., Suri P., Earhardt NB., German RM., Kwon YS., "Microstructural evolution of injection molded gas- and water-atomized 316L stainless steel powder during sintering", *Mater. Sci. Eng. A*, c. 390, ss. 171–177, 2005.
[10] D. JR, *Stainless Steels, ASM International*. 1994.
[11] S. L. Y. Shan, X. Luo, X. Hu, "Journal of Materials Science & Technology", c. 27, ss. 352–358, 2011.
[12] C. I. G. and A. J. D. M. HUA, "Precipitation Behavior in Ultra-Low-Carbon Steels Containing Titanium and Niobium", *Metall. Mater. Trans. A*, c. 28A, 1997.
[13] K. Taylor, "Scripta Metall.", c. 32, ss. 7–12, 1995.
[14] J. Brnic, G. Turkalj, M. Canadija, D. Lanc, ve S. Krscanski, "Martensitic stainless steel AISI 420—mechanical properties, creep and fracture toughness", *Mech. Time-Dependent Mater.*, c. 15, sayı 4, ss. 341–352, 2011.
[15] F. Khodabakhshi, M. H. Farshidianfar, A. P. Gerlich, M. Nosko, V. Trembošová, ve A. Khajepour, "Microstructure, strain-rate sensitivity, work hardening, and fracture behavior of laser additive manufactured austenitic and martensitic stainless steel structures", *ELSEVIER*, c. 756, ss. 545–561, 2019.

The Effect of Crystallographic Texture and Microstructure on Hydrogen Permability of Enamel Steels

Ümran BAŞKAYA[1], Kemal DAVUT[2], Ramazan UZUN[1], Yasemin KILIÇ[1], Oğuz GÜNDÜZ[1]
[1]Eregli Iron and Steel Works, Co., [2]Atılım University
Turkey

Abstract
In this study, the influence of deformation on crystallographic texture and on hydrogen permeability were investigated. For that purpose, specimens from a commercial enamel steel grade have been deformed in tension up to 40% strain. The microstructure and crystallographic texture of the specimens were characterized by the electron back-scatter diffraction (EBSD) technique. The results show that, the gamma-fiber intensity and local misorientations increase, whereas the hydrogen diffusion coefficient decrease with increasing strain.

1. Introduction

Successful enameling requires specific steel grades that have adequate enamel capability and do not cause any surface problems such as fish scale, carbon boiling, adhesion etc. The most common surface defect is fish scale, which is influenced mainly by the hydrogen permeability properties of the steel [1]. Typical microstructure of enamel steels are composed of second phase particles such as carbides, nitrides, sulfides etc. in a ferritic matrix. In this microstructure precipitations, inclusions, dislocations and grain boundaries can act as hydrogen trapping sites [2]. As the fraction of hydrogen trapping sites increase, the probability of fish scale formation decreases [3]. Moreover, the hydrogen permeability has been reported to be influenced by crystallographic texture and fraction of low angle grain boundaries [4].

2. Materials and Methods

Crystallographic texture and hydrogen permeability behavior of steel samples were analyzed as a function of strain. Different strain levels (10% and 40%) were achieved on deep drawing test samples by using Marciniak die, in order to simulate customer's forming process. For comparison a set of unstrained samples were also characterized. Hydrogen diffusion coefficient was measured with Helios II system. Microstructure characterization studies were carried out with scanning electron microscope (SEM/Jeol JSM 7100F) equipped with an EBSD system (Oxford Nordlys Nano EBSD detector). Post processing of raw EBSD data, including texture analysis was performed by the EDAX TSL-OIM Analysis (v.7.3.1) software.

3. Conclusions

In this study, the effect of strain on crystallographic texture and hydrogen permeability were investigated. The results of the study can be summarized as follows:

- Gamma fiber ({111}//ND) is the most dominant fiber in all samples; strained and unstrained. With increasing strain, the intensities of both gamma and alpha fibers increase. Nevertheless, regardless of the increase in alpha fiber intensity the gamma fiber is the most dominant texture component.
- The local misorientations and the fraction of low angle grain boundaries (LAGB) are highest for the sample deformed to 40% strain. The increase in local misorientation value indicates that the dislocation density also increases.
- Considering the decrease of hydrogen diffusion coefficient with increasing strain, the results indicate that dislocations and LAGB can act as trapping sites for hydrogen atoms. Lowering the hydrogen diffusion coefficient prevents the fish scale formation.

References

[1] D. Fu-tao, D. Lin-xiu, L. Xiang-hua, H. Jun and X. Fei, Journal of Iron And Steel Research, International, 20(4) (2013) 39-45.
[2] F. Enikő-Réka, Materials Science Forum, 659 (2010) 7-12.
[3] F. Enikő-Réka and S. Péter János, Materials Science Forum, 659 (2010) 301-306.
[4] H. M. Krom, A.Bakker, Metallurgical and Materials Transactions B , (2000), 1475–1482

Influence of Hydrochloric Acid Temperature on Pickling Efficiency Before Wire Drawing

Murat Alper CEDİMAĞAR
Çelik Halat ve Tel Sanayii A.Ş
Turkey

Abstract

In the production of spring wires or rope wires, phosphate coating is applied to the surface of the wire rods before the cold drawing process. Before phosphate coating on the steel surface, the scale/rust layer on the surface of the wire rods must be removed. Cleaning the oxide layer from the metal surface with acid solution is one of the most common methods. The dipping efficiency varies depending on the basic steel components, the strength of oxides to bind to the base layer, the concentration of acid and iron content, solution temperature, agitation, immersion time and inhibitor used. Within the scope of the experiments, the cleaning times and weight losses of steel wires with a certain chemical composition and diameter in hydrochloric acid solutions with different acid and iron concentrations at varying temperatures are studied.

1. Introduction

The presence of oxide on the steel surface creates disadvantages when the steel is subjected to coating, shaping or cold drawing, and it is undesirable to have an oxide layer on the surface. This oxide layer needs to be cleaned from the wire before phosphating process [1].

The oxide layer on the steel surface can be removed by mechanical or chemical methods. A wide variety of methods are used for iron oxide removal from metal surfaces. These methods include abrasive blasting, wire brushing, grinding, water jetting, thermal cleaning, immersion in acid [2].

In industry, cleaning the oxide layer from the metal surface with acid solution is one of the most common methods. This is usually done by immersing the metal in an acid bath and is called pickling. Various chemicals such as hydrochloric acid (HCl), nitric acid (HNO_3) and sulfuric acid (H_2SO_4) are used to remove the oxidized surface by this process. Apart from being low cost, HCl is widely used because of its faster surface cleaning, lower acid consumption, more efficient use of the acid, less heat consumption and lower amount of waste acid formation, easier operability and more uniform product quality [3].

Scale on the surface of wire rod consists of three layers of iron oxide: wustite (FeO) magnetite (Fe_3O_4) and hematite (Fe_2O_3). By dipping the wire rod into the acid bath, the acid passes through the cracks, piercing the magnetite and hematite layers and reacts with the wustite layer. The acid also reacts with the base metal layer and hydrogen gas is formed. Gas bubbles help separate the magnetite layer and speed up the process [4].

When iron oxides dissolve in HCl, iron chlorides are formed in the following reactions;

$$Fe_2O_3 + Fe + 6HCl = 3FeCl_2 + 3H_2O \quad (1)$$

$$Fe_3O4 + Fe + 8HCl = 4FeCl_2 + 4H_2O \quad (2)$$

$$FeO + 2HCl = FeCl_2 + H_2O \quad (3)$$

Hydrochloric acid also performs the following reaction with the steel layer;

$$Fe + 2HCl = FeCl_2 + H_2 \quad (4)$$

The dipping efficiency varies depending on the basic steel components, the strength of oxides to bind to the base layer, the concentration of acid and iron chloride, solution temperature, agitation, immersion time and inhibitor used [5].

Further understanding of these parameters over pickling efficiency can be useful for the steel wire industry to operate acid baths in optimum conditions and therefore use the acid more effectively that would result in improved cleaning operation performances and creation of less waste.

In this study, effects of temperature, acid and iron concentrations of HCl baths over pickling were investigated.

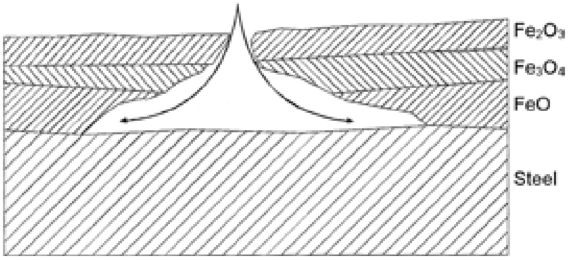

Figure 1. Mechanism of pickling

2. Experimental Procedure

Different acid concentrations are prepared from 30% HCl solution and analytical grade water. For preparing acid solutions of certain iron concentrations, spent acid from Çelik Halat ve Tel Sanayii A.Ş.'s pickling baths are used. Each solution's acid and iron concentrations are determined by NaOH and $KMnO_4$ titrations respectively. In all experiments, a magnetic stirrer (MTPOS MS300HS) and a thermometer was used to adjust solution temperatures. Wire rods were weighted by a digital scale (METTLER AJ100).

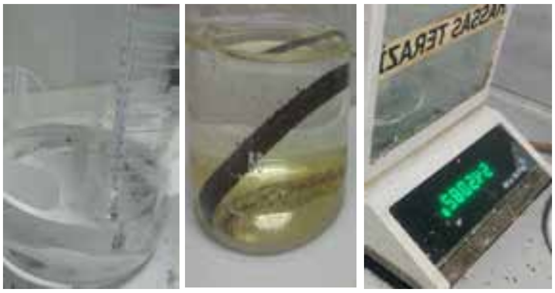

Figure 2. Experimental setup for pickling tests

In the study, wire rods with a 0.70% carbon content and 5.5 mm diameter were used. All rods were cut into lengths of 50 mm. In all experiments which pickling times are observed, 100 ml of solutions were put in beakers, steel wire rods were immersed separately to these beakers and complete pickling times are recorded. In the experiments where effect of HCl concentration on pickling is investigated, wire rods were weighted before immersing in acid solutions and collected from beakers in every 50 seconds, rinsed dried and weighed.

3. Results and Discussion

In order to investigate effect of HCl concentration on pickling, acid solutions with 5%, 10%, 15%, 20%, 25% and 30% concentrations were prepared at adjusted to 30 °C. Wire rods were put in the acid after weighing and immersed for 50 second duration, rinsed, dried and weighed again. This procedure was repeated until 500 seconds total immersion time reached. Figure 3 shows % weight losses against immersion times for different acid concentrations.

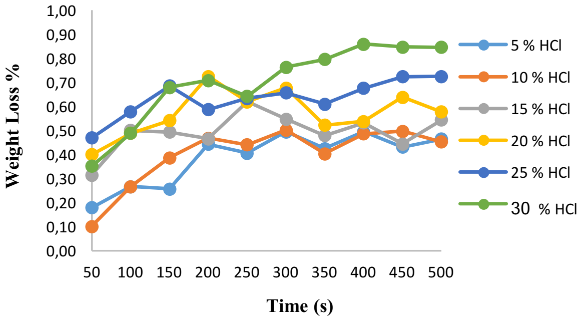

Figure 3. Effect of HCl concentration on pickling

As can be seen from Figure 3, higher acid concentrations resulted in faster pickling ratios. At 20% and 25% acid concentrations pickling started faster compared to 30% and in fist 250 seconds after immersion average pickling rates for 15%, 20%, 25% and 30% concentrations are very close. After first 250 seconds there is a clear difference of pickling ratios between high and low acid concentrations.

To determine the effect of temperature over pickling, acid solutions with 5%, 10%, 15%, 20%, 25% and 30% concentrations were prepared at 25°C, 30°C, 40°C and 50°C.

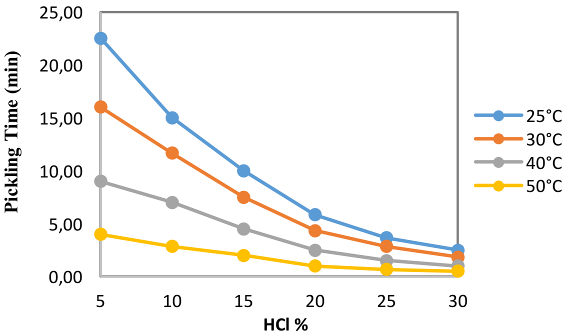

Figure 4. Effect of temperature on pickling time

From figure 4, it can be seen that at all concentrations, higher temperatures resulted in faster pickling times. When the solution temperatures rise from 25 to 50°C overall pickling speed increased more than 4 times. Required pickling time difference at different temperatures reduced considerably at 20% and higher concentrations.

To investigate iron content effect over pickling, 5%, 10%, 15%, 20% and 25% acid solutions were prepared with various (0, 20, 40, 60, 80 and 100 g/L) iron contents. These experiments were carried out at 30°C.

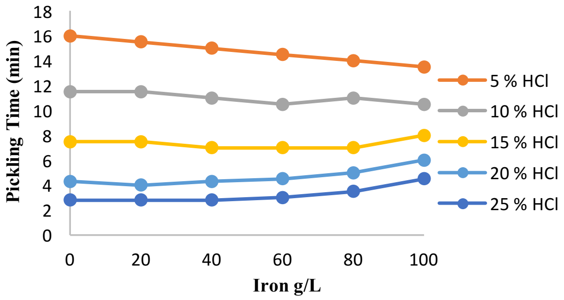

Figure 5. Effect of iron content over pickling time

As can be seen in Figure 5, at 5% and 10% acid concentrations, pickling time decreased with the increasing iron content. This could be related to the base iron's role in the HCl cleaning mechanism. At higher acid concentrations, as the iron content increased the solution approached to saturation and the overall pickling time showed an increase.

With the aim to simulate a batched HCl pickling system, solutions were prepared with a 200, 180, 160, 140, 120, 100 and 80 g/L acid and 0, 20, 40, 60, 80, 100 and 120 g/L iron concentrations respectively. Pickling times were observed for these solutions and the experiments were conducted on 3 different temperature sets (30, 40 and 50°C) (Figure 6).

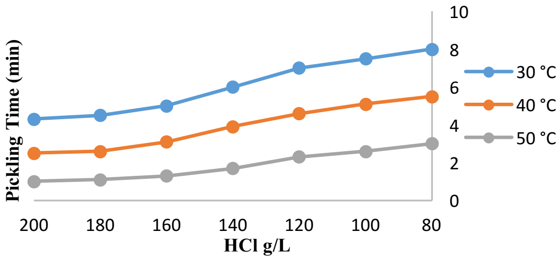

Figure 6. Depleting pickling efficiency of batch HCl bath

From Figure 6, it can be seen that pickling efficiency increases at higher temperatures. When pickling times of 50 and 30°C solutions are compared it is seen that 30°C solution tooks almost 3 times more to clean the wire rod's surface. Another thing to mention is that at all concentrations and temperatures, solutions with iron content showed better pickling efficiency when compared to same acid concentrations at same temperatures.

4. Conclusions

HCl pickling of oxide layers of steel surface depends on various factors. Temperature, acid and iron content of the solution are among the most important factors on pickling performance. In this study, only one type of steel wire rod with same dimensions were used. Also all the solutions were in same volume and were not stirred during pickling process.

The experiments showed that as temperature rises the pickling ratio increases considerably. When compared, acid solutions at 50°C pickles 4 times faster than acid solutions of 30°C on same concentrations. With increasing acid concentrations pickling rate increased dramatically. At high acid concentrations such as 30% and 25% HCl started to remove base steel from the wire rods way sooner than lower concentrations.

Presence of iron in acid solutions slightly accelerates the pickling efficiency until the solutions approaches saturation limit. Especially at high acid concentrations iron content must be taken into account to decide whether to add acid or water to keep the pickling at optimum performances.

Increased temperatures and acid concentrations provide faster pickling but holds a great risk to attack to the base steel and create unwanted cavities on surface. Therefore it is very important to use an inhibitor at such conditions and further investigation of pickling additives/inhibitors could prove useful in achieving optimal bath conditions.

Acknowledgment

The author would like to thank Çelik Halat ve Tel Sanayii A.Ş for opening up all its possibilities for experimental studies and the creation of process conditions.

References

[1] Y. Liu, L. Wang, L. Liu, W. Han, X. Sun, J. Li and J. Shen, International Journal of Simulation -- Systems, Science & Technology, 16 (2015) 1-6.

[2] M. Maanonen, Steel Pickling in Challenging Conditions, M.Sc. Thesis, Helsinki Metropolia University of Applied Sciences, 2014, Helsinki, Finland, pp. 2-18.[3] L. Luo, W. Cuiming, W. Yonghui, X. Tongwen, Separation and Purification Technology, 118 (2013) 716‑722

[4] A. Agrawal, K.K. Sahu, Journal of Hazardous Materials, 171 (2009) 61-75.

[5] W.F. Kladnig, Journal of Iron And Steel Research, 15 (2008) 1-6.

Boriding of AISI 304L Stainless Steel via CRTD-BOR Method

Mehran KARIMZADEHKHOEI, Merve SERT, Oguz Kagan COSKUN, Mehtap ARSLAN, Guldem KARTAL SİRELİ, Servet TİMUR
İstanbul Technical University
Turkey

Abstract

In this study, the effects of process time and temperature on the thickness, morphology and hardness of grown boride layers on AISI 304L stainless steel substrate were investigated. For this purpose, a rapid boriding technique named as Cathodic Reduction and Thermal Diffusion based boriding (CRTD-Bor) method was chosen. The main advantages of this boriding method are its high boride layer growth rates and its environmentally friendly nature as well as its applicability on different substrates including titanium and its alloys. CRTD-Bor of AISI 304L substrates was conducted in an electrochemical cell which contains a mixture of sodium tetraborate and sodium carbonate (%90 $Na_2B_4O_7$ + %10 Na_2CO_3) as molten electrolyte at various electrolyte temperatures (950-1050ºC) and durations (15-60 min) at constant current density (200 mA/cm^2). The XRD diffraction analysis revealed sole CRTD-Bor application cause to form the mixed boride phase formations including Fe_2B, FeB, Cr_5B_3, Ni_2B, $B_6Cr_2Ni_3$ on AISI 304L matrixes. Also cross-sectional Scanning Electron Microscopy (SEM) examinations confirmed the boride layer growth with these phases. Thickness of FeB layer and followed by the total thickness of the boride layer were increased with increasing the process time and temperature and the hardness value of produced boride layer at 1000ºC for 15 min. was achieved as high as with 1950 ± 50 HV boride layer hardness along with the excellent adhesion to the substrate (HF1). Moreover, the kinetic investigations relieved that the activation energy (Q) of boriding layer growth calculated as 161.13 KJ/mol.

1. Introduction

Austenitic stainless steels (ASS) comprise over 70 percent of the total ratio of stainless steel production. The larger subgroup of ASS is 300 series, where the austenitic structure is attained mainly by a nickel addition. Among 300 series, AISI 304 ASS has been distinguished due to its good corrosion resistance, high ductility and excellent drawing and found many applications including car headers, machinery parts, storage containers, door and window frames and so on. Compared to 304 ASS, the carbon content of 304L is restricted to a maximum of 0.03%, in order to increase the intergranular corrosion resistance which prevents welding sensitization due to the formation of chromium carbides along grain boundaries [1]. Thermochemical processes such as carburizing, nitriding, nitro-carburizing, and boriding are good choices to modify the surface chemical chemistry and improve wear and corrosion resistance of those materials and make them last much longer and perform better [2]. However, among these methods, extremely high hardness values (i.e. 1500 HV for steel substrates) and high melting points (i.e. 1390°C for Fe_2B) are achieved using the boriding process. This process is mainly used for iron and its alloys and occasionally for few non-ferrous metals and alloys has been reported [3]. Todays, various boriding methods exist for ferrous materials including pack/paste boriding, plasma boriding and molten salt boriding [4]. Among, pack boriding, despite some problems involved long processing time (up to 40 h) and generation of huge amounts of solid wastes as well as toxic gaseous emissions, has been applied to iron and steels extensively in the industry [5]. Alternatively, electrochemical boriding is considerably fast, environmentally clean, and much more effective in boriding of the various substrates including ferrous and non-ferrous materials in comparison with pack boriding [6, 7]. Regarding, in this study, boriding of AISI 304L stainless steel substrate was carried out by using a rapid electrochemical boriding technique named as Cathodic Reduction and Thermal Diffusion based boriding (CRTD-Bor) method [6]. The main advantages of this method are: i) high boride layer growth rates, ii) environmentally friendly nature, and iii) applicability on different substrates including titanium and its alloys. This paper aims to investigate the effects of processing time and temperature on the chemistry, thickness, morphology, and hardness of grown boride layers on AISI 304L stainless steel substrate and calculate the activation energy of borided AISI 304L stainless steel.

2. Experimental procedure

Rectangular specimen of AISI 304L stainless steel was cut into smaller pieces (i.e., 1.5×5 mm and 1 mm thick). Prior to the electrochemical experiments, the samples were progressively ground with SiC sandpaper up to 800 grit size to remove oxide layers, then ultrasonically cleaned in acetone and dried in air. Boriding experiments of the samples were carried out at a constant current density of 200 mA/cm^2 in the stable composition of molten salt (%90 $Na_2B_4O_7$ + %10 Na_2CO_3) at a temperature range of 950-1050ºC for periods of 15-60 min. The constant parameters taken in this study were initial optimized conditions reported by Kartal et al. [4]. A high-frequency induction furnace (180 kHz, 5 kW, 7 A) was employed to heat electrochemical cell which consists of graphite crucible as an anode and AISI 304L stainless steel substrate as a cathode. During the electrolysis process, the temperature of electrolyte was measured using a K-type thermocouple. After completion of CRTD-Bor, the samples were withdrawn from the electrolyte and left into the air to cool down. In order to remove the solidified remnant electrolyte from the samples, they were washed in the boiling water. Borided samples were cut and metallographically prepared by progressively ground with SiC sandpaper up to 1200 grit size. After that, polished with 1 µm diamond solution, and finally etched by a %5 Nital solution to reveal the morphology of boride layer. Phase composition of the produced layer was characterized by X-ray diffractometer (XRD-Philips PW-3710) using Cu-Kα radiation (40 kV, 40 mA). Thickness, cross-sectional morphology and chemical analyses of the boride layers were determined using an optical microscopy (Olympus TGH-BH2), SEM and EDS (JSM-7000F Model). Furthermore, the micro hardness value and adhesion strength of the layers were measured using Vickers micro hardness tester (Zwick Roell ZHVµ) with a 50 gf of indentation load and Daimler–Benz Rockwell-C adhesion test, respectively.

3. Results and Discussion

3.1. Characterization of the borided layer

X-ray diffraction (XRD) analysis of the borided samples at different process time and temperatures (Figure 1) confirmed the existence of both FeB and Fe_2B phases. In addition, some other phases such as Cr_5B_3, Ni_2B and $B_6Cr_2Ni_3$ were detected in the XRD results. In the case of borided samples at 950ºC for all process time, the most intense peaks belong to FeB and $B_6Cr_2Ni_3$. In addition, Cr_5B_3 phase was determined. However, there is no specified peaks belonging to Fe_2B which is related to the low temperature of the boriding process. The process temperature was increased to 1000ºC in order to produce the Fe_2B. In this case, in addition to FeB, $B_6Cr_2Ni_3$ and Cr_5B_3, Ni_2B phase was detected. Also, Fe_2B peaks were more intense. Finally, at 1050ºC, the most intense peaks belong to FeB and $B_6Cr_2Ni_3$ and there is no detectable Fe_2B peaks. Optical images of the borided AISI 304L stainless steel samples at different temperatures and time periods are shown in Figure 2. As can be seen, Boride layer has a smooth and flat morphology compared to the tooth-like growth morphology of that on low carbon steel due to the existence of the alloying elements such as chromium and nickel in the AISI 304L stainless steel which are concentrated at the grain boundaries and disrupt diffusion of boron atoms to the substrate and hinder formation of boride layer [8, 9]. As is clear, the thickness of FeB layer and followed by the total thickness of the boride layer were increased with increasing the process time and temperature. A SEM image of the borided sample at 1000ºC for 15 min. was shown in Figure 3, and the chemical composition of the defined points is given in Table 1. According to the results, it is seen that the boron content was generally decreased from the surface to the substrate, however, a sudden increase was observed in the grain boundaries (point 5). On the other hand, chromium has been distributed from the surface to the substrate. Additionally, chromium highly concentrated below the boride layer (named as chromium-rich region) and grain boundaries. Besides, nickel was spread into the structure while its content was decreased where the chromium has been concentrated.

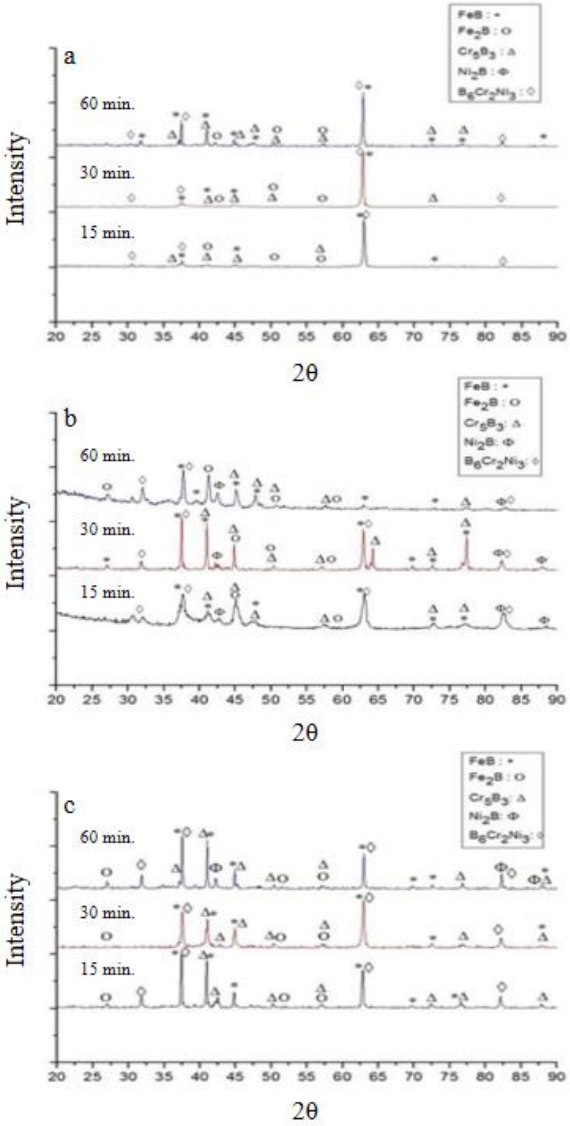

Figure 1. XRD diffraction pattern of the boride layer at a) 950ºC, b) 1000ºC, and c) 1050ºC

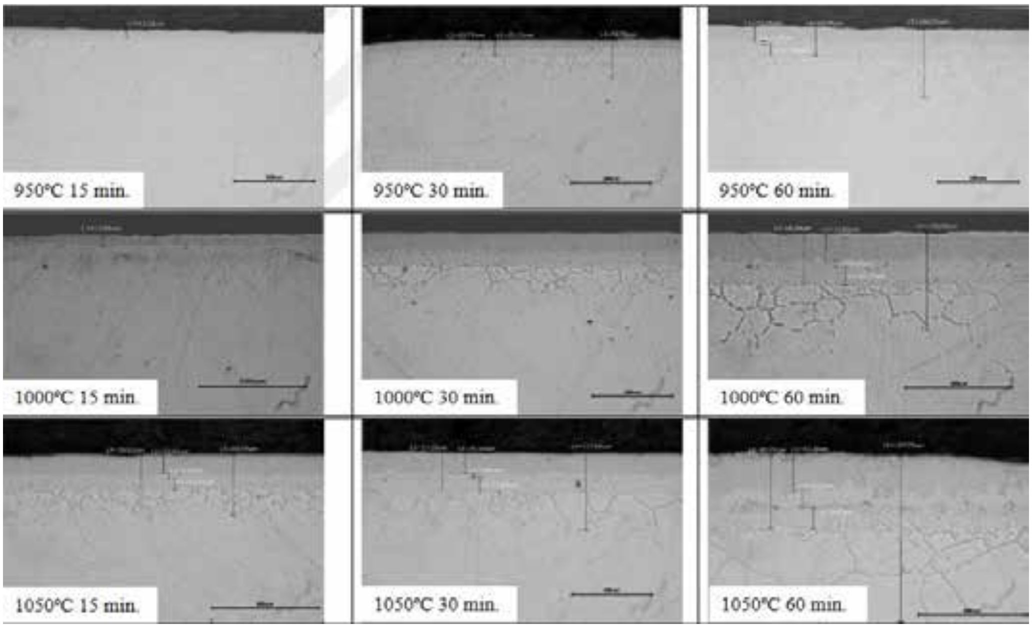

Figure 2. Optical micrographs of the borided samples at different process temperatures and time durations [200 mA/cm^2, %90 $Na_2B_4O_7$ + %10 Na_2CO_3].

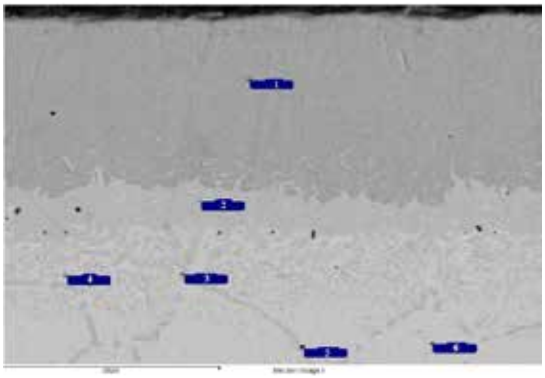

Figure 3. SEM image of the borided sample at 1000°C for 15 min [200 mA/cm^2, %90 $Na_2B_4O_7$ + %10 Na_2CO_3].

Table 1. Chemical composition of the point on Figure 3

Point	B	Si	Cr	Mn	Fe	Ni
1	58.22	-	7.98	1.20	30.39	2.21
2	44.74	-	10.39	0.93	40.22	3.72
3	43.10	0.29	26.46	1.40	28.75	-
4	22.28	2.03	12.29	1.18	54.16	8.06
5	40.64	0.13	22.70	1.41	33.06	2.06
6	-	1.26	19.95	2.43	68.34	8.02

3.2. Kinetic approach to boride layer growth

Thickness variation of the total boride layer as a function of process time at different temperature is shown in Figure 4. As it clear, the relation between rate of boride layer formation and process time is parabolic at all process temperatures. This verifies that the diffusion of boron atoms into the substrate is the most important rate-controlling step in the process. The growth rate constant (K) for iron borides for different temperatures (T), which is calculated by the slope of d^2 versus t (Eq. 1), is given in Figure 5. Also, according to Eq. 2, the activation energy (Q) for the boriding process is calculated by the plot ln K versus 1/T which is shown in Figure 6 and the activation energies (Q) was determined as 161.13 kJ/mol which is %28 lower than the value achieved by Kayali Y. [10] using pack boriding method for AISI 304L stainless steel.

$$d^2 = K.t \qquad \text{Eq. 1}$$

$$K = K0\ exp\ (-\frac{Q}{RT}) \qquad \text{Eq. 2}$$

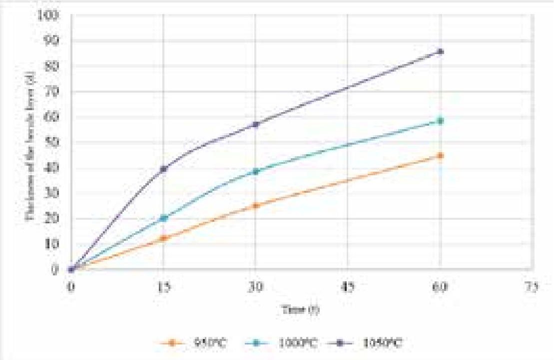

Figure 4. Variations of boride layer thickness, d as a function of boriding time, t at different process temperatures.

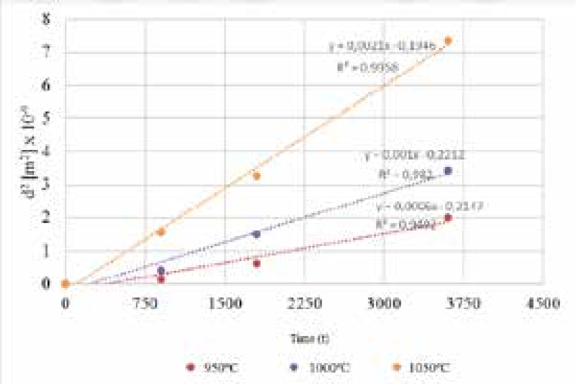

Figure 5. Variations of d^2 versus t.

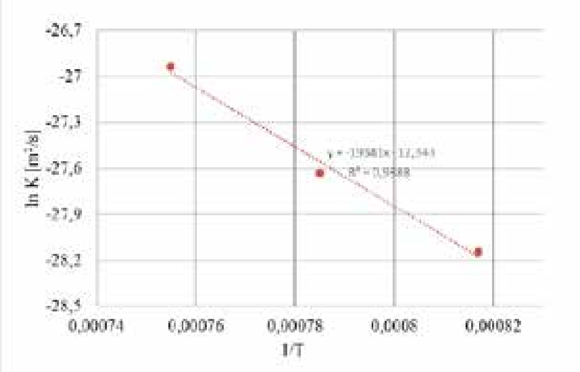

Figure 6. The values of ln K with respect to 1/T.

The hardness value for the borided sample at 1000ºC for 15 min. was measured as high as 1950 ± 50 HV for the boride layer at 20 µm from the surface and decreased to 200 ± 20 HV at 25 µm from the surface where is the hardness value of the substrate. Also, The Daimler–Benz Rockwell-C adhesion test was done to evaluate the adhesion strength of the boride layer. The adhesion strength quality of the boride layer at the mentioned condition was related to HF1.

4. Conclusion

In this study, boriding of AISI 304L stainless steel was carried out via CRTD-Bor method at a constant current density (200 mA/cm^2) in the stable composition of the electrolyte (%90 Na_2B4O_7 + %10 Na_2CO_3) at a temperature range of 950-1050ºC for periods of 15-60 min. Additionally, effects of the processing time and temperature of boriding on the thickness, morphology and hardness of grown boride layers were investigated. According to the results reported, the thickness of FeB layer and followed by the total thickness of the boride layer were increased with increasing the process time and temperature and the hardness value of produced boride layer at 1000ºC for 15 min. was measured as high as 1950 ± 50 HV along with the sufficient adhesion strength (HF1) to the substrate. Moreover, the activation energy (Q) of boride layer growth calculated as 161.13 KJ/mol by the kinetic investigations which was %28 lower than the value achieved by Kayali Y. [10] using pack boriding method for AISI 304L stainless steel.

References

[1] A. Abou-Elazm, R. Abdel-Karim, I. Elmahallawi, and R. Rashad, “Correlation between the degree of sensitization and stress corrosion cracking susceptibility of type 304H stainless steel,” *Corros. Sci.*, 2009, doi: 10.1016/j.corsci.2008.10.015.

[2] I. Campos, O. Bautista, G. Ramírez, M. Islas, J. De La Parra, and L. Zúñiga, “Effect of boron paste thickness on the growth kinetics of Fe 2 B boride layers during the boriding process,” *Appl. Surf. Sci.*, 2005, doi: 10.1016/j.apsusc.2004.09.099.

[3] G. Kartal, O. Kahvecioglu, and S. Timur, “Investigating the morphology and corrosion behavior of electrochemically borided steel,” *Surf. Coatings Technol.*, 2006, doi: 10.1016/j.surfcoat.2005.02.210.

[4] G. Kartal, S. Timur, and C. Arslan, “Effects of process current density and temperature on electrochemical boriding of steel in molten salts,” in *Journal of Electronic Materials*, 2005, doi: 10.1007/s11664-005-0162-x.

[5] T. W. Spence and M. M. Makhlouf, “Characterization of the operative mechanism in potassium fluoborate activated pack boriding of steels,” *J. Mater. Process. Technol.*, 2005, doi: 10.1016/j.jmatprotec.2004.10.015.

[6] G. Kartal, S. Timur, M. Urgen, and A. Erdemir, “Electrochemical boriding of titanium for improved mechanical properties,” *Surf. Coatings Technol.*, 2010, doi: 10.1016/j.surfcoat.2010.05.021.

[7] L. Segers, A. Fontana, and R. Winand, “Electrochemical boriding of iron in molten salts,” *Electrochim. Acta*, 1991, doi: 10.1016/0013-4686(91)85177-9.

[8] M. Kulka and A. Pertek, “Characterization of complex (B + C + N) diffusion layers formed on chromium and nickel-based low-carbon steel,” *Appl. Surf. Sci.*, 2003, doi: 10.1016/S0169-4332(03)00563-4.

[9] I. Campos, M. Palomar-Pardavé, A. Amador, C. VillaVelázquez, and J. Hadad, “Corrosion behavior of boride layers evaluated by the EIS technique,” *Appl. Surf. Sci.*, 2007, doi: 10.1016/j.apsusc.2007.05.016.

[10] Y. Kayali, “Investigation of the diffusion kinetics of borided stainless steels,” *Phys. Met. Metallogr.*, 2013, doi: 10.1134/s0031918x1322002x.

Comparison of Microstructural and Optical Properties of TiO_2 Thin Films Synthesized by Sol-Gel Dip Coating and Spin Coating Techniques

Özge ÖZGÜN, Muhammed NAJAR, Aslı ÇAKIR, Tolga TAVŞANOĞLU
Muğla Sıtkı Koçman University
Turkey

Abstract
In this study, TiO_2 thin films having about 100 nm thicknesses were deposited on glass substrates by sol-gel dip coating and spin coating techniques. Their microstructural and optical properties were comparatively discussed.

1. Introduction

Titanium dioxide is commonly used in optical thin films because it has superior physical and chemical properties, in addition it is highly transparent in the visible, UV and near-infrared regions of the electromagnetic spectrum [1-2].

2. Materials and Methods

A solution composed of titanium (IV) isopropoxide (TTIP) as the precursor material, ethanol (EtOH) as solvent, HCl as catalyst were used to deposit TiO_2 thin films on soda-lime glass substrates by both dip coating and spin coating techniques. Molar ratios of 1:40:0.2 were used for TTIP:EtOH:HCl respectively. The solution was mixed by a magnetic stirrer during 3 hours and aged for 7 days. The pH and viscosity values of as-prepared and aged solution were measured by pHmeter and viscometer. pH values were stable at 0.8 and viscosity increased from 2.1 to 2.9 as a result of the polymerization reactions. Microstructural properties of TiO_2 thin films were characterized by high-resolution SEM observations and results are presented in Figure1. Chemical composion was measured by EDS analyses. Spectrophotometer analyses over the spectral range of 280-1100 nm were conducted to determine the optical properties as can be seen in Figure 2.

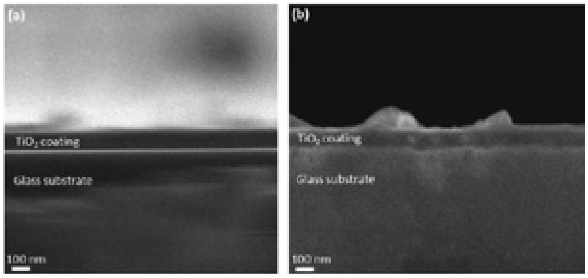

Figure 1. Cross-sections of TiO_2 coatings deposited (a) by dip coating (b) spin coating having both 100 nm thickness

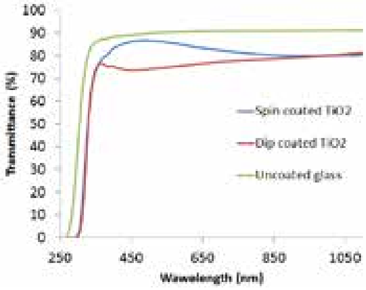

Figure 2. Transmittance values of spin coated TiO_2, dip coated TiO_2 and uncoated glass

3. Conclusion

The results demonstrated that homogenous and well-adherent TiO_2 thin films with thicknesses about 100 nm were successfully deposited on glass substrates. According to EDS analyses both coatings have near stoichiometric TiO_2 composition. It is believed that the difference in the optical properties of TiO_2 thin films having the same thicknesses originated due to the nature of the deposition techniques; in spin coating only one-side of the substrate was coated whereas both sides were coated by dip coating technique. It is thus concluded that the most important parameter is the preparation and composition of the sol. Different sol-gel deposition techniques do not have considerable effects on the coating properties while using the same sol.

References

[1] C.Y. Wu, Y.L. Lee, Y.S. Lo, C.J. Lin, C.H. Wu, Applied Surface Science, 280 (2013) 737– 744.
[2] B. Guo, Z. Liu, L. Hong, H. Jiang, Surface & Coatings Technology, 198 (2005) 24– 29.

Investigation of Delaying Cold Heading Crack Formation with Shot Peening Process

Cenk KILIÇASLAN, M. Burak TOPARLI, Sezgin YURTDAŞ, Doğuş ZEREN, Barış TANRIKULU
Norm Cıvata San. ve Tic A.Ş.
Turkey

Abstract
In this study, steel coil samples were subjected to shot peening process to delay crack initiation during cold heading. By this way, it was aimed to forge products having high head diameter / shaft diameter ratio. After shot peening of steel samples, compression experiments were conducted to samples having two different geometries as tapered and flanged. It was seen after shot peening, surface roughness and hardness values were increased after shot peening. However, compression test results revealed that expected improvement in crack initiation retardation to increase forgeability limit was not achieved after shot peening due to heavily deformed steel surface.

1. Introduction

Shot peening is one of the mechanical surface treatment methods used especially in aviation. Metal or ceramic spheres accelerated with compressed air are directed to the surface of the material to be processed. As a result of plastic deformation in the area close to the surface, compressive residual stresses occur and hardness increases. In this way, crack initiation and propagation can be delayed and fatigue life of the material can be increased significantly [1,2].

2. Materials and Methods

In this study, two different compression test geometry made of 41Cr4 were employed. Characterization tests including surface roughness and hardness were carried out. Compression tests were conducted in order to determine crack initiation limit, which is very important parameter in terms of metal forming via cold forging. Compression tests up to 350 kN were done to obtain the maximum load at which crack initiation was not observed. The limiting study was carried out on samples with and without shot peening treatment. Two of the post-compression test sample images after shot peening with surface cracks can be seen in Fig. 1.

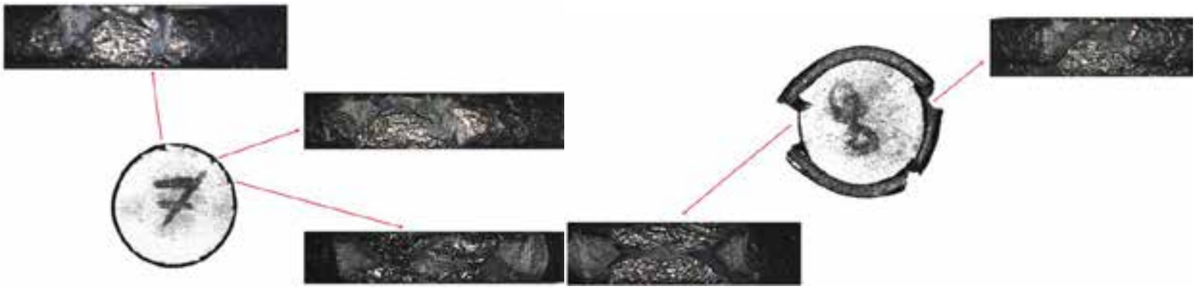

Figure 1. Surface cracks and their locations of two different shot peened samples subjected to compression tests

3. Results and Conclusions

In the characterization tests performed after the shot peening, a 25% hardness increase was obtained on the material surfaces. However, the surface morphology deteriorated and the surface roughness values (R_a and R_z) increased by up to 7.5 times. As a result of the compression tests, it was determined that this process does not have a positive effect on the forging of the products with high target head diameter / shaft diameter ratio after the shot peening, and the expected improvement in the delay and progression of the crack has not been achieved.

Acknowledgment
The authors would like to acknowledge Deniz Civan Özuğurlu for his contribution.

References

[1] M.B. Toparli, Experimental Techniques, 44 (2020), 37-47.
[2] B. Karahan and U. İnce, Derin, 5 (2015), 74-90.

Effect of Heat Treatment Parameters on the Microstructure and Mechanical Properties of 30CrNiMo8 Steel

Hakan ERÇAY[1], Gürcan TATLICAN[1], Tuncay DİKİCİ[2]
[1]Özkan Iron and Steel Industry, [2]Dokuz Eylul University
Turkey

Abstract

In this study, the effect of tempering temperature on the microstructure and mechanical behaviors of 30CrNiMo8 steel were investigated. The steel samples were austenitized at 860 °C followed by polymer added water quenching, and then tempered at four different temperatures. The microstructures, tensile strength, hardness and impact toughness of the samples were analyzed and compared with each others. The results indicated that microstructure and mechanical properties of the 30CrNiMo8 steel samples change with the increasing of tempering temperature. As the tempering temperature increased, the yield strength, tensile strength and the hardness decreased but the elongation and impact energy increased.

1. Introduction

30CrNiMo8 is used for automotive and general components which require high demands on strength, toughness, and good hardenability [1]. It is especially suitable for production of heavily loaded parts, shafts, discs and drive axes, crank shafts of engines, steering shafts, screws and elements exposed to temperatures in the power industry [2]. It is a heat treatable and low alloy steel containing chromium, nickel and molybdenum as strengthening alloy elements [3]. It is known for is toughness and capability of developing high strength in the heat treated condition while retaining good fatigue strength [4].

2. Materials and Methods

The chemical composition of 30CrNiMo8 low-alloy steel is shown in Table 1. In the present work, all the samples were austenitized at 860 °C, followed by polymer added water quenching, and then tempered at different temperatures, 540, 580, 600 and 640°. The microstructural and mechanical properties of the treated samples were evaluated by optical microscopy (OM), tensile test and hardness test.

Table 1. Chemical composition of 30CrNiMo8 steel

C	Si	Mn	Cr	Ni	Mo	P	S
0,28	0,19	0,53	1,91	1,86	0,311	0,010	0,004

3. Conclusion

The results showed that tempering had a significant effect on both the microstructure and mechanical properties of the steel. The tensile strength, yield strength and hardness decrease with the increase of the tempering temperature. The hardness of 30CrNiMo8 steel gradually decreases from 42.5 to 31 HRc with increasing the tempering temperatures in the range of 540-640 °C. Moreover, the hardness of the steel without tempering is the highest and reaches 51.5 HRc. The results showed that the absorbed energies of 30CrNiMo8 steel increase from 43 J to 131 J with increasing tempering temperature from 540 °C to 640 °C.

References

[1] T. DebRoy, S.A. David, J.N. DuPont, T. Koseki and H.K. Bhadeshia, Trends in Welding Research 2012: Proceedings of the 9th International Conference, 2013, ASM International, pp. 753-754.
[2] L. Zumofen, A. Kirchheim and H.J. Dennig. Laser powder bed fusion of 30CrNiMo8 steel for quenching and tempering: examination of the processability and mechanical properties. Progress in Additive Manufacturing, (2020) 1-7.
[3] S. Ahangarani, A.R. Sabour and F. Mahboubi, Surface modification of 30CrNiMo8 low-alloy steel by active screen setup and conventional plasma nitriding methods. Applied Surface Science, 254 (2007)1427-1435.
[4] Brnic, J., Krscanski, S., & Brcic, M. (2019, September). Analysis of the mechanical response of materials used in design for highly stressed components. In *IOP* Conference Series: Materials Science and Engineering (Vol. 625, No. 1, p. 012003). IOP Publishing.
[6] http://www.metal-powder.net> Dated: 08.11.2019.

Temperature Distribution Analysis of Thin Metal Surfaces by Induction Heating

Basar SUER, Arcan F. DERICIOGLU
Middle East Technical University
Turkey

Abstract

The aim of this study is to investigate the effect of several parameters such as film thickness and applied electromagnetic frequency on the induction heating potential of metallic thin films on various surfaces. Achievement of effective and homogeneous temperature distribution has been analyzed in detail by integrating “ANSYS Maxwell” and “ANSYS Transient Thermal” software.

1. Introduction

Induction heating is the heating process which involves an electrically conductive material that is subjected to electromagnetic waves generated by high-frequency alternating current passing through a coil. Interaction of the electromagnetic wave with the subjected material induces eddy-currents inside the material up to a certain thickness defined as *skin depth*. Using finite element analysis approach via ANSYS Maxwell and ANSYS Transient Thermal software, it is possible to understand the heating response of the material subjected to electromagnetic induction.

2. Materials and Methods

In order to understand the heating response of the material subjected to electromagnetic induction, three different metals have been selected for the investigation namely nickel (Ni), silver (Ag) and tungsten (W). On the other hand, to understand the skin depth related consequences, three different sheet-thickness of 10, 20 and 50 µm and frequencies of 25, 50 and 100 kHz were selected. Finally, as the temperature distribution is also affected by the coil design, two different coil designs, namely basic flat spiral design and zigzag-pattern design, were studied. With the help of ANSYS, it was possible to investigate the magnetic field (B) distribution (Figure 1) and eddy-current generated inside the thin film from surface-to-bulk.

3. Conclusion

ANSYS Maxwell and ANSYS Thermal Transient software are capable of solving the induction heating potential of thin films with micron level thicknesses on various surfaces. Effect of film thickness, frequency of the applied electromagnetic radiation and coil design has been studied effectively by means of finite element analysis approach. Detailed simulation analysis yielded the optimum film thickness for different materials and ideal conditions to achieve effective induction heating on various materials.

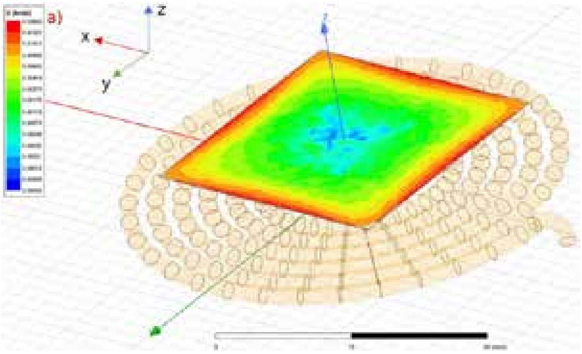

Figure 1. Distribution of magnetic field (B) at the surface of the thin material.

Improvement of Orbital Cutting Blade Life With Tin Coating

Muhammed Cemil ENSAROĞLU, Bedri Onur KÜÇÜKYILDIRIM
Yıldız Technical University
Turkey

1. Introduction

Tube fabricators [1] use a variety of methods; sawing, lathe cutting, orbital cutting and laser cutting to cut tubing from mill lengths into shorter pieces for use in final fabrication. The orbital cutting method is the main application in the field of white goods copper components, copper heating, cooling, ventilation components and automotive aluminum air conditioning lines.

Many companies [2] prefer the orbital cutting method, which has proven its economic contribution over time. The main feature of orbital cutting is that it cuts without producing sawdust and reduces material waste.

In many studies [3,4] in the literature, it has been proven that TiN coating provides different rates of life increase on cutting tools. The purpose of this study is to improve orbital cutting blade life with TiN coating.

2. Materials and Methods

The experiments were carried out on an automatic orbital cutting machine (OAK STCOS M5-695). Coil stocks copper tubes with an outer diameter of 20 mm and wall thickness of 1 mm was selected for this study. Tests were conducted using uncoated and coated orbital cutting blade. Cutting speed was 1800 rpm and depth of cut was 0.95 mm. Coating process was carried out on VACOTEC Alpha400P119 brand machine. Nitrogen was used as reactive gas, the bias voltage was 150 volt, the evaporating current was 60 ampere. Coating process at 450 degrees took 87.6 minutes in total.

3. Results and discussion

The orbital cutting blades that used in experiment were presented in Fig. 1. It was experimentally found that coated blade has greater tool life of 25.200 cuts compared to uncoated blade tool life of 13.700 cuts. Schintlmeister [4] summarized the effect of coatings in the following statements: (1) reduction in friction, in generation heat, and in cutting force; (2) reduction in the diffusion between the chip and the surface of the tool, especially at higher speeds which explains the results of this study as well. From Fig.1, considering the SEM images, it was determined that the ductile-brittle mixed fracture type emerged. Fracture surfaces present evidence of dimpled rupture, the characteristic signature of ductile fracture. At the same time, the high loading to which the material is subjected in terms of where it was used has been an important factor in promoting brittle fracture.

Fig.1- a) Uncoated orbital cutting blade **b)** TiN coated orbital cutting blade **c)** Secondary electron image of the fracture surface of uncoated orbital cutting blade. **d)** Secondary electron image of the fracture surface of coated orbital cutting blade

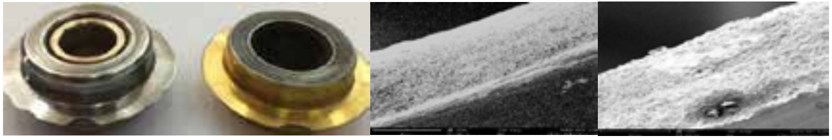

a **b** **c** **d**

4. Conclusion

In the first studies, it was found experimentally that TiN coated orbital cutting blade has %84 longer work life than uncoated blade. Experimental studies will continue with different samples with the same features and parameters.

Acknowledgement

This research has been supported by Konveyör A.Ş and Kapco Kaplama. Thanks to Mr. Metehan Demirkol and Advanced Materials Research Group (AMRG) from Yildiz Technical University for their technical support.

References

[1] A. Banish, “Selecting a tube cutting process Methods and applications , pros and cons,” *Tube Pipe Fabr.*, 2004.
[2] S. Dejesus, “Making the cut - Understanding rotary cutoff blades and extending blade life” Tube Pipe Fabr., pp. 6–8, 2019.
[3] H. V Puneeth and B. S. Smitha, “Studies on Tool Life and Cutting forces for drilling operation using Uncoated and coated HSS tool,” Int. Res. J. Eng. Technol., vol. 4, no. 6, 2017.
[4]W. Schintlmeister, W. Wallgram, J. Kanz, K. Gigl, “Cutting tool materials coated by chemical vapour deposition,” *Wear*, vol. 100, no. 1–3, pp. 153–169, 1984,

Microstructural and Mechanical Characterization of Spot Welds on AISI 430 Ferritic Stainless Steel Sheets

Maazouz MURAD[1,2], Allaoui OMAR[1], Belhocine ABDELGHANI[1], Djendel MOKHTAR[1,3]
[1]Amar Telidji University of Laghouat, [2]Mohamed Boudief University of M'sila,
[3]University Mohamed EL-Bachir El-Ibrahimi

Algeria

Abstract

Electric resistance spot welding is a simple and fast process that is widely applied on stainless steel sheets. During this process, a high electric current flows between the electrodes through the pressure parts. By the Joule effect, a nugget of molten solder is formed between the welded parts.

In this study, AISI 430 ferritic stainless steel sheets were spot welded by electrical resistance with different welding parameters. The effect of the welding current and the holding time during welding on the microstructure and the mechanical properties of the welded joints have been investigated. Tensile tests and microhardness measurements were carried out to assess the mechanical properties and the breaking characteristics of the welded joints.

The obtained results show that the nugget size, the tensile strength of the welded sheets and the microhardness distribution depend on the welding parameters. The microstructural study allowed us to explain the transformations produced during welding.

1. Introduction

Resistance spot welding on a flat counter electrode is widely used in the welding of difficult places such as cabinets or metal boxes or reinforcement ribs, etc.

The device often consists of a downward electrode which presents the work table; the workpiece can be placed directly on the table. The surface under the welding point is smooth so that no welding point and no deformation can appear which avoids re-polishing. The AISI 430 ferritic stainless steels (FSS) are the most important in the family of stainless steels because of their good ductility and resistance [1, 2]. The microstructure of ferritic stainless steel changes during spot resistance welding on a flat counter electrode. When the welding cycle is carried out, the solidification of the fused zones produces a very strong bond between the two welded parts. The merged and solidified areas are called weld nuggets and consist of three areas. They are classified into Fusion Zones (FZ), Heat Affected Zones (HAZ), and Base Metal (BM).

Fusion welding is always accompanied by excessive and undesirable grain growth in the Fusion Zone (FZ) and the Heat Affected Zone (HAZ). This leads to the appearance of grains and the precipitation of secondary phases, including components rich in chromium, which contributes to the decrease in toughness and ductility and to reduce the corrosion resistance of steel [3 -4].

The aim of this work is to study the effect of variations in welding current and time on the mechanical and metallurgical properties of welded joints in Ferritic Stainless Steel AISI 430.

2. Materials and Methods

0.8 mm thick AISI 430 FSS sheets were used as the base metal. The chemical composition of the 430 steel is given in Table 1.

Table 1. The chemical composition of AISI 430 (wt.%).

Cr	Ni	Mn	C	Si	S	Fe
17.5	0.141	0.769	0.12	0.471	0.01	Bal.

The welding operations were carried out by an RSW machine of PTDN-C-616 type with 80 kVA AC, and 50 Hz. The upper electrode is carried on an articulated arm equipped with a pneumatic jack of 1.8 KN, which ensures the pressure required for welding. The contact at the bottom is made on a copper table 15 mm thick, and not at a point, so the heat dissipates in the worktop. Figure 1 illustrates the assembly used for welding operations.

Various welding variables were used to obtain different sizes of welding nuggets. At the beginning, we carried out welding tests on control samples to have the best working parameters without bad welding and without expulsion. The main experimental parameters used in this work, are indicated in table 2. The upper electrode was kept unchanged during all the tests, and it is of (RWMA) type, class 2 with a 45 ° truncated cone and a diameter 4 mm front [5].

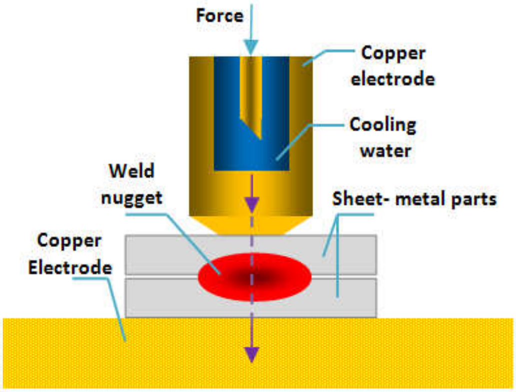

Figure 1. RSW welding on flat counter-electrode

Table 2. Parameters for welding similar AISI 430 FSS.

Weld schedule	Exp. N°	Current (KA)	Time (cycle)	Force (KN)	Electrode Tip (mm)
(a)	1	6.0	15	1.8	4
	2	6.4			
(b)	3	6.0	20		
	4	6.4			
(c)	5	6.0	25		
	6	6.4			

The welded samples were cut by EDM in the center of the weld nugget, then placed in a hard resin, polished and etched to observe the weld microstructures. To have the microstructures of the three zones of the nugget, we carried out a chemical attack according to standard ASTM E407-07 [6].

The microstructure and morphology of the different areas of the welds that appears during the welding cycle were observed using a LEICA DMLM metallurgical microscope optical microscope. Microhardness tests were used to evaluate the hardness profile on the transverse face of the nugget in the vertical direction, by applying a load of 100 g for 15 s on a Mutotoyu VH2 Vickers microhardness tester. Tensile shear test samples were prepared according to JIS Z 3136 [7]. Figure 2 shows the dimensions of the samples used in the tensile test. The tensile tests were carried out on a ZWICK / ROELLZ 050 machine. The values considered in this work present the average of five tests

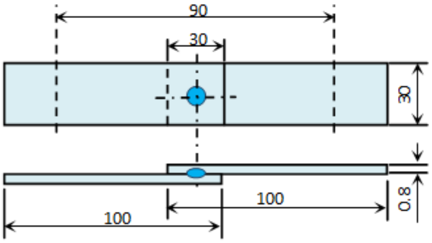

Figure 2. Dimensions of samples used in the tensile tests

3. Results and discussion

3.1. Microstructures

In the welding of Ferritic stainless steels (FSS), the thermal conductivity and the melting point are identical, and the nugget formed is often symmetrical when thermal energy is applied to the tips of the electrodes. The weld sections of the spot resistance welded joints undergo a temperature gradient indicating the metallurgical changes which occur during the formation of a weld. The typical microstructure of these welds reveals three large distinct microstructural zones: the Base Metal (BM), the Heat Affected Zone (HAZ) and the Molten Zone (FZ) Figure. 3a.

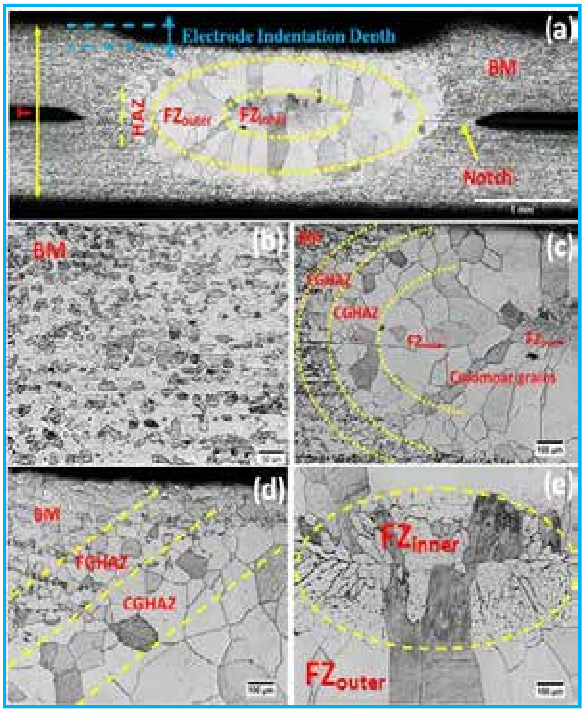

Figure 3. a) typical macrography of resistance spot welding; b) Base metal; c) gradient three zones HAZ, FZ and BM ; d) CGHAZ and FGHAZ ; e) ZF inner and outer.

The microstructure of the Base Metal (BM) is mainly composed of a ferritic phase with entirely fine grain, with an average size of about 5 to 10 µm (figure 3b), and characterized by vast fine precipitates of martensite grain boundaries. Depending on the temperature distribution (Figure 3d), the HAZ can be divided into:

- ❖ A coarse-grained heat affected area (CGHAZ), which is located in the areas immediately adjacent to the melted area. This zone is characterized by a significant growth of the equiaxed ferrite grains without precipitates, with a size between 200 and 300 µm.

- ❖ And a fine-grained heat affected zone (FGHAZ), bordering the BM zone [8]. This zone is relatively coarser than the BM zone, mainly composed of a ferritic phase with chromium carbide precipitates in the form of dispersed islands.

Likewise, the Fused zone (FZ) can be presented in two distinct regions in the weld nugget as shown in Figure 3e: the internal fusion zone having a fine dendritic morphology and the external fusion zone having a coarse dendritic morphology.

3.2. Microhardness

The microhardness profiles of the welded samples with a welding current of 6.0 and 6.4 kA and welding times of 15 to 25 cycles are presented in Figure 4. The obtained values confirm the structural modification during the welding process, where the current plays a key role in the development of microhardness during welding processes by RSW.

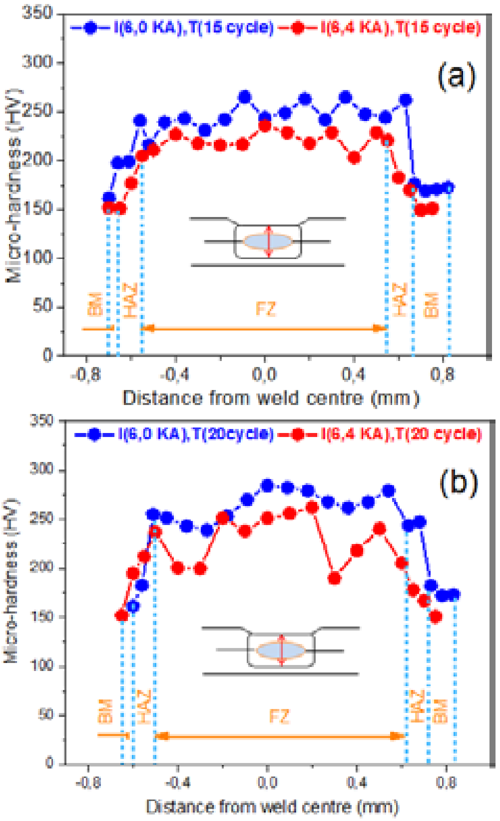

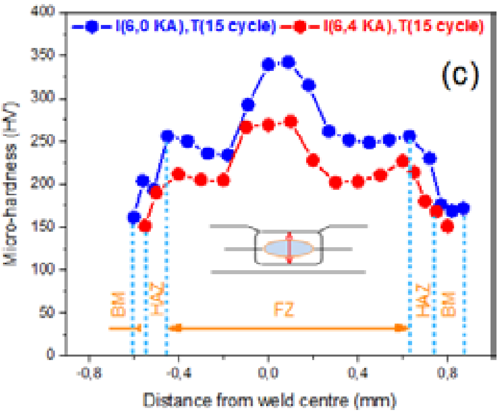

Figure 4. Microhardness profiles of welded samples with welding current of 6.0 and 6.4 kA: (a) 15; (b) 20 and (c) 25 cycles.

According to Figure 4, we can advance the following remarks and observations:

- ❖ The microhardness of different zones (FZ, HAZ and BM) obtained by 6.0 KA current are larger than those obtained by 6.4 KA current whatever the number of cycles. This allows us to say that the welding current does not have a great influence on the microstructure transformations of the welded zone. According to Pouranvari [9], as time and temperature increase, the cooling rate also increases, which leads to microstructures with higher micro-hardness.
- ❖ The shape of the microhardness profiles as a function of the welding current and the number of cycles makes it possible to say that the microhardness of the welding increases when the number of cycles increases.
- ❖ In all cases the microhardness of the Melted Zone (FZ) is larger than the Heat Affected Zone (HAZ) and the Base Metal (BM). Indeed, the hardness of each zone depends on its structure and on the grain size of this structure [10]. Figure 4c shows a hardness of 155 HV in the Base Metal (BM), followed by a hardness of around 250 HV for the Fine Grain Heat Affected Zone (FGHAZ). Then a slight drop in hardness which corresponds to the Coarse Grain Heat Affected Zone (FGHAZ) and which is justified by the enlargement of grains during cooling. The fluctuation of the microhardness values in this Heat Affected Zone is justified by the presence of precipitation of chromium carbides during the thermal cycle.
- ❖ A maximum microhardness of around 350 HV is obtained in the Fused Zone (FZ) after welding with a current of 6.0 KA and 25 cycles. The high hardness value in this area is justified by the rapid solidification immediately after its fusion.

3.3. Traction Results

The tensile curves as a function of the welding current and the number of cycles are presented in Figure 5. According to this figure, the tensile strength increases with the welding current. This is justified by the increase in the diameters of the nuggets formed [11, 12] because of the greater heat in the welded areas. From the results, we can say that the effect of the number of cycles is more important than the effect of the welding current.

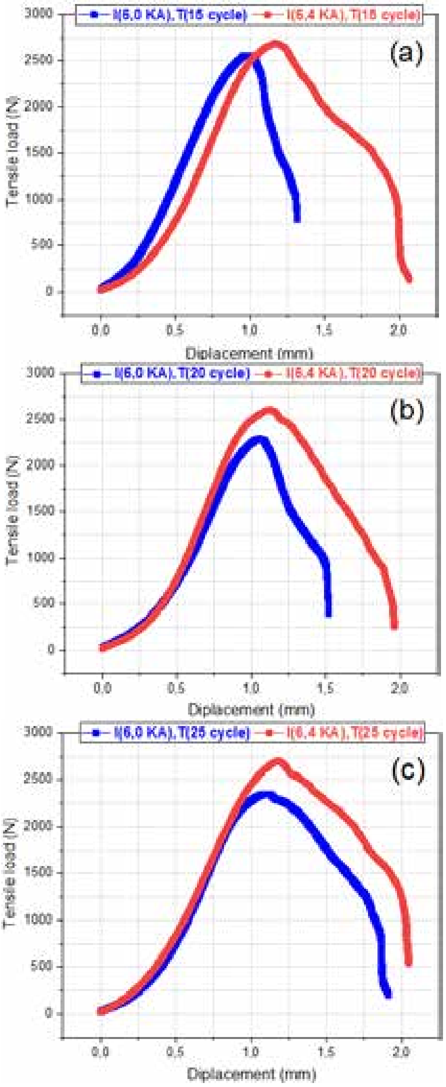

Figure 5. Tensile curves of under 6.0 and 6.4 KA welding currents, with: (a) 15; (b) 20; (c) 25 cycles.

4. Conclusion

After this work, we can advance the following conclusions:

- The Fused Zone (FZ) is constituted of two distinct regions in the weld nugget: an interior fusion zone with a fine dendritic morphology and an external zone with a coarse ferritic columnar structure.
- When the current increases the hardness decreases. On the other hand, when the number of cycles increases the hardness increases.
- The increase of the nuggets size during welding is accompanied by an increase in mechanical strength (a strong bond between the sheets).

5. References:

[1] Amuda, Moh, and S. Mridha. "Microstructural features of AISI 430 ferritic stainless steel (fss) weld produced under varying proc."*International Journal of Mechanical and Materials Engineering* 4, no. 2 (1970)

[2] S. Zaman, M. A. Khattak, and M. N. Tamin, "Akademia Baru Effects of Welding on the Microstructural Properties of AISI 430 Ferritic Stainless Steel Akademia Baru," vol. 1, no. 1, pp. 25–32, 2018.

[3] Amuda MOH, Mridha S. Microstructural features of AISI 430 ferritic stainless steel weld produced under varying process parameters. International Journal of Mechanical and Materials Engineering.2009; 4:160-166.

[4] C. N. Gonçalves, G. Mendes, D. A. Carvalho, J. S. Siqueira, and R. Â. Renzetti, "Influence of Nb Content on Sensitization and Pitting Corrosion of Welded AISI 430 Ferritic Stainless Steel," vol. 6973, pp. 1–10, 2019.

[5] J.R. Davis, B.R. Sanders (Eds.), Welding, Brazing and Soldering, Metals Handbook, ninth ed., vol. 6, American Society for Metals, Metals Park, OH, 1983, pp. 525–534.

[6] A. Standard, "E407-07: Standard Practice for Micro-etching Metals and Alloys,"*ASTM Int. West Conshohocken, PA*, vol.11, November,pp.1–21, 2012.

[7] Z. Al, M. Si, A. Coated, and S. Sheets, "Welding of SuperDyma," 2012.

[8] M. Alizadeh-Sh, S. P. H. Marashi, and M. Pouranvari, "Resistance spot welding of AISI 430 ferritic stainless steel: Phase transformations and mechanical properties," *Mater. Des.*, vol. 56, pp. 258–263, 2014,

[9] M. Pouranvari, "On the failure mode of resistance spot welded HSLA 420 steel," *Arch. Metall. Mater.*, vol. 58, no.1, pp.67–72, 2013, doi: 10.2478/v10172-012-0152y.

[10] M. Pouranvari and S. P. H. Marashi, "Welding metallurgy of stainless steels during resistance spot welding Part I : fusion zone," vol. 20, no. 6, pp. 502–511, 2015, doi: 10.1179/1362171815Y.0000000015.

[11] Jamasri MN, Ilman R, Soekrisno, Triyono. Corrosion Fatique Behaviour of RSW Dissimilar Metal Welds Between Carbon Steel and Austenitic Stainless Steel with Different Thickness. Procedia Engineering, 10: 649-654. 2011.

[12] N. Charde, "Spot Weld Growth on 304L Austenitic Stainless Steel for Equal and Unequal Thicknesses," *Casp. J. Appl. Sci. Res.*, vol. 1, no. 11, pp. 83–91, 2012.

The Optimization of Super Impact MIG Welding Process of ETIAL 171 Alloy Diameter Parts Produced By Die Casting

Hafizittin Hakan YUDAR, Ahmet ÇALIM, Deniz KARABULUT, Güliz TURHAN, Gizem KAPLAN

Demircioğlu Şase A.Ş.

Turkey

Abstract

The Lighten of vehicles requires significant development of the production process, especially for the development of aluminum alloy-intensive vehicles, the assembly and assembly of aluminum alloy structures. Aluminum's widely used series in the automotive industry; 6xxx and 7xxx series for body profiles, 3xxx series for the parts that require sealing and rims, 5xxx series for parts and axles that form the chassis and frame. In this study, pulse metal inert gas (MIG) welding-brazing is used to weld cast Etial 171 alloy products. The main objective of this study is to develop optimum weld process parameters for pieces of Etial 171 aluminum alloy. The factors selected to understand the effect of welding process parameters on the mechanical properties and welding penetration include power input (torch speed, voltage, current, wire feed), pulse frequency and gas flow rate. The filler wire used for this research is AlSi and has a constant thickness (1.2 mm). The effect of the welding grooves, welding current, gas flow rate and wire feed rate on mechanical properties were investigated. The joint strengths and weld penetrations are measured for various operating ranges of weld factors. Depending on joint strength and weld penetration, the best welding process factors were determined.

1. Introduction

Aluminum and its alloys are widely used in the assembly line of various industrial sectors, due to its easy thermal and electrical conductivity, low density, high strength and good corrosion resistance, as well as easy supply and economy [1,2]. Aluminum alloys find wide applications in automobile, aerospace, rail vehicles, bridges, ship transport, and high-speed ships due to their low density and high strength / weight ratio [1,3]. Aluminum alloys also have good fracture toughness at low temperatures and are antimagnetic. Some aluminum alloys can compete with some steels, show a tendency towards lower notch toughness and questionable fatigue life.

The different joining methods are preferred for the assembly of aluminum and alloys according to the areas where it is used [3,4]. One of these joining methods is the welding. Welding methods attract more attention than other methods due to their features such as the practical application, the use capability, the high joint reliability and the leak-proof [3,4]. In all case, the welding is the primary method of assembly, which always represents a major challenge for designers, technologists and manufacturers. The most preferred the methods are arc welding, metal inert gas (MIG) welding, tungsten inert gas (TIG) welding, flux arc welding and friction stir welding [5,6].

In particular, welding of aluminum alloys with high strength values is made easily and economically by MIG welding methods [7,8]. However, the welding quality is affected by the welding method and parameters (welding channels, welding voltage, gas flow rate and wire feed rate) [7–9].

In this study, the feasibility of AlSi (Etial 171) alloy products used in the manufacturing of parts of the air suspension system used in the automotive industry with MIG welding method at different voltage and different wire feed rate was investigated. Tightness checks are carried out to determine whether there are leakage in the weld areas of the samples. The effects of welding parameters on the tensile strength, fatigue strength, and hardness of welding joints were experimentally investigated.

2. Experimental Procedure

The major part of this study was conducted on two pieces aluminum alloy with 212mm body and 194.8mm bottom plate, which are air suspension piston parts. The chemical compositions of the base materials (Etial 171) used in this study are seen in Table 1.

Table 1. Chemical composition of Etial 171

Si	Fe	Cu	Zn	Mn	Mg
9.11	0.39	0.03	0.02	0.03	0.31

Experimental samples, 500 x 500 x 140 mm and 500 x 500 x 300 size Etial 171 Aluminum alloy were poured into the steel mold and in the figure 1 were obtained the bottom plate and body. The molded parts were checked and the surfaces were cleaned before welding. The bottom plate was placed on the body after the body of sample was placed in the sample holder of welding machine.

Figure 1. The bottom plate (a) and the body (b) for Alüminum piston

The parts were welded using MIG welding process super pulse method with the welding wire of diameter 1.2 mm. The chemical composition and mechanical properties of base metal and welding wire were tabulated in tables 2 and 3 respectively.

Table 2. The chemical composition of the wire material

C (%)	Si (%)	Mn (%)	P (%)	S (%)
0.07	0.83	1.48	0.017	0.02

Table 3. The mechanical properties of the wire material

Yield Strengh (MPa)	Tensile Strength (MPa)	Elongation (%)
430	540	28

In this MIG welding process, an electric arc was established among a consumable electrode (welding wire) and the work-piece. The shielding gas which prevents the weld zone from atmospheric contamination, used for this experiment was argon which is the high purity (99.999%) as buffer gas with the constant flow rate of 17 liters/minute. After placing the work piece to be welded in the workstation through proper fixture, welding process is initiated by setting of pre-flow time which is 0.5 s, initial conditions, main conditions, crater conditions, post-flow time which is 1 s. The angle chosen for the welding torch is 75 degrees to the work piece with the distance of 10mm between the tip and the work piece.

With the power source ESAB Aristo MIG 4004i Pulse, the setting of the parameters namely voltage, current, wire feed rate, welding method and gas rate could be achieved separately with the individual adjustment mode through the Multifunctional teach pendant (ARISTO U82 Controller). The automatic feeding mechanism of the electrode wire based on the self-adjusting amperage setting keeps the arc length constant up to a certain distance between the welding torch and the work piece. Synergic + Super Pulse feature could be used to control the welding process with U82 Control panel. Thus, the solidification of the source was ensured by the time between each pulse current. Welding fumes of the alloys are removed by fumes extractor placed nearer to the welding torch.

3. Result and Discussion

Welding wire rate and voltage parameters are used in welding of body and bottom plate. Welding wire rate and voltage parameters are as in Table 4. MIG welding was carried out with a wire feed speed of 5.5 m / min using

1.2 mm diameter welding wires as filler to join the alloys. In addition, argon gas was used for protection in welding method. The image of the sources made with the parameters in Table 4 is shown in Figure 2. The reason for using different welding voltage is to avoid overflows in the welding area and burning of the welding seams.

Table 4. Welding process parameters and levels.

Samples	Wire Feed Rate (m/min)	Welding Voltage (V)
S-1	5,5	23,1
S-2	5,5	22,5

Figure 2. The welding joints of S-1(a) and S-2(b)

The leakage tests of the welded samples were carried out in the leakage test machine which is a special design, shown in figure 3.

Figure 3. Leakage tests

The welding strength of the product welded with the breaking test was tested. For the compression test, a breaking test machine specially developed for the pistons was used.

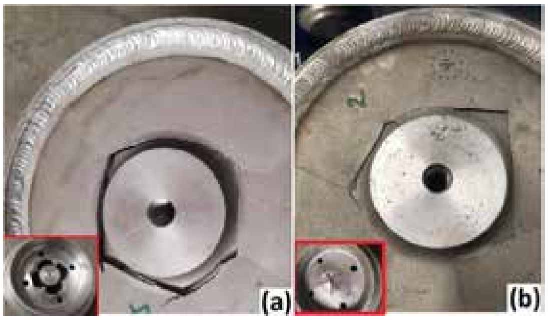

Figure 4.

As a result of this test, breakage occurred in the buffer zone, not in the welding zone. S-1 was broken at 10.62 tons and S-2 at 13.19 tons. The force-displacement plot of the samples is as given in figure 4.

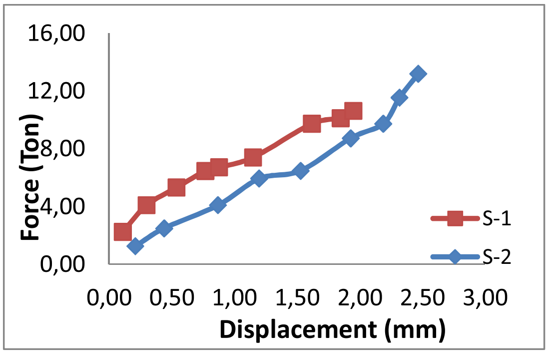

Figure 5. Force-Displacement for Alumium piston

For each samples, the welding cutaway views were taken with the ISM PM200S digital microscope and shown in figure 6.

Figure 6 were shown the source penetration in the samples and the welding status of the body and bottom plate products. Compared to S-1, S-2 has been shown to have less space between the body and the bottom plate, more welding area, more welding cap ratio, and more penetration of the weld to the body.

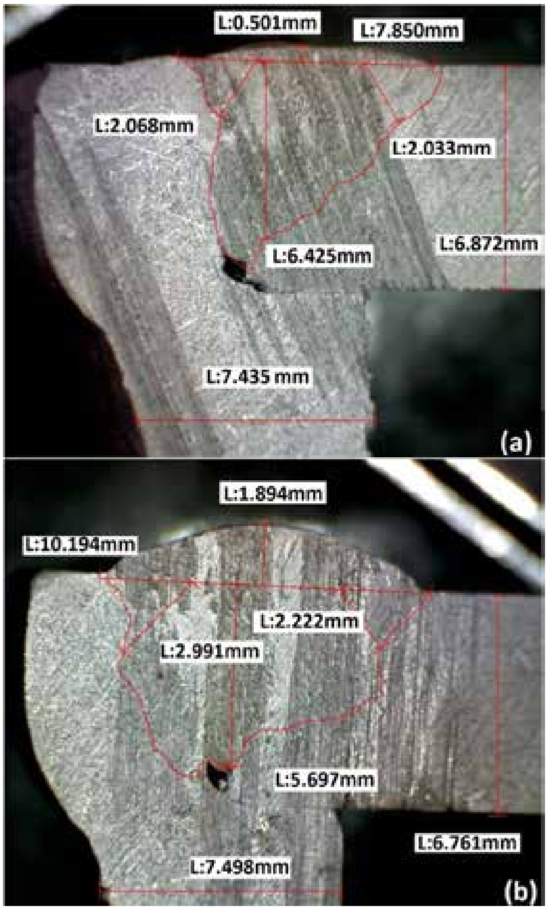

Figure 6. Zones in the weld cutaways

4. Conclusion

In this study, welding of body and sub-base piston parts obtained from Etial 171 Aluminum alloy with MIG has been investigated. In this welding, the welding wire advance speed was held at different voltages by keeping it constant at 5.5 m / min. After the welding process, the leak test was carried out and both samples were found to be leak proof. In order to measure the welding strength, an aluminum piston breaking test was performed. With this test, it was observed tthat the welding regions are based on at least 11 tons. The cross section was taken from the welding area and the welding structure was examined more closely with a microscope. In this context, it was understood that S-2 was the best source between the two samples. With this examination, it was seen that S2 sample had a better welding structure than S1.

Referances

[1] X. Cao, W. Wallace, C. Poon, J.-P. Immarigeon, Research and Progress in Laser Welding of Wrought Aluminum Alloys. I. Laser Welding Processes, Materials and Manufacturing Processes. 18 (2003) 1–22. https://doi.org/10.1081/AMP-120017586.

[2] F. Nie, H. Dong, S. Chen, P. Li, L. Wang, Z. Zhao, X. Li, H. Zhang, Microstructure and Mechanical Properties of Pulse MIG Welded 6061/A356 Aluminum Alloy Dissimilar Butt Joints, Journal of Materials Science & Technology. 34 (2018) 551–560. https://doi.org/10.1016/j.jmst.2016.11.004.

[3] Y. Zhang, J. Huang, Z. Cheng, Z. Ye, H. Chi, L. Peng, S. Chen, Study on MIG-TIG double-sided arc welding-brazing of aluminum and stainless steel, Materials Letters. 172 (2016) 146–148. https://doi.org/10.1016/j.matlet.2016.02.146.

[4] H.T. Zhang, J.Q. Song, Microstructural evolution of aluminum/magnesium lap joints welded using MIG process with zinc foil as an interlayer, Materials Letters. 65 (2011) 3292–3294. https://doi.org/10.1016/j.matlet.2011.05.080.

[5] I. Sevim, F. Hayat, Y. Kaya, N. Kahraman, S. Şahin, The study of MIG weldability of heat-treated aluminum alloys, Int J Adv Manuf Technol. 66 (2013) 1825–1834. https://doi.org/10.1007/s00170-012-4462-z.

[6] A. Patel, Effect of variable process parameter of MIG welding on aluminium alloy 6061-T6, (2018) 4.

[7] A.M. Milani, M. Paidar, A. Khodabandeh, S. Nategh, Influence of filler wire and wire feed speed on metallurgical and mechanical properties of MIG welding–brazing of automotive galvanized steel/5754 aluminum alloy in a lap joint configuration, Int J Adv Manuf Technol. 82 (2016) 1495–1506. https://doi.org/10.1007/s00170-015-7505-4.

[8] J. Li, H. Li, H. Wei, Y. Gao, Effect of torch position and angle on welding quality and welding process stability in Pulse on Pulse MIG welding–brazing of aluminum alloy to stainless steel, Int J Adv Manuf Technol. 84 (2016) 705–716. https://doi.org/10.1007/s00170-015-7734-6.

[9] D. Ye, X. Hua, C. Xu, F. Li, Y. Wu, Research on arc interference and welding operating point change of twin wire MIG welding, Int J Adv Manuf Technol. 89 (2017) 493–502. https://doi.org/10.1007/s00170-016-9110-6.

New Ideas in X-Ray Diffractive Characterization of Nanomaterials

Hande ÖZTÜRK[1], I. Cevdet NOYAN[2]
[1]Özyeğin University, [2]Columbia University
[1]Turkey, [2]USA

1. Introduction

The potentials of facilitating nanomaterials in novel materials design and of enhancing existing materials in the form of advanced composite systems are attracting increasing attentiton to nanomaterials research. Due to the strong correlation between physical properties of nanomaterials and their sizes as well as atomic configurations, manufacturing these materials requires utmost control and precision. Hence developing accurate, reliable and robust characterization methods targeting nanomaterials is becoming and even larger component of manufacturing processes. X-ray diffraction, being the gold standard of non-destructive characterization methods, is increasingly used in nanocharacterization practices and the resulting data are processed under the assumptions of regular crystalline material properties. This increases the uncertainty in interpretation of x-ray diffraction data from nanomaterials and results in inaccurate conclusions.

2. Materials and Methods

In this talk, we will present a computational methodology from which realistic diffraction data from monodispersed crystalline nanopowders with partcle sizes below 20 nm are generated [1,2]. Based on the processing of these idealized diffraction datasets, we will show how existing X-ray analysis constructs are not applicable for small nanocrystalline powders and discuss potential ways to solve the problem of nanodiffraction [1,2,3].

3. Conclusion

Analysis of diffraction data measured from nanocrystalline powders needs to be done with extreme care. Existing crystallographic analysis algorithms such as Rietveld refinement method are based on the presence of infinitely long periodic stacks of atoms in the diffracing materials which is an invalid assumption for the description of nanocrystalline powders especially when the individual particle size is below 20 nm. Therefore, computer simulations of expected diffraction data from such small nanocrystalline powders have the potential to develop appropriate diffraction analysis methodologies and quantify uncertainties in structural parameters derived from existing mehods. Without such effort, measurements from x-ray diffraction experiments with nanocrystalline powders are underutilized or misinterpreted.

References

[1] Xiong S., Öztürk H., Lee SY., Mooney PM., and Noyan IC.,*The nanodiffraction problem*, Journal of Applied Crystallography, 51(4), 2018.

[2] Öztürk H., Yan H., Hill JP., Noyan IC., *Correlating sampling and intensity statistics in nanoparticle diffraction experiments, Journal of Applied* Crystallography, 48(4), 2015.

[3] Fewster PF., *A new theory for X-ray diffraction*, Acta Crystallographica A70: 257-282, 2014.

A Microstructural Investigation of 1 Mol% H_3BO_3 and 0.5 Mol% MnO Added ZnO Ceramics

Berat YÜKSEL PRICE, Gökhan HARDAL
Istanbul University-Cerrahpaşa
Turkey

Abstract

The effects of 1 mol% H_3BO_3 and 0.5 mol% MnO additions on the microstructure properties of ZnO ceramics were investigated. Undoped ZnO (composition code Z), 0.5 mol% MnO doped ZnO (composition code M) and 0.5 mol% MnO-1 mol% H_3BO_3 doped ZnO (composition code MB) compositions were prepared by the conventional ceramic processing techniques. The samples were sintered at 1100 °C for 3 hours. The bulk density of the sintered samples was calculated from their weight and dimensions. The microstructure of samples was investigated using an optical microscope. The relative bulk density of undoped ZnO, 0.5 mol% MnO doped ZnO and 0.5 mol% MnO-1 mol% H_3BO_3 doped ZnO samples sintered at 1100 °C for 3 hours were obtained as 77, 83 and 95%, respectively. The average grain size of 4.9 and 8.2 µm was observed for the undoped ZnO and 0.5 mol% MnO doped ZnO samples sintered at 1100 °C for 3 hours. The average grain size increased to 41 µm with the addition of H_3BO_3. This result indicated that the addition of H_3BO_3 promotes the grain growth of MnO doped ZnO ceramics by forming a liquid phase during sintering.

1. Introduction

ZnO shows the n-type semiconductivity. It is a wide direct-gap semiconductor (Eg=3.3 eV). It is widely known that the electrical properties change significantly with the microstructure of ZnO-based varistors. Also, the control of grain size, which is affected by the content of the compositions and sintering conditions, is an essential parameter to obtain desired microstructural properties. In the present study, the dual doping effect of MnO and B_2O_3 additions on the microstructural properties of ZnO is investigated.

2. Materials and Methods

ZnO, MnO and H_3BO_3 powders were used to prepare the compositions by the conventional ceramic processing techniques. Powder mixtures were ball milled for 6 hours and dried in the oven at 110 °C. Granulated powders were pressed under a pressure of 100 MPa to produce a disc-shaped sample. The samples were sintered at 1100°C for 3 hours. The bulk density of the sintered samples was calculated from their weights and dimensions. The microstructure features of samples were analysed using an optical microscope. The grain sizes of the etched samples were determined from optical images by the linear intercept method [1].

3. Conclusion

The bulk density of Z, M and MB samples sintered at 1100°C for 3 hours were 4.3, 4.7 and 5.3 g/cm^3, respectively.

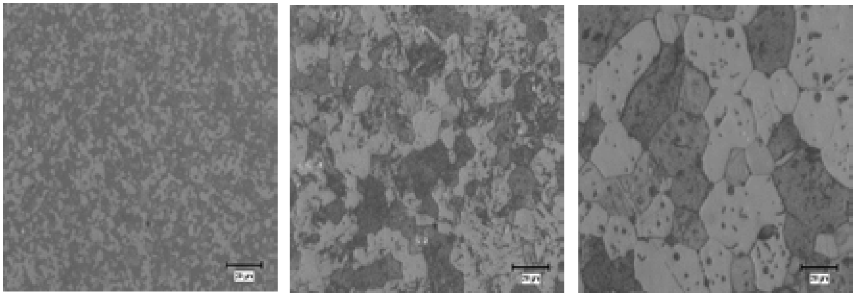

Figure 1. Optical microscope images of Z (left side), M (middle) and MB (right side) samples sintered at 1100°C for 3 hours.

The optical microscope images of samples sintered at 1100°C for 3 hours was shown in Figure 1. The average grain size of samples was tabulated in Table 1. As can be seen in this table, the grain size of M sample sintered for 3 hours was higher than Z sample. In addition, the grain size increased dramatically with the addition of 0.5 mol% H_3BO_3. This indicated that the favourable effect on the grain growth of liquid phase resulting from H_3BO_3 additive.

Table 1. Average grain size of Z, M and MB samples sintered at 1100°C

Grain Size (µm)		
Z	**M**	**MB**
4.9	8.2	41

Acknowledgment

This work was supported by the Scientific Research Projects Coordination Unit of Istanbul University. Project number 38186. It was partially based on a MSc. thesis pursued by Gökhan Hardal.

Reference

[1] M.I. Mendelson, Journal of the American Ceramic Society, 52 (1969) 443–446

Preparation and Structural Characterization of $NiMn_2O_4$ Ceramics

Berat YÜKSEL PRICE, Gökhan HARDAL
Istanbul University-Cerrahpaşa
Turkey

Abstract

In this study, the electrical and microstructural properties of $NiMn_2O_4$ NTC thermistors was investigated. These properties depend on many factors such as the chemical composition, and production routes (such as ball milling time, calcination, sintering conditions). The $NiMn_2O_4$ ceramics were produced by the conventional ceramic processing technique. The bulk density of sintered sample was calculated using the Archimedes method. The phases in the sintered sample were determined by X-Ray diffraction method. The microstructure of sample was observed using a scanning electron microscope on fracture surfaces. The electrical resistance was measured, the material constant "B" and the sensitivity coefficient "α" values were calculated.

1. Introduction

There are two types of thermistors: PTC (positive temperature coefficient) and NTC (negative temperature coefficient). The electrical resistance of NTC thermistors decreases with increasing temperature. Nickel manganite, $NiMn_2O_4$, is widely used as an NTC thermistor material and shows good electrical properties. The advantages of nickel manganite NTC thermistors are high temperature sensitivity, low cost, and fast response. Nickel manganite thermistors exhibit the spinel-type crystal structure with the general formula AB_2O_4 [1]. The electrical conduction of nickel manganite takes place with electron hopping mechanism, depends on an electron jump between the Mn^{3+} and Mn^{4+} ions located on the octahedral sites. The aim of this study is to understand electrical and microstructure properties of NTC thermistors sintered at high temperature.

2. Materials and Methods

$NiMn_2O_4$ ceramics are produced using the conventional solid-state reaction method. This method has some advantages such as being non-polluting and obtaining accurate stoichiometry. The Mn_2O_3 and NiO powders mixed with ethanol, dried at 110 °C and were calcined at 900 °C for 2 hours. The disc-shaped sample were sintered at 1300 °C for 5 hours. The phases in the sintered sample were determined by X-ray diffraction method. The microstructure of sample was observed using a scanning electron microscope. The bulk density of sintered sample was calculated using the Archimedes principle. The electrical resistance was measured in a temperature programmable furnace between 25 and 85 °C in steps of 0.1 °C. The resistivity at room temperature (ρ_{25}, Ω.cm), material constant (B, K), and the sensitivity coefficient (α, %/K) values were calculated for the NTC thermistors.

3. Conclusion

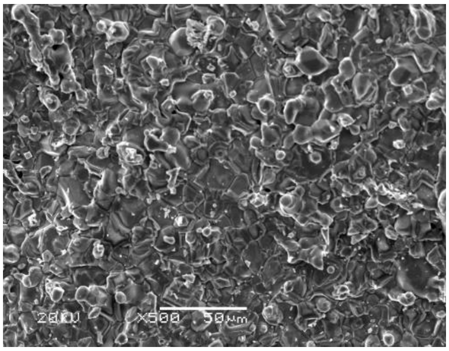

Figure 1. SEM micrograph of the $NiMn_2O_4$ sample sintered at 1300°C.

The cubic spinel phase as the main phase, a small amount of nickel-rich and tetragonal spinel phases were determined by XRD diffraction analysis in the $NiMn_20_4$ sample sintered at 1300 °C for 5 hours. The bulk density value of the $NiMn_2O_4$ sample was calculated as 4.84 g cm^{-3}. SEM micrograph of sample is shown in Figure 1. The electrical resistance at room temperature was measured as 937 Ω, the electrical resistivity was also calculated as 4430 Ω.cm. The material constant from 25°C to 85°C ($B_{25/85}$) and sensitivity coefficient were found 4017 K and 4.523 %/K.

Acknowledgment

This study is supported by TÜBİTAK (The Scientific and Technical Research Council of Turkey). Project Number: 3001-114M860. We would like to thank TÜBİTAK for its financial support.

References

[1] B. Issa, I.M. Obaidat, B.A. Albiss, Y. Haik, Int. J. Mol. Sci., 14 (11) (2013), 21266-21305

Experimental Study of the Solidification of Sn-10wt.%Pb Alloy Under Forced and Natural Convection in Benchmark Experiment

Abdelhafid ABDELHAKEM[1], Lakhdar HACHANI[1], Kader ZAIDAT[2], Yves FAUTRELLE[2]
[1]Université Amar Telidji de Laghouat, [2]CNRS Grenoble Institute of Technology
[1]Algérie, [2]France

Abstract

A comparative research was performed on a benchmark experiment model under the same experimental conditions between natural convection and forced convection at different times during the solidification of the metal alloy (Sn-10 wt. %Pb).The originality of the present study is to examine the effect of forced convection driven by a traveling magnetic field (TMF) (electromagnetic stirring in the opposite direction to natural convection). The domain is a 3D rectangular ingot (100 * 60 * 10 mm), the temperature difference betweet the two lateral sides is 40 K. Experimental findings consist of instantaneous temperature maps given by a lattice of 50 thermocouples in order to calculate the instantaneous temperature.

1.Introduction:

The study of solidification of metallic alloy is increasingly important, as the properties of most alloys depend largely on the degree of control that can be applied during solidification. One of the major problems inherent in solidification is the non-uniform distribution of the concentration of the solutions. These variations in concentration, also known as segregations, appear at different scales in a solidified sample: microscopic, mesoscopic (freckles), and/or ingot (macrosegregation)[1, 2]. Of course, these differences in concentration have major effects on material properties.Therefore, Minimizing segregation is therefore important with regard to performance of alloys. It appears that the gravity role may be prominent for segregation evolution and may establish unexpected patterns of concentration. One solution against this effect is the imposition of a forced convection driven by electromagnetic stirring.

The aim of the present work is to experimentally investigate the effect of different types of electromagnetic stirring on the solidification of a model alloy (Sn-10wt. percent Pb). In terms of temperature background, velocity field, structures and solvent distribution in the solid sample, we analyze the effect of the forced convection driven by a moving magnetic field on the solidification process. The theory of experimentation is similar to the Hebditch and Hunt one[2], with particular focus on monitoring initial and thermal boundary conditions and obtaining reproducible quantitative measurements[19, 21]; One case of stirring was investigated in this study: in the opposite direction to the natural convection.

2. **Experimental process:**

The experimental apparatus is represented in Fig. 1. The experiment consists of solidifying a rectangular ingot of Sn–10 wt. percent Pb alloy using two lateral heat exchangers, allowing the heat flux to be collected from one or two vertical sides of the specimen. The domain is a rectangular ingot (100 60 10 mm) of quasi two dimensions. The DT difference between the two lateral sides is 40 K, and the cooling rate CR = 0.03 K/s. The instrumentation consists in recording the instantaneous temperature maps each second The instrumentation consists of recording the maps of the instant temperature every second by means of a 50 thermocouple lattice. An electromagnetic stirrer is placed beneath the sample to generate forced convection during the solidification process, which will be described later. To have some flow estimate, ultrasonic Doppler velocimetry (UDV) method measurements of the velocity field in a Ga – In – Sn pool with the same dimensions were taken and transposed to the tin – lead alloy case prior to solidification. Post mortem segregation patterns were obtained by X-ray radiography, and confirmed by quantitative analysis of the solut distribution obtained by chemical process coupled with scientific ICP (Inductively Coupled Plasma). Details of both the facility and the experimental method can be found at [9,10].

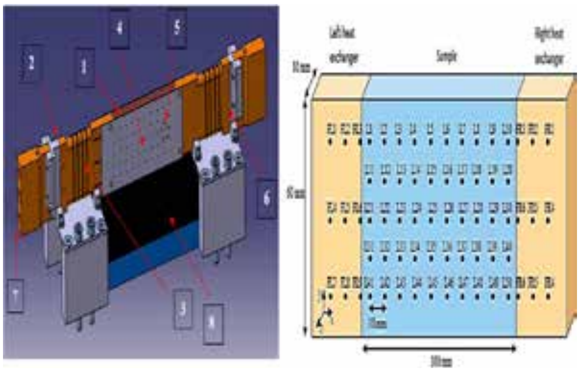

Fig. 1. (a) Schematic view of the experimental facility. 1. Sn–Pb sample, 2. Left ''cold'' heat exchanger, 3. Resistance, 4. Stainless steel crucible, 5. Thermocouple position matrix, 6. Right ''hot'' heat exchanger, 7. Water cooling system, 8. Linear motor. (b) Sketch of the sample surrounded by the two lateral heat exchangers. The location of the lateral thermocouple lattice (L1 to L50) welded on one of the largest surfaces of the crucible is also shown.

4. Temperature field evolution during solidification:

The entire experimental process consists of five steps, as illustrated in Figure 2, First smelting and then temperature stability for fluid pool homogenisation. Then we add a difference (HT) between the thermal initiators, the second temperature stability and the sample's final cooling.

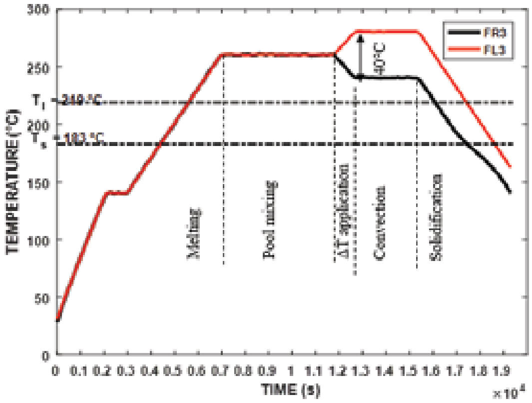

Fig. 2. *Description of the experimental protocol. Time evolution of imposed heater temperature during solidification of Sn–10 wt.%Pb alloy without electromagnetic stirring . Applied temperature difference (ΔT) = 40 K, cooling rate CR = 0.03 K/s. FR3 and FL3 correspond to thermocouples located on the side of the heat exchangers as shown in Fig.1*

In the present experimental study we are primarily interested in analyzing the effect of forced convection on the solidification process powered by a moving magnetic field. A linear motor mounted 5 mm under the bottom wall of the stainless steel crucible generates the moving magnetic field as shown in Fig. 1.a . The next section will provide a detailed characterisation of the magnetic field as well as some indication of the corresponding flow. During the entire experimental process, that is from the beginning of the sample melting to the end of the solidification, the electromagnetic force is imposed. It investigated four types of electromagnetic stirring conditions (see Fig. 3)

Case I: the melt solidifies under natural convection only. The temperature difference between the two lateral sides of the sample produces a clockwise eddy flow (Fig. 3.a), where the cold wall is located on the right.

Case II: the experimental conditions are the same as in Case I, but the electromagnetic force direction is reversed with respect to natural convection as presented in Fig. 3.b.

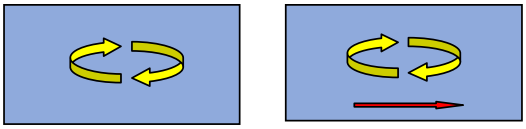

Case I **Case II**

Fig 3. The different electromagnetic stirring modes compared to the direction of thermosolutal convection

5. Results and discussions:

5.1.Temperature field evolution during solidification

During cooling, the temperature contours and the thermal gradients are shown in the next section at three selected times (Fig. 3). The experimental conditions are: some = 40K. At the initial point, the difference in temperature between the two sides of the heat exchangers corresponds to Th = 280 ° C in the left wall temperature and Tc = 240 ° C in the rightwall.Note that there is a thermal contactresistance between the heat exchangers and the walls of thesample.

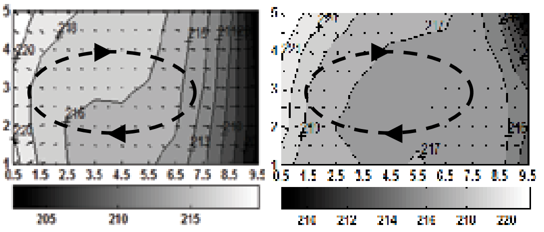

Case I Case II

(a) t = 9min

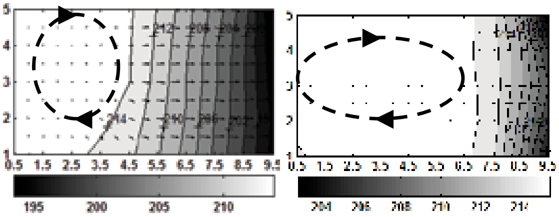

Case I Case II

(b) t =15 min

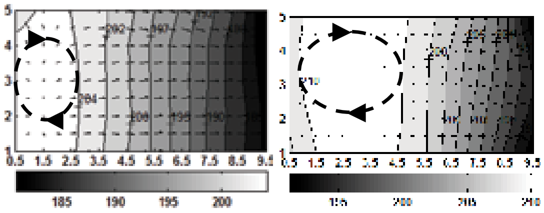

Case I Case II

(c) t = 24min

Fig. 4*. Instantaneous temperature maps with superimposed local temperature gradient vectors* ($-\vec{\nabla}T$) *for the four solidification experiments at (a)* t_1 *= 9 min, (b)* t_2 *= 15min and (c)* t_3 *= 24min. The experimental conditions are: Sn-10wt%Pb alloy, ΔT = 40 K, CR = 0.03 K/s, inductor current I = 8.2A*

In t=9min. We found that Case II (stirring in the opposite direction of convection) significantly modifies the flow configuration. This is shown by isotherm deformation, indicating that a vortex emerges in the opposite direction as regards thermosolutal convection.

Results are shown at t2 = 15min in Fig. 4.b As regards DT, we find a similar pattern to that of the previous period. In fact, in Cases II through IV, DT decreases from 22.6 K without EM stirring to 16.0 K, 13.8 K and 13.9 K respectively. Regarding the evolution of the minimum temperature Tmin from 193.5 ° C to 200.4 ° C, 202.8 ° C and 203.4 ° C a substantial increase was noted. The maximum Tmax temperature varies just slightly from 216.1 ° C to 217.0 ° C. On the map of the Case III temperature field, a second solidification front was observed at the bottom left corner. This is because the temperature of the left heat exchanger drops below TL, while the bulk temperature is still above TL due to the latent heat released in the equiaxed area.

Illustration. 4.c corresponds to t3 = 24mn for moment. We noticed the same behavior as in the instants chosen previously. With one exception DT dropped from 25.9 K to 20.9 K. Indeed the difference in temperature in Case II (DT = 24.0 K) is higher than in Cases III and IV. Tmin and Tmax values are higher than those that correspond to the natural case of convection (Case I). The isotherm deformation in the stirred cases and the low local temperature gradient values clearly indicate the operation of electromagnetic stirring in the last liquid. Temperature maps however clearly show the existence of isotherms on the left side, indicating a temperature level ranging from 204 to 210 ° C, particularly in cases II and III. This corresponds to a degree of undercooling of 24.14 and 18.14 K below the liquid temperature (TL = 228.14 ° C). Indeed an estimated calculation of this alloy's undercooling, presented in the Hachani et al.[21] work, provides a new range between 0.5 and 10 K. But we credit the success of these isotherms to the development of a second front of the left solidification. This conclusion is quite consistent with the shrinkage positions which suit the last solidified liquid presented in the next section (5).

5.2. Effect of electromagnetic stirring on grain structures

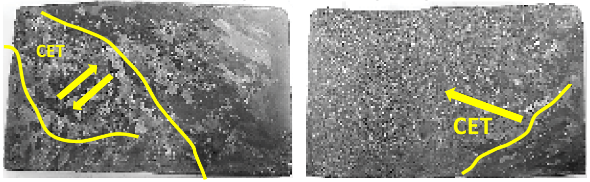

Case I (a) Case II(b)

Fig. 5. Macrostructure on the lateral plane of different ingots of Sn-10wt.%Pb. The experimental conditions are: temperature difference ΔT = 40 K, cooling rate CR = 0.03 K/s and the applied current intensity I = 8.2A. Four cases are presented: (a) Case I solidification under the effect of natural convection only (b) Case II solidification under the effect of electromagnetic stirring in the opposite direction to natural convection.

The procedure outlined in the work of Hachani et al.[21] revealed macrostructures of ingots obtained from four solidification experiments to assess the effect of various electromagnetic stirring modes on the final metallographic structure and grain size. Illustration. 5.A displays the Sn-10wt.%Pb solidification macrostructure under a thermosolutal convection effect only. We observe that, in this case, the dominant morphology of the macrostructure is columnar with an equiaxed zone at the end of solidification corresponding to the last liquid. The columnar-to-equiaxed transformation phase can be accounted for by the decrease in temperature gradient in the liquid bath, as shown by temperature maps in Fig. 9.A (Box I). The tilting of the columnary grains upwind is consistent with the normal convection direction. At the base of the ingot we notice a growth of a different oriented second columnar structure. A possible explanation is the effect of convection, as indicated by Fig, which supplies "cold" liquid to the bottom part of the ingot. 9. A. A. Note that column orientation in that region is supportive of the above argument.

The case of thermosolutal convection stirrings in the opposite direction is shown in Fig. 5.b. The structure consists essentially of equiaxed grains of fine quality. In the ingot bottom right angle is a small columnar area. It's important to remember that when we reversed the direction of stirring toward natural convection, the efficiency of electromagnetic stirring in refining the structure is significantly improved. Parallel to the mechanical fragmentation effect, this mode of stirring appears to have a major impact on the dendrite remelting process. EM stirring immediately produces an upward flow of lead-enriched liquid around the front of the columnar.

Conclusion:

Having regard to the experimental comparative study presented in this work, we may deduce some findings and general conclusions about the effect of various electromagnetic stirring modes applied to the solidification process, especially regarding the morphology of segregation.

1. The various morphologies of segregation are created substantially by fluid movement within the mushy region. Three different mechanisms will produce the movement:

- In the mushy zone, thermosolutal convection which carries the solute inside the mush.

- Electromagnetic stirring, which directly acts on the liquid phase in the mushy zone to produce fluid movement and transport of solute.

- Convection in the liquid region, which can cause differences in pressure along the solidification front, resulting in a flow within the mushy zone (interdendritic liquid) as in a porous medium. Stirring in the opposite direction to natural convection has demonstrated its efficacy in achieving the finest equiaxed structures on almost all ingots. This type of stirring incorporates the processes of remelting as well as mechanical fragmentation.

References

[1] A-M .Bianchi, Y. Fautrelle, J. Etay Italy 2004*Transfert Thermiques, first édition*, , page (5)

[2] L. Hachani, K. Zaidat and Y. Fautrelle 2016 Multiscale statistical analysis of the tin-lead alloy solidification process *Int. J. Thermal Sciences* 186-205.

[3] X. Wang, P. Petitpas, C. Garnier, J. P. Paulin and Y. Fautrelle 2007 A quasi two- dimensional benchmark experiment for the solidification of a tin-lead binary alloy *C. R. Mecanique*, 335 (2007) 336-341.

[4] X. Wang and Y. Fautrelle. 2009 An investigation of the influence of natural convection on tin solidification using a quasi-two-dimensional experimental benchmark *Int. J. Heat Mass Transfer*56245633.

[5] L. Hachani, B. Saadi, X. Wang, A. Nouri, K. Zaidat, A. Belgacem-Bouzida, L. Ayouni-Derouiche, G. Raimondi and Y. Fautrelle 2012 Experimental analysis of the solidification of Sn-3 wt%Pb alloy under natural convection *Int. J. Heat Mass Transfer,* 55 (2012) 1986-1996.

[6] R. Boussaa, O. Budenkova, L. Hachani, X. D. Wang, B. Saadi, K. Zaidat, H. Ben Hadid and Y. Fautrelle 2012 in:CFD Modeling and Simulation in Materials Processing, John Wiley & Sons*, Inc., Hoboken, NJ, USA* 163-170.

[7] L. Hachani, K. Zaidat and Y. Fautrelle 2016 Multiscale statistical analysis of the tin-lead alloy solidification process, *Int. J. Thermal Sciences* 186-205.

[8] R. Boussaa, L. Hachani, O. Budenkova, V. Botton, D. Henry, K. Zaidat, H. Ben Hadid and Y. Fautrelle 2016 Macrosegregations in Sn-3 wt%Pb alloy solidification: Experimental and 3D numerical simulation investigations *Int. J. Heat Mass Transfer* 680-690

[9] X.D. Wang, Y. Fautrelle 2009 An investigation of the influence of natural convection on tin solidification using a quasi-two-dimensional experimental benchmark, *Int. J. Heat Mass Transfer* 52 (23–24) 5624–5633.

[10] L. Hachani, B. Saadi, X.D. Wang, A. Nouri, K. Zaidat, A. Belgacem-Bouzida, L. Ayouni-Derouiche, G. Raimondi, Y. Fautrelle 2012 Experimental analysis of the solidification of Sn–3 wt.%Pb alloy under natural convection, *Int. J. Heat Mass Transfer* 55 (7–8) 1986–1996.

The Effect of Cooling Rate on the Mechanical Properties, Microstructure and Formation of Oxide Scale in Welding Wire Rod Grade for Submerged Arc Welding

Ahmet SAĞLAM, Erdi GÖNÜLALAN
İskenderun Demir ve Çelik A. Ş.
Turkey

Abstract

In the present work, influence of different cooling rate on the mechanical properties, microstructure and formation of easy to remove oxide scale in Welding Wire Rod Grade For Submerged Arc Welding during the process of wire rod rolling. It is aimed to optimize strength, microstructure and easily removable scale in S1 steel wire rod grade used as submerged welding wire. CCT / TTT diagrams were acquired by using JMatPro software transformation temperatures were determined. According to the diagrams obtained, wire rod produced with variable laying head temperatures (880 °C and 960 °C) in similar chemical compositions, were subjected to cooling with a cooling rate of 4,6 – 5,5°C/sec. The mechanical and microstructure results were examined after trial productions. The aimed mechanical properties were provided at all cooling rates. According to ASTM E112-13, grain sizes were similar value at all cooling rates. The oxide scale layer formed was analysed by using optical metallography. It has been determined that the layer of the scale is thicker in productions when the laying head temperature is between 950 °C - 960 °C and the cooling rate is about 5 °C/sec.

1. Introduction

DIN EN ISO 14171 S1 grade steels are suitable for electrode and welding manufacturing. It uses as submerged welding wire. 6.3008_01 is used in order steel grade in ISDEMIR Co. and produced between Ø5,5-6 mm. The billet with 130X130 mm dimensions is annealed in the Wire Rolling Mill Reheating Furnace. It is reduced to Ø 40 mm diameter after 9 stands in roughing mill group, Ø25 mm diameter after 4 stands in 1st intermediate mill group, and Ø18 mm after 2 stands in group 2nd intermediate mill group.

The main customers' requirements for this grade are good wire drawability, ferritic-perlitic microstructure, good surface quality, tensile strength less than 460 MPa, easy to remove oxide scale. Typical chemical composition and mechanical properties for this grade of the previous trials were given in Table 1.

Table 1. Chemical composition and mechanical properties

	Chemical Composition (%)			
	6.3008_01	**C**	**Mn**	**Si**
Typical Range	Min	0,055	0,445	0,000
	Max	0,0949	0,555	0,075

Mechanical Properties			
	Tensile Strength (MPa)	**Reduction in Area (%)**	**Elongation (%)**
Min	-	70	35
Max	460	-	-

Therefore, this study aims to provide customer requirements by optimizing process parameters.

2. Experimental Procedure

The effect of laying head temperature and cooling rate on mechanical properties, microstructure and form of oxide layer was examined.

Advance CCT and TTT diagrams were created in JMatPro software in accordance with the chemical composition in Table 2.

Table 2. Chemical analysis of the of trials (wt%)

Heat No	Grade	C	Mn	Si.
1	6.3008_01	0,078	0,470	0,034
2	6.3008_01	0,079	0,490	0,054

According to the analysis in Table 2, the Advance CCT and TTT diagrams were created in Figure 1-4 in JMatPro software were prepared and possible phases and rates were determined according to the cooling ratio at different laying head temperatures.

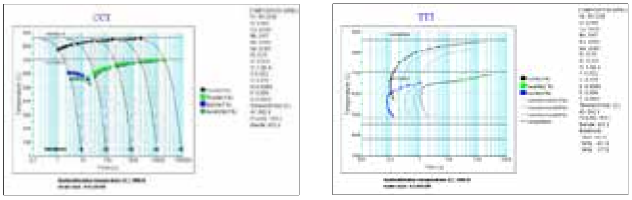

Figure 1. TTT and CCT diagrams of analysis in Heat 1 (T_{aust} = 880°C, ASTM 9)

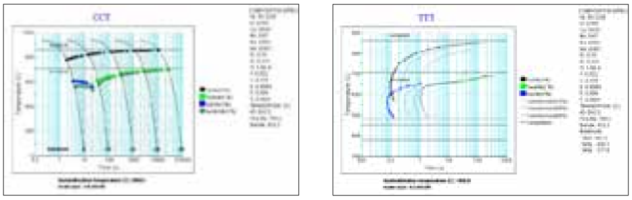

Figure 2. TTT and CCT diagrams of analysis in Heat 1 (T_{aust} = 960°C, ASTM 9)

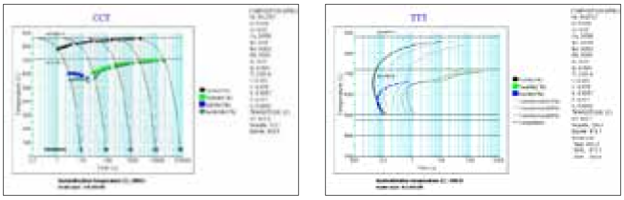

Figure 3. TTT and CCT diagrams of analysis in Heat 2 (T_{aust} = 880°C, ASTM 9)

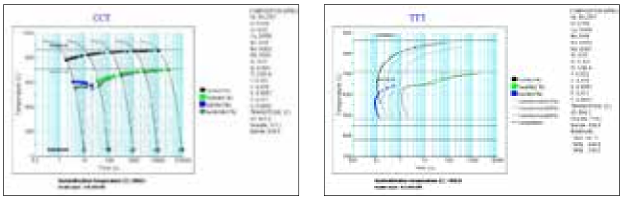

Figure 4. TTT and CCT diagrams of analysis in Heat 2 (T_{aust} = 960°C, ASTM 9)

Industrial trials were done after preliminary studies. According to the diagrams obtained, wire rod produced with variable laying head temperatures (880 °C and 960 °C) in similar chemical compositions, were subjected to cooling with a cooling rate of 4,6 – 5,5°C/sec.(Table 3.)

Table 3. Stelmor® line Cooling Patterns for Trial1 & Trial2

Grade	Heat No	Laying Head Temperature (°C)	Trial No	Avarage Cooling Rate (°C/sec.)
6.3008_01	1	880	1	4,57
			2	5,14
		960	1	4,95
			2	5,52
	2	880	1	4,57
			2	5,05
		960	1	4,95
			2	5,52

As a result of the trial productions, mechanical properties, microstructure and formation of oxide scale were evaluated.

3. Results and Discussion

Trial production has been done according to the chemical compositions in Table 2 and the laying head temperatures and cooling rate in Table 3.

Microstructure of wire rod samples of trial production were examined and mechanical test was performed.

In Table 4, mechanical tests were performed on wire samples in accordance with TS EN ISO 6892-1 standard.

The relationship between the tensile strength and the cooling head temperature depending on the cooling rate is given in Figure 5.

Table 4. Mechanical properties

Grade	Heat No	Laying Head Temperature	Trial No	Avg. Tensile Strength (MPa)	Avg. Elongation (%)	Avg. Reduction in Area (%)
6.3008_01	1,00	880	1	413	41	77
			2	427	42	79
		960	1	415	42	78
			2	427	41	78
	2,00	880	1	413	43	79
			2	419	43	78
		960	1	407	44	80
			2	417	42	79

The structural morphology and the thicknesses of the oxide scales were observed .Microstructure results are shown in Figure 6. Microstructure study was prepared and examined according to ASTM E3 - 11 standard. Samples were examined with 2% Nital etching. In addition, grain size was measured according to ASTM E112-13 standard. The relationship between the grain size and the cooling head temperature depending on the cooling rate is given in Figure 7.

Figure 5. Relationship between Tensile Strenght with LHT for cooling rate

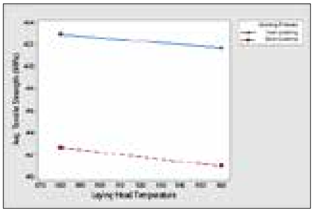

Figure 7. Relationship between Grain Size with LHT for cooling rate

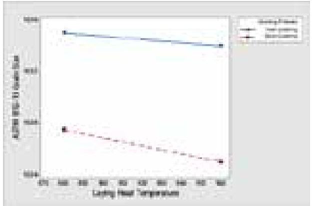

The laying head temperature and cooling rate are directly related to the thickness of the oxide scale layer. Therefore, these process parameters directly effect the easily removable oxide scale layer. As the laying head temperature increases and the cooling rate decreases, the thickness of the oxide scale layer increases. (Figure 8)

Figure 8. Relationship between Thicknesses of The Oxide Scale with LHT for cooling rate

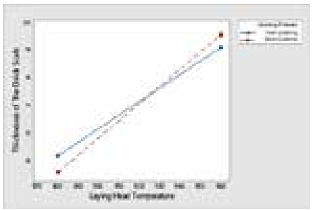

Figure 6. Structural Morphology and Thicknesses of The Oxide

Process Parameter - Grain Size	Structural Morphology	Thicknesses of The Oxide Scale
LHT : 880 °C Heat No:1 Trial No :1 ASTM E112-13 Grain Size :10,2		
LHT : 880 °C Heat No:1 Trial No :2 ASTM E112-13 Grain Size :10,3		
LHT : 960°C Heat No:1 Trial No :1 ASTM E112-13 Grain Size :10,4		
LHT : 960 °C Heat No:1 Trial No :2 ASTM E112-13 Grain Size :10,3		
LHT : 880 °C Heat No:2 Trial No :1 ASTM E112-13 Grain Size :10,3		
LHT : 880 °C Heat No:2 Trial No :2 ASTM E112-13 Grain Size :10,4		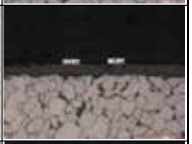
LHT : 960°C Heat No:2 Trial No :1 ASTM E112-13 Grain Size :10,2		
LHT : 960 °C Heat No:2 Trial No :2 ASTM E112-13 Grain Size :10,3		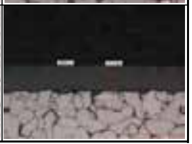

4. Conclusions

In this study, It is aimed to optimum strength, microstructure and easily removable scale in S1 steel wire rod grade used as submerged welding wire.
The trials are designed according to the cooling patterns determined according to Advance CCT and TTT diagrams of the JMatPro software.
With the wire rods produced at 880 ° C, which is the existing laying head temperature, trial productions with different laying head temperatures and cooling rates were made.

- Lower tensile strength values were obtained at the same laying head temperature at a low cooling rate. Tensile strength decreased about 10 MPa.
- The effect of the laying of head temperature and cooling rate on the grain size is insignificant.
- Ferritic-pearlitic structure was obtained at different laying head temperatures and cooling rates.
- It has been determined that the thickness of the easily removable oxide layer increases in the production of high laying head temperature and low cooling rate.

As a result, the mechanical properties, microstructure and easily removable oxide layer of S1 coil grade used as submerged welding wire were obtained with high laying head temperature and low cooling rate.

Definition of Martensite Structures by XRD Method in Carbon Steel (C80)

Sadık POLAT, Onur OREL, Memduh Kağan KELER
İskenderun Demir ve Çelik A. Ş.
Turkey

Abstract

Martensitic transformations, as we observe in steels, are realized by transforming the austenite phase with a surface-centered cubic (FCC) structure into a martensitic phase with a volume-centered tetragonal (BCT) structure. This hard phase atomic structure is generated by rolling and cooling operations. While cooling rate increases, the possibility of occurance martensitic structure also increases. To get accurate content of martensitic phase, XRD method was used in this study. Sample preparation, peak analysis and refinement methods were discussed to resolve the martensitic structure and crystallographic effect in high carbon steels.

1. Introduction

To detect and analyze the exact martensitic phase ratio is crucial for rolling and quenching processes. Martensitic transformation is related some metallurgical phenomenon such as cooling rate, carbon equivalent in the steel grade and crystal transformation effect. With crystallographic changes in the structure, atoms are realigned. During this transformation, energy levels between the interface atoms need more energy which is quite related with diffusionless growth rate. As altering the lattice parameters in the whole pattern, martensitic structures can be identified via using XRD-peak analyse methods.

The body-centered tetragonal (BCT) structure in quenched steels is generated by carbon content. The linear change for lattice parameters (c and a) is correlative at increasing carbon content in steel grade. Studies on this subject show that this continuous linear relationship can be variant at different steel grades[1]. Rather, it was shown that the body-centered-cubic (BCC) structure is the stable structure from 0 to 0.6 wt% C with the c/a ratio equal to an exact value.

Change in the c/a ratio starts at 0.6 wt% C. The BCT structure forms, and the c/a ratio increases with further increase in carbon content. This discontinuity is explained by a change in the transformation process, which is defined upward. It is proposed that a two-step transformation process occurs in the low carbon region, with the FCC first transforming to HCP and then from HCP to BCC. In the high carbon region, the FCC structure transforms to the BCT structure.

Peaks are characteristic wave shape geometry which define the correlation between diffraction intensity and angle variation (2ϴ). In metallographic studies martensitic structure can be easily defined with its sharp and acicular formation after etching and polishing. But there is no exact ratio can be gained after optical microscope operation.

In XRD studies, adjusting and fitting the parameter of with *full width half maximum (FWHM)* is correlated with peak broad and extent function of spectrum curve. At this point Theta (ϴ), which is measured between the points of y-axis to correspond to amplitude of peak, also another factor for define characteristic FWHM value.

The other key parameters are also very important for Rietveld refinement. *Profile variable Caglioti W left* and *profile variable peak shape 1 left* are employed to get correct phase formation in the material. Broader peaks, Kα1 and Kα2 splitting and solve to peak overlap problems are usually preferred for refinement module. The quantification of martensitic phase is fitted the more, the better.

An understanding of the strength of quenched iron-carbon steels plays a key role in the proposed explanation of the c/a anomaly based on interstitial solutes and precipitates[2].

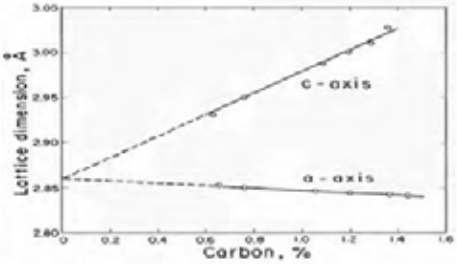

Figure 1. The Relation Between Lattice Parameters and Carbon Content of Quenched Martensite in Fe-C Steels

Figure 1 presents the lattice parameters versus carbon content of quenched martensite in Fe-C steels [2]. The tetragonality of the martensite, measure by X-ray diffraction, c/a, increases with carbon percentage:

$$c/a = 1 + 0.045 \text{ wt\% C} \quad (1)$$

However, it seems this equation lacks data when the

carbon
content in steel is less than 0.6 wt %. The dotted line in *Figure 1* was the assumption, but widely accepted. Sherby claimed after searching references, the c/a ratio relationship was not linear [1].

To accurate XRD patterns, splitting away the two peaks with different carbon content is critical for crystal structure transformation. By using the XRD method in line with this information, we will determine the martensitic structures in steels with a content above 0.6 carbon and we will verify them by metallographic examination.

2. Experimental Procedure

In experimental studies, samples of 3 different heats in C80 steel quality were used. The chemical composition of these castings is given below.

Table 1. Chemical Analysis of the Material (wt%)

Sample	**Grade**	**C**	**Mn**	**Si**	**P**	**S**	**V**	**Cr**
35355 O	C80	0.817	0.75	0.226	0.012	0.0110	0.032	0.29
35401	C80	0.833	0.72	0.182	0.013	0.0032	0.032	0.25
35402	C80	0.833	0.72	0.182	0.013	0.0032	0.032	0.25
35292	C80	0.810	0.70	0.185	0.013	0.0052	0.037	0,26
35355 S	C80	0.817	0.75	0.226	0.012	0.0110	0.032	0.29

2.1. XRD Analysis

XRD could detect bcc and fcc structures but could not distinguish the ferrite, martensite and bainite in steel samples. For that reason Optical Microscope is one of the method, used to detect martensite and bainite qualitatively in the steel manufacturing process. But it is time consuming method because of its long sample preparation time and difficulty of detection. In this work, Qualitative results which is obtained from the optical microscope will be graded between 0-10 and compared with the width of the peak at 100 degrees 2 ϴ obtained by XRD scanning by using Full Width Half Maximum of bcc peak difference of samples.

To calculate full width half maximum in the scan. Profile fitting is applied in X'Pert HighScore Plus 4.9. Vitalij K. Pecharsky&Peter Y. Zavalij defined that profile fitting is the most accurate, although the slowest procedure resulting in observed peak positions, full widths at half maximum(FWHM), and integrated intensities of individual Bragg reflections. It is based on minimization of the difference between observed and calculated profiles using a non-linear least squares technique.

X-ray diffraction (XRD) measurements were performed by means of a PANalytical Cubix3 Series 2 diffractometer. The following software packages were used for the measurements and subsequent analysis: X'Pert Industry (for data collection and instrument control and for data display),) X'Pert HighScore Plus 4.9 (for peak profile fit). The scan was done 0 to 130 degree 2θ with Co LFF X-ray tube for better resolution was performed. A correlation was established between the FWHM of XRD peaks which is in 2ϴ 100° and martensitic phase percentage in a samples when simultaneous changes.

5 different C80 grade steel sample investigated. The XRD patterns are given below.

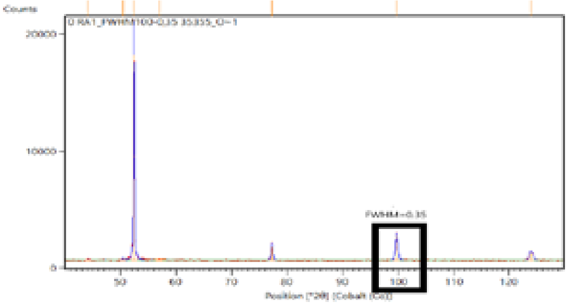

Figure 2. 35355 O-1 XRD scan result

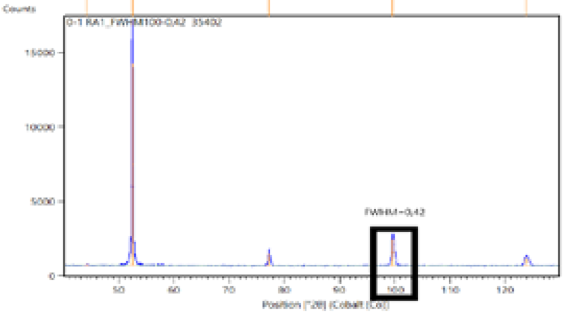

Figure 3. 35402 XRD scan result

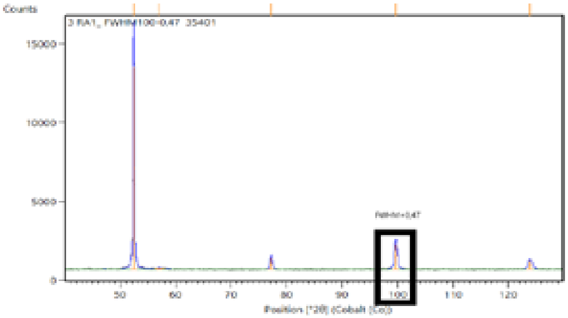

Figure 4. 35401 XRD scan result

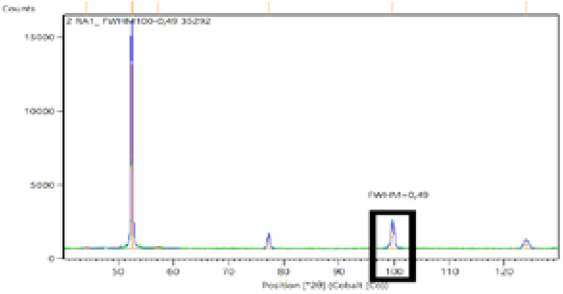

Figure 5. 35292 XRD scan result

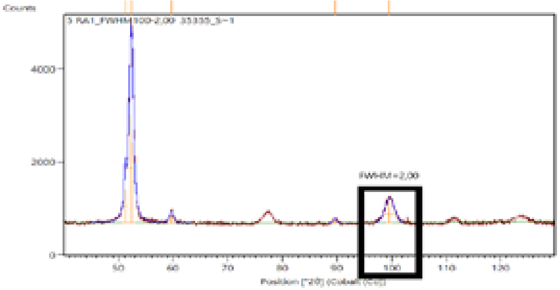

Figure 6. 35355 O-1 XRD scan result

The wire rods grounded and polished by the conventional metallographic methods and etched in %2 nital solution.

Figure 7. 35355 O-1 X500 Micro Structure

Figure 8. 35402 XRD X500 Micro Structure

Figure 9. 35401 XRD X500 Micro Structure

Figure 10. 35292 XRD X500 Micro Structure

Figure 11. 35355 S-1 XRD X500 Micro Structure

Comparison table of microstructura martensite density value and FWHM of XRD peaks value of 2ϴ 100 ° is given below.

Table 2. Microstructural martensite density comparison with FWHM of XRD peaks

Sample	Microstructural martensite density (rated between 1 and 10)	FWHM of XRD peaks in 2ϴ 100°
35355 O	0	0,35
35401	1	0,42
35402	4	0,47
35292	5	0,49
35355 S	10	2

3. Results and Discussion

The graph established between the FWHM of XRD peaks which is in 2ϴ 100° and qualitatively graded martensitic phase detected by optic microscope in a samples.

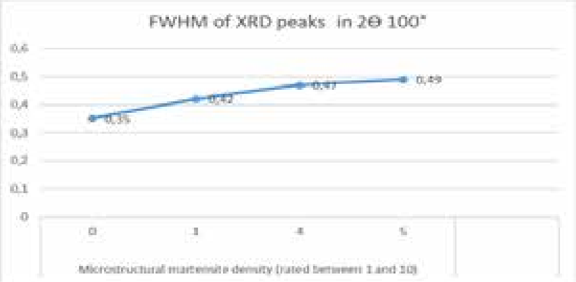

Figure 12. Relation between FWHM and Martensite Density

The correlation between FWHM of XRD peak and martensitic phase appears to be linear. Increasing Martensitic structure amount in the sample broadening the bcc peaks.

References

[1] Sherby, Oleg & Wadsworth, Jeffrey & Lesuer, D. & Syn, C.. (2007). The c/a Ratio in Quenched FeC and FeN Steels - A Heuristic Story. Materials Science Forum - MATER SCI FORUM. 539-543. 215-222. 10.4028/www.scientific.net/MSF.539-543.215.

[2] Lu, Yuan & Yu, Haixuan & Jr, R.. (2017). The effect of carbon content on the c/a ratio of as-quenched martensite in Fe-C alloys. Materials Science and Engineering: A. 700. 10.1016/j.msea.2017.05.094.

[3] Lu, Yuan. (2016). Martensite Lattice Parameter Measured by Modern X-ray Diffraction in Fe-C alloy.

[4] Scott A Speakman, Ph.D. Introduction to PANalytical X'Pert HighScore Plus v3.0 MIT Center for Materials Science and Engineering, http://prism.mit.edu/xray/

[5] Vitalij K. Pecharsky&Peter Y. Zavalij Fundamentals of Powder Diffraction and Structural Characterization of Materials 2009, pp. 360-361.

[6] M. Vashista & S. Paul (2012) Correlation between full width at half maximum (FWHM) of XRD peak with residual stress on ground surfaces, Philosophical Magazine, 92:33, 4194-4204, DOI: 10.1080/14786435.2012.704429

BF No4 Slag Granulation (INBA) Facility Solution of Chimney Floor Abrasion Problems

İbrahim ÇAKMAK, Mehmet Atıl TUNÇ, Ümit GEBENLİ
İskenderun Demir ve Çelik A. Ş.
Turkey

Abstract

This study examines the Slab 4 Blast Furnace Slag Granulated Inba system used by İskenderun Demir ve Çelik A.Ş. (İSDEMİR) in August 2011. The slag, which comes out as a by-product for the production of liquid crude iron in blast furnaces, is used in the granulated inba facility and is made into granules by using pressurized water. The slag turned into granulated is a must as raw material in the cement industry. Slag broadcast contains 42% SiO_2, 33% CaO, 12% Al_2O_3, 6.63% MgO, 0.22% FeO, 0.6% S.
4. For 1 ton liquid raw iron in blast furnace, slag quantity 300-320kg / t and daily slag production quantity min.1680t and max. It is planned as 2200t. 4. The blast furnace has a total of 2 INBA slag granulation systems, one in the north and south casting halls

In this paper, Slag granulation and conveying system (INBA) rotating drum screens improvement work is examined at BF No. 4, Iskenderun Iron & Steel Works Corp. (ISDEMIR) which was commissioned in August 2011.

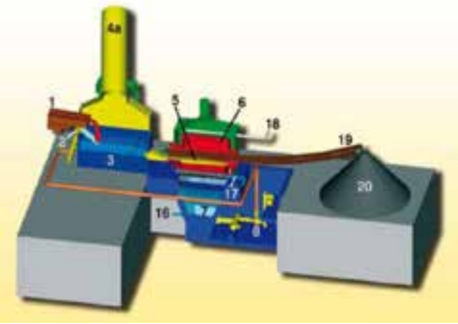

Figure 1. Granulated İnba System

1. Granule Head
2. Water supply
3. Granule tank
4. Flue
5. Distributor
6. Dewatering Tank
7. Hot Water Tank
8. Granulated Water Pump
17. Tank Cleaning Water
18. Tank Cleaning Air
19. Konveyor Belt
20. Stock area

1. Introduction

ISDEMIR's 4th blast furnace is newest and largest blast furnaces of Turkey. Blast furnaces No:4 started the production with 2500 m3 net working volume at 17 August 2011. Daily production rate is 6500 THM/day also daily slag production rate is 2000 Ton/daily.
Liquid hot metal and slag discharge from the blast furnace to the casting channels via tap holes the number of tap holes changing upon volume of the blast furnace hearth. Drill machines drill the tap hole and air pressure poured to hot metal and blast furnace slag to the casting channels . Hot metal and slag seperated from to each other via density at the casting channels. After this process blast furnaces slag poured INBA granulated system. Slag granulated at this plant
In this study examined wear mechanism at the INBA stack's floor.

Figure 2. Granulated Inba İnside Chimney

Figure 3. Granulated Inba Chimney

Figure 4. Granulated Inba İnside Chimney Floor Wear

Figure5.Granulated Inba Chimney Floor Drilling

1. Blast Furnace Slag Granulation İnba System

At the INBA system blast furnace slag granulated with pressured water. Granulated slags use at the cements plant for raw material. Composition of blast furnace slag including 42 SiO_2, %33 CaO, %12 Al_2O_3, 6,63 %MgO, %0,22 FeO, %0,6 S. At the blast furnace No.4 approximately 300-320 kg/T slag procuded for getting one tonne hot metal and daily slag production rate changing between 1.680 tonnes and 2.200 tonnes.

Figure 6. Granulated İnba System

2. Solving method of wear problem of INBA's Stack Floor

Blast furnace slags have abrassive structure due to chemical ad physical composition of slag. This situation cause wear at the INBA stack's floor. Becuse of this situation INBA stack's floor must replaced specific periods.

At the normal situation calcret composite grout used for covering material. This covering material weared time by time. Weared floor are shown at figure 4-5. Weared floor can be damaged or punctured and cause stop of the INBA system. Masterflow material used to fix the puncture problems. This solving method area which Masterlow applied can punctured again and again.

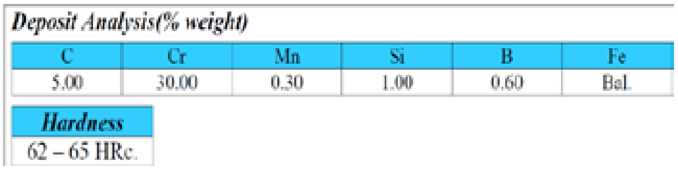

Deposit Analysis(% weight)

C	Cr	Mn	Si	B	Fe
5.00	30.00	0.30	1.00	0.60	Bal.

Hardness
62 – 65 HRc.

Figure 7. Granulated Inba Flue Internal Welding Coating Sheet

Figure 8. Granulated Inba Flue Internal Weldin Coating Sheet

3. Benefits of Welding Coating Sheet

The welding coating sheet, which was first applied to the inba chimney floor in 2018, has been operating in the system for two years without any problems, and there was no puncture problem in the chimney floor area.

50% cost savings were achieved compared to basalt concrete repair.

In 2019, 6 repairs were made in the North Inba chimney and the system was operated. Since the southern inba chimney is a welding sheet metal, no repairs have been made.

References

[1] İSDEMİR A.Ş. 4. Blast Furnace Slag Granulated İnba Projects, 2011.

[1] 4.Blast Furnace Working Parameters

[1] 4. Blast Furnace Slag Chemical Analyzes

[1] Welding Coating Sheet Specs.

The Microstructural Effects of Positioning in Manufacturing on Selective Laser Melted AlSi10Mg

Gülten KAFADAR[1,2], Sertaç ALTINOK[1,2], Burcu ARSLAN HAMAT[1,2],
Ahmet Alptuğ TANRIKULU[1], Akın DAĞKOLU[1], Hakan YAVAŞ[1]
[1]Turkish Aerospace Industries Inc., [2]Middle East Technical University
Turkey

Abstract

Additive manufacturing technologies have gained importance on a global scale especially due to their competencies and fast production capacities, which enable the production of complex geometry parts that cannot be produced using traditional production methods, and their impact is expected to increase exponentially in the coming years. In this study, AlSi10Mg is used as an alloy. Silicon content of AlSi10Mg provides stable melt pools during the process which has higher fluidity comparing to 7xxx series. A detailed study will be carried out on witnessed samples by using advanced material characterization methods, image processing and statistical analysis of microstructures to examine the effects of positioning in manufacturing.

1. Introduction

Due to the considerable design freedom, manufacturing flexibility and light weighting opportunities offered by the PBF (Powder Bed Fusion) systems, the demand for critical lightweight components to be built in this way. However, the most commonly used Al alloys for PBF systems are mainly based on the Al_Si eutectic system due to their good castability and weldability [1]. AlSi10Mg alloys in the as-built condition have supersaturated α-Al matrix and eutectic Si phase. The presence of the Si phase is related by rapid solidification [2]. Si precipitation during solidification defines mechanical properties. Therefore, precipitation distribution and size of Si in α-Al matrix are subjected in this present study.

2. Materials and Methods

The specimens were fabricated with SLM process in different machines but the same energy density level. The samples for fracture toughness property of the material were fabricated with three different orientations with building direction, Z-axis (0-45-90). Fracture toughness tests executed acc. ASTM E399 standard. The tests were carried out with the cross-head speed set to a constant 3 mm/min until failure occurred. The microstructural characterization was carried out in a local excellence center using Scanning Electron Microscope (SEM). The crystallographic texture and the grain morphology of the as-built samples were characterized using an electron backscattered diffraction (EBSD) system. The raw data obtained from EBSD was processed by a high-end software. Grain orientation, internal residual stresses in microstructure, grain size and strain values of the material were evaluated by the software. Fracture surface evaluation executed for failure analysis and mechanisms.

3. Conclusion

This study aims to relate the AlSi10Mg alloy to its mechanical behavior with microstructure and positioning. The data obtained with fracture toughness are associated with microstructure analysis and observed the effect of the presence of Si precipitates. This alloy has different microstructures when compared to casting one. EBSD used as a tool for microstructural analysis. It is observed that melt pools have major effect on microstructure because of the cooling direction and the solidification vector of the components. In the present study the grain size distribution, average grain size, residual stress and strain rate are correlated with mechanical properties of different samples in order to define optimum building direction for future studies.

Acknowledgement

This research is part of the TÜBİTAK 1515 Frontier R&D laboratory support programme and is fully financed by TÜBİTAK. In order to learn for more details about the project, please apply/refer to Turkish Aerospace Inc. Authors would like to thank Bilkent University UNAM for contribution in the microstructural characterization and METU Welding Technology and Non-Destructive Testing Research/Application Center for contribution in the mechanical tests.

References

[1] N. T. Aboulkhair, N. M. Everitt, I. Maskery, I. Ashcroft, C. Tuck, MRS Bull. (2017) 42 311-319.
[2] D. Knoop, A. Lutz, B. Mais, A. von Hehl, Metals (2020) 10 514.

Production and Characterization of Electron Beam Melted (EBM) Ti-6Al-4V Parts

Burcu Arslan Hamat[1,2]; Ahmet Alptuğ Tanrıkulu[1], Gülten Kafadar[1,2], Sertaç Altınok[1,2]
Akın Dağkolu[1], Hakan Yavaş[1]
[1]Turkish Aerospace Industries Inc., [2]Middle East Technical University
Turkey

Abstract

Additive manufacturing (AM) is a layer-by-layer process that enables us to design and produce complex, lighter and stiffer parts without the need for molds, tools, etc., which cannot be achieved by its subtractive manufacturing counterpart. Electron Beam Melting (EBM) is one of the powder bed additive manufacturing techniques which enables to produce almost dense and complex parts with relatively low residual stress compared to selective laser melting technique. This study aims to provide input for the determination of qualification methodologies to produce certified parts. The quality of the parts was evaluated in terms of mechanical and materials properties. Test methodologies for machine capability and acceptance criteria were defined for parts and representative samples.

1. Introduction

Ti-6Al-4V is a highly preferred alloy using in many cutting-edge applications such as defense and aerospace industry due to its high specific strength, high-temperature mechanical properties, and good corrosion properties, etc. However, the cost of related to raw material and processing/tooling limits the use of these alloys in demanding applications. Additive manufacturing provides advantages in the design of Ti-6Al-4V alloys with enhanced mechanical and metallurgical properties. Even though AM provides advantages, produced parts must be qualified in terms of mechanical properties and repeatability of results. In the history of additive manufacturing, the focus has always been on selective laser melting. Our knowledge about the qualification of electron beam melted Ti-6Al-4V parts is largely based on very limited data.

2. Materials and Methods

Parts and representative test samples were built by an EBM Q20 plus machine and Ti-6Al-4V alloys (Arcam AB®, 45-106 µm) were used as starting powder. The EBM 2.24 melt build theme provided by Arcam AB® for 90 µm layer thickness was used to produce parts. Bearing, tensile, compression, and fracture toughness specimens were chosen according to ASTM E238, E8, E9, and E399-19, respectively. The test samples were oriented at different angles (0-45-90). The effects of build direction, part size, surface processing (machining, polishing), and powder on microstructure and mechanical properties were tested. Characterization studies were done in detail to obtain a relation between the microstructures and mechanical properties.

3. Conclusion

Test specimens were located in five different locations on the build table. Microstructures obtained at different locations and orientations were correlated with the mechanical properties such as hardness, bearing strength, yield stress, elastic modulus, ultimate tensile stress, fracture toughness, and elongation at break. The effects of roughness, surface preparation, and sample size on mechanical properties were also examined in detail. Virgin and recycled powders were used to build samples and results were compared.

Acknowledgment

This research is part of the TÜBİTAK 1515 Frontier R&D laboratory support programme and is fully financed by TÜBİTAK. In order to learn for more details about the project, please apply/refer to Turkish Aerospace Inc. Authors would like to thank Bilkent University UNAM for contributing to the microstructural characterization and METU Welding Technology and Non-Destructive Testing Research/Application Center for contribution in the mechanical tests.

Production of PLA/Hydroxyapatite/Graphene Oxide Nanostructured Composite Scaffold

Büşra OKTAY[1], Esma ÖZEROL[1], Oğuzhan GÜNDÜZ[2], Cem Bülent ÜSTÜNDAĞ[1]
[1]Yildiz Technical University, [2]Marmara University
Turkey

Abstract

Polylactic acid (PLA) is an aliphatic biodegradable polyester. The monomer unit is lactic acid, which can be used in several biomedical applications. In this study, hydroxyapatite (HA) and graphene oxide (GO) incorporated nanocomposite fibers were produced. Morphological, chemical, characteristics of the nanostructured scaffolds were investigated. According to the SEM results, diameters of smooth and beadles nanocomposite fibers were obtained by electrospinning.

1. Introduction

Tissue engineering can use the applications of engineering and life science to improve tissue biologic function. These applications are about seeding cells onto a scaffold, creating artificial organs and tissues, triggering new tissue formation, etc. Creating the scaffold is one of the most important applications in tissue engineering. The scaffold should be formed by mimicking the extra-cellular matrix. It is important that scaffolds are made of biocompatible and biodegradable materials and support cell adhesion, differentiation, and growth. The scaffold should have similar mechanical properties to the host tissue. Nanostructured scaffolds exhibit higher performance than micro-structured scaffolds. The electrospinning technique can be used to produce biocompatible nanofibers for tissue engineering applications. The aim of this study is to fabricate a nanostructured scaffold consisting of a mixture of polylactic acid (PLA), hydroxyapatite (HA), and graphene oxide (GO) using electrospinning.

2. Materials and Methods

Hydroxyapatite and Graphene Oxide Synthesis: Nano HA was synthesized wet chemical prepetition method, Calcium nitrate tetra hydrate ($Ca(NO_3)_2.4H_2O$) and Di-ammonium hydrogen phosphate ($(NH_4)_2HPO_4$) as precursors to synthesize Nano HA [1]. GO nanosheet was synthesized modified hummers method and graphite powder was used a starting material [2]. *Formation of solution:* PLA and chloroform were chosen for solute and solvent, respectively. *Production of nanofibers:* To fabricate nanofiber by electrospinning, HA and GO in different amounts were added in the PLA solution. The mixture of PLA/HA/GO was spin by electrospinning [3]. *Evaluation of produced nanofiber:* Nanomaterials and Nanofiber morphology were evaluated by SEM, TEM, and then FT-IR was used for molecular interaction between components, and mechanical characterization of nanofibers was also evaluated.

3. Result

The morphology analysis of synthesized HA and GO was proved using TEM. Evaluation results of HA and GO are shown in Figure 1 and report the crystalized nano-HA (fig. 1 (a)) has a width of 10 nm and a length of 25 nm. As shown in Figure 1 (b) GO revealed a partially uniform transparent sheet morphology due to its characteristic single-layered feature.

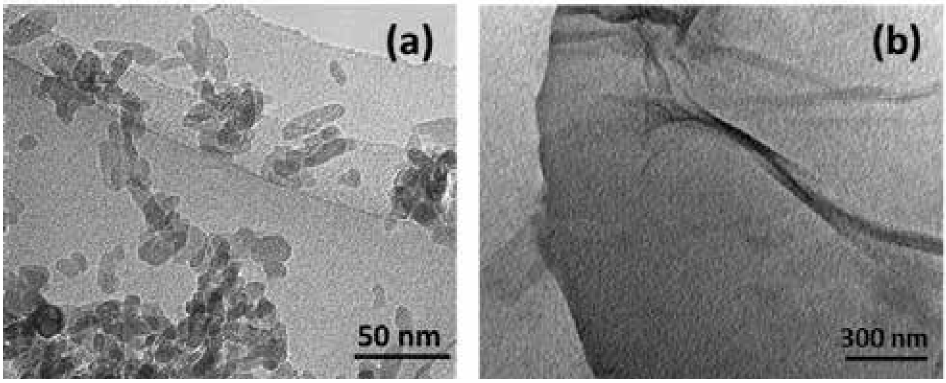

Figure 1. TEM micrograph of hydroxyapatite (a) and graphene oxide (b)

Fourier transform infrared spectroscopy was analyzed to determine the functional groups on PLA/HA/GO and given in Figure 2. According to the FT-IR study, with the addition of HA and GO to PLA, it was seen that there was a similarity in spectrum characteristics between PLA nanofibers and PLA/HA/GO nanofibers. It was monitored because of the overlap of the vibration bands of HA and GO with PLA.

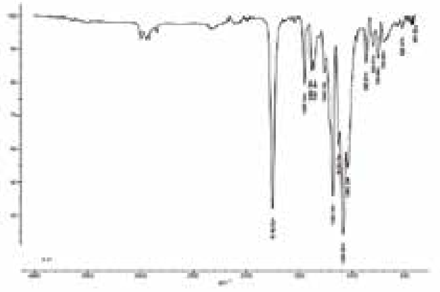

Figure 2. FT-IR spectra of PLA/HA/GO electrospun nanofibers

All fibers were successfully produced by electrospinning and they were obtained three-dimensional (3D) frames (fig 3). Adding HA and Go into PLA increased the surface roughness of obtained composite fibers. Composite of PLA / HA / GO nanofibers in a 3D structure would create a potential scaffold to promote cell adhesion and growth.

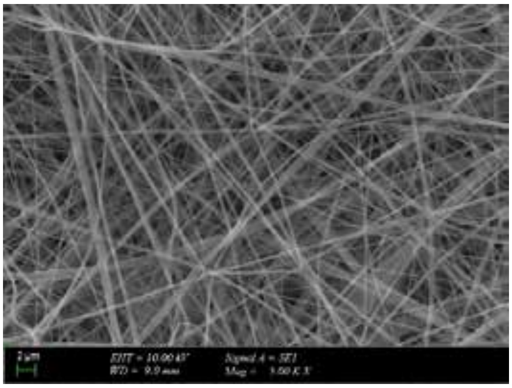

Figure 3. SEM images of PLA/HA/GO nanofibers

4. Conclusion

The nanostructured PLA/HA/GO composite nanofibers were successfully fabricated via the electrospinning method. The addition of HA and GO to PLA can provide better performance for tissue engineering applications due to their unique properties, such as biocompatibility, porous fibrous 3D structure, and mechanic properties. These advantages of composite scaffold show that the scaffolds can be used for tissue engineering applications as a promising material.

References

[1] Ustundag, C. B. (2016). Fabrication of porous hydroxyapatite-carbon nanotubes composite. Materials Letters, 167, 89-92.

[2] Ulucan-Altuntas, K., Debik, E., Ustundag, C. B., Guven, M. D., & Gocen, K. A. (2020). Effect of visible light on the removal of trichloromethane by graphene oxide. Diamond and Related Materials, 106, 107814.

[3] Duygulu, N. E., Ciftci, F., & Ustundag, C. B. (2020). Electrospun drug blended poly (lactic acid)(PLA) nanofibers and their antimicrobial activities. *Journal of Polymer Research*, *27*(8), 1-11.

Polycarbonate / Graphene Oxide Composite Membrane Production

Meryem MUSLU[1], Muhammed Enes Oruc[2], Cem Bulent USTUNDAG[1], Hasan SADIKOGLU[1]
[1]Yildiz Technical University, [2]Gebze Technical University
Turkey

Abstract

Graphene oxide (GO) is a superior hydrophilic material obtained by oxidation of graphite, containing functional groups such as hydroxyl, carbonyl, epoxy. Polycarbonate (PC), on the other hand, is a versatile material with its hydrophilic structure, biologically inertness, good physical and chemical resistance, and asymmetric structure. In this study, PC / GO composite membranes were produced by adding graphene oxide (GO) to the polycarbonate membrane structure. The performance of nanocomposite membranes in terms of dye rejection was examined with a U-tube assembly. The membranes exhibited improved dye rejection after GO was added to the polymer.

1. Introduction

Dyes in the water have serious adverse effects on both humans and the environment. Therefore, it is critical to remove the dyes from the water, even at low concentrations. To overcome this problem, nanoporous membranes, which are of great interest in various places, can be used [1]. Polymer nanocomposite can be produced by adding nanometer-sized nanofillers to their structures to improve polymers' dye rejection. High-aspect ratio nanostructured pores can be incorporated into polymers, thereby preventing the passage of much smaller molecules such as paint, heavy metals, and salt. These membranes produced with nanoporous structure exhibit large pore distribution and curved pore paths [2]. To this end, this study aims to improve dye rejection by adding graphene oxide (GO) to the structure of a polycarbonate (PC) membrane using electrophoretic deposition (EPD) and drop-casting methods.

2. Materials and Methods

Graphene Oxide Synthesis: Graphite powder was used as the starting material in the production of graphene oxide and was synthesized by the Modified Hummers method [3]. Polycarbonate membrane has been taken from Sterlitech with a pore size of 200nm. *Membrane production:* Firstly, with the electrophoretic deposition (EPD) method, which enables the production of porous membranes [4], then PC / GO with different GO concentrations was produced by drop-casting. *Evaluation of the membrane:* The morphology of the nanostructure used was evaluated by SEM and the composite materials produced were characterized by filtration tests.

3. Result

Optimum coating conditions were investigated for the thin film fabricated to have minimum dye permeability. Membranes were first produced with EPD and then with drop-casting that is a faster and relatively more economical method. The U-tube osmosis assembly was used to determine the dye rejection property of the PC / GO membrane. According to the U-tube test setup, with the addition of GO to the PC, GO nanostructures formed long narrow channels to prevent dye passage on the PC, thus an improvement in the dye rejection was achieved. The membranes produced via drop-casting exhibited a higher resistance performance for dye molecules than the produced via EPD.

We observed that dye rejection depends on the GO density in the membrane and the number of layers in the membrane. The dye rejection showed an increasing trend with the increase in the GO concentration and the number of membranes in the membrane. The results show that the four-layer GO / PC membrane has a high dye rejection rate compared to the single-layer GO / PC membrane.

4. Conclusion

PC / GO composite membranes have been successfully produced by the drop-casting method. The addition of GO to PC membrane can alter the removal of waste paint from water in environmental applications due to smaller pore size and hydrophilic property. These promising results show that the composite material produced can take place as an interesting material in environmental applications.

References

[1] Agonafer, D.D., Oruc, M.E., Chainani, E., Lee, K.S., Hu, H. and Shannon, M.A. (2014). Study of ionic transport through metalized nanoporous membranes functionalized with self-assembled monolayers;Journal of Membrane Science, 461, pp.106-113.

[2] Zhou, C., Segal- Peretz, T., Oruc, M.E., Suh, H.S., Wu, G. and Nealey, P.F., (2017). Fabrication of Nanoporous Alumina Ultrafiltration Membrane with Tunable Pore Size Using Block Copolymer Templates. Advanced Functional Materials, 27(34).

[3] Ulucan-Altuntas, K., Debik, E., Ustundag, C. B., Guven, M. D., & Gocen, K. A. (2020). Effect of visible light on the removal of trichloromethane by graphene oxide. Diamond and Related Materials, 106, 107814.dkd

[4] Ustundag, C. B. , Kaya, F., Kamitakahara, M., Kaya, C., & Ioku, K., (2012). Production of tubular porous hydroxyapatite using electrophoretic deposition. Journal Of The Ceramıc Socıety Of Japan , vol.120, no.1408, 569-573.

Production of $AlFe_2B_2$ Intermetallic Compound by Using Mill Scale via Self Propagating High-Temperature Synthesis Method

Ecem Turhan, Faruk Kaya, Bora Derin

Istanbul Technical University

Turkey

Abstract

In this study, $AlFe_2B_2$ intermetallic compounds were produced for the first time via a simple and low-cost aluminothermic self-propagating high-temperature synthesis (SHS) method. The raw materials were selected as boron trioxide (B_2O_3), mill scale from the continuous steel casting process, and aluminum. Thermochemical calculations were made with FactSage to determine precursor amount, the composition of the cast alloy, and the adiabatic temperature of the combustion reaction. The effect of Al addition, heat treatment, and leaching processes on the product phases were investigated. A detailed examination on the products was made by X-ray fluorescence (XRF), X-ray diffraction (XRD), and scanning electron microscopy (SEM/EDS).

1. Introduction

$AlFe_2B_2$ is an intermetallic compound that has recently gained attention due to its exceptional magnetocaloric effect. Its potential use has been suggested for magnetic cooling systems [1-3]. In-operando tests have demonstrated that $AlFe_2B_2$ is a successful material in magnetic refrigeration [4]. In the synthesis studies, the most commonly used method for the production of $AlFe_2B_2$ intermetallic compound is arc melting method. Obviously, this method is costly due to the use of pure elemental precursors, also rather energy and time-consuming. Therefore, in this study, the $AlFe_2B_2$ intermetallic compound was produced from oxides by self-propagating high-temperature synthesis (SHS) method to reduce energy use/raw material costs and provide a shorter process time [5-6]. In order to contribute to recycling, the mill scale was also used as an alternate iron source.

2. Materials and methods

In the SHS method, mill scale or hematite were used as iron (Fe) source, boron oxide (B_2O_3) used as boron source, aluminum powder used as both aluminum source and reducing agent. Prior to the experiments, thermochemical simulations were done by FactSage. Then, the powders were weighed and dried at 110 °C for 30 min in a drying oven. After thoroughly mixing the powders for 45 min, the SHS process were realized in a Cu crucible. The experiments were carried out in three stages. Firstly, $AlFe_2B_2$ intermetallic compounds with different Al:Fe:B ratios were produced by the SHS method. In the second stage, the obtained materials were heat treated at 1000 ˚C for 1 hour under argon atmosphere. In the final stage, the heat treated materials were ground and leached with 50% HCl acid in 1:1 ratio.

3. Conclusions

According to the XRD results, ternary $AlFe_2B_2$ intermetallic compound was successfully produced by SHS method together with binary Fe-B and Al-Fe phases. Increasing aluminum content had a positive effect on the ternary boride content. The best result was obtained when hematite was used as iron source instead of mill scale. After the heat treatment, the amount of binary Fe-B phases decreased due to the peritectic reaction. Ternary boride content further increased by leaching.

References

[1] Lejeune, B. (2014). Designing ‘Cool’ Magnetic Materials for Efficient Refrigeration: Tailoring $AlFe_2B_2$ Magnetism-Structure Relationships for Magnetocaloric Applications.

[2] Barua, R., Hadjipanayis, G., Ke, L., Kramer, M.J., Lejeune, B.T., Levin, E.M., Lewisa, L.H., McCallum, R.W. (2018). Anisotropic magnetocaloric response in $AlFe_2B_2$.

[3] Lee, J.W., Song, M.S., Chob B.K., Nam C. (2019). Magnetic properties of pure $AlFe_2B_2$ formed through annealing followed by acid-treatment.

[4] X. Zhang, B.T. Lejeune, R. Barua, R.W. McCallum, L.H. Lewis, Estimating the in-operando stabilities of $AlFe_2B_2$-Based compounds for magnetic refrigeration, J. Alloys Compd. 823 (2020) 153693. doi:https://doi.org/10.1016/j.jallcom.2020.153693.

[5] Derin, B. (2017). Yanma Sentezi Yöntemiyle İleri Malzemelerin Üretimi.

[6] Pacheco, M.M. (2007). Self-Sustained High-Temperature Reactions- Initiation, propagation and synthesis, Doctoral thesis, Delft University of Technology.

A Review of Composite Lattica Structures: Properties, Design, Manufacturing and Applications

Tayfun DURMAZ[1], Ronan O'HIGGINS[1], Robert TELFORD[2]
[1]University of Limerick, [2]ATG-Innovation
Ireland

ABSTRACT

Composite lattice structures, also known as grid-stiffened, anisogrid and composite isogrid structures **[1]** are a highly efficient structural application of unidirectional carbon fiber reinforced polymer matrix composites **[2]**. These structures are of increasing interest due to their light-weight characteristics. In particular, recent developments have focused on their application in space launcher applications. However, composite lattice structures are still a novel technology **[3]** which require more research to examine their behavior under different loading conditions. This review covers published research on the basic properties and design approaches adopted for development of composite lattice structures. Recent development in terms of manufacturing processes and applications areas for composite lattice structures will be also reviewed. In addition, information about testing and analysis of composite lattice structures will be presented.

1. INTRODUCTION

Composite materials are widely used in different industries due to their excellent properties, such as high specific stiffness and strength. Most advanced composite structures take the form of a laminate skin(s) stiffened by either a core, in the case of a sandwich structure, or more commonly stiffeners, which enhance the structural efficiency and rigidity. Examples of the stiffeners can be found in nature, as shown in Figure 1 **[4]**.

Figure 1. *Examples of natural stiffeners: A Victoria leaf (a), peanut shells (b) and insect wings (c)* **[4]**

Composite lattice structures can be described as a structural architecture that is made up of continuous fiber-reinforced materials as stiffeners. These structures are manufactured by the intersection of stiffeners usually described as ribs **[2]**. The intersection points of ribs are usually referred to as nodes **[2]**. Lattice structures can be manufactured with or without skin. If structure contains an inner or outer skin, it is called a grid-stiffened structure whereas; they are simply called a lattice if only ribs without skin **[2]**.

I. Properties

Lattice and grid-stiffened composite structures can be seen as advanced light-weight periodic materials that have high specific strength and stiffness. Due to these superior properties, they are highly attractive for use in light-weight structures, such as composite beams, panels and cylinders in aerospace industry **[5]**. In the literature, most of the studies focus on the application of carbon fiber-reinforced polymer systems in composite lattice structures. Carbon fiber-reinforced epoxy lattice grids have been found to be much stiffer and stronger that aluminum lattices, carbon foams and honeycomb structures **[6]**.

Huybrechts et al. **[7]** identified additional advantages of grid-stiffened composite structures; grid structures have environmentally robustness, i.e. they have significantly higher inherent damage tolerance when compared to alternative structures, such as honeycomb sandwich composite structures. They also indicate that as grid-stiffened structures are generally open structures, they are less susceptible to issues associated with water or moisture absorption **[7]**. In addition, composite lattice structures lend themselves well to automated manufacturing processes potentially reducing production costs **[7]**. Structural efficiency is also considered to be an advantage, in most of the cases, ribs redistribute both tensile and compressive loads well, in particular helping to suppress the global buckling mode of failure. In most loading scenarios, a skin is not necessary to achieve optimum structural efficiency. As a result, grid-stiffened structures are much stiffer than honeycomb structures for equivalent weight **[7]**.

Huybrechts et al. **[7]** also identified disadvantages with grid-stiffened composites. The behavior of grid-stiffened structures is still not well understood. While numerical and analytical models for these structures exist, there is still a lack of information about their performance under different loading conditions **[7]**. The complexity of grid patterns can lead to potentially longer manufacturing time **[7]**. Because of this complexity, it is hard to produce flat grid-stiffened plates. Moreover, there is an asymmetric geometry of grid structures through the thickness. This situation leads to thermal induced springback during curing between the grids and the skin of the composite structure **[7]**. In addition, the production of complex grid-stiffened structures can lead to complicated and expensive tooling requirements **[7]**. Furthermore, tools can degrade after repeated use requiring them to be replaced periodically **[7]**.

II. Design

There are some basic finite element analysis approaches about that can be used to predict grid-stiffened composite panel behavior and allow the development of analytical models. Using these models, the buckling mode of grid-stiffened composite structure can be evaluated. Jaunky et. al. **[8]** indicate that these models may be grouped as (a) discrete approach, (b) branched plate and shell approach and (c) smeared stiffened approach.

There are some differences in between these approaches according to Wodesenbet et al. **[9]**. The discrete approach may be challenging to use if there are more than two directions and the panel is not symmetrical under axial and torsional loads. It can be used for simpler stiffener arrangements. The branched plate and shell approach may be more flexible and accurate **[9]**. It enables to use finite element modeling for different types of panels. On the other hand, the smeared stiffened approach focuses on skin stiffener interaction. According to the minimum potential energy principle and static conditions, this approach is presented for the derivation of neutral surface profile of the grid/shell assembly **[9]**.

In their research study, Fan et al. **[10]** indicate there are different types of grid structures including honeycomb, square grid, isogrid, Kagome grid, diamond grid and mixed triangle grid (Figure 2). The beam-column theory is used to determine the local buckling strength of lattice composite structures under uniaxial normal stresses. Fan et al. **[10]** compare the analytical and numerical results for different composite lattice grid structures (Figure 3).

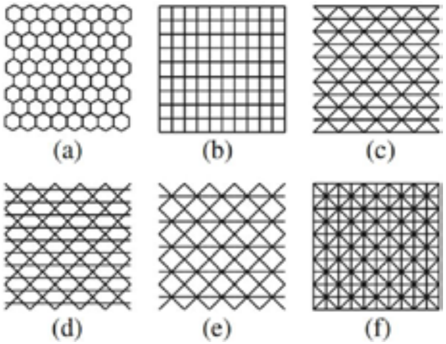

Figure 2. *Different types of lattice grids: honeycomb (a), square grid (b), isogrid (c), Kagome grid (d), diamond grid (e), mixed triangle grid (f)* **[10]**

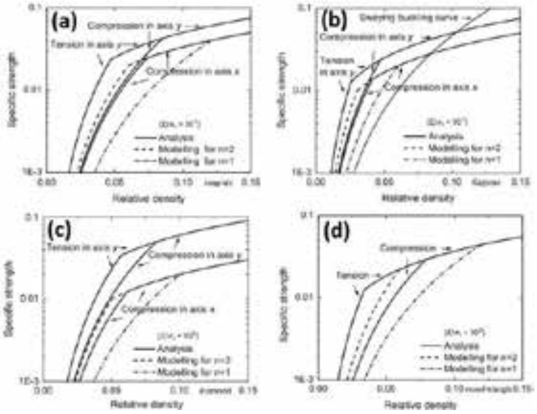

Figure 3. *Uniaxial strength of different types of grids: isogrid (a), Kagome grid (b), diamond grid (c), mixed triangle grid (d) for different n values where n is the end of constraint factor* **[10]**

It should be noted that different grid structures show different structural properties. Grids with three strut stacks have stronger constraints at the nodes than square and regular hexagonal honeycomb composite structures **[10]**. Nodes with more connectivity can create stronger constraints. Fan et al. **[10]** mention that an isogrid structure has six constraint points, whereas the Kagome grid has only four connectivity nodes. While it may be thought that buckling strength can be higher in isogrid structures, but in the reality, for shorter struts the local buckling strength of the Kagome grids are much greater than that of the isogrid with identical relative densities **[10]**. It is indicated that this analysis can be used to design ultralight-weight designs with low relative density grid structures **[10]**.

III. Manufacturing

Various different manufacturing processes can be used to produce fiber-reinforced polymer composite lattice structures. These processes differ with respect to the design expectations. According to Huybrechts et al. **[7]**, grid structures for stiffness control can be manufactured easily. Solar panel substrates, spacecraft structures and optical benches can be given as examples for these applications **[7]**. Similarly, they indicate that strength-controlled applications can also be manufactured relatively easily for cylinders, conical applications, and domes. In these applications, low rib volume fraction, less than 40% is achieved **[7]**. On the other hand, there are some limitations for high rib fiber volume fraction in strength-controlled applications. They state that this manufacturing process is used for low rib-skin dimensions **[7]**. In addition, different manufacturing methods with different developers are noted in their study (Table 1). There can be different options according to the technical background, infrastructure and equipment available. Tooling is the key consideration for manufacturing of fiber-reinforced polymer composite lattice structures, no matter which process is chosen **[7]**.

Table 1. *Different manufacturing methods and their developers* **[7]**

Manufacturing Method	Details
Wet Winding Around Pins	Russian Manufacturing Method
Wet Winding in Hard Tooling	Developed at Boeing
Nodal Spreading	Developed at Stanford University
Winding into Solid Rubber Tooling	Developed at Philips Lab
The Hybrid Tooling Method	Developed at US Air Force Research Laboratory (AFRL)
Fiber Placement with hybrid Tooling	Developed at AFRL & Boeing)
Fiber Placement with Expansion Inserts	Developed at Alliant Tech & Boeing
The Located Expansion Tooling Method	Developed at AFRL & Boeing
Wet Winding: The Brute Force Approach	-
The SnapSat Method	Developed at Composite Optics, Inc
The TRIG Method	Developed at Stanford University

IV. Applications

There is no doubt that grid-stiffened structures are used in some special programs within the aerospace industry. It is possible to see different applications in different countries and organizations. For example, the application of grid-stiffened structures were proposed about 30 years ago by the Central Research Institute of Space Machinery (CRISM) in Russia (and USSR) according to Vasiliev et al. **[11]**. They state that about 40 successful launches have been carried out with anisogrid composite lattice structures by the Russian Space Program **[11]**. Similarly, it is possible to see grid-stiffened composite structures in the various projects in the USA such as ballistic applications by the National Air İntelligence Center (1997), MightySat I satellite (1998), fuselage applications by the Scaled Composite Company (V-Jet, Boomarang, Vantage), interstage parts of Delta II and some launch vehicles by The Boeing Company (2000) **[7]**. Besides Russia and the USA, it is also possible to find some applications of grid-stiffened structures in Europe. The Italian company AVIO has experienced in manufacturing composite lattice structures **[12]**. In the official webpage of this company, it is noted that grid-stiffened structures are preferred in the interstage 2/3 that connect the Zefiro 40 (Z40) second stage with the Zefiro 9 (Z9) third stage of the VEGA-C launch vehicle **[12]**. In addition, it is also possible to see the applications of lattice structures in China. Jingxuan et al. **[13]** state that grid-stiffened structures are used for spacecraft, rockets and commercial airplanes manufactured by Xi'an Aerospace Composite Materials Research Institute in China. In the most of these applications, carbon fiber reinforced epoxy systems are used.

Figure 4. *Internal (left) and external (right) view of the upper interstage of Proton M Launcher* **[11]**

2. EXPERIMENTAL STUDIES

There are various experimental studies of lattice structures. Giannis et al. **[14]** tested grid elements of various different configurations (Figure 5). Wodesenbet et al. **[9]** compared analysis predictions for a grid-stiffened component with experimental test results (Figure 6). In both of these studies, compression tests are carried out.

3. RESULTS AND DISCUSSION

According to Giannis et al. **[14]**, different behaviors were observed for their specimens that were prepared to test particular properties. In the Type-1 specimen, important out-plane deformation of the skin is observed. Similarly, the same deformation is seen in the middle of the ribs (upper triangular area) as demonstrated by the local strain measurement **[14],** i.e. local buckling exists on the skin. Until fracture, the ribs continue to carry the load after local buckling is seen in the skin. It can be said that, there is a detrimental effect of the skin failure on the whole specimen. This situation can be described as a combination of skin-to-rib debonding and local compressive failure of the ribs **[14]**. It is also mentioned that the behavior of the Type-2 specimen is unstable without the skin above a compression load of 10kN (Figure 6) **[14]**. After this point, the ribs started to deform until failing locally (Figure 6).

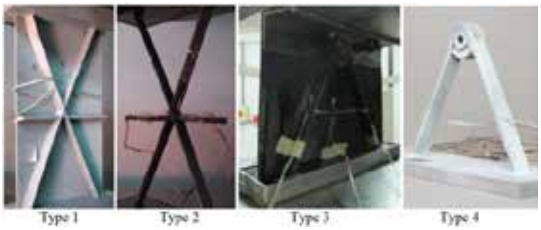

Figure 5. *View of the Type-1, Type-2, Type-3 and Type-4 specimens before mechanical testing* **[14]**

Similar failure characteristics are observed for Type-3 and Type-4 specimens. The loads to failure of these components were measured as very close to each other. However, the modes of failure were different **[14]**. The load was directly applied through a pin for the Type-4 specimen because it does not have any skin structure. As such, the load was directly transferred to the ribs by shear of the adhesively bonded and mechanically interlocked metallic reel. Failure was found to occur in this metal-composite interface **[14]**. Unlike the Type-4 specimen, the load path is divided to the metallic reel through the ribs and the metallic reel itself directly. Hence, the failure mode may be characterized as skin-to-ribs separation prior to failure around the metallic component for Type-3 and Type-4 specimens respectively **[14]**.

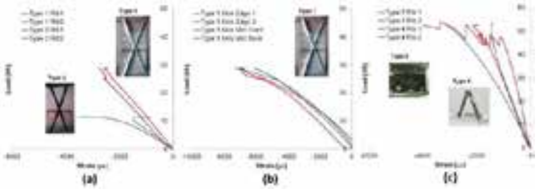

Figure 6. *Mechanical test results of Type-1, Type-2, Type-3 and Type-4 specimens* **[14]**

The numerical test results and the summary of the failure types of the specimens are given in the Table 2. Giannis et al. **[14]** state that composite skins of the grid-stiffened structure carry a significant portion of the load, although the results are close to each other, particularly for Type-3 and Type-4 specimens **[14]**. The skin prevents and delays buckling of the ribs. Nevertheless, the skin is also susceptible to debonding due to the stiffness differences between the unidirectional ribs and skin **[14]**.

Table 2. *Summary of the failure mode and measured failure loads of Type-1, Type-2, Type-3 and Type-4 specimens* **[14]**

Specimen Type	Failure Load (kN)	Failure Type
1	29 - 33	Ribs compression / skin-to-rib debond
2	11 - 12	Ribs buckling and ribs compression
3	54 - 62	Skin-to-ribs debond / reel failure
4	29 - 53	Reel failure

Finite element analysis shows local skin bucking failure at a load of 44.9 kN whereas, the test result on the real composite grid-stiffened part is measured as 46 kN (Figure 7 (a)) according to Wodesenbet et al **[9]**. It means that there is 2.5% deviation between the predictions and experiment. These results indicate that the analytical predictions of the grid-stiffened structure have good agreement with the test results **[9]**.

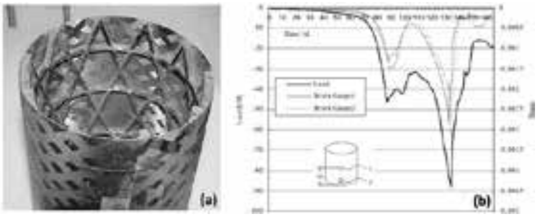

Figure 7. *The view of grid-stiffened test specimen (a) and real component test results (b)* **[9]**

4. CONCLUSION

In this paper, a review of information in the open literature about composite lattice structures in terms of their properties, design approaches, manufacturing processes and applications was carried out. In addition, results of testing of composite grid structures were presented.

Based on this review, a few important conclusions can be draw for composite lattice structures.

a) While composite lattice structures have been known for some decades, more research is needed to evaluate their behavior under different loading scenarios.
b) Lattice structures can be seen as a good alternative for honeycomb structures because of their light-weight nature.
c) There are various manufacturing techniques to produce these structures. Tooling can be seen as one of the most crucial parts of manufacturing as the structures are complex, requiring complicated tooling configurations.

Overall, composite lattice structures exhibit properties that make them a good potential choice for aerospace structures. With the increasing proliferation of space launch vehicles, there is greater potential for more applications of composite lattice structures in the future.

ACKNOWLEDGEMENTS

Sincere appreciation is expressed to Kelly Matthews and Brendan Murray for their participation to discussions. This study is fully funded by Science Foundation Ireland Confirm Centre targeted project (Grant Number: 16/RC/3918 004) in conjunction with ATG Innovation Ltd.

5. REFERENCES

[1] Pavlov, L., Smeets, B., Simonian, S.M., Kloeze, I. (2016). *Optimization of a composite lattice satellite central cylinder structures using an efficient semi-automated approach.* AIAA/ASCE/AHS/ASC Structures, Structural Dynamics, and Materials Conference, 1497.

[2] Smeets, B., Papenhuijzen, T., Pavlov, L., Koot, M. *Development logic and building block testing approach for pre-preg lattice satellite central cylinder applications.* ATG Innovation Ltd.

[3] Maes, V.K., Pavlov, L., Simonian, S.M. (2019). *An efficient semi-automated optimization approach for (grid-stiffened) composite structures: applications to ariane 6 interstage.* Composite Structures, 209, 1042-1049.

[4] Wang, D., Abdallah, M.M., Wang, Z.P., Su, Z. (2018). *Streamline stiffener path optimization (SSPO) for embedded stiffener layout design of non-uniform curved grid-stiffened composite (NCGC) structures. Computer Methods in Applied Mechanics and Engineering.* DOI: 10.1016/j.cma.2018.09.013.

[5] Pavlov, L., Kloeze, I., Smeets, B.J.R., Simonian, S.M. (2016). *Development of mass and cost efficient grid-stiffened and lattice structures for space applications.* ATG Europe BV.

[6] Fan, H.L., Meng, F.H., Yang, W. (2007). *Sandwich panels with kagome lattice cores reinforced by carbon fibers.* Composite Structures, 81, 533-539.

[7] Huybrechts, S.N., Hahn, S., Meink, T.E. *Grid stiffened structures: a survey of fabrication, analysis and design methods.*

[8] Jaunky, N., Knight, N.F. (1996). Jr. *Formulation of an improved smeared stiffener theory for buckling analysis of grid-stiffened composite panels.* Composites: Part B, 27B, 519-526.

[9] Wodesenbet, E., Kidane, S., Pang, Su-Seng. (2003). *Optimization for buckling loads of grid stiffened composite panels.* Composite Structures, 60, 159-169.

[10] Fan, H., Jin, F., Fang, D. (2009). *Uniaxial local bucking strength of periodic lattice composites.* Materials and Design, 30, 4136-4145.

[11] Vasiliev, V.V., Barynin, V.A., Razin, A.F. (2012). *Anisogrid composite lattice structures – development and aerospace applications*. Composite Structures, 94, 1117-1127.

[12] Grid stiffened structure picture from AVIO. Retrieved from https://www.avio.com/who-we-are on 11st of April 2020.

[13] Jingxuan, H., Mingfa, R., Shiyong, S., Qizhong, H., Xiannian, S. (2011). *Failure prediction on advanced grid stiffened composite cylinder under axial compression.* Composite Structures, 93, 1939-1946.

[14] Giannis, S., Hajdaei, A., Matejak, V., Taulitsis, A. (2014). *Testing and analysis of grid-stiffened composite structural panels.* ECCM16-16th European Conference on Composite Materials.

[15] Rana, S., Fangueiro, R. (Ed.). (2016). *Advanced composite materials for aerospace engineering.* Elsevies, Woodhead Publishing Series in Composites Science and Engineering: Number 70.

[16] Mrazova, M. (2013). Advanced composite materials of the future in aerospace industry. Incas Bulletin, Volume 5, Issue/3, pp. 139-150.

[17] Mangalgiri, P.D. (1999). Composite materials for aerospace applications. Bull. Mater. Sci. Vol22, No.3, pp. 675-664.

[18] Totaro, G., Nicola, F.D. (2012). Recent advance on design and manufacturing of composite anisogrid structures for space launchers. Acta Astromautica, 81, 570-577.

[19] Vasiliev, V.V., Morozov, E.V. (2018). Advanced Mechanics of Composite Materials and Structures, Fourth Edition. Elsevier Ltd.

[20] Sorrentino, K., Marchett, M., Bellini, C., Delfini, A., Sette, F.D. (2017). Manufacturing of high performance isogrid structure by robotic filament winding. Composite Structures, 164, 42-50.

[21] Higgins, J., VanWest, B. (2005). NDE and repair of damaged minotaur fairing shell. Composite Structures 67, 189-195.

[22] Wegner, P.M., Ganley, J.M., Huybrechts, S.M., Meink, T.E. Advanced grid stiffened composite payload shroud for the OSP launch vehicle. Air Force Research Laboratory Space Vehicles Directorate (AFRL/VS)

[23] Müller, J.M., Nijhuis, P. (2019). Automated manufacturing of grid stiffened panels. Netherlands Aerospace Center, Report Number NLR-TP-2019-288.

[24] Vasiliev, V.V., Razin A.F. (2006). Anisogrid composite lattice structures for spacecraft and aircraft applications. Composite Structures, 76, 182-189.

Microstructural and Morphological Characterization of Directionally Solidfied Copper-Boron Eutectic System

Samira MOHAGHEGHI, Shabnam Fadaei CHATROUDI, Melis ŞEREFOĞLU

Koç University

Turkey

1. Introduction

The Cu - B system is an irregular eutectic alloy in which boron phase has a faceted solid/liquid interface. The two best known examples of these irregular eutectic systems are the gray cast iron and the aluminum – silicon eutectics which have similar features with Cu – B microstructures. Therefore, studying Cu – B microstructure evolution may shed light on the unknowns of both alloy systems and examine the different kind of morphologies obtained in irregular eutectics. In this study, various Cu – B solidification microstructures and morphologies obtained at different growth velocities are characterized.

2. Materials and Methods

The commercial Cu – B alloy close to the eutectic composition (2 wt.% B), was casted in the form of rods using an induction system. Subsequently, the samples were directionally solidified in a vertical Bridgman-type setup at the growth velocities ranging from 0.5 to 20 µm/s. The samples were then metallographically prepared for post-mortem microstructural analysis at different growth lengths.

3. Results and discussion

Solidification microstructures obtained from the cross-sections at various growth velocities showed that the boron phase morphology substantially changes as a function of velocity. By decreasing the growth velocity, the microstructure coarsens, as expected from the general scaling law. In addition, we identified three main growth morphologies of the eutectic boron as a function of the growth velocities. At high velocity, *i.e.* 20 µm/s, the eutectic boron generally grows with multi-faceted needle-like morphology. The outlines of these needles are polyhedral, indicating that the anisotropy of the boron/liquid interface is an important factor which determines the crystal shape. On the other hand, at a lower growth velocity, *i.e.* 0.5 µm/s, the boron evolves to large crystals with very complex morphologies. In these large crystals, well-defined facets of the crystal can be clearly detected. The 3D morphologies of the eutectic boron phases are obtained by etching the copper phase and the 3D shapes of boron particles revealed that the smaller boron particles around the main chunk are in fact the branches of the neighboring large crystal. In the intermediate velocities, *i.e.* 4 and 2 µm/s, both needle- and plate-like morphologies are observed. All these morphologies are characterized quantitatively using advance image processing techniques.

4. Conclusion

In this study, we identified three distinct growth morphologies of the eutectic boron phase, and thus the solidification microstructures, in the Cu – B irregular eutectic system. By increasing the growth velocity, not only the scale of microstructures decreased but also the morphology of eutectic boron dramatically changed from large and complex to very thin plate-like and needle-like ones. Nevertheless, the facets are apparent in all the cross-sections obtained at different growth velocities, which shows that the boron phase has very high anisotropy in the solid/liquid interface energy.

Acknowledgment

This work is funded by TÜBİTAK 2509 (Grant no: 217M089).

On the Role of Both Pulse Current and Electrolyte Bath on the Mechanical Behavior of Ni Foam

Mansooreh Jafari ESFAD, Ahmad MOLOODI
Academic Center for Education, Culture and Research (ACECR)
Iran

Abstract. Nowadays, Ni foam has a new application in gas and petroleum, automotive and aerospace industry owing to high strength and corrosion resistance. In this study, the effect of the current in two types (Pulse and Non-Pulse) and two electrolytes bath (Watts and Sulphate) was investigated on the mechanical properties and microstructures of Ni foam produced via electrochemical deposition method. For this reason, the first porous polyurethane as a substrate was conducted via an electroless method and finally placed in an electrolyte bath in different conditions. A compression test was used to evaluate mechanical properties and the optical and stereomicroscope was used to study the microstructure. The results of stress-strain curves showed that using watts electrolyte cause to more strength and ductility. Also, in comparison to the effect of the current density, using pulse current causes the increase of ductility in the same strength. It was while the pattern of growth in the watts bath was dendritic.

1. Introduction

Metal foams are new advanced materials that have specific properties like great energy absorption, high ductility, and good acoustic properties because of the spongy structure. In recent years the use of metal foam increased especially in the automotive, defence and oil and petroleum industries [1-2]. Ni foams are one of the main metallic foams that used mostly as a catalyst and heat exchanger because of high corrosion resistant and strength [3].

The main method that used for production open cell Ni foam is electrochemical deposition method. In this method, the Ni ions were deposited on the initial substrate. Polyurethane foams were generally used as an initial substrate [3]. First, the polyurethane foams are conducted using electroless coating bath and then immersed in the electrolyte bath. The kind of electrolyte and current density are very important in the final properties of produced Ni foams [3-4].

The previous studies show applying pulse deposition techniques cause to extremely compact and durable layer in electrodeposited method [5-7].

This research describes the effect of current (pulse and non-pulse) and kind of electrolyte on the microstructure and mechanical properties of Ni foams produced via electrodeposition method.

2. Experimental Procedure

2×2×2 cm dimension polyurethane foam with 20 ppi and 97% porosity was used as an initial substrate to produce Ni foam via electrochemical deposition method. In this method, polyurethane foam was initially conductive using the electroless bath showed in table 1.

Table1. The electroless bath composition

pH	Temperature	Ammonia	Sodium hypophosphate	Sodium pyrophosphate	Nickel sulfate
9-11	60°C	2ml/L	10g/L	25g/L	45g/L

Two types of electrolyte named watts and nickel sulphate electrolytes were used in order to investigate the effect of electrolyte on the rate of the deposition. The combinations of the electrolytes are listed in tables 2 and 3.

Table 2. The composition of the nickel sulphate's electrolyte

pH	Temperature	Sodium chloride	Sodium sulphate	Magnesium sulphate	Nickel sulphate
4-5.5	25°C	20g/L	75g/L	70g/L	360g/L

Table 3. The composition of the watts electrolyte

pH	Temperature	Nickel chloride	Boric acid	Nickel sulphate
4-5.5	60°C	10g/L	25g/L	45g/L

Two kinds of current density namely non-pulse (direct current) with 1.5 A/dm^2 and pulse current with 1.5A/dm^2 and 0.2 duty cycle ($\frac{t_{off}}{t_{on}} = \frac{1}{5}$) was applied. Ni plate was used as a cathode and the electroless sample was used as an anode in electrolyte baths. The optical and stereomicroscope was used to study the microstructure. The compression test was performed according to standard ISO 13314, using strain rate 1×10^{-3} s^{-1} by universal testing equipment ZWICK Z250.

Four mechanical parameters which are investigated in this study are yield stress (σ_y), plateau stress (σ_p), densification strain (ε_d) and energy absorption (E_a).

3. Results and Discussion

3.1. Mechanical properties

Fig. 1 shows the compressive stress–strain curves for nickel foams produced in different conditions. As shown in Fig. 1, there are three regions that are clearly observed for all specimens except non-pulse sample. In general, typical compressive stress-strain curves of open cell metal foam have three regions: yielding (i.e. plastic collapse) followed by a plateau region and then hardening stage due to metal densification [8-9].

Table 4 shows the average of yield stress (σ_y), plateau stress (σ_p), densification strain (ε_d) and Energy absorption (E_a) of all specimens.

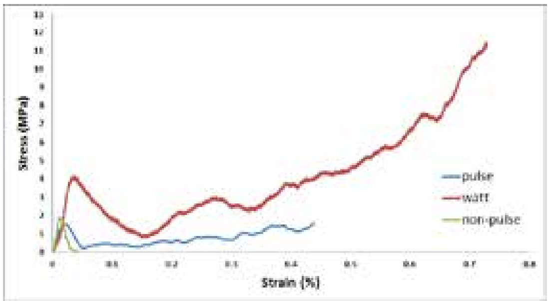

Fig. 1. Compressive stress−strain curves of nickel foams produced in different conditions.

Table 4. Mechanical properties of samples

	Yield stress (σ_y) (MPa)	Plateau stress (σ_p) (MPa)	Densification strain (ε_d) (%)	Energy absorption (E_a) (MJ/mm^2)
Non-pulse	2	-	-	-
Pulse sulphate	1.8	0.6	0.33	0.19
Pulse watts	4.2	1.7	0.41	0.65

The non-pulse specimen is very brittle and the fracture was accurate below 0.1 strains. However, the pulse and watts specimens have the 0.5 and 0.8 fracture strain, respectively. Using pulse current density due to reach the fine grain size [5] and therefore according to Hall-Petch relation, more ductility was achieved. On the other hand, the plating in watts electrolyte was performed at 60°C, which caused passing more current density in low voltage. The low voltage the high ductility in the electroplating deposition method [5-7].

3.2. The rate of electrodepositing

The thickness of cell walls in different specimens was shown in Fig. 2. As can be seen, the thickness of the watts sample is the most. The rates of electrodepositing in non-pulse, pulse and watts samples were about 2µm/h, 2.5µm/h, and 3µm/h, respectively. It means that using the pulse current and watts electrolyte instead of non-pulse and sulphate electrolyte cause to increase the rate of electrodepositing about 1.2 times. The fine grain and high temperature of electrolyte in watts specimen is the reason for this phenomena.

Fig. 2. The microstructure of thickness of cell walls in different specimens; (a) non-pulse, (b) pulse, (c) Watts

3.3. Macrostructures

The macrostructure of specimens produced in different conditions which are made by stereomicroscope was shown in Fig. 3. The dendritic-like growth in watts sample is shown in the figure. The irregular growth in electroplating is due to the non-homogeneous dispersion of current density on the surface. As the watts sample was produced in high temperature, the current density may have more intensity and therefore the Ni ion cannot deposit uniformly on the surface.

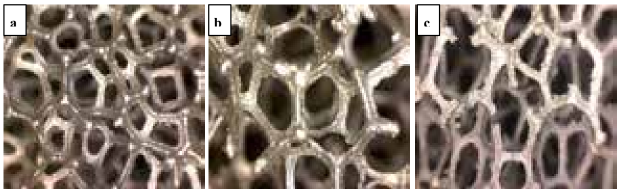

Fig. 3. The macrostructure of specimens (Mag. 40X) (a) non-pulse, (b) pulse and (c) watts

4. Conclusion

In this work, the Ni foam was produced via electrochemical deposition method. The effect of pulse current density and the electrolyte solution on the microstructure and mechanical behavior was investigated. The results can summarize to the following:

1- The use of pulse current cause to more ductility of produced Ni foams.

2- The strength of samples produced in watts electrolyte was higher than the other one.

3- The rate of Ni electrodepositing in watts electrolyte was 1.2 times higher than the sulphate electrolyte and also the pulse current 1.25 times higher than the non-pulse current.

4- The dendritic-like growth was absorbed in watts electrolyte.

References

[1] P. S. Liu, G. F. Chen, "Porous Materials, Processing and Applications". Chapter Three - Application of Porous Metals, (2014) 113-188.

[2] CAO Xiao-qing, WANG Zhi-hua, MA Hong-wei, ZHAO Long-mao, YANG Gui-tong. "Effects of cell size on compressive properties of aluminum foam". Trans Nonferrous Met Soc China, 16(2), (2006) 351−356.

[3] A. Jung, "Electrodeposition of nanocrystalline metals on open cell metal foams: improved mechanical properties", ECS Transactions, 25.41, (2010), 165-172.

[4] A. Jung, M. Weinmannb and H. Natterb, "Electroforming and Electrodeposition on Complex 3D Geometries: Special Requirements and New Methods", (2015).

[5] N. Kanani, "Electroplating: basic principles, processes and practice", Elsevier, 2004.

[6] D. Bari, "Electrodeposition of nickel", Modern Electroplating, 5, (2000), 79-114.

[7] W. Kim, R.Weil, "Pulse plating effects in Nickel electrodeposition", Surface and Coatings Technology, 38 (1989) 289 – 298.

[8] P. Liu, H. Chen, K. Liang, S. Gu, Q. Yu, T. Li and C. Fu, Journal of applied electrochemistry, 2000, vol. 30, 1183-1186

[9] J.-W. Park and C. J. Altstetter, Metallurgical Transactions A, 1987, vol. 18, 43-50.

IMMC 2021

"in Digital Platform"

20th

International Metallurgy and Materials Congress

Uluslararası Metalurji ve Malzeme Kongresi

10-12

June / Haziran 2021

"in Digital Platform"

METEM

www.immc-mtm.com

immc@immc-mtm.com

immc2021

UCTEA CHAMBER OF METALLURGICAL AND MATERIALS ENGINEERS

TMMOB METALURJİ VE MALZEME MÜHENDİSLERİ ODASI